A UNITED STATES DEPARTMENT OF COMMERCE PUBLICATION

NBS SPECIAL PUBLICATION 364

Solid State Chemistry

U.S. DEPARTMENT OF COMMERCE
National Bureau of Standards

Solid State Chemistry

Proceedings of the 5th Materials Research Symposium sponsored by the Institute for Materials Research, National Bureau of Standards, October 18-21, 1971 held at Gaithersburg, Maryland

---

Edited by

Robert S. Roth and Samuel J. Schneider, Jr.

Institute for Materials Research
National Bureau of Standards
Washington, D.C. 20234

U.S. DEPARTMENT OF COMMERCE, Peter G. Peterson, *Secretary*
NATIONAL BUREAU OF STANDARDS, Lawrence M. Kushner, *Acting Director*

Issued July 1972

Library of Congress Catalog Card Number: 72-600031

National Bureau of Standards Special Publication 364

Nat. Bur. Stand. (U.S.), Spec. Publ. 364, 799 pages (July 1972)

Issued July 1972

For sale by the Superintendent of Documents, U.S. Government Printing Office
Washington, D.C. 20402 (Order by SD Catalog No. C 13.10:364). Price $7.50.
Stock Number 0303-1007

GENERAL ABSTRACT

This book presents the proceedings of the 5th Materials Research Symposium on "Solid State Chemistry" held at the National Bureau of Standards, Gaithersburg, Maryland on October 18-21, 1971. The symposium was sponsored by the Institute for Materials Research, NBS. The purpose of the conference was to explore the realm of new inorganic crystalline materials emphasizing crystal chemical and structural aspects, providing a forum for discussion of new research problems and techniques. A total of 56 invited and contributed papers were presented. In addition, the symposium included three unscheduled talks and an open discussion period consisting of four impromptu lectures on very current subjects dealing with nonstoichiometry. The proceedings are divided into four main groupings, I Oxides, II Bromides, Carbides, Silicides, and Related Materials, III Chalcogenides and IV Open Discussion and Nonstoichiometry. An edited version is given on the floor discussion following each paper.

Key Words: Chalcogenides; crystallographic shear; electron optical lattice images; lone pair geometry; nonstoichiometry; oxides; refractory hard metals; Solid State Chemistry.

FOREWORD

Progress of modern technology requires a cooperative and intensive effort on the part of academic, industrial, and government scientists to provide fundamental data on the properties of materials. Effective dissemination of these data are essential for maximum impact on technology and the Institute for Materials Research, through its regularly scheduled symposia, strives to assure the availability of this basic information. These symposia provide an ideal platform for discussion of current research problems and for a free exchange of ideas and thoughts.

The 5th Materials Research Symposium has as its subject, Solid State Chemistry, a seemingly broad and all encompassing field. Research in this area, however, is materials oriented rather than along traditional disciplines, and chemists, ceramists, metallurgists, and crystallographers alike, are intimately involved. The field of Solid State Chemistry primarily is concerned with the structures, chemical properties, reactivities, and general chemical character of solids *per se*, and consequently an overlap of disciplines is required for significant research. Only in the past ten years or so has Solid State Chemistry as an entity come to the forefront. The Institute for Materials Research, through the Inorganic Materials Division, organized the symposium to bring together world wide experts and in doing so, hopes to stimulate further growth in this promising new field.

The National Bureau of Standards is pleased to present the Proceedings of the Symposium on Solid State Chemistry. Publication of this text expresses our appreciation to the participants and to all those who contributed to make this a successful conference.

J. B. WACHTMAN, JR.
Chief, Inorganic Materials Division

J. D. HOFFMAN
Director, Institute for Materials Research

PREFACE

The purpose of this conference was to explore the realm of new inorganic materials, emphasizing crystal-chemical and structural aspects, thus providing a forum for discussion of new research problems and techniques.

The conference was concerned with all aspects of research on the chemical behavior of crystalline inorganic substances in the solid state. Investigations of the reaction mechanisms and products and characterization of the solid state were covered, including crystalline materials produced by chemical reactions between solid-solid and between solid-liquid and solid-gas phases.

The symposium dealt in particular with those "novel" materials which have not yet been well characterized as to crystal chemical and other properties, such as melting points, crystal structure and equilibrium relations. Studies of synthesis and characterizations were highlighted. Although emphasis was on the experimental approach, discussion was included on theoretical aspects as well.

Of primary interest to the conference were fundamental studies on oxides and other chalcogenides as well as borides, carbides, nitrides, silicides and similar materials. Specifically excluded from the symposium subject matter were halides and ductile metals and alloys although mixed materials like oxyhalides were discussed. Papers were primarily on current research although the invited papers also included some reviews.

The proceedings of the conference are presented in an order very similar, though not exactly the same, as was followed for the presentations. The book is divided on the basis of material types into three parts: I Oxides, II Borides, Carbides, Silicides and Related Materials, and III Chalcogenides.

Some very stimulating talks were provided by a group of distinguished foreign participants. The opening invited lecture by Sten Andersson of the Lund Institute of Technology, Sweden on "The Structural Chemistry of Some Solid Trivalent Antimony Compounds" generated considerable discussion throughout the meeting. The paper dealt with lone pair geometry and the crystallographic location in solids of the $5S^2$ electrons, especially those of antimony. Andersson's work was complimented by the contributed paper of J. Galy of CNRS Bordeaux, France, who discussed similar aspects in relation to tellurium +IV oxides.

Throughout the entire symposium reference constantly was made to the late David Wadsley (CSIRO) and his contributions to the science of Solid State Chemistry. The invited papers of Sten Andersson, John Allpress, CSIRO, Australia and J. S. Anderson, Oxford University, England, as well as numerous contributed papers paid tribute to Wadsley by highlighting scientific research which was either a direct or indirect outgrowth of his pioneering work. With the death of David Wadsely, we in solid state chemistry have truly lost a great leader. Nevertheless, Wadsley's work in the field of geometrical structural crystallography is being carried forward by many scientists who were personally motivated by him.

The lattice image electron microscope techniques discussed by J. G. Allpress and by J. S. Anderson and many others at the conference have contributed greatly to our knowledge of the mechanism of structural accommodation of variable valence states in crystalline solids. One of the most exciting new results shown at the conference was the presentation for the first time of high resolution lattice image photographs which seem to actually show the spaces between atoms. These photographs, illustrated in the papers by J. G. Allpress and J. S. Anderson, are truly spectacular. Still another outgrowth of the lattice image technique is the important new concept of "swinging shear planes." (See open Discussion Session, L. Bursill, also frontispiece). The symposium fittingly concluded with an "Open Discussion Section" on "Nonstoichiometry". This session was organized around four impromptu lectures by L. Bursill, University of Western Australia; E. Kostiner, Cornell University; D. J. M. Bevan, Flinders University, South Australia; and L. Eyring, Arizona State University. Several very informative and stimulating discussions were generated and their essence is reproduced in the final section.

The editors of this book would like to thank their co-members of the program committee; Drs. H. S. Bennett, T. D. Coyle, H. P. R. Frederikse, J. L. Torgesen, H. T. Yolken, and J. B. Wachtman, Jr.; R. T. Cook, R. B. Johnson, R. F. Martin, and Mrs. S. R. Torrence of the arrangements and finance committee; and Mrs. S. J. Schneider and Mrs. H. T. Yolken of the ladies' program committee. Additional thanks go to the session chairmen: W. L. Roth, General Electric; B. Hyde, University of Western Australia; R. Ward, University of Connecticut; B. Post, Polytechnical Institute of Brooklyn; D. J. M. Bevan, Flinders University, South Australia; H. Young, Princeton University; and F. Holtzberg, IBM, and all of the speakers and participants of the symposium who together made the whole meeting a very worthwhile occasion for all concerned. Special thanks are due to Mrs. Mary Clevinger who handled the organization of this volume including retyping of the manuscripts and reproduction of the figures and tables, and to her assistants.

R. S. Roth

S. J. Schneider

Drs. Les Bursill and Bruce Hyde, Australia (foreground) authors of the concept of "swinging shear planes" discuss this revolutionary theory with Drs. Jean Galy, France, and Sten Andersson, Sweden (background). In the improvised model, golf balls represent Ti^{+4} ions, ping-pong balls are Cr^{+3} ions and aluminum cans are O^{-2} ions.

WELCOME

Lewis M. Branscomb
Director, National Bureau of Standards

It is my pleasure to welcome you this morning to the National Bureau of Standards for the 5th Materials Research Symposium. We are pleased to join many of our colleagues in universities and industry in a symposium dealing with an area of research of considerable interest to NBS that gets at a cross section of technical problems of unconventional dimension. Also gratifying is the attendance of a substantial number of very distinguished scientists from laboratories in other countries. I think the participation of our guests from overseas will add much to the distinction and to the pleasure of our meeting together. We are personally grateful to those who have traveled long distances to be with us.

The title of the conference, "Solid State Chemistry," and its subtitle, "Novel High Temperature Materials," suggest the sweep of the subject matter from very basic questions to a more practical interest in some of the new materials technologies on which future industrial progress may depend. As I have already noted, we have a very productive blend of academic, industrial, and government people. Perhaps that's not worthy to comment on because it is no novelty to most of you to have your professional interests expressed in forms that involve such a mixture. However, I would like to make a quick comment on this subject. I feel that, in this country anyway, there is a very widespread and publicly expressed sense of lack of confidence in the country's basic research enterprise and its value to the society. There is also a lack of understanding and perhaps again, a lack of confidence in the technical strength of our industrial life. You now see both of these views expressed simultaneously, particularly in the latter case, in connection with the balance of payments and other economic questions. Many people propose various cures for these economic ills which either are of a type designed to say, "all our basic research hasn't been very useful; let's re-channel the funds and do applied research and development," or on the other hand, they may take the attitude that industry hasn't been very imaginative in its research, and that the Government should somehow pay for or do the research that the industries should have been doing all along.

We at the National Bureau of Standards find ourselves often in a minority in these policy arguments. We insist that there is a very, very important common ground of scientific research that has the characteristic of being very sophisticated and intellectually compelling; work that can challenge the best of our bright young students in the universities and at the same time is of direct importance to the industrial scene. Industrial organizations can best take advantage of the materials potential that they see without the necessity of either graduate students or Government scientists engaging in new materials development, and work of that character which is not appropriate to the academic or the Government scene.

In my view, the emphasis in this conference on the fundamental questions of the characterization of the properties and the behavior of high temperature materials of broad general interest is a splendid example of that common ground; one of great scientific interest and one of important utility to those who wish to exploit this knowledge. I share with you my thought that there is encouragement for this kind of work, not just here at NBS, but in both industries and universities. On this basis rests the true proper meeting ground of basic and applied science and technology. Thank you very much. I hope you have a very good meeting.

WELCOME

E. Horowitz
Deputy Director, Institute for Materials Research

The 5th Materials Research Symposium sponsored by the NBS Institute for Materials Research will deal with the chemical behavior of crystalline inorganic substances in the solid state. As in the past, the Materials Research Symposium is intended to provide a platform for scientific discussion and exchange of ideas. This time it will be related to new research, new techniques in solid state chemistry, particularly subjects related to novel high temperature compounds. Dr. Robert S. Roth, the general chairman, and his symposium committee have worked very hard to put together a very interesting program. We are especially pleased to note that participants from fourteen countries are in attendance today, and that at the first morning's session alone, there will be a number of distinguished speakers from abroad. I was interested in looking over the program to note several words that appeared in the text which rang very close to my own feelings--words like synthesis, reaction mechanisms, chemical properties, characterization and new techniques. I promised that I would not be long; I would like, however, to give a brief summary of activities for the Institute for Materials Research (below). Important here are standard reference materials, well-characterized pure materials that the NBS provides to industry and the academic community to calibrate instruments and maintain quality control. Closer to your own interests are research materials which involve both the preparation and purification of special materials. Other important activities include the measurement of properties of materials, compilation of physical and chemical data, the development of improved methods of measurement dealing both with instrumentation and procedures, the analysis and characterization of materials, and finally the composition and structure of inorganic materials.

To all our guests from overseas and the United States, I want to welcome you to the Bureau of Standards and to the Institute for Materials Research.

Thank you.

INSTITUTE FOR MATERIALS RESEARCH

Major Areas of Activity

° STANDARD REFERENCE MATERIALS

° RESEARCH MATERIALS

- Preparation
- Purification

° MEASUREMENT OF PROPERTIES OF MATERIALS

- Physical Data
- Chemical Data

° DEVELOPMENT OF IMPROVED METHODS OF MEASUREMENT

- Instrumentation
- Procedures

° ANALYSIS AND CHARACTERIZATION OF MATERIALS

- Composition
- Structure

° TECHNICAL AND ADVISORY SERVICES

- Other Government Agencies
- State Governments
- Industry
- Standards Bodies

CONTENTS

I. OXIDES

465-504 O - 72 - 2

National Bureau of Standards Special Publication 364, Solid State Chemistry, Proceedings of 5th Materials Research Symposium, issued July 1972.

THE STEREOCHEMISTRY OF THE INERT PAIR IN SOME SOLID OXIDES OR OXIDE FLUORIDES OF Sb^{3+}, Bi^{3+} AND Pb^{2+}

Sten Andersson and Anders Åström

Division of Inorganic Chemistry 2, Chemical Centre, Lund
Box 540, S-220 07, Lund 7, Sweden

Geometrically it is shown that the inert electron pair in some solid oxides or oxide fluorides requires space comparable with that of an anion. If the lone pairs are located on certain sites in a lattice, nets consisting of lone pairs and anions are obtained which correspond to hexagonal, or cubic closest packing of atoms. Other more complex nets, comparable with those in alloy structures, are also found. The lone pairs are thus found in positions which are normally occupied by anions. Using this observation, direct structural relationships with the transition metal compounds can be shown to exist.

Key words: Antimony oxides; antimony oxide fluorides; bismuth oxide fluorides; lead oxides; lone pairs.

1. INTRODUCTION

In the type of compounds to be discussed here, there are three or four anions bonded to the cation, all to one side. They can be arranged in such a way that the lone pair in the equatorial plane completes a trigonal bi-pyramidal configuration. In another way the lone pair is at the apex of a tetragonal pyramid. Finally, in the third way, the lone pair completes a tetrahedron. These arrangements of electron pairs have been predicted by Gillespie and Nyholm [10][1]. The distortions of the various polyhedra that occur are explained by the valence shell electron pair repulsion theory of Gillespie and Nyholm. A stereochemically active lone pair is larger than a bonding pair and takes up more room on the surface of an atom. The bonding pairs are therefore squeezed together and the angles between them greatly reduced.

Crystallographic constants and references for the various compounds to be discussed here are given in table 1.

In order to denote that a compound A_xB_y contains stereochemically active lone pairs, we will often add E_z to the chemical formula, $A_xB_yE_z$, where E stands for lone pair, and z for the number of lone pairs per formula unit.

2. VOLUME OF LONE PAIRS

In table 2 the volumes in $Å^3$ per anion are compared for SbOF, β-Sb_2O_4 and some transition metal oxides. For TiO_2 (rutile), which has an approximately hexagonally close packed arrangement of oxygens, the volume is 15.6 $Å^3$, which is a typical value. For both $BaTiO_3$ and $BaNiO_3$ the oxygen volume is rather high, and comparable with that of the antimony compounds. However, it is well known that in both of these compounds, the barium atom enters the close packed layers of oxygens, formally substituting for an oxygen, giving the layers the composition BaO_3. Thus, if barium is treated as an anion in the calculations, the volume per close packed atom is greatly reduced (column II in table 2), and becomes comparable with the oxygen volume for TiO_2. Regarded in this way, $BaTiO_3$ is a cubic close packed structure,

[1]Figures in brackets indicate the literature references at the end of this paper.

Table 1

Compounds	Unit Cell	*a*	*b*	*c*	β	Space group	Reference
Yellow PbO(E)	orthorhombic	5.489	4.775	5.891		*Pbma*	[1]
Red PbO(E)	tetragonal	3.975		5.023		*P4/nmm*	[2]
BiOF(E)	"	3.7469		6.226		*P4/nmm*	[3]
Pb_3O_4 (E_2)	"	8.80		6.56		*P4/mbc*	[4]
L-SbOF(E)	orthorhombic	8.873	4.099	5.483		*Pnma*	[5]
M-SbOF(E)	"	11.618	5.616	12.281		*Pbca*	[6]
β-Sb_2O_4(E)	monoclinic	12.060	4.834	5.383	104.58	C 2/c	[7]
B-Nb_2O_5	"	12.73	4.88	5.56	105.1	C 2/c*	[8]
α-PbO_2	orthorhombic	4.947	5.951	5.497		*Pbcn*	[9]

*Transformed into standard crystallographic setting.

Table 2

	I(Å^3)	II(Å^3)	anion(+E) packing
L-SbOF(E)	24.9	16.6	Complex
M-SbOF(E)	25.1	16.7	Complex
β-Sb_2O_4(E)	19.0	15.2	h.c.p.
SbF_3(E)	22.3	16.8	Complex
$BaNiO_3$	21.8	16.3	h.c.p.
$BaTiO_3$	21.4	16.0	c.c.p.
TiO_2 (rutile)	15.6	15.6	h.c.p.
Yellow PbO(E)	38.8	19.4	h.c.p.
α-PbO_2	20.2	20.2	h.c.p.

In Column I volume in Å^3 per anion is given; in Column II lone paris or barium atoms are included formally as anions in the corresponding calculations.

and $BaNiO_3$ hexagonally close packed. From table 2 we see that if the lone pairs are included in the calculations as anions, we obtain volumes for the Sb^{3+} compounds which are comparable with those of TiO_2, $BaTiO_3$ and $BaNiO_3$.

It is important to note that the oxygen and the lone pairs in yellow PbO occupy almost the same volume as the oxygens in α-PbO_2, as shown in table 2. The two unit cells are almost identical (if the axes in table 1 are interchanged) and we will point out below that a very close structural relationship between the two oxides exists. The same is true for β-Sb_2O_4(E) and B-Nb_2O_5; the two structures are almost identical, as also will be discussed below.

3. DISCUSSION OF STRUCTURES

We will now show with a number of structures that *the lone pair is stereochemically active as an anion of the size of* F^- *or* O^{2-} *and also that it takes a position in a structure equivalent to such anions.*

3.1. YELLOW PbO

In figure 1 the structure of yellow PbO is projected along the *b*-axis. The structure consists of PbO_4 polyhedra, joined by edges and corners along *b*, and by corners in the *ac* plane. The oxygen positions within each separate PbO sheet are in almost ideal hexagonal closest packing as demonstrated in the left part of figure 2. These sheets are far apart, and if the structure is imagined to be compressed $\frac{1}{2}$ *c*, (fig. 2, right part) an oxygen net is obtained which is hexagonally close packed in three dimensions. (Such an AB structure, containing cations with five coordination is not known, but only small shifts of the lead atoms are required to move them into tetrahedral positions, and then the wurtzite structure is obtained.) Alternatively, there is formally space enough between the sheets for an extra identical sheet. If this is inserted the structure becomes hexagonally close packed. If the lone pairs are placed in these positions, they complete a trigonal bipyramidal polyhedron around Pb^{2+}, as required by the Gillespie-Nyholm theory (Cf fig. 3). With this position of a lone pair, the distance between its center and the Pb^{2+} cation becomes approximately one Å. In the structures described in this article, this distance is used when the lone pairs are located in order to construct OE (oxygen-lone pair) or OFE (oxygen-fluorine-lone pair) nets. The very regular hexagonally close packed OE net for yellow PbO is given in figure 4.

The structure of yellow PbO(E) should thus be compared with AB_2 structures, and only small shifts of the Pb^{2+} ions are required to obtain a structure of the α-PbO_2 type. We pointed out above that the volumes of the unit cells of α-PbO_2 and PbO(E) (table 1) are very close in size, and it is tempting to carry out the mental experiment of oxidizing yellow PbO directly to α-PbO_2 or β-PbO_2, under pressure, with the mechanism that oxygen enters the structure of PbO, captures the lone pairs and takes their positions as O^{2-}. Simultaneously, Pb^{2+} is oxidized to Pb^{4+}, and is also pushed into octahedral position by the oxygen. The new structure can then be of rutile or α-PbO_2 type. A very simple mechanism for the transformation α-$PbO_2 \rightleftarrows \beta$-$PbO_2$ has been given [11]. The main part of the structure stays intact. The reverse of this mechanism might be true for the thermal decomposition of PbO_2 to yellow PbO, which occurs at elevated temperatures.

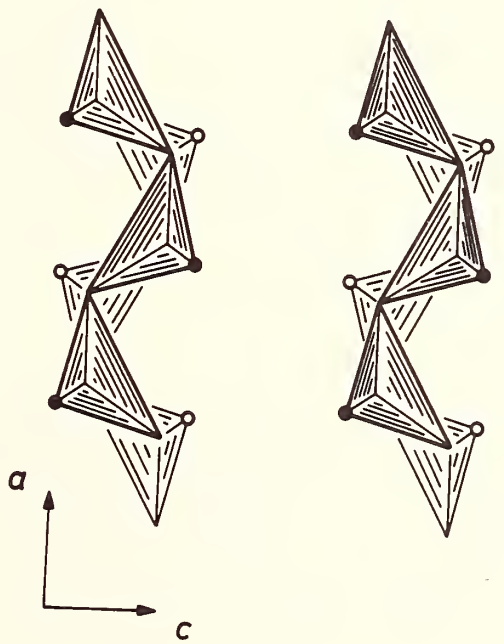

Fig. 1. The structure of yellow PbO. The heavier and lighter polyhedra are b/2 apart, as are the Pb-atoms, marked with filled and open circles. All atoms are on y = 0 or $\frac{1}{2}$.

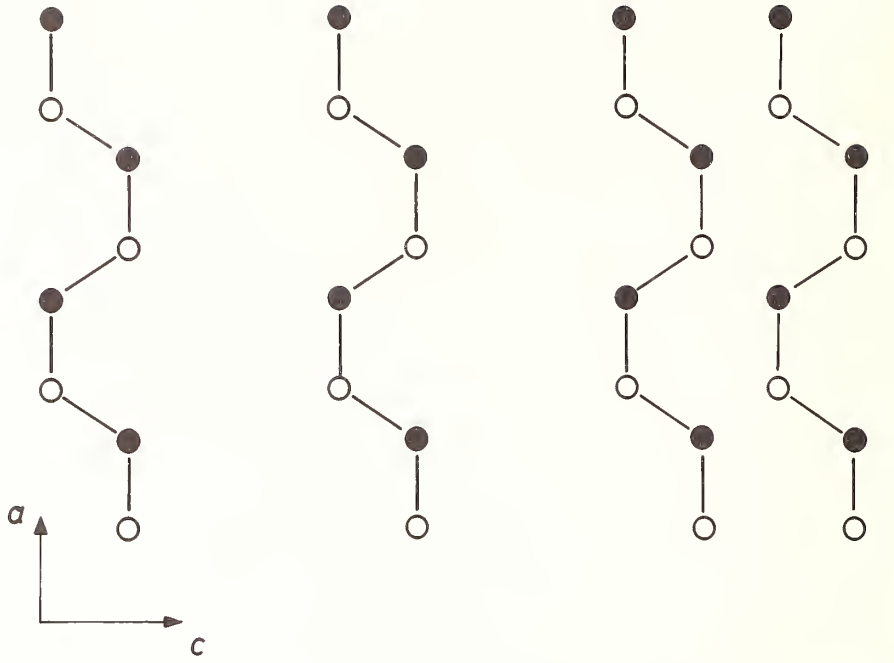

Fig. 2. Oxygen positions in yellow PbO. The structure is compressed by c/2 in the right part of the figure.

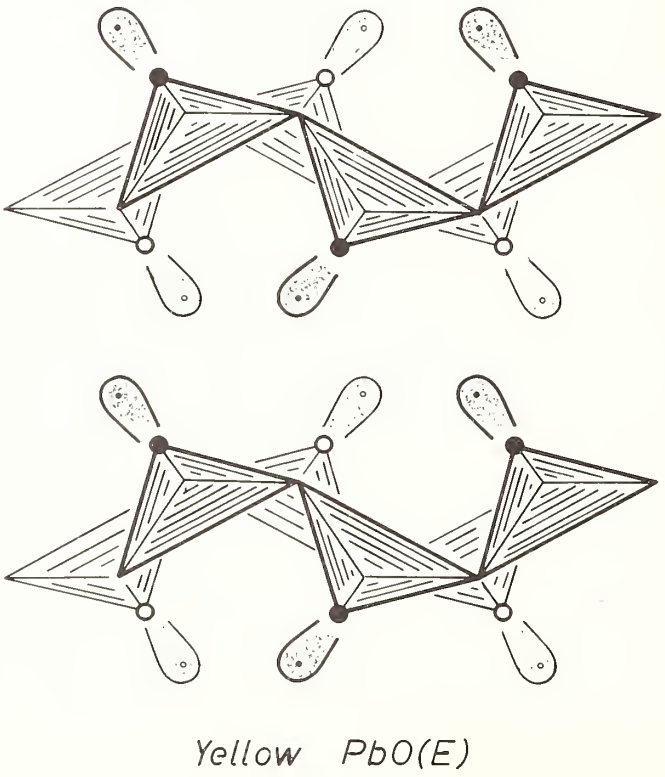

Fig. 3. Yellow PbO with the lone pairs located. Heavier and lighter pairs on y = 0 or $\frac{1}{2}$.

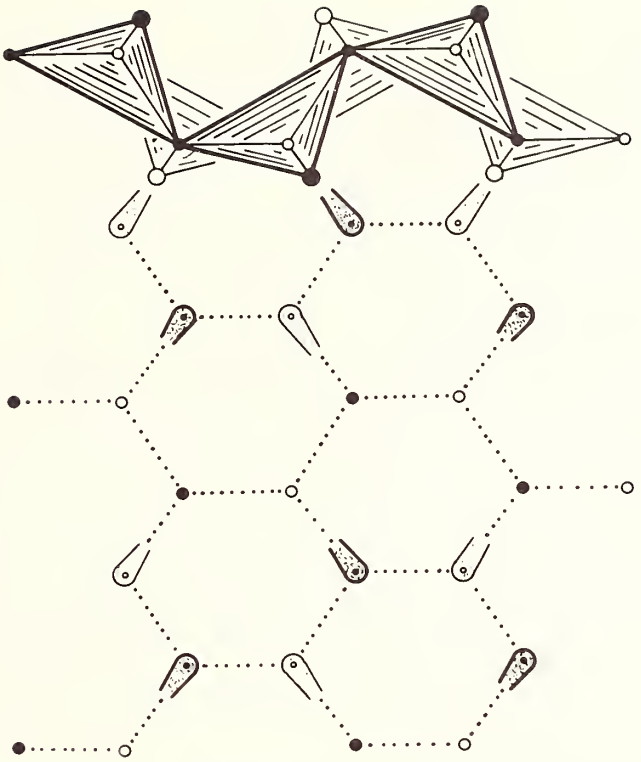

Fig. 4. The hexagonally close packed OE net in yellow PbO.

3.2. RED PbO

In figure 5 the red, tetragonal form of PbO is projected along an *a*-axis. Each square pyramid has a lone pair at the apex, and in this way the oxygens and the lone pairs form a somewhat distorted cubic close packed arrangement. Again it is easy to see a path for the Pb^{2+} cations to move into the octahedra formed by the OE net. The AB_2 structure formed is simple and esthetically attractive, but no compound has been reported to have this particular structure.

3.3. β-Sb_2O_4

The structure of β-Sb_2O_4(E), given in projection along *b* in figure 6, is another example in which oxygens and lone pairs form a hexagonally close packed net. This kind of projection is useful for describing many common structure types, and especially for predicting new ones; it has been described in more detail in reference 12. Octahedra in the structure of β-Sb_2O_4, containing Sb^{5+}, form sheets by sharing corners in the *bc* plane. SbO_4 polyhedra, of the same kind as in yellow PbO, form chains in the *c*-direction by edge-sharing. The structure is then built up by corner-sharing of the sheets and the SbO_4 chains.

In table 1 it is shown that the B-Nb_2O_5 and β-Sb_2O_4 structures have the same space group, and very nearly the same unit cell dimensions. The structures are indeed very similar (fig. 6 a and *b*); the lone pairs in β-Sb_2O_4 are in the same positions as certain oxygens in B-Nb_2O_5, the other oxygens and SB^{5+} and half the Nb^{5+} are in the same positions in the two structures. The only difference is in the Sb^{3+} positions. However, if they are shifted into neighboring octahedral sites, they do correspond to the rest of the Nb^{5+} in the B-Nb_2O_5 structure. B-Nb_2O_5 is the high pressure, high temperature form of all the known Nb_2O_5 modifications [13]. In its structure the oxygens are hexagonally close packed, and it is easily related to the common structural types of rutile and PdF_3 [12].

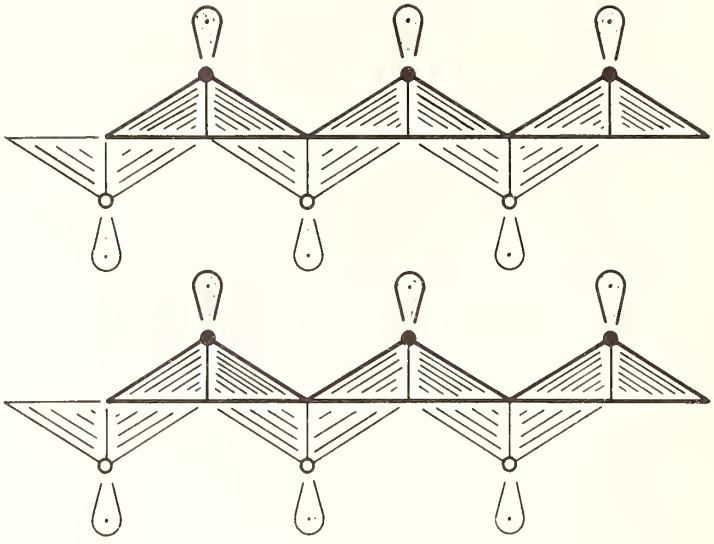

Fig. 5. Tetragonal PbO. The heavier and lighter polyhedra and lone pairs are b/2 apart, as are the Pb-atoms, marked with filled and open circles. All atoms and lone pairs on y = 0 or $\frac{1}{2}$.

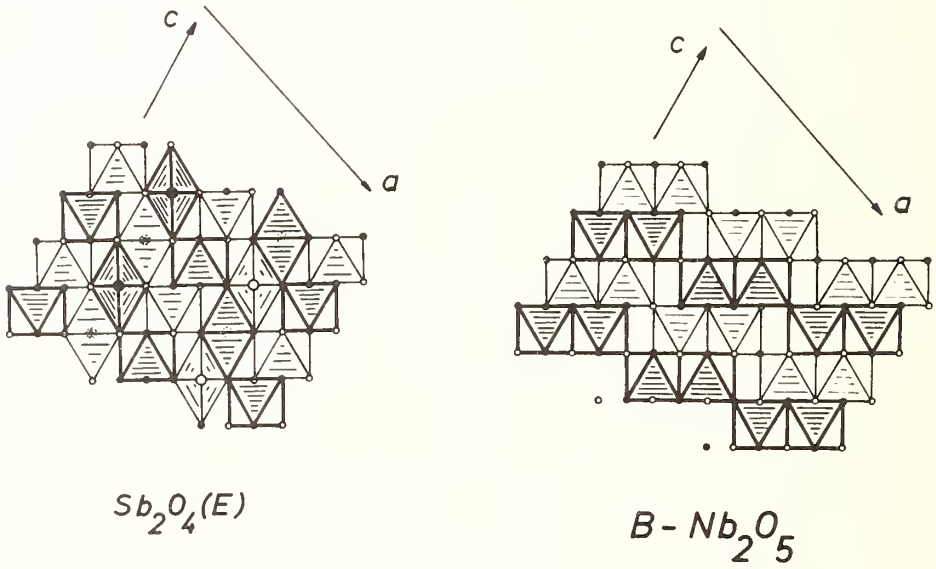

Fig. 6 a. The structure of β-Sb_2O_4 somewhat idealized. The rhombohedral shaped figures are the SbO_4 polyhedra in projection with lone pairs pointing upwards (filled or open circles) or downwards (dotted circles). The Sb^{3+} ions are above or below the lone pairs. Small circles are oxygens, larger circles are lone pairs. The SbO_4 polyhedra form chains which are joined to the octahedral Sb^{5+} sheets by corner sharing.

b. The structure of B-Nb_2O_5. Note that the oxygens and half the Nb atoms in B-Nb_2O_5 are in the same positions as the oxygens, Sb^{5+} and lone pairs in β-Sb_2O_4.

3.4. TETRAGONAL BiOF

The tetragonal BiOF is projected along an *a*-axis in figure 7. In the BiO_4 polyhedra, the lone pairs complete square pyramids. The same metal oxygen lone pair layer is present in this structure as in the structure of red PbO. But in BiOF these layers are pushed further apart by the entrance of fluorine ions. The arrangement of anions and lone pairs are no longer close packed. In figure 8 the OFE net is drawn, and the two different polyhedra that can be found are line-shadowed. One is an octahedron, while the other is a bi-capped cube with 10 vertices. This net is very similar to that of Si atoms in $MoSi_2$ or the net of Aℓ atoms in the alloy $OsAℓ_2$ [14,15]. Again the lone pair is equivalent to an anion in its stereochemical activity.

3.5. TETRAGONAL Pb_3O_4

The tetragonal structure of $Pb_3O_4(E_2)$ is shown in figure 9, projected along the c-axis. As seen in figure 9, the net formed by the oxygens is the same as that formed by the Al atoms in the $CuAl_2$ structure type. The Pb^{2+} ions are coordinated by three oxygens, and the lone pairs complete a tetrahedron. The oxygens in Pb_3O_4 form square antiprisms, which by sharing faces form tunnels along *c*. Inside these tunnels the Pb^{2+} ions are situated, and the lone pairs approach the Cu positions in $CuAl_2$. Due to the positions of the Pb^{2+} ions in Pb_3O_4, its *c*-axis is doubled compared with the *c*-axis of $CuAl_2$. The square antiprisms are joined by edges in the *ab* plane so that octahedral positions for Pb^{4+} ions are created, and these octahedra share edges in the *c*-direction. Due to the arrangements of the lone pairs, the square antiprisms are rather flat compared to those in $CuAℓ_2$.

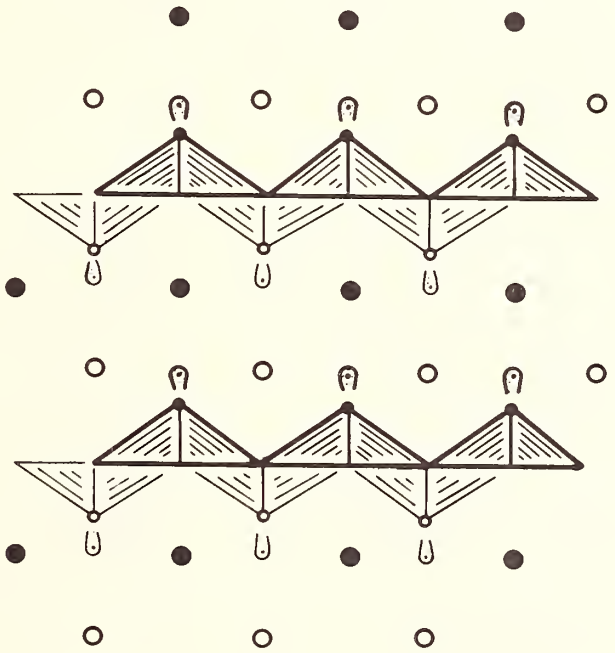

Fig. 7. The structure of BiOF, projected after an *a*-axis. All atoms on y = 0 or $\frac{1}{2}$.

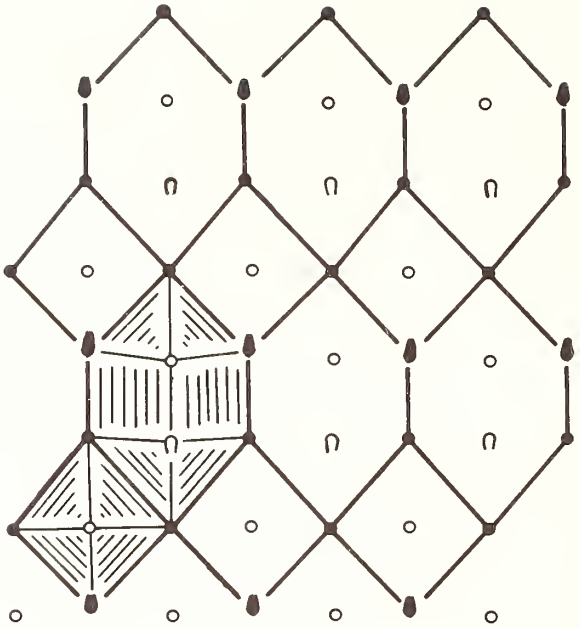

Fig. 8. The OFE net of BiOF, the same projection as in figure 7.

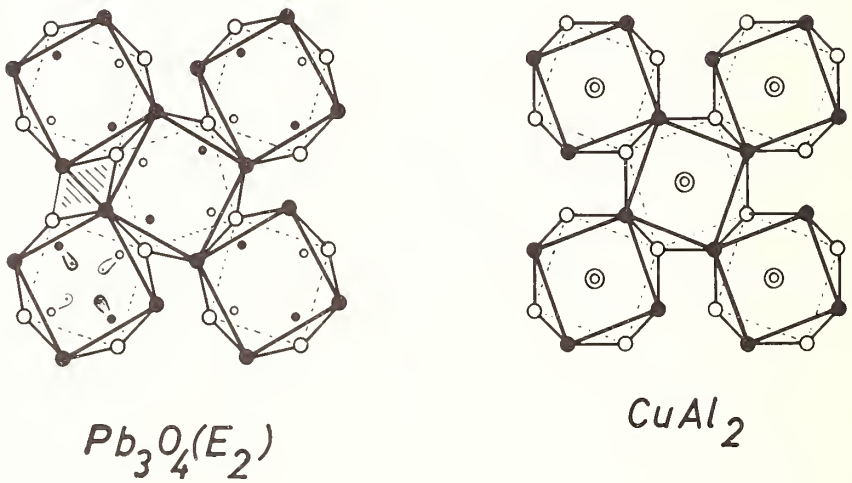

Fig. 9. The structures of Pb_3O_4 and $CuAl_2$, projected along the *c*-axis. In Pb_3O_4 the oxygens (large filled and open circles) are on z = 0, $\frac{1}{4}$, $\frac{1}{2}$, and $\frac{3}{4}$, lead atoms (small circles) are on 0 or $\frac{1}{2}$. The line-shadowed polyhedron represents two octahedra, superimposed in this projection, containing Pb^{4+}. In $CuAl_2$, open and filled circles are Aℓ atoms on 0 or $\frac{1}{2}$, double circles are two Cu atoms superimposed on $\frac{1}{4}$ and $\frac{3}{4}$.

3.6. L-SbOF AND M-SbOF

Different forms of SbOF were made by heating mixtures of SbF_3 and Sb_2O_3 in the molar ratio 1:1 in sealed gold or platinum capsules, at temperatures in the range 150-450 °C [5]. The structures of two of them, L-SbOF and M-SbOF, have been determined [5,6]. L-SbOF, projected in figure 10 down the *b*-axis, consists of SbO_4 polyhedra, with the lone pairs completing trigonal bypyramids. Such octahedra edge-share to form endless chains in the *b*-direction. If alternate chains are translated, $\frac{1}{2}$ c, and the structure is allowed to shrink along *a* so that the chains can join up by edge sharing, the structure of yellow PbO is formed.

In figure 11 the packing of two identical OFE nets of L-SbOF is given, at z=0 and z = $\frac{1}{2}$. The lone pairs are geometrically equivalent to anions; the packing is complex like in alloys, and the net, described in figure 11 is also the same as that of the Rh-atoms in one section of the crystal structure of Rh_5Ge_3 [16].

The structure of M-SbOF is more difficult to describe. A polyhedral drawing in projection down the b-axis is shown in figure 12. SbO_4 polyhedra of the same kind as in L-SbOF join by edges and corners to form a layer structure. Anions and lone pairs can be approximated to be b/2 apart, and in figure 13 it is shown that the packing again is complex. The pentagonal antiprism is often found in complex alloy structures. The lone pairs and anions in M-SbOF are arranged so that they can be described as forming the 10 vertices of a somewhat distorted antiprism shown in figure 13. In the right part of the figure a regular antiprism is drawn, for comparison.

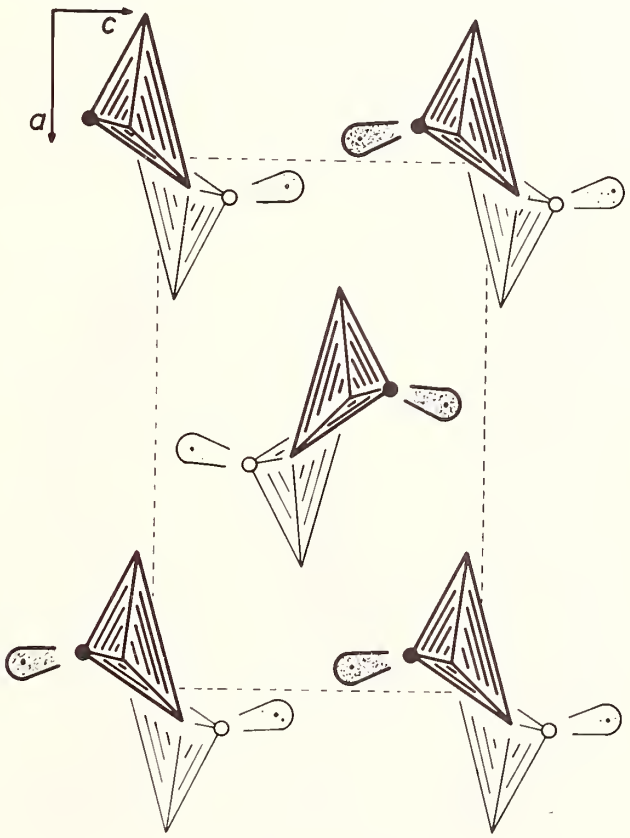

Fig. 10. The structure of L-SbOF projected down the *b*-axis. The heavier and lighter polyhedra and lone pairs are b/2 apart, as are the Sb-atoms, marked with filled and open circles. All atoms are on y = 0 or $\frac{1}{2}$.

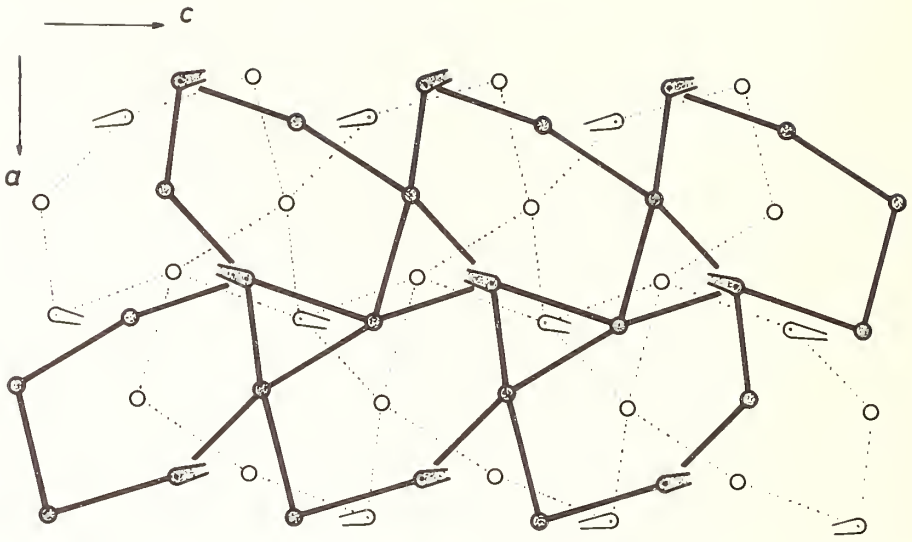

Fig. 11. The OFE net of L-SbOF, Dotted lines connect atoms and lone pairs on y = 0, heavy lines connect atoms and lone pairs on y = $\frac{1}{2}$.

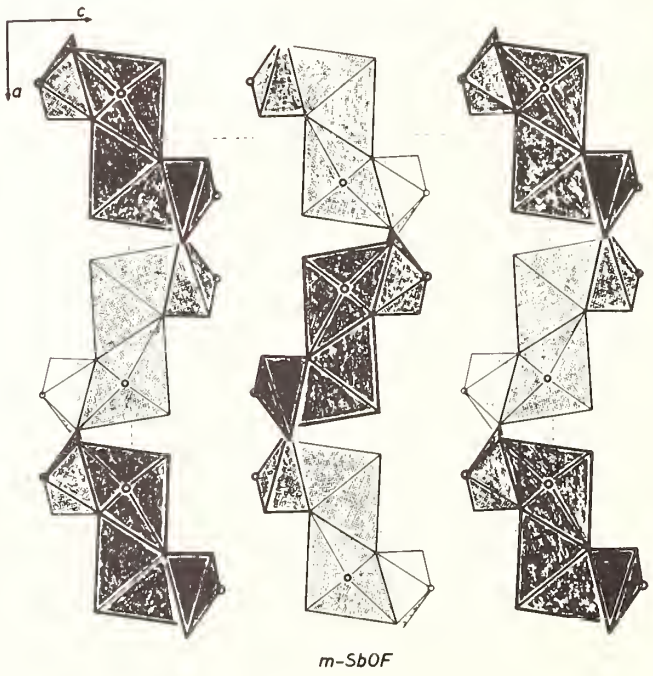

Fig. 12. The structure of M-SbOF. SbO_4 polyhedra of the same kind as in L-SbOF join by corner- and edge-sharing to form SbOF layers.

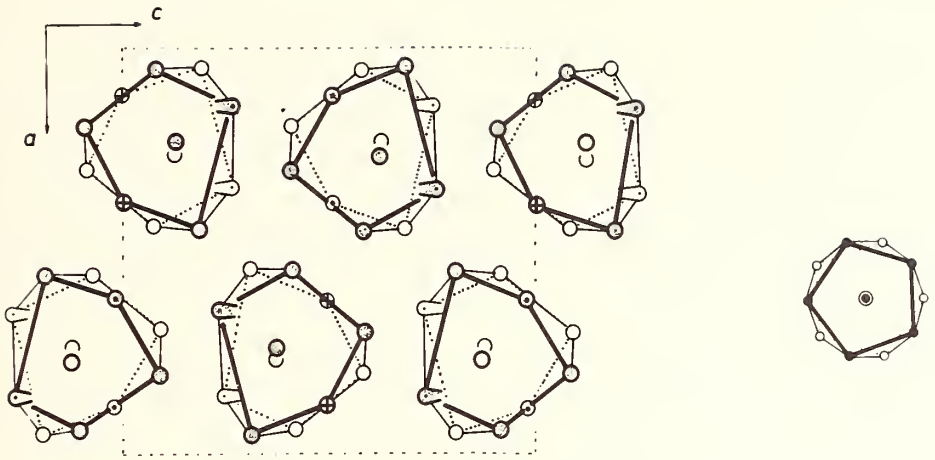

Fig. 13. Distorted antiprisms of anions and lone pairs found in M-SbOF. Heavily or lightly drawn anions and lone pairs are approximately b/2 apart. The tail-shaped figures are lone pairs, parallel to the plane of the paper. Circles with crosses inside are lone pairs pointing downwards, circles with dots inside are lone pairs pointing upwards. The remaining circles are oxygen or fluorine. A regular antiprism is drawn in the right part of the figure.

4. ACKNOWLEDGMENTS

We would like to thank Professor Bengt Aurivillius for valuable discussions. This investigation forms a part of a research program sponsored by the Swedish Natural Science Research Council.

5. REFERENCES

[1] Kay, M.J., Acta Cryst. 14, 80 (1961).
[2] Leciejewicz, J., Acta Cryst. 14, 1304 (1961).
[3] Aurivillius, B., Acta Chem. Scand. 18, 1823 (1964).
[4] Fayek, M.K., and Leciejewicz, J., A. Anorg. Allgem. Chem. 336, 104 (1965).
[5] Åström, A., and Andersson, S., Acta Chem. Scand. 25, 1519 (1971).
[6] Åström, A., to be published.
[7] Skapski, A.C., and Rogers, D., Chem. Communication 23, 611 (1965).
[8] Laves, F., Petter, W., and Wulf, H., Naturwissenschaft, 51, 633 (1964).
[9] Zaslavskii, A.I., and Tolkachev, S.S., Zh. Fiz. Khim., 26, 743 (1952).
[10] Gillespie, R.J., and Nyholm, R.S., Quart. Rev. 11, 339 (1957).
[11] Andersson, S., and Galy, J., Bull. Soc. Chim. France 1065 (1969).
[12] Andersson, S., and Galy, J., J. of Solid State Chemistry 1, 576 (1970).
[13] Wadsley, A.D., and Andersson, S., in *Perspectives in Structural Chemistry*, Vol. 1, John Wiley and Sons, Inc., New York, 1970.
[14] Edshammar, L-E., *X-Ray Studies on Binary Alloys of Aluminium with Platinum Metals*. Dissertation, SUPERB-tryck, Stockholm, 1969.
[15] Edshammar, L-E., Acta Chem. Scand. 19, 871 (1965).
[16] Bhan, S., and Schubert, K., Z. Metallk 51, 327 (1960).

DISCUSSION

J. B. Goodenough: Some years ago, I think you are familiar with the work, Sten, we at Lincoln Laboratory were considering the defect-pyrochlore structures containing lead. It appeared that we transferred the lone-pair electrons into an anion vacancy in that particular structure. So my question is, have you tried, or is it feasible to do, some electron-density distribution studies to see whether these electrons, which you describe as electron lone pairs, are still attached to the parent antimony 3+ ion? Or is it possible that they have really been contributed, or donated, from the antimony to a site that has a positive potential as a result of the crystalline fields? Have they really been donated to the empty space in the structure?

S. Andersson: You have to pick a light element for such studies. I think with arsenic, for example, arsenic 3+, it would be possible with very accurate data. However, what you need is to derive new form factors, non-spherical, just the sort that Barrie Dawson has developed in Melbourne. That has some very advanced mathematics involved, but it should be possible. It is not enough just to make a difference Fourier synthesis, you have to go back to the origin of scattering because you have a non-spherical arrangement.

Note added in proof: There is no donation from the antimony of the lone pair. The distance, according to this geometry, between the lone pair and the metal nucleus is always, in these structures, between 1.0 - 1.20 Å.

E. Banks: The experimental problem here might be solvable by a combination of x-ray and neutron diffraction techniques because one of your difficulties is that the center of electron density is different from the nuclear center. Phil Coppens has done that at Brookhaven. He is continuing at Buffalo on some organic compounds, and he does get, with difference maps, evidence of bonding electron density and this is the sort of thing that we are looking for.

J. M. Honig: I was wondering, in view of the fact that you have these lone electron pairs so close together, whether this endows these compounds with any unusual mechanical and electrical properties? Is this known?

S. Andersson: This is a very interesting point. I think it should involve some interesting properties, but as far as I know nothing has been done.

F. Jellinek: This is just a remark to the last question. There have been several examples of ferroelectricity in antimony 3+ compounds, SbIS, and related compounds, Sb_2S_3, and so on. Probably this ferroelectricity is related to the non-spherical character of the antimony 3+ ion in these compounds.

National Bureau of Standards Special Publication 364, Solid State Chemistry, Proceedings of 5th Materials Research Symposium, issued July 1972.

THE SINGLE CRYSTAL X-RAY STRUCTURE DETERMINATION OF SOME ALKALI METAL MOLYBDATES AND NIOBATES

B. M. Gatehouse, D. J. Lloyd and B. K. Miskin
Chemistry Department
Monash University
Clayton, Victoria, Australia 3168

Crystal structures have been determined for the compounds "$Rb_3Nb_{54}O_{146}$," "$RbNb_3O_9$" $Na_xMo_6O_{17}$, $K_xMo_6O_{17}$ (x approximately 0.8 and 1.0 respectively) and $Li_2Mo_4O_{13}$ (low temperature form). Preliminary results are communicated for the compounds $Li_xMo_6O_{17}$ ($x \leq 1.0$) and $Li_2Mo_4O_{13}$ (high temperature form).

For "$Rb_3Nb_{54}O_{146}$" an unusual structure occurs where niobium-oxygen octahedra are grouped forming four, five, six and seven-sided tunnels through the structure, with the hexagonal tunnels partly filled with rubidium atoms. The unbalanced electrostatic charge is discussed in terms of the possible presence of fluoride, or fractional occupancy of oxygen sites.

Unusual features are discussed for the $M^I_xMo_6O_{17}$ structures (M^I = Li, Na, K) in terms of the presence or absence of Mo-O_6 octahedra or Mo-O_4 tetrahedra in the structure. It appears that the lithium analogue will have a somewhat different structure in spite of similarity in unit cell dimensions.

The ordering of lithium-oxygen octahedra in planes in $Li_2Mo_4O_{13}$ is pointed out in an accurate structure determination of this compound, which is basically a cubic close-packed oxygen lattice with Li and Mo occupying octahedral sites. Systematically absent oxygen atoms result in the presence of pairs of strings of cube octahedral holes in the structure.

Key words: Alkali metal; bronze; heptagonal holes; hexagonal tungsten bronze; lattice image; molybdate; molybdenum; niobate; niobium; oxide; single crystal; tetramolybdate; x-ray structure determination.

This paper sets out some current research on the structures of a number of compounds, and for convenience these will be described in three parts, the formulae of the compounds discussed will be used as headings for each part.

Thus 1. "$Rb_3Nb_{54}O_{146}$" and "$RbNb_3O_9$"
2. $Li_xMo_6O_{17}$, $Na_xMo_6O_{17}$, and $K_xMo_6O_{17}$
3. $Li_2Mo_4O_{13}$ (low temperature form).

1. "$Rb_3Nb_{54}O_{146}$" and "$RbNb_3O_9$"

1.1. INTRODUCTION

A study by Reisman and Holtzberg [1][1] in 1960 of equilibria in the system Rb_2O:Nb_2O_5 indicated the existence of eight intermediate compounds; the compositions of these are listed in table 1 together with the results of a recent examination [2] of some of these, in which unit cell dimensions and crystal systems were given. Samples obtained from Reisman and

[1]Figures in brackets indicate the literature references at the end of this paper.

Table 1

Compositions (Expressed as Ratio $Rb_2O:Nb_2O_5$) and Unit Cell Dimensions Previously Reported

Reference	[1]	[2]	[2]				
			a	b	c	β	Crystal System
	2:15	1:13	20.17	3.83	20.75	123.5°	monoclinic
	1:4	1:4	26.55		3.85		tetragonal
	4:11	1:3	7.45		7.66		hexagonal
	1:2	6:11	12.95	7.48	14.92	106.4°	monoclinic
	2:3	4:7	6.42	7.68	38.55		orthorhombic
	1:1	not examined, as highly hygroscopic materials					
	4:3						
	4:1						

Holtzberg by the late Dr. A. D. Wadsley were subsequently passed on to one of us (B.M.G.). Two compounds from these samples have been examined so far, a third is currently being studied.

1.2. "$Rb_3Nb_{54}O_{146}$"

1.2.a. EXPERIMENTAL

A clear tetragonal, acicular crystal selected from the 12:88 mol percent $Rb_2O:Nb_2O_5$ sample had the unit cell dimensions, a = 27.69, c = 3.98 Å. Absent reflections were h00 (or 0k0), h (or k) = 2n + 1 indicating space group $P42_12$ or $P\bar{4}2_1m$. At this stage the composition was thought to be $RbNb_7O_{18}$ with z = 8, dc = 4.46 $g \cdot cm^{-3}$, compared with dm = 4.59 $g \cdot cm^{-3}$ [1]. The doubt concerning composition arose because microscopic examination of the bulk material using polarizing optics showed that there are several phases present, one in particular being the tetragonal phase reported here. One other isotropic phase was noted but not identified to date.

Data was collected using the integrating equi-inclination Weissenberg technique and 796 observed reflections out of a total of 1327 were estimated visually in the usual manner from the hk0-2 levels. A very small crystal of approximate dimensions 0.02 x 0.02 x 0.2 mm was used. The linear absorption coefficient for CuKα radiation, which was used, is 450 cm^{-1}. No absorption correction was applied.

1.2.b. STRUCTURE SOLUTION

Following a number of unsuccessful attempts to solve the structure by conventional Patterson methods, a solution was obtained in projection (hk0) using the direct methods suite (GSR, LSAM1, LSAM2) of programs of the York-Louvain group kindly supplied by Dr. P. Main of the University of York. The E-map, calculated for this centrosymmetric projection using 193 phased E-values greater than 1.30, contained major maxima corresponding to all metal atom positions together with minor maxima which were subsequently confirmed to be oxygen atom positions.

The niobium atoms are all located in the xy0 plane with rubidium in the xy1/2 plane. Following several cycles of full matrix least squares refinement varying the metal parameters, the oxygen atoms were located in a difference Fourier synthesis calculated using the three-dimensional data. It was clear at this stage that the rubidium site was partially occupied, and the following adjustment of this occupancy on the basis of difference syntheses (three rubidium atoms distributed over four sites), together with

refinement of atomic positional and isotropic thermal parameters the conventional R factor was 11.5% (observed data only, 17.0% for all data). No attempt has been made to vary oxygen or niobium occupancy or to use anisotropic thermal parameters. Individual scales were adjusted for each level in the final stages of the refinement as reported here.

The structure is illustrated in figure 1 (not idealized) and consists of a framework of niobium - oxygen octahedra and pentagonal bipyramidal groups, with rubidium atoms located in hexagonal tunnels formed by the grouping of octahedra. The arrangement of octahedra around an unoccupied heptagonal tunnel is the most notable feature of this structure. The only evidence for any scattering matter in this tunnel was a small peak in the difference Fourier synthesis (approximately 1/3 to 1/4 of an oxygen atom) situated at $z = 1/2$ near one side of the tunnel, slightly off-center.

Selected interatomic distances are listed in table 2, from which it may be seen that Nb - O distances in the octahedra range from 1.80 to 2.16 Å and in the pentagonal bipyramidal units from 1.99 to 2.21 Å. The Rb - O distances range from 3.36 to 3.91 Å in the hexagonal tunnels. The numbering scheme used is given in figure 2.

1.2.c. DISCUSSION

The chemical formula determined by counting the atoms in the unit cell is "$Rb_3Nb_{54}O_{146}$" which represents an electrical unbalance of nineteen negative charges. This proved to be rather disturbing and several possibilities for accounting for this unbalance are being considered.

First, it should be noted that these samples were prepared prior to the observation by Andersson and Aström [3] that some spectroscopically pure Nb_2O_5 preparations contain appreciable amounts of fluoride ion. A formula can be deduced which is electrically neutral by postulating the formula $Rb_3Nb_{54}O_{127}F_{19}$, *i.e.* 19 fluoride ions in place of a like number of oxygen. This represents approximately 4.7% fluoride in the rubidium compound, and about 2.8% fluoride in the starting Nb_2O_5 preparation. Andersson and Aström [3] observed an approximately 2% weight loss from the Nb_2O_5 sample they studied.

A sample of the rubidium compound was submitted for microanalysis which proved unprofitable as attempts to get it into solution by fusion with sodium peroxide were unsuccessful. At present this compound is being examined by the I.E.E. or Induced Electron Emission technique by Professor R. D. Brown and Dr. A. Buckley of this department.

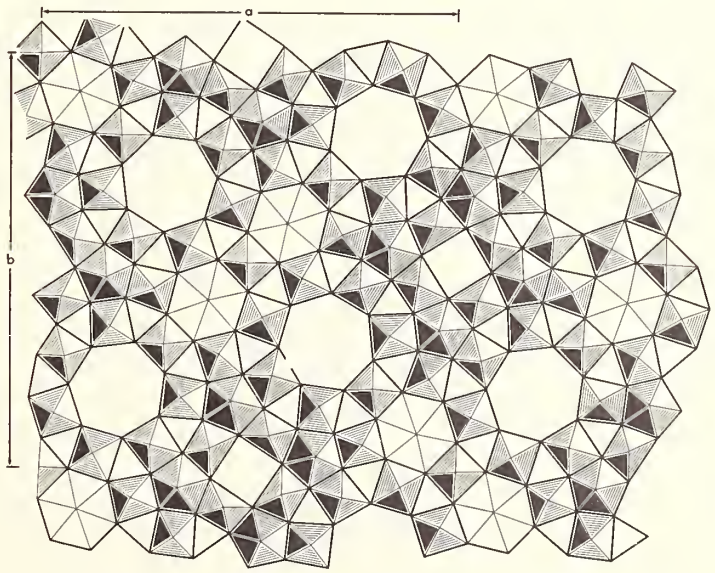

Fig. 1. Structure of "$Rb_3Nb_{54}O_{146}$".

465-504 O - 72 - 3

Table 2

Selected Interatomic Distances (in Ångstrom Units in "$Rb_3Nb_{54}O_{146}$")

Nb1	- O19	2.03 (4x)		Nb6	- O13	2.07 (2x)	
	- O22	1.99 (2x)			- O14	1.94	
					- O16	1.97	
Nb2	- O12	1.96 (2x)			- O27	2.00 (2x)	
	- O21	1.94 (2x)					
	- O23	1.99 (2x)		Nb7	- O10	1.96	
					- O15	1.88	
					- O16	2.16	
					- O17	1.93	
Nb3	- O17	2.16			- O28	1.99 (2x)	
	- O18	2.07					
	- O19	1.88					
	- O20	2.04					
	- O29	2.00 (2x)		Nb8	- O10	2.02	
					- O11	2.01	
					- O13	2.21	
					- O14	2.13	
					- O16	2.17	
Nb5	- O11	2.02			- O25	1.99 (2x)	
	- O12	1.95					
	- O14	2.12					
	- O15	1.93					
	- O26	1.99 (2x)					
Rb	- O18	3.36	- O23	3.87			
	- O19	3.37	- O24	3.60			
	- O21	3.49	- O29	3.91			
	- O22	3.67					

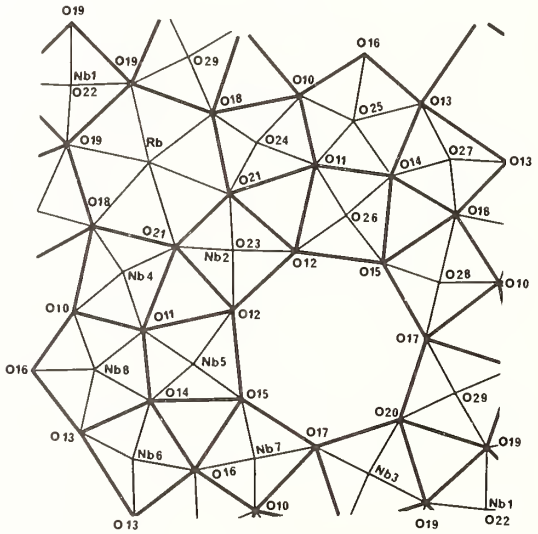

Fig. 2. Number scheme used in "$Rb_3Nb_{54}O_{146}$".

Second, in spite of the use of integrated photographic data it was not felt that a reliable refinement of oxygen occupancy was possible. At present this seems to be the most practical explanation available. Perhaps some of the niobium atoms are five coordinate or even tetrahedral in parts of the structure, although no evidence of this was apparent in the difference Fourier syntheses. Data will be collected shortly using a Picker four-circle diffractometer[2] from which a more complete analysis should be possible.

A preliminary examination of this compound by Dr. J. Allpress using the lattice imaging technique has shown the presence of anti phase boundaries probably arising as a result of a change in the ordering of the three rubidium atoms over four possible sites.

1.3. "$RbNb_3O_9$"

1.3.a. EXPERIMENTAL

This compound crystallizes as minute hexagonal plates, a = 7.39, c = 3.89 Å, space group P6/mmm (z = 1). For convenience the data was examined in the orthorhombic space group Cmmm, a = 13.038, b = 7.502, c = 3.89 Å. Absences were hkℓ for h + k = 2n + 1 indicating space group Cmmm (z = 2).

A total of 130 reflections were measured visually from the hk0 - 2 levels collected using the integrating Weissenberg technique with CuKα radiation.

1.3.b. STRUCTURE SOLUTION AND DISCUSSION

It was noted from the unit cell dimensions and confirmed from the Patterson synthesis that this structure would be very similar to that of the hexagonal tungsten bronzes (fig. 3). The principal difference was that the c axis of "$RbNb_3O_9$" is half that reported for the hexagonal tungsten bronzes. For example, $Rb_{0.27}WO_3$ has dimensions [4], a = 7.39, c = 7.54 Å. Iyer and Smith [2] reported a compound with unit cell dimensions a = 7.45, c = 7.66 Å, formula $RbNb_3O_8$ (z = 2), space group $P6_322$.

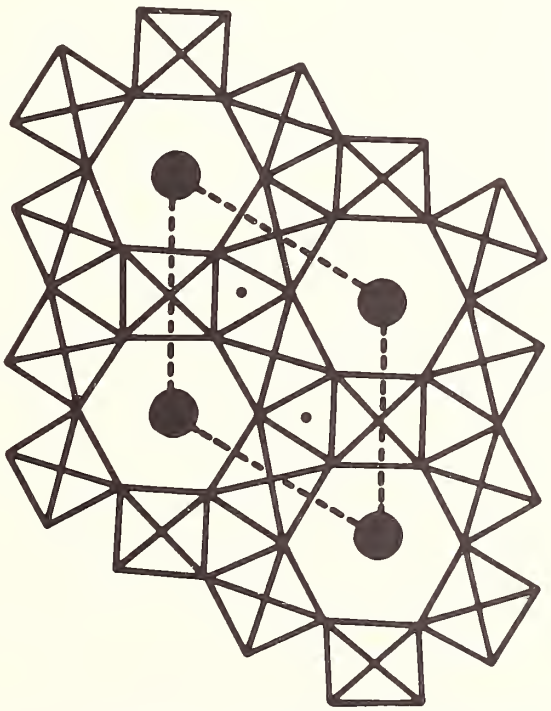

Fig. 3. Hexagonal tungsten bronze structure. The s-tricapped trigonal prismatic site is marked by •.

[2]By courtesy of Dr. A. McL. Mathieson and Dr. W. Denne of the C.S.I.R.O. Division of Chemical Physics.

The structure refined smoothly with both metal and oxygen atoms in the model to an R factor of 14.0%. The formula at this stage corresponded to $RbNb_3O_9$ (cf 3 x $Rb_{0.27}WO_3$), obviously two negative charges in excess. The fact that both this compound and "$Rb_3Nb_{54}O_{146}$" are almost colorless suggests that all the niobium is Nb^{5+}; any reduction would enhance the charge unbalance. It was noted that the 9 coordinate site, marked • in figure 3, showed evidence in the difference Fourier synthesis of containing a small amount of scattering matter (approximately 3/5 of an oxygen atom). The interatomic distances from the center of this hole to neighboring oxygen atoms are approximately 2.2 Å to oxygen in the xy0 plane, and approximately 2.50 Å to oxygens in the xy1/2 plane. These distances are too short for Rb - O (3.3 to 3.8 Å in this compound) and although a little long for Nb - O, it appears quite feasible for a fraction of Nb^{5+} to be in this site, a symmetrically tricapped trigonal prism. Possibly the best known example of this coordination is the ion $Nd(OH_2)_9^{3+}$ in $Nd(OH_2)_9(BrO_3)_3$ reported by Helmholtz [5]. With a 0.2 occupancy of this two-fold site the formula becomes $RbNb_{3.4}O_9$ ($Rb_5Nb_{17}O_{45}$). The possibility of fluoride contamination is considered unlikely in connection with this compound, and therefore for $Rb_3Nb_{54}O_{146}$ also, as $RbNb_3O_7F_2$ would require about 7% of fluoride.

Selected interatomic distances are given in table 3.

2. $Li_xMo_6O_{17}$, $Na_xMo_6O_{17}$, and $K_xMo_6O_{17}$.

2.1. INTRODUCTION

Stephenson [6] partly solved the structure of the sodium compound using data collected from a twinned crystal which had been prepared by melt electrolysis and characterized by Wold, Kunnmann, Arnott and Ferretti [7]; however, the structure presented here accounts for features not readily explained by Stephenson's model.

2.2. EXPERIMENTAL AND STRUCTURE SOLUTION

The lithium, sodium and potassium molybdenum oxide bronzes of composition $Li_xMo_6O_{17}$, $Na_xMo_6O_{17}$, and $K_xMo_6O_{17}$ (where $x \leq 1.0$, 0.8, and 1.0 approximately, respectively) were prepared as untwinned crystals by heating the respective alkali metal hydride with an excess of MoO_3 in open Pythagoras furnaceware over a gas flame. The loose matrix left after reaction was extracted with ammonia solution and the crystals collected. The crystals of the sodium and potassium compounds exhibited a pronounced cleavage plane which was not observed for the lithium compound.

Crystal data for all three compounds is set out in table 4, together with the means by which the data were collected. Two sets of unit cell dimensions are reported for the sodium compound to illustrate the degree of variation that is found with these compounds; a variation which can presumably be correlated with the variable alkali metal content. The presence of an ReO_3 sub-cell was noted in the Weissenberg photographs, and can be seen in figure 4 for the sodium compound where this is compared with the less obvious sub-cell for the lithium compound.

Table 3

Interatomic Distances in "$RbNb_3O_9$" in Angstrom Units

Rb - O	3.33 (6x)	
	3.75 (6x)	
Nb - O	1.94 (2x)	Octahedra
	1.95 (2x)	
	1.98 (2x)	
Nb - O	2.16 (3x)	s-tricapped
	2.52 (6x)	trigonal prims

Table 4

Crystal Data for the Lithium, sodium and Potassium Bronzes

$Li_xMo_6O_{17}$ a = 9.482, b = 5.521, c = 12.737, β = 90.59°.
Monoclinic, space group $P2_1$ or $P2_1/m$. Total number of reflections 1757, with 742 observed.
Picker four circle diffractometer.(a)
MoKα radiation.

$Na_xMo_6O_{17}$ Crystal 1. a = 9.524, b = 5.519, c = 12.975, β = 90.03°.
Crystal 2. a = 9.578, b = 5.517, c = 12.992, β = 90.11°.
Monoclinic, space group C2, Cm or $C2/m$. Total number of reflections 1123, with 861 observed.
Picker four circle diffractometer.
MoKα radiation.

$K_xMo_6O_{17}$ a = 9.60, b = 5.54, c = 13.66, β = 90.1°.
Monoclinic, space group C2, Cm or $C2/m$. Total number of reflections 604, with 277 observed. Weissenberg multiple film technique. CuKα radiation.
Unit cell dimensions corrected for film shrinkage.

(a) Courtesy of Dr. A. McL. Mathieson and Dr. W. A. Denne, C.S.I.R.O. Division of Chemical Physics.

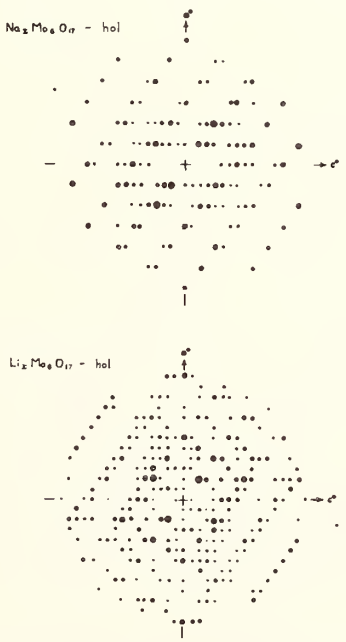

Fig. 4. Intensity weighted reciprocal lattice zero levels for $Li_xMo_6O_{17}$ and $Na_xMo_6O_{17}$.

The structures of the sodium and potassium compounds, which were reported as being isotypic by Reau [8], were solved by conventional Patterson methods, and refined by full matrix least squares and Fourier techniques to conventional R values of 7.8% and 8.2% respectively, for isotropic models.

2.3. DISCUSSION

The structure consists basically of ReO_3 type slabs of corner-shared molybdenum - oxygen octahedra perpendicular to the c-axis, with molybdenum atoms in tetrahedral coordination to oxygen at the surfaces of these slabs. The slabs are weakly held together by sodium (or potassium) ions in distorted cube octahedral sites along the plane at z = 1/2 as shown in figure 5 which illustrates the structure of the sodium compound. In the potassium compound the slabs of ReO_3 type octahedra are pushed further apart to accommodate the larger potassium ions. The planes at z = 1/2 correspond to the pronounced cleavage planes noted above.

There is evidence, found in difference Fourier syntheses principally, that in small areas of the crystal of the sodium compound some of the molybdenum tetrahedra near the z = 1/2 plane are replaced by molybdenum octahedra thus extending and cross-linking the ReO_3 slabs by corner-sharing of octahedra. It is interesting to note that the potassium compound refined smoothly to an R of 8.2% on the basis of film data, compared with the present R of 7.8% from diffractometer data for the sodium compound. It is suggested [9] that this may result from the fact that the potassium site is almost fully occupied resulting in *all* of the molybdenum at the surface of the slabs being in tetrahedral coordination. The lower sodium content in the sodium bronze suggests that less molybdenum is tetrahedrally coordinated compared with the potassium compound, with more octahedra cross-linking the slabs probably in a disordered manner throughout the crystal. The sodium coordination is nearly regular cube octahedral when this cross-linking is present. The sodium site is about 80% occupied in $Na_xMo_6O_{17}$ and the potassium site about 100% occupied in $K_xMo_6O_{17}$.

In comparison with Stephenson's model the localization of the sodium or potassium ions in the z = 1/2 plane, and the reported composition $Na_{0.9}Mo_6O_{17}$ (which is realized if the tetrahedral sites are fully occupied) are more readily explained on the basis of the model described here.

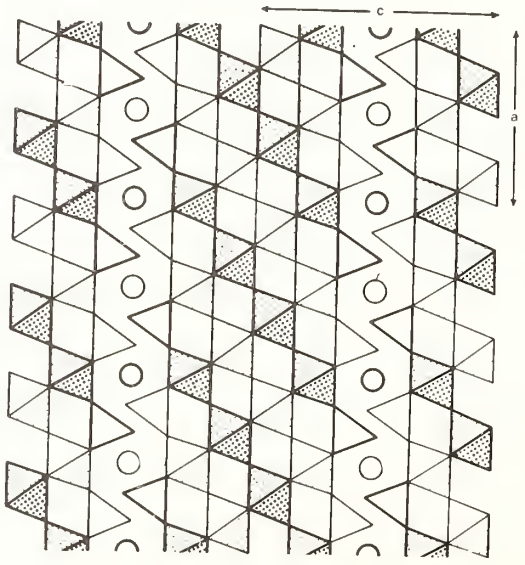

Fig. 5. An 010 projection of part of the structure of $Na_{0.9}Mo_6O_{17}$ represented as MoO_6 octahedra, MoO_4 tetrahedra, and sodium atoms. Heavy lines represent species at y = 0, 1, lighter ones represent those at y = 1/2.

Selected interatomic distances and angles are given in table 5.

In spite of the trend in the unit cell dimensions from the potassium to the sodium and the lithium compound, and the fact that we have not yet been able to solve the structure of the lithium compound, it is apparent that there are going to be significant differences between the structure of the lithium compound and the other two. Crystals of the lithium compound do not have the pronounced cleavage shown by the other crystals, suggesting that the sites occupied by sodium and potassium are too large for lithium, and a different structure exists. The Patterson syntheses are different in features attributable to Mo - O vectors, and some peaks are in such positions that Mo - O and O - O distances both need to be very short if the structure is centrosymmetric. A solution to this structure is being sought in the non-centrosymmetric space group ($P2_1$) using both Patterson and direct methods. The same preliminary metal atom structure has been found using both methods, but we have not been able to proceed further at this stage.

A preliminary report of the structure of the sodium compound was published recently [10].

3. $Li_2Mo_4O_{13}$

3.1. INTRODUCTION

As part of a general study of alkali metal molybdates, which was briefly summarized in the introduction to a recent report [11] on the structure of the compound $K_2Mo_4O_{13}$, we present here a preliminary account of the single crystal structure determination of the low temperature form of lithium tetramolybdate. Following the commencement of this work, samples of both the low temperature and a high temperature modification were obtained from Dr. R. S. Roth of the National Bureau of Standards, Washington, D. C. [12].

3.2. EXPERIMENTAL

A suitable single crystal of $Li_2Mo_4O_{13}$ was obtained from a slowly cooled melt of Li_2CO_3 and MoO_3 in the ratio 1:4. The crystals were plate-like, very pale green in color and possessed a cleavage plane.

Table 5

Selected Bond Lengths and Angles in $Na_xMo_6O_{17}$ and $K_xMo_6O_{17}$.

	$Na_xMo_6O_{17}$	$K_xMo_6O_{17}$
Mo - O (tetrahedra) Å	1 x 1.74	1 x 6.2
	2 x 1.77	2 x 1.77
	1 x 1.78	1 x 1.76
O - Mo - O degrees (tetrahedra)	2 x 108.6	2 x 108.4
	3 x 109.8	1 x 106.7
	1 x 110.3	2 x 112.2
		1 x 108.7
Mo - O (octahedra 1) Å	1 x 1.87	1 x 1.84
	2 x 1.77	2 x 1.86
	2 x 2.04	2 x 1.99
	1 x 2.02	1 x 1.95
	Av. 1.92 Å	Av. 1.92 Å
Mo - O (octahedra 2) Å	2 x 1.75	2 x 1.78
	1 x 1.77	1 x 1.86
	1 x 2.08	2 x 2.08
	2 x 2.09	1 x 2.08
	Av. 1.92 Å	Av. 1.94 Å

Crystal data: $Li_2Mo_4O_{13}$, triclinic, a = 8.225, b = 8.578, c = 11.450 Å, α = 95.95°, β = 109.25°, γ = 96.03°. Space group P1, Cu Kα radiation λ = 1.5405 Å was used. U = 750.17 Å^3, dm = 4.1 $\pm$ 0.1 g·cm^{-3} and dc = 4.02 g·cm^{-3} for z = 3. A total of 2600 reflections, of which the 1813 observed reflections were used to solve the structure, were collected using a Picker FACS1 four-circle automatic diffractometer (by courtesy of Dr. G. B. Robertson of the Research School of Chemistry, Australian National University).

3.3. STRUCTURE SOLUTION

The structure was solved by the method outlined earlier for triclinic compounds [13]. Following the location of all molybdenum atoms, refinement of positional parameters by full matrix least squares techniques resulted in a conventional R factor of 16.6%. All oxygen atoms were found in the subsequent difference Fourier synthesis, and refinement of all positional parameters (R = 9.6%) led to the unambiguous location of the lithium atoms in the next difference synthesis. Refinement of positional and isotropic thermal parameters has given R = 3.9% at present.

3.4. STRUCTURE DESCRIPTION AND DISCUSSION

The structure consists essentially of a cubic close packed array of oxygen atoms, some oxygen atoms being absent in a systematic manner, with Li and Mo atoms occupying octahedral sites. It is interesting to note that the ionic radius of Li^+ (0.74 Å) is the same as the covalent radius of Mo^{VI} [14]. Figure 6, a view perpendicular to the close packed oxygen layers, shows the layer of (idealized) octahedra which is repeated by edge- and corner-sharing to form the three-dimensional framework of the structure. Every third layer consists of Li octahedra only, making the sequence of layers of octahedra in this direction, ---Mo - Mo - Li - Mo - Mo - Li ---. The layer sequence can be seen in figure 7, as can the positions of the oxygens which are absent from the ccp arrangement (marked with *). These absences result in the formation of strings of face-shared (square face) cube-octahedral holes. These strings are in pairs through the structure as a result of additional face-sharing of the same type between adjacent cube-octahedral holes.

Figure 8 shows an alternative view of the structure from which the relationship to the $K_2Mo_4O_{13}$ structure and the structures of other complex molybdates can be more easily seen [11]. In this view, the lithium - oxygen and molybdenum - oxygen octahedra are edge- and corner-shared to form a sheet. This sheet is repeated by edge-sharing to form a double layer as shown in the figure. These double layers are then linked by corner-sharing through a single sheet resulting in a double layer - single layer - double layer sequence reminiscent of the - S - D - S - D - sequence of Andersson and Wadsley [15].

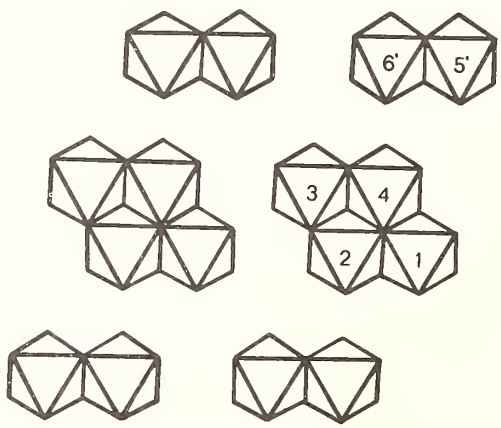

Fig. 6. The basic layer of octahedra in $Li_2Mo_4O_{13}$ with c.c.p. layers of oxygen in the plane of the paper.

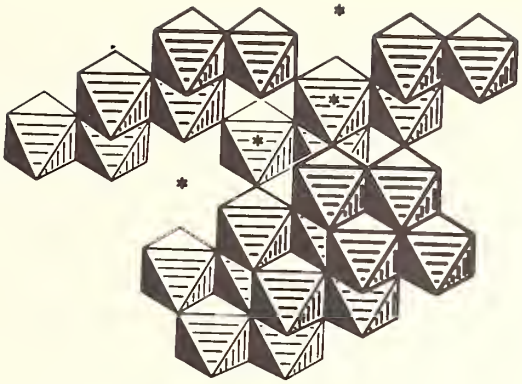

Fig. 7. View of $Li_2Mo_4O_{13}$ structure illustrating the packing together of the layers shown in figure 6.

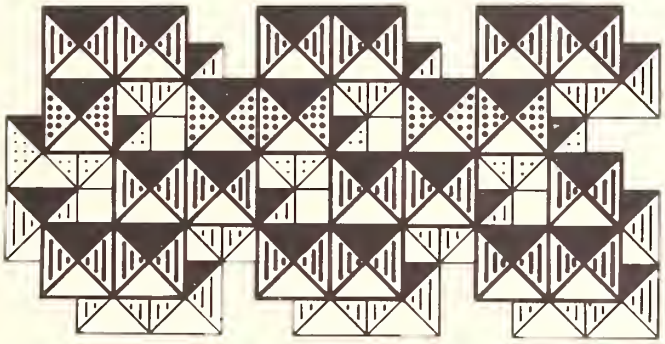

Fig. 8. An alternative view of the structure from which the relationship to $K_2Mo_4O_{13}$ and other complex molybdates can be seen.

The octahedra are considerably distorted from ideal symmetry, in particular for Mo (6) which shows a distortion towards a square-pyramidal coordination. It can be seen from table 6, in which ranges of interatomic distances are listed, that the Mo - Li edge-shared distance is shorter than the Mo - Mo and Li - Li edge-shared distance. Similarly the Mo - Li corner-shared distance is less than the Mo - Mo corner-shared distance. It may be concluded from these observations that the lithium ions are acting to draw the layers of molybdenum octahedra towards one another.

The structures of $Li_2Mo_4O_{13}$ (high temperature form) and of $Cs_2Mo_4O_{13}$ are currently being examined in this laboratory. The former compound is triclinic (a = 8.22, b = 8.63, c - 11.51 Å, α = 111.4°, β = 94.6°, γ = 96.2°) and from the unit cell dimensions and the distribution of intensities observed on Weissenberg films is expected to have a very similar structure to that of the low temperature form.

4. ACKNOWLEDGEMENTS

One of us (B.M.G.) is grateful to the organizers of the 5th Materials Research Symposium, and to the Overseas Travel Grants Committee of Monash University for the opportunity of presenting this work at the Symposium. Two of us (D.J.L. and B.K.M.) are grateful for the award of a Monash Graduate Studentship and a Commonwealth Post-graduate Studentship respectively. This work forms part of a project (No. C65/15891) supported by the Australian Research Grants Committee.

Table 6

Selected Interatomic Distances in $Li_2Mo_4O_{13}$

Mo (1) - O	1.677 - 2.334	octahedra
Mo (2) - O	1.673 - 2.495	
Mo (3) - O	1.695 - 2.379	
Mo (4) - O	1.678 - 2.389	Average Mo - O 1.985
Mo (5) - O	1.694 - 2.475	
Mo (6) - O	1.685 - 2.640	

Each Octahedron Has Two Short, Two Medium and Two Long Mo - O Distances

Li (1) - O	1.924 - 2.562	octahedra
Li (2) - O	1.953 - 2.573	Average Li - O 2.162
Li (3) - O	1.924 - 2.464	

Mo - Mo	edge-shared	(10)	3.239 - 3.574	(Av. 3.378)
Mo - Mo	corner-shared	(7)	3.733 - 4.307	(Av. 3.978)
Mo - Li	edge-shared	(5)	3.130 - 3.335	(Av. 3.218)
Mo - Li	corner-shared	(13)	3.532 - 3.934	(Av. 3.673)
Li - Li	edge-shared	(4)	3.359 - 3.549	(Av. 3.445)

5. REFERENCES

[1] Reisman, A., and Holtzberg, F., J. Phys. Chem., 64, 748 (1960).
[2] Iyer, P. N., and Smith, A. J., Acta Cryst., B27, 731 (1971).
[3] Andersson, S., and Aström, A., Acta Chem. Scand., 18, 2233 (1964).
[4] Magneli, A., Acta Chem. Scand., 7, 315 (1953).
[5] Helmholtz, L., J.A.C.S., 61, 1544 (1939).
[6] Stephenson, N. C., Acta Cryst., 20, 59 (1966).
[7] Wold, A., Kunnmann, W., Arnott, R. J., and Ferretti, A., Inorg. Chem., 3, [4], 545 (1964).
[8] Reau, Jean-Maurice, Thesis, University of Bordeaux, (1970).
[9] Lloyd, D. J., Ph.D. Thesis, Monash University, (1971).
[10] Gatehouse, B. M., and Lloyd, D. J., Chem. Comm., 13 (1971).
[11] Gatehouse, B. M., and Leverett, P., J. Chem. Soc., [A], 2107 (1971).
[12] Roth, R. S., Private Communication, August 1970.
[13] Gatehouse, B. M., and Leverett, P., J. Solid State Chem., 1, 484 (1970).
[14] Shannon, R. D., and Prewitt, C. T., Acta Cryst., B25, 925 (1969).
[15] Andersson, S., and Wadsley, A. D., Acta Cryst., 15, 201 (1962).

E. Banks: Your structure for the pseudohexagonal bronze phase with atoms in the trigonal prism vacancies is reminiscent of some work we did a few years ago in putting lithium into potassium hexagonal tungsten bronze and I am glad to see someone else has been able to do it. I wanted to comment further on this point though. Have you considered the possibility that you have only, say half as many, or some fraction of that many, niobiums in those sites with the remaining electron excess being compensated by fluoride in place of oxygen as you had in the other niobium compound?

B. M. Gatehouse: I have certainly considered this, Professor Banks, but I think that unitl I can get a successful analysis of fluoride in these materials ....

E. Banks: Have you tried the electron microprobe?

B. M. Gatehouse: Yes, I think we have one in Australia, probably BHP, the steel people. We are certainly going to get someone to look at these niobates using that technique.

N. C. Stephenson: These problems you have with charge imbalance are very similar to the ones we had with a sodium niobate. We had diffractometer data and were able to refine on population parameters and we found that the residual electron densities in those tunnels were in fact atoms. In fact, one of the very small electron peaks of about six electrons turned out to be one-eighth of a niobium atom which was in square-fold coordination, and this could very well be what you have in your seven-sided tunnels. We also found that we had a domain structure where we had a slip along the b-axis, and you consider that to be due to an anti-phase boundry. Now I noticed that your little insert into the host matrix was related to the host matrix by a two-fold axis. We consider that these slips are due to anti-polar ferroelectric domains. You also said that the domain boundary had finite width and I would think that in an anti-phase boundary you wouldn't have a finite width boundary, but you might expect a definite boundary width in a ferroelectric domain. One other thing, if you are substituting oxygen ions with fluorine ions to account for your charge imbalance, what sort of a correlation do you get between your observed and calculated densities?

B. M. Gatehouse: There are four or five questions there. I don't think I've got time to adequately answer them all at the moment, but I'll do so later on. The one thing I would like is to get diffractometer data on this compound. Our diffractometer arrives in March next year. Perhaps you could help me out.

T. Negas: For that first rubidium niobium oxide you perhaps made fluorine the culprit. What is the possibility of hydroxyl?

B. M. Gatehouse: This is indeed a possibility. The material was prepared, I think, at 1350 °C. I would probably have to consult either Dr. Andersson or Dr. Holtzberg on that point, but it is indeed a possibility.

S. Andersson: There is a simple way to decide here if you have fluorine or not. You can make the compound, can't you. You can buy pure Nb_2O_5 these days and you mix it with RbF or with $Rb_2O(RbNbO_3)$ in a sealed platinum tube. Two experiments and you will see.

B. M. Gatehouse: Thank you Sten. Yes, we certainly will be trying this. As you can imagine this was rather a recent solution and I am going back to do these experiments.

National Bureau of Standards Special Publication 364, Solid State Chemistry, Proceedings of 5th Materials Research Symposium, issued July 1972.

THE CRYSTAL CHEMISTRY OF SOME NEW MIXED OXIDES OF TELLURIUM +IV

Jean Galy

National Center of Scientific Research Laboratory
of Inorganic and Structural Chemistry
University of Bordeaux I
33 Talence, France

The structural chemistry of some new mixed oxides between TeO_2 and some transition metal oxides is discussed.

A new structural type MTe_3O_8 has been found in the TeO_2 - MO_2 systems (M = Ti, Zr, Hf and Sn). The structure of $TiTe_3O_8$ determined by x-ray single crystal analysis is cubic, space group Ia3 with a = 10.956 Å. The relationships with the fluorite structure type have been established. $ZrTe_3O_8$ as well as fourteen new compounds with the general formula $A_{\frac{1}{2}}B_{\frac{1}{2}}Te_3O_8$ (A = Sc, Cr, Fe, Ga, Rh, In, Bi and B = Nb, Ta) are isostructural with $TiTe_3O_8$.

In the system TeO_2 - VO_2 the phase $TeVO_4$ has been prepared in two different crystalline forms, which we designate α and β here. A reversible polymorphic transformation occurs at 650 °C $\alpha \rightleftarrows \beta$. Both phases crystallize in the monoclinic system. The α-$TeVO_4$ crystals are black and the β-$TeVO_4$ crystals green; a melt of $TeVO_4$ gives a black glass by quenching. In α-$TeVO_4$ the coordination number of vanadium and tellurium is 6 and 3, in β-$TeVO_4$ the C.N. is 5 and 4.

The crystal structure of $NaVTeO_5$ ($KVTeO_5$, $RbVTeO_5$ and $AgVTeO_5$ are isostructural) exhibits isolated chains with $(VTeO_5)_n^{n-}$ formula surrounded by sodium atoms.

Finally, relationship between the structure of α- and β- $TeVO_4$ and other "lone pair" structures such as α-Sb_2O_4 or $SbNbO_4$, β-Sb_2O_4 and Pb_3O_4 is discussed, and comparison with such simple structures as α-PbO_2, ReO_3, PdF_3 and TiO_2 rutile also made.

Key words: Crystal structure; "lone pair" structures; tellurites; tellurium dioxide; tellurium hypovanadate; titanium tellurite.

1. INTRODUCTION

Tellurium differs from the other elements of the 6th group of the periodic table by its ability to form mixed oxides with other elements. Such compounds have typical ionic crystal structures when tellurium is in the oxidation state six (+VI) or four (+IV). Tellurium +IV is characterized by an electronic configuration [Kr] $4d^{10}5s^2$; the pair of s electrons shows a reluctance or inability to act as bonding electrons and this fact will be illustrated by the non-symmetric coordination polyhedra, which occur in the crystal structures of the tellurium +IV compounds.

2. TeO_2

Tellurium dioxide exists in nature as the minerals tellurite and paratellurite with two different crystal structures.

Tellurite crystallizes in the orthorhombic system; the crystal structure has been reported by Beyer, Sahl and Zeman [1][1] and Beyer [2]. The cell dimensions and the space group

[1] Figures in brackets indicate the literature references at the end of this paper.

are given in table 1.

The other modification of TeO_2, paratellurite, crystallizes in the tetragonal system; the crystal structure has been refined by Leciejewicz [3] using neutron diffraction (data are given in table 1).

The tellurium oxide TeO_2 used in our experiments was prepared by the thermal decomposition of orthotelluric acid:

$$H_6TeO_6 \longrightarrow TeO_2 + 3H_2O + \tfrac{1}{2}O_2$$

The synthetic TeO_2 has the paratellurite crystal structure.

Table 1

Oxide	System	Space group	Parameters	Literature
TeO_2 (tellurite)	orthorhombic	P b c a	a = 12.035 Å b = 5.464 Å c = 5.607 Å	Beyer, Sahl and Zemann (1965) [1] Beyer (1967) [2]
TeO_2 (paratellurite)	tetragonal	$P4_12_12$ or $P4_32_12$	a = 4.796 Å c = 7.626 Å	Leciejewicz (1961) [3]
$TiTe_3O_8$	cubic	Ia3	a = 10.956 Å	Galy and Meunier (1969) [5]
$SnTe_3O_8$	"	"	a = 11.144 Å	Meunier and Galy (1971) [7]
$HfTe_3O_8$	"	"	a = 11.291 Å	
$ZrTe_3O_8$	"	"	a = 11.308 Å	
$Ga_{\frac{1}{2}}Te_{\frac{1}{2}}Te_3O_8$	"	"	a = 10.956 Å	Meunier, Galy and Hagenmuller (1970) [16]
$Ga_{\frac{1}{2}}Ta_{\frac{1}{2}}Te_3O_8$	"	"	a = 10.965 Å	
$Cr_{\frac{1}{2}}Nb_{\frac{1}{2}}Te_3O_8$	"	"	a = 11.007 Å	
$Cr_{\frac{1}{2}}Ta_{\frac{1}{2}}Te_3O_8$	"	"	a = 11.012 Å	
$Rh_{\frac{1}{2}}Nb_{\frac{1}{2}}Te_3O_8$	"	"	a = 11.014 Å	
$Rh_{\frac{1}{2}}Ta_{\frac{1}{2}}Te_3O_8$	"	"	a = 11.018 Å	
$Fe_{\frac{1}{2}}Nb_{\frac{1}{2}}Te_3O_8$	"	"	a = 11.027 Å	
$Fe_{\frac{1}{2}}Ta_{\frac{1}{2}}Te_3O_8$	"	"	a = 11.036 Å	
$Sc_{\frac{1}{2}}Nb_{\frac{1}{2}}Te_3O_8$	"	"	a = 11.136 Å	
$Sc_{\frac{1}{2}}Ta_{\frac{1}{2}}Te_3O_8$	"	"	a = 11.150 Å	
$In_{\frac{1}{2}}Nb_{\frac{1}{2}}Te_3O_8$	"	"	a = 11.169 Å	
$In_{\frac{1}{2}}Ta_{\frac{1}{2}}Te_3O_8$	"	"	a = 11.186 Å	
$Bi_{\frac{1}{2}}Nb_{\frac{1}{2}}Te_3O_8$	"	"	a = 11.275 Å	
$Bi_{\frac{1}{2}}Ta_{\frac{1}{2}}Te_3O_8$	"	"	a = 11.289 Å	
α-$TeVO_4$ (black)	monoclinic	$P2_1/c$	a = 5.099 Å b = 4.934 Å c = 12.672 Å β = 105.85°	Meunier, Darriet and Galy (1971) [15]
β-$TeVO_4$ (green)	monoclinic	$P2_1/c$	a = 4.379 Å b = 13.502 Å c = 5.446 Å β = 91.72°	

Table 1 (continued)

$NaVTeO_5$	monoclinic	$P2_1/c$	a = 5.891 Å b = 11.389 Å c = 6.823 Å β = 103.08°	Darriet, Guillaume Wilhelmi, Galy (1971) [9]
$KVTeO_5$	"	"	a = 6.393 Å b = 11.608 Å c = 6.885 Å β = 105.09°	
$RbVTeO_5$	"	"	a = 6.700 Å b = 11.833 Å c = 6.945 Å β = 106.46°	
$AgVTeO_5$	"	"	a = 5.877 Å b = 11.400 Å c = 6.817 Å β = 102.63°	
$LiVTeO_5$	orthorhombic	$P2_12_12_1$	a = 9.509 Å b = 8.353 Å c = 5.285 Å	Darriet, Guillaume Galy (1970) [19]

3. TELLURIUM +IV COORDINATION

Tellurium +IV shows two types of coordination towards oxygen, both one-sided.

The fourfold coordination is the most common; in this case the coordination polyhedron of the tellurium atom can be described as a trigonal bipyramid with one corner of the equatorial triangle unoccupied, or, as a distorted square pyramid with Te at the apex (fig. 1a). Such coordination occurs in several minerals like tellurite [2], paratellurite [3], spiroffite (Mn, Zn) Te_3O_8 [4], "cliffordite" UTe_3O_9 [5] and the synthetic compounds, $Zn_2Te_3O_8$ [6], $TiTe_3O_8$ [7] β-$TeVO_4$ [8] and $NaVTeO_5$ [9].

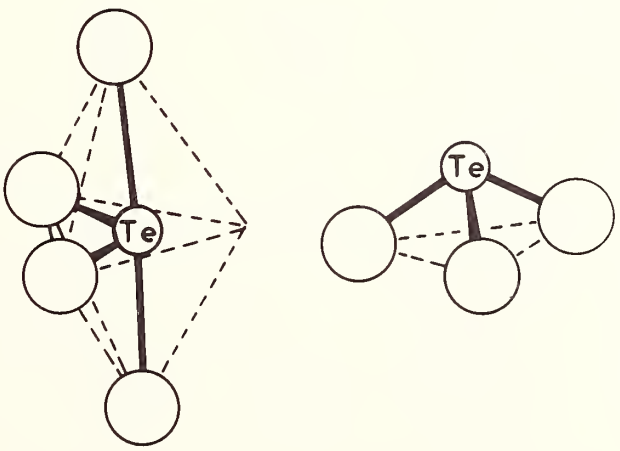

Fig. 1. a) Fourfold coordination of Te +IV.
b) Threefold coordination of Te +IV.

Threefold coordination is characterized by a trigonal pyramid with Te at the apex (fig. 1b). Such TeO_3 pyramids have been found in minerals like teineite $CuTeO_3 \cdot 2H_2O$ [10], the "unnamed hexagonal tellurite" [11], the denningite $(Mn, Ca, Zn)Te_2O_5$ [12], rodalquilarite [13] and also in the synthetic compounds $ZnTeO_3$ [14] and α-$TeVO_4$ [15].

4. DESCRIPTION OF STRUCTURES

4.1. MTe_3O_8 PHASES (M = Ti, Sn, Hf, Zr)

The structure type of the MTe_3O_8 phases where M is titanium, tin, hafnium or zirconium has been determined from x-ray single crystal analysis [17].

$TiTe_3O_8$ crystallizes in the cubic system, space group Ia3 (table 1). The structure has been deduced from a cubic face centered subcell (Ca - atoms in CaF_2) of a' = $a_{TiTe_3O_8}/2$ parameter, in which titanium and tellurium atoms occupy ordered positions (fig. 2).

The structure is built up of TiO_6 octahedra and TeO_4 polyhedra sharing corners to form a threedimensional network. In figures 3 and 4 sections of the structure are given. In figure 3 there are TiO_6 octahedra mixed with TeO_4 polyhedra, while in figure 4 there are only TeO_4 polyhedra. The structure of $TiTe_3O_8$ can be related to the CaF_2 structure type. If

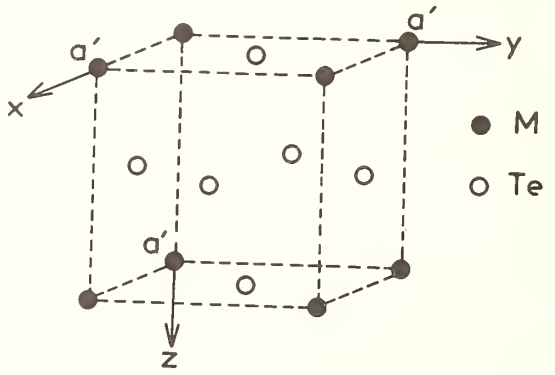

Fig. 2. The ordered f. c. c. subcell of cations in $TiTe_3O_8$ (a' = a/2).

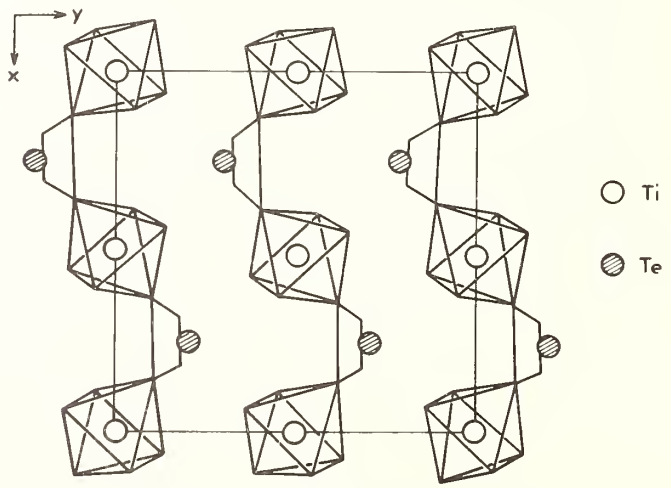

Fig. 3. Sequence of Ti and Te polyhedra in a plane at Z = 0 and 1/2.

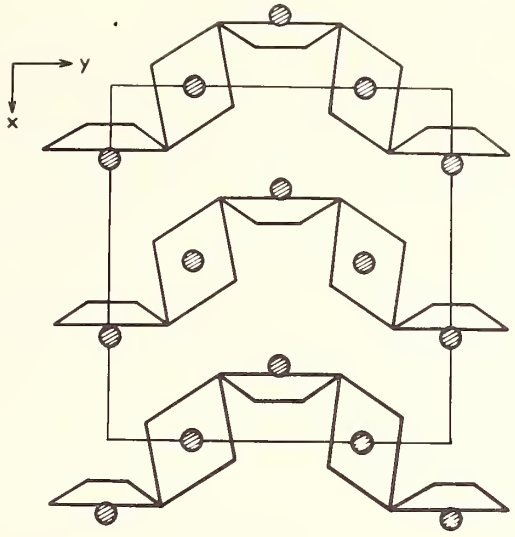

Fig. 4. Sequence of Te polyhedra in a plane at Z = 1/4 and 3/4.

anions (large open circles) move in the directions demonstrated by arrows into the filled circles in figures 5 and 6, the TiO_6 octahedron and TeO_4 polyhedron are obtained from the fluorine positions in CaF_2 structure.

4.2. $A_{\frac{1}{2}}B_{\frac{1}{2}}Te_3O_8$ = A SERIES OF COMPOUNDS WITH THE $TiTe_3O_8$ STRUCTURE TYPE

Fourteen compounds with the general formula $A_{\frac{1}{2}}B_{\frac{1}{2}}Te_3O_8$ where A = Sc, Cr, Fe, Ga, Rh, In, Bi and B = Nb and Ta, have been prepared by solid state reaction [16].

$$A_2O_3 + B_2O_5 + 12TeO_2 \rightarrow 4\ A_{\frac{1}{2}}B_{\frac{1}{2}}Te_3O_8$$

X-ray powder pattern analysis show that these phases are isostructural with $TiTe_3O_8$. A and B atoms are disordered in the octahedral titanium sites.

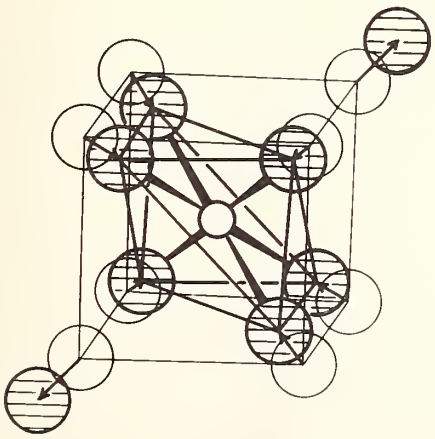

Fig. 5. Titanium coordination octahedron deduced from CaF_2 structure type.

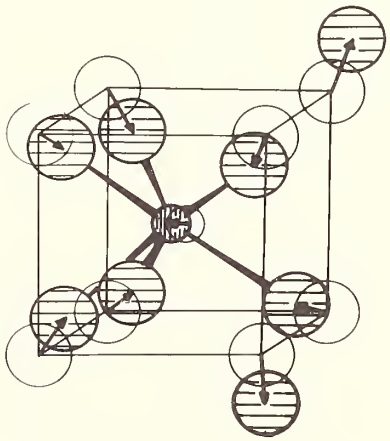

Fig. 6. Tellurium coordination polyhedron deduced from CaF_2 structure type.

465-504 O - 72 - 4

4.3. $TeVO_4$ = A TELLURIUM AND VANADIUM +IV OXIDE PHASE

$TeVO_4$ has been synthesized by direct solid state reaction between the vanadium and tellurium dioxides VO_2 and TeO_2, at 600 °C [8,15]. D.T.A. measurements show a reversible polymorphic transformation at 650° ± 10 °C. Crystals of both phases, designed α- and β-, have been prepared using transport reaction with tellurium tetrachloride $TeCl_4$. The α-$TeVO_4$ crystals are black and β-$TeVO_4$ crystals green. The two crystalline forms of $TeVO_4$ crystallize in the monoclinic system

$$\alpha\text{-}TeVO_4 \underset{650\ °C}{\overset{\rightarrow}{\leftarrow}} \beta\text{-}TeVO_4$$

(black) monoclinic — (green) monoclinic

A melt of $TeVO_4$ gives a black glass upon quenching.

4.3.a. α-$TeVO_4$ STRUCTURE

Projection of the α-$TeVO_4$ structure on the a c plane is given in figure 7. The structure consists of isolated chains of VO_6 octahedra sharing edges and running parallel to the b-axis (fig. 8); these chains are joined to TeO_3 polyhedra by corner sharing.

Tellurium has a threefold coordination in the form of a trigonal pyramid with Te at the apex.

4.3.b. β-$TeVO_4$ STRUCTURE

A projection on the (100) plane of the β-$TeVO_4$ structure is given in figure 9 (data in table 1). This figure shows the general scheme of the structure, which consists of very distorted octahedra sharing corners to form puckered sheets parallel to (010). These sheets are linked by tellurium atoms.

In fact, the VO_6 octahedra are so distorted along the b-axis that it is more reasonable to consider a fivefold coordination for the vanadium +IV.

The VO_5 polyhedron can be described as a square pyramid of oxygens with the V in the center. The 6th oxygen is at 2.77 Å from the vanadium; this appears in the (100) projection (fig. 10).

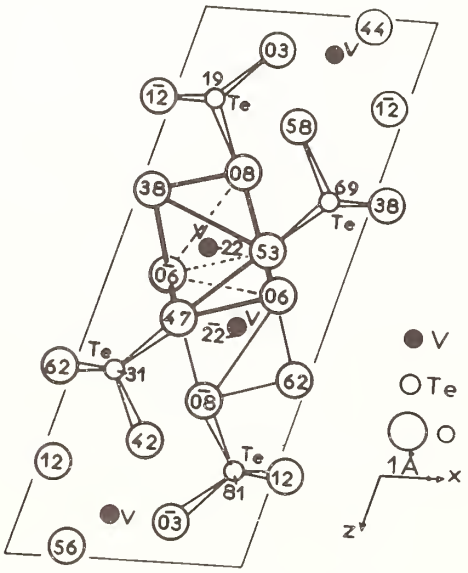

Fig. 7. (010) projection of α - $TeVO_4$.

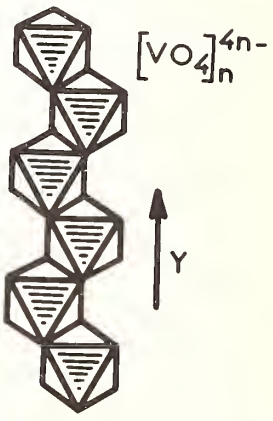

Fig. 8. $[VO_4]_n^{4n-}$ chains of VO_6 octahedra in α-$TeVO_4$.

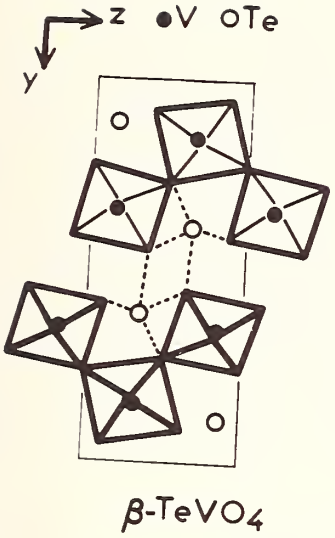

Fig. 9. (100) projection of β-$TeVO_4$.

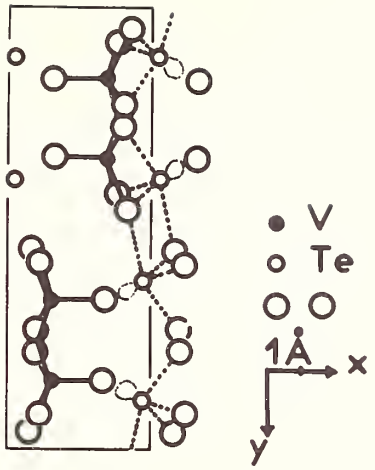

Fig. 10. (001) projection of β-$TeVO_4$.

Tellurium has a fourfold coordination; pairs of TeO_4 groups are connected by common edges to form Te_2O_6 units. The lone pair repulses two extra oxygen in the equatorial plane (O-Te-O) at more than 2.50 Å; its influence seems to be marked by the displacement of the 6th oxygen of the VO_6 octahedron.

This fact gives a $[VO_4]_n$ layer elongated in the direction of the a-axis, a = 4.379 Å instead of ~ 3.80 Å.

This structure shows resemblances with the triclinic $BiNbO_4$ phase [17] and the fluoride $BaZnF_4$ [18].

4.4. $MVTeO_5$ PHASES - (M = Li, Na, K, Rb, Ag)

Yellow crystalline $MVTeO_5$ compounds have been prepared by heating intimate mixtures of metavanadates MVO_3 and tellurium dioxide TeO_2 [19].

$$MVO_3 + TeO_2 \longrightarrow MVTeO_5$$

$LiVTeO_5$ crystallizes in the orthorhombic system (table 1); the structure determination is in progress. When M is the sodium, potassium, rubidium or silver they are all isostructurals and crystallize in the monoclinic system (table 1) [19,9].

The (100) projection of the structure is given in figure 11.

Vanadium atoms occupy the center of an oxygen tetrahedron; tellurium with a fourfold coordination form Te_2O_6 units as in β-$TeVO_4$.

Two Te_2O_6 units are linked together by two independent VO_4 tetrahedra (fig. 12). In this way, isolated chains with $(VTeO_5)_n^{n-}$ formula are built; they are parallel to the [110] direction. The sodium atoms surround these chains and assume the rigidity of the network.

5. STRUCTURAL RELATIONSHIPS

Our aim now is to show some relationships between these new tellurium compounds and some "lone pair" compounds of antimony Sb +III and lead Pb +II with simple structures.

In the first paragraph structural relations between the $TiTe_3O_8$ structure type and calcium fluorite have been established.

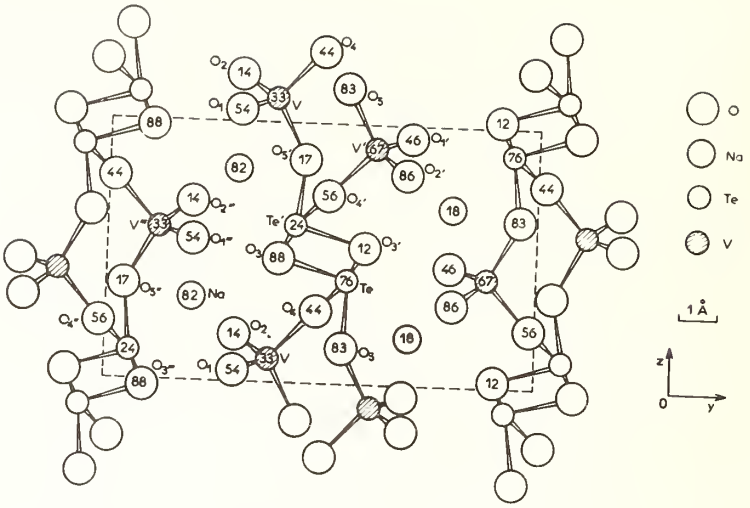

Fig. 11. (100) projection of $NaVTeO_5$.

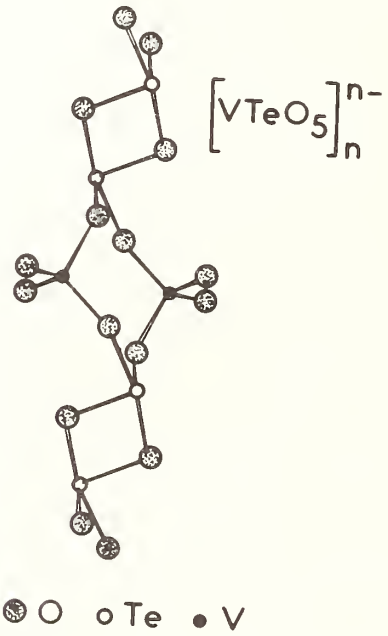

Fig. 12. $(VTeO_5)^{n-}_n$ chains in $NaVTeO_5$ crystal structure.

If we consider now the low temperature form of the tellurium vanadium oxide, α-$TeVO_4$, relationship with the α-PbO_2 structure type can be developed. Idealized drawings of both structures are given in figures 13 and 14. In both structures similar chains of MO_6 octahedra sharing edges are found. In α-PbO_2 these chains share corners; in α-$TeVO_4$ isolated chains of octahedra have identical orientation, the tellurium atoms just play a joining role.

An identical phenomenon is illustrated in the β-$TeVO_4$ structure where the $(VO_4)_n$ layers can be derived from the ReO_3 structure type if it is cut in the way indicated by the arrows (fig. 15). Tellurium atoms are inserted between the layers.

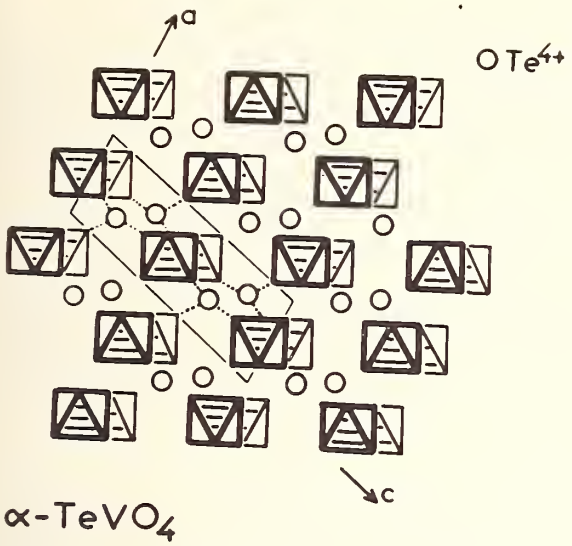

Fig. 13. Idealized α-$TeVO_4$ structure.

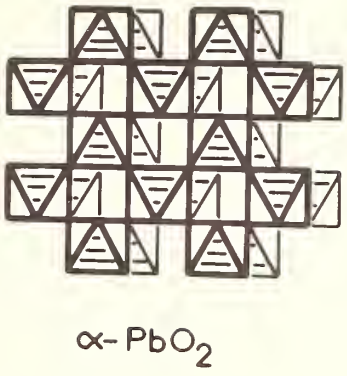

Fig. 14. Idealized α-PbO_2 structure.

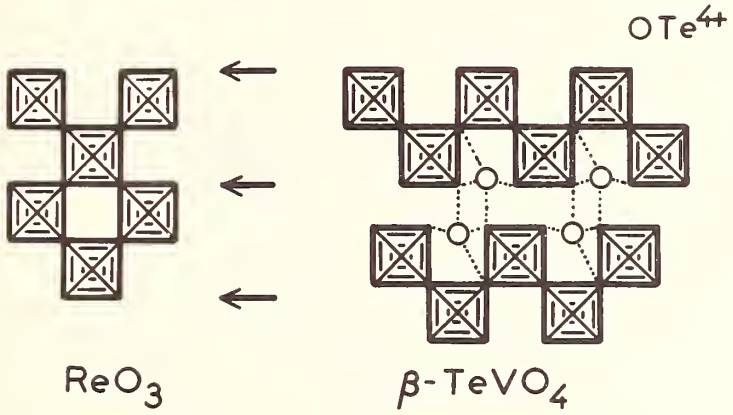

Fig. 15. Idealized β-$TeVO_4$ and its relation with the ReO_3 structure type.

In both the crystallographic forms of $TeVO_4$ the structural principles are the same: 1. A sub-array built around the transition element by the oxygens and deriving from simple structure like the α-PbO_2 and ReO_3 types. 2. Tellurium is inserted in these sub-arrays and do not disturb their orientation.

Some similar examples can be provided in other lone pair compounds. α-Sb_2O_4 and the isostructural compound $SbNbO_4$ exhibit layers of $(SbO_4)_n^{3n-}$ or $(NbO_4)_n^{3n-}$ (fig. 16) [20]; the antimony +III, which is characterized by a lone pair like the tellurium +IV, is inserted between the layers. These are directly derived from the PdF_3 structure if sections are made in the direction indicated by the arrows (fig. 17). The β-Sb_2O_4 structure is built on the same principle (fig. 18).

Pb_3O_4 constitutes another interesting example. The structure of Pb_3O_4 consists of isolated infinite chains of $Pb^{4+}O_6$ octahedra sharing edges (fig. 19) [21]; Pb^{2+} ions with a threefold coordination give the stability to the network. Here again, if we geometrically pack together the $(PbO_4)_n^{4n-}$ chains by corner sharing, the rutile structure is obtained (fig. 20). The chains in Pb_3O_4 have exactly the same orientation as in rutile.

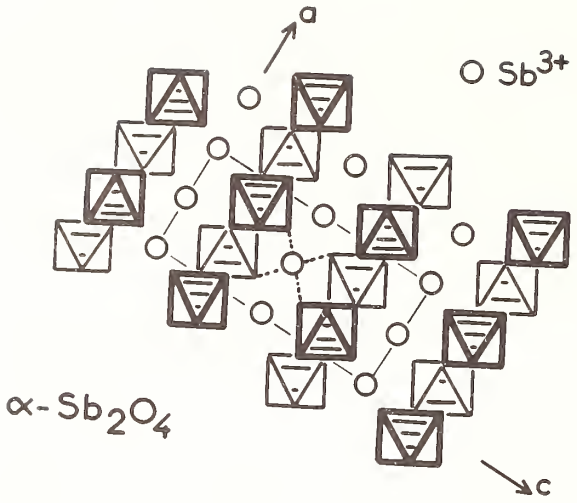

Fig. 16. Idealized α-Sb_2O_4 or $SbNbO_4$ structure.

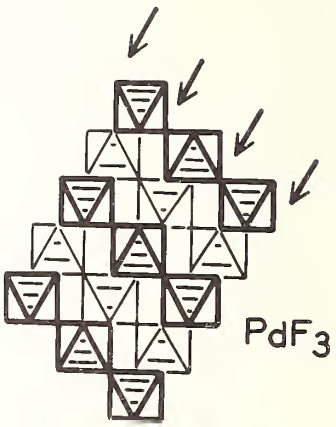

Fig. 17. Idealized PdF_3 structure.

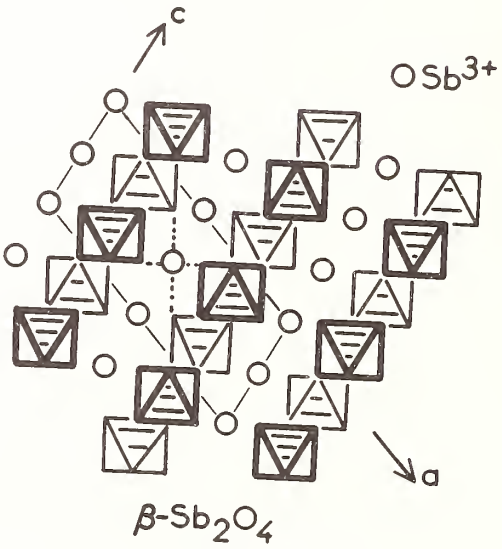

Fig. 18. Idealized β-Sb_2O_4 structure.

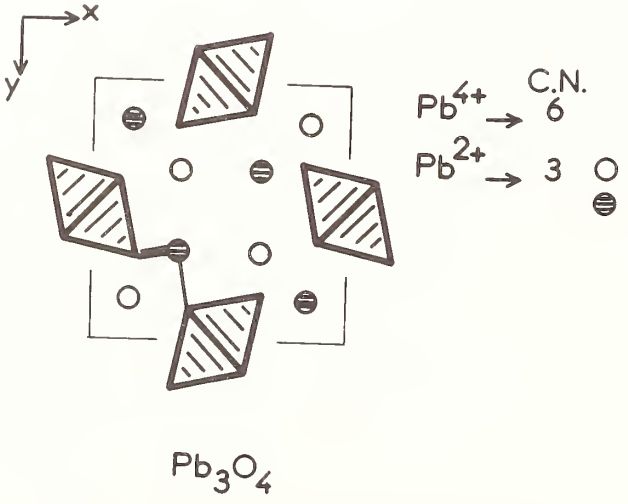

Fig. 19. Idealized Pb_3O_4 structure.

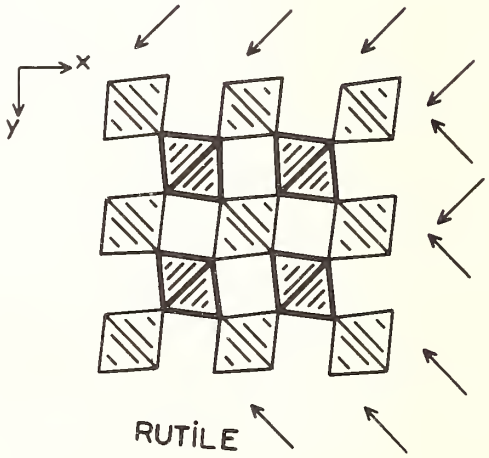

Fig. 20. Rutile structure.

In conclusion, these investigations on the crystal chemistry of some new mixed oxides of tellurium +IV have given some new interesting compounds; we have pointed out the ability of this element characterized by a lone pair to give structures with three-, two- or one-dimensional networks. Some physical measurements could be done, for example on the single and isolated chains $(VO_4)_n^{4n+}$ and such information should then be compared with the physical properties of vanadium +IV compounds.

The chemistry and structural chemistry of the elements like Ge^{2+}, Sn^{2+}, Sb^{3+}, Te^{4+}, I^{5+}, Xe^{6+}, Tl^{+}, Pb^{2+}, Bi^{3+} constitutes an important field of investigation.

The lone pair plays an important role in the structure formation of mixed compounds of these elements. We expect from the study of its influence on the structures and the coordination polyhedra, that results of great importance can be obtained to further our knowledge of the chemical bond.

6. REFERENCES

[1] Beyer, H., Sahl, K. and Zemann, J., Naturwiss, 52, 155 (1965).
[2] Beyer, H., Z. Kristollogr., 124, 228 (1965).
[3] Leciejewicz, J., Z. Kristallogr., 116, 345 (1961).
[4] Mandarino, J. A., Williams, S. J. and Mitchell, R. S., Mineral. Soc. Am. Spec. Paper, 1, 305 (1963).
[5] Galy, J. and Meunier, G., Acta Cryst., B27, 608 (1971).
[6] Hanke, K., Naturwiss., 53, 273 (1966).
[7] Meunier, G. and Galy, J., Acta Cryst., B27, 602 (1971).
[8] Meunier, G., Darriet, J. and Galy, J., to be published.
[9] Darriet, J., Guillaume, G., Wilhelmi, K. A. and Galy, J. Acta Chem. Scand., in print.
[10] Zemann, A. and Zemann, J., Acta Cryst., 15, 698 (1962).
[11] Matzat, E. Tschermaks Mineralog. Petrogr. Mitt., 12, 108 (1967).
[12] Walitzi, E. M., Tschermaks Mineralog. Petrog. Mitt., 10, 241 (1965).
[13] Dusausoy, Y. and Protas, J., C. R. Acad. Sc., 266C, 91 (1968).
[14] Hanke K., Naturwiss., 54, 199 (1967).
[15] Meunier, G., Darriet, J. and Galy, J., to be published.
[16] Meunier, G., Galy, J. and Hagenmuller, P., C. R. Acad. Sc., 270C, 1987 (1970).
[17] Keve, E. T. and Skapski, A. C., Chem. Commun., 281 (1967).
[18] Schnering, H. G. and Bleckmann, P., Naturwiss., 55, 342 (1968).
[19] Darriet, J., Guillaume, G. and Galy, J., C. R. Acad. Sc., 269C, 23 (1970)
[20] Skapski, A. C. and Rogers, D., Chem. Commun., 611 (1965).
[21] Fayek, M. K. and Leciejewicz, J., Report 499/II, Institute of Nuclear Research, Warsaw, Poland (1964).

DISCUSSION

N. C. Stephenson: You mentioned a repulsion of one of the oxygens by the lone pair electrons. Is it possible by looking at these types of distortions in these structures to determine roughly the size, the volume of these lone pair electrons and whether they vary from cation to cation?

J. Galy: You mean if it is possible to find exactly where is the center of the lone pair? I think in these compounds they do not fit in networks so nicely as in the compounds Dr. Andersson told us about in the first talk. However, in $TiTe_3O_8$ for example, I think it is possible perhaps because in $TiTe_3O_8$ you have two extra oxygens, which complete the central plane of the octahedra around tellurium with this oxygen around 2.9Å. In the structure of $TeVO_4$ for example, you have also two extra oxygens at around 2.7, 2.8Å. I think it could be possible to localize the importance of the lone pair. Perhaps, Dr. Andersson has an idea.

S. Andersson: On the airplane coming down here we did calculate oxygen volumes for your compounds.

J. Galy: They fit in your model.

S. Andersson: They do, yes. So you can see that the volume is the same as for the anion. But the packing and the nets here are more complicated. We are working with them.

National Bureau of Standards Special Publication 364, Solid State Chemistry, Proceedings of 5th Materials Research Symposium, issued July 1972.

CRYSTAL STRUCTURE AND PHYSICAL PROPERTIES OF A TRICLINIC SODIUM TUNGSTEN OXIDE*

H. F. Franzen,† H. R. Shanks,†† and B. H. W. S. deJong†

Institute of Atomic Research and Departments of Chemistry† and Physics††
Iowa State University, Ames, Iowa 50010

A triclinic sodium tungstate was prepared by the method of electrolysis of molten mixtures of Na_2WO_4 and WO_3 which has been used extensively in the preparation of sodium tungsten bronzes. The electrical resistivities and Seebeck coefficients of several samples were measured and are reported. A single crystal x-ray diffraction study yielded the tungsten atom positions. A structure is suggested which is consistent with the tungsten positions and the electrical properties. The suggested stiochiometry is $Na_6W_{14}O_{45}$. In the suggested structure the tungsten atoms are coordinated by distorted octahedra of oxygen atoms in all cases but one, in which case the tungsten is coordinated by a trigonal-bipyramid of oxygen atoms. The octahedra share corners in planes in a fashion similar to that found in the hexagonal bronze, and the sodium atoms are located in the resulting hexagonal holes.

Key words: Resistivity; Seebeck coefficient; sodium tungstate; structure.

1. INTRODUCTION

Large single crystals of sodium tungsten bronzes (Na_xWO_3) have been routinely prepared by fused salt electrolysis [1][1]. The stoichiometry of the crystals has been shown to be determined by the temperature and composition of the melt, and a variety of structures has been prepared in the Ames Laboratory. During the process of growing tetragonal sodium tungsten bronze crystals with x-values near 0.30 we obtained on a number of occasions crystals with apparent hexagonal symmetry. After additional investigation it was found that these crystals grow at or just above the melting point of the solution (fig. 1). When the temperature of the melt is increased 10 or 15 °C above the melting point the expected tetragonal bronze crystals are obtained. A photograph of a cluster of the triclinic crystals is shown in figure 2.

This paper is a report on the characterization of this material by crystallographic and electrical measurements.

2. EXPERIMENTAL

2.1. ANALYTICAL

The composition of the crystals was determined by neutron activation analysis. The sodium and tungsten concentrations were determined by the method reported by Reuland and Voigt [2] and the oxygen concentration was obtained by fast neutron activation analysis making use of the T(d,n) reaction. The results for five different samples are listed in table 1. On the basis of these results the compound was initially assigned the formula $Na_{0.33}WO_3$ although the data indicated a somewhat higher oxygen content.

*Work was performed in the Ames Laboratory of the U.S. Atomic Energy Commission. Contribution No. 3126.

[1] Figures in brackets indicate the literature references at the end of this paper.

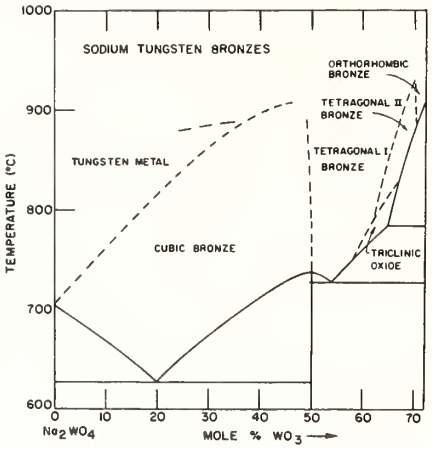

Fig. 1. The phases of sodium tungsten bronzes obtained by electrolysis as a function of melt composition.

Fig. 2. Crystals prepared by electrolysis.

Table 1

Crystal Composition from Neutron Activation Analysis

Sample No.	Wt % W ± σ	Wt 5 Na ± σ	Wt % O ± σ
1	76.09 ± 0.74	3.49 ± 0.04	19.9 ± 0.7
2	75.86 ± 0.81	3.14 ± 0.09	19.8 ± 0.3
3	76.81 ± 3.74	3.10 ± 0.13	19.7 ± 0.1
4	74.58 ± 1.15	3.33 ± 0.07	19.9 ± 0.3
5	77.42 ± 1.78	3.28 ± 0.06	20.0 ± 0.7
$Na_6W_{14}O_{45}$ (calc)	75.00	4.02	20.98
$Na_{0.33}WO_3$ (calc)	76.76	3.20	20.04

2.2. CRYSTALLOGRAPHIC

The sample was examined microscopically. The crystal habit was platy, with more or less well formed hexagonal plates forming aggregates with the plates joined by their flat surfaces. No optical twins were observed under a polarizing microscope. The aggregates were dark blue, however thin plates were transparent with a light green color. A fragment with the dimensions 30 μm x 53 μm x 73 μm was selected from a crushed portion of the sample, and this fragment was examined by the methods of single crystal x-ray diffraction.

Zero and first level Weissenberg patterns with the *a* axis as the rotation axis and a precession pattern with the *b* axis parallel to the x-ray beam were obtained. Single crystal x-ray diffraction data were collected using an automated Hilger-Watts diffractometer which is described elsewhere [3]. The data were collected using MoKα radiation filtered by zirconium. Integrated intensities were measured for all reflections with $0 \leq 30°$. A total of 2506 reflections with intensities greater than four times their estimated standard deviations was obtained.

To obtain data for the refinement of the lattice parameters the θ angles of 12 strong reflections were measured each 4 times to ± 0.01°. The 12 average values were used for a least squares refinement of the lattice parameters.

The Weissenberg and precession patterns showed that none of the arbitrarily chosen axes were symmetry axes. The lattice parameters obtained by a least squares refinement of the diffraction angles indexed on the basis of the arbitrary axes are: a = 18.474 Å, b = 12.577 Å, c = 7.300 Å, α = 29.94°, β = 85.43°, γ = 84.34°. The corresponding conventional reduced cell was found to have the parameters: a = 7.287 Å, b = 18.474 Å, c = 7.235 Å, α = 95.22°, β = 119.64°, γ = 89.40°. The density of the sample was determined using a pycnometer and was found to be 6.536 $g \cdot cm^{-3}$. Assuming the composition reported above there are 13.9 formula units per unit cell.

The diffraction intensities were corrected for Lorentz and polarization effects and for adsorption. The transmission factor coefficients were obtained using a computer program by Busing and Levy [4]. A Howells, Phillips and Rogers plot [5] gave a strong indication that the structure has a center of symmetry and a Wilson plot [6] yielded an overall temperature factor of 0.44 $Å^2$. The tungsten positions were determined both by the interpretation of the Patterson map and, later, by the direct method using Sayre's [7] relation. The two sets of tungsten positions were in complete agreement. The positions were refined by least squares refinement [8] to yield a conventional R factor of 18%. The resulting tungsten positions are given in table 2.

Table 2

Tungsten Atom Positions

Atom	x	y	z
W1	0.250(2)	0.0944(6)	0.014(2)
W2	0.759(2)	0.1291(6)	0.030(2)
W3	0.743(2)	0.0979(7)	0.512(2)
W4	0.269(2)	0.3137(6)	0.093(2)
W5	0.291(2)	0.3194(6)	0.619(2)
W6	0.776(2)	0.3159(6)	0.584(2)
W7	0.175(2)	0.4735(6)	0.331(2)

(a) Uncertainties in the last place are given in parentheses

Attempts to further refine the structure and locate the oxygen and sodium positions by Fourier techniques were unsuccessful. Difference Fourier syntheses did not provide definite locations for the light atoms, nor did least squares refinement of the structure obtained by positioning the oxygen atoms by analogy with other tungsten-oxide and tungsten-bronze structures, as discussed in a later section. A crystal θ, counter 2θ scan measuring the intensity at θ intervals of 0.01° over several of the diffraction peaks revealed two principal maxima separated by 0.06° independent of θ.

It was concluded that the sample chosen for the collection of intensity data was not suitable for a precise structure determination, and that the data obtained were not suitable for the positioning of the light atoms and refinement of the structure. Attempts to isolate smaller fragments suitable for the collection of data for a refinement were not successful. It was concluded that the electrolytically deposited samples consist of aggregates of plate shaped crystals with variations of alignment, and that the smallest samples that were selected (*ca.* 10 μm in the dimension perpendicular to the plates) consisted of such aggregates. The failure to obtain a suitable single crystal from the available samples of the material resulted in the termination of the x-ray crystallographic study at the point of the determination of the tungsten positions and a rough overall temperature factor, as described above.

2.3. ELECTRICAL

Electrical resistivity measurements were made on the a-b plane on four samples in the temperature range between 77 and 300 K. The resistivity decreased exponentially with increasing temperature in all the samples as shown in figure 3. The activation energy as determined from the slope of the plot $\ln_{\rho}$ versus $10^3/T$ was found to vary from one sample to another. The Seebeck coefficients were also measured for three of the four samples (fig. 4). The Seebeck coefficient of sample 4 increased rapidly near 77 K which *indicates a possible large phonon drag effect*. Electrical resistivities, activation energies, and Seebeck coefficients at 77 and 300 K are given in table 3.

The Hall effect was measured at 300 K on an additional sample with the use of an a.c. method. A value of -1.4×10^{-2} cm^3/coulomb was obtained. The sample had an electrical resistivity of 0.4 Ω - cm. If one assumes that the Hall coefficient R = 1/ne then the number of electrons n, is $4 \times 10^{20}/cm^3$ and the Hall mobility is $3.5 \times 10^{-2} cm^2$/volt sec.

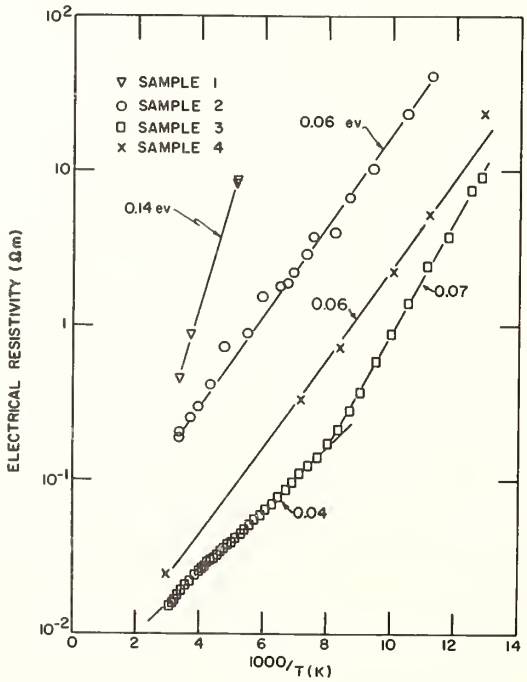

Fig. 3. Resistivities as functions of temperature.

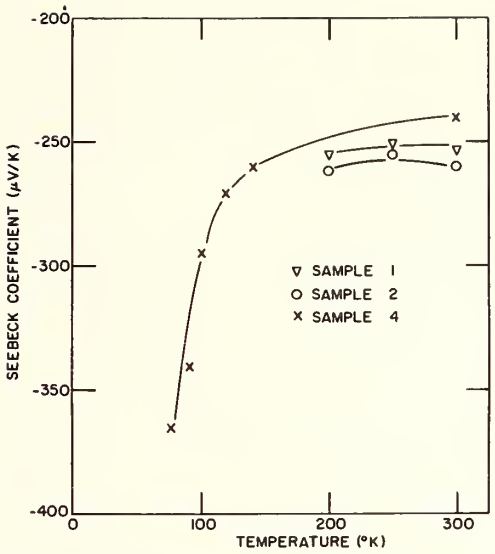

Fig. 4. Seebeck coefficients as functions of temperature.

Table 3

Electrical Resistivity, Activation Energy and Seebeck Coefficient for $Na_6W_{14}O_{45}$

Sample	ρ (Ω-m) 300 K	ρ (Ω-m) 77 K	Eg (ev)	S (mV/K) 300 K	S (mV/K) 77 K
1	0.47		0.14	-253	
2	0.19	100	0.06	-260	
3	1.5×10^{-2}	10	0.04 - 0.07		
4	2.5×10^{-2}	23	0.06	-241	-365

3. DISCUSSION

Figure 5 shows a vertical projection of the tungsten atoms within ±0.32 Å of 2.05 Å above the z = 0 plane onto that plane. The tungsten atoms in this region are considered to constitute the "first layer" in a structure which consists, to a first approximation, of five layers in a nearly hexagonal cell. The Slater [9] radius for tungsten of 1.35 Å was used in constructing the figure.

The tungsten atoms in the first layer are positioned relative to each other in a fashion similar to that found in the hexagonal bronze structure *e.g.* the hexagonal bronze $K_{0.27}WO_3$ with a = 7.40 Å [10]. This similarity leads to the suggestion that the tungsten atoms W1, W2 and W3 are separated by oxygen atoms at positions about 0.9 Å from the triangle connecting centers and midway between the centers, as are the tungsten atoms in the hexagonal bronzes. The W-W distances, given in table 4, are in good agreement with this suggestion.

The second layer consists of tungsten atoms within ±0.045 Å of 5.825 Å above the z = 0 plane and is shown in projection in figure 6. The tungsten atoms in the second layer are,

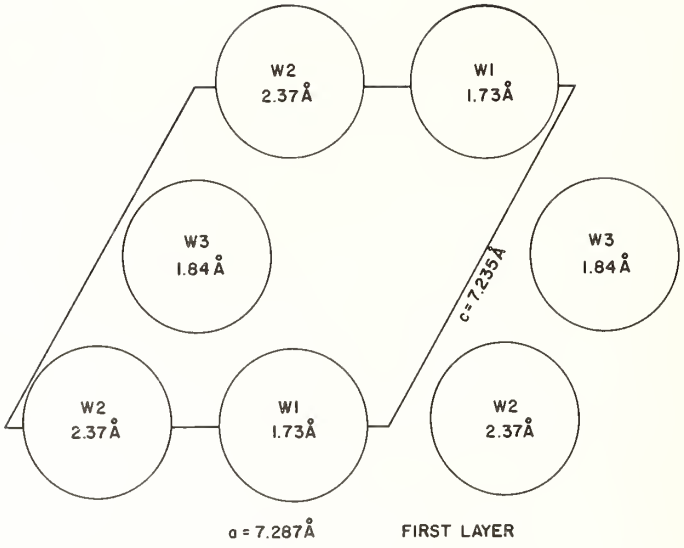

Fig. 5. Tungsten positions in the first layer.

Table 4

Tungsten-tungsten Distances

Atoms	Distances (Å)
W1-W2	3.71
W2-W3	3.67
W1-W3	3.65
W4-W5	3.70
W5-W6	3.68
W4-W6	3.62
W7-W7	4.17
W1-W4	4.09
W3-W6	4.01
W6-W7	3.89
W5-W7	3.52
W4-W7	3.47
W1-W2	4.17

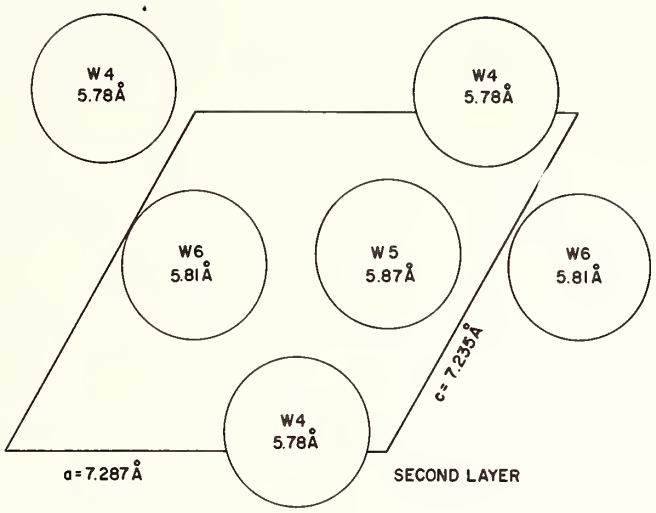

Fig. 6. Tungsten positions in the second layer.

as in the case of the first layer, structurally similar to the layers in the hexagonal bronzes. W4, W5 and W6 are separated by distances in the range 3.62 - 3.70 Å (the distances are given in table 4) which are again consistent with the suggestion that there are oxygen atoms located midway between the tungsten atom centers.

The position of the second layer relative to the first layer is shown in projection in figure 7. In this figure it can be seen that the two nearly hexagonal layers are located such that W2 in the first layer is below a hexagonal hole in the second layer, and W5 in the second layer is above a hexagonal hole in the first layer. Furthermore, W4 in the second layer is nearly vertically above W1 in the first layer, as is also the case of W6 relative to W3. The W1 - W4 distance is 4.09 Å and the W3- W6 distance is 4.01 Å, again leading to the suggestion of W-O-W separations.

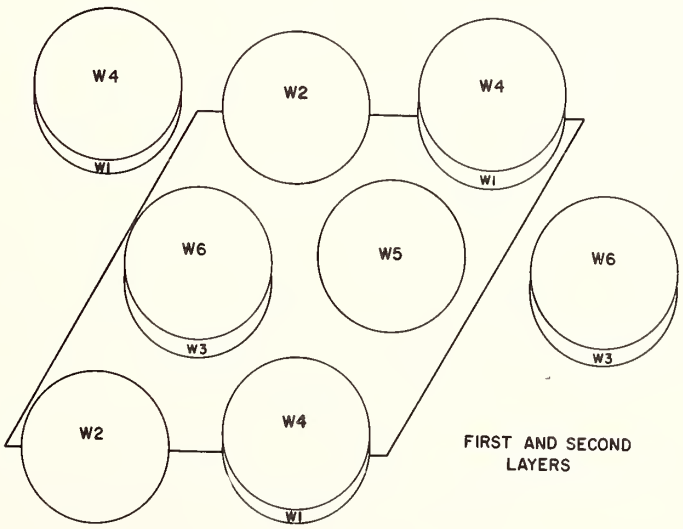

Fig. 7. The first and second layers in projection.

The third layer is shown in projection in figure 8 and the common projection of the second and third layers is shown in figure 9. The distances from the W7 atoms in the third layer to atoms in the second layer are 3.47 Å, 3.52 Å and 3.89 Å, again indicating W-O-W interactions.

The remaining two layers in the structure are related to the first and second layers by the centers of symmetry. The first layer is located relative to the fifth layer in the same way that the first is located relative to the second, and the W-W distance between layers is 4.09 Å, again suggesting a W-O-W distance.

In summary, the suggested structure consists of groups of four layers with roughly the structure found in the layers of the hexagonal bronzes, but with the layers arranged so that the hexagonal holes are not in vertical alignment, and a fifth, new type of layer linking the groups of four layers. The fifth layer contains tungsten atoms which are apparently linked to two tungsten atoms via oxygen atoms in one adjacent plane and to a third tungsten (again *via* an oxygen) in the plane adjacent in the opposite direction. The coordination of the tungsten atoms in the third layer is completed, it is suggested, by oxygen atoms completing the trigonal bipyramids. One oxygen is located at the center of symmetry at $\frac{1}{2}, \frac{1}{2}, \frac{1}{2}$ yielding pairs of corner sharing trigonal bipyramids (the W7-W7 distance is 4.19). It seems

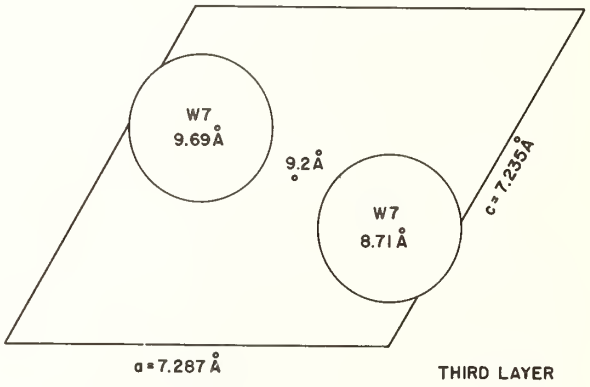

Fig. 8. Tungsten positions in the third layer.

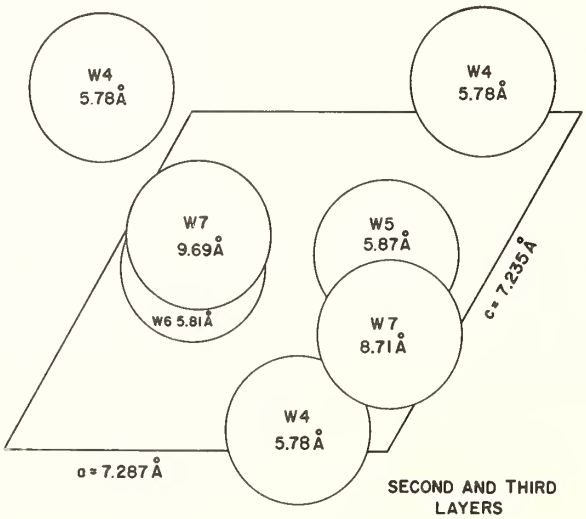

Fig. 9. The second and third layers in projection.

reasonable to suggest that the tungsten atoms located above or below the hexagonal holes in the adjacent layers complete coordination octahedra with oxygen atoms which project into the holes. The W/O ratio in the proposed structure is 14/45 = 0.311, which is in good agreement with the analytical results.

The occurence of oxygen atoms in excess of the O:W = 3:1 stoichiometry suggests an interpretation for the observed electrical properties of the solid. Namely, rather than being a bronze, the solid is a tungstate with the formula $Na_6W_{14}O_{45}$. The six sodium atoms per unit cell would then fit very nicely into the holes in the layers, and complete the coordinations of the oxygen atoms surrounding the holes.

Conduction is by electrons in this material since for all samples the Seebeck coefficient was found to be negative. The decrease in electrical resistivity in all samples with increasing temperature implies an activation energy. This activation energy may be associated with some impurity donor level just below the conduction band but, since different samples exhibit different activation energies, more than one donor level must exist.

An alternate explanation for the observed electronic properties is polaron type conduction similar to that proposed for doped NiO by Ksendzov et al. [11]. In this case, the changes in the slope of the $\ln\rho$ versus 1000/T curves are associated with the changes in the impurity concentrations. However, one can then not assume that the Hall coefficient measures the carrier concentration nor can the Hall mobility be calculated directly.

In either case the electrical properties of the material are not similar to the bronzes but do support crystallographic findings that it is a tungstate compound.

4. ACKNOWLEDGEMENT

The authors would like to thank A. Voigt's group for the neutron activation analysis work on this material.

5. REFERENCES

[1] Shanks, H. R., J. Cryst. Growth (to be published).
[2] Reuland, R. J., and Voigt, A. F., Anal. Chem. 35, 1263 (1963).
[3] Dahm, D. J., Benson, J. E., Nimrod, D. M., Fitzwater, D. R., and Jacobson, R. A., USAEC Report IS-1701 (1967).
[4] Busing, W., and Levy, H., Acta Cryst. 10, 180 (1957).
[5] Howells, E. R., Phillips, D. C., and Rogers, D., Acta Cryst. 3, 210 (1950).
[6] Wilson, A. J. C., Mature, 150, 152 (1942).
[7] Sayre, D., Acta Cryst. 6, 60 (1953).
[8] Busing, W. R., Martin, K. O., and Levy, H. A., USAEC Report ORNL-TM-305 (1962).
[9] Slater, J. C., Chem. Phys. 41, 3199 (1964).
[10] Magneli, A., Acta Chem. Scand. 7, 315 (1953).
[11] Ksendzov, Ya. M., Ansel'm, L. N., Vasil'era, L. L., and Latyshera, V. M., Soviet Physics - Solid State, 5, 116 (1963).

DISCUSSION

S. Andersson: The last thing you said, if you take out sodium, then you have too much oxygen, don't you?

H. F. Franzen: Yes, that's correct.

S. Andersson: Tungsten is only hexavalent in this phase isn't it?

H. F. Franzen: Yes, I would say that, and that does present some problems. I don't know how to rationalize the composition results but this ($Na_6W_{14}O_{45}$) is my preferred stoichiometry. Actually, if pressed, I would suggest that there is some trouble with the neutron activation analyses.

465-504 O - 72 - 5

M. J. Sienko: Your problems in reproducing the activation energy may actually reflect an anisotropy in the electrical conductivity. Did you try to orient the crystals for the conductivity measurements?

H. F. Franzen: They were necessarily oriented. The conductivities were measured by the four probe method and the only dimension suitable for that measurement was the flat plate direction. Oh, orientation within the plane, no, no attempt was made to do that.

B. M. Gatehouse: You didn't comment on the possible stereochemistry of the sodium site, or did I miss that?

H. F. Franzen: You mean the configuration of the oxygen atoms around the sodium sites? The resultant configuration in the bronze layers is a hexagonal ring of oxygen atoms, an oxygen atom above and an oxygen atom below. The configuration in the trigonal bi-pyramidal layer is a pretty severe distortion of that although elongated somewhat. Of course we can't give an accurate estimate of the distortion because the oxygens have been positioned only by conjecture and we don't have refined parameters for the oxygen positions.

E. Banks: Have you considered the possibility that the electrical measurements may actually be measurements of a composite in which you have a bronze phase interleaved with some tungsten 6^+ tungstate? This would easily account for the kind of variability that has been observed. What you would really be measuring would be a contact resistance which is variable with all sorts of things.

H. F. Franzen: No.

J. H. Perlstein: I would like to agree with Dr. Banks. I would think that your statement that the material is probably not a single crystal would agree with your electrical conductivity measurements of showing a semiconductor type of behavior. I am also a little confused about your statement that the material is insulating, yet you report conductivities that seem to be extremely high, almost as high as some bronzes that have conductivities of 10 to 100 inverse ohm centimeters.

H. F. Franzen: Well, if I said that it was insulating then I made a slip of the tongue. What I meant was relative to the metallic bronzes. There is present an activation energy for the conductivity. The conductivity is down by a couple of orders of magnitude from the related bronzes in the same composition region. No, I don't claim that it is an insulator, but it is far more to that side than are the metallic bronzes.

J. H. Perlstein: Okay, then it seems very plausible that until you can get some single crystals from this phase, that to conclude that the ground state is insulating is open to question. It is possible that the material really is metallic, and that the semi-conducting behavior is due to the grain boundaries that might be present in the material.

National Bureau of Standards Special Publication 364, Solid State Chemistry, Proceedings of 5th Materials Research Symposium, issued July 1972.

ELECTROCHEMICAL PREPARATION AND CHARACTERIZATION OF ALKALI METAL TUNGSTEN BRONZES, M_xWO_3

M. S. Whittingham and R. A. Huggins

Department of Materials Science and Engineering
Stanford University
Stanford, California 94305

When a current is passed through two inert electrodes immersed in a molten solution (~750 °C) of alkali metal tungstate, M_2WO_4, and tungsten oxide, WO_3, oxygen is liberated at the anode and a crystal of tungsten bronze, M_xWO_3, where $0<x<1$, formed at the cathode. The potential difference between the electrodes is related to the oxygen concentration gradient across the cell. Thus, if the electrical potential difference across the cell, rather than the current or current density, is kept constant, crystals with a fixed oxygen activity and hence composition (stoichiometry) will be grown. Measurements of the decomposition potential of melts of M_2WO_4 and WO_3 of different composition, and of the oxygen activity in tungsten bronzes allows a type of phase diagram relating oxygen activity to the alkali metal/tungsten ratio in both liquid and solid phases to be constructed. Using this thermodynamic approach, it is possible to rule out certain suggested reaction intermediates in the electrolytic process and to explain both the overlapping stoichiometric ranges of some phases and the effects of reacting electrodes on the decomposition potential.

Key words: Crystal growth; electrolysis; nonstoichiometry; reaction mechanisms; thermodynamics; tungsten bronze.

1. INTRODUCTION

The tungsten bronzes are nonstoichiometric compounds of general formula M_xWO_3 where M is usually a monovalent cation and x is in the range 0 to 1. These materials have been the subject of a number of reviews in recent years [1-3][1], and so their general properties will not be repeated here. They are of much interest particularly because of their exceptionally wide stoichiometry ranges, which are most marked for the case of sodium where x may vary all the way from zero to unity.

The sodium tungsten bronzes were first prepared by the electrolysis of molten mixtures of sodium tungstate and tungsten trioxide over a century ago by Scheibler [4]. In this method a tungsten bronze is formed at the cathode, and oxygen is generated at the anode; both electrodes are usually platinum wire. Since that time bronzes, with sodium replaced by Li, K, Rb, Cs, Tℓ, Cu, Ag and the rare earth metals have been formed by this technique. Although voltages and currents as high as 6 volts and 5 amps (with "current densities" as high as 60 amp/cm^2) [5,6] have been used, more typical values are 1-1.5 volts, and 10-20 ma. The effect of these very different electrical parameters on the nature of the bronze product formed has not previously been considered, and frequently even details of the preparative procedures are omitted. Apart from the recent work of Fleischmann [7], who made a study of the electrodeposition of the bronzes to elucidate the species present in solution, there has been no serious attempt made to understand the processes occurring during the decomposition of these melts to form tungsten bronzes.

[1]Figures in brackets indicate the literature references at the end of this paper.

Although discovered originally by Wöhler [9] in 1824, there is still today no published thermodynamic data on any tungsten bronze system. It is the purpose of this paper to discuss the thermodynamic aspects of the processes occurring during the electrolytic decomposition of tungsten melts to form sodium and potassium tungsten bronzes.

2. EXPERIMENTAL ASPECTS

2.1. MATERIALS AND APPARATUS

Sodium tungstate, potassium tungstate, and tungsten trioxide of reagent grade were obtained from Alfa Inorganics and Research Inorganic Chemicals. All were dried by heating at 500 °C, and checked for purity of phase by x-ray analysis.

The electrolyte cell arrangement consisted of a Coors 3 Gooch crucible set inside a Coors 1A crucible, and is shown in figure 1. This setup keeps the oxygen liberated at the anode away from the bronze formed at the cathode. The electrodes were usually pure platinum or gold; whereas the platinum anode was found to be attacked, no reaction appeared to occur with gold. No inert atmosphere was used, as it has been shown here and previously [7] that the presence of oxygen in the atmosphere has no measurable influence upon the current-potential relationships obtained.

2.2. PROCEDURE

Before any current-potential relationships were measured, a current of 10 ma was passed through the cell overnight so that the cathode was first covered with bronze. The potential across the cell was then measured as a function of the current flowing, for currents from 5 to 40 ma and over about a 150 °C temperature range above the melting point. At least twenty readings were taken at each temperature, either manually or by means of a Digital Equipment Corporation Lab 8 computer system; a linear relationship was found, and the decomposition potential, E_o, was then calculated by means of a least squares analysis on the computer. To insure maximum linearity only potential values obtained for currents in excess of 15 ma were considered. The shape of the curves obtained is shown in figure 2.

In addition, the open circuit voltage, OCV, was determined in a number of cases. If potentials less than the OCV were applied, the current flowed in the opposite direction, causing bronze to be dissolved from the cathode. As this caused poor reproducibility in the current-voltage curves, a current rather than a voltage source was used so that the voltage could never fall below the OCV value.

The phases formed at the cathode were characterized by x-ray analysis, using a Picker x-ray diffractometer with a solid state detector and CuKα radiation, as well as by crystal form and color.

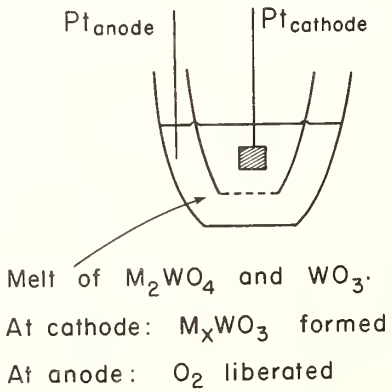

Fig. 1. Cell system for the electrolytic growth of the tungsten bronzes, M_xWO_3.

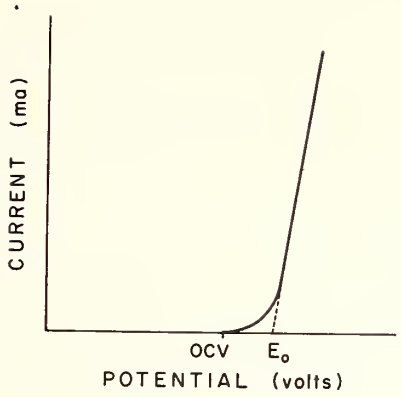

Fig. 2. Typical current-potential relationship, using platinum electrodes.

3. RESULTS

3.1. DECOMPOSITION POTENTIAL

The decomposition potential, E_o, is plotted as a function of the bath composition at 750 °C for the sodium and potassium systems in figures 3 and 4 respectively. It was found that gold electrodes gave values of E_o about 10 mV higher than those obtained with platinum electrodes. As the error in these measurements is also about 10 mV, no differentiation will be made here between the two sets of results. It is to be noted that the slopes of the E_o-composition curves change at the phase boundaries.

The shape of the crystals prepared in this reaction was determined by the crystal structure. Thus those with the hexagonal crystal structure were formed as rods of hexagonal cross-section, up to 1 cm on an edge, and the tetragonal as rods of square or rectangular cross-section. The latter could be grown readily as rather thin needles, but in order to form material of large cross-section (up to 0.7 cm) it was found necessary to use a seed crystal and to mechanically prevent growth along the rod axis. The phase with the cubic perovskite structure grew as cubes in melts of high sodium content but as dodecahedrons at

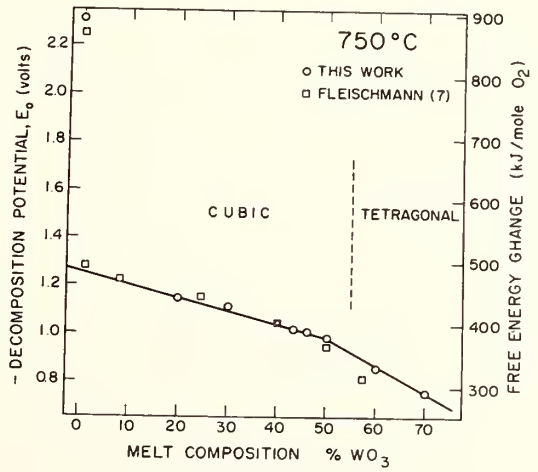

Fig. 3. Decomposition potential, E_o, versus melt composition for sodium system.

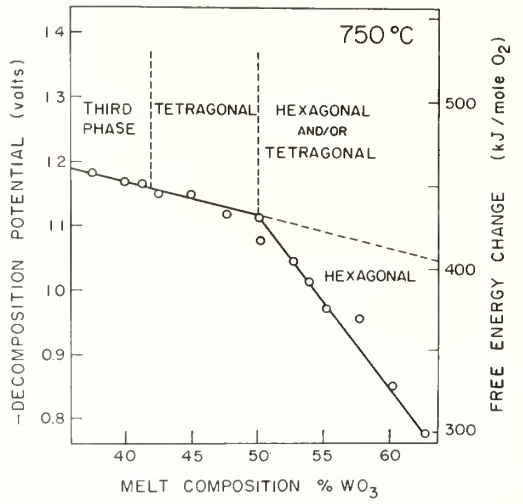

Fig. 4. Decomposition potential, E_o, versus melt composition for potassium system.

the low sodium content end of this phase. The third phase in the potassium system did not have a well defined crystal form, and was of unknown composition. Attempts to interpret the x-ray data have not been successful to date. However, this phase is of interest because its color, blue, indicates that it has fewer free electrons [10] than the purple tetragonal structure and about the same number as the hexagonal, blue, phase despite being formed from baths of highest potassium content.

A number of different electrodes were used in a bath of composition 46%WO_3:54%Na_2WO_4; in every case the anode and cathode were of identical material. The results of these experiments are shown in figure 5.

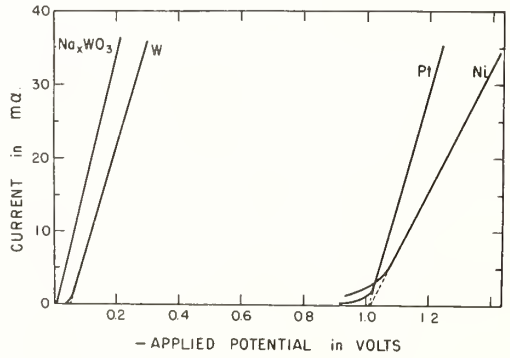

Fig. 5. Current-applied potential curves for 46% WO_3: 54% Na_2WO_4 at 750 °C using various electrode materials.

3.2. OPEN CIRCUIT VOLTAGE

The open circuit voltage was measured on a number of cells after bronze had been deposited at the cathode. These values are plotted in figure 6 as a function of the bath composition for both the sodium and potassium systems.

A zirconia solid electrolyte tube was used as the cathode in one experiment, 42.3%WO_3: 57.7%Na_2WO_4, so as to measure the oxygen activity; the setup is shown in figure 7. The potential across this tube was found at 750 °C to be 0.87 V compared to a cell OCV of 0.90 V. This difference of 30 mV is due to the difference in oxygen partial pressure between that at the anode (1 atmosphere) and that on the inside of the zirconia tube (0.2 atmospheres). The potential drop across the zirconia electrolyte was also measured as a function of the potential applied to the cell. It was found to increase by less than 2% for a change of the latter from open circuit to 4 V. The results are shown in figure 8.

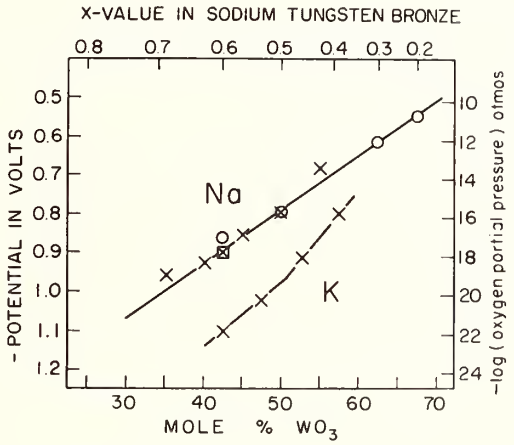

Fig. 6. Open circuit voltage, OCV, measurements. (Potentials relative to oxygen electrode at 1 atmosphere O_2). X OCV on cell; □ zirconia cathode potential; ○ powder preparation zirconia potential.

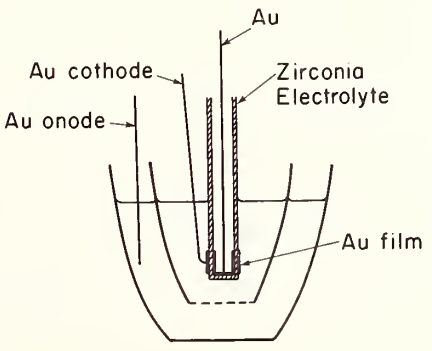

Fig. 7. Zirconia tube cathode cell assembly.

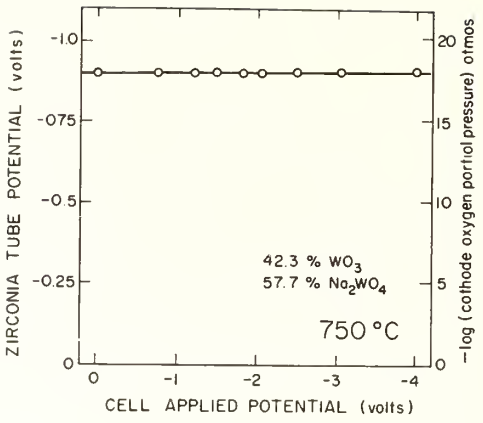

Fig. 8. Zirconia tube potential versus cell potential. (Potentials relative to oxygen electrode at 1 atmosphere O_2).

The potential drop across a zirconia tube was also measured during the solid-state reaction [1,11]:

$$x/2\ Na_2WO_4 + \frac{3-2x}{3}\ WO_3 + x/6W \rightarrow Na_xWO_3. \qquad (1)$$

These results are included in figure 6 as a function of the x value.

4. DISCUSSION

The values of decomposition potential obtained here are in reasonable agreement with those of Fleischmann, et al. [7,8]. In addition, they and Sienko [12] also observed a sharp decrease in E_o when a tungsten or tungsten bronze anode was used rather than a noble metal. The sodium bronze system was found to obey the approximate empirical relationship [7,8]

$$m(\text{bronze}) \approx 1/2\ m(\text{melt}) \qquad (2)$$

where m = (atoms of metal)/(atoms of metal + molecules of WO_3), suggested for the sodium and copper systems. However, this relationship clearly does not hold for the potassium system, as the hexagonal phase may be formed at compositions exceeding 50%WO_3 where m is unity, yet the maximum possible value of x in this phase is 0.33, thus the maximum value of m in this bronze is 0.25.

In the electrolytic preparation of the tungsten bronzes, the melt composition is being depleted in oxygen forming the lower oxygen content bronze at the cathode with evolution of oxygen at the anode. The decomposition potential is a direct measure of the energy required for this reaction. Thus it is possible to calculate the free energy of the reaction, ΔG, using the expression, $\Delta G = -4\ E_oF$ (per mole of oxygen) where F is Faraday's constant. These values are given in figures 3 and 4. Following the method of Johnson [13] the most probable electrode reactions can be deduced. For the sake of simplicity it will be assumed that the only tungstate specie present is M_2WO_4, the tungsten oxides between WO_3 and WO_2 will be ignored, and in the initial analysis that the bath has a composition of $M_2WO_4 \cdot WO_3$, *i.e.*, $M_2W_2O_7$.

The anode reaction is then:

$$W_2O_7^{2-} = 2WO_3 + 2e^- + 1/2\ O_2. \qquad (3)$$

The possible cathode reactions are:

$$W_2O_7^{2-} + xe^- = WO_4^{2-} + WO_3^{x-} \quad (4)$$

$$2W_2O_7^{2-} + 2e^- = 3WO_4^{2-} + WO_2 \quad (5)$$

$$4W_2O_7^{2-} + 6e^- = 7WO_4^{2-} + W \quad (6)$$

$$M^+ + e^- = M. \quad (7)$$

These give four possible overall reactions:

$$\frac{2(2+x)}{x} M_2W_2O_7 = 4WO_3 + \frac{4}{x} M_2WO_4 + \frac{4}{x} M_xWO_3 + O_2 \quad (8)$$

$$6M_2W_2O_7 = 4WO_3 + 6M_2WO_4 + 2WO_2 + O_2 \quad (9)$$

$$\frac{14}{3} M_2W_2O_7 = \frac{14}{3} M_2WO_4 + WO_3 + 2/3\ W + O_2 \quad (10)$$

$$2M_2W_2O_7 = 4WO_3 + 4M + O_2. \quad (11)$$

The measured free energy of reaction corresponds to one of the above. However, because of the sparcity of thermodynamic data for the tungstates, it is not possible in this case to calculate the theoretical decomposition potentials.

There is, however, one further piece of information that gives more insight into the most probable reaction; that is the open circuit voltage, OCV. As the OCV measured on the cell was the same as that measured by the zirconia tube cathode, it must be a measure of the oxygen concentration change across the cell. This OCV can be related to the oxygen partial pressures at the cathode and anode by the Nernst expression:

$$OCV = \frac{RT}{4F} \ln (p_{O_2} \text{ cathode} / p_{O_2} \text{ anode}). \quad (12)$$

At 750 °C, and for a 1 atmosphere pressure of oxygen at the anode this reduces to

$$OCV = 0.0507 \log_{10} (\text{oxygen partial pressure at cathode}). \quad (13)$$

These values of cathodic oxygen pressure are given in figure 6. If any of the species in Eqs (8-11) are oxidized at these partial pressures then they cannot exist in the melt. The oxygen pressures at which oxidation of WO_2, W [14], K, and Na [15] will take place at 750 °C are given in table 1. Thus, at the electrical potentials and compositions considered here there is no possibility of the presence of either sodium or potassium in an unoxidized state. WO_2 and W also can only be formed over a limited melt composition range, and indeed there have been no reports of their formation from either sodium or potassium melts at this temperature and at the applied voltages used, < 1.5V. However, we have made single crystals of the dioxide from a lithium tungstate-tungsten trioxide bath under these conditions. The suggestion proferred by Sienko and Mazumber [16] that the metal M might be a primary cathode product, or WO_2 a primary anode product, and that these species reduce the melt to form the bronze, is thus not possible, (the oxygen activity at the anode is 1 atmosphere when oxygen gas is being evolved, and thus there is no possibility of reduced species in the anode region). In addition, as figure 6 shows, the oxygen activity at the cathode is the same as that of the sodium tungsten bronzes, measured in an independent reaction.

Equation (8), the most likely reaction, can be rewritten in a more general form to cover any melt composition:

$$2\left(\frac{2+xy}{xy}\right)(M_2WO_4 \cdot yWO_3) = 2(1+y)WO_3 + \frac{4}{xy} M_2WO_4 + \frac{4}{x} M_xWO_3 + O_2. \quad (14)$$

Table 1

Oxidation Pressures for Metal Species at 750 °C.

Specie	- log p_{O_2} (atmospheres)	-OCV (volts)
WO_2	18.8	0.95
W	20.3	1.03
K	24.0	1.22
Na	28.5	1.45

The results of figure 5 can now be readily explained in terms of the change in free energy of the reaction. For platinum or gold electrodes the oxygen is liberated at the anode and the free energy change is that for equation (14). In the case of nickel, the anode rapidly becomes covered with a protective layer of oxide and behavior typical of an inert metal is observed. The different slope for the nickel is due to the increased electrical resistance of the system due to this protective oxide layer. The slope of the current-applied potential curve is simply due to the resistive load between the electrodes. For tungsten electrodes, oxygen is not evolved at the anode, but instead tungstic oxide is formed, so that the free energy of reaction in this case will be reduced by the free energy of formation of WO_3, which is equivalent to about 1 volt of applied potential. Thus, the decomposition potential observed in this case is almost zero. This is a slight over-simplification as the tungsten oxide formed will be dissolved by the melt, with an associated free energy change. For the bronze electrodes, no free energy change is expected as the bronze is simply being dissolved from one electrode and deposited at the other.

Equation (14) can be simplified still further to give

$$2\ (\frac{2-x}{xy})M_2WO_4 \cdot yWO_3 = 2\ (\frac{2-x-xy}{xy})M_2WO_4 + \frac{4}{x}M_xWO_3 + O_2. \qquad (15)$$

This expression does not represent the reaction for which the free energy is known but merely indicates the stoichiometry of the reaction. It is clear from this, however, that as the bronze is grown, the bath becomes enriched in the alkali metal, which will cause the decomposition potential to increase with time. This has been observed to occur in both the sodium and potassium systems. It is important to recognize that this may cause a change in the x-value of the growing bronze with time; in cases where the homogeneity of the bronze formed is of importance, it will thus be necessary to use a large volume of melt so as to minimize any possible composition changes. It should be pointed out that in the case of the hexagonal and tetragonal I phases, the mobility of the M ions within the solid is probably high enough to prevent the maintenance of any appreciable concentration gradient within the crystal as a result of changes in the bath composition. This is probably not the case, however, for the cubic sodium tungsten bronzes.

From figures 3, 4, and 6 it can be clearly seen that the decomposition potential is directly related to the oxygen activity at the cathode. As the oxygen activity is a function of the bronze composition it may be possible by varying the applied potential to change the stoichiometry and even the structure of the phase formed at the cathode. These possibilities may be seen by consideration of figures 9 and 10, in which both the melt and the resultant bronze compositions are plotted as a function of the decomposition potential. These figures are analogous to the familiar temperature-composition phase diagrams, but here the electric potential rather than the temperature is the variable. It is quite common to saturate a solution by lowering the temperature, causing precipitation of a solid phase, and this is readily describable in terms of a conventional temperature-composition phase diagram in which the compositions of both the solid precipitating phase and the liquid are given by a horizontal isothermal tie-line joining the liquidus and solidus lines. In the present case,

however, saturation is accomplished by lowering the oxygen activity, rather than the temperature. Nevertheless, one can draw an analogous potential-composition phase diagram, and represent the compositions of the liquid and product phases at any specified potential by means of a horizontal isopotential tie-line.

To cause crystal growth at the cathode, it is necessary to exceed the decomposition potential, so as to cross the liquidus line. This excess potential is used primarily to overcome the resistive drop across the cell but part may be used to further decrease the oxygen activity at the cathode. Figure 8 shows the effect of the applied potential on the cathodic oxygen activity. An increase of about 14 mV in the potential across the zirconia tube was observed in increasing the cell applied potential from open circuit to 4 volts. This corresponds to a change in the x value of the bronze of less than 0.02. However, the effects of a long term high voltage were not determined. The effect of the cell potential is much more important for compositions close to phase boundaries. Figures 9 and 10 show

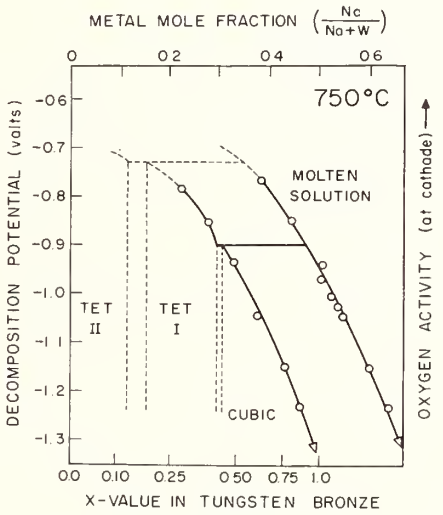

Fig. 9. Oxygen activity - composition diagram for sodium system.

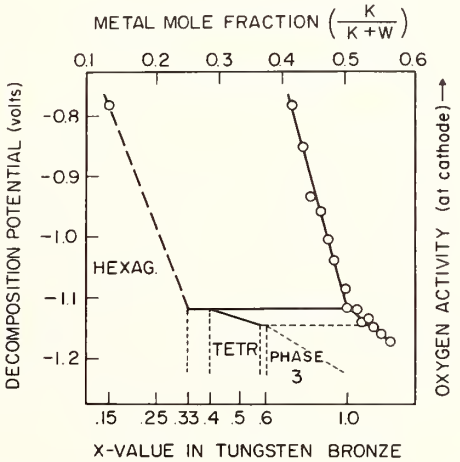

Fig. 10. Oxygen activity - composition diagram for potassium system.

that if the melt composition is at the edge of the tetragonal I phase in the sodium system or the hexagonal phase in the potassium system, the application of a slightly greater potential could readily lead to the formation of a different phase, cubic in the former case, and tetragonal in the latter. That this does, in fact, occur is shown in figure 4. If potentials above the dashed line, in the hexagonal composition range, were used, the tetragonal, the hexagonal, or both phases were formed. However, if the potential was kept below this line only the hexagonal phase was found. Thus, it is important to carefully control the potential drop across the cell in the growth process in order to obtain homogeneous material of a single phase.

The linearity of the sodium curve in figure 6 indicates that there is very little thermodynamic driving force for interconversion of the cubic and tetragonal I bronze phases. As the crystal structures are very different, so that interconversion requires complete rearrangement of the WO_6 octahedra, it is not surprising that the cubic phase is sometimes found at low x values [17] more typical of the tetragonal I structure [18].

5. CONCLUSIONS

By a consideration of the thermodynamic aspects of the electrolytic growth of the tungsten bronzes, it has been possible to rationalize both the structures and compositions of the products formed, as well as the composition dependence of the decomposition potential. In addition, this approach provides insight into the conditions necessary for the growth of homogeneous products of desired composition and phase.

6. ACKNOWLEDGEMENT

We should like to thank the Advanced Research Projects Agency (through its IDL Program) and the National Science Foundation for support of this program; also Professor Ephraim Banks for providing a copy of C. Fleischmann's thesis, and G. Gür and J. Ross for help in the experimental part of this work.

7. REFERENCES

[1] Dickens, P. G. and Whittingham, M. S., Quart. Rev. 22, 30 (1968).
[2] Banks, E. and Wold, A., in *Preparative Inorganic Reactions* (W. L. Jolly, Ed.) 4, 237 (1968).
[3] Hagenmuller, P., in *Progress in Solid State Chemistry* (H. Reiss, Ed.) 5, 71 (1971).
[4] Scheibler, C., J. Prakt. Chem. 83, 273 (1861).
[5] Conroy, L. E. and Sienko, M. J., J. Amer. Chem. Soc. 74, 3520 (1952).
[6] Utsumi, S. and Fujieda, S., Bull. Chem. Soc. Japan 43, 1714 (1970).
[7] Fleischmann, C. W., PhD Dissertation, Polytechnic Institute of Brooklyn, June 1970.
[8] Banks, E., Fleischmann, C. W., and Meites, L., J. Solid State Chem. 1, 372 (1970).
[9] Wöhler, F., Ann. Physik 2, 345 (1824).
[10] Dickens, P. G., Quilliam, R. M. P., and Whittingham, M. S., Mat. Res. Bull. 3, 941 (1968).
[11] Dickens, P. G. and Whittingham, M. S., Trans. Faraday Soc. 61, 1226 (1965).
[12] Sienko, M. J., J. Amer. Chem. Soc. 81, 5556 (1959).
[13] Johnson, K. E., in Proc. 3rd Int. Symp. High Temp. Mat., California, 1967. Butterworths (1969).
[14] Rizzo, F. E., Bidwell, L. R., and Frank, D. F., Trans. Met. Soc. AIME 239, 1901 (1967).
[15] Swalin, R. A., *Thermodynamics of Solids*, John Wiley and Son (1962).
[16] Sienko, M. J. and Mazumber, B. R., J. Amer. Chem. Soc. 82, 3508 (1960).
[17] McNeill, W. and Conroy, L. E., J. Chem. Phys. 36, 87 (1962).
[18] Ribnick, A. S., Post, B., and Banks, E., in *Nonstoichiometric Compounds* (R. Ward, Ed.) Amer. Chem. Soc. Advances in Chemistry Series 39, 246 (1963).

DISCUSSION

E. Kostiner: Just a point of information. We were using sodium tungstate melt a few years ago to grow transition metal oxides by anodic electrolysis. I believe we were at the eutectic in the sodium tungstate-tungsten trioxide system using essentially the same potentials as used for bronze growth. We found the formation of sponge tungsten on the cathode.

E. Banks: Bronzes also.

E. Kostiner: And bronzes, but there was sponge tungsten formed on the cathode. This of course, may be a function of the transition metals present in the system.

M. S. Whittingham: In order to form tungsten at the cathode you must exceed about 1.4 volts across that cell. Otherwise, it's just not possible to form it, unless you were using a tungsten or some other reacting metal anode, thereby lowering the oxygen activity at that electrode. This would make a lot of difference. (This value of 1.4 volts is about 350 mV higher than the OCV, shown in Table 1 for tungsten formation, and the excess is used to overcome the decomposition potential and to provide a reasonable current flow.)

E. Kostiner: Well, perhaps we were then, but we were using platinum electrodes. I don't think we were above one and a half volts.

M. S. Whittingham: It's about 1.4 volts where you would expect tungsten may be formed.

P. Hagenmuller: You raise a question in my mind. You fix your potential having a constant d-electron density, but I believe it can be due to two reasons. The first one, you have a constant sodium rate, but the second one is you are also able to have an oxygen-tungsten ratio below three. So, in fact you have two composition parameters which can be influenced by your potential. Is it true?

M. S. Whittingham: Yes, we have made one major assumption in all this and it is that the tungsten to oxygen ratio is fixed and we are in fact at the moment doing measurements to determine whether this tungsten-oxygen ratio can change and if so, by how much.

R. Ward: It might be of interest to mention that some years ago one of our students was trying to make a mixed tungsten-molybdenum bronze by electrolytic reduction. The product he got was a black crystalline hexagonal looking plate, very similar to the ones described in the previous paper. They were also very poor conductors and they were multiply twinned. One could see the striations on the faces. We never did get any idea of what the structure was. The composition was somewhere around about sodium .25 with about a tenth of molybdenum in there as a maximum and nine-tenths tungsten. And these were produced using platinum electrodes. Later on, in further investigations, the student found that you get these just at higher temperatures without any electrodes at all. I don't know what the composition was, but they were very black and they were non-conductors. We thought we had a lower oxidation state of molybdenum present just as the higher temperatures can get sometimes, but we could get them without any source of reduction.

M. S. Whittingham: This is similarly observed in the vanadium system. One can, in fact, form sodium-vanadium bronzes without any electrolytic reduction[1]. The oxygen has just evolved by itself. In other words, the oxygen partial pressure is in excess of that in one atmosphere of air[2] and this may be similar to what you have observed.

D. J. Lloyd: If I may just add to that, and it's also relevant to the previous paper, you can readily determine whether you have a mixed crystal phase of bronze and an unreduced phase by a simple solvent extraction type process, say with ammonia solution. This will normally remove the unreduced phase leaving behind the bronze, if you choose your conditions carefully.

[1] M. S. Whittingham, unpublished results.
[2] V. L. Volkov, A. A. Fotiev, and A. D. Neuimin, Russ. J. Phys. Chem. 44, 1163 (1970).

M. S. Whittingham: Yes, you can do that with the perovskite phases, but you certainly have to worry that if you treat the hexagonal phase or even possibly the tetragonal phase with an aqueous medium of any sort you may start removing ions from them. This is very clearly shown by changes in superconductivity if you heat these materials in aqueous media[3-5].

[3]J. P. Remeika, T. H. Geballe, B. T. Matthias, A. S. Cooper, G. W. Hull, and E. M. Kelly, Phys. Letters 24A, 565 (1967).
[4]C. N. King, Stanford University, unpublished results.
[5]D. Vanles, Cornell University, unpublished results.

National Bureau of Standards Special Publication 364, Solid State Chemistry, Proceedings of 5th Materials Research Symposium, issued July 1972.

SOME ASPECTS OF THE INVESTIGATION OF INTERGROWTH PHASES IN Nb_2O_5-RICH SYSTEMS

Reginald Gruehn

Justus Liebig University
Institute of Inorganic and Analytical Chemistry II
63 Giessen, West Germany

Numerous Nb_2O_5-rich compounds with complicated compositions could be prepared as monophasic samples. The preparative and analytical work in this field was supplemented by x-ray investigations using the Guinier technique. In addition to 5 phases ($Nb_{11}O_{27}$, $Nb_{25}O_{62}$, $Nb_{28}O_{70}$, $Nb_{31}O_{77}F$, $Nb_{34}O_{84}F_2$) whose structures are known from investigations by Wadsley, Andersson, and Norin, we found 4 "hybrid" phases also called intergrowth-phases. The building principle of the hybrid phases $NbO_{2.464}$, $NbO_{2.483}$, $Nb(O,F)_{2.510}$, and $Nb(O,F)_{2.523}$ is a combination of building elements of both neighbor phases *e.g.* $NbO_{2.483}$ combines component rows of the $Nb_{25}O_{62}$-structure and the $Nb_{28}O_{70}$-structure in a ratio 1:1.

It is of special interest that the phases $Nb_{25}O_{62}$, $Nb_{28}O_{70}$, $Nb_{31}O_{77}F$, and $Nb_{34}O_{84}F_2$ have small but exactly reproducible ranges of homogeneity. The fundamental reason for this deviation from the ideal composition is still unknown. It may be that the deviation from the ideal composition is due to the special properties of the building elements. According to this the non-ideal composition of a hybrid phase may be derived from the non-ideal composition of both neighbor phases *e.g.* the actual composition $NbO_{2.483\pm0.001}$ of the hybrid phase may be calculated from the actual limits of the phases $Nb_{25}O_{62}$ (2.478 O/Nb) and $Nb_{28}O_{70}$ (2.489 O/Nb). A hybrid phase with the ideal composition 2.491 O/Nb ($Nb_{25}O_{62}$+$Nb_{28}O_{70}$) is nonexisting.

In addition to the combination of compositions of neighbor phases there may be relationship between the stabilities of the basic structures and the resulting hybrid phases.

Key words: Analysis; hybrid phase; intergrowth phase; niobium pentoxide; preparation; ranges of homogeneity; stability; systems.

1. INTRODUCTION

More than 10 years ago the author began in the group of Harald Schäfer in Münster (Westfalia) with the preparative and analytical investigation of Nb_2O_5-rich systems. The main interest was given to results that were inconsistent with the picture of distinct narrow phases with separated structures. Thus in 1963 Gruehn and Schäfer [1][1] reported a new phase $(Ti,Nb)O_{2.483}$ with a composition[2,3] not to be described by one of Wadsley's structural related series $Me_{3n}O_{8n-3}$ [2] and $Me_{3n+1}O_{8n-2}$ [3]. Later on the identification of $(Ti,Nb)O_{2.483}$, of the isomorphous phase $NbO_{2.483}$ and of $NbO_{2.464}$ [4][4] as intergrowth- or hybrid[5] phases became possible, since a new phase $W_2Nb_{26}W_2O_{77}$ in the Nb_2O_5-WO_3 system could be prepared and since its composition could be interpreted as a combination of the

[1] Figures in brackets indicate the literature references at the end of this paper.

[2] In reference [1] the composition $(Ti,Nb)O_{2.482}$ was published.

[3] For the system of notation see tables 2 through 6.

[4] In reference [2] the composition $NbO_{2.460}$ was published.

[5] The notation "hybrid phase" proposed by S. Andersson might be preferable.

neighbor phases $WNb_{12}O_{33}$ + $WNb_{14}W_2O_{44}$ [5]. From these samples single crystals were selected and used by Andersson, Mumme, and Wadsley [6] for the first complete crystal structure determination of an intergrowth or hybrid structure.

To characterize the subsequent development the parallel work, done by two groups with different methods, may be mentioned. In Münster "simple" hybrid phases which combine neighboring structures in the 1:1 ratio were prepared as monophase samples and investigated by chemical analysis. In this way 4 hybrid phases (1:1) were found [7,8] one at a time intermediate to two known members of the series $Me_{3n+1}(O,F)_{8n-2}$ (n = 7,8,9,10,11). In Melbourne, Wadsley introduced electron optical methods as a powerful means of structure investigation [9]. Continuing this work Allpress observed more complicated hybrids *e.g.* with a 1:2 ratio of the building elements, Wadsley defects and microdomains of new related phases [10,11,12]. From these structural results also new important aspects arise for further preparative work.

2. METHODS FOR PREPARATIVE AND ANALYTICAL INVESTIGATION

2.1. PRINCIPLE PROCEDURE

The main interest was turned to the Nb_2O_5-rich part of the systems NbO_2 - Nb_2O_5, TiO_2 - Nb_2O_5, Nb_2O_5 - WO_3, and Nb_2O_5 - NbO_2F. Additional experiments were performed in the systems MgO - Nb_2O_5, Al_2O_3 - Nb_2O_5, Ga_2O_3 - Nb_2O_5, Fe_2O_3 - Nb_2O_5, GeO_2 - Nb_2O_5, WO_2 - Nb_2O_5-WO_3, NbO_2 - Nb_2O_5 - WO_3, and Nb_2O_5 - WO_3 - NbO_2F. The detection of hybrid phases mostly required a very subtle technique of investigation because the differences of composition between phases were very small. A sensitive x-ray method was necessary because of the structural similarity of these phases. Our criterion for a single phase region was that a sample could be prepared as a monophase substance. Accordingly, in two phase regions only two phases should exist. Therefore we needed methods to prepare samples near to equilibrium conditions (paragraph 2.2). The monophase character of a substance was established with the sensitive Guinier method (paragraph 2.3). Because monophase samples could be prepared, special chemical methods could be applied for an analysis (paragraph 2.4).

2.2. PREPARATIVE METHODS

Methods, suitable for the investigation of oxide systems and for the preparation of monophase samples, are compiled in table 1. From top to bottom of the table the mobility of the components increases. In the same direction the chance to approach equilibrium conditions *i.e.* defined final states increases.

Table 1

Preparative Methods Used for the Investigation of Nb_2O_5 - Rich Systems

	Method(a)	Temperature °C	Additional Component(s) of the Investigated System	Figure
1	heating of the mechanically mixed components (b)	1100 -1400	TiO_2 [13] ; Al_2O_3 [13,16] ; Fe_2O_3 [13,16] ; Ga_2O_3 [13,16] ; MgO [13,16]	
		1000 -1100	WO_3 [5,13]	
2	heating of mixed precipitations (b)	1100 -1400	TiO_2 [1,13] ; ZrO_2 [17]	

Table 1 - continued

	Method(a)	Temperature °C	Additional Component(s) of the Investigated System	Figure
3	heating of solid solutions $(Ti,Nb)O_2$ with spontaneous oxidation of the lower oxidation states (b)	1200 -1400	TiO_2 [13]	
4	isothermal heating of tablets (mechanical mixtures) in sealed tubes; checking of weight (b,c)	1100 -1420	NbO_2 [13] ; WO_3 [5] ; WO_2+WO_3 [5,17] ; NbO_2+WO_3 [5,17]	1a
5	isothermal heating of mechanical mixtures in sealed platinum tubes (c,d)	1200 -1350 1100 -1300	WO_3 [17] ; GeO_2 [17] NbO_2F [8,17] ; WO_3+NbO_2F [17]	1b
6	equilibration of niobium oxides with gaseous mixtures of H_2O/H_2 (c)	1100 1300	"NbO_2" [13] [14]	cf. [18]
7	chemical transport reactions in quartz tubes under extrem temperature conditions (d)	1200 -1350	NbO_2 [13] ; TiO_2 [13] ; Al_2O_3 [13] ; Fe_2O_3 [13] ; ZrO_2 [17]	1c
8	chemical transport reactions in sealed platinum tubes (d)	1100 -1300	NbO_2F [8,17]	1d
9	chemical transport reactions using a well established temperature gradient(d)	600 -1100	NbO_2 [1,7,13,19] ; TiO_2 [13] ; Al_2O_3 [13] Fe_2O_3 [20]	1e

(a) for specific details see paragraph 2.2.
(b) heating in air or in O_2. No significant participation of a vapor phase reaction.
(c) transport of one component by reaction with the vapor phase (vaporization of WO_3; transport of oxygen as H_2O).
(d) transport of all components by chemical transport reactions.

465-504 O - 72 - 6

2.2.a. METHOD 1

This extremely simple way of a solid state reaction often did not yield well defined products, a fact, proved by the presence of three or more phases in samples belonging to a two phase region. If the composition of neighboring phases differed only slightly a complete reaction was unobtainable, even when the samples were heated at extremely high temperatures or after melting. Therefore monophase samples of the hybrid phase $(Ti,Nb)O_{2.483}$ were not obtained in this way, even when prolonged heating with repeated intermediate grinding was performed. The formation of only a small amount of this phase mixed with neighboring phases indicates that $(Ti,Nb)O_{2.483}$ might be stable under these conditions of heating. The incompleteness of the reaction probably is due to the insufficient rate of diffusion of the components.

2.2.b. METHOD 2 [1,13]

Exactly weighed amounts of Nb_2O_5 and TiO_2 (or ZrO_2) were dissolved in a molten mixture of $(NH_4)_2SO_4$ and H_2SO_4. After the reaction was finished the oxides were precipitated by diluting and adding of NH_3. The resulting mixture of hydrated oxides was carefully dehydrated at 600 - 800 °C and annealed at the reaction temperature (table 1). With this method we could prepare monophase samples of phases that could not be obtained with method 1 because like $Ti_2Nb_{10}O_{29}$ (monoclinic) and $(Zr,Nb)O_{2.464}$ [17] they form in a limited range of temperature. The main advantage of this method is the possibility to prepare phases with small differences in composition.

2.2.c. METHOD 3 [13]

Tablets of the mechanically mixed components TiO_2 and Nb_2O_5 (in a known ratio) were reduced with weighed amount of Nb-foil in sealed tubes at 1250 °C (fig. 1a). In this way homogenous samples consisting of $(Ti,Nb)O_2$ solid solutions (Guinier method) were obtained. In a second step $(Ti_{2y}Nb_{1-2y})O_{2.0}$ was heated in air or in O_2 and thereby spontaneously oxidized. Like method 2 the oxidation of solid solutions provides for a close contact of the components in the resulting $(Ti_{2y}Nb_{1-2y})O_{2.5-y}$. Method 3 is limited to the systems $(Me,Nb)O_x$ $(x>2.0)$ which are adjacent to solid solutions with the composition $(Me,Nb)O_{2.0}$.

2.2.d. METHOD 4 [5,13]

Tablets of the mechanically mixed components $Nb_2O_5 + WO_3$, $Nb_2O_5 + NbO_2 + WO_3$, and $Nb_2O_5 + WO_2 + WO_3$ were isothermally heated in sealed quartz tubes (fig. 1a). Before sealing the tubes were filled with air or O_2 (for experiments with $Nb_2O_5 + WO_3$) or evacuated in all other cases. The weight of the tablets was checked before heating and after the experiment was finished. In this way vaporization of WO_3 could be noticed. In experiments with $Nb_2O_5 + WO_3$ a loss of oxygen was effectively suppressed by the O_2 content of the quartz tube.

2.2.e. METHOD 5 [8,13]

Isothermal heating of the mixed components $Nb_2O_5 + NbO_2F$, $Nb_2O_5 + NbO_2F + WO_3$, and $Nb_2O_5 + GeO_2$ was performed in sealed platinum tubes. A loss of oxygen was suppressed by partly filling the tubes with air or O_2. After sealing the platinum tubes were inserted into quartz tubes which remained filled with air (1 atm at room temperature) when sealed. At reaction temperature this filling of air exerts a pressure of 3 - 4 atm and prevents the platinum tubes from bursting (fig. 1b).

2.2.f. METHOD 6 [14]

In the NbO_2 - Nb_2O_5 system NbO_x phases can be prepared from niobium oxides having higher $(O/Nb>x)$ or lower $(O/Nb<x)$ oxygen content by equilibrating them with well defined H_2O - H_2 mixtures at high temperature. For details of the equipment see [18].

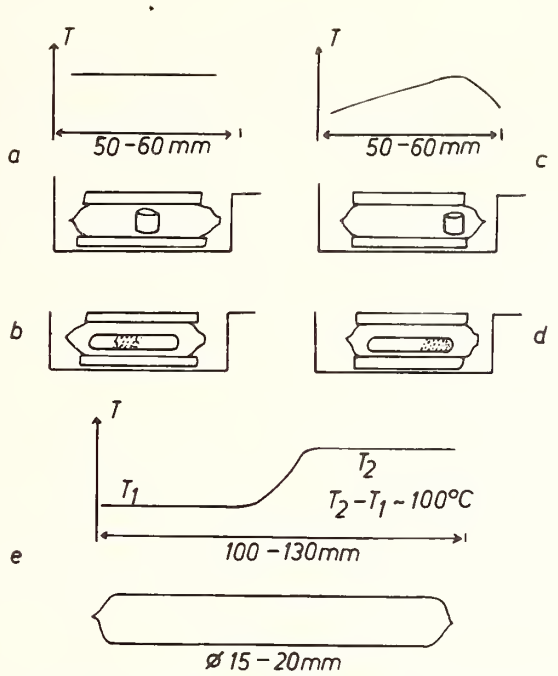

Fig. 1. Heating of samples in closed vessels (a) isothermal heating in a sealed quartz tube (method 4); (b) isothermal heating in a sealed platinum tube enclosed in a sealed quartz tube (method 5); (c) heating in a temperature gradient using a sealed quartz tube (method 7); (d) heating in a temperature gradient using a sealed platinum tube enclosed in a sealed quartz tube (method 8). In figures a through d the sealed quartz tubes are reinforced by surrounding open quartz tubes. During an experiment the filled tubes were placed in platinum boats. (e) chemical transport in a well defined temperature gradient (method 9) using sealed quartz tubes.

2.2.g. METHOD 7 [13]

Small quartz tubes surrounded by a belt tube (fig. 1c, cf. method 4) made it possible to use closed quartz vessels for chemical transport reactions at temperatures of 1200 - 1250 °C. For the principle see method 9. The temperature gradient in method 7 is less well established, of course, than in method 9.

It is favorable to use the inert compound Nb_3O_7Cl to introduce the transporting agent $NbOCl_3/NbCl_5$ (eq (2)) into small tubes with a low volume [7]. At higher temperature Nb_3O_7Cl mainly decomposes as described by equation (1).

$$3Nb_3O_7Cl_{,s} = 4Nb_2O_{5,s} + NbOCl_{3,g} \qquad (1)$$

The additional Nb_2O_5 formed after equation (1) may be taken into account by the starting weight of the other components.

By this method it became possible to prepare crystals of $NbO_{2.453}$, $NbO_{2.464}$, and $Ti_2Nb_{10}O_{29}$ (orthorhombic) which were not obtainable by method 9.

2.2.h. METHOD 8 [8,13]

Using a temperature gradient and sealed platinum tubes it was also possible to study transport reactions with niobium oxide fluorides. By this way larger crystals may be obtained than with method 5. Both methods are similar in equipment (fig. 1d).

2.2.i. METHOD 9 [15]

The method of chemical transport was a particularly suitable one for the preparation of well crystallized samples of the NbO_2 - Nb_2O_5 system and for numerous ternary phases containing niobium. The deposition of substances by means of a well established temperature gradient (*e.g.* T_2 - T_1 = 100°) can be carried out in sealed quartz tubes of sufficient length (*e.g.* l = 100 mm; v = 25 cm^3). They can be used at temperatures up to $T_2 \approx 1100$ °C. Experiments at higher temperatures required smaller tubes (v = 1 - 2 cm^3) cf. method 7.

Nb_2O_5 is transported along a temperature gradient to the less hot zone at T_1 by endothermic reactions as described by equations (2) or (3).

$$Nb_2O_{5,s} + 3NbCl_{5,g} = 5NbOCl_{3,g} \quad (2)$$

$$Nb_2O_{5,s} + 6HCl = 2NbOCl_{3,g} + 3H_2O_{,g} \quad (3)$$

The ratio O/Nb in the solid is controlled by the composition of the vapor phase. In the presence of chlorine ($P(Cl_2)$ = 1 atm, 20 °C) the niobium in the solid is in its maximum oxidation state. Other possible O/Nb values may be established by using a CO_2 - CO mixture ("buffering of the vapor phase")[6]. Lower O/Nb ratios are also obtainable if in reactions, described in equations (2) and (3), chlorine is replaced by bromine or iodine [19].

Ternary oxides *e.g.* $Ti_2Nb_{10}O_{29}$ can be transported in a temperature gradient if a reaction for the transport of Nb_2O_5 (eqs (2) or (3)) and also a similar parallel reaction for the transport of the other component cf. for TiO_2 (eqs (4) or (5)) exists.

$$TiO_{2,s} + 2NbCl_{5,g} = TiCl_{4,g} + 2NbOCl_{3,g} \quad (4)$$

$$TiO_{2,s} + 4HCl = TiCl_{4,g} + 2H_2O_{,g} \quad (5)$$

The composition of the solid deposited at T_1 is given by the ratio Nb/Ti and depends on the ratio Q of the partial pressures $P(NbOCl_3)$ and $P(TiCl_4)$ in the vapor phase and on the temperature.

The rate of chemical transport for both oxides is only sufficient[7] if Q has no extreme value. This statement shows that chemical transport of ternary oxides is only possible if the transport reactions for both components (eqs (2) and (4) or (3) and (5)) do not combine to a reaction (eq (6)) the equilibrium of which is shifted extremely to one side [17]. This can be demonstrated for a system MeO_2 - Nb_2O_5 with the simplified equation (6).

$$2Nb_2O_{5,s} + 3MeCl_{4,g} = 4NbOCl_{3,g} + 3MeO_{2,s} \quad (6)$$

If according to equation (6) $MeCl_4$ disappears from the gas phase the chemical transport of MeO_2 comes to a standstill. Similarly Nb_2O_5 cannot be transported if $NbOCl_3$ disappears. For an accurate discussion of the position of equilibrium of equation (6) the free enthalpy of formation of the ternary oxides (and of possibly existing complex molecules in the vapor phase) has to be taken into account.

For Me = Ti a calculation of the equilibrium (eq (6)) is in accordance with the observation that chemical transport takes place for ternary titanium niobium oxides. The solid in the zone with the higher temperature T_2 showed a small increase in the TiO_2 content. This is in agreement with the sign of $\Delta H°_R$ for this reaction.

2.3. X-RAY WORK

In all cases the x-ray investigation was performed with a Jagodzinsky powder camera equipped with one chamber. The circumference of 360 mm and the $CuK\alpha_1$ radiation used per-

---

[6] See H. Schäfer's paper at this meeting.

[7] For further conditions necessary for chemical transport see [15].

mitted a high resolution. For instance the small amount of 1% of the additional phase NbO_2 was still detectable in $NbO_{2.417}$. The sensitivity was decreased with increasing similarity of the diagrams. In samples of $NbO_{2.483}$ 17% of the neighboring phases $NbO_{2.478}$ or $NbO_{2.489}$ were detectable. In this case the accuracy with regard to the gross composition was 0.001 O/Nb which is still high.

Samples which proved to be monophasic by x-rays may, within the limits of ±0.001 O/Nb, in special cases contain up to 1/6 of the neighboring phase. This may possibly explain why neighboring phases could be detected in these samples with electron optics [11].

In all cases the samples were quenched and Guinier diagrams were taken at room temperature.

2.4. ANALYTICAL WORK

For the identification and relation of phases the gross composition O/Nb (O/ΣMe = O/Σ (Me + Nb(V)) in ternary systems) of these phases is of main interest. Generally a reaction was started with components[8] the ratio of which was accurately determined by weighing. A chemical analysis was not performed provided no volatilization occurred or the possibility of a loss of substance could be excluded by check of weight. In all other cases the composition was determined by chemical analysis.

For investigation of the region 2.417 - 2.500 O/Nb of the NbO_2 - Nb_2O_5 system a special micro analytical method [21] was available. The method is based on the principle that the Nb(IV) portion of the NbO_x oxides reacts with a molten KOH - KBr mixture to form niobate(V) and hydrogen. The amount of hydrogen evolved is measured. The weight of the analyzed samples amounts to 6 - 12 mg. The accuracy depends on the amount of hydrogen. Its limits are 2.420±0.003; 2.460±0.002; 2.490±0.001 O/Nb.

The composition of samples of the systems TiO_2 - Nb_2O_5, Nb_2O_5 - WO_3 or Nb_2O_5 - NbO_2F is given by the content of Ti, W or F, if the metals are completely in their maximum state of oxydation. The absence of lower oxidation states [*e.g.* Nb(IV), Ti(III)] in these cases was established with the micro method [21].

In samples of the system TiO_2 - Nb_2O_5 the portion of Ti was determined and thereby also the composition O/Σ (Ti + Nb) [13]. The samples were melted with $K_2S_2O_7$ and subsequently dissolved with a solution of oxalic acid. Then chromotropic acid was added and the resulting color was compared with the color of similarly prepared standard solutions of titanium. The accuracy depends on the content of titanium and may be gathered from the following resulting formulas: $(Ti,Nb)O_{2.42\pm0.003}$; $(Ti,Nb)O_{2.460\pm0.002}$; $(Ti,Nb)O_{2.49\pm0.001}$ O/Σ (Ti+Nb).

For the Nb_2O_5 - NbO_2F system a micro method for determination of low fluorine contents was developed [17]. In a closed system a mixture of the sample with $K_2S_2O_7$ is melted. HF is distilled off and absorbed in NaOH. The photometric determination of fluorine is performed by the method of Belcher [22][9].

3. RESULTS

3.1. GENERAL ASPECTS

An investigation of hybrid phases necessarily requires an investigation of neighboring phases with closely related structures, particularly phases with simpler basic structures. Observations were collected in tables 2 to 6 with the phases arranged according to structural relationships.

According to their building principle (paragraph 3.2) each ideal structure has a definite gross composition O/Σ Me (or (O,F)/Σ Me, respectively). Therefore it is particularly interesting to see that the observed O/Σ Me of a structurally well defined phase often disagrees

[8] The starting materials were of highest purity if available. As to the problem of additional contamination of substances in the course of an experiment see [13,14].

[9] The experiments were performed by G. Köpke.

Table 2

Phases With the Basic Structure $(Me^{z+},Nb)_{3n}(O,X)_{8n-3}$ (with $Me^{z+}+Nb(V) = \Sigma Me$) (a)

system of notation (type)	ideal structure [2,23]			chemical analysis $O/\Sigma Me$ (b)	monophasic samples with the following Me^{z+}-cations. preparation by method ( ) (c)	additional results (d)
	formula	$O/\Sigma Me$	block size			
$(Ti,Nb)_9O_{21}$ (monoclinic)	Me_9O_{21}	2.33	3x3	2.33 (e)	Ti (1,2,3,7,9)	orthorhombic phase cf. [25]
$(Me,Nb)_{12}O_{29}$ (monoclinic)	$Me_{12}O_{29}$ (monocl.)	2.417	3x4	2.417(e,f)	Nb(IV)(4,6,7,9); Ti(2,3,9); Al(1,7,9); Fe(9)	V(IV) [26] ; Cr [27] ; Co [27] Ni [27] ; Mg [28] ; Zn [29]
$(Me,Nb)_{12}O_{29}$ (orthorhomb.)	$Me_{12}O_{29}$ (orthorh.)	2.417	3x4	2.417(e,f)	Nb(IV)(4,6,7,9); Ti(1,2,3,7,9); Ga(1); Fe(1,7,9); Mg(1)	Co [30] ; Ni [30] ; Zn [29]
$MgNb_{14}O_{35}F_2$ (monoclinic)	$Me_{15}(O,X)_{37}$ (monocl.)(a)	2.467	3x5		$MgNb_{14}O_{35}F_2$ (5)	$MgNb_{14}O_{35}F_2$ [23]
$Nb_{18}O_{45}$	$Nb_{18}O_{45}$	2.50	3x6			not yet observed

(a) With X = O for n = 3,4; X = F for n = 5.
(b) See paragraph 2.4.
(c) Methods ( ) and references see table 1.
(d) For additional references cf. [7,13,16].
(e) Samples $(Ti^4,Nb^5)O_x$; analysis by determination of Ti [13]; in $Ti_3Nb_6O_{21}$ niobium can be replaced by tantalum up to $Ti_3Ta_6O_{21}$; in $Ti_2Nb_{10}O_{29}$ up to 50% Nb can be replaced by Ta [24].
(f) Samples NbO_x, analysis by determination of O/Nb [21].

Table 3

Phases With the Basic Structure $(Me^{z+},Nb)_{3n+1}(O,X)_{8n+1}$ (with $Me^{z+}+Nb(V) = \Sigma Me$) (a)

system of notation (type)	ideal structure [31,32] formula	ideal structure [31,32] O/Σ Me	ideal structure [31,32] block size	chemical composition O/Σ Me (b)	monophasic samples with the following Me^{z+}-cations. preparation by method ( ) (c)	additional results (d)
$(Me,Nb)_{10}O_{29}$	$Me_{4/4}Me_9O_{29}$	2.50	3x3	2.474 (e) 2.50	Ge (5) $2Nb_2O_5.Ta_2O_5$(1,2,4) [33]	PNb_9O_{25}; $AsNb_9O_{25}$ [34] VNb_9O_{25} [34] ; PNb_9O_{25} -$P_{0.6}Nb_{9.4}O_{25}$ [35] (i) $P_{0.36}Nb_{9.64}O_{25}$ [35]
$(Me,Nb)_{13}O_{33}$	$Me_{4/4}Me_{12}O_{33}$	2.538	3x4	2.516 -2.538 (f) 2.529 -2.538 (g)	W (4,5) $WNb_{12}O_{33}$ - $WNb_{10}W_2O_{33}$ (WO_2- added)(4)	$MoNb_{12}O_{33}$ [36] $MoTi_{0.5}Nb_{11}Mo_{0.5}O_{33}$ [36]
$MeNb_{15}O_{40}F$	$Me_{4/4}Me_{15}(O,X)_{41}$(a)	2.562	3x5	2.562 (h)	W (5)	Mo [36]

(a) With X = O for n = 3,4; X = F for n = 5. 1 Me is in tetrahedral positions of the structure according to 4/4 Me per block.
(b) See paragraph 2.4; accurate starting composition, check of weight.
(c) Methods ( ) and references see table 1.
(d) For additional references cf. [7,13].
(e) Monophasic samples of $GeNb_{18}O_{47}$.
(f) Samples Nb_2O_5:WO_3 = 15:1 through 6:1 (1420 °C) [17].
(g) Samples Nb_2O_5:WO_3 = 8:1 through 6:1 (1300 °C) [5,17].
(h) Accurate determination of the chemical composition not yet performed.
(i) The ratio of P/Nb is variable.

Table 4

Phases With the Basic Structures $(Me^{z+},Nb)_{4n+1}O_{11n}$ and $(Me^{z+},Nb)_{5n+1}O_{14n-1}$ (with $Me^{z+}+Nb(V) = \Sigma Me$) [a]

system of notation (type)	ideal structure [32]			chemical composition O/Σ Me (b)	monophasic samples with the following Me^{z+}-cations. preparation by method ( ) (c)	additional results (d)
	formula	O/Σ Me	block size			
$(Me,Nb)_{13}O_{33}$	$Me_{4/4}Me_{12}O_{33}$	2.538	3x4	cf.table 3	cf.table 3	
$(Me,Nb)_{17}O_{44}$	$Me_{4/4}Me_{16}O_{44}$	2.589	4x4	2.589	W (4,5) $WNb_{14}W_2O_{44}$ - $WNb_{10}W_6O_{44}$ (e) (WO_2-added)(4)	Mo [36]
$(Me,Nb)_{21}O_{55}$	$Me_{4/4}Me_{20}O_{55}$	2.619	4x5	2.619	W (4,5) $WNb_{16}W_4O_{55}$ - $WNb_{12}W_8O_{55}$ (e) (WO_2-added)(4)	
$(Me,Nb)_{26}O_{69}$	$Me_{4/4}Me_{25}O_{69}$	2.653	5x5	2.653	W (4,5) $WNb_{18}W_7O_{69}$ - $WNb_{16}W_9O_{69}$ (e) (WO_2 added)	

(a) The phase with 3x4 blocks can be represented by the formulas of both series $(Me,Nb)_{3n+1}O_{8n+1}$ and $(Me,Nb)_{4n+1}O_{11n}$, the phase with 4x5 blocks by the formulas $(Me,Nb)_{4n+1}O_{11n}$ and $(Me,Nb)_{5n+1}O_{14n-1}$ [32]; 1 Me is in tetrahedral positions of these structures according to 4/4 Me per block.

(b) See paragraph 2.4; accurate starting composition; check of weight.

(c) Methods ( ) and references see table 1.

(d) For additional references cf. [13].

(e) The ratio of W/Nb is variable.

Table 5

Phases With Complex Block Structures $(Me^{z+},Nb)_{3n+1}(O,X)_{8n-2}$ [a] and Intermediate Hybrid Phases With a 1:1 Sequence

system of notation (type)	ideal structure [3,38,39]				chemical analysis (b) O/Σ Me resp. (O,F)/Nb	monophasic samples with the following Me^{z+}-cations. preparation by method ( ) (c)	additional results (d)
	formula	O/Σ Me	block size	refe-rences			
$Nb_{22}O_{54}$	$Me_{4/4}Me_{21}O_{54}$	2.4545	3x3 3x4	[38,40]	2.453(e)	Nb(IV)(6,7)	
$NbO_{2.464}$	$Me_{8/4}Me_{45}O_{116}$ (hybrid 1:1)	2.468	3x3 3x4	[7]	2.464-2.467(e) 2.460 (f)	Nb(IV)(6,7); Zr(2)	
$(Me,Nb)_{25}O_{62}$	$Me_{4/4}Me_{24}O_{62}$	2.480	3x4	[3,40]	2.472-2.478(e) 2.467(f) 2.467-2.477(g)	Nb(IV)(6,7,9); Ti(1,2,3,7); Al(1,7), Ga(1,7); Fe(1,7); Zr(2)	V [26]; Co [30]; Ni [30]
$(Me,Nb)O_{2.483}$	$Me_{8/4}Me_{51}O_{132}$ (hybrid 1:1)	2.491	3x4 3x5	[40,11]	2.483(e,f,g)	Nb(IV)(6,7,9); Ti(2,3,7)	V [26]; Al [37]
$Nb_{28}O_{70}$	$Nb_{4/4}Nb_{27}O_{70}$	2.50	3x4 3x5	[38]	2.489-2.50(e,f,g) 2.50-2.504(h)	Nb(IV)(6,9); Ti(2,3,7)(i) Nb(V)(4)	
$Nb(O,F)_{2.510}$	$Nb_{8/4}Nb_{57}O_{147}F$ (hybrid 1:1)	2.508	3x4 3x5	[42,43]	2.510(h)	Nb(V)(4)	
$Nb_{31}O_{77}F$	$Nb_{4/4}Nb_{30}O_{77}F$	2.516	3x5	[39]	2.515-2.519(h)	Nb(V)(4,8)	
$Nb(O,F)_{2.523}$	$Nb_{8/4}Nb_{63}O_{161}F_3$ (hybrid 1:1)	2.523	3x5 3x6	[42,43]	2.523(h)	Nb(V)(4,8)	
$Nb_{34}O_{84}F_2$	$Nb_{4/4}Nb_{33}O_{84}F_2$	2.529	3x5 3x6	[39]	2.527-2.532(h)	Nb(V)(4,8)	

See footnotes on next page.

Footnotes for table 5.

(a) With $Me^{z+}+Nb(V) = \Sigma$ Me; X = O for n = 7,8,9; X = F for n = 9 (h),10,11; 1 Me is in tetrahedral positions of these structures according to 4/4 Me per two blocks. Each member of the series can be derived from basic structures of the tables 2 and 3, cf. paragraph 3.3.
(b) See paragraph 2.4.
(c) Methods ( ) and references see table 1.
(d) For additional references cf. [7,13].
(e) Samples NbO_x from measurements of equilibrium at 1350 °C [14]; chemical analysis by determination of O/Nb [21].
(f) Samples NbO_x prepared by chemical transport, chemical analysis as in (e).
(g) Samples $(Ti^4, Nb^5)O_x$, chemical analysis by determination of the Ti-content [13].
(h) Samples of the Nb_2O_5 - NbO_2F system, chemical analysis by determinqtion of the F-content [17].
(i) The range of solid solution with V_2O_5, "Mo_2O_5", "W_2O_5" [17]; P_2O_5 [31] can be neglected.

Footnotes for table 6.

(a) See paragraph 2.4, accurate starting composition, check of weight in the Nb_2O_5 - WO_3 system.
(b) This complex structure (cf. table 5) can be derived from the basic structures "$WNb_{12}O_{33}$" and "$MgNb_{14}O_{35}F_2$".
(c) This complex structure (cf. table 5) can be derived from the basic structures "$WNb_{12}O_{33}$" and $Ti_2Nb_{10}O_{29}$.
(d) These samples were homogeneous in x-ray investigations but by electron optical methods [10] they were found to be mixtures of the hybrids 1:3, 2:1, and 3:2 with respect to the basic structures.

Table 6

Additional Hybrid Phases

ideal structure					chemical composition O/Σ Me	monophasic samples preparation by method ( )	type of hybrid phase
formula	building elements (sequence)	block size	O/Σ Me	references			
$W_{8/4}Nb_{26}W_2O_{77}$	$WNb_{12}O_{33}$ (1:1) $WNb_{14}W_2O_{44}$	3x4 4x4	2.567	[6]	2.567(a)	(4,5)	1
$PNb_{22}O_{58}$	PNb_9O_{25} (1:1) "$WNb_{12}O_{33}$"	3x3 3x4	2.522	[35]	2.50(a) ($PNb_{22}O_{57.5}$)	[35]	1
$TiNb_{38}O_{97}$	$Nb_{28}O_{70}$(b) (1:2) $TiNb_{24}O_{62}$(c)	3x4 +3x5 3x4	2.487	[11]	unknown	not yet prepared	1
$Ti_3Nb_{34}O_{91}$	"$WNb_{12}O_{33}$" (1:2) $Ti_2Nb_{10}O_{29}$	3x4 3x4	2.459	[11]	"	"	2a
$Ti_5Nb_{44}O_{120}$	"$WNb_{12}O_{33}$" (1:3) $Ti_2Nb_{10}O_{29}$	3x4 3x4	2.449	[11]	"	"	2a
$WNb_{26}O_{68}$	"$WNb_{12}O_{33}$" (3:1) "$MgNb_{14}O_{35}F_2$"	3x4 3x5	2.518	[10]	"	(4)(d)	2b
$WNb_{40}O_{103}$	"$WNb_{12}O_{33}$" (2:1) "$MgNb_{14}O_{35}F_2$"	3x4 3x5	2.513	[10]	"	(4)(d)	2b
$WNb_{68}O_{173}$	"$WNb_{12}O_{33}$" (3:2) "$MgNb_{14}O_{35}F_2$"	3x4 3x5	2.509	[10]	"	(4)(d)	2b

See footnotes for table 6 on preceding page.

with the ideal composition corresponding to a perfect occupied lattice. In these cases either ranges of homogeneity exist or narrow phases with noticeable deviations of composition from ideal structures (paragraph 3.4).

It may be derived from experimental results up to what extent the replacement of a Me cation or of O by F is tolerated by each type of the compounds without change in the O/Σ Me ratio. This derived result is compared with the type of the observed hybrid structure (paragraph 3.3) and discussed from the aspects of stability (paragraph 3.5).

3.2. BUILDING PRINCIPLE

The structures most of which were solved by Wadsley and Andersson [43] can be characterized by building elements, which are "blocks" of different sizes that look like sections of a ReO_3 lattice. The blocks consist of octahedra having corners in common and also sharing edges when connecting blocks.

Structures with the same type of connection may be described as members of a structural related series (*e.g.* $Me_{3n}O_{8n-3}$; $Me_{3n+1}O_{8n+1}$). Members of a series differ in the width of the building elements (blocks) which in one direction is described by the value of n. Within a series the width of blocks in a second direction, perpendicular to the first one, is constant. In the third direction which generally coincides with the b axis of the structures the width of the blocks is not limited. In figure 2 a typical section of a block structure is depicted.

3.3. TYPES OF HYBRID PHASES

The principle of hybrid structures is a combination of the building elements (blocks) of two simpler[10] structures resulting in new more complicated sequences [6]. Since the blocks are clearly distinguished by their width and their connection with neighboring blocks they represent the basic elements of this type of structures. Therefore one might consider that they transmit some properties *e.g.* the actual composition and the stability of a lattice from the basic structure to a hybrid phase (paragraph 3.5). A transition of properties in this assumed way might be most effective if the original surrounding ("sphere of coordination") of the blocks is transmitted unchanged to the new hybrid structure. In accordance with results of Allpress [10,11] two types of hybrid structures exist which can be distinguished by the extent of change of the surrounding of the blocks.

3.3.a. TYPE 1

The surrounding of the blocks remains unchanged (fig. 3) if both basic structures consist of identically connected blocks, *i.e.* if a hybrid structure is built up from different members of the same series.

Examples of this type:

$Me_{4n+1}O_{11n}$; $Me_{13}O_{33} + Me_{17}O_{44} = Me_{30}O_{77}$ (table 6)

$Me_{3n+1}O_{8n+1}$; $Me_{10}O_{25} + Me_{13}O_{33} =$ "$Me_{23}O_{58}$" (table 6)

$Me_{3n+1}O_{8n-2}$; between two neighboring members (n = 7,8,9,10,11) exists one 1:1 hybrid phase (table 5). For additional hybrid phases see table 6 [11].

$Me_{3_n}O_{8n-3}$; within this series ordered hybrids are not yet known (except for orthorhombic $Me_{12}O_{29}$; cf. paragraph 3.5.b).

---

[10] The most simple structures containing only one type of blocks are called "basic structures" in this paper.

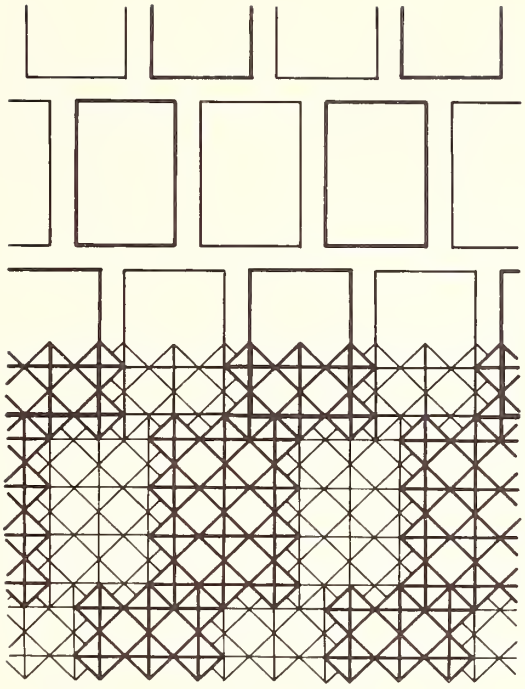

Fig. 2. Idealized drawing illustrating the principle of block structures. The picture shows a section of the structure of monoclinic $(Me,Nb)_{12}O_{29}$ (cf. table 2) projected parallel to the crystallographic b axis. In the lower part of the figure each square represents an Me - O octahedron viewed down a body diagonal. The lighter and darker squares are centered on parallel planes half a body diagonal apart. For the connection of octahedra see paragraph 3.2. The blocks are 3 octahedra x 4 octahedra in size. In the upper part of the drawing each block is represented by a rectangle which joins the metal atoms of the corners of a block. This highly idealized model is also used in figures 3 to 5.

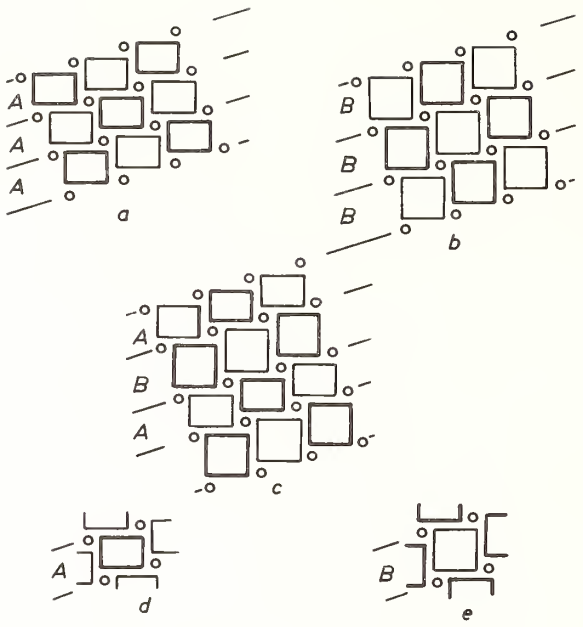

Fig. 3. Combination of building elements leading to a hybrid structure of type 1. Rows of blocks of the basic structures AA and BB combine to the resulting hybrid phase with the sequence ABAB. The blocks are represented by rectangles; the atoms in tetrahedral coordination by circles. (a) 3x4 blocks arranged as in $WNb_{12}O_{33}$; (b) 4x4 blocks arranged as in $WNb_{14}W_2O_{44}$; (c) hybrid phase $W_2Nb_{26}W_2O_{77}$ containing rows of 3x4 and 4x4 blocks; (d and e) the surrounding of blocks remains unchanged with respect to 4/4 tetrahedral positions per block.

3.3.b. TYPE 2

The surrounding of the blocks is a changed one in the hybrid phase with respect to the basic structure, if these basic structures are members of different series that differ in the manner by which the blocks are connected.

Type 2a is characterized by a combination of blocks identical in size (fig. 4). Planes in which connection of the blocks occurs remain only partially unchanged (E,F in fig. 4) compared to each one of the basic structures. The resulting different surrounding of the blocks is shown in figure 4f.

Examples are all phases of the series $Me_{3n+1}O_{8n-2}$ with n even, which can be built up by the basic structures $Me_{3n}O_{8n-3}$ and $Me_{3n+1}O_{8n+1}$ with equal values of n. For additional hybrid phases see table 6.

Type 2b differs from type 2a by having blocks of different size (fig. 5). The surrounding of the blocks and the planes in which connection occurs are totally changed in the hybrid structure when compared with the basic structures. The resulting type of surrounding with 2/4 tetrahedral positions per block corresponding to a sequence 1:1 is given in figure 5f,g. More complicated sequences lead to blocks surrounded by 1/4 or 3/4 tetrahedral positions [10].

Examples of a sequence 1:1 are the phases of the series $Me_{3n+1}O_{8n-2}$ with n odd, which result from the basic structures already mentioned with type 2a if the value of n in $Me_{3n}O_{8n-3}$ exceeds the one in $Me_{3n+1}O_{8n+1}$ by 1. For additional examples of more complicated sequences see table 6.

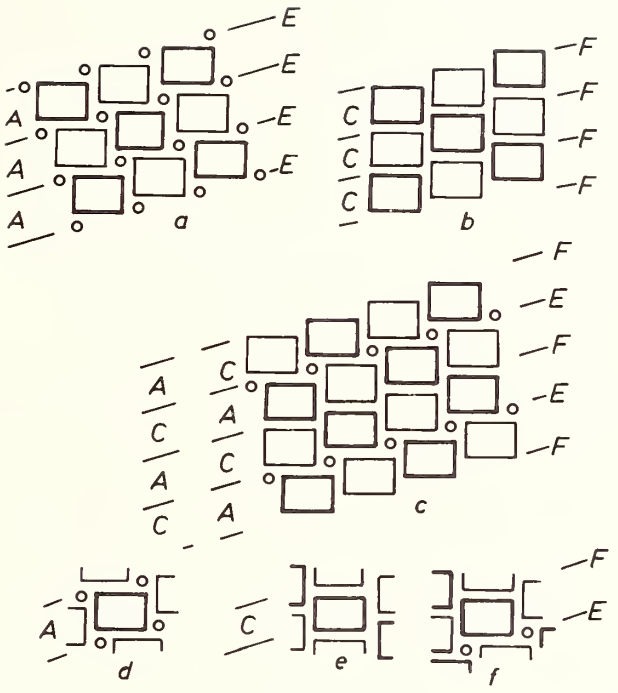

Fig. 4. Combination of building elementd leading to a hybrid structure of type 2a. Rows of blocks of the basic structures AA (series $Me_{3n+1}O_{8n+1}$) and CC (series $Me_{3n}O_{8n-3}$) combine to the resulting hybrid phase of the series $Me_{3n+1}O_{8n-2}$ (n = even). The blocks are represented by rectangles, the atoms in tetrahedral coordination by circles. (a) 3x4 blocks surrounded by atoms in tetrahedral positions as in $WNb_{12}O_{33}$; (b) 3x4 blocks arranged as in $Nb_{12}O_{29}$; (c) hybrid phase $Nb_{25}O_{62}$ in which the rows A and C can no longer be distinguished, because the surrounding of each block has changed. Only shear planes E,F of the basic structures remain unchanged; (d and e) blocks with unchanged surroundings of 4/4 tetrahedral positions per block respectively without tetrahedral positions; (f) surrounding of blocks of the hybrid phase with the sequence 1:1 resulting in 2/4 tetrahedral positions per block.

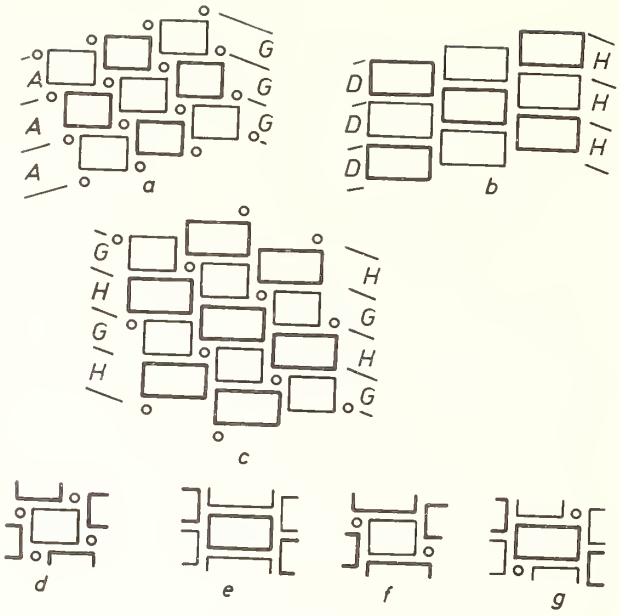

Fig. 5. Combination of building elements leading to a hybrid structure of type 2b. Rows of blocks of the basic structures AA (series $Me_{3n+1}O_{8n+1}$) and DD (series $Me_{3n}(O,F)_{8n-3}$) combine to the resulting hybrid phase of the series $Me_{3n+1}(O,F)_{8n-2}$ (n = odd). The blocks are represented by rectangles, the atoms in tetrahedral coordination by circles. (a) 3x4 blocks surrounded by atoms in tetrahedral positions as in $WNb_{12}O_{33}$; (b) 3x5 blocks as in $MgNb_{14}O_{35}F_2$; (c) hybrid phase $Nb_{28}O_{70}$ (H-Nb_2O_5) formed by combination of rows G and H, not by combination of A and D. In this case shear planes were changed completely. (d and e) blocks with unchanged surrounding corresponding to the basic structures; (f and g) surrounding of the blocks in the hybrid phase with a sequence 1:1 resulting in 2/4 tetrahedral positions per block.

3.4. DEVIATION OF CHEMICAL COMPOSITION FROM IDEAL STRUCTURAL VALUES

3.4.a. RANGES OF HOMOGENEITY

It seems to be characteristic of some types of compounds to exist monophasic in a certain range of gross composition O/Σ Me. In these cases no measurable change in the lattice constants depending on a variation of the chemical composition was detectable. The accurate determination of the limits of a range of homogeneity is based on the sensitivity of the determination of neighbor phases by the Guinier method[11]. Explanation for the existence of these deviations from ideal structures, based on structural arguments, are not consistent at the moment. Explanations by microdomains of neighbor phases or Wadsley defects proved to be insufficient as shown by electron optical investigations [44].

A comparison of the results of investigation (table 2 to 6) shows that ranges of homogeneity are especially realized with certain types of structures if equilibrium conditions are considered.[12]

---

[11] These ranges of homogeneity must be clearly distinguished from solid solutions resulting from the substitution of a cation or an anion but leaving the ratio (O,F)/Σ Me unchanged. In these cases changes in the lattice constants were observed.

[12] Additional metastable ranges of homogeneity are especially observed at lower temperature [13].

No stable ranges of homogeneity could be detected for basic structures of the series $Me_{3n}O_{8n-3}$.

Among the basic structures of the series $Me_{3n+1}O_{8n+1}$ and related structures ($Me_{4n+1}O_{11n}$; $Me_{5n+1}O_{14n-1}$) only one phase ($WNb_{12}O_{33}$) is known to have a range of homogeneity (table 2).

Hybrid phases of type 1 *e.g.* $W_2Nb_{26}W_2O_{77}$ (table 6), $NbO_{2.483}$, $Nb(O,F)_{2.510}$, and $Nb(O,F)_{2.523}$ (table 5) have no detectable ranges of homogeneity[13].

Well known hybrids of type 2 are phases of the series $Me_{3n+1}O_{8n-2}$. In this case each phase (n = 8,9,10,11) has a range of homogeneity with the exception of $Nb_{22}O_{54}$ (n = 7), cf. table 5 and figure 6. It is of special interest, that among these phases $Nb_{25}O_{62}$ (2.467 - 2.478 O/Nb) and $Nb_{28}O_{70}$ (H-Nb_2O_5; 2.489 - 2.50 O/Nb) have the largest ranges of homogeneity. Both structures contain the basic element $Me_{13}O_{33}$ that by itself has a range of homogeneity of 2.516 - 2.538 = 0.022 O/Σ Me. Therefore one may consider, that the element $Me_{13}O_{33}$ transmits a portion of its properties corresponding to $\approx \frac{0.022}{2}$ O/Me to both hybrid phases. Ranges of homogeneity calculated in this way (in brackets) agree well with the observed ones:

$Nb_{25}O_{62}$ (2.469 - 2.480 O/Nb),

$Nb_{28}O_{70}$ (2.490 - 2.500 O/Nb).

A corresponding relation concerning the phases $Nb_{31}O_{77}F$ (2.515 - 2.519 (O,F)/Nb) and $Nb_{34}O_{84}F_2$ (2.527 - 2.532 (F,O)/Nb) which have smaller ranges of homogeneity can not be discussed because accurate knowledge of ranges of homogeneity have not been established for the basic structures $MgNb_{14}O_{35}F_2$ and $WNb_{15}O_{40}F$.

3.4.b. NARROW PHASES WITH DEVIATIONS OF COMPOSITION

Phases with a sharp composition determined by chemical analysis, but differing from the ideal composition derived from structural conditions, mainly belong to the hybrid phases of type 1 (tables 5 and 6). According to paragraph 3.4.a. these phases have no ranges of homogeneity under equilibrium conditions.

Because the structures of hybrid phases of type 1 are combinations of the building elements of neighbor phases, their composition should result from the combination of the compositions of the building elements. These ideal compositions according to their ideal structures could be observed for only two phases (eqs (7) and (8)).

$$WNb_{12}O_{33}(2.538\ O/\Sigma\ Me) + WNb_{14}W_2O_{44}\ (2.589\ O/\Sigma\ Me) \triangleq W_2Nb_{26}W_2O_{77}(2.567\ O/\Sigma\ Me;\ ideal)^{14} \quad (7)$$

$$Nb_{31}O_{77}F(2.517\ X/Nb) + Nb_{34}O_{84}F_2\ (2.529\ X/Nb) \triangleq Nb(O,F)_{2.523}\ (Nb_{65}O_{161}F_3;\ ideal) \quad (8)$$

For equation (7) the actual limits of the neighboring phases are identical with the ideal compositions. For equation (8) the actual limits of both neighboring phases deviate from the ideal composition. For the actual limits of the neighboring phases see equation (9). As shown, the actual composition of the hybrid phase $Nb(O,F)_{2.523}$ may result from the actual limits of the neighboring phases (eq (9)) as well as from their ideal compositions (eq (8)).

$$Nb_{31}O_{77}F\ (2.519\ X/Nb) + Nb_{34}O_{84}F_2\ (2.527\ X/Nb) \triangleq Nb(O,F)_{2.523}\ (actual) \quad (9)$$

---

[13] The observed range of homogeneity of the hybrid phase $NbO_{2.464}$ may possibly be metastable [7].

[14] For additional specifications see tables 5 and 6.

465-504 O - 72 - 7

The actual composition of the following hybrid phases (see fig. 6) can only be explained by a combination of the actual phase limits of both neighbor phases. The relationships with respect to the phases $Nb(O,F)_{2.510}$, $NbO_{2.483}$, and $NbO_{2.464}$ are recognizable from equations 10 through 16.

$$Nb_{28}O_{70}(2.50\ O/Nb)^{15} + Nb_{31}O_{77}F\ (2.517\ X/Nb) \triangleq Nb(O,F)_{2.508}\ (Nb_{59}O_{147}F;\ ideal) \quad (10)$$

$$Nb_{28}O_{70}(2.504\ X/Nb)^{15} + Nb_{31}O_{77}(2.515\ X/Nb) \triangleq Nb(O,F)_{2.510}\ (actual) \quad (11)$$

$$Nb_{25}O_{62}(2.480\ O/Nb) + Nb_{28}O_{70}(2.50\ O/Nb)^{15} \triangleq NbO_{2.491}\ (Nb_{53}O_{132};\ ideal) \quad (12)$$

$$Nb_{25}O_{62}(2.478\ O/Nb) + Nb_{28}O_{70}(2.489\ O/Nb)^{15} \triangleq NbO_{2.483}\ (actual) \quad (13)$$

$$Nb_{22}O_{54}(2.4545\ O/Nb) + Nb_{25}O_{62}(2.480\ O/Nb) \triangleq NbO_{2.468}\ (Nb_{47}O_{116};\ ideal) \quad (14)$$

$$Nb_{22}O_{54}(2.453\ O/Nb) + Nb_{25}O_{62}(2.472\ O/Nb) \triangleq NbO_{2.464}\ (actual;\ method\ 6) \quad (15)$$

$$Nb_{22}O_{54}(2.453\ O/Nb) + Nb_{25}O_{62}(2.467\ O/Nb) \triangleq NbO_{2.460}\ (actual;\ method\ 7) \quad (16)$$

The chemically determined values of the actual composition *e.g.* 2.483 O/Σ Me were obtained from samples prepared in a different way, or prepared by substituting Ti for Nb(IV). Therefore the resulting values are representative for the phases and consequently the differences in composition cannot be explained by microdomains consisting of neighbor phases [11].

Additional hybrid phases known from the electron optical investigations of Allpress [10,11] so far have not been prepared in a monophasic state. Therefore the real chemical composition is still unknown.

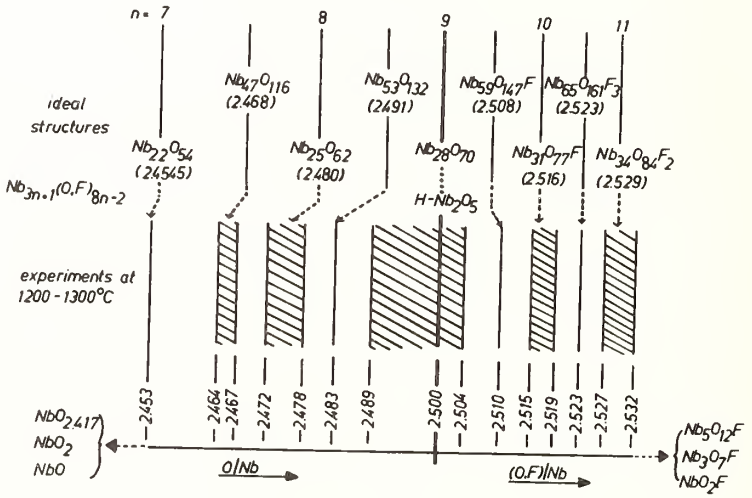

Fig. 6. Section of the systems NbO_2 - Nb_2O_5 and Nb_2O_5 - NbO_2F. Compositions derived from chemical analysis (lower part of the figure) and from ideal structures (upper part) are given for the systems in a high temperature region, in which all known members (n = 7 - 11) of the series $Nb_{3n+1}(O,F)_{8n-2}$ and the corresponding 1:1 hybrid phases exist.

---

15 As modification $H\text{-}Nb_2O_5$.

Additional phases having a composition which deviates from the ideal one are $GeNb_{18}O_{47}$ (table 3) and the hybrid phase $PNb_{22}O_{57.5}$ (table 6). $GeNb_{18}O_{47}$ with the ideal structure $(Me,Nb)_{10}O_{25}$ has a deficiency of oxygen of the same order of magnitude (0.022 O/Σ Me) as $WNb_{12}O_{33}$ (paragraph 3.4.a). This value may be compared with the deviation of the actual composition $PNb_{22}O_{57.5}$ from the ideal formula "$PNb_{22}O_{58}$". As yet these actual compositions cannot be explained by structural considerations.

3.5. STABILITY

According to numerous observations the experimental results gained at higher temperatures (table 2 through 6) may be near to equilibrium conditions of a thermodynamically stable system. This was mainly confirmed by the measurement of equilibrium conditions in the system NbO_2 - Nb_2O_5 at 1300 °C [14]. Values measured in this investigation made it possible to develop a model of the relations [13] between the stability of these phases and the size of the blocks in these structures[16]. It must be mentioned that according to this, the stability of a phase can be considered only in relation to the neighboring phases.

The numerous results of experiments in which one component of a typical compound was replaced in several different ways, suggested that it might be possible to compare qualitatively the stabilities of those compounds (represented by definite structures) with regard to different systems. That means, the situations in a region between two limiting types of structures realized in different investigated systems (*e.g.* between $(Me,Nb)_{12}O_{29}$ and H-Nb_2O_5) may be comparable. The extent to which a structure tolerates the replacement of Me or of O by F may be a rough criterion for the stability of the structure in this region. A supplementary indication of the stability may be the extent of the temperature region in which a structure is stable.

3.5.a. BASIC STRUCTURES

With respect to the basic structures $Me_{3n}(O,F)_{8n-3}$ and $Me_{3n+1}(O,F)_{8n-2}$ members with 3x4 blocks (tables 2 and 3) may be most stable. The structure types $(Me,Nb)_{12}O_{29}$ and $(Me,Nb)_{13}O_{33}$, being stable in an extended range of temperature[17], tolerate different Me cations. Within the series $Me_{3n}(O,F)_{8n-3}$ and $Me_{3n+1}(O,F)_{8n+1}$ the stability decreases with an increasing value of n. Phases with n = 5, such as $MgNb_{14}O_{35}F_2$ and $WNb_{15}O_{40}F$ ($MoNb_{15}O_{40}F$), only show an insignificant tolerance for the replacement of Me, and phases with n = 6 (*e. g.*, $Nb_{18}O_{45}$) are non existent. Related basic structures $Me_{4n+1}O_{11n}$ and $Me_{5n+1}O_{14n-1}$ tolerate a certain replacement of the Me particles but their ranges of existence decrease with increasing block size and are shifted to higher temperatures [5].

3.5.b. HYBRID STRUCTURES OF TYPE 1

Hybrid phases of type 1 are closely related to their neighbor phases (paragraph 3.3). In addition to relations concerning the compositions (paragraph 3.4.b.) they show relationships concerning the stabilities of the neighbor phases. According to this, a hybrid of type 1 could only be observed if both building elements of the hybrid phase were realized by neighbor phases of the same system (tables 5 and 6)[18]. These relationships between the 1:1 hybrids and the series $Me_{3n+1}(O,F)_{8n-2}$ (Me = Nb(v)) are shown in figure 6.

According to the assumed relation of stability the hybrid $NbO_{2.464}$ was only observed in the NbO_2 - Nb_2O_5 system in which also the phase $Nb_{22}O_{54}$ exists as one building element. Though an analogous $(Zr,Nb)_{22}O_{54}$ is non existent, the observation of the phase $(Zr,Nb)O_{2.464}$ does not disagree with this conception, bacause $(Zr,Nb)O_{2.464}$ very probably is metastable [17].

---

[16] This model and the considerations following do not take into account the distortion of octahedra in the actual structures.

[17] The transformation of the monoclinic form of $(Me,Nb)_{12}O_{29}$ into the orthorhombic form was neglected.

[18] The existence of $PNb_{22}O_{57.5}$ seems to be an exception to this.

It is of special interest that the 1:1 hybrid phases observed so far could only be obtained at temperatures higher than needed to prepare the basic structures [13]. It may be possible that the stability of hybrid phases is enhanced by a small increase of entropy[19] with respect to the simpler basic structures. If this is correct it may be understandable why hybrid phases, with the phases $WNb_{16}W_4O_{55}$ and $WNb_{18}W_7O_{69}$ as building elements, could not be observed. Since these (basic) phases are only stable in a region of high temperature, the resulting hybrid phases may be unstable because their range of existence can be expected to be above their melting points. It also fits into this picture that monclinic $Me_{12}O_{29}$, the only phase existing in an especially low temperature region, shows a transformation into its own hybrid[20] which is the orthorhombic form of $Me_{12}O_{29}$. The other monoclinic phases which already exist in a region of high temperature obviously do not show a transformation to orthorhombic modifications because the temperatures required would be above their melting points. According to that, more complicated sequences should not be stable if the 1:1 hybrid phases only exist at higher temperature.

3.5.c. HYBRID STRUCTURES OF TYPE 2

Hybrid phases of type 2 show less clear relationships of stability with respect to the basic structures.

Basic structures of the series $Me_{3n}O_{8n-3}$ and $Me_{3n+1}O_{8n+1}$ combine to hybrids (1:1) represented by the series $Me_{3n+1}O_{8n-2}$. In the following these 1:1 hybrids are tabulated according to decreasing stability.

$(Me,Nb)_{25}O_{62}$ with the building elements $(Me,Nb)_{19}O_{29}$ and $(Me,Nb)_{13}O_{33}$ exists, like its basic structures, in a wide range of temperature and with a considerable variability of composition with respect to the Me cations.

$Nb_{28}O_{70}$ (H-Nb_2O_5) allowed no replacement of Nb without changing the O/Σ Me ratio (*cf.* table 5 (i)); the $Nb_{31}O_{77}F$ structure is only stable in the fluoride system. Both have extended ranges of existance with respect to temperature.

The members $Nb_{22}O_{54}$ and $Nb_{34}O_{84}F_2$ limiting the series $Me_{3n+1}(O,F)_{8n-2}$ (fig. 6), tolerate no replacement of Me. Their range of stability is limited to a small region at high temperature. It is remarkable that these phases are stable though they contain blocks of the non existing structures "$Nb_{10}O_{25}$" and "$Nb_{18}O_{45}$" (tables 2 and 3).

4. SCOPE OF FURTHER INVESTIGATION

With the aid of electron optical methods combined with subtle methods of preparation and chemical analysis it may be possible to perform chemical investigations of hybrid phases, such as $TiNb_{38}O_{97}$, which have more complicated sequences than 1:1. Furthermore it may be possible to determine ranges of homogeneity, suspected for hybrid phases like $WNb_{26}O_{68}$ because of a comparison[21] with the related phases $Nb_{25}O_{62}$ and $Nb_{28}O_{70}$. With respect to this, it is important to know whether the thermodynamic stability of the phases decreases with increasing complexity of sequences in these structures. This question should be solved in further investigations. In addition to this the thermodynamic concept of a phase must be reconsidered if the sequences become extremely complicated. Metastable regions of homogeneity not mentioned in this paper (*c. f.*, [13]), should also be investigated with the new methods.

---

[19] In principle the existence of block structures is favored at high temperatures because of the increase in entropy [13,17].

[20] The orthorhombic form may be described as a hybrid consisting of component rows of the monoclinic form [11].

[21] A calculation according to paragraph 3.4.a. leads to a range of homogeneity of 2.502 - 2.518 O/Σ Me for $WNb_{26}O_{68}$.

5. ACKNOWLEDGEMENTS

The author thanks Professor Harald Schäfer for his stimulating interest and for continuous support during a long time of cooperation in the institute at Münster. He also thanks D. Bergner, M. Görbing, G. Köpke, W. Mertin, M. Trenkel, and E. Vogel for their cooperation. The author is obliged to the Landesamt für Forschung, Düsseldorf and to the Verband der Chemischen Industrie - Fonds der Chemischen Industrie - for their support.

6. REFERENCES

[1] Gruehn, R., and Schäfer, H., Naturwissenschaften, 50, 642 (1963).
[2] Wadsley, A. D., Acta Cryst., 14, 664 (1961).
[3] Roth, R. S., and Wadsley, A. D., Acta Cryst., 18, 724 (1965).
[4] Schäfer, H., Gruehn, R., Schulte, F., and Mertin, W., Bull. Soc. Chim. France, 1965, 1161.
[5] Gruehn, Monatshefte Chemie, 96, 1789 (1965).
[6] Andersson, S., Mumme, W. G., and Wadsley, A. D., Acta Cryst., 21, 802 (1966).
[7] Gruehn, R., and Norin, R., Z. anorg. u. allgem. Chem., 367, 209 (1969).
[8] Gruehn, R., Naturwissenschaften, 54, 645 (1967).
[9] Allpress, J. G., Sanders, J. V., and Wadsley, A. D., Phys. Stat. Sol., 25, 541 (1968).
[10] Allpress, J. G., and Wadsley, A. D., J. Solid State Chem., 1, 28 (1969).
[11] Allpress, J. G., J. Solid State Chem., 1, 66 (1969).
[12] Allpress, J. G., J. Solid State Chem., 2, 78 (1970).
[13] Gruehn, R., Habilitationsschrift, Münster 1968.
[14] Schäfer, H., Bergner, D., and Gruehn, R., Z. anorg. u. allgem. Chem., 365, 31 (1969).
[15] Schäfer, H., Chemical Transport Reactions, Academic Press, N. Y., London 1964.
[16] Gruehn, R., and Schäfer, H., J. Less-Common Metals [Amsterdam] 10, 152 (1966).
[17] Gruehn, R., unpublished work.
[18] Bergner, D., Ph.D. Thesis, Münster 1966.
[19] Schäfer, H., and Huesker, M., Z. anorg. u. allg. Chem., 317, 321 (1962).
[20] Gruehn, R., and Brunner, H., unpublished work.
[21] Gruehn, R., Z. analyt. Chem., 221, 146 (1966).
[22] Quentin, K.-E. and Rosopulo, A., Z. analyt. Chem. 241, 241 (1968).
[23] Lundberg, M., J. Solid State Chem., 1, 463 (1970).
[24] Gruehn, R., Mertin, W., and Schäfer, H., J. Solid State Chem., 1, 425 (1970).
[25] Eror, N. G. and Smyth, D. M., in *The Chemistry of Extended Defects in Non-Metallic Solids*", North-Holland Publ. Comp., 1970.
[26] Waring, J. L., and Roth, R. S., J. Res., NBS, 69A, (phys. and chem.) No. 2, 119 (1965).
[27] The phases were identified through samples from Professor Dr. F. P. Emmenegger, *c.f.*, Emmenegger, F. P., and Petermann, A., J. of Crystal Growth, 2, 33 (1968).
[28] Norin, R., and Arbin, C. G., unpublished work.
[29] Norin, R., and Dahlen, B., Acta Chem. Scand., 23, 1826 (1969).
[30] Burdese, A., Bolera, M. L., and Rolando, P., Atti Accad. Sci. Torino I, Cl, Sci. fisiche, mat., natur., 99, 565 (1964/65).
[31] Roth, R. S., Wadsley, A. D., and Andersson, S., Acta Cryst., 18, 643 (1965).
[32] Roth, R. S., and Wadsley, A. D., Acta Cryst., 19, 42 (1965).
[33] Mertin, W., Diplomarbeit, Münster 1964.
[34] Waring, J. L., and Roth, R. S., Acta Cryst., 17, 455 (1964).
[35] Levin, E. M., and Roth, R. S., J. Solid State Chem., 2, 250 (1970).
[36] Andersson, S., Z. anorg. u. allg. Chem., 366, 96 (1969).
[37] Norin, R., Acta chem. Scand., 23, 1210-1214 (1969).
[38] Gatehouse, B. M., and Wadsley, A. D., Acta Cryst., 17, 1545 (1964).
[39] Åström, A., Acta chem. Scand., 20, 969 (1966).
[40] Norin, R., Carlsson, M., and Elgquist, B., Acta. chem. Scand., 20, 2892 (1966).
[41] Gruehn, R., and Norin, R., Z. anorg. u. allgem. Chem., 355, 176 (1967).
[42] Norin, R., private communication.
[43] Wadsley, A. D., and Andersson, S., in *Perspectives in Structural Chemistry*, (Dunitz, J. D., and Ibers, J. A., eds.), Vol. III, Wiley, New York 1969.
[44] Allpress, J. G., and Roth, R. S., J. Solid State Chem., 3, 209 (1971).

DISCUSSION

J. G. Allpress: I would just like to make the comment that in the circumstances where you have a series of very closely related phases, perhaps the Guinier techniques are not sufficiently sensitive as a means of determining phase boundaries. One really has to look at the samples at the unit cell level using an electron microscope in order to tell whether one has randomly distributed Wadsley defects which will contribute to the change in stoichiometry.

R. Gruehn: Yes, that is a very important point. I had not mentioned it because the time was too short. For the investigation of this field in the future, it is very important to use the methods you have used in this field. However, I think the compositions of the mono-phasic state can be determined by Guinier investigations with a deviation of only one in the third place for phases with small differences in composition. The two phase regions are very small in this case and there is a detection limit of ~0.001 in the oxygen to metal ratio (O/M≈0.001). The uncertainty of 0.001 in the O/M ratio may correspond to a content of 20 percent of a very closely related neighbor phase. This must be the reason why you find regions of neighbor phases in a sample that was homogeneous on x-ray photographs. I think for the investigation of the differences in the present work this is a sufficient accuracy but I hope, in the future, we will also investigate this field with the electron optic technique.

B. Cox: Would you like to speculate on what fraction of the composition range of these compounds is due to extended defects of the type that John Allpress looks at, which presumably don't contribute to the high temperature electrical conductivity, and what fraction is due to point defects which would contribute to the high temperature electrical conductivity of these compounds.

R. Gruehn: We do not know exactly the reasons for these ranges, but I think it is important to know that these ranges of homogeneity are observed also in phases without electric conductivites. You can have a range of homogeneity from O/M 2.500 to 2.489 in the system with niobium 4^+ as well as in the system with titanium 4^+. In the system with niobium 4^+ we have electrical conductivity, increasing with increasing niobium 4^+ content; but in the other system we have no electrical conductivity and it has exactly the same range. It may be that there are defects within the blocks or additional matter, metal, and oxygen within the blocks. I have spoken with Sten Andersson on this point. Some years ago, we considered that there may be additional metal in the tetrahedral holes. You have seen these holes on the drawings pictured with circles. If these deviations are due to additional metal in tetrahedral positions they could not be transmitted from one phase to the other, in the way mentioned in my paper, because the surrounding of the block is not the same in the hybrid as in the original phase. I think there must be defects within the blocks.

National Bureau of Standards Special Publication 364, Solid State Chemistry, Proceedings of 5th Materials Research Symposium, issued July 1972.

THE APPLICATION OF ELECTRON OPTICAL TECHNIQUES TO HIGH TEMPERATURE MATERIALS

John G. Allpress

Commonwealth Scientific and Industrial Research Organization
Division of Tribophysics
Melbourne, Australia

Careful studies of phase equilibria in many high temperature systems have revealed unexpectedly complex structural relationships, which are frequently very difficult to unravel by means of conventional x-ray techniques. The purpose of this contribution is to indicate how and why the electron microscope can be used to advantage in these circumstances. The value of the technique will be demonstrated by referring to the following recent applications in the field of the structural chemistry of oxides: (1) The determination of unit cell data for microcrystalline samples of alkali metal rare earth titanates, using electron diffraction. These materials have orthorhombic superlattices of the perovskite structure; (2) The use of dark field microscopy to study the precipitation of the ferrimagnetic spinel $LiFe_5O_8$ from a nonstoichiometric matrix of α-$LiFeO_2$. The morphology of the precipitate depends critically upon prior thermal treatment; (3) The direct observation of crystallographic shear planes in WO_{3-x} ($x<0.05$) and $WO_3 \cdot yNb_2O_5$ ($y=0.03$-0.09). The results show how changes of composition are accommodated in these systems, and provide clues as to the mode of formation and diffusion of crystallographic shear defects; (4) The study of regions of 'solid solution' in the system TiO_2-Nb_2O_5 (>50 mol % Nb_2O_5), by lattice imaging. Variations in composition are accommodated by coherent intergrowth, at the unit cell level, of thin slabs of several parent phases; and (5) The study of phases in the system WO_3-Nb_2O_5 which have structures related to that of tetragonal tungsten bronze. Several different superlattices are possible, and lattice images provide direct evidence for order-disorder, microdomain formation, and intergrowth with material having a much simpler cubic structure.

Key words: Crystal structure; crystallographic shear planes; electron diffraction; electron microscopy; lattice images; lithium ferrites; lithium lutetium titanate; niobium-titanium oxides; niobium-tungsten oxides; tungsten oxides; Wadsley defects.

1. INTRODUCTION

Of all the techniques available to the solid state chemist, x-ray diffraction is undoubtedly the most important. Even when structural information is not the primary aim of a particular investigation, x-ray methods are almost universally used to establish the identity and purity of a phase, before proceeding to any study of its properties. However, it frequently happens that for one reason or another, the structural results obtained by x-ray diffraction procedures may be incomplete or inconclusive, and other methods of approach must be sought. Some common instances where this situation arises are as follows: (a) The crystallite size of the material is too small for the application of single crystal x-ray methods. In these circumstances, it is often difficult or impossible to determine the unit cell dimensions and symmetry unambiguously from x-ray powder data. (b) The material is disordered in some way, which may or may not be indicated by the x-ray data. Even when disorder is suspected, its nature and extent may be impossible to determine with certainty.

These and other similar problems occur quite frequently in high temperature solid state chemistry. The purpose of this paper is to show how and why electron optical techniques can be used to advantage in conjunction with x-ray diffraction procedures for tackling them.

2. ELECTRON AND X-RAY DIFFRACTION

Although the diffraction of electrons is basically similar to that of x-rays, important differences arise as a consequence of differences in the properties of the two radiations. In what follows, the properties of 100 kV electrons will be compared with those of Cu Kα X-radiation.

2.1. WAVELENGTH

Electron wavelengths $\lambda \simeq 0.04$ Å ($\lambda \simeq 0.004$ nm) are about one fortieth of those of x-rays $\lambda \simeq 1.5$ Å ($\lambda \simeq 0.15$ nm). It follows from Bragg's Law that the scattering angles θ are very small, and the simple formula $\lambda = 2d\theta$, where d is the interplanar spacing, is a good approximation.

A second very important consequence of the shorter wavelengths is demonstrated by the Ewald construction, illustrated in figure 1. The array of dots represents a two-dimensional section through a reciprocal lattice, with origin O. The direction of an incident beam of radiation is indicated by the dashed line, and the vector k_o, terminating at O, is of length $1/\lambda$ for x-rays. Any reciprocal lattice point $hk\ell$ which falls on the surface of the sphere of radius $1/\lambda$, centred on the dashed line and passing through O, represents a set of planes for which Bragg's Law is satisfied. In the section shown in figure 1, the circle (in two dimensions) for x-rays, centred at A, passes through only one point (encircled), in addition to the origin. However, for electrons, $1/\lambda$ is forty times larger, and an arc BOC of the corresponding circle is shown. It cuts up to four points on either side of the origin.

Thus, in general, for any one angle of incidence, a much larger number of Bragg reflections will be excited by electrons than by x-rays. In the particular case when the beam is incident down a zone axis, an extended area of a reciprocal lattice section may be excited at one time. Figure 2 shows electron diffraction patterns from a crystal of high temperature (H-) Nb_2O_5, which has a large unit cell. In (a), the electron beam is incident down the b axis, and (b), (c) and (d) were recorded after tilting the crystal about the c^* axis by 1°, 4°, and 24° respectively. The appearance of these patterns can be explained readily using diagrams, similar to figure 1, by altering the angle of incidence of the radiation. In figure 2d, the arcs which do not include the central beam of the pattern contain upper layer reflections of the type $h1\ell$ and $h\bar{1}\ell$.

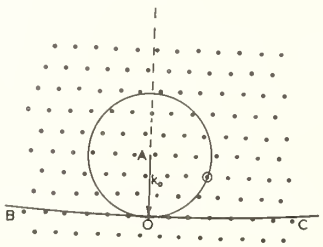

Fig. 1. The Ewald construction. The array of dots represents a section through a reciprocal lattice, with origin O. k_o is a vector in the incident beam direction, of magnitude $1/\lambda$. The circle is a section through the Ewald sphere appropriate for x-rays, and the arc BOC is part of the section for 100kV electrons. Points which lie on the circle (or arc) represent planes for which Bragg's Law is satisfied.

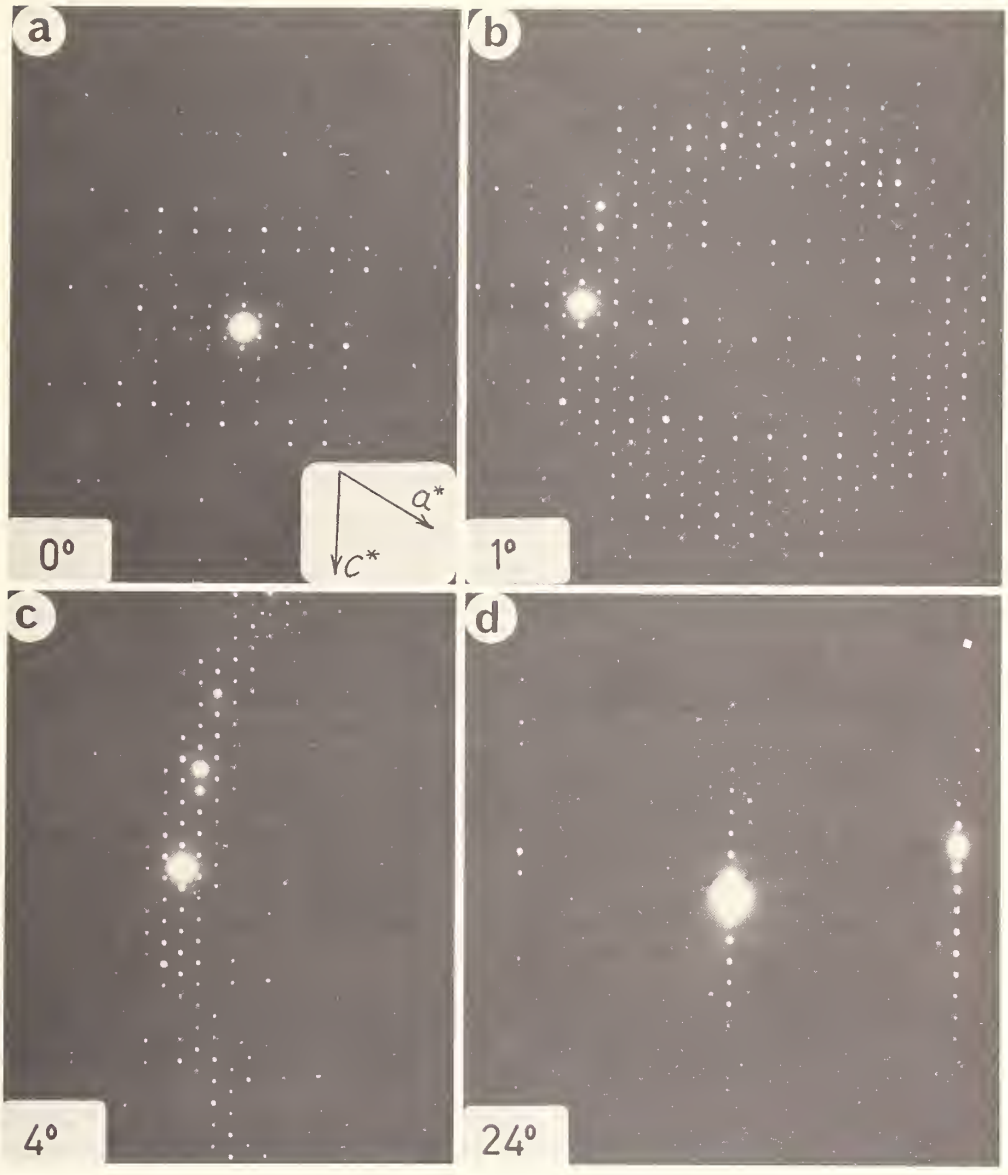

Fig. 2. Electron diffraction patterns from a fragment of H-Nb_2O_5. (a) (0l0) reciprocal lattice section. (b-d) after tilting away from (0l0) about c^*, through the angles shown.

Other factors also contribute to the ease with which simultaneous excitation of many Bragg reflections occurs in electron diffraction. In particular, the reciprocal lattice spots are extended in the direction of the incident radiation, because the specimens are necessarily very thin in this direction. Secondly, the samples may be sufficiently buckled over the illuminated area to allow additional reflections to satisfy the Bragg condition.

The overall result of the difference in wavelength is therefore that using electrons, extended sections of the reciprocal lattice can be easily recorded from a stationary crystal. The equivalent data are obtainable with x-rays only by using a moving crystal technique, or by employing white radiation. The geometry of electron diffraction patterns is exceedingly simple, and corresponds closely to that obtained by the x-ray precession method.

2.2. SCATTERING FACTORS

The interaction of electrons with atoms is about 1000 times greater than that of x-rays. For this reason, a large proportion of electron radiation incident on a thin crystal is diffracted; the diffraction pattern can be observed visually on a fluorescent screen and recorded in a few seconds on a photographic emulsion. Adjustments to the orientations of a crystal can therefore be made while watching the diffraction pattern, and zone axis orientations such as figure 2a indicates can be obtained quickly and easily. The facility with which very thin crystals can be examined, combined with the ability to select individual crystals or parts of crystals as small as $10^{-10}cm^2$ in cross section, makes it a straightforward matter to record reciprocal lattice sections from 'single crystals' which may be only $10^{-15}cm^3$ in volume.

The high scattering factors for electrons have other less favourable consequences. The limitations on specimen thickness are severe - about 200 nm is the maximum for most materials. This immediately raises the problem of sample preparation. Thin foils are perhaps the most ideal form of specimen, but apart from metals and a few other materials which cleave readily, they are not easily prepared. Thinning by ion bombardment shows promise in this respect [1][1]. The simplest method of obtaining thin samples is by grinding, dispersing the resulting fine powder on carbon-coated specimen grids and searching in the electron microscope for thin fracture fragments. Most inorganic materials are brittle, and can be ground without introducing deformation, but the possibility of observing artefacts which are a consequence of the method of specimen preparation must always be taken into account.

Multiple scattering of diffracted beams is a serious problem for samples thicker than 10 nm or even less. Diffracted electrons are themselves subject to further diffraction as they traverse the crystal, and the intensity of emergent beams frequently bears no relation to values expected for single or kinematic scattering. For example, figure 3 shows the results of computations of the variation of intensity of some 00ℓ beams with thickness, for a perfect crystal of $TiNb_{24}O_{62}$ [2]. For each beam, there is a thickness at which the intensity drops to zero, and this thickness is known as the extinction distance. Clearly, these extinction distances vary widely for different beams, and any attempt to interpret electron diffraction intensities must take these effects into account. This requires the application of *n*-beam dynamical theory [3].

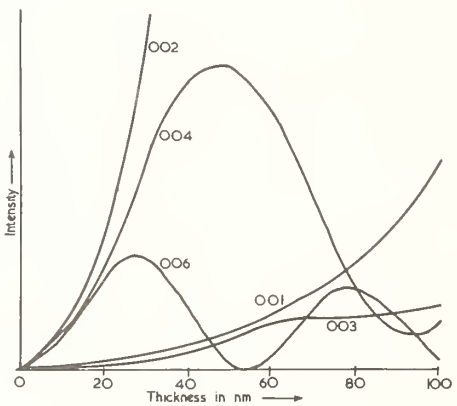

Fig. 3. Computed electron diffraction intensities for some 00ℓ beams from $TiNb_{24}O_{62}$, showing that the variation with thickness is non-linear, and changes drastically for different beams.

[1] Figures in brackets indicate the literature references at the end of this paper.

The modification of diffraction intensities by multiple scattering extends to reflections which are formally forbidden by space group symmetry. Very frequently, these forbidden reflections can be excited with appreciable intensity in electron diffraction, and the effect is illustrated in figure 4, which shows several patterns from a fragment of $LiLuTi_2O_6$ [4]. Figure 4b was recorded after tilting the fragment about its *c* axis by *ca.* 48° from its position in figure 4a. Figure 4b contains 00ℓ spots for $\ell \neq 2n$ (arrowed), which are absent in figure 3a, and forbidden by the space group, Pbcm. This is a consequence of multiple scattering, which can operate to produce intensity at forbidden spots in figure 3b, but not in figure 3a. The appearance of forbidden spots can usually be predicted, and correct symmetry information can be derived, provided that a sufficient number of reciprocal lattice sections are examined.

Finally, a large proportion of the electron radiation incident on a crystal is scattered inelastically, and the energy lost to the crystal appears as heat. It is possible to melt refractory materials such as Nb_2O_5 in the electron beam, but provided thin crystals and moderate beam intensities are used, the heating effect can be controlled. Nevertheless, it is not easy to examine heat-sensitive materials such as hydrates, or crystals which undergo transformations at temperatures below about 600 K, unless special cooled sample stages are employed.

2.3. CHARGE

The fact that the electron beam carries a charge, in contrast to x-rays, means that magnified images can be obtained, using magnetic focussing. This fact lies at the basis of electron microscopy. It allows the direct observation of very small fragments or selected areas, and correlation with the electron diffraction pattern of the same area. Specific features in a diffraction pattern can be investigated by dark-field imaging, using selected diffracted beams. A great deal of information on the nature of defects can be obtained by recording their images at a number of different but known orientations. These techniques have been largely developed and refined for application to metals [5], but their use for the study of non-metallic materials is equally appropriate and rewarding [6,7].

Finally, the examination of samples at high magnifications is in principle capable of yielding structural information at the unit cell level. This technique of lattice imaging has been used for specifying resolution, and some spectacular results have been achieved -

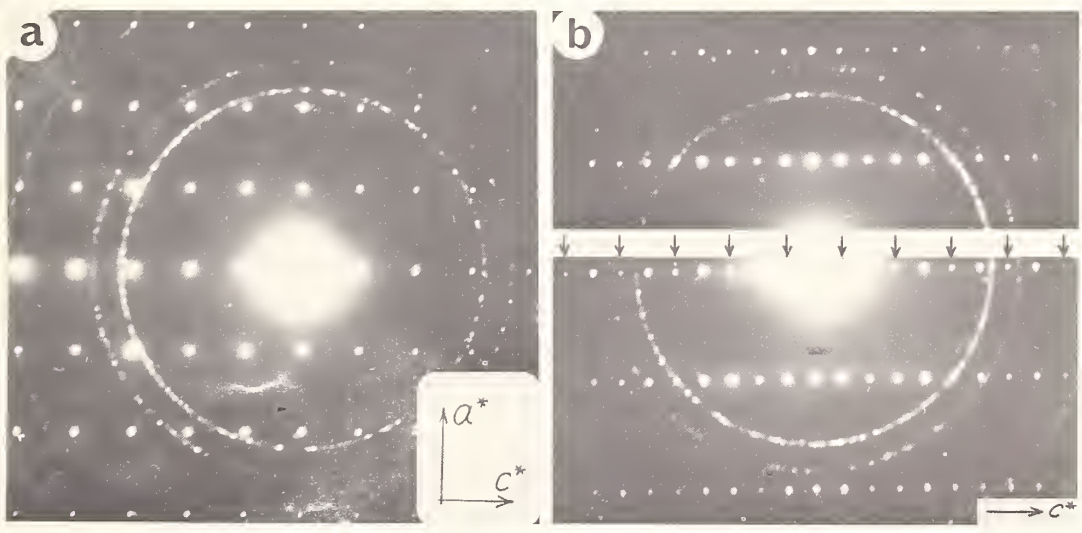

Fig. 4. Electron diffraction patterns from a fragment of $LiLuTi_2O_6$. (a). (010) reciprocal lattice section. (b). $(1\bar{1}0)$ section, obtained by tilting the fragment about *c* by 48°. In this orientation, multiple scattering produces strong reflections in the forbidden positions $0k0$, $k \neq 2n$ (arrowed). The rings in the patterns come from a thin deposit of aluminium, and are used as a calibration.

spacings down to 0.088 nm have been resolved using metal foil samples [8]. Much of this work requires special skill and equipment, but for materials with large unit cells, useful results can be obtained relatively easily, using instruments with more moderate resolution capabilities; say 0.5 - 1 nm. The underlying principle, as stated by Cowley and Moodie [9], is that for very thin specimens which can be regarded as phase gratings, the contrast in the slightly underfocussed image is a representation of the charge distribution within the object. This distribution need not be periodic, and it is therefore possible to examine disordered materials and obtain direct information about their structure.

In the following sections, we shall examine some applications of electron microscopy to high temperature oxides, which illustrate the advantages of the technique as indicated by the foregoing discussion.

3. THE STRUCTURE OF ALKALI METAL RARE EARTH TITANATES, $MRTi_2O_6$ [4]

A series of powder samples of $MRTi_2O_6$ (M = Li, Na; R = Y, La, Nd - Lu) was prepared and examined by x-ray diffraction. The powder data showed obvious similarities to data from perovskites, but the patterns from the lithium compounds could not be indexed with certainty. We therefore obtained 'single crystal' electron diffraction patterns from minute fragments at several different orientations (*e.g.* fig. 4). A thin layer (*ca.* 2 nm) of aluminum was evaporated on to the specimen grids in order to provide an internal standard for the determination of interplanar spacings. $LiLuTi_2O_6$ was studied in detail, and its space group (Pbcm) and approximate unit cell dimensions were obtained from these patterns. The x-ray data were then indexed, and accurate unit cell dimensions were derived. The compound is orthorhombic, with a = 5.175, b = 5.409, c = 15.007 Å. The limited amount of x-ray powder intensity data were used to test several possible structural models, all based on a perovskite subcell. It was quickly established that the octahedral sites were occupied by titanium, and that lithium and lutetium shared the twelve-co-ordinate sites in an ordered manner. Refinement of this model is at present being attempted, in order to determine the distortions from the ideal arrangement.

The sodium compounds proved to orthorhombic, with $a \simeq b \simeq 5.4$ Å, $c \simeq 7.6$ Å, space group Pbnm. They are isostructural with the rare earth orthoferrites [10], and an analysis of the x-ray powder intensity data showed that the sodium and rare earth cations share the twelve-co-ordinate sites randomly. Electron diffraction patterns from these phases (which were prepared by solid state reaction at about 1300 K) gave a completely false impression of pseudo-cubic symmetry, with $a \simeq 7.6$ Å, as a consequence of twinning on a very fine scale. When the samples were sintered for several hours at 1470 K, the twinned domains became large enough to be readily distinguished by dark field microscopy. For example, figure 5a shows an electron diffraction pattern from a fragment of sintered $NaEuTi_2O_6$. On its own, it indicates a square unit mesh with a dimension of about 7.6 Å. However, by selecting the reflections circled in this pattern, and using them to obtain dark field images (see sec. 4), the micrographs in figure 5b and 5c respectively, were obtained. They show that the circled diffracted beams come from different parts of the same fragment. By selecting these parts separately and recording their diffraction patterns, it was established that the pattern in figure 5a is a composite one, in which two (110) sections, rotated 90° with respect to each other, and a third (001) section, of the true orthorhombic reciprocal lattice are superimposed. Within each part of the fragment which is imaged in figures 5b, c, there are boundaries separating regions of similar contrast. We believe that these are probably anti-phase boundaries (see sec. 7) and are currently investigating their origin.

4. PRECIPITATION OF $LiFe_5O_8$ FROM NON-STOICHIOMETRIC α-$LiFeO_2$ [11]

α-$LiFeO_2$ has the cubic rocksalt structure with lithium and iron sharing the cation sites [12]. Electron diffraction patterns from this material (fig. 6a) show distinctive patterns of diffuse scattering, indicative of short range order of the cations. At temperatures below about 840 K, ordering of the cations takes place, and the diffuse intensity is replaced by additional sharp reflections from one or other of several tetragonal modifications [2].

When α-$LiFeO_2$ is heated at temperatures above about 1250 K for prolonged periods, it loses lithium, and when quenched in air, extra spots appear in the diffraction patterns (*e.g.* fig. 6b). The origin of these spots was established by the technique of dark field microscopy - images were recorded with the objective aperture centered on one of the extra

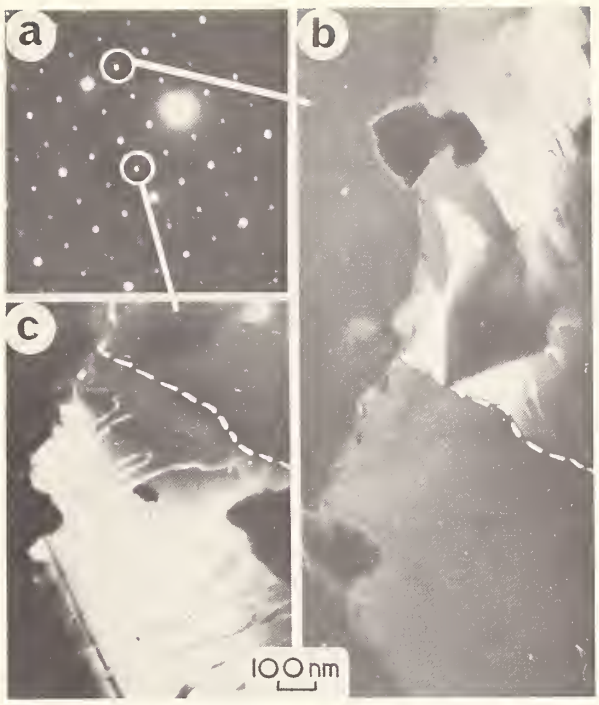

Fig. 5. (a). Electron diffraction pattern from a twinned fragment of $NaEuTi_2O_6$. (b-c). Dark field images from the same fragment, using the reflections identified in (a). A white dashed line marks the boundary between the two regions of the fragment from which these two reflections were diffracted.

spots, and all others, including the central beam, were excluded. Bright areas in these dark field images correspond to regions which diffract into the position selected by the objective aperture. Thus, in figure 6c, the star-shaped particles embedded in the matrix of α-$LiFeO_2$ are responsible for the extra spots in figure 6b. When the same sample was annealed at 870 K, octahedral particles were obtained, which have square projections when viewed down <001> (fig. 6d), and by rapid quenching from 1300 K into water, a homogeneous material giving patterns without extra spots (*i.e.* similar to fig. 6a) was obtained. We were able to identify the particles as $LiFe_5O_8$, a ferrimagnetic spinel having a lattice parameter almost exactly twice that of α-$LiFeO_2$ [13]. The anion lattices of the rocksalt and spinel structures are identical, hence the particles are coherent with the matrix, and are accommodated with negligible strain.

The lithium deficiency caused by heating α-$LiFeO_2$ at 1300 K can be retained by rapid quenching, but slower rates of cooling result in the precipitation of $LiFe_5O_8$. The morphology of the precipitate is a function of the rate of cooling, and in addition to the shapes in figure 6, filamentary dendritic growths have been observed.

Intergrowth of the rocksalt and spinel structures has also been observed in thin flakes grown from borate fluxes [14]. During an attempt to grow larger crystals of α-$LiFeO_2$ by this method [15], we obtained dendrites which were apparently non-stoichiometric. Some of these contained extensive regions of $LiFe_5O_8$ in association with α-$LiFeO_2$, as illustrated by the bright field image in figure 7. The featureless region marked P is α-$LiFeO_2$, and the dark region S, which contains numerous domain boundaries (*e.g.* D) and holes (H) is ordered $LiFe_5O_8$. The interface between the two phases is very well defined, and lies on {111} planes.

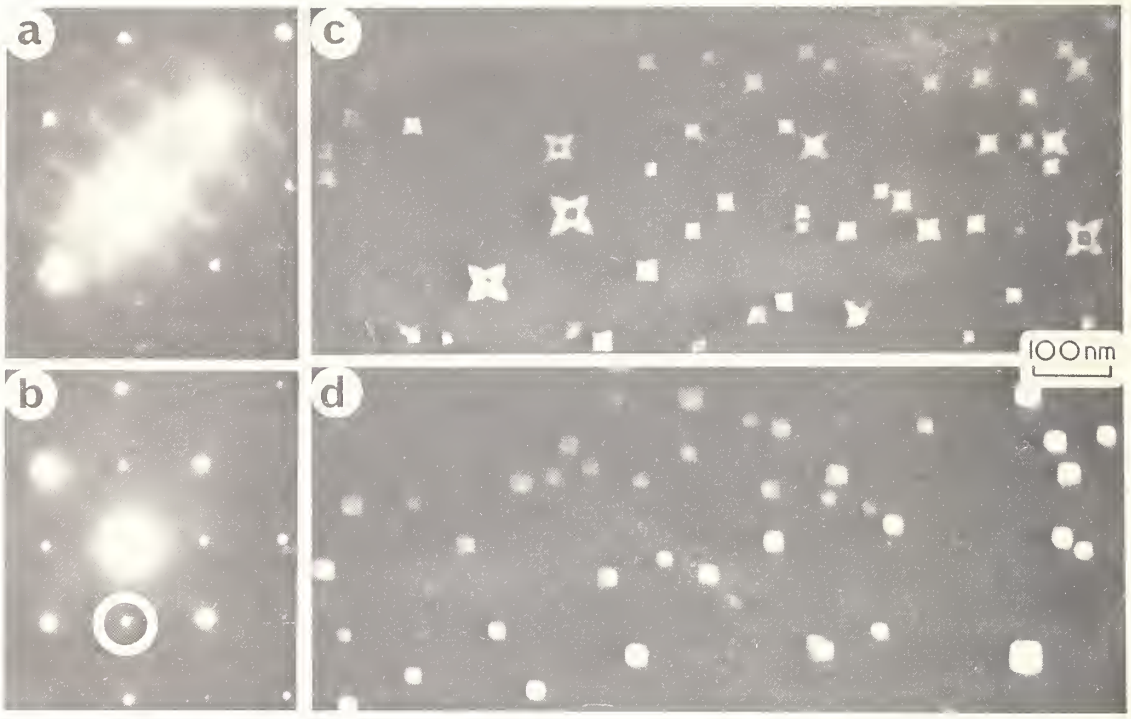

Fig. 6. (a). (001) electron diffraction pattern from α-$LiFeO_2$, showing diffuse scattering in addition to sharp Bragg reflections. (b). (001) pattern from α-$LiFeO_2$, after heating at 1270 K for 65 hours. Note the extra reflections as compared with (a). (c-d). Dark field images, using the reflection circled in (b), from samples quenched in air from 1270 K (c), and annealed at 870 K (d). The star-shaped and square images come from precipitates of $LiFe_5O_8$.

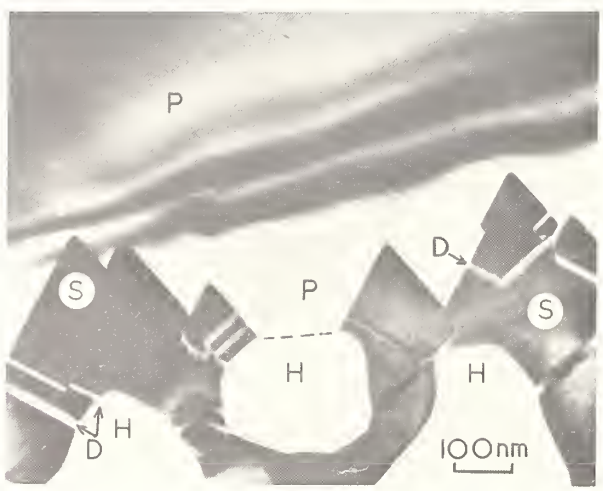

Fig. 7. Bright field image from a dendritic fragment, showing intergrowth of α-$LiFeO_2$ (P) with ordered $LiFe_5O_8$ (S). Domain boundaries (D) are present in the $LiFe_5O_8$. The boundary between the region P and a hole in the fragment (H) is marked by a dashed line.

This investigation illustrates the value of selected area diffraction and dark field microscopy as means of identifying the source of unexpected features in diffraction patterns. Systems which exhibit order-disorder phenomena, such as TiO_x [16] afford many opportunities for the application of these techniques.

5. CRYSTALLOGRAPHIC SHEAR IN MO_{3-x} [17-19]

In a series of careful x-ray studies, Magnéli et al. [20] have shown that a family of phases, closely related to ReO_3 but slightly deficient in oxygen, contain 'recurrent dislocations' or 'crystallographic shear (CS) planes' [21]. In these phases, the regular arrangement of corner-shared octahedra characteristic of cubic ReO_3 (fig. 8a) is interrupted periodically by parallel regions where octahedra share edges (arrowed in fig. 8b, c). This reduces the overall oxygen/metal ratio, and is an important means of accommodating non-stoichiometry in ReO_3-related systems. The idealized structure of ordered $W_{20}O_{58}$ [22] is shown in figure 8b. In this case, the CS planes lie parallel to $(310)_R$ (R = ReO_3-type parent structure). In the series $(Mo,W)_nO_{3n-1}$, represented in figure 8c by the member n = 8 [20], the CS planes are parallel to $(210)_R$. The composition of any particular phase is a function of the direction and spacing of the CS planes, and Magnéli [20] has indicated how the unit cell dimensions and structures of any hypothetical ordered compound of this type, containing CS planes parallel to $\{m10\}_R$ can be predicted with reasonable accuracy.

In most of these phases, the periodicity of the CS planes is large (>2 nm)(>20 Å), and spacings of this magnitude are very readily resolved in the electron microscope. In addition, it seemed probable that an ordered arrangement of CS planes might be the exception rather than the rule, since the interaction between planes spaced so far apart is likely to be small. While indications of disorder have been obtained from x-ray studies, electron microscopy should allow the arrangement of CS planes to be observed directly. We have therefore made an electron optical study of WO_{3-x} (x<0.05) [17,18] and $WO_3 \cdot yNb_2O_5$ (y=0.03=0.09) [19], since both these systems were reported to contain phases of this type.

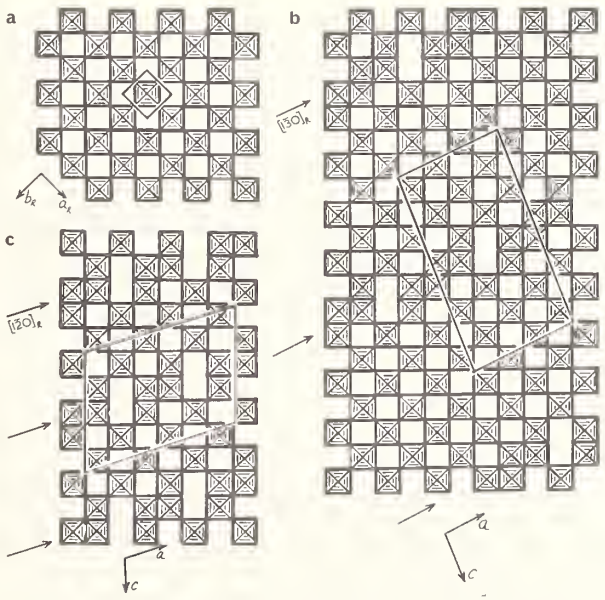

Fig. 8. Idealized models of (a) ReO_3, (b) $W_{20}O_{58}$, and (c) Mo_8O_{23}. Each square represents an octahedron of oxygen atoms surrounding a central metal atom, viewed down a body-diagonal. The corner oxygen atoms are shared between neighboring octahedra. In the crystallographic shear planes (arrowed) the octahedra share edges rather than corners. The subscript R refers to the ReO_3-type subcell.

Figure 9 shows some results typical of WO_{3-x}. The electron diffraction patterns (a, c) contain a square array of strong spots, characteristic of the ReO_3-type parent lattice. In addition, there are lines of spots (a) or streaks (c) lying parallel to $(310)_R$ and $(210)_R$ respectively. The corresponding images (b, d) contain dark lines, more or less regularly arranged in (b), but randomly spaced in (d), lying parallel to $[1\bar{3}0]_R$ and $[1\bar{2}0]_R$ respectively. We believe that these dark lines correspond to the CS planes, and it has been shown [17,18,23] that their direction and spacing is consistent with the known compositions of the samples, $x \approx 0.05$ (a, b) and $x = 0.006$ (c, d), if it is assumed that they have structures analogous to those in figure 8.

In $WO_3 \cdot yNb_2O_5$, [19], the situation is more complex. As the Nb_2O_5 content increases, the direction of the CS planes changes from $\langle 120 \rangle_R$ (at $y \approx 0.03$) through $\langle 140 \rangle_R$ ($y \approx 0.06$) to $\langle 010 \rangle_R$ ($y \approx 0.09$), while the spacing of the planes tends to remain relatively constant in the region 5-7 nm. Using Magnéli's data [20], it has been possible to postulate idealized structures whose lattice parameters and compositions agree with the observed results. In the case of $Nb_2O_5 \cdot 11WO_3$, in which the CS planes lie parallel to $(010)_R$, Roth and Waring's x-ray powder data [24] were successfully indexed using parameters derived from electron diffraction patterns.

In principle, it is possible to cover the whole range of compositions represented in these studies by a single series of phases, with CS planes parallel to a specific direction (say $(210)_R$), and varying only in spacing. In practice, a variety of directions is observed, and there is an increasing amount of evidence that a narrow range of spacings is preferred over others, for any particular system. The present results confirm similar observations on TiO_{2-x} [25-27] that as the composition tends towards that of the parent structure, the plane of crystallographic shear tends towards that which has the least effect on the stoichiometry. These planes are {210} for ReO_3-type systems, and {132} for rutile [27]. Possible reasons for a preferred spacing of CS planes have been discussed recently by Bursill and Hyde [28].

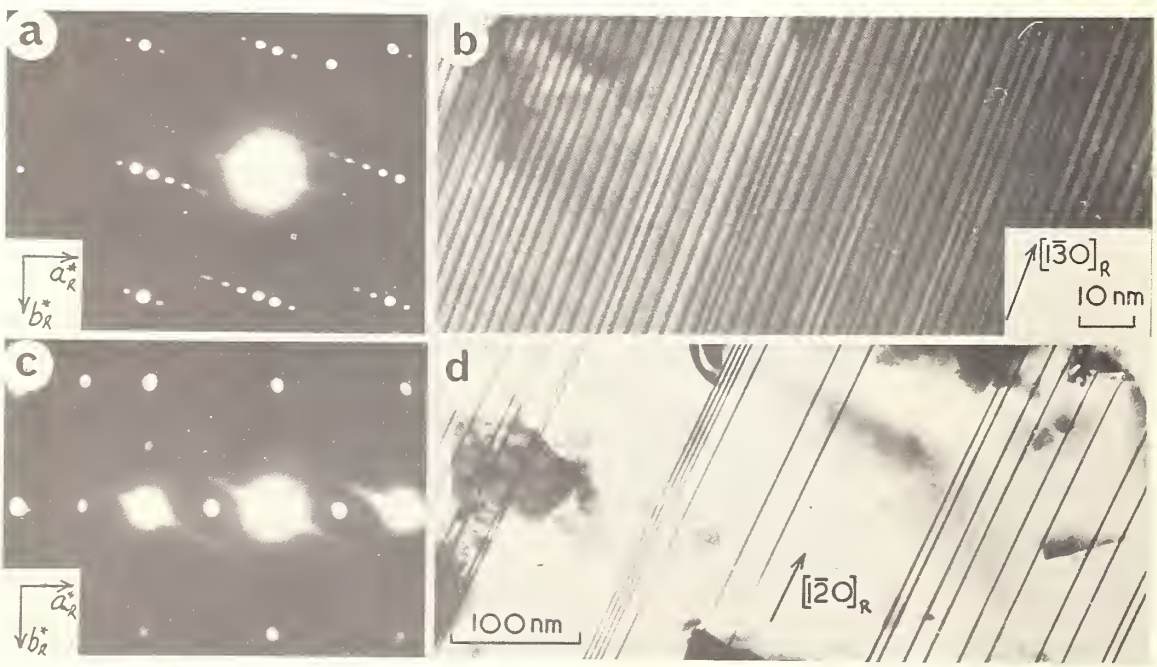

Fig. 9. Electron diffraction patterns and lattice images from (a-b) $WO_{2.90}$ and (c-d) $WO_{2.994}$. The axes and directions refer to the ReO_3-type subcell of the structure. The black lines in (b) and (d) correspond to crystallographic shear planes, whose average spacing is about 2.5 nm in (b) and about 25 nm in (d).

The micrographs in figure 9 show dark lines which are straight, but this is by no means always true. Several examples, which appear to indicate much greater departures from equilibrium, are shown in figure 10. In these fragments, the black lines indicate the presence of CS *surfaces* rather than planes. Most of them are clearly non-planar, and some terminate abruptly within the fragments, presumably at dislocations. Observations of this kind immediately raise questions about the formation and ordering of CS planes, and there is now a considerable amount of evidence which can be used to discuss various models for these processes [21,29]. At this stage, it seems clear that a dislocation model [18] is appropriate for describing the formation of CS surfaces, and that their subsequent movements, including their straightening into planes in specific directions involves a sequence of diffusive movements of particular ions over short distances [19]. In cases where the formation of CS planes is associated with the presence of a foreign ion (*e.g.* doping of WO_3 with Nb_2O_5), long-range migration of the new species must accompany the movement of the CS surfaces.

While the application of electron optical techniques in this area has been very rewarding, most of the work has been qualitative, and there is a great need for carefully designed experiments to be carried out under conditions selected to yield results which will enable the proposed models to be tested more specifically.

6. STRUCTURES IN THE SYSTEM $Nb_2O_5.xTiO_2$ ($x \leqslant 1$)

6.1. THE Nb_2O_5-BASED FAMILY OF STRUCTURES

Until quite recently, it was generally thought that Nb_2O_5 could take up very large amounts of TiO_2 (and other oxides, such as WO_3) into solid solution [30]. However, the meticulous x-ray work of A. D. Wadsley and his collaborators [31] has led to the recognition of a large number of phases in these 'solid solution' regions, including four in the system Nb_2O_5 - TiO_2 (<50 mol % of TiO_2). A fifth was discovered by Gruehn and Norin [32]. These phases all contain elements of the ReO_3-type structure, which are joined to one another along CS planes in *two* directions. They are therefore more complex than the WO_3-based Magnéli phases which we have discussed in section 5. Idealized drawings of some of their structures are shown in figure 11. In all cases, the intersecting sets of CS planes (arrowed) subdivide the structures into blocks or columns, each of which has the ReO_3-type of structure. The blocks are joined by sharing octahedral edges, and the structures differ only in the sizes of the blocks, and the structures of their corner junctions.

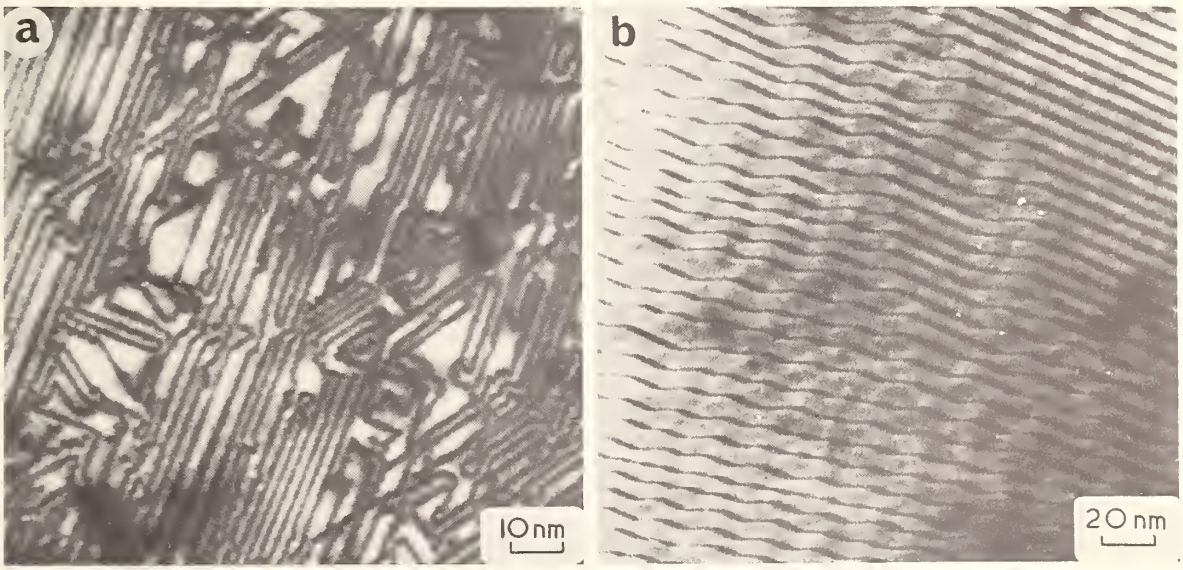

Fig. 10. Non-planar CS surfaces in (a) $WO_{2.90}$ and (b) $WO_3 \cdot yNb_2O_5$ (y = 0.07). The straight portions of the dark lines (CS planes) lie along $\langle 130 \rangle_R$ in (a) and $[010]_R$ in (b).

465-504 O - 72 - 8

Figure 11a shows the structure of monoclinic $Ti_2Nb_{10}O_{29}$ [33], in which the blocks are 4 octahedra wide by 3 long, and the corner junctions contain edge-shared octahedra, marked X. A second structure, containing blocks of the same size, but with the corner junctions occupied by metal atoms in tetrahedral co-ordination (circles) is shown in figure 11b. This structure is adopted by $WNb_{12}O_{33}$ [34], one of a family of eight phases in the closely related system, Nb_2O_5-WO_3 [31]. The structure of $TiNb_{24}O_{62}$ [35] (fig. 10c) may be regarded as an ordered *intergrowth* of these two simpler structures. All of the blocks are 4 x 3 in size, but only half the junctions are of the type marked X in figure 11a, the remainder contain metal atoms in tetrahedral co-ordination, represented by black dots. Figure 11d shows the structure of the most stable (*H*-) form of Nb_2O_5 [36], which is even more complex. Not only does it contain corner junctions of the two types but it is built from blocks of two sizes - 4 x 3 (dark) and 5 x 3 (light). It can be regarded as an intergrowth of the structure shown in figure 11b with another, which is analogous to that in figure 11a, but containing 5 x 3 blocks rather than 4 x 3. The composition of the latter would be $M_{15}O_{37}$, and this structure is adopted by the phase $MgNb_{14}O_{35}F_2$ [37].

In all these phases, the CS planes can be observed in the electron microscope [38-44], either separately or simultaneously, depending upon the orientation of the fragment being examined. For example, figure 12 shows images obtained from fragments of $TiNb_{24}O_{62}$ [41]. The images (a) and (b) were recorded from fragments oriented so that the CS planes parallel to *a* and *c* respectively (fig. 11c) were parallel to the incident electron beam. They show a series of dark lines, which are alternately wide and narrow in (a) but have constant thickness in (b). These differences can be attributed to the fact that in the structure (fig. 11c), the CS planes parallel to *a* contain corner junctions which are either of the type X, or O but those parallel to *c* are indistinguishable.

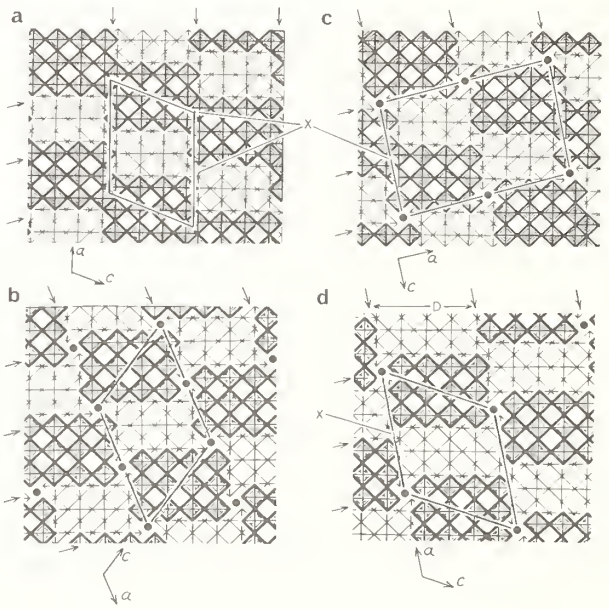

Fig. 11. Idealized models of (a) orthorhombic $Ti_2Nb_{10}O_{29}$, (b) $WNb_{12}O_{33}$, (c) $TiNb_{24}O_{62}$, (d) *H*-Nb_2O_5. The light and dark octahedra lie at different levels in the structure, half a unit cell apart down the short (0.38 nm) *b* axis. The CS planes, where the component ReO_3-type blocks of octahedra are joined by sharing edges, are marked by arrows. Blocks at any one level are either joined together by edge-sharing (*e.g.* at x) or separated by metal atoms in tetrahedral co-ordination (circles).

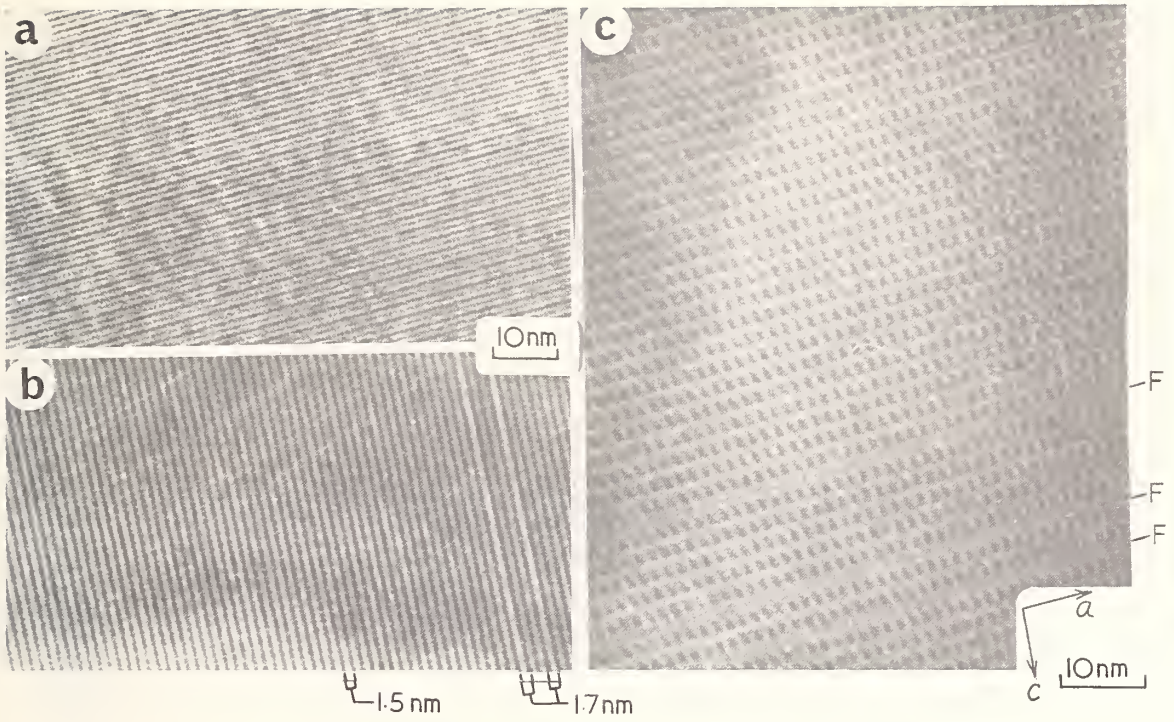

Fig. 12. Lattice images from fragments of $TiNb_{24}O_{62}$ recorded at several different orientations: (a) $0k\ell$ reflections only contribute to the image, (b) $h00$ reflections only contribute to the image, (c) $h0\ell$ reflections contribute - electron beam incident parallel to the *b* axis. Interruptions to the regular pattern in (b) and (c) are due to the presence of Wadsley defects - slabs of H-Nb_2O_5 (b) and $Ti_2Nb_{10}O_{29}$ (c) coherently intergrown in the matrix of $TiNb_{24}O_{62}$.

When both sets of CS planes are parallel to the incident electron beam, the orientation is exactly that of the projection shown in figure 11c, and two-dimensional images, such as figure 12c, are obtained. These images contain dark dots rather than lines, and the arrangement and spacing of these dots over most of the field is exactly the same as that of the tetrahedral sites in the structure. This correlation has been found to hold for all the phases in this family which have been examined by lattice imaging [42].

6.2. WADSLEY DEFECTS

The application of the technique of lattice imaging has greatly increased our understanding of structural relationships in Nb_2O_5-based systems. All the phases in this family may contain *Wadsley defects* - coherent intergrowths, often only half a unit cell wide, of one member of the family in a matrix of another. For example, figure 12b contains several fringe spacings of 1.7 nm amongst a majority of 1.5 nm. The latter are typical of CS planes parallel to *c* in $TiNb_{24}O_{62}$, which have a periodically of 1.49 nm. The 1.7 nm spacing is characteristic of CS planes parallel to *a* in *H*-Nb_2O_5 (fig. 11d), and it is easy to show that a 1.68 nm slab of this structure (marked D in fig. 11d), bounded by CS planes, can fit coherently into the structure of $TiNb_{24}O_{62}$. Similarly, figure 12c contains interuptions to the regular arrangement of dark dots along the lines marked F. These are caused by the presence of additional slabs of the $Ti_2Nb_{10}O_{29}$ structure. We have already noted that $TiNb_{24}O_{62}$ can be regarded as an intergrowth of the structures shown in figures 11a and 11b, hence it is not surprising that extra slabs of $Ti_2Nb_{10}O_{29}$ can be incorporated readily.

The *Wadsley defects* in figures 12b and 12c have opposite effects on the composition. If we increase the departure from the ideal composition by deliberately adding either Nb_2O_5 or TiO_2, the number of Wadsley defects may increase, and new ordered arrangements may appear.

Figure 13a shows a one-dimensional lattice image from a fragment of nominal composition $TiO_2 \cdot 26Nb_2O_5$, oriented to reveal the CS planes parallel to *c*, as in figure 11b. The additional niobium content has greatly increased the number of slabs typical of *H*-Nb_2O_5, with spacings of 1.7 nm. In the region marked X, these slabs form an ordered sequence with the narrower slabs of $TiNb_{24}O_{62}$. This intergrowth of the structures shown in figures 11c and 11d has also been recognized by x-ray diffraction [32], and it may be regarded as a distinct phase of composition $TiNb_{52}O_{132}$ [41].

More complex defects are found in samples which have been quenched from temperatures in the neighbourhood of the melting point [43]. It is often possible to make a detailed analysis of the contrast in two-dimensional images, and to propose models for these defects which fit coherently into the structure of the surrounding matrix. Figure 13b shows such an image from a quenched fragment $TiO_2 \cdot 7Nb_2O_5$. Several domains labelled Y show contrast typical of $TiNb_{24}O_{62}$, but in other areas, vertical lines of dark dots, which correspond to CS planes containing metal atoms in tetrahedral co-ordination, are more widely spaced. This

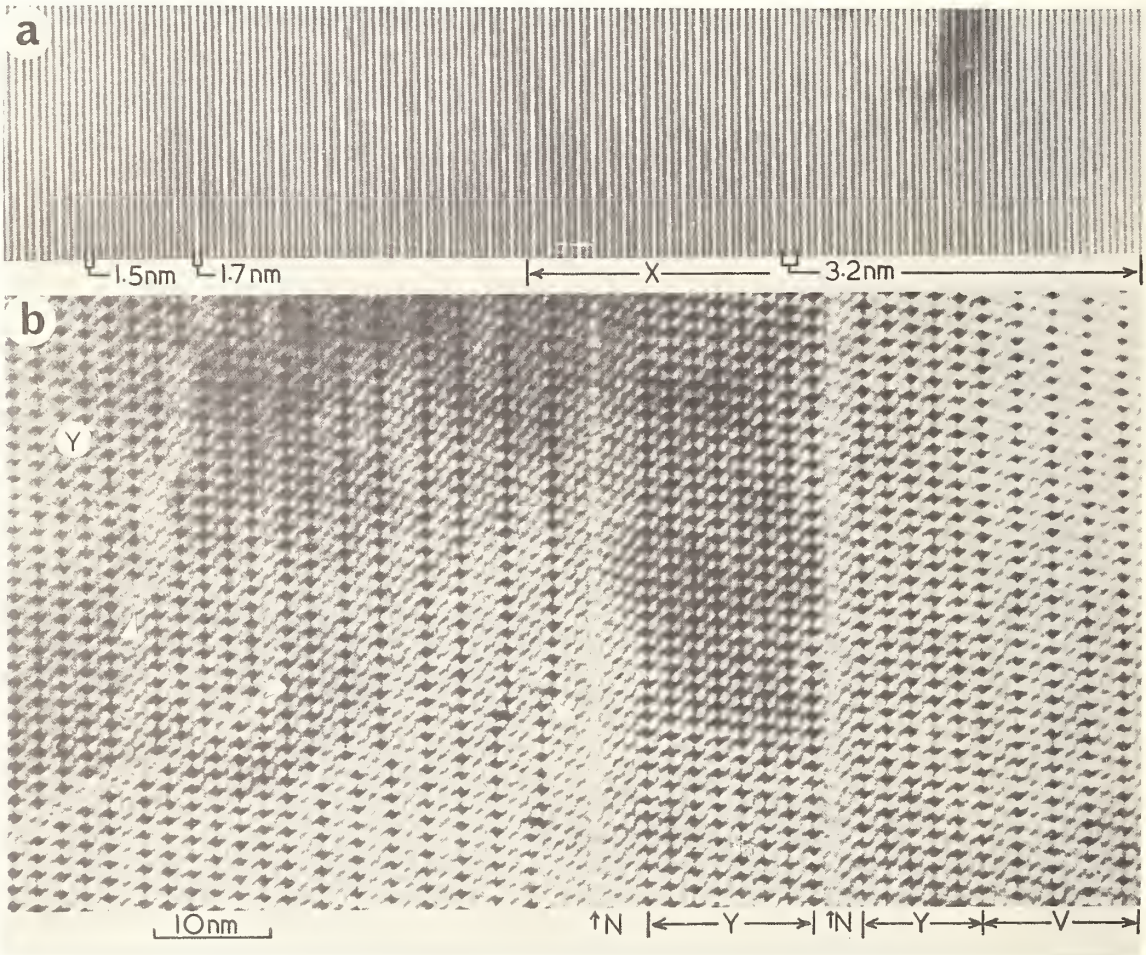

Fig. 13. (a) Lattice image from a sample of $TiO_2 \cdot 26Nb_2O_5$, using *h*00 reflections. Fringes of width 1.5 and 1.7 nm correspond to slabs of $TiNb_{24}O_{62}$ and *H*-Nb_2O_5 respectively. In the region X, these slabs form an ordered sequence, and an intergrowth structure, $TiNb_{52}O_{132}$ can be recognized. (b) Two-dimensional lattice image from a fragment of $TiO_2 \cdot 7Nb_2O_5$, using *h*0ℓ reflections. Domains of $TiNb_{24}O_{62}$ (Y) and $Ti_3Nb_{34}O_{91}$ (V) can be identified by their patterns of dark dots, which correspond to the arrangement of tetrahedral metal atoms. The Wadsley defects marked N are slabs of 4 x 4 blocks. A number of more complex defects (arrowed) produce displacements in the lines of dark dots.

is due to the insertion of extra slabs of $Ti_2Nb_{10}O_{29}$, whose presence alters the composition in the required direction, i.e. towards $TiO_2 \cdot 7Nb_2O_5$. The area V may be regarded as an ordered microdomain of $Ti_3Nb_{34}O_{91}$ [41]. Several slabs, labelled N, differ from all the others in the field, and their width suggests that they contain 4 x 4 blocks of octahedra. It is easy to show that a slab of blocks of this size, otherwise identical to the slabs of 4 x 3 blocks of $Ti_2Nb_{10}O_{29}$, can intergrow readily with the latter. They can be regarded as component slabs of the structure of the *N*-form of Nb_2O_5 [45]. By counting the numbers of slabs of each composition across the field along the top of figure 13b, one arrives at an overall stoichiometry of TiO_2 ($6.9Nb_2O_5$), in good agreement with the nominal value.

In the bottom half of figure 13b, a number of the lines of dark dots suffer displacements, some of which are marked by arrows. These displacements have only been observed in quenched samples, and they appear to involve the insertion of a single block which differs in size from the remainder. Satisfactory models of these defects, in which a 3 x 3 or 5 x 3 block occurs amongst slabs of 4 x 3 blocks have been proposed [43].

6.3. HIGH RESOLUTION IMAGES

Striking confirmation of these defect structures has recently been obtained by Dr. Sumio Iijima, using a high resolution instrument at the Arizona State University. Several micrographs of fragments which were taken from the same sample of $TiO_2 \cdot 7Nb_2O_5$ as we have been using, are reproduced in figures 14 and 15, with his permission. The resolution of these lattice images is of the order of 0.3 nm (3.0 Å), and it has been demonstrated [46] that there is a 1:1 correspondence between the white dots in the images and the tunnels between corner-shared octahedra in the structures. Idealized models of the areas outlined in figures 14 and 15 are shown below the images. The groups of six white dots, corresponding to the six tunnels in each 4 x 3 block of octahedra, are easily seen, and it is very easy to characterize the *Wadsley defect* labelled N in figure 14 as a slab of 4 x 4 blocks, similar to those labelled N in figure 13b. Similarly, several single 3 x 3 blocks can be seen (arrowed) in figure 15 and their presence confirms the model proposed previously for displacements of the kind which are arrowed in figure 13b.

The examination of these and other materials at high resolution obviously offers the possibility of solving complex structures directly. Micrographs of the quality and resolution evident in figures 14 and 15 should at least provide sufficient information to enable reliable trial structures and approximate atomic positions to be derived, which could subsequently be refined using x-ray intensity data. In addition, the technique yields detailed information about the structure of defects, which cannot be obtained by other methods.

6.4. 'SOLID SOLUTION' NON-STOICHIOMETRY

It is now quite clear that composition regions in many Nb_2O_5-based systems, which were once referred to as 'solid solutions' are in fact occupied by series of closely related phases, which can form intergrowths at the unit cell level. The presence of *Wadsley defects* provides a means for accommodating very small discrepancies in composition, and it is tempting to conclude that regions of true solid solution, *i.e.* random distributions of point defects, may not exist in these systems. However, positive evidence for a departure from stoichiometry which is *not* accompanied by *Wadsley defects* has been found in $WO_3 \cdot yNb_2O_5$, for y = 6 - 8 [47].

Crystals of $WO_3 \cdot 8Nb_2O_5$, when prepared from the component oxides by heating for short times (2-5 hours at 1700 K), contained *Wadsley defects* due to the intergrowth of *H*-Nb_2O_5 (fig. 11d) with a matrix of $WNb_{12}O_{33}$ (fig. 11b). On further annealing, these defects were entirely removed, leaving a homogeneous material, whose lattice images (at *ca.* 0.8 nm resolution) and electron diffraction patterns were indistinguishable from those of $WNb_{12}O_{33}$. Thus it appears that the composition region $WO_3 \cdot yNb_2O_5$, y = 6 - 8 may be a true solid solution. The ideal composition of this phase is $M_{13}O_{33}$, but $WO_3 \cdot 8Nb_2O_5$ corresponds to $M_{13.05}O_{33}$ or $M_{13}O_{32.88}$. Because the structure contains potential sites for interstitial atoms (e.g. in the tunnels between the octahedra), an excess of metal (0.4% of the total cations in $WO_3 \cdot 8Nb_2O_5$), accommodated interstitially in some random manner, may explain this region of homogeneity.

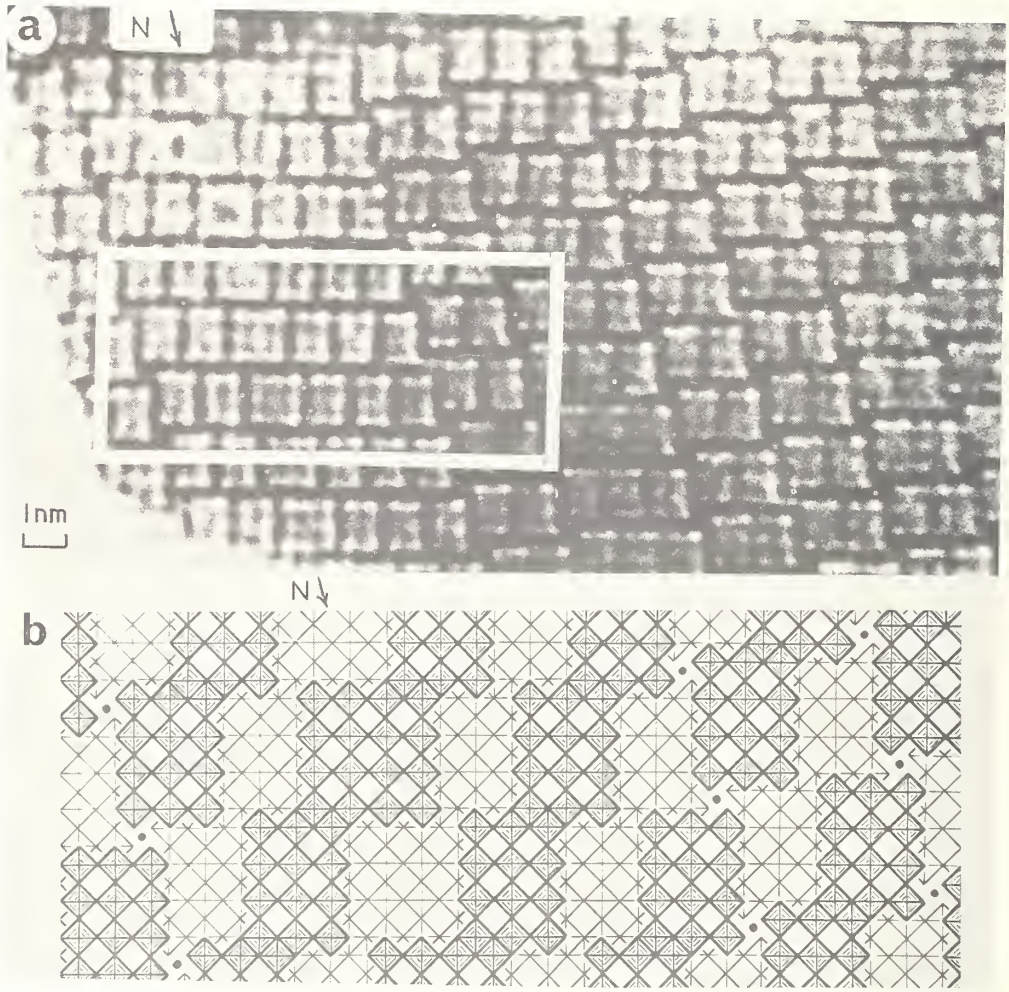

Fig. 14. (a) High resolution two-dimensional lattice image from a fragment of $TiO_2 \cdot 7Nb_2O_5$ (courtesy S. Iijima). (b) Idealized model of the area outlined in (a) showing the intergrowth of a slab of 4 x 4 blocks (N) in the matrix of 4 x 3 blocks. Note the correspondence between the white dots in (a) and the projections of tunnels between octahedra within the blocks in (b).

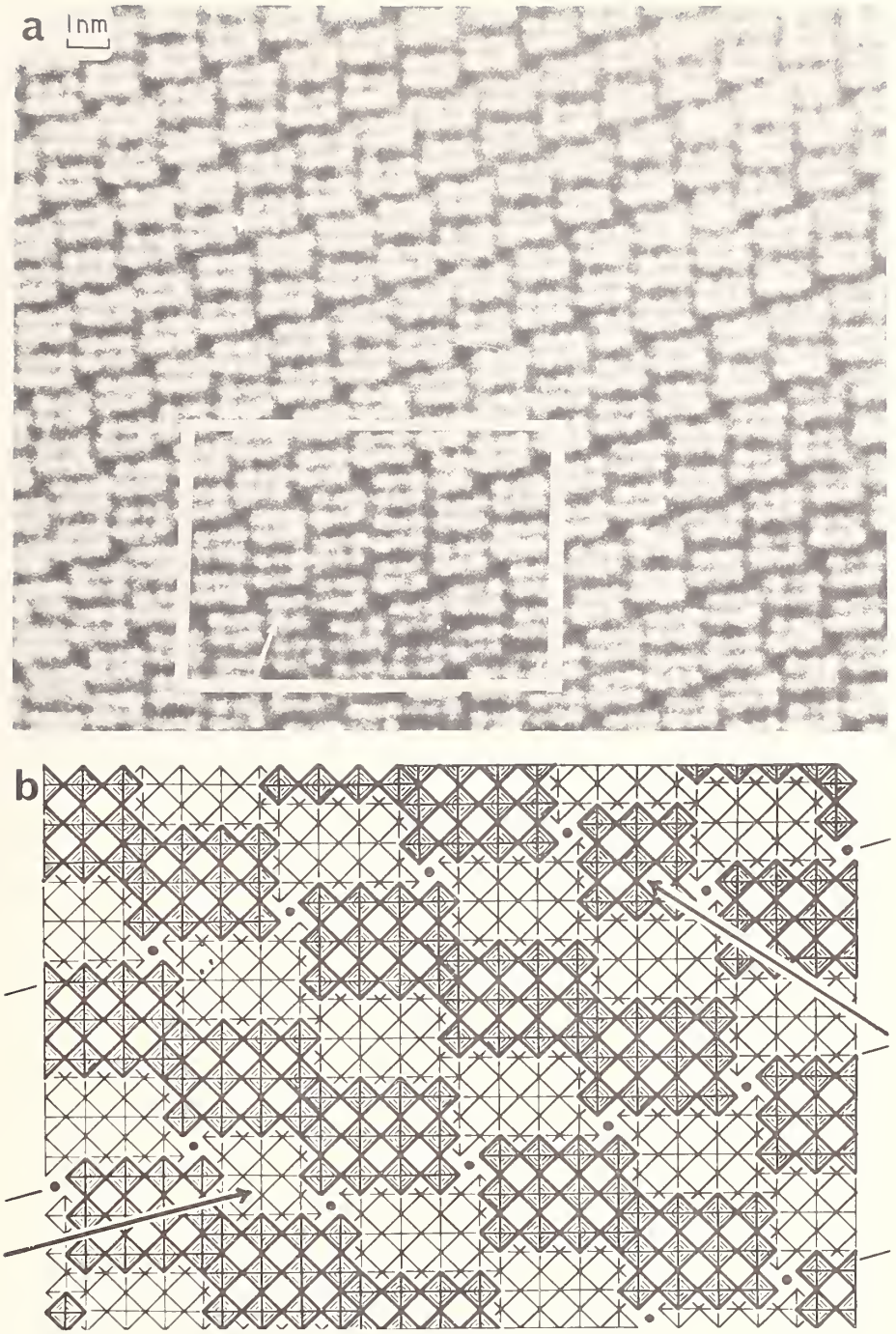

Fig. 15. (a) High resolution two-dimensional lattice image from a fragment of $TiO_2 \cdot 7Nb_2O_5$, showing several displacements of the kind which are arrowed in figure 13b. (Courtesy S. Iijima). The displacements are associated with the presence of isolated 3 x 3 blocks (arrowed) in the matrix of 4 x 3 blocks. (b) Idealized model of the area outlined in (a). The CS planes which contain tetrahedral metal atoms are marked. They suffer a displacement at the points where 3 x 3 blocks (arrowed) occur.

In any event, it seems clear that *Wadsley defects* are the major source of variable compositions in the systems we have been discussing, and that any contribution from randomly distributed point defects is probably limited to levels which are found more generally in numerous other inorganic materials.

7. STRUCTURES IN THE SYSTEM $WO_3 \cdot xNb_2O_5$ (x = 0.2 - 0.35)

Apart from the Magnéli phases (x<0.09, see sec. 5) and the block structures of the type discussed in section 6 ($x \geqslant 1.125$) there is a series of compounds containing 20 - 50 mol % of Nb_2O_5 in which corner-shared octahedra are still the principal structural units, but they are arranged in a more complex manner than in ReO_3. One of these is WNb_2O_8 (x = 1.0) which is structurally related to $LiNb_6O_{15}F$ [48], and the remaining four ($x \approx 0.25$-0.6) have the tetragonal bronze host lattice [24]. The arrangement of octahedra in this structure is shown in figure 16a. The unit cell is tetragonal, with $a \approx 12.5$ Å, $c \approx 3.8$ Å, and contains tunnels which may be occupied by additional ions. In the $WO_3 \cdot Nb_2O_5$ system, a proportion of the pentagonal tunnels are filled by metal and oxygen ions, the metal being in pentagonal bipyramid co-ordination. The number of filled tunnels depends on the composition, and several ordered and disordered phases have been identified [24]. Figure 16b shows the structure of $W_9Nb_8O_{47}$, in which one third of the pentagonal tunnels are filled in an ordered way, and the superlattice is consequently orthorhombic, with $a \approx 37.5$, $b \approx 12.5$, $c \approx 3.8$ Å [49].

A preliminary electron optical study of several of these phases has yielded interesting results, which have thrown further light on some of the questions raised by previous x-ray studies.

7.1. DOMAINS IN $W_9Nb_8O_{47}$

Craig and Stephenson, in a recent x-ray study of $W_9Nb_8O_{47}$ [50], were unable to distinguish unequivocally between two possible structures: (a) an orthorhombic 3 x 1 superlattice of the tetragonal subcell similar to figure 16b, but twinned about the [130] aixs (arrowed). (b) a pseudotetragonal 3 x 3 superlattice of the same subcell. Figure 17 shows some typical electron optical results, from minute fragments of this phase. The diffraction pattern (a) is a (*hk*o) reciprocal lattice section down the short 3.8 Å axis, and contains a square array of strong reflections due to the tetragonal subcell. Each of the major axes of this subcell appears to be trebled, but the complete absence of reflections *within* the squares defined by the subcell reflections immediately suggests some form of twinning, because there is no space group which requires that this combination of reflections be forbidden. This conclusion is confirmed directly by the lattice image in figure 17b, which was recorded at an orientation a few degrees away from that of the diffraction pattern in (a). The image shows that the fragment contains domains, in which fringes with a spacing of 3.7 nm occur in mutually perpendicular directions. The domains labelled A are twinned with respect to those labelled B, and there is a tendency for the twin boundaries to lie on (310) planes of

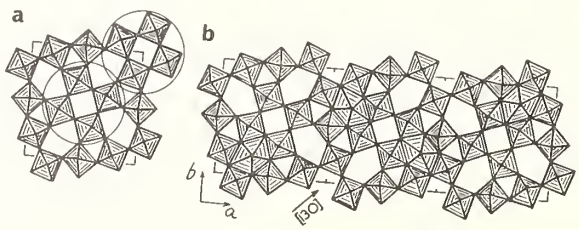

Fig. 16. (a) The arrangement of corner-shared octahedra in the tetragonal tungsten bronze structure. Elements of this structure which closely resemble that of ReO_3 are circled. The corners of the tetragonal unit cell are marked. (b) The structure of $W_9Nb_8O_{47}$, which is a superlattice containing three unit cells of the type shown in (a). Four of the twelve pentagonal tunnels in the orthorhombic unit cell are occupied by metal and oxygen ions.

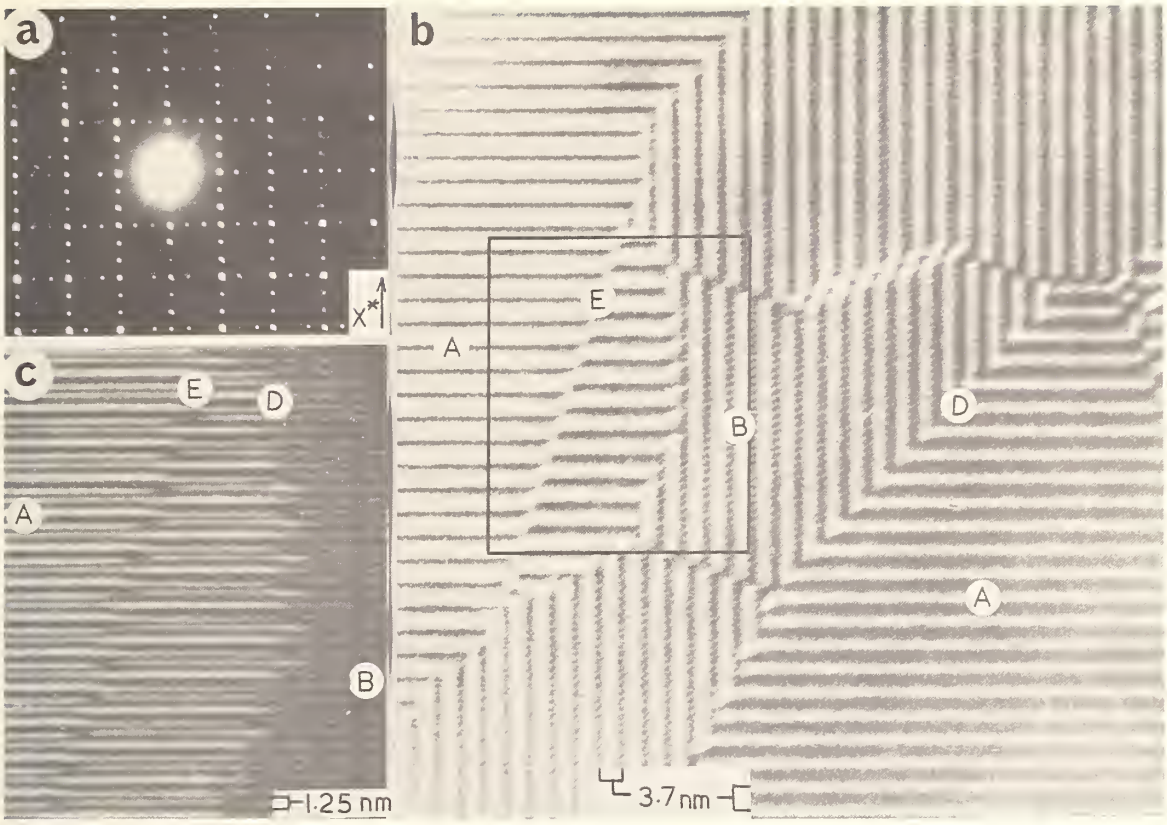

Fig. 17. (a) (001) electron diffraction pattern from a twinned fragment of $W_9Nb_8O_{47}$. (b) Lattice image from a similar fragment, showing two perpendicular orientations of the 3.75 nm superlattice spacing, in the areas of A and B, separated by twin boundaries, *e.g.* at D. Out-of-phase boundaries, such as E, cause a displacement of the superlattice fringes of one third of a unit cell. (c) Lattice image of the area outlined in (b), after tilting slightly to reveal the 1.25 nm subcell fringes. The sublattice is continuous across both the twin boundary D and the out-of-phase boundary E, but the superimposed 3.75 nm periodically in A suffers a displacement of one subcell unit across E.

the orthorhombic superlattice (or 110 planes of the tetragonal subcell), *e.g.* at D. Another type of domain boundary, labelled E, is associated with a displacement of the superlattice fringes by about one third of a unit cell.

Further information on these boundaries can be obtained from figure 17c, which is a one-dimensional image showing the same area as is outlined in (b), but recorded after tilting the fragment until only reflections from the systematic set parallel to *X** in the figure 17a were operating. These reflections are of the type *h*OO for the regions A, and O*k*O for the twinned areas B. In B, the fringes are 1.25 nm apart, corresponding to the periodicity of the structure along the *b* axis. On the other side of the twin boundary (T), this pattern is modified by the superposition of the 3.75 nm periodicity along the *a* axis of the superlattice. Nevertheless, the 1.25 nm fringes can still be seen in this area, and it is clear that they are continuous across the domain boundary E, while the superlattice periodicity is displaced by one subcell unit.

The occurrence of domain boundaries in this material is readily explained in terms of variations in the occupancy of pentagonal tunnels in an otherwise continuous tetragonal bronze-type host lattice. The unit cell in figure 16b contains twelve pentagonal tunnels, but only four of these are occupied. In this situation, there is every possibility that the filled tunnels in different regions of the same crystal may be either twinned or 'out of phase' with respect to each other. The presence of boundaries similar to those in figure 17, at the interface between these regions, is an inevitable consequence of this freedom of choice of tunnels to be occupied. A model of a twin boundary and an out-of-phase boundary in $W_9Nb_8O_{47}$ is shown in figure 18. Each square represents one tetragonal subcell of the structure, and the full and open circles correspond to occupied and empty pentagonal tunnels respectively. The orthorhombic superlattice is heavily outlined, and its displacement by one subcell along the out-of-phase boundary is obvious.

Because the pentagonal tunnels are relatively widely separated (>0.6 nm), interactions between occupied tunnels and hence domain boundary energies are probably very small. For this reason, the microdomain structure which is evident in figure 17, while it undoubtedly represents a metastable condition, probably persists even after long annealing. This accounts for the fact that untwinned crystals large enough for x-ray studies have not been found [49,50].

7.2. DOMAINS AND INTERGROWTH IN $2Nb_2O_5 \cdot 7WO_3$

Stephenson [51] attempted to study the phase $W_7Nb_4O_{31}$ [24] using x-rays, but he was unable to select suitable crystals for this purpose. Nevertheless, he predicted that several structures were likely, all of which contained 4 tetragonal subcell units, to give a superlattice with $a \approx b \approx 25$ Å, $c \approx 3.8$ Å. This unit cell contains sixteen pentagonal tunnels, and the correct composition is achieved by filling four of these with metal and oxygen atoms. There are four different possible arrangements of these filled tunnels, hence the opportunities for domain formation are even greater than for $W_9Nb_8O_{47}$. This is illustrated by the lattice image in figure 19a, in which a square array of white dots, 2.5 nm on a side, corresponding to the projection of the unit cell on (001), is interrupted by out-of-phase boundaries of several different types.

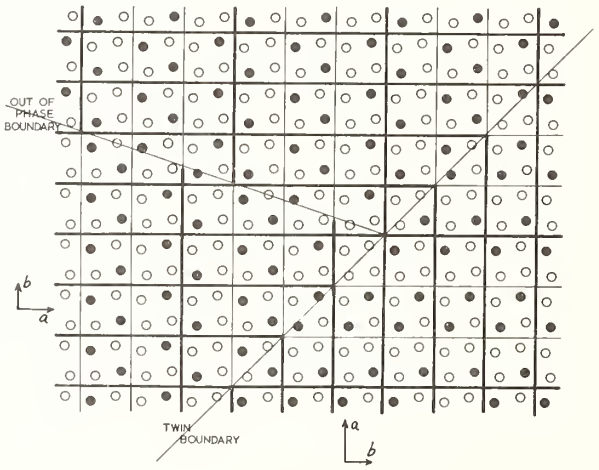

Fig. 18. Model of twin and out-of-phase boundaries in $W_9Nb_8O_{47}$. Each square represents a tetragonal bronze-type subcell, and the open and filled circles correspond to empty and occupied pentagonal tunnels respectively. The orthorhombic unit cells of the superlattice are heavily outlined.

In many cases, the domain structure is not fully developed, and lattice images show ordered regions separated from each other by areas in which only the square projection of the tetragonal subcell, 1.25 nm on a side, is visible. Figures 19b and c illustrate this situation, which probably corresponds to an early stage in the ordering process. Electron diffraction patterns from fragments which give images similar to figure 19c contain sharp subcell reflections surrounded by diffuse scattering due to short range order. This confirms the supposition that the structure consists of a continuous host lattice in which the filling of pentagonal tunnels is random, except in isolated patches where a few unit cells of the 2.5 x 2.5 nm ordered structure occurs.

The contrast within the ordered domains varies considerably, even in the same fragment, as figure 19 shows. These differences are a consequence of the fact that the micrographs were recorded at slightly different orientations, and they do not necessarily represent real differences in the structure of individual domains.

A few fragments contained domains of a much simpler structure, in which lattice fringes were not resolved at 0.8 nm resolution. An example of this intergrowth is shown in figure 20a, in which the region C, which is free of detailed contrast, is embedded in a matrix of tetragonal bronze-type structure, similar to figure 19b. An attempt was made to characterize the region C by selected area electron diffraction. The technique is difficult to

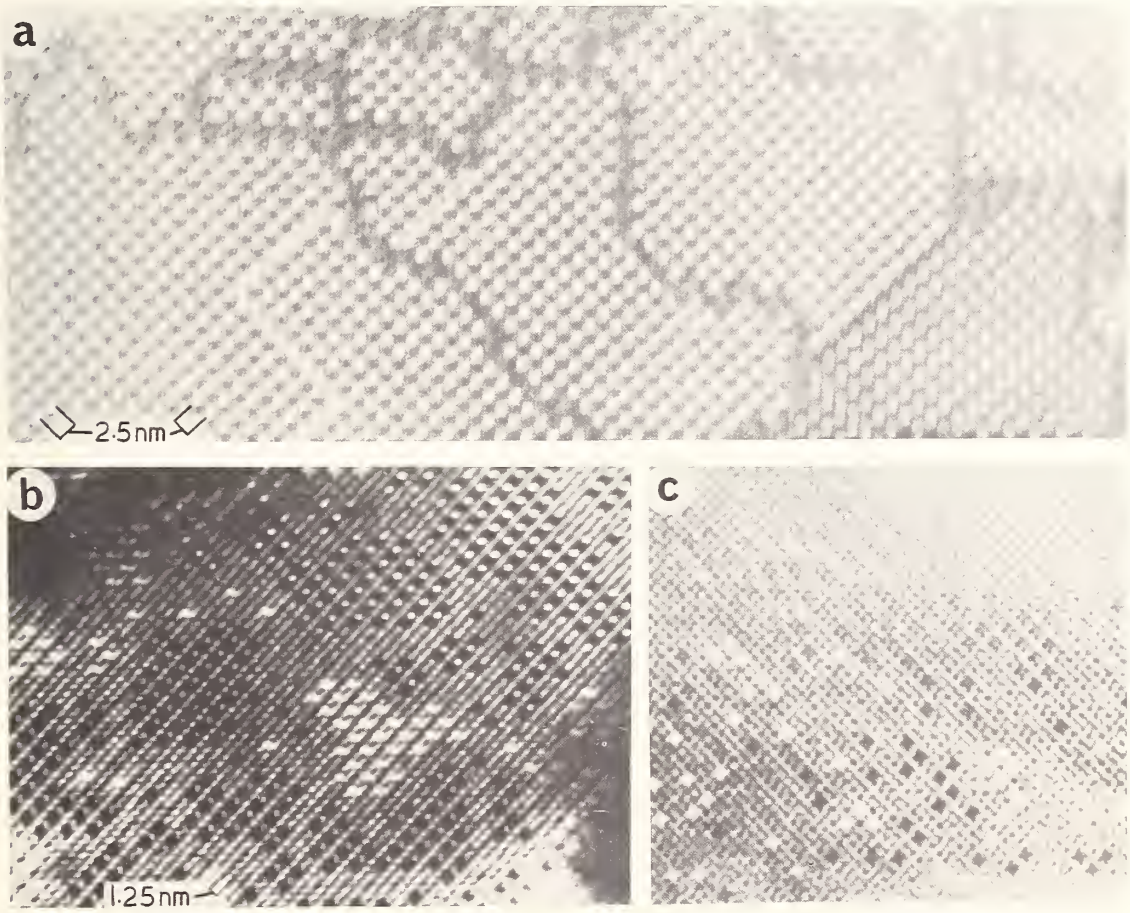

Fig. 19. Lattice images from fragments with compositions near $2Nb_2O_5 \cdot 7WO_3$. (a). Ordered domains of $W_7Nb_4O_{31}$, separated by out-of-phase boundaries of several different types. (b). Small ordered domains of $W_7Nb_4O_{31}$, separated by disordered regions where only the 1.25 nm host lattice fringes are visible. (c). Short-range order - groups of a few unit cells of the 2.5 x 2.5 nm superstructure of $W_7Nb_4O_{31}$ are scattered in a matrix where the host lattice is continuous, but the pentagonal tunnels are filled randomly.

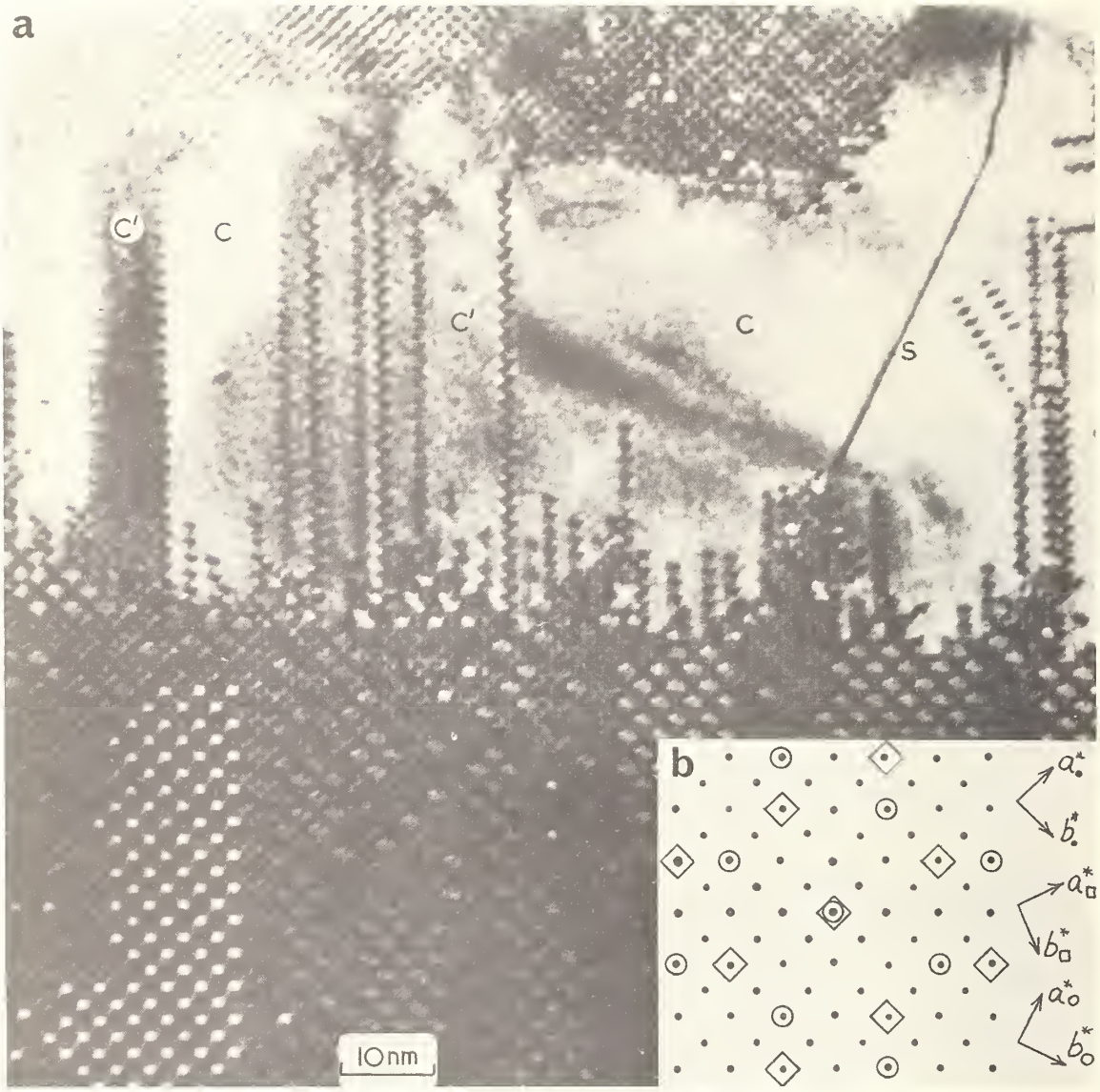

Fig. 20. (a). Two-dimensional lattice image showing intergrowth between a tetragonal bronze host lattice (containing domains of ordered $W_7Nb_4O_{31}$), and a simpler cubic or pseudo cubic structure C, C' in which no lattice fringes are visible. The defect S may be a CS plane. (b). Sketch of (001) electron diffraction pattern showing the relationship between reflections from the tetragonal bronze host lattice (dots) and the two orientations of the cubic intergrowth, C (open circles) and C' (squares).

apply to such small areas, but nevertheless, evidence for a cubic or pseudocubic unit cell with a = 0.38 nm was obtained. Two orientations of this cell were observed; they probably apply to adjacent regions such as C and C', which are separated by zig-zag boundaries. Both these orientations bear specific relationships to the tetragonal bronze subcell, as shown by the diagrammatic sketch of the electron diffraction patterns in figure 20b.

The most likely structure for the region C is the ReO_3-type structure (fig. 8a) or some variant of this, such as the cubic tungsten bronze structure [52]. Elements of this simple 'chess-board' arrangement of octahedra can be recognized in the tetragonal bronze structure, and they are circled in figure 16a. These groups of four corner-shared octahedra, centred on the corners and centre of the tetragonal unit cell, lie in two orientations, which are the same as those of the regions C and C' in figure 20a, as indicated by the orientation relationship in figure 20b. It therefore seems possible that a ReO_3-type structure can be coherently interfaced with the tetragonal bronze structure, and that this is the explanation for observations such as figure 20a.

Models of the interface between the two structures, and of the zig-zag boundary between the two orientations C and C' of ReO_3-type material, are shown in figures 21a and b respectively. Some of the octahedra in the vicinity of the boundaries may be distorted excessively, but in general, the models give a satisfactory explanation to what appeared at first sight to be a most unlikely type of intergrowth. No attempt has been made to explain a number of other features which appear in the region C of figure 20a. However, it is possible that the extended defect marked S may be a crystallographic shear plane. Micrographs such as this clearly contain an enormous amount of structural information about structures and structural relationships which cannot be obtained by other means.

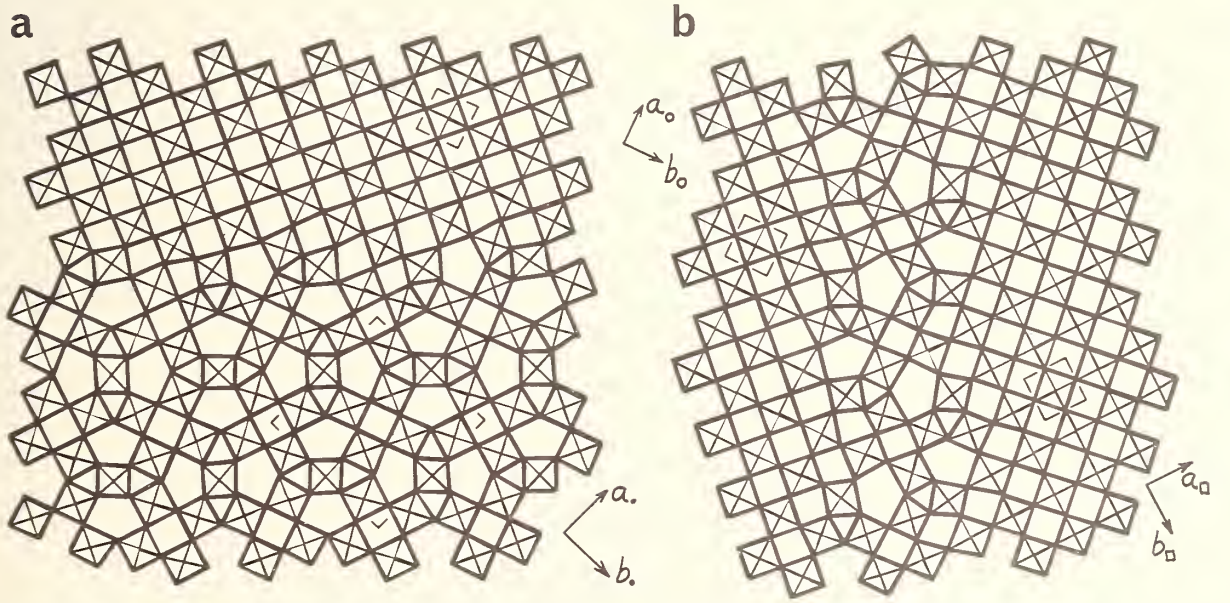

Fig. 21. Models of proposed structures for interfaces between (a) the tetragonal bronze structure (lower) and a ReO_3-type lattice (upper) and (b) two orientations of the ReO_3-type lattice, separated by a zig-zag boundary of the kind seen between the regions C and C' in figure 20a. The orientation of these diagrams is consistent with figure 20, and the axes are labelled in the same way as those in figure 20b.

8. CONCLUSION

The examples cited in sections 3-7 are sufficient to indicate that the electron microscope has considerable potential as a tool for structural investigations on high temperature materials. They do not cover the whole range of possible applications by any means; in particular, the field of dislocation structures has been omitted entirely. This area is an extension of the voluminous work on metals which is very thoroughly documented (5,6).

Perhaps the most interesting new results have been obtained by lattice imaging, and this technique undoubtedly has a bright future. It is clear that the structures we have studied by this method have been favorable ones, because of the presence of a very short projection axis (0.38 nm) and minimal overlap of atoms down this axis. However, using the improved resolution provided by many modern electron microscopes, it should be possible to handle many other types of structure successfully. Concurrent with experimental studies of this kind, there is a need for theoretical investigations of the relationship between lattice image contrast and structure. It cannot be assumed that this relationship will always be as direct and as obvious as is indicated by the results on Nb_2O_5-related phases, ***e.g.*** figures 14, 15.

Finally, there are many opportunities for the study of reactions in and between solids *in situ*, using a high-temperature specimen stage. For example, the formation and migration of CS planes in WO_{3-x} could probably be studied by this means. A few qualitative observations have already been made [18] using the heating effect of the incident electron beam, but meaningful kinetic data might be obtainable with better temperature control provided by a hot stage.

9. ACKNOWLEDGEMENTS

I am indebted to Dr. J. V. Sanders for his continued interest and encouragement, and to Prof. J. M. Cowley and Dr. Sumio Iijima for permission to reproduce figures 14a and 15a.

10. REFERENCES

[1] Hirthe, W. M., Melville, A. T., and Wackman, P. H., Rev. Sci. Inst. 38, 223 (1967).
[2] O'Keefe, M. A., unpublished results, CSIRO.
[3] Cowley, J. M., in *Progress in Materials Science* (B. Chalmers and W. Hume-Rothery, eds.), Pergamon Press, Vol. 13, No. 6(1967).
[4] Li, C., Reid, A. F., and Allpress, J. G., to be published.
[5] Hirsch, P. B., Howie, A., Nicholson, R. B., Pashley, D. W., and Whelan, M. J., *Electron Microscopy of Thin Crystals*, Butterworths (London) 1965.
[6] Amelinekx, S., *The Direct Observation of Dislocations*, Academic Press (New York) 1964.
[7] See, for example, papers in *The Chemistry of Extended Defects in Non-Metallic Solids* (L. Eyring and M. O'Keefe, eds.) North Holland, 1970.
[8] Yada, K. and Hibi, T., J. Electron Microscopy 18, 266 (1969).
[9] Cowley, J. M. and Moodie, A. F., Proc. Phys. Soc. 76, 382 (1960).
[10] Marezio, M., Remeika, J. P., and Dernier, P. D., Acta Cryst. B26, 2008 (1970).
[11] Allpress, J. G., J. Mat. Sci. 6, 313 (1971).
[12] Posnjak, E. and Barth, T., Phys. Rev. 38, 2234 (1931).
[13] Hoffmann, A., Naturwiss 26, 431 (1938).
[14] Allpress, J. G. and O'Keefe, M. A., unpublished results.
[15] Anderson, J. C. and Schieber, M., J. Phys. Chem. 67, 1838 (1963).
[16] Watanabe, D., Terasaki, O., Jostsons, A., and Castles, J. R., in ref. 7, p. 238.
[17] Allpress, J. G. and Gádo, P., Crystal Lattice Defects 1, 311 (1970).
[18] Allpress, J. G., Tilley, R. J. D., and Sienko, M. J., J. Solid State Chem. 3, 440 (1971).
[19] Allpress, J. G., J. Solid State Chem., in press.
[20] Magnéli, A., Acta Cryst. 6, 495 (1953).
[21] Andersson, S. and Wadsley, A. D., Nature 211, 581 (1966).
[22] Magnéli, A., Arkiv. Kemi. 1, 513 (1950).
[23] Tilley, R. J. D., Mat. Res. Bull. 5, 813 (1970).
[24] Roth, R. S. and Waring, J. L., J. Res. NBS 70A, 281 (1966).
[25] Bursill, L. A., Hyde, B. G., Terasaki, O., and Watanabe, D., Phil. Mag. 20, 347 (1969).
[26] Anderson, J. S. and Tilley, R. J. D., J. Solid State Chem. 2, 472 (1970).
[27] Bursill, L. A., Hyde, B. G., and Philp, D. K., Phil. Mag. 23, 1501 (1971).

[28] Bursill, L. A. and Hyde, B. G., Phil. Mag. 23, 3 (1971).
[29] Anderson, J. S. and Hyde, B. G., J. Phys. Chem. Solids 28, 1393 (1967).
[30] Goldschmidt, H. J., *Interstitial Alloys*, p. 419-421, Butterworths (London) 1967.
[31] Wadsley, A. D. and Andersson, S., in *Perspectives in Structural Chemistry* (J. D. Dunitz and J. A. Ibers, eds.) Wiley (New York) Vol. 3, 1970.
[32] Gruehn, R. and Norin, R., Z. Anorg. Allgem. Chem. 355, 176 (1967).
[33] Wadsley, A. D., Acta Cryst. 14, 664 (1961).
[34] Roth, R. S. and Wadsley, A. D.,Acta Cryst. 19, 32 (1965).
[35] Roth, R. S. and Wadsley, A. D., Acta Cryst. 18, 724 (1965).
[36] Gatehouse, B. M. and Wadsley, A. D., Acta Cryst. 17, 1545 (1964).
[37] Lundberg, M., J. Solid State Chem. 1, 463 (1970).
[38] Allpress, J. G., Sanders, J. V., and Wadsley, A. D., Phys. Stat. Sol. 25, 541 (1968).
[39] Allpress, J. G., Sanders, J. V., and Wadsley, A. D., Acta Cryst. B25, 1156 (1969).
[40] Allpress, J. G. and Wadsley, A. D., J. Solid State Chem. 1, 28 (1969).
[41] Allpress, J. G., J. Solid State Chem. 1, 66 (1969).
[42] Allpress, J. G., Mat. Res. Bull. 4, 707 (1969).
[43] Allpress, J. G., J. Solid State Chem. 2, 78 (1970).
[44] Allpress, J. G. and Roth, R.S., J. Solid State Chem. 2, 366 (1970).
[45] Andersson, S., Z. Anorg. Allgem. Chem. 351, 106 (1967).
[46] Iijima, S., J. Appl. Phys., in press.
[47] Allpress, J. G. and Roth, R.S., J. Solid State Chem. 3, 209 (1971).
[48] Lundberg, M., Acta Chem. Scand. 19, 2274 (1965).
[49] Sleight, A. W., Acta Chem. Scand. 20, 1102 (1966).
[50] Craig, D. C. and Stephenson, N. C., Acta Cryst. B25, 2071 (1969).
[51] Stephenson, N. C., Acta Cryst. B24, 637 (1968).
[52] Wadsley, A. D., in *Non-Stoichiometric Compounds* (L. Mandelcorn, ed.) Academic Press (New York) 1964.

National Bureau of Standards Special Publication 364, Solid State Chemistry, Proceedings of 5th Materials Research Symposium, issued July 1972.

APPLICATION OF INFRARED AND RAMAN SPECTROSCOPY TO THE CHARACTERIZATION OF ORDER-DISORDER IN HIGH TEMPERATURE OXIDES

William B. White and Vassilis G. Keramidas

Materials Research Laboratory
The Pennsylvania State University
University Park, Pennsylvania 16802

The vibrational spectra of oxides are remarkably sensitive to ordering effects and are a useful characterization tool. Cation ordering can be classified into: (a) preferential distribution of non-equivalent cations onto non-equivalent sites with no change in space group symmetry or unit cell size, (b) preferential distribution onto equivalent sites with decrease in space group symmetry only, (c) building of superstructures with same symmetry as parent structure, (d) both (b) and (c) combined. Experimental Raman spectra of various structures are compared with these schemes. Ordering of type (a) produces only frequency shifts with no change in spectral pattern and is exemplified by normal-inverse ordering in spinels. Ordering of type (b) produces additional bands due to selection rule relaxation and is exemplified by ilmenite, $LiNbO_3$, and Ni_3TeO_6 orderings on corundum and by spinels with 1:1 ordering on tetrahedral sites. Ordering of type (c) produces a multiplicity of bands as is illustrated by the trirutile structure. Ordering of type (d) produces very complex spectra. Examples include: $P\bar{3}c1$ ordering on corundum, 1:1 ordering on rocksalt and the Ruddlesden-Popper superstructures. Raman spectra are sharp but intensities are highly variable. Simple ordering schemes are easy to discern, but complex schemes produce spectra difficult to interpret.

Key words: Corundum structure; order-disorder; Raman spectra; rocksalt structure; rutile structure; spinel structure.

1. INTRODUCTION

It was proposed several years ago [1][1] that the infrared spectra of solids are exceptionally sensitive to cation ordering. Although the theory is simple to apply, the actual measurement of the ir spectra of many types of structures is difficult if only powder or ceramic specimens are available. Long-range polarization forces in structures such as corundum and perovskite cause a large separation of the transverse and longitudinal optic modes. As a result, the ir spectra are very broad and represent some composite of specular reflectivity and Fröhlich-type surface modes rather than the transverse optic modes. Furthermore, the broadening of the bands obscures splittings and multiplicites of bands that may occur because of ordering.

In this paper we examine the Raman spectra of various classes of compounds with ordering schemes derived from the rocksalt, rutile, corundum, perovskite, and spinel structures. The objective is to test the extent to which the ordering arrangement affects the Raman spectrum. Corresponding infrared spectra are drawn from the literature as needed.

2. EXPERIMENTAL

The ilmenite phases $ZnTiO_3$, $MnTiO_3$, and $MgTiO_3$ were synthesized by dry-firing appropriate mixtures of TiO_2 with the carbonates of the other cation at 1200 °C in air.

[1]Figures in brackets indicate the literature references at the end of this paper.

465-504 O - 72 - 9

$MgSb_2O_6$ and $ZnSb_2O_6$ were prepared by heating pressed pellets of the oxides at 950 °C for 48 hours. Phase identification and purity were checked by x-ray diffraction. The complex niobates were synthesized according to the method of Bertaut et al. [2]. The strontium titanates were obtained from a previous phase equilibrium study [3].

Raman spectra were measured on pressed pellets or sintered chips of pure compounds using a Spex Ramalog spectrometer with an Ar^+ laser source. Since internal scattering of powders destroys the depolarization effects, no information on the polarization dependence of the materials was obtained.

3. INFLUENCE OF ORDER ON VIBRATIONAL SPECTRA

Consider first what is meant by order. We begin with a parent structure with a certain set of equivalent cation sites. In the case of the rocksalt, rutile, and corundum structures there is only one equivalent set of cations. There are two kinds of sites in the spinel and perovskite structures. If we substitute some different kind of cation into a one-cation-sublattice structure in such a way that the substitution takes place at random positions in the structure, there is no change in symmetry. Because of the random substitution, all sites remain equivalent under the various symmetry operations of the space group, the space group remains the same, and the unit cell size does not change. This corresponds to the disordered structure and has the highest symmetry. In contrast, if the foreign cation is substituted in a regular way, say in alternate sites in the cation sublattice, symmetry operations that would exchange non-equivalent cations are lost. The space group symmetry may be lowered, the cell size enlarged, or both.

The number of zone-center phonon modes active in the infrared or Raman spectrum is determined by the factor group symmetry of the structure and by the population of the primitive unit cell. If an ordered arrangement of cations lowers the factor group symmetry, in general, there will be a change in the number of modes in both the infrared and Raman spectra caused by a relaxation of selection rules. An enlargement of the primitive cell, without a change in space group symmetry will cause an increase in the number of allowed modes usually by some multiplicity factor. A summary of the possible situations is given in table 1.

Table 1

Types of Cation Order

Ordering Scheme	Change in Symmetry	Spectral Behavior	Examples
Cation ordering on non-equivalent sites	Same cell size Same space group	No new bands Shift in frequency	Normal-Inverse order in spinels
Cation ordering on equivalent sites	Same cell size Derivative space group	New bands superimposed on parent spectrum	1:1 order on tetrahedral sites in spinel. Ilmenite ordering on corundum
	Larger cell Lower symmetry	New spectrum with many more bands	Octahedral site ordering on spinel. 1:1 ordering on rocksalt. 1:3 ordering on corundum
Cation ordering with superstructure	Superstructure cell Same space group	Parent spectrum develops multiplicity of lines	Trirutile ordering
	Superstructure cell Lower space group	Complex spectrum may not be directly related to parent	Ruddlesden-Popper phases 1:2 ordering on corundum

There is also an effect of the long-range coupling fields in the structure. The polarization field splits the infrared active modes into a transverse and longitudinal component, a splitting that is not accounted for by the factor group analysis. The magnitude of separation between similar motions of vibration is also controlled by the effectiveness of coupling. If, for example, the tetrahedral sites in spinel contain two kinds of weakly coupled cations, the spectrum may exhibit molecular-like bands of both tetrahedra in spite of factor group predictions of a single average spectrum. Even if internal coupling is reasonably strong, as unit cells become large due to superstructure, it may be impossible to resolve the full predicted number of frequencies because of the large number of overlapping bands.

4. RESULTS AND DISCUSSION

4.1. STRUCTURES ORDERING ON NON-EQUIVALENT SITES

The best known example of ordering between non-equivalent sites is the normal-inverse ordering in spinels. Normal spinel has a cation distribution $(A_2)^{VI}B^{IV}X_4$ and an inverse spinel has the distribution $(AB)^{VI}A^{IV}X_4$. Many real spinels have a mixed cation distribution $(A_{2-x}B_x)^{VI}(B_{1-x}A_x)^{IV}X_4$. Throughout this series of substitutions there is no change of space group or unit cell size. It was shown [4] by factor group analysis that the expected modes of spinel are:

$$\Gamma = A_{1g}(R) + E_g(R) + T_{1g} + 3T_{2g}(R) + 2A_{2u} + 2E_u + 4T_{1u}(ir) + 2T_{2u}$$

Four bands are expected in the infrared and five bands in the Raman for a normal spinel. Many infrared studies show that only the expected four bands appear in the infrared spectrum of either normal or inverse spinels. As predicted by simple symmetry arguments, the spectrum does not change with changing cation distribution. Of course frequency shifts occur because the average mass on particular cation sites and the average force constants for the bonds change with changing cation distribution. New data (DeAngelis, Keramidas, and White, to be published) show that the same is true in the Raman effect. Five bands are predicted and only five are observed for a wide variety of oxide spinels with normal, inverse, and mixed cation distributions.

The same would be expected for any other structure in which cations are substituting in an ordered way on distinct crystallographic sites. For example, olivine, Mg_2SiO_4, has two cation positions M(I) and M(II). An ordered substitution of iron onto one site in preference to the other would be revealed in the electronic spectrum or the Mössbauer spectrum, both of which are mainly sensitive to nearest neighbor environment only, but the ordering should manifest itself in the ir and Raman spectra merely by a frequency shift in the lattice modes. No new bands should appear.

4.2. ORDERING WITH LOWER SPACE GROUP SYMMETRY

There are many examples of structures in which cation ordering lowers the space group symmetry without changing the size of the unit cell. We shall examine two, 1:1 ordering an tetrahedral sites in spinel and several orderings on corundum.

A 1:1 ordering of the tetrahedral cations in the spinel structure lowers the space group

$$O_h^{\ 7}(Fd3m) \rightarrow T_d^{\ 2}(F\bar{4}3m)$$

The face-centered cubic cell is retained with nearly the same cell parameter but the point symmetry is lowered. The ir spectral consequences as given by the factor group analysis of [4] are:

	Spinel	1:1 ordered	
$4T_{1u}$	ν_3 tetrahedral stretch	AX_4 asymm. stretch	$7T_2$
		BX_4 asymm. stretch	
	ν_4 tetrahedral deformation	AX_4 bend	
		BX_4 bend	
	Octahedral stretch	Octahedral stretch	
	Antiphase motion of tetrahedra	Antiphase motion	
		Octahedral deformation	

The description of vibrational motion assumes a quasi-molecular behavior from the isolated spinel tetrahedron and the notation ν_1, ν_2, etc., is the standard usage given by Herzberg [5]. The Raman spectrum of the ordered spinel is expected to exhibit 15 bands in contrast to 5 in the disordered form.

	Spinel	1:1 ordered	
A_{1g}	ν_1 Symmetric stretch	AX_4 sym. stretch	A_1
		BX_4 sym. stretch	
		Translatory mode	
E_g	ν_2 Symmetric bend	AX_4 sym. bend	E
		BX_4 sym. bend	
		Translatory mode	
T_{2g}	ν_3 Asymmetric strecth	AX_4 assym. stretch	T_2
		BX_4 asymm. stretch	
	ν_4 Asymmetric bend	AX_4 asymm. bend	
		BX_4 asymm. bend	
	Translatory mode	Three translatory modes (same as ir)	

The group theoretical consequence of the ordering is the removal of the center of symmetry. Two effects can be seen in the spectra. The first is the loss of the mutual exclusion rule, so that all infrared modes also become active in the Raman spectra. The second is a relaxation of selection rules that permits certain modes forbidden in both ir and Raman to become active in the ordered structure. Important among these are the vibrations of the two tetrahedra of the primitive spinel cell. There are two sets of tetrahedral (quasi-molecular) modes in spinel, differing in frequency by the factor group splitting. In the ordered form, both sets of tetrahedral modes appear in both the ir and in the Raman as indicated. If no coupling between tetrahedra were operative, we would expect to see a superposition of spectra with frequencies close to those of the free parent tetrahedra.

Measured ir and Raman spectra [6] show a more complex situation. The infrared spectra show the expected seven bands, but the frequencies of those assigned to tetrahedral modes are not as expected from the de-coupled tetrahedra. Likewise the intensity of one member of the pair is very strong, while the intensity of the other is very weak. It was concluded that coupling forces still act to mix the pairs of tetrahedral vibrations (which is permitted

by symmetry, since all modes have T_2 symmetry). The expected large number of Raman modes appears and can be assigned, but no easy correlation with the parent spinel is apparent in the spectra.

We turn now to cation ordering in the corundum structure. Introduction of two distinct cations into the corundum structure can produce a variety of cation ordering schemes depending on how the atoms are arranged in the cation layers. These have been summarized by Newnham and Meagher [7]. The pertinent crystallographic data are given in table 2. The ilmenite and $LiNbO_3$ ordering schemes reduce the space group symmetry, but the size and contents of the unit cell do not change. The ordering arrangement of $Mg_4Nb_2O_9$ destroys the rhombohedral centering of the cell. In this case the factor group symmetry remains the same, but the system contains thrice as many degrees of freedom as the primitive cell. The Ni_3TeO_6 structure, on the other hand, preserves the rhombohedral centering and thus the primitive cell contains the same number of atoms as the parent corundum.

Factor group analyses for the vibrational modes of these structures are listed in table 3. Seven Raman bands are expected in the completely disordered corundum structure [8]. This number increases to 10 in the ilmenite structure and to 13 in the $LiNbO_3$ structure. The increase in number of modes arises simply from the relaxation of selection rules in the lower symmetry ordered structures. In the case of ilmenite, the 3 A_{2g} inactive modes of corundum are grouped with the Raman active A_g representation in C_{3i} symmetry. The loss of the center of symmetry in the $LiNbO_3$ structure combined the ir and Raman active sets into single representations. In both cases the final result can be obtained by a simple descent of symmetry argument, since both ordered space groups are subgroups of the space group of corundum.

Raman spectra of three ilmenite structure compounds, $ZnTiO_3$, $MnTiO_3$, and $MgTiO_3$ are shown in figure 1. The spectra of $ZnTiO_3$ and $MgTiO_3$ are sharp and well defined, while the spectrum of $MnTiO_3$ is surprisingly weak. The spectrum of $ZnTiO_3$ contains 16 lines and the spectrum of $MgTiO_3$ contains 13 lines in contrast to the 10 predicted by factor group analysis. The positions of these lines are compared with the vibrational levels of Al_2O_3 [8] and $LiNbO_3$ [9] in figure 2. Since A_1 and E species of the $LiNbO_3$ ordering are both ir and Raman active, the comparison with the infrared data should be valid. It can be seen that the three highest frequencies correlate with the three highest frequency modes of corundum and also with $LiNbO_3$. The lower frequency group of lines do not show an obvious relationship to those of corundum. The effect of ordering in this case, then, is the appearance of many low-frequency modes corresponding to lattice vibrations forbidden in the corundum structure. We do not see any pairs of characteristic frequencies that might be associated with Mg-O and Ti-O or Zn-O and Ti-O stretching motions. These remain strongly coupled in the ordered structure and the three high-frequency bands that do occur have exact analogs in the higher symmetry corundum structure.

The bands in excess of those permitted by the factor group analysis of ilmenite pose a problem. Since ilmenite is centrosymmetric, the longitudinal modes should not appear in the Raman spectrum. Perhaps the easy way out is to assign the weaker bands to multi-phonon processes, although there is really no good evidence for this or criteria for making the selection.

Table 2

Cation Ordering Schemes Based on Corundum Structure

Space Group	$R\bar{3}c$	$R\bar{3}$	$R3c$	$P\bar{3}c1$	$R3$
	D^6_{3d}	C^2_{3i}	C^6_{3v}	D^4_{3d}	C^4_3
Structure Type	Corundum	Ilmenite	$LiNbO_3$	$Mn_4Nb_2O_9$	Ni_3TeO_6
Z (Hexagonal Cell)	6	6	6	2	3

Table 3

Factor Group Analyses for Corundum-Related Structures

D_{3d}	Number of Modes		Selection Rules
	Al_2O_3(a)	$Mn_4Nb_2O_9$	
A_{1g}	2	7	Raman
A_{2g}	3	8	Inactive
E_g	5	15	Raman
A_{1u}	2	7	Inactive
A_{2u}	2	7	IR(E$\|\|$C)
E_u	4	14	IR(E$\perp$C)

C_{3i}	Number of Modes	Selection Rules
A_g	5	Raman
E_g	5	Raman
A_u	4	IR(E$\|\|$C)
E_u	4	IR(E$\perp$C)
C_{3v}(b)		
A_1	4	Raman + IR
A_2	5	Inactive
E	9	Raman + IR
C_3		
A	10	Raman + IR
E	10	Raman + IR

(a) Porto and Krishnan [8]

(b) Axe and O'Kane [9]

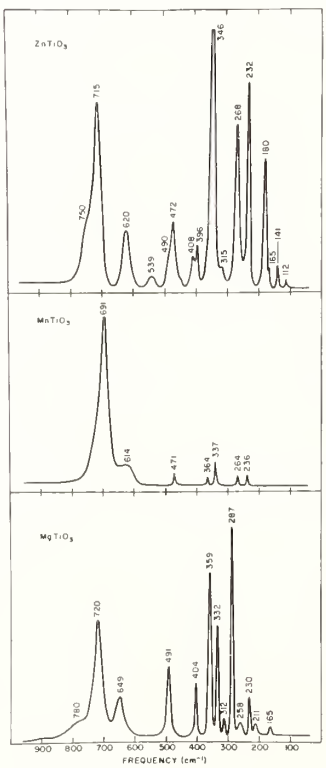

Fig. 1. Raman spectra of ilmenite structure compounds.

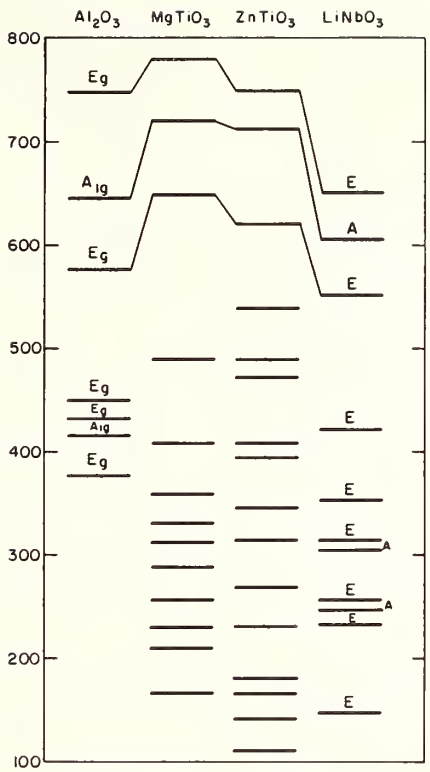

Fig. 2. Correlation of vibrational frequencies between corundum ($R\bar{3}c$), ilmenite ($R\bar{3}$), and $LiNbO_3$ (R3c). Corundum data are from reference [8], and $LiNbO_3$ data are from reference [9].

The Ni_3TeO_6 structure is of similar sort, except that it represents a 1:3 ordering instead of a 1:1 ordering in the cation stacking sequence. The factor group analysis of table 3 predicts a total of 20 modes active in both ir and Raman. The Raman spectrum of Ni_3TeO_6 shown in figure 3 exhibits only 10 lines, exactly half the predicted number. The symmetry here is so low that all vibrational modes are permitted and much of the detail is not resolved.

4.3. ORDERINGS WITH SUPERSTRUCTURE CELL AND SAME SYMMETRY

The trirutile structure is a rare example in which a 3-fold increase in the size of the unit cell is obtained by stacking three rutile cells along the c-axis. The space group remains D_{4h}^{14} ($P4_2/mnm$), the distribution of atoms over the equipoints remains the same, but the total number of degrees of freedom is tripled. A factor group analysis of rutile [10] yields:

$$\Gamma = A_{1g}(R) + A_{2g} + B_{1g}(R) + B_{2g}(R) + E_g(R) + A_{2u}(ir) + 2B_{1u} + 3E_u(ir)$$

Four modes are active in the infrared and four in the Raman. A tripled unit cell with no change in symmetry or site population would simply triple the number of modes appearing in each irreducible representation. We would expect 12 Raman active modes in the trirutile structure but might question whether these would all be distinct, since the individual segments of the enlarged cell might be poorly coupled.

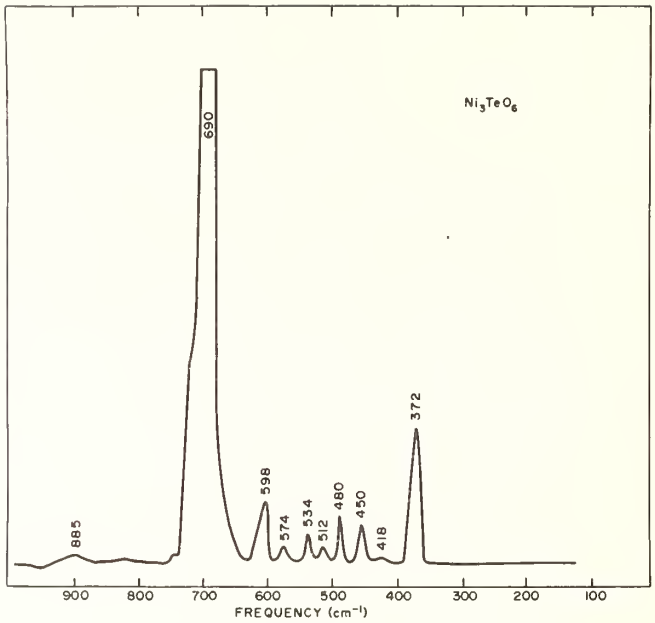

Fig. 3. Raman spectrum of Ni_3TeO_6, a 1:3 (R3) ordering on corundum.

Raman spectra of two trirutile ordered compounds, $ZnSb_2O_6$ and $MgSb_2O_6$, are shown in figure 4. Spectra of these colorless compounds, unlike the ilmenites, are almost identical except for small frequency shifts. The predicted 12 frequencies are observed in the zinc compound and 11 frequencies are observed in the magnesium compound. Direct comparison suggests that the 326 cm^{-1} band of $MgSb_2O_6$ may represent two modes which exactly overlap. The bands, however, are not clumped in readily discernible groups of three. Porto et al. [10] show that the A_{1g} mode of a variety of rutile structures is quite intense, while the higher frequency B_{2g} mode is weak. Using this as a guide, the following association of the bands can be made:

TiO_2 (rutile)		$ZnSb_2O_6$	$MgSb_2O_6$ (trirutile)
		814	810
B_{2g}	826 cm^{-1}	606	615
		412	481
		785	744
A_{1g}	612 cm^{-1}	657	668
		526	537

The 447 cm^{-1} E_g band and the 143 cm^{-1} B_{1g} band of rutile must be represented by the six weak lines in the 200 to 400 cm^{-1} region, but there is no clear-cut criterion for separating them. These spectra show quite clearly the strong coupling that must exist in the ordered trirutile structure. Without coupling we would have expected a strong line at frequencies higher than that of TiO_2 associated with an Sb-O vibration and two rather closely spaced lines in the 500 to 600 cm^{-1} region due to the Zn-O or Mg-O vibrations. What we observe are three strong lines about evenly spaced and with the highest frequency component close to the A_{1g} mode of TiO_2. Likewise, the B_{1g} set of modes is spread over a wide frequency range so that there is complete overlap with the A_{1g} set. Although static trirutile is very similar to rutile, the dynamics of the structure strongly reflect the ordering.

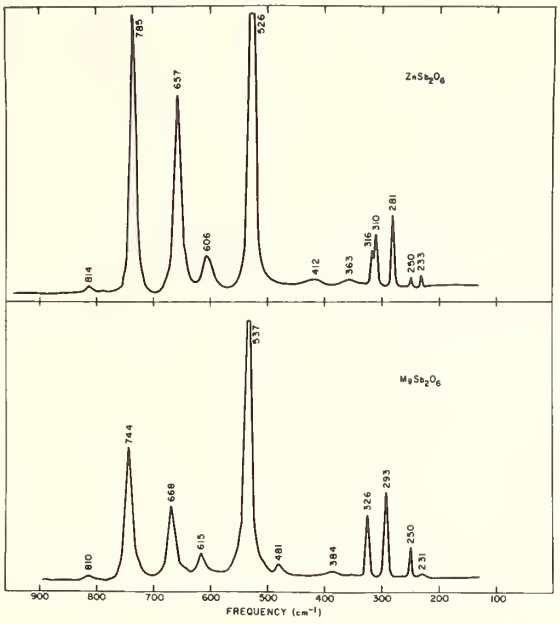

Fig. 4. Raman spectra of $ZnSb_2O_6$ and $MgSb_2O_6$ with the trirutile ($P4_2/mnm$) structure.

4.4. ORDERINGS WITH CHANGE OF BOTH SYMMETRY AND UNIT CELL

When the ordered structure requires both a lower space group and a larger unit cell, the spectra become quite complicated and the relationship to the parent structure becomes hard to discern. We consider here orderings on rocksalt and on corundum.

All of the corundum-related structures are based on a hexagonal unit cell containing 18 oxygens. All except $Mn_4Nb_2O_9$ have rhombohedral centering which introduces a 3-fold redundancy in the calculation of vibrational modes and reduces the effective motion of that of a primitive cell containing 6 oxygens. The $Mn_4Nb_2O_9$ cell is primitive, and the vibrations of the 18-oxygen cell must be considered. The ordering scheme of $Mg_4Nb_2O_9$ requires a superstructure cell which has the same factor group as corundum but requires a different space group. There are 3 times as many degrees of freedom in the primitive cell, but because of the different space group symmetry, these are distributed differently among the irreducible representations of D_{3d}. Had there been no change in space group symmetry (the case of the trirutile structure) each mode of corundum would have been tripled.

Raman spectra for three compounds with the superstructure cell are shown in figure 5. Twenty-two lines are predicted by factor group analysis. Fifteen are observed in $Ni_4Nb_2O_9$, 24 in $Mg_4Nb_2O_9$, and only 7 in $Co_4Nb_2O_9$. The problem here seems quite clearly to be the color of the cobalt and nickel compounds which reduces the intensity of the Raman scattering.

The highest frequency peaks should be assigned to stretching motions of the NbO octahedra. The frequencies are unusually high. Nb^{5+} will have a higher force constant than Al^{3+} but is much heavier. In contrast, the highest frequency mode in $LiNbO_3$ is at 657 cm^{-1} about the expected value for face-sharing octahedra. Since the $Mg_4Nb_2O_9$ space group is centrosymmetric, the longitudinal modes are not allowed in the Raman spectrum. Likewise, the mode-tripling relationship observed in the spectra of trirutile superstructure is not observed. The resemblance to corundum is completery lost, and this places a limitation on the complexity of structural ordering that can be investigated by Raman spectroscopy.

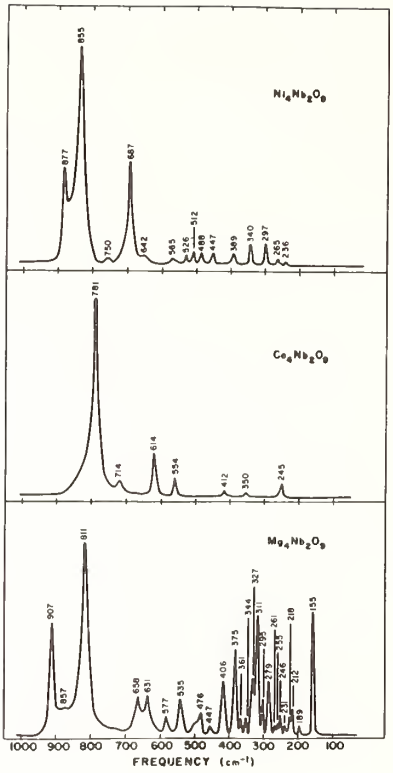

Fig. 5. Raman spectra of compounds with 1:2 ($P\bar{3}c1$) ordering on corundum.

The rocksalt structure, O_h^5, Fm3m contains only one AX forumla unit in the primitive unit cell and has a single infrared active T_{1u} vibrational mode. There are no one-phonon Raman modes. Compounds of the formula ABX_2 may exhibit a 1:1 ordering on the rocksalt structure which reduces the space group symmetry to D_{4h}^{19} $I4_1/amd$ with four formula units in the body-centered cell. Thus the cation ordering produces a lower symmetry, a distortion of the symmetry from cubic to tetragonal, and an enlarged unit cell. A previously published factor group analysis [11] shows:

$$\Gamma = A_{1g}(R) + 2B_{1g}(R) + B_{2g}(R) + 4E_g(R) + 2A_{2u}(ir) + B_{2u} + 3E_u(ir)$$

Examined of the infrared spectra [11] shows that the predicted five ir modes are indeed observed, but the bands are broad and indistinct as is typical of powder infrared spectra of highly polar compounds.

Raman spectra of four compounds with a 1:1 ordering on the rocksalt structure are shown in figure 6. The spectrum of $\gamma LiFeO_2$ is weak, because the compound is strongly colored. Spectra of the other three compounds exhibit more than the predicted 8 Raman bands as did the ilmenite structures. The intense band at low frequencies seems unusually sharp, and one might ascribe it to a fluorescence line, except that the frequency is different in $LiInO_2$, and further, the line appears in $\gamma LiFeO_2$ which should not be fluorescent. The original spectra of the two rare earth compounds were cluttered with fluorescence lines. Only lines which appeared with both 488 and 514.5 nm excitation were included in figure 6.

Although strong resemblances can been seen, the relative intensities are surprisingly different for compounds that are structurally similar. The band near 500 cm^{-1} is most intense in $LiErO_2$ with the second strongest band near 400 cm^{-1}. The two are comparably intense in $LiLuO_2$, and in $LiInO_2$ the 380 cm^{-1} band is far stronger than the 502 cm^{-1} band.

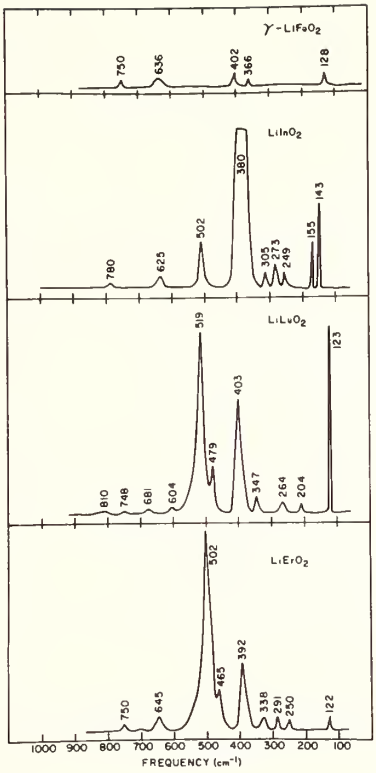

Fig. 6. Raman spectra of compounds with 1:1 ($I4_1/amd$) ordering on rocksalt structure.

The effect of the ordering is to produce strong bands in the Raman spectrum where none are permitted in the disordered structure. In this particular situation the Raman spectrum would be a sensitive tool for the detection of ordering in rocksalt structure mixed oxides.

4.5. ORDERING BASED ON SUPERSTRUCTURE STACKING

Sr_2TiO_4, $Sr_3Ti_2O_7$, and $Sr_4Ti_3O_{10}$ are examples of the Ruddlesden-Popper type of superstructures [3,12,13]. Sr_2TiO_4 has the tetragonal K_2NiF_4 structure which can be constructed from a perovskite block and a rocksalt block stacked along the *c*-axis. The other two compounds can be written $SrO \cdot 2SrTiO_3$ and $SrO \cdot 3SrTiO_3$ and are thus seen to be the same type of stacking with two and three perovskite blocks respectively. The space group is D_{4h}^{17}, I4/mmm for all three compounds. The *a*-axis is ∿3.90 Å for all compounds, while the *c*-axis increases from 13.71 to 20.3 to 28.1 as the number of perovskite blocks increases from one to three.

A factor group analysis for the Ruddlesden-Popper phases is given in table 4. Four Raman modes are expected for Sr_2TiO_4, 10 for $Sr_3Ti_2O_7$, and 14 for $Sr_4Ti_3O_{10}$. Raman spectra are shown in figure 7. Of greatest interest are the strong bands in the range of 500 - 700 cm^{-1}. A single band at 579 cm^{-1} appears in Sr_2TiO_4, two bands appear in $Sr_3Ti_2O_7$, and three in $Sr_4Ti_3O_{10}$. The A_{1g} modes should be the most intense and should correspond to a symmetric stretch of the oxygen lattice corresponding in a first approximation ot the TiO_6 octahedra.

It must be remembered that the basic perovskite block has no first order Raman spectrum [$3T_{1u} + T_{2u}$] and neither does rocksalt [T_{1u} only]. In D_{4h} symmetry, $T_{1u} \rightarrow E_u + A_u$ and $T_{2u} \rightarrow E_u + B_{2u}$. The single perovskite block in Sr_2TiO_4 accounts very nicely for the predicted infrared active $4E_u + 3A_{2u}$ modes. As the number of perovskite blocks is increased the number of ungerade modes no longer accounts for all degrees of freedom. It is apparent

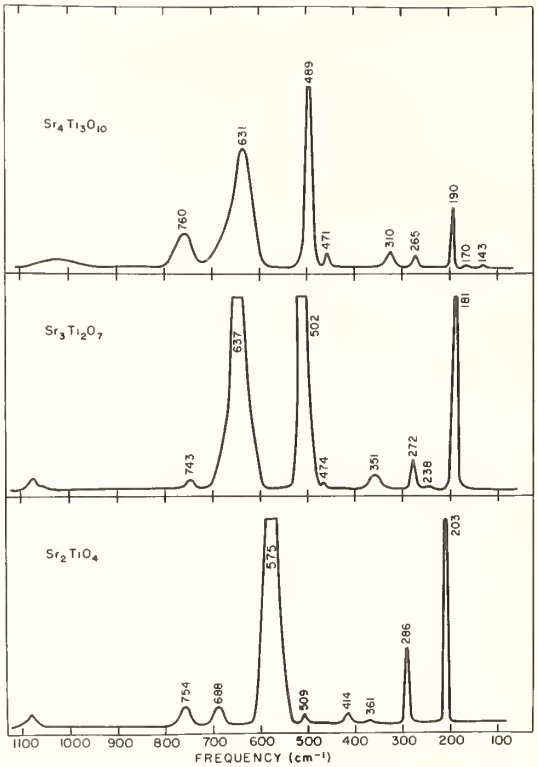

Fig. 7. Raman spectra of the Ruddlesden-Popper phases with I4/mmm symmetry.

Table 4

Factor Group Analyses for the Ruddlesden-Popper Phases

D_{4h}	Acoustic Modes	Vibrational Modes			Selection Rules
		Sr_2TiO_4	$Sr_3Ti_2O_7$	$Sr_4Ti_3O_{10}$	
A_{1g}		2	4	6	Raman
A_{2g}		0	0	0	---
B_{1g}		0	1	1	Raman
B_{2g}		0	0	0	---
E_g		2	5	7	Raman
A_{1u}		0	0	0	---
A_{2u}	z	3	5	7	Ir, E$\|\|$C
B_{1u}		0	0	0	---
B_{2u}		1	1	2	Inactive
E_u	(x,y)	4	6	9	Ir, E$\perp$C

that a stacking superstructure, although the space group is preserved, does not yield a simple multiplicity of bands. The new bands that appear in the Raman have no counterparts in the parent structures.

5. CONCLUSIONS

The overall conclusions reached from the study of order-disorder may be summarized:

1. Vibrational spectroscopy is an exceptionally sensitive tool for the *detection* of ordering. We were able to detect ordering in some spinels where no evidence for it occurred in the x-ray patterns.

2. In general, ir spectra are easier to interpret than Raman spectra. Intensities in particular are more predictable. Raman intensities tend to be very variable, even between very similar compounds.

3. Specific crystallographic models can be tested if the unit cell is not too large. Spectra of very large cells show evidence for ordering, but all predicted detail is generally not resolved.

4. Although ordering seems a rather mild effect crystallographically, it produces dramatic changes in the dynamics of the unit cell. Spectra of ordered structures frequently bear no resemblance to the spectra of the parent. Atoms or molecules that are equivalent in the disordered structure may be non-equivalent in the ordered structure but are still strongly coupled.

This work was supported by the Air Force Materials Laboratory, Wright Patterson Air Force Base, under Contract F33615-69-C-1105.

6. REFERENCES

[1] White, W. B., Mat. Res. Bull., 2, 381 (1967).
[2] Bertaut, E. F., Corliss, L., Forrat, F., Aleonard, R., and Pauthenet, R., J. Phys. Chem. Solids, 21, 234 (1961).
[3] McCarthy, G. J., White, W. B., and Roy, R., J. Amer. Ceram. Soc., 52, 463 (1969).
[4] White, W. B. and DeAngelis, B. A., Spectrochim. Acta, 23A, 485 (1967).
[5] Herzberg, G., *Ir and Raman Spectra of Polyatomic Molecules*, (Van Nostrand, New York, 1945).
[6] DeAngelis, B. A., Keramidas, V. G., and White, W. B., J. Solid State Chem., 3, 358 (1971).
[7] Newnham, R. E. and Meagher, E. P., Mat. Res. Bull., 2, 549 (1967).
[8] Porto, S. P. S., Krishnan, R. S., J. Chem. Phys., 47, 1009 (1967).
[9] Axe, J. D. and O'Kane, D. F., Appl. Phys. Lett., 9, 58 (1966).
[10] Porto, S. P. S., Fleury, P. A., and Damen, T. C., Phys. Rev., 154, 522 (1967).
[11] Moore, R. K. and White, W. B., J. Amer. Ceram. Soc., 53, 679 (1970).
[12] Ruddlesden, S. N. and Popper, P., Acta Cryst., 10, 538 (1957).
[13] Ruddlesden, S. N. and Popper, P., Acta Cryst., 11, 54 (1958).

DISCUSSION

J. Shamir: I would like to ask if the spectra you presented are from single crystals. I would like to add that we have just recently studied a polycrystalline solid solution of zinc and cadium sulfide and found that the frequency of the LO phonon shifts linearly with the composition of zinc sulfide and cadium sulfide. Now my question is have you observed it only in single crystals or in polycrystals as well?

W. B. White: The data that I have shown you here are all on polycrystalline, pressed powder materials. However, they are single phases, not solid solutions. If you do look at solid solutions either by single crystal measurement or by powders you run into this one mode or two mode behavior phenomenon which has been observed in rock salt and sphalerite structures pretty commonly.

W. R. Cook: I note on your slide on lithium iron oxide that the Raman lines were extremely weak in comparison with virtually everything else you showed. Does this mean that the compound is only partly ordered?

W. B. White: No, I'm afraid that what it means in this case is that lithium iron oxide is very strongly colored and with scattering from a blue line of the ionized argon laser it just absorbs like the devil.

National Bureau of Standards Special Publication 364, Solid State Chemistry, Proceedings of 5th Materials Research Symposium, issued July 1972.

A STUDY OF V_2O_3 BY PHOTOELECTRON SPECTROSCOPY*†

J. M. Honig

Department of Chemistry
Purdue University
West Lafayette, Indiana 47907

H. E. Weaver and R. D. Board

Scientific Instruments Division
Hewlett Packard Company
Palo Alto, California 94304

The occupied energy states of single crystal and polycrystalline V_2O_3 have been studied by x-ray photoelectron spectroscopy both above and below the metallic-antiferromagnetic insulator (M-AFI) transition. All of the elemental Vanadium and Oxygen states in the range 20 to 640 ev below the Fermi level were also encountered in V_2O_3. In addition, a valence band with structure was observed in the range 0 to 10 ev. In the metallic phase this band was intersected by the Fermi level; below the transition temperature the topmost portion of the band was no longer observable, and may have disappeared under increased noise. Under the experimental conditions involving a resolution of 0.3 to 0.5 ev, a search was made for the presence of localized states in the energy spectrum of the insulating phase at 77 K. No such states were encountered; unless they were masked by the residual valence band approximately 4 ev in width it must be concluded that the transition does not involve a change from a localized to an itinerant electron regime.

Key words: Metallic-insulator transition; photoelectron spectroscopy; V_2O_3.

---

*Supported in part by the National Science Foundation under Grant GP 8302 to Purdue Univ.

†As this is a post-deadline paper only a brief abstract is presented here.

National Bureau of Standards Special Publication 364, Solid State Chemistry, Proceedings of 5th Materials Research Symposium, issued July 1972.

OBSERVATIONS IN THE ELECTRON MICROSCOPE OF LATTICE PLANES AND MIGRATION OF SILVER IN BETA ALUMINA

W. L. Roth

General Electric Corporate Research and Development
Schenectady, New York 12301

Beta alumina is the commonly accepted name for a sodium aluminate of variable composition and structure with "ideal" formula $NaAl_{11}O_{17}$. There is considerable interest in beta alumina and its isomorphs because the monovalent ions diffuse rapidly at temperatures of 300 °C and below. Crystal structure and density studies of the sodium and silver isomorphs have shown the compound is non-stoichiometric and contains approximately 25% excess sodium or silver. All of the monovalent ions lie in basal planes at z=1/4 and 3/4. The planes are separated by 11 Å and ion conduction takes place by two dimensional diffusion in these planes.

The conducting planes have been resolved in the electron microscope and their identity established by electron diffraction. High resolution photographs show lattice bending and rotation.

When relatively thick crystals of silver beta alumina are observed in the electron microscope, worm-like filaments or whiskers about 50 Å in diameter exude from the edge of the crystal. The filaments were shown by electron diffraction to be silver. The filaments are produced by diffusion of Ag^+ ions down channels in the conducting planes to neutralize the negative charge of absorbed electrons.

Key words: Beta alumina; electron microscope; lattice images; migration of silver; silver whiskers.

1. INTRODUCTION

Motivated by the discovery of solids with exceptionally high ionic conductivity, there has been renewed interest in the structure of beta alumina and some of its isomorphs. Beta alumina is a member of a small class of unique materials, called super ionic conductors [1][1] that exhibit extremely large ionic diffusivities at temperatures which are low with respect to their melting points. For example, the self diffusion constants for sodium and silver ions in beta alumina [2] are given by $D(Na^+) = 2.4 \times 10^{-4} \exp(-3810/RT)$ and $D(Ag^+) = 1.65 \times 10^{-4} \exp(-4050/RT)$ $cm^2 sec^{-1}$, corresponding to room temperature diffusivities of $D(Na^+) = 4.0 \times 10^{-7}$ and $D(Ag^+) = 1.7 \times 10^{-7}$ $cm^2 sec^{-1}$. A particularly important property of the structure is the extreme anisotropy of the diffusion. Movement of ions occurs by two dimensional flow in widely separated planes which are perpendicular to the hexagonal axis of the crystal and there is virtually no diffusion between the planes. X-ray diffraction has provided considerable insight into the structure at the atomic level, the stoichiometry, crystal structure, and paths the conducting ions follow in migrating through the crystal [3,4].

Beta alumina is an unfortunate misnomer commonly used to refer to the refractory sodium aluminate with hexagonal crystal structure which has composition about $Na_2O \cdot 11Al_2O_3$ to $Na_2O \cdot 9Al_2O_3$. The general features of the atomic arrangement was originally solved by Bragg et al. [5] and Beevers and Ross [6], and the structure has been refined with modern methods by Felsche [7] and Peters et al. [3]. The crystal is composed of *spinel-like* blocks which consist of four close packed layers of oxygen atoms with aluminum atoms distributed among the

[1] Figures in brackets indicate literature references at the end of this paper.

465-504 O - 72 - 10

octahedral and tetrahedral interstices. The blocks are bound together by planes of loosely packed Na^+ and O^{-2} ions. The binding between the spinel-like layers is weak, resulting in easy cleavage of the crystals parallel to the basal planes. The sodium may be replaced by other monovalent ions of appropriate size [2] and the structures of the K^+ [6] Ag^+ [4,8] and H_3O^+ [9] derivatives have been shown to be isomorphous with beta alumina.

Beta alumina is non-stoichiometric and crystals usually contain about 15-25% Na^+ in excess of the "ideal" formula $NaAl_{11}O_{17}$ [2,4]. The precise mechanism of charge compensation has not been established and it is not definitely known whether the positive charge due to the excess monovalent cations is neutralized by aluminum vacancies, interstitial oxygens, or bound electrons.

The present paper describes electron microscope observations on sodium and silver beta alumina that were undertaken to provide information on a different scale relevant to the structure and movement of ions through the crystal. Crystals of the sodium and silver isomorphs have been studied in the electron microscope. The lattice planes responsible for conduction in sodium beta alumina have been resolved and the migration and reduction of Ag^+ to Ag by electrons has been observed.

2. IDENTIFICATION OF CONDUCTING PLANES IN SODIUM BETA ALUMINA

Crystals of beta alumina (Monofrax H, Carborundum Company) were gently crushed and scattered on a carbon substrate for examination. Electron microscope observations were made with an updated Sieman's Elmiscope 1, and a Philips EM 300 operated at 100 kV. The observation of lattice fringes due to the conducting planes requires the beam strike the planes at the Bragg angle which for 100 kV electrons is near grazing incidence. The desired orientation is perpendicular to the easy cleavage plane and it was necessary to seek out fragments that had fallen with their c-axis roughly parallel to the plane of the supporting grid. Suitable fragments were identified by scanning the field and observing the diffraction patterns on a fluorescent screen. The c-axis was easily recognized by the close spacing of reflections corresponding to the large c_o = 22.6 Å lattice parameter. After an appropriate fragment was selected, the orientation was sometimes extended to two dimensions by rotation of the crystal about the c-axis.

Figure 1 is an electron micrograph taken at 100,000 magnification of a beta alumina fragment. The long edge is parallel to the hexagonal axis and the fragment appears to be made up of bands about 0.1_μ wide which are parallel to (00.1) planes. The arc-like segments near the lower fracture edge which appear to intersect the crystal surface at an angle to the cleavage planes are probably deformation structures produced when the crystal was crushed.

The diffraction pattern (fig. 2) shows the fragment consisted of two principal crystals. The major individual is oriented with the a*c* plane perpendicular to the electron beam and the c-axis of the second is tilted about 8° with respect to the first. The observed lattice parameters were found to be a_o = 5.46 Å and c_o = 23.8 Å, in reasonable agreement with more accurate values, a_o = 5.594 and c_o = 22.603 Å, measured with x-rays and bulk crystals. The diffraction spots contain considerable substructure indicative of twinning or lattice bending and rotation. The substructure is probably related to the bands in figure 1 and the fragment appears to be composed of lamellae about 0.1_μ thick. The intense pattern shows reflections of the form h-k = 3n, ℓ = 2n + 1 which are not allowed by the space group $P6_3/mmc$. The reflections are absent in the weaker pattern which indicates they are due to dynamic or multiple scattering effects in the thick crystal.

Figure 3 is an electron micrograph taken at magnification 500,000 from a thin wedge near the edge of the same crystal. The region is marked with an X in figure 1. Relatively perfect lattice fringes approximately perpendicular to the c-axis of the fragment are resolved. The fringe separation obtained by direct measurement on the electron micrograph plate is 22 Å, equal to the c_o parameter of beta alumina. The fringes are tilted about 8° with respect to the edge of the dense (absorbing) crystal, approximately the angle between the c-axes of the individuals in figure 2. The fringes were obtained by insertion of a 50_μ objective aperture which isolated the (000) and several low order (00ℓ) reflections. The angular correlation of fringes and diffraction pattern was established after correcting for

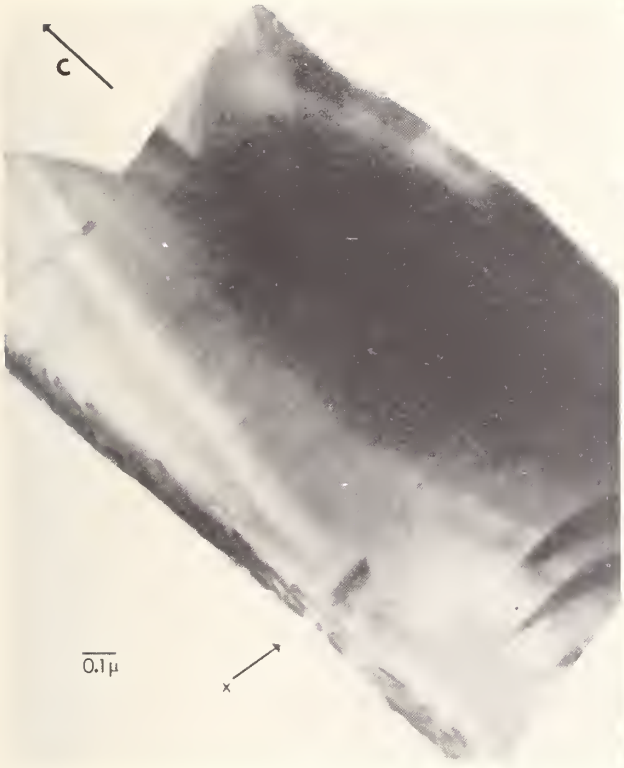

Fig. 1. Beta alumina magnified 100,000X. The region marked with an X is shown at higher magnification in figure 3.

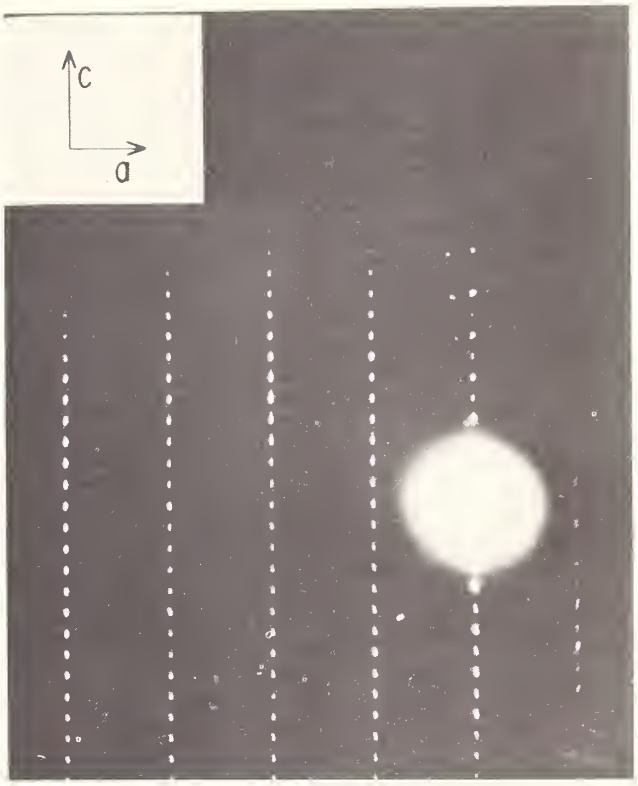

Fig. 2. Electron diffraction pattern of beta alumina crystal shown in figure 1.

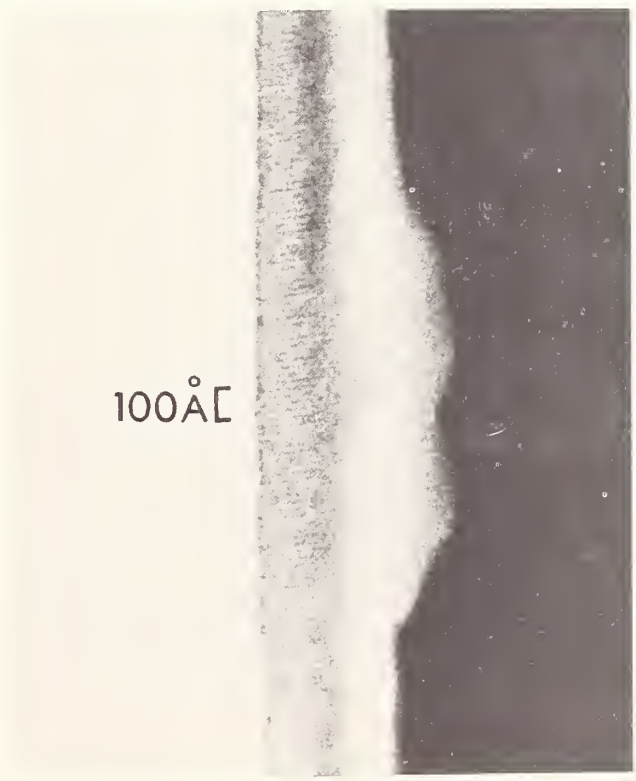

Fig. 3. Beta alumina magnified 500,000X. Same region marked with X in figure 1.

rotation of the image by the magnetic field of the lens. The orientation and spacing identify the lattice fringes with the conducting planes in beta alumina. The fringe separation corresponds to (00.1) planes. Adjacent conducting planes are only 11 Å apart and the double fringe separation is probably due to inclusion of the forbidden (00.1) reflection. The 11 Å separation corresponding to the (00.2) planes was resolved in the patterns to be described next.

Figures 4, 5, 6 are high resolution electron micrographs taken by V.A. Phillips and J.A. Hugo with the Philips EM 300 microscope, axial illumination, and 30μ or 50μ diameter objective apertures. Lattice fringes separated by 11 Å, equal to the separation of the adjacent conducting planes in beta alumina, are clearly resolved in figure 4. The intensity reversals along the fringes are attributable to electron optical effects caused by the crystal thickness tapering toward the edge.

The micrograph in figure 5 taken at magnification of 570,000 shows a cross grating pattern of 11.4 Å fringes inclined at about 68° to a set of 4.5 Å fringes. The wide fringes correspond to the (00.2) planes (d=11.3 Å) and the fine fringes to (10·2) planes (d=4.45 Å). The computed angle between (00.2) and 10.2) planes is 67°15', in agreement with the observed angle. Marked bending of the (00.2) lattice planes which is a consequence of the weak bonding between spinel blocks is visible in the lower position of the crystal.

Figure 6 shows a well developed set of 4.8 Å fringes traversing a broad expanse of nearly perfect crystal except for mottled patches about 25-50 Å wide. The lattice fringes pass continuously through the patches and the similar structure at the edge of the crystal indicates the mottled appearance may arise from microcleavages in the surface. An alternative interpretation, which is highly speculative based on the limited information at hand, is the regions may be the B- and D-domains that have been suggested to account for the nonstoichiometry of beta alumina [4].

Fig. 4. Lattice fringes corresponding to (00.2) planes in beta alumina. The fringe separation is about 11 Å.

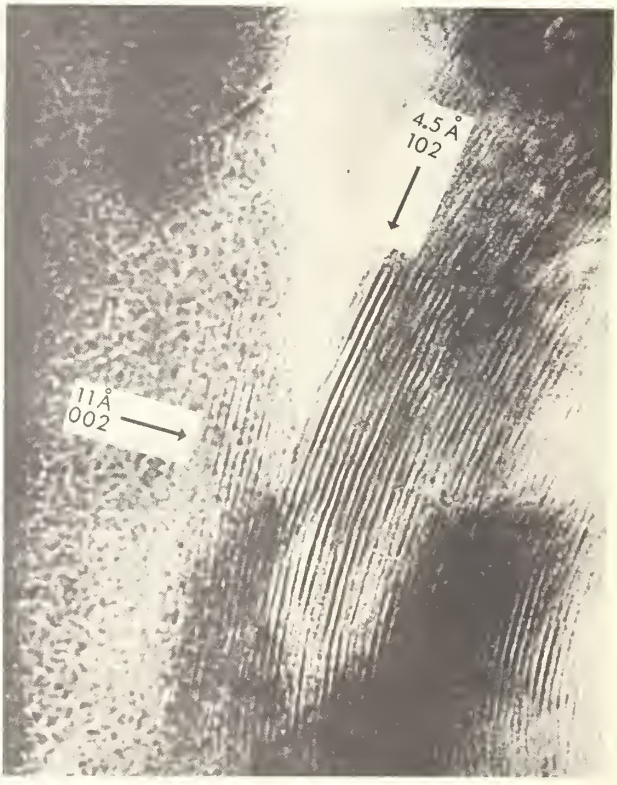

Fig. 5. Beta alumina cross grating pattern. Wide fringes are (00.2) planes (d=11.3Å) and fine fringes are (10.2) planes (d=4.45Å). Note curvature of the (00.2) planes.

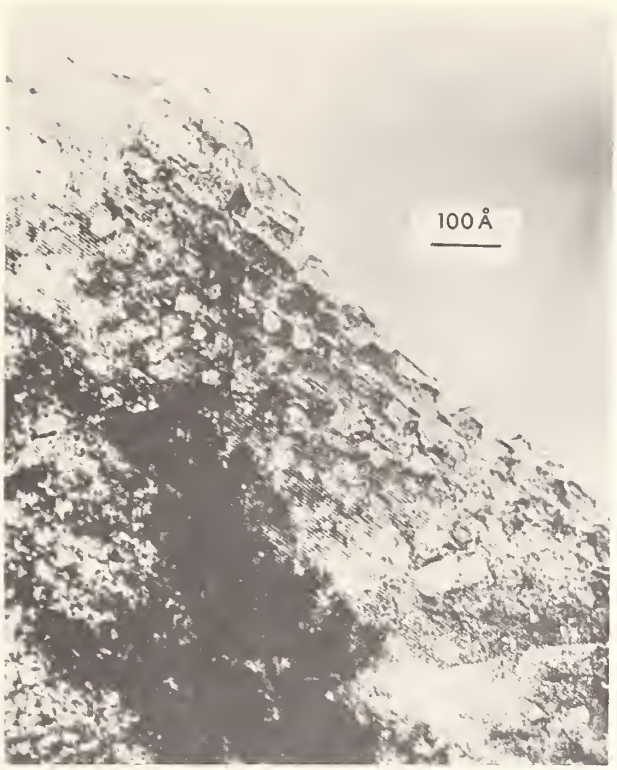

Fig. 6. Lattice fringes corresponding to (10.0) planes in beta alumina (d=4.84Å).

3. REDUCTION OF Ag^+ IN SILVER BETA ALUMINA BY ELECTRONS

The sodium in beta alumina crystals was replaced with silver by exchanging in molten silver nitrate as described by Yao and Kummer [2]. Crystals were crushed and examined with the electron microscope in similar fashion to beta alumina. The phenomena to be described were observed in thick crystals that were opaque to the electron beam. Thin crystal fragments that were highly transparent to electrons appeared to behave in more normal fashion.

Figure 7 is a diffraction pattern obtained from a silver beta alumina crystal which had been only slightly exposed to the electron beam. The electron micrograph of the same crystal (fig. 8) shows opaque regions, roughly globular or disc-like in shape, with sizes ranging from about 50 to 300 Å. Similar opaque regions observed in other fragments had a worm-like appearance. A set of weak, diffuse rings were generally superimposed on the sharp reciprocal lattice of the silver beta alumina. The d-values calculated from the diffuse rings agreed with the first four reflections of metallic silver. The most probable interpretation of these observations is that some of the Ag^+ ions in silver beta alumina were reduced in the electron beam to form metallic silver.

Attempts to observe the precipitation of silver by working with weak beams focused near the edge of crystals resulted in the formation of whisker-like filaments which started at the edge and grew outward in worm-like fashion (fig. 9). Electron diffraction confirmed their identity as crystalline silver (fig. 10). The filaments were about 50-100 Å in diameter and had relatively uniform cross section. Initially the filaments grew straight and parallel to each other, and parallel to the crystal surface. Figure 11 is enlarged to show a banded substructure in the filaments which may be the result of deformation or twinning.

The evident interpretation of these observations is that metallic silver is formed by reduction of Ag^+ by electrons incident on the silver beta alumina. Several processes are involved in the growth of the globs and whiskers.

Fig. 7. [110] zone of silver beta alumina.

Fig. 8. Electron micrograph of silver beta alumina crystal corresponding to diffraction pattern in figure 7.

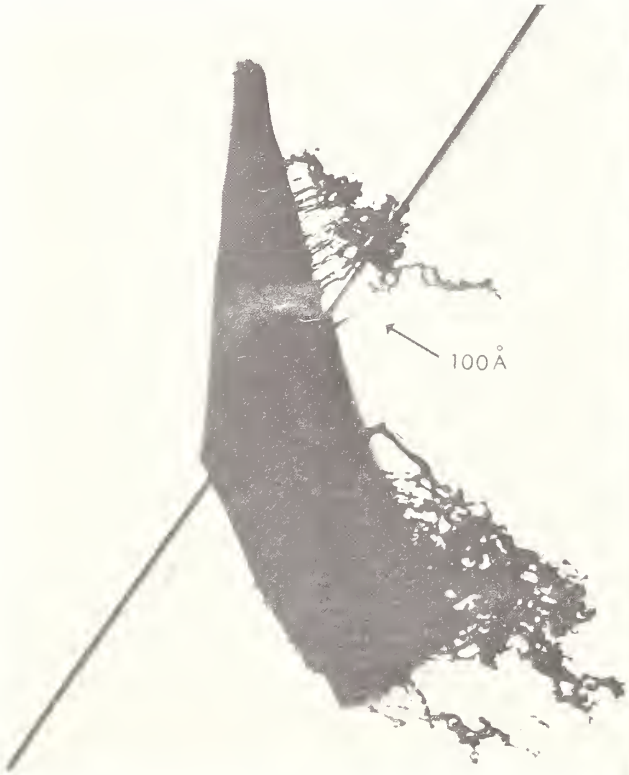

Fig. 9. Silver whiskers growing from silver beta alumina.

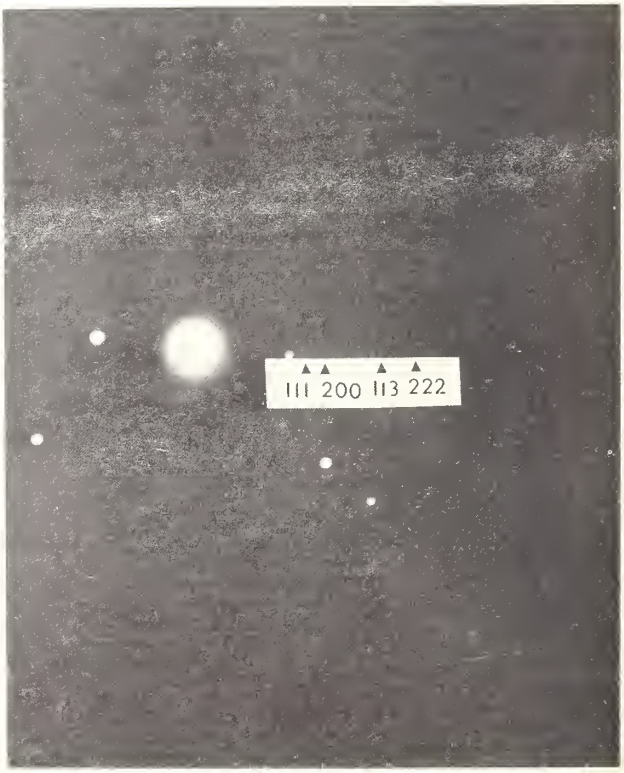

Fig. 10. Diffraction pattern of whiskers.

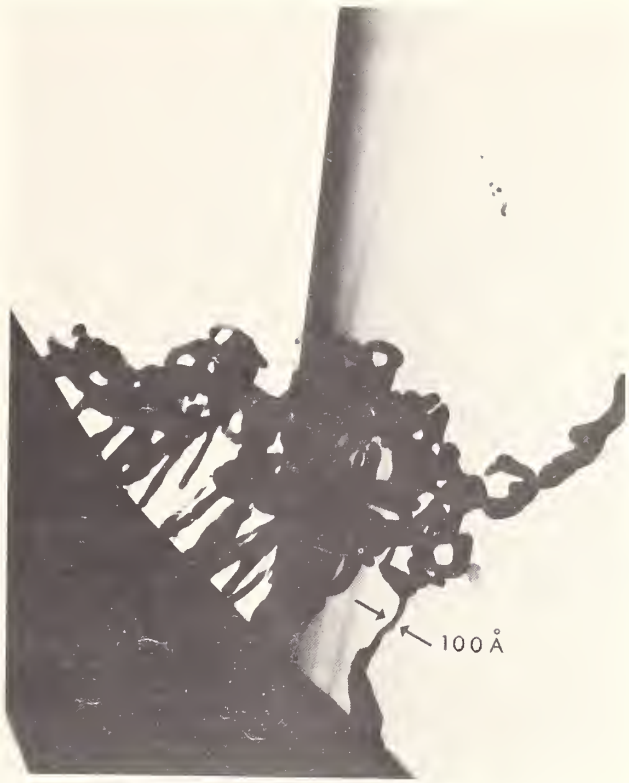

Fig. 11. Enlargement showing detail in whiskers growing from silver beta alumina.

1. The absorption of electrons generates heat and the temperature rise increases the rate of diffusion of Ag^+. The effect is more pronounced in thick crystals which absorb a larger number of electrons.

2. When the beam is directly incident on a thick crystal, Ag^+ ions are attracted and diffuse toward the negative charge where they are reduced to atomic silver. The rounded edges of the silver globs suggest high temperatures may be attained in small local regions.

3. The heating is less severe when the electron beam is incident at the edge of the fragment. The Ag^+ ions are attracted to the negative charge at the crystal edge where they are reduced to atomic silver. The movement of Ag^+ down the crystal channels is probably enhanced by collapse of the beta alumina structure into α-Al_2O_3 behind the advancing front of silver. When the accumulation of silver at the edge exceeds that required to form a nucleus of critical size [10], a crystal nucleates and grows in whisker-fashion as it continues to be fed from the interior of the beta alumina crystal. As the filament extends farther from the surface, elastic strains due to thermal and electrical gradients at the edge of the crystal increase and ultimately are relieved by kinking.

The proposed mechanism of whisker growth is associated with the very high mobility of the Ag^+ ions and resembles the growth of whiskers on silver iodide [11]. The observed whisker cross section indicates the critical size of the silver nucleus is about 50 Å, which agrees with 100 Å found by Price et al. [12] for silver whiskers electrolytically grown from $AgNO_3$. According to the suggested mechanism, the crystals in the whisker should be relatively perfect, in agreement with the sharp reflections making up the Debye Sherrer rings in figure 10. The sharpness of this pattern contrasts with the diffuse rings obtained from the globular precipitate inside beta alumina crystals.

4. REDUCTION OF Na^+ IN SODIUM BETA ALUMINA BY ELECTRONS

The reduction of Na^+ to metallic sodium in beta alumina crystals was not observed in the electron microscope but there is reason to believe that the reaction may occur. Electron microprobe experiments with sodium beta alumina crystals have shown a gradual increase with time of the intensity of NaKα x-rays when the electron beam remained focused on a single region. This is believed to be due to an increase in the concentration of sodium by diffusion of Na^+ toward the electrons. If the beam continues to be focused on the same point, the crystal decomposes and the NaKα x-ray intensity decreases. This is probably due to the sublimation of sodium and a concomitant collapse of the structure into α-Al_2O_3.

5. SUMMARY

1. Lattice fringes due to the conducting planes in beta alumina have been resolved in the electron microscope. Direct measurement of the separation of the conducting planes agrees with that obtained by x-ray diffraction.

2. Reduction of Ag^+ to atomic silver occurs when thick crystals of silver beta alumina are observed in the electron microscope. If the beam strikes the beta alumina directly, globs or worm-like clusters of metallic silver, about 50 Å in diameter, precipitate within the crystal. If the beam impinges near the edge, Ag^+ ions diffuse toward the beam and are reduced to metallic silver to form filament-like whiskers approximately 50 Å in diameter.

3. Evidence is presented that Na^+ is also reduced to atomic sodium by electrons incident on beta alumina.

6. ACKNOWLEDGEMENTS

The cooperation of E.F. Koch in obtaining the electron diffraction and electron microscope patterns of sodium and silver beta alumina is gratefully acknowledged. I am grateful to R.B. Bolon for microprobe observations and to V.A. Phillips and J.A. Hugo for the high resolution electron micrographs.

7. REFERENCES

[1] Rice, M. J., and Roth, W. L., J. Solid State Chem., 4, 294 (1972).
[2] Yao, Y. Y., and Kummer, J. T., J. Inorg. Nucl. Chem., 29, 2453 (1967).
[3] Peters, C. R., Bettman, M., Moore, J. W., and Glick, M. D., Acta Cryst., B27, 1826 (1971).
[4] Roth, W. L., J. Solid State Chem., 4, 60 (1972).
[5] Bragg, W. L., Gottfried, C., and West, J., Z. Krist., 77, 255 (1931).
[6] Beevers, C.A., and Ross, M.A.S., Z. Krist., 97, 59 (1937).
[7] Felsche, J., Naturwissen., 54, 612 (1967).
[8] Whittingham, M.S., and Huggins, R.A., J. Chem. Phys., 54, 414 (1971).
[9] Kato, K., Ph.D. Thesis, University of Hamburg, (1968).
[10] See, for example, Nabarro, F.R.N., and Jackson, P.J., in *Growth and Perfection of Crystals*, Ed. by Doremus, R.H., Roberts, B.W., and Turnbull, D., *Proceedings of International Conference on Crystal Growth*, held at Cooperstown, N. Y., Aug. 27-29(1958), publ. by John Wiley & Sons, Inc., New York (1958).
[11] Berry, C.R., J. Opt. Soc. Amer., 40, 615 (1950).
[12] Price, P.B., Vermilyea, D.A., and Webb, M.B., Acta Metallurgica, 6, 524 (1958).

DISCUSSION

N. C. Stephenson: By looking at the growth of these whiskers, is it possible to tell whether the movement of the silver atoms on the planes are coordinated, whether they move with respect to other atoms, or just have individual paths?

W. L. Roth: No, except the whiskers seem to have a periodic spacing so that one feels one is seeing the consequences of silver atoms moving down channels. Of course, we do not see the structure at the atomic level since the whiskers are 50 to 100 angstroms in diameter.

N. C. Stephenson: Are they all coming out at the same rate?

W. L. Roth: They are all roughly coming out at the same rate, but I do not know to what extent the intensity of the field is constant at the edge of the crystal.

B. Cox: This is a comment which was originally intended for John Allpress, but I think it's just as appropriate here. This is to insert a note of caution into the interpretation of lattice fringe images when one is interpreting detail on the scale where the dynamical theory of electron diffraction is breaking down. I would also like to point out the situation in the imaging of lattice fringes in metals for the study of dislocations where, in a given area of the sample imaged using two symmetrical but opposite reflections, the actual number of terminating fringes or dislocations which appear in the same area, can vary from image to image[1]. I don't think we can go into the reasons for this here, but I would just like to point out that things like wavy fringes are not direct images of the lattice. They are still an interference phenomenon, to use a simplification in terms.

W. L. Roth: I agree completely. However, I should have pointed out the reason for showing the first set of fringes was because I had direct evidence that we were looking at the 00ℓ fringes. We correlated the orientation of the diffraction pattern precisely with the orientation of the fringes by measuring the rotation of the image in the microscope. We know that we are looking at diffraction effects from the 00ℓ planes. Our aperture was such that we probably included other reflections so that I agree some of the detail may not represent real images of the lattice.

J. G. Allpress: I agree with that last comment of Brian Cox. In fact, it is very important. The actual conditions under which you take the pictures are very important, the conditions of focus and so on, the orientation, and the crystal thickness. We really have to do a lot of quite heavy calculations in order to prove that we are seeing structures directly in the particular case that we are interested in. However, I think we've got to take each case on its own merits, we can't make generalizations about this technique.

B. Post: In the first place I agree with Dr. Cox about the caution that has to be exercised in interpreting these fringes. I think you are familiar with Pendelosung fringes which are seen with x-rays and with electrons. There is no reason why you shouldn't see them in some of these cases. But what I wanted to ask was a very simple question, really. Why does silver always act as the anomalous metal, not always, but why does silver always act as the ionic conductor as the material that causes shorting out in semiconductors and so on? Have you any thoughts on that matter?

W. L. Roth: Well, it may not be that anomalous. For example, consider the beta alumina structure. One can substitute lithium, sodium, potassium, ammonia or silver ions, and the base structure, the matrix, changes very little. The diffusion and conduction of silver ions in beta alumina are similar. The activation energies are within a third of a kilocalorie of each other and there is very little difference between them. Silver is a small ion which fits well in open structures. If lithium ions are substituted for silver or sodium, there is a larger activation energy for diffusion because the lithium is too small. The opposite is true for potassium because it is too large. There also may be some effects due to the polarizing power of the silver ion.

B. M. Gatehouse: You seem to stress that the silver was growing out from the surface for 500 angstroms or maybe more along what may possibly be channels. However, I thought I could see one there that seemed to be turning and coming back or was that some odd effect in the photograph?

W. L. Roth: You should understand one is looking at a dynamic process in the microscope and must decide at a given instant to take a photograph. The whiskers start out initially parallel and grow to perhaps three or four times their diameter in length. Then they may deform in a complex way. There probably are intense fields and temperature gradients in the vicinity of the surface. The incident electrons introduce surface charges which result in deformation and the whiskers kink and take off in a new direction. I don't know whether the whiskers are twinned, but the electron diffraction patterns, the Debye-Scherrer rings, are made up of individual reflections which are quite sharp. Each of the 100 to 200 angstroms silver elements in the unkinked region of a whisker seems to be a fairly perfect crystal.

[1]D. J. H. Cockayne, J. R. Parsons and C. W. Hoelke, Phil. Mag., 24, 130 (1971).

National Bureau of Standards Special Publication 364, Solid State Chemistry, Proceedings of 5th Materials Research Symposium, issued July 1972.

BETA ALUMINA - PRELUDE TO A REVOLUTION IN SOLID STATE ELECTROCHEMISTRY

M. S. Whittingham and R. A. Huggins

Department of Materials Science and Engineering
Stanford University
Stanford, California 94305

For almost two decades solid state electrochemical techniques have been used to study the thermodynamic and transport properties of a number of materials. However, these studies have been restricted essentially to systems utilizing electrolytes containing mobile silver or copper ions at low temperatures, and oxygen ions at high temperatures.

Transport measurements have been made on single crystals of beta alumina, which has the nominal formula $MA\ell_{11}O_{17}$ where M is usually a monovalent cation, to test its suitability as a solid electrolyte. In this and related structures, the monovalent cation can be extremely mobile. By use of a group of novel non-polarizing solid electrodes, which are fully reversible to the monovalent cation, it has been possible to study the ionic conductivity of a series of beta aluminas containing alkali metals as well as thallium over a wide temperature range. The electronic conductivity of silver beta alumina has also been determined by use of the Wagner asymmetric polarization technique over wide ranges of temperature and oxygen partial pressure.

The results of these studies clearly indicate that the beta alumina family shows excellent promise for use as solid electrolytes, exhibiting high values of ionic conductivity and a very low electronic transference number. These properties were exhibited over extremely wide ranges of temperature, -150 °C to +820 °C, and oxygen partial pressure, 10^{-24} to 1 atm. The use of beta alumina opens up many new opportunities in solid state electrochemistry, particularly in the study of materials containing monovalent cations.

Key words: Beta alumina; diffusion; electrochemical cell; electrochemical transducer; ionic conductivity; mass transport; solid electrolyte.

1. INTRODUCTION

There has recently been a great deal of interest in a material called "beta alumina", whose nominal formula is $MA\ell_{11}O_{17}$, in which M represents a cation, normally monovalent. This interest has arisen primarily because of the possibility of using materials of this phase, or more probably a related phase called "β" alumina", whose nominal formula is $MA\ell_5O_8$, as solid electrolytes in new types of batteries. This interest arose as a result of the important pioneering work at the Ford Motor Company [1,2][1] which not only focused attention upon the unusual physical properties of this type of material, but also [3] showed that it was possible to take a rather revolutionary approach to the battery problem, using liquid electrodes and a solid electrolyte; this is, of course, just the inverse of traditional battery designs, and leads to some very distinct advantages.

Interest in the practical application of these materials and concepts has spread rather widely, and research is under way in a number of laboratories at the present time. In addition, serious battery development efforts have been undertaken by several companies in the United States, as well as others in England and Japan. At the present time the commerical

[1]Figures in brackets indicate the literature references at the end of this paper.

interest seems to be focused upon the use of configurations involving a liquid sodium anode, a solid β or β" alumina electrolyte and a liquid sulfide cathode. Although there are surely various alternative approaches, it now appears that such a cell is expected to be a serious contender for widespread application as high energy density and power density secondary cells.

One can find reviews of various new battery possibilities in a number of places [4-14], and it is not our intent to discuss this matter here other than to point out that the theoretically limiting value of energy density for a sodium-sulfur cell operating at 300 °C is about 1030 watt hours per kilogram [3], whereas the familiar lead-lead oxide cell typically gives 5 to 30 watt hours per kilogram at room temperature.

This paper will not discuss the possibility of the use of the beta aluminas as battery or fuel cell components. Instead, attention will be focused upon the potential use of these and related materials for a wide range of other purposes, primarily as experimental tools for the measurement of thermodynamic and kinetic data. We shall see that their unusual properties open up a very wide vista for the use of solid electrolytes as electrochemical transducers in a great variety of scientific as well as engineering applications.

2. ELECTROCHEMICAL TRANSDUCERS

2.1. INTRODUCTION

Although there had previously been a few papers in which solid electrolytes had been used for thermodynamic studies [15], attention was drawn to the broad possibility of using such ionically conducting solids as electrochemical transducers for a number of purposes in an important paper by Carl Wagner in 1953 [16], in which he used silver iodide in a simple solid state cell configuration to measure a number of properties of silver sulfide. A few years later, a pair of papers by Kiukkola and Wagner [17,18] expanded this horizon considerably by pointing out a variety of possible applications, as well as indicating several other ionically conducting solids which could be used as solid electrolytes. In addition to discussing the extension of this type of work by the use of other simple binary salts, they pointed out that cubic oxides with the fluorite structure, such as calcium-doped zirconium dioxide, could be used in a similar manner at temperatures in the range 750 to 1150 °C. Since that time, there have been a number of laboratories who have pursued these ideas, as well as extending them, and one can find reviews of much of this work in several places [15, 19-21].

Before mentioning some of these areas of application and pointing out the implications of beta alumina and related materials to them, we shall very briefly review a few elementary concepts for those who are not familiar with this particular field.

If two neighboring regions within a solid are in thermodynamic equilibrium with each other under isothermal conditions, the concentrations of all species (including all defects) in both regions will be time-independent. This means that there must be no net forces present in such a system which tend to cause the transport of either mass or charge from one microscopic region to the other.

Let us focus our attention upon this question of forces acting upon species. We know that in general one can express the force F_i acting on any species i as

$$Fi = - \text{grad } Ui \tag{1}$$

where U_i is the total potential energy or thermodynamic potential of species i at a given location. The requirement for equilibrium, then, is that the gradient in U_i must be equal to zero for all species.

There are several different kinds of potential that can contribute toward the total thermodynamic potential of a particular species in a solid. Here we will restrict ourselves to the discussion of only two, the chemical potential, (or partial molar free energy) μ_i, and the electrostatic potential, $z_iF\phi$ (ϕ is the local value of the electrostatic macropotential, whereas z_iF is the electrostatic charge carried per mole of i). The sum of these two is known as the electrochemical potential, η_i, so we can write

$$\eta_i = \mu_i + z_iF\phi \tag{2}$$

For simple one-dimensional transport, the flux density of a species i can be written as

$$J_i = c_i v_i \qquad (J_i = \text{no./cm}^2\text{sec}) \tag{3}$$

where c_i is the concentration (no./cm^3) and v_i is the average velocity of the species i (cm/sec) relative to a stationary observer. The absolute mobility B is defined as the velocity per unit force,

$$B_i = \frac{v_i}{F_i} . \tag{4}$$

Note that this is a different quantity from the electrical mobility u, which is defined as the velocity per unit electrostatic field, or

$$u_i = \frac{v_i}{\left(\frac{d\phi}{dx}\right)} . \tag{5}$$

We find that although these two different "mobilities" have different dimensions, they are related by

$$u_i = z_i q B_i , \tag{6}$$

where q is the electronic charge. If there are two gradients present, a chemical gradient and an electrostatic gradient, we can write the force acting upon a particle of species i as

$$F_i = -\frac{1}{N}\frac{d\eta_i}{dx} = -\left[\frac{1}{N}\frac{d\mu_i}{dx} + z_i q \frac{d\phi}{dx}\right] \tag{7}$$

where N is Avogadro's number. These equations can be combined to get a general expression for the flux density,

$$J_i = -c_i B_i \left[\frac{1}{N}\frac{d\mu_i}{dx} + z_i q \frac{d\phi}{dx}\right] . \tag{8}$$

It is obvious from this expression that under equilibrium conditions, when the particle and charge flux are both zero, one could have a chemical gradient that is just balanced by an electrostatic gradient.

$$\frac{1}{N}\frac{d\mu_i}{dx} = -z_i q \frac{d\phi}{dx} . \tag{9}$$

If one deals with a material in which the transference number for ionic species is close to unity, essentially all the charge transport is by means of ions, and such an equilibrium situation can exist and, in fact, be used to transduce between chemical and electrical quantities. This simple case is illustrated schematically in figure 1. In that figure, a difference in the chemical potential of species i is assumed to exist upon the two sides of a solid that is an ionic conductor for species i. Integrating eq. (9) between the two interfaces, we find that

$$\mu_i^{I} - \mu_i^{II} = -z_i F E, \tag{10}$$

where E is the electric potential difference between the electrodes placed at the two interfaces. By substitution of the general relation between chemical potential and activity

$$\mu_i = \mu_i^\circ + R\,T\,\ell n\,a_i \qquad (11)$$

it can be rewritten as

$$E = -\frac{R\,T}{z_i F}\,\ell n\,(a_i^{I}/a_i^{II}), \qquad (12)$$

which is the familiar Nernst equation.

It is obvious from these simple considerations that if one has a situation in which no current passes through the ionic conductor, that is, if the forces causing transport of the ions are exactly balanced, a measurement of the open circuit electric potential difference between the two interfaces is a direct measure of the difference in chemical potential or activity in the pertinent species at those locations. If some care is taken, one can play this game both ways and use a chemical potential difference to generate an electrical voltage, or an electric potential difference to generate a difference in chemical activity.

In addition, if no charge-generating or charge-consuming reaction takes place at the interfaces, one can obtain a direct measurement of the ionic transport through the electrolyte by evaluation of the electronic current through the electrode circuit. As will be mentioned shortly, this allows the use of this type of system for measurements of mass transport and related matters.

2.2. RANGE OF APPLICATIONS

Although most of the earlier applications of solid electrolytes as electrochemical transducers involved their being employed in emf cells to measure free energy changes of various reactions, recent work has extended over quite a range of different applications. Some of these are listed in table 1.

3. PRACTICAL CONSIDERATIONS

Although this appears quite simple, there are several practical considerations that must be given attention. These include the magnitude of the ionic conductivity of the transducer phase under the conditions (*e.g.*, temperature and chemical environment) in which it is to be used. In a static situation, this conductivity must be high enough that equilibrium can be established within a reasonable period of time. This typically means that one must have a conductance value of about 10^{-10}ohm^{-1} or greater. Furthermore, if the transducer phase is to be used for transport measurements, or under conditions in which transport is expected to occur within it, its conductivity must be considerably greater, so that the electric potential difference across it (the IR drop) does not seriously interfere with the operation of the cell. Under these conditions, it is generally considered necessary that the conductance be equal to 10^{-4}ohm^{-1} or greater.

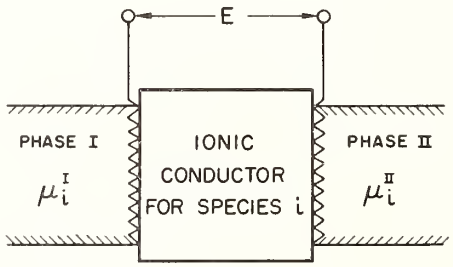

Fig. 1. Schematic representation of simple electrochemical cell with solid electrolyte.

Table 1

Examples of the Application of Solid State Electrochemical Techniques

Static Emf Measurements
- Free energy of formation of binary and ternary compounds
- Free energy changes accompanying various cell reactions
- Thermodynamics of binary phases
- Determination of limits of stoichiometry of compounds
- Phase diagram determination
- Thermodynamics of phase transformations
- Effective mass of electrons or holes in semiconductors
- Solubility of gases in liquids

Time-dependent Emf Measurements
- Phase boundary migration kinetics
- Supersaturation required for nucleation within and upon solids and liquids

Combinations of Emf and Current Measurements
- Diffusion in liquid and solid metals and mixed conductors
- Transport of both ionic and electronic species across phase boundaries
- Kinetics of condensation and vaporization processes
- Oxidation and reduction reactions on solid surfaces
- Thermodynamics of gaseous species
- Studies of the mechanism of catalysis
- Ionic and electronic partial conductivities in mixed conductors
- Structure of electrode-electrolyte interfaces

Technological Applications
- Batteries
- Fuel cells
- Thermoelectric devices
- Memory elements
- Solute valence control in semiconductors and ionic solids
- Purification of liquids and gases
- Measurement and control of gas compositions

Another important consideration is the assumption made in the simple discussion of the Nernst equation that the only charge-carrying mobile species is the ionic species in question. Obviously, if the transducing phase is also an electronic conductor, electronic transport will seriously interfere with, if not completely nullify, the electric potential difference generated by the difference in chemical potentials at the two interfaces. This is obviously a matter of real concern. For, instead of needing to know just the ionic conductivity, one must also know the value of the electronic conductivity or the ratio of electronic conductivity to total conductivity (the transference number for electronic species, t_e). The influence of a small but significant electronic transference number results in a measured open circuit potential, E_m, for a simple cell of the type illustrated in figure 1, given by [17,22,23]

$$E_m = E - \frac{I}{zF} \int_{\mu_i^{II}}^{\mu_i^{I}} t_e \, d\mu_i . \qquad (13)$$

As a rule of thumb, it is normally considered that the electronic transference number should be less than 10^{-2} throughout the usable range in order for a solid electrolyte to be useful as an electrochemical transducer under static conditions. Since the electronic transference number typically varies with the stoichiometry, the thermodynamic range over which an

electrolyte is useful can thus be quite severely restricted.

Another important matter is the thermodynamic stability of the transducer phase with respect to reactions with chemical species present at its interfaces. As a first approximation, if a solid electrolyte MX is in contact with species N, it is necessary that the displacement reaction

$$MX + N \not\geq NX + M, \tag{14}$$

not proceed in the forward direction. Another way of saying this is that it is normally necessary that the element N be more noble than the element M.

4. PROPERTIES OF SOME SOLID STATE ELECTROCHEMICAL TRANSDUCERS

4.1. MAGNITUDE OF THE IONIC CONDUCTIVITY

As we have mentioned, it is important that electrochemical transducers have relatively large values of ionic conductivity. Typical values for such materials are indicated in figure 2, which also shows conductivity data for several other common ionic solids as a function of temperature. It is clear that the conductivity of ionic conductors can vary over an immense range. Materials which are useful as solid electrochemical transducers must have good values of conductivity in the temperature range in which they are to be used. Thus, it is quite obvious, for example, that the fluorite structure oxides will not be very useful below about 600 °C. On the other hand, it is clear that there are several materials which have large ionic conductivities at unusually low values of temperature. These are of two general types, materials which are closely related to the body-centered cubic α AgI structure, in which silver is typically the mobile ion, and the beta aluminas. An important aspect of the latter case is that there are several choices for the mobile cation.

One of the difficulties encountered in the evaluation of the ionic transport in these unusually good ionic conductors (for which the term "super ionic conductors" was coined by Rice and Roth [24]) is the avoidance of polarization effects at measuring electrodes. It is common practice to use ac conductivity techniques to evaluate ionic motion in ionic conductors. If polarization occurs at the electrodes, the conductivity appears to be frequency dependent and the normal procedure is to increase the frequency until it is in a range at which this frequency dependence disappears. This is not a great difficulty in the case of the traditional ionic conductors such as the alkali halides, but it becomes a very severe problem with solids in which the conductivity is high. Even frequencies of the order of 10^8 Hz are often not high enough to avoid polarization effects in the beta aluminas [25].

An alternate approach to this problem is to use reversible electrodes. If this is properly done, the frequency dependence is eliminated. It has been shown [26] that with proper care it is possible to use solid elemental Ag as a reversible electrode to get reliable values of the ionic conductivity of the silver ion in beta alumina from 800 °C all the way down to room temperature.

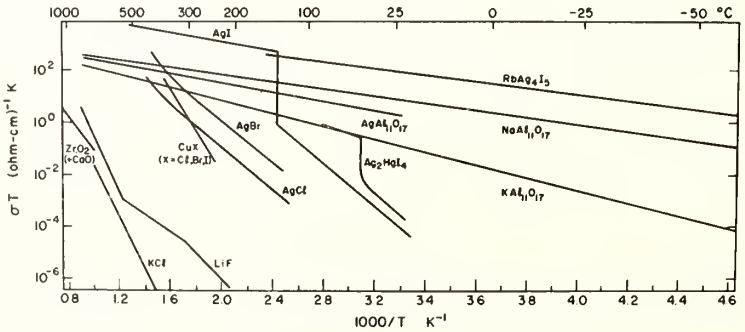

Fig. 2. Conductivity data for various ionic conductors.

Another more novel approach was the demonstration [27] that a mixed conductor, in which the important ion has a high diffusion coefficient, can also be used as a nonpolarizing electrode in connection with materials such as the beta aluminas. By use of this technique, it was possible to measure the conductivity of the sodium ion in sodium beta alumina from 820 °C all the way down to -150 °C.

By use of this nonpolarizing electrode technique, reliable data on the ionic conductivity of single crystals of several of the beta aluminas have now been obtained over a wide temperature range. These are illustrated in figures 3-6 for silver, sodium, potassium and thallium ions. Also included in those figures are data obtained by the Ford research group by means of radiotracer [1,2,28] and the dielectric loss [2] techniques. Allowing for correlation effects, it is seen that the results obtained by the conductivity and radiotracer methods coincide very well in all cases. The dielectric loss data also give good agreement in the sodium and potassium cases, and moderate agreement in the silver case, but deviate by about a factor of ten for thallium beta alumina. It appears that the absolute values of the conductivity obtained by these various techniques agree better than one might expect from just consideration of the activation energy values determined separately over relatively small temperature spans [2].

Conductivity measurements have also been made on a single crystal sample of beta alumina containing lithium. In this case, electrodes of a cubic lithium tungsten bronze were used, rather than the tetragonal or hexagonal bronze phases used with the others. This was necessary as the small lithium ion is only found in the cubic phase. Although we were thus apparently able to avoid a frequency dependence in the conductivity, indicating reversible electrodes, more scatter was present in the data in this case. In addition, the conductivity data seem to fall along two different straight lines when plotted in the normal way to determine the temperature dependence. This is clearly evident in figure 7. Although the conductivity and tracer diffusion data lie comfortably close to one another above 180 °C, it is not obvious that the low temperature conductivity measurements and the dielectric loss experiment are evaluating the same physical process. As a further complication, it was found that annealing the sample above 800 °C caused a marked drop in the low temperature conductivity.

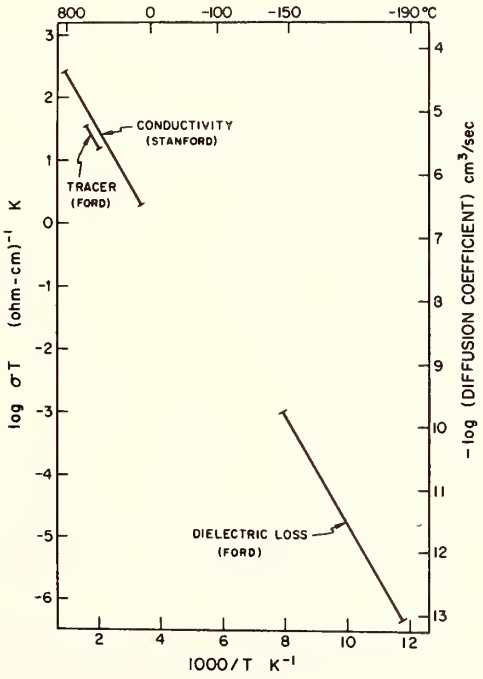

Fig. 3. Conductivity, tracer diffusion, and dielectric loss data for silver beta alumina.

465-504 O - 72 - 11

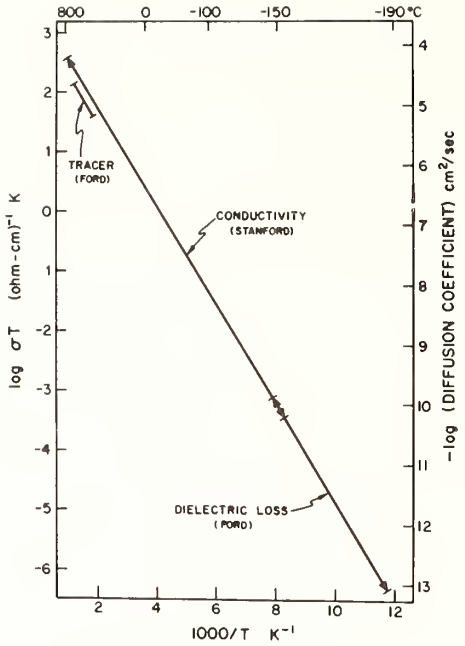

Fig. 4. Conductivity, tracer diffusion, and dielectric loss data for sodium beta alumina.

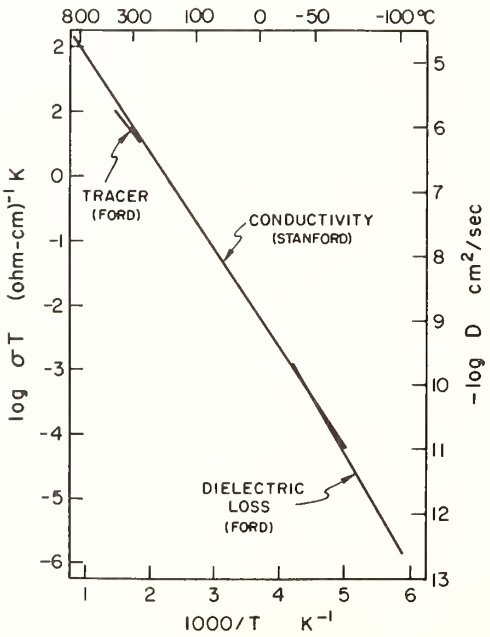

Fig. 5. Conductivity, tracer diffusion, and dielectric loss data for potassium beta alumina.

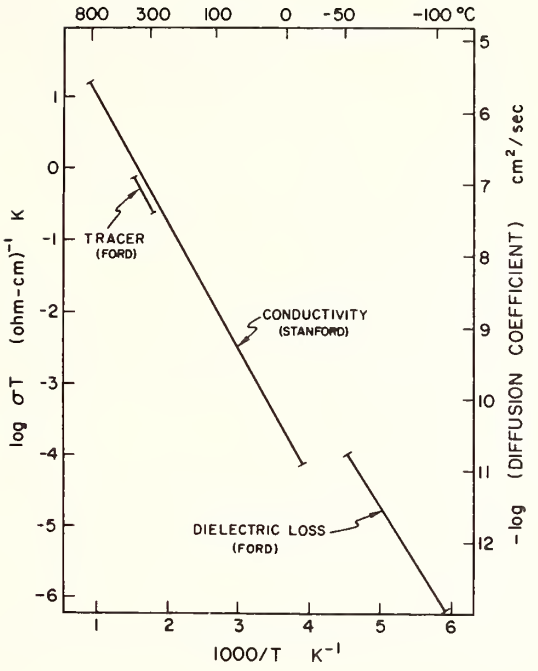

Fig. 6. Conductivity, tracer diffusion, and dielectric loss data for thallium beta alumina.

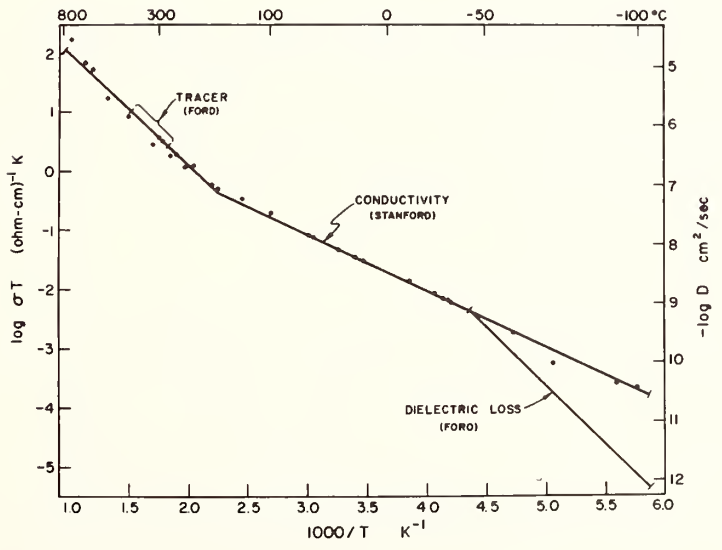

Fig. 7. Conductivity, tracer diffusion, and dielectric loss data for lithium beta alumina.

There is evidently more to do before we should feel that we understand what is happening in lithium beta alumina. One possibility that should certainly be given consideration is that at high temperatures a direct interstitial jump mechanism is becoming important, rather than transport being dominated by the interstitialcy mechanism that seems to prevail [26] in the other beta aluminas.

These conductivity data are compiled in table 2, assuming an Arrhenius relation of the form

$$\sigma_o = (\sigma_o/T)\exp(-H/RT) . \qquad (15)$$

Also included are values of the apparent correlation factor, f, the ratio of the radiotracer diffusion coefficient to the diffusion coefficient obtained from the ionic conductivity data, calculated for temperatures at the center of the tracer data. It is seen that the correspondence to the theoretical value [26] for the interstitially diffusion mechanism in this structure, 0.599, is quite good.

Some measurements have also been made upon samples of the phase β" alumina. It has been reported [29] that both sodium and potassium ions have greater conductivities in this phase than in the beta alumina structure. This appears to be true for both single crystals and dense sintered polycrystalline bodies.

Using the reversible solid electrode technique, we have done a few experiments on hot pressed polycrystalline samples of the β" phase. The results are indicated in figure 8, along with data from the Ford laboratory [29]. Also shown (dotted line) is the conductivity of single crystal sodium beta alumina [27]. Above 315 °C the polycrystalline data are essentially frequency-independent and evidently lie upon a straight line parallel to the single crystal beta alumina data. At lower temperatures, a frequency dependence appears and there is a deviation from linearity. Preliminary measurements [30] using the complex admittance method [31] gave essentially the same value of conductivity at room temperature, as also indicated on figure 8. A plot of these data on the complex admittance plane is shown in figure 9.

4.2. ELECTRONIC CONDUCTIVITY

It was pointed out earlier that a desirable electrochemical transducer should have an electronic transference number less than 10^{-2}. Measurements have been made of the electronic component of the total conductivity of silver beta alumina [26] by use of the Wagner asymmetric polarization technique [23,32-34] from 555 to 790 °C over a wide range of oxygen partial pressure. Below about 750 °C changes in oxygen partial pressure did not appear to influence the electronic conductivity beyond normal experimental scatter. It was not possible to extend these measurements to lower temperatures because of prohibitively long times required for

Table 2

Summary of Data on Ionic Conductivity in Single Crystal Beta Aluminas

Ion	Temp. Range °C	σ_o $(ohm\text{-}cm)^{-1}K$	Activation Energy kJ/mole	Conductivity at 25 °C $(ohm\text{-}cm)^{-1}$	Correlation Factor, f
Ag	25 - 800	1.6×10^3	16.5	6.7×10^{-3}	0.61
Na	-150 - 820	2.4×10^3	15.8	1.4×10^{-2}	0.61
K	-70 - 820	1.5×10^3	28.4	6.5×10^{-5}	-
Tℓ	-20 - 800	6.8×10^2	34.3	2.2×10^{-6}	0.58
Li	180 - 800	9.7×10^3	35.8	-	-
Li	-100 - 180	5.4×10^1	18.0	1.3×10^{-4}	-

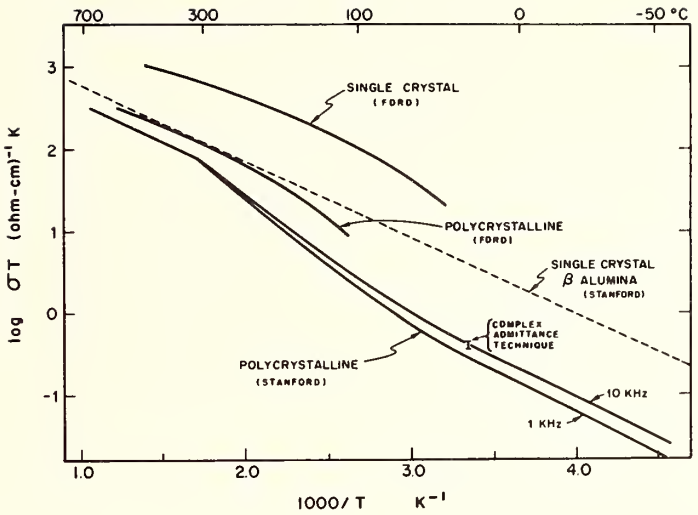

Fig. 8. Conductivity data for single crystal and polycrystalline sodium β" alumina. Also shown (dotted line) are values for single crystal sodium beta alumina, and measurement made by complex admittance method.

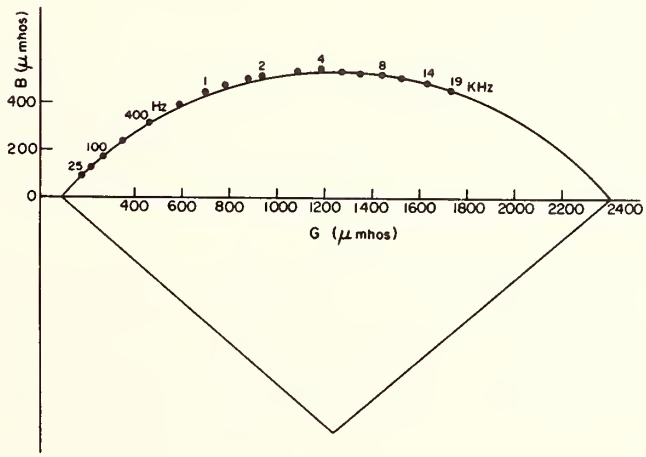

Fig. 9. Admittance plot for polycrystalline β" alumina at 25 °C.

equilibration (presumably due to very slow electron diffusion). From these results and total conductivity values one can compute the electronic transference number t_e over this temperature range. Figure 10 shows the variation of the electronic transference number for single crystalline silver beta alumina with temperature. It is obvious that an extrapolation of these data to lower temperatures indicates that the beta alumina phase should have an extremely low electronic conductivity at temperatures at which its high ionic conductivity makes it a very interesting electrochemical transducer.

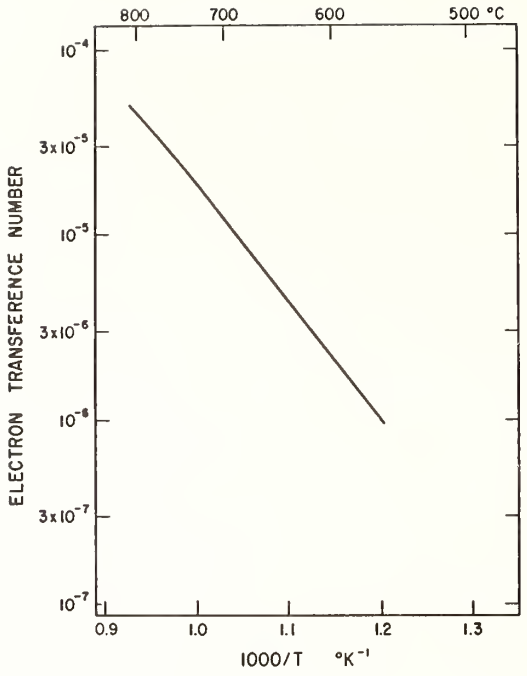

Fig. 10. Temperature dependence of the electronic transference number, silver beta alumina.

4.3. RANGE OF APPLICABILITY

It was pointed out earlier that the range of thermodynamic conditions over which a solid electrolyte can be beneficially used can be limited by two general types of problems, the appearance of an appreciable component of electronic conduction, or what might be referred to as chemical instability with respect to interaction with adjacent phases or structural changes such as phase transformations.

Information concerning the thermodynamic conditions under which solid electrolytes are usable and have sufficiently low values of electronic transference numbers has been compiled by Patterson [35,36], as an extension of an approach initiated by Schmalzried [37,38]. Such information is included in figure 11 for beta alumina and several of the common solid electrolytes. As pointed out by Patterson, reliable information of this type is only available for a relatively few materials. These fall into two general groups, the fluorite structure oxides, which are good conductors for oxygen ions and are generally useful only above about 700 °C, and a group of halides, primarily the silver and copper families. These halides have low melting points and tend to be relatively unstable, reactive and hard to handle. They are only useful under limited conditions between about 150 and 450 °C. Thus the roster of available solid electrolytes that can be used as electrochemical transducers has been quite limited until recently. Essentially only three ions could be considered, silver, copper and oxygen, and each of these over only limited temperature and thermodynamic ranges.

Two important changes have occurred in the solid electrolyte business in the last few years. A group of ternary silver salts, generally related to the α AgI structure, have been discovered, and the beta aluminas have appeared. This first group includes materials such as Ag_3SI and $RbAg_4I_5$ that have very high values of ionic conductivity to remarkably low temperatures. They have attracted a lot of attention as possible battery components, and a good review of much of this work has recently been presented by Owens [9].

Although these materials have impressive values of ionic conductivity at low temperatures, one should not have too much enthusiasm concerning their potential use as electrochemical transducers because all present members of this group are only good conductors for

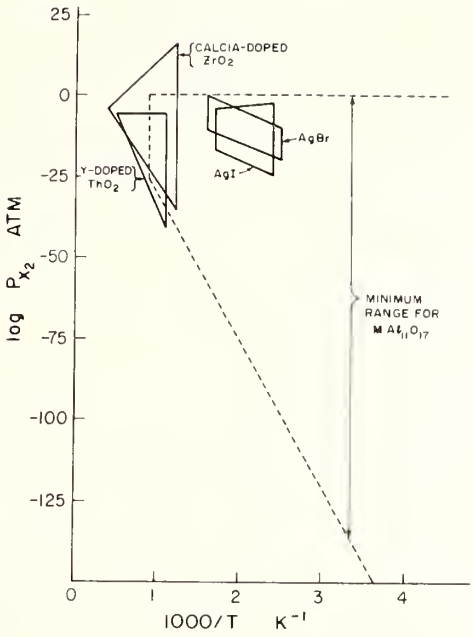

Fig. 11. Electrolytic conduction domains for several common solid electrolytes and beta alumina.

one ion, silver. Also, they tend to have relatively poor thermodynamic stability. As an example of this latter point, the material Ag_3SI is apparently not sufficiently ionic (t_e > 0.01) in contact with iodine at 25 °C to be very usable as a solid electrolyte. Also, their general structural instability is indicated by the fact that a number of them undergo phase transformations at quite low temperatures. Some examples of this are shown in table 3.

In contrast to these limitations, the stability and scope of apparent applicability of the beta aluminas is very impressive. This phase is essentially an oxide ceramic with a rigid structural skeleton. It is mechanically very stable, melting incongruently at about 2000 °C [39]. We shall not discuss the available information concerning either its structure or its various other properties here, however, as such information, as well as discussions of possible transport mechanisms, can be found in a number of other places [24-27, 29, 39-43].

The chemical stability of the beta alumina phase is also very impressive. This phase is apparently stable at temperatures in the vicinity of 300 °C and lower in contact with the alkali metals. This is equivalent to being in equilibrium with extremely low oxygen partial pressures.

We should hasten to point out, of course, that we are not talking about true equilibrium in this respect but practical noninteraction, or if you will, "selective equilibrium". In materials like beta alumina, the oxide structural skeleton is apparently stable enough that one can treat it as an inert matrix or framework within which the M cations can readily move about in response to various forces and achieve their own version of equilibrium.

Experiments upon silver beta alumina [26] between 600 and 800 °C showed that there was no apparent influence of oxygen partial pressure in the range from 0.2 to 10^{-24} atm. upon the ionic conductivity of this phase. The indications [26] that the beta alumina phase has unusually low electronic conductivity and its apparent lack of oxygen pressure dependence below about 750 °C also show the broad range of its applicability.

Perhaps the most important feature of the beta aluminas is the fact that this phase can act as a transducer for a whole new set of ions for which no satisfactory transducer was previously available. Instead of being able to work with just silver, copper, and oxygen, the

Table 3

Examples of Solid Ionic Conductors that have Phase Transformations at Relatively Low Temperatures [9,44]

Material	Transition Temperature
CuBr	470, 420 °C
CuI	400 °C
Ag_3SI	235 °C
AgI	144 °C
Cu_2HgI_4	67 °C
Ag_2HgI_4	50 °C
$[C_5H_5NH]Ag_5I_6$	50 °C
KAg_4I_5	-136 °C
$RbAg_4I_5$	-155 °C

solid state electrochemistry community now has a much wider range of available species with which to deal. Although well defined transport measurements have only been made on beta aluminas containing silver, sodium, potassium, and thallium, it has been demonstrated that this phase can also contain Rb^+, Cu^+, Li^+, NH_4^+, In^+, NO^+, Ga^+, amd H_3O^+ ions [29], and it is reasonable to expect it to be usable as a transducer for some, if not all of those as well. The ability to exchange one type of cation for another by equilibration techniques [1] or in some cases by electrochemical pumping [25], adds a new degree of freedom to the materials synthesis problem.

5. SOME APPLICATIONS

Although, as mentioned already, most of the work that has been done by the use of solid electrolytes as electrochemical transducers has involved either oxide, copper- or silver-containing systems, one begins to see the use of the beta alumina family for such purposes. For example, Belton and Morzenti [45] reported the use of sodium beta alumina for thermodynamic studies of liquid sodium-lead alloys, and Gupta and Tischer [46] employed this phase for measurements of the sodium-sulfur system. Likewise, Hsueh and Bennion [47] have used this material to make emf measurements of the sodium activity in liquid sodium-mercury alloys at 30 °C.

Measurements in our laboratory have indicated that single crystal potassium beta alumina can be used as a transducer to evaluate the difference in potassium activity between two solids. In this case, a difference in potassium activity of 300 mV was found at 500 °C between two samples (x values of 0.2 and 0.33) of potassium tungsten bronze, whose nominal formula is K_xWO_3. These bronzes, which are mixed conductors, as mentioned earlier, were prepared by electrolytic growth from molten salts, as described elsewhere [48]. In addition to being the first use of beta alumina for electrochemical measurements upon solids, this is the first time that successful thermochemical measurements have been made on a tungsten bronze. Previous attempts [49,50] have been unsuccessful, and it was assumed that some kind of alkali ion-deficient surface layer was an inevitable structural feature of these phases.

6. SUMMARY

In this paper we have endeavored to indicate that the beta alumina phase represents a new departure in solid electrolytes. Enough information is now available about its inherent ionic conductivity, electronic transference number, and thermodynamic stability to make it reasonable to expect that it and related materials can be used in a wide variety of scientific and perhaps engineering applications as an electrochemical transducer for a group of important species not heretofore measurable and controllable.

Beta alumina and similar rigid framework materials also represent a major change in another sense. Heretofore, all useful solid electrolytes were expected to attain thermodynamic equilibrium with their environment. In these materials, however, the mobility of one constit-

uent within the structure is so much greater than that of the others that it is quite realistic to think in terms of selective equilibrium for only certain species within an essentially inert crystalline environment. This has many potential advantages, not the least of which involves mechanical properties.

A further unusual and particularly useful characteristic of this class of materials is the ability that they afford for the synthesis of different solid electrolytes themselves. The technique of ion exchange within solids means that one can think in terms of preparing a material, or perhaps even a device, with one composition, and by use of ion exchange methods, convert it to something else in situ.

Because of these factors, we contend that beta alumina truly represents a first step across a vast new frontier.

7. ACKNOWLEDGEMENT

Work in this area at Stanford has been supported by the Office of Naval Research, the Environmental Protection Agency, and the Advanced Research Projects Agency (through Stanford's Center for Materials Research).

8. REFERENCES

[1] Yao, Y. F. Y. and Kummer, J. T., J. Inorg. Nucl. Chem. 29, 2453 (1967).
[2] Radzilowski, R. H., Yao, Y. F. and Kummer, J. T., J. Appl. Phys. 40, 4716 (1969).
[3] Weber, N. and Kummer, J. T., Proc. Ann. Power Sources Conf. 21, 37 (1967).
[4] Foley, R. T., J. Electrochem. Soc. 116, 161 (1969).
[5] Hull, M. N., Energy Conversion 10, 215 (1970).
[6] Mrgudich, J. N., "Solid Electrolyte Batteries," *Encyclopedia of Electrochemistry*, Reinhold, New York, p. 84 (1964).
[7] Takahashi, T., Denki Kagaku, 36, 402 (1968).
[8] Takahashi, T., Denki Kagaku, 36, 481 (1968).
[9] Owens, B. B., Advances in Electrochemistry and Electrochemical Engineering 8, 1 (1971).
[10] Cairns, E. J. and Shimotake, H., Science 164, 1347 (1969).
[11] Jasinski, R., *High Energy Batteries*, Plenum Press (1967).
[12] U. S. Department of Commerce Report, "The Automobile and Air Pollution," (1967).
[13] Sudworth, J. L. and Dugdale, I., Power Sources 2, 547 (1968).
[14] Sudworth, J. L. and Hames, M. D., Power Sources 4, 1 (1970).
[15] Schmalzried, H., *Thermodynamics and Atomic Transport in Solids*, Int. Atomic Energy Agency, Vienna (1965).
[16] Wagner, C., J. Chem. Phys. 21, 1819 (1953).
[17] Kiukkola, K. and Wagner, C., J. Electrochem. Soc. 104, 308 (1957).
[18] Kiukkola, K. and Wagner, C., J. Electrochem. Soc. 104, 379 (1957).
[19] Wagner, C., Advances in Electrochemistry and Electrochemical Enginering, 4, 1 (1966).
[20] Raleigh, D. O., Prog. in Solid State Chem. 3, 83 (1967).
[21] Alcock, C. B., ed., *Electromotive Force Measurements in High-Temperature Systems*, Inst. of Mining and Metallurgy, London (1968).
[22] Wagner, C., Z. physik. Chem. B21, 25 (1933).
[23] Wagner, C., Proc. Int. Comm. Electrochem. Thermo. Kinetics (CITCE) 7, 361 (1957).
[24] Rice, M. J. and Roth, W. L., "Ionic Transport in Super Ionic Conductors," to be published in J. Solid State Chem. (1972).
[25] Whittingham, M. S., Helliwell, R. W. and Huggins, R. A., U. S. Government Res. and Devel. Rept. 69, 158 (1969).
[26] Whittingham, M. S. and Huggins, R. A., J. Electrochem. Soc. 118, 1 (1971).
[27] Whittingham, M. S. and Huggins, R. A., J. Chem. Phys. 54, 414 (1971).
[28] Kummer, J. T., personal communication.
[29] Kummer, J. T., "β Alumina Electrolytes," to be published in Progress in Solid State Chemistry, 7, (1972).
[30] Nakagawa, Y., unpublished work at Stanford (1971).
[31] Bauerle, J. E., J. Phys. Chem. Solids 30, 2657 (1969).
[32] Wagner, C., Z. Elektrochem. 60, 4 (1956).
[33] Wagner, J. B. and Wagner, C., J. Chem. Phys. 26, 1597 (1957).
[34] Patterson, J. W., Bogren, E. C. and Rapp, R. A., J. Electrochem. Soc. 114, 752 (1967).

[35] Patterson, J. W., in *The Physics of Electronic Ceramics,* ed. by L. L. Hench and D. B. Dove, Marcel Dekker, Inc., New York (1971).
[36] Patterson, J. W., J. Electrochem. Soc. 118, 1033 (1971).
[37] Schmalzried, H., Z. Elektrochem. 66, 572 (1962).
[38] Schmalzried, H., Z. physik. Chem. N.F. 38, 87 (1963).
[39] DeVries, R. C. and Roth, W. L., J. Am. Ceram. Soc. 52, 364 (1969).
[40] Demott, D. S. and Hancock, P., Proc. British Ceramic Soc. 19, 193 (1971).
[41] Roth, W. L., "Stoichiometry and Structure of the Super Ionic Conductor Silver Beta-Alumina," General Electric Report No. 71-C-132 (1971).
[42] Sato, H. and Kikuchi, R., J. Chem. Phys. 55, 677 (1971).
[43] Bettman, M. and Peters, C. R., J. Phys. Chem. 73, 1774 (1969).
[44] Geller, S. and Owens, B. B., "Silver Ion Site-Distribution, Structure and Conductivity of the Solid Electrolyte Pyridinium Hexaiodopentaargentate, $[C_5H_5NH]Ag_5I_6$, Between -30 and 125 °C," to be published.
[45] Belton, G. R. and Morzenti, P. T., J. Metals 22, No. 12, 26A (1970).
[46] Gupta, N. K. and Tischer, R. P., J. Electrochem. Soc. 117, 125C (1970).
[47] Hsueh, L. and Bennion, D. N., J. Electrochem. Soc. 118, 1128 (1971).
[48] Whittingham, M. S. and Huggins, R. A. , "Electrochemical Preparation and Characterization of Alkali Tungsten Bronzes, M_xWO_3," to be published in the Proceedings of the 5th Materials Research Symposium, Solid State Chemistry, National Bureau of Standards, (1971).
[49] Swanson, A. B., D. Phil. Thesis, Oxford University (1968).
[50] Koch, D. F. A. and Becker, H., Personal communication quoted by G. H. Taylor, J. Solid State Chem. 1, 359 (1969).

DISCUSSION

G. K. Johnson: I guess this question is for either you or Dr. W. L. Roth. Would you comment on what size crystals can be grown of this material and what techniques are used?

R. A. Huggins: Walter, why don't you answer that?

W. L. Roth: Most of the work was with crystals obtained from the Carborundum Corporation. The crystals were frequently 1 or more centimeters in diameter, but only one or two-tenths of a millimeter thick. They are mica-like and the quality of thick individuals is poor. We have grown crystals in the laboratory that were a bit better in perfection and thickness, but only one or two millimeters in size.

G. K. Johnson: Well, what's the general method that is used for producing these?

W. L. Roth: We passed current between carbon electrodes inserted in a large mass of sodium carbonate and Al_2O_3. The melting point is around 2000 °C and the materials react and crystals of β-Al_2O_3 appear to grow from the melt.

National Bureau of Standards Special Publication 364, Solid State Chemistry, Proceedings of 5th Materials Research Symposium, issued July 1972.

EXPERIMENTAL STUDY ON THE IONICITY IN THE TiO PHASE. AN APPLICATION OF THE NEW METHOD OF DETERMINING THE STRUCTURE FACTOR BY HIGH VOLTAGE ELECTRON DIFFRACTION

D. Watanabe and O. Terasaki

Department of Physics
Tohoku University
Sendai, Japan

It was reported recently that the second order reflection in electron diffraction vanishes at a certain accelerating voltage E_c, owing to the many-beam dynamical interaction combined with the relativistic change of electron mass [Watanabe, Uyeda and Kogiso, Acta Cryst., A24, 249 (1968).]. A measured value of E_c makes it possible to determine very accurately the Fourier coefficient of the potential for the first order, and thus the corresponding value of the x-ray scattering factor [Watanabe, Uyeda and Fukuhara, Acta Cryst. A24, 580 (1968), A25, 138 (1969)].

In the present study, the method has been applied to the disordered TiO phase. The accelerating voltages E_c, for which Kikuchi lines of the 400 reflection vanish, have been measured using a 500 kV electron microscope. The measured values are 340, 354, 389 and 425 kV, respectively, for $TiO_{0.82}$, $TiO_{0.96}$, $TiO_{1.16}$, and $TiO_{1.25}$. To compare the experimental values with calculation, the values of E_c have been calculated for $TiO_{0.82}$ and $TiO_{1.25}$, using theoretical scattering factors of titanium and oxygen atoms of various atomic states. The calculations have been made for free neutral atoms Ti^0, O^0, monovalent ions Ti^{1+}, O^{1-} and divalent ions Ti^{2+}, O^{2-}. The structure factors of the first order have been determined using the measured values of E_c.

Comparison of the experimental values of E_c and the first order structure factors with theoretical ones enables us to discuss the ionicity in a TiO crystal. The result shows that the ionicity depends on the oxygen concentration in the crystal, *i.e.*, titanium and oxygen atoms in the oxygen-deficient TiO crystal are considered to be almost neutral, while the elements in the titanium-deficient crystal appear to be in the ionic states.

The possibility of applying the present method to a TiO_2 crystal of the rutile type is discussed as well.

Key words: Critical voltage for the 400 of TiO; critical voltage for the 110 of TiO_2 (rutile); determination of structure factor by high voltage electron diffraction; disappearing effect of the second order reflection in electron diffraction; ionicity in TiO crystal; many-beam dynamical interaction in electron diffraction; structure factors for electrons of TiO.

1. INTRODUCTION

It was found by Watanabe, Uyeda and Kogiso [1][1] that the second order reflection in electron diffraction disappears at a certain value of the incident electron accelerating voltage E_c owing to the many-beam dynamical systematic interaction combined with the relativistic change of electron mass. The effect has been observed on Kikuchi lines with a 500 kV electron microscope for f. c. c. and b. c. c. metals, such as Al, Fe, Ni,

[1]Figures in brackets indicate the literature references at the end of this paper.

and Cu [2, 3]. Nagata and Fukuhara [4] and Fisher et al. [5] observed a similar effect in the vanishing of the second order extinction contour in electron micrographs at the critical voltage E_c. A measured value of E_c makes it possible to determine very accurately the Fourier coefficient of crystal potential for the first order V_1, and thus the corresponding value of the x-ray atomic scattering factor f_1^x, assuming those for the second and higher order reflections. Previously, the values of E_c were measured for the 220 reflection of Fe and the 222 reflection of Al, Ni, and Cu, and the x-ray atomic scattering factors for the first order reflection f_1^x were determined by many-beam calculation, with an accuracy as good as that obtained by the most accurate x-ray measurement [2,3].

In the present study, the method has been used for accurate determination of the structure factors of titanium monoxide TiO. The NaCl type TiO phase exists over a wide range of composition depending on temperature, *e.g.*, from $TiO_{0.7}$ to $TiO_{1.25}$ at 1400 °C and $TiO_{0.9}$ to $TiO_{1.25}$ at temperatures below about 990 °C, and its crystal structure has a large number of vacancies [6,7]. At the composition $TiO_{1.0}$, about 150% of both metal and oxygen sites are vacant, and titanium-rich crystals have more of the metal sites filled, together with an increase in the number of oxygen vacancies, and vice versa. The vacancies are arranged randomly in the NaCl type structure at temperatures above 990 °C, while ordering of vacancies occurs at lower temperatures [8]. The present method was applied to the disordered phase.

Since atomic scattering factors for electrons at small scattering angles are very sensitive to the configuration of outer atomic electrons, accurate determination of the structure factors for low angle scattering from the TiO crystal would be very useful to discuss the ionic state. The present method provides one of the most sensitive means of measuring low angle structure factors.

The purpose of this paper is to give a brief description of the principle of the method and to report the result obtained from the NaCl type TiO crystals. In addition, the possibility of applying the present method to TiO_2 crystal of rutile type will be discussed.

2. PRINCIPLE

In high energy electron diffraction many weak beams are generally excited in addition to strong ones. Among weak beams, the effect of higher and lower order reflections of the main reflection (systematic interaction) does not depend on the crystal azimuth around the normal of the reflecting plane and is always important; while the effect of other reflections (accidental interaction) depends on the azimuth and is generally small unless simultaneous reflections occur. For the second order reflection at the exact Bragg condition, the intensity I_2 depends not only on the Fourier coefficient of the second order V_2 but also on V_1, V_3, V_4, etc. I_2 depends, at the same time, on the accelerating voltage E due to the relativistic effect. That is, I_2 is expressed by the relation,

$$I_2 = f(V_1, V_2, V_3, \ldots; E). \tag{1}$$

The theoretical description of this effect has been given by the many-beam dynamical theory [4] as well as by Bethe's second approximation [9] and higher-order approximation [10].

In terms of Bethe's second approximation, the apparent value of the structure factor of the h reflection $U_h'(E)$ is expressed by

$$U_h'(E) = R[U_h(0) - R\cdot d^2 \sum_g{}'' \frac{U_g(0)\cdot U_{h-g}(0)}{g(h-g)}], \tag{2}$$

if the effect of accidental interaction can be neglected. In (eq 2), $R = 1 + (eE/m_0c^2)$, $m_0c^2 = 511$ kV, $U_g = (2m_0e/h^2)V_g$, d is the lattice spacing of the first order reflection and $\sum_g{}''$ means the summation over positive and negative integers except for g = 0 and h. For the second order reflection, $U_2'(E)$ is given by

$$U_2'(E) = R[U_2(0) - R\cdot d^2\{U_1(0)^2 - \frac{2}{3}U_1(0)\cdot U_3(0) - \frac{2}{8}U_2(0)\cdot U_4(0)$$

$$- \frac{2}{15}U_3(0)\cdot U_5(0) - \frac{2}{24}U_4(0)\cdot U_6(0) \ldots\}]. \quad (3)$$

If the value of $U_1(0)$ is large and $U_2(0)$ is positive, the apparent structure factor of the second order reflection $U_2'(E)$ decreases with increasing accelerating voltage, vanishes at a certain voltage (E_c) and increases its absolute value with further increase of the voltage. At the critical voltage E_c, (eq. 3) is reduced to

$$U_2(0) - (1 + \frac{eE_c}{m_0c^2})\, d^2\{U_1(0)^2 - \frac{2}{3}U_1(0)\cdot U_3(0) - \frac{2}{8}U_2(0)\cdot U_4(0)$$

$$- \frac{2}{15}U_3(0)\cdot U_5(0) - \frac{2}{24}U_4(0)\cdot U_6(0) \ldots\} = 0. \quad (4)$$

If E_c is determined experimentally, V_1 can be calculated assuming the values of V_2, V_3, etc., and the value V_1 gives the atomic scattering factor for electrons f^e at the first order reflection and thus that for x-rays, f^x.

The percentage error of f^x thus obtained can be estimated as follows. From (eq. 4), $|\Delta U_1/U_1|$ is roughly given by the relation

$$|\frac{\Delta U_1}{U_1}| \simeq \frac{1}{2}\left[\frac{eE_c}{m_0c^2 + eE_c}|\frac{\Delta E_c}{E_c}| + |\frac{\Delta U_2}{U_2}|\right]. \quad (5)$$

From this equation and the well-known formula

$$f^e = \frac{8\pi^2 m_0 e^2}{h^2}\,\frac{Z - f^x}{(4\pi\sin\theta/\lambda)^2}, \quad (6)$$

$|\Delta f_1^x/f_1^x|$ is expressed approximately by the equation

$$|\frac{\Delta f_1^x}{f_1^x}| \simeq \frac{1}{2}\,\frac{Z - f_1^x}{f_1^x}\left[\frac{eE_c}{m_0c^2 + eE_c}\,|\frac{\Delta E_c}{E_c}| + \frac{f_2^x}{Z - f_2^x}\,|\frac{\Delta f_2^x}{f_2^x}|\right]. \quad (7)$$

Since $(Z - f_1^x)/f_1^x \simeq 0.4$ and $f_2^x/(Z - f_2^x) \simeq 0.8 - 1.0$ in many cases, the contribution of Δf_2^x to $|\Delta f_1^x/f_1^x|$ is about 1/6 - 1/5 of $|\Delta f_2^x/f_2^x|$. If $E_c \simeq 400$ kV, then $eE_c/(m_0c^2 + eE_c) \simeq 4/9$ and therefore the contribution of ΔE_c to $|\Delta f_1^x/f_1^x|$ is less than one tenth of $|\Delta E_c/E_c|$. Contributions of Δf_3^x etc., are less because the factors multiplying $|\Delta f_3^x/f_3^x|$ etc., are much smaller.

In the experiment, the accelerating voltage of each diffraction pattern is determined from the analysis of the Kikuchi pattern with an accuracy of 1% [11], and the value of E_c can be determined with an accuracy of 10 kV by examining a series of diffraction patterns taken at various accelerating voltages. In the calculation of the scattering factor, the theoretical Hartree-Fock values of f_2^x, f_3^x, etc., [12] for the free atoms or ions are used. The errors of f_2^x estimated from reliable theoretical and x-ray experimental data are about 1 - 2% for f. c. c. and b. c. c. metals such as Al, Fe, Ni and Cu [3]. Since E_c is usually measured at room temperature, the values of V_2, V_3, etc., including the Debye-Waller factors $\exp(-B\sin^2\theta/\lambda^2)$ must be used in the calculation of V_1. For many crystals the Debye characteristic temperature appropriate to crystal diffraction have been accurately measured, and these can be assumed in the evaluation of V_g. The contribution to the error of f_1^x from that of the assumed B values, ΔB, is estimated to be, for example, less than 0.2% for $\Delta B = 0.05$ Å^2.

The calculations of V_1 and therefore f_1^x can be carried out by Bethe's second approximation, (eq. 4), taking eleven beams (g = -4, -3, .., +6) into account, and also by an orthodox many-beam theory [13] covering nine beams (i = -3, -2, ..., +5). In the many-beam calculation, the accelerating voltage at which two main branches of the dispersion surface contributing to the second order reflection contact with each other is defined as a critical voltage E_c. The results of both calculations agree almost exactly for f. c. c., b. c. c. metals and for NaCl type crystals.

The values of f_1^x at the 110 reflection of Fe and the 111 reflection of Al, Ni and Cu have been calculated from the measured values of E_c and compared with the theoretical and x-ray experimental data [3]. The estimated errors of f_1^x were in fact less than 1%, *i. e.*, about 0.6% for Fe, Ni and Cu and 0.9% for Al. It is to be noted that the values of f_1^x are smaller than those for the free atoms calculated by Freeman and Watson [14] by 0.5% for Ni, 0.9% for Al and Fe and 1.6% for Cu, but agree well with the values for the atoms bound in a crystal obtained by Wakoh and Yamashita [15] on the basis of band structure calculation. Recently, the high voltage electron diffraction experiments have been done for V and Cr as well and the x-ray atomic scattering factors f_1^x for the 110 reflection have been obtained [16], which are also in good agreement with the theoretical values obtained by Wakoh and Yamashita.

3. EXPERIMENTAL METHOD

Four different specimens were prepared by arc melting appropriate mixtures of TiO_2 (99.9% pure) and sponge titanium (99.8% pure) under argon atmosphere. Repeated melting was made to ensure the homogeneity in composition. The buttons were rapidly cooled to room temperature in the argon atmosphere.

For determining the specimen composition, lattice parameters of the powdered specimens were measured, using an x-ray diffractometer method and making a Nelson-Riley plot. Measured values were a = 4.191, 4.184, 4.174, and 4.168 Å, respectively, for four different specimens, the errors being $\pm$ 0.0005 Å. Comparing these values with the lattice parameter–composition relation established by Andersson et al. [7], the compositions of the present specimens were estimated to be $TiO_{0.82}$, $TiO_{0.96}$, $TiO_{1.16}$, and $TiO_{1.25}$, respectively.

The specimens were thinned mechanically to approximately 0.1 mm thickness. Thin foils suitable for transmission electron microscopy were then prepared by electropolishing at room temperature in a solution of 60% HNO_3, 20% HF and 20% glacial acetic acid at 4 V. Final polishing was achieved by chemical thinning in a solution containing 33% HF, 50% HNO_3, and 17% H_2O.

The x-ray diffraction patterns showed sharp diffraction lines of the NaCl type structure, indicating that the disordered state was retained at room temperature. The electron diffraction patterns contained a distribution of weak diffuse scattering, in addition to the fundamental spots. The diffuse scattering is due to the existence of some short range order to vacancies.

Thin foils were examined with a 500 kV electron microscope. Diffraction patterns were taken from areas of 1 μm diameter or smaller by the selected area diffraction technique at various accelerating voltages. Inspecting intensity variation of the 400 Kikuchi line and contrast change of the middle line of the Kikuchi band [1, 17] with the accelerating voltage, the critical voltage E_c for the 400 reflection was determined.

4. RESULTS

Figure 1 shows examples of diffraction patterns of $TiO_{0.82}$ taken at accelerating voltages 325, 345 and 365 kV. The 400 Kikuchi lines are clearly visible in figure 1 (a) and (c), but almost invisible in (b). Moreover, the middle line of the Kikuchi band is clearly seen in figure 1 (a) and (c), and vanishes in (b). Asymmetry of excess-deficient profile of the middle line is reversed in (a) and (c). The critical voltages E_c for the 400 reflection determined from a series of such diffraction patterns were 340, 354, 389, and 425 kV, respectively, for $TiO_{0.82}$, $TiO_{0.96}$, $TiO_{1.16}$, and $TiO_{1.25}$.

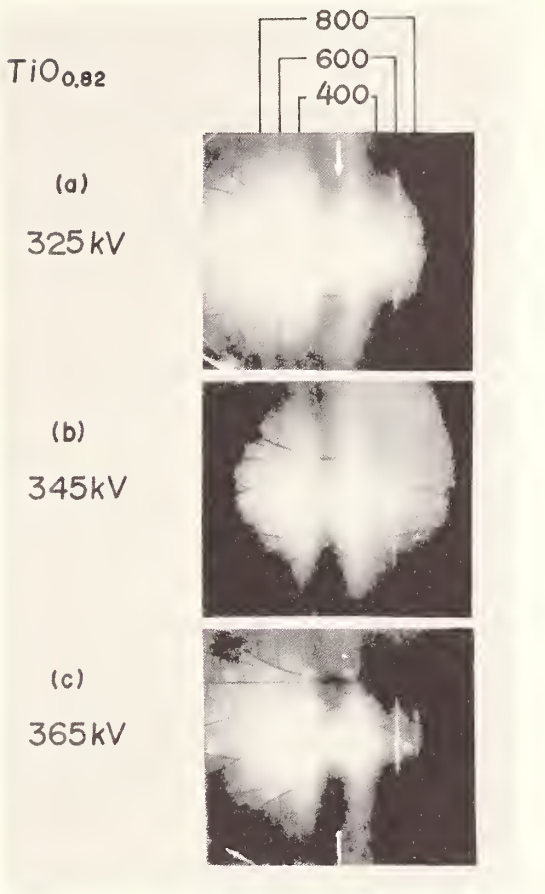

Fig. 1. Electron diffraction patterns from $TiO_{0.82}$ taken at 325 kV (a), 345 (b) and 365 (c). Arrows in (a) and (c) show the middle line of the Kikuchi band.

To compare the experimental values with calculated ones, the values of E_c were calculated for $TiO_{0.82}$ and $TiO_{1.25}$, using available theoretical scattering factors of titanium and oxygen atoms or ions of various atomic states. The calculations were made for free neutral titanium and oxygen atoms Ti^0, O^0, monovalent ions Ti^{1+}, O^{1-} and divalent ions Ti^{2+}, O^{2-}. For the divalent oxygen ion, three models were considered, *i. e.*, O^{2-} ion in a hypothetical potential well with a spherical distribution of +1 or +2 charge calculated by Watson [18, 19], and O^{2-} ion model calculated for magnesium oxide crystal by Yamashita and Asano [20, 21]. For neutral atoms, positive ions and monovalent oxygen ions, x-ray scattering factors calculated by Fukamachi [22] from analytical Roothaan-Hartree-Fock wave functions of Clementi [23] were used. The respective electron configurations are as follows:

Ti^0 ; K(2)L(8)3s(2)3p(6)3d(2)4s(2),

Ti^{1+} ; K(2)L(8)3s(2)3p(6)3d(3)4s(0),

Ti^{2+} ; K(2)L(8)3s(2)3p(6)3d(2)4s(0),

O^0 ; 1s(2)2s(2)2p(4),

O^{1-} ; 1s(2)2s(2)2p(5),

The structure factors for electrons $\pi v_0 U_h$ of the h00 reflections (h = 2, 4, ..., 14) calculated for $TiO_{0.82}$ and $TiO_{1.25}$ at 293 K are shown in table 1, where v_0 is the volume of the unit cell of the crystal lattice. In the calculation, titanium and oxygen vacancies have been treated as if they are distributed uniformly throughout the titanium and oxygen sublattices, respectively, with the probabilities corresponding to vacancy concentrations; since the vacancies are almost randomly arranged in the NaCl type crystal. The effective B factors of 0.56Å^2 for $TiO_{0.8}$ and 0.80 Å^2 for $TiO_{1.2}$ determined by neutron diffraction experiment of Yamada et al. [24], which include the effect of static atom displacements near vacancies as well as thermal vibration effect, were assumed for $TiO_{0.82}$ and $TiO_{1.25}$, respectively.

Table 1

Structure Factors for Electrons, $\pi v_0 U_h$(Å), of the h00 Reflections Calculated for $TiO_{0.82}$ and $TiO_{1.25}$

h00	Ti^0,O^0	Ti^{1+},O^{1-}	Ti^{2+},O^{2-} (a)	Ti^{2+},O^{2-} (b)	Ti^{2+},O^{2-} (c)	experimental value
			$TiO_{0.82}$ (d)			
200	14.41	14.03	14.20	14.11	13.77	14.59±0.08
400	5.85	5.87	5.87	5.87	5.84	
600	2.60	2.60	2.60	2.60	2.60	
800	1.25	1.25	1.25	1.25	1.25	
1000	0.637	0.637	0.637	0.637	0.637	
1200	0.327	0.327	0.327	0.327	0.327	
1400	0.165	0.166	0.165	0.165	0.165	
			$TiO_{1.25}$ (e)			
200	13.55	13.23	13.38	13.26	12.84	13.08±0.11
400	5.27	5.30	5.30	5.30	5.26	
600	2.18	2.18	2.18	2.18	2.17	
800	0.947	0.947	0.946	0.946	0.946	
1000	0.422	0.422	0.422	0.422	0.422	
1200	0.185	0.185	0.185	0.185	0.185	
1400	0.078	0.078	0.078	0.078	0.078	

(a) O^{2-}, Watson +1 well.

(b) O^{2-}, Watson +2 well.

(c) O^{2-}, Yamashita & Asano.

(d) Occupation probabilities are 0.925 and 0.755 for titanium and oxygen sublattices, respectively.

(e) Occupation probabilities are 0.78 and 0.975 for titanium and oxygen sublattices, respectively.

Table 2

Calculated and Measured Values of E_c (kV) for TiO.

	Ti^0,O^0	Ti^{1+},O^{1-}	Ti^{2+},O^{2-} (a)	Ti^{2+},O^{2-} (b)	Ti^{2+},O^{2-} (c)	measured value
$TiO_{0.82}$	359	414	389	403	447	340 ± 5
$TiO_{1.25}$	359	408	385	403	462	425 ± 10

(a) O^{2-}, Watson +1 well.

(b) O^{2-}, Watson +2 well.

(c) O^{2-}, Yamashita & Asano.

The values of E_c calculated using the theoretical structure factors given in table 1 are shown in table 2, together with the experimental values. Although the values of E_c change considerably with the atomic state of constituent elements, the values for each model are almost independent of specimen composition. This is due to the systematic changes of temperature factor, lattice parameter and occupation probabilities of both titanium and oxygen sublattices with composition. That is, the effects of temperature factor and lattice parameter changes compensate the effect of occupation probability change, and almost the same values of E_c are obtained. The measured values of E_c, however, change considerably with specimen composition.

The structure factors $\pi v_0 U_1$ of the first order reflection 200 for $TiO_{0.82}$ and $TiO_{1.25}$ calculated using the measured values of E_c and assuming the structure factors of higher order reflections given in table 1 are shown in the same table. It is to be noted that the theoretical structure factors of higher order reflections are almost the same for various models, as seen in table 1. The contribution to the error of the first order structure factor $|\Delta U_1/U_1|$ from that of the second order structure factor $|\Delta U_2/U_2|$ is estimated to be less than 0.4%.

5. DISCUSSION

Comparison of the experimental values of E_c and $\pi v_0 U_1$ with the theoretical ones enables us to discuss the ionicity in the TiO crystal. As seen in tables 1 and 2, the experimental values of E_c and $\pi v_0 U_1$ for $TiO_{0.82}$ are approximately equal to those calculated for neutral atoms Ti^0 and O^0, while the experimental values for $TiO_{1.25}$ are far different from those for neutral atoms. Since the values of E_c calculated for each model are almost independent of specimen composition, as already mentioned in the preceding section, the E_c values, 354 and 389 kV, measured for $TiO_{0.96}$ and $TiO_{1.16}$, respectively, can also be compared with those calculated for various models in table 2. These results mean that the ionicity in the TiO phase depends on the oxygen concentration in the crystal. That is, titanium and oxygen atoms in the oxygen-deficient TiO crystal are considered to be almost neutral, while the elements in the titanium-deficient crystal appear to be in the ionic states.

The calculation of the structure factors have been based on the atoms in neutral or ionic states with spherically symmetric electron distribution. Since TiO crystals examined in the present study have the cubic close packed structure and the vacancies are almost randomly distributed, the electron distribition in the crystal is considered to be spherically symmetric. On the other hand, the condition of charge neutrality has not been satisfied in the present calculation. The correction to this is not possible to make at present,

465-504 O - 72 - 12

because the actual electronic structure of a TiO crystal is not yet known. Although an attempt to make this correction is in progress, assuming several models for the electronic structure, it seems that at least the conclusion for the oxygen-deficient crystal does not change even if the correction is properly made, since the correction for $TiO_{0.96}$ must be negligible.

It should be emphasized that the structure factors U_1 of the first order reflection 200 estimated from the measured values of E_c are most reliable. Since the structure factor at low angle scattering is very sensitive to the configuration of outer atomic electrons, the present result on the first order structure factors would contribute greatly to the study of the electronic structure of TiO crystals.

In order to find the possibility of applying the present method to other compounds with different crystal structures, the values of E_c for TiO_2 crystal of the rutile type were calculated. The lattice parameters of TiO_2 are a = 4.594 Å and c = 2.959 Å, and the scattering angles of the 110 and 101 reflections are relatively small, *i. e.*, $\sin\theta/\lambda$ = 0.1539 and 0.2010 $Å^{-1}$, respectively. Consequently, the structure factors of these reflections are extremely sensitive to the configuration of outer atomic electrons. In fact, the calculated values of E_c for the second order reflections change remarkedly with atomic state of the constituent elements, as shown in table 3. In the calculation, the B factor of 0.7 $Å^2$ determined by the x-ray experiment of Baur [25] was assumed.

The preliminary experiment on the 220 reflection of a TiO_2 crystal was carried out by use of a 500 kV electron microscope. Figure 2 shows examples of diffraction patterns taken at 333 and 380 kV, where the 220 Kikuchi lines are clearly visible. Observation of a series of such diffraction patterns revealed that the critical voltage E_c is about 350 kV, which can not be explained by any model shown in table 3.

Since it is thought that TiO_2 does not retain the spherical symmetry of electron distribution and has some covalent character in its bonds, the measured value of E_c can not be compared directly with the calculated values shown in table 3. However, it would be very useful for the study of electronic structure to determine accurately the structure factors of the 110, 101, and other reflections by the present method. Attempts are in progress on this line.

Table 3

Calculated Values of E_c (kV) for TiO_2 (rutile).

Model \ reflection	110	101
Ti^0, O^0	444	386
Ti^{2+}, O^{1-}	502	406
Ti^{4+}, O^{1-} (a)	96	58
Ti^{4+}, O^{2-} (b)	102	39
Ti^{4+}, O^{2-} (c)	104	28

(a) O^{2-}, Watson +1 well.

(b) O^{2-}, Watson +2 well.

(c) O^{2-}, Yamashita & Asano.

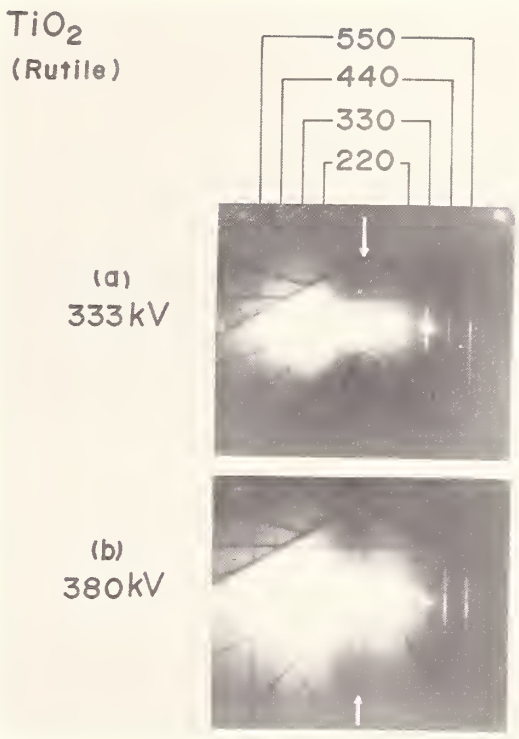

Fig. 2. Electron diffraction patterns from TiO_2 (rutile) taken at 333 kV (a) and 380 kV (b). Arrows show the middle line of the Kikuchi band.

6. ACKNOWLEDGEMENT

The electron diffraction experiments in the present study were carried out by using a 500 kV electron microscope installed in the Institute for Solid State Physics, the University of Tokyo. The authors wish to thank the ISSP for giving them opportunities of using the equipment and for financing the present study. They are indebted to Professor S. Hosoya and Mr. T. Fukamachi for valuable discussions. Thanks are also due to Mr. K. Suzuki and Mr. M. Ichihara for their help in the electron diffraction experiments, and to Dr. H. Iwasaki of Tohoku University for his aid in specimen preparation. This work was partly supported by a Science Research Grant of the Ministry of Education (1969 - 1971). Grateful acknowledgement is made to the Sakkokai foundation for the provision of a research grant (O.T.).

7. REFERENCES

[1] Watanabe, D., Uyeda, R. and Kogiso, M., Acta Cryst., A24, 249 (1968).
[2] Watanabe, D., Uyeda, R., and Fukuhara, A., Acta Cryst., A24, 580 (1968).
[3] Watanabe, D., Uyeda, R., and Fukuhara, A., Acta Cryst., A25, 138 (1969).
[4] Nagata, F., and Fukuhara, A., Japan J. Apply. Phys., 6, 1233 (1967).
[5] Fisher, R. M., Lally, J. S., Humphreys, C. J., and Metherell, A. J. E., Proc. septieme congres international de microscopie electronique, Grenoble, 1, 107 (1970).
[6] Ehrlich, P., Z. anorg. allg. Chem., 247, 53 (1941).
[7] Andersson, S., Collen, B., Kuylenstierna, U., and Magneli, A., Acta Chem. Scand., 11, 1641 (1957).
[8] Watanabe, D., Terasaki, O., Jostsons, A., and Castles, J. R., *The Chemistry of Extended Defects in Non-Metallic Solids*, North-Holland Pub. Co., Amsterdam 238 (1970).
[9] Uyeda, R., Acta Cryst., A24, 175 (1968).
[10] Cowley, J. M., Z. angew. Phys., 26, 149 (1969).
[11] Uyeda, R., Nonoyama, M., and Kogiso, M., J. Electronmicroscopy, 14, 296 (1965).

[12] International Tables for x-ray Crystallography, III, (1962), Birmingham: Kynoch Press.
[13] Fukuhara, A., J. Phys. Soc., Japan 21, 2645 (1966).
[14] Freeman, A. J., and Watson, R. E., Acta Cryst., 14, 231 (1961).
[15] Wakoh, S., and Yamashita, J., J. Phys. Soc. Japan, 30, 422 (1971).
[16] Fujimoto, M., Terasaki, O., and Watanabe, D., to be published.
[17] Kainuma, Y., and Kogiso, M., Acta Cryst., A24, 81 (1968).
[18] Watson, R. E., Phys. Rev. 111, 1108 (1958).
[19] Sanger, P. L., Acta Cryst., A25, 694 (1969).
[20] Yamashita, J., and Asano, S., J. Phys. Soc. Japan, 28, 1143 (1970).
[21] Fukamachi, T., and Hosoya, S., Tech. Rep. ISSP, ser. A No. 453 (1971).
[22] Fukamachi, T., Tech. Rep. ISSP, ser. B, No. 12 (1971).
[23] Clementi, E., Tables of Atomic Functions, A supplement to the paper appearing in IBM J. Res. Developm., 9, 2 (1965).
[24] Yamada, Y., Terasaki, O., and Watanabe, D., to be published.
[25] Baur, W. H., Acta Cryst., 9, 515 (1956).

National Bureau of Standards Special Publication 364, Solid State Chemistry, Proceedings of 5th Materials Research Symposium, issued July 1972.

THE STRUCTURE AND INTERGROWTH OF THE POLYMORPHIC FORMS OF $ZrO_2.16Nb_2O_5$

N. C. Stephenson, J. P. Beale, and D. C. Craig

School of Chemistry
University of New South Wales
Kensington, N. S. W.
Australia

The compound $ZrO_2.12Nb_2O_5$ has been reported to exist in three polymorphic forms, one of which is isostructural with $TiNb_{24}O_{62}$.

The crystal structures of the remaining two polymorphs have been determined by examining x-ray data collected from a single crystal of the β-monoclinic form. The unit-cell dimensions are a = 39.693, b = 3.830, c = 35.488 Å, β = 116.53°. 2948 data were collected using a single crystal diffractometer and CuKα radiation.

No assumptions were made about the structural features and the basic subcell unit was deduced from the Patterson function. Modifications of this subcell give rise to the remaining two polymorphs, which contain blocks of 3x3, 4x4, and 3x4 corner sharing octahedra. The 3x4 blocks are all at the one level and form sheets running parallel to (100). The 3x3 and 4x4 blocks form sheets which alternate with those just described. The manner in which the sheets fit together determines which polymorph is formed.

Although the structures were solved using standard x-ray procedures, the solutions were facilitated by using features of electron transmission micrographs. These consisted of a regular array of dots and streaks (plane group p2) arranged in lines parallel to c. The spacial distribution and contrast of these dots and streaks, together with their arrangements at antiphase boundaries and fault areas, impose certain restrictions upon structures that can be derived by modifications of the basic subcell.

In terms of structure, the areas of contrast on transmission micrographs can be identified with the different types of block junctions.

Key words: Crystal structure; intergrowth; lattice-image; polymorphism; zirconium-niobium oxide.

1. INTRODUCTION

The compound $ZrO_2.12Nb_2O_5$ was first identified by Roth [1][1] as the initial product of the reaction of the component oxides in 1:12 proportion. It was shown to be isostructural with $TiNb_{24}O_{62}$ [2], (fig. 1), but on annealing it transforms to a much more complex structure. Single crystal x-ray studies of the transformed material suggested that the unit cell was monoclinic with a=c=71.04 Å, b = 3.82 Å, and β=90°.

In a later study, Allpress and Roth [3] investigated this monoclinic form using electron diffraction and transmission microscopy. It was shown that the transformed material contained two polymorphs which were capable of intergrowth at the unit-cell level. These polymorphs were called the β and γ forms of $ZrO_2.12Nb_2O_5$ while the product of the initial reaction was called the α form. The relevant crystallographic data are given in table 1.

[1]Figures in brackets indicate the literature references at the end of this paper.

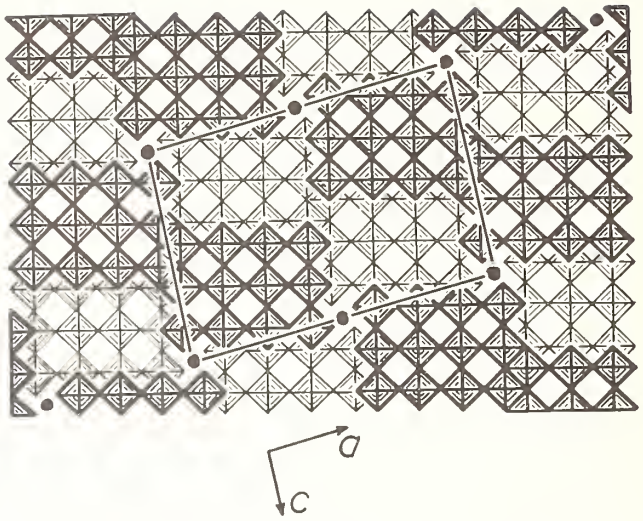

Fig. 1. An idealized model representing the structure of the α form of $ZrNb_{24}O_{62}$. Each square represents an octahedra viewed down a body diagonal, the lighter and darker squares being centred on parallel planes 1.9 Å apart. The circles represent metal atoms in tetrahedral coordination.

Table 1

Crystallographic Data for the $ZrO_2.12Nb_2O_5$ Polymorphs

	a(Å)	b(Å)	c(Å)	α	β	γ	
α-Form	29.78	3.821	21.21	90°	94.9°	90°	(cell dimensions of $TiNb_{24}O_{62}$)
β-Form	39.693	3.830	35.488	90°	116.53°	90°	
γ-Form	35.5	3.83	35.5	90°	90°	90°	

The identification of the β and γ polymorphic forms of $ZrO_2.12Nb_2O_5$ which intergrow in a single crystal formerly thought to have the enormous unit-cell dimensions reported by Roth [1], beautifully demonstrates the power of combined electron diffraction and optical techniques.

Figures 2 and 3 are reproduced with the permission of Drs. Allpress and Roth. The h0l reciprocal lattice plane of the β phase (fig. 2a) can be identified in the combined h0l data from the β and γ forms (fig. 2b). Apart from the fact that these photographs are easier and quicker to obtain than corresponding x-ray photographs, the information contained in figure 2(b) is nevertheless available in the x-ray photographs. Early recognition of intergrowth phases is however facilitated by the use of electron transmission microscopy (fig. 3b).

2. ELECTRON TRANSMISSION MICROGRAPHS OF $ZrO_2.12Nb_2O_5$

Figure 3a shows a lattice image of a fragment of α-$ZrO_2.12Nb_2O_5$. Most of the fringes have a separation of 15 Å, which is the characteristic spacing between shear planes parallel to c in the $TiNb_{24}O_{62}$ structure. The 17 Å separations are indicative of the intergrowth of planar slabs of the H-Nb_2O_5 structure and show that the original preparation was slightly off stoichiometry.

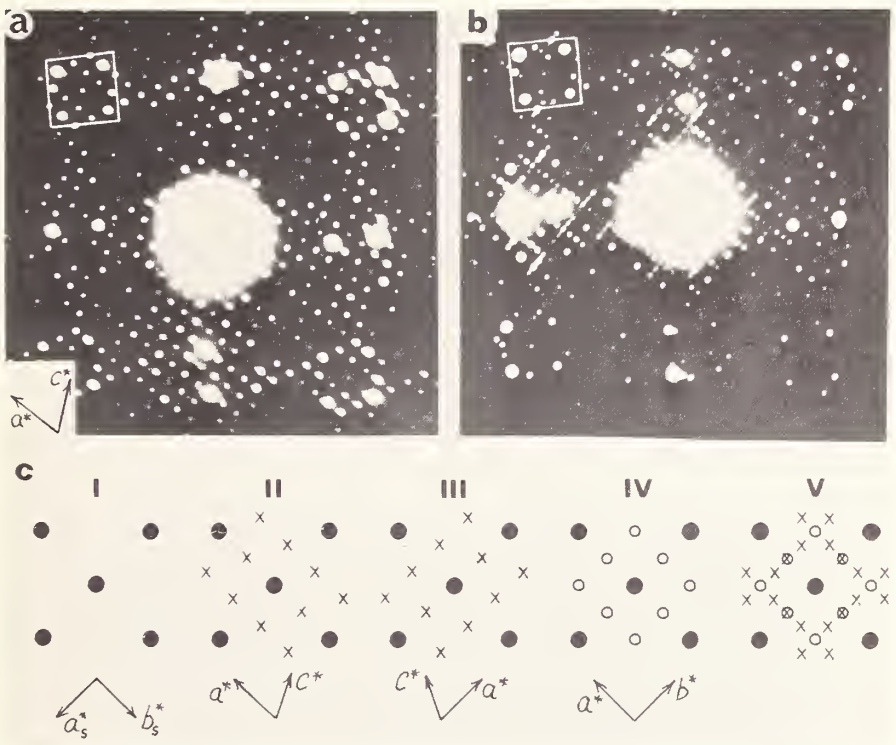

Fig. 2. Electron diffraction photographs.
(a) The h01 reciprocal lattice net of the β-polymorph.
(b) The h01 reciprocal lattice net taken from a crystal containing twinned domains of the β-polymorph and domains of the γ-polymorph.
(c) A diagrammatic representation of the component reciprocal lattice net evident in 2(b)
(i) basic tetragonal subcell lattice;
(ii) a domain of the β-polymorph;
(iii) a domain of the β-polymorph related to the previous one by a two-fold axis;
(iv) a domain of the γ-polymorph;
(v) a combination of (i)-(iv).

The contrast in figure 3b consists of an array of white dots and this lattice image was formed with the electron beam incident a few degrees to [010]. This photograph clearly shows intergrowth domains of the β-form (area H) and γ-forms (area S). Area H, is a domain of the β-form in different orientation to H.

Allpress and Roth [3] were able to postulate structures for the β and γ $ZrO_2.12Nb_2O_5$ phases. They did this by modifying the structural components of a tetragonal subcell which was evident from the distribution of spots on electron diffraction photographs. These modifications were carried out on the basis of the contrast shown in figures 3c and d. The lattice image in figure 3c, taken with the electron beam parallel to the b axis of the β-form, shows regular rows of dark dots and streaks. Faults are evident at P, Q, and R. Previous studies [4] have shown that sites occupied by tetrahedral atoms (O-positions) in block structures produce strong contrast in the form of dark dots in lattice images of suitably oriented framgents. An O-position is shown in figure 4a while the other remaining way of joining 4 blocks gives rise to an x-position (fig. 4b). The structures proposed by Allpress and Roth [3] were felt to be inadequate in that they did not satisfactorily explain the streak contrast in figure 3c. The regions which give this contrast were correlated with x-positions, of which there were too many and which previous studies [4] have indicated to give only slight density contrast in lattice images.

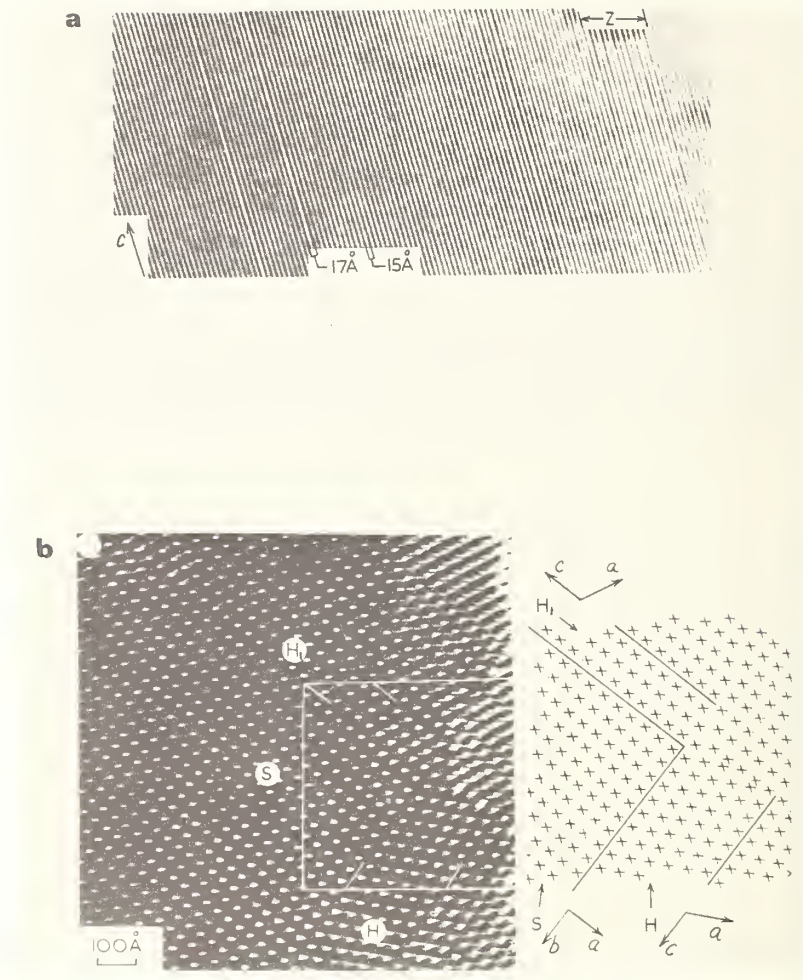

Fig. 3. Lattice image micrographs.

(a) of a crystal of α-$ZrO_2 \cdot 12Nb_2O_5$ tilted to reveal the shear planes parallel to c with spacings of 15 Å. The spacings of 17 Å correspond to planar slabs of H-Nb_2O_5 which form disordered Wadsley intergrowth defects.

(b) taken with the electron beam incident a few degrees away from parallism with the short (3.8 Å) axis. The area contains distinct domains:

(1) H contains the monoclinic β-polymorph.

(2) H_1 is a domain of the β-polymorph but in twinned orientation to H.

(3) S contains the tetragonal γ-polymorph.

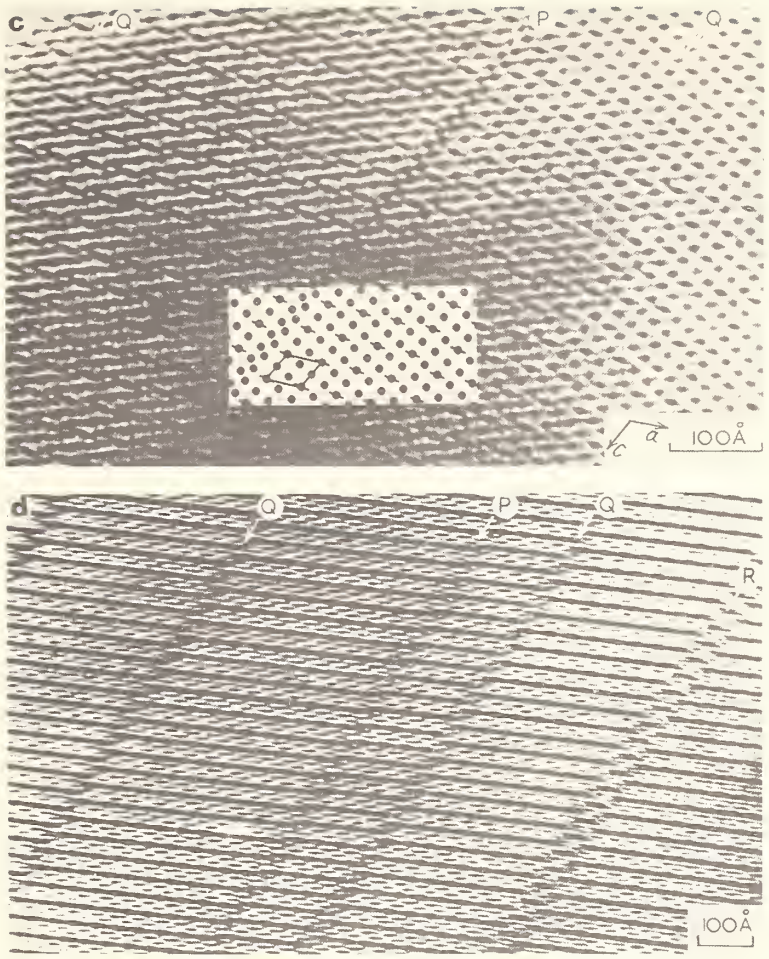

Fig. 3. Lattice image micrographs.
(c) taken with the incident beam exactly parallel to the short b axis of the β-polymorph. The contrast may be approximately described as an array of dots and streaks arranged in lines parallel to c. Faults are evident at P and Q.
(d) similar to (c) but with 00ℓ reflections dominating the diffraction patterns. Another type of fault occurs at R.

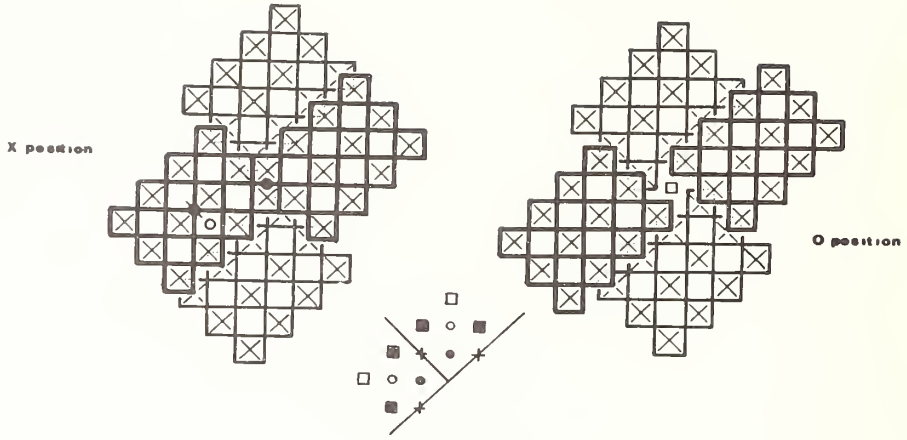

Fig. 4. Block junctions showing the formation of X- and O-positions (full circle and open square respectively). Other positions in the blocks, marked with an open circle or cross, represent centres of symmetry if the blocks are respectively (2n x 2n) or (2n + 1 x 2n) octahedra in size. Vectors across these centers are shown distributed about an origin.

The work described below involves the determination of the structures of the β and γ forms from x-ray diffraction data but with due regard to the spacial distribution and contrast of the lattice image dots and streaks in domains, fault areas and antiphase boundaries.

3. EXPERIMENTAL

Crystals of the compound were mainly fine needles, with twinning and intergrowth particularly common, and it was necessary to examine several by the Weissenberg method before a suitable one was found. The crystal chosen for data collection had dimensions of 0.017 x 0.012 x 0.15 mm.

A Siemens A. E. D. four circle diffractometer controlled by a PDP-8 computer was used for data collection; crystal orientation and angle calculation were accomplished using the method of Busing and Levy [9]. Cell dimensions were determined from selected high angle reflections, which were used also for the refinement of the approximate initial UB matrix.

Integrated intensities for h0l reflections were obtained with CuKα radiation using a θ-2θ scan and a "four value" modification of the "five value method" [10] of measurement. In this modification the third stage of the measurement is omitted, resulting in the peak intensity being obtained as the run of two partial scans, and background measurements being made on each side of the peak. This affords a considerable time saving over the "five value method", and yet maintains the valuable check scanning symmetry obtainable by comparing the values from the two partial scans. The scan range varied from 0.8° at low theta to 1.3° at theta of 70° the limit of the instrument.

The scan rate is controlled by the computer and varies from 6 sec/deg. for the most intense reflections to a maximum, set in this case at 120 sec/deg. for the weak reflections. Attenuation filters are inserted automatically when necessary to keep the count rate within the linear range of the equipment.

Intensities were corrected for instrumental drift, if any, using a periodically measured standard reflection as a reference. Background was assumed to vary linearly though the scan range of each reflection, and corrections for this, Lorentz, polarization and absorption were applied using programs written in this laboratory. Standard deviations (σ) were assigned on the basis of counting statistics, and a reflection was regarded as unobserved if its net intensity was less than 2.58σ, and its intensity was then assigned as 2.58σ.

4. DETERMINATION OF THE STRUCTURE OF THE β-POLYMORPH

4.1. SUBCELL STRUCTURE

The advantages of working with two dimensional h0ℓ data far outweigh the disadvantages, which relate mainly to atomic overlap in projection and to standard deviations in parameters. Overlap in projection is, in fact, minimal because of the short length of the projection axis (3.83 Å) whereas computing and phase determination problems are greatly reduced by using only h0l data.

The Laue symmetry of the reciprocal lattice (2/m) indicated that the crystal class is probably monoclinic. It could, in fact, be triclinic with the heavy metal atoms in a more symmetric array than some of the lighter oxygen atoms. In this case however the form of the two-dimensional Patterson function

$$A(x,z) = \sum_{h=o}^{\infty} \sum_{l=-\infty}^{\infty} | F\ h0\ell |^2 \exp.-2\pi i\ (hx + lz) \qquad (1)$$

is independent of either symmetry requirement and was therefore calculated and contoured. It was immediately apparent from the distribution of peaks that the structure is based upon blocks of corner sharing octahedra similar to the many examined by Wadsley and co-workers.

If the crystal calss is monoclinic then the plane group of the (0l0) projection of the unit-cell contents, or fundamental set, *must* be p2. It would therefore be possible to choose a line from the origin of A(x,z) to a vector point corresponding to a pair of centrosymmetrically situated points in the fundamental set. Image seeking functions [5] based upon this line should not be subject to false symmetry and represent the fundamental set.

The expected location of these centric vectors are shown in figure 4. These were readily identified on the Patterson projection and a number of minimum functions were contoured from superimposed Patterson maps.

The 'fundamental set' which repeatedly resulted from these superposition methods is shown in figure 5. It consists of blocks of 4x3 corner sharing octahedra which are themselves joined by edge sharing. The actual unit-cell is shown dotted and corresponds to the 'tetragonal subcell' which was described by Allpress and Roth [3]. There are four of these subcells in the unit-cell of the β-polymorph.

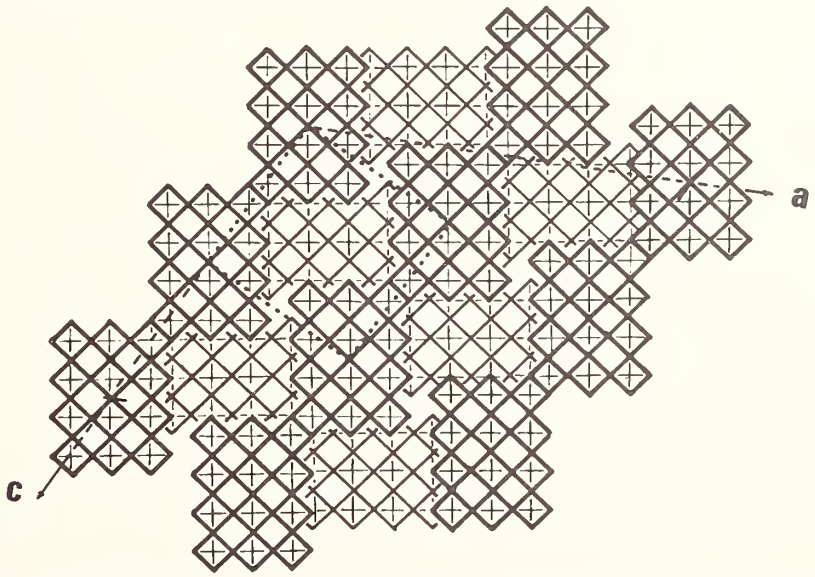

Fig. 5. The β-polymorph structure as determined from the Patterson function by image seeking methods. The monoclinic unit cell axes are shown as dashed. The tetragonal subcell is shown dotted.

4.2. MODIFICATION OF THE SUBCELL STRUCTURE

The relationship between the subcell (dotted) and the true unit cell of the β-polymorph (dashed) is shown again in figure 6. Blocks of corner sharing octahedra are represented by rectangles whose edges run through the centers of the peripheral octahedra.

There are four 0-positions in the β-phase unit-cell depicted in figure 6 (shown as dotted circles). Lattice images of the β-phase (fig. 3c, d) show that there are only three 0-positions and one "modified" 0-position (appearing as a streak). The only way to remove, or modify, an 0-position is to convert it into an X-position by expanding one of the blocks so that it shares edges with some octahedra in an adjacent block at the same level. This position is shown marked with an X in figure 7. The trial partial structure shown in figure 7 thus has the following features:

(1) There are only three 0-positions in the β-polymorph unit-cell and these agree in positions with the distribution of dark dots in figure 3c.

(2) The structure is only a very slight modification of the subcell structure derived from x-ray diffraction data.

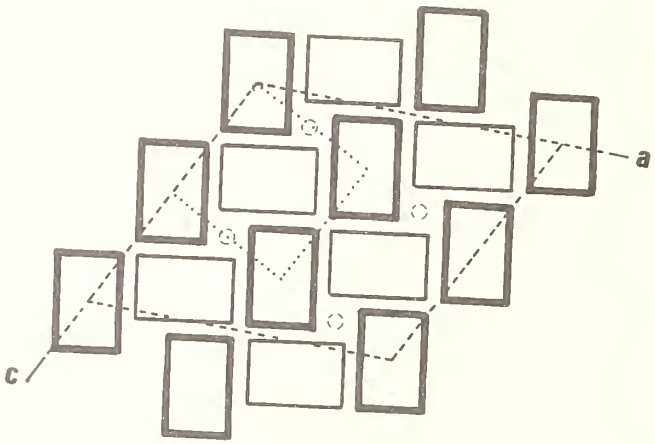

Fig. 6. Block diagram of the subcell structure shown in figure 5. The 4 x 3 blocks are represented by rectangles. 0-positions are shown as broken circles and four such block junctions occur in a unit-cell of the β-polymorph.

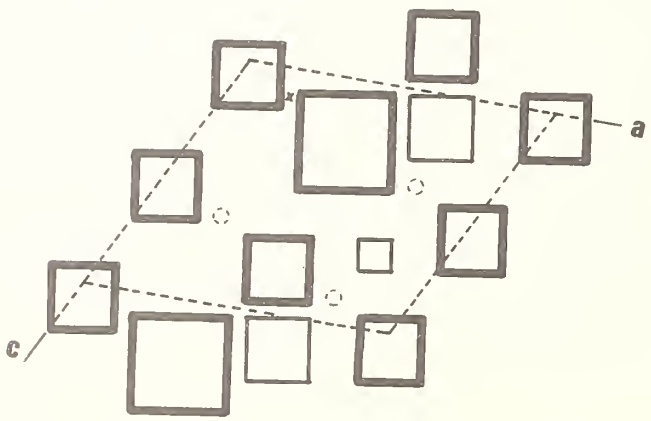

Fig. 7. The initial trial partial structure for the β-polymorph which was obtained from the subcell structure by eliminating one 0-position (marked with an X) and reducing the sizes of the remaining blocks to allow for expansion in either of two directions.

(3) The block sizes (mainly 3x3) and positions are such that they can be expanded to 3x4 (or 4x3) in either of two directions or some can be made 4x4 blocks if atoms are located in the appropriate positions. It is important that the "right" atom be omitted from a trial structure in order to give the structure the utmost flexibility during modification.

(4) The plane group symmetry is p1. If, in fact, the symmetry is higher, then this will become evident as the determination of the true structure from the experimental data proceeds.

4.3. THE TRUE STRUCTURE

Metal atom positions which correspond to the blocks drawn for the trial structure were obtained from the minimum function. The positions of the remaining metal atoms can be located by successive cycles of structure factors (Fc) and difference Fourier syntheses. This involves calculating the function

$$\Delta\rho(x,z) = \frac{1}{A} \sum_{h=0}^{+\infty} \sum_{l=-\infty}^{+\infty} (|Fo|-|Fc|) \cos[2\pi(hx + lz)-\alpha] \qquad (2)$$

where α is the phase angle of individual Fc values and $\Delta\rho(x, z)$ is the residual electron density at the point x,z in the unit-call. As additional metal atoms are found they are included in the calculation of Fc for the next cycle.

After 12 cycles the 99 metal atoms in the asymmetric unit-cell were located. The plane group is p1 and there remained to find over two hundred oxygen atoms. These were located in the manner just described but with the following refinement procedures applied to metal atom parameters and, eventually, to the oxygen atoms.

4.4. REFINEMENT PROCEDURES

Full matric least-sequares methods [6] were used to refine the atomic parameters. Values of $\Sigma\, w\, (|F_o|-|F_c|)^2$ were minimized, where w is the weight of $|F_o|-|F_c|$ and estimated for each observation from counting statistics. The atomic scattering factors for neutral atoms Nb[2] and 0 were computed from numerical Hartree-Fock wave functions using the method of Cromer and Mann [7]. A correction for the real component of the anomalous dispersion of CuKα by Nb was made [8]. An IBM 360/50 computer was used for all calculations together with local versions of well established programs.

A summary of the refinement cycles is given in table 2 and atomic parameters are listed in table 3. Fractional shifts were introduced to rationalize parameter shifts and after cycle 16 the metal atoms were assigned anisotropic temperature factors of the form $\exp [-(\beta_{11}h^2 + \beta_{33}l^2 + 2\beta_{13}hl)]$. Metal atoms, in projection are to a certain extent overlapped by the oxygen atoms which are displaced b/2 Å for them along the [010] direction. Provided the metal atom is located at the center of the octahedron then considerable overlap occurs. These octahedra are usually found in the center area of blocks. Octahedra lying around the periphery of blocks are associated with crystallographic shear planes and metal atoms are significantly displaced towards the body of the block. In these cases the degree of metal-oxygen overlap is lessened and the effect is to elongate the metal peak in projection. An over simplified way of treating these differing degrees of overlap is to treat the composite atom as Nb + 0 and assign anisotropic thermal parameters.

The slow rate of convergence of the least-squares cycles is due, in part, to the non-centric arrangement of the atoms and, in the main, to the parameter interdependence brought about by the underiding symmetry of the subcell. The same difficulty was experienced during the refinement of the Ta_2O_5 - WO_3 structures [11]; atoms not related by the symmetry elements of the real cell are nevertheless related by the symmetry elements of the (tetragonal, in this case) subcell. Correlation coefficients are high and standard deviations in atomic positions are large. Standard deviations in the x and z positional

---

[2]Nb and Zr were assumed to scatter in an identical manner and all metal atoms were treated as niobium atoms.

Table 2

A Summary of the Refinement Cycles

Atoms in Asymmetric Unit	Number of Variables	Number of Cycles	Type of Thermal Parameters	Total Number of Parameters entered	Type of Parameter varied	Fractional Shifts	R(a)	WR(b)
79			TRIAL STRUCTURE				43.2	47.9
79	202	2	Overall B	476	Metal X,Z	.50	39.8	38.1
88	222	2	" "	530	Metal X,Z	.50	35.6	32.5
92	184	2	" "	554	Metal X,Z	.50	33.0	30.6
92	184	4	" "	554	Metal X,Z	.50	30.8	27.8
97	292	2	Individual B	584	Metal X,Z,B	FULL	28.0	23.7
99	198	2	" "	596	Metal X,Z	FULL	26.9	23.1
226	256	1	" "	1358	Oxygen X,Z	.25	23.2	19.4
226	256	1	" "	1358	Oxygen X,Z	.25	23.0	19.0
247	298	1	(ANISO,Metal ISO Oxygen)	2719	Metal β_{11} β_{13},β_{33}	.25	22.0	18.3
247	298	1	"	2719	"	.25	21.2	17.7
247	298	1	"	2719	"	FULL	20.2	16.7
247	197	1	"	2719	Metal X,Z	.30	19.5	16.1
247	197	1	"	2719	Metal X,Z	FULL	18.5	15.1

Number of Obersvations 1486

(a) The normal R factor $\Sigma\left||F_o| - |F_c|\right|/\Sigma|F_o|$

(b) The weighted R factor $[\Sigma w(|F_o| - |F_c|)^2/\Sigma w|F_o|^2]^{\frac{1}{2}}$

parameters of the niobium atoms are of the order 0.05 Å, which is exceptionally large and reflects a degree of intractability in the refinement of the structure.

The large number of parameters associated with atoms in the asymmetric unit imposes an upper limit, approximately 300, on the number of parameters that can be varied in each cycle of least-squares on the IBM 360/50 computer. It is not possible to vary all the parameters of all atoms at the same time. This computing problem, together with the inherent intractability described above, contribute towards a difficult and costly refinement.

The refinement of this present stage cannot be considered as complete. Nevertheless, structural details are sufficiently well resolved to allow for the following discussion.

Table 3

Atomic Parameters for Atoms in the Asymmetric Unit of $ZrO_2.16Nb_2O_5$.

Atom	x	z	β_{11}	β_{33}	β_{13}
M 1	.0253	.0570	36(38)	83(40)	80(34)
M 2	.1206(9)	.0424(10)	-29(15)	-27(20)	-33(14)
M 3	.0064(13)	.2047(15)	20(30)	32(36)	-15(27)
M 4	.0933	.1862(13)	-20(19)	54(37)	36(23)
M 5	.1863(22)	.1733(19)	27(8)	117(57)	91(59)
M 6	.7425(12)	.4037(11)	56(29)	-11(24)	29(23)
M 7	.9715(11)	.4362(20)	-21(23)	144(73)	17(35)
M 8	.0599(7)	.4281(9)	-54(12)	-45(17)	-41(11)
M 9	.2732(15)	.1144(16)	107(44)	128(53)	116(44)
M 10	.3159(16)	.0878(17)	96(47)	92(57)	78(44)
M 11	.4046(4)	.0735(10)	-30(16)	-18(22)	6(17)
M 12	.4917(14)	.0709(18)	56(31)	14(59)	54(36)
M 13	.2891(14)	.2374(12)	96(38)	7(28)	32(30)
M 14	.3842(8)	.2167(9)	-25(17)	-55(18)	-45(14)
M 15	.4661(9)	.1963(11)	-28(18)	-3(25)	2(19)
M 16	.5526(10)	.1755(12)	-14(25)	21(32)	17(25)
M 17	.3587(11)	.3555(14)	19(30)	80(43)	64(32)
M 18	.4517(14)	.3430(16)	76(36)	89(43)	78(35)
M 19	.5309(9)	.3172(11)	-35(17)	-25(21)	-15(16)
M 20	.6190(9)	.2919(11)	-18(20)	30(28)	21(21)
M 21	.4142(11)	.4741(11)	20(27)	-9(23)	-26(20)
M 22	.5808(17)	.4442(18)	195(52)	216(61)	184(52)
M 23	.5920(9)	.4327(9)	-28(17)	-34(19)	-9(16)
M 24	.6742(29)	.4037(26)	183(82)	193(91)	103(72)
M 25	.8296(15)	.3862(16)	86(41)	46(44)	38(36)
M 26	.9263(11)	.3704(17)	-1(21)	158(52)	45(29)
M 27	.0745(13)	.4633(14)	49(30)	26(36)	-1(27)
M 28	.9420(8)	.0818(10)	-55(13)	-76(23)	-16(15)
M 29	.0562(9)	.2890(10)	-13(19)	-38(20)	-17(16)
M 30	.1407(10)	.2729(10)	-6(19)	-17(27)	-9(20)
M 31	.2274(9)	.2512(9)	1(20)	-42(19)	-8(16)
M 32	.1212(11)	.4087(13)	26(30)	77(45)	79(34)
M 33	.2033(17)	.3872(12)	34(31)	9(29)	9(27)
M 34	.2914(14)	.3733(11)	73(33)	-35(19)	18(21)
M 35	.3607(10)	.4935(11)	5(21)	-2(27)	20(21)
M 36	.7368(8)	.5009(8)	-25(14)	-75(12)	-26(11)
M 37	.1816(11)	.0251(16)	-14(23)	104(59)	7(31)
M 38	.2736(14)	.0163(13)	164(54)	65(46)	20(36)
M 39	.6798(9)	.2806(10)	-23(17)	-10(23)	10(18)
M 40	.7575(15)	.2511(16)	96(41)	91(54)	74(42)
M 41	.8544(8)	.2404(10)	-36(17)	-33(19)	-32(15)
M 42	.9167(11)	.2249(14)	9(25)	71(40)	41(27)
M 43	.8467(15)	.0988(15)	94(42)	52(45)	43(38)
M 44	.7927(8)	.1216(11)	58(12)	7(26)	-24(15)
M 45	.7039(10)	.1390(11)	-12(21)	12(28)	31(21)
M 46	.6146(16)	.1576(13)	92(40)	-20(26)	-50(26)
M 47	.5533(13)	.0403(14)	34(30)	39(33)	21(28)
M 48	.6459(24)	.0126(19)	197(85)	92(43)	132(55)
M 49	.9711(6)	.9429(10)	-22(16)	-51(15)	-43(13)
M 50	.8772(13)	.9643(12)	53(33)	-1(30)	12(26)
M 51	.9928(19)	.8040(24)	135(52)	183(74)	50(53)
M 52	.9028(10)	.8220(10)	1(18)	-33(21)	-7(17)
M 53	.8152(9)	.8393(10)	-12(21)	-36(19)	-21(17)

Atom	x	z	β_{11}	β_{33}	β_{13}
M 54	.0113(9)	.7111(13)	-35(16)	68(37)	14(21)
M 55	.0365(11)	.5669(11)	8(22)	-31(20)	-23(17)
M 56	.9410(12)	.5857(13)	45(31)	-3(27)	-10(25)
M 57	.6890(9)	.9209(9)	-10(18)	-35(21)	5(17)
M 58	.5995(7)	.9349(10)	-5(12)	-22(19)	-58(12)
M 59	.5038(9)	.9515(10)	-34(15)	-11(27)	-26(16)
M 60	.8205(11)	.7987(11)	4(30)	-31(19)	-52(19)
M 61	.5339(8)	.8139(10)	40(13)	1(26)	13(17)
M 62	.4535(11)	.8336(12)	33(28)	-3(30)	-26(24)
M 63	.5600(8)	.6757(11)	-34(15)	-4(26)	-3(18)
M 64	.4729(9)	.7011(9)	-7(19)	-54(18)	-27(14)
M 65	.3849(9)	.7138(12)	-21(15)	11(28)	5(17)
M 66	.1875(8)	.6686(9)	-42(13)	-46(15)	-31(11)
M 67	.1036(11)	.6937(12)	26(28)	16(31)	8(25)
M 68	.1222(14)	.5458(13)	51(37)	10(41)	1(32)
M 69	.0632(18)	.9102(20)	104(56)	155(77)	-11(54)
M 70	.8501(10)	.7347(12)	-5(21)	-8(25)	-58(19)
M 71	.7658(10)	.7548(10)	1(20)	-35(21)	-21(17)
M 72	.7959(12)	.6135(12)	23(34)	20(34)	23(29)
M 73	.7101(9)	.6364(9)	-22(16)	-67(15)	-26(13)
M 74	.6470(11)	.5103(14)	10(28)	47(36)	33(28)
M 75	.2731(9)	.5113(12)	-19(18)	24(27)	23(20)
M 76	.1944(12)	.5259(15)	15(30)	51(45)	9(31)
M 77	.7309(24)	.9812(24)	210(72)	201(91)	62(68)
M 78	.2385(20)	.9726(30)	141(85)	61(14)	25(84)
M 79	.1398(22)	.7734(18)	360(90)	98(46)	200(58)
M 80	.0626(28)	.7869(28)	320(90)	190(11)	180(84)
M 81	.1236(18)	.9060(15)	140(57)	15(31)	24(36)
M 82	.2098(28)	.9070(24)	193(78)	114(86)	199(84)
M 83	.2966(8)	.8715(10)	-38(12)	-34(18)	-23(13)
M 84	.7198(16)	.8523(14)	148(58)	36(31)	52(33)
M 85	.7897(13)	.9699(24)	2(40)	50(32)	73(61)
M 86	.3644(14)	.0046(18)	58(51)	145(67)	43(39)
M 87	.6169(21)	.6477(20)	170(51)	137(60)	78(48)
M 88	.6724(33)	.7844(28)	177(61)	192(79)	-40(75)
M 89	.5562(9)	.5370(12)	-10(20)	36(31)	33(25)
M 90	.4494(7)	.9897(8)	-74(9)	-57(14)	52(9)
M 91	.3694(14)	.8503(14)	62(40)	30(39)	7(34)
M 92	.3201(18)	.7331(16)	102(40)	71(41)	-110(33)
M 93	.9405(13)	.7115(12)	96(39)	26(31)	71(32)
M 94	.8961(9)	.5978(9)	-20(14)	-44(17)	-16(13)
M 95	.8223(9)	.4795(12)	-20(16)	33(31)	20(20)
M 96	.2482(10)	.6399(12)	6(26)	52(40)	33(30)
M 97	.3397(10)	.8266(11)	-6(17)	7(27)	5(19)
M 98	.4186(13)	.8069(10)	86(37)	-11(22)	47(26)
M 99	.4907(11)	.5742(12)	11(30)	26(30)	-26(23)

ATOM	X	Z	ATOM	X	Z
O 1 (a)	-0.002(10)	-0.003(10)	O 26	0.813(10)	0.042(10)
O 2	0.076(9)	0.042(10)	O27	0.031(9)	0.298(10)
O 3	0.150(9)	0.168(11)	O 28	0.092(10)	0.281(11)
O 4	0.055(10)	0.200(11)	O 29	0.191(10)	0.284(11)
O 5	0.062	0.120	O 30	0.287(10)	0.317(11)
O 6	0.322(10)	0.003)(11)	O 31	0.175(10)	0.329(12)
O 7	0.224	0.014	O 32	0.080(10)	0.340(10)
O 8	0.350(10)	0.072(11)	O 33	0.260(10)	0.389(11)
O 9	0.446(5)	0.060(10)	O 34	0.412(10)	0.266(11)
O 10	0.274(9)	0.089(10)	O 35	0.318(10)	0.297(11)
O 11	0.246(9)	0.154(10)	O 36	0.143(10)	0.230(11)
O 12	0.877(10)	0.075(11)	O 37	0.496(10)	0.258(11)
O 13	0.527(9)	0.175(10)	O 38	0.404(10)	0.146(11)
O 14	0.661(11)	0.146(12)	O 39	0.494(10)	0.333(12)
O 15	0.760(10)	0.053(11)	O 40	0.411(5)	0.185(10)
O 16	0.750(11)	0.131(12)	O 41	0.476(10)	0.391(11)
O 17	0.596(10)	0.023(11)	O 42	0.560(10)	0.311(11)
O 18	0.585(9)	0.094(10)	O 43	0.724(11)	0.270(12)
O 19	0.680(10)	0.004(11)	O 44	0.736(9)	0.214(11)
O 20	0.986(10)	0.071(12)	O 45	0.648(10)	0.228(11)
O 21	0.876(10)	0.154(11)	O 46	0.580(9)	0.220(10)
O 22	0.969(10)	0.143(11)	O 47	0.714(10)	0.345(11)
O 23	0.830(10)	0.174(11)	O 48	0.831(11)	0.245(11)
O 24	0.892(10)	0.083(11)	O 49	0.882(10)	0.379(11)
O 25	0.909(10)	0.025(11)	O 50	0.802(10)	0.326(11)
O 51	0.892(10)	0.299(11)	O 78	0.397(9)	0.549(10)
O 52	0.968(10)	0.203)(10)	O 77	0.449(9)	0.526(10)
O 53	0.935(9)	0.268(10)	O 78	0.513(9)	0.535(10)
O 54	0.969(9)	0.360(10)	O 79	0.475(9)	0.682(10)
O 55	0.788(10)	0.368(11)	O 80	0.386(9)	0.609(10)
O 56	0.233(11)	0.449(12)	O 81	0.422(11)	0.707(12)
O 57	0.088(10)	0.472(11)	O 82	0.509(11)	0.662(12)
O 58	0.020(9)	0.449(10)	O 83	0.146(10)	0.686(11)
O 59	0.151(11)	0.467(11)	O 84	0.096(9)	0.791(10)
O 60	0.160(10)	0.393(11)	O 85	0.195(10)	0.765(11)
O 61	0.006(10)	0.499(11)	O 86	0.277(9)	0.742(11)
O 62	0.314(10)	0.497(11)	O 87	0.503(11)	0.753(12)
O 63	0.326(10)	0.430(12)	O 88	0.418(10)	0.773(11)
O 64	0.383(10)	0.417(11)	O 89	0.350(9)	0.789(10)
O 65	0.471(10)	0.473(10)	O 90	0.252(9)	0.791(10)
O 66	0.546(9)	0.444(11)	O 91	0.256(11)	0.877(11)
O 67	0.686(10)	0.499(11)	O 92	0.351(10)	0.858(11)
O 68	0.650(9)	0.418(10)	O 93	0.484(11)	0.820(12)
O 69	0.772(10)	0.406(11)	O 94	0.522(9)	0.684(10)
O 70	0.524(10)	0.454(11)	O 95	0.683(11)	0.525(11)
O 71	0.077(10)	0.548(11)	O 96	0.586(10)	0.595(11)
O 72	0.064(10)	0.625(11)	O 97	0.663(10)	0.579(11)
O 73	0.055(10)	0.700(11)	O 98	0.768(11)	0.556(11)
O 74	0.253(10)	0.684(11)	O 99	0.850(9)	0.541(11)
O 75	0.209(9)	0.596(10)	O100	0.910(10)	0.522(11)

ATOM	X	Z	ATOM	X	Z
O 101	0.985(10)	0.568(11)	O 126	0.533(9)	0.941(10)
O 102	0.837(10)	0.681(11)	O 127	0.631(10)	0.921(11)
O 103	0.752(11)	0.621(12)	O 128	0.828(10)	0.956(10)
O 104	0.662(11)	0.646(12)	O 129	0.931(10)	0.956(11)
O 105	0.595(10)	0.741(11)	O 130	0.171	0.100
O 106	0.650(10)	0.714(11)	O 131	0.350	0.152
O 107	0.833(10)	0.682(11)	O 132	0.450	0.125
O 108	0.979(10)	0.649(11)	O 133	0.530	0.085
O 109	0.948(10)	0.809(11)	O 134	0.052	0.376
O 110	0.892(9)	0.723(11)	O 135	0.580	0.365
O 111	0.816(10)	0.749(11)	O 136	0.670	0.339
O 112	0.728(11)	0.766(12)	O 137	0.238	0.520
O 113	0.576(11)	0.806(12)	O 138	0.320	0.547
O 114	0.582(9)	0.879(10)	O 139	0.300	0.634
O 115	0.671(10)	0.852(11)	O 140	0.916	0.658
O 116	0.762(9)	0.837(11)	O 141	0.740	0.690
O 117	0.856(10)	0.828(11)	O 142	0.176	0.838
O 118	0.844(9)	0.860(10)	O 143	0.096	0.856
O 119	0.021(9)	0.929(10)	O 144	0.034	0.868
O 120	0.095(9)	0.925(10)	O 145	0.168	0.904
O 121	0.158(9)	0.970(10)	O 146	0.484	0.889
O 122	0.238(11)	0.949(12)	O 147	0.762	0.914
O 123	0.341(9)	0.911(10)	O 148	0.940	0.880
O 124	0.405(10)	0.981(11)			
O 125	0.425(9)	0.907(10)			

Standard deviations are given in parenthesis and refer to the least significant places of the preceding number. The anisotropic thermal parameters are of the form $T = \exp[-(\beta_{11}h^2 + 2\beta_{13}hl + \beta_{33}l^2)]$. M atoms represent composite atoms of (Nb + O). (a) Parameters listed for oxygen atoms are those obtained from least-squares cycle number 16. An isotropic temperature factor of 0.052 Å was used for each oxygen atom, based upon the value obtained for the overall temperature factor from least-squares cycle number 10.

5. DESCRIPTION OF THE STRUCTURE OF THE β-POLYMORPH

The structure of the unit-cell of the β-polymorph is shown in [010] projection in figure 8. The blocks of distorted, corner-sharing octahedra are either all 4x3 at one level or 4x4 and 3x3 at another level. The two levels are separated by a distance of b/2 Å along [010].

The idealized structure is shown in figure 9 and differs from the real structure in that the blocks are composed of regular octahedra with no distortions at the shear planes.

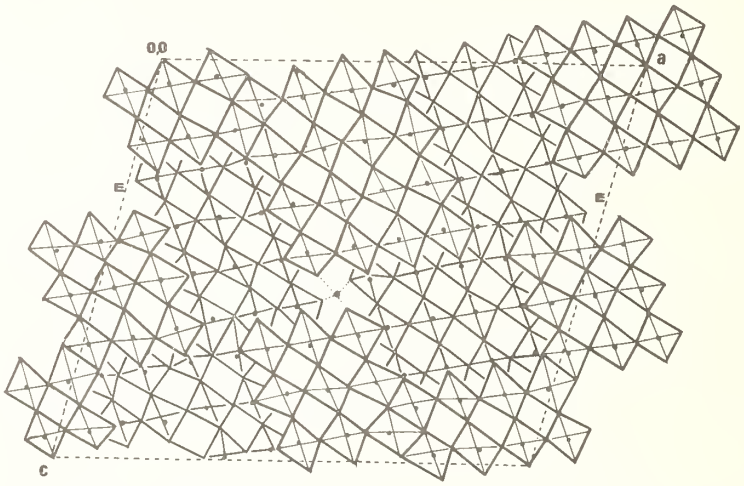

Fig. 8. An (010) projection of the real structure of the β-polymorph of $ZrO_2 \cdot 16Nb_2O_5$. One unit-cell is shown (dashed) which contains 99 metal and 246 oxygen atoms. One metal atom has tetrahedral coordination. The other O-position is empty (marked with an E).

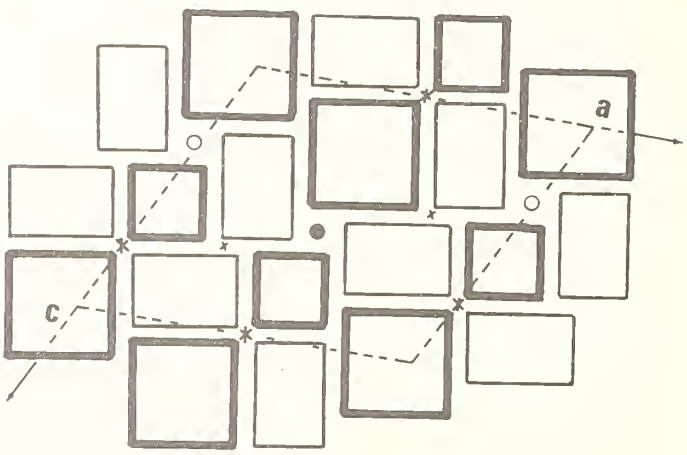

Fig. 9. An idealized block diagram of the unit-cell of the β-polymorph. The full circle represents an atom in tetrahedral coordination (O-position), the open circle is an empty O-position, intersecting shear planes are marked with a cross *, and two of the X-positions are shown.

The 4x3 blocks form strings[3] parallel to [001] in which adjacent blocks are oriented perpendicular to each other while in a direction perpendicular to [001] these blocks are paralleled in pairs with adjacent pairs at right angles to each other. The blocks at the other level again form strings which run parallel and at right angles to c.

The corners of adjacent blocks are joined by either

(i) the sharing of three octahedral edges. There are four of these X-positions in the unit-cell;

(ii) an atom in tetrahedral coordination. There is one 0-position (dark circle) per unit-cell;

(iii) an empty 0-position (open circle). There is one modified 0-position per unit-cell;

(iv) the sharing of one octahedral edge. This new type of block joining is marked by a cross in figure 9. It will be referred to as a Y position.

These are the four different types of block junctions.

Bond distances and angles for individual coordination polyhedra have not been calculated because of the large number of these polyhedra (99) and because of the large standard deviations which make detailed comparisons useless. The interest is rather in the structure at antiphase boundaries and fault areas and in the interpretation of the dots and streaks which appear in lattice image photographs.

6. THE INTERPRETATION OF DOTS AND STREAKS IN LATTICE IMAGE PHOTOGRAPHS OF THE β-POLYMORPH

A surprising feature of the structure of the β-polymorph is that the three 0-positions which were left as such in the trial partial-structure (dotted circles, figure 7) have each been converted to X-positions. Two alternative tetrahedral sites have developed; one site is occupied with a metal atom (shown as a block dot in figure 9) whereas the other tetrahedral site is vacant (shown as an open circle in figure 9). There is only one true 0-position in the unit-cell.

0-positions are regions of high electron density; regions where crystallographic shear planes intersect and where an additional tetrahedrally coordinated metal atom is located. Such positions produce dark dots in lattice image photographs.

Similar positions of high electron density are shown as crosses in figure 9. These Y-positions are at the intersection of shear planes and their contrast effect in transmission micrographs is therefore unknown. If, however, one assumes that they also give rise to a dark dot then the regular alternation of these positions and the 0-position (* ° * in figure 8) would give rise to a line of dark dots, parallel to c and separated by c/2 Å.

Displaced from the * ° * line by a/2 Å but again parallel to c is a line * ° *. Empty 0-positions, *i.e.*, unfilled tetrahedral sites, have not been observed previously and their contrast effect in transmission micrographs is again unknown. They are, however, regions of appreciable electron density and may very well give rise to a streak, particularly as the intersecting shear planes do not intersect precisely at 0 but are displaced slightly.

When the above positions are represented by either dots or streaks then their spacial distribution, shown in figure 10, can be correlated with the arrangemet of dots and streaks in tramsmission micrograph 3c.

A close inspection of transmission micrograph 3c shows areas of lighter contrast which lie between the dark dots and streaks adjacent to each other in the same (102) planes. These lighter areas can be correlated with X-positions (fig. 9) which have been shown by Allpress [4] to be distinguishable from 0 (or Y) positions by their lighter contrast.

---

[3]What appear to be strings in projection are actually sheets in three dimensions.

465-504 O - 72 - 13

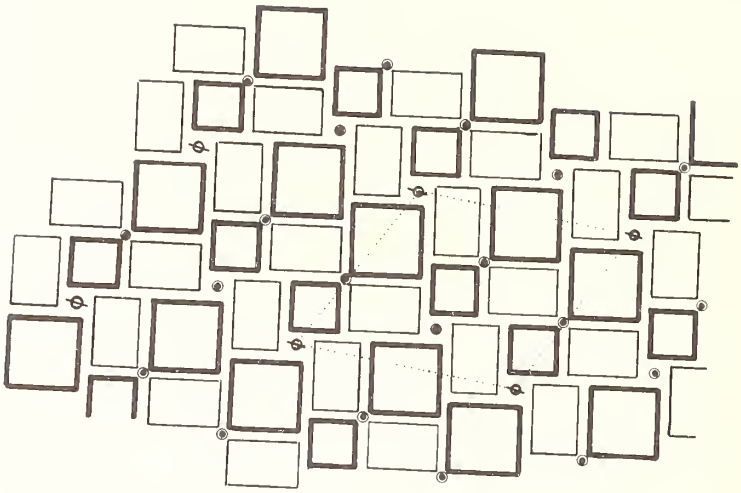

Fig. 10. A domain of the β-polymorph. One unit-cell is shown dotted. O- and Y-positions are marked as large dots. Empty O-positions are streaked. The distribution of these block junctions agrees with the distribution of dots and streaks on lattice image 3c.

The distribution of the four various types of block junctions therefore satisfactorily explains in terms of numbers, spacial arrangement and contrast, the features of the transmission micrograph shown in figure 3c.

7. THE STRUCTURE OF THE γ-POLYMORPH

The structure of the β-polymorph has been described above in terms of sheets of blocks of octahedra which run parallel to (100). A sheet of alternating 4x4 and 3x3 blocks has on either side of it a sheet of 4x3 blocks. These sheets can be displaced parallel to c but remain in the same sequence along a to give the arrangement shown in figure 11. This structure has the same composition as the β-polymorph but the unit-cell has a = b 35.8 Å The structure is that of the γ-polymorph reported by Allpress and Roth.

The distribution of dots and streaks in transmission micrographs of the γ-polymorph can be correlated with the distribution of O (and Y) positions and empty O-positions is the structure drawn in figure 11. The x-positions, located midway between any four adjacent dots and streaks can be identified on the micrograph as areas of lighter contrast.

It is thus possible to explain the contrast features of lattice images of the γ-polymorph in terms of the distribution of the various types of block junctions in the structure.

8. MICRODOMAIN INTERGROWTH AND FAULT STRUCTURE

The faults evident in micrographs 3c and d are labelled as P, Q, and R. Those labelled Q are one unit-cell wide and involve a displacement along [001] of approximately c/2 Å. (Most readily seen in figure 3d). Faults R are two unit-cells in width and involve the domains either side of it in a relative displacement of c Å along [001].

Faults Q and R can be regarded as the intergrowth of domains of the γ form in a matrix of the β form. These structures are shown in figures 12 and 13.

Faults of the P type are of a different character; the displacement along [001] is approximately c/4 Å. Figure 14 illustrates the structure of the P fault. The domain on the left hand side of the fault is displaced by half a unit cell in the b direction from the domain on the right hand side of the fault. Thus the 4x3 blocks on the left hand side are at the same level as the 3x3 and 4x4 blocks on the right hand side of the P fault.

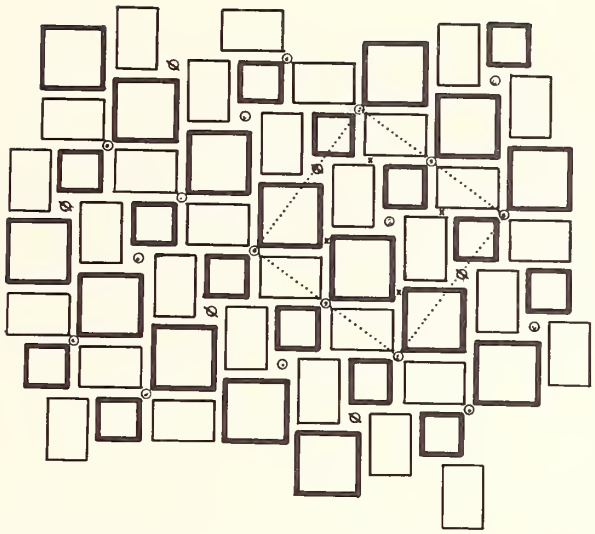

Fig. 11. A domain of the γ-polymorph. A unit-cell is shown dotted. The different types of block junctions are marked as in the β-polymorph and correlate with the contrast shown in transmission micrograph 3c.

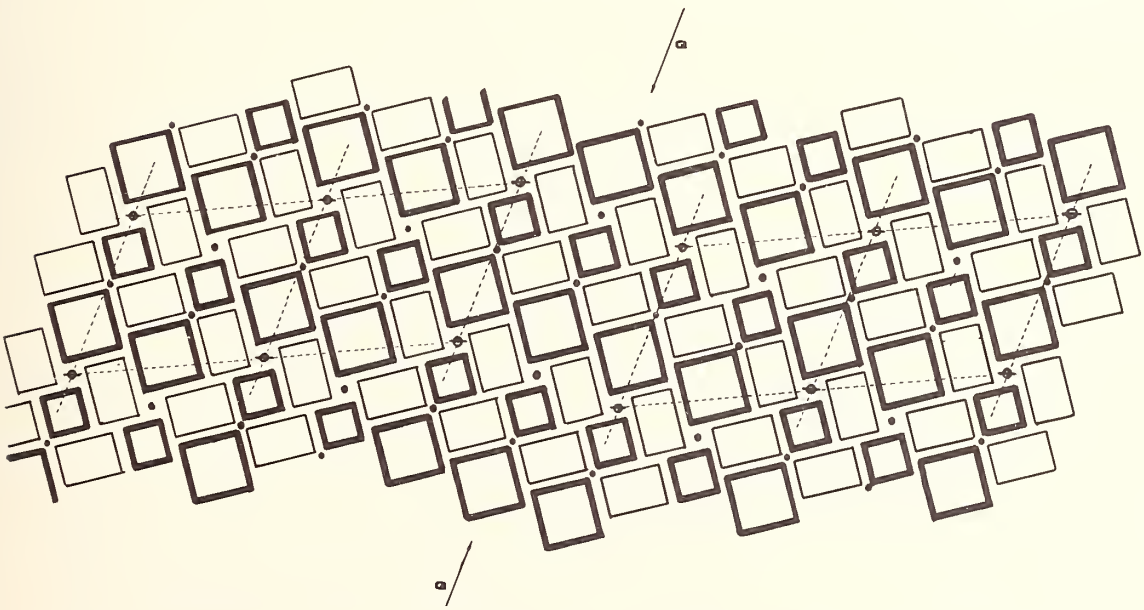

Fig. 12. Structural details at the Q fault. The Q fault can be regarded as a slab of the γ-polymorph, one unit-cell wide, inserted between two domains of the β-polymorph.

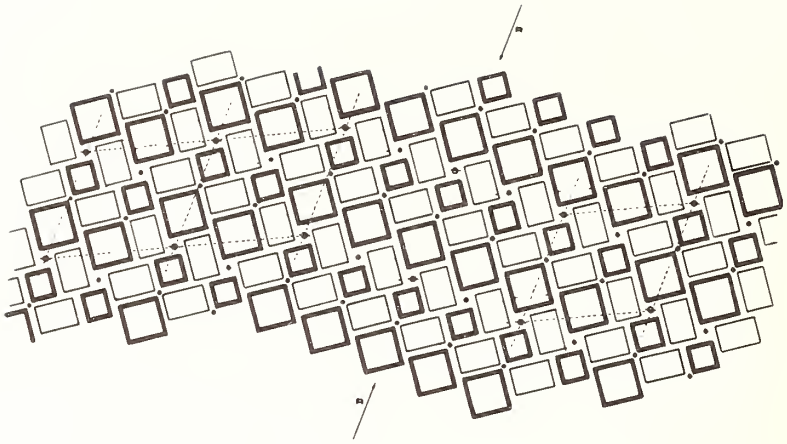

Fig. 13. Structural details at an R fault. A slab of the γ-polymorph, two-unit cells wide, gives rise to a displacement of cÅ along [001] in the adjacent domains of the β-polymorph.

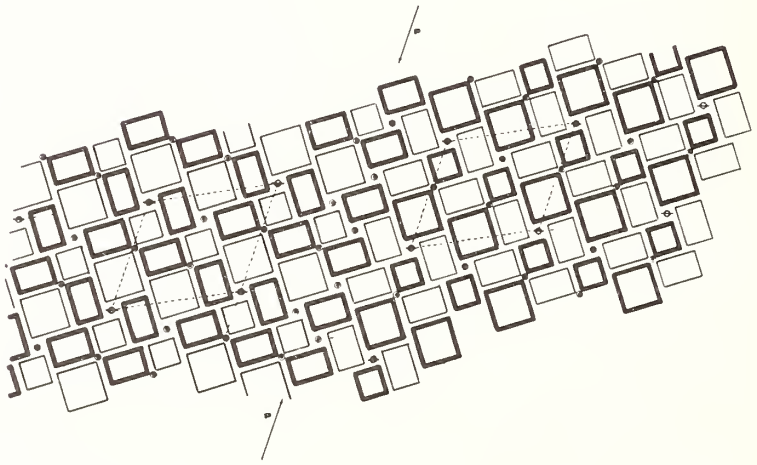

Fig. 14. Structural details at a p fault. Domains either side of the fault are displaced approximately c/4Å along [001].

9. DISCUSSION

A unit cell of either the β or γ polymorph contains 99 metal atoms and 246 oxygen atoms, which corresponds to a composition of $ZrO_2.16Nb_2O_5$. Each unit cell contains the unit $3ZrO_2.48Nb_2O_5$.

It would appear, therefore, that the β and γ forms are not polymorphs of α-$ZrO_2.12Nb_2O_5$ but are polymorphic forms of a substance with stoichiometry $ZrO_2.16Nb_2O_5$.

Allpress and Roth observed that the initial product of their reaction between ZrO_2 and Nb_2O_5 was slightly off stoichiometry and contained slabs of $ZrNb_{24}O_{62}$ and H-Nb_2O_5. These intergrowing domains were readily detected on transmission micrographs of the α form (figure 3a). It would be reasonable to assume that the effect of prolonged annealing is to react the excess Nb_2O_5 with the domains of $ZrO_2.12Nb_2O_5$ to form a new compound(s) *e.g.*, with composition $ZrO_2.16Nb_2O_5$. For such a reaction to occur there would need to be twice as many intergrowth slabs of Nb_2O_5 than appear in figure 3a. This may be the case since the crystal area imaged is but a small fraction of the bulk specimen.

The crystal structure as it stands is the result of the combined use of x-ray diffraction methods and electron diffraction and microscopy techniques. Atomic coordinates are derived from the x-ray data but the identification of intergrowth domains and the use of contrast features to modify subcell structure can only be made using electron optical data.

The work described above represents an attempt to correlate the contrast features of electron micrographs with structure. We believe that the dots and streaks of varying intensities, which result from imaging with the electron beam precisely parallel to the crystallographic *b* axis, can be correlated with the different types of block junctions that occur in the structure of $ZrO_2.16Nb_2O_5$.

We have seen transmission micrographs at this conference [12] in which the contrast features are not merely dots and streaks; these micrographs enable the actual block sizes to be determined merely by inspection. It is clear that a knowledge of block sizes would enable a much better trial structure to be propounded and thereby reduce the uncertainty and the work involved in the refinement of the real structures of these very complicated oxides.

10. ACKNOWLEDGEMENT

We are indebted to John Allpress and Robert S. Roth for permission to reproduce figures 1, 2, and 3 and for providing a sample of the zirconium niobium oxide.

11. REFERENCES

[1] Roth, R. S., unpublished results.
[2] Roth, R. S., and Wadsley, A. D., Acta Cryst., 18, 724 (1965).
[3] Allpress, J. G., and Roth, R. S., J. Solid State Chem., 2, 366 (1970).
[4] Allpress, J. G., Mat. Res. Bull., 4, 707 (1969).
[5] Buerger, M. J., in "Vector Space", John Wiley and Sons., Inc., New York, p. 227 (1959).
[6] Busing, W. R., Martin, K. O., and Levy, H. A., ORFIS, USAEC Report ORNI-TM-305 (1962).
[7] Cromer, D. T., and Mann, J. B., Acta Cryst., A24, 321 (1968).
[8] Dauben, C. H., and Templeton, D. H., Acta Cryst., 8, 841 (1955).
[9] Busing, W. R., and Levy, H. A., Acta Cryst., 22, 457 (1967).
[10] Hoppe, W., Angew, Chem., 77, 484 (1965).
[11] Stephenson, N. C., and Roth, R. S., Acta Cryst., B27, 1010 (1971).
[12] Allpress, J. G., "The Application of Electron Optical Techniques to High Temperature Materials", page 87, this volume.

DISCUSSION

R. S. Roth: I don't want you to feel bad when you say that the composition of the crystal might be different from what I had originally made it up to be. Since the paper that John Allpress and I published on this phase[1], I have been trying to obtain equilibrium data, hopefully, for the polymorphic transitions. I believe that they might have stable equilibrium relationships. So I have re-made a lot of specimens in the high Nb_2O_5 end of this system using the same oxides, the same two end-members (from the same batches) that I had used ten years ago. I found that it was completely impossible to duplicate the number of phases present in a given starting composition two days in a row. I came to the conlcusion that the zirconia that I was using, which was an ultrapure, ultra-spec-pure, zirzonia, had a very abnormal distribution of volatile hydrated material with amorphous zirconia. One can simply not accurately weigh out this "amorphous zirconia". Therefore, it was necessary for me to go to a different technique. I had a metallurgist arc-melt titanium and niobium metal in the proper proportions and I oxydized it. A 10 gram batch at 600 °C took about a month to completely oxydize. You end up with a nice, almost amorphous oxide that you can then equilibrate at higher temperatures. I can now get a single phase x-ray pattern that looks very much like what my old x-ray pattern looked like at the 12 to 1 composition. I don't know what the 16 to 1 ratio would give me.

N. C. Stephenson: Could I ask John Allpress a question, since we didn't ask John questions? In your photographs we saw white features which were the tunnels in the blocks and then we saw the shear planes appearing as dark rims, but you couldn't see what was at the block junctions, everything was just black. Now is it possible to identify the different types of block junctions, not just the tunnels by contrast features?

J. G. Allpress: The detail that you actually see depends very critically on focus and so on, but in fact you can see all those features in the pictures that I showed which were taken at Arizona State (see Allpress, Figs. 14, 15.) The resolution in the pictures I took previously (see Stephenson, Fig. 3) was insufficient to reveal the same details. I'm sure that some good high-resolution images of the same material, recorded under the appropriate conditions of focus, etc., should provide the answer, and enable us to reconcile the various observations which we have made already.

S. Andersson: May I just ask, what kind of R-factor did you get?

N. C. Stephenson: Well, I was afraid you would ask me that. The R at present is fourteen percent. The reason for this is that it takes three and a half hours a cycle and the R comes down by one per cent. The reason for this I believe is....

S. Andersson: But it's going down anyhow?

N. C. Stephenson: Oh, it's coming down every time. As soon as we can get a Saturday to spare, we race in and use the computer for 3 1/2 hours, and drop our R. It's come down from 43 to 14 in about one per cent steps.

S. Andersson: That's very good!

N. C. Stephenson: There is a lot of interdependence of parameters in these supercell structures. Atoms that aren't related by supercell symmetry are related by the subcell symmetry, and the correlation coefficients are extremely high. Standard deviations are very high. The standard deviations for the metal atoms in this structure are .05 of an angstrom and that is due to parameter dependence, as Dr. H. Evans very well knows with his barium titanate.

[1] J. G. Allpress and R. S. Roth, Jour. Solid State Chem. 2, 366 (1970)

National Bureau of Standards Special Publication 364, Solid State Chemistry, Proceedings of 5th Materials Research Symposium, issued July 1972.

SUPERSTRUCTURE OF THE ORTHORHOMBIC $Nb_2O_5 \cdot 6ZrO_2$ TYPE PHASE(S) IN THE Nb_2O_5-ZrO_2 AND Ta_2O_5-ZrO_2 SYSTEMS

Robert S. Roth, J. L. Waring, W. S. Brower and H. S. Parker

National Bureau of Standards
Washington, D.C. 20234

The phase previously described as $Nb_2O_5 \cdot 6ZrO_2$ has been found to have a composition varying from a Nb_2O_5:ZrO_2 ratio of about 2:9 to 2:15. The solidus temperatures of the intermediate compositions studied seem to follow a smooth curve from 1435 °C to 1640 °C rather than a stepwise function expected from a series of compounds. The x-ray diffraction powder patterns indicate a series of phases with subcells similar to α-PbO_2 and orthorhombic symmetry. Superstructure lines indicate that these phases have a multiple *b* axis. The composition 2:9 corresponds approximately to a structure with a *b*-axis multiplicity of seven. The 2:11 composition appears to have a multiplicity of eight, 2:13 a multiplicity of nine and the last composition 2:15, a multiplicity of ten. The intermediate compositions 1:5, 1:6 and 1:7 show superstructure lines halfway between those of the simpler phases on either side, corresponding to multiplicities of 15, 17 and 19 respectively. These multiplicities and compositions thus appear to belong to a homologous series $M_{n-1}O_{2n}$ where *n* varies from 14-20. However the phase equilibria data do not rule out the possibility of a homologous series M_nO_{2n+1}. Compositions in the Ta_2O_5-ZrO_2 system apparently have the same composition *vs* multiplicity arrangement, however, their melting points are considerbly higher.

Single crystals of these phases, prepared by both direct cooling of a melt and utilization of a barium vanadium oxide eutectic flux, have enabled the multiplicities to be completely verified and are now being used for crystal structure determinations. This stabilization of the high pressure form of ZrO_2 (the orthorhombic structure type) by means of higher valence cations provides an alternate process to the anion deficient stabilization of the cubic fluorite phase.

Key words: Equilibrium; Nb_2O_5-ZrO_2; ordered defects; α-PbO_2-type phase(s); single crystals; superstructure; Ta_2O_5-ZrO_2.

1. INTRODUCTION

Zirconium dioxide has long been an attractive material for high temperature applications needing only to be "stabilized" to avoid disruptive phase transitions. Unfortunately most of the additives used for "stabilization" have certain drawbacks and the material is often "destabilized" with use. The systems Nb_2O_5-ZrO_2 [1,2][1] and Ta_2O_5-ZrO_2 contain a phase which appears similar to the α-PbO_2 structure type [3] instead of the "stabilized" cubic (or tetragonal) ZrO_2 phases found for MgO, CaO or Y_2O_3 stabilized ZrO_2. This phase is therefore either cation deficient or anion excess as opposed to the anion deficient phases found in the other systems.

ZrO_2 and HfO_2 are both known to have a high pressure polymorph with orthorhombic symmetry [4,5,6] (fig. 1). The published x-ray pattern [4,6] of this high pressure phase is very similar to that of the α-PbO_2-type structure. Apparently the high pressure phase is stabilized by lowering the average radius of the cation with addition of Nb^{+5} or Ta^{+5}.

---

1 Figures in brackets indicate the literature references at the end of this paper.

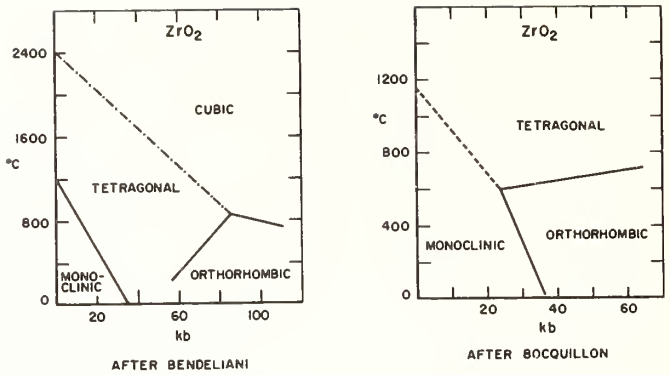

Fig. 1. Pressure-temperature phase diagrams for ZrO_2, after Bendeliani et al. [4] and Bocquillon and Susse [5]. The polymorph labelled orthorhombic has an x-ray pattern similar to α-PbO_2.

However no study has been made of the nature of the defects which occur in this system, although Trunov et al. [2] have indicated the probable existence of a superstructure.

One of the most interesting problems in the field of solid state chemistry is the nature of the non-stoichiometric phases which occur in systems of this type. By a combination of phase equilibria studies, crystal growth, x-ray powder and single crystal diffraction and electron microscopy and diffraction, the methods by which nature compensates a crystallographic phase for non-stoichiometry are gradually beginning to emerge.

The block principle, crystallographic shear and Wadsley defects have been shown to be the major factors affecting non-stoichiometry in Nb_2O_5-type phases [7,8,9]. Ordered oxygen "vacancies" or "distortion planes" causing localized reduced cation coordination is apparently the controlling factor for the appearance of superstructure in low-Ta_2O_5-type phases [10,11]. "Stabilized" cubic ZrO_2 appears to have random anion vacancies which may be ordered at low temperatures with the addition of small cations [12]. The systems Nb_2O_5-ZrO_2 and Ta_2O_5-ZrO_2 have therefore been re-examined to determine the nature of the non-stoichiometric orthorhombic phase(s) found in these systems.

2. SPECIMEN PREPARATION AND TEST METHODS

One gram batches of the appropriate compositions of ZrO_2 and either Nb_2O_5 or Ta_2O_5 were weighed, mixed in a mechanical shaker and pressed into disks at about 10^4 psi. The disks were placed on Pt setters and calcined in air at 1000 °C for 10 hours, ground, repressed and recalcined at 1350 °C for 60 hours. For both heat treatments the specimens were heated and cooled at the rate of approximately 3°C/min. After these preliminary heat treatments the specimens were ground and small portions placed in Pt tubes and heated in the quenching furnace at appropriate temperatures and for various periods of time.

The Pt tubes, open on one end, were quenched either into ice water or onto a chilled metal plate, opened and examined by x-ray diffraction techniques. These specimens were invariably too fine grained for single crystal x-ray diffraction methods. A high angle recording Geiger counter-powder diffractometer and Ni filtered Cu radiation was used in the study. The Geiger counter was rotated at 1/4 deg/min and radiation was recorded on the chart at 1 deg/2θ/in. The unit cell dimensions reported can be considered accurate to about ± 2 in the last decimal place listed.

In order to obtain unambiguous indexing of the powder diffraction patterns it was necessary to grow small single crystals. This was accomplished in two ways. One consisted of direct cooling of a melt rich in Nb_2O_5 (60 mol% Nb_2O_5-40 mol% ZrO_2) which had been heated by induction in a Pt crucible and allowed to slowly cool through the liquidus before being rapidly cooled.

The second method consisted of mixing various proportions of Nb_2O_5 and ZrO_2 with a premelted BaO - V_2O_5 eutectic flux (32.2 wt% BaO:67.8 wt% V_2O_5). These mixtures were heated to 1200 °C and then cooled very slowly (1°/hour) to 800 °C and removed from the furnace.

3. RESULTS AND DISCUSSION

The experimental data is shown in table 1 and the phase diagram derived from this data is shown in figure 2. This diagram differs appreciably from the previously published phase diagram for this system [1] (fig. 3). The orthorhombic phase(s) is shown to have considerably less area than previously thought and the composition and temperature of the maximum

Table 1

Experimental Data

Composition[a] Nb_2O_5 Mol %	ZrO_2 Mol %	Heat treatment Temp[b] °C	Time hrs	Physical Observation	X-ray diffraction analysis	Unit cell dimensions	Position of characteristic superstructure peak 2θ	Multiplicity m
50	50	---	---	---	orth. phase + 12:1			
(1:1)		1444*	18	considerably melted	orth. phase + L-Nb_2O_5 + extra phase[c]			
		1471	21	do	do			
		1492	67	do	do			
		1550	19	do	do			
		1600	16	prob. comp. melted	orth. phase + L-Nb_2O_5			
		1644	1	do	do			
25	75	---	---	---	orth. phase + 12:1			
(1:3)		1399	19	not melted	do			
		1411	21	do	do			
		1423	20	do	do			
		1443	20	partially melted	orth. phase + L-Nb_2O_5 + extra phase[c]			
20	80	---	---	---	orth. phase + 12:1		40.05	
(1:4)		1379	16	not melted	do		40.00	
		1400[d]	60	do	do		39.95	
		1423[e]	17	---	orth. phase + L-Nb_2O_5		39.95	
		1412	64	---	do		39.98	
		1459	20	partially melted	do		39.85	
18.18	81.82	---	---	---	orth. phase + 12:1		40.00	
(2:9)		1400[d]	60	---	orth. phase + L-Nb_2O_5		39.95	
		1430	163	---	do		39.95	
		1436	72	---	do		39.95	
16.67	83.33	---	---	---	orth. phase		39.95	
(1:5)		1400[d]	572	no melting	do	a=4.947, b=5.137×15 c=5.288	39.74	15
		1422[e]	19	do	do		39.75	
		1438[f]	336	---	---			
		1452	21	partially melted	orth. phase + L-Nb_2O_5		39.65	
		1475	19	do	do		39.58	
		1492	64	do	do		39.50	
		1550	114	do	do		39.25	
15.38	84.62	---	---	---	orth. phase		39.70	
(2:11)		1472	17	not melted	do		39.55	
		1489	64	do	do	a=4.959, b=5.132×8 c=5.290	39.45	8
		1502	336[f]	---	---			
		1508	17	partially melted	orth. phase + L-Nb_2O_5		39.45	
14.28$_5$	85.71$_5$	---	---	---	orth. phase		39.40	
(1:6)		1400[d]	572	not melted	do		39.31	
		1432	192	do	do		39.40	
		1482	69	do	do		39.32	
		1499	86	do	do	a=4.965, b=5.126×17 c=5.285	39.23	17
		1510	216[f]	---	---			
		1531	21	partially melted	orth. phase + L-Nb_2O_5		39.15	
		1554	144	do	do		39.15	
		1608	17	do	do		38.85	
		1617	1	do	do		38.80	
		1641	17	do	orth. + L-Nb_2O_5 + Mon ZrO_2(?)		38.76	
		1673	2	do	orth. + L-Nb_2O_5 + Mon ZrO_2			
		1676	17	do	do			
13.33	86.67	---	---	---	orth. phase		39.10	
(2:13)		1543	264[f]	---	---			
		1547	20	not melted	orth. phase	a=4.971, b=5.122×9 c=5.285	39.06	9
		1569	16	partially melted	orth. phase + L-Nb_2O_5		39.10	
12.5	87.5	---	---	---	orth. phase		39.02	
(1:7)		1400[d]	572	not melted	do		38.92	
		1417	168	do	do		38.98	
		1546	139	do	do		38.88	
		1412[e]	64	do	do		38.84	
		1566	19	do	do		38.85	
		1575[f]	168	---	---			
		1590	64	not melted	orth. phase	a=4.979, b=5.119×19 c=5.285	38.84	19
		1607	17	partially melted	orth. phase + L-Nb_2O_5		38.80	
11.76	88.24	---	---	---	orth. phase + Mon ZrO_2			
(2:15)		1594	52	not melted	do		38.72	
		1600	16	do	orth. phase	a=4.982, b=5.118×10 c=5.282	38.70	10
		1617	89		do		38.68	
		1626[f]	168	---	---			
		1633	17	not melted	orth. phase		38.65	
		1657	17	partially melted	orth. phase + L-Nb_2O_5 + Mon ZrO_2			
11.11	88.89	---	---	---	orth. phase + Mon ZrO_2		38.70	
(1:8)		1605[f]	240	---	---			
		1606	17	not melted	orth. phase + Mon ZrO_2		38.65	
		1641	16	partially melted	orth. phase + L-Nb_2O_5 + Mon ZrO_2		38.65	
10.53	89.47	---	---		orth. phase + Mon ZrO_2		38.65	
(2:17)								
10	90	---	---		orth. phase + Mon ZrO_2		38.65	
(1:9)								

a/ All specimens were given two preliminary heat treatments of 1000°C - 10 hrs and 1350°C - 60 hrs with heating and cooling rates of about 3°/min.

b/ Unless otherwise specified all specimens were heated in small open Pt tubes and quenched into H_2O after heat treatment by dropping from vertical quench furnace.

c/ Extra phase, probably formed from quenched liquid, appears to be isostructural with High-Ta_2O_5.

d/ Heated in small Pt tube with heating and cooling rates of about 3°/min.

e/ Previous specimen, reheated.

f/ Specimen sent to Dr. J. Allpress for electron diffraction and electron microscope examination.

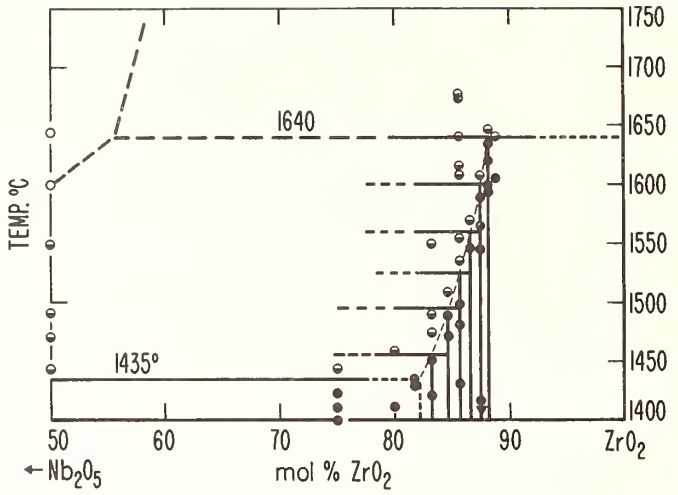

Fig. 2. Proposed phase equilibrium diagram of a portion of the system Nb_2O_5-ZrO_2

- ● - not melted
- ○ - partially melted
- ⊖ - melted
- ▼ - previously equilibrated at higher temperature

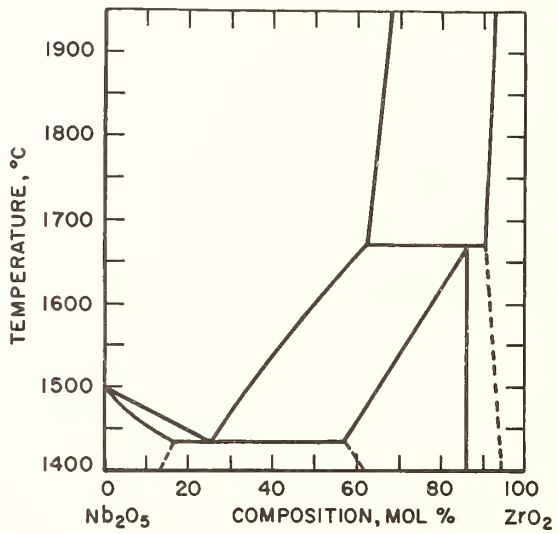

Fig. 3. Previously published phase diagram of the Nb_2O_5-ZrO_2 system after Roth and Coughanour [1].

stability phase is slightly different. The reasons for the differences are probably due to the differences in techniques which in turn are due to improvements in "the state of the art". For the present diagram considerably more specimens were examined; they were heated for much longer periods of time and quenched instead of slow cooled. The solidus temperature could be found with considerably greater accuracy by the onset of the appearance of a low-Nb_2O_5-type phase in the x-ray powder diffraction pattern. Low-Nb_2O_5 is the phase which recrystallizes from a Nb_2O_5 rich liquid upon quenching.

The x-ray powder diffraction pattern of the orthorhombic phase(s) was found to be different in several important details from the two previously published patterns (tables 2 and 3). The stronger lines of the powder pattern could be completely and accurately accounted for on the basis of an α-PbO_2-like orthorhombic subcell with *a*, *b*, and *c* approximately 5 Å. This indexing as listed in table 3 and shown diagramatically in figure 4,

Table 2

Previously Published X-ray Powder Diffraction Patterns of the Orthorhombic Phases in the System Nb_2O_5-ZrO_2.

Reference [1]		Reference [2] 1/
d A	hkℓ	d KX
4.92	100	4.97
3.61	101	3.623
-	-	3.298
-	-	3.140
2.95	111	2.953
-	-	2.839
2.64	002	2.635
2.56	020	2.556
2.48	200	2.488
2.35	012	2.343
2.31	021*	2.326
2.244	201*/210	2.2475
2.179	112*	2.187
2.091	121	2.084
2.020	211*	2.025
-	-	1.952
-	-	1.9363
1.838	022	1.8354
1.809	202	1.8087
1.782	220	1.7816
-	-	1.7417
-	-	1.7246
1.706	212	1.7055
-	-	1.6822
1.660	103	1.6570
-	-	1.6288
1.579	113	1.5756
1.545	131	1.5402
1.511	311	1.5105
1.478	222	1.4762
1.456	023*	
1.435	032	
1.393	123	
1.321	004	
1.281	040/014	
1.243	400	
etc		

1/ hkℓ reported by [2] have the hkℓ values transposed to be in accord with present indexing scheme.

* These hkℓ values do not obey the extinction rules hkℓ:h+ℓ=2n and hkO:k=2n

Table 3

X-ray Powder Diffraction Data for Compositions Which Appear to Correspond to the Homologous Series $M_{n-1}O_{2n}$ (from n=15 to n=20

($Cu_{K\alpha}$ radiation, λ=1.54051)

Orthorhombic Subcell	$Nb_4Zr_{15}O_{40}$					$Nb_4Zr_{14}O_{38}$					$Nb_4Zr_{13}O_{36}$					$Nb_4Zr_{12}O_{34}$					$Nb_4Zr_{11}O_{32}$					$Nb_4Zr_{10}O_{30}$				
	$2Nb_2O_5{\cdot}15ZrO_2$ (m=10)					$Nb_2O_5{\cdot}7ZrO_2$ (m=19)					$2Nb_2O_5{\cdot}13ZrO_2$ (m=9)					$Nb_2O_5{\cdot}6ZrO_2$ (m=17)					$2Nb_2O_5{\cdot}11ZrO_2$ (m=8)					$Nb_2O_5{\cdot}5ZrO_2$ (m=15)				
hkl	d_{obs}	hkl[a]	$2\theta_{obs}$	$2\theta_{calc}$[b]	I[c]	d_{obs}	hkl[a]	$2\theta_{obs}$	$2\theta_{calc}$[b]	I[c]	d_{obs}	hkl[a]	$2\theta_{obs}$	$2\theta_{calc}$[b]	I[c]	d_{obs}	hkl[a]	$2\theta_{obs}$	$2\theta_{calc}$[f]	I[c]	d_{obs}	hkl[g]	$2\theta_{obs}$	$2\theta_{calc}$[g]	I[c]	d_{obs}	hkl[h]	$2\theta_{obs}$	$2\theta_{calc}$[h]	I[c]
---	4.957	110	17.88	17.87	2	4.951	120	17.90	17.89	2	4.946	110	17.92	17.94	2	4.932	120	17.97	17.96	4	4.924	110	18.00	18.00	5	4.910	120	18.05	18.06	3
101	3.621	101	24.56	24.54	37	3.621	101	24.56	24.54	41	3.619	101	24.58	24.57	40	3.616	101	24.60	24.58	42	3.616	101	24.60	24.59	32	3.611	101	24.63	24.62	42
111	2.958	1,10,1	30.19	30.19	285	2.958	1,19,1	30.19	30.19	295	2.956	191	30.21	30.20	280	2.955	1,17,1	30.22	30.21	290	2.955	181	30.22	30.20	275	2.954	1,15,1	30.23	30.22	285
---	2.845	0,18,0	31.42	31.44	5	2.860	0,34,0	31.25	31.24	9	2.882	0.16,0	31.00	31.01	3	2.904	0,30,0	30.76	30.75	8	2.931	0,14,0	30.47	30.47	8	---	0,26,0	---	30.23	---
---	---	---	---	---	---	2.751	1,23,1	32.52	32.51	2	2.742	1,11,1	32.63	32.65	2	2.728	1,21,1	32.80	32.81	2	2.716	1,10,1	32.95	32.97	2	---	1,19,1	---	33.18	---
002	2.641	002	33.92	33.92	60	2.643	002	33.89	33.90	50	2.642	002	33.90	33.90	76	2.642	002	33.90	33.90	72	2.644	002	33.87	33.86	56	2.644	002	33.88	33.88	76
020	2.556	0,20,0	35.05	35.04	106	2.559	0,38,0	35.04	35.03	168	2.561	0.18,0	35.01	35.01	152	2.562	0,34,0	34 99	34.98	170	2.567	0,16,0	34.92	34.93	82	2.567	0,30,0	34.92	34 91	140
200	2.491	200	36.03	36.03	48	2.489	200	36.05	36.05	48	2.484	200	36.13	36.11	85	2.481	200	36.17	36.15	65	2.479	200	36.20	36.20	43	2.473	200	36.30	36.29	68
012	2.347	0,10,2	38.32	38.32	19	2.348	0,19,2	38.30	38.30	14	2.348	092	38.30	38.30	24	2.349	0,17,2	38.28	38.28	27	2.352	082	38.24	38.25	15	2.352	0,15,2	38.23	38.25	26
1/	2.325	0,22,0	38.69	38.67	17	2.317	0,42,0	38.83	38.86	22	2.305	0,20,0	39.05	39.04	14	2.294	0,38,0	39.24	39.25	16	2.291	0,18,0	39.48	39.47	10	2.266	0,34,0	39.74	39.74	15
---	2.251	211	40.03	40.03	4	2.249	221	40.05	40.04	3	2.246	211	40.11	40.11	5	2.245	221	40.14	40.15	3	---	211	---	40.19	---	2.236	221	40.30	40.29	2
---	---	0,12,2	---	---	---	---	---	---	---	---	2.236	0,11,2	40.30	40.32	2	---	---	---	---	---	---	0,10,2	---	40.53	---	---	---	---	---	---
---	2.188	1,21,0	41.22	41.20	8	2.185	1,40,0	41.29	41.29	5	2.180	1.19,0	41.38	41.37	8	2.177	1.36,0	41.45	41.46	7	2.171	1.17,0	41.57	41.55	6	2.165	1,32,0	41.69	41.68	6
---	2.095	291	43.15	43.15	8	2.095	2,17,1	43.14	43.13	10	2.095	281	43.15	43.14	17	---	2,15,1	---	43.13	---	2.097	271	43.10	43.10	10	---	2,13,1	---	43.13	---
121	2.091	1,20,1	43.24	43.25	30	2.091	1,38,1	43.23	43.24	19	2.091	1,18,1	43.23	43.23	30	2.092	1,34,1	43.22	43.22	32	2.093	1,16,1	43.18	43.18	19	2.093	1,30,1	43.18	43.18	35
---	2.086	1,11,2	43.34	43.35	26	2.084	1,21,2	43.38	43.38	19	2.082	1,10,2	43.42	43.43	20	2.080	1,19,2	43.48	43.49	18	2.077	192	43.54	43.52	15	2.074	1,17,2	43.60	43.61	16
---	2.028	2,11,1	44.64	44.65	14	2.026	2,21,1	44.70	44.71	10	2.021	2,10,1	44.81	44.80	15	2.018	2,19,1	44.87	44.88	18	2.014	291	44.98	44.96	12	2.009	2,17,1	45.10	45.10	10
---	---	---	---	---	---	---	---	---	---	---	---	---	---	---	---	---	---	---	---	---	1.963	0,14,2	46.20	46.18	2	---	---	---	---	---
---	1.956	1,22,1	46.39	46.34	1	1.952	1,42,1	46.48	46 50	2	1.944	1,20,1	46.69	46.67	3	1.938	1,38,1	46.85	46.86	1	1.930	1,18,1	47.05	47.05	2	1.919	1,34,1	47.32	47.31	2
---	1.874	2.18,0	48.53	48.55	3	1.878	?,34,0	48.44	48.43	3	1.882	2,16,0	48.32	48.32	3	1.886	2,30,0	48.20	48.18	2	---	2,14,0	---	48.01	---	---	2,26,0	---	47.86	---
022	1.8377	0,20,2	49.56	49.56	83	1.8384	0,30,2	49.54	49.54	68	1.8391	0,18,2	49.52	49.52	116	1.8395	0,34,2	49.51	49.50	90	1.8419	0,16,2	49.44	49.44	60	1.8419	0,30,2	49.44	49.43	111
202	1.8117	202	50.32	50.31	88	1.8121	202	50.31	50.31	79	1.8101	202	50.37	50.36	88	1.8094	202	50.39	50.39	81	1.8087	202	50.41	50.40	74	1.8064	202	50.48	50.48	85
220	1.7849	2,20,0	51.13	51.13	115	1.7846	2,38,0	51.14	51.14	108	1.7836	2,18,0	51.17	51.17	122	1.7833	2,34,0	51.18	51.18	116	1.7830	2,16,0	51.19	51.18	79	1.7813	2,30,0	51.24	51.23	126
---	---	---	---	---	---	---	---	---	---	---	1.7691	1,17,2	51.62	51.64	2	1.7723	1,32,2	51.52	51.54	3	---	---	---	---	---	---	---	---	---	---
---	---	---	---	---	---	1.7421	0,42,2	52.48	52.50	2	---	---	---	---	---	---	---	---	---	---	---	---	---	---	---	---	---	---	---	---
---	---	---	---	---	---	---	---	---	---	---	1.7311	2,17,1	52.84	52.84	2	1.7329	2,32,1	52.78	52.77	4	---	---	---	---	---	---	---	---	---	---
212	1.7081	2,10,2	53.61	53.61	32	1.7081	2,19,2	53.61	53.61	27	1.7072	292	53.64	53.65	35	1.7063	2,17,2	53.67	53.67	37	1.7063	282	53.67	53.68	31	1.7042	2,15,2	53.74	53.75	33
---	1.6851	1,21,2	54.40	54.39	3	1.6837	1,40,2	54.45	54.45	2	1.6814	1,19,2	54.53	54.52	2	1.6797	1,36,2	54.59	54.59	3	1.6785	1,17,2	54.63	54.64	2	1.6754	1,32,2	54.74	54.75	4
103	1.6601	103	55.29	55.29	33	1.6606	103	55.27	55.27	22	1.6606	103	55.27	55.28	27	1.6606	103	55.27	55.28	33	1.6612	103	55.25	55.24	26	1.6609	103	55.26	55.28	32
---	1.5324	1,28,1	56.31	56.32	5	1.6367	1,53,1	56.15	56.14	8	1.6439	1,25,1	55.88	55.90	5	1.6499	1,47,1	55.66	55.65	5	---	1,22,1	---	55.34	---	---	---	---	---	---
301	1.5838	301	58.20	58.19	9	1.5830	301	58.21	58.21	10	---	301	---	58.31	---	---	301	---	58.38	---	---	301	---	58.44	---	---	301	---	58.58	---
113	1.5791	1,10,3	58.39	58.40	49	1.5796	1,19,3	58.37	58.37	51	1.5796	193	58.37	58.37	61	1.5793	1.17,3	58.37	53.38	61	1.5806	183	58.33	58.33	38	1.5803	1,15,3	58.34	58.36	52
131	1.5433	1,30,1	59.88	59.87	100	1.5435	1,57,1	59.87	59.87	89	1.5442	1,27,1	59.84	59.84	92	1.5447	1,51,1	59.82	59.80	105	1.5466	1,24,1	59.74	59.74	80	1.5473	1,45,1	59.71	59.72	70
311	1.5131	3,10,1	61.20	61.19	67	1.5125	3,19,1	61.23	61.22	63	1.5105	391	61.32	61.31	85	1.5091	3,17,1	61.38	61.37	65	1.5076	381	61.45	61.43	65	1.5054	3,15,1	61.55	61.56	66
222	1.4792	2,20,2	62.76	62.78	37	1.4790	2,38,2	62.77	62.78	35	1.4782	2,18,2	62.81	62.80	40	1.4780	2.34.2	62.82	62.81	42	1.4784	2,16,2	62.80	62.79	32	1.4775	2,30,2	62.84	62.84	43
---	1.4631	1,32,1	63.53	63.53	4	1.4590	1,61,1	63.73	63.72	5	1.4556	1,29,1	63.90	63.90	4	1.4519	1,55,1	64.08	64.10	3	1.4471	1,26,1	64.32	64.30	3	---	---	---	---	---
032	1.4312	0,30,2	65.02	65.03	10	1.4338	0,57,2	64.99	64.99	12	1.4344	0,27,2	64.96	64.97	13	1.4351	0,51,2	64.92	64.93	11	1.4365	0,24,2	64.85	64.87	6	1.4375	0,45,2	64.80	64.82	12
---	1.4054	312	66.47	66.48	3	---	---	---	---	---	---	---	---	---	---	1.4018	322	66.66	66.65	3	1.4005	312	66.73	66.71	3	---	---	---	---	---
123	1.3928	1.20,3	67.15	67.15	16	1.3932	1,38,3	67.13	67.13	12	1.3935	1,18,3	67.11	67.13	21	1.3937	1,34,3	67.10	67.11	17	1.3948	1,16,3	67.04	67.05	20	1.3946	1,30,3	67.05	67.07	18

[a] Indexed with the aid of intensities observed from single crystal precession photographs.

[b] Calculated on the basis of an orthorhombic unit cell with a=4.982, b=51.18, c=5.282Å.

[c] Observed Intensity.

[d] Calculated on the basis of an orthorhombic unit cell with a=4.979. b=97.25, c=5.285Å.

[e] Calculated on the basis of an orthorhombic unit cell with a=4.971, b=46.10, c=5.285Å.

[f] Calculated on the basis of an orthorhombic unit cell with a=4.965, b=87.15, c=5.285Å.

[g] Calculated on the basis of an orthorhombic unit cell with a=4.959. b=41.06, c=5.290Å.

[h] Calculated on the basis of an orthorhombic unit cell with a=4.947, b=77.05, c=5.288Å.

[1] This (0k0) spacing is the superstructure line referred to in the text and Table 1 as the "characteristic peak".

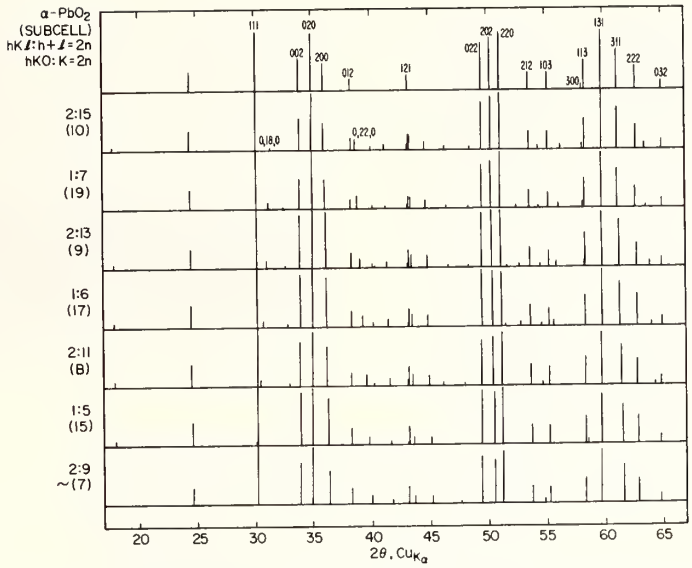

Fig. 4. Diagramatic representation of a portion of the x-ray diffraction powder patterns of the orthorhombic phase(s) in the system Nb_2O_5-ZrO_2.

obeyed the extinction rules hkℓ:h+ℓ=2n and hk0:k=2n when using the convention for the subcell a<b<c. All lines which cannot be indexed on this basis are actually superstructure lines. The d-spacings of the superstructure lines were found to be very strongly dependent on composition and heat treatment. For instance, the peak at d = 2.31 Å mistakenly reported with hkℓ= 021 by Roth and Coughanour [1] was found to vary from $2\theta_{CuK\alpha}$=39.98° (2.2532 Å) at the 1:4 $Nb_2O_5 \cdot ZrO_2$ ratio to a value of 38.67° (2.3263 Å) at the 1:8 Nb_2O_5:ZrO_2 ratio under equilibrium conditions. These two compositions were found to be just on either side of the single phase boundaries. Although other peaks were also found to change positions considerably this peak is the best diagnostic indicator for the change in the superstructure and has been labelled as the "characteristic" peak in tables 1 and 3, similar to the nomenclature used for the low-Ta_2O_5-type phases in a previous publication [13].

In order to arrive at the correct indexing of the superstructure peaks it was necessary to examine single crystals. The specimens prepared by direct melting and by BaO - V_2O_5 flux growth were used for this purpose. Typical crystals from the flux growth experiments are shown in figure 5. These crystals were invariably twinned as shown in the photograph. The twin axis was found to coincide with the *c* axis of the subcell. The *b* axis was always the axis perpendicular to the crystal plate. All superstructure spots in a single crystal x-ray diffraction precession pattern were found to occur only along the *b* axis of the subcell. The tabular crystallographic habit is therefore consistent with the general rule that the short axes grow relatively fast while the long axis grows much more slowly.

From the single crystal photographs shown diagramatically in figures 6, 7 and 8, it can be demonstrated that the only possible hkℓ value for the "characteristic" peak occurring between 2.253 and 2.326 Å is the 0k0 superstructure spot occurring immediately after the 020 substructure reflection. For those compositions where the multiplicity is the smaller whole numbers 7, 8, 9, or 10 the index of the 020 substructure peak would then be (0,14,0), (0,16,0), (0,18,0) or (0,20,0) and the index of the characteristic peak would have a k value of 2 greater or (0,16,0), (0,18,0), (0,20,0) or (0,22,0) respectively. However, for the more complex intermediate compositions where the multiplicity is 15, 17, or 19 and the (020) substructure peak is (0,30,0), (0,34,0) or (0,38,0) the k value of the characteristic peak would be 4 greater or (0,34,0), (0,38,0) or (0,42,0) respectively. The orthorhombic phase(s) in these systems always have only a *b* axis superstructure so that this characteristic line can be used directly to calculate the true unit cell. The distance between this superstructure peak and the 020 substructure reflection increases directly proportional to the

Fig. 5. Photographs of typical twinned crystals of the orthorhombic phase(s) in the Nb_2O_5-ZrO_2 system grown in the $BaO:V_2O_5$ flux.

composition. The distance between the spots is the greatest at the higher Nb_2O_5 concentration and the least at the highest ZrO_2 concentration.

All of the superstructure lines in the x-ray powder diffraction patterns can be accounted for on the basis of a *b*-axis multiplicity varying from approximately seven times the subcell value at a composition of about 2:9 $Nb_2O_5:ZrO_2$ to a value of exactly ten times the subcell at a composition of about 2:15. For those specimens which have been most completely equilibrated by heating at temperatures within about 10 °C of beginning of melting for extended periods of time, it was found that the *b*-axis multiplicity was as follows:

$Nb_2O_5:ZrO_2$	Multiplicity
2:9	~7
1:5	15
2:11	8
1:6	17
2:13	9
1:7	19
2:15	10

Specimens which had not been heated long enough and/or at high enough temperatures always showed the characteristic peak at lower *d* values (higher 2θ) than was achieved at proper equilibriation. However once the specimen had achieved equilibrium it could not be reversed to its former condition by reheating at lower temperatures.

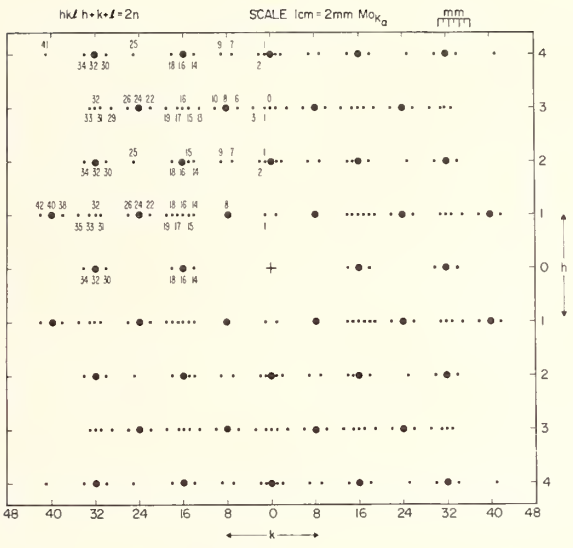

Fig. 6. Diagramatic representation of superimposed (h0ℓ) and (h1ℓ) single crystal precession patterns of the orthorhombic phase with superstructure of eight times the subcell. Spots are labelled in upper left quadrant. Numbers below the spots indicate those present at the h0ℓ level and numbers above the spots indicate those present on h1ℓ level. Indices of spots obey the extinction rule hkℓ:h+k+ℓ=2n.

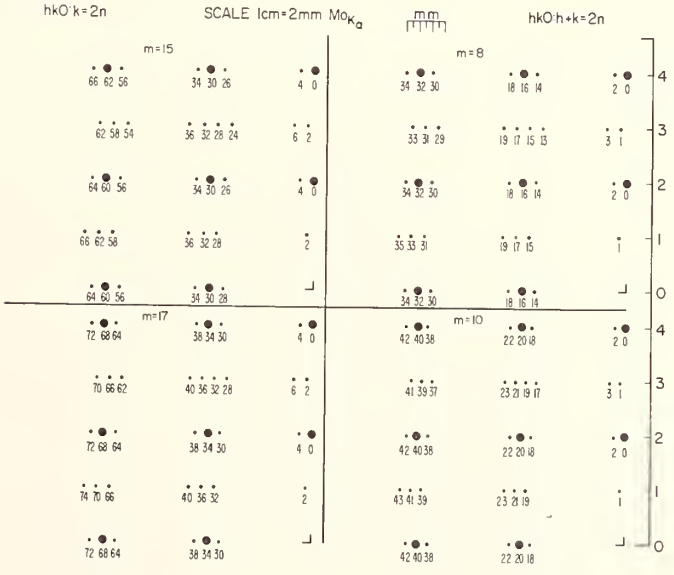

Fig. 7. Diagramatic representation of upper left portions of (h0ℓ) single crystal precession patterns of the orthorhombic phase(s) with superstructure of 15, 8, 17 and 10 times the subcell. Indices of spots obey the extinction rule hk0:k=2n.

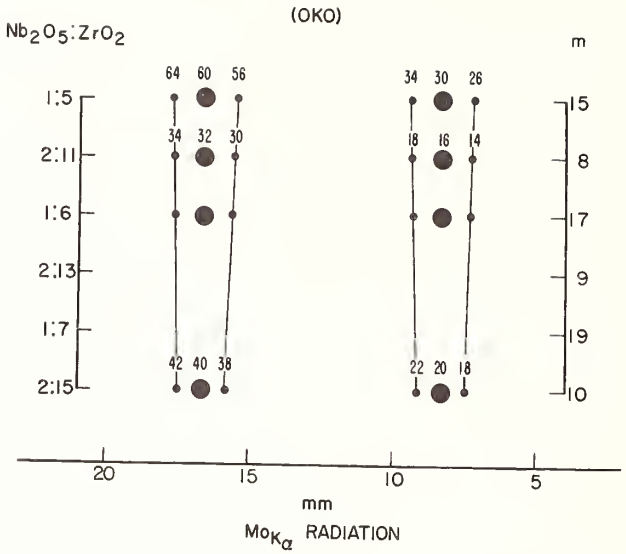

Fig. 8. Diagramatic representation of the left hand portion of the (0k0) level of single crystal precession patterns of the orthorhombic phases with superstructures of 15, 8, 17 and 10 times the subcell. This picture illustrates the way in which the superstructure spots approach the subcell spot as the composition approaches ZrO_2.

The above results most nearly correspond to a group of phases (or a solid solution) which belong to a homologous series $M_{n-1}O_{2n}$.

$M_{n-1}O_{2n}$

n	M:O	Nb_2O_5:ZrO_2	Formula	m
14	$M_{13}O_{28}$	~2:9	$Nb_4Zr_9O_{28}$	~7
15	$M_{14}O_{30}$	1:5	$Nb_4Zr_{10}O_{30}$	15
16	$M_{15}O_{32}$	2:11	$Nb_4Zr_{11}O_{32}$	8
17	$M_{16}O_{34}$	1:6	$Nb_4Zr_{12}O_{34}$	17
18	$M_{17}O_{36}$	2:13	$Nb_4Zr_{13}O_{36}$	9
19	$M_{18}O_{38}$	1:7	$Nb_4Zr_{14}O_{38}$	19
20	$M_{19}O_{40}$	2:15	$Nb_4Zr_{15}O_{40}$	10

However the real compositions of the specimens are probably not accurately enough known to eliminate the possibility of a homologous series M_nO_{2n+2}.

M_nO_{2n+2}

n	M:O	$Nb_2O_5:ZrO_2$	Formula	m
14	$M_{14}O_{30}$	1:5	$Nb_4Zr_{10}O_{30}$	7
15	$M_{15}O_{32}$	2:11	$Nb_4Zr_{11}O_{32}$	15
16	$M_{16}O_{34}$	1:6	$Nb_4Zr_{12}O_{34}$	8
17	$M_{17}O_{36}$	2:13	$Nb_4Zr_{13}O_{36}$	17
18	$M_{18}O_{38}$	1:7	$Nb_4Zr_{14}O_{38}$	9
19	$M_{19}O_{40}$	2:15	$Nb_4Zr_{15}O_{40}$	19
20	$M_{20}O_{52}$	1:8	$Nb_4Zr_{16}O_{42}$	10

Actually no region containing two orthorhombic phases has been seen in this system. It seems unlikely that a two phase region exists and completely or almost completely ordered mixtures of the above phases must exist at all compositions in the single phase region. This rather untenable conclusion may seem more reasonable if stated another way. At low temperatures a metastable solid solution region exists with some type of structural defect containing very little long range order and no superstructure peaks. As the composition is equilibrated at higher temperatures the structural defects tend to diffuse through the individual crystallites and regroup into ordered arrangements. This clustering of defects continues until equilibrium is established. Further heat treatment will then no longer affect the ordering process.

Electron microscope lattice image photographs show only fringes characteristic of the *b* axis unit cell. However electron diffraction patterns were very complex, often requiring much larger multiplicities than the x-ray data would indicate. Only specimens from the two phase region containing the m=10 phase co-existing with monoclinic ZrO_2 allowed the same simple explanation for both x-ray and electron diffraction. A possible explanation for this disagreement is that the specimens are not exactly at equilibrium and/or at exactly the intended composition (all electron microscope and diffraction data were obtained by J. Allpress, CSIRO, Melbourne, Australia).

4. REFERENCES

[1] Roth, R. S. and Coughanour, L. W., J. Res. NBS 55 [4], 209-213 (1955).
[2] Trunov, V. K., Vladimirova, Z. A., Kovba, L. M., and Komissarova, L. N., Izv. Akad. Nauk. SSSR Neorgan. Materials 1 [7], 1152-4 (1965).
[3] Roth, R. S. and Waring, J. L., Am. Min. 49, 242-246 (1964).
[4] Bendeliani, N. A., Popova, S. V., and Vereschchagin, L. P., Geokhimiya 6, 677-683 (1967).
[5] Bocquillon, G. and Susse, C., Rev. Int. Hautes Temper. et Refract. 6, 263-266 (1969).
[6] Bocquillon, G., Susse, C., and Vodar, B., Rev. Int. Hautes Temper. et Refract. 5, 247-251 (1968).
[7] Roth, R. S. and Wadsley, A. D., Acta Cryst. 19 [1], 26-47 (1965).
[8] Wadsley, A. D. and Andersson, S., in *Perspectives in Structural Chemistry III*, ed. J. D. Dunitz and J. A. Ibers, pp. 1-58 (1970). John Wiley & Sons, New York.
[9] Allpress, J. G. and Roth, R. S., Solid State Chem. 3, 209-216 (1971).
[10] Roth, R. S. and Stephenson, N. C., in *The Chemistry of Extended Defects in Non-metallic Solids*, ed. L. Eyring & M. O'Keeffe, pp. 167-182 (1970). North Holland Publishing Co., Amsterdam.
[11] Stephenson, N. C. and Roth, R. S., Acta Cryst. B27, 1010-1044 (1971).
[12] Thornber, M. R., Bevan, D. J. M., and Graham, J., Acta Cryst. B24, 1183-1190 (1968).
[13] Roth, R. S. and Waring, J. L., J. Res. NBS 74A [4], 485-493 (1970).

465-504 O - 72 - 14

W. R. Cook: I noticed the shifting of the superstructure lines with respect to the substructure lines. We have observed this on another zirconium compound. I don't know whether it's characteristic of zirconium or not, but if you dope lead zirconate with a little strontium or lanthanum and titanium you get a tetragonal anti-ferroelectric structure which has weak superstructure which, working from powder diagrams, shift in the same way. You can always convince yourself that you can resolve individual phases out of these apparently continuous shifts, but you are never sure that you've got it.

R. S. Roth: My answer to that is, I think, a very important point, namely you can do all sorts of things with x-ray diffraction powder patterns, but I don't believe them anymore. You have to have a single crystal and at least look at the single crystal x-ray diffraction data or obtain electron diffraction data or something else to help. Now, my guess is that what you are talking about is probably some kind of Ruddlesden-Popper type phases, maybe ordered, maybe disordered. If there really is this continuous type of a structure in the lanthanum titanate-lead zirconate system, then this is something new, and if you can prove it with single crystals, then it's not a Ruddlesden-Popper phase.

D. J. M. Bevan: Perhaps I can just comment very briefly. This sort of phenomenon seems to be cropping up rather more. We have much the same sort of thing in the rare earth oxide-fluorides where you have an anion excess. There is a region of composition in the yttrium case between $YX_{2.13}$ or there-abouts to $YX_{2.22}$ where X is oxygen plus fluorine. On the evidence of both single crystal and powder data, both sets of which correlate very nicely, I believe we have a virtual infinity of ordered phases, some with very large superstructures. I think the biggest we've seen so far is a one dimensional stack of fluorite unit cells, 57 fluorites in length. I think the *b*-axis of the orthorhombic system is something of the order of 350 angstroms in this case. This is within the fluorite type structure and hasn't gone as far as the α-PbO_2 type.

J. G. Allpress: One possible explanation that we have come up with recently is that you may have a super-lattice which extends for a long period in one direction and then has a kink in it. We have been looking at chromium titanium oxides of the α-PbO_2 type which have shear planes in them. The shear planes can go in either of two directions. They seem to go in one direction for a long time and then a small segment in the other direction. If you build up a very large superstructure on this basis, I think you may be able to explain some of the orientation anomalies in the diffraction patterns. We're following this up right now.

B. G. Hyde: I might interpolate. I think this has been seen in several places, and is due to exactly that. In fact, I have noticed throughout this afternoon that several of the micrographs that have had wavy plane images in them, have the waves very closely correlated. If the correlation were perfect this would give rise to very high index ordered planes.

L. A. Bursill: Earlier this year we published a paper on what we call swinging shear planes in reduced rutile[1] and that will be discussed in the next paper by Mike O'Keeffe. In this paper we discuss a simple model whereby you can produce very high index planar faults in crystals. You can have a continuous rotation of the planes from one simple plane to another. We also suggested this as a new way of accommodating nonstoichiometry, instead of varying the shear plane spacing we have an ordered variation in orientation. You have two reciprocal lattices, one due to the superstructure and one due to the subcell, and these rotate relative to each other. This explains the orientation and spacing anomalies on the single crystal diffraction patterns. This type of special reciprocal lattice geometry will not be restricted to shear structures alone.

R. S. Roth: Yes, that wavy lattice image which John Allpress made of poorly annealed Nb_2O_5:$5ZrO_2$ definitely must be telling us something about the method of approaching equilibrium in this system. I don't think that we should be led astray by the very, very large *apparent* unit cells that one can get in a system where there is a continuous infinite series of phases with no two-phase regions between them. I think we are looking at some phenomenon that isn't quite a series of isolated phases. I don't know what it is, but I am not inclined to believe myself these 300 angstrom unit cells. Certainly not in terms of it being a phase,

a structure all by itself because you never find two-phase regions. We need an explanation for why these systems do not have two-phase regions.

B. G. Hyde: Bob, you didn't have the spacing on that wavy plane picture. What was the interplanar spacing there, do you remember?

R. S. Roth: It would have been on the order of magnitude of about 19 angstroms.

Note Added in Proof: During the course of this study it became apparent that the "ZrO_2" used in this study did not have reproducible weight losses (see discussions after papers by N. C. Stephenson and by B. Gatehouse - this proceedings). After personal discussions with Drs. J. Galy, S. Andersson and J. Allpress during the meeting, it was decided that a few more experiments to determine the correct compositions of the phases would help to determine the crystallographic nature of this material. Therefore specimens were prepared of four Nb/Zr alloys by arc fusion of the pure end member metals. The compositions used were 2:5, 2:6, 2:7, and 2:8 Nb:Zr ratios. These specimens were oxidized at 850 °C, each specimen taking about one week for complete oxidation of the alloy. The specimens were then ground and reheated at 1000 °C (with repeated intermittent grindings) for another week. These specimens then represented 1:5, 1:6, 1:7 and 1:8 Nb_2O_5:ZrO_2 ratios with compositions known to a much higher degree of accuracy than was true of the original specimens.

A small portion of each specimen was then heated for approximately one week just below solidus temperatures in a high temperature quench furnace as described in the text of this paper. The 1:5 specimen could now be indexed on the basis of a multiple cell very close to m=7. The 1:6 phase, $Nb_2Zr_6O_{17}$ was now found to have a multiplicity of exactly m=8. The 1:7 phase had a multiplicity very close to m=9 and the 1:8 composition was now essentially single phase with a multiplicity of m=10.

It can be concluded from the above experiments that the original specimens were actually low in ZrO_2 content compared to their "as prepared" mole ratios. Each specimen is approximately 1/2 - 1 1/2 mole percent lower in ZrO_2 than the stated value. The results of these experiments can be interpreted as indicating that these orthorhombic phases belong to the homologous series M_nO_{2n+2} rather than $M_{n-1}O_{2n}$ and are anion excess fluorite type phases rather than cation deficient α-PbO_2 type compounds (see L. Nagel and M. O'Keeffe, Matl. Res. Bull. 6, 1318 (1971) for discussion of similarity of these structures).

[1]Bursill, L. A., Hyde, B. G., and Philp, D. K., Phil. Mag. 23, 1501, (1971).

National Bureau of Standards Special Publication 364, Solid State Chemistry, Proceedings of 5th Materials Research Symposium, issued July 1972.

PHYSICAL AND GEOMETRICAL PRINCIPLES OF CRYSTALLOGRAPHIC SHEAR IN RUTILE

L. A. Bursill and B. G. Hyde

School of Chemistry
University of Western Australia
Nedlands W. A.

M. O'Keeffe

Department of Chemistry
Arizona State University
Tempe, Arizona 85281

Recent studies by electron microscopy and diffraction have elucidated many of the strutural patterns of formation of homologous series of oxides derived from the rutile structure by crystallographic shear. In this paper, the physical and geometrical principles underlying the formation of planar defects are considered. It is shown that the only crystallographic shear planes expected in systems derived from rutile are those containing <111> as observed *e.g.* in TiO_{2-x} and TiO_2--Cr_2O_3. These results enable us to establish likely criteria for the development of homologous series in oxide systems. The kinetic consequences of the existence of disordered shear planes (Wadsley defects) are further examined in the light of these developments.

Key words: Crystallographic shear; rutile; swinging shear planes; TiO_2; TiO_2-Cr_2O_3 system.

1. INTRODUCTION

The study of the "homologous series" of reduced oxides MO_{2-x} with structures derived from that of rutile (TiO_2) has played a central role in the development of our knowledge of the crystallographic and chemical behavior of Wadsley defects in solids. In this paper we examine some of the physical principles possibly important in dictating that non-stoichiometry shall be accommodated in some instances by Wadsley defects (in the MO_{2-x} systems under consideration here, these are crystallographic shear, CS, planes) and in other cases by point defects. We shall be guided by the now extensive accumulation of experimental data mainly obtained by x-ray and electron diffraction and by electron microscopy of TiO_{2-x} and $Ti_{1-2x}Cr_{2x}O_{2-x}$. These data have been the subject of a recent review [1][1] to which the interested reader is referred. Here we simply will quote the appropriate experimental observations when pertinent.

The first question to which we must address ourselves is: Why are extended defects rather than point defects observed in non-stoichiometric crystals? Some clues are provided by an examination of the physical properties of the host crystal and the insight they give into the nature of interionic forces. The second question is: Why do particular extended defects, in this case CS planes of certain indices, occur and not others? The essence of the answer to this question is to be found in a consideration of crystal structure and it will prove necessary to particularize here to the case of rutile-derived materials.

---

[1] Figures in brackets indicate the literature references at the end of this paper.

2. POINT DEFECTS VERSUS EXTENDED DEFECTS

An observation that we feel has received insufficient attention is that Wadsley defects of the CS plane type appear to be confined to materials containing ions of high formal charge and in crystals which either have a very high dielectric constant (>100) or are ferroelectric. Local fields due to an asymmetric distribution of charge in such crystals will therefore be screened rapidly by polarization of the surrounding matrix and polarization energy will be of some importance. As a result the ionic description of these materials must be employed with caution and the contribution of ionic and electronic polarization to the total energy must be considered. The situation is exacerbated by the fact that in materials exhibiting high dielectric constants, the Lorenz correction to the local field is quite different from the normal value of $4\pi/3$ so that ionic polarization, or displacement from the normal site, is accompanied by large local electric field and a large energy contribution from electronic polarization of the anions which in turn stabilize the ionic displacements.

In the case of rutile, calculation of the Lorenz correction [2] satisfactorily accounts for the high dielectric constant (ca. 200) [3]. Examination of the normal coordinates of the corresponding soft IR-active modes [4] shows that the response of this crystal to an electric field is mainly an off-center displacement of the titanium ion in the TiO_2 octahedra (see fig. 1).

A recent calculation on Ti_4O_7 by Anderson and Burch [5], based on a rigid ion model, found no significant difference in electrostatic energy for an ordered vacancy structure and the (observed) shear structure. In view of the above remarks, it is hardly surprising that the less symmetrical shear structure is indeed observed.

It is worth noting also that rutile-structure materials also exhibit a soft Raman-active mode which suggests that the crystal can also accommodate local elastic strains without large stresses [6]. In general one might expect unsymmetrical structures, coherent intergrowth, etc., in systems based on parent crystals with such properties. The term *compliant crystals* [7] is proposed for materials of this type.

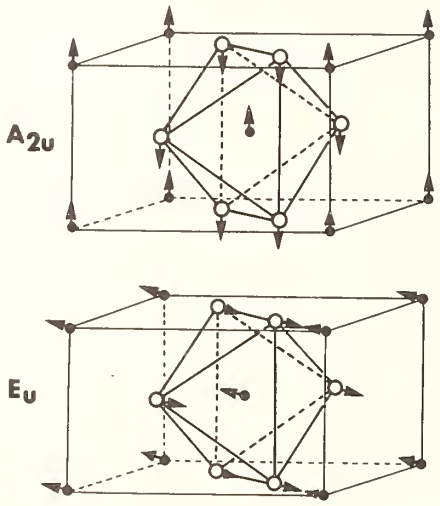

Fig. 1. Normal coordinates of the low-frequency infrared-active modes of rutile. Large open circles represent oxygen and small filled circles titanium. The A_{2u} mode makes the main contribution to $\varepsilon_{\parallel}$. The E_u which makes the main contribution to $\varepsilon_{\perp}$ is doubly degenerate, displacements in the second E_u mode are obtained by rotating to displacement vectors by 90° around the c-axis (vertical in the figure).

In what follows we shall suppose that the interaction of two titanium ions in close proximity, corresponding to TiO_6 octahedra sharing faces, can be fairly readily accommodated by displacement of the titanium ions towards the opposite faces of the octahedra. The occurrence of this configuration in hexagonal $BaTiO_3$, which is very close in energy to the cubic form, is already familiar. An octahedron sharing two opposite faces will present a much less favorable configuration, as in this more-symmetrical arrangement off-center displacement cannot occur.

3. STRUCTURAL ASPECTS OF DEFECTS IN RUTILE

3.1. THE RUTILE STRUCTURE

It proves convenient at this stage to slightly idealize the rutile structure by considering that the anions are in hexagonal close packing (hcp)[2]. In this description (100) layers of anions are hexagonally close-packed and the [100] direction corresponds to the hcp c-axis. The octahedral sites, of which half are occupied by cations in rutile are primitive hexagonal: it is these upon which we shall focus. There are, of course, also tetrahedral sites. However, the experimental work has largely been confined to date to systems containing in addition to Ti^{4+}, ions such as Ti^{3+} and Cr^{3+} with strong octahedral site preferences, so that the possibility of tetrahedral site occupancy is not considered.

Figure 2 shows the two layer repeat-sequence of cation sites in TiO_2. The pattern of filled sites in one layer is immediately above and below empty sites in adjacent layers. A useful geometric property to keep in mind is that the octahedra around the cation sites share edges with adjacent octahedra within a close-packed layer, share faces with octahedra immediately above and below in adjacent layers and share corners with the next nearest octahedra in adjacent layers. Thus in rutile each TiO_6 octahedron shares edges with two other such octahedra and corners with eight octahedra (fig. 2).

3.2. DEFECTS IN RUTILE

An interstitial octahedrally-coordinated ion inserted in the parent structure will be in close proximity to two other cations: its coordination octahedron will share two faces, four edges and only two corners with neighboring octahedra. As discussed above, this is likely to be a high-energy configuration so we search for other ways of accommodating extra cations without destroying the oxygen close packing.

An important step in the argument is to recognize that extra cations can be introduced with octahedra sharing only one face in the region of antiphase boundaries (APB) in the crystal. The only possible APB that does not change the connectivity of coordination polyhedra (specifically that does not introduce face-sharing) is that derived by shear by the vector $1/2\langle 0\bar{1}1\rangle$ in planes of form $\{011\}$. Only vectors of the type $1/2\langle 0\bar{1}\bar{1}\rangle$ connect full and empty octahedral sites and leave the oxygen lattice invariant. The plane must, therefore, be of type $(h\ell\ell)$. The restriction on face-sharing in turn requires $h = 0$. Figure 3 represents two cation layers in rutile with such an APB.

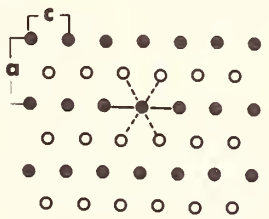

Fig. 2. Two (100) layers of cations in rutile (filled and empty circles respectively). Solid lines connect cations in edge sharing octahedra and broken lines connect cations in corner sharing octahedra.

[2] As hcp and body-centered cubic (bcc) are closely related, the structure could also be idealized to have the anions in a bcc array. This latter was the representation preferred by Anderson and Hyde [8].

Systematic examination of possibilities shows that cations can be added to the crystal with octahedra sharing not more than one face in just one way. This involves "chains" of face-sharing octahedra along [111] and the simultaneous production of a step in the APB. A chain terminating within the crystal will require the presence of either a vacant cation site (neighboring octahedra less connected than normally) or octahedra sharing more than one face. Such a chain is illustrated in figure 4; we return below to a fuller description of its geometrical properties.

We observe at this point that the normal terminology of point defects is not adequate for the description of structural defects such as those under consideration. Part of the difficulty arises because it is not clear which are normal and which are interstitial sites in the proximity of an antiphase boundary. It is more useful, therefore, to discuss defects

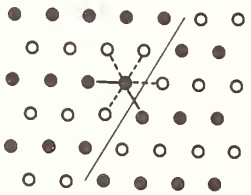

Fig. 3. Cations layers in rutile with an antiphase boundary. Symbols as in figure 2.

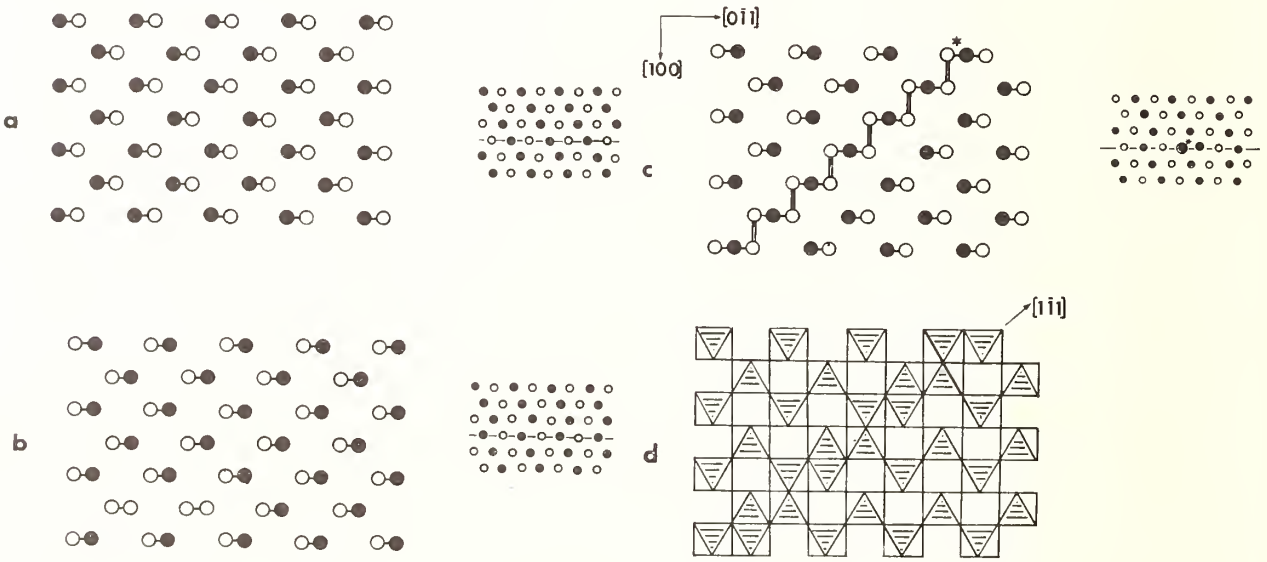

Fig. 4. The small circles on the right in (a) and (b) represent (100) cation layers in rutile and in rutile with an antiphase boundary as in figures 2 and 3 respectively. The larger circles on the left in these diagrams represent two (011) cation layers. Open circles represent cations in the plane shown by a line on the right, filled circles represent cations in the layer underneath. Cations in edge-sharing octahedra are connected by a line. In (c), the same projections are shown by a [1$\bar{1}$1] chain of face-sharing octahedra in an APB. Cations in face-sharing octahedra are connected by a double line. In (d) the octahedra coordinating the open-circle cations of (c) are drawn.

at a higher levelof organization - in this instance in terms of the connectivity of coordination polyhedra. In rutile each octahedron shares edges with two and corners with eight of its neighbors. This situation is unchanged by introducing an APB. In the chains of face-sharing octahedra described above, there is introduced for each extra cation a pair of octahedra that share one face, three edges and six corners in the place of one "normally" connected octahedron. The topology of the structure requires that these pairs of octahedra occur in chains along [$\bar{1}11$] in an APB unless other connectivity defects are introduced. For the sake of completeness it should be noted that in general the connectivity of empty octahedra should also be considered. For example, a cation vacancy corresponds to an empty O_6 octhhedron sharing two faces, *etc.*, in the same way as does an occupied TiO_6 octahedron corresponding to a titanium interstitial. Here we are considering cation-excess structures so only occupied (*i.e.* TiO_6) octahedra are discussed.

3.3. EVOLUTION OF SHEAR STRUCTURES

A formal description of the process of reduction of the crystal can now be given. We will consider later the evidence as to whether, and under what circumstances, this might correspond to the actual steps occurring.

Loss of oxygen at the surface will produce a local excess of cations. Either a pre-existing APB or a fragment of an APB nucleated at this point can accommodate a chain of face-sharing octahedra containing the extra cations in a step on the APB plane. Figure 5 illustrates how the step can migrate into the crystal by a cooperative series of cation jumps along [$0\bar{1}\bar{1}$] transporting the cation excess into the crystal. A second step corresponding to a new [$\bar{1}11$] chain can now form at the surface. Eventually we might envisage a number of steps in the APB being formed.

The chains of pairs of face-sharing octahedra producing steps in the APB contain an excess of cations and require polarization of the surroundings for stability, so it is plausible to suppose that the next stage in the development is that they order in the plane to maximize the distance between adjacent steps. When this occurs we no longer have a (011) APB but a new plane whose indices depend on the spacing between steps. A detailed account of the geometry has been given elsewhere [1,9]. Here we simply note that if there are n rows of "normal" ions between each step the indices of the plane are (1 n+2 n+1), the limiting case n = 0 corresponding to (121) planes. The last illustration in figure 5 shows one layer of cations intersecting a (132) plane (n = 1).

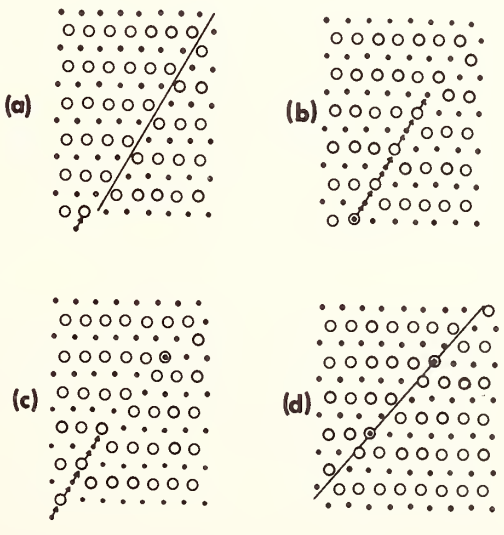

Fig. 5. Two (100) layers of cations in rutile with (a) an antiphase boundary, proceeding by the jumps shown in (b) and (c) to a segment of a (132) CS plane in (d).

Intermediate cation densities can and do occur. For example, regularly alternating n = 1 and n = 0 will result in a (253) plane. In fact, progressive reduction of TiO_2, and more particularly increasing chromium concentration in $(Ti,Cr)O_{2-x}$, results in a great number of planes of different and very high indices being observed [9] by electron-optical techniques as the plane "swings" from (132) to (121). In every instance, however, the observed planes can be considered as derived by ordering of chains of pairs of face-sharing octahedra in an APB in the manner we have described. The occurrence of only particular types of CS planes is seen therefore to be required by the particular structure of rutile and by the principle of minimizing face sharing of octahedra without disrupting the oxygen framework.

The final stage in the evolution of the structure corresponds to the situation in which there is a high density of extra cations and hence a high density of CS planes. Again the requirement of polarization of the surrounding medium suggests that at least at short interplanar distances shear planes will tend to order to maximize the interplanar spacing, producing the now familiar families of reduced oxides [1]. An analysis [10] of interplanar spacings of isolated groups of (132) CS planes has demonstrated this short-range repulsion and shown that in addition there is a longer-range attractive force between pairs of CS planes. This latter is difficult to interpret but may be related to the tendency to eliminate the out-of-phase material between the two APBs.

The particular system of CS planes found in an ordered structure will depend on the balance between the tendency on the one hand for CS planes to order as far apart as possible and on the other hand for the individual chains within a plane to order likewise. One can understand qualitatively in this way the evolution from (132) planes at small degrees of reduction to (121) planes at greater cation/anion ratios.

4. MASS TRANSPORT MECHANISMS

In the absence of detailed kinetic studies, a discussion of mass transport mechanisms must be somewhat speculative at this state. However, we can recognize [1] a number of related, but distinct, processes that might occur in oxidation or reduction of TiO_2 or in interdiffusion of *e.g.* TiO_2 and Cr_2O_3. These processes will probably occur simultaneously but their relative importance will to some extent at least depend on the degree of reduction and previous history of the crystal.

4.1. NUCLEATION AND GROWTH OF SHEAR PLANES

It was suggested earlier [8] that the first stage of reduction of rutile might occur by the aggregation of anion vacancies into planar regions ("discs"). Local collapse and shear of the lattice subsequently produces a region of CS plane surrounded by a partial dislocation. In view of the above discussion a more attractive possibility would now appear to involve nucleation of a CS plane at the surface, eliminating the need for mobile point defects. In this mechanism an APB (which may terminate inside the crystal at a partial dislocation) acts to allow easy incorporation of a cation-rich step of $[1\bar{1}1]$ chains of face-sharing octahedra. Cooperative jumps of a *line* of atoms by 1/2 $[0\bar{1}1]$ moves this chain into the crystal (cf fig. 5). This process moves a step on the APB into the crystal and leaves a "perfect" APB extending back to the surface ready to accommodate another step. Ordering of steps then produces a shear plane of appropriate indices.

4.2. SWINGING SHEAR PLANES

A closely related process that is favored by a certain stoichiometry [1,9] involves change of indices of a CS plane. As should be clear from the above discussion, this requires the identical process of cooperative jumps by $1/2[0\bar{1}1]$ by strings of cations, and is a logical extension of the process of nucleation.

4.3. LATERAL DISPLACEMENT OF SHEAR PLANES

The observation of well ordered crystals with large regions of uniformly spaced CS planes requires that CS planes can move laterally after growing into the crystal. This process can also occur by $1/2[0\bar{1}1]$ jumps [1,11], the difference now being that cooperation of a whole *plane* of atoms is required. Clearly such a process will not be thermally activated but will require repulsion between adjacent CS planes to provide the driving force [11].

4.4. CONSEQUENCE OF THE MODEL

There are some interesting consequences of the model we have described. A key role is played by the APB in providing a path for incorporation of extra cations in the early stages of reduction. Nucleation of a CS plane/APB would appear to be a difficult step and asymmetry in oxidation and reduction in both the kinetic and thermodynamic aspects is expected in certain ranges of stoichiometry. Indeed hysteresis in oxidation-reduction isotherms can be satisfactorily interpreted in terms of this method [1].

Surprisingly there have been no measurements of chemical diffusion in the $Ti-O_2$ system. As well as expecting different rates of oxidation and reduction, it is entirely possible that there will be memory effects, in that APBs left on reoxidation of a slightly reduced sample will provide sites for subsequent reductions. Experiments designed to test these ideas are planned.

Recently a study was made [13] of interdiffusion of Cr_2O_3 and TiO_2. Some features of those measurements are worthy of attention here. Most striking was the observation of a lack of any pronounced anistropy in the interdiffusion coefficient $\tilde{D}$. Now every step in oxidation or reduction we have discussed involves atomic jumps on the type 1/2[011] so that the net flux in each process will have components, on average, of a/4 = 0.12 nm and c/2 = 0.14 nm. Transport along the c- or a-axes will therefore occur at comparable rates. We can also understand qualitatively the variation of the magnitude of $\tilde{D}$ with composition (fig. 6). The initial rapid rise of $\tilde{D}$ with chromium concentration corresponds to nucleation of increasing numbers of APB/CS planes. The almost constant D at higher chromium concentrations corresponds to cooperative movement of *planes* of atoms.

It should be remarked that the above account is really too facile and a completely satisfactory account of interdiffusion, particularly in ternary systems, remains to be given. Conspicuous among the difficulties for ternary systems is that counter-diffusion of *e.g.* Ti and Cr is necessary (in the binary system electronic conduction assures the appropriate Ti^{4+}/Ti^{3+} ratio at all times). Movement of a CS plane incorporates new atoms into the plane and strands the atoms originally in face-sharing octahedra in regions of "perfect" crystal; a mechanism must exist to return Cr^{3+} to the CS plane.

A second point which has not received the attention it deserves is that a CS plane migrating due to cation displacements does not move parallel to the normal to the plane but along $[0\bar{1}1]$. For a CS plane extending right through the crystal this can only be accomplished by adding cations (or substracting oxygen) at one surface and removing them (adding oxygen) at the opposite surface. The role of gas phase transport of material should therefore not be discounted.

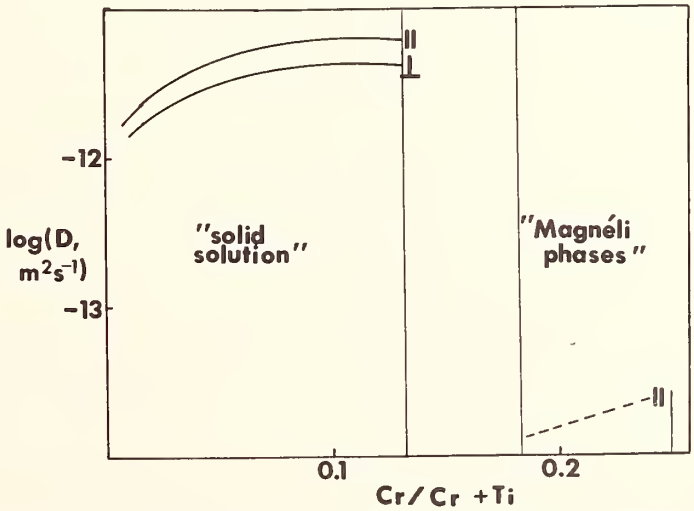

Fig. 6. Interdiffusion coefficient, $\tilde{D}$, for interdiffusion of TiO_2 and Cr_2O_3 at 1450 °C. Based on experiments by T. J. Ribble [13].

The difficulty is mitigated to some extent when systems of defects are considered. For example, ions stranded by one moving CS plane can be incorporated into an adjacent one. Changes in stoichiometry can also occur by movement of a coherent interface [1] between two regions of different density of CS planes.

Clearly many more experiments are needed before the full picture will emerge with any clarity. When this happens, however, we will have substantially enhanced our understanding of the way in which inorganic materials can change in composition.

5. ACKNOWLEDGEMENTS

This paper is based on experimental research at Perth supported by the Australian Research Grants Committee, the U. S. Air Force Office of Scientific Research and the University of Western Australia. One of us (M. O'K) would also like to acknowledge support from the National Science Foundation and a grant from Arizona State University which helped make possible a visit to Western Australia.

6. REFERENCES

[1] Bursill, L. A. and Hyde, B. G., Progr. Solid State Chem., in press (1971).
[2] Parker, R. A., Phys. Rev. 124, 1713 (1961).
[3] Parker, R. A., Phys. Rev. 124, 1719 (1961).
[4] Traylor, J. G., Smith, H. G., Nicklow, R. M., and Wilkinson, M. K., Phys. Rev. B3, 3546 (1971).
[5] Anderson, J. S. and Burch, R., J. Phys. Chem. Solids, 32, 923 (1971).
[6] Nagel, L. E. and O'Keeffe, M., Mat. Sci. Bull. 6, 1317 (1971).
[7] Nagel, L. E. and O'Keeffe, M., to be published.
[8] Anderson, J. S. and Hyde, B. G., J. Phys. Chem. Solids 28, 1393 (1967).
[9] Bursill, L. A., Hyde, B. G., and Philp, D., Phil. Mag. 23, 1501 (1971).
[10] Bursill, L. A. and Hyde, B. G., Phil. Mag. 23, 3 (1971).
[11] Anderson, S. and Wadsley, A. D., Nature 211, 581 (1966).
[12] O'Keeffe, M., Proc. Brit. Ceram. Soc. 19, 1 (1971).
[13] O'Keeffe M. and Ribble, T. J., J. Solid State Chem. 4 (1972) in press and unpublished results.

National Bureau of Standards Special Publication 364, Solid State Chemistry, Proceedings of 5th Materials Research Symposium, issued July 1972.

STRUCTURES AND CHEMICAL BOND PROBLEMS IN VANADIUM OXIDES

Dr. Paul Hagenmuller

Service de Chimie Minérale Structurale de l'Université de Bordeaux I associé au CNRS, 351 Cours de la Libération, 33 - Talence, France

In the transition metal oxides the d-electrons may be either in a localized or a collective state depending essentially on the structure, the transition element and its oxidation state. Some significant examples will be given resulting from recent investigations in the field of the vanadium oxycompounds:

1. A study of the magnetic and electrical properties of the phase $K_{2-x}V_{3+2x}O_{8+2x\pm\kappa}$ ϕ in the system V_2O_5-VO_2-K_2O shows that it can be written formally as

$$K_{2-x}V^{4+}V^{5\pm}_{2-3x\pm2\kappa}(V^{4\pm}_{3x\pm2\kappa})_{subst.}(V^{4\pm}_{2-x})_{ins.}O_8(O_{2x\pm\kappa})_{ins.}$$

$K_2V_3O_8$ is actually an insulator in which the V^{5+} and V^{4+} ions occupy well defined sites ($K_2V^{4+}(V^{5+})_2O_8$). It does not become a conductor until the progressive appearance of d-electrons in the V^{5+} sites as a result of a hopping mechanism. The variation with x of the Curie constant shows that the vanadium, inserted in the form of chain links (O)-V-O-V-(O) in the tunnels emptied by the potassium, also occupies a particular site. These properties were confirmed by the determination of the structure: the phase ϕ, which is isostructural with $Ba_2TiSi_2O_8$, is actually made-up of three types of cationic sites.

2. VO_2 has an allotropic transformation at 340 K of the type homopolar bonding $\rightleftarrows$ metal. This transformation is characterized by a change of symmetry from monoclinic to tetragonal of the rutile type. The replacement of vandium 4+ by cationic substitution of the type $2V^{4+}=M^{5+}(Nb^{5+}f.e.)+V^{3+}$ or by anionic substitution $V^{4+} + O^{2-} = V^{3+} + F^-$ results in the lowering of the transition temperature. It seems to be the result of the progressive occupancy of a π band. On the other hand the transformation temperature is raised by a substitution of the type $2V^{4+} = M^{3+}(Cr^{3+}f.e.) + V^{5+}$, and there appears an intermediate semi-conducting phase of orthorhombic symmetry. The existence of this phase can be explained by the ferroelectric distortions due to vanadium 5+. The change of the physical properties with the substitution rate is analyzed on the basis of the obtained structures.

3. The phase $La_{1-x}Sr_xVO_3$ ($0 \leqslant x \leqslant 0.40$) with a structure derived from $GdFeO_3$ is characterized by an evolution from semi-conductor to metal with increasing x. This latter results from the strengthening of the π(B-O) bond which is a consequence of the weakening of the σ(A-O) bond and the partial replacement of vanadium 3+ by vanadium 4+. This change is less sensitive for the phase $Gd_{1-x}Sr_xVO_3$, Gd^{3+} being more acidic than La^{3+} and hence σ(A-O) stronger and π(B-O) weaker.

These results are compared with those obtained for the homologous $LnTO_3$ phases, Ln being a lanthanide and T a 3d-transition element, on the basis of Goodenough's covalent mixing parameters λ_π and λ_σ. The influence of various factors on the physical properties is discussed.

Key words: Covalence parameters; insulator-metal transitions; perovskite like structures; relations between structures and physical properties; vanadium oxides.

1. INTRODUCTION

The interest in vanadium oxycompounds lies in the fact that the d-electrons may be either localized or delocalized through the lattice. The degree of localization is intimately related to the V-O distances. In other words, it depends on the structure. Factors such as the average degree of oxidation of vanadium, nature of other elements present, temperature, *etc.*, can influence this localization. We are going to show, on the basis of some examples, that the crystal structure of these vanadium oxides and the properties resulting from such an electronic localization are closely related. One is largely responsible for the other. We shall also stress the influence which other cations present can exercise on these properties and therefore on the structure.

2. THE SYSTEM V_2O_5-VO_2-K_2O

The first example deals with the phase ϕ of the system V_2O_5-VO_2-K_2O. In the ternary diagram at 500 °C this phase extends from the composition $K_2V_3O_8$, for which one atom of vanadium in three has an oxidation state of 4+, to the line of the vanadates (IV) in which vanadium is exclusively tetravalent (the composition limits are here $K_2V_6O_{13}$ and $K_2V_8O_{17}$)(fig. 1)[1][1]. The phase ϕ is tetragonal with parameters which do not vary perceptibly with the composition (a = 8.897 ± .001 Å, c = 5.246 ± .002 Å for the composition $K_2V_3O_8$).

The unit cell of $K_2V_3O_8$ contains two formula units. A comparison of the density measured by a very precise hydrostatic method [2] and the densities calculated for various structural hypotheses allows one to assign to a segment inside of the homogeneity range of phase ϕ a structural formula $K_{2-x}V_{3+2x}O_{8+2x}$(fig. 2). Outside of this segment the amount of included oxygen can be either greater or lesser than 2x. The formula can be written as $K_{2-x}V_{3+2x}O_{8+x\pm k}$ for the entire range. In other words the phase ϕ is derived from $K_2V_3O_8$ by replacing the cations K^+ by the chains(O)-V-O-V-(O).

The electrical and magnetic properties along the $K_{2-x}V_{3+2x}O_{8+2x}$ segment [3] have been studied. When we assign to the vanadium atoms their formal degree of oxidation, this formula can be written $K_{2-x}V^{4+}{}_{2-3x}^{5\pm}V_{5x}^{4+}O_{8+2x}$. This means that during the departure of x K^+ ions, 3x atoms of vanadium pass from the 5+ state to the 4+ state, and 2x atoms insert themselves in the available sites in the form of chains of average length O-V-O-V. The formula can now be written as: $K_{2-x}V^{4+}{}_{2-3x}^{5\pm}(V_{3x}^{4\pm})_{\text{subst.}}(V_{2x}^{4\pm})_{\text{ins.}}O_8(O_{2x})_{\text{ins.}}$

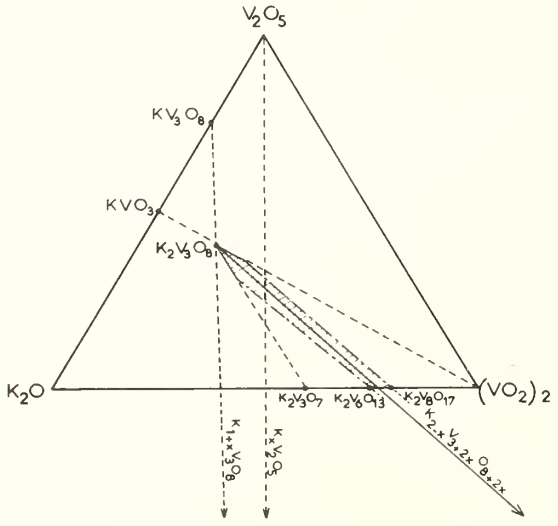

Fig. 1. Homogeneity range of the phase ϕ at 550 °C in the equilibrium diagram V_2O_5 - VO_2 - K_2O.

[1] Figures in brackets indicate the literature references at the end of this paper.

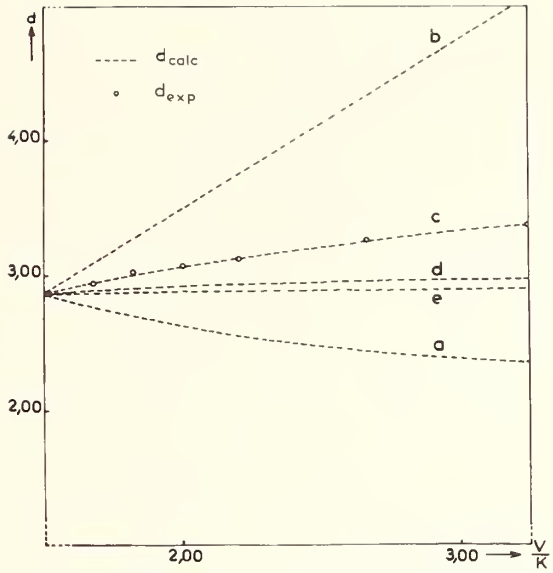

Fig. 2. Determination of the structural formula of the phase $K_{2-x}V_{3+2x}O_{8+2x}$ ϕ by comparison of the calculated and observed densities for various hypotheses.

$K_2V_3O_8$ is an insulator at room temperature with a resistivity above 10^8 Ω cm. One can deduce therefore the absence of a hopping mechanism, the two vanadium 5+ atoms occupying crystallographic sites different from that of vanadium 4+. The conductivity increases with rising x along the $K_{2x}V_{3+2x}O_{8+2x}$ segment: at room temperature it is approximately 10^{-6} ohm^{-1} cm^{-1} for x = 0.33, 10^{-4} ohm^{-1} cm^{-1} for x = 0.67. The activation energies decrease also as x increases: at 600 K it is 1.2 eV for x = 0.33, 0.79 eV for x = 0.50, 0.67 eV for x = 0.60 and 0.16 eV for x = 0.67. Apparently it is the substitution of vanadium 5+ by vanadium 4+ for x > 0 which allows a hopping mechanism in the ϕ phase.

Magnetic measurements indicate that the phases $K_{2-x}V_{3+2x}O_{8+2x}$ at sufficiently high temperatures obey the Curie-Weiss law. The low value of the Weiss constant (T_p = -18 K) observed for $K_2V_3O_8$ could indicate that the vanadium 4+ occupies distant and isolated crystallographic sites. But the fact that the Néel temperature does not vary as x increases allows us to assume that not only the inserted V^{4+}, but also those of the host oxide lattice are arranged in clusters of two (fig. 3).

The molar Curie constant varies linearly (fig. 4): $C_m = 0.37 + 0.59$.

Whereas in $K_2V_3O_8$ the effective magnetic moment is 1.73 μ_B per V^{4+}, for each V^{4+} added either by substitution or insertion, the moment becomes on the average 2.17 μ_B. This result confirms that, when x > 0, V^{4+} occupies three different sites in the lattice.

The structural determination by x-ray diffraction confirmed these conclusions. The phase $K_2V_3O_8$ has the same structure as $Ba_2TiSi_2O_8$ [4]. The lattice is formed by layers of composition $(K_2V_3O_8)_n$. The pentavalent vanadium has a tetrahedral coordination, the tetravalent vanadium is surrounded by five oxygens forming a square pyramid. The potassium occupies the tunnels of pentagonal cross-section. In the network of the ϕ phase potassium is replaced by (O)-V-O-V-(O) chains. Figures 5 and 6 show the projections of the structure of $K_2V_3O_8$ on the xyO and xOz planes.

3. THE TRANSFORMATION POINT OF VO_2

The next example deals with the influence of substitution on the transformation point of VO_2 at 340 K VO_2, which has a rutile structure, is metallic. Below 340 K VO_2 becomes monoclinic and semi-conducting. This change results from the formation of d-d bonds between pairs of neighboring atoms. The distance V-V is alternatively 3.12 and 2.65 Å, these pairs twist slightly about the c axis in creating ferroelectric distortions [5 to 13].

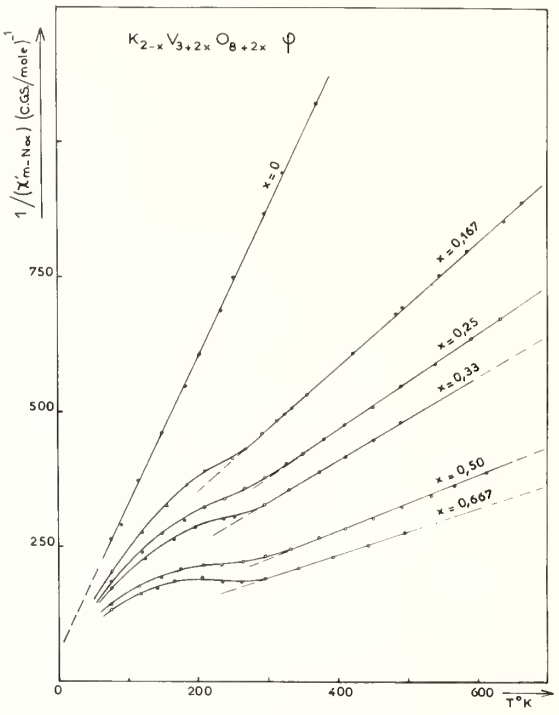

Fig. 3. Variations of the reciprocal molecular susceptibility as a function of temperature for the phases $K_{2-x}V_{3+2x}O_{8+2x}$ ϕ.

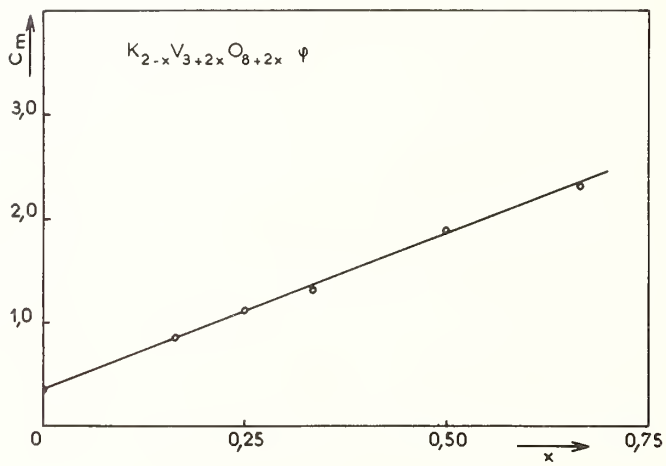

Fig. 4. Variation of the molecular Curie constant of the phases $K_{2-x}V_{3+2x}O_{8+2x}$ as a function of x.

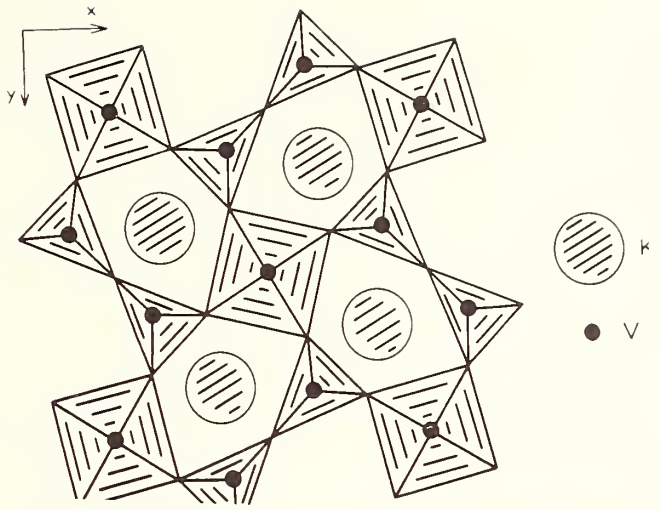

Fig. 5. Projection of the structure of the phase $K_2V_3O_8$ ϕ on the (001) plane.

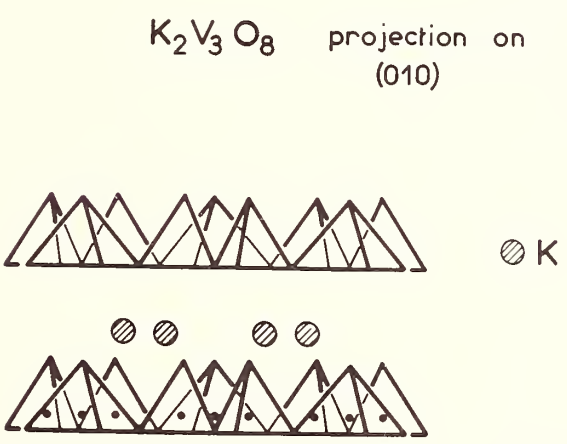

Fig. 6. Projection of the structure of the phase $K_2V_3O_8$ ϕ on the (010) plane.

The change in the transformation point is different depending whether the substitution gives V^{5+} or V^{3+}.

The chromium doped $Cr_xV_{1-x}O_2$ oxide has been studied in a detailed manner [14]. Three phases have been found in place of two: a rutile phase R at high temperature derived from the corresponding VO_2 phase, which cannot be stabilized at room temperature even by very quick quenching, an orthorhombic variety O closely related to the previous one ($a_O \geq a_R\sqrt{2}$, $b_O \leq a_R\sqrt{2}$, $c_O \simeq c_R$), and a monoclinic phase M at low temperature. The transformation points T_1 and T_2 were determined by DTA and x-ray analysis:

$$R \underset{\leftarrow}{\overset{T_1}{\rightleftarrows}} O \underset{\leftarrow}{\overset{T_2}{\rightarrow}} M \qquad \text{(fig. 7 and 8).}$$

T_1 increases with rising x while T_2 decreases: in other words the homogeneity range of the orthorhombic phase increases while the rate of substitution of chromium increases. This result is confirmed by the variation of the magnetic susceptibility as a function of temperature for various values of x (fig. 9). The amplitude of the two magnetic discontinuities decreases with rising x, T_2 is no longer observable for $x > 0.10$. The existence of the two

465-504 O - 72 - 15

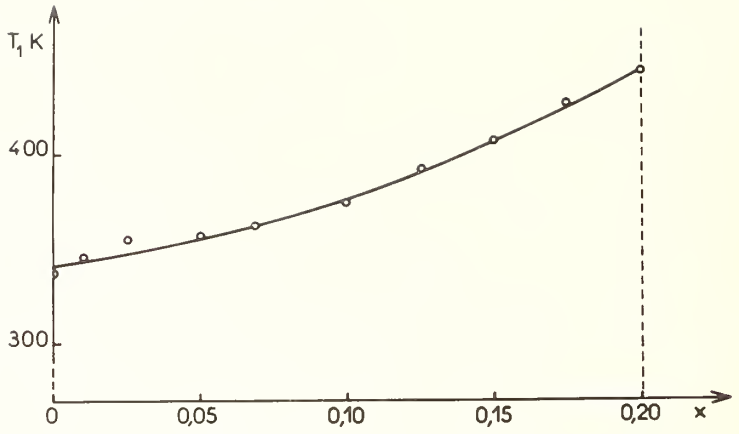

Fig. 7. Transformation temperature T_1 between phases O and R as determined by DTA.

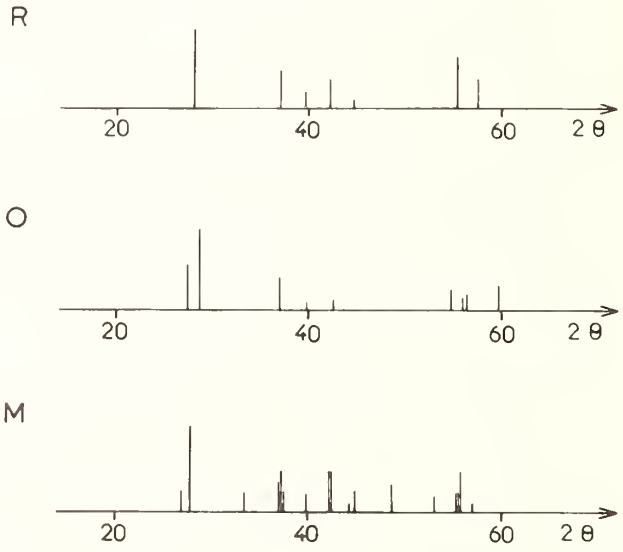

Fig. 8. Diffraction patterns of the phases R, O and M of composition $Cr_{0.01}V_{0.99}O_2$.

transition temperatures is also shown by conductivity measurements as a function of temperature (fig. 10). The phases M and O behave as semi-conductors, while R is metallic as x is small, for x > 0.10 the R phase becomes in turn semi-conducting.

All these facts now allow one to construct a phase diagram of the three phases as a function of x and temperature (fig. 11)(*).

The similarity of the parameters c_O and c_R shows that the d-d bonds that exist in the phase M are all broken in the phase O. The comparison of the parameters a_O, b_O and a_R indicates that in the orthorhombic phase a ferroelectric distortion takes place in the vanadium surroundings (fig. 12). This distortion is itself a result of the substitution: $2V^{4+} = Cr^{3+} + V^{5+}$ in the $Cr_xV_{1-x}O_2$ phase. One can assume that vanadium 5+ having a much smaller size induces the distortion of the coordination octahedron. The increase of T_1 with x can be explained by the fact that the energy necessary to transform O to R is higher as the V^{5+} atoms become more numerous.

*A recent Guinier investigation shows that for $x \leqslant 0.05$ the intermediate phase is actually monoclinic with only 50% of the d-d bonds broken, whereas the rupture is complete in the orthorhombic phase. It was detected the first time by Marezio, McWhan, Remeika and Dernier [33].

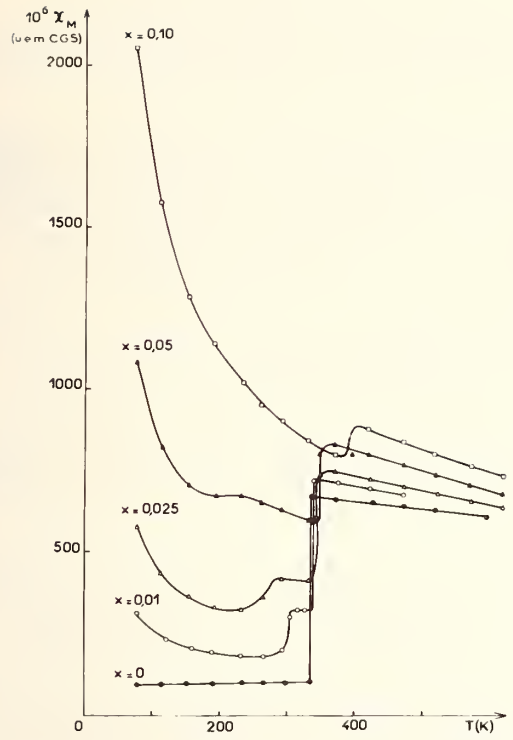

Fig. 9. Magnetic susceptibility of $Cr_xV_{1-x}O_2$.

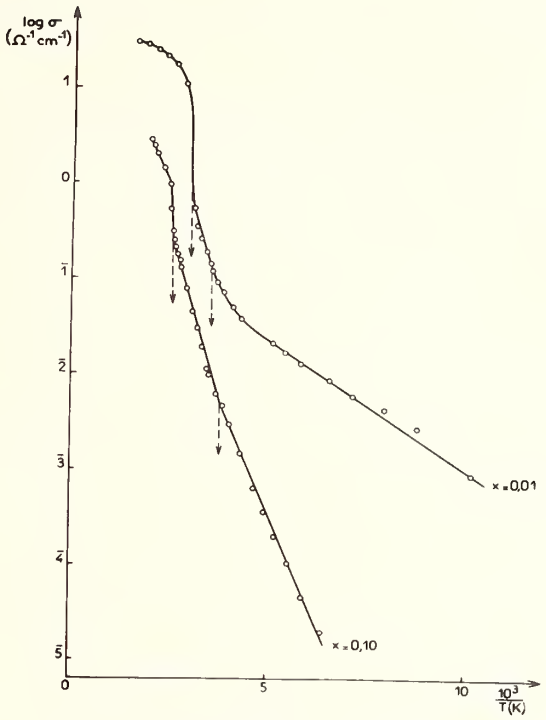

Fig. 10. Electrical conductivity of $Cr_xV_{1-x}O_2$.

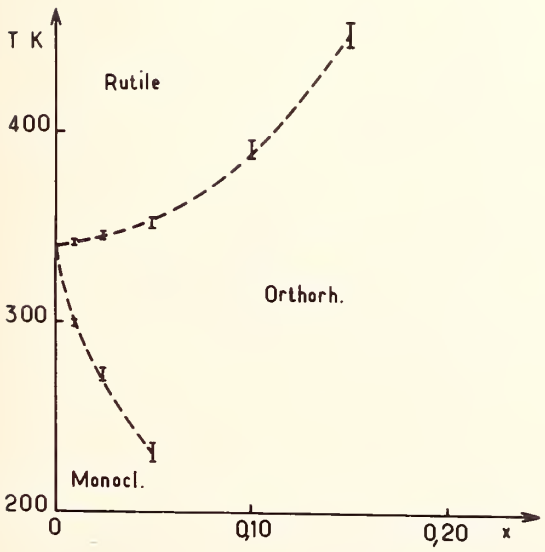

Fig. 11. Phase diagram of phases $Cr_xV_{1-x}O_2$.

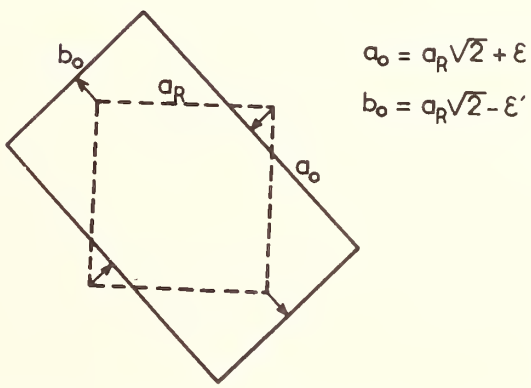

Fig. 12. Ferroelectric distortion during the O⇄R transition.

On the other hand the replacement of vanadium by chromium brings about a progressive rupture of the d-d bonds which are characteristic of the phase M, and so T_2 should decrease as x increases.

The metallic properties of phase R for small values of x result, as in the case of high temperature VO_2, from the delocalization of d electrons which occupy, according to Goodenough's model, a part of the levels available in the $t_{//}$ band characteristic of the bonds between vanadium atoms along the c axis, and in the a $\pi^* t_\perp$ band, which overlaps it, due to the π(V-O-V) bonds perpendicular to the c axis (fig. 13)[15 to 17]. As x increases, the progressive decrease in the metallic character results from the presence of Cr^{3+} ions which break the sequence V-V-V and intercalate between the vanadium atoms.

The structural change seems to be analogous in the phases $Al_xV_{1-x}O_2$ and $Fe_xV_{1-x}O_2$ characterized respectively by substitution such as: $2V^{4+} = Al^{3+} + V^{5+}$ and $2V^{4+} = Fe^{3+} + V^{5+}$.

The aspect of the phase diagrams obtained are completely different when the substitution creates vanadium 3+. Various authors have studied the system VO_2-NbO_2, and have shown that it is characterized by the formation of a compound $Nb_xV_{1-x}O_2$ which for $x < 0.50$ can be denoted by the substitution: $2V^{4+} = Nb^{5+} + V^{3+}$ [18,19].

Studies by x-ray diffraction, DTA, electrical conductivity and thermoelectric power measurements indicate that, at least for $x < 0.15$, two phases only appear: the rutile phase R at high temperatures and the monoclinic phase M. The transformation point decreases about 11° per Nb °/₀ introduced (fig. 14)[20].

For $x > 0.10$ the phase R passes gradually from metallic behavior to semi-conducting, with an increasing activation energy. One is tempted to attribute this change, which is analogous to that observed for $Cr_xV_{1-x}O_2$(R), to the interruption of the sequences V-V-V by the Nb^{5+} ions.

The lowering of the transformation point with increasing x can be attributed either to the decrease of the number of d-d bonds by the introduction of niobium 5+, or to the introduction of supplementary electrons, due to V^{3+}, into a distinct antibonding band $\pi^* t_\perp$. The absence of phase O can be explained by the absence of V^{5+} ions able to induce a ferroelectric distortion.

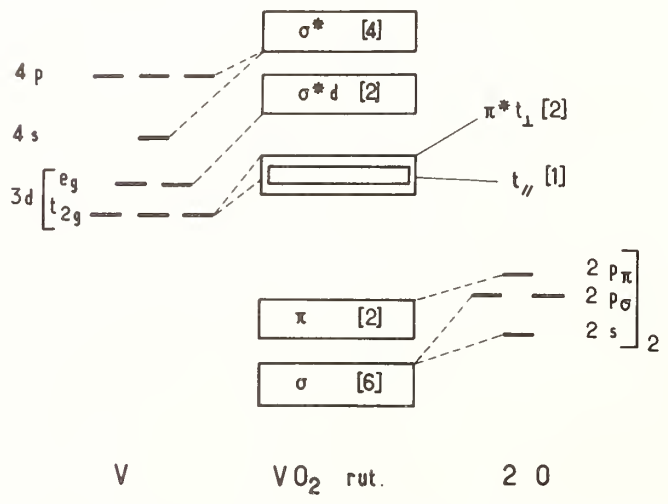

Fig. 13. Band structure of the high temperature variety of VO_2.

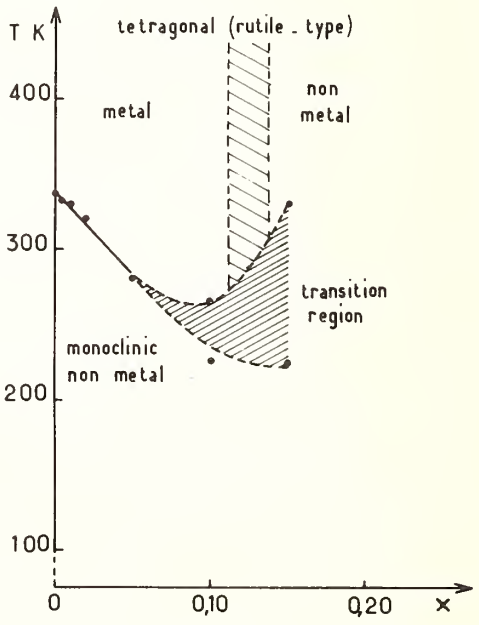

Fig. 14. Phase diagram of the compound $Nb_xV_{1-x}O_2$ for $x < 0.15$.

An analogous diagram has been observed in the neighborhood of VO_2 for the substitutions: $2V^{4+} = Ta^{5+} + V^{3+}$, $3V^{4+} = Mo^{6+} + 2V^{3+}$ and $3V^{4+} = W^{6+} + 2V^{3+}$ [21,22,23]. The lowering of the transformation point is particularly fast in both last cases.

This analogy reappears again in the system $VO_{2-x}F_x$ obtained by partial replacement of oxygen by fluorine, the substitution relation can be written here as: $V^{4+} + O^{2-} = V^{3+} + F^-$ [24,25]. The decrease of the transition temperature is about 12° C per F °/₀. The absence of any cation other than vanadium suggests the conclusion that the lowering of the transition point results effectively from the appearance of d electrons in the $\pi^* t_{\downarrow}$ band.

The structures of the phases derived from VO_2 are therefore closely related to the degree of oxidation and to the temperature.

4 PEROVSKITE RELATED COMPOUNDS

The last example deals with series of compounds of structure derived from the perovskite in which the vanadium has an oxidation state intermediate between 4+ and 3+.

Let us consider for instance the case of the series $La_{1-x}Sr_xVO_3$ [26]. For $0 < x \leqslant 0.40$ it forms, at 1100°C, a phase with the $GdFeO_3$ structure with a slight rhombohedral distortion (fig. 15).

The effective magnetic moment seems to follow the Curie-Weiss law. However, instead of decreasing as one could predict by the progressive replacement of V^{3+} by V^{4+} with increasing x, it rises rapidly with x and then levels off (fig. 16). The paramagnetic Curie temperature tends towards very high values (fig. 17). Electrical conductivity measurements as a function of temperature show that the activation energy which is about 0.10 eV for $x = 0$ tends towards zero for $x \simeq 0.20$ (fig. 18). All these properties are characteristic of a progressive transition with x of the type semiconductor → metal.

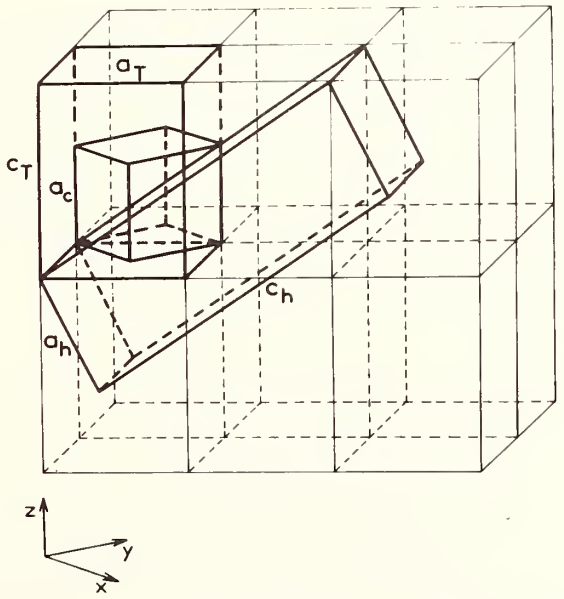

Fig. 15. Relationship between the parameters of the cubic, tetragonal (or orthorhombic) and hexagonal perovskite unit cell ($a_h = a_c\sqrt{2}$, $c_h = 2a_c\sqrt{3}$).

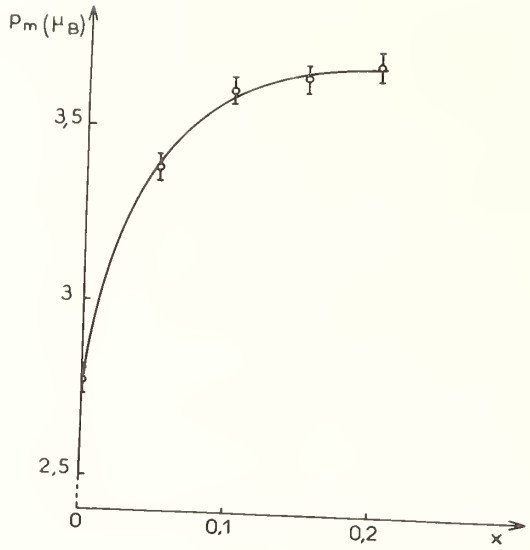

Fig. 16. Variation of the effective magnetic moment as a function of x for the phase $La_{1-x}Sr_xVO_3$.

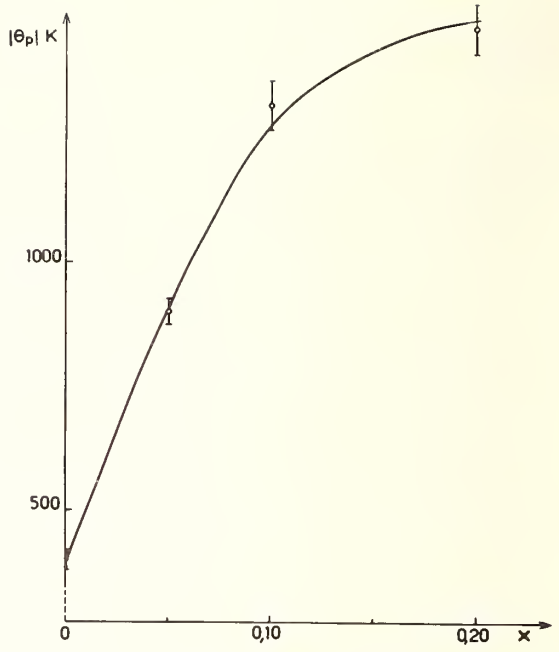

Fig. 17. Variation of the Curie paramagnetic temperature as a function of x for the phase $La_{1-x}Sr_xVO_3$.

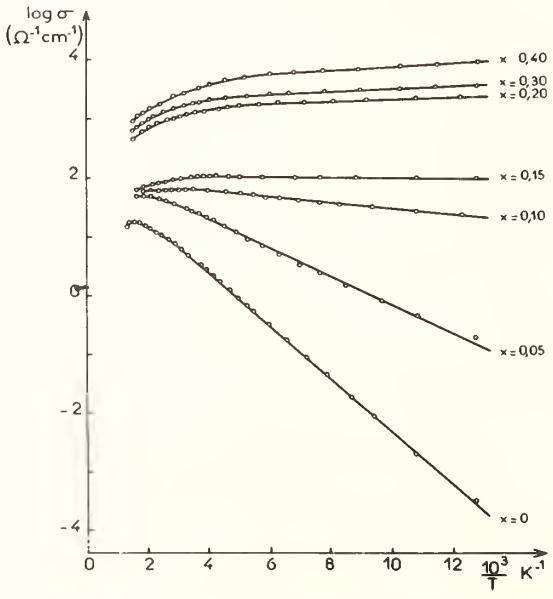

Fig. 18. Variation of the logarithm of the conductivity with the inverse absolute temperature for various phases of $La_{1-x}Sr_xVO_3$.

This phenomenon can be explained by the compositional change in this phase. The replacement of the lanthanum by strontium gives rise to an average weakening of the bond σ (A-O) due to the reduction of charge at the A site. This weakening in turn causes a strengthening of the bond π (B-O) with which the σ (A-O) bond is in competition. The corresponding π^* band becomes broader as the substitution increases. Since this band is only partially filled, it gradually results in metallic conductivity (fig. 19). This broadening of the π^* band is enhanced by the progressive increase in the average oxidation state of vanadium which strengthens the bonds σ (B-O) and π(B-O). The covalence parameters λ_σ and λ_π of Goodenough are now $\lambda_\sigma > \lambda_\pi > \lambda_c$, λ_c being the critical value above which the d electrons are collective [17].

A similar phenomenon is observed in the case of the orthorhombic $Gd_{1-x}Sr_xVO_3$ phase ($0 < x < 0.17$) of the type $GdFeO_3$. Figure 20 allows the comparison of the activation energies of $La_{1-x}SrVO_3$ and $Gd_{1-x}Sr_xVO_3$: the σ(Gd-O) bond being stronger than the σ(La-O) bond, ΔE_{Gd} is greater for the same value of x. For two phases of homologous composition the metallic character is more pronounced in the case of lanthanum than in that of gadolinium. This result shows conclusively that the change in the physical properties is not due exclusively to the charge increase on the vanadium atom.

However, one can wonder whether the semiconductor→metal transition is not the result of a structural evolution induced by the substitution. The Goldschmidt critical radii increase with x ($r_{Sr^{2+}} = 1.16$ Å, $r_{La^{3+}} = 1.06$ Å, $r_{Gd^{3+}} = 0.94$ Å, in the Shannon and Prewitt classification), this results in a small increase of the angle V-O-V which tends towards 180° and therefore in a strengthening of the π (V-O) bond, whose metallic character is enhanced. This explanation is in agreement with the fact that the activation energy of $LaVO_3$ is smaller than that of $GdVO_3$, as the angle V-O-V is larger in the former case than in the latter. It is not sure that the competition between bonds has a greater influence than the bond angles on the mechanism of conduction.

It is of interest to compare the properties of $LaVO_3$ and $GdVO_3$ with those of the corresponding compounds of the first series of transition elements having a perovskite type structure.

$LaTiO_3$ is metallic and Pauli paramagnetic, whereas $GdTiO_3$ is semiconducting and antiferromagnetic at low temperatures [27,28]. If λ_W is the value of the covalence parameter for which the Curie-Weiss electronic correlations give rise to Pauli paramagnetism ($\lambda_W > \lambda_c$), $\lambda_\pi > \lambda_W$ for $LaTiO_3$ and $\lambda_W > \lambda_\pi > \lambda_c$ for $GdTiO_3$, the weakening of the π (Ti-O) bond is still due to the fact that σ (Gd-O) is stronger than σ (La-O). The difference of behavior between $LaTiO_3$ and $LaVO_3$ results from the much greater extension of the titanium t_{2g} orbitals ($\lambda_W > \lambda_c > \lambda_\pi$ for $LaVO_3$ and $GdVO_3$).

On the other hand $LaCrO_3$ and $GdCrO_3$, whose t_{2g} orbitals are less extended than those of $LaVO_3$ and $GdVO_3$, have localized d electrons ($\lambda_W > \lambda_c > \lambda_\pi$).

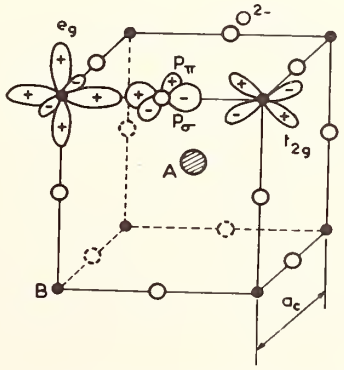

Fig. 19. Competition between the σ(A-O) and π(B-O) bonds in a perovskite lattice.

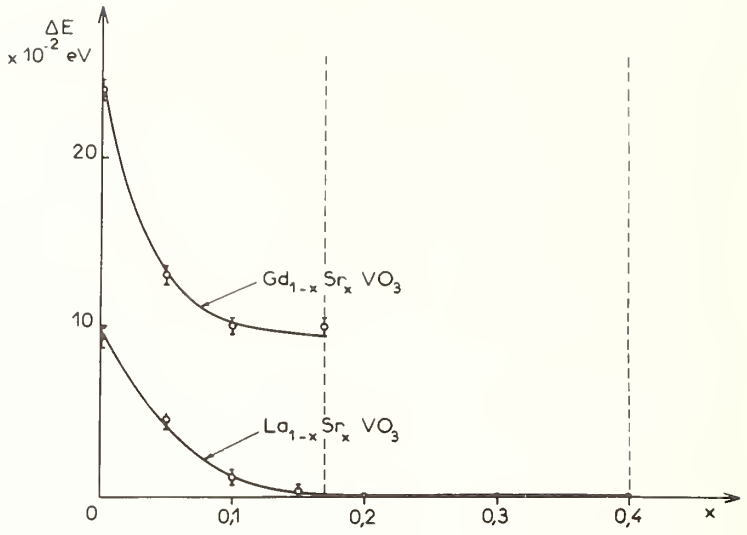

Fig. 20. Variation of the activation energy as a function of the rate of substitution in the compounds $La_{1-x}Sr_xVO_3$ and $Gd_{1-x}Sr_xVO_3$.

$LaMnO_3$ and $GdMnO_3$ show a Jahn-Teller distortion and a A type magnetic structure due to the presence of manganese 3+ ($t_{2g}^3\ e_g^1$). Under these conditions the d electrons are obviously localized and $\lambda_c > \lambda_\sigma > \lambda_\pi$. A localization is also observed for $LaFeO_3$ and $GdFeO_3$, where the high value of the intraatomic exchange energy for the Fe^{3+} ions ($t_{2g}^3\ e_g^2$) implies that λ_σ and λ_π are becoming smaller.

$LaCoO_3$ has simultaneously Co^{III} ions in the low spin state ($t_{2g}^6\ e_g^0$) and Co^{3+} in the high spin state ($t_{2g}^4\ e_g^2$). For $GdCoO_3$ the Co^{III} ions exist alone at low temperatures and the Co^{3+} ions at high temperatures. It has been shown that in both phases a transition temperature exists for localized electrons $\rightleftarrows$ collective electrons (of different nature). One can conclude in both cases that $\lambda_\sigma \simeq \lambda_c$ for the e_g electrons in the high spin state of cobalt [29,30]. The difference in behavior with the analogous iron compounds can doubtlessly be explained in part by the greater tendency of cobalt, whose nucleus has a greater charge, to give to the ions a low spin, and also by the decrease in the intra-atomic exchange energy.

The behavior of the nickel 3+ compounds confirms this point of view. These compounds have been recently prepared under an oxygen pressure of 4 kbars, and their physical properties studied in detail [31]. Nickel is found to exist in the low spin state in the whole temperature range studied ($t_{2g}^6\ e_g^1$). $LaNiO_3$ is metallic ($\lambda_\sigma > \lambda_W$). To the contrary $YNiO_3$ and $LuNiO_3$ are Curie-Weiss paramagnetic, but the absence of the Jahn-Teller effect gives rise to a magnetic structure of type G($\lambda_W > \lambda_\sigma > \lambda_c$). The only explanation for this weakening of λ_σ is the decrease in the bond angle Ni-O-Ni as the size of the A^{3+} ion decreases.

In brief the properties of the oxides of the rare earths and transition elements having perovskite-like structures; depend not only on the nature of the bonds, in particular the σ (A-O) bond, but also on their crystal structures. The results concerning these various phases are condensed in figure 21.

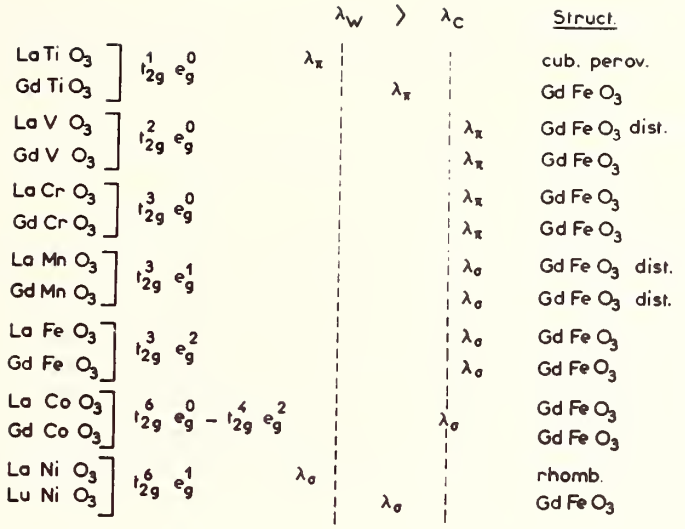

Fig. 21. The change in the covalence parameters of Goodenough in some phases with perovskite-like structure containing a lanthanide in site A and a transition 3d ion in the B site.

5. REFERENCES

[1] Pouchard, M., Galy, J., Rabardel, L., Hagenmuller, P., C.R. Acad. Sc. 264, 1943, 1967.
[2] Rabardel, L., Pouchard, M., Hagenmuller, P., brevet CNRS n° 72.118, 1966.
[3] Pouchard, M., Casalot, A., Villeneuve, G., Bull. Soc. Chim. Fr. 1, 81, 1968.
[4] Galy, J., Andersson, S., private communication.
[5] Morin, F. J., Phys. Rev. Letters, 3, 34, 1959.
[6] Kitahiro, I., Ohashi, T., Watanabe, A., J. Phys. Soc. Japan, 21, 2422, 1966.
[7] Paul, W., Mat. Res. Bull., 5, 691, 1970.
[8] Rudorff, W., Walter, G., Stadler, J., Z. anorg. allg. Chem., 297, 1, 1958.
[9] Minomura, S., Nagasaki, H., J. Phys. Soc. Japan, 19, 131, 1964.
[10] Andersson, G., Acta Chem. Scand. 10, 623, 1956.
[11] Adler, D., Brooks, H., Phys. Rev., 155, 826, 1967.
[12] Goodenough, J. B., id., 117, 1442, 1960.
[13] Zinanon, Z., Mott, N. F., Phil. Mag., 21, 881, 1970.
[14] Villeneuve, Bordet, A., Casalot, A., Hagenmuller, P., Mat. Res. Bull., 6, 119, 1971.
[15] Bongers, P. F., Sol. State Comm. 3, 275, 1965.
[16] Knoeugue, K., J. Phys. Soc. Japan, 22, 551, 1967.
[17] Goodenough, J. B., Progress Sol. State Chemistry V, Pergamon, 1971.
[18] Rüdorff, W., Marklin, J., Z. anorg. allg. Chem., 334, 142, 1966.
[19] Trarieux, H., Bernier, J. C., Michel, A., Ann. Chim. 4, 183, 1969.
[20] Villeneuve, G., Casalot, A., Bordet, A., Hagenmuller, P., Pouget, J. P., Launois, H., Lederer, P., J. Chem. Phys. Sol., to be published.
[21] Israelsson, M., Kihlborg, L., Mat. Res. Bull. 5, 19, 1970.
[22] Nygren, M., Israelsson, M., id., 4, 881, 1969.
[23] Rao, C. N. R., Natarajan, M., Subba Rao, G. V., Loehman, R. E., J. Phys. Chem. Sol., 32, 1147, 1971.
[24] Chamberland, B. L., id., 6, 425, 1971.
[25] Bayard, M., Reynolds, T. G., Vlasse, M., McKinzie, H. L., Arnott, R. J., Wold, A., J. Solid State Chem. 3, 484 (1971).
[26] Dougier, P., Casalot, A., J. Sol. State Chem., 2, 396, 1970.
[27] Koehler, W. C., Wollan, E. O., J. Phys. Chem. Sol. 2, 100, 1957.
[28] Bozorth, R. M., Williams, H. J., Walsh, D. E., Phys. Rev., 103, 572, 1956.
[29] Raccah, P., Goodenough, J. B., J. Appl. Phys., 39, 1209, 1968.
[30] Casalot, A., Dougier, P., Hagenmuller, P., J. Phys. Chem. Solids, 32, 407, 1971.
[31] Demazeau, G., Marbeuf, A., Pouchard, M., Hagenmuller, P., J. Solid State Chem. 3, 582 (1971).

[32] Goodenough, J. B., id. 3, 490 (1971).
[33] Marezio, M., McWhan, D. B., Remeika, J. P., Dernier, P. D., private communication.

DISCUSSION

D. B. McWhan: I just wanted to emphasize the point that Professor Hagenmuller had made with regard to VO_2 and chromium in VO_2. It has been traditional to explain the insulating properties and the lack of magnetism in the low temperature form of VO_2 entirely on the basis of the d-electron being pulled up into covalent bonds. Of the four studies that I am aware of, in the chromium doped VO_2 system, only the one at Bell Labs has been done on a single crystal refinement. As Professor Hagenmuller has said, it shows that only half of the vanadium atoms are paired. Therefore, we have to go back and reexamine our simple picture of the metal to insulator transition because the chromium doped VO_2 at low temperatures is still insulating. It is still non-magnetic but only half of the vandiums are paired. As we learn more about the band structures of the rutile phases from the careful work that is being done on TiO_2 and 4d and 5d oxides, we can hope to go back and get a more realistic picture of this transition.

P. Hagenmuller: I agree with you. Both phases, your monoclinic phase for a very low value of x and our orthorhombic phase are semiconductors. I hope that the contributions we can make from both sides will offer the opportunity for a practical cooperation.

J. B. Goodenough: I am making a response, Paul, to the last remark by McWhan rather than to your paper and I hope that you will forgive me. Ten years ago we emphasized the metal-metal bonding as a way in which one could tie up the electrons in homopolar bonds and therefore explain the lack of magnetic order as well as the semiconducting properties. Since that time we have taken note of the fact that there are displacements of the vanadium 4^+ ions within the octahedra, which you have described in a vague way as a twisting. These form one short vanadium oxygen bond very characteristic of a ferroelectric or an antiferroelectric type displacement of the cations. I think such a motion makes an important contribution to the semiconductor-to-metal transition. One of the things of interest in this class of materials is to determine what is the driving mechanism for this transition. Is it the desire to form the metal-metal bonds or is it a softening of the vibrational mode associated with the ferroelectric-type displacement? I personally find the Bell result most interesting, because they find a 50-50 contribution in their monoclinic phase. It appears that both are contributing about the same amount of driving mechanism. Half the chains form homopolar bonds. The other half, which does not form homopolar bonds, actually shows the antiferroelectric type of displacements, ments, forming one short metaloxygen bond in the material. Antiferroelectric displacements along the chains are also enough to account for the semiconductor-to-metal properties in this particular material. I won't go into the reason at this point, but both mechanisms, homopolar bonding and antiferroelectric displacements, are playing a role. That's all I wish to emphasize at this point. If one considers both these mechanisms, I think one can understand why we find a metal-to-insulator transition. I will make one other comment. It is about the addition tion of fluorine, thereby introducing vanadium 3^+ ions. A vanadium 3^+ ion does not participate in the ferroelectric-type displacement. Therefore, it does not encourage that particular component of the distortion. In addition, vanadium does not form a close bond with the fluorine. Therefore, that also discourages any antiferroelectric-type displacement in this particular material. So one gets a rather sharp decrease in the transition temperature, or addition of fluorine favors the rutile phase all the way down to lowest temperatures, for both those reasons [32].

P. Hagenmuller: I agree completely. It seems the orthorhombic phase is a consequence of a type of ferroelectric distortion and there are two arguments to support this. The first one is that in the case of the chromium-vanadium oxide system the transition temperature increases all the more when one has vanadium 5+. The second argument is given by the fact that one never obtains the orthorhombic or McWhan monoclinic phase, as long as one has vanadium 3+.

National Bureau of Standards Special Publication 364, Solid State Chemistry, Proceedings of 5th Materials Research Symposium, issued July 1972.

PREPARATION AND STRUCTURE OF A PYROCHLORE AND PEROVSKITE IN THE $BiRhO_{3+x}$ SYSTEM*

J. M. Longo,† P. M. Raccah,+ J. A. Kafalas, and J. W. Pierce

Lincoln Laboratory
Massachusetts Institute of Technology
Lexington, Massachusetts 02173

The pyrochlore structure with general formula $A_2B_2O_7$ is formed with a wide variety of ions and tolerates a high degree of nonstoichiometry on the anion and A cation sites *e.g.* $Pb_{1.5}Nb_2O_{6.5}$. We have found that the reaction of Bi_2O_3 with either Rh metal or Rh_2O_3 (Bi/Rh = 1:1) at 600-1000 °C in air or oxygen forms a compound with a face-centered cubic unit cell (a = 10.238 ± .008 Å) and the pyrochlore structure. X-ray fluorescence for the Bi/Rh ratio and thermogravimetric analysis for the oxygen content gave $Bi_{2.0}Rh_{2.0}O_{6.8}$.

In the pyrochlore structure the cations are in fixed positions, and there are two types of oxygen. Six oxygen atoms are of one type (O_1) with one position parameter and form the octahedra around the B cations. The last oxygen (O_2) is fixed and coordinated only to the A cations. It is not essential to the B_2O_6-octahedra network. Taking the origin at the B cation, we have refined the position parameter for O_1, the occupancy factor (OF) for O_2 and atomic temperature factors (B) by R-factor minimization of integrated powder diffraction intensity data. The results are as follows:

$$B_{Bi} = 0.7,\ B_{Rh} = 0.1,\ B_{O_1} = 0.1,\ B_{O_2} = 0.0,\ x_{O_1} = 0.326,\ OF_{O_2} = 0.7.$$

The position parameter for O_1 is in agreement with those found in other pyrochlores, and the occupancy factor (OF) is consistent with the chemical analysis. Resistivity measurements on sintered samples at room temperature gave $\rho = 3.2 \times 10^{-3}$ Ω-cm. We will discuss the stability of the defect structure in terms of the availability of the "inert pair" of electrons of the A cation.

When Bi_2O_3 and Rh_2O_3 were reacted in sealed, evacuated quartz tubes at 750-1100 °C, the product could not be identified. When the same reactants were placed in platinum capsules and subjected to over 65 kbar pressure at 1000-1300 °C for 1/2 hour, the perovskite $BiRhO_3$ was formed. Its unit cell is orthorhombic (a = 5.354 ± .005 Å, b = 5.813 ± .005 Å, c = 7.776 ± .005 Å) as in $GdFeO_3$ or the series of $LnRhO_3$. The relationship between the defect pyrochlore and perovskite structures will be discussed.

Key words: $BiRhO_3$; defect structures; perovskite; pressure-synthesis; pyrochlore.

1. INTRODUCTION

As part of a broad study of mixed metal oxides, the previously unreported Bi-Rh-O system was investigated in the vicinity of the bismuth to rhodium ratio 1:1.

2. EXPERIMENTAL METHODS

When intimately mixed Bi_2O_3 and Rh_2O_3 were reacted at 800 °C for 20 hours in air (rhodium metal or a variety of bismuth salts could also be used), a single-phase, black compound

*This work was sponsored by the Department of the Air Force.
†Present address: Esso Research & Engineering Co., Linden, New Jersey 07036
+Present address: Belfer Graduate School, Yeshiva University, New York, New York 10033

was formed. X-ray powder diffraction patterns of this new phase were subsequently indexed on the basis of a face-centered-cubic unit cell with $a = 10.238 \pm 0.008$ Å. A chemical analysis was then performed to eliminate composition ambiguities arising from the volatility of bismuth (III) oxide and the variable oxidation states of both rhodium and bismuth. The bismuth to rhodium ratio as determined by x-ray fluorescence was 1.00 ± 0.03 and a weight loss of 14.85% was observed when the bismuth-rhodium oxide sample was reduced under flowing 15% hydrogen/85% argon in a du Pont Thermogravimetric Analysis System. The observed bismuth to rhodium ratio and the assumption that the weight change could be totally attributed to loss of oxygen lead to the formula $BiRhO_{3.4}$.

All identification and structural investigations were made on powders using a Norelco diffractometer with CuKα radiation and a LiF crystal diffracted-beam monochromator. X-ray intensity data used for the refinement of structural parameters were collected by slow scanning (1/4°/min.) through each peak and accumulating both time and counts. Background corrections, determined from a smooth plot of values between peaks, were subtracted from each observation. Where reflections could not be resolved, they were recorded as a single peak and similarly treated in the refinement. A total of twenty-one intensities were collected in this way over the interval $20° < 2\theta < 120°$.

3. RESULTS AND DISCUSSION

The x-ray intensity profile, cell dimensions, and observed stoichiometry lead to the conclusion that the structure of the new phase was similar to that of pyrochlore, space group Fd3m. In this structure the bismuth atoms would have a six plus two oxygen coordination while the rhodium atoms would occupy slightly distorted octahedra that share corners with other rhodium octahedra to form a three dimensional network as shown in figure 1. The site with 3m symmetry was chosen as the origin, and the atomic positions given in table 1 were assigned to each atom.

We then refined the single variable-position parameter for the oxygen of the octahedron, the occupancy factor for the oxygen atom associated only with bismuth, and the isotropic atomic temperature factors for Bi, Rh, O_1, and O_2 using a simplex program developed in our laboratory for minimization of the function $R = 100 \times \Sigma|I_{obs}-I_{cal}|/\Sigma I_{obs}$. In the refinement, the atomic scattering factors for Bi^{3+}, Rh^{3+} [1][1], and O^{-2} [2] were corrected for the real and imaginary parts of the anomalous-dispersion term [3]. The theoretical polarization correction for a LiF diffracted-beam monochromator was also applied to our data. The parameters,

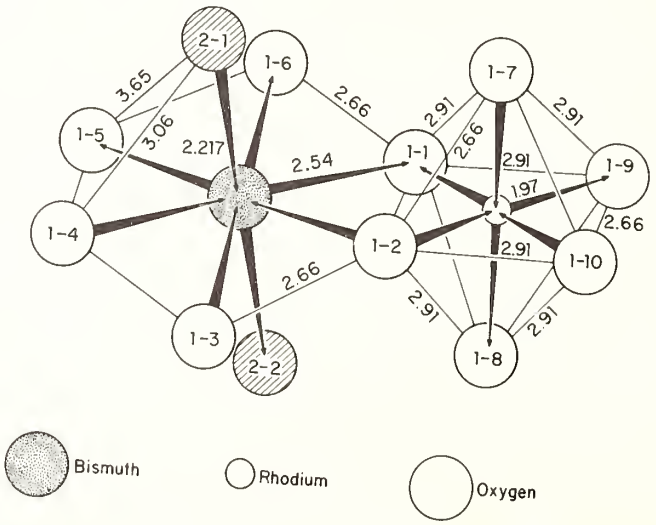

Fig. 1. Octahedra network in the pyrochlore structure.

[1]Figures in brackets indicate the literature references at the end of this paper.

resulting from the final refinement to R = 3.3, are given in table 1, and table 2 lists the observed and calculated intensities for comparison. The refined occupancy factor 0.7 ± 0.1 (70% of the O_2 sites filled) is within experimental error of the 0.8 found by chemical analysis. The occupancy factor for O_1 always remained at 1.0 when allowed to vary, so it was fixed at unity during final refinements to increase the data to parameter ratio. The crystal chemistry of pyrochlores shows that the seventh oxygen (O_2) is not essential to the stability of the octahedra network [4] and that the oxygen content can vary from six to seven ($Pb_2Ru_2O_6$ [5], $Pb_2Pt_2O_{6.7}$, and $Pb_2Rh_2O_7$ [6]).

The position parameter for O_1 (x = 0.326) is well within the range of reported values ($0.305 \leq x \leq 0.355$) for all pyrochlores and is very close to the values found for trivalent rare-earth pyrochlores ($0.322 \leq x \leq 0.333$). A thorough discussion of the pyrochlore structure and the values of all known u-parameters has been given by Sleight [7]. A list of all Rh-O and Bi-O distances as well as selected O-O distances and interatomic angles is given in table 3. Figure 2 shows a rhodium octahedron edge-shared to the bismuth polyhedron and includes some important interatomic distances. The six equivalent Rh-O distances of 1.97 Å agrees exactly with that predicted assuming 80% Rh^{4+}/20% Rh^{3+} and the ionic radii of Shannon and Prewitt [8]. The average Bi-O distance is also in excellent agreement with that predicted [8] for Bi^{+3} in eight-fold coordination. The O-O distances found range from 2.66 Å to 3.65 Å and are similar to those found in most mixed metal oxides.

The resistivity of $Bi_2Rh_2O_{6.8}$ was determined using a four-probe technique on sintered material. At room temperature $\rho = 3.2 \times 10^{-3}$ Ωcm. while $\rho = 3.0 \times 10^{-3}$ Ωcm. at liquid-nitrogen temperature. These values are characteristic of metallic oxides. Similar resistivities have been found in sintered samples of $Pb_2Ru_2O_6$ [5], $Pb_2Ir_2O_{6.5}$ [6] and $Bi_2Ru_2O_7$ [9]. In fields to 14 kOe the magnetic susceptibility of $Bi_2Rh_2O_{6.8}$ was less than the 10^{-5} emu/g sensitivity limit of our vibrating sample magnetometer over the entire range from room temperature to 4.2 K. Such behavior is consistent with the small, temperature-independent susceptibility characteristic of the Pauli paramagnetism often observed in metallic oxides.

When Bi_2O_3 and Rh_2O_3 were sealed in evacuated silica tubes and reacted at 700-1000 °C, the pyrochlore did not form and the products could not be identified. However, when the same reactants were subjected to high pressure (65-90 kbar) and high temperatures (1000-1300 °C), a compound with an orthorhombic perovskite structure was formed along with a small amount of a second phase. The composition $BiRhO_3$ was assumed and was not confirmed by chemical analysis since we could not obtain pure material.

In a typical high-pressure experiment, the well mixed reactants are tightly packed into a cylindrical (4 mm dia. x 10 mm) platinum capsule that is inserted into a high-pressure cell equipped with a graphite sleeve heater. The entire assembly is next placed in a belt apparatus capable of developing 90 kbar and subjected to the desired pressure. The sample is then brought rapidly to the desired temperature and held there for five to thirty minutes. At this point the sample is quenched before the pressure is released.

Table 1

Crystallographic Data for $Bi_2Rh_2O_{6.8}$

Space Group:	Fd3m
Unit Cell Parameter:	10.238(8) Å
Cell Content:	$8Bi_2Rh_2O_{6.8}$

Rh in (16c)	(0,0,0; 0,1/4,1/4; 1/4,0,1/4; 1/4,1/4,0) F.C.
Bi in (16d)	(1/2,1/2,1/2; 1/2,1/4,1/4; 1/4,1/4,1/4; 1/4,1/4,1/2) F.C.
O_1 in (48f)	(x,1/8,1/8; x,7/8,7/8; 1/4-x,1/8,1/8; 3/4+x,7/8,7/8)tr; F.C.
O_2 in (8b)	(3/8,3/8,3/8; 5/8,5/8,5/8) F.C.
$x_{O_1} = 0.326$	Occupany Factor (O_2) = 0.7
$B_{Bi} = 0.7$	$B_{Rh} = 0.1$ $B_{O_1} = 0.1$ $B_{O_2} = 0.0$

Table 2

Comparison of Observed and Calculated Intensities for $Bi_2Rh_2O_{6.8}$

I_{obsd}	I_{calc}	hkℓ	d_{calc}
5.8	5.51	311	3.087
100.00	100.00	222	2.955
39.5	36.97	400	2.559
7.3	7.03	331	2.349
0.4	0.45	422	2.090
3.3	4.03	333 511	1.970
46.1	46.07	440	1.810
2.7	2.42	531	1.731
48.9	47.64	533 622	1.561
11.5	12.24	444	1.478
1.1	1.14	551 711	1.434
1.0	1.44	553 731	1.333
7.5	7.22	800	1.280
0.6	1.11	733	1.251
21.7	21.14	555 751 662	1.182 1.174
16.7	17.51	840	1.145
0.8	1.13	753 911	1.124
14.4	14.79	844	1.045
0.6	1.00	933 755 771	1.029
17.0	18.36	951 773 666 1022	0.990 0.985
6.4	5.97	880	0.905

Table 3

Interatomic Distances and Angles in $Bi_2Rh_2O_{6.8}$ [a/]

Bi-O:	$Bi\text{-}6O_1$	= 2.54
	$Bi\text{-}2O_2$	= 2.22
Rh-O:	$Rh\text{-}6O_1$	= 1.97
O-O:	$O_2\text{-}6O_1$	= 3 x 3.06
		= 3 x 3.65
	$O_1\text{-}8O_1$	= 4 x 2.66
		= 4 x 2.91

$O_{1\text{-}1}$-Bi-$O_{1\text{-}2}$ (6)	= 63.1°
$O_{1\text{-}1}$-Bi-$O_{1\text{-}3}$ (5)	= 116.9°
$O_{1\text{-}1}$-Bi-$O_{1\text{-}4}$	= 180°
$O_{2\text{-}1}$-Bi-$O_{1\text{-}1}$ (3,5)	= 100.2°
$O_{2\text{-}1}$-Bi-$O_{1\text{-}2}$ (4,6)	= 79.8°
$O_{1\text{-}1}$-Rh-$O_{1\text{-}2}$ (8)	= 84.8°
$O_{1\text{-}1}$-Rh-$O_{1\text{-}7}$ (9)	= 95.2°

a/ Notation consistent with figure 2.

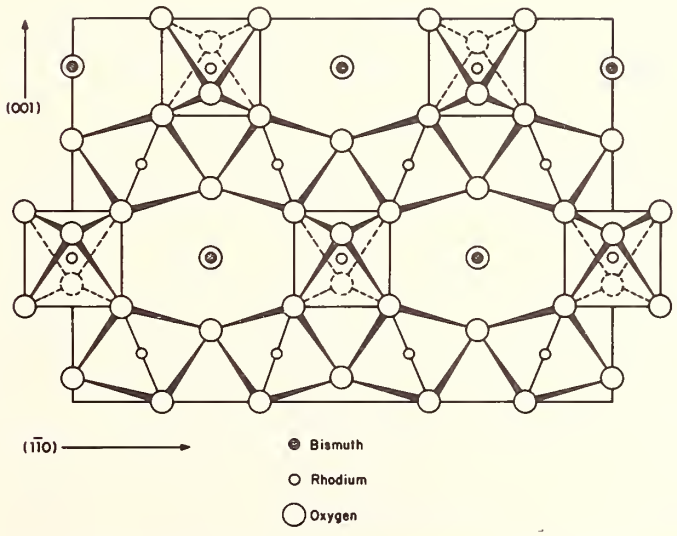

Fig. 2. Ruthenium and bismuth coordination with oxygen.

The lattice parameters for high-pressure orthorhombic $BiRhO_3$, as refined by the minimization of the differences between 2θ obs and 2θ calc for 26 peaks over the range 22° < 2θ < 84°, were a = 5.354 Å, b = 5.813 Å, and c = 7.776 Å with about 0.1% error. The intensities of diffraction peaks were then assigned on a 1 to 100 basis and are compared in table 4 to intensities calculated assuming that the atoms of $BiRhO_3$ are in positions corresponding to those found in orthorhombic $GdFeO_3$ [10]. Table 4 also lists for comparison the observed and calculated interplanar spacings.

Meaningful electrical and magnetic measurements were not possible on the high-pressure material since it was not prepared as a single phase.

The high-pressure perovskite phase could be retained at atmospheric pressure and withstood heating to 800 °C in nitrogen. Such stability is similar to that observed in other quenched, high-pressure, perovskite-related phases [11,12].

In the Bi-Rh-O system, the pyrochlore structure is stable when reaction is carried out in air. The rhodium atoms adjust their oxidation states to a formal +3.8. The formation of partially filled bands allows all rhodium to be equivalent and is the origin of the metallic conductivity and Pauli paramagnetism found for $Bi_2Rh_2O_{6.8}$. The oxygen vacancies resulting from inability of the rhodium atoms to achieve a full +4 oxidation state in this structure are directly associated with the bismuth atoms. These O_2-vacancies are located at the centers of bismuth tetrahedra and are stabilized by the high polarizability of bismuth. The

Table 4

Comparison of Observed and Calculated Intensities for High Pressure $BiRhO_3$

hkℓ	d(obs)	d(cal)	I(obs)	I(cal)	hkℓ	d(obs)	d(cal)	I(obs)	I(cal)
101		4.410		1.79	040	1.453	1.453	1	0.96
110	3.940	3.939	8	5.56	115	1.447	1.447	1	0.88
002	3.892	3.888	4	4.89	041	1.429	1.428	5	3.36
111	3.513	3.513	13	13.39	224	1.383	1.383	10	10.53
020	2.908	2.906	24	20.94	025	1.371	1.371	<1	1.20
112	2.764	2.767	100	100.0	042	1.361	1.361	<1	0.69
021	2.722	2.722	11	10.29	400	1.338	1.338	5	3.10
200	2.677	2.677	23	24.83	331	1.295	1.294	6	3.00
022	2.326	2.328	5	2.85	411	*	1.288	*	1.01
211	2.320	2.321	*	2.29	043	1.268	1.268	3	1.92
202	2.205	2.205	8	5.72	402	*	1.266	*	0.31
113	2.166	2.165	7	4.63	241	1.260	1.260	6	3.90
122	2.136	2.135	1	0.42	332	1.244	1.244	6	3.16
212	2.061	2.062	2	0.43	116	1.231	1.231	8	8.01
220	1.969	1.969	15	20.58	225	1.221	1.220	3	1.90
004	1.945	1.944	13	13.27	420	1.216	1.216	7	2.54
023	1.935	1.935	7	4.64	242	*	1.213	*	0.49
221	1.908	1.909	11	7.97	421	1.201	1.201	4	1.42
131	1.774	1.774	19	13.04	324	*	1.198	*	0.24
213	*	1.773	*	0.85	026	1.183	1.184	6	0.11
114	1.743	1.743	3	1.61	135	*	1.183	*	3.33
310	1.706	1.706	2	0.60	305	1.171	1.172	6	0.09
311	1.666	1.666	3	1.75	333	*	1.171	*	3.04
132	1.650	1.650	12	9.27	413	1.165	1.165	5	0.77
024	1.616	1.616	12	8.62	044	*	1.164	*	0.70
204	1.573	1.573	18	11.11	315	1.150	1.150	<1	0.60
230	*	1.570	*	0.28	243	1.146	1.146	6	3.27
223	*	1.568	*	3.71	150	1.136	1.136	1	1.10
312	1.562	1.562	20	17.80	151	1.124	1.124	6	3.04
133	1.491	1.491	7	6.71	* not separable from above line				

bonding possibilities of Bi^{3+} ions in the defect-pyrochlore structure is analogous to that of Pb^{2+} ions [5]. A discussion of the bonding possibilities has also been given by Bouchard and Gillson [9].

It is interesting to note that the only transition-metal pyrochlores formed with all, or a significant fraction, of the anion sites vacant have Tl^{+1}, Pb^{2+}, or Bi^{3+} ions as the A cation. In all cases, these A cations have $6s^2$ core electrons that are easily polarized because of a relatively small hybridization energy. We speculate that compounds like $Pb_2Ru_2O_6$ [5] and $Tl_2Nb_2O_6$ [13] are stabilized by a transfer of electron density from the A cation to the vicinity of the anion vacancy, thus forming what Goodenough has called a trap-mediated bond [14]. The exact extent and location of the core-electron density is not easily established, but it has been discussed in considerable detail for $Pb_2Ru_2O_6$ [5,11]. The compound $Ag_2Sb_2O_6$ also crystallizes in a defect-pyrochlore structure [15]. In this case it appears that the relatively small effective charge on the Ag^+ ions plus the relative instability of 180° Sb^{5+}-O^{2-}-Sb^{5+} bonds [15,16] allows this structure to be competitive with the perovskite structure.

Transition-metal $BiT^{3+}O$ oxides do not generally form perovskite structures at atmospheric pressure. $BiCrO_3$ and $BiMnO_3$, for example, require high pressure for their formation (17] and, like $BiFeO_3$, have distorted perovskite structures [18]. This is in marked contrast with the rare-earth $LnT^{3+}O_3$ perovskites, which generally form stable perovskite structures if the T^{3+} ion is able to have octahedral coordination [18]. Furthermore, with the smaller T^{3+} ions low spin Co^{III}, low spin Ni^{III} and Al^{3+}, the reported $BiT^{3+}O_3$ phase [19] stable at atmospheric pressure appears to have a structure similar to that of $KSbO_3$ [20]. If the stoichiometry of this phase is ABO_3, then a Bi^{3+}-ion array consisting of linked clusters of six cations unscreened by any intervening anion is indicated, and Goodenough has pointed out to us that a trap-mediated bond may be implicated in these phases also.

The perovskite structure (ABO_3) is strongly favored by high pressure, since it consists of close-packed AO_3 layers having B cations occupying all the all-anion octahedral sites, which share common corners because of cubic stacking of the AO_3 layers. The defect pyrochlore $Pb_2Ru_2O_6$ ($PbRuO_3$) transforms to the orthorhombic perovskite structure at 1400 °C and pressures P > 90 kbar [11], and it is reasonable to anticipate that all transition-metal $A_2B_2O_6$ pyrochlores would also transform similarly at high pressures. The formation of high-pressure $BiRhO_3$ is consistent with this idea.

4. ACKNOWLEDGMENT

We wish to thank J. B. Goodenough for many stimulating discussions, E. B. Owens for chemical analysis, and D. A. Batson and C. H. Anderson, Jr. for valuable technical support.

5. REFERENCES

[1] Cromer, D. T. and Waber, J. T., Acta Cryst. 18, 104 (1965).
[2] Tokonomi, M., Acta Cryst. 19, 486 (1965).
[3] Cromer, D. T., Acta Cryst. 18, 17 (1965).
[4] Jona, F., Shirane, G., and Pepinsky, R., Phys. Rev. 98, 903 (1955).
[5] Longo, J. M., Raccah, P. M., and Goodenough, J. B., Mater. Res. Bull. 4, 191 (1969).
[6] Sleight, A. W., Mater. Res. Bull. 6, 775 (1971).
[7] Sleight, A. W., Inorg. Chem. 7, 1704 (1968).
[8] Shannon, R. D. and Prewitt, C. T., Acta Cryst. B26, 1046 (1970).
[9] Bouchard, R. J. and Gillson, J. L., Mater. Res. Bull. 6, 669 (1971).
[10] Geller, S., J. Chem. Phys. 24, 1236 (1956).
[11] Kafalas, J. A. and Longo, J. M., Mater. Res. Bull. 5, 193 (1970).
[12] Longo, J. M. and Kafalas, J. A., Mater. Res. Bull. 3, 687 (1968).
[13] Belyaev, I. N., Lesnykh, D. S., and Lupeiko, T. G., Zh. Neorg. Khim. 14, 648 (1969).
[14] Goodenough, J. B., *Chemical Bond in Crystals*, N. N. Sirota, Ed. (HAYKA TEXH KA, Minsk, 1969) p. 94.
[15] Sleight, A. W., Mater. Res. Bull. 4, 377 (1969).
[16] Kafalas, J. A., this conference
[17] Sugawara, F., Iida, S., Syono, Y., and Akimoto, S., J. Phys. Soc. Japan 20, 1529 (1965).
[18] Goodenough, J. B. and Longo, J. M., Landolt-Bornstein Tabellen Neue Serie III/4a (Springer-Verlag, Berlin, 1970) p. 126

465-504 O - 72 - 16

[19] Bucci, Joseph D., Ph.D. Thesis, University of Missouri-Rolla (1971).
[20] Spiegelberg, P., Arkiv för Kemi, Min. Och Geol 14 (5), 1-12 (1940).

DISCUSSION

E. Banks: Did you mention anything about the properties of this perovskite?

J. M. Longo: No, we were really unable to measure any meaningful properties because we had small amounts of a second phase which we were unable to separate out.

P. Hagenmuller: Don't you believe it would be interesting to try to introduce some fluorine. Very often when one is able to replace holes by oxygen or oxygen by holes if you prefer, it is interesting to have an intermediate situation by using fluorine.

J. M. Longo: Yes, certainly pyrochlore is known to accept fluorine, hydroxide or even sulfide ions, on that seventh site and one can certainly speculate on a compound which would have no vacancies and they would be taken up by fluorine.

B. Post: There usually is a high degree of correlation between the occupancy factor and the temperature factor. I noticed that you had a rather low temperature factor for vacancies on O_2 sites, namely zero. Of course, this is what came out of your computer. Supposing you had changed the occupancy factor to .9 regardless of the stoichiometry. Did you try anything like that?

J. M. Longo: As I recall, we did change temperature factors because, as you noted, things like oxygen were very small, zero, and bismuth was .7 and we looked for some correlation there. The way I recall it there wasn't really very much change in this 0.7 occupancy factor. Even trying to hold oxygen temperature factors at a value of .2 or .3 and allowing it to refine, the occupancy factor did not change very much and we just got an increased R factor.

B. Post: Well, there is something wrong, seriously wrong!

R. Ward: I'd like to ask one question myself. Are all these oxygen deficient pyrochlores associated with elements which have lone pairs, or do you have oxygen deficiencies without them?

J. M. Longo: The pyrochlore compounds which have the oxygen deficiency are certainly most prevalent with lead 2+, thallium 1+, and bismuth 3+. Also the silver antimony oxide is known where the seventh oxygen position is totally vacant. To my knowledge that's the only exception to the vacancy type where there would not be the inert pair. Perhaps John Goodenough would like to make a comment there.

J. B. Goodenough: I would just like to point out that the original motivation for this work was because the lead compounds had no oxygen in that site and seemed to be associated with a lone pair. We tried with the bismuth compound and there was a certain disappointment that we actually had $O_{6.8}$ instead of $O_{6.0}$. In answer to your question, let me say that, as John Longo has pointed out, silver antimony oxide is the exception of a cation that has no lone pair and still forms a defect pyrochlore structure. However, as Jim Kafalas, in the last paper this morning will point out, we believe that is a peculiarity of the antimony 5+ ion. A 180 degree antimony 5+-oxygen-antimony 5+ bond does not like to form because of the very strong covalent bonding with the oxygen, and there are no d-orbitals involved. Antimony 5+, therefore, is willing to go into this particular structure with the silver in order to avoid having to make that particular kind of a bond connection. So I think it is a peculiarity of antimony 5+ that induces the silver ion to be stabilized in this defect-pyrochlore structure.

National Bureau of Standards Special Publication 364, Solid State Chemistry, Proceedings of 5th Materials Research Symposium, issued July 1972.

PRECIOUS METAL PYROCHLORES*

A. W. Sleight and R. J. Bouchard

Central Research Department
E. I. du Pont de Nemours and Company
Experimental Station
Wilmington, Delaware 19898

Rare earth pyrochlores of the type $A_2M_2O_7$ where A is a rare earth and M is Ru, Ir, Pd, or Pt have been reported, but little is known of their physical properties. We have grown crystals of the rare earth ruthenate and iridate pyrochlores. Four-probe electrical resistivity measurements on single crystals show that both rare earth ruthenates and iridates are semiconducting with an activation energy of about 0.1 eV for the ruthenates and about 0.08 eV for the iridates. Very different behavior is found for the iridate and ruthenate pyrochlores when the A cation is a post-transition metal. Although $Tl_2Ru_2O_7$ is also semiconducting, it has an activation energy of only about 0.01 eV. Metallic conduction is found for $Tl_2Ir_2O_7$, $Tl_2Os_2O_7$, $Bi_2Ru_2O_7$, and $Bi_2Ir_2O_7$. Magnetic susceptibility measurements confirm the localized electron behavior for the semiconductors and delocalized electron behavior for the metallic compounds. Structural refinements have been carried out for $Nd_2Ru_2O_7$, $Yb_2Ru_2O_7$, and $Bi_2Ru_2O_7$. The Ru-O distance is 2.00 ± .01 Å for all three compounds; however, an anomalously high temperature coefficient was found for Bi.

Key words: Metallic conductivity; oxides; pyrochlore structure; semiconductivity.

1. INTRODUCTION

Precious metal oxides with the pyrochlore structure and the formula $A_2^{+3}M_2^{+4}O_7$ have been known for some time where M is Ru or Ir and A is a rare earth [1,2][1]. Recent high pressure work has extended M to include Pd and Pt [3]. Another recent development is the use of post-transition elements (In, Tl, Pb, and Bi) as A cations [3-8]. When the A cation is Pb, the formula is generally better represented as $Pb_2M_2O_{7-x}$, and phases of this type will not be considered here.

An extensive program on precious metal pyrochlores is underway at this laboratory, including the preparation of new phases, crystal growth, crystallographic studies, and numerous physical measurements. Some of the results are given in this paper.

2. EXPERIMENTAL

The methods of preparing polycrystalline samples as well as $Tl_2Ru_2O_7$ crystals have been described previously [6,8]. Single crystals of $Bi_2Ru_2O_7$ and $Bi_2Ir_2O_7$ were grown in a Bi_2O_3 flux. Single crystals of rare earth ruthenates and iridates were grown hydrothermally or in a rare earth chloride flux.

Electrical resistivity was measured on single crystals when they were available. However, sintered bars of $Tl_2M_2O_7$ compounds were used except for $Tl_2Ru_2O_7$. In all cases the four-probe method was used.

---

*Contribution No. 1871.

[1] Figures in brackets indicate the literature references at the end of this paper.

3. RESULTS

Table 1 summarizes some results on precious metal pyrochlores. All the precious metal pyrochlores are black and appear to be cubic (Fd3m). Ruthenates are the easiest to obtain in a highly pure form, and ruthenate crystals are the easiest to grow.

3.1. RUTHENATES

Electrical resistivities of the ruthenate single crystals are given in table 1 and figure 1. All rare earth ruthenate pyrochlores are semiconducting with an activation energy of about 0.1 eV. A very low activation energy is found for $Tl_2Ru_2O_7$, and $Bi_2Ru_2O_7$ is not semiconducting at any temperature. Seebeck coefficients of +350 μV/°C for $Eu_2Ru_2O_7$, +20 μV/°C for $Tl_2Ru_2O_7$, and -7 μV/°C for $Bi_2Ru_2O_7$ also indicate a change from semiconducting to metallic behavior.

Extensive magnetic susceptibility data on the ruthenate pyrochlores have been obtained [9]. However, octahedral Ru^{+4} is nonmagnetic in its ground state, and this leads to complex magnetic behavior. Nonetheless, these data are compatible with localized Ru electron behavior when A is a rare earth or Tl and delocalized behavior when A is Bi.

Single crystals of $Tl_2Ru_2O_7$ and $Bi_2Ru_2O_7$ were examined on a precession camera and found to have the Fd3m space group. Structural refinements have been carried out on semiconducting $Nd_2Ru_2O_7$ and $Lu_2Ru_2O_7$, and metallic $Bi_2Ru_2O_7$. The details will be published elsewhere. The Ru-O distance is 2.00 ± .01 Å for all three pyrochlores, and the O-Ru-O angles are likewise very similar. Thus, it appears unlikely that the change from semiconducting to metallic properties can be attributed to changes in Ru-O distances or O-Ru-O angles. A high Bi temperature factor is the only result which distinguishes $Bi_2Ru_2O_7$ from $Nd_2Ru_2O_7$ and $Lu_2Ru_2O_7$. This high Bi temperature factor appears to be characteristic of inert pair cations on high symmetry sites.

3.2. IRIDATES

Rare earth iridates are semiconducting with activation energies somewhat lower than found for the ruthenates. Metallic behavior is indicated for $Tl_2Ir_2O_7$ and $Bi_2Ir_2O_7$. Thus, the iridate pyrochlores show the same trend found for ruthenate pyrochlores.

Table 1

Electrical Data and Cell Dimensions

Compound	$\rho_{298\ K}$, ohm-cm	Ea or R[(a)]	a, Å
$Nd_2Ru_2O_7$	2.0	0.07 eV	10.33
$Eu_2Ru_2O_7$	1.2	0.08 Ev	10.25
$Gd_2Ru_2O_7$	0.2	0.10 eV	10.23
$Yb_2Ru_2O_7$	1.0	0.12 eV	10.09
$Eu_2Ir_2O_7$	7×10^{-2}	0.09 eV	10.29
$Dy_2Ir_2O_7$	0.2	0.06 eV	10.21
$Tl_2Ru_2O_7$	2.3×10^{-4}	0.01 eV	10.20
$Bi_2Ru_2O_7$	2.5×10^{-4}	1.2	10.30
$Tl_2Ir_2O_7$	1.5×10^{-3}	1.2	10.21
$Bi_2Ir_2O_7$	1.1×10^{-3}	1.6	10.33
$Tl_2Pt_2O_7$	0.25	0.03 eV	10.13
$Tl_2Os_2O_7$	1.8×10^{-4}	1.4	10.31
$Tl_2Rh_2O_7$	6×10^{-4}	0.03 eV	10.16

(a) Resistivity ratio ($R = \rho_{298\ K}/\rho_{4.2\ K}$) is given for the metallic compounds; for semiconductors, the activation energy is given in electron-volts.

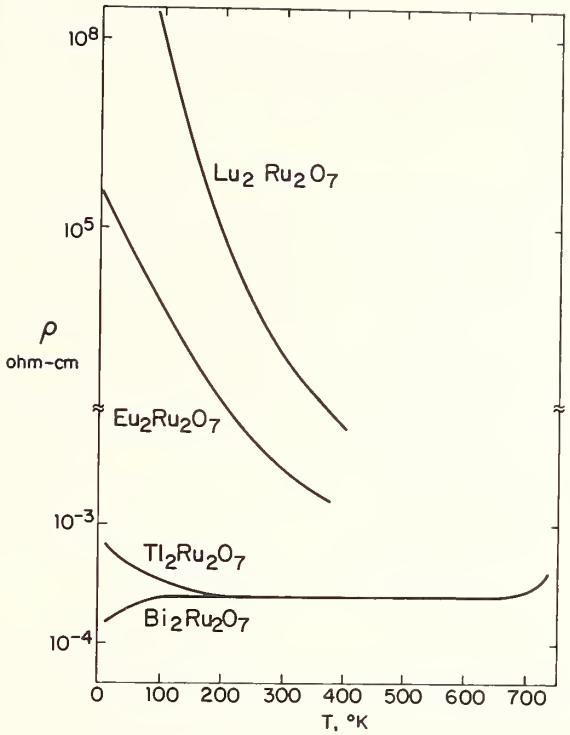

Fig. 1. Resistivity *vs.* temperature for some ruthenate pyrochlores.

4. DISCUSSION

Other metallic oxides containing Ru^{+4} or Ir^{+4} are RuO_2, IrO_2, $SrRuO_3$, and $SrIrO_3$ [10,11 12]. Presumably, this metallic behavior results from a partially filled π^* band [10,13] which arises from an interaction between oxygen *p* and metal t_{2g} orbitals. In perovskites, Goodenough [14] has argued that the A cation competes for these oxygen *p* orbitals. This competition becomes stronger as A becomes less basic. Eventually the π^* band may break down and localized electron behavior will be observed. Thus, the semiconducting behavior of the rare earth pyrochlore *vs.* the metallic behavior of $SrRuO_3$ and $SrIrO_3$ may be due to the less basic character of the rare earths.

The Ru-O-Ru angles, which are close to 180° in the perovskite structure, are around 130° in the pyrochlore structure; this difference in angle may contribute to the localization of electrons in the pyrochlore structure. However, this same geometry is present when A is Bi and then the electrons are apparently not localized. Furthermore, Bi and Tℓ are much less basic than the rare earths, and thus they should compete even more strongly for the oxygen *p* orbitals. Therefore, the rules developed for the perovskite structure seem to fail for the pyrochlore structure.

Ruthenium-oxygen octahedra share only corners in both the perovskite and pyrochlore structures. There is some distortion of the octahedron in $SrRuO_3$ and $SrIrO_3$ as well as in the pyrochlores, but these distortions are small. A more significant difference lies in the arrangement of A cations around Ru. In the perovskite structure, the A cations are positioned around Ru at the corners of a cube; the six A cations around Ru in the pyrochlore structure are in the same plane as Ru. Thus, strong crystal fields may be present in the pyrochlore structure, which would tend to trap electrons at Ru. This field would be stronger when A is a rare earth than when A is a post-transition metal. We can now rationalize trapped, localized electrons when A is a rare earth and delocalized electrons when A is Tℓ or Bi. The activation energy should be a measure of the trap potential; it should increase as the cell dimension and A-M distance decrease, and in fact this appears to occur (table 1). Finally, Tℓ

should exert more of a trapping influence than Bi because (a) Tℓ is slightly more electropositive than Bi; (b) Tℓ is smaller than Bi which leads to smaller A-M distances; and (c) the inert pair of Bi is probably directed toward the M cations. The question remains as to whether the crystal field of the A cations is really sufficient to cause localization; thus, alternate models are being developed.

The pyrochlore structure may be viewed as two inter-penetrating networks (fig. 2), and the formula rewritten accordingly is $A_2O' \cdot 2MO_3$. The schematic MO diagram given in figure 3 emphasizes this two-network feature in that the strongest bonding is within the two separate networks. However, the half-filled band arises from an interaction between the two networks. Since Bi is linearly coordinated to two close oxygens, *s-p* bonding is assumed. Thus, the "inert pair" of Bi now has only *p* character. In this model the metallic properties of $Bi_2Ru_2O_7$ are due to delocalization of this inert pair, and the Ru electrons could be localized. Since $Tℓ^{+3}$ has no inert pair, the half-filled band would be empty in $Tℓ_2Ru_2O_7$, but there would be only a small gap between this conduction band and the lower energy Ru electrons. In the rare earth ruthenates this conduction band would be at much higher energies.

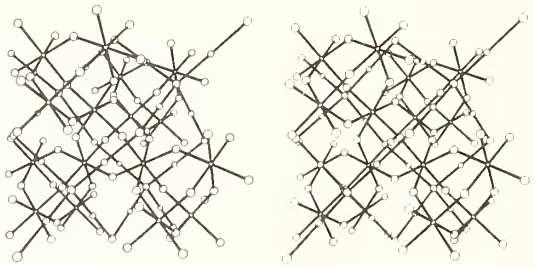

Fig. 2. Stereoscopic view of the pyrochlore structure as two interpenetrating networks. The smallest atoms (M cations) are in octahedral coordination, the next largest atoms (A cations) are in linear coordination, and the remaining larger atoms are the anions.

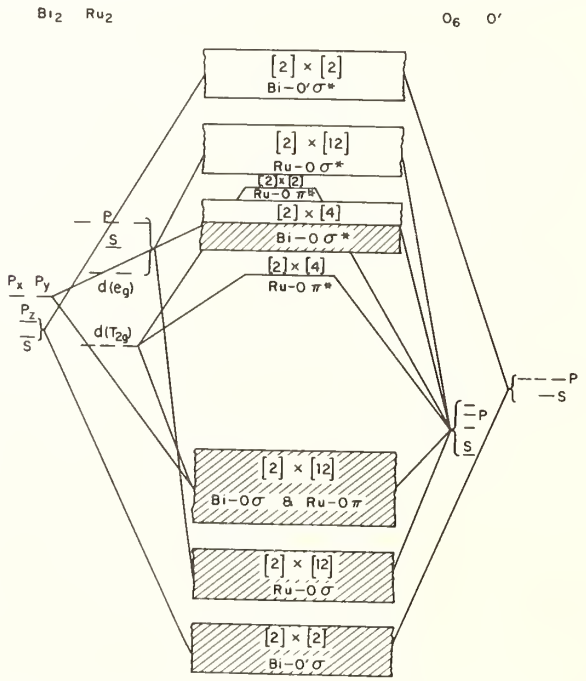

Fig. 3. Schematic MO diagram for $Bi_2Ru_2O_7$.

Further studies of precious metal pyrochlores are in progress, and we hope to determine whether or not one of the qualitative models described here, or a combination of them, is basically correct.

5. ACKNOWLEDGMENTS

We thank J. L. Gillson for electrical measurements, J. F. Weiher for magnetic measurements, and M. S. Licis and C. M. Foris for crystallographic data. Helpful discussions with W. Bindloss and D. B. Rogers are gratefully acknowledged.

6. REFERENCES

[1] Bertaut, E. F., Forrat, F., and Montmory, M. C., Compt. rend. 249, 829 (1959).
[2] Montmory, M. C. and Bertaut, E. F., Compt. rend. 252, 4171 (1961).
[3] Sleight, A. W., Mater. Res. Bull. 3, 699 (1968).
[4] Hoekstra, H. R. and Siegel, S., Inorg. Chem. 7, 4171 (1961).
[5] Longo, J. M., Raccah, P. M., and Goodenough, J. B., Mater. Res. Bull. 4, 191 (1969).
[6] Bouchard, R. J. and Gillson, J. L., Mater. Res. Bull. 6, 669 (1971).
[7] Sleight, A. W., Mater. Res. Bull. 6, 775 (1971).
[8] Sleight, A. W. and Gillson, J. L., Mater. Res. Bull. 6, 781 (1971).
[9] Weiher, J. F., Private communication
[10] Rogers, D. B., Shannon, R. D., Sleight, A. W., and Gillson, J. L., Inorg. Chem. 8, 841 (1969).
[11] Callaghan, A., Moeller, C. W., and Ward. R., Inorg. Chem. 5, 1572 (1966).
[12] Longo, J. M., Kafalas, J. A., and Arnott, R. J., J. Solid State Chem. 3, 174 (1971).
[13] Goodenough, J. B., Bull. Soc. Chim. France 4, 1200 (1965).
[14] Goodenough, J. B., Phys. Rev. 164, 785 (1967).

DISCUSSION

E. Banks: I'm going to steal Post's thunder this time. It seems to me that in this phase where you have a very large temperature factor for bismuth and bismuth only, it might have been very informative if you could have done a low temperature single crystal study. I don't mean necessarily on the low temperature phase, which I assume you are probably planning to do, but if you could have determined whether that was a real temperature factor or due to other considerations, like disorder or something.

A. W. Sleight: This has been done and unfortunately, it was hard to get everything in this talk. We have measured intensity data as a function of temperature at about six temperatures below room temperature and we find that the temperature factor of bismuth stays anomalously high all the way down. Of course below the transition we are not truly measuring a temperature factor anymore. However, the apparent temperature factor drops slightly when we go through that transition. The drop is really within experimental error, I mean the temperature factor appears to drop 2.1 to about 1.8 through that transition. Our error is probably greater than that change, but it's significant in that all the points lie on a nice line.

F. Jellinek: This high temperature factor of bismuth looks like what you could call a dynamic ferroelectric distortion. If this is so, you would expect an anomaly in the dielectric properties. I wonder whether you have done any measurements of that kind.

A. W. Sleight: Well, it's metallic so I don't think it's really possible to measure the dielectric constant. I think a dielectric anomaly is what you would expect for an insulator but for a metal I think this is exactly the kind of effect you expect to see. A break in the resistivity curve at the Curie temperature could in fact be a peak in resistivity because that could be where you have a maximum in the scattering. I don't think we can really measure a dielectric constant in a metal.

E. Kostiner: Are your thermal parameters based on powder diffractions measurements or single crystals?

A. W. Sleight: They are based on powder diffraction data.

E. Kostiner: I think that the point made by Professor Post before is very important here. Perhaps you should consider a single crystal structure analysis even at room temperature. You are measuring thermal parameters from very few data. You probably have a fairly low data:parameter ratio and I question what those high thermal parameters really mean. Certainly you can get much more information out of a single crystal study.

A. W. Sleight: Well, I won't agree with that. I think it would be way over determined in the single crystal. I think it's very adequately determined already. There is only one positional parameter to determine.

E. Kostiner: Are you sure about your stoichiometry (your occupancy factors)?

A. W. Sleight: The occupancy factor was allowed to vary at the same time that the temperature factor was allowed to vary and there was nil correlation between the two, and the occupation parameter stays at one. Chemical analysis indicates that there is one bismuth for one ruthenium.

E. Kostiner: I believe that you should still investigate this possibility using single crystal data.

N. C. Stephenson: I was just wondering what sort of a scattering curve you used for the bismuth.

A. W. Sleight: Well, I don't remember. We've generally used both atomic and ionic and I don't think in this case it made much of any difference but I don't really recall now.

B. Post: Was there any evidence of preferred orientation in the powder data? I mean everyone talks about the programs, what about the data?

A. W. Sleight: No, there was no evidence for preferred orientation in the sample that we ended up using. I should perhaps point out that the single crystal photographs show exactly the same trend as we see in the powder data and that we can compare the two. There are reflections for which the cation contributions add and there are reflections for which they subtract and you can see in the single crystal photographs that in bismuth ruthenate these reflections are acting entirely differently as you go out in theta, in confirmation of the powder data.

J. B. Goodenough: Just a quick comment. Certainly there is a difference between the rare earth ion and bismuth in that the bismuth ions have a lone pair. I wondered if you had any information as to what the energy of the lone pair electrons was on the bismuth, relative to the d-levels on the ruthenium.

A. W. Sleight: No, we don't have any evidence on that and I think that is something that has to be considered. In the paper submitted in conjunction with this talk, I did discuss the possibility of bismuth oxygen bands and I think this is something which can't be ruled out entirely.

National Bureau of Standards Special Publication 364, Solid State Chemistry, Proceedings of 5th Materials Research Symposium, issued July 1972.

PHASES IN THE SYSTEMS BaO-NiO-O-CO_2 AND BaO-CoO-O-CO_2

T. Negas and R. S. Roth

National Bureau of Standards
Washington, D.C. 20234

Several new materials apparently related to the aragonite form of $BaCO_3$ and to the 2H form of "$BaNiO_3$" were prepared at elevated temperature *in air*. The phases $Ba_3NiC_xO_{9-y}$ and $Ba_3Ni_2C_xO_{9-y}$ ([Ni+C] $\leq$ 3) were prepared in powder and single crystal form. Both phases are hexagonal with *a*-axes related to the 2H "$BaNiO_3$" by $a \simeq a_{2H}\sqrt{3}$. Single crystal x-ray and electron diffraction patterns of the Ba:Ni = 3:1 phase reveal $c \simeq 2c_{2H}$. The structure was refined in space group $P\bar{6}$ to R = 5.9% using 639 x-ray reflections. $BaCO_3$-3:2 (Ba:Ni) phase composite crystals were prepared by decomposition of 3:1 phase crystals in air at 800 °C. The structure for these composites is discussed. A similar 3:2 compound, $Ba_3Co_2C_xO_{9-y}$, containing low-spin octahedral Co^{4+}, was prepared in powder form.

Although 2H "$BaNiO_3$" is not stable in air, single crystals of two phases near Ba:Ni = 1:1 were obtained. Both are rhombohedral with hexagonal $a \simeq a_{2H}\sqrt{3}$ and large *c*-axis multiplicities but exact stoichiometries are unknown. Two-layer-like forms of $BaCoO_{3-x}$ can be prepared in air, however, below 890 °C. Similar phases exist at compositions slightly deficient in cobalt. A 12-layer form of $BaCoO_{3-x}$ exists from 890° to 925 °C. It transforms to a phase of unknown structure above 925 °C. The compound Ba_2CoO_4, related to Ba_2TiO_4, can be prepared above 825 °C. Ba_2CoO_4 has a reversible, non-quenchable, monoclinic $\rightleftarrows$ orthorhombic inversion at 145 °C. The Co^{4+} is in a high-spin, tetrahedral, configuration.

Key words: Ba/Co-oxide phases; Ba/Ni-oxide phases; crystal structure; phase equilibria; transition-metal oxides.

1. INTRODUCTION

Determination of phase relations in oxide systems containing transition metals is complicated by the familiar tendency of the metals to exist in variable oxidation states. Stoichiometry therefore becomes dependent on $P[O_2]$. However, the importance of other available and possible components such as H_2O and CO_2 has been generally overlooked, especially in investigations at ambient atmospheric pressure. The systems BaO - "cobalt oxide" and BaO - "nickel oxide" provide excellent examples of these potential problems.

Subsolidus relations over a wide range of Ba/Me (Me = Co or Ni) ratios were deduced at ambient atmospheric pressures and <1000 °C. Only the high baria portion of the nickel system was investigated in any great detail. As the important Ba:Ni = 1:1 ratio was not studied at temperatures >850 °C, phase relations are considered tentative.

Several Ba-Me oxide phases, especially at the 1:1 ratio, have been reported. Strauss et al. [1][1] prepared cubic $BaCoO_{2.72}$ (*a* = 4.82 Å), a $BaCoO_{2.31}$ phase, and a cubic perovskite $BaCoO_{2.23}$ phase (*a* = 4.072 Å). The x-ray powder data reported for the cubic forms, however, cannot be indexed completely on the basis of the *a* dimensions given. Gushee et al. [2] prepared $BaCoO_{2.85}$, similar to $BaCoO_{2.72}$ [1], at 680 °C in air. They found that this phase was hexagonal (*a* = 5.59 Å, *c* = 4.82 Å) rather than cubic, and that it was apparently isostructural with the "$BaNiO_3$" phase reported by Lander [3,4]. This phase as well as, for

[1] Figures in brackets indicate the literature references at the end of this paper.

example, $BaMnO_3$ [5] is commonly referred to as a 2H phase. It consists of two hexagonal close-packed BaO_3-layers perpendicular to *c*. Infinite strings, parallel to *c*, of face-sharing oxygen octahedra containing transition metals further characterize the 2H structure. Recently, Greaves [6] using thermogravimetric techniques, studied $BaCoO_{3-x}$-type phases at $P[O_2]$ = 1.0, 0.10, and 0.316 atm in the range 350° to 1000 °C. Although his interpretation of the x-ray data is improbable the gravimetric data appear to be reasonably reliable.

While the data for this study were in preparation for publication, Krischner et al. [7] reported the preparation of $BaNiO_3$ by oxidation of $BaNiO_2$ in flowing oxygen between 450-600 °C. Their phase is hexagonal and of the 2H form with *a* = 5.631 Å, *c* = 4.808 Å. They also prepared $BaNiO_x$ phases with x between about 2.75 and 2.55 at lower $P[O_2]$. These phases are similar to $BaNiO_3$ but have considerably larger *a* and smaller *c* subcell parameters.

2. EXPERIMENTAL PROCEDURE

Various combinations of starting materials were used. Sources for BaO included spectrographic grades of $BaCO_3$ and $Ba(NO_3)_2$. Spectrographic grades of Co_3O_4 (calcined at 800 °C in air), $Co(NO_3)_2 \cdot 6H_2O$ and NiO provided the transition metal oxides. Weighed starting materials were mixed under acetone, packed in Au trays and calcined at 750-800 °C for two weeks with almost daily remixing. The 1:1 Ba:Co composition was also calcined at 1000 °C for 3 days, followed by six weeks at 600 °C. Compositions formulated from nitrates were slowly (~1°/min) heated from room temperature to the calcining temperature. Portions of the calcined materials were equilibrated in Au tubes within a vertical tube resistance-type quench furnace. After sufficient heating they were quenched in solid-CO_2 or liquid-N_2. The temperatures were measured with Pt-Pt10%Rh thermocouples calibrated against the melting points of NaCℓ and Au. The quench furnaces were controlled by a-c Wheatstone bridge-type instruments capable of maintaining temperature to at least ±2 °C.

Phases were identified at room temperature by x-ray powder diffraction using Ni-filtered Cu radiation and a 1/4° 2θ/min scanning rate. Interplanar *d*-spacings from x-ray powder diffraction measurements were used to compute unit cell dimensions by a least squares refinement computer program. Unit cell dimensions are estimated to be accurate to within three standard deviations. When obtainable, single crystals were investigated with an x-ray diffraction precession camera. Quantitative intensity data were collected with an automatic diffractometer using MoKα radiation. Computer programs from *The X-ray System*, 1970 [8] were used for structural analysis and least squares refinement.

Chemical analyses for several phases were performed by a company independent of the National Bureau of Standards.

3. EXPERIMENTAL RESULTS AND DISCUSSION

3.1. THE BaO-"COBALT OXIDE" SYSTEM

Subsolidus phase relations *in air* for starting Ba/Co ratios are shown in figure 1 which was derived from the data of table 1. Chemical analyses for various phases are given in table 2. As will become evident, the system is not binary, as O_2 and CO_2 must be considered as additional components. Nevertheless, phase relations can be depicted in the simplest manner as a function of temperature and Ba/Co ratio.

3.1.a. Ba_2CoO_4

At the 2:1 Ba:Co ratio a red-brown phase of stoichiometry Ba_2CoO_4 exists from ~790° to at least 1050 °C. Above 1050 °C, which precludes use of Au, experimental difficulties are encountered as the material reacts with Pt-containers. At room temperature, the phase is monoclinic with *a* = 5.909 Å, *b* = 7.617 Å, *c* = 10.406 Å and β = 91°6.8'. Indexed powder data are given in table 3. Ba_2CoO_4 appears to be isostructural with Ba_2TiO_4 [9] which is a distorted form of the orthorhombic K_2SO_4 structure type. The transition metal has tetrahedral coordination. A high temperature x-ray investigation showed that Ba_2CoO_4 has a reversible, non-quenchable, monoclinic to orthorhombic transition near 145 ± 10 °C. Magnetic susceptibility measurements to be published [10] are consistent with tetrahedral $Co^{4+}(d^5)$ in a high-spin state.

Table 1

Summary of Subsolidus Data In Air For The System
BaO-"Cobalt Oxide"[a]

Composition	Heat Treatment[b]		Phase Analysis[c]	Other Information
8a/Co ratio	Temp.(°C)	Time(hr)	X-ray diffraction	
7:3	721	432	BC + 3:2 phase	
	754	168	BC + 3:2 phase	
	763	264	BC + 3:2 phase	reheet of 890° specimen initially consisting of ortho.-$8a_2CoO_4$(ss)+(tr.)BC
	838	1344	ortho.-Ba_2CoO_4(as)+ BC(tr.)	reheat of 754°C specimen
	890	168	ortho.-Ba_2CoO_4(ss)+ BC(tr.)	
	917	144	ortho.-Ba_2CoO_4(ss)+ BC(tr.)	
	953	264	ortho.-Ba_2CoO_4(ss)+ BC(tr.)	
2:1	754	168	BC + 3:2 phese	
	763	264	BC + 3:2 phase	reheat of 998°C specimen conaisting of mono.-$8e_2CoO_4$
	838	1344	mono.-Ba_2CoO_4	reheat of 754°C specimen
	917	144	mono.-Ba_2CoO_4	reheat of 998°C specimen
	953	264	mono.-$8a_2CoO_4$	
	976	168	mono.-$8a_2CoO_4$	
	998	120	mono.-Ba_2CoO_4	
3:2	700	144	3:2 phase	reheat of 750°C specimen
	721	432	3:2 phese	reheat of 763°C specimen
	750	264	3:2 phase	
	754	168	3:2 phase	
	763	264	3:2 phase	reheet of 890°C specimen containing mono.-$8a_2CoO_4$+(tr.)(1:1)ss
	771	144	3:2 phase	
	800	48	3:2 phase	reheat of 838°C specimen containing mono.-$8a_2CoO_4$+(tr.)(1:1)ss
	814	168	3:2 phese + (tr.)mono.-$8a_2CoO_4$ +(tr.)(1:1)ss	reheet of 771°C specimen
	838	1344	mono.-Ba_2CoO_4+(1:1)ss	3:2 phase not completely dacomposed " reheat of 754°C specimen
	884	96	mono.-$8e_2CoO_4$+(1:1)ss	
	890	168	mono.-Ba_2CoO_4+(1:1)ss	
	903	288	mono.-Ba_2CoO_4+(1:1)ss	
	917	144	mono.-Ba_2CoO_4+(1:1)ss	
	935	144	mono.-$8e_2CoO_4$+(1:1)ss	reheat of 884°C speciman
	953	264	mono.-Ba_2CoO_4+(1:1)ss	
29:21	721	432	3:2(ss)+$BaCO_{3-x}$, 2H-type	
	754	168	3:2(ss)+(1:1)ss=(1:1)ss	
	838	1344	mono.-Ba_2CoO_4+(1:1)ss	
	890	168	" " " "	
	953	264	" " " "	
14:11	754	168	3:2(ss)+(1:1)xx=(1:1)ss	
	890	168	mono.-Ba_2CoO_4+(1:1)xx=(1:1)ss	
53:47	721	432	3:2(ss)+$BaCoO_{3-x}$, 2H-type	
	754	168	3:2(ss)+(1:1)ss	
	763	264	3:2(ss)+(1:1)ss	reheat of 890°C specimen
	838	1344	(1:1)ss+(tr.)mono.-Ba_2CoO_4	
	890	168	" " " " "	
	917	144	" " " " "	
	953	264	" " " " "	
1:1	600	240	$BaCoO_3$,2H-type	reheat of a specimen heeted 4 dy at 1100°C
	721	432	$BaCoO_{3-x}$,2H-type	
	763	264	$BaCoO_{3-x}$	reheat of 976°C specimen
	771	144	$BaCoO_{3-x}$+(tr.)2H-type	incomplete reection
	814	168	$BaCoO_{3-x}$	
	814	168	"	reheat of 771°C specimen
	838	1344	$BaCoO_{3-x}$	
	884	96	$BaCoO_{3-x}$	
	890	168	$BaCoO_{3-x}$+12-leyer $8eCoO_{3-x}$	$8aCoO_{3-x}$ incompletely decomposed
	907	168	12-layer $8aCoO_{3-x}$	reheat of 917°C specimen
	907	288	" " "	
	907	168	" " "	reheat of 890°C specimen
	917	144	" " "	
	917	144	" " "	reheat of 890°C specimen
	935	144	12-layer $8aCoO_{3-x}$+ unknown $BaCoO_{3-x}$	incomplete decomposition of 12-layer phase
	935	144	" " " " "	incomplete decomposition of 12-layer phase; reheat of 884°C spacimen
	953	264	unknown $8aCoO_{3-x}$ phase	
	976	168	" " "	
	976	168	" " "	reheet of 814°C specimen
	1003	192	" " "	reheat of 814°C+ 976°C specimen
unknown ratio between 53:47 and 1:1	903	288	12-layer $8aCoO_{3-x}$+(1:1)ss	
2:3	721	432	$BaCoO_{3-x}$,2H-type+Co_3O_4	
	763	264	$BaCoO_{3-x}$+Co_3O_4	reheat of 903°C speciman
	814	168	" " "	
	838	1344	" " "	
	884	96	" " "	
	903	288	12-leyer$8aCoO_{3-x}$+Co_3O_4	
	935	144	unknown $BaCoO_{3-x}$+Co_3O_4	reheet of 884°C specimen
	953	264	" " " "	
	976	168	" " +CoO	
	1003	192	" " +CoO	reheet of 976°C specimen

[a] The system is not binary because of reactions with atmospheric CO_2 and O_2.

[b] Does not include prior calcining. Specimens were heated in Au-tubes.

[c] At room temperature

8C = $8aCO_3$; (tr.) = trace; ss = solid solution; ortho. = orthorhombic; mono. = monoclinic

3:2 phase = carbon-containing oxide phase at 3:2 8a/Co ratio. See table 2 for chemical analysis deta.

$(1:1)_{ss}$ - cobalt deficient oxide phases similar to those at 8e:Co = 1:1.

$BaCoO_{3-x}$, 2H-type = two-layer hexagonal, oxygen deficient phase.

2H-type = two-layer hexagonal phase.

12-layer $BeCoO_{3-x}$ = 12-leyer hexagonal, oxygen deficient phase.

unknown $8aCoO_{3-x}$ = oxygen deficient phase similar (but not identical) to a perovskite or brownmillerite-like phase.

$BaCoO_{3-x}$ = oxygen deficient phases related to 2H-type structure (see text).

Table 2

Summary of Chemical Analyses for Ba/Co - Oxide Phases

%	Analysis	Formula	% Calculated [1]
H	0.00	Ba_2CoO_4	---
C	0.00		---
Ba	68.32		69.083
Co	14.48		14.822
0	---		16.095
Ba/Co	2.02		2.00
	#1		
C	0.00	$BaCoO_3$	---
Ba	56.61	600°C, in air	56.22
Co	24.02		24.13
0	---		19.65
Ba/Co	1.01		1.00
	#2		
C	0.00		
Ba	55.56	$BaCoO_3$	
Co	23.11	#1 specimen	
0	---	annealed in O_2	
Ba/Co	1.03	300-350°	1.00
	#1		
C	1.37		1.75
Ba	61.27		60.07
Co	16.93	$Ba_3Co_2CO_9$ *	17.18
0	20.14		20.99
Ba/Co	1.55		1.50
	#2		
C	1.38		1.33
Ba	61.00	$Ba_3Co_2C_{0.75}O_{8.5}$ *	61.05
Co	18.06		17.46
0	---		20.15
Ba/Co	1.45		1.50
	#3		
C	1.71		
Ba	61.10		
Co	17.61		
0	---		
Ba/Co	1.49		1.50

[1] Based on the proposed formulas.

*The analyses are not unequivocable but appear to represent formulas within these compositions.

Table 3

X-ray Powder Data for Ba_2CoO_4

d_{obs}	d_{calc}	$hk\ell$[a]	I_{obs}
5.170	5.181	$\bar{1}01$	6
4.287	4.284	$\bar{1}11$	7
3.577	3.576	021	19
3.502	3.501	$\bar{1}12$	37
3.446	3.448	112	41
3.201	3.201	120	32
3.156	3.156	013	31
3.068	3.073 3.069	022 $\bar{1}21$	79
3.051	3.050	121	54
3.016	3.017	$\bar{1}03$	55
-- 2.953	2.966 2.954	103(S) 200	100
2.739	2.739	$\bar{1}22$	8
2.713	2.713	122	12
2.600	2.601	004	10
2.565	2.564	023	26
2.466 -- --	2.467 2.462 2.452	031 014(S) 212(S)	35
2.416	2.416	212	8
2.336	2.334	$\bar{2}20$	7
2.284	2.287 2.285 2.282 2.280	$\bar{1}14$ $\bar{2}21$ 032 $\bar{1}31$	21(b)
2.272	2.272 2.270	131 $\bar{2}21$	20(b)
2.258	2.258	$\bar{1}14$	8
2.178	2.176	$\bar{2}13$	13
2.140	2.142 2.138	$\bar{2}22$ 213	21(b)
2.118	2.117	222	15
2.051	2.049	033	13
2.009	2.008 2.007	124 015	20
1.9750	1.9748	$\bar{1}05$	5
1.9509	1.9508 1.9504	105 $\bar{2}23$	13(b)
1.9229	1.9228	$\bar{2}23$	10
1.8975	1.8976	$\bar{2}31$	9
1.8886	1.8890	231	9
1.8134	1.8133	$\bar{2}32$	8
1.7879	1.7882 1.7874	042 $\bar{1}41$	16
1.7839	1.7838	141	15
1.7431	1.7433	$\bar{1}34$	22
1.7296	1.7300 1.7300 1.7270	$\bar{1}34$ $\bar{3}21$ $\bar{3}03$	29
1.7205	1.7202	321	10
1.6981	1.6983	303	7
1.6752	1.6749	$\bar{2}15$	10
1.6461	1.6460	215	8
1.5788	1.5782	026	11
1.5322	1.5315	$\bar{1}26$	6
1.5179	1.5180	126	6
1.4769	1.4770	400	12

[a] Indexed on the basis of a monoclinic cell with $a = 5.909 \pm 0.001$ Å, $b = 7.617 \pm 0.001$ Å, $c = 10.406 \pm 0.002$ Å, and $\beta = 91° 6.8 \pm 1.2'$.

(S) = shoulder

(b) = broad

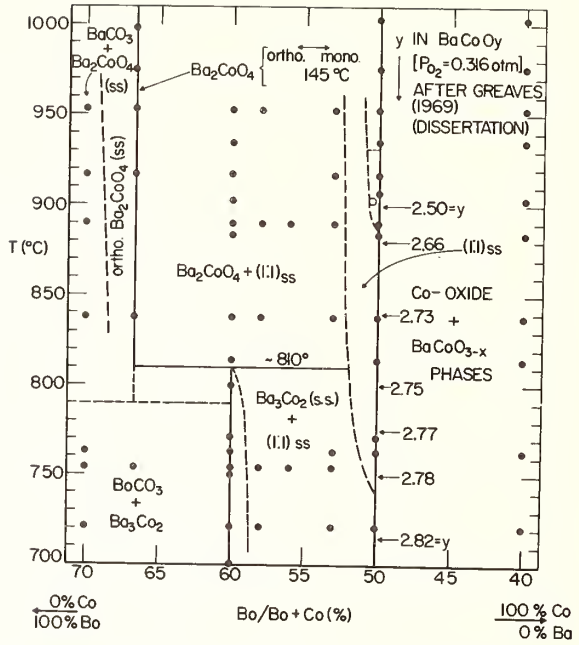

Fig. 1. Subsolidus phase relations *in air* for the system BaO-"cobalt oxide". The system is not binary because of reactions with atmospheric CO_2 and O_2. Compositions are plotted in terms of cation (%) of starting mixtures. $(1:1)_{ss}$ = phases similar to those found at the 1:1 Ba/Co ratio. See table 2 for probable stoichiometries of indicated phases.

● - quench runs, solid
o - unknown Ba/Co ratio near 1:1

When exposed to air (at room temperature) for extended time intervals Ba_2CoO_4 is unstable, reacting apparently with CO_2. Although $BaCO_3$ is easily identified as a decomposition product the cobalt must remain in a non-crystalline oxide form as its presence is not evident in powder patterns. Near 790 °C, Ba_2CoO_4 reacts with atmospheric CO_2 to form $BaCO_3$ plus a phase with Ba:Co = 3:2. The reaction is reversible but decomposition is so rapid that Ba_2CoO_4 cannot be brought to room temperature by a "slow-cooling" process. In oxygen, Ba_2CoO_4 does not decompose.

Evidence for a Ba_2CoO_4(ss) region was obtained from Ba:Co = 7:3. The orthorhombic form (plus a trace of $BaCO_3$) can be retained at room temperature. This indicates that the monoclinic ↔ orthorhombic transition temperature is lowered by addition of excess barium carbonate. X-ray diffraction powder data for the orthorhombic phase obtained from the 7:3 composition are given in table 4. A comparison of pertinent x-ray data for Ba_2CoO_4, Ba_2TiO_4, and K_2SO_4 [11] is provided in table 5.

The physical nature and magnetic properties of Ba_2CoO_4(ss) are subjects for future investigation. It should be of interest to determine whether stabilization of the orthorhombic solid solution is structurally accomplished by excess Ba or deficiency in Co content or is one involving stabilization by an additional component such as CO_2 (*i.e.* - a $BaCO_3$ - Ba_2CoO_4 solid solution).

3.1.b. THE 3:2 Ba:Co RATIO AND $BaCoO_3$

Below about 810 °C *in air* a single phase material exists at Ba:Co = 3:2. Above 810 °C it decomposes reversibly to Ba_2CoO_4 plus a phase near the 1:1 ratio [shown as $(1:1)_{ss}$ in fig. 1]. On each side of the 3:2 ratio two-phase assemblages exist except for a narrow solid solution region in the cobalt-rich portion. This region is inferred because the unit cell of single phase 3:2 and 3:2 in equilibrium with 1:1-type phases are similar but not identical.

Table 4

X-ray Powder Data for Ba_2CoO_4 (ss)[a/]

d_{obs}	d_{calc}	hkℓ[b/]	I_{obs}
5.106	5.109	110	5
4.250	4.246	111	6
3.584	3.583	012	15
3.462	3.463	121	75
3.201	3.201	102	34
3.148	3.147	031	27
3.073	3.074	022	50
3.058	3.059	112	80
2.975	2.977	130	88
2.935	2.936	200	100
2.722	2.723	122	15
2.589	2.590	040	8
2.562	2.562	032	20
2.472	2.472	013	30
2.452	2.453	041	6
2.422	2.423	221	15
2.328	2.328	202	5
2.278	2.278	113	16(b)
2.272	2.271	212	20(b)
2.147	2.147	231	23
2.124	2.123	222	38
2.050	2.049	033	15
2.000	2.000	051	12(b)
1.9541	1.9542	150	8
1.9306	1.9303	232	21
1.8910	1.8912	213	20
1.8156	{1.8158 1.8157}	{104 043}	10
1.7916	1.7915	024	15
1.7886	1.7885	114	25
1.7808	1.7807	321	15
1.7418	1.7420	302	11
1.7351	1.7347	143	28
1.7179	1.7179	312	17
1.7031	1.7031	330	8
1.6805	1.6805	233	6
1.6518	1.6512	322	15
1.6186	1.6191	161	4(b)
1.5300	1.5301	341	5
1.4680	1.4682	400	12

[a/] Obtained from a 7:3 Ba:Co ratio composition. Contains a trace of $BaCO_3$ which is excluded from the data.

[b/] Indexed on the basis of an orthorhombic cell with a = 5.873±0.001 Å, b = 10.362±0.003 Å, and c = 7.637±0.001 Å.

(b) = broad

Table 5

Comparison of Similar A_2BO_4 Structure Types

	Ba_2TiO_4	Ba_2CoO_4 monoclinic	Ba_2CoO_4(ss)[a] orthorhomibc	K_2SO_4
Space Group	$P2_1/n$			Pmcn
a (Å)	6.12	5.909±0.001	5.873±0.001	5.772
b (Å)	7.70	7.617±0.001	10.362±0.003	10.072
c (Å)	10.50	10.406±0.002	7.637±0.001	7.483
β	93°8'	91° 6.8±1.2'		
	(Bland, 1961)	(this study)		(Swanson et al. 1954)

[a] From a 7:3 Ba:Co ratio composition. Contains a trace of free $BaCO_3$.

The powder pattern of the 3:2 phase, given in table 6, is of excellent quality and shows no evidence of unreacted starting materials or other Ba/Co phases. It can be completely and unambiguously indexed on the basis of a hexagonal cell with a = 9.688 Å and c = 4.757 Å. $BaCoO_3$ was prepared at the 1:1 ratio and 600 °C in air. This material was annealed at 300 - 350 °C as suggested by Greaves [6] to maximize anion content. The x-ray powder pattern, given in table 7, represents the phases prepared in air and in O_2. Furthermore, magnetic susceptibilities [10] of both phases were identical within experimental error. The magnetic data are consistent with octahedral Co^{4+} in a low-spin state. $BaCoO_3$ was indexed on the basis of a hexagonal cell with a = 5.648 Å and c = 4.756 Å. Based on the similarity of their cell dimensions and line intensities, this phase appears to be isostructural with 2H $BaMnO_3$ [5]. The x-ray data are in particularly good accord with those of Greaves [6]. Our x-ray evidence, however, does not support a doubling of the c-axis. Additionally, strong lines indicative of the presence of cubic-type stacking are absent.

The powder patterns of $BaCoO_3$ and the 3:2 phase are strikingly similar as shown by pertinent portions of each in figure 2. The similarity suggests that the 3:2 phase has a structure related to the 2H form. Several additional lines, however, appear in the 3:2 pattern which can only be accounted for by choosing a cell with the relations $a_{2H}\sqrt{3} \approx a_{3:2}$ and $c_{2H} \approx c_{3:2}$. This choice creates several problems involving the stoichiometry of the phase and especially the oxidation state of Co. Chemical analyses (table 2) unequivocally established the presence of carbon in the material and yield possible formulas ranging from $Ba_3Co_2^{4+}C_{0.75}O_{8.5}$ to $Ba_3Co_2^{4+}CO_9$. The structural implications will be discussed later. Magnetic susceptibility data [10] are not identical with those of $BaCoO_3$ but remain consistent with octahedral, low-spin, Co^{4+}. Electron diffraction data confirmed the $a_{2H}\sqrt{3} \approx a_{3:2}$ relationship but also suggested that the true c-axis is at least four times that determined from x-ray powder data.

3.1.c. $BaCoO_{3-x}$ AND $(1:1)_{ss}$ PHASES

$BaCoO_3$ releases oxygen to form $BaCoO_{3-x}$-type phases from 600 °C to near 740 °C. As shown in figure 3, a increases while c decreases slightly with increasing temperature. Powder patterns show very little change from 2H $BaCoO_3$. If the gravimetric data of Greaves [6] are nearly correct the maximum value of x in $BaCoO_{3-x}$ must approach ~0.20 for this series. A second series of $BaCoO_{3-x}$ phases appears above 740 °C. As shown in figures 3, 4, 5, and 6 this series is characterized by an abrupt increase in a and decrease in c near 740 °C. The

a dimension remains essentially constant while *c* gradually decreases up to about 890 °C. The gravimetric data of Greaves suggest that x varies from ~0.20 to 0.35 in this range. From powder data alone it cannot be ascertained whether this second series represents an oxygen deficient solid solution or a series of discrete, ordered, 1:1 phases. It is clear, however, that for either case the basic structural framework is a close packing of Ba and O atoms similar to the 2H structure. Furthermore, the *a* and *c* parameters shown in figure 3, represent those of a subcell. Each phase, however, has at least two weak-medium intensity x-ray lines in the vicinity of d = 1.97 Å and 1.54 Å. As their exact position is temperature dependent, they are not considered to be lines of a second phase. They cannot be indexed on the basis of a simple 2H cell. Recently, Krischner et al. [7] reported a similar phenomenon for $BaNiO_{3-x}$ phases. Their subcell *a*-axes remained essentially constant (5.705 Å) while subcell *c* decreased from 4.335 to 4.311 Å between x ≈ 0.25 and about 0.45.

As shown in figure 1, a second $BaCoO_{3-x}$ series extends to Co-deficient compositions. This region, labelled $(1:1)_{ss}$, extends to temperatures at least 60 °C above the last similar phase observed at the 1:1 ratio. The dashed solvus curve was placed between Ba/Co = 53/47 and 1:1 as the former was always a two phase assemblage. From powder patterns of the 53/47 ratio, subcell parameters were calculated for the $(1:1)_{ss}$ near the solvus. As shown in figure 3, *a* remains relatively constant to 953 °C while *c* decreases with increasing temperature. Although $(1:1)_{ss}$ patterns are similar to $BaCoO_{3-x}$ it is clear that the corresponding *a* and *c* subcell parameters are significantly different. As in the case of $BaCoO_{3-x}$ it remains unclear whether the $(1:1)_{ss}$ region includes a series of Co and oxygen deficient solid solutions or represents a series of ordered compounds. For convenience a solid solution series is depicted in figure 1.

Table 6

X-ray Powder Data for the 3:2 Ba:Co Ratio Phase [a]

$d_{obs.}$	$d_{calc.}$	$hk\ell$ [b]	$I_{obs.}$
8.402	8.390	100	14
3.392	3.394	111	94
2.797	2.797	300	100
2.422	2.422	220	7
2.379	2.379	002	10
2.328	2.327	310	4
2.158	2.158	221	77
2.135	2.135	112	19
1.8309	1.8310	410	4
1.8125	1.8120	302	11
1.7087	1.7088	411	30
1.6970	1.6971	222	18
1.6146	1.6147	330	20
1.5068	1.5071 1.5070	113 510	8
1.4963	1.4963	322	3
1.4509	1.4509	412	13
1.3985	1.3984	600	18
1.3361	1.3360	332	5
1.3266	1.3267	223	7
1.2930	1.2930	521	14
1.2055	1.2055	602	5
1.1985	1.1987 1.1986	413 530	7
1.1894	1.1893	004	3
1.1735	1.1736	441	6
1.1700	1.1698	522	7
1.0945	1.0945	304	3

[a] See table 2 for chemical analysis data.

[b] Indexed on the basis of a hexagonal cell with *a* = 9.688±0.001 Å and *c* = 4.757±0.001 Å.

465-504 O - 72 - 17

Table 7

X-ray Powder Data for $BaCoO_3$ [a]

$d_{obs.}$	$d_{calc.}$	$hk\ell$ [b]	$I_{obs.}$ [c]
3.409	3.410	101	66
2.825	2.824	110	100
2.447	2.446	200	10
2.378	2.378	002	14
2.174	2.175	201	54
2.140	2.139	102	31
1.8192	1.8191	112	7
1.7227	1.7232	211	20
1.7049	1.7050	202	20
1.6306	1.6305	300	15
1.5078	1.5082	103	6
1.4592	1.4596	212	12
1.4124	1.4120	220	12
1.3305	1.3304	203	5
1.3042	1.3046	311	7

[a] Prepared at 600 °C in air and annealed in oxygen at 300-350 °C.

[b] Indexed on the basis of a hexagonal cell with a = 5.648±0.001 Å and c = 4.756±0.001 Å.

[c] All peaks are broad.

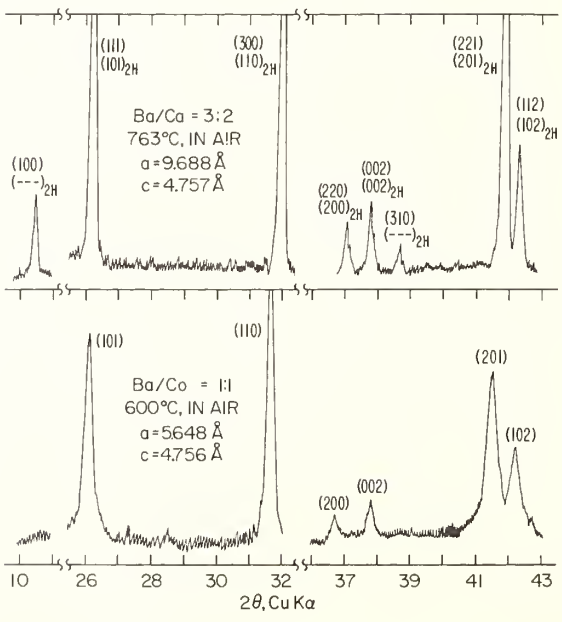

Fig. 2. Portions of x-ray diffraction powder patterns illustrating the similarity between the 2H-type $BaCoO_3$ and the carbon-containing compound existing at the 3:2 Ba:Co ratio.

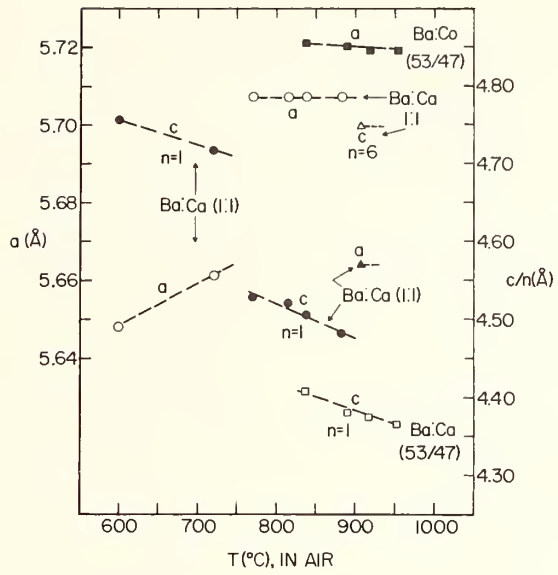

Fig. 3. Variation of *a* and *c* parameters of quenched 1:1 $BaCoO_{3-x}$-type and $(1:1)_{ss}$ -type phases. The latter were determined from the 53/47 Ba/Co ratio which is in a two phase field (see fig. 1). All parameters above 750 °C represent subcells except the *a* associated with the symbol ▲.

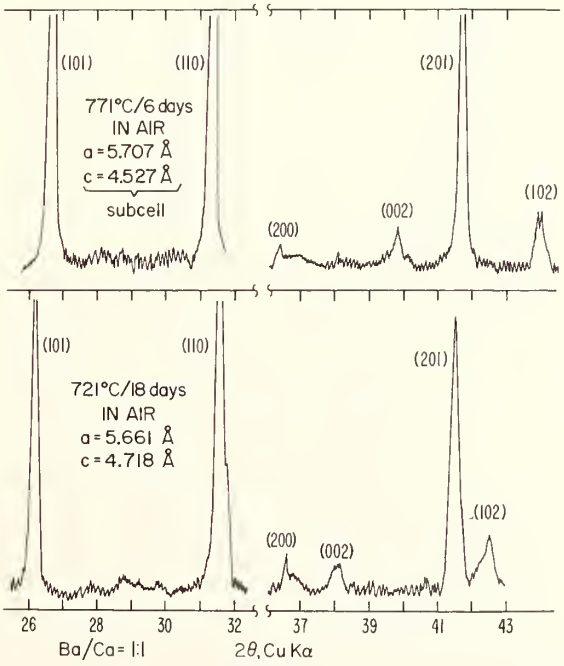

Fig. 4. Portions of x-ray diffraction powder patterns illustrating the changes in $BaCoO_{3-x}$ from 721 °C to 771 °C in air.

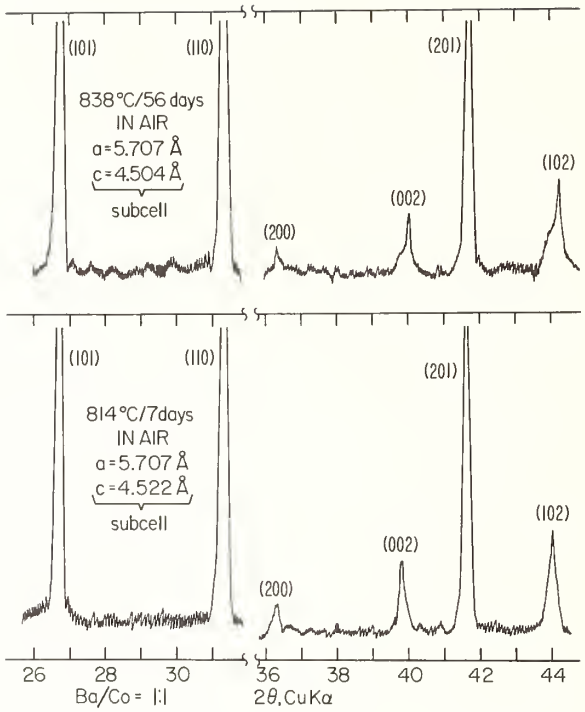

Fig. 5. Portions of x-ray diffraction powder patterns illustrating changes in $BaCoO_{3-x}$ from 814 °C to 838 °C in air. Compare with fig. 4.

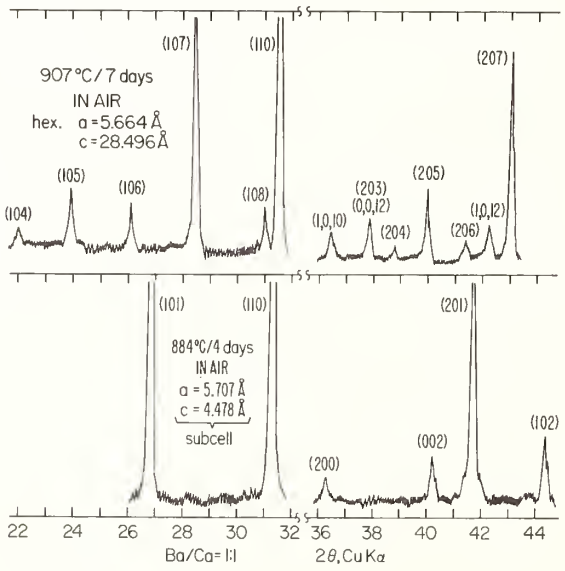

Fig. 6. Portions of x-ray diffraction powder patterns illustrating the transformation of a 2H-like $BaCoO_{3-x}$ to a hexagonal twelve-layer $BaCoO_{3-x}$ phase. Compare with figs. 4, 5.

Near 890 °C and Ba:Co = 1:1 a sluggish transformation to a third modification occurs as shown in figures 1, 3 and 6. X-ray diffraction powder data are completely indexed on the basis of a hexagonal cell with a = 5.664 Å and c = 28.496 Å in table 8. Based on the a dimension which is typical of a close packing of Ba and O and assuming an average thickness of about 2.4 Å for a BaO_3-type layer it is suggested that the compound is a 12-layer (12 x 2.4 = 28.8 Å ≈ c) form of $BaCoO_{3-x}$. Furthermore, the appearance of the powder pattern strongly suggests that the stacking is of the mixed hexagonal-cubic type rather than purely hexagonal. *The International Tables for X-ray Crystallography* [12] lists 42 possible hexagonal (non-rhombohedral) cases for the stacking of 12-close-packed layers. Until powder pattern intensities for each case are calculated or single crystals are available the structure cannot be assigned unambiguously.

Above approximately 925 °C the 12-layer form transforms to yet another modification which is stable to at least 1000 °C *in air*. Powder data for this phase are given in table 9. The data resemble that for a perovskite or brownmillerite-type phase but cannot be indexed on either basis. The phase slowly deteriorates upon exposure to air at room temperature.

3.2. THE BaO - "NICKEL OXIDE" SYSTEM

Portions of the nickel system were investigated *in air* partly for the purpose of preparing an analogous 3:2 Ba:Ni phase and partly to prepare other possible carbon-containing phases. From structural considerations to be later discussed it became apparent that a phase at Ba:Ni = 3:1 might exist. Very little work was done with Ba:Ni = 1:1, a particularly formidable and entirely separate project. The system as shown in figure 7 therefore represents subsolidus relations only *in air* and is incomplete with respect to 1:1. Some of the data points (table 10) represent conditions under which single crystals were grown.

3.2.a. THE 3:2 AND 1:1 Ba:Ni RATIOS

At the 3:2 Ba:Ni ratio a phase analogous to that of cobalt is easily prepared. The powder pattern given in table 11 was indexed on the basis of a hexagonal cell with a = 9.671 Å, c = 4.836 Å. The phase is pseudocubic and suspiciously similar to Lander's [3,4] $BaNiO_3$ (a = 5.580 Å, c = 4.832 Å). If the a dimension reported by Lander is multiplied by $\sqrt{3}$ the new cell with a = 9.665 Å would strongly resemble that herein reported. Furthermore, Greaves [6] reported the formation in air of what he considered to be a 1:1 phase with a = 5.596 Å,

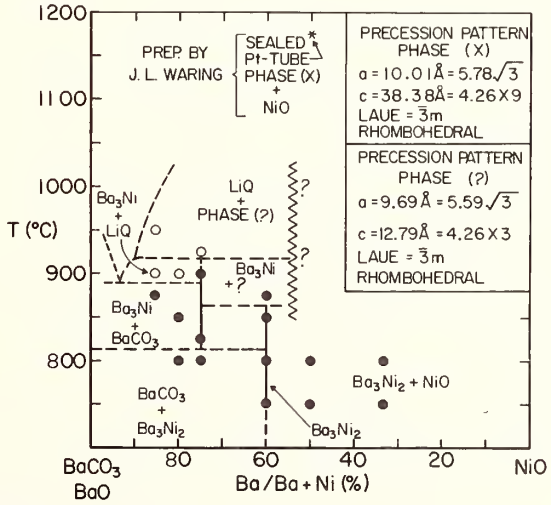

Fig. 7. Phase relations (incomplete) *in air* for the system BaO-"nickel oxide". The system is not binary because of reactions with atmospheric O_2 and CO_2. Compositions are shown only in terms of cation content. See table 12 for probable stoichiometries of Ba_3Ni- and Ba_3Ni_2-oxides. Single crystals of phases (X) and phase (?) were grown under conditions shown in the figure.

Table 8

X-ray Powder Data for the Twelve-Layer Form of $BaCoO_{3-x}$ [a]

$d_{obs.}$	$d_{calc.}$	hkℓ [b]	$I_{obs.}$
4.037	4.040	104	4 (b)
3.720	3.718	105	12
3.411	3.412	106	11
3.131	3.132	107	62
2.883	2.882	108	10
2.832	2.832	110	100
2.463	2.464	1,0,10	5 (b)
2.416	2.417	202	3
2.374	2.375 2.375	203 0,0,12	9
2.320	2.319	204	3
2.252	2.253	205	13
2.180	2.179	206	5
2.137	2.137	1,0,12	8
2.101	2.101	207	40
2.036	2.035	0,0,14	8
2.020	2.020	208	9 (b)
2.010	2.009	1,1,10	9 (b)
1.8800	1.8800	1,0,14	10
1.8590	1.8589	2,0,10	5
1.8196	1.8197 1.8196	213 1,1,12	7 (b)
1.7942	1.7942	214	3 (b)
1.7632	1.7630	215	3 (b)
1.7060	1.7060	2,0,12	10
1.6874	1.6872	217	24
1.6526	1.6528	1,1,14	3
1.6446	1.6446	218	5
1.6353	1.6351	300	18
1.5829	1.5831	0,0,18	3
1.5662	1.5663	2,0,14	5 (b)
1.5076	1.5077 1.5076	2,1,11 1,1,16	4
1.4613	1.4614	2,1,12	5
1.4342	1.4342	1,0,19	5
1.4160	1.4160	220	19
1.3705	1.3706	2,1,14	5
1.3467	1.3467 1.3467	313 3,0,12	3
1.3081	1.3079 1.3078	316 1,0,21	3 (b)
1.2904	1.2903	317	10
1.2794	1.2795	2,0,19	5
1.2160	1.2162 1.2162	403 2,2,12	4 (b)

[a] Prepared at 907 °C in air; x in $BaCoO_{3-x}$ unknown.

[b] Indexed on the basis of a hexagonal cell with $a = 5.664 \pm 0.001$ Å and $c = 28.496 \pm 0.004$ Å.

(b) broad

Table 9

X-ray Powder Data for $BaCoO_{3-x}$ Above 925 °C in Air.

$d_{obs.}$	$I_{obs.}$ [a]
4.15	10
4.01	3
3.36	8
2.914	100 vb
2.882	25 s,b
2.842	20* b
2.577	8 b
2.382	11
2.208	7
2.069	15
2.052	15
1.937	14
1.835	6 b
1.751	6 b
1.686	15
1.614	7 b
1.456	7 b
1.334	5 vb
1.212	5 vb
1.119	5 vb

[a] This is a poor powder pattern, a characteristic of this phase. The pattern further deteriorates with time.

b = broad, vb = very broad, s = shoulder

* Increases to this intensity from a much weaker, broad line upon long exposure to ambient conditions.

Table 10

Summary of Subsolidus and Single Crystal Growth Data In Air for the System BaO-"Nickel Oxide"[a/]

Composition	Heat Treatment[b/]		Phase Analysis	
Ba/Ni ratio	Temp.(°C)	Time(hr)	X-ray diffraction[c/]	Other Information
6:1	875	168	3:1 phase + BC	
	900	24	3:1 phase + L (partly melted)	crystals of 3:1 phase
	950	24	Phase (?) + L (partly melted)	crystals of phase (?)
4:1	800	696	3:2 phase + BC	
	850	48	3:1 phase + BC	
	900	24	3:1 phase + L (partly melted)	crystals of 3:1 phase
3:1	800	696	3:2 phase + BC	
	800	48	3:2 phase + BC	reheat of 900°C specimen
	825	240	3:1 phase	
	850	72	3:1 phase	in Pt - container
	900	36	3:1 phase	reheat of 800°C specimen, 48 hr
	925	96	Phase (?) + L (partly melted)	crystals of phase (?)
	800	360	BC - 3:2 phase composite crystals	crystals of 3:1 phase reversed to composite crystals (see text)
3:2	750	696	3:2 phase + BC + NiO	incomplete reaction
	750	144	3:2 phase	reheat of 800°C, 432 hr, specimen
	800	168	3:2 phase	reheat of 750°C 696 hr, specimen
	800	432	3:2 phase	
	800	168	3:2 phase	reheat of 900°C specimen containing 3:1 phase + phase (?)
	800	696	3:2 phase	
	850	504	3:2 phase	reheat of 800°C, 696 hr, specimen
	875	148	3:1 phase + phase (?)	
	900	148	3:1 phase + phase (?)	
1:1	750	696	BC + NiO + (tr.) 3:2 phase	incomplete, sluggish reaction
	800	696	3:2 phase + NiO	reheat of 750°C specimen
	1175	504	crystals of phase (X) + NiO + amorphous white material	sealed Pt-tube
1:2	750	696	BC + NiO (tr.) 3:2 phase	incomplete, sluggish reaction
	800	696	3:2 phase + NiO	reheat of 750°C specimen

[a/] The system is not binary because of reactions with atmospheric CO_2 and O_2.

[b/] Does not include prior calcining. Specimens heated in Au-tubes.

[c/] At room temperature.

BC = $BaCO_3$; L = liquid (highly reactive with Au-container), (tr.) = trace
3:1 phase = hexagonal, carbon-containing oxide phase at Ba:Ni = 3:1 (see text).
3:2 phase = hexagonal, carbon-containing oxide phase at Ba:Ni = 3:2 (see text).
Phase (?) = rhombohedral Ba:Ni-oxide near 1:1 ratio but of unknown stoichiometry.
Phase (X) = rhombohedral Ba:Ni-oxide of unknown stoichiometry, possibly near 1:1.

Table 11

X-ray Powder Data for the 3:2 Ba:Ni Ratio Phase[a/]

$d_{obs.}$	$d_{calc.}$	hkℓ[b/]	$I_{obs.}$
8.378	8.375	100	14
4.837	4.835	110	2
3.420	3.419	111	100
2.792	2.792	300	92
2.418	2.418 2.418	220 002	15
2.322	2.323 2.323	102 310	4
2.163	2.163 2.163	112 221	78
2.094	2.094 2.094 2.094	202 311 400	5
1.9215	1.9216 1.9214	212 320	3
1.8277	1.8278 1.8276	302 410	12
1.7099	1.7097 1.7096	222 411	42
1.6122	1.6118	330	18
1.5290	1.5293 1.5291	113 331	7
1.5043	1.5043 1.5042 1.5042	322 421 510	3
1.4578	1.4580	412	13
1.3958	1.3958	600	14
1.3413	1.3412 1.3412 1.3411	223 332 520	10
1.2925	1.2923	521	12
1.2088	1.2090 1.2090 1.2089 1.2088	004 413 602 440	11
1.1728	1.1729 1.1728 1.1728	114 522 441	11
1.1092	1.1095 1.1093	304 710	4
1.0811	1.0814 1.0812 1.0812	224 442 711	8
1.0551	1.0552	630	6
1.0307	1.0310 1.0309	523 631	3
1.0082	1.0084 1.0083	414 712	3

[a/] See table 12 for chemical analysis data.

[b/] Indexed on the basis of a hexagonal cell with a = 9.671 0.001 Å and c = 4.836 0.002 Å. The phase is pseudocubic.

c = 4.847 Å. This phase was admixed with $BaCO_3$ + NiO. If his a were multiplied by $\sqrt{3}$, a_{new} = 9.692 Å, the cell would again resemble the 3:2 phase of this study. Since both 1:1 and 3:2 phases exist in the cobalt system, the 1:1 ratio was investigated below 850 °C. If the 3:2 phase is truly of 1:1 stoichiometry an additional phase such as $BaCO_3$ should be apparent in powder patterns. This is not the case. If the phase is of 3:2 stoichiometry then a possible 1:1 phase should be similar to $BaCoO_3$. If $BaNiO_3$ does not exist, the 1:1 composition must then consist of 3:2 plus free NiO. The portions of powder patterns shown in figure 8 clearly demonstrate the latter case, with free NiO evident in both the 1:1 and 1:2 Ba:Ni ratio patterns. Although some of the NiO lines are nearly coincident with those of the 3:2, the (220) line of NiO is clearly present in the compositions richer in Ni. It is therefore concluded that at least in air or in an oxidizing atmosphere containing a sufficient $P[CO_2]$, $BaNiO_3$ is unstable. Further evidence for this was obtained from an experiment involving the compound $BaNiO_2$ [3,4]. At 20,000 psi air and 600 °C this compound instead of oxidizing to $BaNiO_3$ decomposed completely to $BaCO_3$ + NiO. The CO_2 pressure was sufficently increased to prevent even the formation of the 3:2. Additional evidence for the behavior of $BaNiO_3$ was provided by preparing the compound at 810 °C and 1000 psi oxygen. Cell parameters for this phase which has a powder pattern shown superimposed on that of 3:2 in figure 8, are a = 5.631 Å and c = 4.797 Å. Greaves [6] prepared a similar phase at low temperature in flowing O_2. His phase, also different from that which he prepared in air, has a = 5.637 Å and c = 9.618 Å. The c-axis was doubled (4.809 Å x 2) because of several weak lines in his powder pattern. Our patterns do not show these lines nor is the phase (even with a doubled c) isostructural with the 4H form of $BaMnO_3$ [5] as suggested by Greaves. Recently, Krischner et al. [7] prepared $BaNiO_3$ with a = 5.631 Å, c = 4.808 Å in O_2. The data of Greaves [6], Krischner et al. [7], and this study for $BaNiO_3$ are consistent with our view that the phase observed in air is the 3:2.

Electron diffraction data for the 3:2 phase confirmed the $a\sqrt{3}$ axis but showed streaking and additional spots along c^* indicating at least a doubling of that axis. Chemical analyses (table 12) unequivocally established the presence of carbon in this phase. The composition appears to lie near $Ba_3Ni_2CO_8$ although $Ba_3Ni_2CO_9$ is not precluded. The first (or possible formulas intermediate in oxygen content) suggests the presence of Ni^{3+} or perhaps a disproportion to Ni^{4+} and Ni^{2+}. Magnetic susceptibility measurements by Lander [3] on his "$BaNiO_3$"

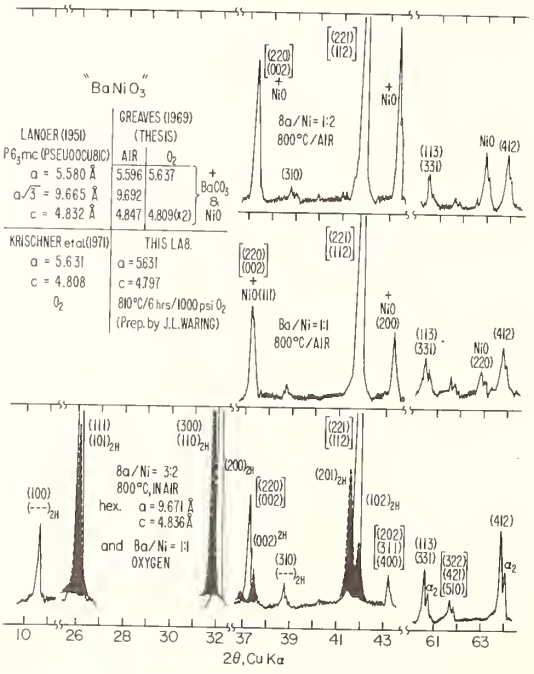

Fig. 8. Summary of x-ray diffraction powder data for "$BaNiO_3$" and the 3:2 Ba:Ni ratio phase. Compositions Ba:Ni = 1:1 and 1:2 show free NiO. The dashed overlay pattern in the bottom powder pattern represents $BaNiO_3$ (this lab).

Table 12

Chemical Analyses for Ba/Ni-Oxide Phases

%	Analysis	Formula	Calculated 1/
		3:2 Ba/Ni Phase	
H_2O	--		--
CO_2	6.96		6.57
BaO	67.98	$Ba_3Ni_2CO_8$	68.72
NiO	22.67		22.32
O	--	or	2.39
Ba/Ni	1.46		1.50
Ni/C	1.92		2.00
CO_2		$Ba_3Ni_2CO_9$	6.42
BaO			67.11
NiO			21.80
O			4.67
	#1	3:1 Ba/Ni Phase	
C	2.52		2.48
Ni	10.30	$*Ba_{12}Ni_4C_5O_{30}$	9.69
C/Ni	1.20		1.25
	#2		
C	3.03	$*Ba_{12}Ni_4C_6O_{30}$	2.96
Ni	10.29		9.64
C/Ni	1.44		1.50

1/ Based on the proposed formulas.

* Possible formulas indicating between 5 and 6 carbons per unit cell. See structural discussion of 3:1 Ba/Ni in text.

suggested a moment corresponding to 0.8 unpaired electrons. Greaves [6] and Krischner et al. [7], however, found their $BaNiO_3$ to be diamagnetic as might be expected for octahedral Ni^{4+} (d^6). This discrepancy is understandable if Lander really measured a phase containing the non-diamagnetic (d^7) ion Ni^{3+}. His x-ray and magnetic data appear to be more consistent with the 3:2 phase of this study.

3.2.b. THE 3:1 Ba:Ni RATIO

Above 875 °C, the 3:2 phase decomposes reversibly in air to an unidentified phase near 1:1 and a reddish-brown (in fine powder form) phase with a 3:1 Ba:Ni ratio. This latter material has a reversible minimum in air near 825 °C, decomposing to $BaCO_3$ plus the 3:2 phase. The x-ray powder pattern given in table 13 was completely indexed on the basis of a hexagonal cell with a = 9.587 Å and c = 4.880 Å. The portion shown in figure 9 clearly shows the apparent similarity with the 3:2 Ni and Co phases as well as with the 2H $BaCoO_3$ structure. Cell dimensions for the 3:1 phase show a larger c and smaller a by comparison with the 3:2. The compound melts incongruently above 925 °C in air to a solid phase (?), possibly near 1:1, plus a liquid which is especially reactive with Au containers. Chemical analyses (table 12) clearly established the presence of carbon in the compound and suggest the ideal formula to be between $Ba_3NiC_{1.25}O_{7.5}$ and $Ba_3NiC_{1.5}O_{8.25}$ or $Ba_2NiC_{1.5}O_{7.5}$.

3.3. SINGLE CRYSTAL GROWTH AND ANALYSIS OF Ba/Ni PHASES

3.3.a. PHASE (?)

Small black crystals (<0.1 mm) of a phase (?) were easily grown by melting the 6:1 or 3:1 ratios above ~925 °C [within the primary field of phase (?)]. Precession photographs revealed that this phase is rhombohedral (Laue = $\bar{3}$m) with $a = 5.59\sqrt{3} = 9.69$ Å and $c = 4.26 \times (3) = 12.79$ Å. The cell dimensions and subcell suggest a similarity with 2H $BaNiO_{3-x}$ and the 1:1-type Ba:Co phases previously discussed. From powder patterns and without evidence

Table 13

X-ray Powder Data for the 3:1 Ba:Ni Ratio Phase[a/]

$d_{obs.}$	$d_{calc.}$	$hk\ell$[b/]	$I_{obs.}$
8.292	8.303	100	34
4.792	4.793	110	13
3.415	3.420	111	100
2.765	2.767	300	63
2.441	2.440	002	6
2.396	2.397	220	12
2.302	2.303	310	8
2.174	2.175	112	11
2.150	2.151	221	52
2.079	2.082 2.076	311 400	4(b)
1.9259	1.9263	212	3
1.8309	1.8303	302	14
1.8121	1.8118	410	5
1.7746	1.7744	321	2
1.7099	1.7099	222	8
1.6990	1.6985	411	23
1.5976	1.5978	330	16
1.5705	1.5720 1.5691	501 420	4(b)
1.5406	1.5405	113	5
1.5019	1.5015	322	3(b)
1.4934	1.4938	421	3(b)
1.4545	1.4547	412	8
1.4258	1.4261	511	3
1.3841	1.3838	600	7
1.3454	1.3460	223	3(b)
1.3371	1.3368	332	2
1.2829	1.2827	521	11
1.2663	1.2661	610	2(b)
1.2097	1.2104 1.2071	413 104	4(b)
1.2033	1.2037	602	5
1.1672	1.1675	522	3
1.1638	1.1638	441	5

[a/] See table 12 for chemical analysis data.

[b/] Indexed on the basis of a hexagonal cell with a = 9.587±0.001 Å and c = 4.880±0.001 Å. Single crystal precession pictures indicate that the true c-axis is (4.880)(2) = 9.760 Å.

(b) = broad

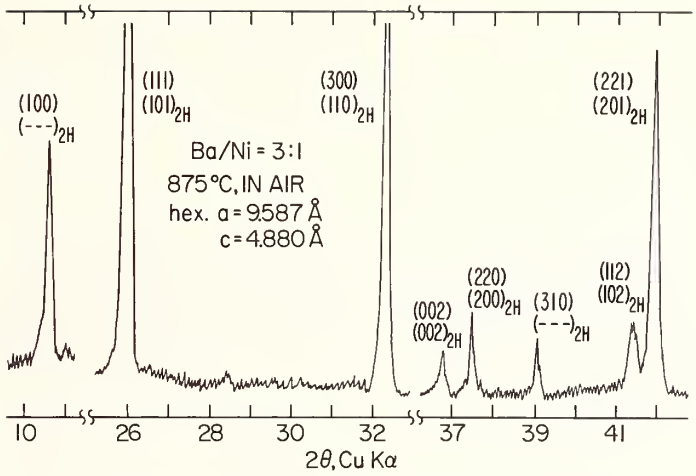

Fig. 9. Portion of the x-ray diffraction powder pattern for the 3:1 Ba:Ni ratio phase illustrating its similarity with 3:2 Ba:Ni and Co and 2H-type phases. Compare with figures 2 and 8.

of superstructure lines Krischner et al. [7] suggested that phases between $BaNiO_{2.73}$ and $BaNiO_{2.55}$ are rhombohedral with tripled subcell c-axes (4.355-4.311 Åx3) and subcell a-axes (5.705 Å) which are multiplied by $\sqrt{3}$. If our phase (?) is a (1:1) or even near a 1:1 ratio in composition it appears that Krischner et al. made a rather good educated guess about their powder patterns. Our precession photos clearly show superstructure spots. All crystals examined, however, are twinned with variable twin volume ratios.

3.3.b. PHASE (X)

Unrelated to the "in air" equilibria is an experiment conducted using the 1:1 ratio. This was heated at 1175 °C (3 weeks) in a sealed Pt-tube and quenched. Resulting products were black single crystals (<0.1 mm) of a phase (X) and considerable quantities of NiO plus a white amorphous material. Precession photos of phase (X) are similar to phase (?). The material is rhombohedral (Laue = $\bar{3}$m) with $a = 5.78\sqrt{3} = 10.01$ Å but with $c = 4.26x(9) \simeq 38.38$ Å.

3.3.c. 3:1 CRYSTALS

By heating compositions more Ba-rich than 3:1 within the primary field of the 3:1 phase (see fig. 7), small hexagonal prisms (<0.1 mm) are easily obtained. Precession pictures show 6/m Laue symmetry. With no extinctions, possible space groups are P6, P$\bar{6}$ and P6/m. Furthermore, the c-axis is doubled, $c = 4.880 \times (2) = 9.760$ Å, although this is not evident in x-ray powder patterns (see table 13). The a and c parameters were confirmed by electron diffraction.

3.3.d. TRANSFORMATION OF 3:1 to "3:2 CRYSTALS"

Crystals of the 3:2 phase could not be grown by conventional techniques as the phase has a decomposition maximum at relatively low temperature. Crystals of the 3:1, however, were available. As the 3:1 has a decomposition minimum, the 3:1 crystals were heated at 800 °C within the stability field of $BaCO_3$ plus the 3:2. The idea was based on the assumption that since the 3:1 and 3:2 phases appeared to be structurally similar there was a good possibility that $BaCO_3$ would segregate or diffuse from the 3:1 leaving the 3:2 phase in essentially single crystal form.

The transformation (followed by powder and single crystal patterns), was completed within 15 days. Within the first day, the 3:1 crystals did not transform to 3:2 but seemingly changed to the higher hexagonal Laue group 6/mmm. This conclusion ultimately proved incorrect after x-ray intensity data using an automatic diffractometer were collected. For example,

although the (hkℓ), ℓ = odd data showed equivalency consistent with 6/mmm Laue symmetry, the (hkℓ), ℓ = even data remained consistent with 6/m. A Laue group check using 2507 measured x-ray reflections and a sorting - averaging routine for equivalent reflections (written by Dr. A. D. Mighell, National Bureau of Standards) yielded an R = 1.6% for equivalent reflections based on 6/m. It was concluded that a symmetry change does not occur since the agreement factor in 6/mmm was 11%. At this time we do not understand why the 3:1 when annealed at lower temperatures (even at 350 °C for 10 min.) exhibits rather large x-ray diffraction intensity changes particularly for (hkℓ), ℓ = odd. The intensity changes are continuous with annealing time.

With continued heating the 3:1 crystals slowly transform to $BaCO_3$ and what appears to be the 3:2 phase. The precession pictures (figs. 10, 11, 12) for the transformed crystals are noteworthy in that they consist of intergrowths or at least oriented domains of $BaCO_3$ intergrown with the 3:2 phase. If the additional spots shown as $BaCO_3$ in figures 10, 11, and 12, belong to the 3:2 phase unusually large *a* and *c* axes must necessarily be chosen. Fortunately, the extra spots were easily identified by their d-spacings as the strongest reflections of $BaCO_3$. These are also somewhat streaked indicating that $BaCO_3$ is probably not truly single crystal in nature. Significantly, the *a* and *c* axes of orthorhombic $BaCO_3$ coincide with *a** and *c** of the 3:2. The *b*-axis of $BaCO_3$ coincides with an [hh0]* direction. The assemblage is an oriented, intimate intergrowth of two phases. The cause of this assemblage is the experimental conditions imposed for crystal growth. Although a 3:1 single crystal initially more Ba-rich than 3:2 must exsolve $BaCO_3$ to form a two phase assemblage, $BaCO_3$ simply does not diffuse to the crystal surface but remains as domains or perhaps as an intracrystalline growth with 3:2. Structural implications will be discussed in following sections. Neglecting the spots belonging to $BaCO_3$, the remainder of the precession pattern is consistent with the powder data for the 3:2 phase. The Laue symmetry appears to be 6/mmm. No superstructure along *c** is apparent. The x-ray pattern of crystals which were powdered showed $BaCO_3$ plus the 3:2 phase.

4. STRUCTURAL CONSIDERATIONS

4.1. GENERAL

It is possible to account for the chemistry, thermal behavior, and possible structure of non-1:1 type phases by considering the structure of the 2H modification. The structure of a 2H-type $A^{2+}B^{4+}O_3$ is shown as the cell with the shortest *a* dimension in figure 13. Ideally the cell contains the formula $A_2B_2O_6$. The space group is $P6_3/mmc$ or $P6_3mc$. Typical *a* and *c* dimensions are ~5.7 Å and ~4.8 Å respectively. A larger hexagonal cell with *a'* related to *a* by the factor $\sqrt{3}$ and with a content $A_6B_6O_{18}$ can also be chosen as shown. This unit, of course, is not the smallest repeat unit consistent with ABO_3 stoichiometry, although it could become the real unit cell if the stoichiometry and particularly the A/B ratio were varied. The two simplest ways of achieving the $a\sqrt{3}$ configuration, starting for convenience with $A_6B_6O_{18}$ stoichiometry are:

a) "removal" of the two Me(B) cations from the corners of the $a\sqrt{3}$ cell or

b) "removal" of the four Me cations from the 1/3 2/3 z and 2/3 1/3 z sites.

The resulting ideal stoichiometries which would justify the choice of an $a\sqrt{3}$ cell are $A_6B_4O_{18}$ and $A_6B_2O_{18}$. These are not satisfactory with respect to oxygen content as charge compensation must necessarily be accomplished by increasing the charge of the transition metal (B). The formula $A_6^{2+}B_4O_{18}$ requires a B^{6+} while $A_6^{2+}B_2O_{18}$ requires a B^{12+}. Both clearly are unrealistic. To maintain a B^{4+} oxygen vacancies can be hypothesized yielding $A_6B_4O_{14}$ and $A_6B_2O_{10}$ stoichiometries. The resulting structures would be skeletal in nature with quite large voids. This mechanism is not particularly feasible. The only remaining possibility is the incorporation of an additional component which, a) would permit the B cation to exist in a reasonable oxidation state and, b) would coordinate with available oxygen to preclude large structural cavities. The 3:2 (6:4) Ba:Ni (and Co) and 3:1 (6:2) Ba:Ni phases have the two simple A/B ratios described. Furthermore, these phases are characterized by $\sqrt{3}$-type cells. The only missing link is the identity of the additional component. From the known affinity

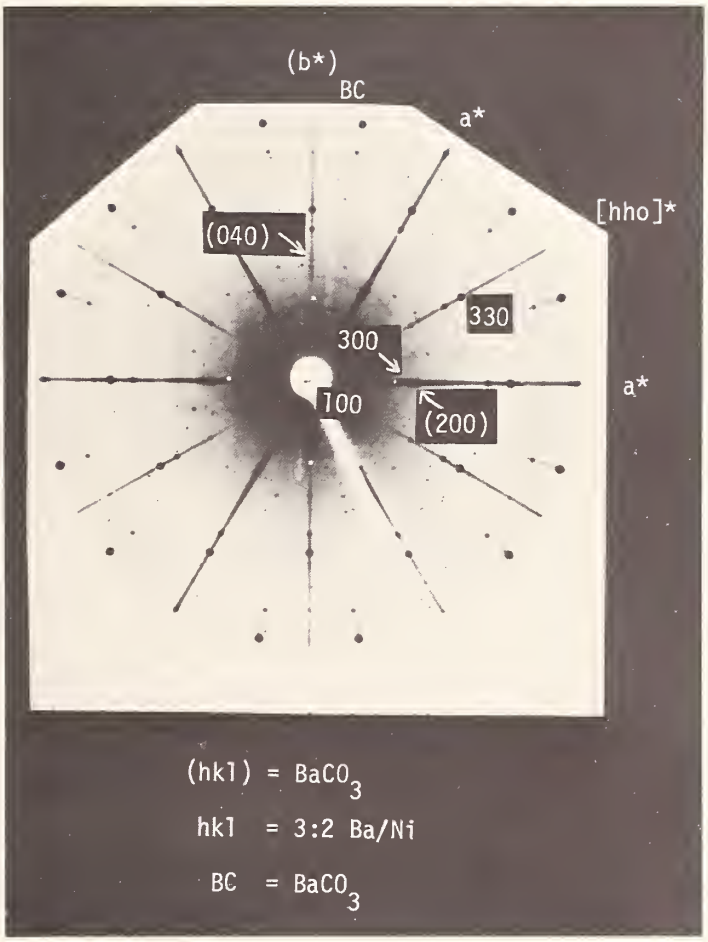

Fig. 10. X-ray precession photograph, hko view, of a $BaCO_3$ - 3:2 Ba:Ni composite crystal. The *a** directions for orthorhombic $BaCO_3$ and the hexagonal 3:2 coincide while *b** for $BaCO_3$ coincides with one of the [hho]* directions (unfiltered Mo radiation).

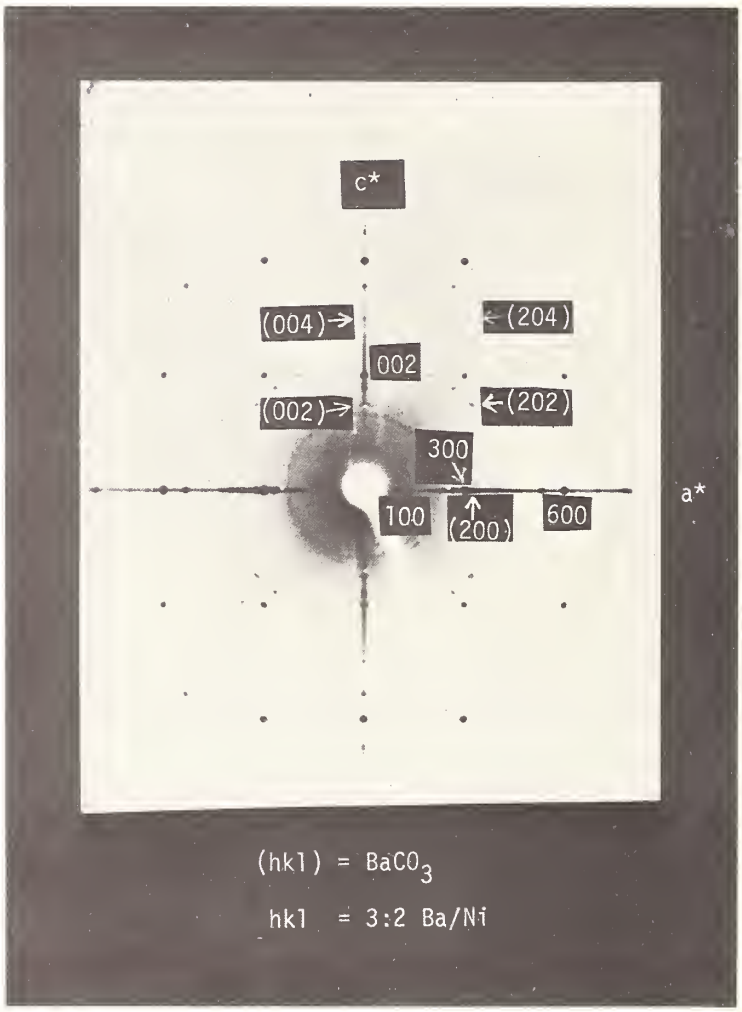

Fig. 11. X-ray precession photograph, h0ℓ view, of a $BaCO_3$ - 3:2 Ba:Ni composite crystal. The *c** directions for both phases coincide. The (204) of $BaCO_3$ is very very weak (unfiltered Mo radiation).

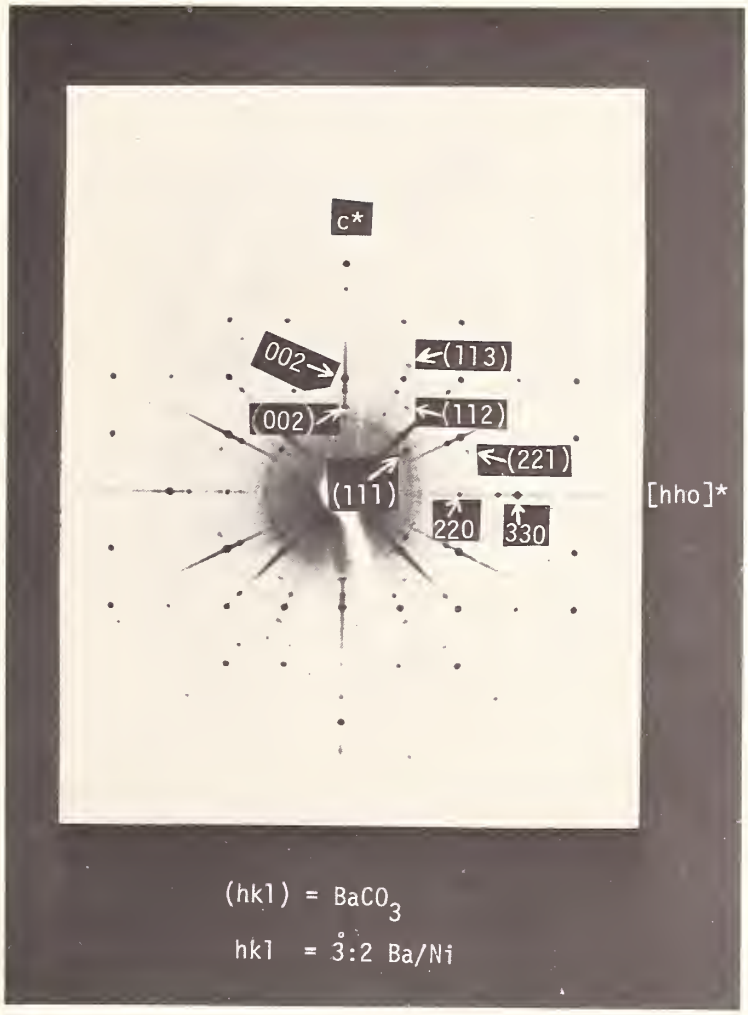

Fig. 12. X-ray precession photograph, hhℓ view, of a $BaCO_3$ - 2:2 Ba:Ni composite crystal. The c^* directions of both phases coincide and (hhℓ) spots for orthorhombic $BaCO_3$ are present (unfiltered Mo radiation).

of BaO for CO_2 and from the structural nature of $BaCO_3$, it appeared likely that this component was CO_2. Chemical analyses later verified this assumption. Consider the dashed-line cell in figure 13. The unit cell outlined may be regarded as being orthorhombic with $a_{ortho.} \simeq a_{hex.}$, $b_{ortho.} \simeq a_{hex.}\sqrt{3}$, and $c_{ortho.} \simeq c_{hex.}$ This cell is nearly identical with that of the structure of $BaCO_3$ which has a = 5.314 Å, b = 8.904 Å, and c = 6.430 Å [11]. The Me cations must be removed from the centers of the face-sharing octahedra and replaced with carbon within the triangular oxygen groups. Except for an expansion of c from ~4.8 Å to 6.430 Å necessitated by, a) the tendency of parallel CO_3 groups to maximize their separation and, b) the "staggering" of adjacent CO_3 units to form "puckered" oxygen layers, the disposition of atoms in figure 13 is similar to aragonite. It is also obvious that for a close packing of large A cations and oxygens, space is inherently available for carbon within nearly perfect trigonal oxygen groups.

The 2H, $a\sqrt{3}$, and $BaCO_3$-type cells all appear to be related. It was therefore not surprising to find the oriented intergrowth of $BaCO_3$ and 3:2 Ba:Ni. The systematic c-axis expansion in, for example, the Ba:Ni series:

465-504 O - 72 - 18

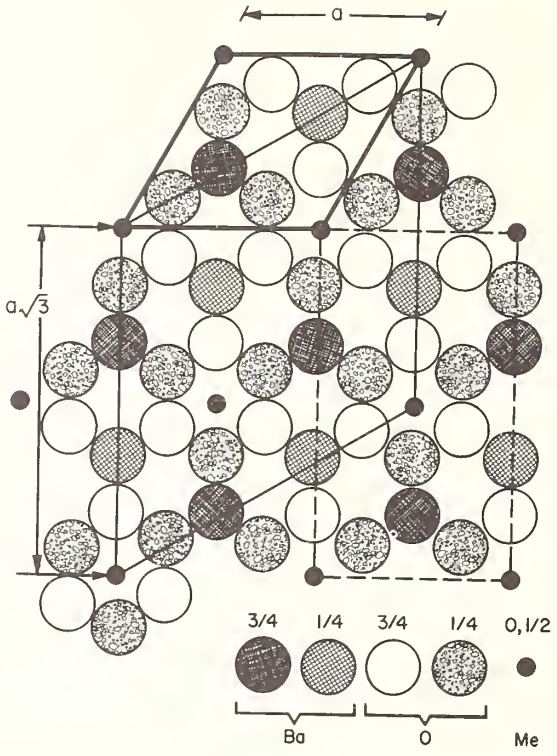

Fig. 13. A close-packing of barium and oxygens with octahedrally coordinated transition metals (Me). Atoms, projected on (001), have fractional z coordinates. The small (heavy line) hexagonal cell describes the 2H structure. The larger (fine line) hexagonal cell is related to 2H by the factor $\sqrt{3}$. The orthorhombic (dashed) cell represents the aragonite form of $BaCO_3$ only in the general disposition of atoms excluding Me atoms. See discussion in text.

4.797 Å (no carbonate, 1:1) → 4.836 Å (3:2, carbon containing) → 9.760/2 = 4.880 Å (3:1, carbon containing → 6.430 Å ($BaCO_3$),

is in accord with incorporation of increased amounts of carbonate. The high temperature decomposition of the 3:2 phases appears to reflect the structural instability due to loss of CO_2.

4.2. THE 3:2 Ba:Ni-$BaCO_3$ COMPOSITE CRYSTALS

Using an automatic diffractometer, 1385 x-ray reflections were measured for the 3:2 Ba:Ni - $BaCO_3$ composite crystals. The $BaCO_3$ maxima were ignored. The data were sorted and equivalent reflections based on the assumed 6/mmm symmetry were averaged to yield 111 independent observations. It was anticipated that the quality of the intensity data would be poor considering the nature of the 3:2 crystals grown. The agreement factor for "equivalent" reflections, for example, was somewhat high at 10.1%. Although it was further realized that the electron diffraction data for the 3:2 indicate a tendency toward at least a doubling of *c*, a structural analysis was nevertheless attempted.

A three-dimensional Patterson map suggested the coordinates xoz, z ≈ 1/4 for six Ba atoms but also was characterized by, a) numerous additional maxima which could not be reconciled with Ba-Ni, Ni-Ni, or Ba-O vectors and, b) a "smearing" out of the Ba-Ba vectors along [oow] especially for o < w < 1/8. The following structural observations proved to be consistent with these features of the Patterson. The condition $hh\bar{o}\ell$, ℓ = 2n derived from the data suggested the space groups $P6_3cm$ or $P6_3/mcm$. Using $P6_3cm$ and the 6(c) site with x ≈ 2/3, z ≈ 1/4, Ba would not refine. The x parameter refined to 0.6817 ± 0.0019 but z was

shifted to a numerically huge coordinate effectively outside the unit cell. The isotropic temperature factor, however, remained positive and < 1.0. Refinement of Ba was possible in 6(g), x0 1/4, of $P6_3/mcm$. The x parameter refined to 0.6804 ± 0.0019 when z was fixed at 1/4. The R-factor was 36.4%. A difference map at this point immediately revealed several problems. Two Ni atoms were clearly evident at (000) and (001/2) but the remaining two were distributed in the 4(d) site, (1/3 2/3 0), indicating possible disorder. Of greater importance, however, were maxima, approximately 1/10 the magnitude of Ba in 6(g), related by the xoz coordinates of the 12(k) position. Three distinct sets were evident with the following parameters:

$$12(k);\ x \approx \frac{2}{3},\ z \approx \frac{1}{6}$$

$$12(k);\ x \approx \frac{1}{3},\ z \approx \frac{1}{6}$$

$$12(k);\ x \approx \frac{1}{3},\ z \approx 0$$

It is proposed that the atoms in 12(k) are bariums which are arranged in layers perpendicular to *c*. Consider layers of the 2H structure-type as generated by the bariums in 6(g). Eight of these layers separated by ~ 2.4 Å yield a distance along *c* of ~ 19.2 Å. In the $BaCO_3$ structure, Ba-layers are separated by 1/2 *c* or (6.43/2) ≈ 3.2 Å. Six $BaCO_3$-type layers therefore can occupy the space provided by a distance of 19.2 Å. A mixture of the two types of layers together with the symmetry imposed by $P6_3/mcm$ can generate a composite cell with $c \approx 4.8$ Å (19.2/4). This "average" cell accounts not only for the Ba in 6(g) but also for the possible Ba in 12(k). Although the ratio of the two types of layers remains unknown, the Ba in 12(k) together with the Ba in 6(g) yield vectors which are consistent with the Patterson. The precession pictures in figures 10, 11, and 12 further substantiate this interpretation. Based on these observations the conclusion that the 3:2 crystals are not perfectly ordered but are $BaCO_3$-3:2 composites seems justified. This interpretation may not be true for a 3:2 phase grown "on composition" but seems applicable to those crystals grown purposely (and from necessity) from a more Ba-rich composition.

Confronted with the possibility that the asymmetric unit could not be deduced by conventional methods the refinement was continued. Instead of partially occupying the 12(k) sites with unknown multiplicity factors (which may also be refined) it was decided to vary the β_{33} parameter of the Ba in 6(g). This is realistic since the z parameters near, for example, 1/4, are ~ 1/6 to ~ 1/3. The 6 Ba (anisotropic) and 2 Ni in (b), refined to 17.1%. Addition of the half-occupied 4(d) nickel site plus 6 oxygens in x0 1/4 ($x \approx 1/6$) and 12 in xy 1/4 ($x \approx 1/2$, $y \approx 1/6$) also observed in the difference map gave R = 13.5%. The oxygens in 6(g) provide for octahedral coordination for Ni in (b). Those in 12(j) are associated with the partially occupied nickel 4(d) site but were approximately 1/2 the magnitude of oxygen in 6(g) in the difference map. The oxygen in 12(j) refined but has a large (12.185 ± 5.97) isotropic temperature factor. This was expected since, a) the oxygen is associated with the partially occupied 4(d) Ni site and, b) the oxygen multiplicity factor was not permitted to vary. The refinement was terminated at this stage as further information about the structure especially with respect to the light atoms could not be derived.

4.3. THE 3:1 Ba:Ni PHASE

Using 639 independent reflections collected with an automatic diffractometer a structure analysis of the 3:1 Ba:Ni compound ($a = 9.587$ Å, $c = 9.760$ Å) was initiated. Of the possible space groups (without extinctions) of Laue symmetry 6/m, $P\bar{6}$ contains symmetry elements which permit a close packing of Ba and O atoms. After an analysis of the Patterson map, the structure was refined to R = 5.9% using full-matrix least squares and successive $F_{obs.}$ and/or $F_{diff.}$ maps. The asymmetric unit was not clearly established, however. Positional coordinates are given in table 14. The preliminary structure is shown in figure 14 and 15. Refinement proceeded normally until the very last stages. Refinement of the atoms in the unit $Ba_{12}Ni_4C_2O_{21}$ gave R = 6.5%. The Ni atoms are in strings of face-sharing octahedra parallel with *c* (fig. 15). They are separated by a normal distance of ~ 2.50 Å as in the 2H structure. The two carbon atoms are located within triangular O groups centered about 2/3 1/3 z, near $z \approx 1/3, 2/3$. This appears to account for the doubling (2 x 4.880 Å) of the *c*-axis. They are separated by ~ 3.40 Å, nearly that observed in $BaCO_3$. The C - O distances, 1.28 - 1.30 Å are typical for a CO_3-group. A possible third carbon at (000) was observed in difference

Table 14

Summary of Positional Coordinates from
Single Crystal Data for the 3:1 Ba:Ni-Oxide Phase

Space Group	-	$P\bar{6}$	639 reflections	
$Ba_{12}Ni_4C_2O_{21}$	m[a]	x	y	z
6Ba (ℓ)	1	0.3296(5)	0.3115(5)	0.2426(2)
3Ba (k)	1/2	0.0223(4)	0.3268(5)	1/2
3Ba (j)	1/2	0.3206(5)	0.0067(5)	0
2Ni (g)	1/3	0	0	0.122(1)
2Ni (g)	1/3	0	0	0.378(1)
6 O (ℓ)[b]	1	0.836(4)	0.842(5)	0.242(2)
3 O (k)[b]	1/2	0.831(5)	0.013(5)	1/2
3 O (j)[b]	1/2	-0.006(6)	0.838(8)	0
3 O (j)[c]	1/2	0.531(4)	0.330(4)	0
6 O (j)[d]	1	0.536(2)	0.196(2)	0.326(2)
2 C (i)	1/3	2/3	1/3	0.318(4)
Possible Carbonate Groups from F_{diff} Maps:				
3 O (ℓ)	1/2[e]	0.195(4)	0.665(5)	0.031(4)
3 O (ℓ)	1/2[e]	0.196(8)	0.649(8)	0.446(6)
3 O (ℓ)	1/2[e]	0.205(8)	0.542(8)	0.260(5)

R = 6.5% for $Ba_{12}Ni_4C_2O_{21}$

R = 5.9% after addition of half-occupied oxygens of the possible carbonate groups.

Suggested Stoichiometry (chemical analysis):
$Ba_{12}Ni_4C_5O_{30}$ or $Ba_{12}Ni_4C_6O_{30}$

[a] multiplicity factor (occupancy)

[b] oxygens of the octahedra associated with Ni

[c] potential carbonate group

[d] carbonate group

[e] normal multiplicity is halved (half-occupied oxygens) (see text).

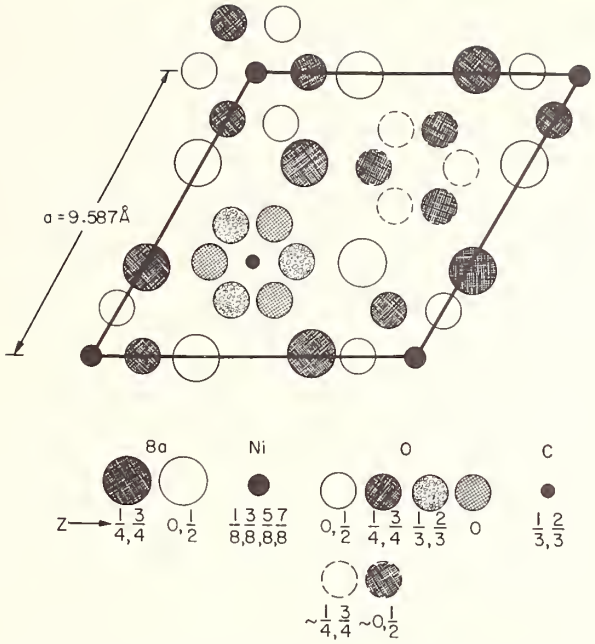

Fig. 14. Proposed structure, (001) view, of the hexagonal 3:1 Ba:Ni phase. Fractional coordinates are approximate z parameters. Space group = $P\bar{6}$. Oxygens that are dashed are images observed in $F_{diff.}$ maps and are possible carbonate groups.

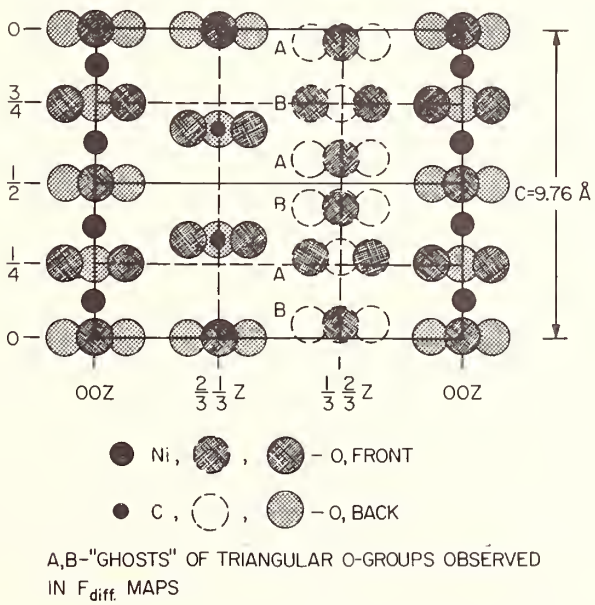

Fig. 15. Proposed structure, (110) view, of the hexagonal 3:1 Ba:Ni phase. The Ni atoms are in strings of face-sharing octahedra. Two carbonate groups at z ≈ 1/3, 2/3 are shown. The triangular oxygen group around 2/3 1/3 O is a probable carbonate group. Groups A and B are "ghosts" or images of possible carbonate groups observed in $F_{diff.}$ maps. All cannot exist in the structure. Barium atoms are not shown. See discussion in text.

maps within the triangular oxygen group centered about 2/3 1/3 0. When refined, the isotropic temperature factor for this atom was slightly negative at -1.6 ± 0.5. Of greater importance are "images" (in $F_{diff.}$ maps) of possible CO_3-groups centered about 1/3 2/3 z as shown labelled A and B in figure 15. Both A and B groups cannot exist simultaneously within the same cell as the distance between parallel groups is far too short, ranging from 0.58 to 2.25 Å. With a *c*-axis of 9.76 Å, space is available for a maximum of three parallel CO_3-groups separated by 3.2 Å. The three groups in set A or B would be satisfactory although the corresponding distances range from ~ 2.9 to ~ 4.3 Å. These distances were derived after a refinement in which the oxygens in sets A and B were half-occupied (see table 14). The R-factor dropped slightly to 5.9%. Prior to refinement, the oxygens were positioned where they were observed in difference maps. From z parameters initially at 0.06, 0.24, and 0.43 they shifted in the refinement to .03, 0.26 and 0.45, respectively. The initial set of z parameters more closely resembles the appropriate distances of 3.2 - 3.4 Å for parallel carbonate groups. As multiplicity, temperature factor, and z parameters are strongly correlated, the refined parameters may not be particularly accurate. It may be concluded that these groups are disordered to remain within the confines of $P\bar{6}$. Other possibilities for the observed phenomenon include, a) absorption effects for which correction was not made, b) twinning from a lower symmetry space group to $P\bar{6}$ and/or, c) the data is so dominated by heavy Ba and Ni that a possible monoclinic or orthorhombic space group cannot be discerned. Chemical analyses established the number of carbon atoms per cell to be between 5 and 6. It is seen (fig. 15) that a maximum of 6 C can be distributed within triangular oxygen groups observed. Two are at z ≈ 1/3, 2/3; one is possible at z = 0; and three are physically reasonable within either the A or B groups. If the correct number of carbons is 5 then the stoichiometry $Ba_{12}Ni_4C_5O_{30}$ $[Ba_{12}(Ni_4O_{12})(CO_3)_5(\square O_3)_v$; v - vacant] yields an oxidation state of 4+ for nickel. If the number is 6 the $Ba_{12}Ni_4C_6O_{30}$ $[Ba_{12}(Ni_4O_{12})(CO_3)_6]$ stoichiometry yields Ni^{3+}. Magnetic susceptibility data should elucidate this aspect of the problem.

5. SUMMARY

Phase relations in the systems BaO-"cobalt oxide" and BaO-"nickel oxide" are directly influenced by the presence of CO_2. In air and at elevated temperatures carbonated phases related to a 2H-type structure are stable and easily prepared. The presence of CO_2 causes decomposition of Ba_2CoO_4 and prevents the formation of 2H-$BaNiO_3$.

6. ACKNOWLEDGMENTS

We wish to thank Dr. J. G. Allpress, University of Melbourne, for the electron diffraction data and Dr. A. D. Mighell, National Bureau of Standards, for numerous discussions concerning the computer programs used in this study. J. L. Waring, National Bureau of Standards, prepared several 1:1 phases in the nickel system.

7. REFERENCES

[1] Strauss, S. W., Fankuchen, I., and Ward, R., J. Amer. Chem. Soc. 73, 5084 (1951).
[2] Gushee, B. E., Katz, L., and Ward, R., J. Amer. Chem. Soc. 79, 5601 (1957).
[3] Lander, J. J., and Wooten, L. A., J. Amer. Chem. Soc. 73, 2452 (1951).
[4] Lander, J. J., Acta Cryst. 4, 148 (1951).
[5] Hardy, A., Acta Cryst. 15, 179 (1962).
[6] Greaves, J. R., *Thermodynamic Properties of Mixed Metal Oxides* (dissertation), Oxford Univ., England (1969).
[7] Krischner, H., Torkar, K., and Kolbesen, B. O., J. Solid State Chem. 3, 349 (1971).
[8] *The X-ray System*, edited by J. M. Steward, F. A. Kundell, and J. C. Baldwin, Univ. of Maryland Computer Science Center, 1970.
[9] Bland, J. A., Acta Cryst. 14, 875 (1961).
[10] Candela, G. A., and Negas, T., to be published.
[11] Swanson, H. E., Fuyat, R. K., and Ugrinic, G. M., NBS Circular 539, Vol. III, p. 62, 1954.
[12] *International Tables for X-ray Crystallography*, Vol. II, p. 342, Kynoch Press, Birmingham, 1959.

DISCUSSION

R. Ward: May I ask one question? The position of the carbons couldn't possibly be within an octahedron could it?

T. Negas: No, all our electron density indicative of a carbon was always in or near the oxygen plane. There is this idea now that carbonate groups are no longer truly planar and indeed the two carbons that were actually well refined, pulled out of that trigonal plane very, very slightly, but not into the center of the octahedron. The possible octahedra within that 110 plane which you saw--these were devoid of nickel, completely devoid of nickel.

R. Ward: They will be sharing faces. In the carbides, the carbon is always in the octahedral sites, and it looks like that would be a good place for carbon to be.

T. Negas: Yes, but they were definitely well within the triangular oxygen group, not at a lower elevation. This is definitely a carbonate phase, not a carbide.

National Bureau of Standards Special Publication 364, Solid State Chemistry, Proceedings of 5th Materials Research Symposium, issued July 1972.

PREPARATION OF $SrFe_xMn_{1-x}O_{3-y}$ AND $CaFe_xMn_{1-x}O_{3-y}$ CRYSTALS AND SOME OF THEIR PROPERTIES[1]

E. Banks, O. Berkooz[2] and T. Nakagawa[3]

Department of Chemistry
Polytechnic Institute of Brooklyn
Brooklyn, New York 11201

Single crystals of $SrFe_xMn_{1-x}O_{3-y}$ and $CaFe_xMn_{1-x}O_{3-y}$ were grown by the usual technique from fluxes of excess $SrCl_2$ and $CaCl_2$, respectively. Apparently cubic perovskites were obtained in the $SrFe_xMn_{1-x}O_{3-y}$ system where x is in the range $0.4 \leq x \leq 0.7$ and in the $CaFe_xMn_{1-x}O_{3-y}$ where x is $0.2 \leq x < 0.4$. Hexagonal crystals, isostructural with the reported high temperature phase of $BaMnO_3$, were obtained in the $SrFe_xMn_{1-x}O_{3-y}$ where x is 0.1 and 0. Chemical analysis showed that the values of Fe:Mn ratio in these crystals were very close to the expected ones. From the density and X-ray measurements the existence of substantial amounts of oxygen vacancies ($0.26 \leq y \leq 0.44$) in the perovskite crystals was observed. For the hexagonal crystals, lower concentrations of oxygen vacancies ($y \sim 0.11$) were observed. The Mössbauer spectra of crystals having $x = 0.4 - 0.7$ in the $SrFe_xMn_{1-x}O_{3-y}$ system were found to consist of two kinds of quadrupole-split lines of Fe^{3+} ions, Fe^{3+}(I) which are present in regular oxygen octahedra and Fe^{3+}(II) which are associated with oxygen vacancies. From the magnetic measurements, Neél temperatures in the $SrFe_xMn_{1-x}O_{3-y}$ were found to be T_N = 130 K, 35 K and 20 K for x = 0.7, 0.5 and 0.4, respectively. Using the experimental data of the densities, the Mössbauer effect and effective magnetic moments, discussions concerning the amount of oxygen vacancies in the perovskite compounds are given.

The perovskite-like phases exhibited semiconducting behavior with activation energies of about 0.16 eV, which was almost independent of composition.

Key words: Antiferromagnetism; $CaFe_xMn_{1-x}O_{3-y}$; defect structure; mixed metal oxides; Mössbauer effect; oxygen vacancies; perovskite; semiconductivity; $SrFe_xMn_{1-x}O_{3-y}$.

1. INTRODUCTION

Oxygen deficiencies have often been observed in perovskite-type oxides containing transition metal ions. It is well known [1-4][4] that the deficiencies can be tolerated over wide ranges of composition without changes in structure. Investigations of the perovskite phases in the systems $SrFeO_{3-y}$ [5-7] and $CaMnO_{3-y}$ [8,9], have shown that the oxygen concentration is dependent upon the temperature and oxygen pressure at which samples are equilibrated and that their magnetic and electrical properties are greatly affected by the oxygen deficiencies.

This report describes the preparation of single crystals in the systems $SrFe_xMn_{1-x}O_{3-y}$ and $CaFe_xMn_{1-x}O_{3-y}$, and some observations on their magnetic and electrical properties.

---

[1] Work sponsored by U.S. Army Research Office (Durham) Grant No. DA-ARO-D-31-124-G-1036 and Air Force Office of Scientific Research, Grant No. F 44620-69-C-0047.

[2] Permanent address: 11 Azar Street, Holon, Israel.

[3] Permanent address: Department of Physical Electronics, Tokyo Institute of Technology, Ohkayama, Meguro-ku, Tokyo, Japan.

[4] Figures in brackets indicate the literature references at the end of this paper.

2. EXPERIMENTAL PROCEDURES AND RESULTS

2.1. PREPARATIONS OF SAMPLES AND CRYSTALLOGRAPHIC PROPERTIES

Single crystals of $SrFe_xMn_{1-x}O_{3-y}$ and $CaFe_xMn_{1-x}O_{3-y}$ were grown by slow cooling from fluxes of excess $SrCl_2$ and $CaCl_2$, respectively. Sintered powders with compositions $SrFe_xMn_{1-x}O_{3-y}$ and $CaFe_xMn_{1-x}O_{3-y}$, produced by mixing $SrCO_3$ or $CaCO_3$, Fe_2O_3 and $MnCO_3$ and firing at 1100 °C in air for 12 hours, were used as starting materials.

For the preparation of $SrFe_xMn_{1-x}O_{3-y}$ crystals, weighed amounts of the starting materials and reagent-grade $SrCl_2$ with a molar ratio of 1:4 were heated in 40 ml platinum crucibles at 1330 °C for 12 hours so as to allow complete solution. The furnace was then cooled at 5-10° per hour to 900 °C, at which temperature the crucible was removed from the furnace. For the crystallization of $CaFe_xMn_{1-x}O_{3-y}$ the best results were obtained from a soaking temperature of 1280 °C.

The crystals were separated by leaching in dilute hot nitric acid. Crystals were located mostly at the surface on the crucible wall. Cubic crystals generally about 1 x 1 x 1 mm in dimension were obtained in the $SrFe_xMn_{1-x}O_{3-y}$ system ($0.4 < x < 0.7$). For higher manganese concentrations ($SrMnO_{3-y}$ and $SrMn_{0.9}Fe_{0.1}O_{3-y}$) hexagonal crystals were obtained. In the $CaFe_xMn_{1-x}O_{3-y}$ system, only cubic crystals were obtained in the range $0.2 \leq x \leq 0.4$. The largest crystals obtained were 3 x 3 x 3 mm in dimension for a composition of $CaFe_{0.4}Mn_{0.6}O_{3-y}$.

X-ray diffraction measurements were made on powdered samples of these crystals using monochromatized CuKα radiation. The powder patterns of cubic crystals are consistent with a cubic perovskite structure. The lattice constants in the $SrFe_xMn_{1-x}O_{3-y}$ system are plotted in figure 1. The powder patterns of hexagonal crystals were indexed on the basis of the high temperature phase of $BaMnO_3$ [10]. The lattice constants were calculated from the high angle reflections.

Crystals from several different runs were chemically analyzed. Results of crystallographic properties and chemical analysis of selected crystals are shown in table 1. Observed values of the Fe:Mn ratio in these crystals are found to be very close to the nominal compositions.

Densities of the crystals were measured with a pycnometric method using toluene at room temperature. Observed values of the densities in the perovskite phase, $SrFe_xMn_{1-x}O_{3-y}$, are plotted in figure 2. Solid lines in the figure show the calculated x-ray densities, assuming oxygen vacancies based upon y = 0, 0.25 and 0.5, respectively.

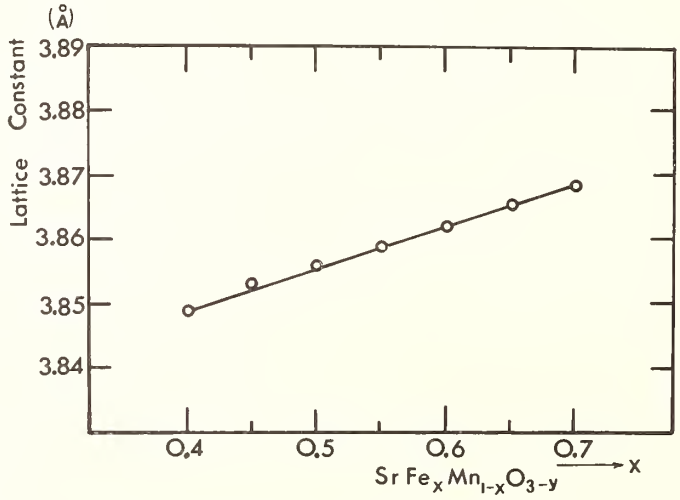

Fig. 1. Variation of the lattice constants in the $SrFe_xMn_{1-x}O_{3-y}$ system.

Table 1

Chemical Analysis and Lattice Parameters of $SrFe_xMn_{1-x}O_{3-y}$ and $CaFe_xMn_{1-x}O_{3-y}$

Starting composition	Chemical Analysis	Lattice parameters (Å)
$SrFe_{0.7}Mn_{0.3}O_{3-y}$	$SrFe_{0.703}Mn_{0.300}O_{3-y}$	a = 3.868 ± 0.001
$SrFe_{0.6}Mn_{0.4}O_{3-y}$	$SrFe_{0.648}Mn_{0.349}O_{3-y}$	a = 3.862 ± 0.001
$SrFe_{0.5}Mn_{0.5}O_{3-y}$	$SrFe_{0.526}Mn_{0.446}O_{3-y}$	a = 3.856 ± 0.001
$SrFe_{0.4}Mn_{0.6}O_{3-y}$	$SrFe_{0.421}Mn_{0.553}O_{3-y}$	a = 3.849 ± 0.001
$CaFe_{0.4}Mn_{0.6}O_{3-y}$	$CaFe_{0.378}Mn_{0.624}O_{3-y}$	a = 3.760 ± 0.001
$CaFe_{0.3}Mn_{0.7}O_{3-y}$	$CaFe_{0.283}Mn_{0.733}O_{3-y}$	a = 3.754 ± 0.001

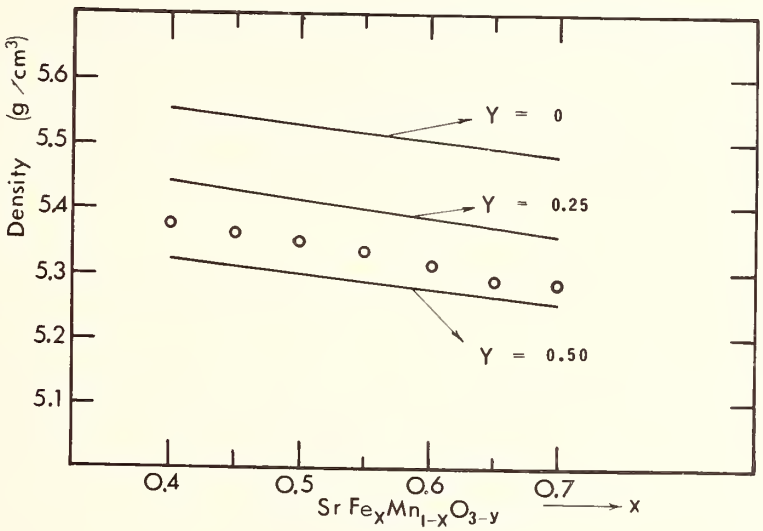

Fig. 2. Observed values of the densities (dots) in the materials $SrFe_xMn_{1-x}O_{3-y}$.

It is interesting to note that for all the compositions the vacancy concentrations lie in the region between y = 0.25 and y - 0.5. The existence of substantial amounts of oxygen vacancies in the $CaFe_xMn_{1-x}O_{3-y}$ crystals was also observed in the same way.

For the hexagonal crystals, on the contrary, lower concentrations of oxygen vacancies were estimated. The results are shown in table 2 together with the Ca-Fe-Mn-O system, in which oxygen vacancy concentrations, y, were estimated from the experimental values of unit cell volume and density.

Table 2

Density and Oxygen Vacancy Concentration, Y, of $CaFe_xMn_{1-x}O_{3-y}$ and Hexagonal $SrFe_xMn_{1-x}O_{3-y}$

Sample	Density (g cm^3)	y
$CaFe_{0.4}Mn_{0.6}O_{3-y}$	4.32 ± 0.01	0.30
$CaFe_{0.3}Mn_{0.7}O_{3-y}$	4.35 ± 0.01	0.26
$CaFe_{0.2}Mn_{0.8}O_{3-y}$	4.32 ± 0.01	0.30
$SrFe_{0.1}Mn_{0.9}O_{3-y}$	5.37 ± 0.01	0.11
$SrMnO_3$	5.37 ± 0.01	0.11

2.2. MAGNETIC PROPERTIES

The Mössbauer spectra of the perovskite single crystals, $SrFe_xMn_{1-x}O_{3-y}$, which had been crushed to powder, were measured at room temperature using a $^{57}Co(Pd)$ source. A typical example of the Mössbauer spectra of $SrFe_{0.5}Mn_{0.5}O_{3-y}$, is shown in figure 3. The spectra of the samples having x = 0.4-0.7 were found to consist of two sets of quadrupole split peaks of Fe^{3+} ions, $Fe^{3+}(I)$, and $Fe^{3+}(II)$ indicating Fe^{3+} ions are located in two nonequivalent sites. Isomer shifts of $Fe^{3+}(I)$ and $Fe^{3+}(II)$ are about 0.50 mm/sec. and 0.30 mm/sec., respectively, which are in reasonable agreement with literature values for high-spin Fe^{3+} [11].

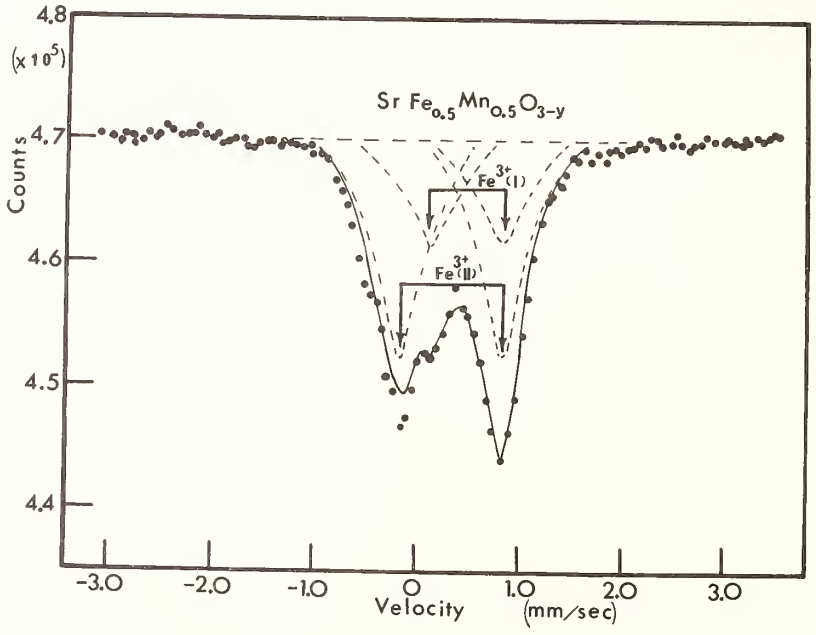

Fig. 3. The Mössbauer spectrum of $SrFe_{0.5}Mn_{0.5}O_{3-y}$ at room temperature.

In the iron rich compound, $SrFe_{0.7}Mn_{0.3}O_{3-y}$, the presence of small amounts (~ 15%) of Fe^{4+} ions (IS = -0.17 mm/sec.) [6] was detected in the spectra (fig. 4). The Mössbauer data in $SrFe_xMn_{1-x}O_{3-y}$ are summarized in table 3.

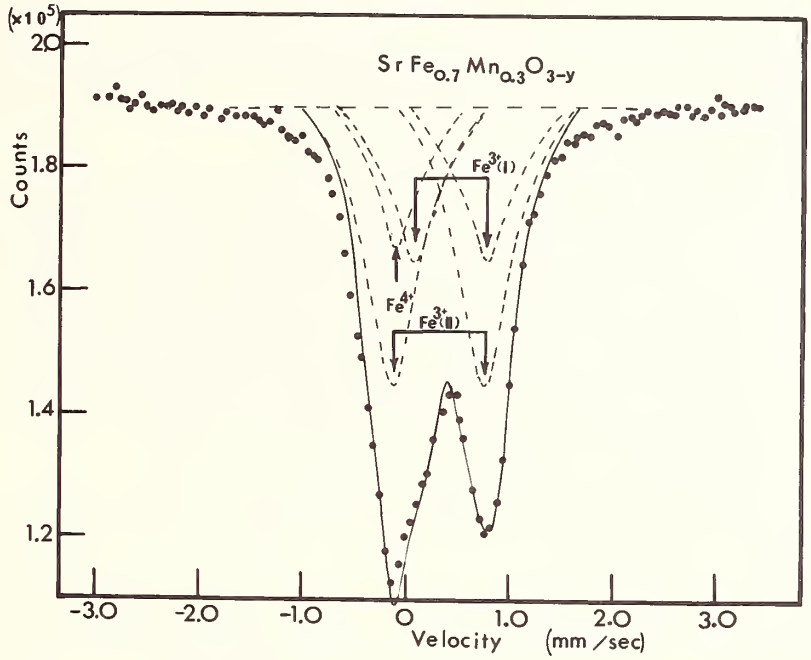

Fig. 4. The Mössbauer spectrum of $SrFe_{0.7}Mn_{0.3}O_{3-y}$ at room temperature.

Table 3

Mössbauer Data for $SrFe_xMn_{1-x}O_{3-y}$.

Sample	Ion	Isomer shifts* (mm/sec.)	Quadrupole splittings (mm/sec.)
$SrFe_{0.7}Mn_{0.3}O_{3-y}$	Fe^{4+}	-0.17	0
	Fe^{3+}(I)	0.50	0.57
	Fe^{3+}(II)	0.30	0.90
$SrFe_{0.6}Mn_{0.4}O_{3-y}$	Fe^{3+}(I)	0.50	0.66
	Fe^{3+}(II)	0.30	0.96
$SrFe_{0.5}Mn_{0.5}O_{3-y}$	Fe^{3+}(I)	0.50	0.66
	Fe^{3+}(II)	0.30	1.02
$SrFe_{0.4}Mn_{0.6}O_{3-y}$	Fe^{3+}(I)	0.50	0.60
	Fe^{3+}(II)	0.30	1.02

*relative to ^{57}Co in Pd source.

The magnetic susceptibilities (χ) of selected compositions in the Sr-Fe-Mn-O system with x = 0.7, 0.6 and 0.45 were measured with a Foner-type magnetometer between 4.2 K and room temperature. There was no appreciable magnetic moment for these compositions down to 4.2 K. These samples were found to become antiferromagnetic with Neél temperatures of 130 K, and 30 K, respectively. The $1/\chi$ *vs* T curve of $SrFe_{0.6}Mn_{0.4}O_{3-y}$ is shown in figure 5. The linear portion of the $1/\chi$ *vs* T curve yielded an effective moment of about 4.23 μ_B. The asymptotic paramagnetic Curie temperature of this compound is -48 K. The magnetic properties of $SrFe_xMn_{1-x}O_{3-y}$ are shown in table 4.

2.3. ELECTRICAL PROPERTIES

Electrical resistivity was measured from liquid nitrogen temperature to about 500 K. Surfaces of the crystal were polished and contacted to the platinum electrodes using In amalgam for ohmic contact. Appreciable semiconductivity in the perovskite compounds, Sr-Fe-Mn-O and Ca-Fe-Mn-O, was observed. Room temperature resistivity of these compounds is about 10^2-10^3 ohm·cm regardless of composition. Semilog plots of resistivity against temperature are straight lines. Typical examples of temperature dependence of resistivity are shown in figure 6. The activation energies of these compounds 0.16 eV, are almost equal for all the samples. The resistivity of the hexagonal crystals, $SrMnO_{3-y}$ and $SrMn_{0.9}Fe_{0.1}O_{3-y}$, was rather high, approximately ~ 10^8 ohm·cm at room temperature.

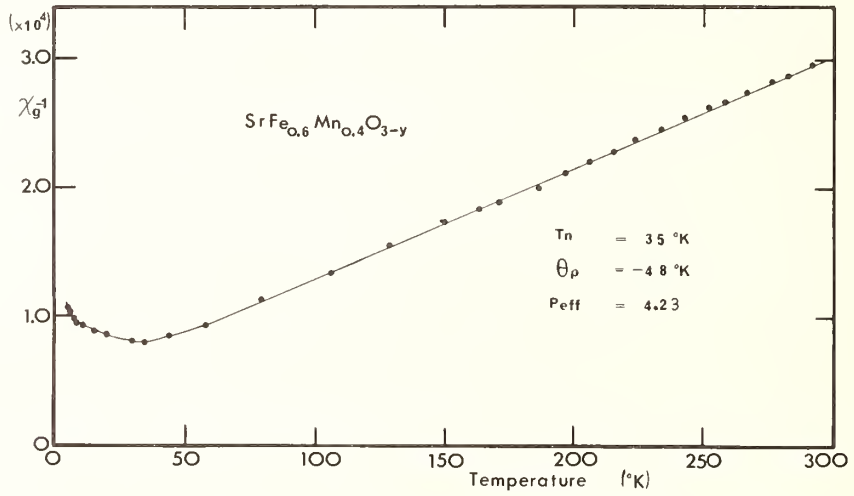

Fig. 5. The reciprocal magnetic susceptibility as a function of temperature for $SrFe_{0.6}Mn_{0.4}O_{3-y}$.

Table 4

Magnetic Properties of $SrFe_xMn_{1-x}O_{3-y}$

Sample	Neél temp. (K)	Effective magnetic moment (μ_B)	Paramagnetic Curie temp. (K)
$SrFe_{0.7}Mn_{0.3}O_{3-y}$	130	-	-
$SrFe_{0.6}Mn_{0.4}O_{3-y}$	35	4.23	-48
$SrFe_{0.45}Mn_{0.55}O_{3-y}$	20	4.43	-58

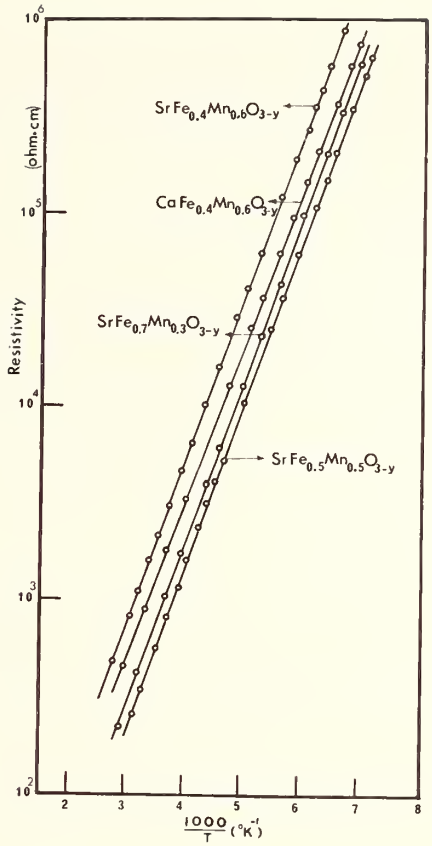

Fig. 6. Variation of log resistivity versus 1/T for $SrFe_{0.4}Mn_{0.6}O_{3-y}$, $SrFe_{0.5}Mn_{0.5}O_{3-y}$, $SrFe_{0.7}Mn_{0.3}O_{3-y}$ and $CaFe_{0.4}Mn_{0.6}O_{3-y}$.

3. DISCUSSION

The lattice constants of the perovskite phases, Sr-Fe-Mn-O and Ca-Fe-Mn-O, vary almost linearly with the change of Fe:Mn ratio, indicating the formation of simple solid solutions. Besides the diffraction patterns of the simple cubic perovskite structure, no superstructure lines due to the ordering of Fe and Mn ions or oxygen vacancies were detected by the conventional x-ray diffractometer. Owing to the similarity of the x-ray scattering factor of the Fe and Mn ions, we might not expect to observe the superstructure lines but it may be safely said that the difference of the ionic sizes and charge between Fe^{3+} and $Mn^{4+,3+}$ ions is too small to promote any long range ordering.

Gallagher, et al. [6] reported that the oxygen deficient perovskite phase, $SrFeO_{3-y}$, could exist stably in the range $0 \leq y \leq 0.25$ depending upon the temperature and oxygen pressure of the sample preparation condition. Recently Mizutani, et al. and Negas and Roth [12] both reported that they could obtain the perovskite $SrMnO_{3-y}$ by rapid quenching from 1500 °C. Their results indicate that $y \geq 0.26$ and the perovskite can be reoxidized at ~300 °C to $SrMnO_3$.

From the density and x-ray data, the perovskite crystals of $SrFe_xMn_{1-x}O_{3-y}$ and $CaFe_xMn_{1-x}O_{3-y}$ were shown to have a high concentration of oxygen vacancies ($0.25 \leq y \leq 0.44$) unlike the previous $SrFeO_{3-y}$. However, under present crystal growth conditions, the brownmillerite-type crystals such as $SrFeO_{2.5}$ and $SrMnO_{2.5}$ were not formed.

As for the hexagonal crystals, $SrMnO_{3-y}$ and $SrMn_{0.9}Fe_{0.1}O_{3-y}$, lower concentrations of oxygen vacancies were observed (y = 0.11). This indicates that, in the perovskite structure, oxygen vacancies can be tolerated over a larger range of composition than in the hexagonal structure although the major difference between the perovskite structure and hexagonal structure is in the mode of stacking of layers consisting of AO_3.

Mössbauer spectra of the material $SrFe_xMn_{1-x}O_{3-y}$ with $0.4 \leq x \leq 0.6$ showed only Fe^{3+} ions, with large quadrupole splittings. With better resolution of the spectra we could assign the two kinds of Fe^{3+} ions, Fe^{3+}(I) and Fe^{3+}(II) ions, in the following way.

There are two Fe^{3+}(II) ions which are associated with every oxygen vacancy in addition to Fe^{3+}(I) ions which are present in regular oxygen octahedra. The location of an oxygen vacancy adjacent to the Fe^{3+}(II) ions would be expected to introduce a larger quadrupole splitting than that of Fe^{3+}(I) ion. If we assume that vacancies are randomly distributed in the crystals, simple calculation gives the result that there would be 50% Fe^{3+}(II) ions for compositions such as $SrFe_xMn_{1-x}O_{2.75}$ and 100% Fe^{3+}(II) ions for $SrFe_xMn_{1-x}O_{2.5}$. Alternatively, one can estimate amounts of oxygen vacancies from the Mössbauer data in the perovskites, $SrFe_xMn_{1-x}O_{3-y}$. This gives a value for y of approximately 0.35 ± 0.05, which is close to the values obtained from density measurements.

There appear to be about 15% Fe^{4+} ions for the iron rich composition $SrFe_{0.7}Mn_{0.3}O_{3-y}$.

The effective Bohr magneton numbers calculated from the straight line part of $1/\chi$ - T curve were 4.43 μ_B for $SrFe_{0.45}Mn_{0.55}O_{3-y}$ and 4.23 μ_B for $SrFe_{0.6}Mn_{0.4}O_{3-y}$, respectively. Using the values of y obtained from the density measurements, the charge distributions for these crystals are estimated to be $SrFe^{3+}_{0.45}Mn^{3+}_{0.29}Mn^{4+}_{0.26}O_{2.63}$ and $SrFe^{3+}_{0.60}Mn^{4+}_{0.24}Mn^{4+}_{0.16}O_{2.58}$, respectively. The measured moments were smaller than the expected values (spin only) of 5.02 μ_B for $SrFe_{0.45}Mn_{0.55}O_{3-y}$ and 5.27 μ_B for $SrFe_{0.6}Mn_{0.4}O_{3-y}$. This may be due either to the incorrect estimates of the charge distribution in the crystals or inaccurate extrapolation of the linear part of $1/\chi$ - T curve, which was obtained in a relatively narrow range of temperature.

The Neél temperature is reported to be 138 K in $SrFeO_3$ [7]. The Neél temperature of $SrFeO_{2.86}$ has decreased to 80 K with the increased concentration of vacancies [7]. The Neél temperatures in the present perovskite system Sr-Fe-Mn-O (T_N = 130 K, 35 K, and 20 K for x = 0.7, 0.6 and 0.45, respectively) were found to be much lower than for stoichiometric orthoferrites.

The main exchange interactions in the Sr-Fe-Mn-O system would be Fe^{3+}-Mn^{4+}, Fe^{3+}-Mn^{3+} and Mn^{3+}-Mn^{4+}, although there are various combinations of exchange interactions such as Fe^{3+}-Fe^{3+} owing to the random distribution.

All the perovskite compounds exhibited semiconducting behavior with large temperature coefficients and activation energies of about 0.16 eV, which were almost independent of composition. It also appeared that the room temperature electrical resistivity of the perovskite compounds fell in the region of about 10^2-10^3 ohm·cm.

Investigation of the $La_{0.85}Ba_{0.15}Fe_xMn_{1-x}O_3$ [13], and $La_{1-x}Ca_xFe_{1-x}Mn_xO_3$ [14] system suggested the conduction mechanism for hopping might be:

$$Mn^{4+} + Mn^{3+} \rightleftarrows Mn^{3+} + Mn^{4+} \quad \text{and} \quad Fe^{3+} + Fe^{4+} \rightleftarrows Fe^{4+} + Fe^{3+}$$

The electrical conductivity in the present perovskite phase may be attributed to the mixed valence states (Mn^{3+} and Mn^{4+}); however, we cannot deny that there might be a large contribution from lattice defects. Further study is necessary to clarify these problems.

4. REFERENCES

[1] Erchak, M., Fankuchen, I., and Ward, R., J.Am.Chem.Soc. 68, 2085 (1946).
[2] Strauss, S.W., Fankuchen, I., and Ward, R., *ibid.* 73, 5084 (1951).
[3] Kestigian, M., Dickinson, J.G., and Ward, R., *ibid.* 79, 5598 (1957).
[4] Brixner, L., *ibid.*80, 3214 (1958).
[5] Watanabe, H., J.Phys.Soc., Japan, 12, 515 (1957).

[6] Gallagher, P.K., MacChesney, J.B., and Buchanan, D.N.E., J.Chem.Phys. 41, 2429 (1964).
[7] MacChesney, J.B., Sherwood, R.C., and Potter, J.F., *ibid.*43, 1907 (1965).
[8] Yakel, H.L., Acta Cryst. 8, 394 (1955).
[9] Jonker, G.H., and Van Santen, J.H., Physica 16, 337 (1950).
[10] Hardy, A., Acta Cryst. 15, 179 (1962).
[11] Stevens, J.G., and Stevens, V.E., *Mossbauer Effect Data Index,* Plenum Publishing Co., New York, 1970.
[12] Mizutani, N., Ohkuma, N., Kitazawa, A., and Kato, M., Kogyo Kagaku Zasshi 73, 1103 (1970).
Negas, T. and Roth, R.S., J. Solid State Chem. 1, 409 (1970).
[13] Jonker, G.H., Physica 20, 1118 (1954).
[14] Banks, E., and Tashima, N., J. Appl. Phys. 41, 1186 (1970).

465-504 O - 72 - 19

National Bureau of Standards Special Publication 364, Solid State Chemistry, Proceedings of 5th Materials Research Symposium, issued July 1972.

$La_xSr_{1-x}RuO_3$: A NEW PEROVSKITE SERIES*

R. J. Bouchard and J. F. Weiher

Central Research Department
E. I. du Pont de Nemours and Company
Experimental Station
Wilmington, Delaware 19898

The compound $LaRuO_3$ was prepared for the first time. It appears to be metallic and antiferromagnetic. Solid solutions with ferromagnetic $SrRuO_3$ of the type $La_xSr_{1-x}RuO_3$ exist for all values of x. All compounds have the orthorhombic $GdFeO_3$-type perovskite structure. The ferromagnetism observed for $SrRuO_3$ (x = 0) diminishes rapidly with increasing La content, and antiferromagnetism or parasitic ferromagnetism sets in at approximately 35% La. All compounds show Curie-Weiss behavior at fairly low temperatures. The properties of $LaRhO_3$ are also discussed.

Key words: Antiferromagnetism; Curie-Weiss paramagnetism; ferromagnetism; metallic conductivity; oxide; perovskite; solid solution.

1. INTRODUCTION

The number of compounds with the perovskite structure having the general formula ABO_3 is legion. Typical oxidation states are $A^{+3}B^{+3}O_3$ and $A^{+2}B^{+4}O_3$, and the crystal structure is usually cubic or orthorhombic (D_{2h}^{16}-Pbnm, Z = 4), as typified by $GdFeO_3$. Magnetic and electrical transport properties can vary from metallic and Pauli paramagnetic, *e.g.*, $LaNiO_3$ [1][1], through metallic and ferromagnetic, *e.g.*, $SrRuO_3$ [2], to insulating and antiferromagnetic, *e.g.*, $LaCrO_3$ [1]. $SrRuO_3$ is particularly interesting since it represents the only known example where ferromagnetism results solely from a 2nd row transition element. The metallic conductivity has been attributed [2,3] to a 2/3-filled, six-fold degenerate, π^*-type band formed by the interaction of the t_{2g} orbitals of Ru with suitable directed p orbitals of oxygen. We were interested in examining the effects on the magnetic and electrical properties of $SrRuO_3$ caused by substitution of the Sr^{+2} with a large trivalent cation like La^{+3}. This process would change the number of electrons in the π^* band, adding one electron/La^{+3} as the formal valence of Ru changed from +4 in $SrRuO_3$ to +3 in $LaRuO_3$, simultaneously progressing from a 2/3 (d^4)- to a 5/6 (d^5)-filled band. In addition, we consider $LaRuO_3$ itself to be unusual, representing the only known example of Ru in a formally trivalent state in an oxide lattice.

2. EXPERIMENTAL

The starting materials for the $LaRuO_3$ end member were La_2O_3, RuO_2, and Ru metal, accurately weighed according to the reaction:

$$2La_2O_3 + 3RuO_2 + Ru \rightarrow 4LaRuO_3$$

The La_2O_3 was high purity, heated to 1000 °C ~16 hours, kept in a vacuum dessicator, and weighed quickly because of the well-known tendency of this oxide to react with atmospheric water and carbon dioxide. Preparation of "reactive" La_2O_3 by decomposition of the oxalate

---

*Contribution No. 1803.

[1] Figures in brackets indicate the literature references at the end of this paper.

did not affect the reaction rate or the crystallinity of the product. The Ru metal was high-purity 325-mesh powder, which was also used to prepare the RuO_2 starting material by heating in O_2 at 1000 °C for ~12 hours, grinding for 1 hour in a mechanical mortar grinder, and refiring at 1000 °C in O_2 for another 12 hours. The resulting product had a single-phase rutile x-ray pattern and hydrogen reduction indicated RuO_2 stoichiometry within experimental error.

$SrRuO_3$ was prepared by firing $SrCO_3$ + Ru in O_2 at 1000 °C, after Randall [4]. The $SrRuO_3$ and the components of the $LaRuO_3$ (La_2O_3, RuO_2, and Ru) were mixed in the proper ratios to give $La_xSr_{1-x}RuO_3$ where x = 0.1, 0.25, 0.50, 0.75, and 1.

These starting materials were ground together for approximately 1 hour under dry nitrogen and quickly pressed into a pellet in a small hand press. The pellet was then preheated to red heat in a silica tube under vacuum to remove any trace water picked up during the pressing operation and sealed in a Pt tube under vacuum. The tube was heated at 1300-1350 °C for approximately 48 hours, then at 1100 °C for approximately 48 hours, and cooled in the furnace. When silica tubes were used for the firing, or the 1100 °C heating cycle was omitted, excess Ru was always present in the x-ray patterns.

A pellet of $LaRhO_3$ was also prepared. An equimolar mixture of La_2O_3 and Rh_2O_3 was ground for approximately 1 hour, pressed, sealed in Pt under vacuum, and fired at 1200 °C for 16 hours. While the resultant product was reasonably well sintered and suitable for gross electrical characterization, x-ray examination revealed a trace of unreacted La_2O_3. Another sample was prepared by reaction at 1300 °C and 3 kb external pressure for 12 hours, slow cooled at 50 °C/hr. to 900 °C, after which the furnace was shut off to cool. The product was now single-phase and noticeably more crystalline. This sample was used for obtaining x-ray data.

The products were examined with a Guinier-Hägg x-ray camera using an internal KCl standard (a_o = 6.2931 Å) and monochromatic CuKα radiation. The films were overexposed to emphasize the weak reflections. Cell dimensions were derived from a least squares refinement of the d-values. For the ferromagnetic samples, a vibrating-sample magnetometer was used for magnetic susceptibility data, while a Faraday balance was used for the antiferromagnetic and diamagnetic compounds. Electrical resistivity was measured for two of the samples, using bars cut from polycrystalline pellets. Standard 4-probe techniques were employed. Attempts to grow single crystals by flux reactions for accurate electrical data were unsuccessful.

3. RESULTS AND DISCUSSION

3.1. CRYSTALLOGRAPHIC

The products were single-phase, fairly well-crystallized orthorhombic perovskites. The space group Pbnm (same as $GdFeO_3$) was verified by the occurrence of the 021 reflection and the absence of the 201, which is not allowed. The refined lattice dimensions are listed in table 1. The parameters for $LaRuO_3$ are similar to those reported for $LaRhO_3$ [5] with a very slightly larger unit cell volume, reflecting the larger size of Ru^{+3} *vs* Rh^{+3} [6]. The refined lattice constants for $LaRhO_3$ are also included in table 1. They are in good agreement with reference [5]. The d-values and relative intensities for $LaRuO_3$ are listed in table 2. Volumes of the solid-solution unit cells *vs* increasing x in $La_xSr_{1-x}RuO_3$ will be the resultant of two opposing factors: (1) substitution of the smaller La^{+3} (1.18 Å) for Sr^{+2} (1.25 Å) and (2) substitution of the larger Ru^{+3} (0.68 Å) for Ru^{+4} (0.62 Å), using Shannon-Prewitt radii for the six-fold B-ion and eight-fold A-ion coordination in the orthorhombic perovskite [6]. The observed cell volumes increase with increasing x, indicating factor 2 to be dominant. The lattice constants *vs* x are plotted in figure 1. While the unit cell volume increases smoothly with x, the *a*, *b*, and *c*-axes do not. The *a*- and *c*-axes appear to go through a maximum and there is a crossover from $a > b$ to $a < b$ at x ~0.5. Most striking is the rapid increase in *b*, the rate of increase becoming much larger at higher x. The large decrease in the *b* axis from $LaRuO_3$ to $SrRuO_3$ suggests that a factor other than size considerations may be important. Also, the dimensions for $SrRuO_3$ are much closer than $LaRuO_3$ to being cubic ($a = b = c/\sqrt{2}$ for cubic symmetry). This behavior may be related to the occurrence of ferromagnetism at the Sr-rich end of the solid solution series as discussed in the magnetic section. Because the orthorhombic perovskite structure is

Table 1

Compound	a(Å)	b(Å)	c(Å)	V(Å^3)
$LaRuO_3$	5.4944(6)	5.7789(5)	7.8548(7)	249.40(3)
$La_{.75}Sr_{.25}RuO_3$	5.5648(7)	5.6278(7)	7.8800(12)	246.78(4)
$La_{.5}Sr_{.5}RuO_3$	5.5777(2)	5.5749(8)	7.8881(5)	245.28(3)
$La_{.4}Sr_{.6}RuO_3$	5.5798(7)	5.5652(9)	7.8780(8)	244.63(4)
$La_{.25}Sr_{.75}RuO_3$	5.5782(7)	5.5488(6)	7.8646(12)	243.44(4)
$La_{.1}Sr_{.9}RuO_3$	5.5745(7)	5.5397(7)	7.8554(12)	242.58(5)
$SrRuO_3$	5.5702(4)	5.5324(4)	7.8494(7)	241.89(2)
$LaRhO_3$	5.5226(3)	5.7024(4)	7.9857(6)	248.65(2)

Refined lattice dimensions for the $La_xSr_{1-x}RuO_3$ compounds and $LaRhO_3$. Numbers in parentheses are standard deviations in the last place.

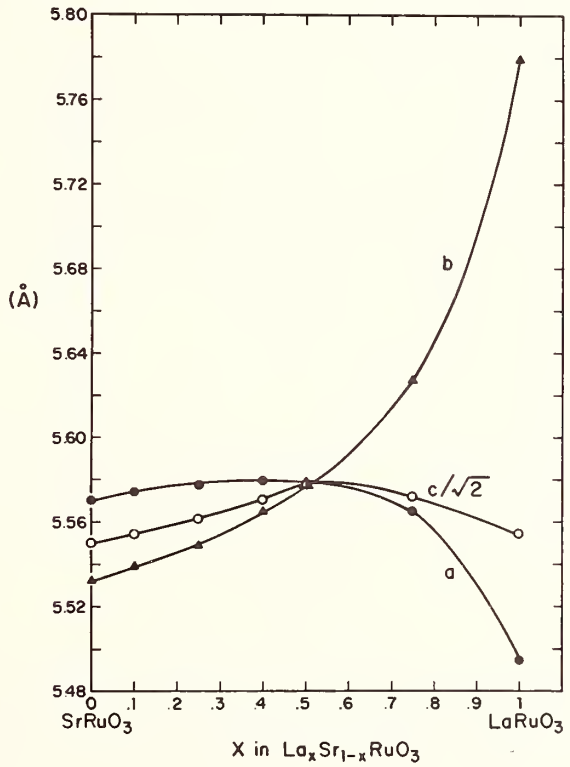

Fig. 1. The variation in lattice parameters *vs.* x in $La_xSr_{1-x}RuO_3$. $c/\sqrt{2}$ is plotted rather than c so as to better illustrate the distortion from cubic symmetry.

Table 2

I/I_o	h	k	ℓ	d_{obs}	d_{calc}
1	1	1	0	3.9812	3.9818
1	0	0	2	3.9256	3.9274
11	1	1	1	3.5498	3.5516
15	0	2	0	2.8882	2.8894
100	1	1	2	2.7970	2.7961
23	2	0	0	2.7477	2.7471
5	0	2	1	2.7114	2.7117
2	2	1	1	2.3654	2.3658
	1	0	3		
1	0	2	2	2.3273	2.3274
2	2	0	2	2.2521	2.2511
3	1	1	3	2.1879	2.1877
1	1	2	2	2.1423	2.1430
18	2	2	0	1.9910	1.9909
12	0	0	4	1.9639	1.9637
2	0	2	3	1.9401	1.9402
6	2	2	1	1.9300	1.9299
5	1	3	1	1.7711	1.7710
1	3	1	1	1.7042	1.7042
5	1	3	2	1.6498	1.6496
5	0	2	4	1.6241	1.6241
17	2	0	4	1.5968	1.5975
	3	1	2		
2	2	2	3	1.5854	1.5848
2	1	3	3	1.4932	1.4932
1	1	1	5	1.4620	1.4613
	2	3	2		
1	0	4	0	1.4447	1.4447
1	0	4	1	1.4208	1.4208
6	2	2	4	1.3981	1.3980
	1	4	0		
1	0	2	5	1.3795	1.3801
2	4	0	0	1.3733	1.3735
1	3	3	1	1.3087	1.3087
	0	0	6		

X-ray data for $LaRuO_3$. The intensities were estimated from relative peak heights on a diffractometer tracing. The observed d-values were taken from a Guinier-Hägg film, and the calculated d-values resulted from a least-squares treatment of the Guinier data.

somewhat complex, the relationship between the unit cell axes and individual MO_6 octahedra involved in superexchange interactions is obscured, especially for large departures from cubic symmetry. It is clear, however, that the RuO_6 octahedra in $SrRuO_3$ are more symmetrically arranged, suggesting that overlap of Ru and O orbitals is maximized.

Wold et al. [5], who first reported $LaRhO_3$, noted that $NdRhO_3$ could also be prepared, but not $SmRhO_3$ or $YRhO_3$. It was assumed that the smaller size of Sm^{+3} and Y^{+3} could not satisfy the tolerance factor requirements for the stability of the perovskite phase. That is, for a given B^{+3} ion size, there is a minimum size requirement for the A ion, below which no perovskite can form. Since Ru^{+3} is larger than Rh^{+3}, it should be even more difficult to prepare any $MRuO_3$ where M is a rare earth ion smaller than La. This is in accord with experimental observations. $GdRuO_3$, $NdRuO_3$, and $PrRuO_3$ could not be prepared under the same conditions used for $LaRuO_3$. Instead, the pyrochlores, $A_2Ru_2O_7$, were the major phases.

(However, single-phase $Nd_xSr_{1-x}RuO_3$ solid solutions could be prepared up to x ~0.3.) It therefore appears that compared to $MRhO_3$, the phase field defining the perovskite structure for $MRuO_3$ compounds is shifted further to the left in the lanthanide series so that only La^{+3}, the largest ion, is included. In this connection, it may also be significant that no $La_2Ru_2O_7$ pyrochlore exists.

The almost universal adoption of the tetravalent state for Ru in oxides would seem to indicate a special stability. Therefore, Ru^{+3} should oxidize in air to Ru^{+4} at some reasonably low temperature. Surprisingly, $LaRuO_3$ can be heated in air to 700 °C, suffering only a slight broadening of x-ray diffraction peaks after about 16 hours. At 900 °C, the x-ray pattern becomes almost amorphous indicating destruction of the perovskite lattice.

3.2. ELECTRICAL

The electrical data plotted in figure 2 show a fairly low resistivity of approximately 5×10^{-3} ohm-cm for both $LaRuO_3$ and $La_{.5}Sr_{.5}RuO_3$. The positive temperature dependence is characteristic of metallic materials, but the low resistivity ratio and relatively high resistivity suggest that these oxides are poor "metals". It is fair to assume that the resistivity of single crystals would be considerably lower. Although the electrical results are qualitative, they do point to the same type of metallic-like behavior found for other Ru oxides like $SrRuO_3$ and RuO_2 [2,7].

From qualitative band model considerations of the type discussed by Goodenough [8], $LaRuO_3$ should be metallic with a 5/6-filled π^*band formed from (Ru)t_{2g}-(O)$p\pi$ covalent interactions. A Seebeck coefficient of +42 μV/°C was measured on a sintered piece of $LaRuO_3$ (hot junction = 60 °C; cold junction = 27 °C). The small positive voltage is consistent with hole conductivity in a nearly full band. The relatively high values for the resistivity may indicate that the conduction band is very narrow, leading to high masses and low mobilities; more likely, they result from the difficulties associated with resistivity measurements on polycrystalline samples.

If a model with a conduction band composed mainly of t_{2g} (π) states is valid, the electrical properties of $LaRuO_3$ should be considerably different from $LaRhO_3$. For the latter, the 6-fold degenerate π^*-band should be completely filled (trivalent rhodium has a $4d^6$ configuration), leading to semiconducting properties, rather than metallic. Electrical

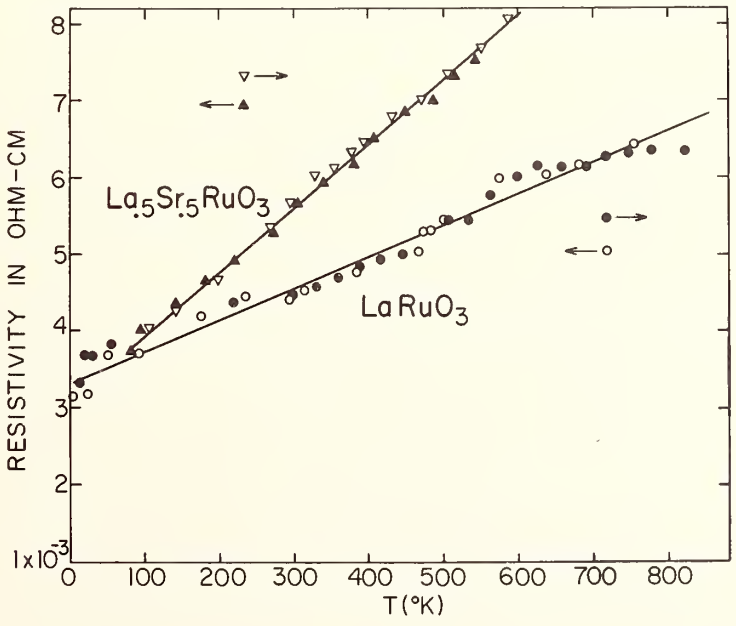

Fig. 2. The resistivity of $LaRuO_3$ and $La_{.5}Sr_{.5}RuO_3$ *vs.* temperature. Arrows indicate measurements taken on heating (→) or cooling (←).

conduction would then become an activated process, *via* transfer of electrons from $t2_g$ (π) to e_g (σ) levels, which would presumably also exist as band states, σ-bonding being stronger than π-bonding. A crude 2-probe resistivity of about 1 x 10^4 ohm-cm was measured on a pellet of $LaRhO_3$ at room temperature. This difference in resistivity of approximately seven orders of magnitude between $LaRuO_3$ and $LaRhO_3$ is consistent with a partially filled conduction band in the former and a filled band in the latter.

3.3 MAGNETIC

Magnetic susceptibility was measured as a function of temperature on five solid-solutions. The $1/\chi$ *vs* T plots are shown in figure 3. To assure that the upper temperature portions of the curves correspond to the paramagnetic (Curie-Weiss) region, one sample was taken to high temperatures (fig. 4). The calculated magnetic parameters are listed in table 3. No corrections were made for temperature-independent contributions to the susceptibility because of the difficulty in accurately estimating this term. In addition to the negative contribution from core diamagnetism, there should be a positive Pauli contribution from conduction electrons. These are small, about the same order of magnitude, and tend to cancel one another.

All the compounds appear to show Curie-Weiss behavior at the higher end of the temperature region scanned. The straight line to 700 K for one sample supports this conclusion. The values for the paramagnetic moment are in the range 2.4-2.8 B.M., with no particular dependence on composition. Part of this fluctuation may be experimental error, although error propagation analysis indicates that the standard deviation in μ should be no greater than ~2% or ~ $\pm$ 0.05 B.M. Another factor that is probably more important is the temperature range of the Curie-Weiss portion of the susceptibility data, which may be too small for the derivation of very accurate C and θ values. This is illustrated by the low and high-temperature measurements on $La_{.75}Sr_{.25}RuO_3$, as shown in figures 3 and 4, respectively. Data in both temperature ranges were taken on the same sample preparation. From the high-temperature run, μ = 2.56 B.M. and θ = -127 K (table 2). The corresponding low-temperature data are 2.70 B.M. and -118 K. Given such scatter, no particular significance can be attached to the variation of μ with composition.

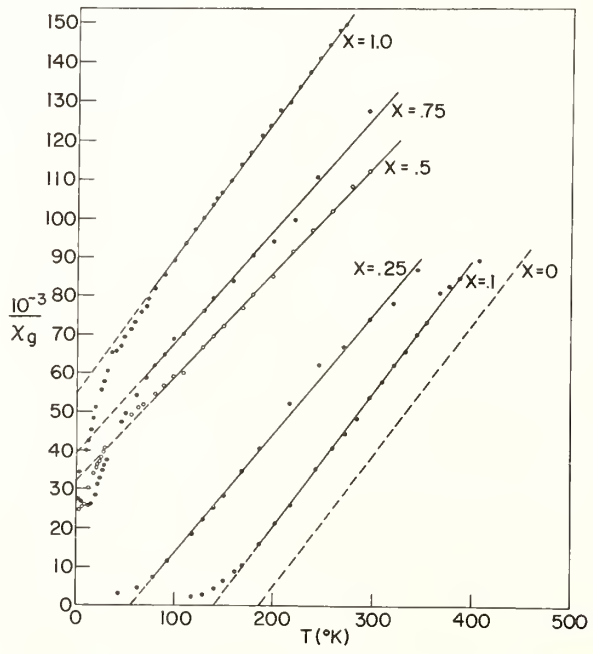

Fig. 3. Inverse susceptibility *vs.* temperature of various members of the $La_xSr_{1-x}RuO_3$ solid solution series. The data for x = 0 ($SrRuO_3$) were calculated from reference (b) and are included for comparison.

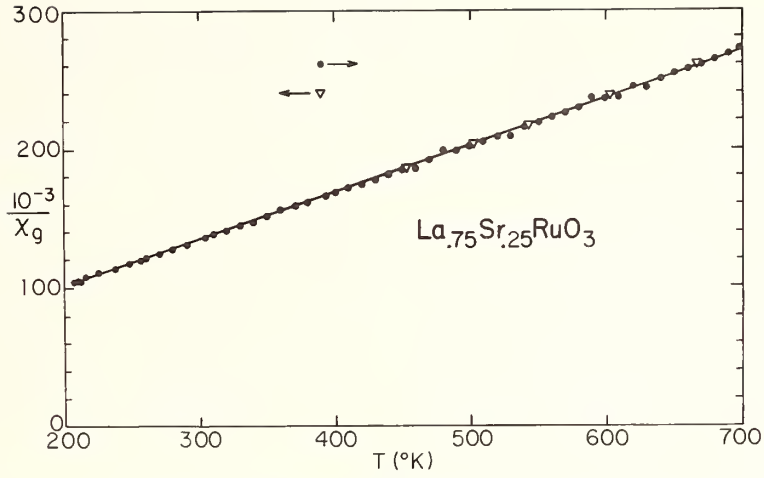

Fig. 4. Inverse susceptibility at high temperatures for $La_{.75}Sr_{.25}RuO_3$.

Table 3

Compound	C ($\frac{emu°K}{mole\ Oe}$)	μ_p (B.M.)	θ (°K)	μ_F (B.M.)	T_c (°K)	$\sigma_s(\vec{H} \to 0, T \to 0)$ emu/gm
$SrRuO_3$	--	2.65	+160	.85	160	
$La_{.1}Sr_{.9}RuO_3$	.709	2.39	+142	.75	133	17.4
$La_{.25}Sr_{.75}RuO_3$	.809	2.54	+59	.35	79	7.75
$La_{.5}Sr_{.5}RuO_3$	.946	2.75	-107	--	--	
$La_{.75}Sr_{.25}RuO_3$	.817	2.55	-127	--	--	
$LaRuO_3$	.841	2.59	-160	--	--	

Magnetic parameters for $La_xSr_{1-x}RuO_3$. The $SrRuO_3$ data were taken from reference (2) and are included for comparison. The paramagnetic moment $\mu_p = \left[\frac{3k}{N\beta} 2\chi(T-\theta)\right]^{1/2}$ from susceptibility data in the Curie-Weiss region.

The formulas for the solid solutions can be written as $La_xSr_{1-x}Ru_x^{+3}Ru_{1-x}^{+4}O_3$. It can be safely assumed that both Ru^{+4} and Ru^{+3} are in the low-spin state because of strong covalency effects (large e_g-t_{2g} splitting) characteristic of 4d-ion interactions. An ESR study [9] of Ru^{+3} in a corundum (Al_2O_3) matrix confirms this even for the trivalent ion, where covalency should be weaker. The spin-only moments corresponding to the low-spin states of Ru^{+3} (d^5) in $LaRuO_3$ and Ru^{+4} (d^4) in $SrRuO_3$ are 1.73 and 2.83 B.M., respectively. Although $SrRuO_3$ appears to exhibit a paramagnetic moment near the spin-only value, the $LaRuO_3$ moment is considerably higher than expected. However, d^5 systems can show greatly enhanced paramagnetic moments [10,11] because of spin-orbit contributions and various other factors. While it may be tempting to contemplate the effect of a distorted octahedral environment of the Ru ion, a structure determination [12] of $GdFeO_3$ has shown that the distortion effected by the orthorhombic symmetry is mainly borne by Gd^{+3}, the Fe^{+3}-O octahedra remaining almost purely octahedral.

The most obvious trend in the magnetic properties of $La_xSr_{1-x}RuO_3$ is the appearance of antiferromagnetism with increasing x. The ferromagnetism characteristic of $SrRuO_3$ disappears at approximately 35% La, where the Weiss constant θ becomes negative (fig. 5).

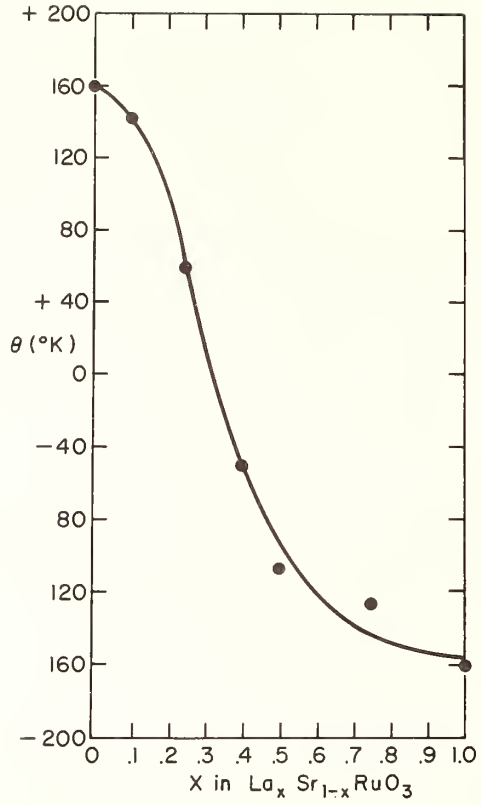

Fig. 5. Weiss constant θ *vs.* x for $La_xSr_{1-x}RuO_3$.

The shapes of the $1/\chi$ *vs* T curves for those samples which exhibit a negative θ are not completely typical of antiferromagnets. The lack of a pronounced minimum may mean weak parasitic ferromagnetism or trace ferromagnetic impurities. The only reasonable ferromagnetic impurity in the solid solution system would be $SrRuO_3$. Since the effect is present even for $LaRuO_3$, however, this seems unlikely to be the cause. Also, some of the curves are very similar to that of $CaRuO_3$ [3,13], which is thought to be an example of band antiferromagnetism with parasitic ferromagnetism below T_N. In addition, the fact that an orthorhombic distortion almost by definition prohibits exactly compensated antiferromagnetism suggests that parasitic ferromagnetism is a reasonable explanation for the magnetic behavior at low temperatures.

In an ABO_3 perovskite, both the A- and the B-ion compete in a covalent sense for the oxygen electrons. In $SrRuO_3$, Ru^{+4} is able to interact strongly because of its relatively high charge and small size. The two unpaired electrons in Ru $t2_g$ levels are not localized on the Ru^{+4}, and can take part in ferromagnetic band interactions at low temperatures. Although paramagentic behavior is found above T_C, the moment is below the spin-only value, consistent with some delocalization. When La^{+3} is substituted for Sr^{+2}, its smaller size and higher charge enable it to compete more strongly for oxygen electrons. At the same time, the Ru^{+3} resulting from the substitution is less strongly bonded than the Ru^{+4}, because of its larger size and smaller charge. These effects are additive, both leading to a decreasing Ru-O interaction, and presumably a narrower π^*-band. At $LaRuO_3$, the bandwidth has been sufficiently decreased so that antiferromagnetic behavior is observed which appears to be more characteristic of narrower bands [3]. The paramagnetic moment is considerably higher than the spin-only value; this may result from orbital contributions and has been observed, for example, in Ru complexes [14] where presumably the electrons are localized rather than collective. Evidence that the bandwidth has not decreased to zero is provided by the metallic-like electrical behavior.

Similar reasoning was used [3] to explain the contrast between $CaRuO_3$ (antiferromagnetic, unit cell volume V = 227Å^3) and $SrRuO_3$ (ferromagnetic, V = 242Å^3). In that example, the more acidic Ca^{+2} decreased the strength of the Ru^{+4}-O interactions in $CaRuO_3$ to such an extent that antiferromagnetism resulted, *for the same number of d electrons per Ru ion*. Clearly, the sign of the superexchange interaction between Ru ions is determined not so much by the *number* of d electrons in the π^* band as by other considerations such as Ru-O covalency and bandwidth of the π^* states.

Finally, the magnetic properties of $LaRhO_3$ should reflect the filled t_{2g} band previously discussed. This is essentially confirmed, with minor complications. A value of $\chi_g = 1.2 \times 10^{-7}$ emu/gm was found at 300 K. However, there was a small but definite temperature dependence and slight field dependence. The temperature dependence indicates a small amount of paramagnetic impurity ($C_m = 0.0082$, $\mu^2_{eff} = 0.066$; corresponds to 0.2 mole % of an S = 5/2 ion). The field dependence corresponds to a trace ferromagnetic component with a magnetization of $\sigma_g = 5.5 \times 10^{-4}$ emu.

4. ACKNOWLEDGMENTS

Mrs. C. G. Frederick is thanked for the magnetic measurements on the ferromagnetic compounds, as is Mr. J. L. Gillson for the electrical resistivity data. The comments and suggestions of Dr. D. B. Rogers are gratefully acknowledged, as are several helpful discussions with Dr. A. W. Sleight concerning the crystallographic details of the perovskite structure.

5. REFERENCES

[1] Goodenough, J. B., J. Appl. Phys. 37, 1414 (1966).
[2] Callaghan, A., Moeller, C. W., and Ward, R., Inorg. Chem. 5, 1572 (1966).
[3] Longo, J. M., Raccah, P. M., and Goodenough, J. B., J. Appl. Phys. 39, 1327 (1968).
[4] Randall, J. J., and Ward, R., J.A.C.S. 81, 2629 (1959).
[5] Wold, A., Arnott, R. J., and Croft, W. J., Inorg. Chem. 2, 972 (1963).
[6] Shannon, R. D. and Prewitt, C. T., Acta Cryst. B25, 925 (1969).
[7] Fletcher, J. M., Gardner, W. E., Greenfield, B. F., Holdoway, J. M., and Rand, M. H., J. Chem. Soc. 1968A, 653.
[8] Goodenough, J. B., Bull. Soc. Chim. France 1965, 1200.
[9] Geschwind, S. and Remeika, J. P., J. Appl. Phys. 33(s), 370 (1962).
[10] Kotani, M., Prog. Theor. Phys. (Kyoto) 14, 1 (1960).
[11] Figgis, B. N., Lewis, J., Hyholm, R. S., and Peacock, R. D., Disc. Faraday Soc. 26, 103 (1958).
[12] Coppens, P. and Eibschutz, M., Acta Cryst. 19, 524 (1965).
[13] Goodenough, J. B., Longo, J. M., and Kalafas, J. A., Matl. Res. Bull. 3, 471 (1968).
[14] Figgis, B. N., Lewis, J., Mabbs, F. E., and Webb, G. A., J. Chem. Soc. 1966A, 422.

DISCUSSION

E. Banks: Did you try to make any Seebeck coefficient measurements?

R. J. Bouchard: Yes, the Seebeck coefficient of lanthium ruthenate is plus 40, which is in the metal range-and it is also the right sign for nearly filled band, incidently.

P. Hagenmuller: It would be interesting, of course, to be able to prepare the other rare earth compounds. Did you try to increase the Goldschmidt factor by working with high pressure?

R. J. Bouchard: I think we did make a 65 kilobar run when we tried to prepare neodymium ruthenate, $NdRuO_3$. Again we got the pyrochlore phase. It is very, very stable for these compounds.

P. Hagenmuller: The pyrochlore phase, of course, is in competition with the formation of a perovskite.

J. M. Longo: You pointed out that you didn't expect to get the perovskites with the rare earths because of the analogy to the rhodium compound. From what we reported this morning on bismuth rhodate, would you expect bismuth ruthenate to be perovskite at pressure where the others did not form.

R. J. Bouchard: Well, we only tried it with bismuth up to 65 kilobars, and again we got exactly the same thing we got under autogenous conditions.

National Bureau of Standards Special Publication 364, Solid State Chemistry, Proceedings of 5th Materials Research Symposium, issued July 1972.

HIGH PRESSURE SYNTHESIS AND CRYSTAL STRUCTURE OF COBALT SESQUIOXIDE AND ITS LOW-SPIN → HIGH-SPIN TRANSITION

M. Marezio and P. D. Dernier

Bell Telephone Laboratories, Incorporated
Murray Hill, New Jersey 07974

J. Chenavas and J.-C. Joubert

Laboratoire d'Electrostatique et de Physique du Metal
CNRS, Grenoble, France

This note reports the high pressure synthesis of Co_2O_3 with the corundum structure. Two different syntheses were performed. In the first the starting material was $Co^{2+}Cr^{6+}O_4$. By applying a pressure of $\geq$ 90 kbar and 1000 °C in the presence of a small amount of water, $CoCrO_4$ was found to decompose into Co_2O_3 with the corundum structure and a solid solution of CoOOH and CrO_2 with the orthorhombic distortion of the rutile structure. The decomposition occurs according to the formula:

$$\text{(I)} \quad 3\ CoCrO_4 + \frac{1}{2}\ H_2O \rightarrow 4\ (CrO_2)_{.75}(CoOOH)_{.25} + Co_2O_3 + \frac{3}{4}\ O_2$$

The second synthesis was based on the following reaction at 80 Kb and 850 °C:

$$\text{(II)} \quad 2\ CoF_3 + 3\ Na_2O_2 \rightarrow 6\ NaF + Co_2O_3 + \frac{3}{2}\ O_2$$

Unfortunately some reduction occurred under pressure and the quenched material contained some Co_3O_4.

The x-ray powder pattern of Co_2O_3 was indexed on a hexagonal cell, a = 4.782 Å, c = 12.96 Å, c/a = 2.710, V = 258.5 Å . It resembles closely that of α - Al_2O_3 as far as the sequence of the d-spacings is concerned, but the intensities of the reflections are similar to those of V_2O_3. This indicates that the Co^{3+} ions must be in the low spin state. On the other hand the arrangement of the structure of Co_2O_3 should be different from that of Al_2O_3 as the relative intensitites indicate.

By annealing Co_2O_3 at 400 °C for a half hour in air, this oxide transforms to a corundum structure with a different volume and c/a ratio. The new values are a = 4.882 Å, c = 13.38 Å, c/a = 2.742, V = 276.2 Å^3. Since the unit cell volume and the d-spacings of this Co_2O_3 are nearly the same as those of α-Fe_2O_3, the Co^{3+} ions must be in the high spin state. The transformation Co_2O_3 (low spin) → Co_2O_3 (high spin) is accompanied by an increase in volume $\Delta V/V$(l.s.) = 6.7%. These results seem to indicate that Co_2O_3 (high spin) is the cobalt sesquioxide stable at atmospheric pressure whereas Co_2O_3 (low spin) is the high pressure phase.

Preliminary refinements of the two structures based on powder intensities gave average Co-O distances of 1.90 Å and 1.99 Å for Co_2O_3 (low spin) and (high spin) respectively. These values are in fairly good agreement with those calculated from Shannon and Prewitt ionic radii, 1.92 Å and 2.01 Å respectively. The Co-Co distances across the shared face between two octahedra are quite short in both compounds. Relative to the ionic radii it is smaller in Co_2O_3 (high spin). Also the Co-Co distance across the shared edge is anomalously short in Co_2O_3 (high spin).

According to the general trends in the transition metal sesquioxides, Co_2O_3 (high spin) should be a magnetic insulator, whereas Co_2O_3 (low spin) a nonmagnetic insulator. In octahedral coordination the Co^{3+} ions in the low spin state have the configuration $t_{2g}^6 e_g$ which corresponds to a zero magnetic moment. The filled t_{2g}^6 band would be compatible with the predicted insulator character of Co_2O_3 (low spin).

DISCUSSION

P. Hagenmuller: A comment, we found always at any pressure a low spin state for nickel 3^+ which is consistent with your results. The question, at what temperature do you begin to observe a loss of oxygen from the cobalt sesquioxide. That's the major difficulty with your interpretation of the data.

M. Marezio: We have tried to prepare nickel sesquioxide with the same methods; it does not work. The reason why it doesn't work, we believe, is because it is difficult to make the nickel ions in the low spin state even at these pressures. If one takes the compound $Ni^{+2}Cr^{+6}O_4$ in the presence of water at 90 kilobars and 1000 degrees one obtains an x-ray pattern of a corundum structure, which we believe is $NiCrO_3$. The lines are very sharp, including the back reflection region, which indicates a single phase of $NiCrO_3$. One could claim that we have made Ni_2O_3 but we don't believe it.

P. Hagenmuller: We don't speak about the same compound. I spoke about the ternary compounds of the rare earths. One has to work with high oxygen pressure.

M. Marezio: We do lose oxygen, in fact, in some preparations we obtained Co_3O_4. We lost oxygen even in an oxidizing environment. In one preparation we used sodium peroxide, which is a very strong oxidizing compound, and we still lost oxygen at 850 °C.

P. Hagenmuller: But there's a problem. In this case you have cobalt 2^+ and there is a question concerning the interpretation of the magnetic moments, but maybe we speak later about it.

B. Chamberland: That particular compound, the $NiCrO_3$, was prepared using nickel oxide and chromium dioxide at high pressure and nickel is definitely 3^+ with a high spin.

M. Marezio: Thank you.

National Bureau of Standards Special Publication 364, Solid State Chemistry, Proceedings of 5th Materials Research Symposium, issued July 1972.

INFLUENCE OF MADELUNG ENERGY AND COVALENCY ON THE STRUCTURE OF $A^+B^{5+}O_3$ COMPOUNDS*

J. A. Kafalas

Massachusetts Institute of Technology
Lincoln Laboratory
Lexington, Massachusetts 02173

The large Goldschmidt tolerance factor t = 1.06 in $BaTiO_3$ appears to be related to its ferroelectric properties and also suggests that relatively large effective charge at a Ti^{4+} ion inhibits formation of the hexagonal-perovskite polytypes generally associated with t > 1.0. In order to test these ideas, $RbNbO_3$ and $RbTaO_3$ (t = 1.08) were prepared under very high pressures. $RbNbO_3$ is an orthorhombic perovskite isostructural with ferroelectric $BaTiO_3$, and it decomposes on heating without formation of an hexagonal-perovskite polytype. Only at 90 kbar and 900 °C did $RbTaO_3$ form a cubic, or nearly cubic, perovskite. Unlike the transition-metal ions, Sb^{5+} and Bi^{5+} have never been stabilized in a cubic perovskite structure. $AgSbO_3$ forms a defect pyrochlore, $NaSbO_3$ and $KSbO_3$ have ilmenite structures, although a cubic (Pn3) form of $KSbO_3$ is stabilized by prolonged annealing above 1000 °C. A body-centered-cubic, disordered form of the cubic $KSbO_3$ having space group I23 was prepared in five minutes at 20 kbar and 800 °C. Preparation of $RbSbO_3$ at 20 kbar and 1000 °C yielded a phase with the same structure. These results are interpreted to mean that strong covalent bonding inhibits the formation of 180° Sb^{5+}-O^{2-}-Sb^{5+} linkages.

Key words: $A^+B^{5+}O_3$ compounds; ferroelectricity; perovskites; phase stability.

1. STRUCTURES OF ABX_3 PEROVSKITE POLYTYPES

Many oxides, fluoride, chlorides and sulfides of chemical formula ABX_3 crystallize in one of the hexagonal-perovskite polytypes [1][1]. These structures consist of ordered, close-packed AX_3 layers stacked in cubic or hexagonal or mixed cubic and hexagonal stacking sequences. The smaller B cations occupy all the interlayer X-anion octahedra, and stabilization of these structures requires not only that the larger A cation have a radius $r_A > 0.9$Å, but also that the B cation be stable in an octahedral interstice.

If the stacking of AX_3 layers is entirely cubic (fig. 1a), the B-cation octahedra share only corners to form the 3C structure of cubic perovskites. In this structure the A cations are confined to a cubic cage of edge B-X-B, where the B-X bond length is a characteristic of the B and X ions that requires considerable energy to increase. This cage creates an upper limit on the A-cation size that can be accommodated in a given BX_3 cubic array. This geometrical reasoning led Goldschmidt [2] to define a tolerance factor

$$t = (r_A + r_X)/\sqrt{2}(r_B + r_X) \quad (1)$$

such that the ideal cubic structure should occur at t = 1.0. For t < 1.0 the BX_3 array may be distorted from cubic to orthorhombic or rhombohedral symmetry so as to optimize the A-X bonding. If this distortion is too large, other structures become competitive, which places a lower limit on t. Therefore the cubic perovskite phase is stable in the interval

$$t_\ell < t < t_u \quad (2)$$

*This work was sponsored by the Department of the Air Force
[1]Figures in brackets indicate the literature references at the end of this paper.

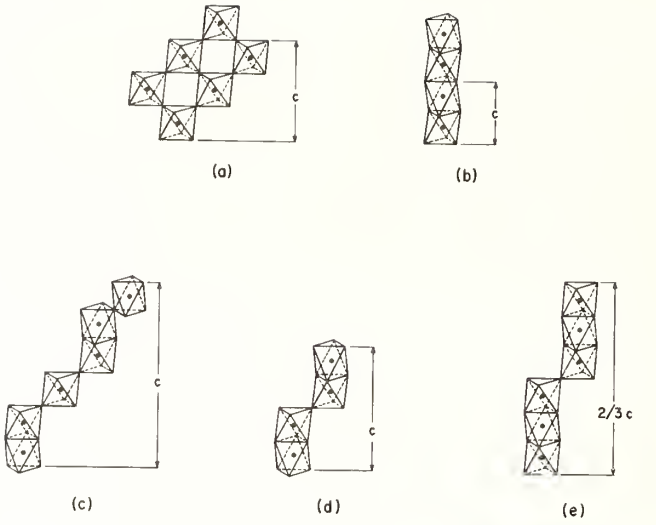

Fig. 1. BX_6-octahedra-network in ABX_3 perovskite polytypes.

where the upper limit is expected to fall close to $t_u = 1.0$.

If the stacking of AX_3 layers is entirely hexagonal (fig. 1b), the B-cation octahedra form face-shared linear chains parallel to the *c* axis of the hexagonal (2H) cell. Since these chains are isolated from one another, relatively large A cations can be accommodated by adjustment of the c/a ratio. Therefore this hexagonal perovskite structure is competitive for larger t>1. However, accommodation of the larger A cation is at the expense of considerable Madelung energy, a large electrostatic repulsive force occurring between B cations in face-shared octahedra.

In a narrow, intermediate range of tolerance factors three intermediate stacking sequences have been identified in stoichiometric ABX_3 compounds: two-to-one cubic to hexagonal stacking (cchcch of the 6H structure, fig. 1c), a one-to-one stacking (chch of the 4H structure, fig. 1d), and a one-to-two stacking (chhchhchh of the 9R structure, fig. 1c). In these intermediate structures the loss of electrostatic Madelung energy is minimized by displacing oppositely-along the *c* axis the B cations in face-shared octahedra. However, changing the stacking sequence within a structure introduces an energy loss that limits the stability range of these phases, and in the halides the 4H structure is entirely suppressed. In a comprehensive survey of ABF_3 polytypes, Babel [3] summarizes the stability of the various fluoroperovskites as follows:

Orthorhombic ($GdFeO_3$-type	t = 0.78-0.88
Cubic (3C)	t = 0.88-1.0
Hexagonal (6H, $BaTiO_3$-type)	t = 1.0-1.06
Hex-Rhombo (9R, $CsCoF_3$-type)	t = 1.07
Hex (2H, $CsNiF_3$-type)	t = 1.08

In the oxides the upper tolerance-factor limit t_u and the range of tolerance factors for the intermediate polytypes are not well defined: they depend more strongly upon the covalency and effective charges of the B cations. The purpose of this study was to investigate further these effects in $A^+B^{5+}O_3$ oxides, for which no hexagonal polytypes have been reported.

Hydrostatic pressure stabilizes a higher cation coordination, which reduces the lower tolerance-factor limit t_ℓ. It also favors a more regular cation coordination, which stabizes cubic *vs* hexagonal stacking [4] and raises t_u. This latter trend is illustrated in figure 2 [5], which shows the effect of B-cation size and pressure on the stability of $CsBF_3$ polymorphs, and in figure 3 [6], which shows the effect of A-cation size and pressure in the system $Br_{1-x}Sr_xRuO_3$. Since high pressure extends the tolerance-factor rante $t_\ell < t < t_u$ at both ends, it always favors formation of the perovskite structure. Therefore high pressures were used in this study for the preparation of several $A^+B^{5+}O_3$ compounds.

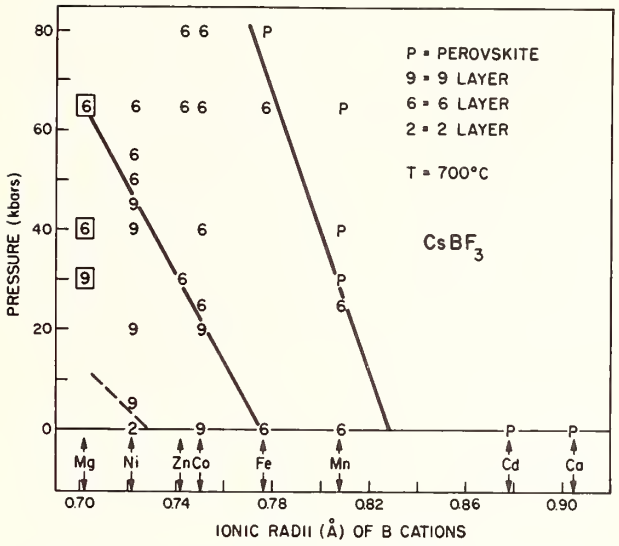

Fig. 2. Effect of pressure and B-cation size on structure of $CsBF_3$ compounds.

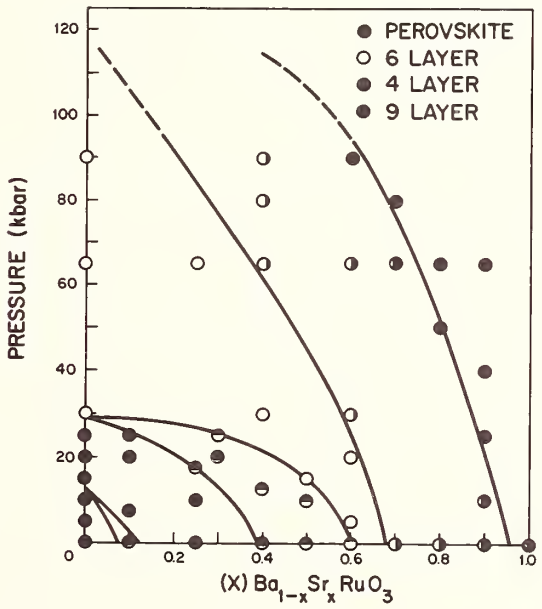

Fig. 3. Pressure-composition phase diagram in the system $Ba_{1-x}Sr_xRuO_3$.

2. TENTATIVE CONCLUSIONS FROM KNOWN $A^+B^{5+}O_3$ STRUCTURES

A striking feature of the known $A^+B^{5+}O_3$ structures is a lack of face-shared octahedra containing B^{5+} ions. Thus no hexagonal $A^+B^{5+}O_3$ perovskites have been reported. Furthermore, compounds containing Sb^{5+} or Bi^{5+} B cations tend to form different structures than those containing Nb^{5+} or Ta^{5+} B cations. These observations suggest two conclusions: (1) The electrostatic repulsion between B cations of large effective charge reduces the stability of the hexagonal-perovskite polytypes, so that these phases are no longer competitive if the B cation has a formal valence B^{5+}. (2) B cations, such as Sb^{5+} or Bi^{5+} ions, that form strong covalent bonds with their oxygen ligands will not be stabilized in structures

465-504 O - 72 - 20

having 180° Sb^{5+}-O^{2-}-Sb^{5+} linkages. Structures that permit the anion to use different p orbitals in covalent-bond formation with two neighboring Sb^{5+} ions will be competitive, so 90° Sb^{5+}-O^{2-5}-Sb^{+} or 120-140° Sb^{5+}-O^{2-}-Sb^{5+} linkages are expected in the stable $A^{+}Sb^{5+}O_3$ structures (Electrostatic forces would tend to open from 120° the tetrahedral angle appropriate to sp^3 hybridization).

The first of these conclusions provides a significant perspective for interpretation of the ferroelectric compound $Ba^{2+}Ti^{4+}O_3$, which crystallizes in the cubic (3C) perovskite structure at high temperatures even tho t = 1.06 is considerably larger than the geometric limit $t_u^g = 1.0$. Of all the $A^{2+}B^{4+}O_3$ compounds, the B^{4+} cations of largest effective charge would be those furthest to the left in the Periodic Table (Ti^{4+}, Zr^{4+}, Hf^{4+}). The fact that cubic $BaTiO_3$ can be stabilized even though t = 1.06 indicates that the effective charges on the Ti^{4+} ions are too large for the hexagonal structures to be competitive, although the 6H polytype is formed in reduced $BaTiO_{3-\delta}$. Since a $t_u > 1.0$ implies stretching of the B-X bond length, the elastic forces that would inhibit ferroelectric-type displacements of the cation toward one or more near-neighbor anions is sharply reduced. Therefore $BaTiO_3$, unlike $CaTiO_3$ or even $SrTiO_3$, exhibits ferroelectricity with a high Curie temperature. $BaZrO_3$ (t = 1.007) and $BaHfO_3$ (t = 1.005) are cubic and have no ferroelectric-type distortions.

Where the A cation is small enough to be accommodated in sixfold-coordination, an ilmenite structure might be anticipated. However, in this structure a B^{5+} cation and an A^{+} cation share a common octahedral face, and the electrostatic repulsion between the ions may be strong enough to stabilize alternate structures. In $LiNbO_3$, for example, the small Li^{+} ion is displaced to the far octahedral-site face midway between the Nb^{5+}-occupied interstices; and in $LiSbO_3$ the Li^{+} ions fill one-third of the *c*-axis octahedral-site chains so that the Sb^{5+} ions may occupy every other octahedral site in the remaining two-thirds of the *c*-axis chains. Ordering of the *c*-axis chains makes ~130° Sb^{5+}-O^{2-}-Sb^{5+} linkages in the $LiSbO_3$ structure.

The compounds $NaNbO_3$ and $NaTaO_3$ (t = 0.94) crystallize in cubic perovskite structures that are distorted to orthorhombic symmetry as a result of Na^{+}-ions displacements [7,8]. However, $NaSbO_3$ crystallizes in the ilmenite structure even though t = 0.96. Clearly the formation of 180° Sb^{5+}-O^{2-}-Sb^{5+} linkages requires the loss of more energy than the formation of face-shared Na^{+} and Sb^{5+} ions. $KNbO_3$, which has a t = 1.04, is ferroelectric like $BaTiO_3$ below 435 °C, whereas $KTaO_3$ (t = 1.04) is cubic at room temperature [9], although an orthorhombic $BaTiO_3$ form has been reported [10]. Again a $t > t_u^g = 1.0$ is associated with a large effective charge on the B cation, which inhibits formation of the hexagonal polytypes, and with ferroelectric-type displacements of the B cations. Surprisingly, $KSbO_3$ has the ilmenite structure (a = 6.8144 Å, α = 46°20') [11] even though t = 1.05 and the large K^{+} ion is stable in twelve-fold coordination. Generally this structure is stable only for $t < t_\ell$. Therefore the 180° Sb^{5+}-O^{2-}-Sb^{5+} linkages of the cubic perovskite phase must be relatively unstable. Spiegelberg [11] further reports that $KSbO_3$ transforms to a cubic (a = 9.56 Å) form if heated at 1000 °C for several weeks. The cubic structure (space group Pn3) consists of Sb_2O_{10} groups of edge-shared octahedra sharing common corners, as illustrated in figure 4. The Sb^{5+}-O^{2-}-Sb^{5+} linkages make 90° and about 130° angles. Clustered about the origin, located at the center of the front face of figure 4, are four K^{+} ions forming a tetrahedron, each at $0.15\sqrt{3}a$ from the origin, and four on the other body diagonals a distance $0.25\sqrt{3}a$ from the origin. This arrangement results in pairs of K^{+} ions between the origin and half the body-center positions, in single K^{+} ions midway between the origin and the remaining four body-center positions. The cubic cell is about 3% more dense than the ilmenite form, and I found that treatment of the $KSbO_3$ ilmenite for five minutes at 800 °C and 20 kbar is adequate to transform the ilmenite phase to a body-centered, disordered (The twofold and single K^{+} positions on the eight $\langle 111 \rangle$ directions are randomized.) form of the cubic structure. The body-centered space group is I23. In this structure clusters of K^{+} ions form unscreened near neighbors, but the associated loss in Madelung energy is apparently smaller than that associated with face-shared Sb^{5+} ions in the hexagonal perovskite structure or with the formation of 180° Sb^{5+}-O^{2-}-Sb^{5+} linkages. Similarly $NaBiO_3$ has the ilmenite structure; $KBiO_3$ and $RbBiO_3$ have the body-centered cubic structure [12].

The silver compounds $AgNbO_3$ and $AgTaO_3$ (t = 0.94) form cubic perovskites above 550 °C and 485 °C, respectively, and are distorted to monoclinic symmetry at lower temperatures as a result of Ag^{+}-ion displacements. $AgSbO_3$ (t = 0.95), on the other hand, forms a defect-pyrochlore structure in which are clusters of four unscreened Ag^{+} ions. The Sb^{5+}-O^{2-}-Sb^{5+}

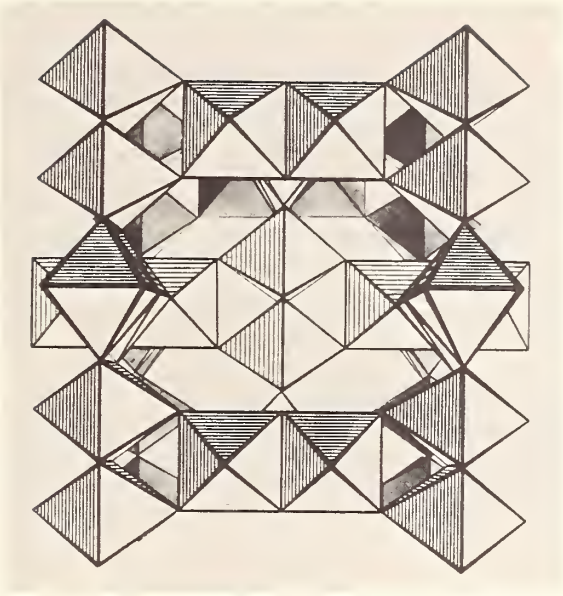

Fig. 4. SbO_6 octahedra network in $KSbO_3$.

linkages form angles of *ca* 135°. Again the loss in Madelung energy associated with the Ag^{+}-ion clusters is apparently less than the loss in covalent-bond energy to be associated with 180° Sb^{5+}-O^{2-}-Sb^{5+} linkages.

3. NEW SYNTHESES

In order to test further these tentative conclusions, the following new compounds have been synthesized under pressure: $RbNbO_3$, $RbTaO_3$, and $RbSbO_3$.

$RbNbO_3$ and $RbTaO_3$ have a large tolerance factor (t = 1.08), but it did not seem to be too large for the cubic perovskite structure to be accessible under very high pressure. Synthesis of $RbNbO_3$ was achieved at 65 kbar and 900 °C, and the atmospheric phase at room temperature was an orthorhombic perovskite (a = 3.9965 Å, b = 5.8360 Å, c = 5.8698 Å) isostructural with the orthorhombic form of ferroelectric $BaTiO_3$. Once again ferroelecrric distortions are associated with a $t > t_{11}^{g} = 1.0$. Preliminary DTA measurements indicate that rhombohedral and tetragonal ferroelectric phases also exist. However, heating above 500 °C leads to disproportionation without the formation of any hexagonal-perovskite polytype. This is to be contrasted with the $A^{2+}B^{4+}O_3$ compounds in which a metastable, cubic-perovskite (3C) phase is stabilized by high-pressure snythesis. Heating of these latter compounds to above 1000 °C induces transformations to the hexagonal-perovskite polytypes stable at atmospheric pressure. Synthesis of $RbTaO_3$ required 90 kbar and 900 °C, which is at the limit of my apparatus, and it was not possible to obtain the high-pressure form as a pure single phase. The structure at atmospheric pressure was cubic or nearly cubic (a = 4.035 Å).

The compound $RbSbO_3$ was synthesized at 20 kbar and 1000 °C. It forms the Pn3 structure of ordered $KSbO_3$ with a = 9.6985 Å.

These additional syntheses lend considerable support to the tentative conclusions that motivated this research.

4. ACKNOWLEDGEMENTS

I would like to express my appreciation to Dr. J. B. Goodenough, who shared in the strategy and interpretation of these experiments. I am also indebted to Drs. J. M. Longo and J. W. Pierce for many stimulating discussions and to D. A. Batson and D. M. Tracy for their technical assistance.

5. REFERENCES

[1] Goodenough, J. B. and Longo, J. M., "Landolt-Bornstein", Vol. III/4a, Springer-Verlag, Berlin (1970). Note: Material not specifically referenced in the text of this paper may be found in this general reference.
[2] Goldschmidt, V. M., Akad. Oslo I. Mat-Natur 2, 7-117 (1926).
[3] Babel, D., Structure and Bonding 3, 1 (1967).
[4] Goodenough, J. B., Kafalas, J. A., and Longo, J. M., "High-pressure Synthesis", in *Preparative Methods in Solid State Chemistry*, P. Hagenmuller, Ed., Academic Press (to be published).
[5] Longo, J. M. and Kafalas, J. A., J. Solid State Chem. 1, 103 (1969).
[6] Longo, J. M. and Kafalas, J. A., Mater. Res. Bull. 3, 687 (1968).
[7] Wood, E. A., Miller, R. C., and Remeika, J. P., Acta Cryst. 15, 1273 (1962).
[8] Kay, H. F. and Miles, J. L., Acta Cryst. 10, 213 (1957).
[9] Vousden, P., Acta Cryst. 4, 68 (1951).
[10] Wyckoff, W. G., Crystal Structures, Vol. 2, 405 (John Wiley & Sons, Inc., 1964).
[11] Spiegelberg, P., Arkiv for Kemi, Min. Och Geol 14A, 5, 1 (1940).
[12] Zemann, J., Mineral. Petrog. Mitt. 1, 361 (1950).

DISCUSSION

E. Banks: Ferroelectric phases in the perovskite structure can't be quite as simple as your comments indicate. Right there on the board you had a very good example when comparing potassium and rubidium niobates and tantalates. The temperature scale for any ferroelectric transition in the tantalates is of the order of 10^3 smaller than in the niobates. Here you have nominally equal radii and essentially the same lattice paramters if you convert them to equivalent volumes and you still don't have ferroelectric phases in tantalates and you do in the niobates.

J. A. Kafalas: True, but tantalum has less of a tendency to accept four-fold coordination than niobium does and the ferroelectric distortion is just a tendency toward four-fold rather than six-fold coordination. However, I agree with you, though, to a certain extent. I had mentioned that I did some DTA measurements on the rubidium niobate and that we did obtain the orthorhombic form. We find that there is a first order transition at something like -15 centigrade and another one at 155 and another one at about 300. One could certainly suggest that these are the same kinds of ferroelectric transitions that you find in barium titanate.

B. Cox: You ascribed the structures of your niobates and tantalates to the high charge on the niobium and the tantalum. Do you have a measured value for the ionicity in these structures?

J. A. Kafalas: Not really, no.

B. Cox: Would you speculate on what the actual charge is?

J. A. Kafalas: I'd rather not at the moment.

J. B. Goodenough: I just wanted to say something with regard to Professor Banks' question. You'll notice that Jim was very careful to say that when he had a tolerance factor greater than one, it enhanced any tendency toward going to a ferroelectric transition. He didn't say that that was a sufficient condition, and certainly there are other conditions that are involved. One of these is, as he mentioned, the need for a near equivalence in the site energies for the ion in tetrahedral and octahedral coordination. That condition certainly provides an important difference between the tantalum and the niobium ions.

A. W. Sleight: I was wondering, Jim, whether you or perhaps John Goodenough would like to tell us why it is that antimony does not like to form the 180° bond with oxygen.

J. A. Kafalas: Do you want to take that one, John?

J. B. Goodenough: Well, the working hypothesis we had in setting up this series of experiments was simply that an antimony 5+ ion is going to have a very strong covalent bond with the oxygen. Greater covalency per antimony occurs if the oxygen ion uses different p-orbitals for bonding rather than shares the same p-orbital with antimony on either side. So, if the Sb-O-Sb linkages can make a 90° bond or something approaching a tetrahedral bond angle, than the oxygen ion can use two different p-orbitals. Presumably a certain amount of covalent-bonding energy is sacrificed by sharing the same p-orbital on two sides. That was the idea we had, and we wanted to see whether one could force the antimony into 180° angles in a perovskite structure. As you can see, we were unable to do it. So it seems as though there is a fair amount of energetics involved in that consideration.

R. Ward: I think you can get antimony in perovskite structures, in the ordered perovskites.

J. B. Goodenough: That's correct. But there, of course, you are dealing with an ion on the opposite side that is not an antimony 5+ and that isn't bonding strongly in a covalent way. There is no reason for the antimony 5+ not to want to be in a perovskite structure if it can form an SbO_6 cluster that is not so tightly bound to the ion on the opposite side of the oxygen ions. So, I think, that fits in very well with the explanation I was giving to you.

National Bureau of Standards Special Publication 364, Solid State Chemistry, Proceedings of 5th Materials Research Symposium, issued July 1972.

DEFECTS IN OXIDES

J. S. Anderson

Inorganic Chemistry Laboratory
University of Oxford
Oxford, England

Defects in ionic crystals, such as the metallic oxides, are so intimately involved in diffusion, reactivity and electronic properties, that an understanding of defect structure is a necessary background for a variety of problems in the chemistry, physics and technology of materials. In the present context consideration will be restricted primarily to thermodynamic defects: the inner equilibrium of oxide structures, stoichiometric changes that displace that equilibrium, and solid solutions in which replacement of one cation by another of different valence involves an analogous change in the ratio of cations to anions in the crystal structure. This paper is largely concerned with structural matters and has two purposes: the first is to draw together what is known about highly defective oxide structures (stoichiometrically variable and solid solution phases); the second is to consider, in more detail, one or two systems that exhibit a remarkable capacity for organizing their defect structures.

It has been customary to treat these problems within the framework of point defect theory. This viewpoint, well rooted in statistical thermodynamics, is certainly applicable to highly ionic uni-univalent crystals (alkali halides) and, perhaps generally to highly dilute defect systems - *e.g.* 10^{19} cm^{-3} or less. We are concerned with concentrations two orders of magnitude greater, with ions of greater formal charge, and (in the important transition metal oxides) with a considerable measure of orbital overlap between cations and anions and, in some cases, direct cation-cation bonding. These last considerations raise questions about the effects exerted by defects, such as anion vacancies, on charge screening and cation repulsions, and about the preservation of cation coordination so as to maximize charge screening and optimize the covalent component of the bonding.

We shall try to trace a progression in our classification of defect structures, and in doing so we shall find effects both of chemical specificity - the electronic configuration, as well as the size of cations - and of influences exerted nonspecifically, by crystal structure type.

Key words: Block structures; crystallographic shear; defect clusters; defect models; high resolution electron microscopy; oxide defects; rutile structure; Wadsley defects.

1. THE SIMPLE DEFECT MODEL

Dissociation of an oxide such as rutile is customarily represented as forming an inherently nonstoichiometric phase:

$$TiO_2 \rightleftarrows TiO_{2-x} + \frac{x}{2} O_2$$

through the formation of point defects - anion vacancies or interstitial cations. For a vacancy model, the basic step is

$$O_O^x \rightleftarrows V_O^x + \frac{1}{2} O_2$$

where V_O^x is a vacant anion site with two trapped electrons, which may ionize in two stages to furnish electrons in the conduction band:

$$V_O^x \rightleftarrows V_O^{\cdot} + e^-$$

$$V_O^{\cdot} \rightleftarrows V_O^{\cdot\cdot} + e^-$$

Application of the law of mass action relates the concentration of defects in each stage of ionization to the chemical potential of oxygen, through the relevant equilibrium constants.

For an oxide such as rutile, with a very low intrinsic electronic conductivity

$$[e^-] = 2[V_O^{\cdot\cdot}] + [V_O^{\cdot}]$$

and

$$[V_O]_{total} = [V_O^X] + [V_O^{\cdot}] + [V_O^{\cdot\cdot}]$$

It is readily shown [1][1] that depending on the vacancy ionization equilibria, the pressure-dependence of the deviation from stoichiometry might vary from $p^{-\frac{1}{2}}$ to $p^{-\frac{1}{6}}$. Only if a single stage of the ionization process dominates the situation is a simple pressure dependence to be expected.

If the defect structure involves interstitial cations, the defect reactions may be written as

$$TiO_2 \rightleftarrows O_2 + Ti_I^X$$

$$Ti_I^X \rightleftarrows Ti_I^{m+} + me^-$$

and the stoichiometric defect becomes proportional to $p^{-1/(m+1)}$.

Numerous careful studies of rutile [1,2,3], Nb_2O_5 [4] and other oxides have been analyzed on this basis. In the case of rutile, Kofstad and Forland considered that the results agreed with the $p^{-\frac{1}{6}}$ law indicative of fully ionized oxygen vacancies over a composition range from $TiO_{1.999}$ to $TiO_{1.997}$ (1050 °C) and $TiO_{1.9923}$(1194 °C) [3], or to $TiO_{1.9905}$ (1227 °C) [1]. Whatever the structure may be at very low deviations from stoichiometry, this fit between experimental data and the point defect model extends into a composition range where as will be seen (below), there is direct evidence that the real structure is quite different. One must conclude that thermodynamic measurements do not suffice to discriminate between alternative structural models, even for defect concentrations at which it might be hoped that the behavior would be simple.

Point defects are customarily regarded as charged entities, located on regular sites of the crystal lattice or on interstitial sites between them, and it is often (though not necessarily) assumed that the interstitial positions are the special sites of high symmetry. In calculations of defect energies, the ions surrounding a defect site are taken to relax symmetrically from their idealized positions under the influence of coulomb forces and repulsions. Various authors have drawn an analogy between defects in a crystal, with their ionization equilibria, and ions in electrolyte solutions, with their protonation equilibria [5,6]. On this basis, such processes as direct defect association and Debye Hückel effects can be treated. The analogy is useful and can be taken further. We are reminded that ions in solution may profoundly modify the local structure of the solvent and that ions of high charge interact so strongly with dipolar solvent molecules that a localized chemical transformation takes place: there is no such species as a Zr^{4+} cation in aqueous solution; it is transformed, at the expense of destroying water molecules, into a hydroxo complex. Similarly, relaxation of the system (point defect in a crystal) may go far beyond a simple rebalancing of coulomb forces, and may effect a structural transformation of the 'solvent' crystal lattice. We can probably summarize the effects of such profound relaxations, and of progressively stronger mutual interaction between the resulting defect centers, as in table 1.

2. APPROXIMATION TO THE SIMPLE DEFECT MODEL

The closest approximation to a random point defect description is afforded at first sight by the NaCℓ structure monoxides of titanium and vanadium. These are remarkable compounds, with surprisingly high concentrations of cation and anion vacancies - 15% vacant sites in each sublattice even in the stoichiometric phases, as is shown by figure 1 [7]. These defect concentrations are so high that, on a simple interpretation, they would imply an absurdly low energetic cost of defect creation. The first thing to note is that these oxides are metals; the formally +2 cations have occupied d-orbitals of sufficient radial extension to overlap, so that there is strong cation-cation metallic bonding throughout the

[1] Figures in brackets indicates the literature references at the end of this paper.

Table 1

Summary of Defect Models.

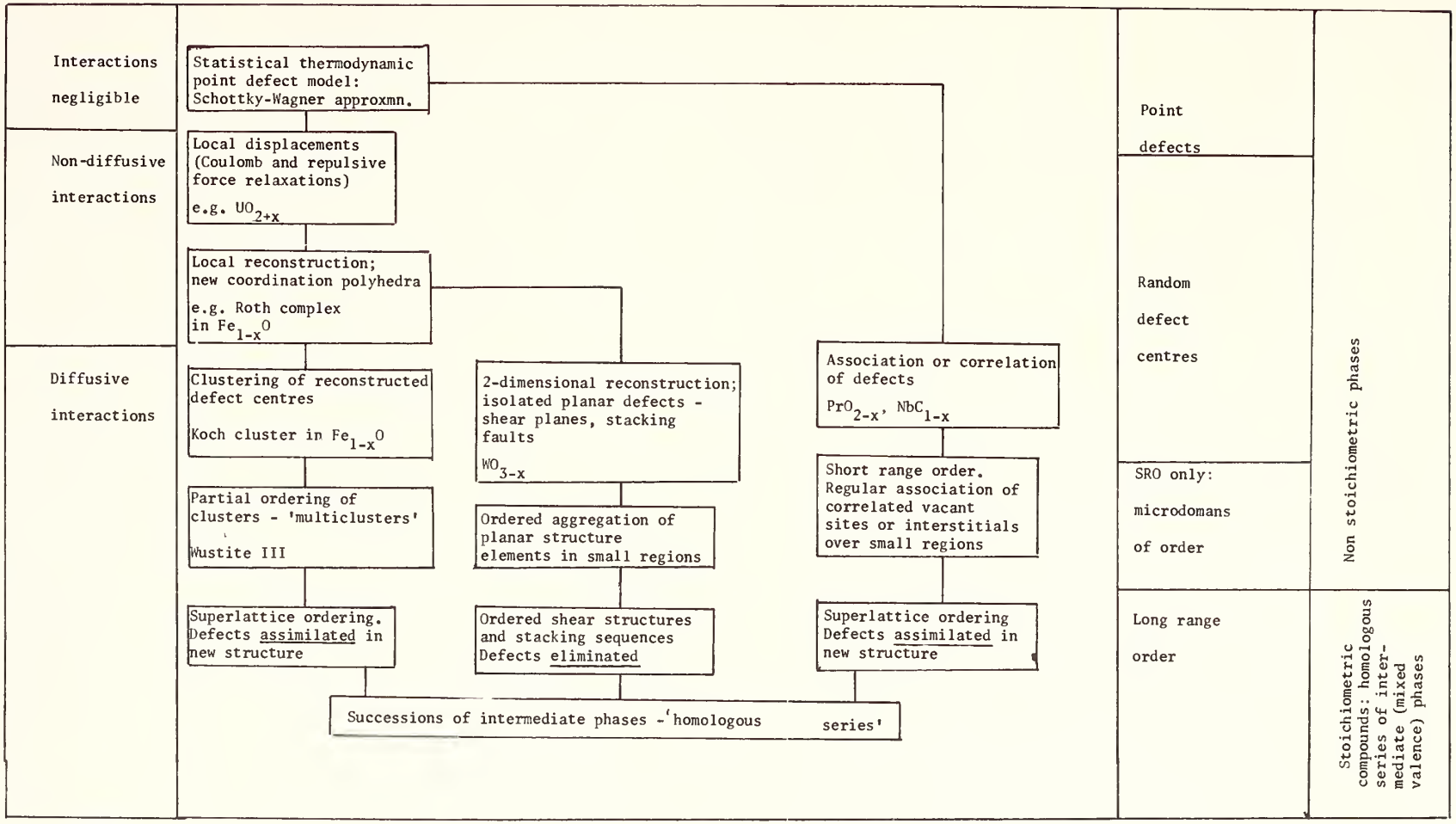

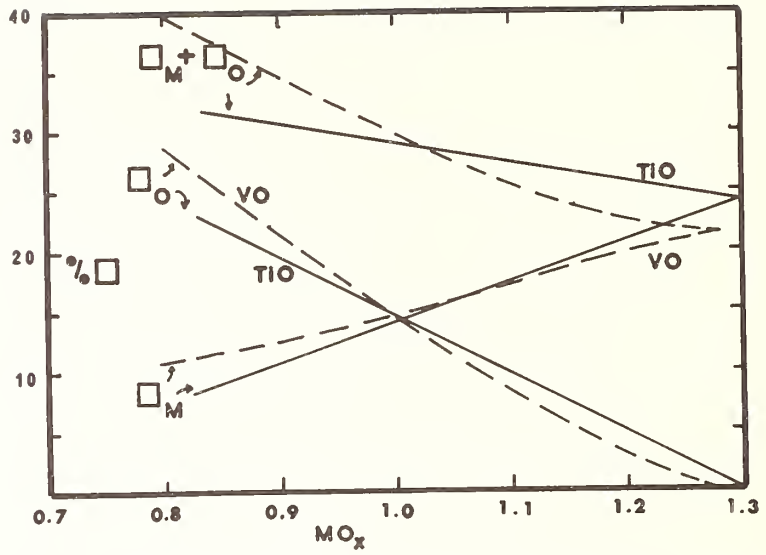

Fig. 1. Concentration of vacant metal atom sites, vacant oxygen sites and total vacant sites, as functions of composition, in nonstoichiometric TiO and VO.

structure. This has two consequences. The first is that the excess negative or positive charges arising from stoichiometric charge are completely delocalized, rather than being trapped as cations of +1 or +3 charge, and the effect of stoichiometric change is only to raise or lower the Fermi level; the states concerned are probably in the non-bonding or antibonding levels of the *d*-band. The second is that the usual role of cation vacancies and anion vacancies as charge trapping centers is effectively screened by the metallic electrons. As a result, coulomb interaction between the vacancies is greatly attenuated. Nevertheless, there are quite strong interactions.

These interactions show themselves in the transformation of the random, high temperature, nonstoichiometric oxides into ordered phases of fixed stoichiometry, below 1000° C. The structure of the TiO ordered phases has been worked out by electron diffraction [8]. There are two distinct structures, at $TiO_{1.00}$ and at $TiO_{1.25}$, shown in figure 2. It will be noted that both structures are superlattices based upon the NaCℓ type, with every occupied lattice site assignable to a site of the parent structure. The vacant sites are now *not* defects but are part of the structural pattern; they are a virtual ternary component of a fully ordered crystal pattern; because of this relation to the NaCℓ structure, the two definite compositions are dimensionally compatible with one another and can intergrow coherently. It has been shown that at compositions between $TiO_{1.00}$ and $TiO_{1.25}$ ordering leads to an unmixing into lamellae of the two separate ordered structures, only a few tens of Angstroms wide. The structure at compositions below $TiO_{1.00}$ in the ordered state has not been worked out, but from analogy with the suboxide Ti_2O, in which oxygen atoms are located in octahedral interstices of the hexagonal titanium structure, it is a plausible prediction that oxygen atoms and oxygen vacancies will order themselves on {111} planes of the sodium chloride structure, with the possibility of giving other additional ordered stoichiometric phases in intergrowth with $TiO_{1.00}$.

In the light of this evidence we return to the question whether the high temperature phases are really random point defect structures. Strongly suggestive evidence to the contrary comes from the fact that although high temperature VO and TiO have similar vacancy concentrations, they are almost immiscible in the solid state, suggesting that they differ in an incompatible way in the ordering of their defects on a short range basis. If the random structures do not actually contain microdomains of the same kind of ordering as can be fully developed in the low temperature phase, along the lines of Ariya's concept of defect solids, [9], then at least it is likely that there is a strong correlation between the positions of vacant sites. My colleague Fender and his pupils have shown that in the somewhat analogous NaCℓ type carbide structures, the carbon deficient NbC_{1-x} phase shows strong

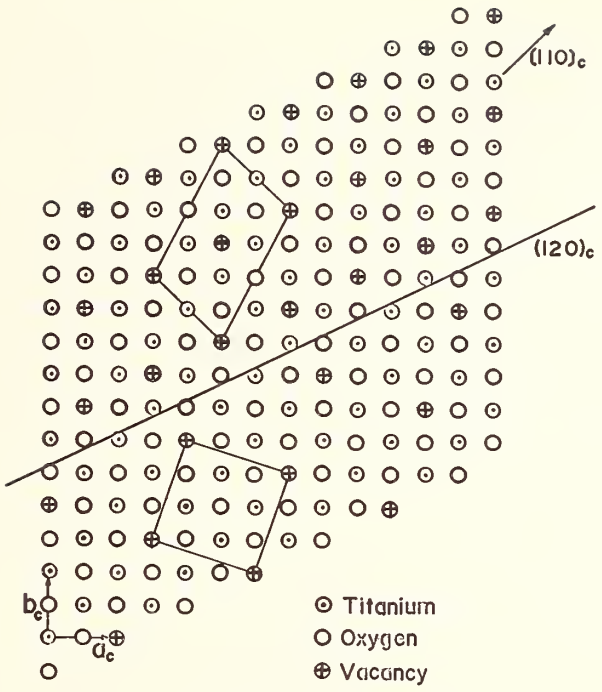

Fig. 2. Structure of ordered, low temperature TiO ($TiO_{0.8}O_{0.8}$), $TiO_{1.25}$ ($Ti_{0.8}O$) and their coherent intergrowth.

correlation, with vacant carbon sites preferentially located in third nearest neighbor positions.

The next stage in the deviation from a point defect model can be exemplified by the oxygen excess fluorite structure oxides such as UO_{2+x}. Here the coulomb repulsion between defects - formally identified as oxygen interstitials - reinforced by closed shell repulsion within a crowded structure, modifies the structure of the parent crystal and transforms a point defect into a defect complex. The Willis structure for UO_{2+x} is shown in figure 3; in the simplest form of the defect complex, the 2:1:2 complex, each interstitial oxygen displaces 2 oxide ions from their lattice sites, creating 2 vacancies, so that there are, in fact, 3 associated interstitial oxygens, located on two sorts of general, interstitial site. The number of such complexes in a crystal is, indeed, given by the number of oxygen atoms introduced; the hyperstoichiometric oxygen is indeed interstitial; the thermodynamics of the system approximates to that of a simple interstitial oxygen model. What has been completely lost is any equivalence between the number of oxygen atoms introduced and the number of point defects which contribute to transport and other properties. The defect complexes interact with one another and can be ordered, as in U_4O_9; they can be imperfectly ordered but must still be quite closely correlated in the oxygen-rich region of the nonstoichiometric UO_{2+x} phase field.

It may be noted that this type of defect transformation appears to be common to hyperstoichiometric fluorite structures of ionic type. It is found in the CaF_2YF_3 solid solutions, as Fender and Cheetham have recently shown.

3. NON-RECONSTRUCTIVE DEFECT CLUSTERS

The next stage we may recognize in the progression is a stereochemically specific association of point defects, to form defect clusters without significant change in the atomic positions of the "solvent" crystal lattice. This is exemplified by what is found in the substoichiometric binary and ternary fluorite type oxides. Bevan has shown that, in these,

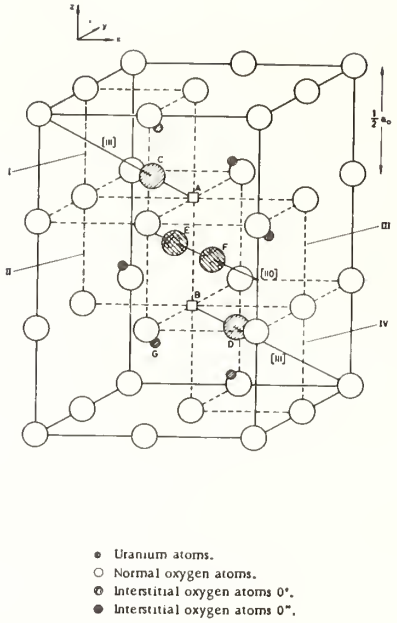

Fig. 3. Model for UO_{2+x} structure. Normal oxygens, at A and B in $UO_{2.00}$, are replaced by interstitial atoms 0" at C, D and 0' atoms at E (2:1:2 structure) or at E and F (2:2:2 structure).

unoccupied anion sites are paired up across the body diagonal of the cubic coordination polyhedra (fig. 4). Depending upon the size of the cation in this polyhedron, which may be symbolized as $[MO_6V_2]$, there may be little or no distortion of the fluorite-type cube. Since every anion site is 4-coordinate, each vacant site is shared with three other cubes, and the whole represents a dumb-bell shaped cluster which could be assigned the symbol $[MO_6V_2][MO_7V]_6$. Every site in this cluster corresponds to a site in the fluorite crystal structure and the whole is dimensionally compatible with the fluorite crystal structure. It constitutes a unit which, if infinitely repeated, builds up a crystal $M_7^{IV}M_6^{III}O_{12}$ (as in Pr_7O_{12} and the ternary oxides of similar formula). It is a sort of 'lattice molecule' which may be plugged into the fluorite oxide structure (or oxyfluoride structure $M^{III}O$ F) in place of a corresponding group of $[MX_8]$ polyhedra [10]. Substitution may be uncorrelated (or imperfectly correlated), or the units can order themselves in one dimension, along their trigonal axis. They can give rise either to the variable composition α-phases of CeO_{2-x} and PrO_{2-x} or to the ordered binary and ternary phases. Bevan has advanced evidence that there is a considerable degree of linear ordering of such strings of complexes even in the nonstoichiometric apparently random phases. Treating the vacant anion positions as potential electron trapping sites, the cluster is an electrostatically neutral entity. However, if the ionization energy is small, then the carrier concentration depends only upon the numbers of rare earth cations in the 2 valence states +3, +4, *i.e.*, upon the stoichiometry of the crystal, and is little dependent upon the actual structure. The electronic properties of the substoichiometric rare earth oxides are simple functions of composition; their structures are not. On the other hand, the mass transport properties of the crystal depend on mobile defects. The formation of such clusters almost completely removes the isolated anion vacancy which is the unit of diffusional mobility. Such mobile vacancies can be formed only by what is effectively a dissociation of the cluster, as represented by the notional equation

$$[MO_8] + \underbrace{[MO_6V_2][MO_7V]_6}_{\text{anchored, paired, structural empty anion sites}} \rightleftarrows 2\ \underbrace{[MO_7V]_4}_{\text{Isolated defect anion vacancy.}}$$

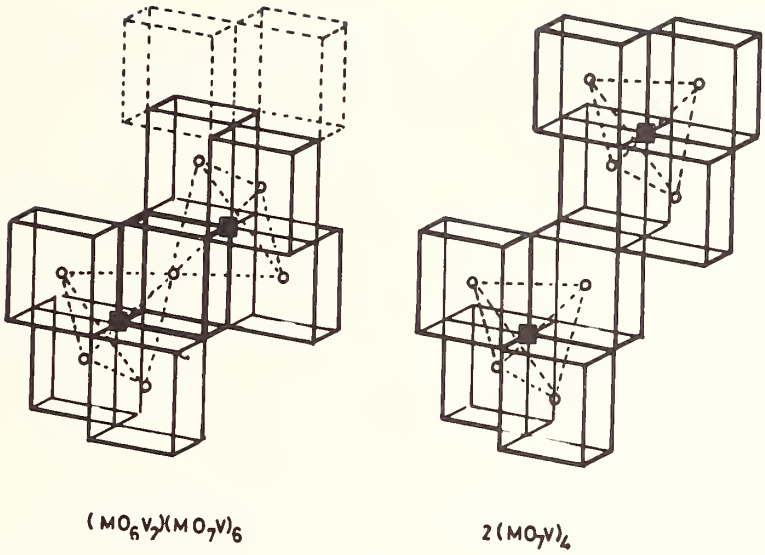

Fig. 4. The Bevan cluster in hypostoichiometric fluorite structures. Creation of mobile point defect vacancies involves dissociation of the tightly bound paired empty anion sites (right).

If the clusters are well ordered, unoccupied anion sites are no longer to be regarded as defects; they are again structure elements of the crystal as it is. Even if the clusters are fully randomized, their stereospecifically paired vacant anion positions are distinct from the anion vacancies of the point defect equilibrium.

4. RECONSTRUCTIVE CLUSTERING

By reconstructive clustering is meant a rather more profound interaction between introduced defects and the crystal structure, which substantially modifies the occupancy of parent lattice sites around the defect and emphasizes the role of non-coulombic interactions, crystal field effects *etc.*, in determining the location of cations of different valence. The case to be considered is the ferrous oxide phase $Fe_{1-x}0$ which exists only as a highly defective structure with 5 - 15% of vacant cation sites (on the point defect description; the real concentration of vacant sites is much higher). $Mn_{1-x}0$ is probably analogous. This is an example of a system where the sparse, but good, thermodynamic measurements of Darken and Gurry and later workers look as if they follow the $p^{-\frac{1}{6}}$ law required for a point defect model, though later and more data intensive oxygen potential measurements [11] show complexities and have not been fitted explicitly to the real structural situation.

The actual structure has now been investigated by a variety of methods, though only on too limited a number of discrete compositions, and on quenched samples: by x-ray diffraction (by Manenc; Koch and Cohen): by Bragg neutron scattering (Roth); by diffuse neutron scattering (Fender and Childs) and by Mössbauer effect. There is always some doubt about the validity of deducing the structures of high temperature phases from quenched samples. It is therefore important that the structure of ferrous oxide at high temperatures, in equilibrium with its gaseous environment, has been investigated by Bragg neutron scattering (Fender and Cheetham) and by Mössbauer methods (Howe). These combine to give a picture which is still incomplete, but from which the main conclusions seem assured. Roth's work showed conclusively that some of the Fe^{3+} cations moved from octahedral sites to tetrahedral sites, thereby creating additional cation vacancies, and the minimum unit would therefore appear to be a complex of a tetrahedral cation bracketted by a pair of vacancies, the octahedral sites; the analogy with the spinel structure of Fe_3O_4 is obvious but slightly misleading, and attempts have been made to fit the thermodynamics of the system to a defect structure based on Roth complexes. [12] At low temperatures, in its metastable existence range, the FeO phase can undergo a considerable amount of superstructure ordering, and from the partially devel-

oped superstructure Koch and Cohen [13] deduced that the actual complex was the unit containing four tetrahedral iron atoms and 13 octahedral vacancies, figure 5. In other words, there has been a considerable aggregation of empty iron sites to the units created by the Roth complexing process. Such a structural unit is virtually a single cube of the zinc blend structure type, and it bears a net anionic charge. It must therefore be surrounded by an ionic atmosphere containing other Fe^{3+} cations in the octahedral sites of the surrounding structure, which can indeed be described as of the NaCl structure type. This basic unit, of Koch cluster plus its atmosphere, defines a certain minimum distance of approach between defect centers, which will tend to order themselves under coulombic forces. There are several ways in which superlattice ordering can take place, which accounts for the apparent variable and fractional multiplicity of the superlattice observed. The diffuse neutron scattering of Fender and Childs gave results compatible with the Koch-Cohen cluster and its partial ordering, but is probably equally compatible with the slightly different structure deduced by Howe from an analysis of the complex Mössbauer structure. This involves the creation of tetrahedral groups, with 5 tetrahedral Fe^{3+} atoms and 16 cation vacancies. The high temperature equilibrium work shows that the defect complexes are not an artifact of quenching and low temperature ordering. The ratio of tetrahedral iron to total Fe^{3+} in oxygen-rich FeO (*e.g.* $Fe_{0.850}$) is consistent with either the Koch-Cohen or the Howe models; it is hardly possible to discriminate on the basis of the evidence. The essentials of the structure are thus retained when long range correlation is lost and a nonstoichiometric phase of pseudo-NaCl type is formed. The rather subtle thermodynamic differences between different parts of the Wüstite phase field, discovered by Vallet and Raccah and confirmed by Fender and Riley, can probably be attributed to some change in the type of defect complex that is present. Within any one part of the phase field, a change of composition is reflected by a change in the ratio of sites that properly be described as FeO structure to sites that are taken up in the complexes and their ionic atmosphere, without a change in the nature of the defects. In fact, at the oxygen rich end of the phase field it might be more correct to describe Wüstite as a coherent solid solution of FeO in a disordered superstructure oxide, of irrational formula given by the Howe or Koch-Cohen complex, than as a defect FeO phase. At the iron rich end of the phase field (*i.e.*, about $Fe_{0.930}$ to $Fe_{0.950}$), and at very high temperatures, the structure is less clear. The basic unit appears to be a tetrahedral ion Fe^{3+} bracketed by

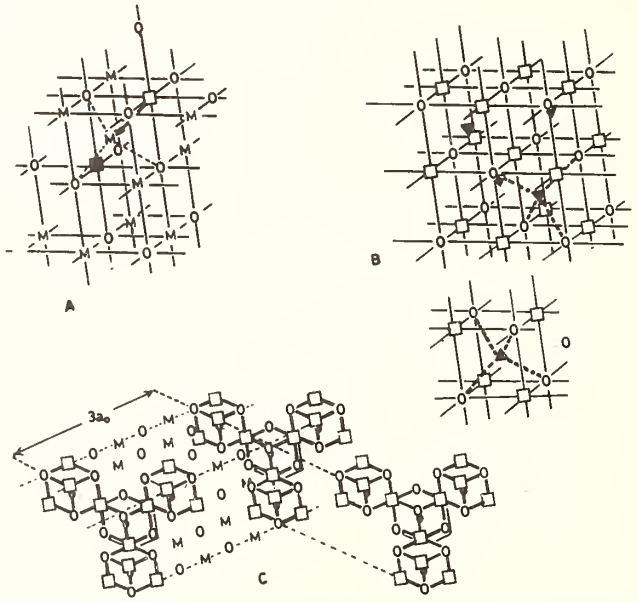

Fig. 5. Wüstite, $Fe_{1-x}O$ *A*. Fe^{3+} ion adjacent to vacancy moves to tetrahedral site, creating a Roth-type cluster. *B*. The Koch-Cohen cluster of 13 empty cation sites and 4 tetrahedral Fe^{3+}. *C*. Alternative cluster with 5 tetrahedral Fe^{3+} and 16 empty sites, and possible superstructure ordering. (Howe) *D*. The basic cluster unit common to B and C.

4 empty octahedral sites, which may be the defect center at the iron rich high temperature end. With increasing concentration, such defect centers aggregate, with the absorption of additional cation vacancies, to build up the more complex clusters. It will be noted that there is again a profound difference between the real defect structure and the inferences to be drawn by applying the point defect concept to the variable composition phase. It remains as a net vacancy structure, in the sense that the anion sublattice is more or less completely occupied and the cation sublattice contains fewer cations than the sites available. The number of unoccupied cation sites is not simply related to the composition, nor can the empty sites within the complexes be regarded as defect vacancies in the usual sense. The diffusion properties become more complex. Chemical diffusion, such as transmission of a composition change in oxidation or reduction, requires a cooperative step whereby the location and average distance between the complex clusters is changed. It probably requires a cooperative diffusive mechanism in which, however, the mobility of the isolated vacancy dissociated from the complexes may be the unit diffusive step. The concentration of such isolated vacancies, is, however, much smaller than the number of vacancies that are subsumed in the clusters. The electronic properties are also likely to be complicated, since the direct electron transfer between cations on equivalent sites, but in different valence states, involves not all the Fe^{3+} but only those in the ionic atmospheres of the clusters. From the standpoint of statistical thermodynamics, it must be noted that the incorporation of a high proportion of the vacant cation sites and of the cations of different valency into clusters of definite structure has the effect of considerably diminishing the configurational entropy of the system. As a consequence, the factor determining the stability, the oxygen potentials and the structure assumed by the material is shifted entirely in the direction of a gain in enthalpy. The factors that enter into this are more subtle than could be extracted from a simple calculation of coulombic energies.

5. ELIMINATION OF DEFECTS BY CRYSTALLOGRAPHIC SHEAR

In the foregoing sections, it is clear that there may be an energetic advantage in processes that reduce the number of defects by subsuming them into larger, but less numerous, extended defects; these may themselves be clustered and partially ordered. In the oxides of the (formally) highly charged transition metal cations a particularly interesting situation arises. It is evidently advantageous to maintain the screening of the cationic charge and the character of the covalent component of the bonding by preserving octahedral coordination and changing the coordination number of anions only. The effective size, charge and *d*-character of the cations are the determining factors. Relaxation then takes the form that has been termed *crystallographic shear*, in which the changed coordination of the anions brings about a closer linkage of coordination polyhedra along some defined crystallographic plane, and thereby eliminates a complete sheet of anion sites from the crystal. This is a cooperative process; its mechanism is open to debate, but it virtually amounts to a two dimensional ordering of anion vacancies, followed by a collapse of the structure across the crystallographic shear plane. It provides a basis both for generating a very large number of mixed valence intermediate phases without any profound change in crystal structure and, as will be seen, of eliminating point defects down to some very low concentration.

Thus in ReO_3-type structures (*e.g.*, idealized WO_3), the coordination number of oxygen is increased from 2 to 3 by changing apex-linking to edge sharing of octahedra: in rutile-based structures, oxygen coordination is changed from 3 to 4 by face-sharing of octahedra. In each case there is a reduction in cation-cation distances across the shear plane; this causes some distortion of the coordination octahedra, which is propagated out into, and progressively attenuated in, the slabs of parent structure between shear planes, and this may be one of the (repulsive) elements in shear plane interaction. Between the cations of face sharing octahedra there may well be direct cation-cation bonding, sensitive to the nature and *d*-character of the cations concerned.

We deal first with the mixed valence intermediate phases. These are formed by recurrent shear, so as to enclose slabs of unchanging parent structure between crystallographic shear planes of a particular orientation at regular intervals. If the slabs are of absolutely regular width, a crystallographically new structure of definite stoichiometry is formed, with a composition that depends upon two factors: (a) the number of anion sites per cation site that are eliminated in the shear plane, and (b) the width of the slab of parent structure between shear planes. For any given shear plane orientation, the latter is a variable, so that a whole homologous series is generated, with the possibility of a very fine scale of

gradation in composition between successive members. If the slabs of parent structure are not of absolutely regular width, then a one-dimensional disorder is introduced, which gives rise to the possibility of a new type of nonstoichiometry. It may be noted that the shear planes, in general, extend by cooperative action across the full width of any crystal. A shear plane that terminates within a crystal must do so at a dislocation and it is energetically advantageous to propagate the shear plane across to the free surface. It can be shown that disorder of shear planes makes a very small contribution to the configurational entropy of a crystal, so that the inner equilibrium is dominated by the enthalpy; ordering is energetically favored and the shear phases do not undergo significant disordering of their shear planes at high temperatures. Such ordering does, however, involve longerange interactions - not yet satisfactorily interpreted - between shear planes that may be from 10 to >40 Å apart. The driving force behind ordering therefore falls off with the spacing. The evidence so far is that the lower members in all series are rather well ordered, although the higher members, with wider shear plane spacings, frequently do not attain perfect order within the time scale of laboratory experiments.

Investigation of such problems is entirely dependent upon electron microscope techniques. The existence of disorder, with narrow domains of a given member of the homologous series, may be inferred from the streaking of electron diffraction spots, but for the detailed investigation of order the only available method is the purposive use of direct lattice imaging as pioneered by Allpress. Thus Allpress and Gado found a considerable degree of randomness in well crystallized $W_{20}O_{58}$; a single crystal, homogeneous to x-rays, showed spacings between successive shear planes (as measured on direct lattice images) varying between the values corresponding to $W_{12}O_{34}$ ($WO_{2.8333}$) and $W_{28}O_{82}$ ($WO_{2.9285}$) and varying in distribution from isolated lamellae to strips of homogeneous structure wide enough to give discrete electron diffraction spots (fig. 6).

Of the crystallographic shear structures, the one most intensely studied is the rutile structure, and this merits more detailed consideration. It is of interest because, (as indicated earlier) the native defect structure of rutile has been a matter of dispute; opinions have been divided whether the n-type conductivity produced on reduction is associated with oxygen vacancies or with titanium interstitials. All the studies of rutile up to 1969, and practically all the physics even today, have been discussed in terms of the point defect model. In fact, the composition range ostensibly covered by point defects in the rutile structure has shrunk progressively as the system has been more carefully investigated. Crystallographic shear not only generates intermediate phases but operates as a means of eliminating point defects in the rutile phase itself.

The real structural situation in reduced and slightly reduced rutile appears to be as summarized by table 2. There are two distinct series of shear phases, both with the general formula Ti_nO_{2n-1}, covering different ranges of composition and with the shear plane on two different orientations. The $\{1\bar{2}1\}$ shear plane family oxides [14] can be obtained as well ordered solids; the $\{1\bar{3}2\}$ family [15] are almost invariably obtained in a one-dimensionally disordered state, with lamellae of different compositions. Occasionally larger domains with a single shear plane spacing are formed, but the thermodynamic individuality of these phases, as will be seen in a moment, is so ill-defined that the driving force behind ordering is relatively small. Between the compositions $TiO_{1.900}$ and about $TiO_{1.937}$ there has to be a reorientation of the shear planes and we return to this point later. The $\{1\bar{3}2\}$ shear plane phases extend to a composition about $TiO_{1.973}$, with *n* around 37 and the shear planes more or less ordered at distances of about 40 Å. Material with a yet smaller oxygen defect contains coherently intergrown domains of the $\{1\bar{3}2\}$ shear plane oxides with domains of rutile structure; [15] [16] these contain randomly disposed shear planes, not now lined up but on all the possible $\{1\bar{3}2\}$ orientations. An isolated shear plane of this kind represents a two dimensionally 'infinite' fault, and has been termed a *Wadsley defect*. Hyde and Bursill [17] have shown that in material brought by coulometric titration to the composition $TiO_{1.9986}$ shear planes still line up in packets of 2-25, to define lamellae of the intermediate oxides, and that, from the concentration and spacing of the random Wadsley defects in the rutile structure (which is now the bulk of the crystal), the composition of material in apparent equilibrium with the nearly ordered packets of shear phases is around $TiO_{1.999}$. Mutual alignment and aggregation of shear phases is thus obviated only at compositions still closer to the ideal formula, and even then much of the oxygen defect is taken up and eliminated by the random Wadsley defects. It follows that the true point defect concentration in reduced rutile must be 10^{-4} or less.

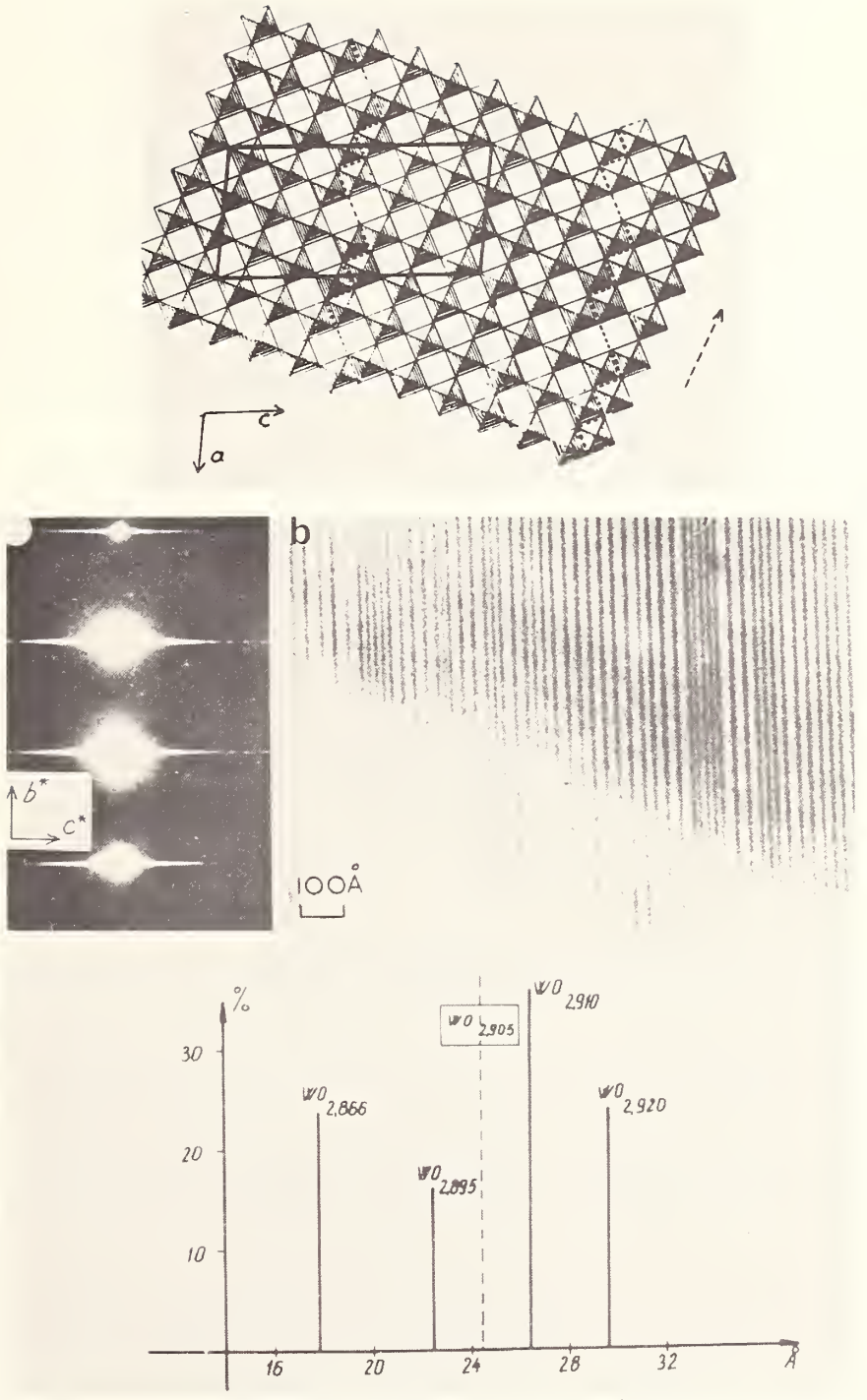

Fig. 6. (a) The structure of $W_{20}O_{58}$: recurrent {130} crystallographic shear planes in the ReO_3-type structure. (b) Single crystal '$WO_{2.90}$': variable spacing between CS planes. (c) Corresponding distribution of CS plane spacing in a "$W_{20}O_{58}$" crystal; proportions of lamellae of different members of W_nO_{3n-2} series.

465-504 O - 72 - 21

Table 2

Summary of the Structural Situation in Reduced Rutile.

Composition	Structure	Thermodynamics $-\bar{G}_{O_2}$ (1300K), kJ mol^{-1}	Equilibration behaviour
$TiO_{1.75}$ - $TiO_{1.90}$	$\{1\bar{2}1\}$ crystallographic shear phases Ti_nO_{2n-1} $4 \leqslant n \leqslant 10$	500 - 455	Hysteresis
$TiO_{1.90}$ - $TiO_{1.937}$ ca.	Shear plane orientation changes from $\{1\bar{2}1\}$ to $\{1\bar{3}2\}$. Either: (a) Discontinuity: intermediate phases of two series coexist; or (b) Continuous change; shear planes pivot around at roughly constant spacing.	455 - 445	Good reversibility
$TiO_{1.9375}$ - ca $TiO_{1.973}$	$\{1\bar{3}2\}$ crystallographic shear phases Ti_nO_{2n-1}, $16 \leqslant n \leqslant$ ca 37	445 - 43-	Hysteresis
ca $TiO_{1.973}$ - ca $TiO_{1.999}$	$\{1\bar{3}2\}$ shear planes group in lamellae defining high members of $\{1\bar{3}2\}$ family, within rutile saturated with $\{1\bar{3}2\}$ Wadsley defects	431 - ca 350	Probably hysteresis
$TiO_{1.999}$ - TiO_{2-x}	Wadsley defects on all $\{1\bar{3}2\}$ orientations, too widely spaced to interact and aline	350 - 250	
TiO_{2-x} - $TiO_{2.00000}$	Point defects in rutile structure $x \ll 0.0001$		

The subtlety of these changes in real structure obviously have thermodynamic implications. Some of the older, careful measurements of the oxygen potentials at compositions close to the ideal overlap into the region where it is now seen that Wadsley defects replace point defects. Thus all the attempts to analyze the results in terms of point defect theory and a simple $p^{-\frac{1}{n}}$ law become meaningless. We may set aside older work on the $\{1\bar{2}1\}$ shear phases, which showed that they were thermodynamic individuals but that transformations were very sluggish except at very high temperatures, and focus attention upon recent work by Hyde and Merritt, which correlates the thermodynamics with the new information on structure. The structural information shows that a very large number of discrete steps of composition have to be fitted in to a relatively small total change of chemical potential between $TiO_{1.75}$ and $TiO_{2.00}$, so that each step in chemical potential must be very small. Hyde and Merritt found that, over each range corresponding to a single set of shear phase compounds, there was gross hysteresis, at the temperature of the experiments (1300 K), at least. The width of the hysteresis loop was very large compared with the height of individual steps within it. In such circumstances, maintenance of internal order and establishment of univariant two-phase equilibria are hardly to be expected. Between these two distinct structural ranges, however, there was a range of composition over which the behavior was truly reversible, and this was just where the shear plane orientation changed over from $\{1\bar{2}1\}$ to $\{1\bar{3}2\}$. This is very remarkable, and contrary to all that one would intuitively foretell.

Consider what is happening as composition of the oxide is changed by oxidation or reduction, or is perturbed by the process of measuring an equilibrium situation. Over the two end ranges, any composition change implies that shear planes have been eliminated or additional shear planes introduced into the crystal and then, for maintenance of order, all shear planes have to adjust themselves to adopt a new regular spacing. It appears that either the creation and annihilation step or the migration and ordering step are kinetically

hindered, slow and responsible for hysteresis. In the middle range the situation is different. The distance between recurrent shear planes in any homologous series is given by the formula

$$D_{cs} = d_{hk\ell} \ (n-X)$$

where $d_{hk\ell}$ is the interplanar distance in the rutile crystal between the planes upon which the shear vector operates and X is the collapse factor in the process of shear (ideally, X = 0.5). When we consider how the shear plane spacing changes in the two homologous series, it becomes apparent that the upper end of the $\{1\bar{2}1\}$ series and the lower end of the $\{1\bar{3}2\}$ series, as found experimentally, have slabs of parent structure of much the same width. This means that, to a first approximation, a change of composition can take place without changing the *number* of shear planes per unit volume, but by changing only their *orientation*. Intuitively, it would seem that this should be a complex process productive of disorder, sluggishness and hysteresis. In fact, it corresponds to ready reversibility. How does it occur? The clue can be obtained with a high degree of probability from work on the ternary anion-deficient rutile oxides, particularly the Cr_2O_3-TiO_2 system.

The anion to cation ratio can be changed by introduction of ions of a different valency and suitable ionic radius, as well as by oxidation and reduction. It must be borne in mind, however, that there is one profound difference between nonstoichiometric binary systems and ternary solid solution systems. In the former, a redistribution of cations in different charge states can be mediated by electron transfer alone, without atomic movement. In the ternary systems, the distribution of charge is firmly anchored to the distribution of atoms of the two kinds. Hence any relaxation process may depend upon an ordering of the hetero-atoms in the structure, and self-diffusion processes, which become important at high temperatures, may interfere with or destroy the charge distribution which is necessary for some extended defect structure. In the crystallographic shear phases, considerations of local electroneutrality suggest that the +3 cations must be associated with the shear plane itself, so that formation of Wadsley defects or of ordered shear structures would depend on cation ordering. If this is not achieved, the crystal is left with some type of local structural defect; either cations in interstitial positions or vacancies which may be bound by coulomb association with the altervalent cations.

A second difference from binary systems is that chemical specificity may enter into the behavior of the ternary defect oxides. Ionic radius differences will bring about small but significant changes in both coulomb attraction and repulsion terms of the lattice energy. The electronic configuration, particularly the d character of the hetero-cations, may have far reaching effects on the non-ionic component of the binding.

Because VO_2 gives rise to its own series of $\{1\bar{2}1\}$ shear phases it is generally assumed that titanium-vanadium ternary oxides will differ little from rutile itself, and the system has not been thoroughly investigated. Doping with chromium brings to light a number of interesting effects that are significant for the understanding of the rutile system. The first is that ordering to shear phases takes place with ease. The $\{1\bar{2}1\}$ series of chromium titanium oxides was known earlier from Swedish work, [18] and electron diffraction and microscopy indicates that this extends roughly up to the member with n = 11 *i.e.*, $Cr_2Ti_9O_{21}$. Preparations with higher oxygen to metal ratios display a remarkable phenomenon which probably sheds light on the behavior of the middle range of the binary oxide system. Between the compositions indicated by n = 11 and n = about 22 at least, the well annealed oxides show very good ordering, with regularly recurrent shear planes, demarcating slabs of rutile structure of nearly constant width, about 20 Å. The orientation of the shear planes swings round progressively in the $[1\bar{1}1]$ zone, from $(1\bar{2}1)$ to close to $(1\bar{3}2)$ in a continuous progression, (fig. 7,8) as has been established by Hyde and Bursill [19] and independently by Gibb [20] in my Laboratory. Only at compositions corresponding to n = 27 or thereabouts, obtained by annealing at lower temperatures, does the shear plane lie in or very close to the $[1\bar{3}2]$ orientation. At about this composition the well-ordered shear phases coexist with rutile structure; (fig. 9) this proves to be a chromium doped solid solution phase, the saturation composition of which varies markedly with temperature, the limiting chromium content going up to about 5 atoms % at 1600°. [21]. This oxygen deficient solid solution does not contain Wadsley defects, except perhaps when some slight reduction of Ti^{4+} to Ti^{3+} has taken place. Since the unbalance between anions and cations is not eliminated by a crystallographic shear rearrangement, we are obliged to consider that there are localized defects in this structure.

Fig. 7. $Cr_2Ti_{n-2}O_{2n-1}$, 12 < n < 22: superlattice direction lying *between* [211] and [312].

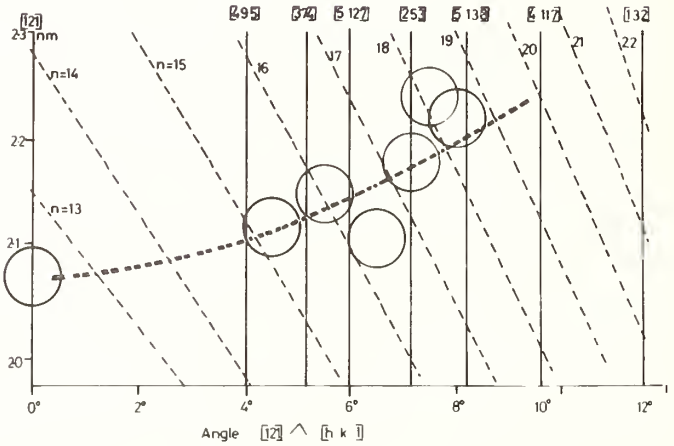

Fig. 8. 'Pivoting' of shear planes: change of composition in $Cr_2Ti_{n-2}O_{2n-1}$ series (n variable) achieved by rotation of CS planes at nearly constant spacing. Dotted lines show how CS plane spacing and CS plane orientation would be related for given, fixed values of *n*.

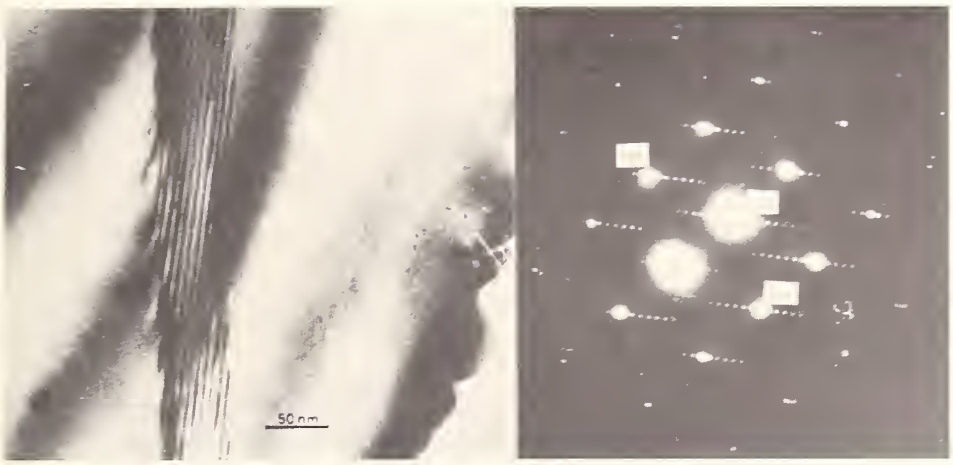

Fig. 9. $Cr_2Ti_{n-2}O_{2n-1}$ at low Cr^{3+} content, rutile structure without Wadsley defects (left hand side) coexists with fairly well ordered limiting-composition shear phase. At right, corresponding diffraction pattern.

At higher chromium contents, the $\{1\bar{2}1\}$ shear phase family ends with $Cr_2Ti_3O_9$, n = 5. $Cr_2Ti_2O_7$, n = 4, has a different structure, and phase analysis has identified it as a non-stoichiometric compound with a composition range that broadens considerably at high temperatures. At low temperatures, it narrows to a 'line phase', but does not come to the ideal composition, [21]. Reid in Melbourne has recently elucidated the constitution of this, and shown that we have another nonstoichiometric phase based on random intergrowth of shear structures. These are not derived from rutile, but from the α-PbO_2 structure and over the composition range of the $Cr_2Ti_2O_7$ phase there is a random intergrowth of the members with n = 3, 4 and 5 of the α-PbO_2 shear phase series $Cr_2Ti_{n-2}O_{2n-1}$.(fig. 10)

In view of the surprising ease with which Cr^{3+} generates well-ordered shear structures at low concentrations, it is of interest to examine the behavior of other trivalent cations and bivalent cations of similar ionic radius as controllers of the anion-cation ratio and to vary, in particular, the electronic configuration of the doping cation. The Al_2O_3-TiO_2 system shows only a narrow range of rutile solid solution, in equilibrium with the pseudo-brookite phase Al_2TiO_5, and the solid solution shows no extended defects of any kind under any conditions that we have examined [22]. It must therefore contain only localized defects.

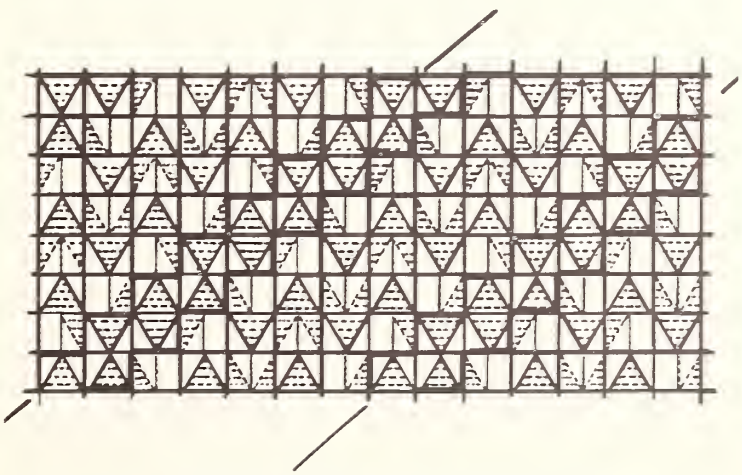

Fig. 10. Recurrent crystallographic shear in the α-PbO_2 structure, as in $Cr_2Ti_2O_7$.

This may be a size effect, or might be associated with the absence of d orbitals available for covalent bonding. If then one turns to Ga_2O_3-TiO_2 systems, with the same outer shell configuration but a somewhat better radius fit for the hetero-cation, one finds that the gross features of the phase diagram are similar to those of the Al_2O_3-TiO_2 system. As before, there is a rutile solid solution range and a phase Ga_2TiO_5, but the rutile solid solution is now laced with Wadsley defects in the form of planar boundaries but on a new orientation, {210} (fig. 11). It emerges, further, that there is an intermediate range of composition in which these {210} planar defects order themselves in regular recurrence, to build up a new family of homologous oxides with the formula

$$Ga_4\ Ti_{n-4}\ O_{2n-2} \quad (7 < n < 11)$$

These are moderately well ordered but show some variations in stacking (fig. 12); they have

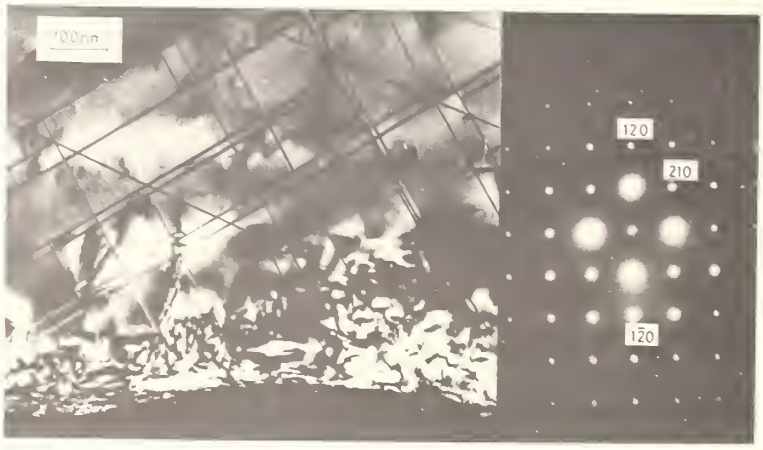

Fig. 11. {210} planar boundaries in Fe_2O_3-TiO_2 solid solutions; Ga_2O_3-TiO_2 similarly.

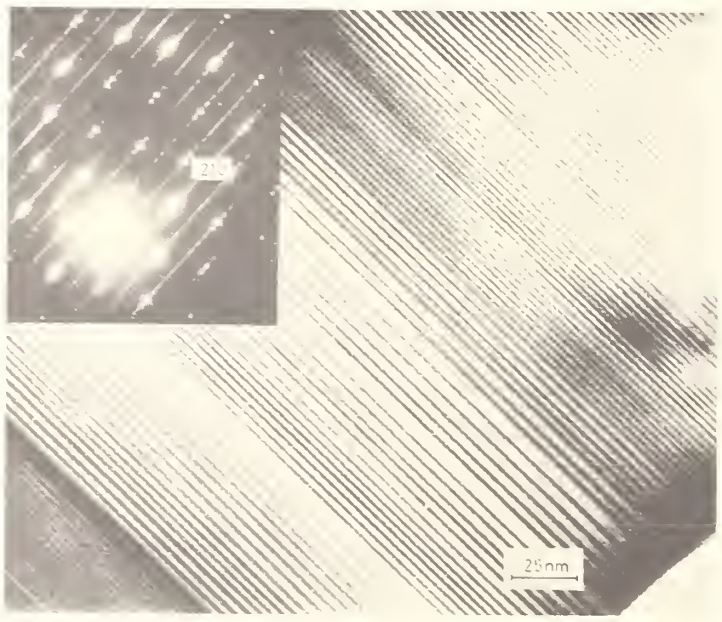

Fig. 12. Ga_2O_3-TiO_2: Incompletely ordered recurrent (210) planar boundaries in crystal of $Ga_4Ti_{n-4}O_{2n-2}$, defining lamellae with variable values of *n*.

not been grown as crystals for crystal structure determination, but consideration of the structural principle, dimensions and the displacement vector across the boundary, as determined from electron microscopy, suggests only one structure for them. This is related to the shear structures but involves a twinned orientation across each boundary. It is a type of recurrent collapsed twinning.

This difference in planar boundary structures cannot be attributed simply to the availability or non-availability of d orbitals for covalent bonding. The Fe_2O_3-TiO_2 system resembles the Ga_2O_3-TiO_2 system in having a solid solution range with Wadsley defects on the {210} orientation. This time, however, there is no ordering into discrete intermediate phases with regularly recurrent boundaries, even after long annealing in the laboratory. It may be, however, that all our laboratory experiments are too short, and that the longer diffusion paths attributable in the course of geological time, even at relatively low temperatures, would enable some ordering process to take place. Professor Buseck and I have therefore recently examined high quality natural rutiles, and it is found that in low temperature hydrothermal rutiles there are both isolated Wadsley defects on the {210} orientation and a regular long periodicity, suggesting that the collapsed twin boundaries have lined up very regularly at very long spacings indeed. This is not the whole story. Rutiles formed and annealed for geological periods at relatively high temperatures, and possibly under pressure with compositions lying in the solid solution range show a remarkably well developed superlattice ordering of a different type, but it would be premature to discuss this now.

This brief survey of the behavior of rutile emphasizes the role that crystallographic shear can play in the elimination of defects, as well as in the formation of intermediate phases. It is appropriate to ask if this is general. The short answer is that the other oxides that generate shear structure intermediate phases also appear to tolerate only minute concentrations of point defects, and replace them by Wadsley defects for very small deviations from ideal stoichiometry.

Thus WO_3 has been examined by Tilley, Allpress and Sienko [23][24], who have found that slightly substoichiometric material, in the composition range $WO_{2.99}$ to $WO_{3.00}$, obtained by loss of oxygen in vacuum at high temperatures, accommodates the oxygen deficit by forming disordered crystallographic shear planes parallel to {120}. These were already sufficiently numerous to cluster into small groups in $WO_{2.9988}$, and were rare, but present, in $WO_{2.9999}$; in $WO_{2.993}$ they had become more or less ordered, albeit imperfectly, at spacings of 40-50A, to define lamellae corresponding to members of the homologous series W_nO_{3n-1}, with n around 30-50 (about $WO_{2.967}$ to $WO_{2.98}$).

It will be noted that this group clustering of shear planes - and indeed, the formation of a simple Wadsley defect - implies that a defective crystal spontaneously assumes a spatially inhomogeneous composition. The problem of how crystallographic shear takes place is, as yet, unsolved. During a reduction process, oxygen atoms can presumably be removed from the crystal over the whole surface: by cooperative displacements and diffusion, the consequences of that oxygen loss are concentrated and organized at a single sheet of crystallographic sites. Possible mechanisms have been discussed by various authors [24][25][26], but the processes of formation and mutual ordering are still obscure. In TiO_2 and WO_3, there is no evidence that oxygen vacancies have to be ordered or collected in a vacancy disc as a precursor to shear collapse. In MoO_3, Bursill [27] has found that a preliminary superlattice ordering of vacancies, at about the composition $Mo_{400}O_{1199}$, may take place but does not appear to be an essential step in the formation of shear planes (in this case on $\{120\}_{MoO_3}$).

For each of these examples, the shear plane orientation adopted by isolated, random Wadsley defects is neither the only observed shear plane nor, necessarily, that found in well characterized intermediate phases; in each case, however, the shear vector remains constant:

In WO_3 : initial shear on $\{120\}_{ReO_3}$; compounds W_nO_{3n-2} ($W_{40}O_{118}$, $W_{20}O_{58}$) have $\{130\}_{ReO_3}$ shear planes. Shear vector $\frac{1}{2}$ <110>

In MoO_3 : initial shear on $\{120\}_{MoO_3} \rightarrow \{211\}_{MoO_3}$ (Mo_nO_{3n-1}, $Mo_{13}O_{31}$)

$\rightarrow \{311\}_{MoO_3}$ (Mo_nO_{3n-2}, $Mo_{18}O_{52}$) $\rightarrow \{411\}_{MoO_3}$ (Mo_nO_{3n-3}, $Mo_{26}O_{75}$)

all with shear vector $\langle \frac{a}{2}, \frac{b}{7}, 0 \rangle$. [6]

In TiO_2 : initial shear on $\{1\bar{3}2\}$; $(1\bar{3}2)$ family $Ti_nO_{2n-1} \rightarrow (1\bar{2}1)$ family Ti_nO_{2n-1}; shear vector (idealized) $\frac{1}{2}\langle 011 \rangle$

There is evidence, as has been seen, that this reorientation of shear planes can take place continuously: each shear plane is, strictly, pleated into a regularly puckered interface, but its trace remains straight as the mean orientation pivots around. In WO_3 however, Allpress [29] has produced striking evidence that - in some circumstances at least, possibly relating to non-equilibrium conditions - the shear planes may kink abruptly from the (120) to the (130) orientation.

6. DEFECTS IN BLOCK STRUCTURES

Related to the crystallographic shear structures are those that have been interpreted by Wadsley and designated 'block' structures [30][31], formed particularly by niobium in its binary oxides between $Nb_{12}O_{29}$ ($NbO_{2.417}$) and Nb_2O_5, and in ternary oxides derived from these. These are based on the ReO_3 structural type, and the modified linkage of coordination octahedra, required by the stoichiometry, is accommodated by edge sharing, as in the ReO_3-based shear phases. They can be roughly described in terms of two sets of shear planes on $(100)_{ReO_3}$ and $(001)_{ReO_3}$, although not strictly derived from the ReO_3 structure by recurrent shear. The ribbons of shear plane-like structure demarcate columns or blocks of ReO_3-structure, (mxn) octahedra in cross section, are infinite along the *b* axis. They have been fully described in a number of places [31][32], and attention need be given in this place only to those aspects that are relevant for the discussion of defects. These substances lend themselves particularly well to the exploitation of direct lattice imaging methods: they have fairly large unit cells, their structural principles are well understood and the lattice images can be interpreted in some detail and with considerable confidence.(fig. 13) In a series of elegant papers, Allpress has shown how much detail can be derived about defects and fluctuations in the local ordering pattern, especially for the ternary niobium oxides containing titanium (Ti,Nb O_x:O/Ti+Nb < 2.500) and tungsten (W,Nb O_x:O/W+Nb > 2.500) [33]. During the past year or two, a great deal of evidence has been accumulated at Oxford about the binary oxides $NbO_{2.500}$ to $NbO_{2.417}$, in relation to nonstoichiometry.

The feature that emerges unmistakably from these studies is this combination of flexibility with a high capacity for local ordering, in response to very small changes in anion: cation ratio. The relation of the block structures to the ReO_3-type subcell imposes a common metric on all the possible structures, while providing extreme possibilities for coherent intergrowth of isolated blocks or rows of blocks of different sizes, or with different linkages between sets of blocks at the same level. This flexibility is subject to certain constraints as the crystal optimizes its microstructure. The sheared ReO_3 substructure must be conserved in the orientation of the $[MO_6]$ octahedra and the location of metal atoms and equatorial oxygen atoms. The assembly of blocks must be space-filling. The permitted sizes of blocks is restricted by considerations of local electroneutrality - one can regard the block structure oxides as assemblages of rod-like anionic structures extending along the *b* axis, balanced by cationic rods constituted by shared corners of blocks, or tunnels filled with tetrahedrally coordinated cations, but the local accumulation of charge must not be excessive.

Subject to these constraints, the compounds reveal a remarkable capacity for discriminating between very small changes in the anion:cation ratio and forming new extended ordering patterns in response, and for assimilating yet smaller compositional fluctuations into 1-dimensional, highly localized structural rearrangements. Changes in composition - in the proportions of the constituents in the TiO_2-Nb_2O_5 and WO_3-Nb_2O_5 ternary oxides, for example, or through oxidation-reduction processes for the mixed valence oxides between Nb_2O_5 and $Nb_{12}O_{29}$ - can be assimilated, through the coherent intergrowth of a dimensionally compatible but different structure, identifiable as lamellae of a different compound [33]. If these are regularly recurrent, a new ordered intergrowth compound is formed - *e.g.*, the $M_{53}O_{132}$

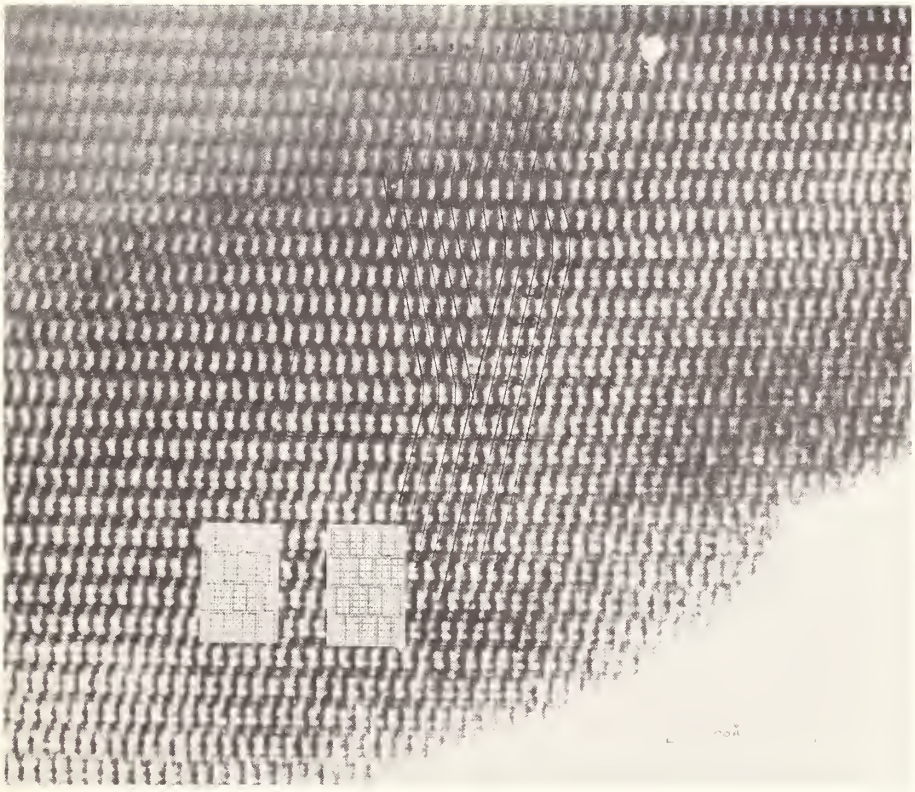

Fig. 13. Lattice image of the $(5x3)_\infty$ structure $M_{15}X_{37}$ ($MgNb_{14}O_{35}F_2$) showing correlation between lattice image and crystal structure (inset). Note twinning and a dislocation.

phases $TiNb_{52}O_{132}$, $Nb_{53}O_{132}$ formed by alternation of unit cell-wide strips of the H-Nb_2O_5 ($Nb_{28}O_{70}$) and the $M_{25}O_{62}$ structures. If the proportion and the distribution of the lamellae are irregular, the crystal is inherently nonstoichiometric. If the strips of new structure associate into packets, several or many unit cells wide, the crystal assumes a domain structure which poses questions - at present with no answers - about the thermodynamic behavior and thermodynamic characterization of the materials. Which of the above configurations minimizes the free energy of the system? The experimental evidence so far - *e.g.*, from the reduction of Nb_2O_5 - is that rearrangement to new block sizes and block linkages can take place at relatively low temperatures (below 1000 °C) and usually results in a small-domain arrangement of the simple structural types. Thus both reduction of Nb_2O_5 and solid state reactions of NbO_2 with Nb_2O_5 at 1000° C yield crystals with domains of the H-Nb_2O_5 structure, of the $(3x4)_2$ structure of $Nb_{25}O_{62}$ and of the $(3x4)_\infty$ structure of $Nb_{12}O_{29}$, in coherent intergrowth. At 1300° C, such domain crystals transform slowly to form large domains of the regular intergrowth structures [34]. (fig. 14)

During the past year, systematic high resolution electron microscopy at Oxford has provided information about the modes of faulting, in block structures, that are permitted by the constraint of conserving the ReO_3 basic structure. The first type is that which creates planar domain boundaries while preserving the stoichiometry of the crystals. These include twinning modes that change the orientation of rectangular blocks, or that reverse the direction in which blocks at the same level are linked in ribbons; because they have to be compatible with the integrity of the basis structure, the possibilities for such boundaries vary considerably from one block structure to another. Different block structures may have the same stoichiometry (*e.g.*, the $(3x4)_1 + (3x5)_\infty$ structure of H-Nb_2O_5 and the two variants of $(4x4)_\infty$ structure found in M- and N-Nb_2O_5). Strips of different structure can therefore be incorporated, as intergrown lamellae or as part of a twinning mechanism, without change of stoichiometry. Small deviations from stoichiometry can arise not only from changes in oxidation state, but also from the incorporation of impurities that may catalyze the production of a particular, possibly metastable, crystal structure. Thus, N-Nb_2O_5, most readily

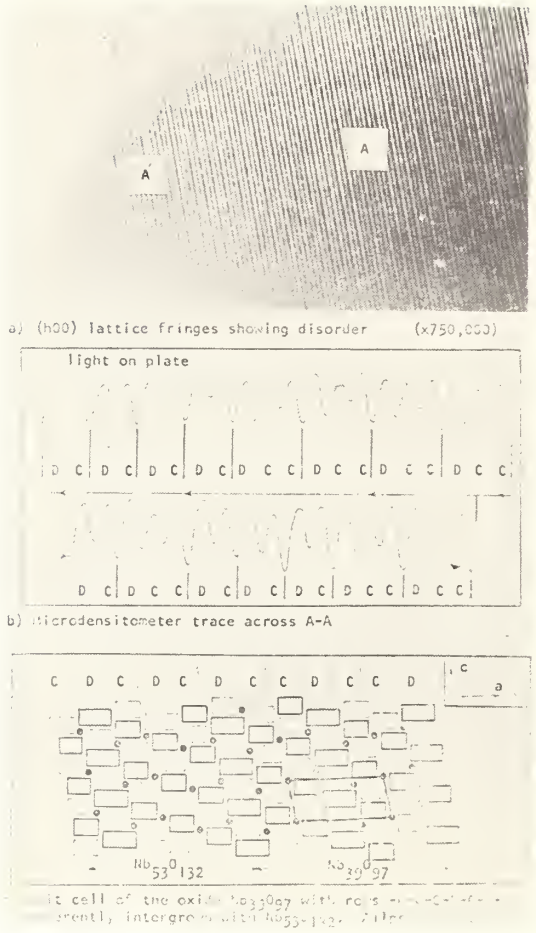

Fig. 14. Nonstoichiometry in Nb_2O_5-x: 1-dimensional (hoo) lattice fringes show intergrowth of $Nb_{39}O_{97}$ and $Nb_{53}O_{132}$ in $Nb_{28}O_{70}$ (H - Nb_2O_5).

obtained in the presence of F^- ions, tends to be doped with a low concentration of fluorine in place of oxygen, to give crystals with O+F/M slightly greater than 2.50000. In these circumstances, the evidence indicates that, as has been seen previously, the stoichiometric defect is concentrated into a localized fluctuation of composition that expresses itself in a local element of new structure, with different block sizes and/or block linkages from that of the surrounding matrix. Short range order is maintained. This may be illustrated by fig. 15, a lattice image of N-Nb_2O_5; the relation between the idealized block structure and the contrast distribution in the lattice image is shown on the micrograph. Over the field as a whole, the ribbons of linked, square (4x4) blocks can be recognized. At A, a strip of (4x3) blocks - unambiguously identified by their dimensions - is coherently incorporated, and this implies a local change in stoichiometry concentrated into this sheet of the crystal. The fault is finite; it terminates within the crystal at B, and reconstruction of the block structure, from the measured fringe positions, leaves no doubt that the crystal reconciles the fit of the blocks meeting at that point by building in a single linear fault - a single tunnel providing an array of tetrahedral cation sites.

These ways in which local order is strongly preserved, by a process analogous to the readjustment of shear plane spacings, prompt the question whether, (as in the crystallographic shear structures themselves) point defects are virtually eliminated. It is not possible, at the present time, to settle this question definitely, but the balance of evidence seems to favor the existence of anion vacancies or cation vacancies in some form. Allpress and Roth [35] have made a careful statistical study of the number and distribution of Wadsley

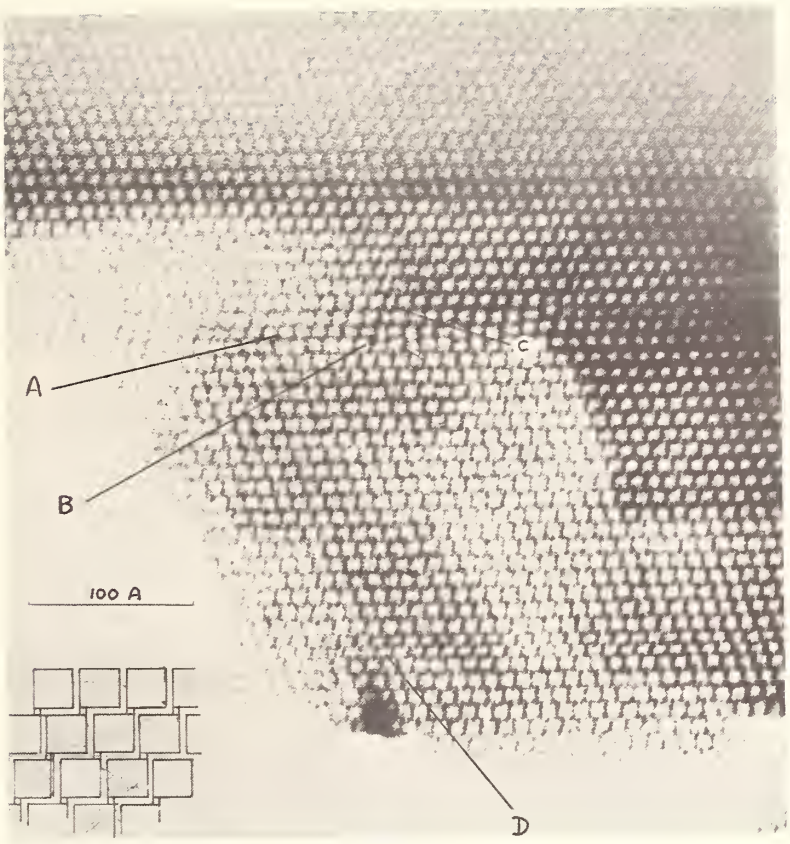

Fig. 15. Lattice image of N-Nb_2O_5 ($(4x4)_\infty$ structure, inset). At A, C, D strips of different ($(4x3)_\infty$) blocks. Faults A, C terminate at B in a single tunnel of tetrahedral sites.

defects in Nb_2O_5-rich $WNb_{12}O_{33}$ (composition range $MO_{2.5000}$- $MO_{2.5385}$). There are regular intergrowth phases in this system, with regularly recurrent ribbons of $(3x5)_\infty$ blocks inserted in the $(3x4)_1$ structure of $WNb_{12}O_{33}$; at low excess concentrations of Nb_2O_5, isolated ribbons of $(3x5)_\infty$ blocks appear as Wadsley defects. In the most carefully annealed preparations, at compositions between $WO_3.6Nb_2O_5$ ($MO_{2.5385}$) and $WO_3.8Nb_2O_5$ ($MO_{2.5294}$), the density of Wadsley defects was too low, and their mean spacing too great, to account for the deviation from the composition of the $(3x4)_1$ block structure. Similarly, in the reduction of H-Nb_2O_5, as mentioned above, the first step is that of conversion to the $(3x4)_2$ structure of $Nb_{25}O_{62}$, and this appears at 1000° in lamellar domains, which are incorporated at higher temperatures into intergrowths of $Nb_{53}O_{132}$ ($NbO_{2.4906}$) and $Nb_{39}O_{97}$ ($NbO_{2.4872}$) [34]. At compositions between $NbO_{2.5000}$ and about $NbO_{2.495}$, however, few Wadsley defects (lamellae of $(3x4)_2$ blocks) can be found. In both these instances there appears to be a narrow but experimentally significant range of anion:cation ratio in which there is a metal excess, with respect to the observed structure, not accounted for by extended defects. Since it is a metal excess, it cannot be explained by a variable occupancy of tetrahedral sites [32], but would seem to imply anion vacancies, interstitial cations or localized defect complexes based upon such point defects.

7. CONCLUSION

The theme underlying this paper has been that information about the real ultramicrostructure of defective crystals is essential for a theoretical treatment of their properties. The evidence advanced has been selective, but it is representative of those structures and systems about which most is now known. It is clear that, in the present state of the subject, no simple generalized treatment is feasible. The common property is an inbuilt ten-

dency towards attainment of order on a local scale if not at long range. Lattice energy calculations by Burch [36], confirm not only that ordered configurations are advantageous as compared with random distributions at significant defect considerations but that, as far as the electrostatic part of the lattice energy is concerned, there is little between radically different ways of achieving order - as between ordered vacancies and crystallographic shear in the rutile structure, for example. How crystals deal with defects thus depends on the more subtle and non-coulombic interactions. Specificity enters in this way, and no one model can embrace the whole of chemistry: neither crystallographic shear nor superlattice ordering is a universal explanation. At the end, and especially in ternary solid solution systems, we are left with localized defects, without information, as yet, whether they are point defects or extended defects. One obvious requirement is an extension of experimental methods to study such problems.

8. REFERENCES

[1] Kofstad, P., J. Phys. Chem. Solids 23 1579 (1962).
[2] Hurlen, T., Acta Chem. Scand. 13 365 (1959).
[3] Forland, K.S., Acta Chem. Scand. 18 1267 (1964).
[4] Kofstad, P. and Anderson, P.B., J. Phys. Chem. Solids 21 280 (1961), Blumenthal, J.B., Mason, J.B. and Whitmore, D.H., J. Amer. Ceram. Soc. 48 620 (1965).
[5] Kröger, F.A., *Chemistry of Imperfect Crystals,* North Holland Publ. Co. Amsterdam Chap. IX (1964).
[6] Reiss, H., Robert A. Welch Foundation Conference on Chemical Research XIV Solid State Chemistry, Houston 1970: in publication.
[7] Banus, M. D. and Reed, T. B., *Extended Defects in Nonmetallic Solids,* North Holland Publ. Co., Amsterdam, p. 488 (1970).
[8] Watanabe, D., Terasaki, O., Jostsons, A., Castles, J.R., *Extended Defects in Non-Metallic Solids,* North Holland Publ. Co. Amsterdam, P. 238 (1970).
[9] Ariya, S.M. and Morozowa, M.P., Russ. J. Chem. 28 2647 (1958), Ariya, S.M. and Popov, Y.G., Russ. J. Gen. Chem. 32 2077 (1962).
[10] Bevan, D.J.M., Baker, W.W. and Martin, R.L., *Rare Earth Research* Vol. 3, p.441, Gordon & Breach N.Y. (1965); Parks, T.C., Thornber, M.R. and Bevan, D.J.M., J. Solid State Chem. 1 536 (1970). Thornber, M.R., Bevan, D.J.M. and Summerville, E., J. Solid State Chem. 1 545 (1970).
[11] Vallet, P. and Raccah, P., Mem. Sci. Rev. Metall. 62 1 (1965). Fender, B.E.F. and Riley, F.D., J. Phys. Chem. Solids 30 793 (1969).
[12] Kofstad, P. and Hed, A.Z., J. Electrochem. Soc. 115 102 (1968.
[13] Koch, F. and Cohen, J.B., Acta Cryst. B25 275 (1969).
[14] Andersson, S. and Magneli, A., Naturwiss 43 (1956).
[15] Bursill, L.A., Hyde, B.G., Terasaki, O. and Watanabe, D., Phil. Mag. 20 347 (1969), Bursill, L.A. and Hyde, B.G., Acta Cryst. B27 210 (1971).
[16] Anderson, J.S. and Tilley, R.J.D., J. Solid State Chem. 2 472 (1970).
[17] Bursill, L.A. and Hyde, B.G., Phil. Mag. 23 3 (1971).
[18] Andersson, S., Sundholm, A. and Magneli, A., Acta Chem. Scand. 13 989 (1959).
[19] Bursill, L.A. Hyde, B.G., Phil. Mag. 23 1501 (1971).
[20] Gibb, R.M. and Anderson, J.S., J. Solid State Chem. In course of publication.
[21] Flörke, O.W. and Lee, C.W., J. Solid State Chem. 1 445 (1969).
[22] Gibb, R.M. and Anderson, J.S., In course of publication
[23] Tilley, R.J.D., Materials Res. Bull. 5 813 (1970).
[24] Allpress, J.G., Tilley, R.J.D. and Sienko, M.J., J. Solid State Chem. 3 440 (1971).
[25] Anderson, J.S. and Hyde, B.G., J. Phys. Chem. Solids 28 1393 (1967), Hyde, B.G., *Extended Defects in Nonmetallic Solids,* North Holland Publ. Co. Amsterdam p.347 (1970).
[26] Andersson, S. and Wadsley, A.D., Nature 211 581 (1966).
[27] Bursill, L.A., Proc. Roy. Soc. A. 311 267 (1969).
[28[Kihlborg, L., Arkiv. Kemi 21 443 (1963).
[29] Allpress, J.G., Personal communication; in course of publication.
[30] Roth, R.S. and Wadsley, A.D., Acta Cryst. 19 42 (1965), Wadsley, A.D., Helv. Chim. Acta Alfred Werner Volume p. 207 (1967).
[3]] Wadsley, A.D. and Andersson, S., *Perspectives in Structural Chemistry,* Vol. III Wiley, New York (1970).
[32] *e.g.*, Anderson, J.S., *Problems of Nonstoichiometry,* Ed. A. Rabenau, North Holland Publ. Co. p.1 (1970).

[33] Allpress, J.G., Sanders, J.V. and Wadsley, A.D., Acta Cryst. B25 1156 (1969, Allpress, J.G., J. Solid State Chem. 1 28, 66 (1970); 2, 78, 366 (1970).
[34] Nimmo, K.M. and Anderson, J.S., To be published.
[35] Allpress, J.G. and Roth, R.S., J. Solid State Chem. 3 209 (1971).
[36] Burch, R. and Anderson, J.S., J. Phys. Chem. Solids and unpublished work.

DISCUSSION

P. Hagenmuller: I would like to make a comment about the rather important question you raised: do we have two phases or one phase in a given specimen? My question would be , do we really have an equilibrium situation because the phase rule only corresponds to an equilibrium situation?

J. S. Anderson: This is a very difficult point to decide, as Dr. Hyde knows from his very careful work on rutile. It is exceedingly difficult to get anything, in operational terms, which corresponds to the purely hypothetical concept of thermodynamic equilibrium and a thermodynamically reversible process. Anything we do perturbs the system and it never can recover. I don't know. I don't know whether one can say any more than that we see steady state situations.

J. M. Honig: I was wondering, in connection with your earlier discussion, whether you could not get screening of point charges in solids whenever you have a lot of mobile electrons around so that you could turn the long range coulomb forces off. In which event I would imagine that those materials would be subject to the laws of independent point charges. Is this a correct assumption?

J. S. Anderson: Certainly, it is a closer approach to it. All I know is that in some materials, not necessarily oxides, but for instance the carbon deficient niobium carbide phase, there is a strong site preference for a third nearest neighbor and this is not something that you control by any simple coulomb interactions, I think.

R. S. Roth: I want to go back to the first comment of Professor Hagenmuller. I think we must remember the original statement that Dave Wadsley made after John Allpress took the first lattice image pictures of the niobium-tungsten oxide shear phases. Wadsley's statement was that "The definition of equilibrium depends upon the wavelength used to examine it." The second point I wish to emphasize is the following. As John Allpress and I have demonstrated with these phases[1], if after examining with the electron microscope and realizing you have not reached equilibrium, you then make a really concerted attempt to obtain equilibrium in such a specimen by month-long heatings just below the melting point, you *can* order up these phases. I think we have to say that when you are looking at a system that has random shear planes, Wadsley defects, it is a non-equilibrium situation. It is neither one phase nor two phases. Perhaps I should coint a new word for a poorly equilibrated specimen, it is gunk, and that is all you can consider it. It may be a little more than just a physical mixture, but it is still a non-equilibrium situation.

J. S. Anderson: Well, I agree with you it is a non-equilibrium situation. What I say we do not know is what an arbitrary composition would come to when it was finally brought to equilibrium. I strongly suspect that *some* of these might really present your concept of an infinity of ordered structures. They would find some way of accommodating any possible composition within some, if necessary very complex, stacking or ordered arrangement.

[1] J. G. Allpress and R. S. Roth, J. Solid State Chem. 3, 209 (1971).

National Bureau of Standards Special Publication 364, Solid State Chemistry, Proceedings of 5th Materials Research Symposium, issued July 1972.

OXYGEN DISSOCIATION PRESSURES AND PHASE BEHAVIOR IN THE TRANSPLUTONIUM OXIDES*

T. D. Chikalla and R. P. Turcotte

Fuels and Materials Department
Battelle Memorial Institute
Pacific Northwest Laboratories
Richland, Washington 99352

The results of recent oxygen vapor pressure measurements over nonstoichiometric AmO_x, CmO_x, and BkO_x are presented. These include derived information concerning the phase relations and partial thermodynamics of oxygen solution over the range $1.5 < x < 2.0$ and $300 < T < 1200$ °C.

The americium-oxygen system has been examined by thermogravimetric techniques in the single phase α region for $1.80 < x < 2.00$ to yield relative partial molar heat and entropy data. Supporting information obtained by quench methods and x-ray diffraction analysis extend the results to lower compositions and, additionally, demonstrate the existence of a bcc σ phase over a wide composition range. Phase relations in the curium-oxygen system have been defined by a series of isobars in the pressure range $2 < p_{O_2}$ (mm) < 730. In addition to α and σ phase, compounds of more narrow compositional width are seen at $CmO_{1.72}$ and $CmO_{1.82}$, and a plausible phase diagram is constructed. Differences obtained on two curium isotypes of greatly different radioactivity are discussed. The berkelium-oxygen system has been examined using a novel capacitance manometer system and a 1.2 mg sample. A set of five isotherms was obtained over the range $852 < T$ (°C) < 1150. The isotherms show a regular variation across α and σ regions separated by a diphasic field at $x \sim 1.79$. In addition, a narrow two-phase region exists between $BkO_{1.91}$ and $BkO_{1.93}$. Certain similarities are shown to exist between this and certain other fluorite related ternary oxide systems.

In addition, melting behavior of the di- and sesquioxides and polymorphism in the sesquioxide is described over the entire actinide series.

Key words: Actinide oxides; actinide sesquioxides; americium oxides; berkelium oxides; curium oxides; melting points of actinide oxides; nonstoichiometry; oxides; thermodynamics.

1. INTRODUCTION

The recent investigations of transplutonium oxides in this laboratory and others have progressed to the point at which compilation of the existing information is of value. Indeed, understanding of the actinide oxide systems in the $M^{3+} - M^{4+}$ regime is yet primative by comparison to other areas of solid state science. In detail, the behavior in each of the systems for $1.5 < x < 2.0$ in MO_x (where M = Am, Cm, Bk) is markedly different and we observe the systematic trends ascribed to these elements as a family only in a coarse comparison.

*This paper covers work performed by Battelle-Northwest under AEC Contract No. AT(45-1)-1830

At the end member compositions (x = 1.500 and x = 2.000), the behavior through the series is more regular, and phase relations (polymorphism) in the sesquioxide are now well documented for both the actinide and lanthanide series [1,2][1]. It is our primary interest to consider the phase behavior in what would normally be considered the nonstoichiometric field where 1.5 < x < 2.0 and the sesquioxide is of the fluorite related C-type structure. In an effort toward completeness, the high temperature phase diagram and melting behavior of the stoichiometric end member oxides is discussed in the first section. We call attention to a previous discussion of the fluorite related actinide oxide systems that serves as a basis in some respects for the extension presented here [3].

2. M_2O_3 AND MO_2

The melting behavior of the actinide dioxides and sesquioxides has recently been reviewed [2]. In addition, polymorphism in the sesquioxide has been correlated with ionic radii for both the actinide and lanthanide series.

There are no melting point data for oxides higher than curium. As shown in figure 1, a reasonably linear decrease in the melting point of the dioxides with increasing Z is observed, while the opposite trend is true for the sesquioxides. The heats of formation of the actinide dioxides decrease in a similar manner which reflects the lowering of bond energies with increasing atomic number. The increasing stability of the sesquioxides with increasing Z parallels behavior in the lanthanides, where the melting point increases to a maximum at Gd_2O_3, whereafter it remains essentially constant [1]. If the same behavior occurs in the actinides, this maximum may exist at Cm_2O_3, which, based on electronic configuration, is the actinide homologue of Gd_2O_3.

Phase transformation behavior for both lanthanide and actinide sesquioxides shows a good correlation of the thermal stability domains of the various polymorphs and ionic radii (fig. 2). The five crystallographic modifications for the sesquioxide include A (hexagonal), B (monoclinic), C (cubic), H (hexagonal), and X (cubic) forms. It is interesting to note that the high temperature H-form sesquioxide is probably the only crystal structure common to all of the lanthanide and actinides with the exception of Lutetium. Relevant to later discussion, the metastability of the C-type structure relative to C → B or C → A transitions in the < 1000 °C temperature range should be pointed out. This is really to be expected at these temperatures, where necessary cation movement is slow.

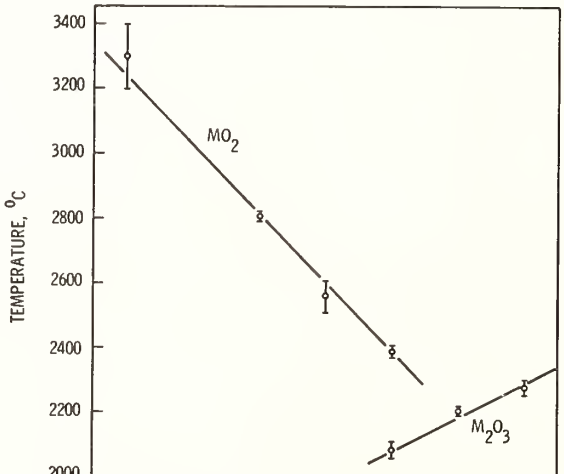

Fig. 1. Melting points of actinide di- and sesquioxides.

[1] Figures in brackets indicate the literature references at the end of this paper.

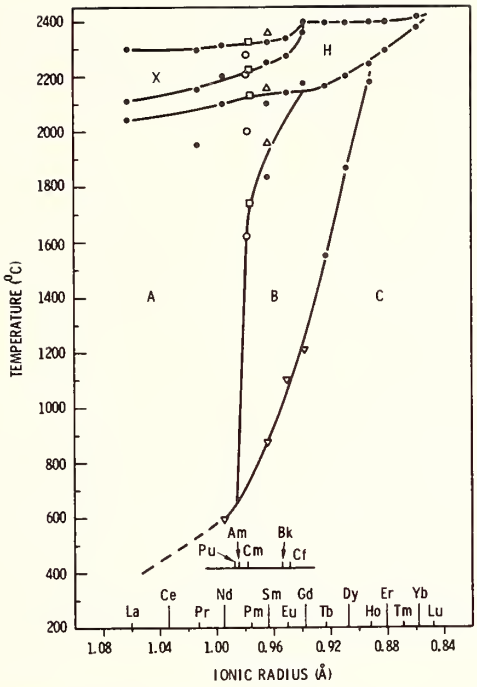

Fig. 2. Stability diagram of polymorphic forms of lanthanide and actinide sesquioxides.

● - high temperature transformations (ref. 1).
○ - Cm_2O_3 transformation temperatures (ref. 2).
□ - Pm_2O_3 transformation temperatures (ref. 2).
△ - Sm_2O_3 transformation temperatures (ref. 2).
▽ - low temperature transformations (ref. 23).

3. AmO_x

The early dissociation pressure measurements of Asprey and Cunningham [4] with a milligram-size sample demonstrated the existence of an AmO_{2-x} (α) phase to at least x = 0.15. More recent work at lower temperatures by Chikalla and Eyring [5] by a tensimetric method agreed with the early measurements and allowed accurate determination of the partial thermodynamic quantities. The isotherms (fig. 3) are smooth curves over the entire measured range 1.80 < O/Am < 2.00. Thermodynamic equilibrium was demonstrated at all but the lowest temperature where data were taken in reduction only. There is a notable change in slope in the isotherms at O/Am = 1.98-1.96, reflecting a change in defect structure, at this time undefined. The partial molar entropy and enthalpy obtained by the relations

$$\Delta\bar{S}_{O_2} = -\partial(\Delta\bar{G}_{O_2})/\partial T \qquad (1)$$

$$\Delta\bar{H}_{O_2} = R\,\partial(\ln p_{O_2})/\partial(1/T) \qquad (2)$$

are given in figure 4, again indicating a larger rate of change at the high composition end of the α field.

An x-ray diffraction analysis of quenched samples was made across the entire compositional width 1.50 < O/Am < 2.00 [6]. These show the formation of a bcc phase (σ) in the range 1.50 < O/Am < 1.67. Samples annealed in the α region could not be quenched but always gave a two-phase mixture of $AmO_{2.00}$ and a phase of estimated composition $AmO_{1.8}$. By implication, it was suggested that another diphasic region must exist in the interval 1.67 < O/Am < 1.8.

465-504 O - 72 - 22

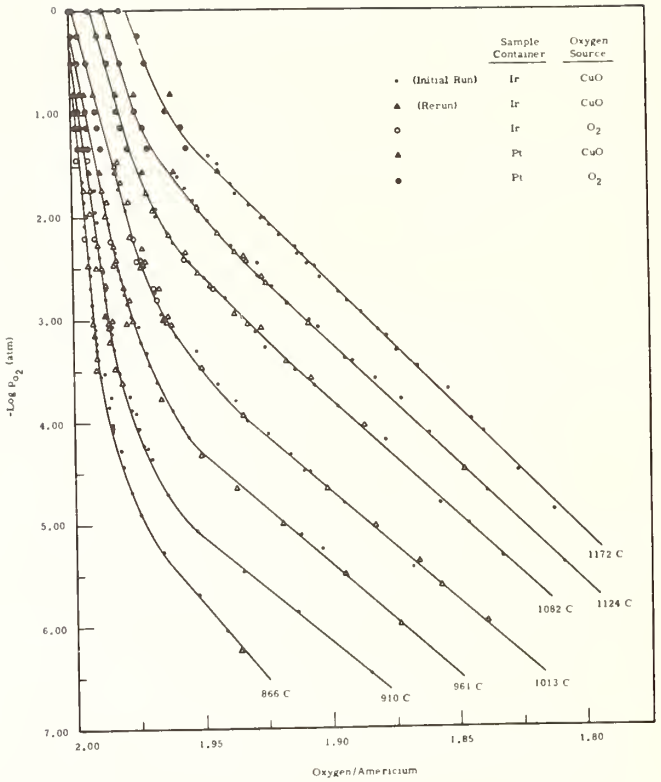

Fig. 3. Dissociation pressure isotherms for AmO_x.

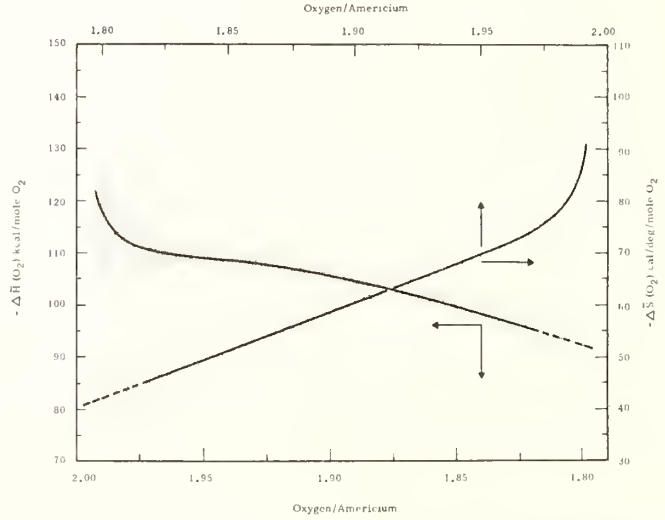

Fig. 4. Partial molar entropy and enthalpy for AmO_x.

These results may be compared to a recent investigation of the system by ceramographic and DTA methods by Sari and Zamorani [7]. A phase diagram is suggested which closely parallels that for the PuO_x system but which is at some variance with these earlier data. A miscibility gap of two α phases shows closure at 1000 °C. The low composition phase intersects the σ field at O/Am $\cong$ 1.98, while the high composition phase approaches O/Am $\simeq$ 1.98 at a temperature of ~ 850 °C.

As discussed above, the x-ray work [6] would suggest a greater complexity in the 1.67-1.80 region and that the σ field extends to the 1.50 composition rather than to 1.63 as indicated by Sari and Zamorani [7]. Clearly, these differences can be resolved only by equilibrium studies over the full range of composition, most importantly by high temperature diffraction methods.

4. CmO_x

Posey et al. [8] reported the first thermograms for the decomposition of CmO_2, followed shortly after by Mosley [9], whose effort concentrated on the sesquioxide as a candidate isotopic fuel. Chikalla and Eyring [10] published results of a detailed study of dissociation pressure - composition - temperature relations obtained using a thermobalance technique. Most recently, a similar study of $^{248}CmO_x$ has been completed on a sub-milligram sample using an automated capacitance manometer system [11]. All previous studies were made on ^{244}Cm, which is an alpha emitter with a half life of 18.1 years compared to 3.7×10^5 years for the ^{248}Cm isotope. It was the objective of this study to assess possible differences in the chemical nature of the Cm-O system due to radiation damage.

Since only 0.68 milligram of ^{248}Cm oxide was available, classical microbalance methods for studying dissociation behavior could not be used. The differential capacitance manometer system employed (fig. 5) is capable of detecting gaseous uptake or evolution of $< 10^{-10}$ moles of gas. The major problem in realizing an accuracy approaching this sensitivity level is the elimination of system effects either due to physical or chemical changes. The capabilities of the system and detailed information concerning its construction and reduction of data have been reported [12].

For the $^{248}CmO_x$ sample, isobaric traces were recorded with a sensitivity which allowed composition to be estimated to 0.001 in x. In the present case, the assumption of three (P-T-x) points (x = 1.500, 1.714, 2.000) was used to fix correction curves (ΔP_{system} versus T) for each isobar independently of any other run. The corrections were very small at lower pressures (< 50 mm Hg), but at 760 mm Hg, approached values as high as 30% of the pressure change due to complete sample reaction. Analysis of the data suggests an uncertainty of ± 0.003 in O/Cm for the stoichiometry measurement.

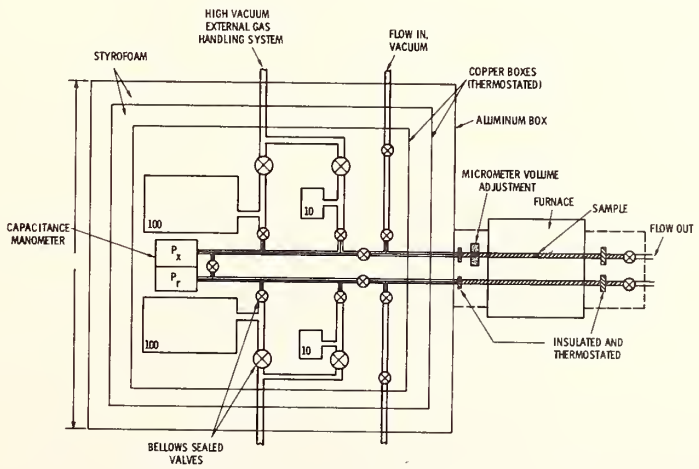

Fig. 5. Capacitance manometer system.

The $^{244}CmO_x$ results [10] demonstrated the existence of a number of intermediate phases in close parallel to the behavior of the rare earth systems CeO_x, PrO_x and TbO_x, now well established. (See [3] for references.) Representative isobars are given in figure 6. The decomposition is seen to proceed through a narrow region of CmO_{2-x} (α), to phases $CmO_{1.82\pm x}$ (δ) and $CmO_{1.72}$ (ι) and finally $CmO_{1.5+x}$ (σ). Complete reduction to the sesquioxide was not achieved even in a H_2 atmosphere.

These results may be compared to isobars of the $^{248}CmO_2$ decomposition at an oxygen pressure of 735 mm Hg in figure 7. The similarities are evident. The major apparent differences are the shift of composition for the δ phase to $CmO_{1.80\pm x}$ and the ease of reduction to the sesquioxide at ~ 865 °C. The three isobars shown demonstrate that the degree of completion of the $\sigma \rightarrow Cm_2O_3$ decomposition relates directly to the subsequent oxidizability of the product. The oxidation resistance of the B-form sesquioxide has been discussed by Mosley [9], where no oxidation was observed in 1 atm O_2 except for $250 < T < 520$ °C. Thus, we interpret the break from σ to lower compositions as a $\sigma \rightarrow B - Cm_2O_3$ decomposition. This interpretation is, however, not consistent with the kinetic data [9] for the transformation $C \rightarrow B$ since no conversion occurred below 900 °C and 1290 °C was required for completion. We ascribe this difference to impurity or crystallite size differences and note the long history of different temperatures reported for the rare earth oxide polymorphic phase transformations.

The ^{244}Cm and ^{248}Cm results may be more completely compared by the phase boundary plot of figure 8. There are marked temperature shifts for several of the reactions and differences in entropy values (slopes of the RT ln p_{O_2} versus T lines). The vertical lines obtained in the low temperature region of the α-δ boundary and the $\sigma \rightarrow B$ boundary are taken to indicate non-thermodynamic behavior (kinetic limitations), while the remaining reaction boundaries give reasonable changes in entropy ~ 40-60 eu. It is remarkable that the $^{244}CmO_x$ data for α-δ do show an acceptable temperature dependence even though occurring at temperatures ~30 °C lower. We ascribe this increased oxygen mobility to self-radiation, and point out the recent observation of Noe and Fuger [13] that $^{244}CmO_2$ may release oxygen even at room temperature when in vacuum.

The large temperature shift in the $\sigma \rightarrow \iota$ boundary to higher values in $^{248}CmO_x$ and the marked change in slope of the $\iota \rightarrow \sigma$ reduction are not well understood. It is to be expected that effects due to radiation damage are much reduced at these temperatures due to annealing.

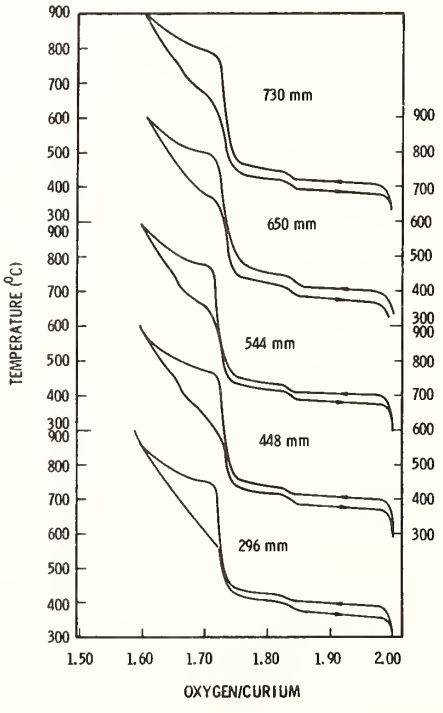

Fig. 6. Selected $^{244}CmO_x$ isobars.

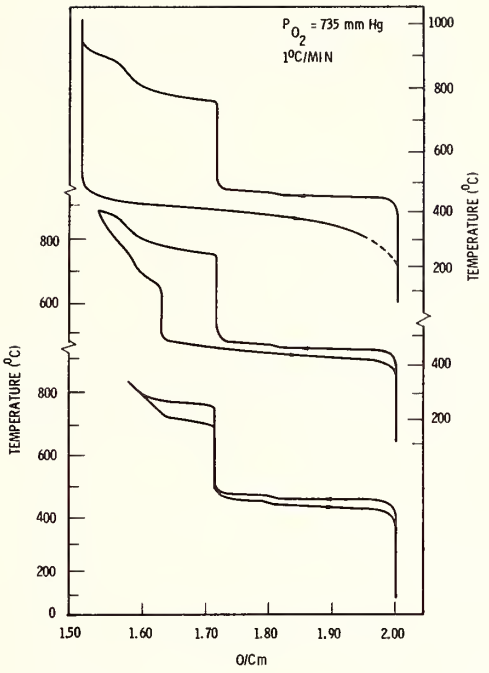

Fig. 7. Isobars for $^{248}CmO_x$ at 735 mm Hg O_2.

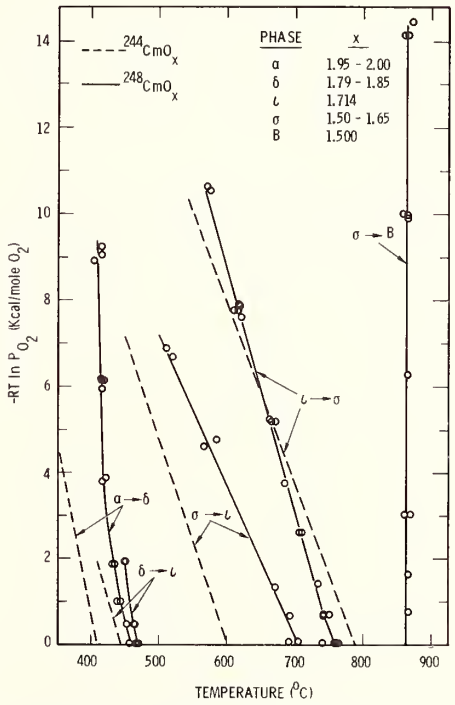

Fig. 8. Partial molar free energy versus T at phase boundaries in CmO_x.

Sample purity of the $^{248}CmO_x$ at 99.9 mol % was higher than for the $^{244}CmO_x$ sample which contained 2.5 mol % AmO_2 and approximately 0.4% other impurities, mainly Fe and Si. Purity and other physical differences must play some role in these types of reaction, at a level, however, which is unknown.

The phase diagram for the CmO_x system (fig. 9) has not been altered from that given previously [10]. The $^{248}CmO_x$ results suggest only minor changes and any significant revision will require a detailed high temperature x-ray diffraction examination of the system under controlled oxygen pressures.

5. BkO_x

With the exception of a few x-ray diffraction studies on Bk_2O_3 and BkO_2, the only work on the BkO_x system was by Turcotte, Chikalla and Eyring [14]. The paucity of data is readily attributable to its scarcity and short (314 day) half life. The decay mechanism predominantly involves a 114 KeV beta, introducing californium-249 ($t_{1/2}$ = 360 yrs) at the rate of about 1.5%/week.

Since only milligram samples of this element were available and the weight loss for a $BkO_2 \rightarrow BkO_{1.5}$ decomposition is 34.2 μg per milligram of BkO_2, balance techniques were ruled out and the capacitance manometer system was developed as described earlier. The 1.22 mg sample was investigated in the temperature interval 852-1150 °C and oxygen partial pressures from 10^{-7} to 10^{-20} atm.

The low oxygen pressures required to attain equilibrium with various nonstoichiometric BkO_x compositions were set by appropriate CO_2/CO mixtures. The equilibration of a given gas mixture with the sample was made isothermally followed by cooling to 500 °C in vacuum. At this point, the reduced sample was quantitatively oxidized to $BkO_{2.00}$. Repetition of this procedure with various CO_2/CO ratios and with appropriate evacuations and flushings resulted in the isotherms shown in figure 10. The data shown are grouped according to ^{249}Cf content which varied from 3 to 13% during the course of the experiment. The conditions of oxidation of the substoichiometric BkO_x preparations (7 mm O_2 and 500 °C) were not sufficient to oxidize the Cf present significantly above O/Cf = 1.50. The ingrowing californium was thus treated as an inert impurity in correlating the raw data and O/Bk values. Structurally, it is virtually certain that the Cf^{+3} was fully incorporated in solid solution and the data obtained refer to the ternary $(Bk_y, Cf_{1-y})O_x$. It is likely, however, that the dissociation pressures are little different for the pure BkO_x system as suggested by the present results and by the small changes observed in other studies as in $U_{1-z}Ce_zO_{2-x}$ [15] relative to CeO_x and in $U_yTh_{1-y}O_{2+x}$ [16] relative to UO_{2+x}.

The interpretation of the plateau regions shown in figure 10 and by the derived thermodynamic quantities (fig. 11) is complicated by a variety of possibilities suggested by phase relations in other binary and ternary fluorite related oxide systems. Without x-ray diffraction analysis, we can only speculate as follows: a single phase $BkO_{1.5+x}$ (σ) region extends

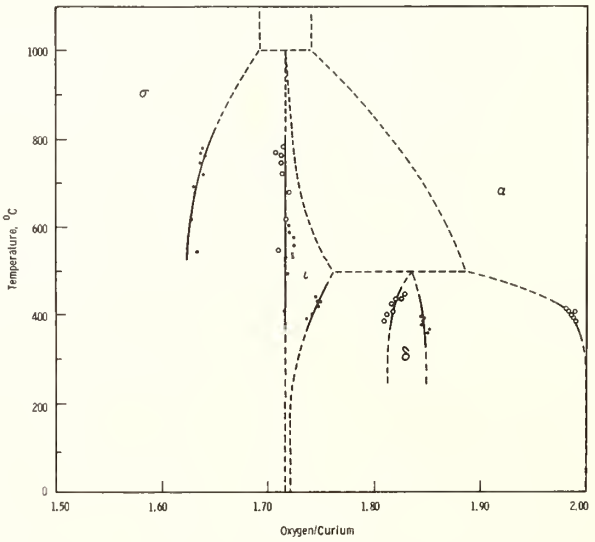

Fig. 9. Phase relations for CmO_x.

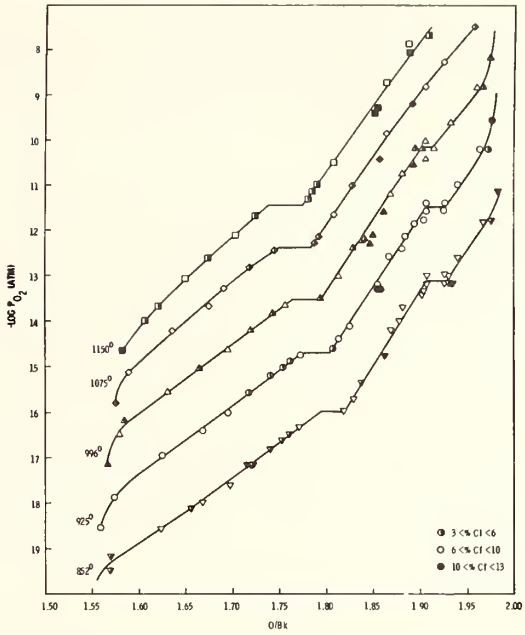

Fig. 10. Dissociation pressure isotherms for BkO_x.

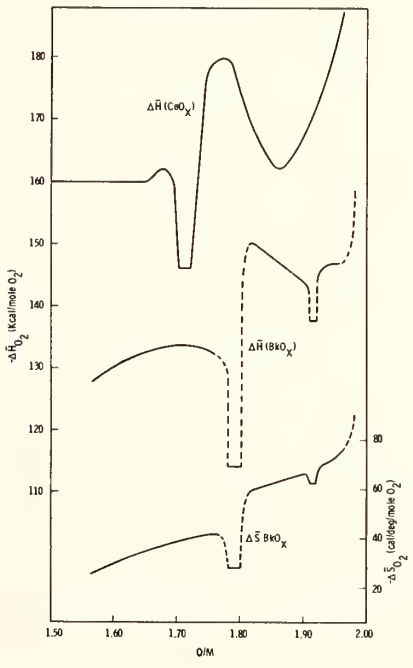

Fig. 11. Partial molar entropy and enthalpy for BkO_x.

from low compositions up to a maximum O/Bk which is a function of temperature (1.73 at 1150 °C and 1.78 at 852 °C). A two-phase region separates σ from the BkO_{2-x} (α) region which extends to near the dioxide composition unperturbed at 1075 and 1150 °C but which is broken into α and α' regions at the lower temperatures.

Alternatively, the observed plateaus (fig. 10) at O/Bk ~ 1.92 may be related to recent observations of several phases of narrow composition width in the ternary systems $(U,Ce)O_x$ [15], $(Zr,Sc)O_x$ [17], $(Hf,Sc)O_x$ [18] and $(Hf,Y)O_x$ [19]. We note in these systems also that,

in general, the major intermediate formed is not $MO_{1.714}$ (as for the pure Ce, Pr, Tb and Cm oxide systems), but the nonstoichiometric pyrochlore phase (mean O/M = 1.75) predominates. Although unobserved in any of the binary systems, radii considerations relative to Roth's data [20] do not rule out this possibility as explaining the mid-field plateau observed at O/Bk = 1.73 - 1.82 in the $(Bk,Cf)O_x$ system.

6. CfO_x AND HIGHER Z OXIDES

The isotopes including californium and all those of higher atomic number, have not been examined tensimetrically. Baybarz et al. [21], however, have prepared $^{249}CfO_2$ by oxidation of Cf_2O_3 in approximately 100 atm O_2 or by use of atomic oxygen. During the course of these preparations, samples of intermediate compositions were obtained which tended to cluster about compositions O/Cf = 1.56, 1.70 and 1.80 as estimated by lattice parameter considerations. By analogy to the rare earth systems, the better crystallized preparations of the 1.7-1.8 compositions showed rhombohedral distortion.

The heavier actinides offer isotopes of increasingly lower half-lives. Einsteinium-253 ($t_{1/2}$ = 20 days) and fermium-257 ($t_{1/2}$ = 94 days) will likely be the last elements amenable to solid state studies (excluding possible stable super-heavy elements) if and when they become available in suitable quantities.

7. SUMMARY

In summary, the chemical behavior of the transplutonium actinide elements as seen through the behavior of the (M^{3+}, M^{4+}) oxides supports the concept that they should be generally similar, but in detail they are clearly individual. Of this series, berkelium would seem anomalous if indeed curium and californium are as similar as indicated. This is perhaps related to the half-filled 5f subshell of Bk (IV) or to perturbation by the ingrowing Cf in the sample studied. On the other hand, AmO_x does not appear to form the ordered intermediate phases suggested for CmO_x and CfO_x.

The thermodynamics obtained from these studies have no general theory to which they can be compared and the influence of impurities on entropy changes, for example, have not been adequately investigated. The structural details to which correlation must be made are not available, particularly in the grossly nonstoichiometric regions.

For the actinide oxides, the question of future studies is related to both the stability and very small quantities in existence as already noted and to the oxygen pressure range and temperatures experimentally accessible. In figure 12, we have compared oxidation-reduction potentials for the M^{III}-M^{IV} couple [22] with dissociation pressures over $MO_{1.90}$ at 900 °C using the known data for Pu, Bk and Am oxides. Error bars for the redox potentials of ± 0.2 V are high and the very excellent fit of the three points should not be taken as too meaningful. The data do predict correctly, however, that the Cf higher oxide requires greater O_2 pressures for formation than Cm. It is clear that measurement of oxidation of Es^{3+} and the heavier elements will be virtually impossible even considering the reduction in dissociation pressures of approximately 15 units in log p_{O_2} for a temperature reduction to 400 °C and another approximately 8 units if one considers a composition $MO_{1.51}$. More clearly stated, the dissociation pressure over a hypothetical $EsO_{1.51}$ oxide at 400 °C would be on the order of 10^{15} atmospheres of oxygen. It is worth pointing out here that a consideration of the lanthanide III-IV potentials reveals that all but Ce, Pr and Tb have similar or lower values than Es and indeed none have been prepared in the +4 state.

A summary of the known phases in the (III-IV) field is given in table 1 for all of the actinides. The progression from high stability for the +4 ion at Th proceeds with increasing Z through a crossover to the case of a highly stable +3 oxidation state as already indicated. It is the intermediate group from Np through Cf which offers the formation of compounds of mixed valence as the pure oxides and a host of ternary systems all showing behavior which in detail we are only now beginning to examine at a level necessary for full understanding and possible utilization.

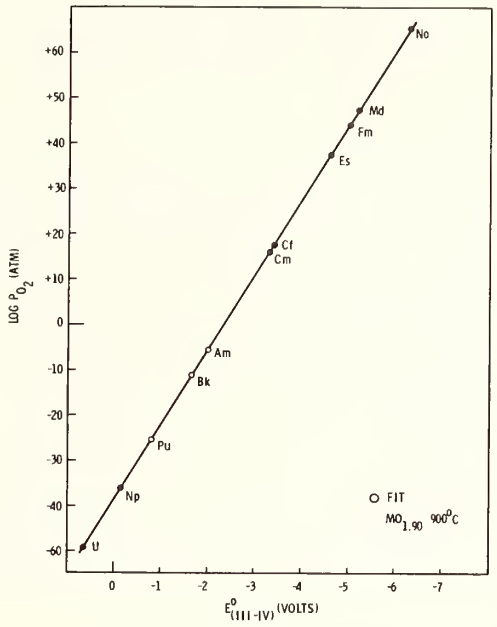

Fig. 12. M^{III-IV} redox potentials versus dissociation pressures over $MO_{1.90}$ at 900 °C.

Table 1

Fluorite Related Phases in the Actinide Oxides

	OBSERVED PHASES $(M^{+3}, M^{+4})O_x$					
M	$MO_{1.500}$ C	$MO_{1.5+x}$ σ	$MO_{1.714}$ i	$MO_{1.82\pm x}$ δ	MO_{2-x} α	$MO_{2.000}$ F
Th					✓	✓
Pa						✓
U					✓	✓
Np					✓	✓
Pu	✓	✓			✓	✓
Am	✓	✓			✓	✓
Cm	✓	✓	✓	✓	✓	✓
Bk	✓	✓			✓	✓
Cf	✓	✓	✓(?)	✓(?)	✓	✓
Es	✓(?)					

8. REFERENCES

[1] Foëx, M. and Traverse, J. P., Bull. Soc. Fr. Miner. Crist. 89, 184 (1966).

[2] Chikalla, T. D., McNeilly, C. E., Bates, J. L. and Rasmussen, J. J., *High Temperature Phase Transformations in Some Lanthanide and Actinide Oxides*, BNWL-SA-3818, presented at the International Colloquium on High Temperature Phase Transformations, Odeillo, France, September 1971.

[3] Eyring, L, Adv. in Chem. Ser. #71, Chapter 6, 1967.

[4] Asprey, L. B. and Cunningham, B. B., USAEC Report UCRL-329, (1949).

[5] Chikalla, T. D. and Eyring, L., J. Inorg. Nucl. Chem. 29, 2281 (1967).

[6] Chikalla, T. D. and Eyring, L., J. Inorg. Nucl. Chem. 30, 133 (1968).
[7] Sari, C. and Zamorani, E., J. Nucl. Mat. 37, 324 (1970).
[8] Posey, J. C., Kuehn, P. R. and McHenry, R. E., Abstr. & Papers, 150th Meeting ACS, Atlantic City (1965).
[9] Mosley, W. C., paper presented at ACS Symposium on Macroscopic Studies of the Actinides, San Francisco, 1968.
[10] Chikalla, T. D. and Eyring, L., J. Inorg. Nucl. Chem. 31, 85 (1969).
[11] Turcotte, R. P., Chikalla, T. D. and Eyring, L., unpublished data.
[12] Turcotte, R. P., Chikalla, T. D. and Eyring, L., Anal. Chem. 43, 958 (1971).
[13] Noe, M. and Fuger, J., Inorg. Nucl. Chem. Letters 7, 421 (1971).
[14] Turcotte, R. P., Chikalla, T. D. and Eyring, L., J. Inorg. Nucl. Chem. 33, 3749 (1971).
[15] Markin, T. L. and Crouch, E. C., J. Inorg. Nucl. Chem. 32, 77 (1970).
[16] Aronson, S. and Clayton, J. C., J. Chem. Phys. 32, 749 (1969).
[17] Thornber, M. R., Bevan, D. J. M. and Sommerville, E., J. Solid State Chem. 1, 545 (1970).
[18] Kalinovskaya, C. A., Spiridinov, E. M. and Komissarova, L. N., J. Less Comm. Metals 17, 151 (1969).
[19] Didcot, M., Vicot, J. and Deportes, C., J. Solid State Chem. 2, 236 (1970).
[20] Roth, R. S., J. Res. NBS 56, 17 (1956).
[21] Baybarz, R. D., Haire, R. G. and Fahey, J. A., ORNL, private communication, submitted to J. Inorg. Nucl. Chem.
[22] Nugent, L. J., Baybarz, R. D., Burnett, J. L., and Ryan, J. L., J. Inorg. Nucl. Chem. 33, 2503 (1971).
[23] Warshaw, I. and Roy, R., J. Phys. Chem. 65, 2048 (1961).

National Bureau of Standards Special Publication 364, Solid State Chemistry, Proceedings of 5th Materials Research Symposium, issued July 1972.

BINARY SOLID SOLUTIONS OF PaO_2 AND OTHER ACTINIDE DIOXIDES AND THEIR EXCHANGE EQUILIBRIA WITH MOLTEN SALT REACTOR FLUORIDES[1]

C. E. Bamberger, R. G. Ross, and C. F. Baes, Jr.

Oak Ridge National Laboratory
Oak Ridge, Tennessee 37830

The dioxides of thorium, protactinium, uranium and plutonium all are relatively insoluble in molten mixtures -- containing LiF, BeF_2, ThF_4, PaF_4, and UF_4 or UF_3 -- which serve as the fuel of the molten salt nuclear power reactors (MSR's). Since these dioxides can form substitutional solid solutions, exchange reactions of the type

$$ThO_2(ss) + MF_4(d) \rightleftarrows ThF_4(d) + MO_2(ss); \quad Q^M_{Th} = \frac{X_{MO_2}}{X_{ThO_2}} \frac{X_{ThF_4}}{X_{MF_4}}$$

involving the solid solution (ss) and the molten fluoride phase (d) become possible. It is of interest to study such exchange equilibria not only because the inadvertent precipitation of fissile oxide solids from an MSR fuel should be avoided, but also because such reactions might provide a means of separating and recycling the fissile and fertile elements.

A study of the exchange reaction involving Pa^{4+} and Th^{4+} has been carried out in which PaO_2-ThO_2 solid solutions ($X_{PaO_2} \leq 0.33$) were formed by equilibration of ThO_2 with molten LiF-BeF_2-ThF_4-PaF_4 (72-16-12-0.05 mol %) in the temperature range 570-730 °C. The resulting values of the distribution quotient Q^{Pa}_{Th}, along with previously measured values of Q^{U}_{Th} and a value of Q^{Pu}_{Th} derived indirectly from other previous measurements, are consistent with the following expressions

$$\ln \gamma_{MO_2} = 10^6\left(\frac{1.228 \pm .15}{T}\right)\left(\frac{\Delta a}{a_{ThO_2}}\right)^2 X^2_{ThO_2} \; ; \; \ln \gamma_{ThO_2} = 10^6\left(\frac{1.228 \pm .15}{T}\right)\left(\frac{\Delta a}{a_{ThO_2}}\right)^2 X^2_{MO_2}$$

$$\ln Q^M_{Th} = 10^6\left(\frac{1.318 \pm .03}{T}\right)\left(\frac{\Delta a}{a_{MO_2}\, a_{ThO_2}}\right) + 10^6\left(\frac{1.228 \pm .15}{T}\right)\left(\frac{\Delta a}{a_{ThO_2}}\right)^2 (2X_{MO_2} - 1)$$

wherein the activity coefficients in the solid solution are related to the difference in the lattice parameters ($\Delta a = a_{ThO_2} - a_{MO_2}$) as suggested by Hietala's model.

Key words: Activity coefficients in solid solutions; equilibrium of actinide oxides and molten fluorides; heat of mixing in solid solutions; ion exchange between solid oxides and molten fluorides; lattice parameter of actinide oxides; molten fluorides; molten salt reactor; oxide solid solutions; equilibria with molten fluorides; plutonium dioxide; protactinium dioxide; thorium dioxide; uranium dioxide.

[1]Research sponsored by the U. S. Atomic Energy Commission under contract with Union Carbide Corporation.

1. INTRODUCTION

Molten salt reactors (MSR's) are nuclear power reactors in which the fissile material can be either $^{233}UF_4$, $^{235}UF_4$, or $^{239}PuF_3$ dissolved in a molten salt consisting mainly of ^7LiF and BeF_2 [1][2]. When $^{232}ThF_4$ is added, it is converted by a neutron capture and successive β-decays first to ^{233}Pa and then to fissile ^{233}U. Such reactors thus can replace a portion or all of the fissile material they consume, or even produce (breed) more fuel than they consume. The oxide chemistry of these actinide elements in this fluoride media is important because: (a) their inadvertent precipitation by oxide impurities within the reactor core could compromise reactor safety; (b) such oxides might be useful in separating and recycling the actinide elements.

If a soluble oxide is added to the $LiF-BeF_2-ThF_4$ molten mixture which serves as the solvent salt for the fuel of an MSR, ThO_2 is precipitated. When UF_4 is present, the oxide precipitate formed at equilibrium is a solid solution of UO_2 and ThO_2 which undergoes the exchange equilibrium

$$ThO_2(ss) + UF_4(d) \leftrightharpoons ThF_4(d) + UO_2(ss) \tag{1}$$

(where *d* and *ss* denote, respectively, species dissolved in the molten fluoride phase and in the oxide solid solution phase). In a study of this equilibrium [2], it was found that the distribution of U^{4+}, which strongly favors the oxide phase, was not significantly dependent on the composition of the fluoride phase but did depend on the composition of the oxide phase; *i.e.*, the equilibrium quotient (Q^U_{Th}) was given by

$$\log Q^U_{Th} = \log \frac{X_{UO_2} X_{ThF_4}}{X_{ThO_2} X_{UF_4}} = (2101 + 550\, X_{UO_2})/T \tag{2}$$

(wherein X denotes mole fraction). The form of this dependence suggested that the solid solution was a regular solution in which

$$\log \gamma_{UO_2} = (275/T) X^2_{ThO_2} \tag{3a}$$

$$\log \gamma_{ThO_2} = (275/T) X^2_{UO_2} \tag{3b}$$

The proportionality of the log of Q^U_{Th} to 1/T indicated, as might have been expected, that the entropy of the exchange is nearly zero.

In a subsequent study [3] it was found that plutonium, which is trivalent in MSR fluorides, can be oxidized and precipitated as a PuO_2-ThO_2 solid solution. The equilibrium, measured in $LiF-BeF_2-ThF_4$ (72-16-12 mol %), was

$$PuF_3(d) + 1/2NiO(c) + 3/4ThO_2(ss) \rightleftharpoons 3/4ThF_4(d) + 1/2Ni(c) + PuO_2(ss) \tag{4}$$

wherein the oxidant was NiO. From the two measured values of this quotient it is possible to derive values (table 1) for the equilibrium quotient Q^{Pu}_{Th} of the exchange reaction

$$ThO_2(ss) + PuF_4(d) \rightleftharpoons ThF_4(d) + PuO_2(ss) \tag{5}$$

The resulting values (table 1) are clearly insufficient to determine the dependence of Q^{Pu}_{Th} on temperature or oxide composition; however, the indicated 60-fold change in Q^{Pu}_{Th} over only a 100° change in temperature and for relatively dilute PuO_2-solutions in ThO_2 is too great to be consistent with the expected zero entropy for the exchange reaction.

The oxide chemistry of protactinium in these fluorides was first explored by Schaffer et al. [4] who found that protactinium could be precipitated quantitatively even at very low

---

[2] Figures in brackets indicate the literature references at the end of this paper.

Table 1

Estimation of the Equilibrium Quotient Q_{Th}^{Pu} for the Exchange of Pu^{4+} and Th^{4+} Between Oxide and Molten Fluoride Phases

	log Q 615 °C	log Q 715 °C	σ(log Q)	Ref.
$ThO_2(ss)+\frac{2}{3}NiO(c)+\frac{4}{3}PuF_3(d) \rightleftarrows ThF_4(d)+\frac{4}{3}PuO_2(ss)+\frac{2}{3}Ni(c)$	1.45	0.14	0.03	[3](a)
$PuF_4(c)+\frac{1}{3}PuO_2(c) \rightleftarrows \frac{4}{3}PuF_3(c)+\frac{1}{3}O_2(g)$	-0.53	-0.41	0.03	[9]
$\frac{2}{3}Ni(c)+\frac{1}{3}O_2(g) \rightleftarrows \frac{2}{3}NiO(c)$	6.26	5.33	0.03	[10]
$\frac{4}{3}PuF_3(c) \rightleftarrows \frac{4}{3}PuF_3(d)$	-2.97	-2.49	0.03	[11]
$PuF_4(d) \rightleftarrows PuF_4(c)$	-0.59	-0.74	0.72	(b)
$ThO_2(ss)+PuF_4(d) \rightleftarrows ThF_4(d)+PuO_2(ss)$	3.63	1.83	0.72	

(a) Calculated for .67LiF-.33BeF_2 from measurements in .72LiF-.16BeF_2-.12ThF_4, using the corresponding activity coefficients for $PuF_3(d)$ and $ThF_4(d)$ from ref. [12].
(b) Assumed to be the same as for $UF_4(d) \rightleftarrows UF_4(c)$ ref. [7].

Table 2

Equilibrium Data Obtained for the Reaction $ThO_2(ss) + PaF_4(d) \rightleftarrows PaO_2(ss) + ThF_4(d)$

Sample	Temperature (°C)	$X_{\Sigma O}$(a)	X_{PaF_4}	X_{PaO_2}(b)	log Q_{Th}^{Pa}	a (Å)
A	567.0	0.35×10^{-3}	4.38×10^{-4}	(.324)	2.12±.48	
B	567.0	$0.58\ 10^{-3}$	4.10×10^{-4}	(.291)	2.08±.26	
C	567.0	1.08×10^{-3}	3.40×10^{-4}	(.292)	2.16±.15	
D	663.0	2.78×10^{-3}	3.38×10^{-4}	(.167)	1.85±.13	
E	727.0	2.70×10^{-3}	4.16×10^{-4}	(.109)	1.55±.08(e)	
F	567.0	2.83×10^{-3}	2.71×10^{-4}	.175±.02(c)	1.97±.06	5.5926±.0003
G	730.0	14.88×10^{-3}	1.91×10^{-4}	.073±.004(d) (.050)	1.69±.05 1.52±.10	5.5910±.0002
H	567.0	8.88×10^{-3}	0.75×10^{-4}	(.062)	2.02±.10	
I	567.0	8.88×10^{-3}	0.69×10^{-4}	(.063)	2.07±.10	

(a) Total moles of oxide added per mole of solvent (LiF+BeF_2+ThF_4).
(b) Number in parenthesis were calculated by material balance.
(c) Determined by x-ray fluorescence.
(d) Determined by γ-spectrometry.
(e) Value assumed for calculating $Q_{s(ThO_2)}$ (Sec. 3.2)

concentrations by oxide. Recent studies by us [5] have confirmed this and have shown that the insoluble oxide involved is either Pa_2O_5 or an addition compound of it with fluoride. In an MSR fuel, however, protactinium will be in the tetravalent state and the precipitation of Pa(V) by traces of oxide will be easily avoided under the reducing conditions which will be normally maintained.

The behavior of Pa(IV) in the presence of oxide remained to be determined. It is to be expected that Pa^{4+} would form solid solutions with ThO_2 and UO_2. Roberts and Walker [6] have reported the formation of solid solutions of ThO_2 containing both Pa_2O_5 and PaO_2. The purpose of the present study was to confirm the exchange equilibrium

$$ThO_2(ss) + PaF_4(d) \rightleftarrows ThF_4(d) + PaO_2(ss) \qquad (6)$$

and determine the corresponding equilibrium quotient (Q_{Th}^{Pa}). With these results, along with previous estimates of Q_{Th}^{U} and Q_{Th}^{Pu}, it should be possible to determine at least approximately how such exchange quotients, and perhaps the properties of these binary solid solutions depend on the lattice parameters of the separate oxides.

2. EXPERIMENTAL

All the work described here was performed with ~ .4g of ^{231}Pa in glove boxes suited for work with α-emitters. The procedure and apparatus for purification of the solvent salt, $LiF-BeF_2-ThF_4$ (72-16-12 mol %), for equilibration with the solid oxide phases, and for sampling of the melt was similar to that described in the previous studies of plutonium [3]. The protactinium solution was prepared by extensive hydrofluorination, at 700 °C, of a mixture of the salt with Pa_2O_5. After this treatment the temperature was lowered to 560 °C. Since this caused no detectable precipitation of the very insoluble Pa(V) oxide, it was concluded that the oxide removal was essentially complete. In order to convert all the protactinium to the tetravalent state and to remove the metallic impurities present (Ni^{2+}, Fe^{2+}), the solution was next extensively reduced by sparging with hydrogen at 720 °C and then at 560 °C. The extent of the reduction was followed by measuring the HF evolved. The reduction was considered complete when the partial pressure of HF reached 2.6×10^{-5} atm ($2.63\ N/m^2$) at 560 °C. This pressure limited the amount of Pa^{5+} to no more than ~5 ppm (0.3% of the total protactinium present) [5].

The equilibrations of the protactinium solution with various amounts of oxide phase (added as ThO_2 microspheres) were conducted by stirring both phases under a flowing hydrogen atmosphere. This maintained reducing conditions while the rate of HF evolution, which was monitored, provided an indication of the rate and amount of oxidation by impurities. Filtered samples of the melt were obtained at various times and at several temperatures, and the content of ^{231}Pa was determined by γ-spectrometry using a lithium-drifted germanium crystal. Equilibrium was assumed if the protactinium concentration remained constant to within ± 5% (the analytical uncertainty) for at least 48 hours.

Two samples of the equilibrated oxide phase (40 to 120 mg) were isolated, one at the end of a series of stepwise additions of oxide. The salt was drawn off through a filter and the remaining fluorides were removed from the residue by washing with a solution of versene, boric acid, and citric acid, followed by two washings with 7N nitric acid at 70 °C. The oxide residue was finally washed with acetone and dried. The protactinium content of the oxides was determined by γ-counting of a weighed sample. Emission spectroscopy and chemical analysis revealed no elements other than Pa, Th, and O to be present in significant amounts (1700 ppm F, less than 200 ppm each of Li, Be, Cr, Fe, Ni). The samples were examined by x-ray diffraction and in a scanning electron microscope. The latter permitted an analysis of individual oxide crystals.

3. RESULTS

3.1. THE Pa^{4+}-Th^{4+} EXCHANGE QUOTIENT

While the first oxide sample (F in table 2) was found by x-ray diffraction to contain two cubic phases, the scanning electron microscope (SEM) revealed that only one of these consisted of relatively large (15 to 25μm) crystals of the type expected to be formed by equilibration with the melt. The second phase was present as small (<1 μm) irregular particles

or aggregates, relatively rich in protactinium (X_{PaO_2} ~ 0.44 by x-ray fluorescence). The latter material was probably an artifact produced by oxidizing impurities introduced during the filtration procedure used to isolate the equilibrated oxide phase. The second oxide sample (G in table 2) was found to consist almost entirely of well formed, relatively large, crystals with a small amount of an extraneous oxide phase. Since the x-ray fluorescence of individual crystals in both samples revealed the presence of both thorium and protactinium there can be little doubt that these crystals were solid solutions of thorium and protactinium oxides.

The analysis of the first sample (F in table 2) is based on the x-ray fluorescence spectra measured for single crystals. (The γ-counting results for the entire sample were complicated by the presence of the second protactinium-rich phase.) The result (X_{PaO_2} = .175) is consistent with the composition which could be crudely estimated from material balance.

Two compositions are shown for the second oxide sample. One is based on direct γ-counting of a weighed portion and the other on material balance, which here is more accurate because of the larger amount of precipitated oxide present in the reaction mixture. X-ray fluorescence was not sufficiently sensitive to give an accurate analysis of this more dilute PaO_2 solid solution. The small amount of extraneous oxide phase probably explains the discrepancy between the two analyses shown.

The lattice parameters measured for these samples (table 2), when plotted (along with the previous results of Roberts and Walker [6]) *vs.* the composition of ThO_2-PaO_2 solid solutions showed in one case a positive deviation from, and in the other good agreement with Vegard's law. While we are not yet sure of the reason for the positive deviation, possibly a result of radiation damage, it is important to note that if any Pa(V) had been present in the solid solution the expected effect would have been in the opposite direction.

The entries A-D in table 2, which resulted from stepwise additions of oxide but without isolation of an oxide sample, include extimates of the composition of the equilibrated oxide solid-solution based on the following material balance calculation: First the total moles of oxide present (Σn_o) at the end of the series of equilibrations A-E was calculated from

$$\Sigma n_o = 2\left(\frac{X^T_{PaF_4} - X_{PaF_4}}{X_{PaO_2}}\right)\Sigma n_F + \left(Q_{S(ThO_2)}\frac{(1-X_{PaO_2})}{X_{ThF_4}}\right)^{\frac{1}{2}}\Sigma n_F \qquad (7)$$

The first term on the right represents the moles of oxide phase, where $X^T_{PaF_4}$ would be the mole fraction of PaF_4 if none had been precipitated, and Σn_F is the sum of the moles of LiF, BeF_2, and ThF_4. The other term represents the moles of oxide in solution, based on the solubility quotient of ThO_2

$$Q_{s(ThO_2)} = X_{ThF_4}\, X^2_{O^{2-}}/X_{ThO_2} \qquad (8)$$

The values of this quotient finally used (sect.3-2) are given by the expression

$$\log Q_{s(ThO_2)} = -2.46 - 3.87\ (10^3/T) \qquad (9)$$

The total moles of oxide thus calculated to be present at the end of the run exceeded the total added by a small but significant amount, assumed to have been present initially. This amount was used to correct upward the total amount of oxide present at each other step in the run. X_{PaO_2} was then calculated by an iterative solution of equation 7. The remaining entries H and I resulted from equilibrations where a large amount of oxide (introduced at G) was present; hence, the uncertainty in the composition of the precipitated phase when calculated by material balance, was significantly reduced. The uncertainties assigned to the resulting Q^{Pa}_{Th} values reflect the effect of estimated uncertainties in the direct determinations of X_{PaO_2} and X_{PaF_4}, and an uncertainty of a factor of two in $Q_{s(ThO_2)}$.

Within their larger uncertainties, the Q_{Th}^{Pa} values derived from the material balance calculation are quite consistent with the results of the two equilibrations in which the oxide phase was analyzed directly. This is most clearly shown by the points plotted in figures 1 and 2, wherein the anticipated effects of temperature and oxide composition have been taken into account (see sect. 4).

3.2. SOLUBILITY OF ThO_2

When the material balance calculation was applied to the equilibration at 727 °C (E in table 2), it was found to be very sensitive to the value assigned to the solubility quotient of ThO_2 (eq 8). In particular, the very fact that some PaO_2-ThO_2 solid solution remained undissolved at this relatively high temperature (as was clearly shown by the protactinium missing from solution) placed an upper limit on $Q_{s(ThO_2)}$ which was within the previously estimated range of values. Indeed, it was found by reversing the calculation and introducing an estimated value of Q_{Th}^{Pa}, based on the present results at lower temperatures, that it was possible to derive a value of $Q_{s(ThO_2)}$ for the conditions of this equilibration which is probably more accurate than any prior estimates.

$$\log Q_{s(ThO_2)} = -6.33 \pm 0.13 \qquad (X_{PaO_2} = .1,\ 727\ °C) \tag{10}$$

Noting that this solubility quotient may be related to the equilibrium constant by

$$Q_{s(ThO_2)} = K_{s(ThO_2)}\ \gamma_{ThO_2} / (\gamma_{O^{2-}}^2\ \gamma_{ThF_4}) \tag{11}$$

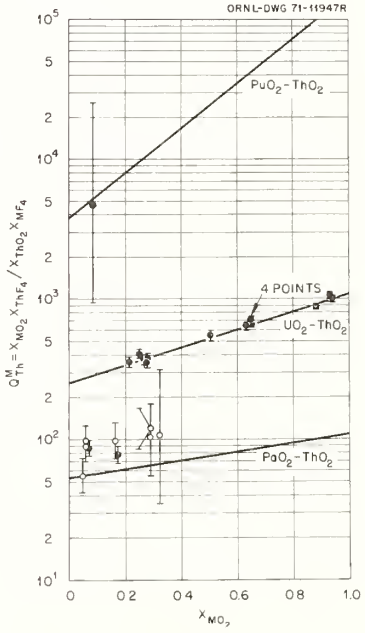

Fig. 1. Exchange quotient Q_{Th}^{M} as a function of the composition of MO_2-ThO_2 solid solutions (in mole fractions X_{MO_2}) at 600 °C. The points are measurements, corrected to 600 °C, in which the composition of the oxide phase was determined directly (●) or by material balance (○). The lines were calculated by means of eq. (25).

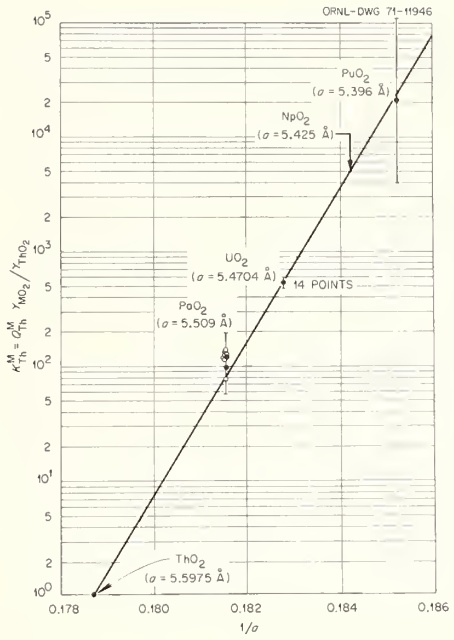

Fig. 2. Equilibrium constant for exchange reactions as a function of the reciprocal of the lattice constants (1/a) of the pure actinide dioxides at 600 °C. The points are derived from those in figure 1 using eq. (26).

$Q_{s(ThO_2)}$ should vary with both melt composition and oxide composition. Since the melt composition was not changed significantly from LiF-BeF_2-ThF_4 (72-16-12 mol %) in the present measurements, and since the solid solutions were all >67 mol % ThO_2 wherein γ_{ThO_2} should be quite close to unity (see sect. 4-1), we may assume here that $Q_{s(ThO_2)}$ was a constant dependent only on the temperature. The expression (eq 9) adopted to represent this dependence is based on the above determination of $Q_{s(ThO_2)}$ at 727 °C and a previous estimate of the entropy of the reaction [7].

$$ThO_2(c) = Th^{4+} + 2O^{2-} \qquad (12)$$

4. DISCUSSION

4.1. BINARY SOLID SOLUTIONS OF ACTINIDE DIOXIDES

Hietala [8] has successfully accounted for the observed heats of mixing of alkali metal halides in binary solid solutions in terms of a simple model which involves the displacement of the common ion in a fixed lattice of the randomly mixed counter-ions. The result is of the approximate form

$$\Delta H_m \approx C \left(\frac{d_2-d_1}{d_1}\right)^2 X_1 X_2 \qquad (13)$$

where d_1 and d_2 are the cation-anion distances for the two pure salts. The constant C contains no adjustable parameters, being a function only of the molar volumes and compressibilities (and their temperature coefficients) of the two pure salts.

While an analogous treatment has not yet been completed for substitutional solid solutions with the fluorite structure such as those of the actinide dioxides, it is clear that

465-504 O - 72 - 23

the result will be of the same form. Hence we will approximate the heat of mixing of MO_2-ThO_2 solid solutions by

$$\Delta H_m = A \left(\frac{a_{ThO_2} - a_{MO_2}}{a_{ThO_2}} \right)^2 X_{MO_2} X_{ThO_2} \qquad (14)$$

where a_{MO2} is the lattice parameter of the pure oxide. From the heat of mixing found for the UO_2-ThO_2 solid solutions [2], we obtain

$$A = 2{,}440 \pm 300 \text{ kcal/mole } (= 10{,}210 \pm 1260 \text{ J/mole}).$$

If we assume random mixing in these solid solutions, the activity coefficients are given by

$$\ln \gamma_{MO_2} = \frac{A}{RT} \left(\frac{a_{ThO_2} - a_{MO_2}}{a_{ThO_2}} \right)^2 X^2_{ThO_2} \qquad (15a)$$

$$\ln \gamma_{ThO_2} = \frac{A}{RT} \left(\frac{a_{ThO_2} - a_{MO_2}}{a_{ThO_2}} \right)^2 X^2_{MO_2} \qquad (15b)$$

Considering the series of binary solid solutions of ThO_2 with PaO_2, UO_2, NpO_2, and PuO_2, these then should show an increasing positive deviation from ideality. In the case of ThO_2-PuO_2 solutions, this deviation should be the largest with

$$\Delta H_m \sim 3.17 X_1 X_2 \quad \text{kcal/mole } (\sim 13.26 \text{ J/mole}).$$

and

$$\ln \gamma_{PuO_2} = \frac{1{,}590}{T} X^2_{ThO_2}.$$

From this it is predicted that ThO_2 and PuO_2 will not be completely miscible at temperatures below about 500 °C.

4.2. ACTINIDE (IV) EXCHANGE EQUILIBRIA

Considering next the exchange reaction

$$ThO_2(ss) + MF_4(d) \rightleftarrows ThF_4(d) + MO_2(ss) \qquad (16)$$

we might expect the entropy change for this reaction to be zero for all the tetravalent actinides from Pa^{4+} to Pu^{4+}. Furthermore we might well expect that the enthalpy change

$$\Delta H° = (H_{MO_2(c)} - H_{ThO_2(c)}) - (\bar{H}_{MF_4(d)} - \bar{H}_{ThF_4(d)}) \qquad (17)$$

would depend on the reciprocal of the M-F and M-O distances, *i.e*,

$$\Delta H° = - B'\left(\frac{1}{d_{M-O}} - \frac{1}{d_{Th-O}}\right) + B''\left(\frac{1}{d_{M-F}} - \frac{1}{d_{Th-F}}\right) \qquad (18)$$

where B' and B" are constants characteristic of the actinide dioxides and of the actinide tetrafluorides dissolved at low concentrations in a molten fluoride solvent. If this last expression is rearranged to

$$\Delta H° = - \left[B' - B'' \left(\frac{d_{Th-O}\, d_{M-O}}{d_{Th-F}\, d_{M-F}} \right) \left(\frac{d_{Th-F} - d_{M-F}}{d_{Th-O} - d_{M-O}} \right) \right] \left(\frac{1}{d_{M-O}} - \frac{1}{d_{Th-O}} \right) \qquad (19)$$

we see that the bracketed term ought to be nearly constant for the series Pa^{4+} - Pu^{4+}, especially since the ion radii of O^{2-} and F^- are quite similar. Hence we might expect the following relationship to be a good approximation

$$\Delta H^\circ = -B''' \left(\frac{1}{d_{M-O}} - \frac{1}{d_{Th-O}} \right) \tag{20}$$

or, replacing d_{M-O} by a_{MO_2}

$$\Delta H^\circ = - B \left(\frac{1}{a_{MO_2}} - \frac{1}{a_{ThO_2}} \right) \tag{21}$$

The equilibrium constant for the above reaction then should be given by

$$\ln K^M_{Th} = \frac{B}{RT} \left(\frac{1}{a_{MO_2}} - \frac{1}{a_{ThO_2}} \right) \tag{22}$$

From the results for the ThO_2 - UO_2 solid solution we estimate

$$B = 2{,}620 \pm 53 \text{ kcal/Å } (= 10{,}960 \pm 220 \text{ J/Å})$$

The exchange quotient Q^M_{Th} is related to K^M_{Th} as follows

$$K^M_{Th} = \frac{X_{MO_2} X_{ThF_4}}{X_{ThO_2} X_{MF_4}} \cdot \frac{\gamma_{MO_2}\gamma_{MF_4}}{\gamma_{ThO_2}\gamma_{MF_4}} = Q^M_{Th} \frac{\gamma_{MO_2}\gamma_{ThF_4}}{\gamma_{ThO_2}\gamma_{MF_4}} \tag{23}$$

We will assume that the ratio of activity coefficients $\gamma_{ThF_4}/\gamma_{MF_4}$ for the tetrafluorides in dilute fluoride solutions is a constant independent of the composition of the solvent. This was found to be the case for the ratio $\gamma_{ThF_4}/\gamma_{UF_4}$ [2]. By choosing the standard states for the tetrafluorides such that $\gamma_{ThF_4}/\gamma_{MF_4}$ is unity, we may then write

$$K^M_{Th} = Q^M_{Th} \gamma_{MO_2}/\gamma_{ThO_2} \tag{24}$$

Introducing the expressions for K^M_{Th} (eq 22), γ_{MO_2} and γ_{ThO_2} (eq 15) we obtain the following expression for Q^M_{Th}

$$\ln Q^M_{Th} = \frac{B}{RT} \left(\frac{1}{a_{MO_2}} - \frac{1}{a_{ThO_2}} \right) + \frac{A}{RT} \left(\frac{a_{ThO_2} - a_{MO_2}}{a_{ThO_2}} \right)^2 (2X_{MO_2} - 1) \tag{25}$$

Thus we expect the log of the quotient for a given exchange to increase linearly with X_{MO_2}, the amount of the increase varying directly as Δa^2. Further, we expect the log of the quotient to increase directly as the difference $\Delta(1/a)$ for the oxides involved.

The present results for Q^{Pa}_{Th}, along with the previous measurements of Q^U_{Th} and the value calculated (table 1) for Q^{Pu}_{Th} at 615 °C are compared with these expectations in figures 1 and 2. In figure 1 the data have been normalized to a temperature of 600 °C by invoking the assumption that the entropy of exchange is zero (and hence that $\ln Q^M_{Th}$ is proportional to 1/T K). The curve drawn through the values for Q^U_{Th} was arrived at previously by a least squares fit of the data. The other curves were constructed from equation 25. Values of K^M_{Th} at 600 °C were then calculated according to the expression

$$\ln K^M_{Th} = \ln Q^M_{Th} - \frac{A}{RT} \left(\frac{a_{ThO_2} - a_{MO_2}}{a_{ThO_2}} \right)^2 (2X_{MO_2} - 1) \tag{26}$$

and these are compared with a line based on equation (22) in figure 2.

As is seen, within their accuracy, the present results and the estimates for Q_{Th}^{Pu} at 615 °C agree quite well with the expected behavior. The results for Q_{Th}^{Pu} at 715 °C derived in table 1, which is not shown in figure 1, would fall far below the curve, being low by a factor of about 40. This discrepancy, we are fairly certain, arises from some unsuspected error in the previous measurement of the equilibrium quotient for reaction (4) at 715 °C. The apparent change in this quotient by a factor of about 10 over the temperature range 615-715 °C is far greater than one would predict from the expected small entropy change for this reaction. The most likely explanation is that the NiO introduced into the system had been reduced at the higher temperature by reaction with lubricant leaking into the system through the stirrer seal.

5. CONCLUSIONS

The present measurements of Q_{Th}^{Pu} are insufficient to test the dependence of ΔH_m on $(\Delta a/a)^2$ suggested by Hietala's appealingly simple model. The composition range of the PaO_2-ThO_2 solid solutions and the expected deviations from ideality are too small. We hope to test further this dependence by making direct measurements of the Pu^{4+}-Th^{4+} exchange between PuO_2-ThO_2 solutions and a molten fluoride. Here ΔH_m should be much larger and hence so should be the dependence of Q_{Th}^{Pu} on the composition of the oxide phase. These measurements will also test more fully the apparent dependence of K_{Th}^{M} on $\Delta(1/a)$.

The application of Hietala's model to these oxide solid solutions with the fluorite structure is still in progress. We hope to include solid solutions containing more than two components, since this should permit the treatment of the important case of the simultaneous exchange of more than two M^{4+} actinide ions (in an oxide phase) with a molten fluoride phase.

For the present, it seems likely that the correlation suggested here (eq 25) will be usefully accurate (1) for predicting binary exchange of cations, (2) for relating the solubilities of the other actinide dioxides to ThO_2, and (3) for estimating thermochemical values for actinide fluorides in solution from such data for the corresponding dioxides.

6. ACKNOWLEDGMENTS

The authors would like to express their appreciation to the following members of the Analytical Chemistry Division of Oak Ridge National Laboratory: H. Dunn for the x-ray diffraction analyses, L. Hulett for the examinations with the Scanning Electron Microscope, and J. Emery for the γ-spectrometric analyses. We are grateful to D. Sood, on leave at ORNL from the Bhabha Atomic Research Center, for his invaluable help in isolating the oxide phases.

7. REFERENCES

[1] Grimes, W. R., Nucl. Appl. Tech. 8, 137 (1970).
[2] Bamberger, C. E. and Baes, C. F., Jr., J. Nucl. Mat'l 35, 177 (1970).
[3] Bamberger, C. E., Ross, R. G., and Baes, C. F. Jr., J. Inorg. & Nucl. Chem. 33, 767 (1971).
[4] Shaffer, J. H., Grimes, W. R., Watson, G. M., Cuneo, D. R., Strain, J. E., and Kelly, M. J., Nucl. Sci. Engr. 18, 177 (1964).
[5] Ross, R. G., Bamberger, C. E., and Baes, C. F., Jr., MSR Prog. Semiann. Progr. Rept. for Period Ending Aug. 31, 1970, ORNL-4622, p. 92 (1971).
[6] Roberts, L. E. J. and Walker, A. J., *Physico-Chemie du Protactinium,* 51 Centre National de la Recherche Scientifique, Paris (1966).
[7] Baes, C. F., Jr., in *Nuclear Metallurgy* (Symposium on the Reprocessing of Nuclear Fuels, edited by P. Chiotti) vol. 15, USAEC-CONF 690801 (1969).
[8] Hietala, J., Ann. Acad. Scient. Fennicae Series A, VI Physica 121-123 (1963).
[9] Dawson, J. K., Elliot, R. M., Hurst, R., and Truswell, A. E., J. Chem. Soc. 558 (1954).
[10] Elliot, J. F. and Gleiser, M., Thermochemistry for Steelmaking, American Iron and Steel Institute, Addison-Wesley, Reading, Mass. (1960).
[11] Barton, C. J., J. Phys. Chem. 64, 306 (1960).
[12] Baes, C. F., Jr., MSR Prog. Semiann Progr. Rept. for Period Ending Feb. 28, 1970, ORNL-4548, p. 149 (1970).

DISCUSSION

P. Hagenmuller: Did you find any evidence of substitution of oxygen by fluorine in your solid phase?

C. E. Bamberger: No sir, at least not in an appreciable amount. Because we could not correlate the lattice parameter of the Pa-rich solid solution with its Pa content, we had considered the possibility that we had formed a Pa(IV) oxyfluoride. So, this sample was analyzed for fluorine and for metallic impurities. The results, in ppm, were 1700 F, 0.1 Be, 10 Li, and 30 each of Ni and Cr, and 200 Fe. The concentration of Li and Be indicated that while the amount of fluorine present did not correspond to residual solvent salt, neither was it sufficient to indicate the presence of an oxyfluoride phase.

Note added in proof: However, from the results obtained, the substitution of oxygen by fluorine cannot be entirely ruled out. The concentration of fluorine would correspond to a maximum of 0.03 mole fluorine per mole of MO_2 (solid solution) or 0.17 mole fluorine per mole of PaO_2 present in the solid solution.

National Bureau of Standards Special Publication 364, Solid State Chemistry, Proceedings of 5th Materials Research Symposium, issued July 1972.

GROWTH AND X-RAY STUDIES OF SINGLE CRYSTALS OF HIGHER OXIDES OF PRASEODYMIUM AND TERBIUM

M. Z. Lowenstein, L. Kihlborg, K. H. Lau,
J. M. Haschke and L. Eyring

Department of Chemistry
Arizona State University
Tempe, Arizona 85281

Single crystals of higher oxides of praseodymium and terbium have been grown successfully using hydrothermal techniques. Cold seal reactors were utilized to study the crystallization process over a temperature range of 600-900 °C and at pressures up to 3.1 kilobar. Crystal growth conditions were optimized using controlled pressure and temperature cycling. Any oxide of praseodymium may be used as starting material. Nitric acid served both as a mineralizer to promote solubility and as a source of oxygen. Two predominant crystal habits are observed; octahedra and trigonal prisms. Faces are smooth and well defined.

Single crystals of praseodymium dioxide have been reduced to $PrO_{1.833}$ in the homologous series Pr_nO_{2n-2} with crystal integrity maintained. X-ray data have been obtained on these crystals using Weissenberg and Hägg-Guinier cameras. The phase has a fluorite-type sublattice with a superstructure of monoclinic symmetry (space group $P2_1/n, C_2^5h$) and a unit cell having a = 6.6874 Å, b = 11.602 Å, c = 15.470 Å, β = 125.257° and V = 979.6 Å^3. Indexing of the powder pattern of this phase has been completed on the basis of this cell. The relationship to the fluorite subcell is shown.

Key words: Higher oxides; hydrothermal crystal growth; oxide structures; praseodymium oxide; single crystal; terbium oxide.

1. CRYSTAL GROWTH

1.1. INTRODUCTION

The PrO_x-O_2 system is ideally suited as a model system for the study of solid state reactions. Its crystal system resembles those of about one third of the known elements; it exhibits polymorphism in its phases of nearly fixed composition; it possesses ordered intermediate phases of narrow composition range belonging to an homologous series; ordered intermediate phases are observed to disorder to nonstoichiometric phases of wide composition range at higher temperatures and pressures; and, in addition, such interesting features as chemical hysteresis and pseudophase formation occur in many regions of its existence range. All these chemical and structural features are accessible at oxygen pressures between vacuum and one atmosphere at temperatures up to 1100 °C.

There has long been a great need for a model system to be thoroughly studied from all points of view including thermodynamics, kinetics and structure. Systems for which structural data are most completely known are frequently very difficult to study thermodynamically and kinetically and vice versa. Structural and some specific kinetic studies on the PrO_x-O_2 system (which is ideally suited to thermodynamic and kinetic measurements) have until now been prevented because of the unavailability of single crystals of most of the oxide phases. While powder diffraction studies have resulted in a model for the structural relationships between the phases, these cannot be tested without single crystals.

Growth of single crystals of praseodymium oxide by the Verneuil technique has produced only high temperature A-type sesquioxide crystals which shatter upon oxidation due to the reconstructive transformation required to produce the fluorite related major sequence of oxides. Similar failures to obtain crystals in the cubic related system have been experienced in flux growth techniques which successfully grew fluorite CeO_2 and ThO_2 crystals [1, 2, 3][1]. The early report of Shafer and Roy [4] made hydrothermal techniques appear well suited to produce the C-type sesquioxide of the rare earths. It was assumed that the C-type sesquioxide could then be oxidized to the intermediate oxides and PrO_2 without loss of crystal integrity.

Experiments by Haschke and Eyring [5] demonstrated that in the presence of an oxidizing medium the oxide produced was PrO_2 or a mixture of $TbO_{1.714}$ and $TbO_{1.818}$ in the praseodymium and terbium oxide [6] systems respectively. An experimental program was inaugurated to perfect the conditions for crystal growth.

1.2. EXPERIMENTAL PART

The basic apparatus and technique has been described previously in detail [5, 7]. An externally heated stellite cold seal reactor was utilized for the hydrothermal vessel. The reactor was connected either to a gas driven water intensifier or to a gas driven diaphragm compressor. In the latter case, argon was used as the pressurizing fluid. Pressure was measured with a bourdon gauge to $\sim$ 34 bars and temperature was measured by means of a thermocouple in a well on the outer surface of the reactor. External temperatures were calibrated to internal temperatures ($\pm$25 °C) which are those reported. The reactors were heated by concentrically wound Kanthal furnaces with the temperature regulated by proportional controllers.

The rare earth oxides used were 99.999% pure provided by Lindsay Division of American Potash and Chemical Corporation. Other chemicals were reagent grade. Since the reactants attack stellite at high temperature and pressure, sample containers were constructed of thin gold tubing (5.0 mm OD, 4.5 mm ID). The tubing was crimped on one end in a three-jaw chuck and welded shut. The sample was weighed into the container; the other end was then crimped and welded. Volatile reactants were frozen in the capsule by cooling it and the chuck with liquid nitrogen before final welding. Leaks were detected by weight loss after extended heating at 110 °C in a drying oven.

1.3. RESULTS

Haschke and Eyring [5] reported that, starting with A-Pr_2O_3 (A-form), a source of oxygen such as NO_3^- was necessary for the oxidation to PrO_2. (Some experiments with H_2O_2 produced PrO_2 but were considered less satisfactory due to decomposition of the peroxide before the capsules could be welded.) The presence of a neutral or acidic medium was also demonstrated as a necessity for dioxide formation. A lower temperature limit of 700 °C was found, below which $Pr(OH)_3$ was the only product. At temperatures above 700 °C A-Pr_2O_3 gave only trihydroxide while β disproportionated into $Pr(OH)_3$and PrO_2. With this information as a start, a series of studies was initiated to determine the conditions necessary for preparation of larger single crystals of PrO_2.

A selective sample of these exploratory studies is shown in table 1. The reactor was pressurized cold to the desired pressure. A preheated furnace was placed around the reactor which was brought to temperature as quickly as possible (1-3 hours) with the pressure maintained constant. The reactor was sealed off from the pressurizing system and maintained at temperature and pressure for the period shown.

Different cooling methods were explored as shown in figure 1. Curve A represents rapid cooling produced by replacing the furnace with a water-cooled jacket. The reactor cools to room temperature in about 20 minutes. Curve B represents cooling produced by switching off the furnace but leaving it around the reactor. The initial cooling rate is 6 °C/min and the system reaches room temperature in about five hours. Curve C represents cooling by switching

[1] Figures in brackets indicate the literature references at the end of this paper.

off the furnace, with the furnace removed at 700 °C. Curves D and E represent slow cooling with a motor-driven temperature controller. Cooling rates of 5-20°/hr were maintained either to 700 °C (D) or to room temperature (E).

Table 1

Selected Hydrothermal Reaction Experiments

1 = A-Pr_2O_3, 2 = β 3 = PrO_2, 4 = $Pr(NO_3)_3$

5 = $Pr(OH)_3$ 6 = Hydroxynitrates

Unless noted, HNO_3 = 70% tr = trace

Starting Materials	Ratio Oxide: HNO_3	Temp (C°)	Press (bar)	Time (hr)	Depressurizations	Cooling Curve	Products	PrO_2 Size
1		800	1150	60		A	5	
1+30%H_2O_2		800	1150	65		A	3, 5	powder
1+1M HNO_3		800	1150	48		A	3, 5	powder
1+4		800	1150	96		A	3, 5	powder
5		500	1000	60		A	6	
1+4		900	900	21		A	3(tr), 5	
1+4		800	900	21		A	3(tr), 5	
1+4		700	900	21		A	5	
1+4		600	900	21		A	5	
1+4		850	1150	21		A	3(50%), 5	powder
1+4		800	1150	21		A	3(30%), 5	powder
1+4		700	1150	21		A	3(tr), 5	
1+4		600	1150	21		A	5	
1+4		800	1500	21		A	3(10%), 5	powder
1+4		700	1500	21		A	5	
1+4		600	1500	21		A	5	
1+4		700	2000	21		A	5	
3+HNO_3	6	800	1150	20		A	3, 5(tr)	small, poor
3+HNO_3	1.5	800	1150	20		A	3, 5(tr)	.08-.1 mm
3+HNO_3	1.2	800	1150	12		A	3, 5(tr)	.05-.08 mm
3+HNO_3	1.5	800	1150	12		B	3(60%), 5	<.1 mm, smooth
3+HNO_3	1.4	810	1150	12		E	3(10%), 5	<.1 mm
3+HNO_3	1.5	820	1250	12		B	3(60%), 5	.05-.1 mm
2+HNO_3	1.5	820	1250	12		B	3(60%), 5	.05-.1 mm
1+HNO_3	1.5	800	1150	10		B	3(60%), 5	.05-.1 mm
3+HNO_3	1.3	800	1650	14	1300 in ½ hr	B	3(80%), 5	small, poor
3+HNO_3	1.1	810	1650	20	1200 in 4 hr	B	3(80%), 5	<.1 mm, smooth
3+HNO_3	1.5	740	2150	15	1250 in 50 hr	C	3(90%), 5	.07-.3mm, smooth
1+HNO_3	1.4	740	2150	15	1250 in 50 hr	C	3(90%), 5	.07-.2mm, smooth
2+HNO_3	1.5	740	2150	15	1250 in 50 hr	C	3(90%), 5	.07-.2 mm
2+HNO_3	1.5	820	1650		1000 in 16 hr up to 1150	B	3(90%), 5	.1-.35mm, biggest
3+HNO_3	1.1	730	3000		2000 in 18 hr	B	3(tr) 5(50%), 6	
3+HNO_3	.9	730	3000	11		B	6	
3+HNO_3	.9	730	1750	12		B	3(90%), 5	.08-.2 mm
3+HNO_3	.9	955	3100	18	on cooling to 340°, P goes to 2500 in 3hr			

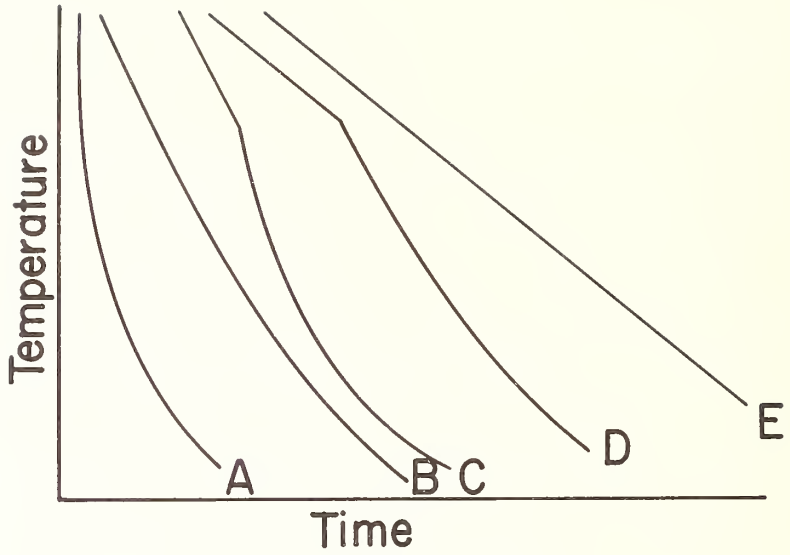

Fig. 1. Cooling Curves

Depressurization at constant temperature was explored. Pressure leak rates varied from 30 to 600 bars/hr. When the reactor reached final pressure it was cooled isobarically to room temperature by switching off the furnace (B).

1.4. DISCUSSION

Several generalizations can be made. Higher temperature and starting pressure (within the limits of the apparatus) tend to result in larger crystals. Long term heating at temperature and pressure (up to 96 hrs) seemed to have no effect on crystal growth. Slow cooling below 700 °C (curve E, fig. 1) resulted in the trihydroxide as the sole product. Depressurization followed by rapid cooling resulted in large crystal clusters but few individually well-formed crystals. Slow cooling produces much larger crystals than fast cooling, the same is true for depressurization. If the pressure drops below 900 bars at high temperature, crystals of dioxide obtained are fractured and disintegrate to powder on touch. The final form of the dioxide crystals seems to be independent of the starting material but is dependent on the relative amounts of starting material (only powder is found if PrO_x:HNO_3 > 1.5). The largest crystals obtained to date were grown under the following conditions.

Pr_6O_{11} (or PrO_2) and 70% HNO_3 (1.4:1 weight ratio) were used as starting materials. The reactor was pressurized to 1650 bars and heated to 820 °C. The pressure was leaked to 1000 bars over a 16 hour period and then raised to 1150 bars and held for two hours. The furnace was switched off and the reactor cooled to room temperature isobarically at 1150 bars. The reactor was depressurized at room temperature; crystals were treated with .2N HNO_3 to dissolve the small amount of $Pr(OH)_3$ present, filtered and dried in a desicator.

From the conditions required to obtain single crystals of PrO_2 one can propose a plausible mechanism for the crystallization process. While the oxides of praseodymium are soluble in concentrated nitric acid, the mole ratios are such that there is insufficient acid for complete reaction and too little water for complete solution (after an initial reaction on mixing, with O_2 released, the reaction mixture is equivalent to a 1:1.85 mixture of $PrO_{1.833}$ and $Pr(NO_3)_3 \cdot 6H_2O$. Such a starting mixture gives identical results to the PrO_2-HNO_3 starting mixture). At reactor temperature and pressure the nitrate decomposes to N_2 and O_2 and the remaining oxide will convert to an intermediate phase, (perhaps $\int$ ($PrO_{1.714}$) or α (PrO_{2-x})). On cooling or depressurization Pr should come out of solution as the intermediate phase, growing on some of the undissolved material present. If the cooling or depressurization is slow enough, one might expect the selective dissolution of smaller crystallites in favor of larger single crystals (as in crystallization from solution under "normal" conditions). The result should be large single crystals of the intermediate phase.

If these crystals are maintained in a temperature range where $Pr(OH)_3$ is the favored phase, one would expect (and actually obtains) hydrolysis to the trihydroxide. If, however, the crystals are passed rapidly through this region of trihydroxide stability, they should reach a temperature where the kinetics of the hydrolysis reaction permits them to remain. At low temperatures with at least 1000 atm. of oxygen pressure the oxidation to the fluorite structure, PrO_2, should proceed with crystal integrity maintained.

The concentrated nitric acid reacts at low temperature to provide water and to solubilize some of the starting oxide. At higher temperatures it decomposes to provide a high oxygen pressure within the sample capsule. Mass spectrometric data on the residual gasses within the capsule are shown in table 2. These data confirm the complete destruction of HNO_3 under reaction conditions. It is interesting to note the increase of $N_2:O_2$ ratio when a reduced oxide (requiring excess oxygen for dioxide formation) was used as starting material.

A product diagram of the type shown in figure 2 is suggested from the experiments summarized in table 1. However, further work will be required to locate exactly the regions of stability.

The suggested mechanism for crystal growth tends to be confirmed by preliminary studies on the TbO_x system. With the same starting conditions as with PrO_x, a mixed crystalline system of $TbO_{1.714}$ and $TbO_{1.818}$ was obtained. When the TbO_x:HNO_3 ratio was decreased to 0.8, a single crystalline phase, $TbO_{1.818}$, was obtained. This is in agreement with the increase in oxygen engendered by the increased HNO_3 content. The oxygen potential is not great enough to produce TbO_2.

These results suggest that the hydrothermal method can be a most useful technique for the growth of single crystals of the rare earth oxides for structural and kinetic studies.

At present crystals up to 0.5 mm on an edge but having a wide range of sizes have been routinely prepared. These crystals have been spherodized by grinding against emory paper as they are swirled about by a low pressure gas flow [8]. These spherical crystals appear suitable for oxygen diffusion studies by a heterogeneous isotope exchange technique.

2. X-RAY STUDIES OF REDUCED CRYSTALS

Now that crystals of PrO_2 of sufficient size and perfection have been grown, a thorough program of structural investigation is begun. The immediate questions to be answered are whether the intermediate oxides can be prepared by reduction without their fracture and if so to discover the details of their structure.

PrO_2 crystals were reduced by heating for various periods of time at 450-475 °C and P_{O_2}= 0.5-1 bar which is within the stability region of the β phase [9].

In the first experiments the crystals were allowed to cool relatively slowly at constant oxygen pressure. The diffraction patterns from these crystals consisted of two sets of reflections; sharp spots corresponding to the lattice of PrO_2 and weaker, diffuse ones corresponding to the lattice of β phase, in parallel orientation. Apparently, the crystals had

Table 2

Gaseous Capsule Contents

Mass No.	HNO_3	HNO_3 + PrO_2	HNO_3 + A-Pr_2O_3
18	.009 (a)	.065	.20
28	.57	.74	.93
30	.002	.002	.003
46	.007	.005	.004

(a) Peak Height Ratio to 32 (O_2)

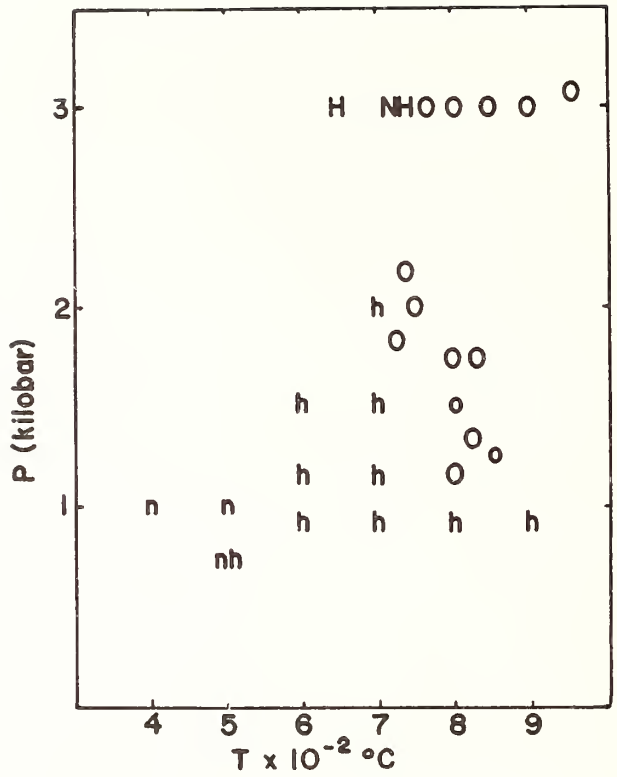

Fig. 2. Product Diagram. Lower case indicates PrO_x + $Pr(NO_3)_3$. Upper case indicates PrO_x + HNO_3, o = PrO_2, h = $Pr(OH)_3$, n = hydroxynitrate.

oxidized coherently during cooling with smaller regions of the reduced phase remaining within the "single" crystals.

When the crystals were cooled slowly to 400 °C (still within the β region) and from there rapidly with pumping to avoid oxidation, they remained monophasic. An x-ray powder pattern taken of some of the crushed crystals showed the faint superstructure lines characteristic of the β-phase [10]. The single crystal patterns revealed a fluorite-type sublattice with a superstructure of monoclinic symmetry. Super-structure unit cell dimensions obtained by least squares refinement are as follows: a = 6.6874±8 Å, b = 11.602±2 Å, c = 15.470±3 Å, β = 125.257±3°, V = 979.6 $Å^3$. Its relation to the fluorite-type subcell, with the three lattice vectors $\underset{\sim}{a}_1$, $\underset{\sim}{a}_2$ and $\underset{\sim}{a}_3$ is

$$\underset{\sim}{a} = -\tfrac{1}{2}\underset{\sim}{a}_1 - \tfrac{1}{2}\underset{\sim}{a}_2 + \underset{\sim}{a}_3,\ \underset{\sim}{b} = \tfrac{3}{2}(-\underset{\sim}{a}_1 + \underset{\sim}{a}_2),\ \underset{\sim}{c} = 2(\underset{\sim}{a}_1 + \underset{\sim}{a}_2) \qquad (1)$$

as shown in figure 3. The volume is six times that of the subcell. (It should be pointed out that the above cell is not the reduced one, but chosen so as to make the c axis fall in the $\underset{\sim}{a}_1$ $\underset{\sim}{a}_2$ plane. A less oblique cell is obtained with $\underset{\sim}{c} = \frac{3}{2}\underset{\sim}{a}_1 + \frac{3}{2}\underset{\sim}{a}_2 + \underset{\sim}{a}_3$.)

Indexing of the powder pattern of the β phase has been accomplished on the basis of this unit cell and is shown in table 3. The systematic absences of reflections are those required by the space group $P2_1/n(C_2^5h$ with a nonstandard choice of axes). Data are now being collected for a complete crystal structure determination of this phase, $Pr_{12}O_{22}$.

In a preliminary run a PrO_2 crystal was reduced under less carefully controlled conditions by heating in air at a temperature in the range 500-600 °C and then rapidly cooled. According to the equilibrium diagram [9] this is within the stability region for the α-phase. The single crystal pattern indicated a subcell with an edge about 0.7% larger than that of the β-phase, which suggested that the crystal was considerably more reduced. Weak superstructure reflections were visible in the high angle region of the Weissenberg photographs,

Table 3

Powder Pattern of Pr_6O_{11} Recorded in a Guinier-Hägg Focussing Camera with ThO_2 as an Internal Standard (a/27°C/=5.59712 Å)

I	d_{obs} (Å)	$hk\ell$	d_{calc} (Å)	I	d_{obs} (Å)	$hk\ell$	d_{calc} (Å)
1	6.574	$\bar{1}01$	6.584			$\bar{2}08$	1.934
1	6.320	002	6.316	s	1.936-	060	1.934
1	5.541	$\bar{1}12$	5.542		1.929	$\bar{1}34$	1.933
2	5.266	021	5.272			$\bar{3}34$	1.931
3	4.609	$\bar{1}13$	4.605	1	1.910	$\bar{1}05$	1.911
3	4.271	$\bar{1}22$	4.270	2	1.896	$\bar{2}52$	1.897
4	4.203	$\bar{1}01$	4.206	3	1.848	$\bar{1}55$	1.850
3	3.980	$\bar{1}20$	3.976	3	1.767	$\bar{1}44$	1.769
s	3.168-	004	3.158			$\bar{3}44$	1.767
	3.152	$\bar{1}30$	3.156	1	1.751	$\bar{2}47$	1.752
		$\bar{2}04$	3.154	3	1.737	$\bar{3}20$	1.737
1	3.064	$\bar{1}05$	3.064	3	1.702	$\bar{3}46$	1.702
2	3.044	$\bar{2}14$	3.044			$\bar{3}42$	1.702
s	2.736-	$\bar{1}34$	2.735	3	1.673	$\bar{2}33$	1.672
	2.731	200	2.730			$\bar{3}01$	1.671
2	2.672	$\bar{1}03$	2.671			$\bar{1}38$	1.649
1	2.659	$\bar{2}10$	2.658			064	1.649
2	2.635	$\bar{1}42$	2.635			$\bar{2}64$	1.649
1	2.562	$\bar{1}40$	2.562	s	1.649-	$\bar{3}38$	1.648
1	2.557	$\bar{2}25$	2.555		1.646	$\bar{2}04$	1.648
1	2.452	$\bar{2}16$	2.452			$\bar{3}30$	1.647
3	2.400	$\bar{2}31$	2.399			$\bar{4}04$	1.646
2	2.388	043	2.389	3	1.604	$\bar{4}25$	1.605
		$\bar{1}41$	2.388			072	1.603
4	2.188	$\bar{1}51$	2.188	1	1.594	$\bar{3}55$	1.595
		243	2.187		1.578-	008	1.579
4	2.178	$\bar{1}42$	2.177	s	1.576	$\bar{2}60$	1.578
4	2.157	$\bar{3}15$	2.157			$\bar{4}08$	1.577
5	2.114	$\bar{1}07$	2.115	1	1.566	$\bar{1}63$	1.566
4	2.105	006	2.105	3	1.542	$\bar{3}40$	1.542
4	2.082	$\bar{1}24$	2.083	2	1.480	$\bar{2}72$	1.480
		$\bar{3}24$	2.081	1	1.478	$\bar{1}07$	1.478
2	2.039	$\bar{2}31$	2.038	1	1.476	$\bar{4}33$	1.476
1	1.943	$\bar{3}17$	1.943	2	1.381	$\bar{2}76$	1.383
		$\bar{3}11$	1.941			$\bar{2}35$	1.380
				s	1.367	$\bar{2}68$	1.367
				s	1.366	$\bar{4}00$	1.365
				1	1.355	$\bar{4}10$	1.356

The intensities of the strong fluorite-type substructure lines are indicated by s; the intensities of the weak superstructure reflections are visually estimated on a scale from 1 to 5.

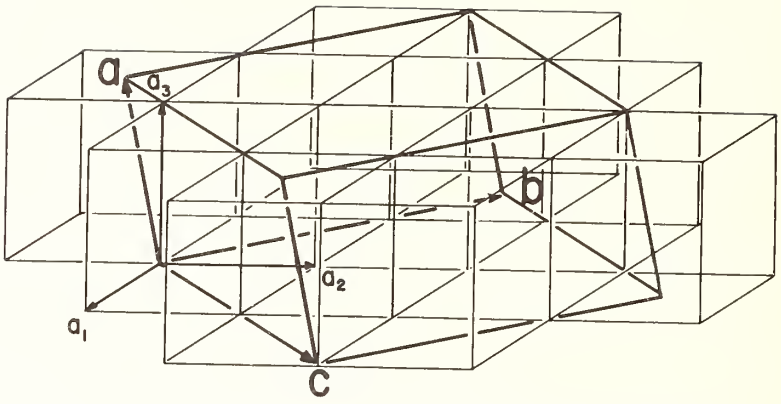

Fig. 3. Relationship between the monoclinic superlattice of $Pr_{12}O_{22}$ and the face-centered, fluorite-type sublattice, twelve unit cells of which are indicated.

and these, as well as the strong spots could be indexed on the basis of the following unit cell,

$$\underset{\sim}{a} = \tfrac{3}{2}\,(-\underset{\sim}{a}_1 - \underset{\sim}{a}_2 + 2\underset{\sim}{a}_3),\ \underset{\sim}{b} = \tfrac{5}{2}\,(-\underset{\sim}{a}_1 + \underset{\sim}{a}_2),\ \underset{\sim}{c} = 2(\underset{\sim}{a}_1 + \underset{\sim}{a}_2 + \underset{\sim}{a}_3). \qquad (2)$$

This lattice is rectangular apart from a possible small distortion of the fluorite-type subcell and the volume is 45 times larger than the volume of the subcell. The fact that the superstructure-reflections are relatively few and confined to high angles makes the derivation of the unit cell somewhat uncertain, however. Although the oxygen content of this phase is uncertain it is obviously less than in the β-phase. The weak superstructure lines indicate long range ordering in either α-phase or some member of the homologous series formed during rapid cooling.

3. ACKNOWLEDGMENTS

We are grateful to the United States Atomic Energy Commission for support of the research of which this is part.

4. REFERENCES

[1] Vinokurov, I. V., Zonn, Z. N. and Ioffe, V. A., Soviet Physics--Solid State, 7, No. 4. October 1965.
[2] Finch, C. B., and Clark, G. W., J. Appl. Phys., 37, 3910 (1966).
[3] Linares, R. C., J. Phys. Chem. Solids, 28, 1285 (1967).
[4] Shafer, M. W., and Roy, R., J. Amer. Ceram. Soc., 42, 563 (1959).
[5] Haschke, J. M., and Eyring, L., Inorg. Chem. In press.
[6] MacChesney,* J. B., Williams, H. J., Sherwood, R. C. and Patter, J. F., J. Chem. Phys. 44, 596 (1966).
[7] Laudise, R. A., and Nielsen, J. W., Solid State Physics, 12, 149 (1961).
[8] Whitmore, R. I., J. Sci. Instrum., 31, 223 (1954).
[9] Hyde, B. G., Bevan, D. J. M. and Eyring, L., Phil. Trans. Roy. Soc., London, Ser. A, No. 1106, 259, 583 (1966).
[10] Sawyer, J. O., Hyde, B. G., and Eyring, L., Bull. Soc. Chim. Fr., 1190 (1965).

* The preparation of TbO_2 by a technique similar to that described above but utilizing $HClO_4 \cdot 2H_2O$ as an oxidant, was called to our attention by Dr. MacChesney at the time of presentation of this paper. No mention was made as to the crystallite size of the unstable TbO_2 prepared.

DISCUSSION

R. S. Roth: I don't want to comment on the praseodymium oxide or fluorite system, I want to comment on the crystal growth technique. I think it is really going to be a very useful method. At a conference that Aaron Wold gave, at Brown University in 1967, Prof. Roland Ward asked the audience "Does anybody know how to make a crystal of two layer hexagonal $BaNiO_3$?" I think for the first time there is a possibility, with this method, that somebody might be able to grow that sort of crystal, and I bet this method will work in a lot of other systems too.

A. S. Nowick: You pointed out that there was an instantaneous transformation as you went from one slide to the other. What change produced that transformation? Was it the temperature?

L. Eyring: Oh, this is a very hostile environment. These crystals are very unstable in the environment of the electron beam in a high vacuum so they are losing oxygen all the time. This sequence of superstructure is the natural result of looking at a crystal of decomposing PrO_2 in the electron microscope.

E. Banks: In your introduction you mentioned terbium oxides and I was wondering whether you had succeeded in growing any crystals of the TbO_2 phase.

L. Eyring: The highest oxide we get is $TbO_{1.818}$, the delta phase. Utilizing a similar technique MacChesney et al. [see reference [6] in the manuscript] have prepared TbO_2.

J. M. Honig: Did you find any nitrogen inclusion in your single crystals?

L. Eyring: There has been no analysis of the crystals other than the gravimetric analysis of a large sample of single crystal material, but this wouldn't show up small amounts of nitrogen. We have no way of saying that there is no nitrogen; I'm sure there is only a very small amount, if any.

National Bureau of Standards Special Publication 364, Solid State Chemistry, Proceedings of 5th Materials Research Symposium, issued July 1972.

DEFECTS AND MASS TRANSPORT IN REDUCED CeO_2 SINGLE CRYSTALS

Y. Ban[1] and A. S. Nowick

Henry Krumb School of Mines
Columbia University
New York, New York 10027

A study is made of reduced CeO_2 in the form of large single crystals grown by arc fusion. It is shown that, so long as $y \geq 1.67$ in the formula CeO_y, all structural changes on reducing CeO_2 occur without loss of coherency of the original fluorite lattice. Comparison of length and lattice parameter changes shows that only oxygen vacancies (and no detectable Ce interstitials) are present in the reduced state. For $y > 1.67$, it is shown that oxidation (in air or in O_2) takes place at reasonable rates just above room temperature. The kinetics of this anomalously rapid mass transport are studied in some detail, including the effects of sample thickness and of oxygen partial pressure. The results show that the kinetics are neither diffusion nor surface controlled. A model of the process is developed which explains the major results. The low temperature oxidation process does not terminate in the pure α (CeO_2) phase, but in a metastable structure, here called α', for which y is very close to 2.0. The properties of α' are discussed.

Key words: Ceria; crystal defects; diffusion; mass transport; nonstoichiometry; oxides.

1. INTRODUCTION

In the study of nonstoichiometry, considerable interest over the past decade has been focused on those rare earth oxides which span the range of composition from the sesquioxide R_2O_3 to the dioxide RO_2. The specific oxides of interest have been CeO_y, PrO_y and TbO_y, all of which take on the fluorite structure in the dioxide. There have been many studies of phase relationships, mass transport and electrical properties of these materials, usually using samples in polycrystalline form. Careful thermal and x-ray investigations have revealed that at the lower temperatures a series of intermediate phases of narrow composition limits is found in the range from y = 1.5 to 2.0. These phases appear always to belong to a homologous series of formula R_nO_{2n-2}. Thus, for CeO_y, the projected phase diagram of Bevan and Kordis [1][2] is given in figure 1 showing three intermediate phases δ, ζ and ι, which appear at y = 1.82 (n = 11), 1.78 (n = 9) and 1.71 (n = 7), respectively.

The availability of large single crystals of CeO_2 through a cooperative project between Columbia University and the Materials Research Corporation (MRC) has resulted in the present study of these crystals. The MRC crystals are grown by arc fusion in a carbon arc [2]. The starting material is ~ 99.98% pure and the final crystals have about the same purity. The lack of a high degree of perfection, probably due to the rapid solidification in the arc, is shown by a lack of transparency of the resulting crystals. Nevertheless, x-ray Laue photographs of crystals annealed in oxygen show sharp spots, indicating "good" single crystals.

The present work,explores the question of the type of defects that are present in reduced CeO_2, and observes an anomalously rapid rate of mass transport in the low-temperature reoxidation of the reduced material. A major part of the work (section 3) is directed toward an attempt to understand the nature of this rapid oxidation process.

---

[1] Now with Fujitsu Ltd. Co., Kawasaki, Japan.

[2] Figures in brackets indicate the literature references at the end of this paper.

465-504 O - 72 - 24

2. OBSERVATIONS CONCERNING DEFECTS AND STRUCTURE

2.1. RESULTS OF REDUCTION-OXIDATION CYCLING

The phase diagram in figure 1 shows that at high temperatures the fluorite (α) phase is maintained down to y = 1.7, while at low temperatures a series of three intermediate phases occurs. It has generally been regarded [3] that these intermediate phases may be considered as distorted fluorite structures produced by appropriate ordering of oxygen vacancies. With the large single crystals now available, it becomes possible to see whether these various structures are, in fact, all formed continuously from the fluorite structure. Thus, we have carried out a series of reductions of <111> oriented CeO_2 crystals and examined the Laue x-ray diffraction pattern at each stage. Reductions were carried out in the range 700° - 900 °C in CO/CO_2 or H_2/H_2O mixtures and the samples were then quenched to room temperature. The most extreme reduction produced by this procedure was to y = 1.67. In all of these cases, the Laue photograph of the reduced crystal still showed the original 3-fold symmetry along the <111> axis[3], although the spots were more blurred than for the fully oxidized material, indicating a distortion of the original cubic structure. When the samples were reoxidized by heating in air at ~ 500 °C the original sharp Laue pattern reappeared in all cases. This result shows that, so long as $y \geq 1.67$, all changes during reduction and reoxidation occur in such a way that the fluorite lattice, although distorted, is maintained intact. From the phase diagram (fig. 1), this result may have been expected for y-values down to 1.71, but it is rather surprising that it also holds in the range 1.67 to 1.71.

To achieve a more drastic reduction to Ce_2O_3, a crystal was sealed in vacuum in a quartz tube with titanium chips, heated for several hours at 800 °C, and rapidly cooled to room temperature. In this case, the Laue photograph shows portions of rings, indicating that the sample is no longer a single crystal. Reoxidation to CeO_2 also verifies that the sample is now polycrystalline. It is concluded that, unlike the intermediate phases, the sesquioxide forms by nucleation and growth of the new phase at the expense of the original fluorite structure.

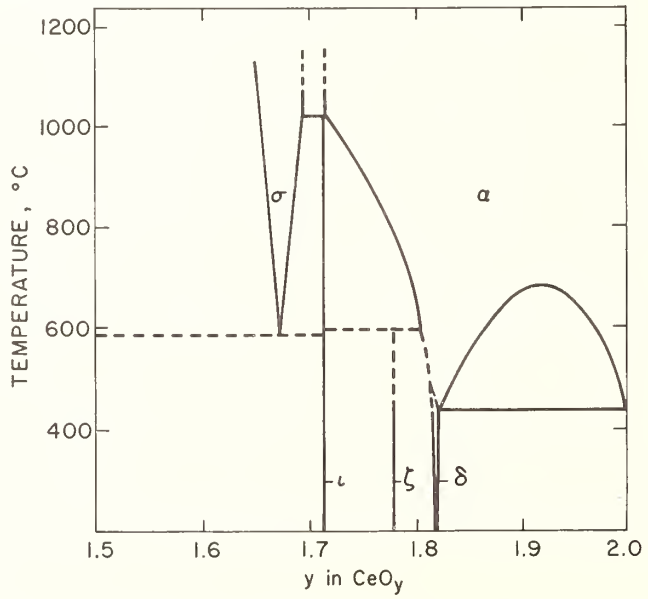

Fig. 1. Temperature-composition projection of the CeO_y - O_2 phase diagram.

[3]However, the pattern for y = 1.67 differs in the number of diffraction spots from those of y = 1.8 or 2.0, probably due to the fact that the 1.67 composition corresponds to the bcc (so-called C-type) structure which has a lattice constant nearly twice that of CeO_2.

2.2. COMPARISON OF LENGTH AND LATTICE-PARAMETER MEASUREMENTS

Although the intermediate phases produced by reduction of CeO_2 are usually regarded as formed by the ordering of anion vacancies on the fluorite lattice, suggestions persist in the literature [4,5] (based on the dependence of properties, particularly electrical conductivity, on oxygen partial pressure) that Ce interstitials are the primary defect involved in reduced CeO_2. It was therefore decided to examine this point by the most direct method, *viz.*, comparison of macroscopic (length) with microscopic (lattice parameter) measurements. The basis for the interpretation of such measurements is the relation

$$V = Nv \tag{1}$$

where V is the sample volume, v the volume of the primitive unit cell and N the number of unit cells. Thus, if reduction occurs by formation of oxygen vacancies, the number of unit cells is unchanged, and one obtains

$$\Delta V/V = \Delta v/v \qquad \text{(0 vacancies)} \tag{2}$$

as the relation between the fractional changes in the macroscopic and the microscopic volumes. (The symbol Δ is conveniently taken as the difference between the oxidized and the reduced states.) On the other hand, if cerium interstitials are formed, it is easy to see that $\Delta N/N = \Delta y/2$ where Δy is the change in composition of CeO_y associated with the reduction. Thus

$$\frac{\Delta V}{V} = \frac{\Delta v}{v} + \frac{\Delta y}{2} \qquad \text{(Ce interstitials)} \tag{3}$$

In practice, it is more convenient to measure lengths, *i.e.*, macroscopic length L, and lattice parameter d, in a given orientation. The corresponding relations to equations (2) and (3) are then

$$\Delta L/L = \Delta d/d \qquad \text{(0 vacancies)} \tag{4}$$

and

$$\Delta L/L = (\Delta d/d) + (\Delta y/6) \qquad \text{(Ce interstitials)} \tag{5}$$

under the reasonable assumption that the change in number of unit cells produces dimensional changes isotropically.

The present experiment involved a series of careful micrometer measurements of the thickness of a crystal before and after reduction to y = 1.81, *i.e.*, to the δ phase. The crystal involved was 1.05 mm thick and its thickness dimension was parallel to <111>. The result of the measurements may be summarized as

$$(L_\alpha - L_\delta)/L_\alpha = -\ 0.017 \pm 0.001$$

where the subscripts α and δ refer to the phases, *i.e.*, to y = 2.00 and 1.81, respectively. Correspondingly, the change in lattice parameter is available from the work of Bevan [6]. However, we have repeated these measurements in an x-ray diffractometer and obtained somewhat more precise values for d-values along <111>:

$$(d_\alpha - d_\delta)/d_\alpha = -\ 0.0164 \pm 0.0003$$

(The value of d_α can be obtained from the lattice parameter of the cubic fluorite structure, but d_δ must be measured directly, since the δ phase is actually rhombohedral). Comparison of these results shows that the agreement with (eq 4) is excellent, and since $\Delta y/6 = 0.03$, that (eq 5) is in complete disagreement. If we allow for the possibility that both defect types may be present simultaneously, these results lead us to conclude that at least 97% of the defects are oxygen-ion vacancies. Thus, we have found no evidence for the formation of Ce-ion interstitials upon reduction.

2.3. THE LOW-TEMPERATURE REOXIDIZED STATE (α')

It was found, both for the MRC single crystals and for sintered polycrystalline samples reduced to $y \geq 1.67$, that reoxidation takes place in air at ambient temperatures with a return to a y-value close to 2.0. Oxidation is so rapid, in fact, that if a thick sample is used and cooling precautions are not taken, the sample heats up appreciably as a result of the exothermic oxidation process[4]. The kinetics of the low-temperature oxidation will be discussed in detail in the next section. Here we are concerned with the state to which the sample returns after this oxidation process. This state is characterized by the following features:

(a) Appearance: The color of the reoxidized crystal remains black, like that of the crystal in the reduced condition. In order to bleach this crystal to the yellowish color of the fluorite (α) phase, it must be heated in air at a temperature of 350 °C or higher. When the bleached crystal is brought back to room temperature, it is stable indefinitely. It is concluded that the low-temperature reoxidized state is a metastable one; henceforth, we shall call it the α' state.

(b) Composition: The y-value in the α' state is very close to 2.0. Samples taken through the bleaching transformation, in a Cahn microbalance, show that the increase in y-value which accompanies the transformation $\alpha' \rightarrow \alpha$ is roughly 0.005. In order to determine whether $\alpha' \rightarrow \alpha$ is primarily a thermally activated structural transformation, or whether the small amount of oxidation that occurs is essential to the transformation, we heated samples sealed in quartz capsules. These samples did not bleach when brought up to 500 °C, while similar samples heated in air are fully bleached. It is therefore concluded that the small amount ($\delta y < 0.01$) of additional oxidation is an essential part of the process by which the metastable α' is transformed to α.

(c) Diffraction Pattern: A Laue photograph of the α' state is similar to that of α except that the spots are blurry for α' and sharp for α. For more careful examination, sintered powder samples in the low-temperature reoxidized state were examined in a diffractometer. Figure 2 shows a comparison of (331) reflection for the α' and α structures. On the

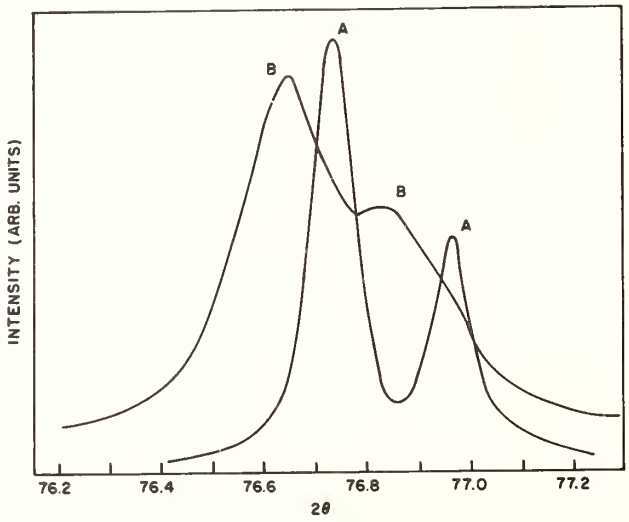

Fig. 2. Comparison of the x-ray (331) reflection for the α' structure, labeled B, with that of the fluorite (α) phase, labeled A. (The doublet in each case is due to the $K\alpha_1$ and $K\alpha_2$ x-radiation.)

[4]The occurrence of this low temperature process is only briefly mentioned in the early literature [6].

one hand, α' shows a slightly larger lattice parameter (~ 0.2% larger) than α, but most strikingly the α' line is distinctly broader than the corresponding one for the α phase. The broadening of the other reflections is about in the same ratio. This line broadening cannot be interpreted as resulting from a two-phase mixture of the α and δ phases, since the lattice parameters of these two phases is sufficiently different that the lines would be well resolved. Instead, it is most reasonably regarded as indicating a microdomain structure [7], *i.e.*, the presence of small regions, of dimensions ~ 100 - 1000 atom distances, which differ in composition from the α phase but are coherent with it.

(d) Chemical Reactivity: A reduced CeO_y crystal sealed in a high humidity chamber reacts rapidly with moisture and disintegrates into a powder which probably consists of a hydroxide. On the other hand, the α' structure is relatively inert toward reaction with moisture.

(e) Electrical Conductivity: The electrical properties of α' are similar to those of the reduced material, *viz.* a conductivity $\sigma \sim 10^{-3}$ $(\text{ohm-cm})^{-1}$. On the other hand, upon bleaching to α, the conductivity drops five decades to $\sigma \sim 10^{-8}$ $(\text{ohm-cm})^{-1}$. Figure 3 shows the change in conductivity during very slow heating and subsequent cooling. Note that once bleaching has occurred, the crystal remains a relatively good insulator at room temperature.

The question of how this metastable α' structure arises will be discussed when we consider the theory of the kinetics of oxidation in the next section.

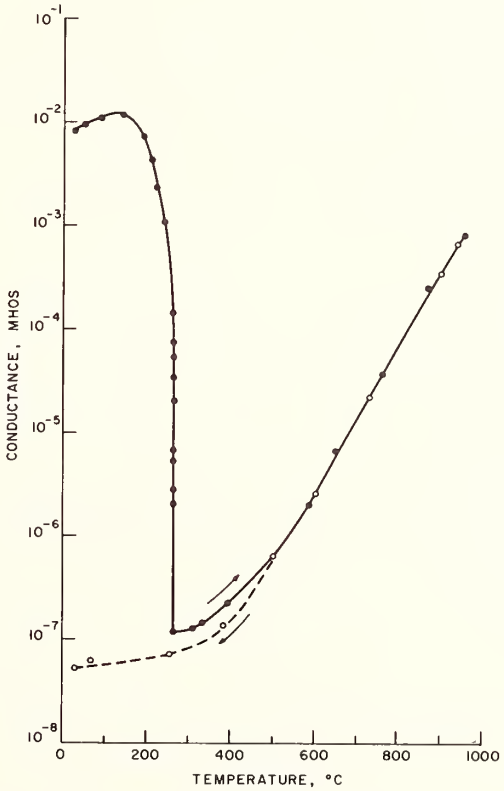

Fig. 3. Changes in conductance with temperature upon heating (solid circles) and subsequent cooling (open circles) of a CeO_2 crystal which had been reoxidized at low temperature. Conductivity = conductance x 0.25.

3. KINETICS OF THE LOW-TEMPERATURE OXIDATION ($\delta \rightarrow \alpha'$)

The oxidation of reduced CeO_2 in the vicinity of room temperature is an example of remarkably rapid mass transport, considering that CeO_2 has a melting point of ~ 2600 °C and, therefore, a Tammann temperature[5] ~ 1200 °C. In order to try to understand the nature of this rapid mass transport, a detailed study of the kinetics of the process was carried out. It was hoped that by using single crystals, mass transport along grain boundaries would be eliminated from consideration.[6]

3.1. EXPERIMENTAL METHODS

To avoid the necessity for mounting and handling the sample after the high temperature reduction, we gave up the idea of using an electrobalance, and instead adopted a classic system employing a fine quartz spring, as shown in figure 4. The quartz spring used was made by Worden Quartz Products, Inc. It allowed a maximum load of 2g and had a sensitivity of 0.039 g/cm. The elongation of the spring was measured by a cathetometer. The samples used were attached to the quartz spring by means of a fine platinum wire. The system was completely enclosed and offered the ability to transfer the sample rapidly from a hot zone to a cool zone (both regulated in temperature), as well as to change the gas flowing through the system. By using thin samples and maintaining a gas flow, it was found that the problem of heating up of the sample during oxidation could be avoided. The procedure, following the mounting of the sample, is as follows:

(1) The sample is oxidized by holding it in the hot zone at 850 °C under an oxygen atmosphere for 10 hours.

(2) The oxygen is replaced with argon over a period of about 1 hour.

(3) The argon is replaced by a gas mixture 99.9% CO/0.1% CO_2 and the sample is held for longer than 12 h at 850 °C in this atmosphere. According to Bevan and Kordis [1], these conditions produce an equilibrium y-value of 1.79 ± 0.02.

(4) The sample is then brought down to the point B in figure 4 over a period of a few seconds by turning the ground joint F, while maintaining the flow of CO/CO_2 (at 0.8 cm/sec). Region B is then at 0 °C.

(5) The tube is then flushed with argon, and the point B is then brought to the desired temperature of measurement (20 - 42 °C). The temperature of point B is controlled to ± 0.02 °C by a mercury relay attached to an immersion heater in water bath I. When this temperature is reached the argon is replaced by oxygen or dry air. This event is taken as the time t = 0 for the kinetic curve. The flow rates of the Ar and O_2 gases are 0.5 cm/sec.

Most of the experiments were carried out on two samples, both from the same MRC crystal. Each had a cross section of 8 mm x 10 mm and its small (thickness) dimension was parallel to <111>. They did differ, however, both in thickness and in surface condition, as follows:

Sample	Thickness	Surface
A	1.45 mm	polished
B	1.08 mm	cleaved

The surface of sample A was polished with emery paper (#180) while that of B was as cleaved. Sample B, therefore, had a much smoother surface than A.

---

[5] The Tammann temperature, roughly 0.5 of the melting temperature (in K) is the point below which atom movements usually cease, for all practical purposes.

[6] The results described earlier (section 2.1.), which show that all changes upon reduction and reoxidation occur without destruction of the basic structure of the fluorite lattice, indicates the absence of any incoherent boundaries in the reduced structure.

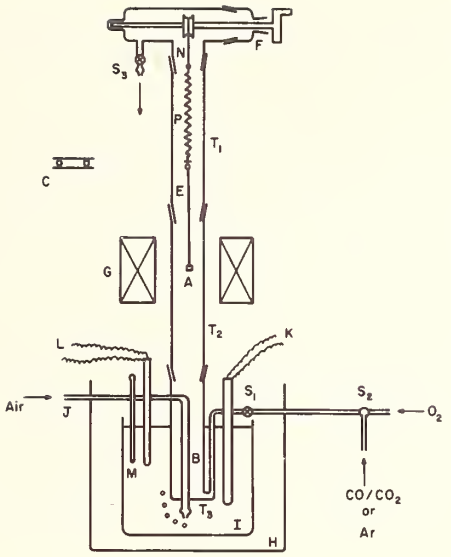

Fig. 4. The quartz spring balance and associated equipment. A - specimen position for reduction at high temperature; B - specimen position for oxidation at low temperature; C - cathetometer; E - platinum wire; F - ground joint; G - furnace; I - temperature regulated water bath; P - quartz spring; S_1, S_2, S_3 - stopcocks.

3.2. RESULTS

Figure 5 presents the kinetics of oxidation at four temperatures for sample A, starting

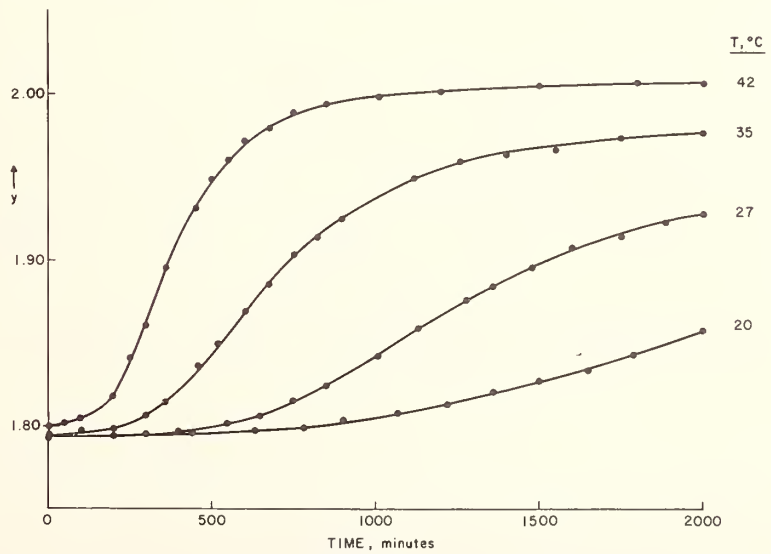

Fig. 5. Kinetics of oxidation of sample A at four different temperatures in pure oxygen.

in each case from a y-value near 1.8. In this figure the changes in weight have been converted to y-values for greater ease of interpretation. In doing so, the reference value of $y = 2.00$ is taken as the value for a sample heated in oxygen at 850 °C prior to reduction[7].

In figure 6, kinetic curves are compared for samples A and B at two temperatures. Although the oxidation of sample B seems to begin more rapidly in both curves, the overall result is that there is surprisingly little difference between these two samples, which indicates the absence of a thickness dependence. Unfortunately, however, the fact that the surface conditions of the two samples are not identical places a possible reservation on this conclusion. This point will be discussed later.

In order to determine the activation energy of the rate controlling step, a series of horizontal cuts have been made through the curves of figure 5, each at a different y-value, say y_i. The corresponding times t_i to reach the value y_i are then plotted as log t_i *versus* $1/T$, as shown in figure 7. If oxidation over the entire range is controlled by a single activation energy, E, the slope of these plots should be independent of y_i. In the present case, there are departures from a constant E at the initial and final stages of the curves, but these regions are also where the precision is poorest. The data of figure 7 shows that for the intermediate range, E is fairly constant at 0.7 eV (16 kcal/mol).

In order to determine the oxygen-pressure dependence of the kinetics of oxidation, the same sample A as had been run in pure O_2 was re-run under dry air, *i.e.*, under oxygen pressure a factor of five times smaller. Figure 8 shows that under higher P_{O_2} the rate of oxidation is faster. If we take the rate of oxidation in the form

$$dy/dt = k\, f(y) \tag{6}$$

the data of figure 8 show that the ratio of rate constants, k_{O_2}/k_{air}, is 1.5 from the 42 °C

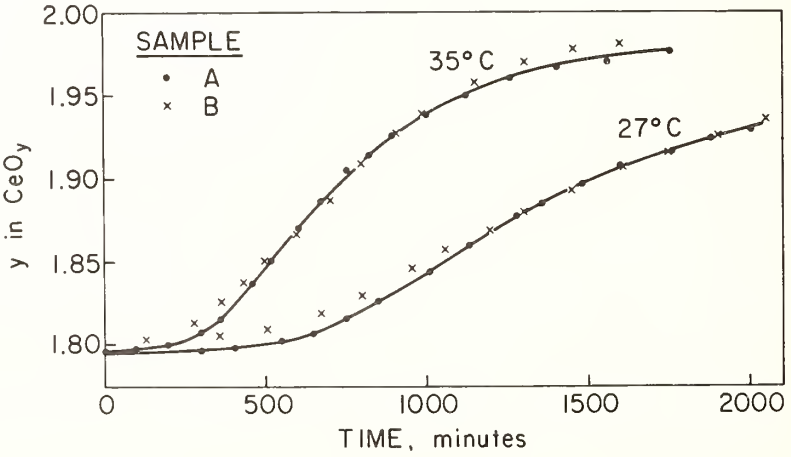

Fig. 6. Comparison of kinetics of oxidation of samples A and B at two temperatures.

7 The fact that the 42 °C curve of figure 5 appears to exceed $y = 2.0$ is a source of concern. Comparing with other experiments, we cannot yet say whether a y-value slightly in excess of 2.0 actually occurs, or whether such a reading is due to experimental error by the spring balance, or the pickup of some CO_2 by the crystal.

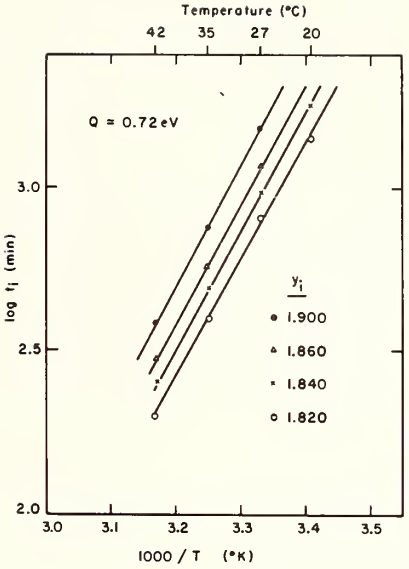

Fig. 7. Plots of time, t_i, to reach a given value y_i as a function of reciprocal absolute temperature, obtained from the data of figure 5.

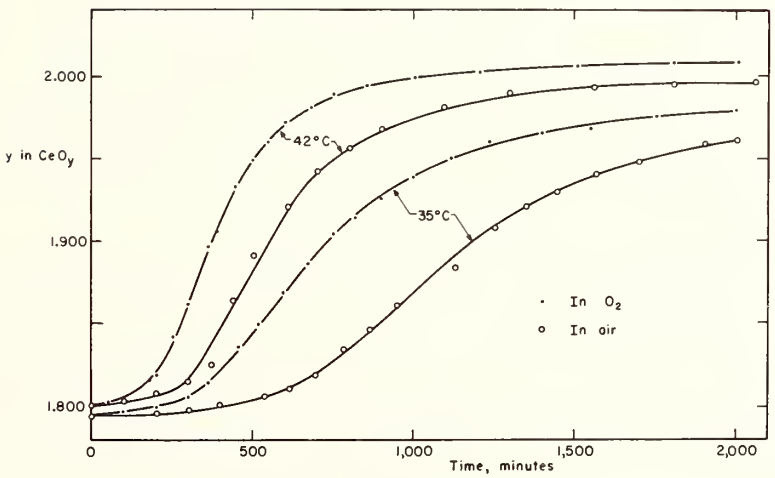

Fig. 8. Effect of oxygen partial pressure on oxidation curves of sample A at two different temperatures.

curves and 1.65 from the 35 °C data. If it is assumed that $k \propto p_{O_2}^n$, these ratios correspond to n = 0.25 and 0.31, respectively.

Finally, some preliminary experiments were carried out on a set of small flux grown crystals (supplied by C. Finch of the Oak Ridge National Laboratory). For these crystals, oxidation does not take place at room temperature but seems to require temperatures near 100 °C. The reason for this difference between the flux-grown and the arc-fusion grown crystals is not clear at present. It may be related to the very smooth external surfaces or

to a higher degree of internal perfection of the flux-grown crystals. Either reason may impose an additional rate-limiting step which was not present in the case of the MRC crystals. This matter will be studied further in the future.

3.3. DISCUSSION

In attempting to understand mass transport processes in reduced CeO_2, one might first turn to the available high temperature oxygen diffusion experiments [8,9]. Extrapolation of data taken near 1000 °C for y ~ 0.9 gives a diffusion coefficient $D \leq 10^{-13}$ cm^2/sec at 35 °C. Such a value is far too small to allow penetration of oxygen through a sample ~ 1 mm thick in reasonable lengths of time. From the phase diagram, however, it is clear that the structure at high temperatures, consisting of random oxygen vacancies on the fluorite lattice, is entirely different from the structure with which we are concerned near room temperature. Accordingly, it is clear that any explanation for the anomalously rapid mass transport at low temperatures, must be given in terms of the structure of the reduced material at low temperatures.

There are several strong indications that the low temperature oxidation is not a diffusion controlled process:

(a) The solution of Fick's second law for a thin slab of thickness *a*, under conditions of constant composition at the surface gives [10] a result which initially takes the form

$$\Delta y \propto (Dt)^{1/2} \tag{7a}$$

and then, over most of the range obeys

$$\ln [1 - (\Delta y/\Delta y_o)] = - \pi^2 \, Dt/a^2 + \ln (8/\pi^2) \tag{7b}$$

Here D is the diffusion coefficient, while Δy is the instantaneous average change in y-value and Δy_o is the total change. The form of (eq 7) disagrees with the kinetic curves of figure 5, since the observed initially increasing slope is not predicted.

(b) In a diffusion controlled process, except for the initial part of the kinetic curve, the time to a given y-value should vary as a^2, as predicted by (eq 7b). The results of figure 6, which compares two samples of different thickness, are in clear disagreement with this prediction.

(c) The observation of an appreciable pressure dependence is difficult to explain on a diffusion model, since the equilibrium y-value is very nearly independent of p_{O_2} in this range of temperature and pressure.

(d) Finally, the value of the measured activation energy, 0.7 eV, is too high to be consistent with a simple diffusion model. For, if it were the activation energy for a diffusion jump, the mean jump time at 35 °C would be[8] $\tau \simeq 10^{-14}$ exp (0.7 eV/kT) ~ 10^{-2} sec. Thus, in the half-time of the experiment (700 min at 35 °C) there would be ~ 10^8 jumps, or a mean diffusion over ~ 10^4 lattice spacings. Such a distance is far smaller than the sample dimensions.

If the observed oxidation process is not diffusion controlled, it is reasonable to consider next the possibility that the rate controlling step is the surface reaction by which oxygen is incorporated into the crystal. In such a case, however, the rate constant k in (eq 6) should be proportional to the oxygen pressure (*i.e.* n = 1) which is not observed. Also, the initial kinetics should be linear [11], *i.e.*, $\Delta y \propto t$, contrary to the observations. Finally, we have the comparison of two samples (A and B) of different surface condition, in figure 6. The situation is complicated by the fact that two variables, *viz.* surface and thickness, are changed simultaneously. However, in the early part of these curves where the thickness effect should be least important, if anything, the smoother sample B shows the faster kinetics. This result is opposite to that which would be expected based on a surface

[8] In virtually all atom and defect jump processes in crystals, a frequency factor of $10^{14 \pm 1}$ sec^{-1} is obtained.

controlled reaction. In view of these arguments, it seems necessary to reject the idea of a surface controlled step.

Accordingly, we turn to the following simple model which seems generally to account for the experimental observations. In this model, we assume that the appropriate defect is *interstitial* oxygen within the reduced δ phase. This suggestion is not in conflict with the earlier evidence (section 2.2.) that reduction of CeO_2 involves exclusively vacancies, since the present interstitials are taken relative to the stoichiometric δ phase. Since the oxidation is not diffusion controlled, it is reasonable to conclude that the interstitial defect migration process is one of very low activation energy ($\lesssim$ 0.4 eV), *i.e.*, sufficiently small to produce diffusion through the entire specimen in times much less than the time of the experiment. In view of this rapid interstitial migration, equilibrium of these defects with the external atmosphere should be quickly established. If the oxygen interstitials are singly ionized, the reaction is (in the Kröger-Vink notation [12]):

$$O_2 \rightleftarrows 2O_i' + 2\oplus$$

which leads to the mass action equation

$$[O_i']^2[\oplus]^2/p_{O_2} = K_1(T) \tag{8}$$

Since $[O_i'] = [\oplus]$, it follows that $[O_i'] \propto p_{O_2}{}^{1/4}$. On the other hand, if the interstitials were unionized or double ionized, their concentration would go as $p_{O_2}{}^{1/2}$ and $p_{O_2}{}^{1/6}$, respectively.

The second assumption of the model is that nuclei of the α phase are already present in the quenched material, *e.g.*, at structural imperfections. The final assumption is that the rate limiting process is the transfer of an interstitial oxygen ion in the δ phase over to the α phase at the δ-α phase boundary.

This model explains why diffusion is not rate controlling, and therefore, why results are independent of sample thickness. It is also consistent with the observed pressure dependence (see below (eq 6)), if one assumes that the singly ionized state of the interstitial is predominant. The model also predicts the shape of the oxidation profiles of the type shown in figures 5, 6 and 8. Thus, if the growing particles of α are initially spherical in shape, the rate of growth is given by

$$dy/dt = k_o n_o \cdot 4\pi r^2 \tag{9}$$

where y is the average composition of the entire sample, r the radius of a growing α region, n_o the number per unit volume of such growing particles (*i.e.*, the original number of nuclei) and k_o a rate constant. Because the rate is controlled by the surface reaction, we also have $r = Kt$, so that $\Delta y \propto t^3$ for the initial portion of the curve. Figure 9 shows that this initial cube law is obeyed reasonably well. The point at which the oxidation curve departs from the cube law and the slope begins to decrease is then interpreted as the beginning of interference of the growing α regions.

Finally, this model permits us to understand why the metastable α′ state is the end product of the low temperature oxidation process. For, only so long as the δ phase is continuous can oxygen be rapidly transported to the growing interfaces. As soon as small regions of δ phase are isolated, the process of further growth requires transport of oxygen through regions of the α phase. This is a much slower process and, therefore, cannot take place until the temperature is further elevated. This interpretation seems to lead to the prediction that the α′ structure is a two-phase mixture of α and δ. However, if the δ regions are small enough, they will be severely strained by the α matrix, since the two are coherent. Accordingly, such small regions would behave more like microdomains than as particles of an independent second phase, which is consistent with the type of diffraction pattern shown in figure 2.

In summary, the present model provides a basis for understanding of several of the key facts associated with the anomalously rapid mass transport of oxygen in the low temperature oxidation of reduced CeO_2. On the other hand, the reader should note that, in the data pre-

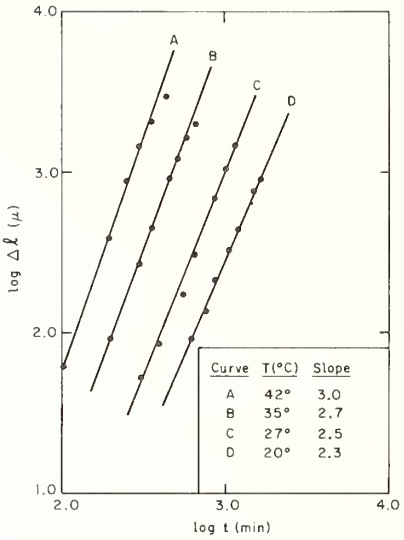

Fig. 9. Log-log plot of initial change in length of quartz spring *versus* time at four temperatures. The slopes of the curves are given in the inset.

sented here, the variables are not always controlled as well as required. For example, whereas the model assumes that the initial reduced state is completely the δ phase, the actual y-values at the start of the runs used to obtain figures 5 and 9 fall somewhat below the ideal value of 1.818 of the δ phase. The structure at the start may therefore be more complex than that assumed in the model. Another example is in figure 6 in which both sample thickness and surface condition have been varied simultaneously. Finally, there is the question of why flux grown crystals show slower oxidation kinetics. It is clear, therefore, that further kinetic studies which will provide a more stringent test of the model are required. Such studies are currently under way in this laboratory.

4. ACKNOWLEDGMENTS

This work was supported by the Advanced Projects Research Agency. The authors are also grateful to Messrs. H. Tuller and S. P. Ray for their valuable assistance in carrying out some of the x-ray and electrical conductivity experiments.

5. REFERENCES

[1] Bevan, D. J. M. and Kordis, J., J. Inorg. Nucl. Chem. 26, 1509 (1964).
[2] *Defects and Mass Transport in Single Crystals of Refractory Oxides,* Semiannual reports to ARPA under Contract DAHC-15-68-C-0129, May 1, 1968 and Nov. 1, 1968.
[3] Sawyer, J. O., Hyde, B. G., and Eyring, L., Bull. Soc. Chim. France 1190 (1965).
[4] Kofstad, P. and Hed, A. Z., J. Am. Cer. Soc. 50, 681 (1967).
[5] Blumenthal, R. N., Lee, P. W., and Panlener, R. J., J. Electrochem. Soc. 118, 123 (1971).
[6] Bevan, D. J. M., J. Inorg. Nucl. Chem. 1, 49 (1955).
[7] See, for example, Anderson, J. S. in *Problems of Nonstoichiometry,* ed. Rabenau, A., North Holland, Amsterdam 1970, Chap. 1.
[8] Steele, B. C. H. and Floyd, J. M., Proc. Brit. Cer. Soc. No. 19, March 1971, p. 55.
[9] Vinokurov, I. V. and Ioffe, V. A., Sov. Phys.-Solid State 11, 207 (1969).
[10] Levin, R. L. and Wagner, J. B., Jr., Trans. AIME 233, 159 (1965).
[11] Childs, P. E. and Wagner, J. B., Jr., in *Heterogenesus Kinetics at Elevated Temperatures,* ed. Belton, G. R. and Worrell, W. L., Plenum Press, New York, 1970, p. 269.
[12] Kröger, F. A. and Vink, H. J., Solid State Physics 3, 310 (1956).

DISCUSSION

A. D. Franklin: Do you know the source of the extremely high conductivity in the alpha prime phase; is it ionic or electronic?

A. S. Nowick: We think it is at least partially electronic, but in view of the observed rapid migration, it must also have a substantially ionic component. We are just now in the process of determining the transference numbers.

L. Eyring: Do I understand that at none of these temperatures up to 45 °C did you see a completely bleached end product?

A. S. Nowick: This is correct. The composition levels off at a final value which represents the metastable state. To produce bleaching is not a matter of a slight increase in temperature or of waiting a somewhat longer time. The kinetics are very slow at the end of each run; to produce the bleaching one must go up another 150 degrees at least.

L. Eyring: So, its something like 200 °C.

A. S. Nowick: Yes, that is correct.

W. Van Gool: I don't see how you are able to deduce something from this defect chemistry by just comparing the macroscopic and lattice dimensions. I should expect that even when you have an interstitial model you should find the same relationship as you found experimentally. You are working here with volumes and the differences between the two defect situations is a difference in mass, but not in volume.

A. S. Nowick: The difference between the two defect situations (oxygen vacancies as against cerium interstitials) is not a difference in mass, but a difference in the number of unit cells in the lattice. The macroscopic dimensions are sensitive to the number of unit cells, while the x-ray lattice parameters are not.

National Bureau of Standards Special Publication 364, Solid State Chemistry, Proceedings of 5th Materials Research Symposium, issued July 1972.

ANION CENTERED COORDINATION POLYHEDRA AND RELATED PHYSICAL PROPERTIES IN RARE EARTH OXIDES AND OXYSALTS

Paul E. Caro

Centre National de la Recherche Scientifique
Laboratoire des Terres Rares
Bellevue, France

The structures of rare earth oxides and oxysalts can be conveniently described in terms of linkages of anion centered coordination polyhedra, namely tetrahedra, yielding two-dimensional or three-dimensional frameworks. A complex "lanthanyl" cation $(LnO)_n^{n+}$ can be recognized. It has two different arrangements of tetrahedra, one of them being identical with the well known "bismuthyl" cation $(BiO)_n^{n+}$. The structural elements are similar to the classical SiO_2 and Si_xO_y ones; SiO_4 tetrahedra frameworks, used for silicates structures classification. Other anions than oxygen (sulfur and halides) yield isomorphous networks.

Such types of structures imply some sort of covalent bonding. The covalence of the bond can be shown from optical measurements on solids. For (OLn_4) compounds the absorption spectrum is displaced to the red (nephelauxetic effect), a phenomenon which corresponds to the lowering of the Racah's parameters of the 4 f^n configuration. The mixing of the $|\ 4\ f^n\rangle$ wave functions with ligand wave functions also yields larger transition probabilities and the $(LnO)_n^{n+}$ materials are very effective phosphors.

The layered oxide structures also yield textured thin films which exhibit epitaxial continuity and intergrowth between the rare earth oxides phases.

The layered polymolecular complex cation concept can be applied to rare earth extended non-stoichiometric systems. It can be shown that the chemical composition of all the known phases of those systems can be accounted for in term of the succession along a main crystallographic axis of four planar chemical units ABCD. Non-stoichiometry occurs because a layered structure AB is able to be interleaved through another layered structure ADCD. A general chemical formula for the ordered phases was derived, for the bastnaesite family of compound (AB = bastnaesite, ADCD = synchisite), the Ln_2O_3-LnF_3 systems (AB = tysonite, ADCD = trigonal EuOF), the LnO_x systems (AB = Ln_6O_{10}, ADCD = $Ln_{12}O_{22}$) and the $LnCl_3$-$LnCl_2$ system (AB = $LnCl_3$, ADCD = $LnCl_2$). All of the compounds contain layered polymolecular complex cations.

Key words: Complex ions; coordination polyhedra; 4 f^n configurations; non-stoichiometry; polymolecular frameworks; refractory materials; rare earth optical spectra; rare earth oxide; thin films.

1. INTRODUCTION

A few years ago [1][1] we introduced a structural description of the rare earth sesquioxides, and of several other rare earth compounds we called "oxysalts", based on the recognition of the importance of the coordination of the oxygen atom. The process is to abstract coordination polyhedra of metallic atoms (the cations) *around* the oxygen atom and to describe the structure in term of linkages of corners, edges, or faces, whatever is convenient, of these polyhedra together. This is a very well known and successful descriptive scheme for structures in inorganic chemistry, but the abstraction is usually applied

[1] Figures in brackets indicate the literature references at the end of this paper.

only to cations coordination polyhedra. Anion centered coordination polyhedra are described but very occasionally [2]. Nevertheless, they sometimes offer a challenging and provocative way to the understanding of structure and bonding.

We think this is indeed the case for a score of rare earth compounds. It turns out that the proposed description applies specially well to those compounds of the rare earths which are high-temperature materials. It may also help to understand some of their fundamental properties and high-temperature behavior. We shall consequently restate briefly, first, our unified description of rare earths oxides and other pertinent refractory materials.

2. THE TETRAHEDRAL COORDINATION OF OXYGEN IN RARE EARTH OXIDES AND OXYSALTS.

The rare earth sesquioxides exhibit, along the rare earth series, three fundamental structural types: A-type Ln_2O_3 (we shall use the symbol Ln as a convenient one for the whole rare earth group cations) which is hexagonal, B-type Ln_2O_3 which is monoclinic, and C-type Ln_2O_3, cubic. At high temperatures there is also two other additional phases the H (hexagonal) and X (cubic), but their structure are still unknown. The rare earth oxides structural pattern versus temperature was investigated up to the melting point by Foëx and Traverse and their papers [3], [4] provide all the informations on transition temperatures, stability domains and the like.

C-type Ln_2O_3 is derived from the fluorite structural type by removing a quarter of the anions. The fluorite structure is the basis for the understanding of the non-stoichiometric rare earth oxide systems LnO_x (Ln_2O_3-LnO_2), which exhibit several sharply defined compounds as the thermodynamical and structural studies of LeRoy Eyring and his school have shown [5], [6]. Of those intermediate compounds only one is of a known structure at the present time, it is the most stable of them all, Ln_7O_{12}. The fluorite structure can be conveniently described in terms of anion centered coordination polyhedra. The oxygen in LnO_2 is at the center of a tetrahedron of metallic atoms and the whole structure may be seen as three-dimensional framework of OLn_4 tetrahedra linked together by their six edges. Then, from the known position of oxygen vacancies in C-Ln_2O_3 and Ln_7O_{12} it is easy to show that C-Ln_2O_3 is a three-dimensional building of OLn_4 tetrahedra linked together by four out of six edges, and Ln_7O_{12} a three-dimensional building of the same OLn_4 tetrahedra, but linked together with five out of six. In other words, for the two structures, all of the OLn_4 tetrahedra have identical linkages and are topologically equivalent. Curiously enough, the observed structures are the only ways to pack tetrahedra into space by linking together only four or five of their edges (although there are other ways for linkage of five edges but far less symmetrical than the one observed in Ln_7O_{12} and of a different stoichiometry).

A OLn_4 tetrahedra packing appears conspicuously in A and B-Ln_2O_3. However this time, there are two types of oxygen atoms in the structure, one is inside a tetrahedron of metallic atoms, the other one is six-coordinated and is further removed from the rare earth atoms than the former one (d. O-Ln = 2.70 Å versus 2.40 Å, in A-La_2O_3). The remote oxygen atom can be replaced by other chemical species: the familiar example is S^{2-}, yielding the oxysulfide $(LnO)_2S$ which is isomorphous to the A-type oxide. We proposed to formulate A-Ln_2O_3:$(LnO)_2O$ because the structure is made along the hexagonal *c*-axis of a succession of slabs of a "complex group" $(LnO)_n^{n+}$-built of OLn_4 tetrahedra edge-linked in a manner derived from the fluorite structure - separated by planes of oxygen anions. The layered character of A-Ln_2O_3 is very clearly exhibited by the easy cleavage of the single crystals perpendicular to the *c*-axis [7].

B-type Ln_2O_3 is very similar to the A-type but is monoclinic because the hexagonal symmetry is lost following a small displacement of the $(LnO)_n^{n+}$ slabs with respect to each other, together with a tetrahedra distortion induced by the lanthanide contraction. The close relationship between A and B-Ln_2O_3 was demonstrated by the author and his associates [8] from electron diffraction and microscopy on thin oxide films.

Other rare earth oxysalts exhibit edge-linked OLn_4 tetrahedra which also develop into a $(LnO)_n^{n+}$ slab but with a different symmetry. This other type of slab is usually associated with monovalent anions (Cl^-, OH^-) and the best structural example is the rare earth oxychloride (LnO)Cl.

Now, the two types of $(LnO)_n^{n+}$ structural slabs, or layers, are simply slices of the fluorite (LnO_2) structure. One of them (A-Ln_2O_3), is a slice perpendicular to the C_3 axis in the fluorite cake and involves a Ln-O-O-Ln succession of fluorite planes parallel to (111), the other one is a slice perpendicular to a C_4 axis and involves a Ln-O-Ln succession of planes. Both slices have the same overall formula $(LnO)_n^{n+}$. To distinguish the two arrangements we will, from now on, label them as $(LnO)_n^{n+}$ (C_3) for the type encountered in A (or B)-Ln_2O_3 and $(LnO)_n^{n+}$ (C_4) for the one found in (LnO)Cl. The labelling *does not* implies that the layers imperatively always exhibit a C_3 or C_4 symmetry axis perpendicular to them through the atomic positions, this fundamental symmetry can be slightly distorted (as in B-Ln_2O_3). An interesting character of both layers is that they do not have a plane of symmetry perpendicular to the C_3 or C_4 axis. (That means there can be "up and down" layers with respect to an oriented C_3 or C_4 axis), (figs. 1 and 2).

Numerous rare earth compounds exhibit one or the other type of complex cation. Such compounds can be recognized, or suspected, easily because for a large number of anions the rare earth derivatives come in two forms: one is a true Ln^{3+} salt, it is usually highly reactive, soluble, has a low melting point or decomposes easily (for instance the rare earth halide series); the other one is an oxycompound and contains the $(LnO)_n^{n+}$ unit, it is on the contrary chemically inert, strictly insoluble, has a high melting point or decomposition temperature. Two good examples are the oxynitrates $(LnO)NO_3$ which are insoluble (a character which is not common for a nitrate), and the oxycarbonates $(LnO)_2CO_3$, which at the beginning of the rare earth series exhibit the highest decomposition temperature for an inorganic carbonate ($(LaO)_2CO_3$ - 950-1000 °C) [9, 10].

The rare earth oxycarbonates $(LnO)_2CO_3$ are polymorphous materials. There is three forms, I (quadratic), Ia (monoclinic) and II (hexagonal). Two of them, I and Ia, correspond apparently to $(LnO)_n^{n+}$ (C_4), the other one to $(LnO)_n^{n+}$ (C_3). This is the only oxysalt for which both infinite cations were reported. At the beginning of the rare earth series, the C_3 oxycarbonate appears to be more stable than the C_4 types. In the middle of the series the C_4 oxycarbonate type I is easier to prepare, and at the end the mere existence of an oxysalt is in doubt. The C_3 oxycarbonate decomposes to A-type Ln_2O_3, but the C_4 types decompose to C-Ln_2O_3.

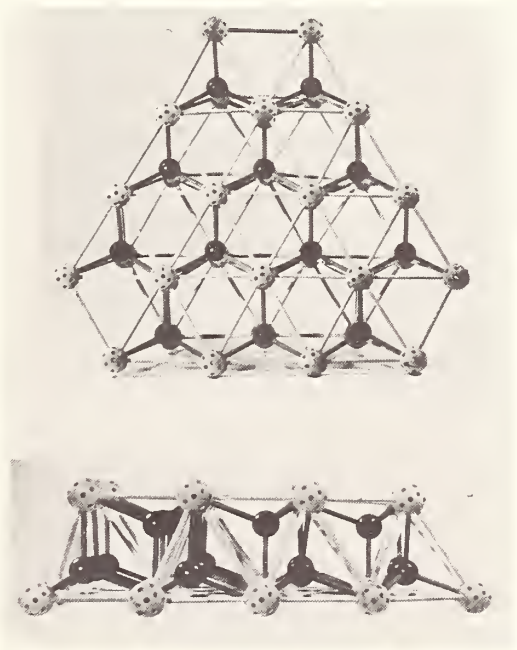

Fig. 1. The "hexagonal" $(LnO)_n^{n+}(C_3)$ polymeric cation. The smaller balls are the oxygen atoms.

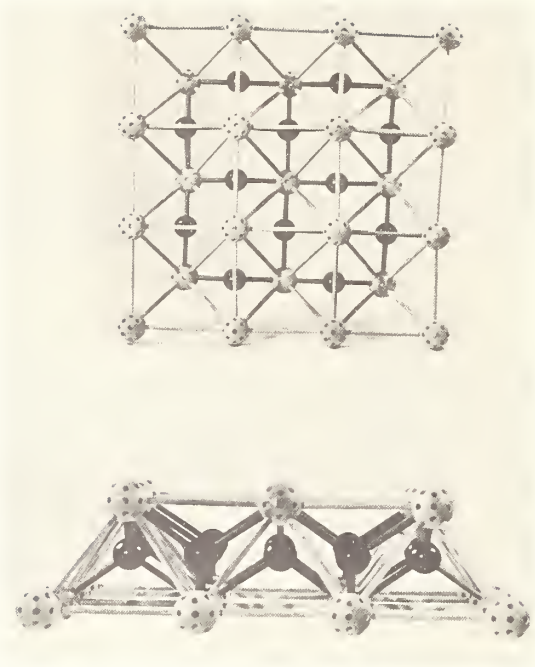

Fig. 2. The "quadratic" $(LnO)_n^{n+}(C_4)$ polymeric cation. The smaller balls are the oxygen atoms.

As a general rule, the rare earth oxysalts are far more easy to synthetize for the ceric group. Their easy occurrence is, in fact, a fundamental chemical property of the ceric group. After gadolinium in the series, the oxycompounds are not so well defined. This is due to the increased difficulties to conserve the compact, fluorite derived, layers, in view of the progressive lanthanide contraction which reduces the Ln-O distance beyond the limit acceptable for the oxygen to oxygen distance in the OLn_4 tetrahedra close packing. In C-type Ln_2O_3, however, the tetrahedra form a less rigid three-dimensional network, they can distort themselves more easily, and the structure, being able to adjust to the reduced cation radii, becomes the stable one in the rare earth oxide series.

$(LnO)_n^{n+}$ (C_4) has a well known counterpart in bismuth chemistry. It is the so-called bismuthyl cation $(BiO)_n^{n+}$. The crystallography of the bismuthyl compounds is known from the work of the swedish scientist Sillen [11]. $(LnO)_n^{n+}$ (C_4) and $(BiO)_n^{n+}$ are strictly identical and the salts of both cations are isomorphous and can exhibit large domains of solid solutions when the Ln-O distance is compatible with the Bi-O one (2.29 Å). Because of that analogy it may be convenient to adopt the word "lanthanyl" to qualify the $(LnO)_n^{n+}$ (C_4) and $(LnO)_n^{n+}$ (C_3) compounds. The bismuthyl group $(BiO)_n^{n+}$ appears as a layer in the structures of numerous complex oxides and complex oxyhalides of bismuth (Wells [12]), providing a good example of the type of structural entities to be expected from the occurrence of such a type of bonding. We will return to the bismuth case in connection with the problem of non-stoichiometric systems.

3. THE SILICON COMPOUNDS ANALOGY

The structural elements we have discussed so far have nothing unusual, but for the fact that the primitive unit is an oxygen centered coordination polyhedron. It will be easily noticed that what we are describing is analogous in principle to the scheme used to classify and describe the silicon oxides and the silicate families [12]. The primitive unit is in that case a cation centered coordination polyhedron which is also a tetrahedron. In the silicon compounds the SiO_4 tetrahedra are linked together by their corners, instead of edges for the OLn_4 tetrahedra. Depending on the number of corners joined together SiO_4 tetrahedra develop complex cations, rings, chains, or bi-dimensional sheets. The sheets are formed by

the sharing of three corners, their overall composition is $(Si_2O_5)_n^{2n-}$, and they can exhibit different geometries (6 ring sheets like in the micas or an alternance of 4 and 8 rings in such minerals as apophyllite). These two $(Si_2O_5)_n^{2n-}$ sheets are seen to have a formal analogy with the two $(LnO)_n^{n+}$. If the SiO_4 tetrahedra share all of their corners we have three-dimensional structures. Those are the different forms of silica SiO_2. There the formal analogy is to the three-dimensional framework of OLn_4 tetrahedra in LnO_2, Ln_7O_{12} and C-Ln_2O_3.

The structures of layered silicates are rather complex and impressive. The negatively charged sheets can be held together by cations (of course the $(LnO)_n^{n+}$ sheets are correspondingly held together by anions), or they can be in structural continuity with other (positively charged) frameworks (like layered hydroxydes), as does the bismuthyl cation in several oxides of bismuth. Also the complexity of the properties come, in part, from the possibility to substitute another cation, with a different charge, Al^{3+}, for the silicon in the $(Si_2O_5)_n^{2n-}$ (and also in other types of SiO_4 frameworks). Similarly the structures in the PrO_x system must accommodate two differently charged cations Ln^{3+} and Ln^{4+}. Polymorphism in layered silicates is frequent because the layers can undergo translations with respect to each other. For $(LnO)_n^{n+}$ compounds the same phenomenon yields polymorphism (A and B-Ln_2O_3, type I and Ia $(LnO)_2CO_3$) and can be a cause of structural disorder (*i.e.* poorly defined powder patterns are frequent for oxysalts, and intense twinning is the rule in B-Ln_2O_3 crystals).

The correspondence we are trying to establish between the classical picture of the well-known silicon family and our descriptive structural scheme for rare earth oxides and oxysalts of high temperature interest is not entirely intended as an illustrative trick. We do mean that the two groups of compounds, although of unequal nature and complexity, have in common a fundamental component. In the silicon family, there is, of course, a strongly covalent σ bonding between silicon and oxygen in the SiO_4 tetrahedral unit. Because of the bonding, one, two, or three-dimensional polymeric atomic frameworks are easily built (see also the Huggins theory of "structons" [13]). We then claim that the occurrence of formally analogous structural entities in the rare earth compounds is a sign of the existence of a formally analogous, not, evidently, identical but practically as efficient, bonding process between the oxygen and the rare earth ligand (in fact the mode of bonding is more likely to be distributed through the complex atomic association). Because of the efficiency of the bonding and its "polymolecular" nature both the silicon and the rare earth compounds are effectively high temperature materials.

4. OTHER TYPES OF ANION CENTERED COORDINATION POLYHEDRA AND LAYER STRUCTURES IN RARE EARTH COMPOUNDS

Complex entities, strictly analogous to the $(LnO)_n^{n+}$, can be formed with other anions than oxygen, namely S^{2-} and F^-, as work undertaken in Professeur Flahaut's laboratory in Paris by Dagron and Thevet has shown recently [14]. In the structures of the rare earth halogenosulfides LnSF, LnSBr, and LnSI, $(LnX)_n$ structural layers appear made of XLn_4 tetrahedra sharing edges. X is fluorine in LnSF, sulfur in LnSBr and LnSI. The layers are held together by two planes of the remaining anions. The complex layer exhibits, like $(LnO)_n^{n+}$, the two C_3 (SmSI) and C_4 (CeSI) polymorphs.

Still another, but different, type of apparent "complex polymeric cation" is exhibited by the rare earth fluorine association in the tysonite structure of the ceric rare earth fluorides LnF_3. There exists a plane, perpendicular to the *c*-hexagonal axis, which contains the same amount of rare earth and fluorine atoms, in an array which can be conveniently described as triangles of rare earth atoms having at their center a fluorine, each metal corner being common to three triangles. The overall composition is $(LnF)_n^{2n+}$. It is known from NMR experiments, that one of the fluorine atoms in tysonite is more strongly bonded to the rare earth than the other two [15]. The tysonite sheet is specially important because it is seen associated with a well documented case of nonstoichiometry and microdomain formation, in the structure of the bastnaesite family of rare earth fluorocarbonates: $(LnF)CO_3$ and its associations with calcium carbonate. Similar $(LnF)_n^{2n+}$ sheets were just reported in LaSeF (α) and Ce_2SeF_4 by Nguyen-Huy-Dung from Flahaut's laboratory [16]. As a pleasant contribution to the power of the tetrahedron abstraction let us mention the discovery by the Flahaut group [17] that the supposed β form of Ln_2S_3 was in fact a ternary compound with a formula $Ln_{10}S_{14}O$ and a structure organized around a single isolated OLn_4 tetrahedron!

Corner sharing of OM_4 tetrahedra (M is not restricted to a rare earth) has been described [18] as a convenient way to visualize the pyrochlore structure. This $A_2B_2X_6X'$ structure is interpreted as two interpenetrating networks, one is a network of classical BX_6 octahedra, but with the B atoms forming a rigid tetrahedron skeleton, the other one is a network of $X'A_4$ tetrahedra sharing corners in an anti-cristobalite way. The AX'A angle stays remarkably close to 110° through the whole range of stability of the pyrochlore structure (for a position parameter x running from 0,300 to 0,375). In that perspective the pyrochlore structure appears to be closely related to the SiO_2 ones and to such classical structures as Cu_2O which can also be entirely viewed in terms of OCu_4 tetrahedra sharing corners. Other familiar examples of structures easily described in terms of linkages of anion centered tetrahedra are zinc-blende and wurtzite.

5. EVIDENCES ON THE BONDING FROM THE OPTICAL PROPERTIES

The bonding in such materials as rare earth oxides is generally considered to have an entirely ionic character on the basis of Madelung's constant calculations [19]. However, as Jorgensen explains [20], a good agreement between the Madelung energy and the heat of formation of a crystal does not mean that the crystal is purely ionic. On the contrary one should expect between 95 and 105% agreement for a covalent compound (but only 90% for a purely ionic one, because of the repulsion between electrons in close shells). Sophisticated methods of evaluating bonds, such as LCAO-MO, have been widely used for organic molecules, but have not been applied extensively to continuous solids. If the compounds under discussion were not rare earths ones, the treatment of the bonding would be restricted to highly speculative models. However, the rare earth atoms having ground 4 f^n configurations and the $^{2S+1}L_J$ levels of the free ion keep their identity in the solid. They are not greatly affected by the crystal field like the $^{2S+1}L_J$ levels of the d^n configurations: the overall splitting is generally less than 500 cm^{-1}. The levels split depending on the symmetry at the rare earth site, into 2J+1 (n even) or J+1/2 (n odd) Stark components at the maximum. The transitions between the levels are well defined and give rise to the sharp lines in the absorption or emission spectra of the rare earth compounds. Rare earth crystal field splittings yield information on the symmetry at the rare earth site and the number of different crystallographic sites, and are generally used as local structural probes sensitive to short range order. Jorgensen (see ref. [20] for an extensive treatment of the spectroscopic problem) pointed out that the change in the position of the barycenter of the $^{2S+1}L_J$ levels with respect to the free ion, or an arbitrary basis compound, was linked to the nature of the bond supported by the rare earth atom. Increased covalency (*i.e.* progressive overlap of the ligand wave functions with the transition electron wave functions) brings a decrease of the positions of the barycenters in the energy scale with respect to the free ion: the absorption spectra is shifted to the red. This is the nephelauxetic effect. The red shift corresponds to a decrease of the Racah parameters describing the matrix elements of the interelectronic repulsion hamiltonian. Because of the sharp rare earth spectra, the nephelauxetic effect, though small, can be quite precisely measured. However it is always necessary to record the absorption spectra at liquid helium temperature, in order to observe transitions to the excited levels, from the lower ground state Stark component only. Fluorescence experiments, or room temperature absorption, must be used to determine the Stark splitting ground state itself and its barycenter (the zero line for the 4 f^n configuration energy levels) [21,22]. The barycenters of the excited levels are usually easily determined from the liquid helium absorption spectra. From their positions, the Racah's parameters of the configuration can be calculated through a computer program [23]. From those experiments a *relative* scale of covalency can be established. The method measures the extent of the pertubation of the 4 f^n electron wave functions by the environment. This does not imply that the 4 f^n electrons participate extensively in the bonding. The bonding may be simply strong enough to carry over a bit of information down to the deep-core 4 f^n electrons beneath the complete $5p^6 5s^2$ shells.

We have recorded the absorption spectra of several characteristic structural types of neodymium compounds. The results are reproduced in figure 3 [24], on the form of the position of the $^4P_{1/2}$ level (which is not split by the crystal field) of the $4f^3$ configuration above the lower Stark component of the $^4I_{9/2}$ ground state. The reason for using the lower Stark component is that for several compounds the ground state barycenter cannot be easily determined. However the crystal field being more or less of comparable magnitude from compound to compound the succession on figure 2 is a reasonably good *nephelauxetic scale* supported by the full calculation of the Racah parameters [23]. Several reliable data from the literature were used to help construct figure 3, pertinent references and

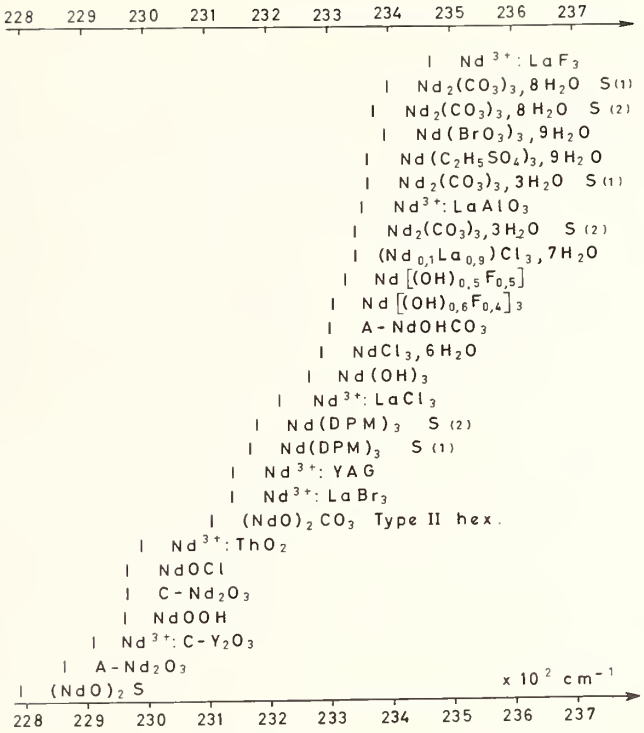

Fig. 3. Position of the $^2P_{1/2}$ levels of neodymium $4f^3$ above the lower Stark component of the ground level $^4I_{9/2}$. (liquid helium temperature).

further details are given in reference [23]. A careful comparison shows that the levels are shifted by an amount proportional to their energy, a fact which incited Jorgensen to introduce a nephelauxetic parameter β.

$$\beta = \frac{\text{Energy } {}^{2S+1}L_J \text{ (compound)}}{\text{Energy } {}^{2S+1}L_J \text{ (free ion or basis compound)}}$$

From figure 3, one sees that β runs from 0.96 to 1.00 (if the basis compound is chosen to be the fluoride).

It is clear from figure 3 that the compounds which have the largest nephelauxetical effects are the rare earth oxides and the salts of the $(LnO)_n^{n+}$. The preferential bonding to the oxygen shows up by the fact that the $(LnO)_n^{n+}$ salts are quite close to each other on the scale, and well separated from the other compounds (compare for instance (NdO)OH and $Nd(OH)_3$). The other immediate fact is, that the effect increases from the fluoride, to the chloride, then to the bromide. This is what is generally observed: the effect depends first on the ligand, and for a given ligand, it depends on the distance between the rare earth atom and the ligand. The method is quite sensitive for the measurement of distances: Nd-O in Nd_2O_3 is 2.34 Å, 2.35 Å in NdOCl 2.48 Å for $Nd(OH)_3$ and one can see that the two crystallographic sites in $Nd_2(CO_3)_3,8H_2O$ with mean distances of 2.60 and 2.61 Å, respectively, are well differenciated. A smaller distance means generally a chance for a tighter bonding, the nephelauxetic effect shows that the 4f electrons wave functions are affected by the presence of a closer ligand.

The relative "covalency" scale exhibited on figure 3 is in agreement with recently [25] reported measurements through Mossbauër spectroscopy of "relative covalency" in a series of europium compounds. As in our studies the europium sesquioxide was found to be the more covalent one and the fluoride the lesser.

An interesting character of the compounds on figure 3, is that all of those which have the largest nephelauxetic effect from $(NdO)_2S$ to $Nd(DPM)_3$ inclusively, and excluding the bromide, have structures characterized by the existence of a Nd-O-Nd angle close to the tetrahedral value 109°. This is true for $Nd(DPM)_3$, a β-diketonate where the rare earth atoms came in pairs in a dimerized molecule, with a seven coordination very similar to the one in the A-type oxide (the molecule is volatile at 150 °C under 10^{-2} mmHg), and also for the garnet where the oxygen atoms in the irregular eight coordination polyhedron of the rare earth are in a tetrahedron of metal atoms, however badly distorted.

There is another proof of the perturbation of the 4 f^n configuration in the $(LnO)_n^{n+}$ compounds. It comes from the intensities of the transitions between the $^{2S+1}L_J$ levels. Theoretically, only magnetic dipole transitions should be observed between those levels and only if $\Delta J = 0 \pm 1$, a $0 \rightarrow 0$ transition being excluded. In fact the transitions are more often of an electric dipole character, mostly because there are a very few crystallographic sites, where the trivalent rare earth is sitting, which exhibit a center of inversion. But those electric dipole transitions must borrow their intensities from a parity mixing in at least one of the energy levels involved. It is well known that the $^{2S+1}L_J$ levels must be described in intermediate coupling as a sum of $|\ ^{2S+1}L >$ with the same J, however parity mixing needs the inclusion of levels from *another* configuration, 4 $f^{n-1}5d$ the next higher configuration is, for instance, a convenient one. The other parity component can be introduced through mixing with the orbitals of the ligands, as is done classically in MO theory. A strong intensity of the transitions is the sure indication of an important degree of mixing. It will be enough to say, to prove the importance of this phenomenon for $(LnO)_n^{n+}$ compounds, that the most efficient rare earth phosphors used for color TV applications are rare earth oxysalts, specially oxysulfides. All rare earth oxysalts, and the oxides, are very bright phosphors. It has been shown [26] that the intensities of the transitions increases exponentially with the magnitude of the nephelauxetic effect.

There is consequently little doubt, from an optical point of view, that the rare earth atom is feeling something in the oxides and oxysalts. However the 4 f^n orbitals are obviously not responsible for the main part of the bonding. The $(LnO)_n^{n+}$ compounds, and the oxides, show strong absorption bands in the ultra-violet (beginning at 2700 Å for A-Nd_2O_3). The U.V. absorption bands in SiO_2 quartz and corundum Al_2O_3 beginning about 1500 Å were recently interpreted [27] on the basis of a covalent LCAO-MO type of bonding extended through the crystals, because an ionic model was inadequate to explain the data. It should be at this point remembered that aluminum replaces silicon quite easily in the frameworks of silicates and that SiO_2 and Al_2O_3, like the rare earth oxides, are rather good refractory materials. However a serious model of bonding for the rare earth compounds should obviously wait until more simple and more classical structures can be precisely described in LCAO-MO, or other appropriate scheme. Anyway, sp^3 hybridization seems to be a logical starting point for the oxygen atom.

6. THE ORIENTED TEXTURES OF RARE EARTH OXIDE THIN FILMS

Rare earth oxide thin films were produced by oxidation of rare earth metal thin films. Their thickness (500 Å to 2500 Å) allows observation by electron diffraction and microscopy. Large crystals (several dozens of microns) of the two layered oxides A and B-Ln_2O_3 can be grown from the low temperature C-type phase small crystals by directly heating the film with the electron beam. Those films have a preferred texture as shown on figures 4 and 5. The plane of the film is perpendicular to the *c*-hexagonal axis (*i.e.* parallel to (002) for the A-type) and parallel to the $(20\bar{1})$ plane for the B-monoclinic type. Both orientations correspond to the planes of the two infinite $(LnO)_n^{n+}$ layers in the structures. Large crystals of the C-type can also be grown, but only for those oxides whose C-type is stable at very high temperatures. The crystals then have also a preferred orientation, the plane of the film being parallel to (111) cubic as shown on figure 6. The image of the crystal (C-Dy_2O_3) is shown on figure 7.

It is technically interesting to be able to grow large oriented crystals of these refractory materials from the small crystals produced by the oxidation of a thin metal film. Dysprosium is specially interesting because the metal is volatile, the oxide is refractory and, being an yttric earth, it is also quite insensitive to atmospheric agents contrary to the ceric oxides.

Fig. 4. Electron diffraction of a crystal of A-Nd_2O_3. The electron beam is along the *c*-hexagonal axis. Plane of the thin film is parallel to (00.2).

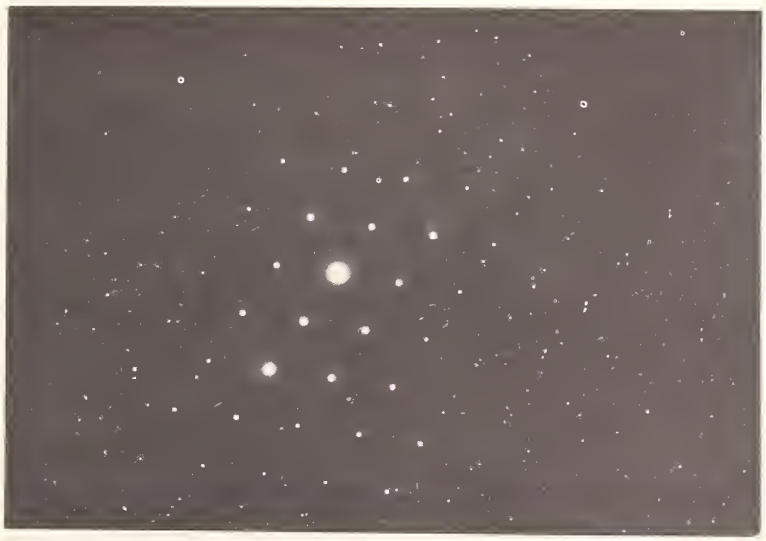

Fig. 5. Electron diffraction of a crystal of monoclinic B-Sm_2O_3. The electron beam is along $[10\bar{1}]$, 3.5° off the plane of the thin film which is parallel to $(20\bar{1})$.

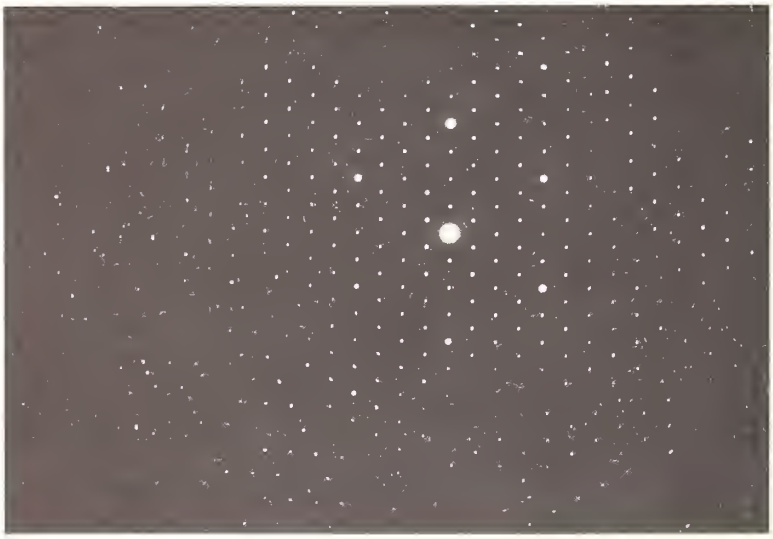

Fig. 6. Electron diffraction of a crystal of C-Dy_2O_3. The electron beam is along [111], the plane of the thin film is parallel to (111).

Fig. 7. Image of C-Dy_2O_3 crystal diffracting the pattern on figure 6 (X 60.000).

Electron diffraction and microscopy shows several modes of crystallographic relations between the rare earth oxides phases. The epitaxial continuity between A and B-Nd_2O_3 was measured after producing B-type crystals (fig. 8) inside the A-type crystals by application of a thermal stress. The B-type bands on figure 8 run in a characteristic zig-zag way. The epitaxial relationship is as follows: (00.2) and (11.0) of the hexagonal A-Nd_2O_3 are parallel respectively to $(20\bar{1})$ and (313) of the monoclinic B-Nd_2O_3 [28]. The situation is complicated by the existence of intense twinning in B-Ln_2O_3 (because there is four possible glide directions in distorting the $(LnO)_n^{n+}$ sheets in A-Ln_2O_3 from above one another) [8]. Twinning occurs principally with respect to {111} and {313} of B-Ln_2O_3. The appearance of the twinned crystals is shown on figure 9. At high temperature B-Dy_2O_3 grows epitaxially on C-Dy_2O_3 with $(20\bar{1})$ of B parallel to (111) of C and (111) of B parallel to (110) of C [29].

Fig. 8. Characteristic zig-zag and triangular domains of B-Nd_2O_3 in crystals of A-Nd_2O_3 (X 30.000).

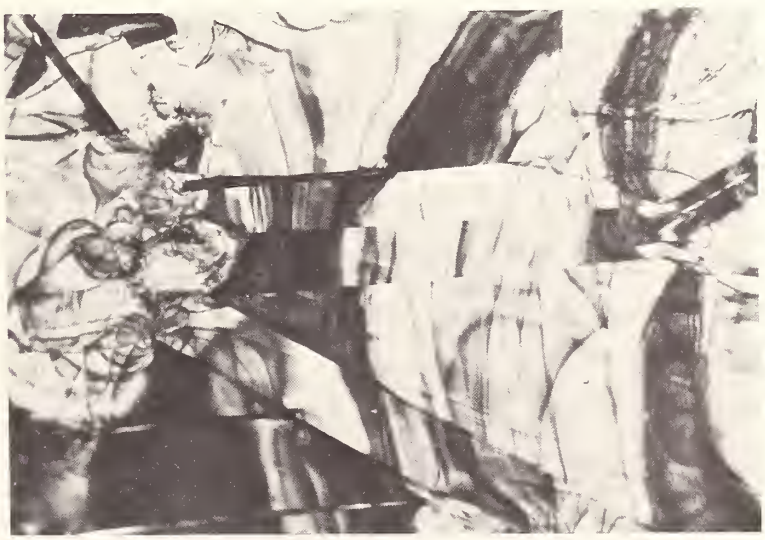

Fig. 9. Twinning and dislocations in B-Sm_2O_3. Twins are {313} and {111} (X 30.000).

Twinning and epitaxy keep the continuity of the $(LnO)_n^{n+}$ layers. The contact planes are usually perpendicular to the layers. However all the phenomena have not been yet investigated and only the most obvious ones were analyzed. The epitaxies can only be studied very briefly (A and B-Nd_2O_3) or at very high temperatures. The B-phase twinning is very complex, a (20$\bar{1}$) twinning (reversal of the layers) was for instance suspected.

The thin film studies entirely confirm, as does the single crystal cleavage habits, the layered character of the $(LnO)_2O$ oxides. The crystallographic axis, with respect to which the layers are stacked, is always perpendicular to the plane of the thin film. This main crystallographic axis turns out to be very important when one considers the implications for non-stoichiometric rare earth oxides.

7. LAYERED POLYMOLECULAR CATIONS AND NON-STOICHIOMETRY

The layered frameworks of atoms $(LnO)_n^{n+}$ (C_3), and $(LnO)_n^{n+}$ (C_4) and $(LnF)_n^{2n+}$ behave as individual cations with their own chemistry. A question may arise as to their possible part in the occurrence of non-stoichiometric compounds in several rare earth systems.

The behavior of the bismuthyl cation $(BiO)_n^{n+}$ may be a clue to this problem. Very complicated structures are known in the complex oxides and oxyhalides of bismuth. The $(BiO)_n^{n+}$ group in those compounds appears to be in epitaxial continuity with other types of structures and interleaved with them. For instance, there is an association of a pseudo-tetragonal symmetry with a perovskite type of structure, and the crystallography depends on the numbers of perovskites layers involved (1,2,3 or 4) between the $(BiO)_n^{n+}$.

Another striking example are the well known, and rather fascinating crystals in "syntaxic intergrowths" formed by the bastnaesite group of minerals $LnFCO_3$ (bastnaesite) $2LnFCO_3CaCO_3$ (parisite) $3LnFCO_3$ $2CaCO_3$ (roentgenite) and $LnFCO_3$ $CaCO_3$ (synchisite) [30]. The different phases have pseudohexagonal structures and can coexist in the same "single crystal" as a succession perpendicular to *c* (interface, planar, parallel to 00.1) of layers of the different minerals (there is also a three-dimensional intergrowth like the one of A and B-Ln_2O_3 in thin film). The structure of the individual compounds is made of a succession perpendicular to *c* of the same $(LnF)_n^{2n+}$ planes we described previously for tysonite (LnF_3), of Ca^{2+} planes, and of two types of carbonate ion CO_3^{2-} planes. We shall see later how these planes organize themselves.

Other complicated non-stoichiometric compounds are the microphases found in the LnF_3 - Ln_2O_3 systems. Bevan et al. [31] suggested the formula $(Ln_nO_{n-}\ F_{n+2})_4$. Compounds for n=7 (yttrium) and n=5 (Erbium) were isolated. Tanguy and Portier [32] found several symmetry types in $Eu(O,F)_x$ $I,5 \leqslant x \leqslant 3$, system. A rhombohedral phase occurs for $1.96 \leqslant x \leqslant 2.06$ (EuOF), a cubic phase (a high temperature one) for $1.96 \leqslant x \leqslant 2.42$ a quadratic phase for $2.16 \leqslant x \leqslant 2.20$, an orthorhombic one for $2.31 \leq x \leq 2.40$. The system exhibits also at high temperature, above 800 °C, a phase of a tysonite type $(LnF)F_2$. The optical examination of the Tanguy and Portier phases shows that only three of them have well defined local crystallographic sites for the rare earth. Those are EuF_3 (orthorhombic), EuOF (rhombohedral) and C-type Eu_2O_3. The other have broad absorption or emission lines, with however a pattern changing regularly with x. A structure has been proposed for rhombohedral EuOF by Mann and Bevan [33]. Along the (III) fluorite axis there is a succession of planes Ln-O-O-Ln-F-F-Ln-O-O-Ln... Such a succession is what is to be expected for the structure of the fluoride of $(LnO)_n^{n+}$ (C_3). The oxyfluorides are the only salts not clearly identified because of the uncertainty in the structures and the possible competition with the $(LnF)_n^{2n+}$ cation. In the Mann and Bevan structure the two fluoride planes between the $(LnO)_n^{n+}$ (C_3) layers are equivalent to the two fluoride planes between the $(LnF)_n^{2n+}$ layers in tysonite LnF_3 (hexagonal). We shall see that the combination of these elements is necessary to the understanding of the system.

The writer and J. D. Corbett [34] reported a most unusual series of non-stoichiometric phases associated with thermal analysis phenomenons in the $TmCl_2$-$TmCl_3$ system. N. A. Fishel from H. Eick Laboratory at Michigan State reported [35] that $YbCl_2$ with which $TmCl_2$ is isostructural, is of the structural type of CeSIα, which made it a chloride of a complex cation of $ClTm_4$ tetrahedra in C_4 symmetry equivalent to the $(LnO)_n^{n+}$ (C_4) according to the structures reported by the Flahaut group for the halogenosulfides [14].

For the famous Ln_2O_3-LnO_2 systems, we have already tried [1] to interprete the chemical composition of some of the compounds by using the $(LnO)_n^{n+}$ concept. We found a satisfactory agreement by using $(LnO)_n^{n+}$ (C_3) slabs separated, like in the $(BiO)_n^{n+}$ compounds, by layers of fluorite structure with one sixth of the anions missing in each oxygen plane. If there is no $(LnO)_n^{n+}$ the stoichiometry of this hypothetical phase is Ln_6O_{10} which is an unknown member of the supposedly Ln_nO_{2n-2} family of compounds. However there is a three-dimensional structure made of OLn_4 tetrahedra topologically equivalent joined by five edges out of six which corresponds to that stoichiometry but the framework looks less symmetrical than the one for Ln_7O_{12}.

From a comparison between the non-stoichiometric systems, we were able to isolate, in each of them, four different planar entities whose succession down a main axis of symmetry (*c* pseudo-hexagonal or [111] fluorite) defines the chemical composition. Let us call them A B C D. Some of the planes (or double planes) are anionic, others cationic. We will consequently have a rule according to which B will be always followed and preceded by A and C will be always followed and preceded by D. In table 1 we have identified our choice of the structural elements in the systems with each one of the code letters A B C D.

The notation "double plane" in table 1 indicates that one consider as a single chemical individual two sequential planes of identical composition. The complex cations may also be represented by a succession of letters, such as DCD, which stands for $(LnO)_n^{n+}$ (C_3). Each of the systems under consideration is characterized by the presence of a structural element corresponding to one or the other of the complex polymeric cations defined previously in this paper.

Table 1

Code for the Identification of the Four Planar Chemical Units in Rare Earth Non-Stoichiometric Systems

Code letter	Bastnaesite system	Ln_2O_3-LnF_3	LnO_x	$LnCl_3$-$LnCl_2$
A	$(LnF)_n^{2n+}$ (as in tysonite)	Double plane of fluoride ions F^- - F^- (as in tysonite)	Two planes of fluorite oxide ions with one sixth vacancies in each	Two planes of chlorides ions
B	a plane of "vertical" CO_3^{2-}	$(LnF)_n^{2n+}$ (as in tysonite)	a Ln plane as in fluorite	a plane of Ln^{3+} and a plane of chloride ions
C	a plane of Ca^{2+} ions	a double plane of oxide ions without vacancies as in fluorite	a double plane of oxide ions without vacancies as in fluorite	a plane of chloride ions similar to the oxygen's one in (LnO)Cl
D	a plane of "twisted" CO_3^{2-}	a plane of Ln^{3+} as in fluorite	a plane of Ln as in fluorite	a plane of Ln^{2+}
Complex ion unit	A is $(LnF)_n^{2n+}$	the succession D C D is $(LnO)_n^{n+}$ (C_3) B is $(LnF)_n^{2n+}$	the succession D C D is $(LnO)_n^{n+}$ (C_3)	the succession D C D is $(LnCl)_n^{n+}$ (C_4)

Then, most, if not *all*, of the known chemical compositions for the phases in all non-stoichiometric systems can be accounted for with *the same succession of letters* if the chemical code in table 1 is respected.

Results are condensed in table 2.

Inspection of the table shows that the non-stoichiometric system occurs because a layered structure AB is able to be interleaved through another layered structure ADCD (the reciprocal is not true). The A elements insure the epitaxial continuity. The result is that an infinite series of compounds can occur in the binary system between the phases AB and ADCD. However ADCD is generally not one of the extremity of the phase diagram under consideration. It is $Ln_{12}O_{22}$ in LnO_x, LnOF in Ln_2O_3-LnF_3. It is remarkable also that in all the systems *one* of the simple combinations AB or CD *does not exist* as a known chemical entity. Whether or not this must be so, is not clear.

Table 2

Experimentally known, chemical compounds in the rare earth non-stoichiometric systems identified and connected by a succession of four coded letters.

Chemical repetitive unit down the axis coded by letters (see code table 1)	Name and formula of compound bastnaesite system Ln = ceric group	Formula of compound LnF_3 - Ln_2O_3 system Ln = Eu, Y, Er	Formula of compound $LnO_x(Ln^{3+}/Ln^{4+})$ system Ln = Ce, Pr, Tb	Formula of compound $LnCl_3$ - $LnCl_2$ system Ln = Dy, Tm
AB	bastnaesite $LnFCO_3$	tysonite LnF_3	Ln_6O_{10} DOES NOT EXIST	$LnCl_3$
AB ADCD	parisite $2LnFCO_3.CaCO_3$	$Ln_3O_2F_5$ $(LnF)(LnO)_2F_4$	$LnO_{1.778}$ (or Ln_9O_{16})	Ln_3Cl_7 (Cl/Ln = 2.33)
AB ADCD ADCD	roentgenite $3LnFCO_3.2CaCO_3$	$Ln_5O_4F_7$ $(LnF)(LnO)_4F_6$	$LnO_{1.800}$ (or $Ln_{10}O_{18}$)	extended series of $LnCl_x$ compounds between x ≃ 2.31 and x = 2.00
AB ADCD ADCD ADCD	?	$Ln_7O_6F_9$ $(LnF)(LnO)_6F_8$	$LnO_{1.809}$	
AB $(ADCD)_4$	?	?	$LnO_{1.815}$	
AB $(ADCD)_5$	?	?	$LnO_{1.818}$ (or $Ln_{11}O_{20}$)	
AB $(ADCD)_m$	(n+1)$(LnFCO_3)$ n$(CaCO_3)$	$Ln_nO_{n-1}F_{n+2}$ (n odd)	$Ln_{6n+3}O_{11n+5}$	Ln_nCl_{2n+1}(n.odd)
ADCD	synchisite $LnFCO_3.CaCO_3$	LnOF (trigonal)	$LnO_{1.833}$ (or $Ln_{12}O_{22}$)	$LnCl_2$=[LnCl] Cl structure (CeS)I
CD	DOES NOT EXIST	DOES NOT EXIST	LnO_2	DOES NOT EXIST

Because of the excellence of the experimental work done on the LnO_x systems the agreement between the theoretical formula and the experimental composition is very good. One can see that the Ln_nO_{2n-2} classical formula is in error. The real one is $Ln_{6n+3}O_{11n+5}$. It emphasizes the fact that $LnO_{1.833}$ is the last compound in the system. It was known that there was no other phases between x = 1.833 and 2.000. Of course, the LnO_x comounds which are three-dimensional frameworks of topologically equivalent OLn_4 tetrahedra (Ln_2O_3, Ln_7O_{12}, LnO_2), not being layered structures, does not come out in the table. The importance of the OLn_4 tetrahedron unit can be seen from the fact that the stability of the Ln_7O_{12} phase is greatly reduced if one tries to make a mixed compound (*i.e.*, Tb and Pr, or Pr and Ce) [36]. This is because the OPr_4 and OTb_4 tetrahedra, for instance, do not have the same size, and consequently edge-linking is difficult. Epitaxial continuity and syntaxic intergrowth are to be expected between the layered compounds because of the bastnaesite system correspondence. In LnO_x the presence of the complex cation $(LnO)_n^{n+}$ (C_3) and the blackness of the phases indicates that the bonding may be able to take care of the charge equilibrium between Ln^{3+} and Ln^{4+}. Recent Mossbauër experiments [37] show a single signal for 141 Pr in $Pr_{12}O_{22}$. That signal is intermediate between the one for PrO_2 and the one for Pr_2O_3 which is itself very close to the signal of the pure metal. This indicates that the praseodymium atoms are more or less equivalent. In $Pr_{12}O_{22}$ all of the praseodymium atoms belongs to $(LnO)_n^{n+}$ (C_3) complex groups, the chemical bonding may insure the fractional valency implied by the Mossbauër results.

The description of rare earth non-stoichiometric LnO_x compounds as being capable of syntaxic intergrowths brings a correspondence between the fact that Donnay and Donnay were able to selectively dissolve by chemical action one or the other of the bastnaesite family intergrowth constituents [30] and the fact that the LnO_x compounds can be leached by atmospheric agents (water, CO_2), or mild chemicals, to yield the end member of the system, pure, very well crystallized, LnO_2, which is (compare CeO_2) chemically inert [38].

The layered polycations offer a way to the interpretation of the chemical compositions of the phases in non-stoichiometric rare earth systems. The scheme does *not* offer a way to understand the *crystallography* of those phases. This is because it is clear, from the bastnaesite family example, that the sequences will orient themselves differently: they have the polytypic choice, the three ABC sites (in the familiar notation AB hcp, ABC fcc). This amounts to a possibility of rotation of the chemical planes around the pseudo-hexagonal or (III) fluorite axis. The unit cell may consequently be very wild. As a consequence, crystallography does not bring out, at all, the fundamental chemical relationship underlying the basic existence of rare earth non-stoichiometric compounds.

8. CONCLUSION

The recognition of polymolecular chemical entities constituted of linked together anion centered coordination polyhedra appears to be quite helpful to understand the basic chemical, optical, and mechanical (thin film textures) properties of several rare earth compounds, especially oxides and oxysalts. The concept extended to non-stoichiometry gives an instantaneous key to the chemical composition and structures of the compounds in the most famous rare earth non-stoichiometric systems. The existence of a layered polymolecular cation is found to be the basic reason for the existence of those systems. As clearly shown by the optical studies, the chemical bond inside the polycation is the ultimate factor responsible for the observed phenomena. This is the problem of explaining the real nature of the bonding of transition elements in solids.

Table 3 collects the layered rare earth polycations discussed in this paper.

Table 3

Rare Earth Layered Polycations

1) (XLn_4) tetrahedra sharing edges

X	Structural type of layered polycation	Typical Compound
O	$(LnO)_n^{n+}$ (C_3)	A - Ln_2O_3
	$(LnO)_n^{n+}$ (C_4)	LnOCl
S	$(LnS)_n^{n+}$ (C_3)	Sm SI
	$(LnS)_n^{n+}$ (C_4)	Ce SI
F	$(LnF)_n^{2n+}(C_4')$	La FS
Cl	$(LnCl)_n^{n+}(C_4)$	Yb Cl_2

2) XLn_3 triangles sharing corners.

X	Structural type of layered polycation	Typical Compound
F	$(LnF)_n^{2n+}$ (C_3)	LaF_3 tysonite

9. REFERENCES

[1] Caro, P. E., J. Less Common Metals 16, 367 (1968).
[2] Bergerhoff, G. and Paeslack, J., Z. Krist 126, 112 (1968).
[3] Foëx, M. and Traverse, J. P., Rev. Int. Htes Temp. et Refract. 3 [4], 429 (1966).
[4] Foëx, M. and Traverse, J. P., Bull. Soc. Franc. Miner. Crist. 89, 184 (1966).
[5] Eyring, L. and Holmberg, B., Advan. Chem. Ser. 39, 46 (1963).
[6] Sawyer, J. O., Hyde, B. G., and Eyring, L., Bull. Soc. Chim. France, 1190 (1965).
[7] Lejus, A. M. and Collongues, R., Personnal communication.
[8] Boulesteix, C., Caro, P. E., Gasgnier, M., Henry la Blanchetais, C., and Pardo, B., Acta Cryst. B27, 216 (1971).
[9] Turcotte, R. P., Sawyer, J. O., and Eyring, L., Inorg. Chem. 8, 238 (1969).
[10] Caro, P. E., Achard, J. C., DePous, O., *Colloque International du C.N.R.S. sur les Elements des Terres Rares*, Vol. I, 285 (1970). C.N.R.S., Paris.
[11] Sillen, L. G., Nature 30, 318 (1942).
[12] Wells, A. F., *Structural Inorganic Chemistry*, 3rd Ed., p. 671 and 765, (1962) Clarendon Press, Oxford.
[13] Huggins, M. L., Inorg. Chem. 7, 2108 (1968).
[14] Dagron, M. C. and Thevet, F., Ann. Chim. 6, 67 (1971).
[15] Goldman, M. and Shen, L., Phys. Rev. 144, 321 (1966).
[16] Nguyen-Huy-Dune, These Doctorat-es-sciences, Paris (1971).
[17] Carre, D., Laruelle, P., and Besancon, P., Compt. Rend. Acad. Sci. Paris, 270C, 537 (1970).
[18] Pannetier, J. and Lucas, J., Matls. Res. Bull. 5, 797 (1970).

[19] Barker, W. W., Graham, J., Knop, O., and Brisse, F., in *The Chemistry of Extended Defects in Non-Metallic Solids*, Eyring, L. and O'Keeffe, M., Ed., p. 198, North Holland, Amsterdam (1970).
[20] Jorgensen, C. K., *Modern Aspects of Ligand Field Theory*, p. 263-264, North Holland, Amsterdam (1971).
[21] Dieke, G. H., *Spectra and Energy Levels of Rare Earth Ions in Crystals*, Interscience, New York (1968).
[22] Wybourne, B. G., *Spectroscopic Properties of Rare Earths*, Interscience, New York (1965).
[23] Caro, P. E. and Derouet, J., Bull. Soc. Chim. France, 46, (1972).
[24] Caro, P. E. and Derouet, J., Compt. Rend. Acad. Sc. Paris, 271C, 1370 (1970).
[25] Dulaney, G. W. and Clifford, A. F., *Proceeding of the 8th Rare Earth Research Conference*, Reno, Nevada, p. 641, April 1970.
[26] Henrie, D. E. and Choppin, G. R., J. Chem. Phys. 32, 639 (1968).
[27] Reilly, M. H., J. Phys. Chem. Solids, 31, 1041 (1970).
[28] Boulesteix, C., Caro, P. E., Gasgnier, M., Henry La Blanchetais, C., and Schiffmacher, G., Acta Cryst. A27, 552 (1971).
[29] Boulesteix, C., Caro, P. E., Gasgnier, M., Henry La Blanchetais, C., and Schiffmacher, G., *Colloque International du C.N.R.S. sur l'etude des Transformations cristallines au-dessus de 2000 °K,* Odeillo, 1971 (to be published C.N.R.S., Paris).
[30] Donnay, G. and Donnay, J.D.H., Amer. Mineralogist 38, 932 (1953).
[31] Bevan, D.J.M., Cameron, R. S., Mann, A. W., Brauer, G., and Roether, V., Inorg. Nucl. Chem. Letters 4, 241 (1968).
[32] Tanguy, B. and Portier, J., Personnal communication.
[33] Mann, A. W. and Bevan, D.J.M., Acta Cryst. B26, 2129 (1970).
[34] Caro, P. E. and Corbett, J. D., J. Less Common Metals 18, 1 (1969).
[35] Fischel, N. A., Dissertation Abstract 31 [11], 6477B (1971).
[36] Kordis, J. and Eyring, L., J. Phys. Chem. 72, 2044 (1968).
[37] Kapfhammer, W., Maurer, W., Wagner, F. E., and Kienle, P., *Proc. Intern. Conf. in Hyperfine Structure Detected by Nuclear Radiation*, Rehovot, Israel, p. 120, Sept. 1970.
[38] Clifford, A. F., in *Rare Earth Research II*, K. S. Vorres, Ed., Gordon and Press, New York, p. 45 (1964).

DISCUSSION

B. G. Hyde: A beautiful model, I would just like to ask, you predict in the rare earth oxides the known structures, that is the known compositions.

P. E. Caro: Yes, the normal composition. I cannot say anything about the structure because it is only a chemical repetition.

B. G. Hyde: Do you predict any that are not known?

P. E. Caro: Well, I don't know. You know by that game of coherent intergrowth, you say there is an infinity of phases as you approach the composition $LnO_{1.833}$, for instance. If you make a design of it you could see that this is, as a matter of fact, intergrowth of one of the preceding structures and the $LnO_{1.833}$. So where do you stop? It is just like a card game, you know you have four cards, for instance, and you just stack that card game with some rules. If you let red and black cards represent anionic and cationic sheets then it's just a mathematical game. You have to have some sort of a distribution as long as you have four chemical units to stack. But, of course, that says nothing about the crystallography.

National Bureau of Standards Special Publication 364, Solid State Chemistry, Proceedings of 5th Materials Research Symposium, issued July 1972.

PLASMA-SYNTHESIZED SUBSTOICHIOMETRIC SCANDIUM OXIDE[1]

J. E. Young, Jr.[2] and M. J. Sienko

Baker Laboratory of Chemistry
Cornell University
Ithaca, New York 14850

Crystals of substoichiometric scandium oxide have been grown in high frequency, induction-coupled, argon plasmas. The composition of the crystals could be varied by addition of small percentages of hydrogen or oxygen to the argon stream. Chemical analysis by reoxidation indicated an oxygen deficiency that could attain 4% before metallic films appeared, concentrated at grain boundaries. The chemical composition of the films could not be established. X-ray studies of the bulk crystals indicated retention of the C-type rare earth structure of Sc_2O_3 with but slight shrinkage of the cubic cell parameter. Transmission electron microscopy showed no evidence for shear plane formation. Attempts to measure Hall voltage and conductivity by a van der Pauw technique gave conductivity values, both a.c. and d.c., too small to measure. Faraday susceptibility measurements from 1.6 to 300 K indicated a very small effective magnetic moment, which decreased below 10 K. Possible models are F and F´ centers in thermal equilibrium or Sc^{+1} ions with thermal equilibrium between ^3D and ^1D or ^3D and ^1S states.

Key words: Crystal growth; F centers; flame fusion; magnetic susceptibility; nonstoichiometry, scandium oxide.

1. INTRODUCTION

Several years ago Morin [1][3] suggested that the electrical-conductivity properties of the transition metal oxides could be interpreted, at least qualitatively, by a model in which the conduction band is made up of overlapping d-orbitals. In such a model, the p_σ-orbitals of the oxygen combine with the $d(e_g)$ orbitals of the transition metal to form a lower, bonding and an upper, antibonding set. The bonding set is believed to be completely populated, corresponding to a filled valence band. The antibonding levels, corresponding to σ^* orbitals, are believed to lie from five to ten electron volts higher and, under normal conditions, are completely empty. In the gap between the two sets of levels are the $d(t_{2g})$ levels. If the transition metal atoms are close enough together and if the spatial extent of the t_{2g} orbitals is large enough, overlap results and a conduction band is formed. Morin went on further to suggest that the extent of orbital overlap should increase as one proceeds from right to left in a row or from the top to bottom in a group of the periodic table. In this view, the widest d bands would be formed in the transition metal oxides of the elements toward the left and bottom of the periodic table. For the first row sequence, the probability of d-orbital overlap would be greatest for the case of scandium oxide, Sc_2O_3.

As a result of this model, it would appear interesting to investigate the carrier characteristics of scandium oxide in comparison with the carrier characteristics of TiO_2, V_2O_5, and CrO_3. If the bandwidth in Sc_2O_3 is indeed the greatest of these oxides, one would expect to find the greatest carrier mobility. The problem, however, is to introduce carriers into

[1]This research was supported by the Air Force Office of Scientific Research and the Advanced Research Projects Agency.
[2]Present address: Gulf Research and Development Co., P. O. Drawer 2038 Pittsburgh, Pa. 15230
[3]Figures in brackets indicate the literature references at the end of this paper.

465-504 O - 72 - 26

the oxides. In their highest oxidation states, the transition metals form oxides that are insulators. They have been described as "electronless metals" because, although they may have conduction bands of appreciable width, the cation has an argon configuration and there is no electrical conductivity because there are no carriers. For example, TiO_2 is such an insulator. The Ti^{4+} ion in stoichiometric TiO_2 has no electrons to supply to a d conduction band. The lower oxides of titanium, however, are fairly good conductors. Electrical conductivity and Hall effect measurements on oxygen-deficient TiO_2 [2] indicated conduction electrons with moderate mobility, decreasing with increasing temperature in a way expected for metals. TiO is a very good metal [3]; Ti_2O_3 exhibits a semiconductor-to-metal transition in the vicinity of 450 K [3]. Morin has suggested that the semiconductor-to-metal transition is due to a splitting of the 3d band by the crystal field into d_γ and d_ε sub-bands. Below the transition temperature, the Fermi level is believed to be in the energy gap between the occupied d_γ and the empty d_ε bands, but at T_n, the sub-bands collapse into a single, partially-filled band, causing metallic conduction.

One can imagine two approaches for introducing carriers into the scandium oxide structure. One might substitute a tetravalent atom for a portion of the trivalent scandium atoms, hoping that the substituent atoms would act as donor centers for contributing electrons to the conduction band. The other possibility would be to remove oxygen atoms from the Sc_2O_3 structure. As has been shown by Sienko and Banerjee [4] for the case of WO_3, extraction of each oxygen atom contributes two conduction electrons in the same way as if two alkali metal atoms had been added. In general, the removal of an oxygen atom from any transition metal oxide should leave two electrons free for carrier properties.

Because the original effort in this research, to insert an easily ionized donor into the Sc_2O_3 structure, proved to be unsuccessful, the alternate approach chosen was to remove oxygen. However, removal of oxygen from Sc_2O_3 is extraordinarily difficult. There have been reports of lower oxides of scandium in the literature [5,6,7], but close examination of this work indicates the possibility that the so-called lower oxides were other compounds, for example, carbides of scandium. It is no simple matter to remove oxygen from the Sc_2O_3 structure, the lattice energy of which is among the greatest of any oxide. Still, a simple thermodynamic argument suggests that extraction of oxygen should be feasible by a thermal method. Writing the chemical equation as:

$$Sc_2O_3(s) \rightarrow Sc_2O_{3-x}(s) + 1/2 \times O_2(g)$$

we can see that no matter what the ΔH for this reaction, a sufficiently high temperature should lead to a negative ΔG because the entropy term must eventually dominate. In the reaction, the entropy change must be positive because there is formation of gas phase. In a preliminary investigation, we tried to produce substoichiometric scandium oxide by heating scandium oxide in a hydrogen-oxygen flame. However, the maximum temperature one can realize with such a flame is just barely greater than that of the melting point of Sc_2O_3, namely 2400 °C. Hence, although we were able to fuse Sc_2O_3 powder and form multi-crystalline boules by use of the Verneuil technique, we were not able to get oxygen deficiency. It was not until we went to the plasma technique that we were able to achieve temperatures high enough to make the free-energy change favorable for the above reaction.

Sc_2O_3 has been the subject of very few investigations. The only electrical conductivity measurements have been made on sintered powders. Noddack et al. [8,9] found in the temperature range 873 - 1573 °C that the conductivity in air varied from 0.02×10^{-9} to 47×10^{-9} ohm^{-1} cm^{-1} with an average activation energy of 1.70 eV and an ionization energy of 6.7 eV. Zyrin et al [10] measured the electrical conductivity and thermoelectric power in air and in vacuum from 1100 to 1600 °C obtaining values for σ of 1×10^{-5} ohm^{-1} cm^{-1} at 1100 °C and 1.6×10^{-3} ohm^{-1} cm^{-1} at 1600 °C, an activation energy of 2.2 eV, and a thermoelectric power of 230 μV/degree. At a pressure of 10^{-5} torr, the conductivity was approximately a factor of eight smaller, with an activation energy of 2.6 eV and thermoelectric power of 760 μV/degree.

Companion [11] observed the diffuse reflectance spectrum of Sc_2O_3, measuring a band gap of 5.4 eV. Tippins [12] studied the ultraviolet absorption spectra of single crystals at room temperature and at approximately 80 K. His results agreed with those of Companion, and he calculated a band gap of 6.0 eV at room temperature and 6.2 eV at 80 K. Barta et al [13] have measured the refractive index of Sc_2O_3, arriving at a value of 1.91, which would yield a value of 1.38 for the dielectric constant at optical frequencies.

Scandium sesquioxide crystallizes in the C-type rare-earth structure. This structure is essentially a body-centered cubic array of eight fluorite-type cells, with 1/4 of the oxygen sites unoccupied in the following manner: the vacancies occur in pairs such that 75% occur along the face diagonals of the anion cubes while the reamining 25% occur along the body diagonals. All the scandium cations are six coordinated, with 25% surrounded by a nearly regular octahedron of oxygen ions and 75% surrounded by a highly distorted octahedral environment of oxygen ions. There have been two recent refinements of the crystal structure: Geller [14,15] reports a lattice constant of 9.844 Å; Norrestam [16] reports a value of 9.849 Å. Reid and Ringwood [17] have reported the existence of a monoclinic B-type rare-earth form of Sc_2O_3, produced at 130 kilobar pressure and 1000 °C. The calculated density of this form represents an increase of 8.3% over the density of C-type Sc_2O_3, reflecting an increase in coordination from six to seven fold for 2/3 of the scandium ions. No other properties of this form have been reported.

The chemistry of scandium is very similar to that of yttrium and the rare-earth metals. Borchardt [18] observed the formation of a blue-black oxide film resulting from oxidation of metallic yttrium; x-ray analysis showed it to be Y_2O_3, with lattice constants identical to those of stoichiometric Y_2O_3. He interpreted this as the presence of metallic yttrium dissolved in stoichiometric Y_2O_3. Miller and Danne [19,20] have reported the preparation of oxygen-deficient oxides of gadolinium, yttrium, erbium, and lutetium. These compounds corresponded to the formulas $GdO_{1.495}$, $YO_{1.49}$, $ErO_{1.489}$, and $LuO_{1.485}$ (crystallizing with the cubic C-type structure) and $GdO_{1.493}$ (crystallizing with the monoclinic B-type structure.) They were produced by vacuum melting of the stoichiometric oxide or by co-distilling and co-melting the rare earth metals with the respective sesquioxide. X-ray and density information indicate that the sesquioxides had lost oxygen, forming Schottky defects in the anion lattice. These defects serve as effective positive ion sites capable of trapping the electrons released by the cations in a lower oxidation state. Miller reports that the magnetic susceptibility data of $GdO_{1.493}$ indicate an antiferromagnetic transition at 3.35 K. The cubic $GdO_{1.495}$ or $ErO_{1.489}$ demonstrate no such transition, although the magnetic susceptibility of both these materials takes a sharp upturn below 20 K indicating possible magnetic ordering at these temperatures. Muller-Buschbaum [21] has reported the preparation of nonstoichiometric La_2O_{3-x} by melting in a high-frequency, induction plasma in a vacuum. X-ray data indicate a structure identical to that of La_2O_3, but no other properties have been reported.

2. EXPERIMENTAL PROCEDURE

2.1. CRYSTAL GROWTH

The scandium sesquioxide used in these studies was obtained from Australian Mineral Development Laboratories, South Australia. It contained nominally 99.5% Sc_2O_3 with the major impurity being silica. An emission spectrographic analysis, performed by the analytical facility of the Cornell Materials Science Center, showed that the starting material contained 0.01 - 0.1% calcium, 0.01 - 0.1% magnesium, 0.01 - 0.1% iron, and 0.001 - 0.01% silicon whereas the plasma-grown crystals contained no detectable calcium, no detectable magnesium, iron at 0.001 - 0.1%, and silicon at 0.001 - 0.01%.

2.2. PLASMA

The equipment used in these experiments consisted of a TAFA Model 58 torch powdered by a Lepel 10-kw, rf generator operating at a frequency at 3.8 megahertz or, in later stages, by a Lepel 20-kw generator, operating at 4.0 megahertz. The powdered oxide was injected into the plasma through a water-cooled copper probe at the center axis of the torch. The powder had to be introduced into the plasma in finely divided form as large particles would disturb the plasma to such an extent that it would be extinguished. The powder-feed mechanism consisted of a bed-type hopper in which the dry powdered oxide was fluidized by gas flowing from a jet at the bottom of a cone. A small portion of this finely divided powder then left the hopper through an exit tube in the upper portion of the hopper. In order to insure smooth flow of the powder, the exit tube extended continuously through the hopper and the water-cooled probe of the torch, terminating just at the tip of the probe. The powder was kept from forming "channels" for the gas flow by continuous vibration of the hopper with an electric vibrator attached to the hopper support.

The gas used for the plasma was generally argon, with small percentages of hydrogen or oxygen occasionally added. Addition of any diatomic gas caused a drastic reduction in the size of the plasma zone and increased the rate of heat transfer to the torch itself, frequently resulting in early torch failure. The torch could be operated reliably only with pure argon, argon mixed with up to 5% hydrogen, or argon mixed with up to 50% oxygen. No efforts were made to operate with nitrogen or air.

The crystals were grown on the end of a 5-mm diameter, 15-cm length magnesia rod which was mounted on a long boron nitride rod, attached to a motor-driven positioning apparatus. The position of the crystal pedestal could be varied over a range of approximately 15 cm; it could also be rotated at a rate of 100 rpm.

Procedures and operating conditions for growing crystals with a plasma technique are difficult to reproduce. Proper compensation for variations in these conditions was developed only after many failures. A reasonably typical set of conditions was as follows: Total flow of gas was 1800 - 2200 liters per hr. The majority of this gas enters through the laminar flow jets; up to 25% may be introduced through swirling flow jets, producing vortex stabilization of the plasma zone. The plasma is initiated by inserting a grounded carbon rod into the center tube of the torch while increasing the power output of the rf generator. The carbon rod couples with the rf field, eventually becoming red hot. At this point the argon gas near the hot rod becomes thermally ionized, coupling with the field and initiating the plasma. The crystal pedestal is raised to a point approximately 8 cm from the end of the torch, just in the lower portion of the plasma tail. The powder flow was begun very gradually, as a quick burst of powder would immediately extinguish the plasma. The total gas flow through the powder feed hopper was approximately 100 liters per hr. -- from 0 to 50 liters per hr. through the powder fluidizing jet and the balance through an auxillary carrier gas opening. If the powder were introduced at a lower total gas flow rate, it would "bounce" off the surface of the hot plasma zone, flowing around the outside surface and missing the pedestal completely. The higher gas flow was necessary to punch a hole partially through the plasma in order to inject the powder into its center. After the powder flow was initiated, a very high rate of flow was used to build up an approximately 5-mm layer of sintered powder on the end of the magnesia pedestal. At high temperatures, Sc_2O_3 reacted with MgO to form the spinel phase $MgSc_2O_4$, which served to bond the Sc_2O_3 boule to the pedestal, while the thick layer of sintered powder prevented contamination of the boule by the magnesia. Eventually a cone of the sintered powder was built up, at which time the powder flow was reduced and the pedestal raised until the tip of the cone was 5 to 10 mm from the end of the torch. The tip of the cone then melted, spread out, and a cap of molten oxide was formed. During growth of the boule, the powder gas flow rate was approximately 15 - 30 liters per hr. through the fluidizing jet. The pedestal was slowly lowered as the molten cap increased in size, allowing the lower portion of the cap to solidify. The boule was allowed to grow until it was approximately 2 cm long, the powder flow terminated, the rf generator turned off, and the boule immediately raised until it was entirely inside the quartz tube of the torch. In this way, the boule was cooled in the flowing gas constituting the plasma, without contact with the air.

The resulting boule was 3 to 12 mm in diameter. The surface of the upper portion frequently showed grain boundaries in the polycrystalline mass. The lower portion of the boule was covered with a dendritic growth of various colors depending on the conditions during growth. The arms of these dendrites grew at 90° angles and were 0.1 to 0.5 mm thick. At the base of the dendrites, there were frequently clusters of whiskers up to 0.5 mm long and approximately 0.01 mm thick. If the plasma contained a high concentration of oxygen during the crystal growth, the resulting boule was nearly clear, but had a brownish haze. The dendrites at the base were clear. When the boule was fractured, the smoky color was evenly distributed throughout the mass. When the boule was grown in a pure argon plasma, a black-colored mass was obtained. The dendrites at the base were dark red in color and were frequently covered with a metallic-appearing film that was blue, violet, red, gold, or silver. The interior of the boule varied from dark red (nearly black) to bluish black. When the crystals of the boule were bluish black, there were frequently observed in the grain boundaries the same multicolored metallic films observed on the dendrites. When the plasma was doped with hydrogen during crystal growth, the boule was the same bluish black in color but with considerably more of the multicolored metallic films on the dendrites and in the interior grain boundaries.

Because of the metallic appearance of the films, the electrical resistance of various portions of the boule was measured with a conventional ohm-meter. It was found that many of the multicolored films, in the interior of the boule or on the surface of the dendrites, demonstrated a resistance of less than 10 ohms, but the resistance of any other portion of the boule was so high as not to be measurable. The colored films were stable in air, demonstrating no change in appearance or in electrical resistance even over a period of a year. Treatment of various portion of the boule with dilute acid showed for a period of approximately 1 hr a very slow evolution of gas bubbles. During this time, the metallic films would disappear, but no apparent change occurred in the dark, nonmetallic crystals. All of the materials were stable in pure water.

2.3. STRUCTURE INVESTIGATIONS

Samples of two boules were selected for structure investigation, electrical and magnetic measurements, and determination of stoichiometry. Crystals were removed from the boules with great care to exclude the metallic films appearing in the grain boundaries. The lattice parameters were measured from x-ray powder patterns taken on a Guinier-type, focused beam camera with CuKα radiation. Sc_2O_3 was photographed on the same film and the Sc_2O_3 pattern was used as an internal standard. The measured values for the lattice parameters are listed in table 1. The diffraction patterns corresponded exactly to that of Sc_2O_3 with the exception of a slight shift in line positions toward slightly smaller values of d. Because of the similarity in powder diffraction patterns, a small, nearly spherically crystal of Sc_2O_{3-x} was aligned along the [100] direction and a rotation photograph was taken with Cukα radiation. This was compared with a rotation photograph taken of a crystal of Sc_2O_3 obtained from the hydrogen-oxygen flame fusion work. No extra reflections or extinctions were observed, and the relative intensities of the reflections agreed between the two photographs.

Electron micrographs and diffraction patterns were kindly taken for us by Professor J. G. Allpress of the University of Melbourne, Australia. He found that the diffraction pattern of all fragments of the material corresponded closely to that expected for Sc_2O_3 except that some of the reflections, which are forbidden by the space group, appeared strongly. This effect was due to multiple scattering and was a consequence of the technique used, rather than any function of sample stoichiometry. None of the patterns contained additional reflections, diffuse scattering, or streaking. There was no evidence for crystallographic shear formation [23].

2.4. ANALYSIS FOR STOICHIOMETRY

The oxygen content of the Sc_2O_{3-x} crystals was measured by reoxidation. Crystals which were free of metallic films were selected and crushed with an Al_2O_3 mortar and pestle to pass a 50-mesh sieve. Several portions of each sample, weighing approximately 30 mg each, were placed in small platinum boats and fired to constant weight at 1000 °C in a slow-flowing stream of oxygen. All weighings were made to the nearest microgram on a Mettler model M5 microbalance. Corrections were applied for the small amounts of platinum vaporized in the oxygen stream. The results of the analysis are shown in table 1. An additional sample grown in a hydrogen-doped plasma and containing many of the metallic films in the grain boundaries showed a composition corresponding to $Sc_2O_{2.516 \pm 0.006}$.

Table 1

Sample Compositions and Lattice Constants

Sample	Starting Material	A	B
Lattice Constant	9.845 Å Ref. [22]	9.831 Å ±0.005	9.826 Å ±0.005
Formula	Sc_2O_3	$Sc_2O_{2.922}$ ±0.008	$Sc_2O_{2.885}$ ±0.008

2.5. ELECTRICAL PROPERTIES

Attempts were made to measure the electrical conductivity and Hall effect of the Sc_2O_{3-x} samples by the van der Pauw technique [24]. The crystals selected for study were approximately 1 mm x 2 mm x 0.2 mm in size, chosen with extreme care to insure that no metallic films were included. The resistance of the Sc_2O_{3-x} crystals proved to be so high that it was impossible to obtain meaningful data by dc measurement techniques, using an electrometer. Because of space charge effects, the electrometer was replaced with a Princeton Applied Research model HR8 lock-in amplifier with an FET input operational amplifier as an impedance matching device, but again the crystal resistance proved to be too high to be measured. Because accurate electrical conductivity data were not obtained, Hall effect measurements were impossible. The conclusion was that the electrical resistance of the crystals was equal to or greater than the input impedance of the measuring instruments -- *i.e.*, 10^{12} ohms.

2.6. MAGNETIC SUSCEPTIBILITY MEASUREMENTS

The Faraday method was used for the measurement of the magnetic susceptibility. The magnet was an Eastern Scientific Instruments Model 7 electromagnet supplied with 18-cm diameter pole caps giving a gap of 3 cm. The force-sensing balance was a Cahn Model RG electrobalance, an electrically recording-type balance with an ultimate sensitivity of 0.1 microgram with a maximum weight of one gram for the sample plus suspension. Temperature was varied over the range from 1.5 to 300 K. The dewar was constructed of stainless steel with the exception of the tail, which was constructed of copper to eliminate any possible effects on the magnetic field. The temperature was measured and controlled by a regulator designed by J. Garland of the Cornell University Department of Physics. The regulator consisted of a resistance bridge driven by an oscillator operating at approximately 200 hertz with the unknown leg being one of two carbon resistors used as thermometers. The imbalance of the bridge was amplified and detected in a lock-in-type amplifier synchronized with the bridge drive oscillator. The sensitivity of the measuring circuit was such that a change of resistance in the thermometer of one part in 10,000 could be detected. The thermometers were calibrated at three temperatures, room temperature, 77 K, and 4.2 K. The latter two points were determined accurately by measuring the vapor pressure over the boiling liquid-nitrogen or helium in the cryostat and applying the appropriate temperature and hydrostatic head corrections. The three calibration points were then fitted to a semi-empirical equation proposed by Clement [25,26] for the temperature-resistance relationship of the carbon radio resistors.

The magnetic field was mapped with the aid of a 0.6 mm-diameter platinum bead, hung from quartz fibers of various lengths. The vertical position of the bead with respect to the peak of the magnet pole caps was measured with a cathetometer. The force was found to be constant within 2% in a region approximately 1 cm high and 5 mm wide. The maximum field used was 12 kilogauss. The field was calibrated using platinum [27,28] and mercury tetrathiocyanato cobaltate [29] as standards.

The force measured by the balance at any given value of the magnetic field is the sum of the force due to the quartz sample bucket and that due to the sample itself. The necessary corrections were determined by measurements on the empty bucket at the same values of the magnet output as those used in the field calibration, throughout the temperature range 1.6 K to 300 K. The correction was temperature-independent from 300 K to approximately 60 K, then its magnitude decreased as temperature decreased. This latter effect was undoubtedly caused by trace impurities in the quartz. Apparently, the distribution of such impurities in the quartz is not uniform since the correction varies somewhat from bucket to bucket. Hence, a measurement of this diamagnetic correction was made for each bucket used in the apparatus.

A slight field dependence was found for the samples of Sc_2O_{3-x} as well as for the Sc_2O_3 starting material, suggesting the presence of trace ferromagnetic impurities. These were corrected for by the extrapolation method of Honda [30] and Owen [31]. The plots of χ_H *vs* $\frac{1}{H}$ were very nearly linear in the range of 5 kilogauss to maximum magnet output, so extrapolation to $\frac{1}{H} = 0$ was a simple matter. The molar susceptibility was also corrected for the diamagnetism of the ion cores. The value for Sc^{3+} was taken as -6×10^{-6} [32] and that for O^{2-} as -10×10^{-6} [4]. As indicated previously, the Sc_2O_3 and the Sc_2O_{3-x} contain small amounts of iron which, according to Geller et al. [33], dissolves in Sc_2O_3 by substitution of Fe^{3+} for Sc^{3+}. The Sc_2O_3 starting material contained 0.01 - 0.1% iron, and the plasma-grown

crystals exhibited a factor of 10 reduction in the iron content. Assuming the presence of 0.02% iron in Sc_2O_3 and 0.002% in the samples of Sc_2O_{3-x}, a correction was made to the observed molar susceptibility by using the equation $\chi = N\mu^2/3kT$, where N is the number of Fe^{3+} ions per mole of Sc_2O_3 and μ is the effective magnetic moment of Fe^{3+} (in this case, 5.9 Bohr magnetons).

3. DISCUSSION

The reduction in impurity levels in the plasma-grown crystals probably results from the fact that sufficiently high temperatures are reached in the plasma to result in vaporization of a considerable amount of the powdered scandium oxide. At high temperatures the vapor pressure of iron or its oxides is higher than that of scandium oxide [34,35], so portions of this impurity, as well as calcium and magnesium, are simply boiled off prior to crystallization of the Sc_2O_3, resulting in effective purification of the Sc_2O_{3-x}.

In the temperature range 2400 - 2570 °C, *i.e.*, very near the melting point of Sc_2O_3, Sc_2O_3 sublimes [36] with the following equilibrium:

$$Sc_2O_3(s) \rightleftarrows 2ScO\ (g) + O(g)$$

The vapor pressure of ScO at 2440 K is 0.001 torr and at 2630 K, 0.01 torr. At 2550 K the ScO partially dissociates to form Sc and O atoms in a ratio of 1 Sc to 8 ScO. In a rapidly moving plasma stream, one could expect a portion of the Sc and ScO vapors to be quenched and dissolved in the molten cap and on the surface of the boule before recombination with oxygen could occur. The net result would be an excess of scandium in the molten cap, but this could have only limited solubility in the solid material. Apparently the composition of sample B is nearer the limit of solubility of scandium in Sc_2O_3, because of greater amounts of a second phase precipitated in the grain boundaries. Unfortunately, the metallic films could not be produced in sufficient quantities for chemical analysis. Their multicolor character could not be attributed to light interference patterns resulting from varying film thickness; the films themselves are metallic, and light penetration would be insignificant. The films could be due to precipitated, colloidal, metal particles of varying size or they could consist of lower oxides of scandium with continuously varying oxygen content. Photoelectron spectroscopy or x-ray microprobe analyses of these films might yield useful information.

Correction of the observed magnetic susceptibility of Sc_2O_3 for diamagnetism of the ions cores and for the contribution due to Fe^{3+} impurity yields a slight paramagnetism that is essentially temperature independent. This has been observed previously in the case of Sc_2O_3, TiO_2, and V_2O_5 [37]; it is just the Van Vleck paramagnetism [38]. Because the structures of Sc_2O_3 and Sc_2O_{3-x} are the same, the Van Vleck paramagnetism should be subtracted from the observed susceptibility of the oxygen-deficient samples in order to study the magnetic contribution of the defects. The resulting plot of the reciprocal susceptibility as a function of temperature is shown in figure 1. Figure 2 shows the temperature dependence of the effective magnetic moment per mole of Sc_2O_{3-x} calculated from the relation $\mu_{eff} = 2.83\sqrt{\chi_M T}$. The error bars at high temperatures are sufficiently large that a linear relation of the Curie-Weiss type, $\chi = C/(T-\theta)$ cannot be ruled out, but the actual data points do indeed show a definite curvature throughout the entire temperature range of measurement.

It can be seen from figure 2 that the effective magnetic moment is extremely small. It would be more meaningful to calculate the μ_{eff} per mole of defect rather than per mole of Sc_2O_{3-x}, but in order to do this one must know the nature of the defects and their concentrations in the samples. The most probably defects are: Sc^0, either interstitial or at a scandium site; Sc^{+1} or Sc^{+2}, probably at a scandium site; and F center, consisting of a single electron trapped at an oxygen vacancy; or an F´ center consisting of an electron pair trapped at an oxygen vacancy. Each of these defects would make a different contribution to the magnetic susceptibility. The contributions are listed in table 2. Column I gives the types of defect and Column II, corresponding formulas of samples A and B. Column III shows the experimentally observed μ_{eff} per mole of defect at three temperatures: 300 K, 77 K, and 4.2 K. Column IV indicates the spin state S of the defect, and Column V, the magnetic moment expected from spin only. In all cases, the observed μ_{eff} is less than the μ predicted for any of the paramagnetic species, thus implying that more than one single species, one paramagnetic and the other diamagnetic, must be contributing to the net magnetic moment. The temperature dependence of the moment suggests either an equilibrium between two species or an equilibrium between two

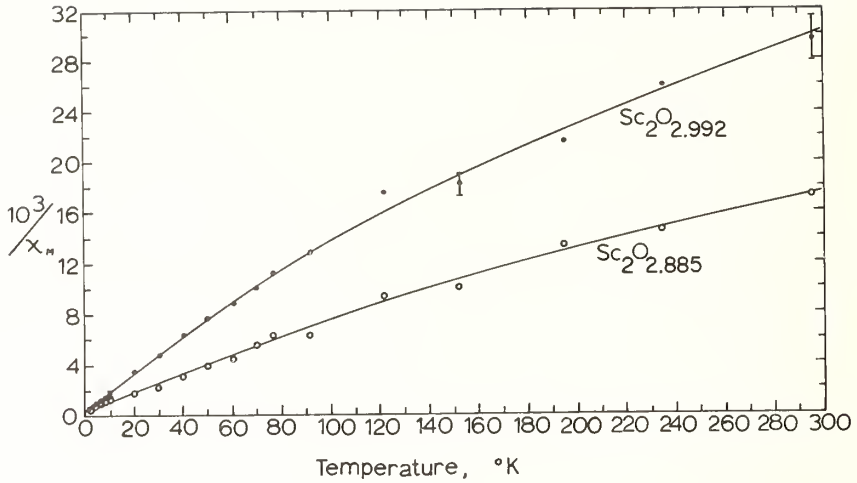

Fig. 1. Reciprocal net molar magnetic susceptibility versus absolute temperature for oxygen-deficient scandium oxide. Values have been corrected for diamagnetism, temperature-independent paramagnetism, and trace iron impurity.

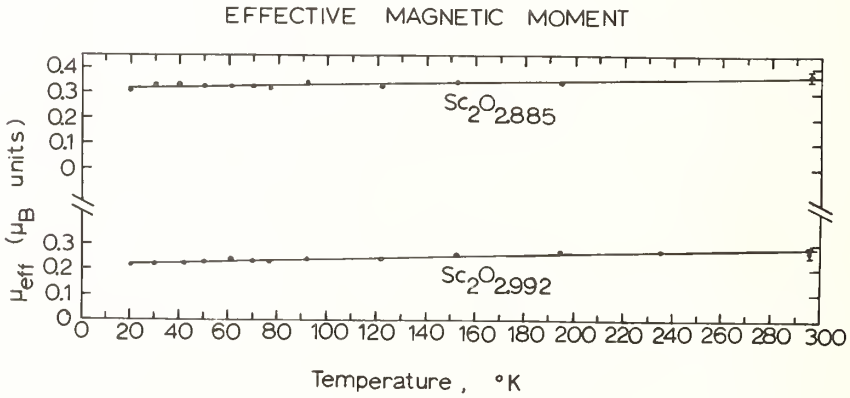

Fig. 2. Effective magnetic moment versus temperature per mole of Sc_2O_{3-x}.

states of the same species. The diamagnetic state or species would have to be more stable at low temperatures.

Of the species listed, there could be an equilibrium between an F center and an F´ center. However, F´ centers are stable only over a relatively narrow temperature range and then only in the vicinity of 70 K in the case of alkali halides. The other possibility arises with the Sc^{+1} ion. The energy difference between the $^3D(s^1d^1)$ ground state and the $^1D(s^1d^1$ antiparallel spin) is 2541 cm^{-1}; that between the ground state and the $^1S(s^2d^0)$ level is 11736 cm^{-1}. However, ligand-field effects may be sufficient to make either the ^1D or the ^1S very close in energy to the ^3D ground state. Furthermore, the orbital moment of the ground state may not be completely quenched, yielding an additional component to the Van Vleck temperature-independent paramagnetism.

The observed electrical properties are not inconsistent with the above models. If the d electron of Sc^+ were delocalized in a d-conduction band as postulated by Morin [1], there should be strongly enhanced conductivity; this was not observed. Apparently, the electron is trapped at a localized site. Application of Goodenough's criterion for metallic conductivity

Table 2

Comparison of Calculated and Observed Magnetic Moments Assuming Different Defect Models for Sc_2O_{3-x}

I	II		III		IV	V
Defect	Formula		Obsd. μ_{eff}		Spin	Calc.
Temp.	Sample A	Sample B	A	B	State	μ
Sc^0	$Sc_2^{3+}Sc_{0.052}^{0}O_{2.922}^{2-}$	$Sc_2^{3+}Sc_{0.076}^{0}O_{2.885}^{2-}$			1/2	1.73
300 K			1.18	1.34		
77 K			1.01	1.16		
4.2 K			0.79	0.80		
Sc^{+1}	$Sc_{1.922}^{3+}Sc_{0.078}^{+}O_{2.922}^{2-}$	$Sc_{1.885}^{3+}Sc_{0.115}^{+}O_{2.885}^{2-}$			1 ^3D	2.83
300			0.97	1.09		
77			0.82	0.94	0	0
4.2			0.64	0.65	^1D or ^1S	
Sc^{2+}	$Sc_{1.944}^{3+}Sc_{0.156}^{2+}O_{2.922}^{2-}$	$Sc_{1.770}^{3+}Sc_{0.230}^{2+}O_{2.885}^{2-}$			1/2	1.73
300			0.68	0.77		
77			0.58	0.67		
4.2			0.45	0.46		
F	$Sc_2^{3+}O_{2.922}^{2-}e_{0.156}^{-}$	$Sc_2^{3+}O_{2.885}^{2-}e_{0.230}^{-}$			1/2	1.73
300			0.68	0.77		
77			0.58	0.67		
4.2			0.45	0.46		
F′	$Sc_2^{3+}O_{2.922}^{2-}2e_{0.078}^{2-}$	$Sc_2^{3+}O_{2.885}^{2-}2e_{0.115}^{2-}$			0	0
300			0.68	0.77		
77			0.58	0.67		
4.2			0.45	0.46		

[39] would give a critical cation-cation distance for Sc_2O_3 of 3.00 Å. The actual nearest neighbor Sc-Sc distance in Sc_2O_3 is 2.14 Å, but this distance is not repeated consecutively; it occurs at isolated sites in the lattice, hence could not contribute to extensive electron delocalization. Furthermore, the application of Goodenough's empirical relationship to the case of scandium oxide is questionable. It was derived from electrical studies of the oxides of titanium, vanadium, chromium, and iron, and is expressed in terms of the nuclear charge of titanium. Also, as Goodenough suggests, the relationship is valid only when the cations are distributed with octahedral coordination in a close-packed array of oxygen ions. The coordination sphere of oxygen around three fourths of the scandium is so distorted that it is difficult to call it octahedral.

There remains the possibility that the poor electrical conductivity observed is the result of passivation of the Sc_2O_{3-x} crystal by a film of stoichiometric Sc_2O_3 although the electrodes for electrical measurements were attached with the aid of an ultrasonic soldering device. If the film were rejuvenated as rapidly as it was broken, then the oxide barrier at the electrode-crystal interface could still inhibit the electrical conductivity, leading to space charge effects such as were observed during the measurements. Unfortunately, electrodeless conductivity measurements are not feasible on intermediate and low conductivity materials.

4. REFERENCES

[1] Morin, F. J., Bell System Tech. Jour. 37, 1047 (1958).
[2] Breckenridge, R. G. and Hosler, W. R., Phys. Rev. 91, 793 (1953).
[3] Morin, F. J., Phys. Rev. Letters, 3, 34 (1959).

[4] Sienko, M. J. and Banerjee, B., J. Amer. Chem. Soc. 83, 4149 (1961).
[5] Petru, F. and Dufek, V., Z. Chem. 6, 345 (1966).
[6] Dufek, V., Petru, F., and Brozek, V., Monat. Chem. 98, 2424 (1967).
[7] Dufek, V., Brozek, V., and Petru, F., Monat. Chem. 100, 1628 (1969).
[8] Noddack, W., Walch, H., and Dobner, W., Z. Physik. Chem. 211, 180 (1959).
[9] Noddack, W. and Walch, H., Z. Elektrochemie 63, 269 (1959).
[10] Zyrin, A. V., Dubok, V. A., and Tresvyatskii, S. G., *Khimiia Vysokotemperaturnykh Materialov*, Trud, Vses. Soveskch. 2nd, Leningrad, 1965, pp. 59-65 (pub. 1967).
[11] Companion, A. L., J. Phys. Chem. Solids 25, 357 (1964).
[12] Tippins, H. H., J. Phys. Chem. Solids 27, 1069 (1966).
[13] Bartá, C., Petru, F., and Hájeck, B., Naturwissenschaften 45, 36 (1958).
[14] Geller, S., Romo, P. and Remeika, J. P., Z. Krist. 124, 136 (1967).
[15] Geller, S., Romo, P. and Remeika, J. P., Z. Krist. 126, 461 (1968).
[16] Norrestam, R., Arkiv für Kemi 29, 343 (1968).
[17] Reid, A. F. and Ringwood, A. E., J. Geophys. Res. 74, 3238 (1969).
[18] Borchardt, H. J., J. Inorg. Nucl. Chem. 26, 711 (1964).
[19] Miller, A. E. and Daane, A. H., J. Inorg. Nucl. Chem. 27, 1955 (1965).
[20] Miller, A. E., Ph.D. thesis, Iowa State University (1964).
[21] Muller-Buschbaum, H. K., J. Inorg. Nucl. Chem. 30, 895 (1968).
[22] Swanson, H. E. and Fuyat, R. K., National Bureau of Standards Circular 539, Vol III, NBS, Washington, D.C., 1953, p. 27.
[23] Allpress, J. G., private communication.
[24] van der Pauw, L. J., Philips Res. Rpts. 13, 1 (1958).
[25] Clement, J. R. and Quinnell, E. H., Rev. Sci. Instr. 23, 213 (1952).
[26] Hoare, F. E., Jackson, L. C., and Kurti, N., *Experimental Cryophysics*, Butterworths, London, 1961, p. 234.
[27] Kojima, H., Tebble, R. S., and Williams, D. E. G., Proc. Roy. Soc. (London) 260, 237 (1961).
[28] Hoare, F. E. and Walling, J. C., Proc. Phys. Soc. B64 337 (1951).
[29] Figgis, B. N. and Nyholm, R. S., J. Chem. Soc. 1958, 4190.
[30] Honda, K., Ann. Phys. 32, 1048 (1910).
[31] Owen, M., Ann. Phys. 37, 657 (1912).
[32] Selwood, P. W., *Magnetochemistry* 2nd edition, Interscience, New York, 1956, p.78.
[33] Geller, S., Williams, H. J., and Sherwood, R. C., J. Chem. Phys. 35, 1908 (1961).
[34] Fedesov, V. N. and Nadolskii, A. P., Trudy Irkutsk. Politekh. Inst. 27, 80 (1966).
[35] Nesmayanov, A. N. and Trapp, G., Zh. Fiz. Khim. 38, 2931 (1964).
[36] Semenov, G. A., Russ. J. Inorg. Chem. 10, 1300 (1965).
[37] Landenburg, R., Z. für Phys. Chem. 126, 133 (1927).
[38] Van Vleck, J. H., *The Theory of Electric and Magnetic Susceptibilities*, Oxford University Press, London, 1932, p. 302.
[39] Goodenough, J. B., *Colloque Internationale du C.N.R.S.*, No. 149, Bordeaux, 1965, pp. 162-169.

DISCUSSION

J. H. Perlstein: You grew the crystals on MgO pedestals, I think you indicated.

M. J. Sienko: The pedestal was so far down that we didn't have any of that: we just took the top part.

J. H. Perlstein: I was going to ask you if there could have been magnesium diffusion up the crystal?

M. J. Sienko: There was no evidence of magnesium in the spectroanalysis. There was no detectable magnesium.

E. Banks: Have you been able to look at any optical spectra?

M. J. Sienko: No, the black is so black that it is hopeless. One might be able to do something with reflectivity, but certainly not with transmission. Incidentally, these things are relatively inert. As I mentioned, those films would stick around for a year or so. If we put the boules in water, they just stayed there. If we put them in acid, there would be

a very slow evolution of bubbles which would continue for hours. We were not able to collect any gas to make an analysis of it, but we assumed it was hydrogen.

W. VanGool: Are you sure there was no hydrogen in your crystals?

M. J. Sienko: No, one is never sure that there is no hydrogen. That is always a possibility, but being in an argon plasma instead of hydrogen-oxygen flame suggests that it was not hydrogen that was producing these properties. Also, I think that hydrogen would probably give reasonable conductivity in these structures because of the proton jump.

R. S. Roth: If we wanted to accurately measure the melting point of scandium oxide for use on an international practical temperature scale and we were going to do this in a vacuum in a tungsten crucible, would we run into the problem of reduction of scandium oxide?

M. J. Sienko: No, I don't think so. No, I think that my first argument would apply. The ΔH for oxygen loss must be very large.

F. Holtzberg: I wondered if you looked for any rare earth impurities?

M. J. Sienko: The effective moment, as you saw, was of the order of 0.3 Bohr magnetons; any rare earths would immediately make this climb up. But you have a point there; there could be traces. We considered that, didn't we John (Young)?

J. E. Young: The detailed spectroanalysis did not really investigate the rare earth possibility to any great extent. They did not look very closely for rare earths.

E. Banks: I think that scandium oxide has a C-rare earth oxide structure, is that correct? In that structure you have two non-equivalent scandium sites in the ratio of three to one, and I would just like to ask whether your ESR spectrum could be partially resolved in terms of a three to one intensity?

M. J. Sienko: That's a very good point and this is precisely what we are trying to do now. The ESR spectrum offers promise of indicating what the nature of the defect is.

National Bureau of Standards Special Publication 364, Solid State Chemistry, Proceedings of 5th Materials Research Symposium, issued July 1972.

CRYSTAL CHEMISTRY AND COMPOUND FORMATION IN THE SYSTEMS RARE EARTH SESQUIOXIDE-WO_3

G. J. McCarthy, R. D. Fischer[1], G. G. Johnson, Jr. and C. E. Gooden

Materials Research Laboratory
The Pennsylvania State University
University Park, Pennsylvania 16802

Compounds with the following stoichiometries have been prepared in the rare earth sesquioxide-tungsten trioxide systems: RE_6WO_{12}, $RE_{10}W_2O_{21}$, $RE_{14}W_4O_{33}$, RE_2WO_6, $RE_2W_2O_9$. Compounds of the first three stoichiometries prepared at 1400 °C have structures apparently related to that of fluorite. RE_6WO_{12} has three structural classes whose symmetries are dependent on the rare earth ionic radius: La-Pr, cubic or pseudocubic; Nd-Gd, pseudotetragonal; Tb-Lu, Y, rhombohedral. $RE_{10}W_2O_{21}$ is stable only for RE = Gd-Ho, Y and has the same pseudotetragonal symmetry as the intermediate RE_6WO_{12} compounds. $RE_{14}W_4O_{33}$ has a pseudo-rhombohedral structure related to the third RE_6WO_{12} structure. The rhombohedral RE_6WO_{12} compounds are known to be isostructural with RE_7O_{12} oxides and it is suggested that $RE_{10}W_2O_{21}$ and $RE_{14}W_4O_{33}$ may be structurally related to RE_4O_7 and RE_6O_{11} respectively. RE_2WO_6 compounds with RE = Pr-Dy have a monoclinic scheelite-related structure. The $RE_2W_2O_9$ compounds, also with a complex monoclinic structure, are stable only for RE = Ce-Gd (or Tb). Compounds of the stoichiometries $RE_4W_3O_{12}$ and $RE_2W_3O_{12}$ were not studied, but the literature information on them is noted. A discussion of the probable sub-solidus phase relations in RE-W-O systems is also included.

Key words: Fluorite-related structures; rare earth tungstates; rare earth tungsten oxides; RE_2O_3-WO_3 compounds; RE-W-O systems.

1. INTRODUCTION

As part of a continuing study of rare earth-transition metal oxide chemistry, we have completed a preliminary examination of the crystal chemistry and compound formation in the systems rare earth sesquioxide-tungsten trioxide. These compounds are of considerable interest in science and technology as phosphors, laser hosts and nuclear control materials, and in crystal chemistry because of the opportunity to examine the behavior of certain structure types as a function of the rare earth ionic radius.

There have been several previous investigations of compound formation in RE_2O_3[2]-WO_3 systems. Ivanova et al. [1][3] studied the system La_2O_3-WO_3 and reported compounds of the molar ratio $3La_2O_3 \cdot WO_3$, $3La_2O_3 \cdot 2WO_3$, $La_2O_3 \cdot WO_3$, $La_2O_3 \cdot 2WO_3$ and $La_2O_3 \cdot 3WO_3$. In the system Nd_2O_3-WO_3 Rode and Karpov [2] found the following compounds: $3Nd_2O_3 \cdot WO_3$, $2Nd_2O_3 \cdot WO_3$, $Nd_2O_3 \cdot WO_3$, $Nd_2O_3 \cdot 2WO_3$, $Nd_2O_3 \cdot 3WO_3$. Chang et al. [3] listed $3Sm_2O_3 \cdot WO_3$, $7Sm_2O_3 \cdot 4WO_3$, $Sm_2O_3 \cdot WO_3$, $Sm_2O_3 \cdot 2WO_3$ and $Sm_2O_3 \cdot 3WO_3$ as the stable compounds in the system Sm_2O_3-WO_3. Finally in the earliest systematic RE_2O_3-WO_3 study, Borchardt [3] reported the following compounds in the system Y_2O_3-WO_3: $3Y_2O_3$-WO_3, $9Y_2O_3 \cdot 4WO_3$, $15Y_2O_3 \cdot WO_3$, $Y_2O_3 \cdot WO_3$, $Y_2O_3 \cdot 3WO_3$.

---

[1] Present address: Institute for Biophysical Chemistry, Max Planck Gesellschaft, Göttingen, West Germany.

[2] RE = rare earth

[3] Figures in brackets indicate literature references at the end of this paper.

Certain stoichiometries are common to all four investigations: $3RE_2O_3 \cdot WO_3 (RE_6WO_{12})$, $RE_2O_3 \cdot WO_3 (RE_2WO_6)$ and $RE_2O_3 \cdot 3WO_3 (RE_2W_3O_{12})$. However, enough variation existed among the reported stoichiometries to justify a compositional study. The systems Nd_2O_3-WO_3, Eu_2O_3-WO_3, and Ho_2O_3-WO_3 were chosen for careful study. The stoichiometries of compounds and the range of stability determined later in the study were:

RE_6WO_{12}	RE = La-Lu, Y
$RE_{10}W_2O_{21}$	RE = Gd-Ho, Y
$RE_{14}W_4O_{33}$	RE = Nd-Lu, Y (La-Ce were not examined)
RE_2WO_6	RE = Nd-Lu, Y (La-Ce were not examined)
$RE_4W_3O_{15}$	RE = La-Nd
$RE_2W_2O_9$	RE = Ce-Gd (La and Tb were not examined)
$RE_2W_3O_{12}$	RE = La-Lu, Y

Only two temperatures were used in this preliminary study: for the range 0-45 mol % WO_3, 1400 °C; for 46-100 mol % WO_3, 1150 °C. Thus, the existence of other stoichiometries at higher or lower temperatures cannot be eliminated and this should be kept in mind. Also, some of the compounds studied probably show a small range of stoichiometry, but it is on the stoichiometric compound that the x-ray powder data were determined and crystal chemistry comparisons were based. It was not feasible in this study to determine the stoichiometry range of each compound for each rare earth.

In reference to nomenclature, the terms "tungstate", "normal tungstate", "oxytungstate", *etc.*, sometimes applied to these compounds have been avoided in favor of the stoichiometric formula.

The larger part of this report will be devoted to the fluorite-structure-related compounds RE_6WO_{12}, $RE_{10}W_2O_{21}$, and $RE_{14}W_4O_{33}$. They were especially interesting because of their probable isostructural relationship to the RE_2O_{2n-2} oxides.

2. EXPERIMENTAL PROCEDURES

Starting materials were high-purity rare earth sesquioxides[4] and tungsten trioxide[5]. Tb_2O_3 and Pr_2O_3 were prepared by hydrogen reduction of "Tb_4O_7" and Pr_6O_{11} at 1400 °C. The oxides were thoroughly dried, weighed to the appropriate ratios to one part in ten thousand, thoroughly ground and mixed in an agate mortar and pressed into pellets at 60,000 psi. These pellets were heated in air (or in argon in the case of compounds containing Tb, Pr, and Ce) for from three to seven days at either 1400 °C (for Re_6WO_{12}, $RE_{10}W_2O_{21}$, $RE_{14}W_4O_{33}$) or 1150 °C (for RE_2WO_6 and $RE_2W_2O_9$). At least once during the heating schedule the pellets were removed from the furnace, reground, and repelletized.

Phases were identified by x-ray powder diffraction. Measurements were performed on a Siemens diffractometer using Nickel-filtered Cu$K\alpha$ radiation (λ = 1.54178 Å). The diffractometer was calibrated with high-purity silicon (a_o = 5.4301 Å) and gold (a_o = 4.0786 Å). Data were refined to yield cell parameters using the least squares computer program of Appleman et al.[5]. Reported intensities are derived from relative peak heights.

3. RESULTS AND DISCUSSION

3.1. RE_6WO_{12}

The RE_6WO_{12} compounds were all prepared at 1400 °C with six days total heating and two intermediate regrindings. They were grouped according to three structural classes, all apparently related to the fluorite structure, whose symmetry depended on the size of the rare earth cation.

La-Pr	Cubic or Pseudocubic
Nd-Gd	Pseudotetragonal
Tb-Lu, Y	Rhombohedral

[4] Research Chemicals, 99.9%
[5] Fischer Scientific, "purified"

Cell parameters for all of these compounds are listed in table 1.

3.1.a. La-Pr

La_6WO_{12} was first studied by Chang and Phillips [6]. They presented powder data indexed on a face centered cubic (f.c.c.) cell with a_o = 11.18 Å and suggested a disordered pyrochlore or ordered defect fluorite structure. We also prepared La_6WO_{12} and confirmed the powder data and cell parameter of Chang and Phillips [6]. However, it should be noted that only two weak reflections [(200) and 422)] could not be indexed on a halved f.c.c. cell with a_o = 5.591 Å.

Ce_6WO_{12} and Pr_6WO_{12} had very similar diffraction patterns except that the (200) and (422) reflections were not observed. Several weak reflections which could not be indexed on a single or doubled f.c.c. cell were present in Ce_6WO_{12} and it is for this reason that the symmetry is termed "pseudocubic" in table 1. Powder diffraction data[6] for Ce_6WO_{12} is given in table 2. Also given in table 2 is the powder data for CeO_2 as listed in the Powder Diffraction File [7]. Both have f.c.c. symmetry (or pseudosymmetry) and there is a striking correspondence between their relative intensities. The pseudocubic cell parameter of Ce_6WO_{12} is only 2% larger than that of CeO_2(a_o = 5.411 Å). This behavior tends to support the suggestion of Chang and Phillips [6] that the structure of these compounds is closely related to that of fluorite.

Table 1

Cell Parameters of RE_6WO_{12} Compounds

Compound	a_o	c_o	Symmetry
La_6WO_{12}	11.182 (1) Å		Cubic
La_6WO_{12} (a)	11.18		Cubic
Ce_6WO_{12}	5.518 (1)		Pseudocubic
Pr_6WO_{12}	5.486 (1)		Cubic
Nd_6WO_{12}	5.467 (1)	5.446 (1) Å	Pseudotetragonal
Nd_6WO_{12} (b)	5.470	5.442	Pseudotetragonal
Sm_6WO_{12}	5.409 (1)	5.389 (2)	Pseudotetragonal
Sm_6WO_{12} (b)	5.412	5.405	Pseudotetragonal
Sm_6WO_{12} (b)	10.80		Cubic
Eu_6WO_{12}	5.384 (1)	5.362 (1)	Pseudotetragonal
Gd_6WO_{12}	5.352 (2)	5.327 (2)	Pseudotetragonal
Tb_6WO_{12}	9.842 (1)	9.406 (2)	Rhombohedral
Dy_6WO_{12}	9.796 (1)	9.371 (2)	Rhombohedral
Ho_6WO_{12}(c)	9.755 (1)	9.308 (2)	Rhombohedral
Er_6WO_{12}	9.723 (1)	9.270 (1)	Rhombohedral
Er_6WO_{12}(b)	9.712	9.264	Rhombohedral
Tm_6WO_{12}(d)	9.679	9.230	Rhombohedral
Yb_6WO_{12}(d)	9.640	9.188	Rhombohedral
Lu_6WO_{12}(d)	9.618	9.145	Rhombohedral
Yb_6WO_{12}(d)	9.757	9.317	Rhombohedral

(a) after ref. [6]
(b) after ref. [8]
(c) after ref. [12]
(d) after ref. [10]

[6]We determined the x-ray powder diffraction data of every compound listed in the cell parameter tables. However, only selected examples are given in this report. The remaining powder patterns have been submitted to the Powder Diffraction File of the Joint Committee on Powder Diffration Standards [7] and, if accepted, will appear in sets 22 and 23.

Table 2

X-Ray Powder Data for Ce_6WO_{12} and CeO_2

	Ce_6WO_{12}			CeO_2(a)	
hkℓ	d_{calc}	d_{obs}	I/Io	d_{obs}	I/Io
111	3.186	3.184	100	3.124	100
200	2.759	2.758	35	3.706	29
---	---	2.215	2		
---	---	2.164	>1		
---	---	2.123	>1		
220	1.9508	1.9507	45	1.913	51
311	1.6636	1.6634	40	1.632	44
222	1.5927	1.5925	9	1.562	5
400	1.3794	1.3791	6	1.353	5
331	1.2658	1.2658	18	1.241	15
420	1.2338	1.2339	12	1.210	6
422	1.1263	1.1263	10	1.1044	12
511	1.0619	1.0617	9	1.0412	9
440	0.9754	0.9753	4	0.9505	5
531	0.9326	0.9328	16	0.9146	13

(a) From reference [7] #4-0593. Data collected by Swanson and Tatge of the U.S. National Bureau of Standards. a_o = 5.411 Å.

The AX_2 fluorite structure has four formula units per unit cell with the eight-fold coordinated A cations in the (4a) equipoints of space group Fm3m and the X anions in (8c). For RE_6WO_{12} to have a simple fluorite structure, the model for the unit cell must be $(RE^{3+}_{3.43}\ W_{0.57})(O_{6.86}\square_{1.14})$ *i.e.*, with every seventh oxygen missing and random distribution of RE^{3+} and W on the (4a) and oxygen defects on the (8c). The extra reflections, and thus doubling of the simple cell, in the case of La_6WO_{12} are probably a result of ordering of cations or oxygen defects or both. When a single-crystal structure analysis is performed, it would not be surprising to find the oxygen defects clustered around the tungsten since W^{6+} in most oxides has four-fold coordination and in the rhombohedral RE_6WO_{12} compounds described below), a coordination of six, and thus would favor the site with the lowest coordination associated with oxygen defects.

In Ce_6WO_{12} and Pr_6WO_{12} there is the possibility of removal of the oxygen defects by partial substitution of RE^{4+}. This may explain why the diffraction patterns of Ce_6WO_{12} and Pr_6WO_{12} are not identical with La_6WO_{12}. Because of difficulties in preparing and storing stoichiometric Ce_2O_3, Ce_6WO_{12} was prepared by heating the appropriate mixture of CeO_2 and WO_3 in a purified argon atmosphere according to the usual schedule. The possibility of incomplete reduction of Ce^{4+} to Ce^{3+} exists. If there is a mixed Ce valence the oxygen defects could be removed giving the simple fluorite model $(Ce^{3+}_{1.15}Ce^{4+}_{2.28}W_{0.57})O_8$. When our "$Ce_6WO_{12}$" was heated in air at 1400 °C it gave a complex x-ray powder pattern with CeO_2 as the major constituent. In the case of Pr_6WO_{12} (prepared from Pr_2O_3 and WO_3) there were no reflections which could not be indexed on a simple f.c.c. cell with a_o = 5.486 Å. When it was heated in air at 1400 °C the cell parameter decreased slightly to a_o = 5.482 Å, probably reflecting the partial substitution of the smaller Pr^{4+} for Pr^{3+}.

3.1.b. Nd-Gd

As the size of the rare earth in the RE_6WO_{12} compounds was decreased, many of the strong f.c.c. reflections showed a slight but resolvable splitting with the addition of a few new weak reflections. This was first noted by Trunov et al. [8] in Nd_6WO_{12} and Sm_6WO_{12} prepared at 1256 °C for 50 hours. Their cell parameters are listed in table 1. The weak reflections

of RE_6WO_{12} compounds in this group could not be indexed on this tetragonal cell or one related to it by simple multiples (2, 3, $\sqrt{2}$, $\sqrt{3}$) of a_o and c_o, and for this reason the symmetry has been termed pseudotetragonal in table 1. The x-ray powder diffraction pattern for Nd_6WO_{12} is given in table 3. We observed significantly fewer unindexed weak reflections than Trunov et al. [8], but this may be due to their lower preparation temperature's favoring further ordering and thus yielding stronger superlattice reflections.

Sm_6WO_{12}, Eu_6WO_{12}, and Gd_6WO_{12} were found to be isostructural with Nd_6WO_{12}. In a recent study, McCarthy [9] prepared Eu_6WO_{12} also at 1400 °C, but with a single one-day heating. The product was cubic with a_o = 5.366 Å, not tetragonal. We repeated this preparation and derived the same cubic phase. Similarly, Chang and Phillips [6] prepared Sm_6WO_{12} at 1400 °C with a 6-hour heating and reported a phase with f.c.c. symmetry and a_o = 10.80 Å. Again, two very weak reflections required doubling of the 5.40 Å f.c.c. subcell. We also observed the same behavior in Gd_6WO_{12} heated for 12 hours at 1400 °C. These results imply that considerable heating time is required in order to develop the equilibrium pseudotetragonal structure.

3.1.c. Tb-Lu, Y

The RE_6WO_{12} compounds with RE = Tb-Lu, Y have the well known RE_6MO_{12} (M = Mo, W, U) structure first elucidated by Aitken et al. [10]. The structure of this class of compounds was described by Bartram [11] who performed a structure analysis and refinement on Y_6UO_{12}. It is a rhombohedrally distorted fluorite (space group $R\bar{3}$) in which the *c*-axis of the hexagonal cell lies along the [111] axis of the f.c.c. fluorite cell. The Y(RE) ions are coordinated with oxygen ions in highly distorted octahedra, while the U(W) ions form regular octahedra with oxygen. These U(W) octahedra alternate along the *c*-axis with similar octahedra not containing a U(W) ion.

Tm_6WO_{12}, Yb_6WO_{12}, Lu_6WO_{12}, and Y_6WO_{12} have been prepared as pure phases by Aitken et al. [10]. Their hexagonal cell parameters of the rhombohedral cell are given in table 1. They also reported that the structure type extended to at least Dy_6WO_{12} but were unable to prepare any of these other compounds as pure phases. We have prepared the RE_6WO_{12} compounds with RE = Tb-Er as pure phases without particular difficulty. We reported on Ho_6WO_{12} in a

Table 3

X-Ray Powder Data of Nd_6WO_{12}

hkℓ	d_{calc}	d_{obs}	I/I_o
---	---	3.62	2
111	3.153	3.153	100
200	3.735	2.735	35(a)
002	2.723	2.722	18
---	---	2.225	2
220	1.9337	1.9336	30
202	1.9297	1.9296	45
311	1.6484	1.6483	30
113	1.6430	1.6432	30
222	1.5765	1.5766	16
400	1.3674	1.3673	3
004	1.3212	1.3613	2
331	1.2544	1.2545	6
313	1.2521	1.2522	15
420	1.2230	1.222	6
402	1.2219		
204	1.2187	1.2189	8
422	1.1156	1.1158	10
224	1.1131	1.1131	10

(a) Indicates overlapping reflections

recent study of the Ho_2O_3-WO_3 system [12]. The hexagonal cell parameters of these compounds are also given in table 1 along with the data of Trunov et al. [8] for Er_6WO_{12}. The extra reflections observed in the powder diffraction patterns by Aitken et al. [10] may have been due to incomplete reaction and the presence of the $RE_{10}W_2O_{21}$ or $RE_{14}W_4O_{33}$ phases described below.

3.1.d. Phase Transitions

It is important to note that the results just reported for RE_6WO_{12} compounds probably pertain only to the 1400 °C isotherm of a temperature vs RE^{3+} ionic radius structure diagram. As a check on the possibility of lower temperature phase transitions, we did water-quench one example of each of the RE_6WO_{12} structure types from 1400 °C to see whether the same phase as that from the usual slow air cooling would form. In each case the rapid-quenched and slow-cooled products were identical. This does not, however, rule out the possibility of a completely reversible phase transition at some temperature below 1400 °C.

If our results are valid for the 1400 °C isotherm, they show that this isotherm intersects the cubic-pseudotetragonal boundary between Pr and Nd and the pseudotetragonal-rhombohedral boundary between Gd and Tb. Using the Shannon and Prewitt [13] effective ionic radii of RE^{3+} in oxides listed in table 4 we can derive the approximate structure boundary-isotherm intercepts. For 6-fold coordination of the RE^{3+} these intercepts are about 0.99 Å and 0.93 Å respectively.

An interesting extension of the research reported here would be a study of the stability of these three structure classes as a function of temperature. Borchardt [4] has reported that rhombohedral Y_6WO_{12} undergoes a phase transition to a f.c.c. phase with a_o = 5.276 Å somewhere between 1700 °C and its melting point (above 2200 °C). Thus it is likely that many of the rhombohedral RE_6WO_{12} compounds will transform to the pseudotetragonal and/or the cubic structure at higher temperatures.

3.2. $RE_{10}W_2O_{21}$

In a recent study of the system Ho_2O_3-WO_3, McCarthy and Fischer [12] described a pseudotetragonal fluorite-structure-related compound with the stoichiometry $Ho_{10}W_2O_{21}$. Isostructural compounds of the stoichiometry $RE_{10}W_2O_{21}$ were found among the other rare earths only for RE = Gd-Ho, Y. For the other rare earths, mixtures with this bulk composition subjected

Table 4

Effective Ionic Radii of the Rare Earths in Oxides(a)

RE^{3+}	Six Coordination	Eight Coordination
La	1.045 Å	1.18 Å
Ce	1.01	1.14
Pr	0.997	1.14
Nd	0.983	1.12
Sm	0.958	1.09
Eu	0.947	1.07
Gd	0.938	1.06
Tb	0.923	1.04
Dy	0.912	1.03
Ho	0.901	1.02
Y	0.900	1.015
Er	0.890	1.00
Tm	0.880	0.99
Yb	0.868	0.98
Lu	0.861	0.97

(a) After Shannon and Prewitt, reference [13]

to the usual 1400 °C heat treatment yielded products which consisted of RE_6WO_{12} plus $RE_{14}W_4O_{33}$. Cell parameters of the $RE_{10}W_2O_{21}$ compounds are listed in table 5. A typical x-ray powder pattern, that of $Dy_{10}W_2O_{21}$, is given in table 6.

After allowance for the shifts in interplanar spacings due to the lanthanide contraction, one sees that the $RE_{10}W_2O_{21}$ x-ray patterns are virtually identical to those of the pseudotetragonal RE_6WO_{12} (RE = Nd-Gd) compounds (compare table 3 with table 6). The stability fields of this pseudotetragonal structure overlap at Gd, and as expected there is complete solid solution between Gd_6WO_{12} and $Gd_{10}W_2O_{21}$. The cell parameters of the $Gd_{10}W_2O_{21}$ end member are somewhat smaller than those of Gd_6WO_{12} because of the partial substitution of the smaller W^{6+} for Gd^{3+}.

The case of $Y_{10}W_2O_{21}$ is interesting. In his study of the system Y_2O_3-WO_3, Borchardt[4] described a compound with the oxide ratio $9Y_2O_3 \cdot 4WO_3$ (30.8 mol % WO_3). This composition is between $Y_{10}W_2O_{21}$ (28.6 mol % WO_3) and $Y_{14}W_4O_{33}$ (36.4 mol % WO_3) and indeed a check of the powder data reported by Borchardt for this "compound" indicated a mixture of about three parts $Y_{10}W_2O_{21}$ to one part $Y_{14}W_4O_{33}$. $Y_{10}W_2O_{21}$ sets the lower limit of the stability field of $RE_{10}W_2O_{21}$. In table 4 the radius of Y^{3+} is between that of Ho^{3+} and Er^{3+} but closer to Ho^{3+}. At 1400 °C, the approximate 6-coordinated RE^{3+} ionic radii limits for $RE_{10}W_2O_{21}$ are 0.94 and 0.895 Å.

3.3. $RE_{14}W_4O_{33}$

In his study of the system Y_2O_3-WO_3, Borchardt [4] also described a compound with the molar ratio $15Y_2O_3 \cdot 8WO_3$ (34.8 mol % WO_3). The powder data given for this compound were very similar to those given by Trunov et al. [8] for $11Er_2O_3 \cdot 6WO_3$ (35.3 mol % WO_3) and (allowing

Table 5

Pseudotetragonal Cell Parameters of $RE_{10}W_2O_{21}$

Compound	a_o	c_o
$Gd_{10}W_2O_{21}$	5.340 (2) Å	5.317 (2) Å
$Tb_{10}W_2O_{21}$	5.327 (1)	5.312 (1)
$Dy_{10}W_2O_{21}$	5.309 (1)	5.292 (2)
$Ho_{10}W_2O_{21}$	5.287 (1)	5.268 (2)
$Y_{10}W_2O_{21}$	5.285 (1)	5.266 (1)

Table 6

X-Ray Powder Data of $Dy_{10}W_2O_{21}$

hkℓ	d_{calc}	d_{obs}	I/I_o
---	---	3.52	2
111	3.062	3.062	100
200	2.655	2.655	30(a)
002	2.646	2.648	20
220	1.877	1.878	30
202	1.875	1.874	45
311	1.600	1.601	30
113	1.596	1.596	30
222	1.5311	1.5310	15
400	1.3274	1.3275	3
004	1.3228	1.3230	4
331	1.2179	1.2177	5
313	1.2162	1.2163	7

(a) Indicates overlapping reflections

for larger interplanar spacings) to the data of Chang et al. [3] for $7Sm_2O_3 \cdot 4WO_3$ (36.4 mol % WO_3). McCarthy and Fischer [12] found a similar compound in the system Ho_2O_3-WO_3 and determined its stoichiometry as $Ho_{14}W_4O_{33}$ ($7Ho_2O_3 \cdot 4WO_3$). A similar examination of part of the systems Nd_2O_3-WO_3 and Eu_2O_3-WO_3 as part of the present investigation also indicated a $RE_{14}W_4O_{33}$ stoichiometry.

All of the rare earths from Nd-Lu, Y (La-Pr were not studied) had a compound of this stoichiometry. The powder diffraction patterns of these compounds were similar, but minor variations caused them to be classed into three groups. The basic pattern strongly resembled that of the rhombohedral RE_6WO_{12} compounds. However, there were extra weak reflections and splitting of strong reflections which could not be indexed on a simple rhombohedral cell. Since satisfactory indexing of all the reflections could not be obtained by the usual trial-and-error methods, the powder data were referred to this rhombohedral pseudocell using only unsplit, unambiguously indexed reflections in the cell parameter refinements (see table 7).

The group of $RE_{14}W_4O_{33}$ closest to rhombohedral in symmetry were RE = Er-Lu. All of the ten strong reflections (to d = $\sim$ 1.3 Å) were unsplit and gave an excellent refinement on the rhombohedral cell. The powder data are given in table 8. In the second group, RE = Ho, Y, three of the strong reflections [the (214), (413), and (422)] were split and could not be used in the refinement based on the simple rhombohedral cell. McCarthy and Fischer [12] suggested indexing of $Ho_{14}W_4O_{33}$ based on doubling the hexagonal c_o of the rhombohedral cell in order to account for the weak reflections and the observed splitting. However, this did not yield a satisfactory refinement when applied to $Y_{14}W_4O_{33}$ which had a sharper, stronger pattern and better development of the weak reflections. Neither did the cell of Trunov [8] with a doubled hexagonal a_o. In the Powder Diffraction File (#15-559) [7], Dr. Benjamin Post suggested indexing for Borchardt's $15Y_2O_3 \cdot 8WO_3$ data based on the hexagonal cell a_o = 7.34 Å and c_o = 9.36 Å. This cell did not yield a satisfactory refinement when the weak reflections and splitting not observed by Borchardt were included.

The third group of compounds, RE = Nd-Dy, showed a more pronounced distortion of the basic rhombohedral symmetry in their powder patterns. Table 8 lists the powder data for $Gd_{14}W_4O_{33}$ side by side with that of $Lu_{14}W_4O_{33}$. It should be noted from this table that only four major reflections of $Gd_{14}W_4O_{33}$ remain unsplit. The pseudorhombohedral cell parameters were calculated and refined from these reflections only. This explains the comparatively large standard deviations of the cell parameters listed in table 7 for RE = Nd-Dy.

3.4. RELATION OF RE_6WO_{12}, $RE_{10}W_2O_{21}$ AND $RE_{14}W_4O_{33}$ TO RE_nO_{2n-2}

Borchardt [4], in communication with Professor LeRoy Eyring, was the first to report that a RE_6WO_{12} compound (Y_6WO_{12}) was apparently isostructural with the higher rare earth oxides Pr_7O_{12} and Tb_7O_{12}. Aitken et al. [10] later confirmed that the rhombohedral

Table 7

Pseudorhombohedral Cell Parameters of $RE_{14}W_4O_{33}$ Compounds

Compound	a	c
$Nd_{14}W_4O_{33}$	10.055 (3) Å	9.762 (6) Å
$Sm_{14}W_4O_{33}$	9.963 (5)	9.622 (8)
$Eu_{14}W_4O_{33}$	9.902 (2)	9.598 (6)
$Gd_{14}W_4O_{33}$	9.894 (4)	9.600 (4)
$Dy_{14}W_4O_{33}$	9.787 (2)	9.465 (3)
$Ho_{14}W_4O_{33}$	9.748 (2)	9.402 (3)
$Er_{14}W_4O_{33}$	9.735 (1)	9.347 (2)
$Tm_{14}W_4O_{33}$	9.688 (1)	9.318 (1)
$Yb_{14}W_4O_{33}$	9.654 (1)	9.263 (1)
$Lu_{14}W_4O_{33}$	9.635 (1)	9.238 (2)
$Y_{14}W_4O_{33}$	9.747 (2)	9.401 (3)

Table 8

X-Ray Powder Data of $Gd_{14}W_4O_{33}$ and $Lu_{14}W_4O_{33}$

	$Gd_{14}W_4O_{33}$			$Lu_{14}W_4O_{33}$		
hkℓ	d_{calc}	d_{obs}	I/Io	d_{calc}	d_{obs}	I/Io
				---	4.49	<1
				---	3.73	4
003	3.187	3.187	30	3.079	3.080	40
211	3.067	3.075 (a)	55	2.985	2.985	100
		3.061	100			
				---	2.884	1
				---	2.768	2
122	2.681	2.681	50	2.605	2.605	65
				---	2.310	2
				---	2.168	1
				---	1.951	2
				---	1.884	2
214	1.923	1.927	14	1.8634	1.8636	45
		1.921	35			
410	1.869	1.871	30	1.8209	1.8213	45
		1.866	30			
				---	1.7741	1
				---	1.6598	3
				---	1.6491	2
125	1.646	1.648	16	1.5943	1.5944	20
		1.644	14			
413	1.613	1.617	12	1.5674	1.5675	40
		1.610	30			
241	1.596	1.596	30	1.5545	1.5546	25
006				1.5397	1.5399	6
422	1.534	1.538	2	1.4924	1.4925	18
		1.530	6			
244	1.341	1.341	12	1.3023	1.3023	14

(a) Indicates split reflection

RE_6MO_{12} compounds were isostructural with RE_7O_{12}. McCarthy and Fischer [12] recently suggested that $RE_{10}W_2O_{21}$ and $RE_{14}W_4O_{33}$, which have metal-oxygen ratios of 4:7 and 6:11 respectively, might be isostructural with "Tb_4O_7" or Pr_6O_{11}. Professor Eyring will report on the structure of Pr_6O_{11} and other RE_nO_{2n-2} compounds elsewhere in these Proceedings. He recently told us of a probable isostructural relationship between $RE_{14}W_4O_{33}$ and Pr_6O_{11} [14].

3.5. RE_2WO_6

A number of investigators have studied RE_2WO_6 compounds. Borchardt [16] prepared all of the compounds for RE = Pr-Lu, Y. He did not determine the structure type but noted that the powder patterns fell into two groups, Pr-Dy and Ho-Lu, Y. Blasse [15] also examined these compounds and found the same two types of powder patterns. He was able to index *most* of the reflections of each type on monoclinic cells typified by the examples

	a_o	b_o	c_o	β
Pr_2WO_6	5.30 Å	5.55 Å	17.15 Å	88.0°
Gd_2WO_6	5.17	5.38	16.65	88.4
Y_2WO_6	5.50	5.34	15.15	88.3

Trunov et al. [8] prepared Nd_2WO_6, Sm_2WO_6, Er_2WO_6, and Y_2WO_6 and reported being able to index *most* reflections on the monoclinic cells, examples of which are

	a_o	b_o	c_o	β
Sm_2WO_6	5.473 Å	11.30 Å	5.260 Å	91°45'
Y_2WO_6	5.505	16.00	5.056	91°46'

A later version of the cell parameters for the two structural types of RE_2WO_6 compounds was reported by Pokrovskii et al. [17]. They confirmed that the structural change occurred between Dy_2WO_6 and Ho_2WO_6 and provided monoclinic unit cell parameters for all of the compounds. For the two examples shown above, these were

	a_o	b_o	c_o	β
Sm_2WO_6	16.81 Å	11.27 Å	5.464 Å	110°39'
Y_2WO_6	11.35	5.333	7.589	104°26'

In a recent crystal structure determination on Nd_2WO_6, Polyanskaya et al. [18] and Wyant et al. [19] described a monoclinic scheelite-related structure with the space group I2/c (No. 15) in which the Nd ions are approximately eight-coordinated and the W ions are approximately five-coordinated.

We prepared the RE_2WO_6 compounds with RE = Nd-Gd, Dy and were able to index all the observed reflections on a monoclinic cell similar to that given by Polyanskaya et al. [18]. The cell parameters of these compounds are given in table 9 and a typical powder pattern, that of Dy_2WO_6, in table 10.

No structure determination has been performed on the second type of RE_2WO_6 structure. We prepared all of the compounds for RE = Ho-Lu, Y and noted many similarities of the strong reflections of the powder patterns to those of the first group. However, we were unable to obtain satisfactory indexing and refinement for their complex powder patterns based on any of the cells described above. We did obtain satisfactory indexing and cell parameter refinement on a cell even larger than any listed above by trial-and-error methods. For example, for Y_2WO_6, the cell a_o = 11.010(4), b_o = 15.962(8), c_o = 10.081(4), β = 91°46(3)' satisfactorily accounted for all 42 reflections observed out to an interplanar spacing of 1.6 Å. Further work on this group of compounds is in progress.

3.6. $RE_4W_3O_{12}$

Compounds of this stoichiometry are reported for RE = La-Nd only. It is emphasized in the three studies describing these compounds [20, 21, 22] that they cannot be prepared by sintering the appropriate RE_2O_3-WO_3 mixtures. They have been prepared only as single crystals by hydrothermal or flux techniques. Thus, on the RE_2O_3-WO_3 phase diagrams they may be metastable compounds or compounds with a very limited range of stability with respect to temperature. The cell parameters of these compounds are listed in table 11. Typical powder patterns are given for $La_4W_3O_{15}$ by Timchenko *et al.* [20] and for $Pr_4W_3O_{15}$ by Kharchenko et al. [21]. The structure has been described by Polyanskaya et al. [22]. Tungsten ions are 6-fold coordinated in two distinct types of octahedra, and Nd ions are 8- and 9-fold coordinated in three types of polyhedra. The space group is $P4_2/nmc$ (No. 137) with four formula units per unit cell.

Table 9

Cell Parameters of RE_2WO_6, RE = Nd-Dy

Compound	a_o	b_o	c_o	β
Nd_2WO_6	15.858 (4) Å	11.387 (3) Å	5.523 (2) Å	91°49 (1)'
Nd_2WO_6(a)	15.92	11.39	5.508	92°
Sm_2WO_6	15.731 (2)	11.264 (1)	5.466 (1)	91°41 (1)'
Eu_2WO_6	15.686 (3)	11.219 (3)	5.422 (1)	91°41 (1)'
Gd_2WO_6	15.619 (4)	11.186 (4)	5.412 (2)	91°38 (2)'
Dy_2WO_6	15.505 (3)	11.064 (2)	5.365 (1)	91°35 (1)'

(a) After reference [18]

Table 10

X-Ray Powder Data of Dy_2WO_6

hkℓ	d_{calc}	d_{obs}	I/I_o
011	4.83	4.83	3
$\bar{2}11$	4.14	4.14	4
$\bar{1}30$	3.588	3.588	7
$\bar{3}21$	3.116	3.117	100
321	3.058	3.059	80
330	3.002	3.002	2
411	2.985	2.985	6
510	2.985		
231	2.814	2.815	3
040	2.765	2.766	30
002	2.681	2.681	25
600	2.583	2.583	20
341	2.208	2.209	2
132	2.1413	2.1412	5
$\bar{5}12$	1.9687	1.9688	2
$\bar{5}41$	1.9380	1.9381	1
042	1.9252	1.9253	30
640	1.8878	1.887	45
$\bar{6}02$	1.8866		
602	1.8351	1.8352	12
451	1.8010	1.8010	6
550	1.8009		
$\bar{3}61$	1.6567	1.656	15
$\bar{7}41$	1.6556		
361	1.6476	1.6477	12

Table 11

Cell Parameters of $Nd_4W_3O_{12}$

Compound	a_o	b_o
$La_4W_3O_{15}$(a)	10.06 (3) Å	12.63 (6) Å
$Pr_4W_3O_{15}$(b)	9.962	12.584
$Nd_4W_3O_{15}$(c)	9.92	12.50

(a) After ref. [20]
(b) After ref. [21]
(c) After ref. [22]

3.7. $RE_2W_2O_9$

The first reports of a compound of this stoichiometry were of $Sm_2W_2O_9$ by Chang et al. [3] and of $Nd_2W_2O_9$ by Rode and Karpov [2]. Klevtsov et al. [23] and Borisov et al. [24] prepared single crystals of $Ce_2W_2O_9$, $Pr_2W_2O_9$, and $Nd_2W_2O_9$ and performed a partial structure analysis on $Pr_2W_2O_9$. They found that the W ions formed deformed octahedra with oxygen which shared edges to yield $[(W_2O_9)^{6-}]$ zig-zag chains and that there were two types of Pr ions with 8- and 9-fold coordination respectively. The space group was $P2_1/c$ (No. 14) with four formula units per unit cell.

We attempted to synthesize all of the remaining $RE_2W_2O_9$ compounds. For RE ions smaller than Gd^{3+} (or Tb^{3+} which was not studied) this stoichiometry was not stable and the products were mixtures of RE_2WO_6 and $RE_2W_3O_{12}$. Based on the powder data of $Nd_2W_2O_9$, $Sm_2W_2O_9$, $Eu_2W_2O_9$, and $Gd_2W_2O_9$, cell parameters were refined and these are listed in table 12. A typical powder pattern, that of $Nd_2W_2O_9$, is given in table 13. The powder data of $Sm_2W_2O_9$ and $Nd_2W_2O_9$ were in good agreement with the unindexed data of Chang et al. [3] and Rode and Karpov [2]. The unindexed powder data of Ivanova et al. [1] for $La_2W_2O_9$ did not appear to be similar to the rest of the $RE_2W_2O_9$ compounds.

3.8. $RE_2W_3O_{12}$

The crystal chemistry and compound formation in this group of compounds have been studied in detail by Nassau and co-workers [25, 26]. A review of this stoichiometry by Dr. Nassau is found elsewhere in these Proceedings.

3.9. RE-W-O System

We recently completed a study of the subsolidus phase relations and compound formation in system Eu-W-O [27]. In addition to the RE_2O_3-WO_3 compounds discussed above, we found a tungsten bronze solid solution Eu_xWO_3 (previously reported by Ostertag [28])and a scheelite structure solid solution Eu_xWO_4. This latter compound contains all Eu^{2+} in its end member $EuWO_4$. McCarthy and White [29] have demonstrated that it is only with europium that one is likely to have stable lower oxidation states of the rare earths in *oxide compounds* prepared at high temperatures. The bronze RE_xWO_3 has been prepared for all of the other rare earths with a value of x of at least 0.1. Thus, except in the vicinity of the bronze, the subsolidus phase diagrams of RE-W-O probably consist of a series of compatibility lines connecting W metal with the appropriate RE_2O_3-WO_3 phases described in the preceding sections. Borchardt [4] has found this to be the case for a large portion of the system Y-W-O sub-solidus phase relations. Near the bronze the phase relations will be more complicated and involve the phases RE_xWO_3, $RE_2W_3O_{12}$, WO_2, $W_{18}O_{49}$, $W_{20}O_{58}$, and WO_3.

4. ACKNOWLEDGMENTS

We appreciate the technical assistance of Maribeth Lovette in the last stages of this study. This work was supported in part by the Joint Committee on Powder Diffraction Standards.

Table 12

Cell Parameters of $RE_2W_2O_9$ Compounds

Compound	a_o	b_o	c_o	β
$Pr_2W_2O_9$ (a)	7.70	9.84	9.27	105°30' (a)
$Nd_2W_2O_9$	7.638 (2)	9.829 (4)	9.218 (2)	107°32 (1)'
$Sm_2W_2O_9$	7.596 (3)	9.762 (4)	9.188 (3)	107°38 (2)'
$Eu_2W_2O_9$	7.590 (1)	9.732 (1)	9.178 (1)	107°40 (1)'
$Gd_2W_2O_9$	7.572 (2)	9.697 (3)	9.149 (3)	107°42 (2)'

(a) From ref. [24]

Table 13

X-Ray Powder Data of $Nd_2W_2O_9$

hkℓ	d_{calc}	d_{obs}	I/I_o
$1\bar{1}0$	5.85	5.86	10
$\bar{1}11$	5.53	5.53	9
020	4.915	4.915	12
111	4.404		
002	4.395	4.396	2
$\bar{1}02$	4.394		
$\bar{1}21$	3.959	3.957	5
$\bar{2}11$	3.538	3.537	7
$\bar{1}02$	3.344	3.345	100
$\bar{2}02$	3.343		
022	3.276	3.275	95
$\bar{1}22$	3.276		
$\bar{1}12$	3.166	3.164	95
$\bar{2}12$	3.164		
031	3.071	3.071	6
$\bar{2}21$	3.003	3.001	16
$1\bar{3}0$	2.988	2.987	70
$\bar{1}31$	2.942	2.941	20
$2\bar{2}0$	2.926	2.926	75
$\bar{1}13$	2.918	2.917	25
211	2.917		
013	2.807	2.809	4
$1\bar{2}2$	2.765	2.766	11
$\bar{2}22$	2.764		
131	2.728	2.728	1
032	2.626	2.626	30
$\bar{1}32$	2.626		
$\bar{2}13$	2.619	2.617	10
$\bar{1}23$	2.595	2.595	8
221	2.595		
023	2.517	2.516	2
$\bar{3}11$	2.463		
202	2.463	2.463	20
$\bar{3}02$	2.462		
040	2.457	2.457	8
$3\bar{1}0$	2.357	2.357	45
$\bar{1}41$	2.306	2.305	2
$\bar{1}04$	2.306		
$\bar{1}14$	2.244	2.244	14
123	2.209	2.209	3
$\bar{2}22$	2.202	2.202	8
$\bar{3}22$	2.201		
004	2.198	2.197	6
$\bar{2}02$	2.197		
033	2.184	2.172	11
$\bar{3}13$	2.173	2.172	11

5. REFERENCES

[1] Ivanova, M.M., Balagina, G.M. and Rode, E. Ya., Izv. Akad. Nauk SSSR, Neorg. Mater. 6, 914 (1970), [Eng. Trans. 6, 801 (1970)].

[2] Rode, E. Ya. and Karpov, V.N., Izv. Akad. Nauk SSSR, Neorg. Mater. 2, 683 (1966), [Eng. Trans., 2, 587 (1966)].

[3] Chang, L.L.Y., Scroger, M.G. and Phillips, B., J.Inorg. Nucl. Chem. 28, 1179 (1966).

[4] Borchardt, H.J., Inorg. Chem. 2, 170 (1963).

[5] Appleman, D.E., Handwerker, D.S. and Evans, H.T., Jr., Annual Meeting of the American Crystallographic Association, Cambridge, Mass., Program pp 42-43 (1963).

[6] Chang, L.L.Y. and Phillips, Bert, Inorg. Chem. 3, 1792 (1964).

[7] Powder Diffraction File of the Joint Committee on Powder Diffraction Standards, Swarthmore, Pa.

[8] Trunov, V.K., Tyushevskaya, G.I. and Afonskii, N.S., Zh. Neorg. Khim. 13, 936 (1968) [Eng. Trans. 13, 491 (1968)].

[9] McCarthy, G.J., Mat. Res. Bull. 6, 31 (1971).

[10] Aitken, E.A., Bartram, S.F. and Juenke, E.F., Inorg. Chem. 3, 949 (1964).

[11] Bartram, S.F., Inorg. Chem. 5, 749 (1965).

[12] McCarthy, G.J. and Fischer, R.D., Mat. Res. Bull. 6, 591 (1971).

[13] Shannon, R.D. and Prewitt, C.T., Acta Cryst. B25, 925 (1969) and B26, 1046 (1970).

[14] Eyring, LeRoy, Personal Communication.

[15] Blasse, G., J. Inorg. Nucl. Chem. 28, 1488 (1966).

[16] Borchardt, H.J., J. Chem. Phys. 39, 504 (1963).

[17] Pokrouskii, A.N.,Rybakov, V.K. and Trunov, V.K., Zh. Neorg. Khim., 14, 2344 (1969) [Eng. Trans. 14, 1233 (1969)].

[18] Polyanskaya, T.M., Borisov, S.V. and Belov, N.V. Dokl. Akad. Nauk. SSSR, 193, 83 (1970) [Eng. Trans. 15, 636 (1971)].

[19] Wyant, J. Klevtsov, P.V., Kharchenko, L. Yu. and Polyanskaya, T.M., Bull. Soc. Fr. Mineral. Cryst. 93, 536 (1970).

[20] Timchenko, T.I., Petushkova, L.V., Pobedinskaya, E.A. and Pashkova, A.V., Dokl. Akad. Nauk SSSR, 185, 573 (1969) [Eng. Trans. 14, 188 (1969)].

[21] Kharchenko, L. Yu., Polyanskaya, T.M. and Klevtsov, P.V., Izv. Akad. Nauk. SSSR, Neorg. Mater. 6, 1720 (1970). [Eng. Trans. 6, 1517 (1970)].

[22] Polyanskaya, T.M., Borisov, S.V. and Belov, N.V., Kristallografiya 15, 1135 (1970), [Eng. Trans. 15, 991 (1971)].

[23] Klevtsov, P.V., Kharchenko, L. Yu. and Klevtsova, R.F., Dokl. Akad. Nauk. SSSR 176, 575 (1967) [Eng. Trans. 12, 851 (1968)].

[24] Borisov, S.V. and Klevtsova, R.F., Kristallografiya 15, 38 (1970) [Eng. Trans. 15, 28 (1970)].

[25] Nassau, K., Levinstein, H.J. and Loiacano, G.M., J. Phys. Chem. Solids 26, 1805 (1965).

[26] Nassau, K., Shiever, J.W. and Keve, E.T., J. Solid State Chem. 3, 411 (1971).

[27] McCarthy, G. J., Fischer, R. D., and Sanzgiri, J., J. Solid State Chem. (in press).

[28] Ostertag, W., Inorg. Chem. 5, 758 (1966).

[29] McCarthy, G.J. and White, W.B., J. Less-Common Metals, 22, 409 (1970).

DISCUSSION

P. Hagenmuller: We investigated in Bordeaux some rare earth alkali-metal-tungstates and we always found tungsten in coordination 6 or 4 in the wolframite or scheelite-like phases. So one can suppose that your anionic sublattice in the fluorite related structures is distorted, giving a coordination number of 6 or maybe of 4. Have you any evidence about the surrounding of tungsten in these fluorite related structures?

G. J. McCarthy: I do not have any evidence of tungsten coordination in the fluorite related compounds based on powder data[1]. Structures have been determined in the case of $RE_4W_3O_{15}$, $RE_2W_2O_9$ and RE_2WO_6. All of these were determined in the USSR[2], and the two with Professor Belov's[3] participation are, I believe, quite good. Tungsten is in 6-fold coordination in the first two and in approximately 5-fold coordination in RE_2WO_6. You don't get 4-fold coordination until the higher WO_3 content $RE_2W_3O_{12}$ compounds with scheelite related structures which Dr. Nassau will talk about this afternoon.

M. J. Sienko: I believe that Tilley at Bradford[4] is studying the europium tungsten bronzes and related systems. He is finding a series of block-type structures, as I recall, with varying integral structural units put together.

G. J. McCarthy: I've been in contact with Ian McColm who is working with Tilley at Bradford. He was quite interested in learning more about the phase relations around the bronze composition range. I have not yet seen their crystallographic results, but I'm looking forward to it.

[1]Since it is very likely that the fluorite related RE_6WO_{12} compounds with RE=Tb-Lu,Y are isostructural with Y_6UO_{12} in which uranium has a regular 6-fold coordination, we can infer that tungsten will also have regular 6-fold coordination in these compounds (see Section 3.1.C).

[2]References [18], [20], and [24].

[3]N. V. Belov, Academy of Sciences of the USSR.

[4]See J. Solid State Chem. 4, 199 (1971) for an article on related Sn_xWO_3 phases.

National Bureau of Standards Special Publication 364, Solid State Chemistry, Proceedings of 5th Materials Research Symposium, issued July 1972.

PREPARATION OF OXIDES AND RELATED COMPOUNDS BY CHEMICAL TRANSPORT

Harald Schäfer

University of Münster
Münster, GERMANY

In a temperature gradient it is possible for solids to migrate by sublimation, by catalytic sublimation (P_{red}/I_2), dissociative sublimation and by chemical transport.

Reversible heterogeneous reactions are utilized in chemical transport. The phenomenon is complex but can normally be treated as gaseous diffusion between spaces in which thermodynamic equilibrium has been established between solid and gaseous phases. The partial pressure drop between these spaces is the quantity which determines the suitability of a chemical reaction for transport processes.

Information is given regarding working techniques and transport agents which have been employed hitherto.

In further chapters there is an account of the binary oxides which have been chemically transported up to now and there is also an account of the types of reaction used for transport.

Using zinc oxide transport as an example, a demonstration is given of the selection of transport reactions on the basis of thermodynamic considerations.

There is a discussion of syntheses in a temperature gradient and of "solid/solid reactions", with regard to the preparative employment of chemical transport processes. This discussion is illustrated with several examples. There is in addition a review of the transport of ternary compounds and of the decomposition of ternary compounds which can occur under the influence of the transport agent.

Examples are given of the crystallization of metastable modifications out of the gas phase.

Key words: Chemical Vapor Transport; crystal growth; oxides; synthesis.

1. INTRODUCTION, PRINCIPLES

1.1. MIGRATION OF SOLIDS IN A TEMPERATURE GRADIENT

If in a reaction space there exists a temperature gradient and if in that space a solid (or a liquid) migrates reversibly through the gas phase from point 2 to point 1 with the temperature T_2 and T_1, this can be a consequence of five distinct causes:

1.1.a. SUBLIMATION

$$I_{2(s)} = I_{2(g)} \quad (1)$$

$$LiF_{(s)} = LiF_{(g)} \quad (0.5\ Li_2F_{2(g)}) \quad (2)$$

1.1.b. SUBLIMATION WITH SUPRESSION OF A THERMAL BREAKDOWN

$$TiCl_{3(s)} = TiCl_{3(g)} \quad (0.5\ Ti_2Cl_{6(g)}) \qquad (3)$$

(in the presence of $TiCl_{4(g)}$

$$NbCl_{4(s)} = NbCl_{4(g)} \qquad (4)$$

(in the presence of $NbCl_{5(g)}$)

The gaseous chlorides $TiCl_4$ or $NbCl_5$ prevent the disproportionation of $TiCl_3$ or $NbCl_4$, however they are not involved in sublimation in the thermodynamic sense.

1.1.c. CATALYTIC SUBLIMATION

There are solids in whose structure the volatile species do not occur as building blocks at the outset, so that during transition into the gas phase it is necessary to break atomic bonds, to rearrange atoms and to establish new atomic bonds; such solids possess lower volatilization coefficients [1].[1] This also applies to the transition of the three-dimensionally linked lattice of red phosphorus into the P_4-molecule. It has been found [2] that red phosphorus sublimates rapidly upon the addition of iodine. It is not a chemical transport through phosphorus iodide which is taking place but rather a catalyzed reversible reaction (5).

$$4\ P_{red} = P_{4(g)} \qquad (5)$$

(I_2, PI_3, P_2I_4)

1.1.d. THERMAL DECOMPOSITION AND RECOMBINATION

(Dissociative Sublimation)

$$NH_4Cl_{(s)} = NH_3 + HCl \qquad (6)$$

$$3SbSI_{(s)} = Sb_2S_{3(g)} + SbI_{3(g)} \qquad (7)$$

$$CdO_{(s)} = Cd_{(g)} + 0.5O_2 \qquad (8)$$

1.1.e. CHEMICAL TRANSPORT

$$Nb_{(s)} + \left\{\begin{matrix} 2\ (2.5)\ I_2 \\ 4\ (5)\ I_1 \end{matrix}\right\} = NbI_{4(g)}\ (NbI_{5(g)}) \qquad (9)$$

$$TiO_{2(s)} + 2Cl_2 = TiCl_{4(g)} + O_2 \qquad (10)$$

$$ZnS_{(s)} + I_2 = ZnI_{2(g)} + 0.5\ S_{2(g)} \qquad (11)$$

$$2GaAs_{(s)} + GaI_{3(g)} = 3GaI_{(g)} + 0.5\ As_{4(g)} \qquad (12)$$

1.2. DISTINGUISHING BETWEEN PROCESSES

When it is necessary to determine which of the processes 1.1.a. through 1.1.e. is operative in an observed migration of a solid, this can be accomplished on the basis of a thermodynamic calculation -- or if data is lacking, on the basis of an experimental equilibrium investigation. In the course of making this determination it will become apparent when several processes overlap.

However, it often happens that quite simple observations supply sufficient information.

---

[1] Figures in brackets indicate the literature references at the end of this paper.

Only the processes 1.1.a. and 1.1.d. also occur in a vacuum; the other processes require the presence of a foreign gaseous partner.

In the processes 1.1.a. through 1.1.d. the forward reaction is in each case *endothermal;* the solid is used up in the warmer zone (T_2) and precipitated in the cooler zone (T_1). On the other hand chemical transport is possible both with endothermal and with exothermal processes. If in the temperature gradient a solid migrates into the warmer zone ($T_1 \rightarrow T_2$) then it is clearly a chemical transport which is taking place.

1.3. THE COMPLEX NATURE OF CHEMICAL TRANSPORT AND ITS POSSIBLE SIMPLIFICATIONS

Chemical transport between points 2 and 1 having temperatures T_2 and T_1 requires gas motion and a partial pressure drop $P_2 - P_1$.

The relationships become clear when a known gas flow transports material from an equilibrium space 2 into an equilibrium space 1. In principle this corresponds to equilibrium measurement by the flow method. If a high degree of precision is required in the computation of transport efficiency then this procedure should be used.

Practically more important, especially for preparative purposes, is chemical transport in closed cylindrical ampules. Here the process is complex indeed. Problems arise both in the unambiguous description of the gas motion and in the partial pressure drop. An exact treatment would have to take the following details into consideration:

(a) Diffusion together with its temperature dependence along the transport path.

(b) The diffusion-coupled flow of the entire gas mass, during reactions involving molecular number change, which moves towards the side where the reaction takes place with decreasing molecular number.

(c) Individual diffusion coefficients, whenever more than two gaseous components are present.

(d) The flow of the entire gas mass by thermal convection with its dependence upon tube dimensions and upon the position (inclination) of the tube in the temperature gradient.

(e) Gas separation by thermodiffusion.

To these factors relating to the *gas motion* should be added those factors affecting the *partial pressure drop:*

(f) In the simplest case the equilibrium pressure is established at the surface of the solid phase. When the tube content is known and whenever *only two gaseous materials* occur, the partial pressure drop $P_2 - P_1$ is unambiguously derivable from the thermodynamic calculation.

(g) When the gas phase contains more than two substances the calculation of the gas composition at the solid phase requires that the individual diffusion constants be taken into consideration also in the case of equilibrium.

(h) Along the gas path homogeneous reactions can occur ($I_2 = 2I_1$; $H_2S = H_2 + 0.5S_2$) which influence the diffusion characteristics and the partial pressure drop.

In addition there are the deviations from the equilibrium case:

(i) The precipitation of the substance requires a certain supersaturation of the gas phase.

(k) In the case of rapid gas movement the heterogeneous reaction (and not the gas motion) becomes the factor which determines velocity.

(l) Finally in the case of small quantities of the transport agent and large surface area of the solid, difficulties can arise. The adsorption of gas constituents at the surface of the solid can significantly affect the given gas composition [3]

It appears hopeless to take all these effects into account exactly. But fortunately in the practically important range of ΣP and T many of these effects are not substantially significant and hence for practical purposes may be neglected:

(a') The diffusion is calculated for the mean temperature of the diffusion path.

(b') The one-directional flow of the total gas mass occurring in the case of reactions with molecular number change is to be neglected whenever the diffusion formula is applied to those varieties of molecule occurring in small concentration (and is not applied to a principal constituent) [4].

(c', g') In calculations the same mean diffusion coefficient is used for all molecules.

(e', h') One proceeds on the basis of a model which assumes that a volume element of the gas is carried unchanged from point 2 to point 1 and reacts there.

(d') Thermal convection acquires significance only for $\Sigma P > 1$ atm., when, for example, one is working with ampules of 18 centimeter length and 2 centimeter diameter. The effect of convection can also be easily checked experimentally: In the case of pure diffusion the inclination of the ampule in the temperature drop is without significance; in addition the quantity transported is proportional to the tube cross-section.

(f', i', k') Normally at $\Sigma P > 10^{-2}$ atm. equilibrium pressure is established at the solid phase with sufficient exactness. If nucleus formation has taken place in the separating zone (or if seed crystals are assumed to be present) then supersaturation of the gas phase need not be considered.

(l') If the solid phase does not have an unusually large surface then at total pressures greater than 10^{-2} atmospheres adsorption will also no longer play a disturbing role.

In closing it should be emphasized that the *uncertainty in the thermodynamic numerical values* is frequently of much more weight than simplifications in the calculation of the gas motion.

1.4. THE SIMPLIFIED CALCULATION OF TRANSPORT EFFICIENCY [4]

Transport experiments were frequently carried out under the following experimental conditions:

Ampule length 10 - 20 cm

Ampule diameter < 3 cm

Temperature > 600 K

Total pressure, lower limit 0.001 - 0.01 atm., upper limit 1 - 10 atm.

Under such conditions one can proceed from the assumption, based upon available experience with many chemical systems, that heterogeneous *equilibrium* exists at the solid phase and that the gas motion by *diffusion* is the slowest component of displacement which contributes to determining the velocity.

For a transport reaction

$$iA_{(s)} + kB_{(g)} = jC_{(g)} + lD_{(g)} + \ldots. \qquad (13)$$

the molecular numbers moving between points 1 and 2 are in the ratio k: j: l, in the stationary state. Thus one can base the calculation upon the absolute values of each of the partial pressure drops ΔP_B, ΔP_C, ΔP_D ($\Delta P = P_2 - P_1$). However on account of the flow of the entire gas phase (*cf.*, 1.3 b, b'), connected with the diffusion, for the calculation of ΔP one selects the smallest (or in any case a small) partial pressure; with $P_B >> P_C$ thus P_C [sic].

The diffusion formula then gives

$$n_A = \frac{i}{j} \cdot \frac{D\ q\ t}{s\ R\ T} \cdot \Delta P_C [\text{Mol}] \qquad (14)$$

where D is the mean diffusion constant for the given experimental conditions, q is the cross-section and s the length of the diffusion path, t is the duration of the experiment and T is the absolute temperature of the diffusion path.

With an average diffusion coefficient for hydrogen-free systems D_o (273 K, 1 atm.) = 0.1 cm^2/sec. and with the introduction of the functional dependence of D upon P and T there follows [4].

$$n_A = \frac{i}{j} \cdot \frac{\Delta P_c}{\Sigma P} \cdot \frac{T^{0.8} \cdot q \cdot t'}{s} \cdot 1.8 \times 10^{-4} \text{ [Mol]} \qquad (15)$$

n_A = gram molecules of transported solid phase

i,j = coefficients of the reaction equation

ΔP_c = difference of the equilibrium pressures (atm.).

ΣP = total pressure (atm.)

T = mean temperature of the diffusion path (K)

q = cross-section of the diffusion path (cm^2)

t' = duration of experiment (h)

s = length of the diffusion path (cm)

This simplified equation has proven to be useful for the approximate calculation of transport efficiencies. When using another value of D_o it is only necessary to change the numerical factor proportionately.

Evidently the quoted $\Delta P/\Sigma P$ is of decisive significance. In conjunction with the above equation and with the usual experimental conditions (T = 1,000 K; q = $1^2\pi$; s = 10 cm) as well as with the gram molecular weight of 100 for the transported solid substance, one can calculate a transport efficiency of around 1 mg/100 h, if $\Delta P/\Sigma P = 10^{-5}$, (5). This value of $\Delta P/\Sigma P$ can be used generally as a practical lower limit. If significant amounts of solid phase are to be transported over distances amounting to centimeters, then a reaction must be selected with the aid of thermodynamic considerations for $\Delta P/\Sigma P > 10^{-5}$.

At the same time it is to be noted that ΣP cannot be arbitrarily lowered, because as a rule at $\Sigma P <$ (0.001 to 0.01) atm. diffusion no longer determines the velocity (*cf.*, 1.3 (k) (k'), and also 1.3. (1)). These considerations are applicable in the case of a transport path (diffusion distance s) of 10 cm. If the reactions between two mingled solids are enhanced by chemical transport (Section 5.3.), then the diffusion paths in the gas space are only of the order of magnitude of 10^{-3} cm. Because of the proportionality between transport efficiency and one/s there is then a lowering of the $\Delta P/\Sigma P$-limit to $10^{-5} \times 10^{-4} = 10^{-9}$(!).

1.5. THE PARTIAL PRESSURE DROP (4)

1.5.a. THE EQUILIBRIUM POSITION

As the simplest case let us consider transport of A with the reversible reaction

$$A_{(s)} + B_{(g)} = C_{(g)} \qquad (16)$$

Everywhere in the closed tube which lies in the temperature gradient $T_2 - T_1$, $\Sigma P = P_B + P_C$. Further, we have for the partial pressure drop $\Delta P = P_2 - P_1$ in absolute values $|\Delta P_B| = |\Delta P_C|$. If now the equilibrium (16) lies far to the left or to the right side then one of the partial pressures and hence also ΔP will become very small:

"A noticeable chemical transport cannot occur at an extreme equilibrium position".

Between these extremes there exists a maximum:

"A large transport effect is to be expected whenever a reaction is chosen for which log $Kp_{(T)}$ *does not differ too much from* zero" [4].

This qualitative rule is useful for the selection of the reaction and is sufficient for many purposes (*cf.*, also Section 4). More extensive questions, such as "under what conditions of P and T is a maximal transport rate to be expected for the selected reaction?", require a more precise thermodynamic discussion.

1.5.b. THE SIGN OF THE REACTION ENTHALPY

From the temperature dependence of the equilibrium position it follows that *exothermal* reactions transport the solid into the warmer zone $T_1 \rightarrow T_2$ and *endothermal* reactions transport it into the colder zone ($T_2 \rightarrow T_1$). Here the solid is always written on the left side of the equilibrium reaction which is being considered.

1.5.c. MULTICOMPONENT SYSTEMS

Often in a given transport system *only one* reaction is responsible for the chemical transport or is at least so strongly predominant that it suffices to consider this reaction only.

In those cases in which several reactions participate to a comparable extent in the formation of the equilibrium gas phase, the situation can be dealt with without difficulty; for example

$$MeO_{(s)} + Cl_2 = MeCl_{2(g)} + 0.5\ O_2 \qquad (17)$$

$$MeO_{(s)} + 2HCl = MeCl_{2(g)} + H_2O_{(g)} \qquad (18)$$

$$Cl_2 + H_2O = 2HCl + 0.5\ O_2 \qquad (19)$$

$$\Delta P = \Delta P(MeCl_2) = \Delta P(H_2O) + 2\Delta P(O_2)$$

A closer view of the matter is provided by systems of the type (20) -- (23).

$$Si_{(s)} + SiI_{4(g)} = 2SiI_{2(g)} \qquad \text{endothermally} \qquad (20)$$

$$Si_{(s)} + 2I_{2(g)} = SiI_{4(g)} \qquad \text{exothermally} \qquad (21)$$

$$Si_{(s)} + 4I_g = SiI_{4(g)} \qquad \text{exothermally} \qquad (22)$$

$$I_{2(g)} = 2I_{(g)} \qquad (23)$$

Here the effective ΔP does not come from the difference of the total Si-contents in the spaces 1 and 2 expressed in each case by $P(SiI_2) + P(SiI_4)$, but from the difference of the Si-contents P^*_{Si} reversibly taken up by the gas phase (and capable of being again precipitated out of it in the case of T-change);

$$P^*_{Si} = 0.5[P(SiI_2) - P(I_2) - 0.5\ P(I)] \qquad (24)$$

$$\Delta P = P(Si^*, T_2) - P(Si^*, T_2) \qquad (25)$$

This expresses the fact that in the case of T-reduction only the SiI_2-portion disproportionates with Si-precipitation, which is not converted into SiI_4 by I_2 or I_1 [4].

If both exothermal and endothermal reactions participate in the chemical transport, then P^* passes with increasing temperature through a maximum or a minimum. Thus there occurs

a change in the transport direction in the temperature drop ($T_2 > T_1$). During the Si-transport discussed above, the events are governed at lower temperatures predominantly by the *endothermal* reaction (2) ($T_2 \rightarrow T_1$) while at a higher temperature the exothermal reactions (21) and (22) prevail ($T_1 \rightarrow T_2$) [4].

For the thermodynamics of chemical transport *cf.*, also [5].

1.6. WORKING TECHNIQUE AND TRANSPORT AGENTS

If transport reactions are to furnish information regarding the controlling gas species then a highly refined working technique is required. The ampule material (normally fused quartz) must be heated thoroughly in high vacuum and the materials -- as pure as possible -- and transport agents which are employed must be introduced with particular care. All this is superfluous for normal preparative purposes.

Preparative transport reactions are as a rule carried out in closed ampules made of glass or quartz glass. Typical dimensions are 10-20 centimeters in length, 1-2 centimeters in diameter. After being loaded up with the solid phase (*e.g.*, 1 g) and with the transport agent quantity calculated, for example, for 1 atm. at the experimental temperature, the ampules are sealed off and heated in a tube furnace possessing two independently controllable heating zones.

At the end of the experiment is is advisable to cool off that side of the ampule on which the initial solid substance lay. The content of the gas phase then precipitates there and not upon the transported substance.

For further suggestions regarding the filling of the ampules, *cf.*, [4].

In special cases ampules can be used having linings made of porcelain or of sintered corundum or having a carbon coating. It is also possible for procelain, sintered corundum, nickle or platinum to be used directly as ampule material.

Table 1 presents a synopsis of transport agents which have been frequently used up to now.

Table 1

Examples of Transport Agents

X_2	HX	NH_4X	(X = F, Cl, Br, I)
H_gX_2	AlX_3	SiX_4	NbX_5
H_2	H_2O	CO	CO_2
O_2	S_2	Se_2	Te_2

Frequently it is more convenient to introduce the corresponding ammonium salt in place of HCl, HBr, HI.

When very great purity or a very precise amount of the transport agent is required, the latter can be generated by a quantitative chemical reaction and condensed into the transport ampule. Examples appear in Equations (27), (28); for further reactions in the synthesis of transport agents *cf.*, [6].

$$AgCl + 0.5\ H_2 = Ag + HCl \qquad (27)$$

$$2CuI + 0.5\ O_2 = CuO + I_2 \qquad (28)$$

2. BINARY OXIDES WHICH UP TO THE PRESENT HAVE BEEN CHEMICALLY TRANSPORTED, A SYNOPSIS

In recent years numerous binary oxides have been chemically transported in situations where the focus of interest was the production of crystals or of thin layers. Tables 2 and 3 give a qualitative synopsis (certainly not a complete one) of the present state of this subject. With regard to each particular modification of the crystals growing out of the gas phase (for example TiO_2, Nb_2O_5) the reader must be referred to the original literature: In addition *cf.*, Section 5.5. Simultaneously, the tables referred to furnish the foundation of the next sections.

Table 2

Chemically Transportable Binary Oxides

																	He
Li	*	Be										B	C	N	O	F	Ne
Na		Mg										Al	Si	P	S	Cl	Ar
K	Ca	Sc	Ti	V	Cr	Mn	Fe	Co	Ni	Cu	Zn	Ga	Ge	As	Se	Br	Kr
Rb	Sr	Y	Zr	Nb	Mo	Tc	Ru	Rh	Pd	Ag	Cd	In	Sn	Sb	Te	I	Xe
Cs	Ba	La	Hf	Ta	W	Re	Os	Ir	Pt	Au	Hg	Tl	Pb	Bi	Po	At	Rn
Fr	Ra	Ac	Th	Pa	U												

* Elements, whose oxides have been transported previously, are marked with □.

Table 3

Chemically Transported Binary Oxides

Oxide	Transport agent	Temperature °C	Reference
Li_2O	H_2O	∿ 1000	[4], [7]
BeO	H_2O	∿ 1500	[4], [8]
BeO	HCl	1100 → 800	[4]
MgO	H_2O	∿ 2000	[9]
MgO	HCl	1000 → 800	[4], [10]
MgO	CO	1700 → 1600	[11]
B_2O_3	H_2O	∿ 900	[12]
Al_2O_3	Cl_2	1240 → T_1	[4]
Al_2O_3	HCl	∿ 1100 → T_1	[4], [13]
Al_2O_3	H_2	2000 → T_1	[4], [14], [15]
Ga_2O_3	I_2 + S	1150 → 1100	[16]
In_2O_3	I_2 + S	1150 → 1100	[16]
SiO_2	H_2O	hydrothermal	[4]
SiO_2	HF	200 → 500	[17], [18], [19], [20]
SiO_2	$TaCl_5$	∿ 1000	[4]
SiO_2	TaI_5	∿ 1000	[4]
SiO_2	SiI_2/SiI_4	1270 → 1000	[4]
SiO_2	$CrCl_4/Cl_2$	1100 → 900	[4]
SiO_2	H_2	1400 → T_1	[4]

Table 3 - continued

Oxide	Transport agent	Temperature °C	Reference
GeO_2	HCl	200 → 500	[21]
GeO_2	H_2/H_2O	700 → 660	[22]
SnO_2	H_2O	1570 → 1500	[23]
SnO_2	HCl		[4], [24]
SnO_2	HBr	T_1 → 800	[25]
SnO_2	S	800 → T_1	[25]
SnO_2	Br_2 + a little S	T_1 → 800	[25]
SnO_2	Br_2 + large amount S	800 → T_1	[25]
SnO_2	H_2	∿ 900	[4]
SnO_2	CO	∿ 900	[4]
TeO_2	H_2O	700 → 600	[26], [27]
TiO_2	Cl_2	1000 → 800	[28], [29]
TiO_2	HCl	∿ 1000 → T_1	[4], [30]
TiO_2	Se/Cl_2	1000 → 800	[29]
TiO_2	$TeCl_4$	1100 → 900	[28], [29]
TiO_2	I_2 + S	1150 → 1100	[16]
Ti_2O_3	HCl	1000 → 900	[31]
ZrO_2	I_2 + S	1050 → 1000	[16]
V_2O_5	H_2O	∿ 600	[32]
V_8O_{15}	$TeCl_4$		[33]
V_7O_{13}	$TeCl_4$	1050	[34]
V_6O_{11}	$TeCl_4$	1040 → 920	[35]
V_5O_9	$TeCl_4$		[36]
V_4O_7	$TeCl_4$	1050	[34]
V_3O_5	$TeCl_4$	1040 → 920	[35]
Nb_2O_5	Cl_2	∿ 1000 → T_1	[37]
Nb_2O_5	HCl (+$NbCl_5$)	∿ 1000 → T_1	[38], [37], [39]
Nb_2O_5	Cl_2 + Te	1000 → 800	[40]
Nb_2O_5	Cl_2 + $NbCl_5$	∿ 1000 → T_1	[39], [41], [42]
Nb_2O_5	$NbCl_5$	∿ 1000 → T_1	[41], [4], [42a]
$NbO_{2.5-x}$	$NbBr_5$	∿ 1000	[43], [4]
$NbO_{2.5-x}$	NbI_5	650 → 550	[4], [39], [42a]
$NbO_{2.483}$	$NbCl_5/NbOCl_3$	1080 → 980	[44]
$NbO_{2.464}$	$NbCl_5/NbOCl_3$	1250 → T_1	[45]
$NbO_{2.417}$ ($Nb_{12}O_{29}$)	NbI_5	920 → 840	[46]
		740 → 650	[47]
NbO_2	I_2	∿ 1000	[47], [4]
NbO	I_2	950 → 1100	[47], [4]
Ta_2O_5	Cl_2	900 → 700	[4]
Ta_2O_5	HCl	1000 → 600	[4]
Ta_2O_5	$TaCl_5$	750 → 650	[48], [4]
Ta_2O_5	Cl_2 + $CrCl_4$	900 → 700	[4]
Cr_2O_3	O_2	≧ 1000	[4]
Cr_2O_3	Cl_2	800 → 600	[49], [39]
		980 → 860	
Cr_2O_3	Cl_2 + O_2	800 → 600	[49]
Cr_2O_3	Br_2; Br_2 + O_2	800 → 600	[49]
MoO_3	H_2O	∿ 700	[4], [50]
MoO_3	Cl_2	500 → 400	[51]
MoO_2	I_2	1000 → 800	[49], [52], [53]
WO_3	H_2O	1100 → T_1	[4], [50]
WO_3	Cl_2	1000 → 900	[54]
WO_3	HCl	1000 → 900	[4], [54], [55]
WO_3	CCl_4	∿ 700	[54]
$W_{20}O_{58}$	HCl	∿ 900	[56]
$W_{18}O_{49}$	I_2 + H_2O	900 → 800	[58]
W_4O_{11}	H_2O (+ H_2)	1000 → T_1	[4]
WO_2	H_2O (+ H_2)	1000 → T_1	[4]

Table 3 - continued

Oxide	Transport agent	Temperature °C	Reference
WO_2	I_2	1000 → 800	[57], [58], [52]
WO_2	HCl	∿ 900	[56]
Mn_2O_3	Cl_2	980 → 860	[39]
Mn_2O_3	$Cl_2 + O_2$	800 → 600	[59]
Mn_3O_4	HCl	1000 → 800	[10], [60]
MnO	HCl	980 → 900	[4], [39]
Re_2O_7	H_2O (+ O_2)	180 → T_1	[61]
ReO_3	I_2	400 → 370	[62], [63], [64]
ReO_2	I_2	700 → 600	[63]
Fe_2O_3	Cl_2	980 → 860	[4], [39]
Fe_2O_3	HCl	300 → 400	[65]
Fe_2O_3	HCl	1000 → 800	[4]
Fe_2O_3	HBr	∿ 600	[25]
Fe_3O_4	HCl	1000 → 800	[4], [66], [67]
FeO	HCl		[4]
RuO_2	O_2	1280 → T_1	[4], [68]
OsO_2	O_2	960 → 900	[4], [69], [70], [71]
Co_3O_4	HCl	900 → 700	[60]
Co_3O_4	Cl_2	980 → 860	[39]
CoO	Cl_2	1000 → 900	[39]
CoO	HCl	970 → 900	[39]
IrO_2	O_2	1100 → 900	[4]
IrO_2	$Cl_2 + O_2$	900 → T_1	[72]
NiO	Cl_2	980 → 860	[39]
NiO	Br_2	930 → T_1	[73]
NiO	HCl	930 → T_1	[73], [10], [39]
NiO	HBr	940 → 915	[73]
CuO	HCl	800 → 700	[74]
Cu_2O	HCl	600 → 900	[4]
Cu_2O	HCl	1100 → 900	[4]
ZnO	H_2		[75]
ZnO	Cl_2	1000 → 800	[76], [29], [39]
ZnO	$HgCl_2$	1000 → 800	[29], [6]
ZnO	HCl	1005 → 935	[39], [29]
ZnO	Br_2	1010 → 990	[77]
ZnO	I_2	800 → 700	[78]
CdO	I_2	540 → 510	[46], [39]
		760 → 700	[79]. [78]
U_3O_8	O_2	> 1300	[80], [81]
U_3O_8	HCl	1000 → 850	[82]
U_4O_9	HCl	1000 → 850	[82]
UO_2	HCl; Br_2; Br_2 + S	1000 → 850	[82]

The arrow indicates the transport direction in the T-drop. To the extent that the reaction has already been covered in [4], the reader is referred to the original literature cited there.

3. TYPES OF REACTION

The transport agent is highly volatile and transforms the solid, which is to be transported, reversibly into volatile reaction products.

Frequently employed transport agents are listed in table 1 (Section 1.6.). Further variations are possible particularly in the case of the metallic halides.

The following, naturally incomplete, picture (for literature citations *cf.*, table 3) is the result of an attempt to make it possible to survey the quite disparate reaction types employed for chemical transport from a unified point of view.

3.1. THE FORMATION OF VOLATILE ELEMENTS OR SUB-COMPOUNDS

The reactions (29) through (31) give examples.

$$MgO_{(s)} + CO = Mg_{(g)} + CO_2; \qquad 1700 \rightarrow 1600\ ^\circ C \tag{29}$$

$$Al_2O_{3(s)} + 2H_2 = Al_2O_{(g)} + 2H_2O; \qquad 2000\ ^\circ C \rightarrow T_1 \tag{30}$$

$$SiO_{2(s)} + H_2 = SiO_{(g)} + H_2O; \qquad 1400\ ^\circ C \rightarrow T_2 \tag{31}$$

Such transport processes require relatively high temperatures which however are still substantially lower than those of a comparable purely thermal volatilization of the solids.

3.2. THE FORMATION OF VOLATILE COMPOUNDS WITH NORMAL OR HIGHER OXIDATION STATES

The volatility of the MeX_n compounds increases with the magnitude of n. This is a consequence of the diminution of the crystal lattice bonding with increasing n and of the simultaneously increasing screening of Me by the X ligands in the gas molecule. For this reason in chemical transport the formation of compounds with monovalent ligands (halides) is frequently a controlling factor. If gaseous oxide-halides or oxides are formed then for the same reason these are, as a rule, of a type having a higher Me oxidation state.

Examples:

$$Mn_2O_{3(s)} + 2Cl_2 = 2MnCl_{2(g)} + 1.5\ O_2 \tag{32}$$

$$NiO_{(s)} + 2HBr = NiBr_{2(g)} + H_2O \tag{33}$$

$$CdO_{(s)} + I_2 = CdI_{2(g)} + 0.5\ O_2 \tag{34}$$

$$Fe_2O_{3(s)} + 6HCl = 2FeCl_{3(g)} + 3H_2O \tag{35}$$

$$SiO_{2(s)} + 4HF = SiF_4 + 2H_2O \tag{36}$$

$$SiO_{2(s)} + 2TaCl_{5(g)} = SiCl_4 + 2TaOCl_{3(g)} \tag{37}$$

$$NbO_{(s)} + 1.5I_2 = NbOI_{3(g)} \tag{38}$$

$$Nb_{12}O_{29(s)} + 19NbCl_{5(g)} = 29NbOCl_{3(g)} + 2NbCl_{4(g)} \tag{39}$$

$$Ta_2O_{5(s)} + 3TaCl_{5(g)} = 5TaOCl_{3(g)} \tag{40}$$

$$2Cr_2O_{3(s)} + 5Cl_2 = 3CrO_2Cl_{2(g)} + CrCl_{4(g)} \tag{41}$$

$$MoO_{3(s)} + Cl_2 = MoO_2Cl_{2(g)} + 0.5\ O_2 \tag{42}$$

$$WO_{2(s)} + I_2 = WO_2I_{2(g)} \tag{43}$$

$$MoO_{3(s)} + H_2O = MoO_2(OH)_{2(g)} \tag{44}$$

$$Re_2O_{7(s)} + H_2O = 2ReO_3(OH)_{(g)} \tag{45}$$

$$OsO_{2(s)} + OsO_{4(g)} = 2OsO_{3(g)} \tag{46}$$

$$IrO_{2(s)} + 0.5\ O_2 = IrO_{3(g)} \tag{47}$$

3.3. THE COMBINATION OF TRANSPORT AGENTS

The heterogeneous reactions become relatively complicated whenever, for stoichiometric reasons, gaseous compounds must arise having various oxidation numbers: *cf.*, (eq. 39,41).

If in the contemplated system there exists *only one* gaseous compound of the metal which is under consideration then it must be made possible to control the oxidation number by means of the simultaneous use of several transport agents: (eq. 48).

$$W_{18}O_{49(s)} + 18I_2 + 13H_2 = 18WO_2I_{2(g)} + 13H_2O \quad (48)$$

It can also be particularly useful to improve the equilibrium position in a thermodynamically predictable manner by means of added supplements; (eq. 49 through 51); also *cf.*, [4].

$$SiO_{2(s)} + Cl_2 + CrCl_{4(g)} = SiCl_{4(g)} + CrO_2Cl_{2(g)} \quad (49)$$

$$ZrO_{2(s)} + 2I_2 + 0.5\ S_{2(g)} = ZrI_{4(g)} + SO_2 \quad (50)$$

$$Cr_2O_{3(s)} + 2Cl_2 + 0.5\ O_2 = 2CrO_2Cl_{2(g)} \quad (51)$$

In the transport of TiO_2 with Cl_2 the addition of Te proved to be especially favorable. However, we still have no clear picture of the gaseous species (TeO_2, $TeOCl_2$?).

3.4. UNEXPECTED TRANSPORT PHENOMENA

As a rule one knows the gas molecules which lie at the basis of the observed transport processes. However, it happens repeatedly that an observed transport effect is not interpretable by means of known gas molecules. If the transport effect persists when the experiments are carried out with a thorough exclusion of impurities suspected of being transport agents (water from the wall of the quartz ampule!), then a more detailed experimental thermodynamic investigation would be desirable. For example it was in such a way that it became known that the molecule which is essential for the functioning of the iodine lamp is not tungsten iodide but is the oxide iodide WO_2I_2. This led to the transport of WO_2 with I_2 on the basis of (eq. 43).

For the transport reactions of MoO_2 and ReO_3 with I_2 the gaseous oxide iodides MoO_2I_2 and ReO_3I were, from the outset, assumed to be of controlling importance. In support of this assumption there is the sequence:

$$NbOI_3 \quad MoO_2I_2$$

$$WO_2I_2 \quad ReO_3I$$

and the fact that corresponding oxide-bromides and oxide-chlorides (MoO_2Cl_2, MoO_2Br_2, ReO_3Cl, ReO_3Br) are known. These ideas have been confirmed by the most recent measurements [53] made in the case of chemical transport of MoO_2 with I_2.

It is not unusual to find that, of the higher halides and oxide-halides of a metal, the one possessing the heavier halogen is, to be sure, no longer stable in the solid state, but certainly occurs in considerable concentrations in the gas phase ($CrCl_4$, FeI_3).

Some more examples of unexpected transport phenomena are:

Numerous metallic sulphides were transported in the presence of high sulphur pressures [83], with the controlling molecule as yet unidentified.

$CrCl_{3(s)}$ is transported by $Al_2Cl_{6(g)}$. The equilibrium study which was carried out in investigation of this phenomenon led to the discovery of the gas molecule ($CrCl_3 \cdot 3\ AlCl_3$) [84], [85].

4. THE SELECTION OF TRANSPORT REACTIONS, ILLUSTRATED BY THE EXAMPLE OF ZINC OXIDE

For the transport of zinc oxide, all those equilibrium reactions are to be discussed in which, besides the solid ZnO, only gaseous reaction partners participate. The only Zn-containing gas species having sufficient thermal stability are Zn and ZnX_2 (X=halogen). Thus it is only in this form that the zinc can migrate through the gas phase. Hence, we

have the following reaction equations:

$$ZnO + H_2 = Zn_{(g)} + H_2O_{(g)} \quad (52)$$

$$ZnO + CO = Zn_{(g)} + CO_2 \quad (53)$$

$$ZnO + X_{2(g)} = ZnX_{2(g)} + 0.5\ O_2 \quad (X = Cl, Br, I) \quad (54)$$

$$ZnO + 2HX = ZnX_{2(g)} + H_2O_{(g)} \quad (55)$$

$$ZnO + HgCl_{2(g)} = ZnCl_{2(g)} + Hg_{(g)} + 0.5\ O_2 \quad (56)$$

Further selection takes place on the basis of thermodynamic considerations.

At a given total pressure the transport rate is proportional to the partial pressure drop: $\Delta P = P_2 - P_1$ (Section 1.4.). Of course the magnitude of ΔP is not equally critical for every preparative purpose.

In the case of powder reactions (section 5.3.) having transport distances of the order of 1 - 100μ, very small values of ΔP suffice (*cf.*, section 1.4.). In the case of *syntheses in the temperature drop* (section 5.2.) or in the case of *the production of small crystals* the selection of a large value of ΔP is necessary if the reaction times are to remain within limits and for *growing large crystals* the selection of the maximum ΔP is especially important -- a fact which nevertheless has evidently not been sufficiently taken into account up to the present. This topic will be discussed in a later paper.

According to section 1.5., ΔP is large whenever *log Kp* for the transporting reaction lies *near zero*. Thus in selecting the transporting reaction, one first studies the equilibrium position and its dependence upon temperature. Figure 1 provides data in this connection.

Since one has to stay above the condensation temperature of zinc or of zinc halide and on the other hand, to avoid attacking the quartz, an unnecessary high temperature should be avoided, it is desirable to set the temperature region, in which ZnO is to migrate through the gas phase, at 1,000/900 °C. Then, referring to figure 1, one can make the following statements:

The *saturation pressure of the solid ZnO* is so low that it can be ignored. The dissociative sublimation of the zinc oxide requires higher temperatures.

With log Kp ranging between -2 and 0 for the corresponding reactions, I_2, CO, H_2, and $HgCl_2$ are suitable transport agents for ZnO, with the special suitability of $HgCl_2$ deserving particular emphasis.

In *reactions having positive values of log Kp* it should be taken into consideration that the saturation pressure of the fluid zinc halide ought not to be exceeded ($ZnCl_2$ boils at 1005 K, 1 atm). Hence one selects a total pressure which is not too high.

Of the remaining transport agents, Br_2 and HCl are especially suitable. However, Cl_2 is also usable, as corresponding experiments have confirmed.

The use of HBr as a transport agent leads to an *exothermal* reaction ($\Delta H_T^\circ = -5.4$ kcal). Hence transport into the warmer zone is to be expected. But because of the quite large value of log Kp the transport properties are not favorable.

These qualitative statements made on the basis of figure 1 are sufficient within our present context. They are confirmed by a more extensive quantitative treatment, in which, at the total pressure prescribed by the condition $\Sigma P = 1$ atm., a calculation is made of the gas composition and of the magnitude of $\Delta P(Zn)$ or $\Delta P(ZnX_2)$.

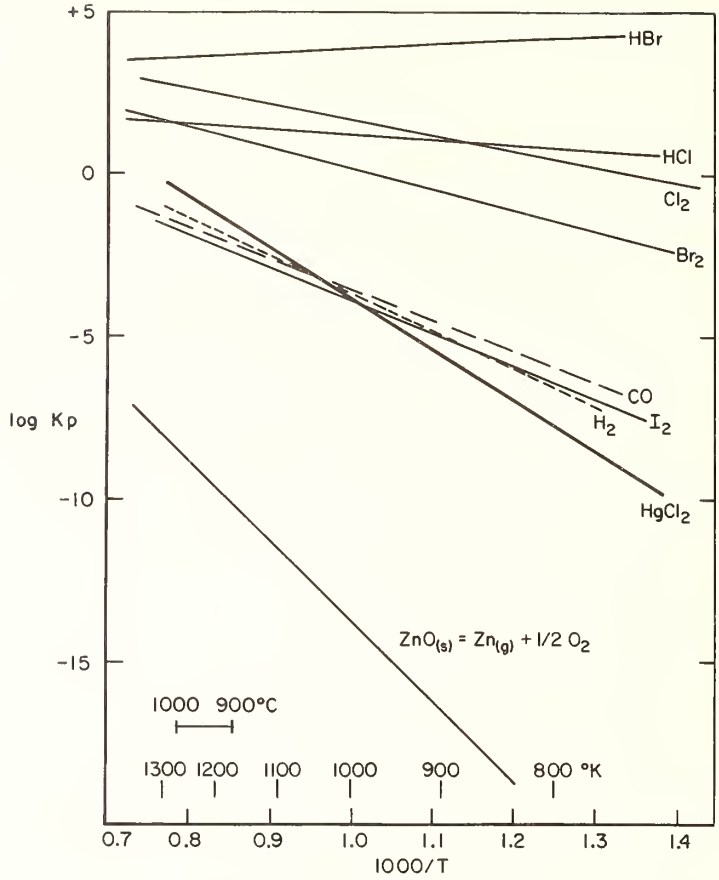

Fig. 1. Equilibria with ZnO as solid phase. Kp refers to the reaction of 1 Mol ZnO.

5. PREPARATIVE USE OF CHEMICAL TRANSPORT

5.1. SYNOPSIS

In the basic process of chemical transport the solid which is initially introduced is chemically identical with the transported material which is precipitated out of the gas phase. This process is suitable for, *e.g.*, crystal growing.

The combination of chemical transport with other processes gives rise to many preparative possibilities. Here chemical transport generally has the effect of furthering equilibration or in other words of promoting the formation of the thermodynamically stable solid phase (for a limitation *cf.*, section 5.5.). The latter, at no particular expense, will usually contain crystals suitable for x-ray purposes.

One can classify the applications of chemical transport in the following way:

A. Crystal growing, precipitation of thin layers

B. Purification of solids (*cf.*, van Arkel-method, and also [4], [86], [87a]

C. Doping of solids

D. Promotion of syntheses (solid + gas) in a temperature gradient [4], [86]

E. Promotion of reactions between solids [4], [86]

(a) Partial transport of one component only (*e.g.*, of oxygen)

(b) Transport of one solid partner only

(c) Transport of the reaction product

(d) Production of closely adjacent phases (Hägg-Magneli-phases); transport using a buffered gas phase

(e) Production of mixed crystals [86]

F. Synthesis with spatially separate precipitation of reaction products [5]

G. Transport of ternary compounds

H. Precipitation of metastable modifications

Of these numerous possibilities only D, E(c), G and H will be discussed in further detail in what follows:

5.2. PROMOTION OF SYNTHESES (SOLID + GAS) IN A TEMPERATURE GRADIENT

During reactions of solids with gases (*e.g.*, O_2, S_2) the reaction product often forms a surface layer which delays the progress of the reaction. With the aid of a transport agent, the reaction product can be transported away and, at another location in the reaction space, be precipitated in crystals (normally at a lower temperature). In this way the reaction is at the same time substantially accelerated. Examples:

Iridium oxide is formed when iridium is heated at 1000 °C in oxygen (1 atm). The IrO_2-surface layer much impedes the reaction. But if the reaction is carried out under transport conditions then IrO_2 precipitates out of the gas phase separately from the Ir and the reaction is complete [4], [86a]. Here oxygen itself has the effect of a transport agent. The behavior may be described by means of the processes (57) and (58), that is to say by IrO_2-formation and transport-away.

$$Ir + O_2 = IrO_{2(s)} \qquad (57)$$

$$IrO_{2(s)} + 0.5\ O_2 = IrO_{3(g)} \qquad (58)$$

If one is working at a temperature of the iridium which is so high that an IrO_2-surface layer is not stable at O_2 = 1 atm., then the reaction sequence is (59), (60).

$$Ir + 1.5\ O_2 = IrO_{3(g)}, \quad T_2 \sim 1150\ °C \qquad (59)$$

$$IrO_{3(g)} = IrO_{2(s)} + 0.5\ O_2, \quad T_1 \sim 1000\ °C \qquad (60)$$

The situation is similar in the case of synthesis of *ruthenium dioxide* [4], [68].

Likewise, in the reaction of excess tungsten with oxygen in a sealed tube with formation of the dioxide, the transport of WO_2 with I_2 (1000 → 800 °C) is advantageous [29].

The oxides ReO_2 and ReO_3 are obtained as crystals if the synthesis out of elements in the sealed tube is combined with transport by means of iodine [63]; *cf.*, also table 3.

Also in the case of synthesis of *sulfides, selenides and tellurides* the reaction-layer formed on the metallic grain or on the molten metal (!) can severely impede the course of the reaction. Hence the removal of the chalcogenide layer by means of iodine decidedly accelerates the course of the reaction. Comparative observations of this sort exist with and without addition of I_2 as a transport agent in the synthesis of ZnS, ZnSe, CdS, CdSe, Al_2S_3, Al_2Se_3 and CrTe [4], [86].

Syntheses of binary, ternary and quaternary chalcogenides from the elements, with iodine being added, were carried out primarily by Nitsche and co-workers [87], [88], [89].

The addition of a transport agent has a similarly favorable effect, for example, in the synthesis of *metallic arsenides* out of the elements.

In general it is possible in the presence of the transport agent, on account of the *reversibility* and *mobility* which it creates, to combine the most conveniently accessible materials, *e.g.*, the elements, into the desired stable compound.

5.3. PROMOTION OF SOLID/SOLID REACTIONS [4], [86]

The recombination of two solids by heating the aggregate of the powdered components is the classical preparative procedure of solid state chemistry. It still plays an important role today although it exhibits clearly recognizable disadvantages:

(a) Diffusion in the solid state requires time and high temperatures.

(b) Diffusion must take place over just a few "contact-bridges" between the grains. Because of the volume reduction which normally occurs during the reaction, this contact becomes steadily worse as the reaction progresses.

(c) Such reactions possess no selective mechanism. Contaminants which have been brought in with the initially introduced material or by reaction with the wall of the vessel, remain in the reaction product.

(d) Because of the absence of selectivity, chemical analysis of the products has scarcely any demonstrative value since one finally recovers only the aggregates of material which have been used.

By the addition of a transport agent these difficulties can be overcome. Even when only one of the initially introduced materials (*e.g.*, the material A) is chemically transportable, the reaction is substantially accelerated. The non-transportable substance B is then to some extent heated in a gaseous solution of A. For this the entire surface of B is available for the reaction. Mechanical contact bridges are no longer a bottle-neck and in fact a mechanical contact between A and B is no longer required.

Still more favorable is the frequently occurring case in which A, B and the product A_xB_y are transportable. In this situation all the above named difficulties (a, b, c, d) are overcome. The reaction product is precipitated out of the gas phase as pure crystals.

The combination of two binary compounds into a ternary as for example occurs in the preparation of spinels or of ternary sulfides can be carried out in the same working procedure along with the chemical transport. Thus if it is desired to secure crystals of the ternary compound the preliminary synthesis of this compound by another route (*e.g.*, by means of a pure solid/solid reaction) is not necessary.

Table 4 shows examples of reactions of oxides carried out in the presence of transport agents. The table is in no sense complete. Thus for example the closely neighboring phases ("Hagg-Magneli phases") occurring between NbO_2 and Nb_2O_5 are obtainable in crystalline form by the reaction of Nb_2O_5 with Nb or a lower oxide in the presence of a transport agent (*cf.*, table 3). The members of the analogous family of the vanadium oxides are attainable in crystalline form from V_2O_5 and a lower oxide in the presence of the transport agent $TeCl_4$ (*cf.*, table 3).

The same principle of synthesis is also used with other classes of compounds.

During the investigation of multi-component systems with determination of the phases occurring in the sub-solid domain, the promotion of equilibration by addition of a transport agent is an essential help [100].

5.4. THERMODYNAMIC CONSIDERATIONS RELATED TO THE TRANSPORT OF TERNARY COMPOUNDS

If two solids A and B exist side by side then they compete for the transport agent X. In consequence the transport of A and B is modified in a predictable way in contrast to the isolated transport of these substances. If the solid compound A_aB_b is formed in addition, then from the thermodynamic point of view very different situations can arise.

Table 4

Reactions of Oxides in the Presence of Transport Agents
Temperatures Around 1000 °C

Starting Material	Product	Transport Agent	Reference
$Nb + Nb_2O_5$	NbO	Cl_2	[4]
$Nb + Nb_2O_5$	NbO	I_2	[4]
$Nb + Nb_2O_5$	NbO_2	I_2	[47]
$W + WO_3$	WO_2	$I_2 + H_2O$	[58]
$Ti + SiO_2$	$Ti_2O_3 + TiSi$	$TiCl_3$	[4]
$V + SiO_2$	$VO + V_3Si$	I_2	[90]
$Nb + SiO_2$	$NbO + Nb_5Si_3$	H_2	[4]
$Nb + SiO_2$	$NbO + Nb_5Si_3$	I_2	
$Ta + SiO_2$	$Ta_2O_5 + Ta_2Si$	I_2	[4]
$Ta + SiO_2$	$Ta_2O_5 + Ta_2Si$	$TaCl_5$	[4]
$TiO + TiI_2 + B_2O_3$	$TiBO_3$	H_2O(HI)	[91]
$V_2O_5 + V + B_2O_3$	VBO_3	H_2O, HCl	[91]
$Cr_2O_3 + B_2O_3$	$CrBO_3$	H_2O, HCl	[91]
$MgO + Cr_2O_3$	$MgCr_2O_4$	O_2	[4]
$MeO + Cr_2O_3$ (Me = Mn, Co, Ni)	$MeCr_2O_4$	Cl_2	[92]
$NiO + Cr_2O_3$	$NiCr_2O_4$	O_2	[4]
$MeO + Fe_2O_3$	$MeFe_2O_4$		
(Me = Mn, Ni, Co)		HCl	[93]
(Me = Mg, Co, Ni, Zn)		HCl, Cl_2	[94]
$NiO + Fe_2O_3$	$NiFe_2O_4$	HCl	[95]
$CoO + SiO_2$	Co_2SiO_4	HF	[96]
$FeO + GeO_2$	$FeGeO_3$	NH_4Cl	[97]
$CaO + SnO_2$	Ca_2SnO_4	H_2, CO	[4]
$SrO + SnO_2$	$SrSnO_3$	H_2, CO	[4]
$MeO + SnO_2$ (Me = Mn, Co, Zn)	Me_2SnO_4	NH_4Cl	[98]
$CoO + SnO_2$	Co_2SnO_4	Cl_2	[92]
$MeO + TiO_2$ (Me = Mg, Ni)	$MeTiO_3$	Cl_2	[92]
$Me_2O_3 + Nb_2O_5$ (Me = Cr, Fe)	$MeNbO_4$	$Cl_2 + NbCl_5$	[39]
$MeO + Nb_2O_5$	$MeNb_2O_6$		[39]
(Me = Co, Ni, Ca)		Cl_2	
(Me = Fe, Mn)		$Cl_2 + NbCl_5$	
(Me = Mg, Zn)		HCl	
$Me_2O_5 + Nb_2O_5$ (Me = V, As)	$Me(Nb_9O_{25})$	Cl_2(+$NbCl_5$)	[92]
$GeO_2 + Nb_2O_5$	$GeO_2 \cdot 9\ Nb_2O_5$	Cl_2	[92]
$Me_2O_3 + Ta_2O_5$ (Me = Fe, Cr)	$MeTaO_4$	Cl_2(+ $TaCl_5$)	[92]
$MeO + Ta_2O_5$ (Me = Mg, Mn, Co, Ni)	$MeTa_2O_6$	Cl_2(+ $TaCl_5$)	[92]
$MeO + MoO_3$ (Me = Mg, Mn, Co, Ni)	Me MoO_4	Cl_2	[92]
$MeO + WO_3$ (Me = Mg, Mn, Fe, Co, Ni, Zn)	$MeWO_4$	Cl_2	[92]
$FeO + WO_3$	$FeWO_4$	HCl	[4]
$Fe_2O_3 + Cr_2O_3$	Me_2O_3 - mixed cryst.	Cl_2	[92]
$ThO_2 + U_3O_8$	MeO_2 - mixed cryst.	O_2	[99]
$ZnO + MnO + Fe_2O_3$	(Zn, Mn) Fe_2O_4	HCl	[25]

It frequently happens that *ternary* compounds are transportable when this is true, under the same circumstances, for the isolated binary compounds. This means that the free enthalpy of formation for the process $aA_{(s)} + bB_{(s)} \rightarrow A_aB_{b(s)}$ is not large. If this is not so then different cases are conceivable:

Transport of the ternary compound *can* occur although the same is not true for one or both components because for these the transport equilibrium lies too far to the right.

Transport of the ternary compound can fail to occur (or be very much diminished) although both components are in themselves transportable. In this case the transporting equilibrium has been pushed too strongly to the left by the exothermal compound formation.

Emmenegger [92] has already discussed qualitative ideas of this sort. Such situations are to be treated quantitatively according to the usual rules of chemical transport on the principle of heterogeneous equilibria. This applies also to the somewhat more complicated question which inquires under what circumstances the reaction of the phase A_aB_b -- in itself thermodynamically stable -- with the transport agent leads to precipitation of one of the components A or B. There exist familiar examples of this: In the attempt to transport $CuFe_2O_4$ with Cl_2, CuO precipitated in the colder zone while Fe_2O_3 remained in the warmer zone as a residue [101]. The analogous experiment with garnet $Y_3Fe_5O_{12}$ and HCl as the transport agent leads to Y_2O_3-precipitation in the warmer zone [102], *cf.*, also [95].

Wehmeier [102] has already studied this question. The solution which he suggests is in principle as follows:

One considers the equilibria (61) and (62) (for simplicity formulated without stoichiometric coefficients) for the given temperature and the selected mixture in the reaction chamber.

$$AB_{(s)} + 2X_{(g)} = AX_{(g)} + BX_{(g)} \quad : K_{61} \tag{61}$$

$$B_{(s)} + X_{(g)} = BX_{(g)} \quad : K_{62} \tag{62}$$

With the equilibrium pressures of (61) one calculates the K_{62}-analogous expression $Q_{61,62} = P_{61}(BX)/P_{61}(X)$. With $Q_{61,62} > K_{62}$ the component $B_{(s)}$ precipitates, together with $AB_{(s)}$, under the influence of the transport agent.

The analogous statement is valid for the precipitation of $A_{(s)}$.

In the extreme case the reaction can lead to complete consumption of $AB_{(s)}$, (eq. (63))

$$AB_{(s)} + X_{(g)} = AX_{(g)} + B_{(s)} \tag{63}$$

Naturally this also depends upon the amounts of the solid phase and of the transport agent which are used.

The following considerations are likewise of interest:

(a) By addition of $AX_{(g)}$ to the system (61) the decomposition of $AB_{(s)}$ can be repressed. Example:
Addition of $FeCl_3$ in the transport of $Y_3Fe_5O_{12}$ [102].

(b) It can suffice (!) to use an increased AB - initial amount and an increased amount of the transport agent. Then a portion of $AB_{(s)}$ is used, with precipitation of $B_{(s)}$, in the construction of the equilibrium gas phase; however the remaining portion of $AB_{(s)}$ can be chemically transported.

(c) During decomposition of $AB_{(s)}$ under the influence of the transport agent it is nevertheless possible, after sufficient transport duration, for $AB_{(s)}$ to exist at T_1:

Step 1 $AB_{(s)} + X_{(g)} = AX_{(g)} + B_{(s)}$ at T_2 (64)

Step 2 $AX_{(g)} = A_{(s)} + X_{(g)}$ at T_1 (65)

This process proceeds until there is no more $AB_{(s)}$ present at T_2: One then has $A_{(s)}$ at T_1 and $B_{(s)}$ at T_2.

Step 3 Now the B-transport begins, $T_2 \rightarrow T_1$

$$B_{(s)} + X_g = BX_{(g)} \qquad \text{at } T_2 \tag{66}$$

Step 4 Re-formation of $AB_{(s)}$

$$A_{(s)} + BX_{(g)} = AB_{(s)} + X_{(g)} \qquad \text{at } T_1 \tag{67}$$

Steps 3 and 4 are not compulsory. It can also happen that the process comes to a stop after Step 2 because the equilibrium gas generated by the presence of $A_{(s)}$ at T_1 interferes with the B-transport. In such a case one could achieve renewed formation of $AB_{(s)}$ by an advance provision of $B_{(s)}$ in the zone with T_1. Of course it would not be possible to grow crystals by this method.

(d) The possibly advantageous transition to another transport agent or the use of an additional transport agent for $B_{(s)}$ were not included in the considerations of the present study. In addition it was assumed that the simultaneous presence of A, B and X does not lead to the formation of new gas molecules. As a rule this is the case but for the system Cu/Fe/Cl the possibility should not be excluded.

Quantitative statements can likewise be attained regarding the effectiveness of the arrangements (a) or (b) and regarding the stable solid phase in zones 1 and 2 of a transport tube. They can be derived from the calculation of the composition of the gas phase over the solid phase $AB_{(s)}$ and $B_{(s)}$ at the temperatures T_1 and T_2 and at constant total pressure in the tube

Such a computation will not be carried out here because the thermochemistry of the two systems which are familiar along these lines CuO/Fe_2O_3 and Y_2O_3/Fe_2O_3 is still too uncertain.

5.5. PRECIPITATION OF METASTABLE SUBSTANCES

In the ideal model chemical transport by gas motion between equilibrium regions is described. In the practical case this model is valid to a degree of approximation which is sufficiently good for the thermodynamic calculation to constitute a basis for the selection of transporting systems and for determining transport rates. In addition the mobility provided by the transport agent favors recrystallization (mineralizer effect [4]) and leads to a transition of the solid phase into the thermodynamically stable state. Also useful, during investigation of phase diagrams, is the decided improvement -- due to transport agents -- of the equilibration in the sub-solid region [100].

Naturally, the equilibration becomes all the more difficult the less the solid phases differ from one another in energy content. Under such circumstances, even in the presence of a transport agent a longer isothermal tempering can be required for the formation of the stable phase -- as has appeared in the case of the Nb_2O_5-modifications [41].

In such systems, during normal transport experiments in the temperature drop, the precipitation of *metastable modifications* is also possible. The following review presents examples of polymorphisms.

Nb_2O_5. Of the numerous modifications of Nb_2O_5 those designated by the letters B, H, M, N, P, R, and T can be obtained by chemical transport in crystalline form [41], [38]. H-Nb_2O_5 is thermodynamically stable at temperatures > 700 ($\pm$ 50 °C). Below this temperature the B-form is stable. ΔH (transformation H-Nb_2O_5 $\rightarrow$ B-Nb_2O_5) $\sim$ -2 kcal [41]. The other modifications, so far as we know up to the present, are metastable.

In our experiments [41] powdered H-Nb_2O_5 served as the initially introduced substance. However the modification of the initial substance was without effect upon the transported product. The following is a synopsis of the *formation conditions:*

B-Nb_2O_5: (a) Transport with $NbCl_5 + Cl_2$, 850 $\rightarrow$ 750 °C;
often in a mixture with the modifications N and P [41].

(b) Transport with NbI_5 (700 → 550 °C) or
$NbCl_5$ (1000 → 700 °C) [42a]

(c) Transport with HCl or HCl + Cl_2 or Cl_2 + H_2O;
750 → 700 °C [37]

H-Nb_2O_5: Transport with $NbCl_5$ + Cl_2, 1100 → 1000 °C [41], [37].

M-Nb_2O_5: (a) Transport with $NbCl_5$ + Cl_2 1000 → 800 °C
in a mixture with the H-form [41].

(b) Transport with $NbCl_5$ + Cl_2, 970 → 860 °C
in the presence of SnO_2, which strongly promotes the formation of the M-form, without the incorporation of significant amounts of Sn - [37].

N-Nb_2O_5: Transport with $NbCl_5$ + Cl_2, 940 → 840 °C, in a mixture with the modifications M and H. The addition of a small amount of F^- (as NbO_2F) strongly promotes the formation of the N-form [41].

P-Nb_2O_5: Transport with Cl_2 + H_2O, 800 → 600 °C; then the P-form is markedly preferred [41], [37].

R-Nb_2O_5: (a) Transport with HCl, 800 → 600 °C, besides P, at times also besides B- and T-Nb_2O_5 [38].

(b) R-Nb_2O_5 was also observed in transport with $NbCl_5/NbOCl_3$ besides other modifications. Slight additions of NbO_2-F appear to promote the formation of the R-modification [38].

T-Nb_2O_5: (a) Transport with $NbCl_5$ + Cl_2, 890 → 835 °C. As a rule besides B- and N-Nb_2O_5. Nucleus selection is possible [41].

(b) Transport with Cl_2, 850 → 750 °C, in a mixture with P-Nb_2O_5 [37].

TiO_2. Rutile is the modification which is thermodynamically stable at all temperatures.

Rutile was obtained (without admixture of anatase) with $TeCl_4$ (or Cl_2 + Te) as the transport agent at 1100 → 900 °C [28]. At 1000 → 800 °C rutile precipitated in one part of the experiment but in others rutile with anatase was precipitated [29].

Anatase without admixture of rutile precipitated with Cl_2 as the transport agent at 1000 → 800 °C. [28], [29]. However, under comparable conditions both modifications often appeared together [29].

Mixtures of Rutile and anatase were obtained in many experiments (1000 → 800 °C; 900 → 700 °C) with Cl_2, Cl_2 + S, Cl_2 + Se, Cl_2 + Te, Cl_2 + P, Cl_2 + C as transport agents [29].

Brookite has not yet been observed in transport experiments.

ZnS. By transport with iodine below 1000 °C, *e.g.*, at 850 → 750 °C pure cyrstals of zinc blend are obtained but at 1170 → 1150 °C crystals of wurtzite were obtained [100], [88]. ΔH (transformation, wurtzite → zinc blend) = -3 kcal. Possibly wurtzite is the stable high temperature form.

In_2Se_3. Of four modifications, three are producible in crystalline form by transport with I_2 [103].

NbS_2. Two polymorphic modifications (2s and 3s) were obtained by transport with I_2 at different temperatures [104]

Taking into consideration that this is not very extensive observational data, one reaches the following conclusions:

In the transport experiments with Nb_2O_5 and with TiO_2 the metastability is manifested by the simultaneous occurrence of several modifications.

In all cases the difference in energy content of the occurring modifications is small, In consequence nucleus formation and nucleus growth acquire significance.

Even at transformation heats of 8 kcal/Mol($\gamma \rightarrow \alpha$-$Fe_2O_3$) and 15 kcal/Mol($\gamma \rightarrow \alpha$-$Al_2O_3$) chemical transport produces only the thermodynamically stable modification. Transport experiments specially conducted to obtain γ -Fe_2O_3-crystals always produced α-Fe_2O_3 [94].

In general one can expect the preparatively -- and of course also structurally -- interesting metastable modifications to have the highest probability of occurrence when the energy difference is small in comparison with the stable phase and when the precipitation temperature is made as low as possible. It would also be possible for transport under conditions of non-equilibrium, *e.g.*, at small total pressure, to promote the formation of metastable modifications. However there exists no data on this subject.

If several modifications occur together then as a rule they can be easily separated mechanically because of the size of the crystals.

In addition there exists the possibility of promoting the formation of metastable modifications by the selection of other transport agents (*cf.*, the case of TiO_2) or by additions to the transporting system (*cf.*, Nb_2O_5, addition of SnO_2, F). Here to be sure one is dependent upon empirical experiments. Certainly in the cases which have been mentioned, owing to the small amount of incorporated foreign material aggregates, one is not dealing with a stabilization in the thermodynamic sense but with a kinetic effect during nucleus formation or during crystal growth.

6. REFERENCES

[1] Brewer, L., and Kane, J. S., J. Phys. Chem., 59, 105 (1955).
[2] Schäfer, H., and M. Trenkel, in Z. anorg. allg. Chem., to be published.
[3] Kleinert, P., Z. anorg. allg. Chem., in press.
[4] Schäfer, H., *Chemische Transportreaktionen,* Weinheim 1962; *Chemical Transport Reactions,* New York, London 1964.
[5] Schäfer, H., J. Crystal Growth, 9, 17 (1971).
[6] Schäfer, H., to be published in W. Bardsley, D. T. J. Hurle, and J. B. Mullin, North Holland Series on Crystal Growth, Vol. I. (North Holland Publishing Co., Amsterdam).
[7] Berkowitz-Mattuck, J. B., and Buchler, A., J. Physic. Chem., 67, 1386 (1963).
[8] Budnikov, P. P., Kusakovskij, V. I., Sandulov, D. B., and Butra, F. P., Izvest. Akad. Nauk. SSSR, Neorg. Mater., 2, 829 (1966).
[9] Alexander, C. A., Ogden, J. S., and Levy, A., J. Chem. Physics, 39, 3057 (1963).
[10] Kleinert, P., in J. W. Mitchell, R. C. DeVries, R. W. Roberts and P. Cannon, *Reactivity of Solids,* J. Wiley 1969.
[11] Budnikov, P. P., and Sandulov, D. B., Kristall u. Techn., 2, 549 (1967).
[12] Schmid, H., J. Physic. Chem. Solids., 26, 973 (1965).
[13] Kerrigan, J. V., J. Appl. Physics 34, 3408 (1963).
[14] Sears, G. W., and DeVries, R. C., J. Chem. Physics., 39, 2837 (1963).
[15] Ready, D. W., and Kuczynski, G. C., J. Amer. Ceram. Soc., 49, 25 (1966).
[16] Nitsche, R., Crystal Growth, Suopl. to J. Phys. Chem. Solids., C 1, 215 (1967).
[17] Schmid, H., Z. anorg. allg. Chem., 327, 110 (1964).
[18] Chu, T. L., Gavaler, J. R., Gruber, G. A., and Kao, Y. C., J. electrochem. Soc., 111, 1433 (1964).
[19] Chu, T. L., and Gruber, G. A., Trans. Met. Soc., AIME, 233, 568 (1965).
[20] Gruehn, R., see Schäfer, H., Festschrift fur Leo Brandt, Westdeutscher Verlag Köln and Opladen 1968.
[21] Chu, T. L., and Gavaler, J. R., J. Inorg. Nuclear Chem., 27, 731 (1965).
[22] Faktor, M. M., and Carasso, J. I., J. electrochem. Soc., 112, 817 (1965).
[23] Ugai, Y. A., Lavrov, V. V., Anokhin, V. Z., and Averbakh, E. M., Izv. Akad. Nauk SSSR, Neorg. Mater., 6, 750 (1970).
[24] Schröcke, H., N. Jb. Min. Mh., 1963, 18.

465-504 O - 72 - 29

[25] Scholz, H., Aachen, Privatmitteilung 1966/67.
[26] Glemser, O., Haeseler, R. V., and Müller, A., Z. anorg. allg. Chem., 329, 51 (1964).
[27] Malinauskas, A. P., Gooch, J. W., and Redman, J. D., Nucl. Appl. Technol., 8, 52 (1970).
[28] Niemyski, T., and Piekarczyk, W., J. Crystal Growth 1, 177 (1967).
[29] Schäfer, H., and Trenkel, M., unpublished (1971).
[30] Anikin, I. N., Naumova, I. I., and Rumjanzewa, G. W., Kristallografija, 10, 230 (1965).
[31] Hauptman, Z., Schmidt, D., and Banerjee, S. K., Collect. czechoslov, chem. Commun., 32, 2421 (1967).
[32] Glemser, O., and Müller, A., Z. anorg. allg. Chem., 325, 220 (1963).
[33] Nagasawa, K., Bando, Y., Takada, T., Horiuchi, H., Tokonami, M., and Morimoto, N., Jap. J. Appl. Physics, 9, 841 (1970).
[34] Nagasawa, K., Bando, Y., and Takada, T., Jap. J. Appl. Physics., 8, 1262 (1969).
[35] Nagasawa, K., Bando, Y., and Takada, T., Jap. J. Appl. Physics., 8, 1267 (1969).
[36] Nagasawa, K., Bando. Y., and Takada, T., Jap. J. Appl. Physics., 9, 407 (1970).
[37] Emmenegger, F. P., and Robinson, M. L. A., J. Physic. Chem. Solids, 29, 1673 (1968).
[38] Gruehn, R., J. Less-Common Metals, 11, 119 (1966).
[39] Emmenegger, F. P., and Petermann, A., J. Crystal Growth, 2, 33 (1968).
[40] Schäfer, H., and Wiemeyer, M., unpublished (1971).
[41] Schäfer, H., Gruehn, R., and Schulte, F., Angew. Chem., 78, 28 (1966).
[42] Schäfer, H., Schulte, F., and Gruehn, R., Angew, Chem., 76, 536 (1964).
[42a] Laves, F., Moser, R., and Petter, W., Naturwissenschaften, 51, 356 (1964).
[43] Schäfer, H., Gruehn, R., Schulte, F., and Mertin, W., Bull. Soc. Chim. France, 1965 1161.
[44] Gruehn, R., and Norin, R., Z. anorg. allg. Chem., 355, 176 (1967).
[45] Gruehn, R., and Norin, R., Z. anorg. allg. Chem., 367, 209 (1969).
[46] Schäfer, H., and Odenbach, H., Z. anorg. allg. Chem., 346, 127 (1966).
[47] Schäfer, H., and Hüesker, M., Z. anorg. allg. Chem., 317, 321 (1962).
[48] Schäfer, H., and Sibbing, E., Z. anorg. allg. Chem., 305, 341 (1960).
[49] Schäfer, H., and Schwarzer, B., unpublished, 1967.
[50] Glemser, O., and Haeseler, R. V., Z. anorg. allg. Chem., 316, 168 (1962).
[51] Tillack, J., and Schäfer, H., unpublished (1963).
[52] Ben-Dor, L., and Conroy, L. E., Isr. J. Chem., 7, 713 (1969).
[53] Oppermann, H., Z. anorg. allg. Chem., 383, 285 (1971).
[54] Kleber, W., Hähnert, M., and Müller, R., Z. anorg. allg. Chem., 346, 113 (1966).
[55] LeBihan, R., and Vacherand, C., Croisance Composes Miner. Monocrist., 2, 147 (1969).
[56] Kleber, W., Raidt, H., and Dehlwes, U., Kristall u. Technik, 3, 153 (1968).
[57] Dettingmeijer, J. H., and Meinders, B., Z. anorg. allg. Chem., 357, 1 (1968).
[58] Dettingmeijer, J. H., Tillack, J., and Schäfer, H., Z. anorg. allg. Chem., 369, 161 (1969).
[59] Schäfer, H., and Schwarzer, B., unpublished, 1969.
[60] Kleinert, P., Z. Chem., 3, 353 (1963).
[61] Müller, A., Krebs, B., and Glemser, O., Naturwissenschaften, 52, 55 (1965).
[62] Ferretti, A., Rogers, D. B., and Goodenough, J. B., J. Physic. Chem. Solids, 26, 2007 (1965).
[63] Bode, M., and Schäfer, H., unpublished (1967).
[64] Quinn, R. K., and Neiswander, P. G., Mater. Res. Bull., 5, 329 (1970).
[65] Kleinert, P., and Schmidt, D., Z. anorg. allg. Chem., 348, 142 (1966).
[66] Hauptman, Z., Czechoslov. J. Physics, 12, 148 (1962).
[67] Kershaw, R., and Wold, A., U. S. Air Force Syst. Command, Air Force Mater. Lab. Tech. Rep., AFML, 1967; TR-67-239, 24-31
[68] Schäfer, H., Schneidereit, G., and Gerhardt, W., Z. anorg. allg. Chem., 319, 327 (1963).
[69] Ruff, O., and Rathsburg, H., Ber. Dtsch. chem. Ges., 50, 484 (1917).
[70] Greedan, J. E., and Willson, D. B., and Haas, T. E., Inorg. Chem., 7, 2461 (1968).
[71] Thiele, G., and Woditsch, P., J. Less-Common Metals, 17, 459 (1969).
[72] Bell, W. E., and Tagami, M., J. Physic. Chem., 70, 640 (1966).
[73] Stolpe, C. van de, J. Physics Chem. Solids, 27, 1952 (1966),
[74] Schäfer, H., and Jagusch, W., (1966) vgl. bei [4].
[75] Hoffman, J. W., and Lauder, I., IUPAC Congr., Australien 1969, Referat R 11 Mon 52.
[76] Kleber, W., and Mlodoch, R., Kristall and Techn., 1, 249 (1966).
[77] Widmer, R., J. Crystal Growth, 8, 216 (1971).
[78] Schäfer, H., and Wehmeier, F., unpublished (1963).

[79] Schäfer, H., and Fuhr, W., unpublished (1964).
[80] Karkhanavala, M. D., and Momin, A. C., J. Nuclear Materials, 11, 114 (1964).
[81] Ackermann, R. J., Thorn, R. J., Alexander, C., and Tetenbaum, M., J. Physic. Chem., 64, 350 (1960).
[82] Naito, K., Kamegashira, N., and Nomura, Y., J. Crystal Growth, 8, 219 (1971).
[83] Schäfer, H., Wehmeier, F., and Trenkel, M., J. Less-Common Metals, 16, 290 (1968).
[84] Lascelles, K., and Schäfer, H., Angew, Chemie, 83, 112 (1971).
[85] Lascelles, K., and Schäfer, H., Z. anorg. allg. Chem., 382, 249 (1971).
[86] Schäfer, H., in P. Hagenmuller, *Preparative Methods in Solid State Chemistry;* Academic Press, in press.
[86a] Schäfer, H., Heitland, H. J., Z. anorg. allg. Chem., 304, 249 (1960).
[87] Greenaway, D. L., and Nitsche, R., J. Phys. Chem. Solids, 26, 1445 (1965).
[87a] Schäfer, H.,Chemische Transportreaktionen. Ihre Grundlagen und Anwendungen, besonders für Trennvorgänge. Reinststoff probleme IV., (*Chemical Transport Reactions. Their Foundations and applications especially for separation processes. Pure substances Problem IV.),* Editor, M. Balarin, Akademie-Verlag Berlin (1971).
[88] Nitsche, R., Bölsterli, H. U., and Lichtenberger, M., J. Phys. Chem. Solids, 21, 199 (1961).
[89] Nitsche, R., Sargent, D. F., and Wild, P., J. Crystal Growth, 1, 52 (1967).
[90] Spear, K. E., Gilles, P. W., and Schäfer, H., J. Less-Common Metals, 14, 69 (1968).
[91] Schmid, H., Acta Cryst., 17, 1080 (1964).
[92] Emmenegger, F., J. Crystal Growth, 3, 135 (1968).
[93] Curtis, B. J., and Wilkinson, J. A., J. Amer. Ceram. Soc., 48, 49 (1965).
[94] Kleber, W., Noack, J., and Berger, B., Monatsber. dtsch. Akad. Wiss., Berlin, 7, 157 (1965).
[95] Kleinert, P., Z. Chem., 4, 434 (1964).
[96] Schmid, H., Z. anorg. allg. Chem., 327, 110 (1964).
[97] Royen, P., and Forwerg, W., Z. anorg. allg. Chem., 326, 113 (1963).
[98] Trömel, M., Z. anorg. allg. Chem., im Druck.
[99] Karkhanavala, M. D., and Momin, A. C., J. Nuclear Materials, 11, 114 (1964).
[100] Nitsche, R., J. Crystal Growth, 9, 238 (1971).
[101] Berger, H., Lecture at the symposium on crystallization by chemical transport reactions, Berlin 11. - 13 April 1967.
[102] Wehmeier, F. H., J. Crystal Growth, 6, 341 (1970).
[103] Medvedeva, Z. S., Guliev, T. N., Neorg. Mater., 1, 848 (1965).
[104] Nitsche, R., and Wild, P., J. Crystal Growth, 3, 153 (1968).

DISCUSSION

R. S. Kirk: What did you use as a container for your hydrogen fluoride transport?

H. Schäfer: That was made with platinum.

J. M. Honig: Is there usually a danger of incorporating some of your transport gas in the crystals that you grow? Is any systematic information available on that point?

H. Schäfer: First of all, the concentration of gas species per cc is small compared to the flux method and therefore the danger is not too high, but I don't wish to escape the question in this way. We looked for the introduction of iodine in sulfides and found that this depends on the system. For example you can have amounts of hundredths of a per cent of iodine in sulfide in some cases, but it depends on the formation of holes. You see, if you introduce an iodine instead of a sulfur then the charge is not balanced and therefore you must have a hole on the cation sites. We did such investigations, and if you go to more highly charged cations, for example to hafnium sulfides, then the introduction of iodine is too small to be measured because now it's too hard to get a four valent hole.

R. Ward: I wonder in the chemical transport and formation of the silica phase, was it tridimite?

H. Schäfer: Yes.

R. Ward: What was the transport agent there?

H. Schäfer: HF.

R. Ward: HF? Was there any incorporation at all of fluorine in the crystals?

H. Schäfer: There are a few, not too much.

R. Ward: I think tridymite is a clathrate, I think there must be something there.

T. Chen: I just wonder if all the tungstate and molybdate phases required the same kind of transport agent. The ternary systems. What kind of agent?

H. Schäfer: Yes. Mostly they use chlorine usually.

J. W. McCauley: I have two questions. Have you ever tried to grow carbonates by this technique? Have you ever tried to limit the number of crystals and grow one large one with any of these materials?

H. Schäfer: We have never grown carbonates, but I believe it must be possible for such things like siderite or manganese carbonate also. We would like to try as it has not been done up to now. We are not crystal growers, that is to say, primarily, but I know that people using such an ampule in a temperature gradient make single crystals from gallium phosphide. They can be obtained some centimeters in size. Zince oxide crystals are made by Fischer with a length, I believe, five centimeters and a diameter of five or six millimeters.

National Bureau of Standards Special Publication 364, Solid State Chemistry, Proceedings of 5th Materials Research Symposium, issued July 1972.

PRECISION PARAMETERS OF THE FERROELECTRIC RARE EARTH MOLYBDATES $Ln_2(MoO_4)_3$*

L. H. Brixner, P. E. Bierstedt, A. W. Sleight and M. S. Licis

Central Research Department
E. I. du Pont de Nemours and Company
Wilmington, Delaware 19898

Lattice parameters to an accuracy of better than ±0.001 Å have been determined for the ferroelectric $Ln_2(MoO_4)_3$ compounds with Ln = Pr, Nd, Sm, Eu, Gd, Tb, Dy and Ho. X-ray patterns were obtained with a Hägg-Guinier camera and the data was refined by a least-squares method using selected reflections. Parameters obtained this way exhibited a systematic trend of the *b-a* dimension as a function of the cation size for the orthorhombic Pba2 room temperature structure. A linear relationship between the cell volume and the cube of the ionic radius of the rare earths has been observed. The first seven compounds are metastable at room temperature and transform from the ferroelectric/ferroelastic Pba2 structure to the parent $P\bar{4}2_1m$ structure between 140 and 235 °C. Only $Ho_2(MoO_4)_3$ is stable in the Pba2 phase at room temperature and transforms into the tetragonal structure at 121 °C. The high temperature structure for this compound is orthorhombic, space group Pnca. The transition temperatures have been accurately determined by differential scanning calorimetry, differential thermal analysis, dielectric measurements and hot-stage optical techniques and are discussed in relationship with the degree of *b-a* distortion. Lattice parameters have also been determined for the stable monoclinic modification of Sm, Eu, Gd, Tb and Dy-molybdate and their transition temperatures, ranging from 800 to 1000 °C, as reported.

Key words: Ferroelectric molybdates of rare earths; lattice parameters; phase transitions.

1. INTRODUCTION

Certain rare earth molybdates of the type $Ln_2(MoO_4)_3$ such as $Nd_2(MoO_4)_3$ have been known for many years [1][1]. More recently, Borchardt [2] grew single crystals of many rare earth molybdates and showed that some members of this group of compounds are ferroelectric. There still was considerable argument about the true structure of the ferroelectric room temperature phase, which is complicated by the fact that for most compounds it only exists in a metastable state. Abrahams et al. [3] and Jeitschko [4] have given detailed accounts of this orthorhombic structure, but even to date some authors [5] insist that the structure is tetragonal. There was also disagreement on the extent of the existence of the Pba2 phase as well as the nature of the stable room temperature α phase. Newnham et al. [6] only included the Sm to Dy-compounds in their parameter studies of the ferroelectric rare earth molybdates and stated that "the orthorhombic distortion *b-a* is constant within experimental error." Nassau et al. [7] carried out a comprehensive study of these rare earth molybdates, recognizing the profusion of different structural types, further complicated by temperature-dependent polymorphisms. Concerning the stable low temperature α structure, Nassau [7] stated that it is unknown.

In the present paper we will show that actually 8 rare earths [from Pr (59) to Ho (67), excepting Pm, which does not occur naturally] crystallize in the Pba2 structure of $Ln_2(MoO_4)_3$ and that there exists a pronounced dependence of b-a upon the ionic radius of the rare earths.

---

* Contribution No. 1801

[1] Figures in brackets indicate the literature references at the end of this paper.

We will also show that the α structure of the compounds of Sm, Eu, Gd, Tb and Dy is actually identical with the structure previously described for $Eu_2(WO_4)_3$ [8]. The remaining non-ferroelectric $Ln_2(MoO_4)_3$ compounds fall into two categories: 1) an isostructural group including La, Ce, Pr and Nd-molybdate, crystallizing in a monoclinic structure different from that given by Jamieson et al. [12] for α$Nd_2(MoO_4)_3$ and 2) an isostructural group, crystallizing in the orthorhombic Pnca space group and including Sc, Y, Er, Tm, Yb and Lu-molybdate. Parameter refinements have been obtained on all of these compounds and will be the subject of a forthcoming publication [13].

2. EXPERIMENTAL

2.1. SAMPLE PREPARATION

All compounds were prepared by standard solid state techniques using Kerr-McGee Co.'s 99.99% pure rare earth oxides and MoO_3 prepared by decomposition of Climax Molybdenum Co.'s ammonium-molybdate $(NH_4)_6Mo_7O_{24}\cdot 4H_2O$. The α-phase compounds had to be prepared below the transition temperatures reported in table 3. Since this temperature may be as low as 800 °C, extensive firing periods of up to 60 hours were necessary to achieve homogeneous products.

2.2. X-RAY STUDIES

For the x-ray studies, powder patterns were obtained at 25.0 ± 0.5 °C with a Hägg-Guinier camera using KCl (a_o = 6.2931 Å at 25 °C) as an internal standard. These data were refined by a least-squares method using selected reflections which could be indexed as single lines. As a guide for the β' modifications, powder pattern intensities were calculated based on the known β'$Gd_2(MoO_4)_3$ structure [4]. Intensities for α$Gd_2(MoO_4)_3$ were estimated with diffractometer data as well as the Guinier data.

2.3. TRANSITION AND DIELECTRIC STUDIES

The Curie temperatures as well as the α/β transition temperatures and melting points were measured with a Du Pont 900 thermal analyzer. Heating and cooling rates of 1 °C or 0.5 °C/min were employed, ensuring accurate T_c values. A sensitive digital voltmeter was used to monitor the output of the thermocouple; thermal hysteresis in the T_c values was always observed, but in no case did it exceed 1 °C.

Dielectric measurements were made at 1 kHz and 10 kHz with a General Radio (Type 716c) capacitance bridge. A Princeton Applied Research Lock-In Amplifier (HR8) was used both as the generator and detector. The output of the detector was fed into an x-y recorder for plotting of the capacitance *vs.* temperature curve. In addition, the DTA apparatus was adapted so that dielectric constant measurements could be made in the DTA cell, and then the thermal anomaly (DTA) and the dielectric anomaly could be measured simultaneously. C-cut single crystals were used for this purpose, and it was observed that the peak in the dielectric constant occurred at the *same time* as the peak in the DTA signal. The precision of the T_c values is ±0.2 °C.

The Curie temperatures were also measured by observing through crossed polars the disappearance and reappearance of the ferroelectric domains as the specimen was heated and cooled through the β'/β transition. A Mettler FP hot stage was used to heat the sample, and it was observed that the transition occurred over temperature intervals less than 0.1 °C. The temperatures were measured with a calibrated platinum resistor and the agreement with T_c values obtained by dielectric and differential thermal analysis techniques was within 0.2 °C.

3. RESULTS AND DISCUSSION

Jamieson et al. [12] have postulated a structure for α$Pr_2(MoO_4)_3$ and α$Nd_2(MoO_4)_3$. We have shown that isomorphism actually exists from $La_2(MoO_4)_3$ to $Nd_2(MoO_4)_3$. In going to $Sm_2(MoO_4)_3$, there is a structural change for the αphase which persists through $Dy_2(MoO_4)_3$. Nassau et al. [7] report that the low temperature modifications of $Sm_2(MoO_4)_3$, $Eu_2(MoO_4)_3$, and $Gd_2(MoO_4)_3$ are isostructural with each other, but they claim that these compounds are not isostructural with any other known molybdates or tungstates. We have found that there are low temperature modifications of $Tb_2(MoO_4)_3$ and $Dy_2(MoO_4)_3$ which are isostructural with α$Sm_2(MoO_4)_3$, α$Eu_2(MoO_4)_3$, and α$Gd_2(MoO_4)_3$. Furthermore, these are in fact isostructural

with the normal modifications of $Ln_2(WO_4)_3$ compounds where Ln is La through Dy. The cell dimensions of the $\alpha Ln_2(MoO_4)_3$ phases where Ln is Sm-Dy are given in table 1 assuming space group C 2/c[2]. These may be compared with the cell dimensions of $Eu_2(WO_4)_3$ which are [8]: a = 7.676 Å, b = 11.463 Å, c = 11.396 Å and β = 109.63°. Intensity calculations were carried out for $\alpha Gd_2(MoO_4)_3$ using the published [8] positional parameters for $Eu_2(WO_4)_3$. The agreement between the calculated intensities and the powder intensities is qualitatively very good (table 2). A comparison of the last 2 columns in table 1 shows that we are dealing with rather substantial differences (~20%) in densities for the 2 structures. This suggested that the application of pressure may have a significant influence on the transformation of the metastable low density, high temperature β structure into the stable, high density, low temperature α structure. At 30 kbars of pressure the β → α transformation for $Gd_2(MoO_4)_3$ was indeed observed at 555 °C, more than 300 °C below the ambient pressure transformation point[3].

Table 3 summarizes the lattice parameters, shear angles, Curie temperatures and transition temperatures of the ferroelectric rare earth molybdates. Figure 1 shows a graphic representation of the various phase relationships for the different rare earth molybdates as a function of temperature.

It is apparent from the data in table 3 that there is a systematic trend for the b-a parameter of the Pba2 structure going from a maximum of 0.053 Å for the Pr compound to a minimum of 0.021 Å for the Ho compound. In going from the ferroelectric mm2 point group to the paraelectric $\bar{4}2m$ point group, the a and b lattice constants become equal and it requires a higher temperature to effect this rearrangement of atoms for the praseodymium compound than for the holmium compound.

The trend for the α/β transformation temperature is in the same direction, that is, going up as the size of the ionic radius of the rare earth increases. The melting point, on the other hand, goes up in the opposite direction due to the fact that the cell volume decreases with a corresponding increase in cohesive energy.

The one minor deviation from a linear relationship between Curie temperature and composition in figure 1 is $\beta' Tb_2(MoO_4)_3$. This compound had essentially the same Curie temperature as the Gd-composition, while the b-a difference is smaller. A recent paper by Keve [10] also gives a higher Curie temperature for $\beta' Tb_2(MoO_4)_3$ but lists a higher b-a difference. Conceivably, small deviations in stoichiometry may account for this discrepancy.

Table 1

Cell Dimensions(a) of the α-Rare Earth Molybdates and a Density Comparison

Compound	a, Å	b, Å	c, Å	β	V, Å^3	$\delta_{\alpha(b)}$	$\delta_{\beta'(c)}$
$Sm_2(MoO_4)_3$	7.562	11.509	11.557	108.98	951.1	5.450	4.405
$Eu_2(MoO_4)_3$	7.554	11.459	11.497	109.08	940.6	5.533	4.463
$Gd_2(MoO_4)_3$	7.575	11.436	11.424	109.28	934.1	5.647	4.555
$Tb_2(MoO_4)_3$	7.529	11.379	11.401	109.21	922.3	5.743	4.708
$Dy_2(MoO_4)_3$	7.514	11.344	11.364	109.31	914.1	5.847	4.628

(a) The cell is C-centered.
(b) Calculated densities based on the x-ray volumes.
(c) Density of the β' form at room temperature for comparison.

[2]C c as the alternative space group has been ruled out based on a negative second harmonic generation test carried out on α-$Sm_2(MoO_4)_3$ (courtesy Professor Cross, Pennsylvania State University).

[3]In a recent paper, Nassau [9] also listed an α modification for $Ho_2(MoO_4)_3$. We were unable to obtain this form even through extended (10 days) sintering between 600 °C and the reported transition temperature of 750 °C. We only obtained $\beta' Ho_2(MoO_4)_3$.

Table 2

X-ray Powder Pattern for α-$Gd_2(MoO_4)_3$

h	k	ℓ	d_{obs}	d_{calc}	I_{obs}	I_{calc}
1	1	0	6.047	6.063	26	10
1	1	-1		6.059		15
0	2	0	5.705	5.718	2	2
0	0	2	5.384	5.391	19	22
0	2	1	5.045	5.052	18	16
1	1	1	4.741	4.747	8	<1
1	1	-2		4.742		1
0	2	2	-	3.923	-	1
2	0	0	3.562	3.575	36	2
2	0	-2		3.572		6
1	1	2		3.564		17
1	1	-3		3.560		17
1	3	0	3.361	3.364	5	5
1	3	-1		3.363		1
2	2	-1	3.158	3.158	100	100
1	3	1	3.074	3.070	7	<1
1	3	-2		3.077		<1
0	2	3	3.043	3.043	84	79
2	2	0	-	3.031	-	<1
2	2	-2	-	3.029	-	<1
0	4	0	2.858	2.859	27	27
1	1	3	-	2.770	-	<1
1	1	-4	-	2.768	-	<1
0	4	1	-	2.764	-	<1
2	2	1	2.723	2.726	8	6
2	2	-3		2.723		3
0	0	4	-	2.696	-	<1
1	3	2	2.673	2.673	7	5
1	3	-3		2.672		6
2	0	2	2.608	2.609	15	15
2	0	-4	2.605	2.605	14	15
0	4	2	2.526	2.526	3	3
3	1	-1	2.447	2.450	1	1
3	1	-2		2.449		<1
0	2	4	-	2.438	-	<1
2	2	2	-	2.374	-	<1
2	2	-4	-	2.371	-	<1
3	1	0	2.333	2.333	2	1
3	1	-3		2.331		<1
1	3	3	2.281	2.285	2	<1
1	3	-4		2.284		<1
2	4	1		2.282		<1

Table 3

Cell Dimensions and Transition Temperatures for the Ferroelectric Rare Earth Molybdates

Composition	Melting Point(a) °C	α/β Transition Temperature, °C	Curie(b) Temperature, °C	a, Å(c)	b, Å	c, Å	b-a, Å	V, Å^3	IR, Å	G(d)
$Pr_2(MoO_4)_3$	1045	987	235.0	10.5255	10.5782	10.9013	0.0527	1213.75	0.991	17' 10"
$Nd_2(MoO_4)_3$	1081	961	244.9	10.4966	10.5426	10.8544	0.0460	1201.16	0.983	15' 04"
$Sm_2(MoO_4)_3$	1122	910	197.2	10.4352	10.4718	10.7687	0.0366	1176.76	0.958	12' 03"
$Eu_2(MoO_4)_3$	1144	881	180.5	10.4109	10.4436	10.7269	0.0327	1166.29	0.947	10' 47"
$Gd_2(MoO_4)_3$	1171	857	159.5	10.3881	10.4194	10.7007	0.0313	1158.19	0.938	10' 20"
$Tb_2(MoO_4)_3$	1172	835	160.4	10.3518	10.3807	10.6531	0.0289	1144.77	0.923	9' 35"
$Dy_2(MoO_4)_3$	1222	1030; 805	144.8	10.3271	10.3513	10.6145	0.0242	1134.68	0.912	8' 02"
$Ho_2(MoO_4)_3$	1245	853 (β to Pnca)	121.0	10.3038	10.3244	10.5783	0.0206	1125.33	0.901	6' 52"

(a) These temperatures are in good agreement with those observed earlier by Nassau [7].

(b) Measured for β' → β transition.

(c) The parameters can be considered accurate to ±0.0005 Å for the a and b dimension and to ±0.0009 Å for the c dimension.

(d) Shear angle (±15") calculated from x-ray data.

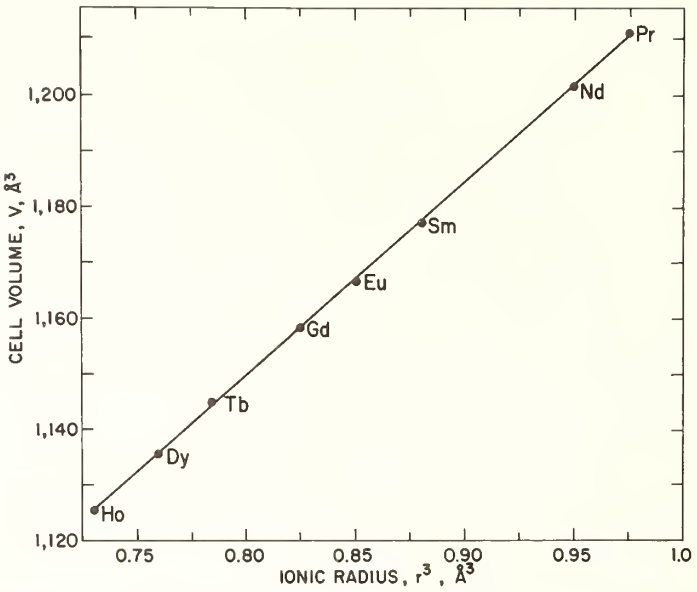

Fig. 1. Cell dimensions and transition temperatures for the ferroelectric rare earth molybdates.

Figure 2 shows a plot of the cell volume of the β' molybdates *vs.* the cube of the ionic radii. The numbers used for the radii are those of Shannon and Prewitt [11]. Based on the cell volume obtained for $Pr_2(MoO_4)_3$, a correction of the ionic radius for Pr^{+3} in octahedral coordination from 0.997 to 0.991 Å would seem indicated.

3. SUMMARY

In conclusion, the ferroelectric rare earth molybdates constitute a highly interesting group of compounds which combine a number of unusual physical properties in the metastable Pba2 room temperature structure. The structure is highly sensitive toward substitutions and transforms at relatively low temperatures (121-235 °C) into the more symmetrical tetragonal $P\bar{4}2_1m$ structure. Prepared below the α/β transformation temperature, the molybdates with Ln = Sm-Dy are isostructural with rare earth tungstates of the type $Ln_2(WO_4)_3$ where Ln is La-Dy.

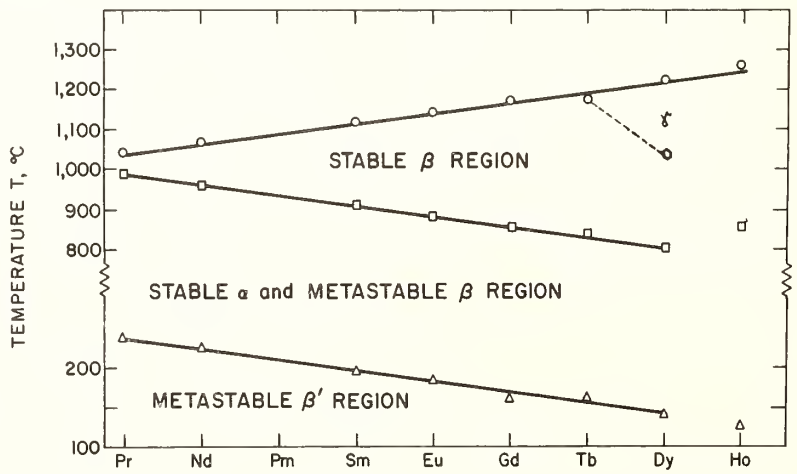

Fig. 2. Ionic radius *vs.* cell volume of the β´ modifications.

4. ACKNOWLEDGMENTS

We are grateful to J. W. Rooney and B. F. Gordon for technical assistance in carrying out this work.

5. REFERENCES

[1] Hitchcock, F. R. M., J. Am. Chem. Soc. 17, 522 (1895).
[2] Borchardt, H. J., U. S. Patent 3,437,432.
[3] Abrahams, S. C., Kurtz, S. K. and Jamieson, P. B., Phys. Rev. 172, 551 (1968).
[4] Jeitschko, W. K., Naturwiss. 57, 544 (1970).
[5] Drobyshev, L. A., Sov. Phys.-Crystallogr. 15, 835 (1971).
[6] Newnham, R. E., McKinstry, H. A., Gregg, C. W. and Stitt, W. R., Phys. Status Solidi 32, 49 (1969).
[7] Nassau, K, Levinstein, H. J. and Loiacono, G. M., J. Phys. Chem. Solids 26, 1805 (1965).
[8] Templeton, D. H. and Zalkin, A., Acta Cryst. 16, 762 (1963).
[9] Nassau, K., Shiever, J. W., Keve, E. T., J. Sol. State Chem. 3, 411 (1971).
[10] Keve, E. T., Abrahams, S. C., Nassau, K. and Glass, A. M., Solid State Commun. 8, 1517 (1970).
[11] Shannon, R. D., Prewitt, C. T., Acta Cryst. B25, 925 (1969), and ibid, B26, 1046 (1970).
[12] Jamieson, P. B. Jamieson, Abrahams, S. C., Bernstein, J. L., J. Chem. Phys. 50, 86 (1969).
[13] Brixner, L. H., Bierstedt, P. E., Sleight, A. W. and Licis, M. S., Mat. Res. Bull. 6, 545 (1971).

DISCUSSION

F. Holtzberg: Do I understand that the metastable transition that you showed, takes place reproducibly at the indicated temperature?

L. H. Brixner: No. You have to prepare the alpha gadolinium molybdate material below the transformation temperature of 800 °C, where it is stable. If you heat that up, it converts rather quickly into the beta structure. Now, if you rapidly quench the beta structure through 850 °C, it will survive. So, in other words, below 850 °C it is at least kinetically stable. If you sit with a crystal of the beta structure at or below the transition temperature, it will convert in a matter of days or perhaps weeks. If it's fine powder, it will go much faster. Thus, equilibrium favors the α phase but the reaction rate is quite slow. The density comparison of α and β indicates the structures are very different, which is consistent with the notion of large energy barrier between β and α.

National Bureau of Standards Special Publication 364, Solid State Chemistry, Proceedings of 5th Materials Research Symposium, issued July 1972.

STRUCTURAL AND PHASE RELATIONSHIPS AMONG TRIVALENT TUNGSTATES AND MOLYBDATES

K. Nassau and J. W. Shiever

Bell Telephone Laboratories, Incorporated
Murray Hill, New Jersey 07974

The trivalent tungstates $L_2(WO_4)_3$, molybdates $L_2(MoO_4)_3$, and mixed systems, $L_2(W_{1-x}Mo_xO_4)_3$ have been studied between room temperature and the melting points (up to 1650 °C). Single crystal and powder x-ray diffraction at room and elevated temperatures, differential thermal analysis, and crystal growth were among the techniques used to characterize phases and determine relationships.

Among the molybdates of the lanthanides, In, Sc, Fe, Cr, and Al, at least five structures were observed: the tungstates show at least three. Particular attention was devoted to $Tb_2(MoO_4)_3$, which, like $Gd_2(MoO_4)_3$, shows transitions at 800, 1040 and melting at 1155 °C and a ferroelectric transition at 163 °C in the metastable phase region; not all of these transitions are easily reversible.

Pseudo-binary tungstate-molybdate phase diagrams and structural parameters were determined for the La, Nd, Sm, Gd, Ho, and In systems. Based on structural determinations together with phase diagram interpretations and crystal growth evidence on the nature of various transitions (destructive or ncndestructive), structural relationships were used to organize the many structures into three groupings and relate the results to the radii of the trivalent atoms:

i) The small size tungstates and molybdates, the $Sc_2(WO_4)_3$ type family, with at least two members, form 6-coordinated structures with unit cell or subcell based on *Pnca*; with rising temperature this family extends to larger size atoms.

ii) The large size tungstates and molybdates form 8-coordination structures with scheelite related subcells; this α-$Eu_2(WO_4)_3$ type family includes at least 4 structures.

iii) The β-$Gd_2(MoO_4)_3$ type family of structures, occurring only in the intermediate size molybdates, have 7-coordinated trivalent atoms; except for $Y_2(MoO_4)_3$ they are stable only above 800 °C, although extensive metastability does occur with ferroelectric transitions in the metastable form near room temperature.

Key words: Crystal structure; lanthanide compounds; molybdates; tungstates.

1. INTRODUCTION

Insight into crystallochemical relationships can be obtained by the study of the variation of structure in a series of closely related compounds. Suitable variables can include the temperature and the substitution of cations of similar size and electronegativity. Structural determinations on single crystals (or powders when crystals are not available) as well as the study of phase transitions and pseudo-binary phase diagrams have been used by us and our co-workers [1-7][1] to clarify the structural relationships here studied.

---

[1] Figures in brackets indicate the literature references at the end of this paper.

The hexavalent tungsten and molybdenum ions have essentially the same size and electronegativity, and the range of these same parameters in the lanthanide series is also limited (6-coordination ionic radii [8] range from La = 1.06 Å to Ln = 0.85 Å). By comparison with other series of rare earth compounds one might therefore expect at most three structures to occur in the trivalent lanthanides tungstates and molybdates of the formula $Ln_2^{3+}(M^{6+}O_4)_3$.

In fact, no less than eight distinct structure types occur, at least four of which show evidence of containing additional variants. Four of these structures have been determined and enough is known about the other three and some of the variants that several patterns can be discerned.

The seven structures may first of all be grouped into families [6] as shown in figure 1. The smallest trivalent cations yield the C* family tungstates and molybdates, where the trivalent cation is 6-coordinated. A number of outer transition metal ions also occur in this family, and in the tungstates this structure occurs in the very wide size range from Al (0.53 Å) to Gd (0.94 Å).

Intermediate size molybdates contain 7-coordinated trivalent cations. With the exception of $Y_2(MoO_4)_3$, these have stability regions only at elevated temperatures but nevertheless do exist metastably at room temperature, showing interesting dielectric, ferroelectric, and ferroelastic properties and serving as laser host lattices [5,9-11].

The largest size trivalent cations yield tungstates and molybdates in the A family structures with 8-coordination, similar to that in the scheelite structure ($CaWO_4$, tetragonal $I4_1/a$). This A family contains four structure types as shown in table 1, namely A, D, M*, and N*, the asterisks on the last two indicating that variants occur. The variability of structures within this A family can be understood by viewing them as derived from the scheelite structure with two trivalent ions replacing three Ca ions, one vacancy (designated ϕ) resulting; one may then describe the substitution as the electroneutrality maintaining transformation: $3\ Ca^{2+}\ WO_4 \rightarrow Nd_2^{3+}\ \phi^0(WO_4)_3$.

This substitution, however, does not occur without an increase in energy, and the strain may be relieved in at least three different ways. First, there may be a change to an arrangement involving other than 8-coordination. With elevated temperature the tendency is to obtain 7-coordinated trivalent cations, with smaller trivalent cation size 6-coordination is observed.

A second way of lowering the energy results from a distortion of the unit cell shape. This occurs, for example, in the A type tungstates (*e.g.* α-$Eu_2(WO_4)_3$, monoclinic, $C2/c$ [12]) where the occupancy arrangement is simple (every third layer of Ca sites in the scheelite structure figure 2a, is vacant as shown in figure 2b) but where the scheelite type sub-cell angle is 94° instead of 90°.

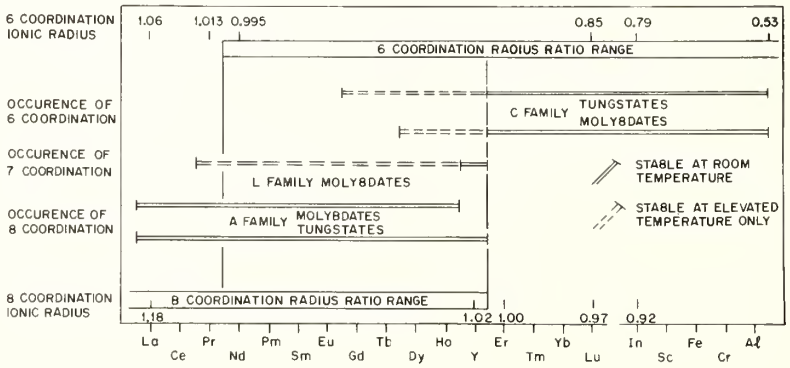

Fig. 1. Occurrence of structure families, coordination about the trivalent cation, and ionic radius of the trivalent cation in $Ln(WO_4)_3$ and $Ln(MoO_4)_3$ (after [6]).

Table 1†

Structure Types of $Ln_2(WO_4)_3$ and $Ln_2(MoO_4)_3$

Structure	Example	Spacegroup	Subcell
A Family (8-coordinated)			
A	α-$Eu_2(WO_4)_3$	$C2/c$	"scheelite" $\gamma \neq 90$
D	β-$Nd_2(WO_4)_3$	-	"scheelite" $\gamma \neq 90$
M*	α-$Tb_2(MoO_4)_3$	-	"scheelite" $\gamma \neq 90$
N*	α-$Nd_2(MoO_4)_3$	$C2$	scheelite $\gamma = 90$
L Family (7-coordinated)			
L´	β´-$Gd_2(MoO_4)_3$	$Pba2$	tetragonal
L	β-$Gd_2(MoO_4)_3$	$P42_1/m$	tetragonal
J	γ-$Tb_2(MoO_4)_3$	$Pm3m$ or subgroup	-
C* Family (6-coordinated)			
C*	$Sc_2(WO_4)_3$	$Pnca$	-
	$Fe_2(MoO_4)_3$	$P2_1/a$	$Pnca$
	α-$Tm_2(MoO_4)_3$	-	$Pnca$

†after table 3 of [6]; several obvious errors there have been corrected.

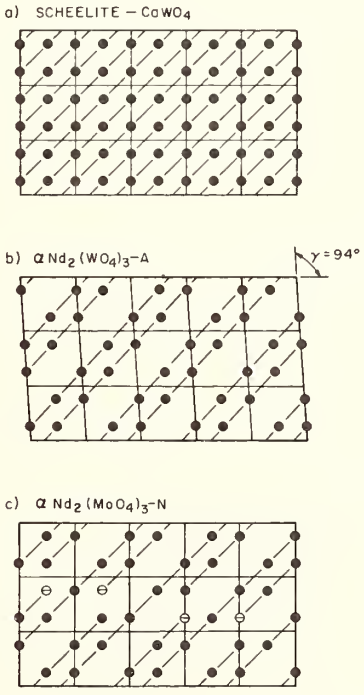

Fig. 2. Position of the Ca atoms in scheelite, viewed down the c (a); equivalent view of the Nd atom positions in α-$Nd_2(WO_4)_3$, structure type A(b); and in α-$Nd_2(MoO_4)_3$, structure type N(c).

A third way of relieving the strain is observed, for example, in the N*-type molybdates (*e.g.* α-$Nd_2(MoO_4)_3$, monoclinic, $C2$); here the sub-cell remains tetragonal ($I4_1/a$ as in scheelite) but the replacement of $2Na^{3+}$ for $3Ca^{2+}$ occurs in the long range order arrangement of figure 2c [3].

The other 8-coordinated structure types, the D tungstates and the M* molybdates, also have distorted scheelite-type sub-cells and structures distinct from type A; it may be suggested that when crystals become available and the structures can be determined, both unit cell distortion as well as disordering of the vacancies will be found.

2. OCCURRENCE OF STRUCTURES

The occurrence of the various structures for the various trivalent tungstates and molybdates is shown in figures 3 and 4, respectively. This is based primarily on our work [1,3,6]; relevant work by others will be found referenced there.

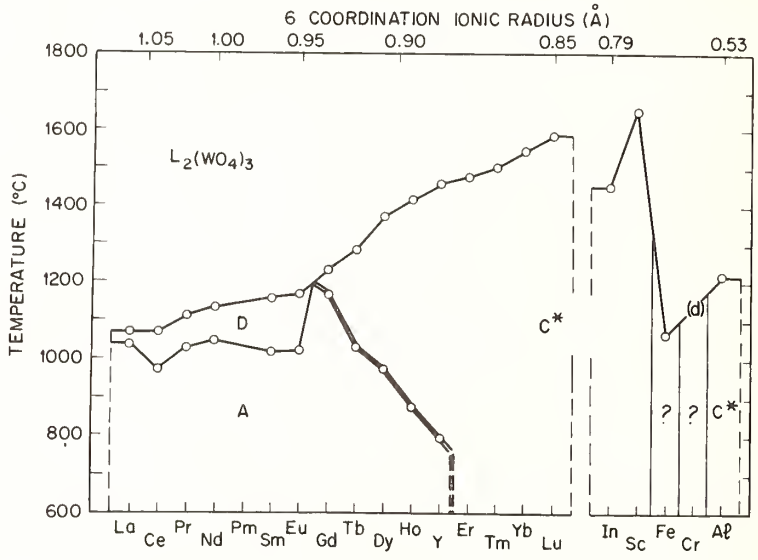

Fig. 3. Occurrence of structures in the $L_2(WO_4)_3$ compounds (after [6]).

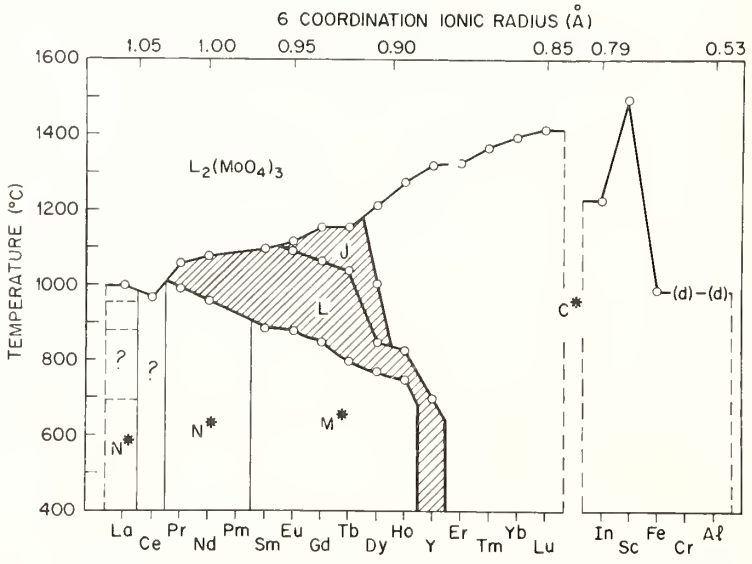

Fig. 4. Occurrence of structures in the $L_2(MoO_4)_3$ compounds (after [6]).

These structures are conveniently designated in three different ways. Successive phases with increasing temperatures are designated α-, β-, etc. as usual. For comparison among different compounds, alphabetic designations such as "A", "C", etc. as in table 1 and figures 3 and 4 provide an easily perceived label. An asterisk following such a designation indicates that the comparison of x-ray powder diffraction data (Debye-Scherrer, Guinier, and diffractometer techniques have all been used) indicates close similarity but not necessarily identity of structures. Thus in the case of the C* family, α-$Sc_2(WO_4)_3$ falls into space group *Pnca*, but $Fe_2(MoO_4)_3$ is $P2_1/a$, with *Pnca* as sub-cell. Structures solved in detail are designated by the specific compound first solved as customary. Thus one may refer to α-$Nd_2(WO_4)_3$ as being part of the "A" field and having the α-$Eu_2(WO_4)_3$ structure. Preparation (powder sintering and single crystal growth) and examination techniques (x-ray examination at ambient and elevated temperatures, DTA (differential thermal analysis), TGA (thermogravimetric analysis), quenching, etc.) have been previously [1,3,6] described. Transition and melting temperatures have been summarized previously [1] with some additions [6].

Some mixed compounds of the type $LaYb(WO_4)_3$ were also examined and found to have the same structures as the compound closest to the average ionic radius, $Sm_2(WO_4)_3$ in this instance. Any possible ordering of the cations was, however, not looked for.

The many phases reported by Drobyshev et al (*e.g.* eight for $Pr_2(MoO_4)_3$ [13]) appear to be inconsistent with this work. Their preparation technique (nonequilibrium, which can produce other nonequilibrium phases by Ostwald's step rule) and x-ray results (only minor intensity changes and invariant diffraction line spacings for many of the phases) make it difficult to relate their results to those of this series of studies.

3. PSEUDO-BINARY PHASE DIAGRAMS

The neodymium tungstate-molybdate $Nd_2(WO_4)_3$ - $Nd_2(MoO_4)_3$ pseudo-binary system has been investigated in most detail [3], and a phase diagram consistent with the data is shown in figure 5. Both α (room-temperature) forms have scheelite-type sub-cells; the variation of the sub-cell parameters with composition is shown in figure 6. The addition of as little as 2-1/2% tungstate permits the long range order α-$Nd_2(MoO_4)_3$ N structure of figure 2b to change into the highly ordered α-$Nd_2(WO_4)_3$ A structure; at first with an α angle of approximately 90°, increasing to 94° as the tungstate content dominates. Whether the A structure can exist with an α-angle of exactly 90° cannot be decided from these data.

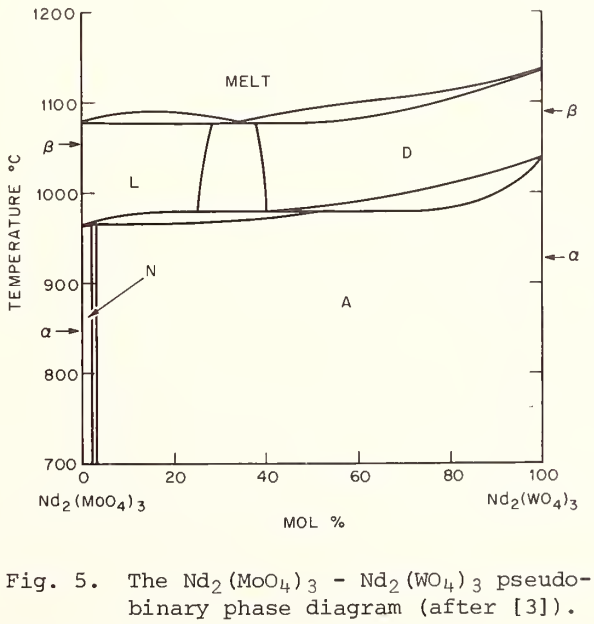

Fig. 5. The $Nd_2(MoO_4)_3$ - $Nd_2(WO_4)_3$ pseudo-binary phase diagram (after [3]).

465-504 O - 72 - 30

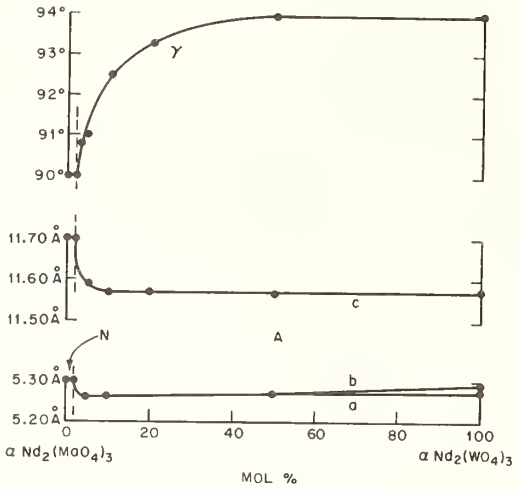

Fig. 6. Scheelite-type sub-cell parameters in the α-$Nd_2(MoO_4)_3$ - α-$Nd_2(WO_4)_3$ system (after [3]).

The gadolinium tungstate-molybdate system is shown in figures 7 and 8. Both the Nd and Gd systems show no significant two-phase region, but the La and Ho systems show wide two phase regions [6]; the sub-cell parameters of the latter are shown in figure 9. In the case of the Sm system [6] the three sub-cell parameters are all continuous between the M and A phases but there is evidence that at least one additional phase may exist in this system. In the indium system there is complete solid solubility, both end members having the same C structure [6].

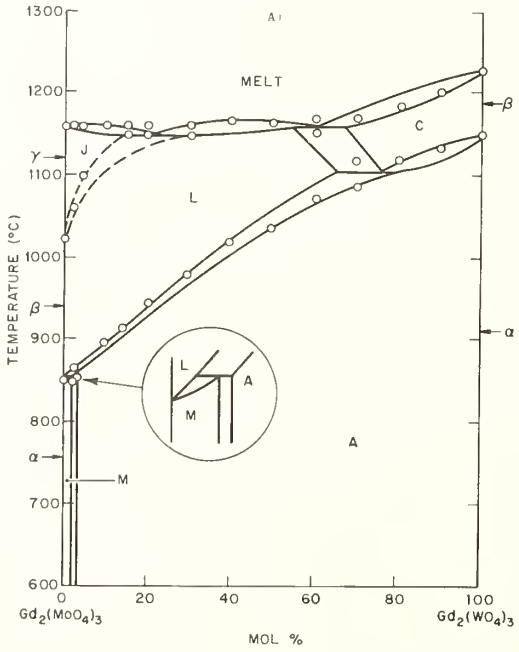

Fig. 7. The $Gd_2(MoO_4)_3$ - $Gd_2(WO_4)_3$ pseudo-binary phase diagram (after [3]).

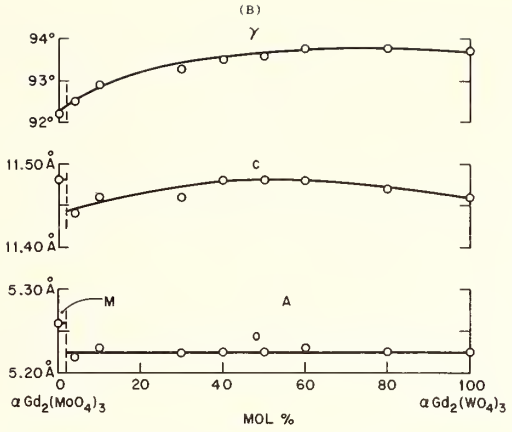

Fig. 8. Scheelite-type sub-cell parameters in the α-$Gd_2(MoO_4)_3$ - α-$Gd_2(WO_4)_3$ system (after [3]).

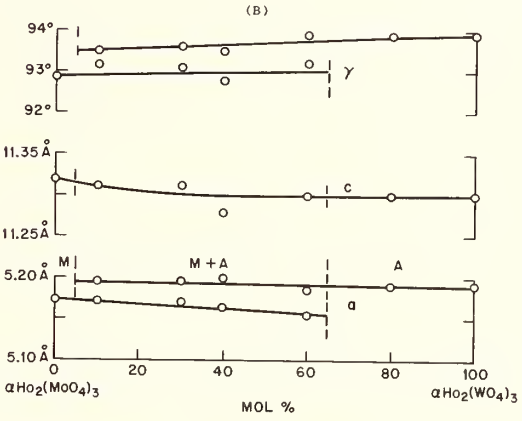

Fig. 9. Scheelite-type sub-cell parameters in the α-$Ho_2(MoO_4)_3$ - α-$Ho_2(WO_4)_3$ system (after [3]).

Even though the sub-cell may not show any discontinuities, *e.g.* between the M and A structures in the Sm binary system [6], there are nevertheless changes seen in a series of x-ray powder diffraction patterns across the system that indicate a change in structure. This was confirmed in the Sm system by the powder second harmonic generation test which showed a center of symmetry in $Sm_2(WO_4)_3$ and in the mixed system to 80% $Sm_2(WO_4)_2$ - 20% $Sm_2(MoO_4)_3$, but a lack of a center of symmetry in $Sm_2(MoO_4)_3$ [6]. The report by Brixner et al. [14] that the A and M compounds are isostructural is based only on x-ray powder diffraction data which does not necessarily show small differences. The type of long range ordering which characterizes the A* family of structures can only be satisfactorily established by single crystal work.

4. DESCRIPTIONS OF THE INDIVIDUAL STRUCTURES, THEIR OCCURRENCE, AND CRYSTAL GROWTH

4.1. A FAMILY STRUCTURES (8-COORDINATED)

4.1.a. STRUCTURE A

This structure is found in the α-form of the tungstates from La to Ho and including Y as shown in figure 3. The structure was first solved for α-$Eu_2(WO_4)_3$ which is monoclinic *C2/c*

with a = 7.73, b = 11.58, c = 11.48 Å, and β = 109.6° [12]. There is a scheelite-related distorted tetragonal sub-cell with a = 5.28, c = 11.58 Å and γ near 94°. Lattice parameters for most of the type A compounds, and an indexed x-ray powder diffraction pattern for α-$Nd_2(WO_4)_3$ have been given [1]; the promethium compound was studied by Weigel and Scherer [15].

The structure is related to that of scheelite as illustrated in figures 2a and 2b, with an ordered replacement of 2Nd for 3Ca. The distortion angle of the pseudo-tetragonal sub-cell decreases from 94° towards 90° as, for example, $Nd_2(MoO_4)_3$ is added to $Nd_2(WO_4)_3$. It also decreases as the temperature is raised, being approximately 92° at the transition temperature for α-$Nd_2(WO_4)_3$ as shown in figure 10.

Single crystals may be grown from the melt, *e.g.* by Czochralski pulling in inch size pieces, for the La to Eu tungstates. The D structure to A transition shown in figure 3 is nondestructive for these compounds; this is not the case for the transition in the remaining compounds, where destruction of the pulled crystals occurs on cooling through the phase transition from C to A.

4.1.b. STRUCTURE D

This structure occurs in the β form of the tungstates from La to Eu as shown in figure 3. Since it transforms nondestructively into Structure A it cannot be examined at room temperature, although a melt sample of $La_2(WO_4)_3$ was successfully quenched in the β-form and an x-ray powder diffraction pattern of this sample has been given [1]. High temperature x-ray diffraction shows a distorted scheelite-type sub-cell with $\gamma \neq 90°$ as shown in part of figure 10 for β-$Nd_2(WO_4)_3$ with sub-cell dimensions a = 5.3 and c = 11.6 Å. On the basis of the absence of a discontinuity in γ in the D to A transition of figure 10 one may assume a structure similar to the A structure of figure 2b, but with some disorder.

4.1.c. STRUCTURE M*

This structure is found as the α-form of the molybdates of Sm to Ho as shown in figure 4. Since the L form in this region is extremely stable with respect to the L to M* transition, preparatory sintering must be performed below the transition temperature and a technique to prepare single crystals has not yet been found.

An x-ray powder pattern has been given [1] for α-$Gd_2(MoO_4)_3$. Monoclinic indexing of the α-$Gd_2(MoO_4)_3$ and cell dimensions for the Sm through Dy compounds has been given by Brixner [14] on the assumption that the structure is $C2/c$, identical with the A structure of α-$Eu_2(WO_4)_3$. This clearly cannot be the true unit as indicated by the absence of a center of symmetry and other evidence as discussed in section 3. It is probably a sub-cell of the true cell.

The scheelite-type sub-cell angle deduced from x-ray diffractometer tracings is in the 92 to 94° range. In pseudo-binary tungstate-molybdate systems the angle γ and the other sub-cell parameters are continuous in some instances and discontinuous in others with those of the A structure (see figures 8, 9, and reference [6]). This structure again may be assumed to be related to the A structures with disorder, but different from that found in the A or D structures. Differences are noted as the x-ray powder patterns of this series are compared and there may be a number of different disorder patterns as implied in the asterisk of M*.

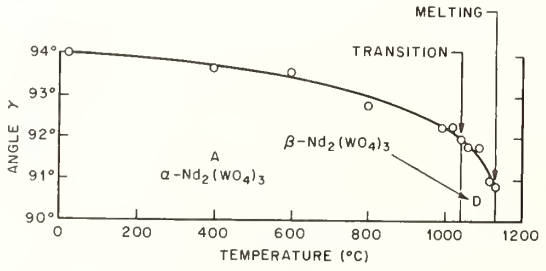

Fig. 10. Sub-cell γ values for $Nd_2(WO_4)_3$.

4.1.d. STRUCTURE N*

This structure is found as the α-form of La, Pr, Nd, and Pm molybdates as shown in figure 4. The structure was solved for α-$Nd_2(MoO_4)_3$ which is monoclinic $C2$ with a = 27.02, b = 11.70, c = 11.85 Å, and β = 105.3° [4]. An indexed x-ray powder diffraction pattern of this compound has been given [1], as well as one for the Pm compound [15]. The sub-cell is tetragonal (*e.g.* γ ≅ 90°), $I4_1/a$ with a = 5.30 and c = 11.70 Å. Crystals were grown by temperature cycling the sintering powder containing excess MoO_3 near the upper temperature limit of the stability region. In the pseudo-binary tungstate-molybdate systems this structure occurs to about 42% tungstate in the La system, but only to about 2-1/2% tungstate in the Nd system.

As shown in figure 2c there is considerable disorder in the α-$Nd(MoO_4)_3$ structure, with partial occupancy in the barred locations as determined from satellite reflections [16]. The comparison of x-ray powder diffraction patterns shows differences among the four N* compounds; all show tetragonal sub-cells and different types of disorder may be assumed.

4.2. L FAMILY STRUCTURES (7-COORDINATED)

4.2.a. STRUCTURES L AND L´

These are the β forms of Pr to Ho molybdates and α-Y molybdate as shown in figure 4. The structure was first solved [7] for β-$Gd_2(MoO_4)_3$ (frequently abbreviated β-GM0 or, less accurately, GM0) which in its ferroelectric form at room temperature is orthorhombic $Pba2$, with a = 10.3858, b = 10.4186, and c = 10.7004 Å. Lower symmetry has been suggested, but this appears to be an artifact produced by a-b type twinning and [001] rotational mosaic misorientations. Above the approximate 160 °C Curie temperature, the structure is tetragonal, $P42_1/m$. An indexed x-ray powder diffraction pattern and lattice parameters on tetragonal indexing [1] and more accurate parameters on orthorhombic indexing and Curie temperatures [14] have been given. The structure has been confirmed by Jeitschko [17]. The designation β´ (and L´) may be used for the ferroelectric phase if a distinction between this and the β (and L) paraelectric phase is desired. The ferroelectric characteristics of this group were first discovered by Borchardt and Biersted [18].

Single crystals can be grown in inch size pieces by the Czochralski technique of pulling from the melt Pr to Tb. For the Eu to Tb compounds the J structure is first formed, but converts nondestructively into L. In the case of the Dy, Ho, and Y compounds, however, the transformation from C is destructive.

The L structure compounds (except for $Y_2(MoO_4)_3$) exist at room temperature in a metastable condition; at temperatures below but close to the transformation temperature the transition to M does occur. Thus a single crystal of $Gd_2(MoO_4)_3$ transforms completely at 800 °C in 3 days to the M form, but at 600 °C the process is imperceptibly slow. The powder transforms completely in less than 3 days at 400 °C. For $Tb_2(MoO_4)_3$ the conversion rate is appreciably slower.

At room temperature β-$Tb_2(MoO_4)_3$ and β-$Gd_2(MoO_4)_3$ are ferroelectric, ferroelastic, and paramagnetic, and a compilation of properties has been published [5,19]. Laser action has been reported in β-$Gd_2(MoO_4)_3$ doped with Nd [9,10]. At very low temperatures gadolinium molybdates become antiferromagnetic [20].

4.2.b. STRUCTURE J

This phase was only recently recognized [6]. It occurs as the γ form of the molybdates from Eu through Dy as shown in figure 4. The DTA curves of figure 11 show that in the case of $Tb_2(MoO_4)_3$ the γ phase does not form on heating but only during solidification of the melt. It should be noted that the amount of heat absorbed during melting, *i.e.* the area under the melting peak, depends on whether the γ phase is present or not. Quantitative measurements indicate that for the β to γ transition ΔH_{1155} = 50 kcals/mole [6]. The powder diffraction trace at 1000 °C can be indexed as cubic with a = 10.44 Å, and is $Pm3m$ or a subgroup [6]. Since the J structure compounds transform nondestructively to L and only exist in a limited temperature region at elevated temperatures, the prospects for single crystal preparation and examination are not encouraging.

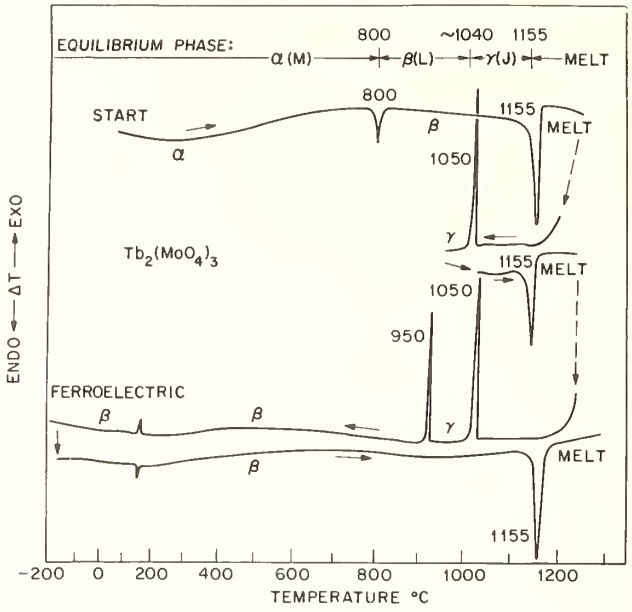

Fig. 11. DTA curve (composite) of $Tb_2(MoO_4)_3$ (after [3]).

4.3. C* FAMILY STRUCTURES (6-COORDINATED)

This family of structures occurs as the only form of the molybdates of Er to Lu, Sc, In, Fe, Cr, Al, the β-form of Y, the γ-form of Ho and the δ-form of Dy; also the tungstates of Er to Lu, In, Sc, Al, and the β-form of Gd to Y. The structure was first solved [2] for $Sc_2(WO_4)_3$, which is orthorhombic *Pnca* with a = 9.596, b = 13.330, and c = 9.512 Å. An indexed x-ray powder diffraction pattern of $Sc_2(WO_4)_3$ and approximate lattice constants for some of the other C* compounds have been given. [1].

Most of these compounds are readily pulled from the melt in large single crystal form. One of the difficulties in working with the lanthanide C* compounds is that they absorb moisture from the atmosphere to form trihydrates destructively; data for hydrates of the tungstates, designated B, and the molybdates, designated K, has been presented [1]. Early workers on lanthanide tungstates did not realize that water was present, and this was first recognized by Borchard as detailed previously [1]. The nonlanthanide compounds do not hydrate in this way.

The In and Fe molybdates have been reported [21,22] to be monoclinic $P2_1a$, but with *Pnca* as a sub-cell. Partial examination of a $Tm_2(MoO_4)_3$ crystal pulled from the melt and protected from hydration indicated a doubling of the c-axis dimension with a = 10.00, b = 13.65, and c = 19.50 Å; this structure has been designated C′ by Rode et al. [23]. This type of structural variation is the justification for using the "family" concept.

5. CONCLUSION

Factors which have complicated, and in fact even vitiated, early and also some more recent work on these compounds include the following:

i) the existence of unexpected components, *e.g.* Na yielding $NaRe(WO_4)_2$ [24] and H_2O in the C* structure lanthanide compound hydrates;

ii) metastability, *e.g.* the slow L→N, L→M, and L→J transitions, resulting in phases being overlooked when sintering is performed at too high a temperature, *etc.*;

iii) sometimes unsuspected nondestructive phase transitions, *e.g.* J→L and D→A;

iv) the occurrence of compounds with highly related but distinct structures within families such as C*;

v) the presence of long range ordering not apparent in powder x-ray diffraction but obvious in single crystal investigations, *e.g.* in the A family M* structures; and

vi) insidious effects which can be produced by deviations from stoichiometry and Ostwald's step rule in metastable systems.

With allowance made for these complications, several patterns emerge. Three in particular may be singled out:

i) the unexpectedly many structures occurring can be grouped into three families with coordination numbers of 6, 7, and 8 for the lanthanons, increase in size and decrease in temperature favoring higher coordination as discussed in Section I;

ii) the change from tungstate to molybdate (or an equivalent smaller rise in temperature [3] has essentially no effect on the coordination but does produce a change from the relatively simple A structure to the more complex members of the A family; and

iii) the various ways in which the A family structures (based on the ordering of vacancies in a scheelite related sub-cell structure) can deform: by deviating from the $\gamma = 90°$ of scheelite with a simple ordering, as in the A structure; by maintaining $\gamma = 90°$ but forming a complex long-range ordering, as in the N* structures; or by doing both, as presumably occurs in the M* and D structures.

Further understanding of this fascinating group of compounds must await the availability in single crystal form (permitting structure determinations) of additional compounds, in particular of the D, M*, and J compounds, as well as further variants within the N* and C* structures.

6. ACKNOWLEDGMENTS

The cooperation of various co-workers of references [1] through [7] and [16] as well as those acknowledged there is gratefully recognized, as are most helpful discussions with S. C. Abrahams.

7. REFERENCES

[1] Nassau, K., Levinstein, H. J., and Loiacono, G. M., J. Phys. Chem. Solids 26, 1805 (1965).
[2] Abrahams, S. C. and Bernstein, J. L., J. Chem. Phys. 45, 2745 (1966).
[3] Nassau, K., Jamieson, P. B., and Shiever, J. W., J. Phys. Chem. Solids 30, 1225 (1969)
[4] Jamieson, P. B., Abrahams, S. C., and Bernstein, J. L., J. Chem. Phys. 50, 86 (1969).
[5] Keve, E. T., Abrahams, S. C., Nassau, K., and Glass, A. M., Solid State Comm. 8, 1517 (1970).
[6] Nassau, K., Shiever, J. W., and Keve, E. T., J. Solid State Chem. 3, 411 (1971).
[7] Keve, E. T., Abrahams, S. C., and Bernstein, J. L., J. Chem. Phys. 54, 3185 (1971).
[8] Shannon, R. D. and Prewitt, C. T., Acta Cryst. B25, 925 (1969).
[9] Borchardt, H. J. and Biersted, P. E., Appl. Phys. Letters 8, 50 (1966).
[10] Borchardt, H. J. and Biersted, P. E., J. Appl. Phys. 38, 2057 (1967).
[11] Cross, L. E., Fouskova, A., and Cummins, S. E., Phys. Rev. Letters 21, 812 (1968).
[12] Templeton, D. H. and Zalkin, A., Acta Cryst. 16, 762 (1963).
[13] Drobyshev, L. A., Ponomarev, V. I., Frolkina, I. T., and Belov, N. V., Sov. Phys. Crystallography 15, 391 (1970).
[14] Brixner, L. H., Biersted, P. E., Sleight, A. W., and Licis, M. S., Mat. Res. Bull. 6, 545 (1971).
[15] Weigel, F. and Scherer, U., Radiochim. Acta 13, 6 (1970).
[16] Jamieson, P. B., de Fontaine, D., and Abrahams, S. C., J. Appl. Cryst. 2, 24 (1969).
[17] Jeitschko, W. K., Naturwiss, 57, 544 (1970).
[18] Borchardt, H. J. and Biersted, P. E., Appl. Phys. Letters 8, 51 (1966).
[19] Cummins, S. E., Ferroelectrics 1, 11 (1970).

[20] Fisher, R. A., Hornung, E. W., Brodale, G. E., and Giauque, W. F. (to be published).
[21] Plyasova, L. M., Klevtsova, R. F., Borisov, S. V., and Kefeli, L. M., Sov. Phys. Crystallogr. 13, 29 (1968).
[22] Plyasova, L. M., Klevtsova, R. F., Borisov, S. V., and Kefeli, L. M., Sov. Phys.-Dokl. 11, 189 (1966).
[23] Rode, E. Y., Lysanova, G. V., Kuznetsov, V. G., and Gokhman, L. Z., Russ. J. Inorg. Chem. 13, 678 (1968).
[24] Sillen, L. G. and Sundvall, H., Arkiv För Kemi, Min. o. Geol. 17A, 1 (1943).

DISCUSSION

L. H. Brixner: I'm glad you left my little diagram up there on the board. I'd like to come back to this gamma phase because I still believe it's metastable. Of course, it would be very difficult to prove really, because one would have to take a high temperature x-ray diagram of a growing crystal. There are two reasons why I believe it is metastable. One, I'm convinced we are growing in equilibrium with the tetragonal beta structure because the macroscopic symmetry of the crystals (as you well know since you've grown enough of them) is in accordance with tetragonal symmetry, not with cubic symmetry, and I believe you called the gamma phase cubic. Two, we do find a lower melting temperature, at least in the case of terbium molybdate, for the gamma phase and we are growing at the beta melting point, not the gamma melting point.

K. Nassau: Two points. First of all, I said that the gamma phase can be indexed cubic, I didn't say it is cubic. Drastic difference: it may well be tetragonal. Secondly, I believe you are taking as the melting point the DTA peak whereas we are taking the shoulder. I believe the shoulder is the correct one to take on theoretical basis and this we find does not change within five degrees from α to β. So we disagree: we agree on the data, but we disagree on the interpretation.

L. H. Brixner: No matter what point we take on the DTA plot, the absolute difference between shoulder or peak is the same.

K. Nassau: We find the shoulders are identical within five degrees.

L. H. Brixner: As best I know you are also using a DuPont analyzer.

K. Nassau: Yes, I'm the first to admit it. However, I should say in line with what we heard in our first talk this morning, who knows what an "equilibrium phase" is anyway. All we can do is report what results we observe.

H. Young: Could we have another kind of question?

R. S. Roth: I think that your surprise that molybdenum and tungsten are so different shouldn't be a surprise. I think, just like niobium and tantalum are so different, molybdenum and tungsten are different when more than 50 percent of the compound is this ion. When it is a 1:1 ratio or less, then they are very, very similar. After all, even the oxides themselves are very different.

K. Nassau: If you look at the phosphates and arsenates and so on, you usually find one structural change in the middle of each lanthanide series. Even if the tungstates and molybdates are different, for instance with calcium the tungstates and molybdates aren't the same structure; I still would not have expected eight structures plus numerous variants within two simple series of compounds like this. I think one is justified at some surprise there. It's true, after one has seen Wadsley's work one shouldn't be surprised at anything, but then I do think we are dealing with equilibrium phases here which is not claimed for Wadsley's structures.

National Bureau of Standards Special Publication 364, Solid State Chemistry, Proceedings of 5th Materials Research Symposium, issued July 1972.

CRYSTAL CHEMISTRY OF TETRAHEDRALLY-COORDINATED OXIDES: Li_3PO_4 DERIVATIVES

A. R. West and F. P. Glasser*

Department of Chemistry
University of Aberdeen
Meston Walk
Old Aberdeen, AB9 2UE, Scotland

The high and low polymorphs of Li_3PO_4 are type structures for a large family of tetrahedrally-coordinated oxides. These are readily synthesized by direct solid state reaction of the constituent oxides or by hydrothermal reaction. The simplest substances which are Li_3PO_4-type include Li_3VO_4 and Li_3AsO_4, although the high-low inversion in the latter two proceeds reversibly through one or more intermediate phases which are thermodynamically stable over a short range of temperatures.

The intermediate phases often undergo further structural distortion during quenching to ambient. Li_3PO_4 itself forms an intermediate phase in the conversion low → high Li_3PO_4. This intermediate phase is readily retained to ambient but is believed to be metastable at all temperatures. More complex Li_3PO_4 derivatives include substances of the general formula Li_2MXO_4, where M = Mg, Zn, Co^{2+} and X = Si, Ge^{4+}. Each compound usually has at least two polymorphs. These fall into three classes: one which is either high or low Li_3PO_4 type, one which includes the distortional derivatives of both high and low Li_3PO_4, and lastly, phases of related but unknown structures. A full explanation of the polymorphism of an individual phase is only possible if effects due to solid solution are taken into account. For example, the stoichiometry of "Li_2ZnSiO_4" varies within the system Li_4SiO_4-Zn_2SiO_4; the solubilities of excess Li^+ and Zn^{2+} have been measured as a function of temperature. Inversion temperatures, and especially, the occurrence and stability of many of the distortional derivative structures, are closely related to the stoichiometry.

The possibilities of making other substitutions, such as replacing ($Li^+ + M^{2+}$) by A^{3+}, where A = Al, Ga^{3+}, etc., are discussed.

This family of phases is probably of widespread occurrence. We have encountered these phases in glass-ceramic systems, such as Li_2O-MgO-ZnO-SiO_2, where they are an important crystallization product of *all* glass composition.

Key words: Crystal chemistry; kinetics; lithium arsenate; lithium phosphates; lithium vanadate; phase transformation; polymorphism.

1. INTRODUCTION

The crystal structures of the low and high forms of Li_3PO_4 have been determined [1,2][1]: the atomic positions are similar in both polymorphs. The oxygen atoms are arranged in approximately hexagonal close packing, similar to that found in olivines. However, the simplest olivines have the stoichiometry $M_2^{2+}SiO_4$, where M^{2+} = Mg, Fe, Ni, Co, Mn, and, at low temperatutes Ca, while lithium phosphate is more cation-rich. Also, the divalent ions

---

*Lecturer and Senior Lecturer, respectively.

[1] Figures in brackets indicate the literature references at the end of this paper.

are octahedrally coordinated in olivine, whereas in Li_3PO_4 all the cations are tetrahedrally coordinated. Despite these differences, Li_3PO_4 and olivines exhibit a remarkable similarity in unit cell dimensions and axial ratios; both have orthorhombic symmetry and the same, or closely related space groups. This relationship can only be fortuitous even allowing for the similar oxygen arrangement in the two structure types. As a result, much confusion has arisen in the past over the distinction between lithium phosphate and olivine structures. Synthetic lithium phosphate was once classified as an olivine [3] and when the low form of Li_3PO_4 was subsequently found in nature as the mineral lithiophosphate [4], it was thought to be an olivine [5].

After the crystal structure of high Li_3PO_4 had been reported [2], one of the first to recognize and study other Li_3PO_4 isotypes was Tarte [6]; he showed that Li_3AsO_4 and Li_3VO_4 were isostructural with the low form of Li_3PO_4, whose synthesis and x-ray powder diffraction data were first reported by Swanson, et al. [7].

The present paper reviews some of the authors recent work on the simple isotypes of Li_3PO_4 and on the crystal chemistry and stoichiometry of some of the more complex derivative structures. Phases which are isostructural with low Li_3PO_4 will be designated β_{II}: those isostructural with high Li_3PO_4 will be designated γ_{II}. Reasons for using this apparently more cumbersome nomenclature will become apparent when the crystal chemistry of the derivative structures is described.

2. LITHIUM PHOSPHATE

2.1. LITHIOPHOSPHATE

Single crystals of lithiophosphate, the naturally occurring form of Li_3PO_4, have been examined by x-ray rotation and Weissenberg photographs.[2] Sufficient photographs were obtained to show that the specimen is isostructural with synthetic β_{II}(low)Li_3PO_4. It had previously been suspected from a comparison of x-ray powder data that the two were closely related, but that they may not have been isostructural. This uncertainty is now removed. The slight differences between the powder patterns of the synthetic and naturally-occurring samples probably arise from their differing degrees of preferred orientation.

2.2. HEATING EXPERIMENTS ON Li_3PO_4

A heat effect has been reported to occur at *ca.* 500 °C on heating low Li_3PO_4 [7]: presumably this was due to conversion of the β_{II}(low) to γ_{II}(high)Li_3PO_4. The reaction is apparently monotropic: hydrothermal recrystallization can be used to reverse the reaction [6]. $\beta_{II}Li_3PO_4$ can also be prepared by direct precipitation from aqueous solution [7].

We have recently studied the $\beta_{II} \rightarrow \gamma_{II}$ inversion of a commercial grade (Hopkin and Williams, Ltd.) of low Li_3PO_4. No sharp event was observed by DTA at or around 500 °C, but instead, a broad endotherm appeared over the range 440° to 520 °C: this heat effect was not reversible on cooling. A sample removed from the DTA apparatus after heating to 550 °C gave, at ambient, a powder pattern intermediate between those of β_{II} and γ_{II}. Li_3PO_4 taken from the same source and heated to 900 °C for 15 hr yielded $\gamma_{II}Li_3PO_4$. The differences between the powder patterns of the high, low and intermediate polymorphs are small, as shown diagramatically in figure 1. A high temperature powder x-ray (HTXR) photograph also showed that the $\beta_{II} \rightarrow \gamma_{II}$ inversion proceeded *via* formation, over a short temperature range, of the same intermediate phase. The thermodynamic stability of this Li_3PO_4 transitional phase is uncertain: it has not yet been obtained by cooling $\gamma_{II}Li_3PO_4$, and the reverse reaction, $\gamma_{II} \rightarrow \beta_{II}Li_3PO_4$, has not been achieved except in the presence of water or water vapor.

Single crystals of the natural mineral, heated rapidly to *ca.* 700 °C, convert topotactically to $\gamma_{II}Li_3PO_4$. The significance of this will be discussed subsequently.

---

[2] This sample was kindly loaned by The United States National Museum, Catalogue number USNM 121266.

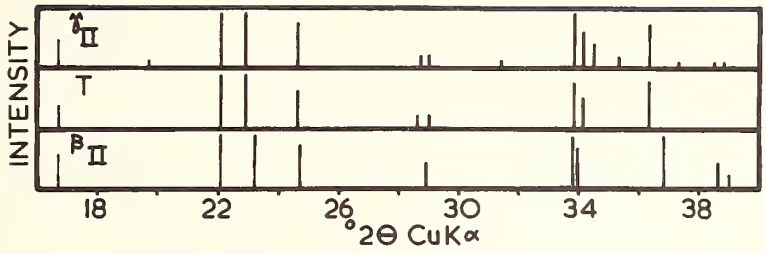

Fig. 1. X-ray powder diffraction data at 25 °C for the polymorphs of Li_3PO_4.

3. ISOTYPES OF Li_3PO_4

3.1. LITHIUM VANADATE, Li_3VO_4

The complex polymorphism of Li_3VO_4 is only partially understood: the present state of knowledge is summed up in figure 2. In addition to the β_{II}(low) form, Li_3VO_4 forms a non-quenchable γ_{II}(high) form and a T (= transitional) phase having a stability field and also, probably a structure intermediate between those of the β_{II} and γ_{II} polymorphs [8]. Both the β_{II} and T polymorphs occur in several variants; these will be discussed presently. The existence of an additional phase, stable between *ca* 1050 °C and the melting temperature, *ca* 1150 °C, is indicated by DTA [8,9]. This high phase gave only weak and diffuse x-ray powder patterns so it is not well characterized, but it appears to be structurally unrelated to the β, γ, or T phases.

The β phase (β_{II} or one of its variants) appears to be stable up to *ca*. 650 °C; above this temperature a T phase forms. The reaction: β phase ⇆ T phase, is reversible and shows some hysteresis, especially at the faster rates used in DTA. One variant of β_{II}, designated X' -β_{II}, was obtained at ambient. It was prepared by annealing a sample of β_{II} at *ca*. 650 °C for several days. X' -β_{II} may be the equilibrium phase at 650 °C. However, HTXR photographs taken at slow heating and cooling rates show that another closely-related phase, designated X-β_{II}, appears between *ca*. 300° and 650 °C. The exact status of X-β_{II} and X' -β_{II} is uncertain; in figure 2 both are shown as being metastable at all temperatures, but this interpretation is provisional.

Several T-phases may be produced for Li_3VO_4. In general, they have a stability field between *ca*. 650° and 750 °C, although two variants have also been quenched metastably to ambient. The conversion of a T phase to γ_{II} takes place reversibly, although with some hysteresis. By HTXR, at heating and cooling rates of approximately 1.0 °C min^{-1} the variant designated T_I Li_3VO_4 is observed in the conversion $\beta_{II} \leftrightarrows T_I \leftrightarrows \gamma_{II}$. This T_I phase appears to be the same as that which is obtained by quenching Li_3VO_4 from *ca*. 740 °C to ambient. However, HTXR photographs taken at slower heating and cooling rates (*ca*. 0.1 °C min^{-1}), show that a number of minor phase changes occur within the T phases. The different T phase variants have proved difficult to classify not only because of the small differences between their x-ray patterns, and the short range of temperatures over which each variant occurs, but also, because different transformation sequences between variants are observed on the heating and cooling runs. The broad features of both heating and cooling runs appear to be: $\beta_{II} \rightleftarrows$ X-$\beta_{II} \rightleftarrows$ T phases (several variants) $\rightleftarrows \gamma_{II}$.

The powder patterns of the T phases, especially T_{II} (produced by quenching Li_3VO_4 from *ca*. 1100 °C), have close similarities to those of β_{II} and γ_{II}: a comparison is shown in figure 3. Indexed powder data for these phases are presented elsewhere [8]; it is shown that many of the differences between the powder patterns can be accounted for by changes in the *c* crystallographic dimension of the orthorhombic cell, or pseudocell, which is common to all three phases. With rising temperature, *c* increases by about 1.0 to 1.5% at each transition. These discontinuous changes in *c* are characteristic of a normal, first-order phase transformation.

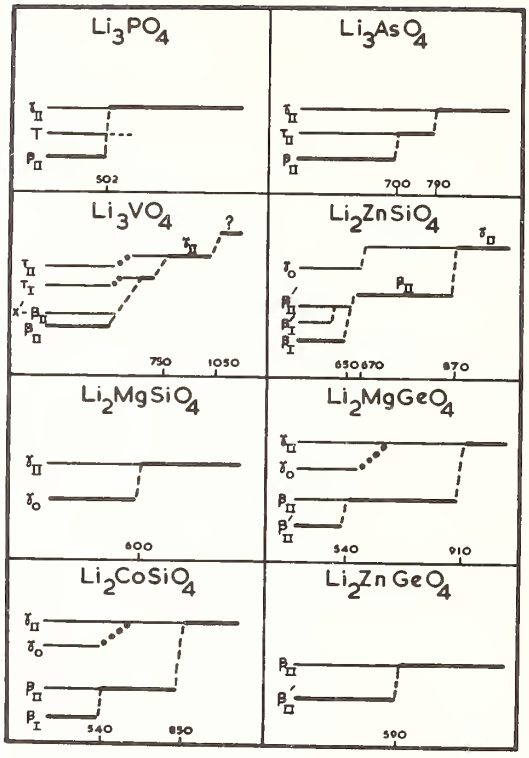

Fig. 2. Schematic temperature-stability relations for the sequence of phase changes in Li_3PO_4 and related structures. The ordinate is a schematic measure of the relative stabilities of the different forms. Heavy lines show the equilibrium state. Broken lines indicate phase changes which could be followed by either DTA or high-temperature x-ray. Small circles represent transformations which could not be followed directly, but which must exist. Where known, transformation temperatures are indicated at the bottom of each figure. For Li_3VO_4, the crystallochemical classification of the high phase is not known; hence the question mark. Also, it is not known if the $T_I Li_3VO_4$ phase which is shown as stable for a short range of temperature below 750 °C, is the same as or is a variant of the T_I phase obtained at ambient by quenching; the figure suggests the latter interpretation.

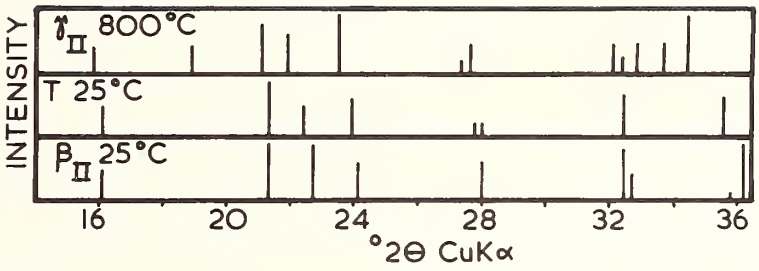

Fig. 3. X-ray powder diffraction data for some Li_3VO_4 polymorphs.

3.2. LITHIUM ARSENATE

The polymorphism of Li_3AsO_4 is shown in figure 2. Like Li_3VO_4, it has γ_{II} and β_{II} phases whose stability fields are separated by that of a transitional phase. This phase, designated T_{II} Li_3AsO_4, is believed to be isostructural with T_{II} Li_3VO_4, a polymorph which is probably always metastable in the Li_3VO_4 system. The T_{II} phase of Li_3AsO_4 forms reversibly from β_{II} Li_3AsO_4 on heating and from γ_{II} Li_3AsO_4 on cooling. The transformations exhibit considerable hysteresis at the faster DTA rates. All three polymorphs may be retained to ambient by a suitable choice of cooling rate for the γ_{II} phase. None of the other transitional phases or the β_{II} variants produced by annealing Li_3VO_4 seem to have any counterpart in the Li_3AsO_4 system.

3.3. STRUCTURAL RELATIONS, KINETICS AND MECHANISM OF THE HIGH $\rightleftarrows$ LOW TRANSFORMATION IN Li_3PO_4 - TYPE STRUCTURES

The structural differences between the high and low forms of Li_3PO_4 are not large. Examination of the atomic positions shows that the oxygens approximate more nearly to hexagonal close packed layers in the low form than in the high, and that one set of lithium and one set of phosphorus atoms occupy different sets of tetrahedral holes in the two structures. These differences are largely confined to displacements occurring in the [001] direction, *i.e.*, the direction which is normal to the close-packed oxygens. Thus, the two structures appear to be very similar in their *ab* projections. Rather surprisingly, the symmetry of the low form is higher than that of the high-temperature form.

Associated with each plane of close-packed oxygens are two sets of available tetrahedral sites, one above and one below the oxygen layer. Only one of these sets is occupied in low Li_3PO_4. By comparison, in high Li_3PO_4 there is a division of lithium and phosphorus atoms into tetrahedral sites on both sides of the oxygen layers. This redistribution of cations in the high form causes a buckling of the oxygen layers, which results in the *c* unit cell edge of high Li_3PO_4 being 1-2% larger than that of low Li_3PO_4.

During the high $\rightleftarrows$ low transformation, half of the cations jump from one set of tetrahedral sites to another and the oxygen framework changes slightly. Evidence for the semi-displacive nature of the transformation is provided by observing single crystals of lithiophosphate which have been heated rapidly to 700 °C. These convert to $\gamma_{II}Li_3PO_4$ which is easily preserved to ambient. Microscopic examination shows that these γ_{II} crystals retain their optical continuity and orientation, thereby indicating that the transformation is topotactic.

The $\beta_{II} \rightleftarrows \gamma_{II}$ transformation is much more rapid for Li_3VO_4 and Li_3AsO_4 than it is for Li_3PO_4. This could be explained in several ways. Firstly, it should become progressively easier to rupture bonds in the order: P-O, V-O, and As-O. Secondly, more thermal energy will be available at the inversion temperatures of Li_3VO_4 and Li_3AsO_4 which are both approximately 700 °C, compared with approximately 500 °C for Li_3PO_4. Thirdly, the possible appearance of a transitional phase will presumably lower the activation energy required for the transition, by allowing the necessary adjustments in atomic positions to occur in two

stages. The question arises: if a phase with intermediate structure eases the transformation, and such a phase occurs during the Li_3PO_4 transformation, why is the $\beta_{II} \rightleftharpoons \gamma_{II}$ transformation apparently irreversible? One possible explanation is that the transitional phase is, in fact, metastable and can only appear monotropically on heating the low phase. This possibility is shown schematically in figure 4. On heating a sample of $\beta_{II}Li_3PO_4$, it follows the free energy curve a-b-c. Beyond point b it is actually metastable: at point c it inverts monotropically to a transitional phase. On further heating, the transitional phase becomes unstable and converts to the equilibrium γ_{II} phase. However, on cooling the γ_{II} phase, it follows the curve e-b-f: beyond point b, γ_{II} becomes metastable relative to β_{II} but no apportunity arises for the formation of a transitional phase, and a large kinetic barrier is created which favors the metastable preservation of the γ_{II} phase.

4. DERIVATIVE Li_3PO_4 STRUCTURES: $Li_2M^{2+}XO_4$ PHASES

4.1. INTRODUCTION

A number of compounds have been prepared which have one, or both, the γ_{II} and β_{II} structure types. These include substances where M^{2+} = Mg, Zn, and Co, and where X = Si^{4+} and Ge^{4+}. In all cases where both γ and β polymorphs can be prepared from the same composition, the β-type phases are stable at the lower temperatures; the polymorphisms of these compounds are summarized in figure 2. Phases of the type Li_2MXO_4 need not conform to this exact stoichiometry, and the polymorphism of the derivative structures is, in fact, very sensitive to the stoichiometry. A fuller explanation of the crystal chemistry of these derivatives and the stability of their various polymorphs, including the effects of changing composition, temperature of preparation, and rate of cooling to ambient, can only be given in terms of the phase diagram for the appropriate system.

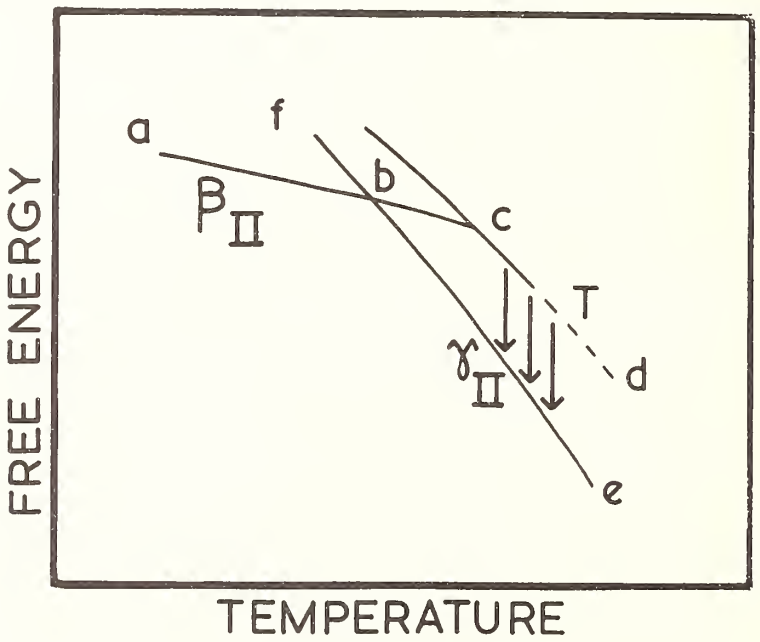

Fig. 4. Schematic temperature - stability relations for the polymorphism of Li_3PO_4 showing the postulated monotropic formation of a metastable T (= transitional) phase on heating low (β_{II}) Li_3PO_4. This T phase transforms irreversibly to γ_{II} (high) Li_3PO_4 on prolonged heating at *ca* 600° - 700 °C (shown by vertical arrows).

4.2. THE SYSTEM Li_4SiO_4-Zn_2SiO_4

4.2.1. PHASE EQUILIBRIA

The phase diagram of this system is shown in figure 5. It was determined by a combination of classical quenching methods and direct, high-temperature investigation [10]. Li_4SiO_4 can accept a considerable amount of zinc into solid solution, but no detectable solid solution of lithium in zinc orthosilicate occurs. Li_2ZnSiO_4 is a congruently melting 1:1 phase and both β- and γ-type polymorphs occur at this ratio. The most remarkable feature of the diagram is the very wide range of solid solutions formed by the γ_{II} polymorph. At 900 °C, the range of single-phase formation extends from approximately 21 to 72 mol % Zn_2SiO_4. At higher temperatures, the zinc-rich limits of solid solution continue to expand but it becomes more difficult to fix accurately the lithia-rich limits, owing to the increasing volatilization of lithia from the sample. It is possible that the narrow two-phase gap, which at 900 °C separates the fields of γ_{II} solid solutions from those of Li_4SiO_4, closes over at higher temperatures, such that complete subsolidus miscibility extends from Li_4SiO_4 to *ca.* 75 mol % Zn_2SiO_4. The extensive solid solution in this system, even at low temperatures, is much larger than any previously reported in other comparable orthosilicate systems.

4.2.2. CHARACTERIZATION AND CRYSTAL CHEMISTRY OF THE ORTHOSILICATE SOLID SOLUTIONS

The x-ray d-spacings of γ-phase solid solutions ranging in comparison from 25 to 71.5 mol % Zn_2SiO_4, have been measured at 700 °C. The end-member compositions mark the approximate limits of homogeneous, single-phase formation at 700 °C and this is also the lowest temperature at which the entire range of solid solutions can be held, without decomposition, for a length of time sufficient to obtain an x-ray pattern. Figure 6 shows the variation in unit cell dimensions with composition of the γ_{II} solid solutions at 700 °C The *c*-dimension remains nearly constant throughout; *a* and *b* change little in the lithia-rich solid solutions but show a more rapid rate of change beyond 50% Zn_2SiO_4. The calculated cell volume of Li_2ZnSiO_4 increases slightly with both lithium and zinc substitution. It is thought that the oxygen array remains unchanged throughout the solid solution series and

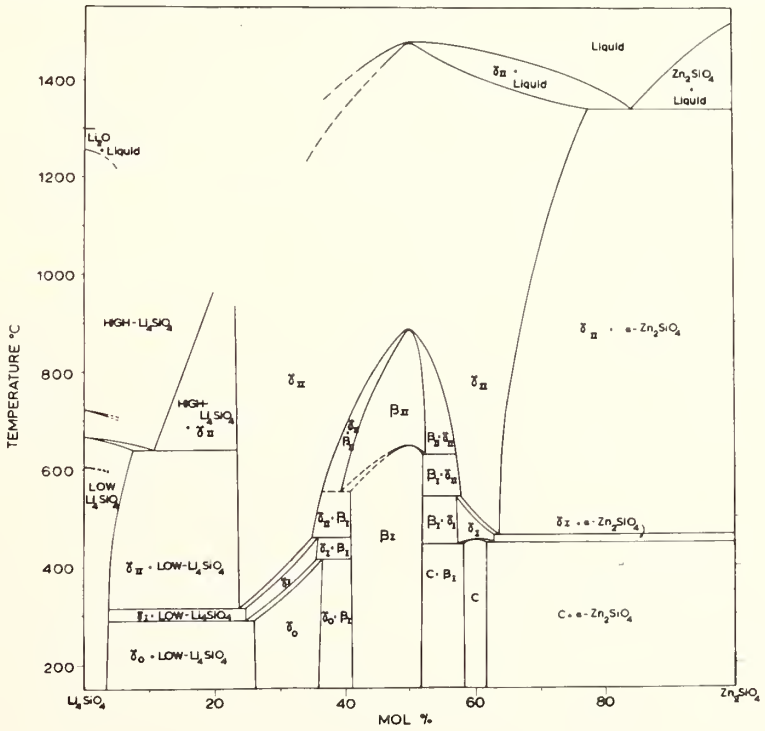

Fig. 5. Phase equilibria in the system Li_4SiO_4-Zn_2SiO_4. The data are taken from reference [10].

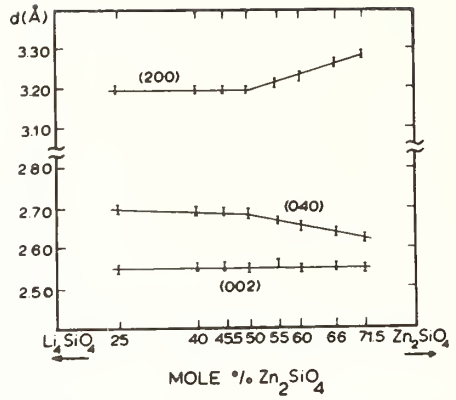

Fig. 6. Variation in the *a*, *b* and *c* unit cell dimensions of the γ_{II} lithium zinc silicates as a function of composition, at 700 °C. The data are taken from reference [10].

that the variable lithium-zinc ratios are achieved by introduction of cation vacancies in the zinc-rich members, and by cation-stuffing in the lithia-rich members. Thus, if the unit cell formula at the 'ideal' ratio is: Li_2ZnSiO_4, substitution of zinc for lithium introduces cation vacancies until, at 75 mol % Zn_2SiO_4, the solid solution has the formula: $(\square\ {}_2Li_4Zn_2)\ (Zn_4)\ Si_4O_{16}$ where $\square$ represents a cation vacancy. On the other hand, the lithia-rich solid solutions substitute two lithiums for one zinc, so that at 25% Zn_2SiO_4, the solid solution composition would be: $(\bigcirc\!\!\!\!\text{Li})_2\ (Li_8)\ (Zn_2Li_2)\ Si_4O_{16}$ where $\bigcirc$ refers to a site, which is unoccupied in solid solutions containing > 50% Zn_2SiO_4, but which is gradually filled in the lithia-rich solid solutions. Li_4SiO_4 may be regraded as the end-member of this stuffing process. Its crystal structure is known [11], and at ambient temperatures it can be regarded as a distorted Li_3PO_4 type structure in which the extra lithiums are stuffed into five and six coordinated sites. With rising temperatures, Li_4SiO_4 undergoes a series of minor phase transformations, until the high form, stable above *ca.* 720 °C, is obtained. Judging by the similarities between HTXR photographs of high Li_4SiO_4 and γ_{II}, high Li_4SiO_4 is probably even more similar to the γ_{II} phase than is low Li_4SiO_4. This similarity in powder patterns, especially at higher temperatures, lends support to the view that, at temperatures just below the solidus, it would be possible for the two-phase gap between Li_4SiO_4 solid solutions and γ_{II} solid solutions to disappear.

4.2.3. LOW-TEMPERATURE PHASE TRANSFORMATIONS

At lower temperatures, several types of phase change may occur. At equilibrium, γ_{II} Li_2ZnSiO_4 and a small range of solid solutions convert to the β_{II} phase. The inversion temperature passes through a maximum at the 50% composition, at which composition the conversion is also kinetically most rapid. At still lower temperatures, the β_{II} phase inverts to another closely related phase, designated β_I, which is a distorted, low Li_3PO_4 derivative structure. Under certain conditions, the $\beta_I \rightleftharpoons \beta_{II}$ inversion passes through an intermediate phase designated β_{II}' which can be quenched to ambient. This β_{II}' phase is closely related in structure to β_{II} Li_2ZnSiO_4, its powder pattern differing only in slight splittings of certain reflections. The nomenclature used is chosen so that Roman subscripts denote patrials, or members of a particular structural family. Where it has been possible to study phase transformations between patrials, these are usually second-order, or have some second-order continuous character: these transformations are characteristically rapid and are often non-quenchable. Thus, the γ_{II} solid solutions undergo various structural distortions on cooling to yield other γ- patrial phases. The more lithia-rich members, for example at 30% Zn_2SiO_4, convert to the patrials designated γ_I and γ_o. At more zinc-rich compositions, typically, 60% Zn_2SiO_4, progressive cooling of γ_{II} solid solutions yields first a γ_{II} and then a new phase, designated phase C. Phase C appears to be structurally related to Li_3PO_4, but has a characteristic Li_2O:ZnO ratio in the region 1:2 to 2:3.

Two general principles serve as a guide to the type of non-equilibria which can arise on cooling. One principle is that any reaction requiring conversion of a γ- patrial phase to a β- patrial will be comparatively sluggish. If a phase fails to convert at an equilibrium transition temperature it may instead follow a metastable pathway which subsequently leads to its undergoing one or more metastable inversions. Nevertheless the results obtained by cooling samples from *ca.* 900 °C at 1-10 °C min^{-1} are so consistent and are so reversible on reheating, that they can be presented as a quasi-equilibrium diagram [12]: this is shown in figure 7. At higher temperatures, where equilibrium is attained more rapidly, the sequence of phase transformations tends to become indistinguishable from those which are shown on the equilibrium diagram (fig. 5), but at lower temperatures, the sluggishness of the $\gamma_{II} \longrightarrow \beta_{II}$ conversion allows the γ- patrial phases to appear metastably across the central region of the diagram. The $\gamma_O \rightleftharpoons \gamma_I$ and $\gamma_I \rightleftharpoons \gamma_{II}$ inversion temperatures also pass through a thermal maximum at the Li_2ZnSiO_4 composition.

The second principle is that equilibrium reactions requiring the exsolution of an initially homogeneous solid solution tend to be sluggish. Quenching of more zinc-rich compositions causes a γ_{II} phase to enter a region where it is metastable with respect to the two-phase assemblage (γ_{II} solid solution plus willemite); at lower temperatures, this undercooled γ_{II} phase inverts to a metastable C-family patrial, designated C'. Another example occurs in more lithia-rich compositions; for example at 16% Zn_2SiO_4 cooling of Li_4SiO_4 solid solutions yields a new lithia-rich phase, designated phase D, which is structurally-related to Li_4SiO_4 and is presumably a more distant relative of the Li_3PO_4 structure types. Powder x-ray data for these phases, as well as more details of their preparation can be found in the references [10,12]. The combinations of metastable and stable phase transformations tend to produce complicated patterns of thermal activity in DTA runs; a few of these sequences have been described in detail [12]. It is also noteworthy that the equilibrium phase relationships cannot, in general, be determined from an analysis of the phases present in runs "quenched" to ambient: it is necessary to use a combination of direct, high-temperature methods (DTA, HTXR) to account for the phase distributions observed at ambient.

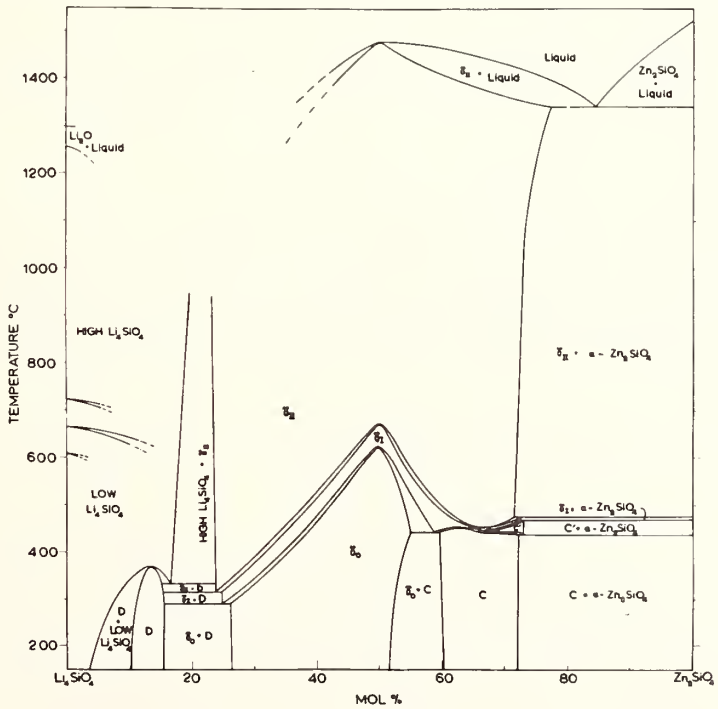

Fig. 7. Phase non-equilibrium diagram representing the sequences of transformations encountered in Li_4SiO_4-Zn_2SiO_4 compositions upon cooling from the liquid, or from solidus temperatures, at moderately slow rates ranging from approximately 2 to 20 °C min^{-1}. The data are taken from reference [12].

Single crystals of most of the low-temperature phases can generally be prepared by conversion of a 'high' solid solution having the appropriate composition. In several cases where these crystals have been examined at ambient, the crystals exhibit complex twinning: this has tended to discourage single crystal x-ray studies. In general, the low-temperature ordering of the solid solutions prepared initially at higher temperatures, bears a phenomenological resemblance to that which occurs in many complex alloy systems. The analogy is strengthened because certain solid solutions which are unable for kinetic reasons to undergo inversion to the stable phase or phases, instead undergo martensitic phase transformations. The formation of phase D from Li_4SiO_4 solid solutions and phase C' from γ_{II} solid solutions are examples of this.

4.2.4. MECHANISM OF THE $\gamma_{II} \longrightarrow \beta_{II}$ TRANSFORMATION IN Li_2ZnSiO_4

Evidence has been presented showing that Li_3VO_4 and Li_3AsO_4 transform from γ_{II} to β_{II} modifications via an intermediate phase. Each of the transformations, $\gamma_{II} \rightleftharpoons T$ and $T \rightleftharpoons \beta_{II}$, approximates to first-order. However, in the various derivative structures, the $\beta_{II} \rightleftharpoons \gamma_{II}$ transformation proceeds in different ways. The $\gamma_{II} \rightleftharpoons \beta_{II}$ inversion for Li_2ZnSiO_4 has a different mechanism to that for $\gamma_{II} \longrightarrow \beta_{II}$ Li_3VO_4. Thus, in one experiment, a homogeneous γ_{II} Li_2ZnSiO_4 preparation was cooled to ambient from 1100 °C over a period of 4 hours. The x-ray powder pattern showed that it contained a mixture of β- and γ- type phases at ambient, indicating that partial conversion of the γ phase to β had occurred. A peculiar feature of the powder pattern of this partially converted product is the appearance of the (002) reflections. Corresponding (002) reflections of the β and γ phases, are normally clearly resolved in well-crystallized mixtures of the two phases, but in the partially converted product the two reflections are connected by a continuous band of diffuse radiation, upon which are superimposed two sharp reflections, one of the β, the other of the γ phase. This phenomenon has been interpreted in terms of coherent growth during the cooling, of β crystallites within the host γ-phase crystals. The extra diffuse reflection band is attributed to disordered or strained regions at or close to the interface. A number of specimens have been examined which differ principally in their degree of conversion In this series of powder photographs, the relative intensities of the sharp portions of the (002) reflections varies, as would be expected, with the relative proportions of γ- and β- phases which are present, but the intensity of the diffuse band always remains approximately constant so long as both the starting phase (γ) and its conversion product (β) are both present.

The reaction apparently proceeds in the reverse direction - that is, $\beta \longrightarrow \gamma$ - in one step. A high-temperature x-ray photograph, taken on heating, showed β converting slowly to γ. The reaction was slow, taking several hours to complete, although the furnance temperature was allowed to rise slowly during the course of the experiment. The powder pattern thus obtained was characterized by a gradual weakening of the (002) reflections of the β phase while the (002) reflections of the γ phase became more intense. Each (002) reflection remained sharp and no intermediate diffuse zone was noted.

These observations show that the $\beta_{II} \rightleftharpoons \gamma_{II}$ transformation in Li_2ZnSiO_4 is not ideally reversible, and provide some support for the suggestion that the γ_{II} phase transforms to β_{II} by a nucleation and coherent growth mechanism.

4.2.5. MECHANISM OF THE $\gamma_{II} \rightleftharpoons \beta_{II}$ TRANSFORMATION IN OTHER Li_2MXO_4 PHASES

A few experiments have been done to find out the mechanism of the $\gamma \rightleftharpoons \beta$ transformation for other derivative phases. Li_2CoSiO_4 transforms in the same way as does Li_2ZnSiO_4. On heating the β_{II} phase the conversion to γ_{II} apparently takes place in one step, but upon slow cooling of γ_{II}, the (002) reflection of β_{II} gradually appears, and the (002) reflections of the two phases are again connected by a diffuse scattering region which persists throughout the transformation. In Li_2MgGeO_4, however, the transformation between β_{II} and γ_{II} proceeds reversibly through a separate intermediate phase, which may be the thermodynamically stable phase over a short range of temperatures close to 1000 °C. This transitional Li_2MgGeO_4 phase is probably isostructural with $T_{II}Li_3VO_4$.

4.3. THE SYSTEM Li_4SiO_4-Mg_2SiO_4

Phase relations in this system, shown in figure 8, were studied by the same techniques as were used for studying the Li_4SiO_4-Zn_2SiO_4 system [13]. The magnesium system bears a considerable resemblance to the zinc system, except that the stoichiometry of the magnesium-containing γ solid solution is more restricted at any temperature chosen for comparison. Also, no β-patrial phases have ever been obtained in this system. Hydrothermal experiments made in the hope of producing a β-patrial phase at the Li_2MgSiO_4 composition yielded negative results, although β solid solutions containing up to 80 mol % Li_2MgSiO_4 can be prepared along the join Li_2ZnSiO_4-Li_2MgSiO_4. Apparently, some zinc is essential to the stability of the β-type phase.

The D-patrial phases, which could only be obtained metastably in Li_4SiO_4-Zn_2SiO_4 compositions, can be obtained at equilibrium for a range of Mg-containing compositions.

5. SUBSTITUTION OF TRIVALENT IONS IN $Li_2M^{2+}XO_4$

Trivalent ions such as aluminum and gallium may be substituted, often in substantial quantities, in these structures. In all cases where solid solution was found to occur, the M^{3+} ion substitutes for $(Li^+ + M^{2+})$, rather than by substitution of two M^{3+} ions for $(M^{2+} + X^{4+})$. Thus, the solid solutions have the formula: $Li_{2-n}M^{2+}_{1-n}M^{3+}_nXO_4$, where n is the number of trivalent ions per formula unit. Table 1 shows the quantitative extent of these solid solutions, at 1000 °C, for the various combinations tried. Compositions on the join Li_2MgSiO_4-$LiAlSiO_4$ did not yield a γ-phase solid solution: instead large quantities of lithium spinel formed. Thus the solid solution of Al in Li_2MgSiO_4 is probably negligible. On the other joins, solid solutions range upwards from *ca.* 5% of $LiAlGeO_4$, or $LiGaGeO_4$ in Li_2ZnGeO_4, to *ca.* 25% of $LiGaSiO_4$ in either Li_2ZnSiO_4 or Li_2MgSiO_4. Apparently, the most favorable substitutions are those where gallium replaces either (Li + Mg) or (Li + Zn) in a silicate phase or where either aluminium or gallium replace (Li + Mg) in a germanate phase.

It is not possible from these few experiments to say whether the solid solutions are compatible with the end-members of the replacement series, $LiM^{3+}XO_4$.

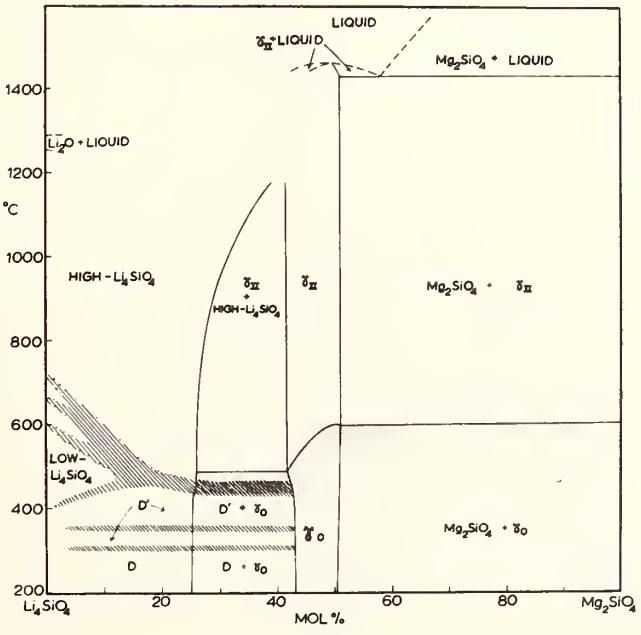

Fig. 8. Phase equilibria in the system Li_4SiO_4-Mg_2SiO_4. The data are taken from reference [13].

TABLE 1

Solid Solution of M^{3+} Ions in $Li_2M^{2+}XO_4$ Phases

System	Extent of Solid Solution at 1000 °C
Li_2ZnSiO_4-$LiAlSiO_4$	10 ± 5%
Li_2ZnSiO_4-$LiGaSiO_4$	25 ± 10%
Li_2ZnGeO_4-$LiAlGeO_4$	5 ± 5%
Li_2ZnGeO_4-$LiGaGeO_4$	5 ± 5%
Li_2MgSiO_4-$LiAlSiO_4$	0 ± 5%
Li_2MgSiO_4-$LiGaSiO_4$	25 ± 10%
Li_2MgGeO_4-$LiAlGeO_4$	20 ± 10%
Li_2MgGeO_4-$LiGaGeO_4$	20 ± 10%

6. OCCURRENCE OF Li_3PO_4 - TYPE PHASES IN MORE COMPLEX SYSTEMS

The interactions between the three orthosilicates: Li_4SiO_4, Mg_2SiO_4 and Zn_2SiO_4 have been studied [13], and it was found that an extensive range of ternary orthosilicate solid solutions having the β or γ type structures occur. The extent of this solid solution and the occurrence of β or γ phases is very temperature dependent. Figure 9 shows the appearance of one such isothermal section at 700 °C.

The distribution of Li_3PO_4 - derivative phases in yet more complex systems has received some study. Data on the quaternary system Li_4SiO_4-Zn_2SiO_4-Mg_2SiO_4-SiO_2 show that at subsolidus temperatures, all compositions, even those highest in silica, will contain a Li_3PO_4 - type phase on equilibrium crystallization [14].

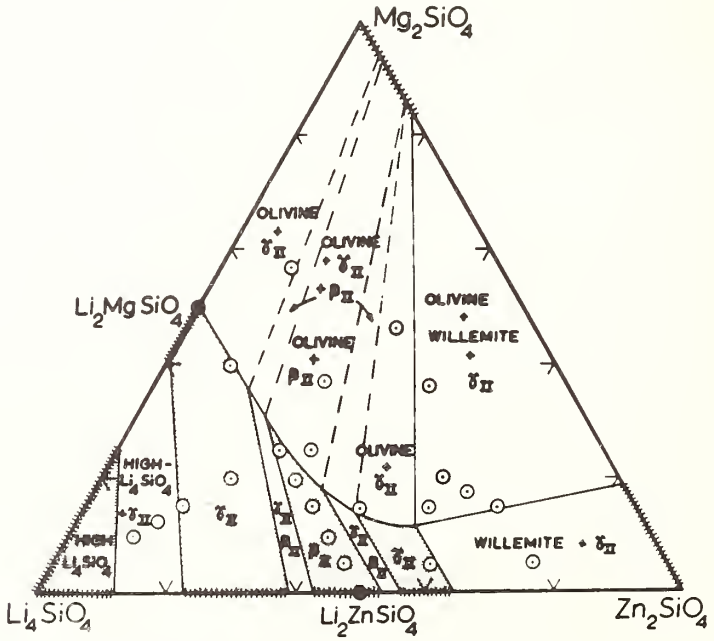

Fig. 9. Phase equilibria in the system Li_4SiO_4-Zn_2SiO_4-Mg_2SiO_4 : the 700 °C isothermal section. The data are taken from reference [13].

7. REFERENCES

[1] Keffer, C., Mighell, A., Mauer, F., Swanson, H., and Block, S., Inorg. Chem., 6, 119 (1967).
[2] Zemann, J., Acta. Cryst., B13, 863 (1960).
[3] Zambonini, F., and Laves, F., Z. Krist., 83, 26 (1932).
[4] Matias, W. S., and Bondareva, A. M., Dokl. Akad, Nauk, S. S. S. R., 112, 124 (1957).
[5] Fischer, D. J., Amer. Miner., 43, 761 (1958).
[6] Tarte, P., J. Inorg. Nucl. Chem., 29, 915 (1967).
[7] Swanson, H. E., Morris, M. C., and Evans, E. H., "Standard X-Ray Diffraction Powder Patterns", Sect. 4, p. 21, National Bureau of Standards, Washington, D. C., monograph No. 25, (1966).
[8] West, A. R., and Glasser, F. P., J. Solid State Chemistry, 4, 20 (1972).
[9] Reisman, A., and Mineo, J., J. Phys. Chem., 66, 1181 (1962).
[10] West, A. R., and Glasser, F. P., J. Mater. Sci., 5, 557 (1970).
[11] Vollenkle, H., Wittmann, A., and Nowotny, H., Monat. Chem., 99, 1360 (1968).
[12] West, A. R., and Glasser, F. P., J. Mater. Sci., 5, 676 (1970).
[13] West, A. R., and Glasser, F. P., J. Mater. Sci., 6, 1100 (1971).
[14] West, A. R., and Glasser, F. P., J. Mater. Sci., in press.

DISCUSSION

R. S. Roth: I'm wondering if these compounds don't have some water in them that might account for some of the strange polymorphic behavior and/or some of the non-stoichiometry. Do you have any way to prove or disprove this?

F. P. Glasser: Well, of course it is always very difficult to disprove the existence of water in a compound, but in the course of doing the experiments on lithium vanadate we certainly did do quite a few weight change measurements and there was no evidence of any water pickup. We have also done some infrared work on these compounds, which time does not permit me to describe, and there was no evidence of any hydroxyl content in them. Also, in many instances the temperatures of preparation were very high, 1300 or 1400 °C in a few instances. I would think the evidence is very reasonable that there is no essential content in any of these phases. It is possible that some of the annealing variants which we described might have picked up water during the long annealing at low temperatures. However, some of these experiments were duplicated in sealed silica tubes in an attempt to check this and they gave identical results.

W. R. Cook: There is a very great similarity between the low and high temperature lithium phosphates in their structure, which doesn't really seem to require intermediate phases. I was wondering if you had any information on why, in fact, you get the intermediate phases.

F. P. Glasser: Yes, we had speculated why these intermediate phases arose. Let me describe the structures very briefly for those who aren't conversant with them. The oxygens in both phases are hexagonally close packed and all cations both lithiums and silicons are in tetrahedral sites. But comparing the two structures, half the lithiums and half the silicons are in different sites. We speculated that the transitional forms arise because of motions of one set of atoms before the other set begin to move. This would, of course, require a structure determination of one of the intermediate forms to prove this speculation. As most of the people who have worked on lithium phosphate, lithium vanadate and so on will tell you, the crystals tend to have a high proportion of twins. Many of the crystals of the related silicate phases also have very complicated internal phase domain structures. These have greatly handicapped single crystal investigations. So, at the moment we are reduced to speculation as to why the transitional forms arise.

I might add that with respect to both questions, I think that all of these oxide systems, when investigated in more detail, are going to turn out to be very complicated. They are going to turn out to be just as complicated as metal alloy systems. I think these intermediate phases and transitional phases will more and more be discovered.

National Bureau of Standards Special Publication 364, Solid State Chemistry, Proceedings of 5th Materials Research Symposium, issued July 1972.

ON THE SOLIDIFICATION TEMPERATURE AND THE NONSTOICHIOMETRY OF COBALTOUS OXIDE IN AN OXIDIZING ATMOSPHERE

J. P. Coutures and M. Foex

Centre National de la Recherche Scientifique
Laboratoire des Ultra Refractaires
B. P. No. 5 - 66 - ODEILLO
France

Liquid cobaltous oxide can dissolve a large amount of oxygen depending on temperature oxygen partial pressure and time. Therefore, the solidification temperature decreases when the amount of oxygen in the liquid phases increases. During solidification, a "spitting" phenomena occurs. The behavior (spitting phenomena for example) and the properties of this oxide (solidification temperature, melt composition, solid composition) are studied by high temperature techniques.

Key words: $CoO-O_2$ system; melting point depression; nonstoichiometry in liquid CoO; solar furnace; thermal analysis.

1. EXPERIMENTAL

In the course of the present study, thermal analysis, thermomanometric, and thermogravimetric, apparatus are used and in each case the oxygen potential in the gaseous phase is determined by gas chromatography.

The thermal analysis apparatus (fig. 1), previously described by Foex and Coutures [1][1] is used in conjunction with an horizontal axis solar furnace. Controlled atmosphere is obtained by the interposition of a silica tube (A) between the centrifugal furnace (B) at the focus of the parabolic mirror. The optical pyrometer works in the visible region (0.65μm). Melting is maintained for ten minutes in order to obtain thermodynamical equilibrium between the melt and the oxygen partial pressure of the atmosphere. The volume of the centrifugal furnace (cooled cooper) is 10 cm^3. The dimensions of the cobaltous oxide crucible are: diameter 8 mm, length 23 mm.

Figure 2 shows different cooling curves of cobaltous oxide melted under: A) mixed gas, 20% argon - 80% oxygen, B) mixed gas, 40% argon - 60% oxygen, C) pure argon. It is evident that only the product melted under pure argon gives a good solidification plateau corresponding to a stoichiometrix oxide (solid composition $\frac{O}{Co} = 1{,}000$). For the other cases, at the end of the solidification, there is a thermal arrest corresponding to the spitting phenomena. As an example, figure 3 gives a view of the spitting phenomenon that occurs at the end of the solidification of cobaltous oxide molten under a pure oxygen atmosphere. The projections (spitting) are the cause of the thermal arrest on the thermal analysis curves.

A schematic diagram of the thermomanometric apparatus [2] (built in our laboratory) associated with the vertical axis solar furnace is shown in figure 4. The product is melted on a small water cooled copper plate which is surrounded by two silica vessels containing water. The change of the pressure inside the vessel, at the solidification point is measured by a differential pressure transducer and recorded by a high speed recorder [3]. The response time of the complete data acquisition system is 2 milliseconds.

---

[1] Figures in brackets indicate the literature references at the end of this paper.

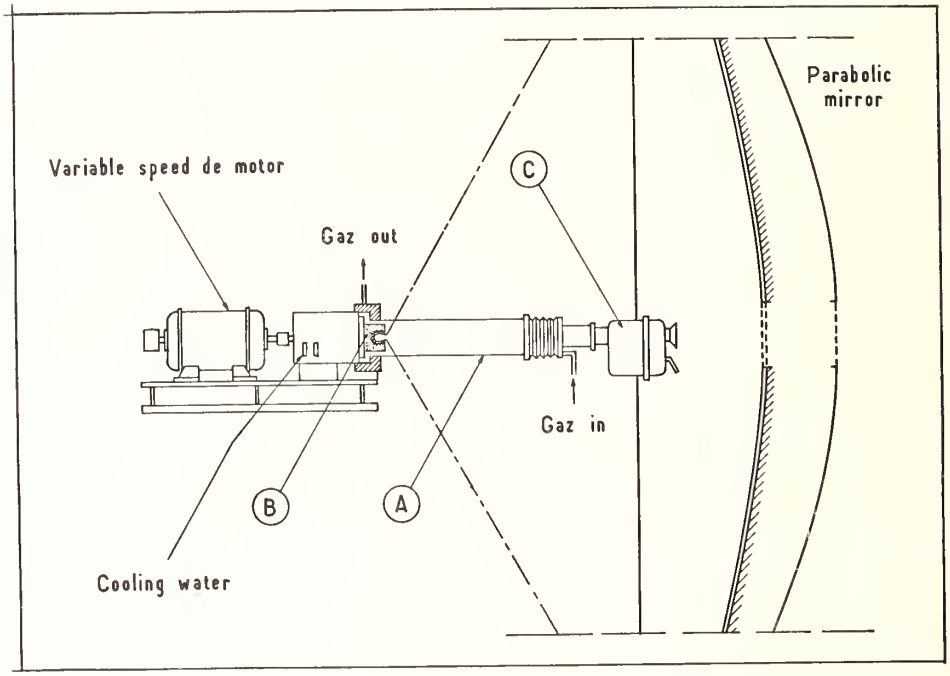

Fig. 1. Thermal analysis apparatus for controlled atmosphere. A - silica tube, B - sample, C - optical pyrometer.

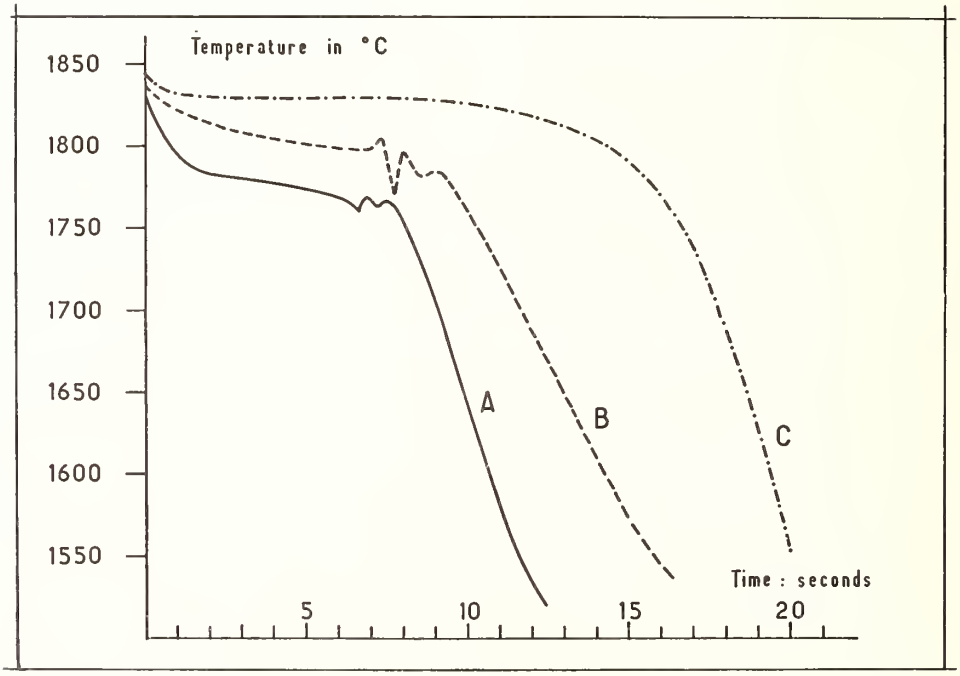

Fig. 2. Cooling curves of cobaltous oxide after melting under: A - mixed gas 20% A - 80% O_2; B - mixed gas 40% A - 60% O_2; C - pure argon.

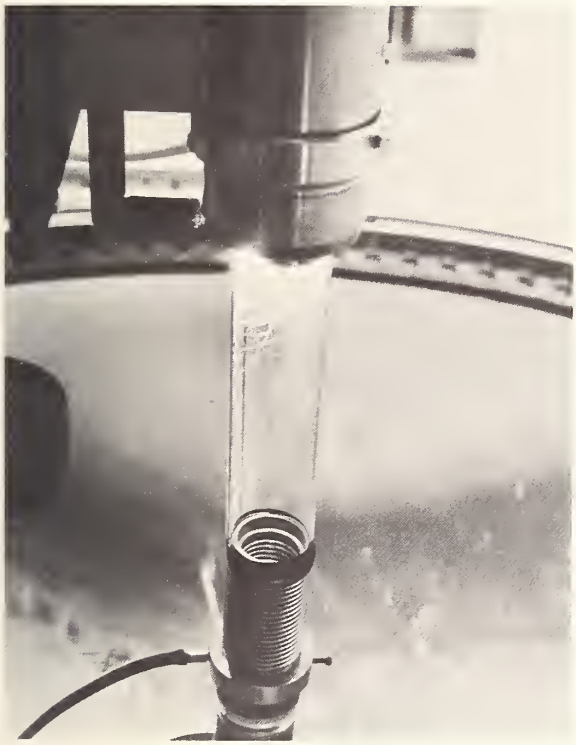

Fig. 3. View of the spitting phenomena occurring at the solidification of CoO after melting in pure oxygen.

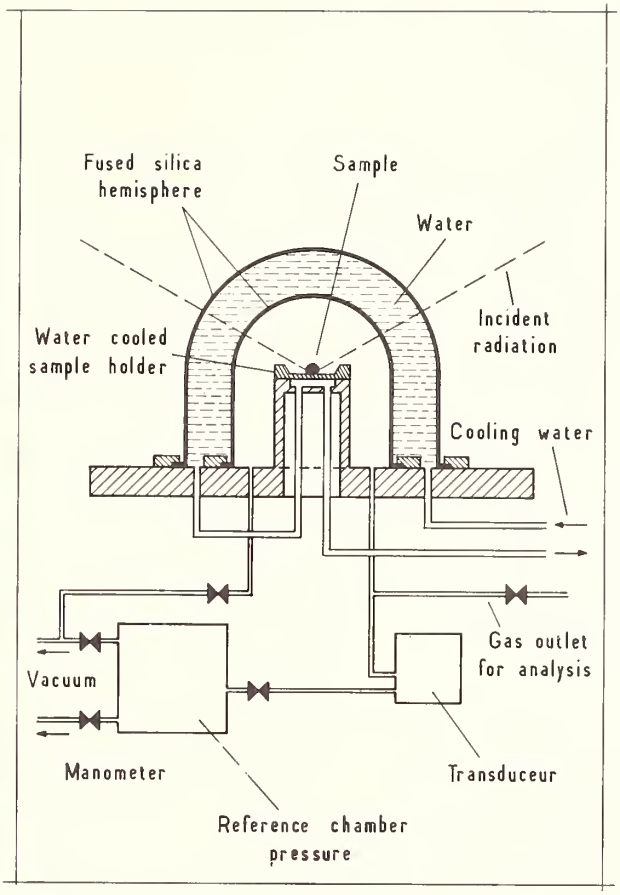

Fig. 4. Schematic drawing of the thermomanometric apparatus associated with a vertical axis solar furnace.

Solidification of the sample is obtained through a variable speed DC motor by vertical translation of the measurement head in the solar heating cone. In such a way the liquid phase can be cooled at different speeds in the range of 1 °C/sec to 250 °C/sec. Figure 5 shows the pressure change at the solidification of cobaltous oxide melted under pure oxygen (weight: 230 mg; time of fusion: 1 minute; atmosphere: pure oxygen at 0.83 atm; cooling speed of the liquid phase: 250 °C/sec). One can note the beginning of the solidification and the plateau due to the evolved oxygen. The final peak is caused by the many thermal effects linked to the spitting [3]. With the help of calibration curves we can calculate the volume of evolved oxygen and the composition of the melt just before the solidification.

Thermogravimetric data, figure 6, are obtained by a high temperature thermobalance manufactured by SETARAM (Lyon-France). This apparatus is composed of an automatic recording balance with a complete data acquisition chain (weight = f(t) and $\frac{d\,(\text{weight})}{dt} = f\,(t)$ and a high temperature furnace working in oxidizing atmosphere. The graphite heating element of this furnace surrounds the alumina laboratory tube. The composition of the working atmosphere (mixed argon-oxygen) is determined by a gas chromatography; the protection of the resistor is obrained by purified argon flowing through the furnace. The temperature of the molten product, in this case contained in an iridium crucible, is measured by an automatic optical pyrometer working at 0.65µm viewing the crucible through a total reflection prism.

An example of a typical thermogravimetric curve obtained with cobaltous oxide molten under a gas mixture containing 20% oxygen and 80% argon is shown in figure 6. One can note, at the beginning of the melting, the weight increase caused by the solution of oxygen in the liquid phase and the weight loss that occurs at the solidification.

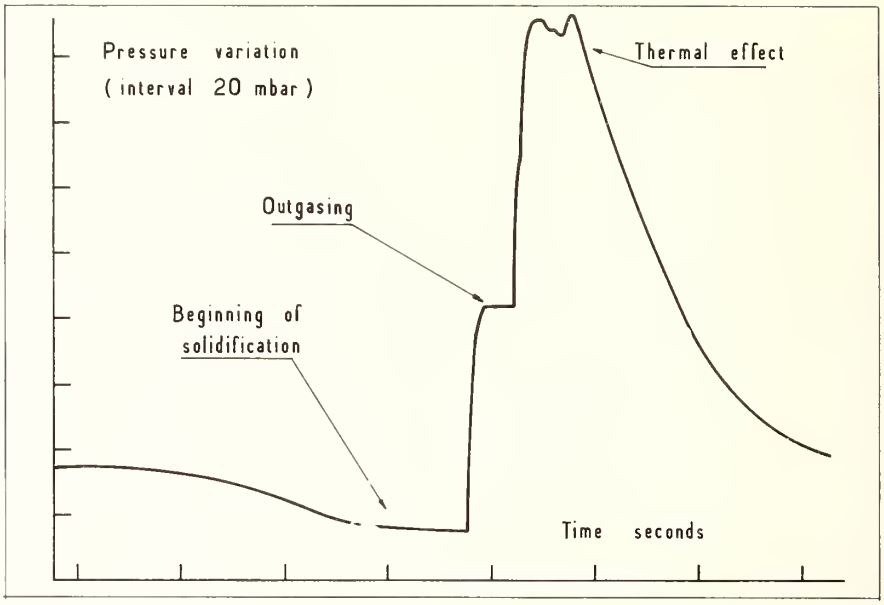

Fig. 5. Pressure variation with time at the solidification of CoO after melting under pure oxygen.

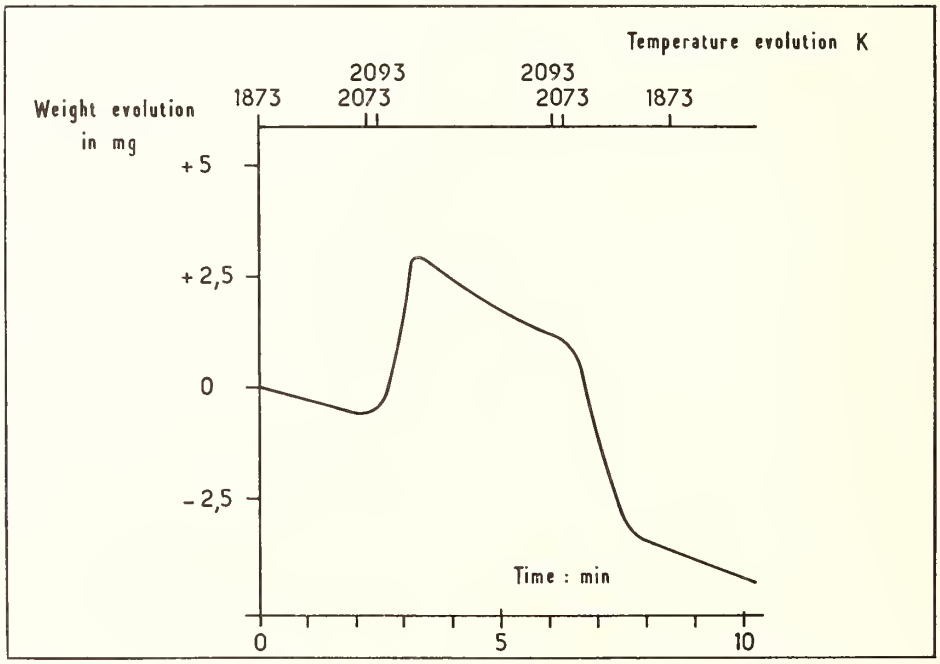

Fig. 6. Thermogravimetric curve showing the solution of oxygen in CoO molten under static atmosphere of 20% oxygen in argon.

2. RESULTS

2.1. INFLUENCE OF THE PARTIAL PRESSURE OF OXYGEN ON THE REFRACTORY CHARACTER OF COBALTOUS OXIDE

By analysis of many cooling curves of cobaltous oxide melted under different oxygen partial pressures one can get some information on the influence of oxygen on the solidification point. We have collected the most important experimental results in table 1, when T is the solidification temperature (IPTS 48), ΔT the depletion of the freezing point (reference: solidification point of cobaltous oxide melted under pure argon), composition of the solid product after melting (ratio $\frac{O}{Co}$) and the nonstoichiometry x for $Co_{1-x}O$ as a function of the composition of the melting atmosphere (mixed oxygen-argon). From these results, one can make the following remarks.

The depletion ΔT of the freezing point is proportionnal to the square root of the partial pressure of oxygen, and this indicates that the oxygen is dissolved in an atomic state.

The solidification temperature of cobaltous oxide versus the oxygen partial pressure is given by the following formula:

$$T_C = 1830 - 40.5\ Po_2^{1/2}$$

(total pressure 0.83 atm, atmospheric pressure of the laboratory).

2.2. INFLUENCE OF THE TEMPERATURE ON THE MELT COMPOSITION

The solution of oxygen for a given partial pressure versus the temperature is studied by means of the thermogravimetric apparatus. To minimize the oxidation of the wire and of the curcible of iridium and also the noise from the flowing gas, the experiment was performed under a static oxidizing atmosphere (mixed oxygen 20% and argon 80%). The temperature range is between 1815 °C and 1885 °C and the pressure is 0.83 atm. The experimental data are collected on figure 7 where the composition of the liquid phase (ratio $\frac{O}{Co}$; O = number of oxygen atoms and Co, the number of Cobalt atoms) is shown versus the temperature. The curve

Table 1

O_2 % del atmosphe	T solidifi	ΔT	$\sqrt{O_2\ \%}$	$\frac{\Delta T}{\sqrt{O_2\ \%}}$	$\frac{(O)}{Co\ sol}$	X	$\frac{X\ 10^3}{\sqrt{O_2\ \%}}$
0	1830	0	0		1.000	0	
10	1820	10	3.16	3.16	1.000	0	
20	1814	16	4.47	3.17	1.002	0.002	0.47
30	1810	20	5.47	3.65	1.005	0.005	0.91
40	1808	22	6.32	3.63	1.006	0.006	0.94
50	1805	25	7.07	3.53	1.008	0.008	1.13
60	1802	28	7.74	3.61	1.009	0.009	1.16
70	1800	30	8.36	3.58	1.010	0.010	1.19
80	1797	33	8.94	3.64	1.011	0.011	1.23
90	1795	35	9.48	3.68	1.012	0.012	1.28
100	1793	37	10	3.70	1.012	0.012	1.20

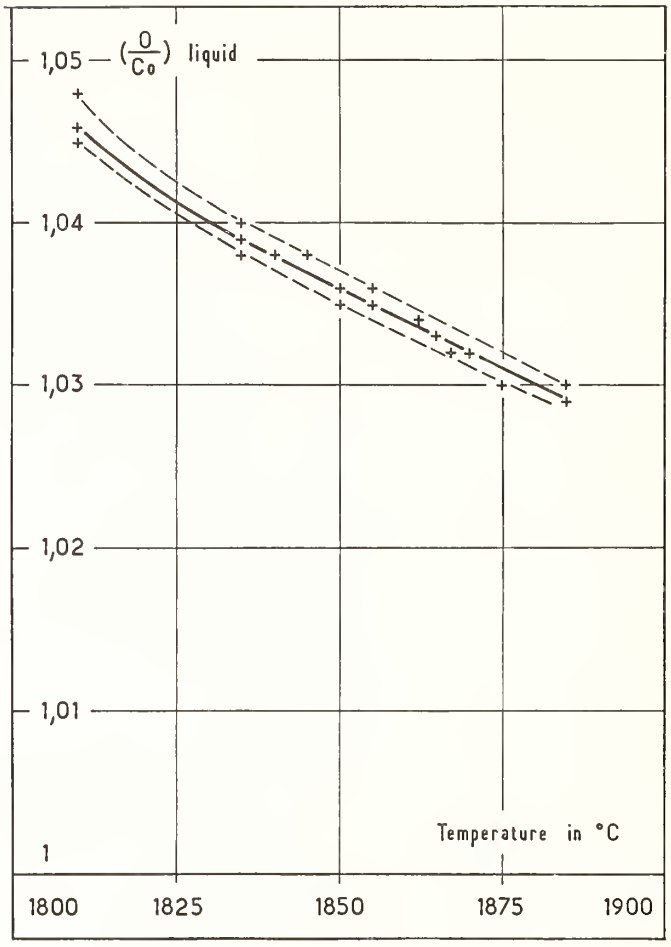

Fig. 7. Change in the ratio $\frac{O}{Co}$ obtained in static atmosphere (20% O_2 in A) with temperature.

of figure 7 shows that, above the melting point, the solution of oxygen in the liquid phase decreases when the temperature increases, which indicates that the heat of the solution reaction is exothermic.

One can note that in such a case the data obtained under static atmosphere are not the true equilibrium values because the solution of oxygen produces a decrease of the oxygen potential near the gas-ligand interface. But, with some improvement, as described previously (3), it is possible to obtain the composition of liquid cobaltous oxide, near the solidification, under an oxygen partial pressure of 0.166 atm. The value is $(\frac{O}{Co})_{liq} = 1.074$.

The data obtained in static atmosphere are however adequate to make some calculations on the enthalpy of the oxygen solution in liquid cobaltous oxide.

2.3. DEPENDENCE OF MELT COMPOSITION ON TIME

Because of the oxidation of the wire and of the crucible in iridium it is impossible to obtain data on the kinetics of oxygen solution in liquid CoO by thermogravimetry. Some qualitative indications are given by thermomanometry, and the results show that the apparent reaction is rapid. In fact, at 2000 °C in pure oxygen, the equilibrium value $(\frac{O}{Co})_{liq}$ is obtained after only 10 seconds of malting. Nevertheless, data on the oxygen desorption are given with argon at low flow as carrier gas. The bath of cobaltous oxide is first saturated by a static gas mixture containing 20% oxygen and 80% argon. Figure 8 shows three thermogravimetric curves (A: 2093 K - B; 2128 K -C; 2153 K). Δm is the weight loss due to the

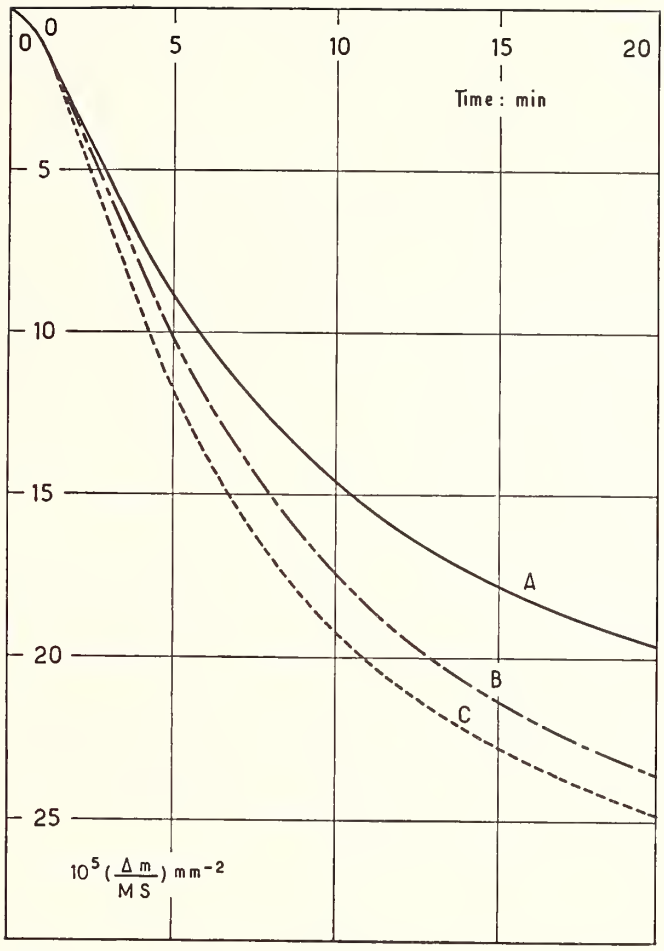

Fig. 8. Thermogravimetric curve obtained for desaturation of cobaltous oxide melts previously saturated in 20% A O_2/A for differents temperatures: A - 2093 K; B - 2128 K; C - 2153 K.

oxygen desorption in mg, M is the weight in mg of the sample, and S in mm^2 the exchange area between the liquid and the gas phase. One can see two steps in the rate of weight loss of the bath. It seems possible that the linear part of the curve is due to the desaturation of the liquid interface, and that the parabolic part is due to the oxygen diffusion in the bath.

2.4. INFLUENCE OF THE LIQUID COOLING SPEED ON THE COBALTOUS OXIDE SOLIDIFICATION, SPITTING PHENOMENON

The thermomanometric apparatus is particularly well adapted for unraveling such a phenomenon, and in this case the experimental conditions are as follows: saturation temperature 2000 °C, melting time: 1 min, oxide weight: 230 mg, atmosphere: pure oxygen at 0.83 atm, range of cooling speed between 1 °C/s and 250 °C/s. Figure 9 shows the experimental results given by these experiments. We have drafted, on curve A, the change in the number of oxygen atoms evolved at the solidification per mol of cobaltous oxide, and on curve B the change in the liquid phase composition just before the solidification. One can see the great influence of the cooling speed on the intensity of the splitting. Table 2 shows the percentage of weight loss of the product versus the cooling speed (in the case of the previously defined experimental conditions).

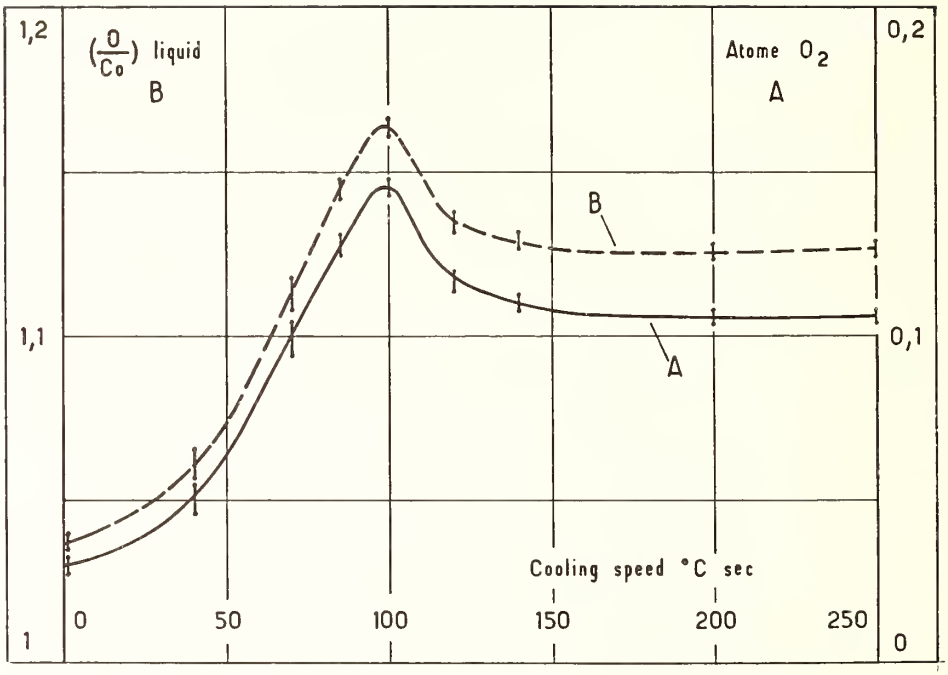

Fig. 9. Evolution of the number of oxygen atoms evolved at the solidification of CoO molten under pure oxygen versus cooling speed. Curve A: the change in the number of evolved oxygen atoms per mole of CoO at solidification. Curve B: melt composition of such a product just before the spitting phenomena.

Table 2

Cooling speed °C/s	250	200	140	120	100	85	70	40	2	1
Weight %	28	26	22	21	17	15	15.5	16	7.5	3

The examination of these results shows that:

- a *true* melt composition for a given saturation temperature is obtained for cooling speeds higher than 150 °C/s
- the mechanical effect (projections) of spitting increases when the cooling speed increases.

2.5. EXAMINATION OF SOLID PRODUCTS

The nonstoichiometry of the products is determined by thermal reduction in hydrogen at 800 °C and knowledge of the thermal history of the liquid. For example, one can see from table 3 the change in composition of solid cobaltous oxide with the cooling speed of the liquid phase (experimental conditions are the same as previously).

Table 3

Cooling speed °C/s	250	200	140	120	100	85	40	2	1
$(\frac{O}{Co})_s$	1.022	1.020	1.019	1.018	1.017	1.014	1.011	1.004	

The nonstoichiometry of the final product increases when the cooling speed increases. After (water quenching) the composition $(\frac{O}{Co})$ (ratio in solid state of the number of atoms of oxygen and to that of cobalt) is 1.044. X-ray analysis, however, does not show any important parameter changes for the above nonstoichiometric cobaltous oxide.

2.6. CONCLUSION OF EXPERIMENTAL RESULTS

On the basis of the experimental results obtained by thermal analysis, thermomanometry and thermogravimetry it is possible to draft, as shown on figure 10 a diagram of cobaltous oxide-oxygen system. The heavy lines represent the liquidus and partail pressure of oxygen. This diagram clearly shows: First: the great importance of oxygen in the atmosphere above the melt and the decrease of the solidification point when the partial pressure of oxygen increases. Second: the exothermicity of the solution of oxygen in the liquid phase, the ratio $(\frac{O}{Co})_{liq}$ decreased when the temperature of the bath increases. Third: the spitting phenomena is to be explained by the great difference of composition between the liquid and the phase at the transition liquid = solid.

3. DISCUSSION OF RESULTS

3.1. KINETICS DATA

It is possible to calculate with the help of Arrhenius equation from the different thermogravimetric curves the apparent activation energy of the two stages occuring during the oxygen desorption. From the slope of the linear curves we obtained

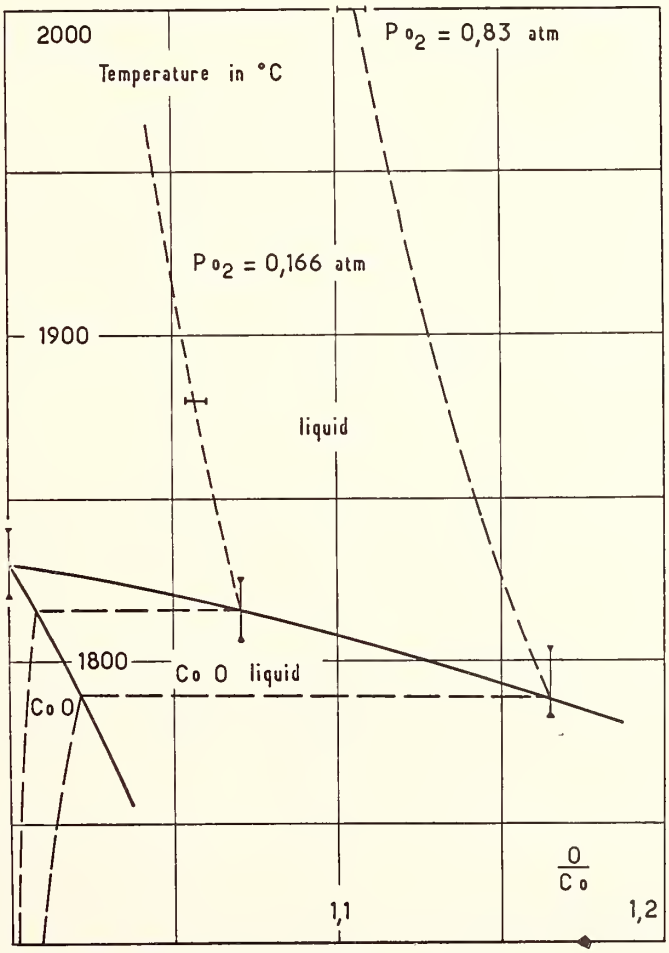

Fig. 10. Diagram of temperature *vs* composition for the system $CoO-O_2$.

E_a	desaturation	51 K cal/mol
E_a	diffusion	72 K cal/mol

3.2. THERMODYNAMICAL APPROACH TO THE OXYGEN DISSOLUTION

The thermomanometric data have shown that the solution is an atomic solution, because the quantity of oxygen evolved at the solidification is a function of the square root of the partial pressure of oxygen in the atmosphere above the melt.

For the calculation of the heat of solution on the assumption of the following equation

$$(O_2)gas = 2\,(O)_{sol}$$

we consider the reference states to be such that

- the gaseous oxygen is under a pressure of one atmosphere
- the dissolved oxygen is an infiniting dilute state.

In that case we can write

$$\frac{d\ Ln\ (o)}{d\ (\frac{1}{T})} = -\frac{\Delta H°}{2R}$$

with $(o) = \frac{no}{n_o + X}$

(O) molar fraction of dissolved oxygen, no the number of dissolved oxygen atoms, X composition of the liquid with all present species except dissolved oxygen.

At that point one must make a remark of great importance. Such a caluclation is impossible with thermomanometric results because of the non thermodynamic equilibrium conditions of the experiments. In the case of saturation by oxygen at 20% in argon $X = n\ CoO$ and n_o is very small with respect to n CoO and consequently we can write $(O) \frac{n_o}{n_{CoO}}$

By measuring the slope of the curve showed on figure 11 we determined the enthalpy of solution of oxygen in liquid cobaltous oxide

$$\Delta H°_{sol} = -\ 103.5\ K\ cal/mol\ O_2$$

In conclusion, one can note great effect of the oxygen on the behavior of cobaltous oxide after melting. For the establishment of correct phase diagrams with this compound, it is necessary to give the nature and composition of the gaseous atmosphere above the melt.

4. REFERENCES

[1] Coutures, J. P., and Foex, M., C. R. Acad. Sci., 267C, 1577 (1968).
[2] Foex, M., and Coutures, J. P., C. R. Acad. Sci., 266C, 796 (1968).
[3] Coutures, J. P., Thesis, Bordeaux, Janvier 1971.

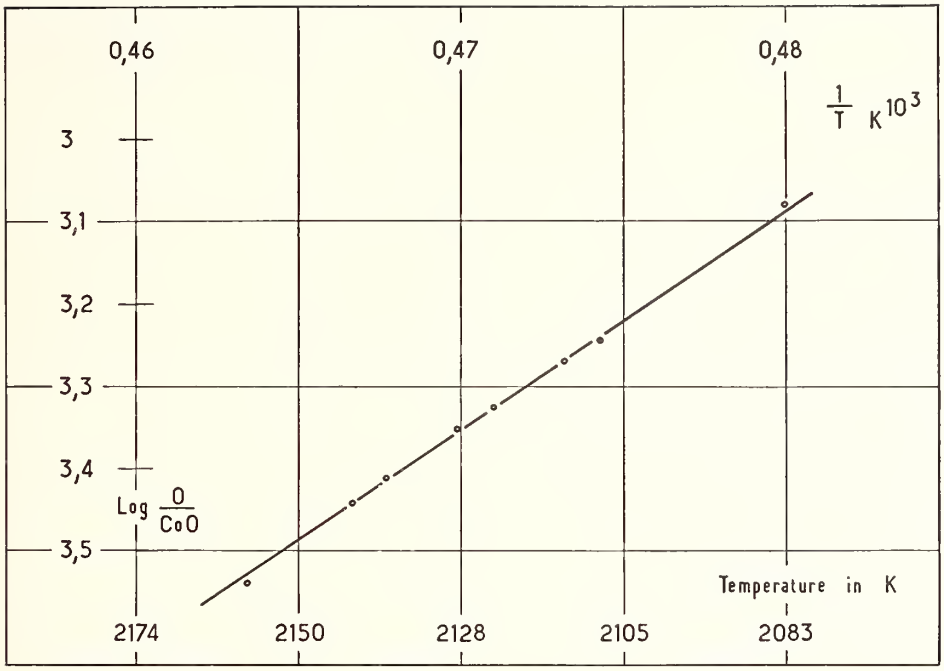

Fig. 11. Ln $\frac{O}{CoO}$ versus the inverse of the absolute temperature.

465-504 O - 72 - 32

National Bureau of Standards Special Publication 364, Solid State Chemistry, Proceedings of 5th Materials Research Symposium, issued July 1972.

THE SYSTEM $FeO-SiO_2-TiO_2$ AT HIGH TEMPERATURES AND HIGH PRESSURES

E. Woermann

Institut fur Kristallographie
Rhein.-Westf. Technische Hochschule Aachen
West Germany

A. Lamprecht

Frankfurt am Main
Germany

ABSTRACT

The investigations of liquidus and solidus relationships in the system $FeO-SiO_2-TiO_2$ in equilibrium with metallic iron at one atmosphere total pressure revealed four ternary invariant points:

1) L = wüstite + fayalite + ulvöspinel (1169° C)

2) L = fayalite + tridymite + ulvöspinel (1145° C)

3) L + ilmenite = tridymite + ulvöspinel (1180° C)

4) L + ferropseudobrookite = tridymite + ilmenite (1254° C)

In the system ferropseudobrookite - tridymite - *rutile* in equilibrium with metallic iron considerable amounts of trivalent titanium are observed at solidus and liquidus temperatures. The titanium bearing phases thus are located outside of the ternary system $FeO-SiO_2-TiO_2$ toward the oxygen deficient side.

At elevated pressures the following reactions occur:

1) Ferropseudobrookite = rutile + ilmenite

2) ulvöspinel + quartz = fayalite + ilmenite

3) fayalite + quartz = ferrosilite

4) ulvöspinel = wüstite + ilmenite

Depending on temperature and pressure the iron titanium phases form limited solid solutions in the system $FeO-SiO_2$, due to the occurrence of defect structures.

II. BORIDES, CARBIDES, SILICIDES, AND RELATED MATERIALS

National Bureau of Standards Special Publication 364, Solid State Chemistry, Proceedings of 5th Materials Research Symposium, issued July 1972.

CARBIDES AND SILICIDES

Hans Nowotny, H. Boller and G. Zwilling

University of Vienna
Vienna, Austria

A brief survey of the structural chemistry of transition element carbides will be presented with emphasis on the problem of carbon-void ordering. The scandium carbides including $Sc_{15}C_{19}$ are to be discussed. Complex carbides which derive from octahedral and trigonal prismatic building elements will be classified. Metal-metal carbides such as VCr_2C_2 and metal-nonmetal carbides such as Ti_3SiC_2, V_4P_2C, Nb_2SC or Ta_2S_2C will be interrelated. The role of nitrogen and hydrogen on the stabilization of complex carbides such as $Cr_3(C,N)_2$ or $Zr_2CH_{0.5}$ will also be treated. Besides the class of typical interstitial carbides, some examples of metal boro-carbides displaying a two-dimensional boron-carbon network will be given (YB_2C). In compounds such as $Cr_2(P,C)$ carbon plays an intermediate role. The present state of the problem of chemical bonding in carbides will be discussed.

Binary metal silicides are numerous and occur almost at any composition. They are commonly classified as valence compounds (electronegative), metal-like silicides (electro-positive) and clathrate silicides (mainly electroneutral). Disilicides and related compounds exhibit a particularly wide occurrence. The continuous change of structural elements and properties of this group will be discussed. So-called defect disilicides of formula T_nSi_{2n-m} (T = transition element) which are derived from the $TiSi_2$ type structure belong to a uniform building principle, where n presents the number of subcells and m the deviation from the disilicide composition. In many cases a relation of the electronic concentration with m can be observed. In general, lowering of the overall electron concentration diminishes the defect m. Single crystal work on $Mn_{27}Si_{47}$ will be described. This phase, a fifth variety having a composition in the vicinity of $MnSi_{\sim 1.7}$, presents the problem of pseudo-homogenous domains. Some ternary silicides such as E-phases will be discussed from the viewpoint of ordered structures.

Key words: Carbides; chemical bonding; defect structures; interstitial compounds; ordering; silicides.

1. INTRODUCTION

With regard to the large number of review articles [1-7][1] it appears to be questionable to add another to this subject. The main problems are still unchanged; *e.g.*, the lack of a breakthrough concerning the theory of bonding, particularly as the transition element carbides are concerned. Hence the predictibility of stable solid compounds for binary and multicomponent systems is still uncertain and even the method of classification of phases is not consistent.

2. CARBON AND SILICON

The striking structural similarity known for carbon in the diamond forms (cubic or hexagonal) and silicon (cubic or hexagonal) disappears more or less with metal carbides and the homologous silicides. The main reason for this is due to the size factor. The silicon atom is considerably larger than the carbon atom evaluated for a neutral state. The same is true for the silicon-metal size ratio as compared to the carbon-metal size ratio. Furthermore

[1] Figures in brackets indicate the literature references at the end of this paper.

there is quite a difference in electronegativities. The position of the 3d-level may also occasionally separate the bonding system in silicides from analogous carbides. It is significant to note that the individual features for SiC polytype modifications are equal to a large extent, obviously favored by the strong valence influence of directed sp^3 bonds, thus obeying the octet rule and not violating a critical radii ratio for tetrahedral structures.

3. BINARY CARBIDES

Very early it was recognized that carbon combines with almost every other element of the Periodic Chart, but all (*e.g.* copper) do not form carbides. According to the proposed rule which considers the difference of the ionization potential of the elements, we classify "carbides" as compounds of carbon with metals and with boron and silicon. Such a classification coincides with a positive sign of the difference in electronegativities of carbon-metal (B, Si).

Alkali and alkaline earth carbides (*e.g.* graphite compounds) exhibit partially ionic character in that carbon atoms easily form anion aggregates *e.g.* pairs such as is the case for $Ca^{++}(C_2)^{=}$. The transition element carbides are metallic and regarded, following the concept by Hägg [8] and Goldschmidt [3], as interstitial compounds or interstitial alloys. A final group consists of Be_2C, Al_4C_3 and SiC type phases. These very likely are of ionic-covalent bond type, obeying the valence rule (octet forming). There is, however, ample overlap in the neighboring areas as far as the bonding and the structural elements are concerned. In other words a stepwise change in bonding, structural elements and hence chemical composition can often be observed. The latter fact has also been emphasized by Goldschmidt [3] studying the systematic structural change within a specific group of elements of the Periodic Chart. The gradual change in bonding is well known as illustrated by the isostructural series: $CaC_2 \rightarrow LaC_2 \rightarrow UC_2$. The first compound, however, is not a transition element carbide. The strong ionic bonding between Ca^{++} ions and the acetylide ions $(C\equiv C)^{2-}$ can be derived from lattice energy calculations [9], from the formation of solid solutions CaC_2-CaS [10], and, as was previously concluded, from the hydrolysis behavior. While the assumption of the triple bond in $(C\equiv C)^{2-}$ is also in agreement with the distance C-C, larger carbon-carbon distances have been observed for R.E.C_2 and UC_2, as was shown by Atoji et al. [11]. It was assumed that six valence electrons of the metal atoms in R.E.C_2 are distributed over one $(C\equiv C)^{2-}$ and one $(C=C)^{4-}$ ion [12]. On the basis of hydrolysis experiments, measurements of specific resistivity, TEF and Hall-coefficients, Makarenko et al. [13] have proposed a similar charge distribution, $La^{+++}\ (C\equiv C)^{2-}(C=C)^{4}_{1/4}\ e^{-}_{1/2}$, assuming 0.5 conduction electron per atom. Another explanation for the larger C-C distance in R.E.C_2 in comparison to that of CaC_2 has been proposed on the basis that the one electron left fills an antibonding level in the carbon dumbbell particle. The R.E.dicarbides were occasionally considered as salt-like-covalent-metallic carbides [14].

The C-C distance in UC_2 increases up to 1.340 Å. Increasing C-C distances correspond, according to Atoji [15], to higher metal valencies (4 for U; 3.4 for Ce). The tendency for increasing C-C distances indicates the competition between pair formation of carbon and isolated carbon atoms in metal carbides. One should emphasize in this context, that the extended C-C aggregations only occur in graphite compounds. This means in a very first approach, that the aggregation of carbon atoms decreases in the carbides going from the left side to the right side of the Periodic Chart.

3.1. BINARY CARBIDES OF TRANSITION ELEMENTS

The carbides of the very first transition element also reveal in a peculiar way the stepwise change with respect to the C-C aggregation. Although no complete phase diagram for the scandium-carbon system is available as yet, the Sc-carbides unify somewhat the features of both the carbides of calcium on the one hand and titanium on the other. The phase $ScC_{0.3-0.5}$, having a defect NaCl type structure within a large homogenous region, can be compared with TiC_{1-x} *etc.* (isolated carbon particles). A superstructure also has been found at the composition Sc_2C. A carbon-void ordering like Y_2C has been proposed by Atoji et al. [16], but a more detailed inspection has been shown to be necessary [17]. The scandium carbide, earlier formulated as Sc_2C_{3-x} [18], was found by Krikorian et al. [19] to be Sc_4C_3 with the Th_3P_4- instead of Pu_2C_3-type structure. Neutron diffraction experiments carried out by the latter named authors indicate the presence of single C particles rather than C_2 pairs as was derived from X-ray powder diagrams. The metal positions in both arrangements are however the

same. Another scandium carbide has been detected beyond this phase [18], having a composition assumed to be $ScC_{1.2-1.3}$ [19]. It turned out that the same phase was also described by Petrů et al. [20] who designated it as "ScC_2". A formula $Sc_{15}C_{19}$ ($ScC_{1.27}$) fits best with a proposal of an atomic arrangement based on single crystal x-ray data (figs. 1-3). $Sc_{15}C_{19}$ can be obtained either from heating scandium metal and carbon or by reduction of Sc_2O_3 with

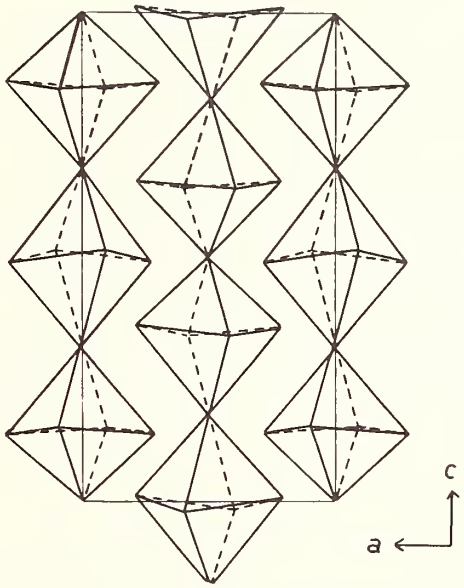

Fig. 1. Array of metal octahedra in $Sc_{15}C_{19}$ (a = 7.50; c = 15.00 Å, $P\bar{4}2_1c$).

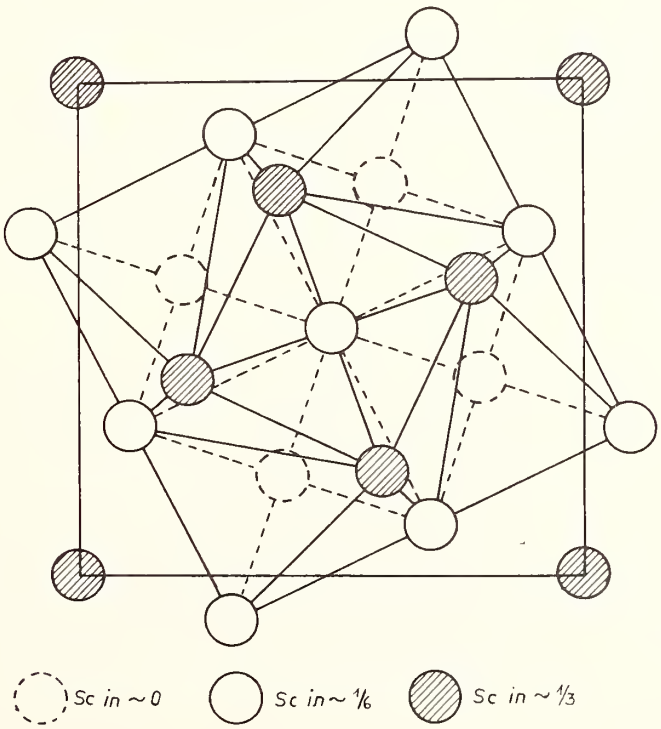

Fig. 2. Positions of the scandium atoms in $Sc_{15}C_{19}$, as seen in the [001] direction.

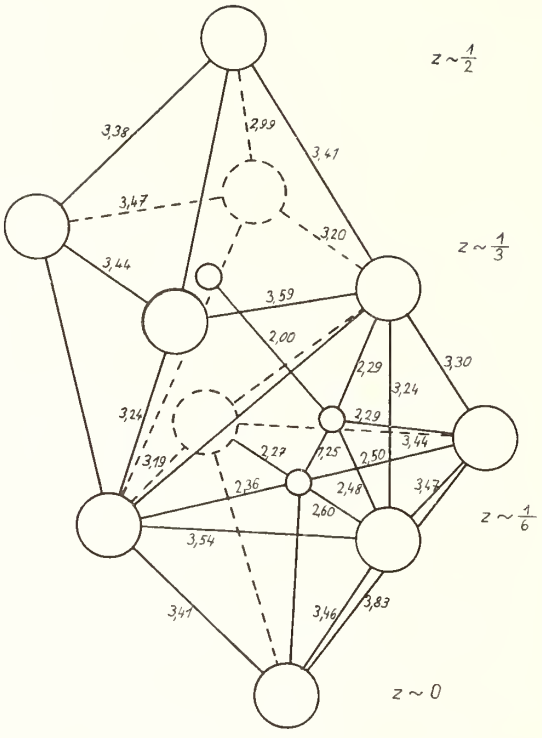

Fig. 3. $[Sc_6C]$- and $[Sc_6C_2]$-groups in $Sc_{15}C_{19}$.

carbon at 2000 °C. The crystal structure of $Sc_{15}C_{19}$ ($ScC_{1.27}$) consists of metal octahedra (somewhat distorted) which are filled by single carbon atoms and carbon pairs, with a C-C-distance of 1.25 Å which compares well to that of CaC_2 or R.E.C_2. As is shown in figure 2 the metal atoms form a parent lattice related to a cubic close packing.

A similar phase, $Y_{15}C_{19}$($YC_{1.27}$) appears to occur in the corresponding yttrium-carbon system. According to Carlson et al. [21] a δ-phase was found to exist between 55 and 58 a% C, transforming to the ε-phase above 1200 °C. This phase obviously corresponds to "Y_2C_3" earlier reported as of low symmetry. Very recently Haschke et al. [22] described a monoclinic $YbC_{1.25+y}$ which most likely also relates to the above mentioned scandium and yttrium carbides $MC_{1.27}$. Although the powder diagrams of the respective carbides $Sc_{15}C_{19}$ and $Y_{15}C_{19}$ clearly indicate an isotypic structure, it may be that the pseudocubic, tetragonal cell is only a first approach.

Although a dicarbide occurs in the Y-C system (Y has a larger metal radius than Sc) no such scandium dicarbide could be synthesized. On the other hand, the similarity between the metal-rich sides in both cases should be mentioned, each having a large region of defect sodium chloride structure (including ordered phases). In the course of mass spectrometric measurements by Drowart et al. [23], the formation of at least five scandium carbides has been described. In addition to $Sc_{15}C_{19}$, Sc_4C_3 (Sc_2C_{3-x}) and Sc_2C, the existence of two more ordered carbide phases derived from the NaCℓ-defect structure has been postulated. No precise measurements of melting points of the Sc-carbides are available as yet. However, a possible eutectic between $Sc_{15}C_{19}$ and graphite lies close to 1800 °C. These carbides seem, therefore, to be thermally less stable than the yttrium carbides. A eutectic between YC_2 and graphite is reported to occur at 2300 °C. As Drowart et al. emphasize, the heat of formation of the scandium carbides is in line with that of other transition element carbides (IIIA, IVA and VA).

3.2. CARBON ORDERING

The carbon-void ordering has clearly been demonstrated for subcarbides of transition elements and more recently for other compositions such as V_6C_5 or V_8C_7. The tendency for carbon ordering is even more pronounced with carbohydrides such as Zr_2CH. The problem of

ordering in carbides has been extensively discussed by the author [24]. In general, low temperatures favor ordering. Probable minor amounts of oxygen or nitrogen contaminants quite often exert an ordering influence upon the transition element carbides. A unique example for the unambiguous determination by neutron diffraction of carbon ordering has been shown for V_2C having the ζ-Fe_2N-type structure. Here the neutron diffraction scattering stems only from the carbon positions (fig. 4). Nevertheless, orthorhombic V_2C has also been reported for $V_2C_{1.01}O_{0.02}$ [25]. On the other hand, the existence of an orthorhombic V_2C (called α-V_2C) was found at low temperatures by Rudy et al. [26].

Whether the ordering phenomenon takes place in a large homogenous region such as for ScC_{1-x} and YC_{1-x} or in a more narrow domain such as for W_2C, the most characteristic feature is obviously the formation of shorter metal-carbon distances than those for randomly distributed carbon atoms in a metal parent lattice with close packed array. Thus the V-C distance of 2.01 Å for the orthorhombic V_2C is distinctly shorter than the V-C distance of 2.03 Å for the hexagonal V_2C with random carbon positions. Similarly the Y-C distance of 2.27 Å in Y_2C (rhombohedral) is remarkably shorter than the Y-C distance of 2.35 Å in YC_{1-x}.

Furthermore, it turned out that the metal atoms in some ordered carbide structures, *e.g.* V_8C_7, are also shifted in such a way that shorter neighboring metal-carbon atomic distances result [27,28]. It has also been shown that shorter distances between metal-carbon-metal occur than for metal-void-metal. This clearly indicates the significance of the structural elements [M_6C]. The concept of the building elements for the generation of the large class of complex carbides has been shown to be particularly useful [7].

From this concept stacking faults in TaC_{1-x} can be understood by gliding in planes in which a metal-void-metal arrangement occurs. Thus areas at high temperatures may exist with some stepwise transition from the cubic close packing (monocarbide) to the hexagonal close packing (subcarbide). This problem is linked to the ζ-carbides recently explored by Yvon et al. [29]. The metal atoms of the fairly unstable ζ-phases (V_4C_3, Nb_4C_3, Ta_4C_3) exhibit a complicated sequence, namely $(hhcc)_3$. In this context VTa_2C_2 detected by Rudy [30], should be mentioned although this phase (stable up to 2600 °C) represents an intermediate ternary carbide, which is characterized by a sequence $(hhc)_3$. However, nothing can be said about the degree of ordering. It has already been emphasized that V_4C_3 can be built up by V_2C and VC structural blocks. From table 1 the evolution of different stacking sequences in carbides can be seen. The corresponding c-axes display a simple ratio. As compared to the early findings of interstitial compounds quite a change has taken place. Still more transition element carbides are to be expected to occur because of more complex ordering and stackings. The mode of stacking immediately influences composition because of the repulsion of two carbon atoms which come too close together, as was assumed for MoC_{1-x} (Mo_3C_2). On the other hand, there was no carbon ordering found for the ζ-carbide V_4C_3.

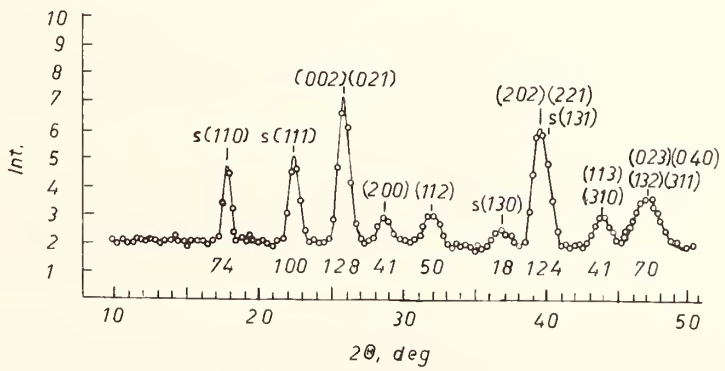

Fig. 4. Neutron diffraction diagram of V_2C, having ζ-Fe_2N-type structure, s = superstructure lines.

Table 1

Metal Stackings in Carbides

number of metal layers n		c-axis, approxim. (Å)		c_n/c_1
3	ABC (cub., hexag. axes)	7.5	(TiC)	1
6	ABCACB	14.7	(γ"MoC_{1-x})	2
9	ABCBCACAB	22	(VTa_2C_2)	3
12	ABCACABCBCAB	30	(Ta_4C_3)	4

Molybdenum and tungsten carbides have recently been reviewed by Morton et al. [31] who have measured the superconducting critical temperatures. These authors confirmed the existence of the well known Mo-C phases [4] including the orthorhombic α-Mo_2C, which is, according to Jack [32], stabilized by very minor amounts of nitrogen.

Nevertheless there is no complete agreement between all data reported in the literature. The same is partially true for the W-C system.

4. COMPLEX CARBIDES (INTERSTITIAL COMPOUNDS)

Only novel carbides of this huge class shall be discussed. For more detail the reader is referred to the above cited literature [7]. Generally the particular problem of transition between metal-metal-carbides and metal-nonmetal-carbides is to be focused here. On the basis of the building elements, mainly octahedral or trigonal prismatic groups [M_6C] or [M_6X] (X = nonmetal), so-called H-phases, the filled Re_3B-type structure and derivatives offer convenient examples to demonstrate the stepwise generation of new structure types of complex carbides. In the H-phase, *e.g.* $Nb_2A\ell C$, the aluminum atoms are still in contact with overall metal packing "$Nb_2A\ell$" (c/3a = 1.49). No such contact (if neutral S atoms are present) can be assumed for Nb_2SC (c/3a = 1.17). In other words the latter H-phase can be considered as a topochemical sum of NbC (octahedra) + NbS (trigonal prism). At this point it is of interest to note that Goldschmidt has introduced the term "inverse" interstitial compounds, *e.g.* 2s-MoS_2, which is, incidentally, an anti-type of the H-phase parent lattice.

4.1. Ta_2S_2C

No H-phase Ta_2SC in the system Ta-S-C has been found so far. However, a complex carbide, Ta_2S_2C, was detected in both low and high temperature forms. The transformation is sensitive to mechanical treatment. As is shown in figure 5, the octahedral structural element [M_6C] linked by edges form a single plane or double plane (Ti_3SiC_2-type structure) combined with trigonal prismatic layers (Ti_2SC- and Ti_3SiC_2-type structures) or typical layer blocks (MoS_2-, TaS_2-structure types). Thus ls-Ta_2S_2C is topochemically composed of ls-MoS_2 + TaC slabs, 3s-Ta_2S_2C of ls-TaS_2 + TaC. Because of the weak bonding between adjacent sulphur layers, mechanical distortion (stacking faults) easily may take place. Both polymorphs are isotypic with valence compounds (Ce_2O_2S and Bi_2Te_2S respectively) [33].

The latter mentioned fact indicates the presence of some ionic fraction in the bonding. One must assume formation of sulphur anions and metal cations. The role of hydrogen in metal carbohydrides is similar. Within the layer sequence -M-C-M-H-M-C-M (cubic or hexagonal) the occurrence of H-anions is most probable, as is the case of many metal hydrides, *e.g.* NdH_2 [34].

4.2. FILLED UP Re_3B-TYPE STRUCTURE CARBIDES AND V_4P_2C.

The occurrence of the filled Re_3B-type structure is shown in table 2. The array represents a simple combination between octahedral and trigonal prismatic building groups. Again VCr_2C_2 is a perfect topochemical sum of $(V,Cr)C_{1-x}$ (octahedra) + Cr_3C_2 (trigonal prism). Similarly $Cr_3C(C_{0.4}N_{0.6})$ [35] is built up by CrN and Cr_3C_2 elements with some nitrogen in CrN being substituted by carbon.

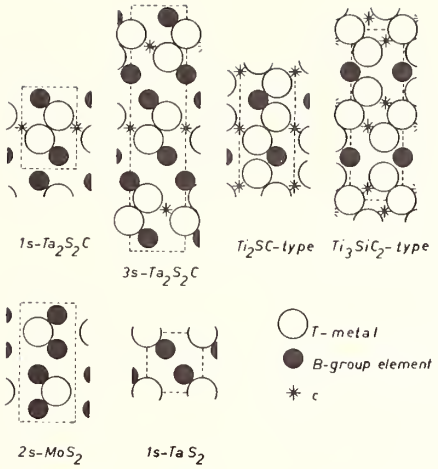

Fig. 5. Transition element sulfocarbides and related compounds, as seen from layer-like stacking.

Table 2

Occurrence of the Filled Re_3B-type Structure

M element	X element	Interstitial element
V	Ga,Ge,P,As	(C),N
V+Cr	C	C
Cr	(B,C),Ge,P,As	C,(N)

Combinations with ( ) are missing

As is well known for the Mo-C and W-C system, the octahedral building group is limited to subcarbides or carbon deficient cubic structures which only occur in a high temperature region. For the monocarbide of tungsten the trigonal prism is characteristic. Ettmayer has recently found that nitrogen at high pressures stabilizes Mo(C,N) in the WC-type structure [36].

Another interesting example of combined building elements is represented by V_4P_2C (fig. 6). Similar to the filled Re_3B-type structure, the metal octahedra are filled by carbon, while the trigonal prisms accommodate the phosphorus atoms. The crystal structure has been derived by Boller [37].

The interchangeability of X-atoms and carbon such as H/C, N/C, B/C is widely extended. In such a way another concept somewhat different from the interstitial principle becomes visible. It was found that phosphorus and arsenic atoms can be replaced by carbon in chromiun containing carbides. Furthermore, formation of boron-carbon aggregates takes place in metal borocarbides (carboborides).

4.3. $Cr_6P_{2.6}C_{0.4}$ and $Cr_2(As,C)$

While the Cr-phosphocarbide is a ternary compound, the isotypic $Cr_2(As,C)$ develops from the high temperature form having Fe_2P-type structure. The lattice parameters, dependent upon the amount of carbon, indicates that carbon not only may enter voids but also substitutes for the X-atom, as is shown in figure 7.

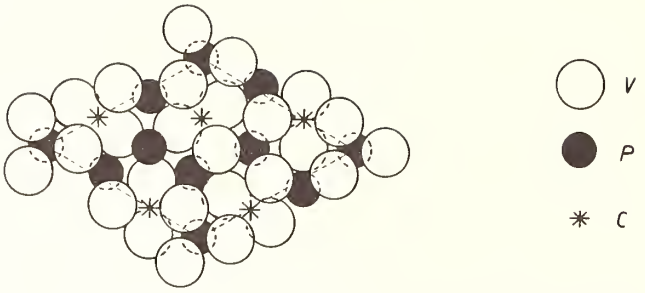

Fig. 6. Crystal structure of V_4P_2C (a = 9.567, c = 3.166 Å, $P\bar{6}2m$).

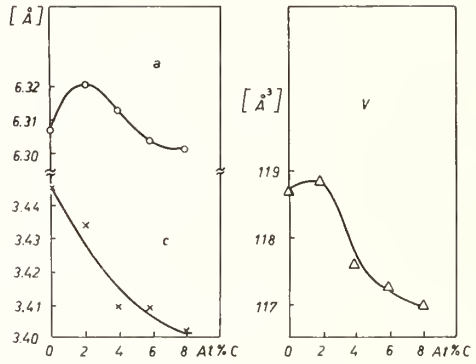

Fig. 7. Lattice spacings for $Cr_6As_{3-x}C_x$.

5. BOROCARBIDES OF TRANSITION ELEMENTS

Boron/carbon substitution in borocarbides of transition elements is well known for $Fe_3(B,C)$ or $Fe_{23}(B,C)_6$. However, carbon atoms in borocarbides such as Mo_2BC do not display a substitutional mode with respect to boron atoms. Mo_2BC, a sum of MoC (octahedral) and MoB (trigonal prismatic group) behaves as the former (interstitial) compounds. UBC and $Cr_3(B,C)C$ look like intermediates between Mo_2BC and $Fe_3(B,C)$. Nevertheless, with borocarbides low in metal content, the aggregation tendency of the nonmetal atoms becomes a distinct feature. The boron-boron chains are linked to carbon atoms like a branched chain as is the case for UBC (fig. 8). Very recently YBC [38] was found to be of a similar arrangement (fig. 8). While for ThB_2C (approximate composition) two-dimensional networks have been assumed, Smith et al. [39] derived the crystal structure of ScB_2C_2 consisting of such boron-carbon networks, built up by 5- and 7-membered rings. In YB_2C_2 such a network also exists, however it contains 4- and 8-membered rings (fig. 9). The same arrangement obviously occurs in a large number of lanthanide borocarbides described by Smith et al. [40]. Finally, YB_2C also exhibits two-dimensional boron-carbon networks characterized by 4- and 7-membered rings (fig. 9).

The array represents a sum of the building elements of YB_2 (diboride type structure) and YB_2C_2. These complex carbides compare somewhat to the alkaline graphite compounds. From this analogue one must assume that the boron-carbon layers bear a slightly negative charge. Within this class of compounds the boron-carbon structural elements constitute a major (covalent) bonding system. No specific data such as melting point for these borocarbides are available as yet.

6. SOME REMARKS ABOUT THE CHEMICAL BONDING IN CARBIDES

The views about the nature of the chemical bonding in transition element carbides are still controversial. There is a particularly wide gap between the various models including quantum chemical results and experimental facts including structural chemical aspects.

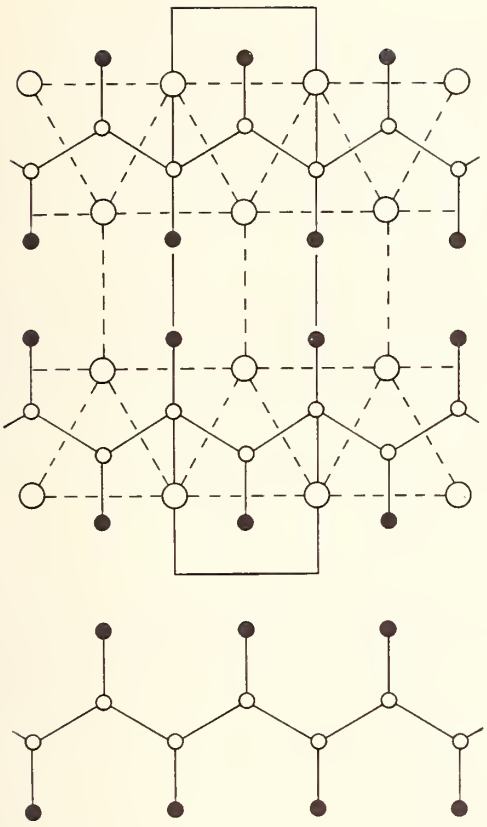

Fig. 8. Branched boron-carbon chains in UBC (below) and crystal structure of YBC ($a = 3.38_8$, $b = 13.69_3$, $c = 3.62_7$ Å, Cmmm).

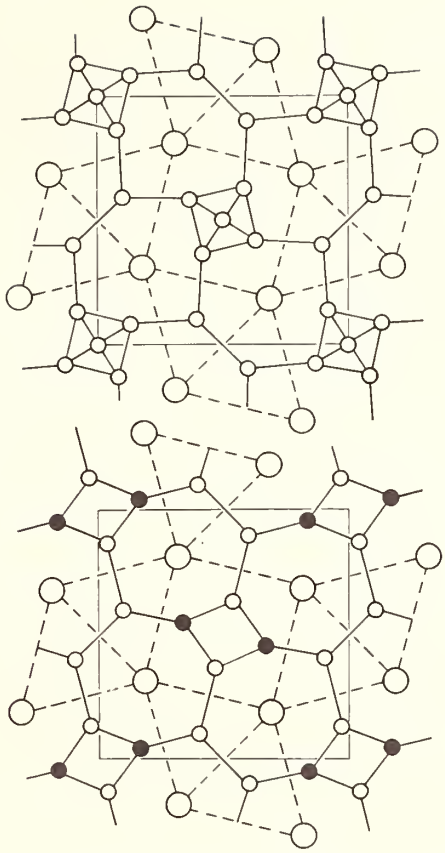

Fig. 9. Boron-carbon networks in YB_2C ($a = 6.76_9$, $c = 7.430$ Å, $P4_2mbc$) generated out of YB_4, (above).

Beattie [41] has recently treated this class of compounds within the "cannonball" structures where octahedral (and occasionally tetrahedral) voids are filled by so-called small nonmetal atoms, in agreement with the early geometrical concept of interstitial carbides. Along these lines the electronic model or "transition-metal like" model has been developed by a number of authors, assuming a transfer of electrons from the carbon atom to the d-band of the metal atom. In such a way bonding between metal-metal atoms was expected to be enhanced, thus, the stability evaluated in terms of the melting point, increases for the carbide over the corresponding metal. In a more detailed, semiquantitative manner, Engel [42] considered the bond system from the spin pairing concept. For ZrC (an sp^2 state is assumed to be characteristic for the fcc array of the metal atoms) the following states are present: $Zr(1-,2-,3-, 4s^2p^6d^5, 5sp^2)^{4-}$ and C^{4+}, yielding five d-bonds (Zr-Zr), three outer sp^2-bonds and in addition, four ionic bonds. The large number of bonds makes one believe that the energy required for ionization of carbon to C^{4+} can easily be overcome.

Quantum chemical calculations carried out by Costa et al. [43] also support the "transition metal-like model". According to these authors the M-M bonding is the essential interaction in monocarbides. It is assumed that about 1.5 electrons are transferred from the carbon atom to the metal atom. In a later paper Costa has expressed the opinion that the d-band filling of the metal does not produce a noticeable positive charge on the carbon atom because of the extending and overlapping d-orbitals which screen the nucleus of the carbon atom. A different approach (using optical data) made by Lye [44] for stoichiometric TiC yields the approximate electronic configuration $3d^4 4s^{3/4} 4p^{1/2}$ for Ti and $2s^2 sp^{3/4}$ for carbon which corresponds to a transfer of 1 1/4 electrons from carbon to the metal atom. The net charge is said to be smaller because the metal wave functions extend to the carbon sites. The main result of these concepts may be interpreted in the following way: the *metal-metal* bonds are

found to be the strongest, followed by *metal-carbon* bonds and surprisingly *carbon-carbon* bonds should also exist.

Other quantum chemical calculations [45,46] and more recent work based on APW and self consistent APW-methods on monocarbides and related compounds [47,48] differ quite a bit with respect to the calculated density - of - state curves as compared to Lye's conclusion. Furthermore, based on the more elaborate quantum chemical methods, it was shown that the results do not indicate any transfer at all from carbon to the transition element in TiC and similar compounds (assuming a perfect NaCℓ type structure).

The presence of M-M-, M-C- and C-C-bonds has also been proposed by Hench [49]. According to this author the electronic bond consists of mutually overlapping tetrahedral hybrid orbitals. The well known hybrid state of carbon sp^3 combines with one of the stable electronic configurations of the metal atom namely sp^3, d^3s, d^2sp, dp^3, d^3p forming a resonance between alternate cells. The arrangement of the respective cores of Ti and C together with the centers of high electron concentration is incidentally similar to that proposed for TiC by Schubert [50] on the basis of a spatial correlation of electrons. There is no doubt that all calculations and specific models are loaded with a number of assumptions.

6.1. COMPOUND-LIKE MODELS

In a more unorthodox manner, considering an isotypic and isoelectronic series such as: KF-CaO-ScN-TiC or CsF-BaO-LaN-HfC, one must accept a stepwise change in bonding, in which the formation of N-anions and C-anions appears favorable [51]. In fact calculations of the lattice energies, particularly for nitrides, yield very satisfactory results on the assumption of M^{3+} and N^{3-} ions, present in the lattice. This has also been shown in great detail by Straumanis et al [52] for TiN, which is even more metallic than TiC as seen from the electrical conductivity.

A similar point of view arose with Rundle's theory [53] on transition element monocarbides which has been expanded by Hume-Rothery [54] and Krebs [55]. In this concept the predominant bonding is believed to be due to a *metal-carbon* interaction rather than metal-metal bonding. Besides the result that this theory is connected with a more or less pronounced electron transfer in the direction opposite to that proposed in the "transition metal-like model", it was widely agreed that the bonding nature in metal carbides is usually considered to be a mixture of covalent and metallic bonding. Hume-Rothery completes the discussion with the idea that the electropositive nature of titanium relative to carbon or nitrogen results in a further electronegativity effect which acts as a stabilizing factor.

In agreement with this concept [45,48] the important role of metal-carbon interaction is distinctly shown by the existence of structural elements in carbides and complex carbides.

A more direct confirmation of the "compound-like" model of transition element carbides (monocarbides) apparently can be obtained by the results of the ESCA-method as Ramqvist [56] has reported. From the negative shift of the carbon 1s-level and the positive shift of the metal levels (1s; $2p_{3/2}$; $3d_{5/2}$; $4f_{7/2}$) a transfer of electrons from the metal atom to the carbon atom in monocarbides has been derived, leading to a average charge of 0.3 to 0.5 units. The calculated Madelung energy from these data turns out to be 30 - 60 Kcal/formula; values which Ramqvist compares to the heats of formation. With respect to the bond system, present in monocarbides, a statistical approach, proposed by Hoch [57] should also be mentioned. From the energy balance it clearly turns out that M-C bonding is by far the most important contribution; furthermore, carbon-carbon repulsion takes place which obviously stems from a Coulomb interaction.

7. BINARY METAL SILICIDES

In view of the radius of the silicon atom in comparison to carbon on the one hand and to aluminum on the other the concept of typical interstitial compounds no longer holds for metal silicides. They rather occupy an intermediate position [3] between interstitial and intermetallic compounds. Metal silicides are also characterized by their wide occurrence and the large variety of compositions which they exhibit. Generally they are line compounds and for some, ordinary valencies apply, at least in a formal way, for metal silicides having

isolated silicon atoms in the lattice. One can further extend the valence principle by taking into account Si-Si aggregates, so-called pseudoanions, as the tendency to form Si_2 pairs, Si-Si chains *etc.* is frequently observed in metal silicides. Alkali and alkaline earth silicides, mainly of composition (M_2Si-MSi_2) belong to the class where the electronegative character is predominary [58]: $Li_4^+[Si_2]^{4-}$; $K_4^+[Si_4]^{4-}$; $Ca_2^{2+}[-Si-Si-]^{4-}$ etc. It is of interest to notice that a number of these compounds *e.g.* CaSi, Ba_5Si_3 are structurally representative of a series of corresponding transition element silicides, although the valence concept no longer holds for these compounds and a mixed type of bonding (metallic - ionic) must be assumed. Along these lines, more metallic character develops, although not necessarily in a predictable way. In metal-rich silicides the cationic function of silicon appears as can be seen from a pronounced metal-silicon interchangeability in numerous phases displaying typical metallic crystal structures such as polyhedra compounds *etc.* This is valid particularly for complex silicides. On the other hand, the silicon like behavior (tetrahedral bonding) in silicides, is revealed in the silicon-rich clathrate compounds such as Na_8Si_{46} [59].

7.1. DISILICIDES AND DEFECT-DISILICIDES

As was early recognized, the formation of stable disilicides extends from Group IIA to VIIIA metals and the gradual change in structure is most characteristic, particularly in the Si-Si aggregation and bonding. The tendency of Si-Si aggregations decreases in a systematic way from IIA to VIIIA metal disilicides and will be replaced by metal-silicon networks within IVA to VIA metal disilicides. While compounds such as $CaSi_2$ or $SrSi_2$ can be explained by valencies (strong ionic portion considering Si-anion aggregates), the disilicides of the latter named group display interchangeability and hence obey regularities of valence electron concentration.

The interchangeability of metal-silicon atoms within the so-called supertype compounds ($TiSi_2$- $TaSi_2$- and $MoSi_2$-type structures [60] is particularly supported by the partial silicon/aluminum substitution, which transforms the various types in agreement with the valence electron concept. Lowering of the electron to atom ratio (on the basis of the outer electrons) leads to a change from the $MoSi_2$-type structure to the $TaSi_2$-type structure and further to the $TiSi_2$-type structure [61]. The hexagon array of the silicon atoms in the supertype which perfectly accommodates the metal atoms (Ti,V,Nb *etc.*) is demonstrated in R.E. disilicides having $A\ell B_2$-type structure or in the $ThSi_2$-type structure. The latter can be generated out of the $A\ell B_2$-type structure by a shift, as was shown by Parthé [62]. The intermetallic character of the supertype structures parallels with the coordination number of 10, although there are semiconductors among these disilicides ($CrSi_2$ or $ReSi_2$ at high temperatures). With respect to thermal stability, the disilicides (two-dimensional networks) compete mainly with monosilicides and silicides of formula M_5Si_3 (exhibiting Si-Si chain formation).

Silicides of the general formula Mn_nSi_{2n-m} have been detected [64-68] as intermediates between the supertype structures and β-$FeSi_2$ [63], $OsSi_2$ [63], $CoSi_2$, $NiSi_2$ which crystallize with a distorted or regular fluorite type (C.N. = 8 for silicon).

7.1.a. MANGANESE SILICIDES Mn_nSi_{2n-m}

Manganese silicides of the above formula corresponding to a defect disilicide $MnSi_{2-x}$ exhibit a unique structural principle first discovered with $Mn_{11}Si_{19}$. As seen from figure 10 the atomic arrangement is generated from the $TiSi_2$-type structure, the subcell of the manganese (transition element) atoms being identical with the titanium (transition element) atoms within the $TiSi_2$ cell. The multiple n refers to the number of the transition element in the formula. The second partial lattice formed by the silicon atoms is expanded, leaving out m silicon atoms out of 2n silicon atoms for n $TiSi_2$ cells. In this way crystal structures occur occasionally having large c-axes (table 3). Also, various defect disilicides have been found to exist either for slightly different compositions in the binary system manganese-silicon or in partially substituted ternary phases. More recently the compound $Mn_{27}Si_{47}$ (fig. 10) has been characterized by single crystal data. Although the melting mode in the region of $MnSi_{\sim 1.7}$ is not unambiguously explored as yet, large single crystals (4cm) could be obtained by means of the Czochralski method at a rate of 0.45 mm/min. Single crystal data confirmed the cell dimensions, earlier derived from powder patterns. In accordance with the regularity for odd m and n, only (0k1) reflections k + l = 2n (space group $P\bar{4}n2$) have been recorded. The atomic positions have been derived in a similar way as for the other

465-504 O - 72 - 33

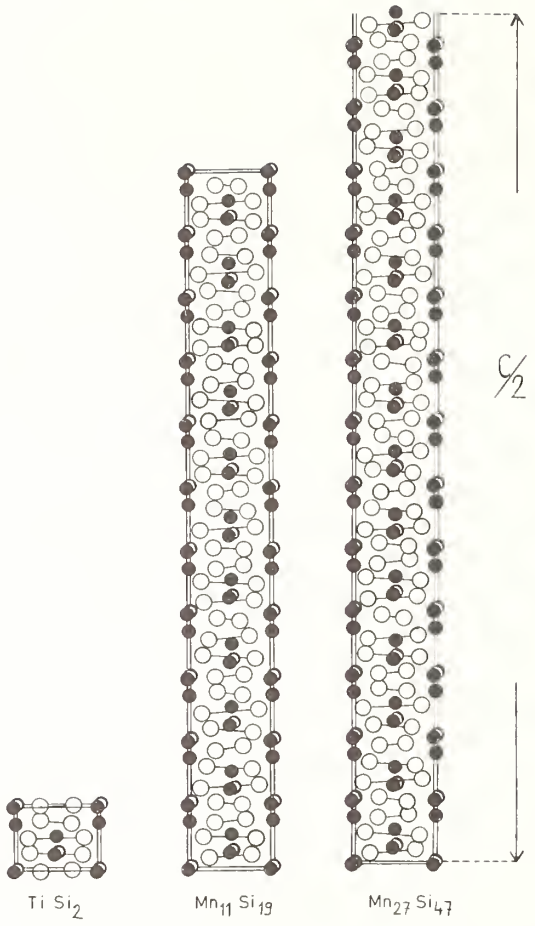

Fig. 10. Atomic arrangement of $TiSi_2$, $Mn_{11}Si_{19}$ and $Mn_{27}Si_{47}$.

manganese silicides with an R-value of 0.095. While the Si-Si-helix which is centered in the (110) plane is essentially going clockwise from top to bottom, the adjacent helix centered in the ($1\bar{1}0$) plane goes anticlockwise (fig. 10). Also it has been shown by neutron diffraction experiments that the same multiple n results as has been determined by x-ray techniques. However the superstructure reflections *e.g.* (21.11) for $Mn_{15}Si_{26}$ are remarkably enhanced [69].

The strong contribution of the magnetic scattering seems to be very complicated. No simple explanation for the magnetic structure of these Mn-silicides can be given as yet. It should be mentioned that the representative superstructure reflections (Weissenberg patterns) as mentioned above or the (21.20) and (11.47) reflections for $Mn_{27}Si_{47}$ occasionally have a diffuse character. Even after a long anneal (150 hrs) at about 1000 °C this phenomenon does not disapper, indicating a domain formation around the multiple n. In this context an observation, reported by Ivanova et al. [70] is of interest, namely microscopically visible fringes perpendicular to the [001] axis, independent of the direction of pulling of a manganese silicide of formula $MnSi_{1.72}$.

7.2. PSEUDO-SOLID SOLUTIONS OF FORMULA $(Mn,T)_nSi_{n-m}$

Substitution of some manganese atoms by other transition elements (Cr,Fe,Co) do not essentially change the subcell, as can be seen from a plot: volume versus composition of the defect disilicide (fig. 11). The dependency mainly reflects the silicon defect and makes one believe that continuous solid solutions have been formed. Similarly, other properties such as the magnetic susceptibility indicate solid solutions, as is determined for (Mn,Fe)-defect disilicides in figure 12. A detailed inspection reveals, however, that the various

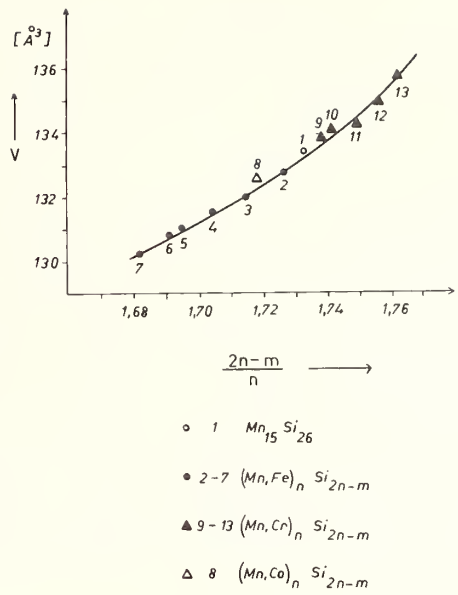

Fig. 11. Volume of the subcell as a function of the amount of silicon for $(Mn,T)_nSi_{2n-m}$ phases.

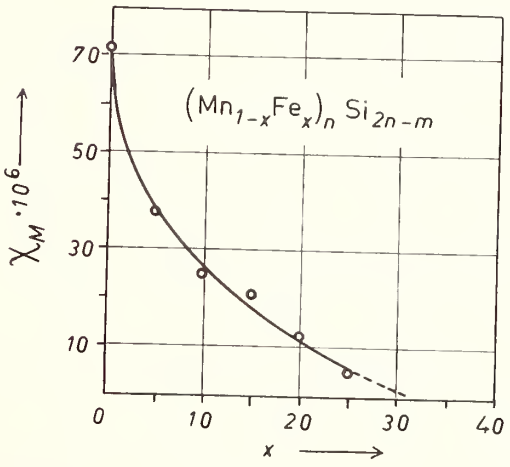

Fig. 12, Susceptibility per formula as a function of the Mn/Fe substitution for $(Mn_{1-x}Fe_x)_nSi_{2n-m}$.

substituted silicides differ generally with respect to n and m. This means only pseudo-solid solutions are present, as is shown in table 3. Some of these phases might develop from one of the manganese defect disilicides such as $(Mn_{0.95}Fe_{0.05})_{11}Si_{19}$ or $(Mn_{0.85}Cr_{0.15})_4Si_7$. The latter obviously is related to the compound Mn_4Si_7 which has been characterized by Fujino et al. [71] and by Karpinskii et al [72]. An analogous behavior has been described for transition element germanides and substituted compounds [7]. From figure 13 it can be seen that an increase in the outer electrons which occurs with Fe and Co-substitution increases the silicon defect while chromium substitution decreases these defects. This fact is closely related to the regularity of the silicon/aluminum substitution in the supertype structures. Here again aluminum, lowering the overall valence electron concentration suppresses the silicon defect, thus stabilizing the supertype structures for $Mn(Si,Al)_2$.

Table 3

$(Mn,T)_nSi_{2n-m}$ Phases

	Formula	n	$\frac{2n-m}{n}$	a	c	c/na
2	$(Mn_{0.95}Fe_{0.05})_{11}Si_{19}$	11	1.727	5.51_8	47.96	0.7914
3	$(Mn_{0.9}Fe_{0.1})_7Si_{12}$	7	1.715	5.51_0	30.46_4	0.7898
4	$(Mn_{0.85}Fe_{0.15})_{17}Si_{29}$	17	1.705	5.50_3	73.86_5	0.7896
5	$(Mn_{0.8}Fe_{0.2})_{23}Si_{39}$	23	1.695	5.49_6	99.79_7	0.7895
6	$(Mn_{0.75}Fe_{0.25})_{29}Si_{49}$	29	1.691	5.49_0	125.68_6	0.7894
7	$(Mn_{0.7}Fe_{0.3})_{22}Si_{37}$	22	1.682	5.48_3	95.17_3	0.7890
8	$(Mn_{0.95}Co_{0.05})_{25}Si_{43}$	25	1.719	5.51_6	108.95_0	0.7901
9	$(Mn_{0.95}Cr_{0.05})_{19}Si_{33}$	19	1.738	5.53_3	83.06_8	0.7902
10	$(Mn_{0.9}Cr_{0.1})_{31}Si_{54}$	31	1.742	5.53_4	135.71_8	0.7911
11	$(Mn_{0.85}Cr_{0.15})_4Si_7$	4	1.750	5.53_7	17.53_2	0.7916
12	$(Mn_{0.8}Cr_{0.2})_{29}Si_{51}$	29	1.757	5.54_6	127.28_1	0.7914
13	$(Mn_{0.75}Cr_{0.25})_{17}Si_{30}$	17	1.763	5.55_2	74.66_4	0.7911

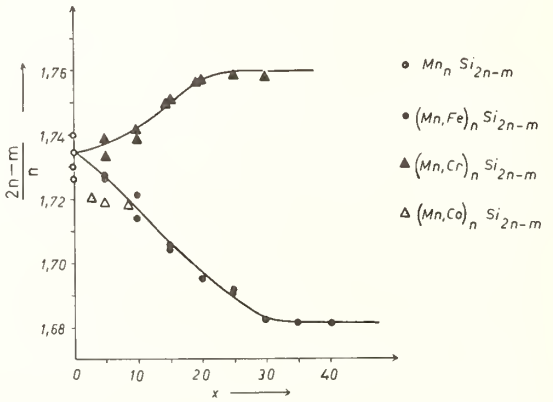

Fig. 13. Silicon concentration as a function of the amount of the manganese-transition element substitution.

An interesting approach to explain the peculair structural principle has been made by Jeitschko et al. [73]. As the transition element atoms form a subcell lattice which is well known for the white tin type structure, the defect disilicides are considered as "stuffed" white tin structures. The silicon atoms act as a filler donating electrons to the white tin array. Application of this concept leads to an electron/atom correlation which shows a relatively small excess contribution of the transition elements as compared to vanadium to the overall electron concentration. More recently Pearson [74] treated the same problem in phases called chimney-ladder structures. From about 40 phases belonging to these super-super-structures a relationship between the transition element valence V_T and the ratio $(2n-m)V_X/nV_T$ has been derived, which is shown in figure 14 (V_X = valence of silicon, *etc.*). The electron concentration for the subcell of the transition element atoms is limited to 14 per atom or 56 outer electrons in the subcell. The composition of phases for lower valences V_T is obviously also controlled by a uniformly decreasing electron concentration (48 outer electrons in the subcell for $V_T = 4$). For the manganese silicides ($V_T = 7$) it is significant to note that a constant electron concentration per subcell governs the stability. However, it is not possible to explain the varieties of multiple n for a relatively narrow region on the basis of the above proposed electron concentration per subcell. According to Pearson the similarity of Mn-Si distances (fig. 15) of neighboring atoms along the c-axis may well be responsible for comparable near-neighbor interaction and hence for comparable enthalpy.

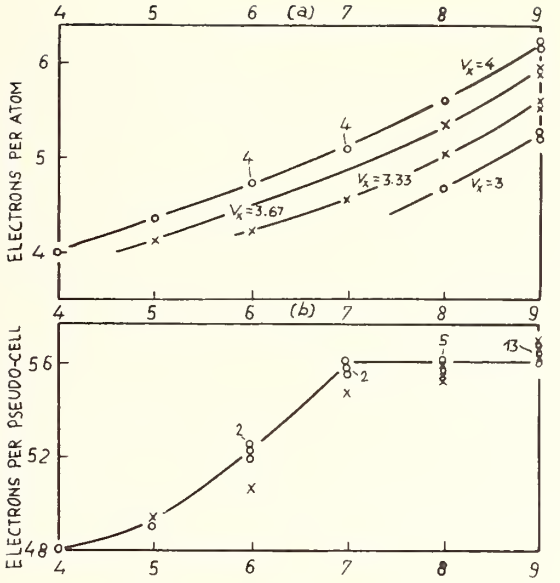

Fig. 14. Electrons per atom (a) and electrons per subcell (b) as dependent on the outer electrons of the transition element for chimney-ladder structures.

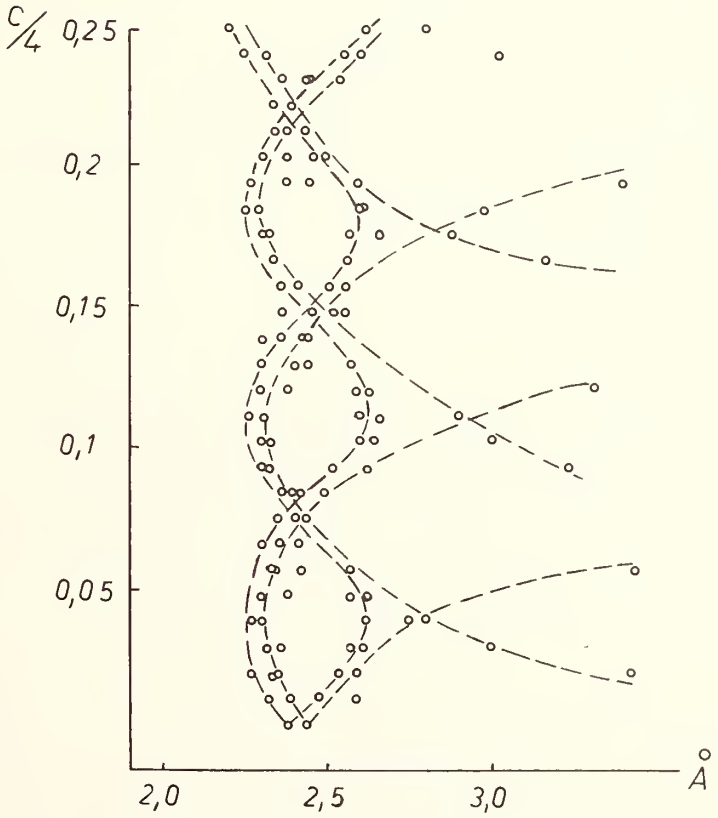

Fig. 15. Mn-Si-distances along c-axis in $Mn_{27}Si_{47}$.

8. TERNARY METAL SILICIDES

There are quite a few review articles [3,6] dealing with ternary and multicomponent silicides. The ability of silicon to act as a non-metal on the one hand and as a metal on the other is clearly demonstrated in a large number of complex silicides. The metal-like behavior can be seen preferentially with metal-rich silicides. This is particularly true in the case of random substitution metal-silicon in equivalent positions such as $Mn(Ni,Si)_2$ or with metal silicides crystallizing with polyhedric structures such as the μ-phase $Mo_6(N,Si)_7$. The non metal like behavior of silicon is again centered around alkali and alkaline earth containing compounds such as Li_2BaSi [75] or MgCaSi [58] which obey ordinary valencies. For ternary silicides, ordered structures derived from the array of binary compounds (salt-like or metallic) are quite characteristic: examples are the ordered $CuAl_2$-, $BaAl_4$- or the anti-$PbCl_2$-type structures. Thus silicon in Nb_4FeSi or $ThCu_2Si_2$ is surrounded by metal atoms forming a so-called quadratic antiprism. In such a way silicon compares somewhat to carbon in metal-rich carbides with a small ratio r_T/r_C such as $Cr_{23}C_6$. Some fifty compounds belonging to the $ThCu_2Si_2$ type structure have been described [6,76]. Another group of ternary metal silicides having a wide occurrence is encountered with so-called E-phases having the ordered anti-$PbCl_2$-type structure. Metal trigonal prisms linked by edges surround the silicon atoms, thus, ignoring three more metal neighbors, some similarity to metal carbides can be recognized. In addition, as is shown in table 4, the valence compounds MgCaSi and MgSrSi [58] are the first members of a series of E-phases containing transition elements.

Finally $CaAl_2Si_2$ and $SrAl_2Si_2$ having an ordered La_2O_3-type structure (La_2O_2S) can also be considered as salt-like compounds and obey normal valencies ($Sr^{II}Al_2^{III}Si_2^{IV}$). A resonance between ionic and covalent bonding must be assumed, as silicon is surrounded by four neighbors, similar to the Mg_2Si proposed by Krebs [77]. It would be of interest to extend Phillips [78] theory on bonding to this class of compounds.

Table 4

Ternary Silicides (E-phases)

Mg {Ca,Sr} Si	Ti {Ni,Cu} Si	V {Co,Ni} Si	Mn {Co,Ni} Si
	Zr {Fe,Co,Ni,Pd,Pt,Cu} Si	Nb {Fe,Co,Ni} Si	
	Hf {Fe,Co,Ni,Cu} Si		

9. REFERENCES

[1] Kieffer, R. and Benesovsky, F., *Hartstoffe,* Springer-Verlag, Wien, 1963.
[2] Storms, E. K., *The Refractory Carbides,* Academic Press, New York - London, 1967.
[3] Goldschmidt, H. J., *Interstitial Alloys,* Butterworth, London, 1967.
[4] Rudy, E., Compendium on Phase Diagram Data, AFML-Report, 1969.
[5] Samsonov, G. V., *Tugoplavkie Karbidi,* Naukova Dumka, Kiev, 1970; Kosolopova, T. Ya., *Carbides Properties, Production and Applications,* Plenum Press, New York, 1971 (Russian text published 1968); Toth, L. E., *Transition Metal Carbides and Nitrides,* in Refractory Materials, J. L. Margrave, Editor, Academic Press, New York, 1971.
[6] Gladyshevskii, E. I., *Kristallochimia Silitsidov i Germanidov,* G. V. Samsonov, Editor, Izdatelstvo Metallurgija, Moscow, 1971.
[7] Nowotny, H., *Progress in Solid-State Chemistry,* Vol. 5, H. Reiss, Editor, Pergamon Press, Oxford, 1971.
[8] Hägg, G., Z. Physik. Chem. B12, 33 (1931).
[9] Vinek, G., Neckel, A. G., and Nowotny, H., Acta Chim. Acad. Sci. Hung. 51, 193 (1967).
[10] Juza, R. and Bünzen, K., Z. Phys. Chem. N. F. 17, 82 (1958).
[11] Atoji, M., Gschneidner, K., Daane, A., Rundle, R., and Spedding, F., JACS, 80, 1804 (1958).
[12] Vickery, R., Sedlacek, R., and Ruben, A., J. Chem. Soc. No. 2, 498 (1958).
[13] Makarenko, G. N., Pustovoit, L. T., Yupko, V. L., and Rud', B. M., Izv. Akad. Nauk SSSR, Neorg. Mat. 1, 1787 (1965).

[14] Samsonov, G. V., Poroshk. Metall. No. 1, 98 (1965).
[15] Atoji, M., J. Chem. Phys. 35, 1950 (1961).
[16] Atoji, M., and Kikuchi, M., Argonne Nat. Lab. ANL-7441, 1968.
[17] Jedlicka, H., Nowotny, H., and Benesovsky, F., Mh. Chem. 102, 389 (1971).
[18] Rassaerts, H., Nowotny, H., Vinek, G., and Benesovsky, F., Mh. Chem. 98, 460 (1967).
[19] Krikorian, N. K., Bowman, A. L., Krupka, M. C., and Arnold, G. B., High Temp. Sci. 1, 360 (1969).
[20] Petrů, F., Brožek, V., Hajek, B., and Dufek, V., Z. Chem. 9, 71 (1969).
[21] Carlson, O. N., and Paulson, W. M., Trans. Met. AIME 242, 846 (1968).
[22] Haschke, J. M., and Eick, H. A., JACS 92, 1526 (1970); High Temp. Sci. 2, 376 (1970).
[23] Drowart, J., Smoes, S., Vander Auwerd-Mahieu, A., and Wagner, S., in press.
[24] Nowotny, H., *Progress in Solid-State Chemistry,* Vol. 5, Pergamon Press, H. Reiss, Editor, Oxford *etc.* 1971.
[25] Alyamovskii, S. I., Shverikin, G. P., and Gel'd, P. V., Zh. Neorg. Khim. 8, 2000 (1963).
[26] Rudy, E., and Brukl, Ch., J. Amer. Ceram. Soc. 50, 265 (1967).
[27] Kordes, D., Phys. Stat. Sol. 20, K 141 (1967).
[28] Henfrey, A. W., and Fender, B. E. F., Acta Cryst. B26, 1882 (1970).
[29] Yvon, K., and Parthé, E., Acta Cryst. B26, 149 (1970).
[30] Rudy, E., J. Less-Common Met. 20, 49 (1970).
[31] Morton, N., James, B. W., Wostenholm, G. H., Pomfret, D. G., Davies, M. R., and Dykins, J. L., J. Less-Common Met. 25, 97 (1971).
[32] Jack, K. H., AIME meeting, Atlanta, Ga. 1971.
[33] Nowotny, H., Boller, H., and Beckmann, O., J. Solid State Chem. 2, 462 (1970).
[34] Bieganski. Z., Phys. Stat. Solidi, in press.
[35] Ettmayer, P., Mh. Chem. 97, 241 (1966).
[36] Ettmayer, P., Mh. Chem. 101, 1720 (1970).
[37] Boller, H., Mh. Chem., in press.
[38] Bauer, J., and Nowotny, H., Mh. Chem. 102, 1129 (1971).
[39] Smith, G. S., Johnson, Q., and Nordine, P. C., Acta Cryst. 19, 668 (1965).
[40] Smith, P. K., and Gilles, P. W., J. Inorg. Nucl. Chem. 29, 375 (1967).
[41] Beattie, H. J., in *Intermetallic Compounds,* J. Wiley and Sons, J. H. Westbrook, Editor, New York, 1967).
[42] Engel, N., in *Development in Structural Chemistry of Alloy Phases,* Plenum Press, B. C. Giessen, Editor, New York, 1969.
[43] Costa, P. and Conte, R. R., in *Compounds of Interest in Nuclear Reactor Techn.,* edited by Waber, J. T., Chiotti, P., and Miner, W. N., IMD Special Rep. No. 3, Met. Soc. AIME, 1964.
[44] Lye, R. G., in *Propriétés Thermodynamiques, Physiques et Structurales des Dérivés Semi-Métalliques,* CNRS, Paris, 1967.
[45] Bilz, H., Z. Phys. 153, 338 (1958).
[46] Ern, V., and Switendick, A. C., Phys. Rev. 137A, 1927 (1965).
[47] Schwarz, Kh., Doctoral Thesis, University of Vienna, 1968; Neckel, A., Nowotny, H., 6th Plansee-Seminary, Reutte-Tirol 1969.
[48] Conklin, J. B., Averill, Ir. F. W., and Hattox, Th., Colloquim, Centre Européen de Calcul Atomique et Moleculaire, Menton, Sept. 1971.
[49] Hench, L. L., Electronic Bonding and Properties of the Carbides, U. of Florida, 1967.
[50] Schubert, K., *Kristallstrukturen zweikomponentiger Verbindungen,* Springer, Berlin, Göttingen, Heidelberg, 1964.
[51] Nowotny, H., Vitovec, F., in F. Benesovsky, 1st Plansee Seminary, Reutte, Tirol, 1953.
[52] Straumanis, M. E., Faunce, C. A., and James, W. J., Inorg. Chem. 5, 2027 (1966).
[53] Rundle, R. E., Acta Cryst. 1, 180 (1948).
[54] Hume-Rothery, W., *Phase Stability of Metals and Alloys,* P. S. Rudman, et al. Editors, McGraw-Hill, New York, 1967.
[55] Krebs, H., Acta Cryst. 9, 95 (1956).
[56] Ramqvist, L., Jernkont. Ann. 153, 1 (1969).
[57] Hoch, M., in Rudman, P. S., Stringer, J., and Jaffee, R. I., *Phase Stability in Metals and Alloys,* McGraw-Hill Book Co., New York, 1967.
[58] Schäfer, H., Angew. Chem. Int. Ed. Engl. 9, 965 (1970).
[59] Kasper, J. S., Hagenmuller, P., Pouchard, R. M., and Cros, C., Science 150, 1713 (1965).
[60] Laves, F., in *The Theory of Alloys,* Am. Soc. for Met. Cleveland, Ohio, 1956.
[61] Nowotny H., in *Electronic Structure and Alloy Chemistry of Transition Elements,* P. A. Beck, Editor, J. Wiley and Sons, New York, 1962.

[62] Parthé, E., in *Propriétés thermodynamiques, physiques et structurales des Dérivés Semi-métalliques*, CNRS, Paris, 1967.
[63] Engström, I., Acta Universitatis Uppsaliensis Söderström and Finn, Uppsala, 1970.
[64] Schwomma, O., Preisinger, A., Nowotny, H., and Wittmann, A., Mh. Chem. 95, 1527 (1964).
[65] Flieher, G., Völlenkle, H., and Nowotny, H., Mh. Chem. 98, 2173 (1967).
[66] Völlenkle, H., Preisinger, A., Nowotny, H., and Wittmann, A., Z. Kristallogr. 124, 9 (1967).
[67] Flieher, G., Völlenkle, H., and Nowotny, H., Mh. Chem. 99, 2408 (1968).
[68] Zwilling, G., and Nowotny, H., Mh. Chem. 102, 672 (1971).
[69] Flieher, G., Doctoral Thesis, University of Vienna, 1968.
[70] Ivanova, L. D., Abrikosov, N. Ch., Elagina, E. I., and Chostikova, W. D., J. Neorg. Mater. 5, 1933 (1969).
[71] Fujino, Y., Shinoda, D., Asanabe, A., and Sasaki, Y., Japan J. Appl. Phys. 3, 431 (1964).
[72] Karpinskii, O. G., and Evsev, B. A., J. Neorgan. Mater. 5, 525 (1969).
[73] Jeitschko, W., Parthé, E., Acta Cryst. 22, 417 (1967).
[74] Pearson, W. B., Acta Cryst. B26, 1044 (1970).
[75] Axel, H., Müller, W., Schäfer, H., and Weiss, A., Z. Naturforschg. 22b, 1081 (1967).
[76] Rieger, W., and Parthé, E., Mh. Chem. 100, 444 (1969).
[77] Krebs, H., Proc. NPL Symposium No. 9, 1958.
[78] Phillips, J. C., Rev. of Modern Phys. 42, 317 (1970).

DISCUSSION

A. L. Bowman: For the intermediate scandium carbide we always come out with a composition of exactly Sc_4C_3. Our diffraction data resulted in a complete determination of the single carbons in the structure which, of course, we didn't expect at all when we started. Structurally, I like to think of the basic structure of the sesquicarbides as being that of the scandium 4 carbon 3 phase. The sesquicarbides of uranium and plutonium would best be thought of, as for instance, $Pu_4(C_2)_3$. Thus we see the exact relationship between them, even though they seem to be totally different. We seem to find, interestingly enough, that we can make both phases in some of the rare earth carbides by using pressure synthesis. Exactly what happens there we don't understand at all, but that's an initial observation.

H. Nowotny: Well, yes, I agree.

N. C. Stephenson: The manganese silicide structure that you showed there contains silicon pairs. What sort of condition was the manganese in? Were they just isolated cations?

H. Nowotny: You mean with respect to the valence state?

N. C. Stephenson: They weren't bonded to anything else were they?

H. Nowotny: No, the manganese forms a more or less white tin structure and it is in itself diamondoid. One silicon spiral fits with the same direction, but the other is anti. I don't know whether I have really answered your question.

R. S. Roth: I would like to ask if, in the phase diagram for a system containing these ladder-like structures, there are two phase regions between such structures, or are you talking about a continuous ladder-like structure?

H. Nowotny: In this system, manganese silicon, we couldn't find a heterogeneous domain, but we get either the one or the other and this depends very much on the thermal treatment and, of course, also on the composition. In a more detailed study, Dr. Zwilling managed to prepare single crystals of a length of a few centimeters, that means one and one-half inches, and all parts of this were uniformly of the last structure, the 27-47 phase. In most of the Weisenberg patterns we nevertheless observed superstructure reflections with some diffuse character. In other words, it may be that the 27 multiple is just an average and we have domains around this 27. So such a crystal is very complicated in its microstructure.

National Bureau of Standards Special Publication 364, Solid State Chemistry, Proceedings of 5th Materials Research Symposium, issued July 1972.

INVESTIGATIONS IN THE TERNARY SYSTEM BORON - CARBON - SILICON

E. Gugel, R. Kieffer, G. Leimer and P. Ettmayer

Forschungs-institut der Cremergruppe
Roedental, Germany

and

Institute für chemische Technologie anorganischer Stoffe
Universität Wien, Austria

Viewing the literature one will notice that the available knowledge about the nonmetallic inorganic systems are rather insufficient and sometimes do not agree with each other. These systems yield a number of attractive high temperature materials and therefore it is essential to improve available information.

The Institut für chemische Technologie anorganischer Stoffe (Institute for Chemical Technology of Inorganic Materials), Technical University of Vienna, and the Research Institute of the Cremer-Group, Rödental-Germany, have systematically worked in this area for several years. This paper will deal with the system Boron-Carbon-Silicon.

In contradiction, some publications confirmed the existence of B_4C only in the enclosing system Boron-Carbon. However, Boron Carbide is able to incorporate excess Boron up to the composition $B_{6,5}$ (in solid solution) clearly showing a lattice expansion. Within the enclosing system Silicon-Boron there are the chemical compounds SiB_{4-x} ($x \leqslant 1$) and SiB_{12+x} ($x \geqslant 8$). According to our investigations the ternary system itself, in contrast to some other scientists, does not contain ternary phases as well as no solid solution between enclosing binary systems. Limited solid solutions exist around B_4C (+Si) and around SiB_{4-x} (+C). The x-ray investigations permit the presentation of phase distributions. By means of a new method for determination the melting temperatures of high temperature materials the liquidus areas (melting isotherms) of this system were investigated.

Key words: Binary system; boron; carbon; chemical analysis; melting-point determination; metallography; phase-field division; silicon; solubilities; ternary system; x-ray investigations.

1. INTRODUCTION

Many of the nonmetallic hard materials existing in nature or those man-made which are used in technology because of their special properties, can be found in the quarternary system, boron-carbon-silicon-nitrogen. These are the elements which combine especially with the transition metals of the IVa - VIa group of the periodic table to form the well known and very important hard alloys of the carbides, borides, nitrides and silicides.

All compounds of this quarternary system lie as can be seen from figure 1, on the binary connecting lines. As far as is known till now either ternary nor quarternary compounds exist.

Last time we studied all the four ternary systems (fig. 2). Here we shall deal with recent work in the system boron-silicon-carbon.

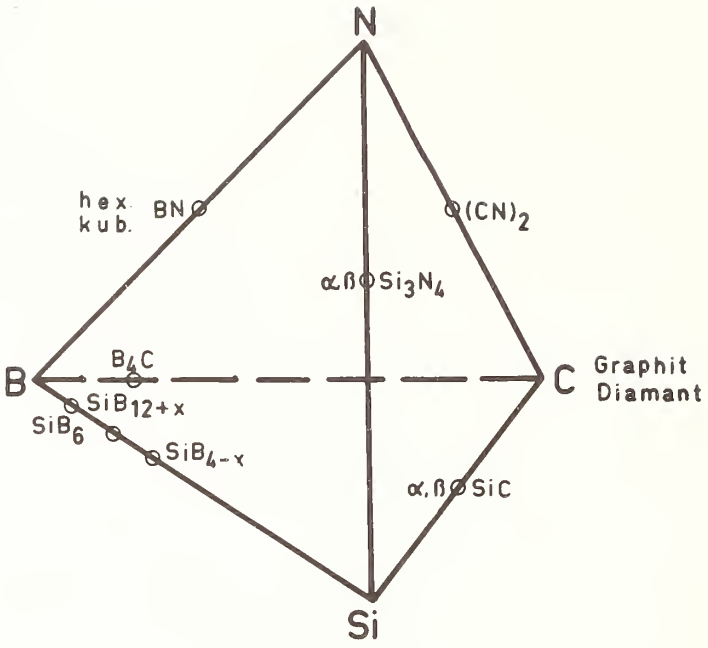

Fig. 1. The quarternary system boron-carbon-silicon-nitrogen.

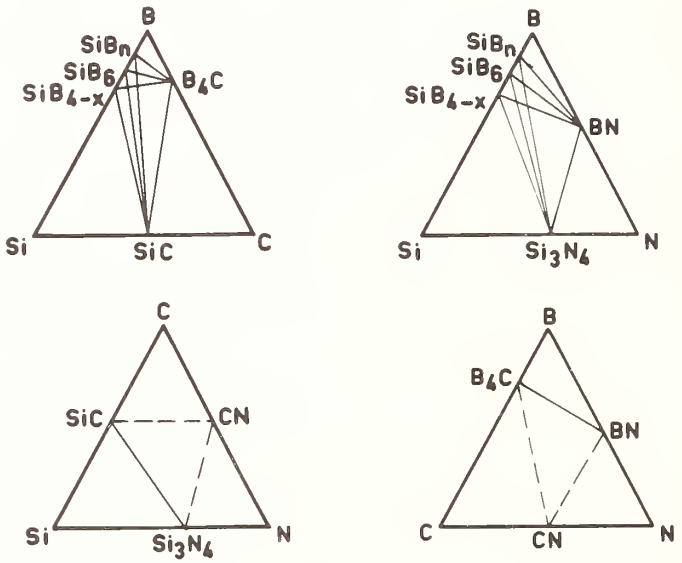

Fig. 2. The ternary systems between the elements boron carbon, silicon and nitrogen.

Of the three boundary binary systems, we have reported recently about the system Si-C [1][1] as well as about the system Si-B [2].

The system B-C, containing the technically very important boron carbide, and therefore investigated many times, has not been covered until now. Russian and American authors, especially, cannot agree about this system. Therefore, we have studied this system once more in detail.

[1]Figures in brackets indicate the literature references at the end of this paper.

The reason for the very different information one can find in the literature for the system B-C, as well as for the ternary system B-Si-C, lies doubtlessly in the experimental difficulties of the investigations. These are caused by the properties of the elements and compounds. These include the high-melting phases B_4C and B, the low-melting element Si with a high vapour pressure, carbon, non-melting under normal conditions, the incongruent-melting siliconborides and SiC, which dissociates to vapour and a solid phase. Boron, carbon and silicon themselves are very reactive at the high temperatures of the investigations and therefore inert crucibles and furnace equipment are hardly available.

Chemical and x-ray analyses, and metallographic investigations were made on samples which were hot- or cold-pressed and then tempered under different conditions. Microhardness, transverse strength and abrasive strength were determined on some selected samples.

Melting point determinations were made in a resistance-heated furnace constructed specially for this purpose (figs. 3 and 4). Melting occurred under an inert atmosphere using pyramid-shaped specimens. Possible support materials were studied. It was possible with this simple equipment to get very exact data.

2. THE SYSTEM B - C

Here we will report only on the results of our own investigations. For the remaining studies of this system, reference should be made to a publication [3] containing an extensive reading list.

The experiments cover compositions of 0 - 60% C, 100 - 40% B, and the temperature range of 1800 - 2300 °C.

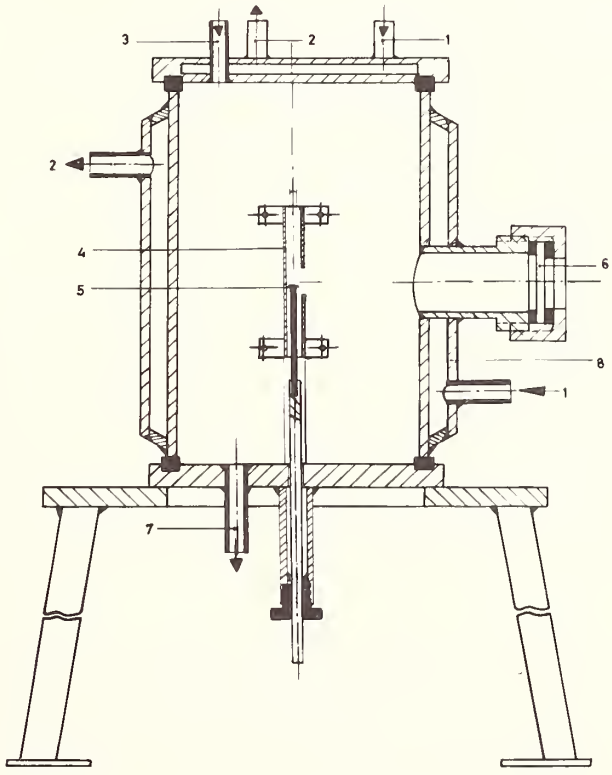

Fig. 3. Furnace for the determination of melting-points.

1. water in
2. water out
3. protecting gas
4. W-heating tube
5. specimen support
6. Pyrex viewing glass
7. vacuum
8. watercooled double casing

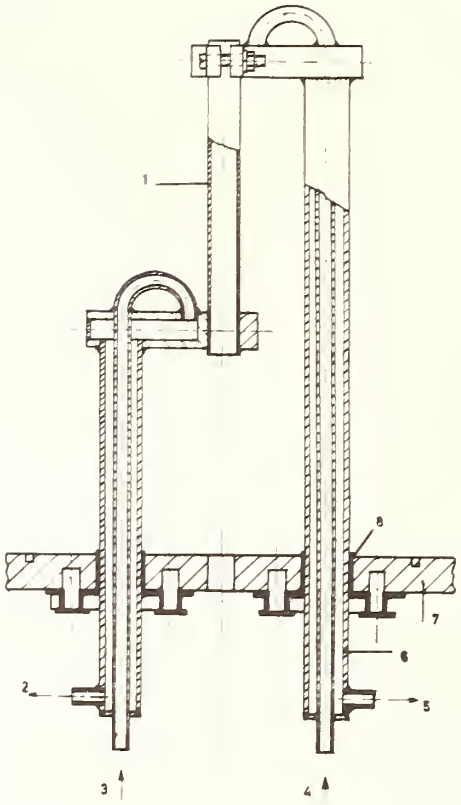

Fig. 4. Electrode arrangement in the furnace for determination of melting-point.

1. W-tube
2. H_2O - out
3. H_2O - in
4. H_2O - in
5. H_2O - out
6. electrode terminals
7. floor plate
8. plastic seal

Above all, x-ray investigations have shown that in the system B-C only one carbide phase exists with a relatively wide range of homogeneity. Figure 5 shows the lattice parameters calculated from the x-ray powder diffraction patterns as a function of the composition of the initial samples. A relatively wide variation in the results of the analysis occurs because of the relatively small displacement of the diffraction lines measured at low angles. Nevertheless, one can recognize a relationship, which could perhaps correspond to the graph line. Therefore the x-ray constants for pure boron carbide, B_4C, are a = 5.60 Å and c = 12.085 Å and those for boron carbide in which the carbon is maximally replaced by boron are a = 5.61 and c = 12.13 Å. The increase of the unit cell dimension along the *c*-axis is very clear. It is easy to interpret as the substitution of larger B-atoms in the carbon chain situated on the *c*-axis.

Comparing this result with the relatively few measurements given in the literature [4-8] one can see that previously a much larger increase of the lattice parameter was determined. However the results confirm in principle the present idea about the lattice of boron carbide.

Figure 6 shows the melting temperatures determined, in comparison with the liquidus temperatures stated by Elliot [9] and Samsonov [10].

As the "melting point", the temperature was estimated at which the pyramid-shaped specimens form a hemispherical pearl. Metallographic investigations have shown that the specimens, even those with a wide melting interval, were totally melted in most cases. The stated values are therefore liquidus temperatures.

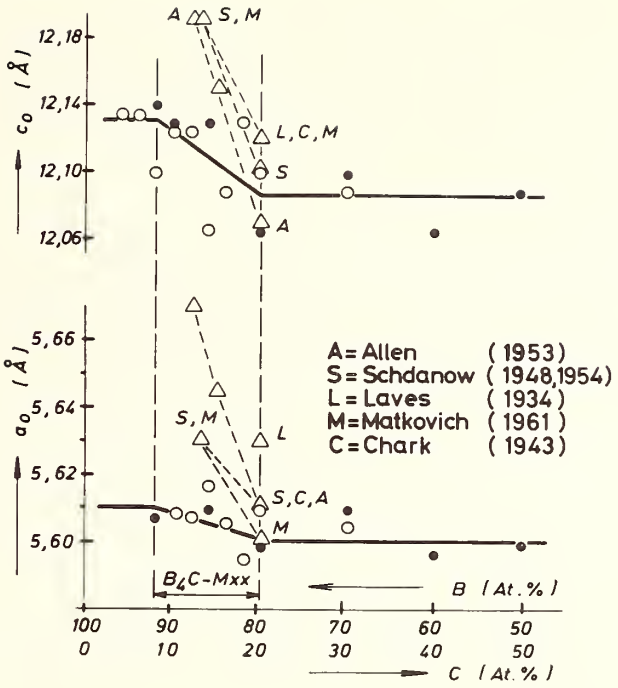

Fig. 5. Lattice constants of B_4C.
● filled circles-hot pressed specimens
○ open circles-cold pressed specimens
△ triangles-literature data

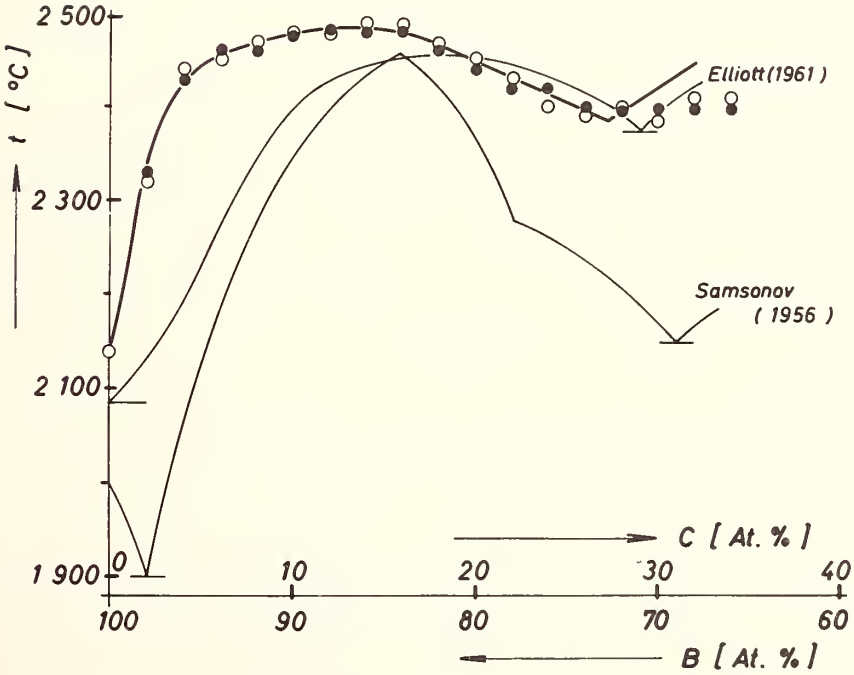

Fig. 6. Liquidus temperatures in the system Boron-carbon.
○ open circles-tungsten tube furnace
● closed circles-Carbon tube furnace

The highest melting temperature in the boron-rich region was measured at 16% C. A eutectic between the supposed compounds $B_{13}C_2$ and $B_{12}C$, as estimated by Schurawlow [11], could not be detected. Furthermore no support was found for the existence of the compound $B_{12}C$ with a melting temperature of about 2400 °C. The melting temperatures in the boron-rich region are, however, higher than estimated previously. In the carbon-rich range our own results are in accord with the liquidus temperatures from Elliot [9] whereas here Samsonov [10] gives too low figures.

All mixtures investigated with C-contents greater than 24%, begin to melt at nearly the same temperature of 2400 ± 10 °C. This is obviously the eutectic temperature. For the identification of the composition of the eutectic the following observation was of use; that samples with more than 26% C do not melt homogeneously. Apparently the eutectic melt infiltrates the porous graphite support leaving a graphitic skeleton. Therefore it can be stated that the eutectic composition contains 26% C in contrast to the 28 and 31% given in the literature. An undetectable diffusion from the graphitic support into the specimens could, however, displace the value to the left side. An eutectic between boron and boron carbide was not detectable, but from results obtained in the experiments with the ternary system one can suppose that it is present. Certainly it lies very close to pure boron and is hard to find because the melting-point of boron is decreased considerably by small amounts of impurities. The eutectic, estimated by Samsonov [10] and Schurawlow [11] seems to be incorrect.

3. THE SYSTEM B - Si - C

The component elements show many similar chemical and physical properties as a result of the horizontal (B, C), the vertical (C, Si) and the diagonal (B, Si) relationship in the periodic table. They are all metalloids with low densities and great hardnesses (for carbon, the diamond). They have, of course, different, but relatively high melting points, are chemically inert and form compounds with similar chemical and physical properties. Among themselves they react to extremely hard compounds, which are the subject of this investigation.

Specimens analysed covered the whole range of the ternary system above 1700 °C.

3.1. THE PSEUDOBINARY SYSTEM B_4C - SiC

Independent of the sintering conditions, x-ray analysis in all cases, showed the two phase SiC and B_4C.

The x-ray diffraction line at 2 θ = 133.5° (copper K-alpha radiation) which exists in all SiC polytypes was constant in the range of ± 0.2°. A solution of boron in the SiC lattice constants of B_4C varied with a relatively intense zone of dispersion between a = 5.58 and 5.61 Å and c = 11,99 and 12.11 Å. As a rule, the lower values can be found by increasing sintering temperatures and in samples with increasing SiC-content. The lattice constants lie below the lowest values we have found in the system B - C and the lowest values we found for SiC-rich samples. Therefore one can assume the existence of a certain slight solubility of SiC in B_4C. Such a solubility is not confirmed in the more recent literature [12], but in older references [13] it seems possible however.

Figure 7 shows the results of the melting-point determinations in comparison with the literature [12]. Therefore the eutectic is closer to B_4C (about 65 mol % B_4C) and the temperature somewhat lower.

3.2. THE PSEUDOBINARY SYSTEM B_4C - Si

In all cases B_4C and SiC were detectable by x-ray determinations. Microscopic investigations indicate the presence of boron silicides, which are required by the stoichiometry. Electron-microanalysis indicated a solubility of 2.2 weight % Si in B_4C. Melting-temperature investigations made on presintered samples are given in the total presentation of the melting-temperatures of the ternary system (fig. 8).

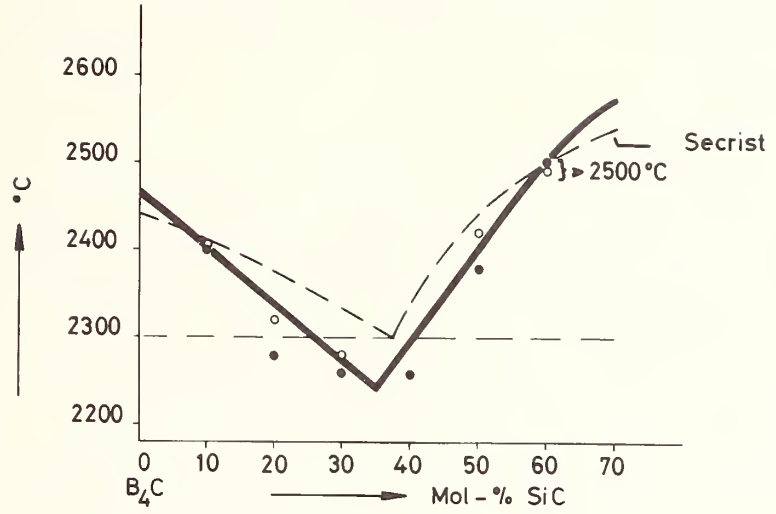

Fig. 7. Liquidus temperatures in the system B_4C - SiC.
● filled circles - C-tube furnace
○ open circles - W-tube furnace

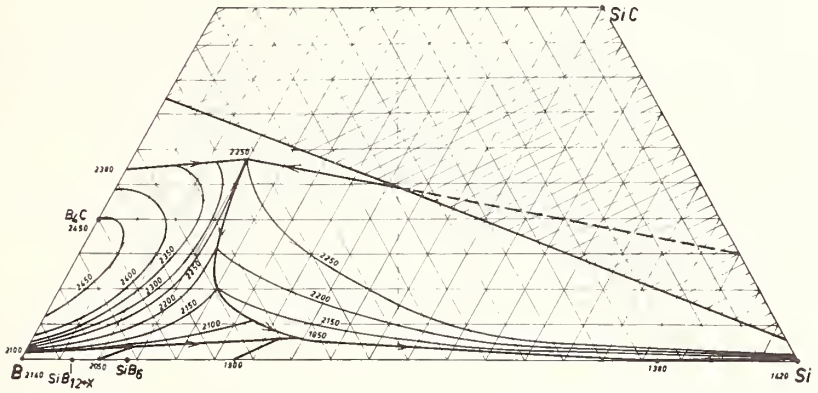

Fig. 8. Melting isotherms and eutectic lines in the system silicon-boron-carbon.

3.3. THE PSEUDOBINARY SYSTEM B - SiC

X-ray analysis showed in all mixtures the two phases SiC and B_4C. Here the formation of boron silicides is also required. The solubility of boron in β-SiC at 1800 °C is 4.9 - 5.2 weight %. This value, contrary to Shaffer [14], is very high. Russian authors [13,15,16] on the other hand have announced a considerable solubility of B in β-SiC. The results of the melting investigations, with those from the system B_4C - B_4Si discussed below are used for the total presentation of the ternary system.

3.4. PSEUDOBINARY SYSTEM B_4C - SiB_4

As starting powders, the end member components were used. The x-ray analysis of the samples, which were sintered at 1900 °C, showed in all cases B_4C. In addition to this, for the starting composition with 10 - 80% B_4Si, SiC appeared as second phase, and for samples with 80 - 90% B_4Si, some SiB_6 as third or second phase. A ternary compound was not detectable. The continuous series of solid solutions as it is stated by several authors [17-21], if at all, is existent only below 1350 °C. At high temperatures SiC always exists, while

SiB_{4-x} dissociates above 1350 °C to SiB_6 and Si, which reacts with the B_4C to SiC. A variation of the lattice parameters of B_4C in equilibrium with silicon-boron alloys was not detectable.

3.5. THE TERNARY SYSTEM

The phases Si, SiC, B_4C, SiB_6, SiB_{12+x} and C were detected. Ternary compounds were not found, not even in the compositions which were stated in the literature [18,19] for them. From melting-point determinations in the ternary system together with those from the boundary systems and the pseudobinaries, the melting isotherms and the eutectic lines as shown in figure 8 can be presented. Therefore the ternary eutectic lies very close to the binary eutectic of the system B - Si.

Figure 9, in conclusion, shows the phase-field divisions at two isothermal sections which would be probable according to the complete results.

4. CONCLUSION

New investigations in the system B - C confirm the statements of Elliot [9] with regard to which phases occur. The only compound is boron carbide, B_4C, with a relatively wide range of composition. With increasing substitution of carbon atoms by boron an increase of the lattice occurs, detectable by x-ray analysis. The liquidus curve of this system has a maximum at 16% C, clearly higher than was assumed previously. The eutectic between B_4C and C lies at 26% C and 2400 °C.

In the ternary system B - Si - C no indication of the existence of a ternary compound could be found. The x-ray diffraction patterns of alloys in the range of the solid solution of Si in B_4C, also showed no indication of the existence of a phase with the character of a ternary compound. However, it seems possible that Si is accommodated in the B_4C-structure, not statistically, but in certain positions. This phenomenon can be observed sometimes in the accommodation of extraneous atoms in the boride lattices.

Based on the results, phase-field divisions at two isothermic sections were determined. As was to be expected from thermodynamic data on SiC and B_4C, at not too high temperatures the Si liquidus is in equilibrium with SiC but not with B_4C.

Melting isotherms and the eutectic lines were determined by melting-point examinations.

There were difficulties in the analysis of the solubilities, but the values were in general not high, and were in agreement with those of other authors. The solubility of boron in SiC was not detectable, neither by x-ray nor by electron-microanalysis. If solid solution occurs, it would be very low.

The range of composition of the compound SiB_6 with regard to the three components has not been investigated, nor has the solubility of carbon in the compound SiB_{12+x}.

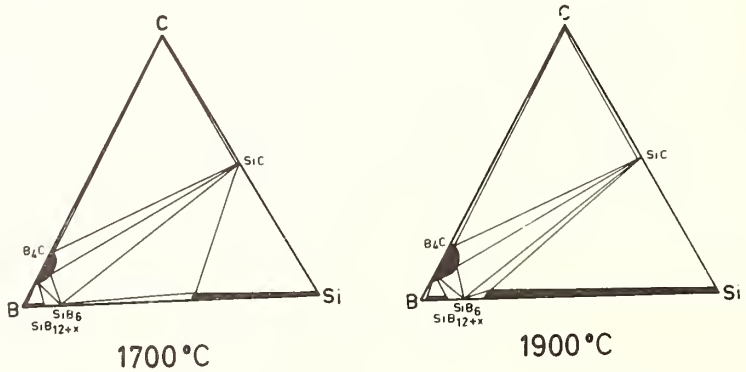

Fig. 9. Phase field divisions in the system Si - B - C at 1700 °C and 1900 °C.

5. REFERENCES

[1] Gugel, E., Ettmayer, P., and Schmidt, A., Ber. Dtsch. Keram. Ges. 45 Nr. 8, 395-402 (1968).

[2] Ettmayer, P., Horn, H. Ch., and Schwetz, K. R., Microchimica Acta (Wien), Suppl. IV, 87-95 (1970).

[3] Kieffer, R., Gugel, E., Leimer, G., and Ettmayer, P., Ber. Dtsch. Keram. Ges. 48, Nr. 9, 385-389 (1971).

[4] Allen, R. D., J. Amer. Chem. Soc. 75, 3582 (1953).

[5] Schdanov, G. S., and Mitarb., J. Phys. Chem. (russ.) 22, 326 (1948).

[6] Laves, F., Nachr. Ges. Wiss. Göttingen, Math.-Physik. Kl., Fachgruppe IV, 1, 57 (1934).

[7] Matkovich, V. J., J. Amer. Chem. Soc. 83, 1804 (1961).

[8] Clark, H. K., and Hoard, J. L., J. Amer. Chem. Soc. 65, 2115 (1943).

[9] Elliott, R. P., IIT Research Institute, ARF-2200-12, Final Rep. US At. Energy Comm. Contract At. (11-1)-578, Projekt Agreement No. 4, p. 44 (1961).

[10] Samsonov, G. V., Schuravlov, N. N., and Amnuel, J. G., Fiz. Met. Metallovad. Akad. Nauk. SSSR Ural. Filial 3, 309 (1956).

[11] Schuravlov, N. N., Makenzenko, G., and Samsonov, G., IZ west. Akad. Nauk. SSSR OTN 1, 133 (1961).

[12] Secrist, D. R., J. Amer. Ceram. Soc. 47, 127 (1964).

[13] Kalinina, A. A., Shamray, F. I., Doklady Inst. Metall. imeni Baykova, A. A., 151 (1960) (trans. J. P. R. S. 4045, Sept. 16, 1960).

[14] Shaffer, P. T. B., Mat. Res. Bull. 4, 213 (1969).

[15] Meerson, G. A., Niselson, L. A., Chu-Ming, C., Izw. Akad. Nauk. SSSR, Met. Topt. 1, 67 (1964).

[16] Meerson, G. A., Kiparisov, S. S., Gurevich, M. A., Den Fen-Syan, Poroshkovaya Met., 2, (26), 15 (1965).

[17] Meerson, G. A., Kiparisov, S. S., Gurevich, M. A., Den Fen-Syan, Poroshkovaya Met., 3, 62 (1966).

[18] Colton, E., J. Amer. Chem. Soc., 82, 1002 (1960).

[19] Matkovich, V. I., Acta Crystall. 13, 679 (1960).

[20] Cline, F., and Sanks, E., Nature 185, 456 (1960).

[21] Brosset, C., Magnusson, B., Nature 187, 54 (1960).

[22] Portnoj, K. I., Samsonov, G. V., Solonikova, L. A., Dokl. Akad. Nauk. SSSR., 125, 823 (1959).

[23] Portnoj, K. I., Samsonov, G. V., Solonikova, L. A., Zhurg. Neorg. Khim, 5, No. 9, 2032, C. A. 55, (1960), No. 7, 6329e (1961).

465-504 O - 72 - 34

National Bureau of Standards Special Publication 364, Solid State Chemistry, Proceedings of 5th Materials Research Symposium, issued July 1972.

VALENCE BONDING IN SOME REFRACTORY TRANSITION METAL COMPOUNDS WITH HIGH COORDINATION

Forrest L. Carter

Naval Research Laboratory
Washington, D. C. 20390

Bond formation in transition metal compounds isomorphous with WC and $A\ell B_2$ is formulated using the bidirectional orbital approximation (BOA) to establish orbital hybridization and a simple but self-consistent application of Pauling's metallic radii with charge transfer to obtain the bond orders. For tungsten carbide seven mutally orthogonal bidirectional bonding orbitals for the negative W atom permits it to simultaneously bond its fourteen neighbors with up to 6.5 electrons. However, bond polarization results in an effective negative charge for carbon of 0.0 to -0.3e. For the diborides the metallic radii results indicate that the group IV diborides have a slightly positive boron which becomes negative with increasing group number but remains below a charge of -1e. Four arguments are given for the pleating of the boron layer were it to be heavily charged as has been proposed earlier in the isoelectronic analogy to graphite. One of these involves a new definition of atomic volume based on the Voronoi polyhedron. Bond formation by the boron and carbon atoms in these compounds is discussed using the nonpaired spin-orbital [NPSO] approach of Linnett.

Madelung constant and Madelung potentials calculations via the method of Bertaut have been made for both the tungsten carbide and the $A\ell B_2(CdI_2)$ structure. These were computed in order to both estimate the magnitude of the electrostatic stability as a function of atomic parameters and to provide a basis for the comparison of ESCA chemical shift data with the calculated effective charge.

The effect of bond formation in distorting the surfaces of constant energy in k space is also considered in these compounds with the aid of a simple square well potential model. The principle directions of these distortions of the unreduced Fermi surface are indicated for the WC structures and as a function of the boron position parameter for the $A\ell B_2$ structures.

Finally, we note that in both of these structures almost all the electrons outside the rare gas cores are involved in bond formation; this is in contrast to the refractory chalcogenides.

Key words: Aluminum diboride - cadmium diiodide structure; bidirectional orbitals; effective charge; ESCA; Fermi surface distortion; Madelung constant; Madelung potential; metallic single bond radii; refractory transition metal compounds; tungsten carbide; valence bonding; Voronoi polyhedra.

1. INTRODUCTION

The materials of principal concern in this paper are those transition metal compounds with the tungsten carbide and the aluminum diboride structures. These generally refractory compounds have in common three features of interest to us:

1) all outer electrons are used in bond formation (largely true),
2) the transition metal atoms have high coordination numbers, 14 and 18 respectively, and
3) the nonmetals, which are usually first row atoms, also have high coordinations for which bond hybrids of the usual types do not apply.

Understanding these compounds then presents a special challenge to the solid state chemist since he must devise new bond hybrids for both the transition metal atom and the nonmetal atom, under the restraint that all electrons outside the rare gas cores are involved in bond formation. This latter fact is, of course, suggested by the unusual refractory nature of many of these compounds.

In view of the commercial importance of some compounds having the tungsten carbide structure, it is surprising that it has not been the subject of extensive theoretical research. That it has not is indicated by the little space devoted to it in reviews such as Nowotny's [1][1] which deal with the bond formation in similar refractory compounds, and in material bibliographies of metals and alloys treating physical properties subject to theoretical interpretation [2]. On the other hand, the diborides which currently are of little commercial value, though of some promise, have a plethora of theoretical bonding interpretations as is indicated in the review of Post [3]. These bonding interpretations are primarily of two forms; electron transport to boron and electron transport away from boron.

Of these two diametrically opposed theories, the theory transporting one electron to boron is the simplest and has considerable appeal to chemists. This theory was probably first proposed by Nowotny [4] in 1950 and Muetterties [5] in 1957, although Pauling [6] had earlier discussed a tetravalent B^- atom in conjunction with FeB. In this description of the diborides the boron is assumed to be isoelectronic and isostructural with graphite, with the boron negative charge neutralized by the intercalated divalent metal ions. For the various other details of this approach it is well to go to the original articles as reviewed by Post [3].

The case for the opposing theory has been discussed by Kiessling [7] in 1950 from a chemical point of view, by Juretschke and Steinitz [8] in 1958, and more recently by Cadeville [9] from physical concepts. In the latter two models various numbers of electrons (3 and 1.7 respectively) are assumed to enter the d band of the transition metal in order to account for experimental mobility and magnetic properties. Taken literally the resultant high positive charges for boron of +3 and +1.7 respectively are difficult to accept from a chemical viewpoint.

In this paper we want to reexamine valence bonding in refractory transition metal materials as represented by the two classes of compounds with the tungsten carbide and aluminum diboride structures. In doing so, use will be made of bond distance information as through Pauling's metallic radii formalism [6; 10, p. 393ff], electrostatic energy calculations, and atomic volume effects. However, instead of applying Pauling's "resonating valence bond" theory [6] in a literal sense, an attempt is made to develop bidirectional orbitals [11] for the transition metal atoms in the two structures and to examine some of the implications of Linnett's [12,13] nonpaired spin-orbitals (NPSO) approach for bonding by the nonmetal atom. The desirability of deviating from the resonating bond approach while retaining many of the desirable features of the valence bond method is related to the incalculable number of different ways of developing equivalent resonant forms in the solid state. The bidirectional orbital approximation (BOA) reduces the number of possibilities to a manageable few which can be ordered.

In particular, the tungsten carbide structure is approached from the metallic radii formalism, electrostatic energy, and valence bond methods in sections 2., 3., and 4., respectively. For the diborides similar considerations are applied in the main sections 5., 7., and 8., while a new concept of atomic volume is developed in section 6. Theoretical and experimental evidence is adduced, in these four sections, against the existence of a planar graphite-like layer composed of B^- ions. Finally, in section 9 the effect of bond formation on the shape of the Fermi surface is discussed in regard to the two different structures along the lines suggested earlier by the author [11].

Prior to proceeding to the body of this primarily theoretical paper, it is of value to the reader to recognize that the most important and difficult portion of working in the area of these refractory materials is the preparation of single phase, well characterized compounds. That this is a nontrivial problem is suggested by the frequency that irregularities

---

[1] Figures in brackets indicate the literature references at the end of this paper.

in the metallic radii results are coincident with the questioning in the literature of the compounds existence.

2. METALLIC VALENCES IN TRANSITION METAL COMPOUNDS

By the use of Pauling's semiempirical metallic radii formalism [6; 10, p. 393ff] it is generally possible with the data from an accurate structure analysis to obtain estimates of the following properties: 1) the relative importance of different bonds, 2) the effective valences V_j, for each atom, 3) an approximate distribution of bonding electrons between the s-p and d orbitals, and 4) the approximate number of unshared and unpaired electrons on each atom. For the transition metals the number of unpaired electrons can be checked against known magnetic properties. In Pauling's approach the atomic valence V_j of atom j is equal to the sum of the bond orders n_{ij} of all important bonds, eq (1). These bond orders are

$$V_j = \sum_i n_{ij} \tag{1}$$

$$d_{ij} = R_i + R_j - 0.600 \log n_{ij} \tag{2}$$

$$R_i = 1.825 - 0.043Z - (1.600 - 0.100)\delta \tag{3}$$

obtained from the bond distances d_{ij} and the single bond metallic radii R_i via eq (2). In eq (3) we give Pauling's formula for estimating the single bond radii R_i, for the iron-transition row elements according to δ, the bonding d character, and Z, the number of electrons outside the rare gas core. These radii are in general a function of the atomic valence, both through the d character, δ, of the bonding orbitals and through the number of electrons Z, associated with the atom in question. This latter factor includes electrons involved in charge transfer but not electrons associated with bond polarization.

In order to apply these equations to a known structure, an Algol program [14] has been developed that solves the above simple equations in an reiterative manner taking into account electronegativity effects like the one of Schomaker and Stevenson [10, p. 228], equations similar to eq (3) for the elements of other rows, and the effect of nonstoichiometry (without site relaxation). While the equations and effects involved are simple, the program is not, due to an inordinate amount of electron bookkeeping required for a program capable of handling a general structure which might involve any combination of the elements (actinides generally excluded). Presumably the only variable permitted is charge transfer since tables of the single bond radii and d character have been provided by Pauling [6,10]. In fact it is often necessary to permit variation of the transition metal d character, δ, in order to achieve selfconsistency between the valence "calculated" by eq (1) and the valence "estimated" from the electrons available and set aside for covalent bond formation (a bookkeeping operation).

In general it is desirable to pay more attention to trends in series of related compounds than it is to focus attention to the details of any one compound. This is particularly true in the refractory carbides and diborides discussed in this paper since it is often the case that the only information reported is the nominal starting preparatory composition and the lattice parameters. In the general absence of detailed information the author has little alternative to the suspect assumption that the compounds reported are pure and stoichiometric. Even when the assumption is correct a detailed analysis might be misleading in a refractory and hard compound since the final structure can be a compromise in which some bonds are stretched while others are compressed. This situation will lead to incorrect bond orders via the application of eq (2) and to incorrect valences, eq (1), in some cases. Even so the use of Pauling's metallic radii are much to be preferred on the basis of the new information obtained than any "hard sphere" or ionic radii model. The parameters associated with the latter models usually are applicable only to a very limited class of compounds while Pauling's approach has general application to intermetallic compounds, semimetals, and most semiconductors.

2.1. METALLIC RADII CALCULATIONS FOR THE TUNGSTEN CARBIDE COMPOUNDS

In compounds with the one-to-one hexagonal tungsten carbide structure the nonmetal has six metal neighbors in the form of a trigonal prism while the metal atom has six basal plane

metal neighbors, and two additional metal neighbors above and below the basal plane. Further, the metal atom has six nonmetal neighbors also in a trigonal prismatic coordination. For the compounds and their lattice parameters tabulated by Wyckoff [15] the results of various metallic radii calculations are given in tables 1 and 2. In general we see from table 1 that the strongest bonds are the metal-nonmetal bonds, labeled M-X, which are somewhat better than halfbonds (bond order equals 1.0 for a single bond). The metal-metal bonds are also quite significant, being only slightly weaker than halfbonds, except in the compound of MoP. Of the metal bonds the vertical pair along the z axis are consistently stronger than the more numerous basal plane bonds. In table 2 it is apparent that the tungsten carbide structure is characterized by a high metal valence of about 5.0 to 6.5 and by a low charge effect.

Details and limitations of the metallic radii approach are indicated by the first two entries in table 1 and 2 for tungsten carbide, as calculated under two different charge transfer restrictions. Under the assumption of 1:1 stoichiometry for tungsten carbide the application of the metallic radii equations as given by Pauling does not lead to self-consistency without some upward adjustment of the tungsten d character (δ, as given by eq (2)). Such a change in d character results in a smaller single bond radius (R_1) and usually a decrease in the calculated valence. If the d character increases too much (*e.g.* 10%) or decreases, the experience of the author suggests that the reason may reside in the incompleteness of the material characterization, and that assumptions as to stoichiometry and purity are inaccurate. In the case of entries 1 and 2, table 2, it is seen that the d character increases from 39% to 42% and to 40% respectively. In the first case, entry 1, no charge transfer was allowed so that all of the adjustment to attain self-consistency was attained by the d character increases. The effective charge of carbon, -0.36, is due to the polarization of the bond according to electronegativity differences in a manner employed by Hedberg [16] and Pauling [10]. In the second case, entry 2, sufficient charge was transferred from carbon to tungsten to make the effective charge of each atom zero, where the effective charge of each atom is taken as the sum of the charge transferred to it plus the sum of the charges due to the polarization of the pure covalent bonds "i" of bond orders n_i. This latter case, which we describe as a "neutral cell" calculation (to be discussed shortly), appears to give the following rather reasonable results for tungsten carbide: 1) first very little adjustment of the tungsten d character is required, 40% *vs* 39.7%; 2) electrons transferred to tungsten are employed in bond formation (no unshared electrons on tungsten) and 3) all the carbon electrons are also used for bond formation or are transferred. The net result is that tungsten has roughly 6-1/2 electrons for forming halfbonds with 14 near neighbors and that all electrons outside the rare gas cores of both atoms are bonding electrons, a situation which is wholly reasonable in light of the refractory nature of tungsten carbide.

Table 1

Metallic Radii and Bond Orders for the Tungsten Carbide Compounds

ENTRY[a]	cpd	RADII (Å)		BOND ORDERS		
		M	X	M-X	M-M(basal)	M-M(vert)
1.[b]	WC	1.322	0.772	0.543	0.318	0.416
2.	WC	1.333	0.770	0.568	0.380	0.495
3.	WN	1.333	0.770	0.486	0.420	0.543
4.	RuC	1.276	0.774	0.528	0.256	0.356
5.	OsC	1.282	0.774	0.539	0.266	0.370
6.	MoP	1.301	1.108	0.826	0.090	0.098
7.	MoP	1.301	1.062	0.693	0.090	0.098

(a) Similar entries of tables 1 and 2 correspond to the same calculations.
(b) Entry 1 was calculated under the restriction of zero charge transfer, the remainder of the table was calculated using the "neutral" cell approach.

Table 2

Metallic Radii Summary for the Tungsten Carbide Structure

ENTRY[a]	cpd.	ELEM.	CHARGE Trans.	CHARGE Eff.	CALC. VALENCE[b]	δ d-CHARACTER[c]	UNSHARED ELECTRONS
1.[d]	WC	W	0.0	+0.37	6.00	0.41(0.39)	0.0
		C	0.0	-0.37	3.26	--	0.74
2.	WC	W	-0.51	0.0	6.57	0.40(0.39)	0.0
		C	+0.51	0.0	3.41	--	0.08
3.	WN	W	-1.00	0.0	6.52	0.39(0.39)	0.49
		N	+1.00	0.0	2.91	--	1.08
4.	RuC	Ru	-0.07	0.0	5.41	0.46(0.50)	2.66
		C	+0.07	0.0	3.17	--	0.76
5.	OsC	OS	-0.07	0.0	5.57	0.46(0.49)	2.50
		C	+0.07	0.0	3.23	--	0.70
6.	MoP	Mo	-0.11	0.0	5.69	0.43(0.43)	0.42
		P	+0.11	0.0	4.95(3.11)	--	1.78
7.	MoP	Mo	-0.09	0.0	4.89	0.43(0.43)	1.20
		P	+0.09	0.0	4.16	0.04(0.0)	0.75

(a) Similar entries in tables 1 and 2 correspond to the same calculation.

(b) Generally the "calculated" valence equals the "estimated" valence, when this is not the case the estimated valence is given in parentheses.

(c) The d-character in parentheses is that given by Pauling or calculated from his table of single bond metallic radii [10].

(d) With the exception of entry 1, all results are for the "neutral" cell restriction, that is, charge transferred is balanced by bond polarization such that the effective charge on each atom is zero. In this case, however, no charge transfer was permitted.

In those cases where bond polarization in a compound is counteracted by charge transfer, see Pauling [10, p. 431ff], a polyhedral cell can be devised [17] such that the total charge in the cell is zero. Such a "neutral" cell about a particular atom is constructed along the lines of a Voronoi or Wigner-Seitz cell by constructing planes which are both perpendicular to the inter-neighbor vectors and which divide in half each bond of the atom of interest. The smallest polyhedron formed by this process is the cell of interest. From atom i, the distance dp of the plane which divides equally the bonding electrons between atoms i and j is taken to be

$$dp = (d_{ij} - R_i - R_j)/2 + R_i = (d_{ij} + R_i - R_j)/2 \qquad (4)$$

where d_{ij} is the internuclear distance and R_i, R_j are the single bond radii. The polarization of this bond is assumed to transport through the bond-bisecting plane that amount of charge to be associated with the electronegativity difference times the bond order [16]. The cell charge is zero when the total bond polarization charge is equal to that transferred to another atom. For tungsten carbide the neutral cells for both kinds of atoms are compared in figure 1 with their Voronoi polyhedra (to be discussed in greater detail later). The neutral cell restriction was employed with the remaining entries of table 1 and 2 in order to clarify any trends. However, in these materials it seems reasonable that the physical situation is bracketed between the results under the restriction of zero charge transfer and those of the

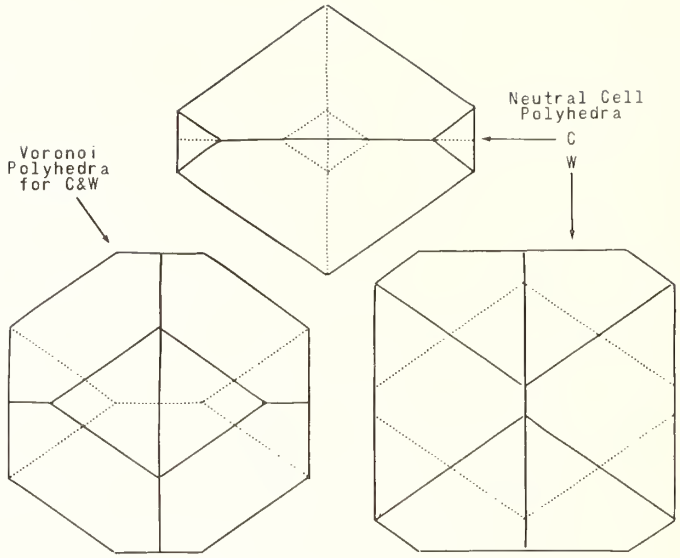

Fig. 1. The Voronoi polyhedron for carbon is the same as that for the tungsten atom in the tungsten carbide structure. This polyhedron, whose volume is half that of the unit cell, is compared with the neutral cell polyhedra for carbon and tungsten. These cells, which more nearly reflect the volume associated with the individual atoms almost pack together perfectly to fill all space. The c axis is vertical.

neutral cell restriction. From table 2, entries 1 and 2, we see that the effective charge of carbon is negative with a maximum value -0.36.

The neutral cell calculation for tungsten nitride is of interest for several reasons. In the first place, the largest electronegativity difference of tungsten and nitrogen polarizes the W-N bonds more, so that the neutral cell calculation requires the largest charge transfer to the metal of any of the compounds in the series of table 2. In the second place, 100% more charge is transferred than seems to be used by the tungsten atom in bond formation since 0.49 tungsten electrons are unused (unshared). Finally, so much charge is transferred that the single bond radius of nitrogen is a near equivalent to that of neutral carbon, table 1.

While the neutral cell restriction seems to be eminently reasonable for application to intermetallic compounds of good electrical conductivity, perhaps its application to compounds exhibiting large electronegativity differences is less desirable. On the other hand, this neutral cell approach seems reasonable when taken in combination with the meager experimental data available. Tungsten mononitride is rather different than the refractory tungsten carbide in that it is reported by Schönberg [18] to decompose at 600 °C to W_2N and nitrogen gas. In addition, Schönberg suggested that the compound was not stoichiometric but probably contained less nitrogen than 50% atomic. A decrease in nitrogen content will tend to produce three desirable effects in terms of the neutral cell calculations: 1) The number of electrons transferred to tungsten but not used for bonding will be directly reduced through composition changes. 2) Similarly, the tungsten charge will also be reduced and appear to more nearly resemble that of tungsten in the carbide. This will have a secondary effect on the charge transferred as the W-N electronegativity difference will be decreased. 3) Finally, the nitrogen radius will be larger and the metallic radii calculation will yield a valence of nitrogen greater than the 2.91 of table 2. These three points taken together suggest that stoichiometric tungsten mononitride might be difficult to prepare and give reasons for the comparative stability of W_2N, that is, provided it has a related structure.

Experimentally little data on the stoichiometry and properties of ruthenium and osmium monocarbide exist. That more is needed is indicated by the neutral cell metallic radii calculations; the results of which are given in tables 1 and 2. Since the electronegativity differences are small, the neutral cell approach may be expected to apply; even so in both cases, entries 4 and 5, the d character had to be decreased (metal radius increased) by 4% and 3% in order to obtain selfconsistency. This suggests an interstitial impurity or that excess carbon may be present. Otherwise the results as well as some of the refractory properties are similar to those of tungsten carbide[2]. The calculated results are similar in the presence of the high metal valence, an apparent carbon valence of less than four, and good metal-metal bonds.

The neutral cell results for molybdenum monophosphide are rather different in regards to this last point as illustrated by entries 6 and 7 in table 1. Here it seems that the metal-metal bonds are a fourth as strong as in the remaining members of the tungsten carbide series. However, the metal and nonmetal valences are comparable to the other members of the series. Another difference is the use of a smaller radius by phosphorous than is normal: this is interpreted as the use of a small amount of d character according to an equation which is an extrapolation of Pauling's equations and is similar to eq(3) . That the normal radius is inappropriate in this case is shown by entry 6, table 2, in which the estimated phosphorous valence of 3.11 is not equal to the calculated valence of 4.95. In order to achieve selfconsistency the insertion of 3 to 8% phosphorous d character was assumed. Entry 7, table 2, gives the results for 4% d character which was approximately the lowest d character giving selfconsistency. At higher d character the Mo-P bond order became more nearly like a halfbond at the expense of slightly decreased valences. The use of d character by phosphorous is understandable and is discussed later in terms of bidirectional orbitals for its trigonal prismatic coordination. An alternative explanation might be metal deficiency; however, the experimental data given does not bear on this point.

The effective charges for the various members of the tungsten carbide compounds might be summarized as follows: Carbon in tungsten carbide has a small negative charge due to bond polarization effects but one which is significantly less than the zero charge transfer case of -0.36. Nitrogen in WN has a somewhat larger negative charge than its carbon analogue, but its lower composition ratio will result in a tungsten charge approaching that in the carbide. The remaining compounds should have quite small charges of less than +0.1. Part of the theoretical information required to verify these expectations is developed in the next section.

3. ELECTROSTATIC AND POTENTIAL ENERGY CALCULATIONS

Any model of bond formation in a heteroatomic material will, in effect, associate with each atom a net effective charge. Accordingly, a comparison of calculated charges with measured charges would be a useful adjunct in a test of the model in addition to the usual test using interatomic distances. While accurate determinations of atomic charges has been attempted by x-ray and optical techniques, generally these have not been too successful. However, new technical advances (x-ray) and interpertations of optical bond data by Phillips [19] may prove useful. Meanwhile, the method of electron spectroscopy for chemical analysis (ESCA) has been developed by Siegbahn and his co-workers [20] at Uppsala and this method promises to be a much more direct and rapid approach to the determination of effective atomic charges in a compound. In short, the technique is to bombard the core electrons with a monochromatic beam of x-rays with the energy E_ν and accurately measure the energy E_k of those electrons which escape the solid without being inelastically scattered. The binding energy E_B of the core electron is then simply $E_B = E_\nu - E_k$. The chemical shift ΔE is the difference $E_B - E_B^o$ where E_B^o is the binding energy for that element in some standard state. Simple potential theory suggests that for a free atom a positive ΔE corresponds to a positively charged atom. In the case of a crystalline compound the approach must be modified to allow for the Madelung potential as has been discussed by Siegbahn et al. [20] and Ramqvist [21].

Although to date little chemical shift information is available on transition metal compounds having the tungsten carbide and aluminum diboride structure, the corresponding

---

[2]Nowotny [1, p. 194] reports that Knapton has demonstrated that these reported carbides of ruthenium and osmium probably were, in fact, tungsten carbide.

Madelung constant and Madelung potentials have been calculated here in anticipation of the rapid maturing of the ESCA technique. Two more immediate reasons for the Madelung constant calculations include the electrostatic estimation of the tungsten carbide heat of formation as per Ramqvist [21] and concern for the stability of the boron position in the diborides when charge has been transferred.

The Madelung constant A, and potentials V_i, have been calculated via the method of Bertaut [22,23]. Using the notation of Templeton [24,25] the appropriate formula for one molecule per unit cell is eq (5) where W_E is the electrostatic energy,

$$A = -\frac{W_E}{\varepsilon^2} L = \frac{gL}{R} \sum_j z_j^2 - \frac{\pi R^2 L}{V} \sum_h F^2 \, \phi(\alpha)/h^2 \tag{5}$$

ε is the electron charge, V is the unit cell volume, L is a standard length taken here as $L = V^{1/3}$, z_j is the charge of the atom j, and h is the length of the reciprocal lattice vector $(h_1 h_2 h_3)$. The structure factor term F is given in eq (6) where the atom j is at the position $(x_1 x_2 x_3)$.

$$F = \sum_j z_j \, e^{2\pi i (h_1 x_1 + h_2 x_2 + h_3 x_3)} \tag{6}$$

The function $\phi(\alpha)$ is simply the square of the Fourier transform of the normalized linear spherical charge distribution f(r) defined by eq (7) with R as the sphere radius. The self-energy factor g is readily shown to be g = 26/35 [23,25]

$$f(r) = \begin{cases} 3(R - r)/\pi R^4 & r \leq R \\ 0 & r > R \end{cases} \tag{7}$$

and the parameter α is defined simply as $\alpha \doteq 2\pi hR$.

The potential V_j, at the position of the atom j is readily calculated by the method of Bertaut [23] at the same time as the Madelung constant. The potentials V_j, are related to the electrostatic energy W_E, by the eqs (8 and 9).

$$V_j = \delta W_E / \delta z_j \tag{8}$$

$$W_E = \frac{1}{2} \sum_j V_j z_j \tag{9}$$

The equivalence of the carbon and tungsten positions in the tungsten carbide structure permits the potentials to be obtained from the Madelung constant without further calculation, thanks to eq (9), as is occasionally the case with other simple structures [21]. However, for the $A\ell B_2$ case the aluminum and boron site potentials must be individually calculated. Unless otherwise stated, all calculations were made by summing over the points in reciprocal space out to a limit of h(max) determined by $\alpha(max) = 2\pi Rh(max) = 5.0$. The value of R in these hexagonal structures was taken as $R = 0.285\ A_o$ where A_o is a basal plane unit cell edge. In both the tungsten carbide and the diboride structure the closest interatomic approach for any value of the metalloid z parameter is $A_o/\sqrt{3}$. The radius R was chosen to be less than $0.2887\ A_o$, or half this value, so that no correction was needed for the overlapping of the charged spheres.

The computer program used [26] is suitable for several simple hexagonal structures and was tested by verifying the work of Zemann [27] who gave the variation of the Madelung constant of the NiAs structure as a function of the c/a ratio. The program was further checked against the empirical "reduced" Madelung constant of Templeton [28] as indicated in the appropriate sections below. The results for the CdI_2 structure also generally supported the work of Hartman [29] who obtained the value $A(R_o) = 4.381890$ rather than the earlier and less accurate value of Hund [30] who obtained $A(R_o) = 4.71$. Both of these values are based on R_o the shortest anion-cation distance. Table 3 gives the present results for the Bozorth CdI_2 structure (see [15, p. 266]) as a function of a few values of the iodine z parameter and two values of the c/a ratio. These calculations are based on a cation charge of +1.0,

an anion charge of -0.5, and a length L equal to a cube root of the volume. When Hartman's value is converted to these conditions, one obtains A = 1.73865 which is lower by 0.00030 than the value shown in table 3 for z = 1/4, c/a = 6.855/4.240 ≐ 1.617, and $\alpha(\max) = 5\pi$. Jones and Templeton [25] have provided a table of corrections for series termination to be applied to Madelung constants calculated using the Bertaut series for values of $\alpha(\max)$ up to $\alpha(\max) = 5\pi$. In the present case this correction amounts to 0.000034 which is about 1/9 the amount required to produce agreement between Hartman and the results obtained here. The CdI_2 calculations were repeated for $\alpha\max = 5.5\pi$ and are indicated in table 3 in parentheses. These results tend to confirm the size of the Jones and Templeton correction and suggest that Hartman's value may be 0.015% smaller than the best estimate of A = 1.738918.

3.1. THE TUNGSTEN CARBIDE MADELUNG CONSTANT

Using Bertaut's method as described above, the Madelung constant for the tungsten carbide structure has been calculated as a function of the c/a ratio as well as a function of carbon z position. In table 4 the Madelung constant $A = W_E L/\varepsilon^2$ is given for the charges $z_W = +1$, $z_C = -1$ where W_E is the electrostatic energy and $L = V^{1/3} = A_o\ (\sqrt{3}\ c/2a)^{1/3}$. As the result of this charge choice and the carbon and tungsten position similarity the same table can be used for the carbon Madelung potential interpreted as $V_C L/\varepsilon$, and with a negative sign as the tungsten Madelung potential, $V_W L/\varepsilon^2$. The symbol ε represents the electron charge. The Jones and Templeton correction for table 4 is $Q = \Delta AR/2L = 5.7 \times 10^{-6}$ and is a slowly varying function of c/a. Thus for c/a = 0.85 the numerical magnitude of A should be decreased by $\Delta A = 0.000036$ and at c/a = 1.2 by $\Delta A = 0.000041$.

The increase of the electrostatic energy (Madelung constant) with the decreasing separation of the tungsten and carbon layers and the decrease of the Madelung constant with increasing c/a ratio is expected from simple electrostatic considerations. The carbon parameter at z(C) = 0.50 and constant c/a ratio is at the Madelung constant minimum. Experimentally determined metalloid positions in this structure at values other than at 2/3, 1/3, 1/2 are not known to the author. Even so, on the basis of L being the cube root of the molecular volume, the Madelung constant 2.137, of the tungsten carbide structure with c/a = 1.0

Table 3

The Cadmium Iodide Madelung Constants
and Potentials for Selected Parameter Values

METALLOID	z =	0.30	0.25	0.20
C/A				
1.617	A	1.481751 (1.481736) (a)	1.738951 (1.738935)	1.957677 (1.957662)
	LV_{Cd}/ε	-1.864629 (-1.864609)	-2.092507 (-2.092485)	-2.340555 (-2.340535)
	LV_I/ε	1.098873 (1.098863)	1.385396 (1.385385)	1.574799 (1.574789)
1.633	A	1.469607 (1.469592)	1.732332 (1.732316)	1.956348 (1.956334)
	LV_{Cd}/ε	-1.846214 (-1.846194)	-2.079068 (-2.079047)	-2.332955 (-2.332936)
	LV_I/ε	1.093000 (1.092991)	1.385596 (1.385585)	1.579742 (1.579732)

(a) Values in parentheses are for $\alpha_{max} = 5.5\pi$, others for $\alpha_{max} = 5.0\pi$.

Table 4

Madelung Constants for the Generalized Tungsten Carbide Structure

C/A	z = 0.50[a]	0.45	0.40	0.35	0.30	0.25	0.20	0.15	0.10	0.05	0.00
0.85	2.16427	2.16929	2.18393	2.20689	2.23611	2.26888	2.30205	2.33232	2.35659	2.37229	2.37772
0.90	2.16559	2.17184	2.19009	2.21876	2.25533	2.29647	2.33825	2.37650	2.40726	2.42719	2.43409
0.95	2.15612	2.16371	2.18589	2.22081	2.26548	2.31589	2.36728	2.41450	2.45257	2.47730	2.48587
1.00	2.13718	2.14622	2.17261	2.21426	2.26769	2.32821	2.39015	2.44728	2.49350	2.52360	2.53405
1.05	2.10988	2.12042	2.15127	2.20006	2.26285	2.33425	2.40763	2.47560	2.53079	2.56683	2.57936
1.10	2.07512	2.08724	2.12273	2.17900	2.25167	2.33464	2.42029	2.49998	2.56495	2.60750	2.62232
1.15	2.03366	2.04740	2.08770	2.15174	2.23473	2.32989	2.42859	2.52085	2.59639	2.64602	2.66333
1.20	1.98617	2.00157	2.04679	2.11883	2.21252	2.32041	2.43287	2.53853	2.62541	2.68269	2.70271

(a) The nonmetal is assumed to be in the 1c site (2/3,1/3,z) of the trigonal space group C_3^1 - P3 (with the metal at the origin) rather than in the more special 1f site (2/3,1/3,1/2) of the D_{3h} - $P\bar{6}m2$ space group.

compares favorably with that of the NaCℓ structure, 2.202, and that of the CsCℓ structure, 2.035.

For tungsten carbide itself with a = 2.9065 and c = 2.8366A we have that the Madelung constant referred to L is 2.1465 and $A(R_o)$ referred to the shortest anion-cation distance R_o, is $A(R_o) = 1.7161$. This latter value is the same as for Templeton's "reduced Madelung constant" α defined by eq (10) where the sum is over all atoms in the

$$a = 2A(R_o)/\sum_i z_i^2 \tag{10}$$

"molecule" [31]. Templeton [28] had shown earlier that α could be approximated by the empirical equation below, eq (11)

$$\alpha = 1.89 - 1.00/m \tag{11}$$

where m is the weighted-harmonic-mean coordination number defined as $1/m = (\sum_i n_i p_i)/(\sum_i n_i)$. Here it is assumed that n_i atoms of one kind have the coordination number p_i, where the sum is again over all atoms in the "molecule" or unit cell. For tungsten carbide 1/m = 1/6 and the empirical $\alpha = 1.72$ in good agreement with the reduced Madelung constant of eq (10), where $\alpha = 1.7161$.

Having calculated the tungsten carbide Madelung constant, we are now in a position to estimate the negative charge on the carbon atom from the reported ESCA chemical shift data [31]. Using a combination of metal x-ray absorption edge (K) and ESCA data, Ramqvist [21] was able to obtain the atomic charge for titanium in TiC and the carbon 1s Coulomb repulsion integral γ_{C1s}, as $z_{Ti} = 0.4$ and $\gamma_{C1s} = 0.73$ Hartree (atomic units). From this start he was able to indicate that the metal charge in a series of cubic transition metal carbides was proportional to the ESCA chemical shift and that the electrostatic energy calculated simply from this charge and the Madelung constant correlated surprisingly well with the heat of formation of these various carbides. Using the ESCA chemical shift value of $S_{C1s} = 2.1$ eV reported by Ramqvist for tungsten carbide and his experimental value of the Coulomb repulsion integral γ_{C1s}, the carbon charge in tungsten carbide is calculated here to be $z_C = -0.245$ from eq (12) as per Ramqvist. The

$$S_{C1s} = z_C\gamma_{C1s} + V_C = z_C\,(\gamma_{C1s} - A/L) \tag{12}$$

resultant electrostatic energy is calculated from the tungsten carbide Madelung constant of 2.146 to be 65.6 kJ/mole which is in rather poor agreement with the experimental heat of formation of 40 ± 2kJ/mole. This suggests that the estimated charge is about 25% too high and that a value of $z_C = -0.20$ would be better. The alternative, that γ_{C1s} should be as large as 0.80 Hartree, seems unlikely since it will later be seen that a strong parallel can be drawn in the carbon bonding and the use of the carbon p orbitals in the tungsten carbide case compared to the cubic transition metal carbides. Recent advances in ESCA instrumentation could be advantageously employed to confirm or deny the Ramqvist reported shift.

The Madelung constant calculations also give support to the ordered carbon position found by Leciejewicz using neutron diffraction techniques [32]. Earlier it was uncertain whether carbon was in the ordered position 2/3, 1/3, 1/2 or was disordered between that position and 1/3, 2/3, 1/2. Using the Bertaut method for the case of perfect disorder [33], the author has employed Madelung constant calculations to show that a statistical distribution of cation vacancies in lanthanide sesquichalcogenides having the Th_3P_4 structure is electrostatically unstable with respect to the complete ordering of vacancies [34]. A similar effect may be expected here. The case with z(C) = 0.5 has not been calculated; however, the case with one carbon atom at 1/3, 2/3, 0 and charge of -1.0 can be compared with the VB_2 - CdI_2 calculations with the boron position z(B) = 0 given in a later section (table 7). In this case we have two atoms of charge -0.5 at the positions 1/3, 2/3, 0 and 2/3, 1/3, 0; this would correspond to the complete disordering of the carbons. By comparing Madelung constants at various c/a ratios, we see that the ordered case is more stable by 0.61 units at c/a = 0.90 to 0.67 units at c/a = 1.2. This result, a 25% increase in electrostatic stability, is suggestive that the ordered case at z(C) = 0.50 is also more stable than the disorder structure, as is indicated by the neutron diffraction findings.

4. BOND FORMATION IN TUNGSTEN CARBIDE STRUCTURE

A discussion of valence bond formation in the tungsten carbide type structures will revolve principally around the approaches used in treating two problems. The first problem involves finding a suitable basis set of valence orbitals for bonding the tungsten atom to its fourteen near neighbors, given only nine atomic orbitals. The other problem is that of devising carbon orbitals which permit the carbon atom to simultaneously bond six neighboring tungsten atoms. If the tungsten atoms were in an octahedral coordination the three p orbitals could be used. However, the coordination about the carbon atom is that of a regular trigonal prism. The approaches to these problems employed here involve the use of bidirectional orbitals (BOA) to obtain bonds in the fourteen directions required by the tungsten atom [11] in combination with Linnett's nonpaired spin-orbitals (NPSO) on carbon to obtain six bonds in the trigonal coordination [12,13].

4.1. TUNGSTEN BIDIRECTIONAL ORBITALS

Twelve of the fourteen neighbors of the tungsten atom have a coordination similar to hexagonal close packing but with a c/a ratio slightly smaller than 1.0 rather than the ideal 1.63. In this case the tungsten atom is surrounded by six metals situated in the basal plane with three carbon atoms above and below the basal plane in the form of a trigonal prism. This HCP coordination suggests that a variation of the C-type bonding orbitals used in a discussion of bonding in the HCP rare earth metals [35] be employed. If a bonding bidirectional orbital ϕ_1 is written in the general form of eq (13) then five other orbitals ϕ_1

$$\phi_1 = A\,s + Bp_x + C\,p_y + D\,p_z + E\,d_{xy} + F\,d_{xz} + G\,d_{yz} + H\,d_{x^2-y^2} + I\,d_{y^2} \tag{13}$$

can be generated from ϕ_1 by rotations of 120° and 240° about the z axis combined with a 180° rotation about the x axis. If this set of six orbitals is required to be orthonormal, then the coefficients, A, . . I, must satisfy equations (14), (15), and (16).

$$A^2 + I^2 = D^2 = 1/6 \tag{14}$$

$$C^2 + E^2 + F^2 = B^2 + 6^2 + H^2 = 1/3 \tag{15}$$

$$BC = EH + FG \tag{16}$$

Of the original nine atomic orbitals, one 6s, three 6p and five 5d's, three orbitals remain which may be hybridized in various ways. Since the two remaining important neighbors of the tungsten atom are directly above and below it on the z axis and since all the p_z character is employed in the six C-type orbitals as per eq (14), then a bidirectional G-type orbital of the form eq (17) first employed by Ganzhorn [36]

$$\phi_G = \bar{A}\,s + \bar{I}\,d_z s \tag{17}$$

might be applicable. The two remaining orbitals then contain no s, p_z, or d_{z2} character. The orthogonality conditions to be satisfied by these last three orbitals are indicated by equations (18), (19), and (20) where the lower case coefficients

$$A\,\bar{A} + I\,\bar{I} = 0 \tag{18}$$

$$Cc + Ee + Ff = Gg + Hh = 0 \tag{19}$$

$$Cb - Bc + He - Eh + Gf - Fg = 0 \tag{20}$$

correspond to the two local orbitals.

Within the above restrictions for the six C-type orbitals, eqs (14-16), the coefficients may be selected such that one lobe of the bidirectional orbital is directed approximately toward a neighbor in the basal plane while the maximum of the other main lobe is directed toward one of the six atoms out of the basal plane. Previously it had been indicated that an effective variation from a c/a ratio above 1.63 to a ratio of about 1.52 could be achieved via use of increasing d character in these orbitals [35]. This decrease in c/a is clearly insufficient for the tungsten carbide coordination. However, if significant s character is included in the orbital much lower effective c/a ratios can be achieved as is indicated in figure 2. Since there are nine coefficients in eq (13) and only five restrictions, eqs (14), (15), and (16), there exists a certain latitude in the choice of the remaining coefficients. However, such considerations as the relative strengths of the two main lobes and alignment of lobes along bond directions are of importance and will be considered later.

The strength of the G orbital along the z axis is determined both by the fact that only one s and one d_z2 orbital are available and that these must be shared by the G orbital and the six C-type orbitals in the manner required by the orthogonality restriction of eq (18). It is a happy circumstance that the s and d_z2 coefficients in the C-type orbitals are of opposite sign since this permits, via eq (18), the same signs of these coefficients in the G-type orbital. As a consequence, this orbital has a strong concentration of electron density along the z axis, thereby permitting the tungsten atom to form halfbonds with its tungsten neighbors directly above and below.

The overall picture for the tungsten atom then may be summarized as follows: six C-type orbitals and one G orbital can employ up to 7 electrons to form bonds simultaneously with its fourteen neighbors. There are, in fact, two different ways in which the C-type orbitals can be formed. These different ways can be related by a mirror plane reflection and are enantiomorphic to one another. However, the G-type orbital is orthogonal to both sets of orthogonal C-type orbitals. In figure 2 a C-type orbital is indicated in relationship to its bond directions. Corresponding to this C orbital figures 3 and 4 show the overall angular distribution of the electron density for six such orbitals while figure 5 illustrates the orthogonal G orbital. The hybridization strength[3] of the two lobes of the C orbital of figure 1 are approximately equal, 2.18 for the carbon directed lobe and 2.09 for the horizontal lobe in the basal plane. The strength of the G lobes is 2.28 when $\tilde{A} = 1/\sqrt{2}$. The carbon directed lobe of the C orbital is misdirected toward a high c/a ratio by about 5°. It will be seen in the next section that this is probably desirable to maximize overlap with

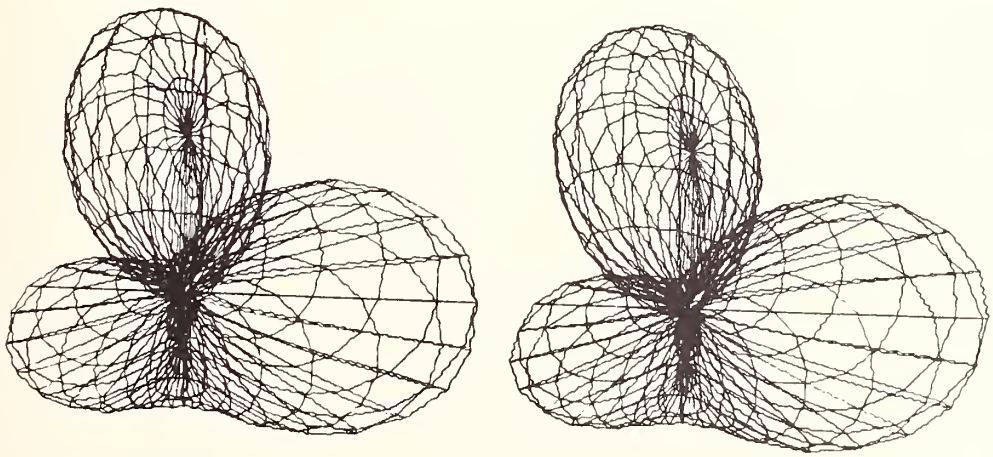

Fig. 2. This stereogram of a C-type orbital for the tungsten atom shows a lobe (taken as positive) in the horizontal plane for forming the basal plane metal-metal bonds and a negative lobe for the metal-carbon bond which projects out toward the viewer. The total d character of the orbital is 60% with the coefficients $A = -I = 1/\sqrt{6}$ and $D = -1/\sqrt{6}$.

[3]See reference [10, p. 108f] for a definition of orbital strength.

the carbon bonding orbital which is also slightly misdirected. The C orbital shown in figure 2 is fairly typical of those available from a coarse net of values of the coefficients of B and H.

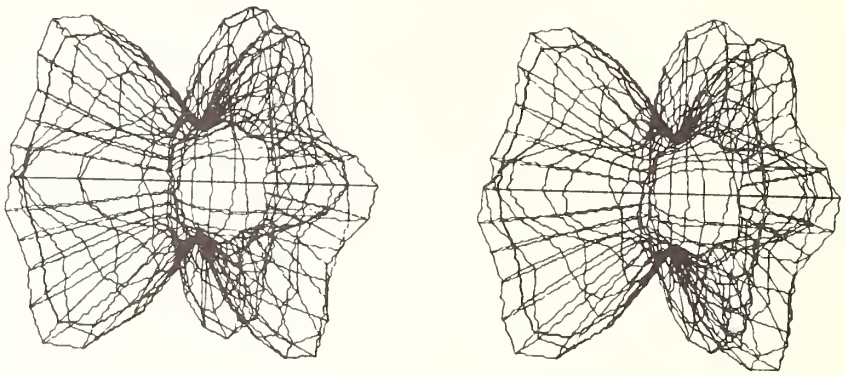

Fig. 3. The total angular density distribution of the six orthogonal C orbitals for the metal atom is shown in this slightly asymmetric stereogram. While the electron density corresponding to the metal-carbon bond has a clear trigonal prismatic configuration the basal angular projections tend to overlap in pairs near the carbon atoms. Although the basal lobe maxima are well directed these lobes are not symmetrical about the metal-metal direction; this is also indicated stereoscoptically in figure 2 and figure 4.

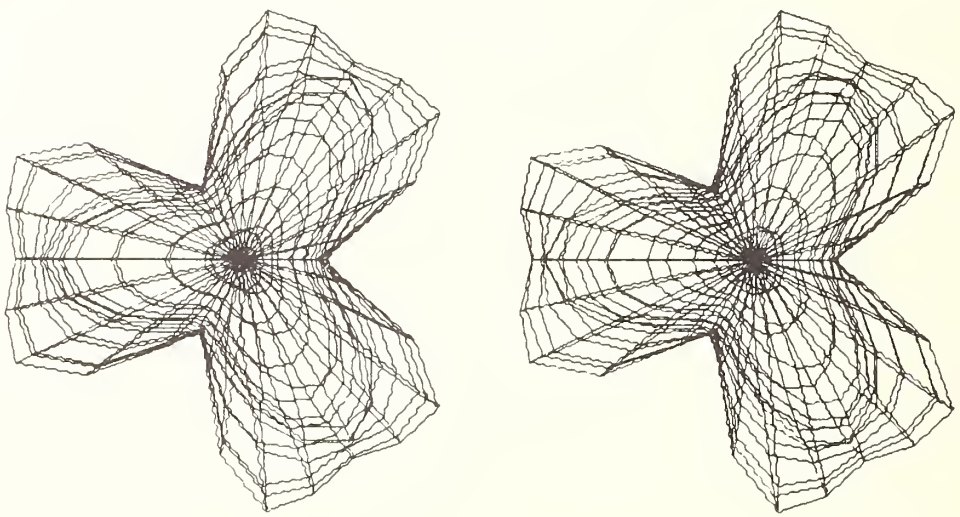

Fig. 4. The stereogram viewed here down the z axis includes the average of the electron density of figure 3 plus its enantiomorph. While the corresponding wavefunction has the full crystal symmetry of the metal site the metal-metal bonds are clearly asymmetric favoring the region near the carbon atoms. Nevertheless the bond maxima in the basal plane are only about 5° away from the hexagonal directions.

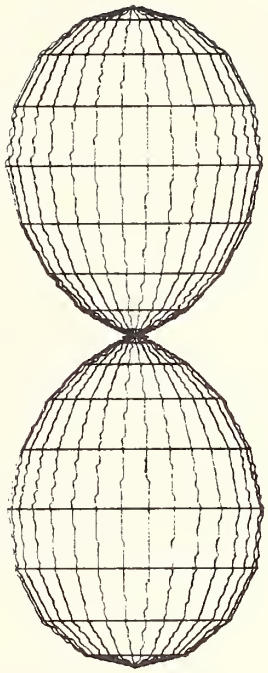

Fig. 5. The remaining two near neighbors which are not bound by the six metal C orbitals in tungsten carbide are other metal atoms directly above and below. These neighbors are bound by the symmetrical (gerade) G orbital shown above whose angular concentration along the + z and - z direction is controlled by the requirement of orthogonality with the six C orbitals.

4.2. BOND ORBITALS FOR CARBON

While the BOA method appears to provide a reasonably satisfying set of bond orbitals for the tungsten type atom, the method is not by itself applicable to carbon in the tungsten carbide structure since carbon has a trigonal prismatic coordination and only s orbitals and p orbitals are available for hybridization. Later it will be seen that prismatic coordination using C-type orbitals of low d character, *ca.* 7.8%, might be considered. However, this gives a coordination $\bar{c}/\bar{a}$ ratio[4] of 1.5 which is not a good fit for carbon in tungsten carbide where its effective coordination $\bar{c}/\bar{a}$ is 1.9. More important, even a usage of 7.8% d character by carbon appears improbable.

The approach which shall be used to discuss the carbon bonding is the non-paired spin-orbital (NPSO) treatment of Linnett. In this case the traditional valence pairing of electrons in a single bonding orbital is abandoned and one deals with eight spin-orbitals for carbon. The real space components of the four of these orbitals for the spin up electron is generally not orthogonal to the real space orbitals for the spin down electron. Accordingly by this method one can obtain eight s-p hybrid orbitals from the four traditional orbitals of carbon. These then may be linked to the bidirectional orbitals of the metal atom to obtain a form of the alternate molecular orbitals (AMO) introduced by P. O. Lowdin and expanded by Pauncz and his coworkers [37]. However, prior to considering the implications of these

---

[4] The definition of coordination $\bar{c}/\bar{a}$ ratio used here defines the height of the metal prism as $\bar{c}/2$ and length of the side of the trigonal base as $\bar{a}$. When this definition is used for a trigonal antiprism a $\bar{c}/\bar{a}$ of 1.633 corresponds to a regular octahedral coordination about the central atom.

465-504 O - 72 - 35

ideas, let us review the variations of bond hybridizations possessing three-fold symmetry. Such a review will be applicable to the boron element in the $A\ell B_2$ structure and will provide limitations for the bonding of carbon in the tungsten carbide structure.

The orthogonality conditions for trigonally related s-p hybrid orbitals can be readily obtained by rotating an orbital of the form a s + b p_z about the x axis. The well known relationship eq (21) then relates

$$b^2 \sin^2\gamma = \frac{2}{3} \tag{21}$$

the angle of rotation γ to the p character, b^2, of the orbital. When $\gamma = 90°$ the three trigonally related orbitals are the familiar planar sp^2 orbitals and the fourth orthogonal orbital is the p_z orbital. At $\gamma = 70° 32'$ one has the four symmetric tetrahedral orbitals, sp^3, with one of these being directed along the -z axis. The minimum angle γ is 54° 44' and corresponds to the three pure p orbitals with $b^2 = 1$. For carbon in the general trigonal prismatic coordination one might employ the following scheme: The three trigonally related s-p hybrids of one spin point to the three metal atoms at the base of the prism with the three trigonal hybrids of the other spin pointing to the top of the metal prism. Reversing the electron spins leads to an equally probable situation. Of course in the final wave function these two different spin arrangements are equally likely to occur in a material of low magnetic moment.

The situation in tungsten carbide is a little bit different from the above. Carbon has a coordination $\bar{c}/\bar{a}$ ratio of 0.975 and a corresponding angle α, as above, of 49° 50'. However, the minimum α for s-p hybrids is 54° 44' corresponding to the three pure p orbitals. Accordingly, the following applies for the carbon hybridization in tungsten carbide: 1) The carbon bonding orbital will be mostly p with the fourth orbital for both electron spin up and spin down being the 2s orbital. 2) The tungsten-carbon bond is bent so that the carbon has a somewhat smaller $\bar{c}/\bar{a}$ ratio than observed while the tungsten has a larger $\bar{c}/\bar{a}$ ratio than observed. 3) The maximum bond order of the tungsten-carbon bond is 0.5 according to this treatment.

This maximum bond order of 1/2 leads to a maximum valence of three for carbon. That carbon should be trivalent in a compound known for its strength and extreme refractory nature is, of course, anathema to all those who believe in the tetravalency of carbon. In the next section, dealing with phase structures in tungsten carbide materials, we will see that not only does the unbonded half of the p orbitals play a role in the bonding but appropriately the s orbital is also important.

4.3. PHASE STRUCTURES IN TUNGSTEN CARBIDE

In the prior two sections bidirectional bond orbital schemes have been devised for both the metal atom and the nonmetal elements of the second row. Now we would like to link these orbitals together throughout the structure to form bonds, in a schematic sense, in order to determine the overall selfconsistency of the method. The approach is to match the phases of the bidirectional orbitals in the bonding region so that bonds rather than antibonds are formed. In the former case, the phases of the two orbitals should both be positive or negative, while in the case of the antibond the phases are of different signs. Thus, in the antibond, a nodal surface exists in the region between the two atoms and the resultant low electron density causes the interbonding force to be repellent. If this were to occur frequently or if many possible bonds were not formed, then one would consider such a "phase structure" as unstable and not representative of the material's ground state. The use of bidirectional orbitals usually leads to the formation of cycles within the phase structure that are composed of rings (cycles) or infinite chains of phase-linked orbitals. Further, these cycles are usually mutually orthogonal within a single phase structure. However, in the tungsten carbide case we will find a different situation in the presence of three centered bonds involving one carbon and two tungsten atoms in addition to the above discussed carbon-tungsten halfbond.

In figure 6 we indicate part of a phase structure involving a layer of tungsten atoms and the neighboring carbons in a view which is a projection down the c axis. The tungsten atoms are small open circles while the carbons are small filled circles numbered 1, 2 and 3. In this phase structure the C orbitals of all the tungsten atoms are assumed to be all of the same sense (like right handed) and only two of the six C orbitals for each metal atom are shown. Also missing are the metal G orbitals and the carbon s and p orbitals. The C orbitals of figure 6 are linked by their lobes in the metal plane to form one-third of the tungsten-tungsten bonds. Although all of the phases of these lobes are arbitrarily taken to be positive, we shall shortly find that this leads to a selfconsistent situation of considerable stability. The negative lobes of these C orbitals point toward the carbon atoms above and below the metal plane. If the carbon 1 is above the plane with one set of NPSO's overlapping the negative lobes of the C orbitals, then we see from figures 6 and 7 that it is phase linked through two C orbitals with carbon 2 which is below the plane and which uses the second set of spin-orbitals. This configuration of phase-matched orbitals might be termed a partial phase structure, $\psi_A(0)$, associated with the zeroth layer of tungsten atoms. This partial phase structure has a repeat unit cell (fig. 6, dotted lines) which is three times the volume of the crystallographic unit cell (solid outline). The carbon atoms in the new unit cell have the coordinates: C1,0,0,1/2; C2,1/3,2/3,-1/2; and C3,2/3,1/3,1/2. The total phase structure consists of two more partial phase structures, $\psi_B(\cap)$ and $\psi_C(0)$, involving different metal C orbitals and a cyclic rotation of the roles played by (and the spin-orbitals used by) carbons 1, 2, and 3. Notice that the total phase structure, using ψ_A,ψ_B, and ψ_C together, can have the crystallographic unit cell size; and that right handed and left handed phase structures, employed in equal proportions, give total wave-functions with full crystallographic symmetry.

At first glance it might seem that these partial phase structures ψ_A, *etc.* are independent of each other, however, we shall now indicate that they are linked through the formation of three centered bonds involving the positive lobe of the carbon p orbitals and its partial overlap with the central portion of the nearby tungsten-tungsten bond. At the top of figure 7 we see two C-type orbitals overlapping to form a metal bond in the z = 0 plane.

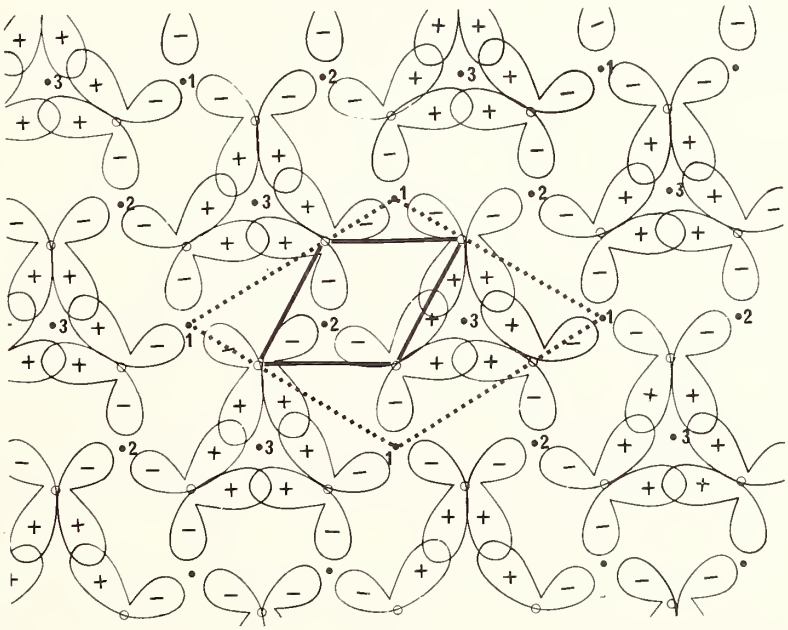

Fig. 6. A partial phase structure, $\Psi_A(0)$, in the tungsten carbide structure basal plane is shown for two of the six C orbitals for each metal atom: the carbon p spin-orbitals are not indicated. The carbon atoms numbered 1 and 3 are taken as above the plane while number 2 carbon is below the plane. The repeat cell for Ψ_A is indicated by the dotted lines while the crystallographic unit cell outline in the (001) plane is shown in the solid lines.

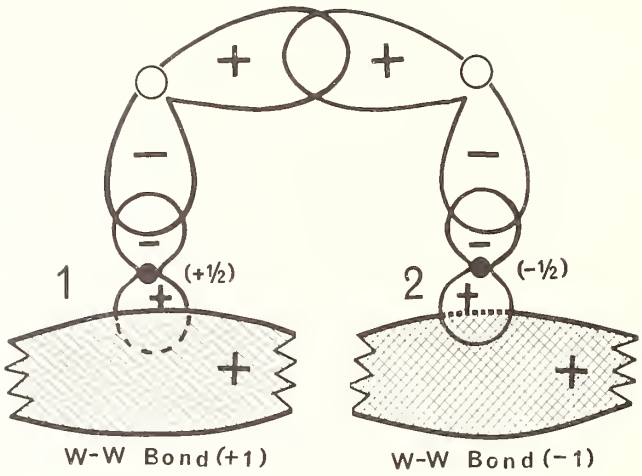

Fig. 7. Partial phase structures associated with neighboring hexagonal packed layers of tungsten atoms are shown to be phase linked by the carbon p spin-orbitals as above. This is seen to involve a metal-metal bond in the z = 0 layer, two metal-carbon halfbonds, and two three-centered bonds, such as between a carbon at z = + 1/2(- 1/2) and a metal-metal bond at z = + 1.0(-1.0).

The carbon atom on the right at z = +1/2 uses a p spin-orbital not only to form a halfbond with the tungsten atom in the z = 0 plane but also to form a three center bond with the metal-metal bond in the layer above. Similarly carbon 2 continues the phase matching to the metal bond in the plane below. The net result is that the phases of all the metal-metal bonds in ψ_A,ψ_B, and ψ_C can be taken as positive and linked by cycles of six bidirectional orbitals indicated by the sequences $\psi_A(0) \rightarrow \psi_B(-1) \rightarrow \psi_A(0)$ and $\psi_A(0) \rightarrow \psi_C(+1) \rightarrow \psi_A(0)$.

In addition to this special use of the carbon p orbitals, it is seen that the carbon 2s orbital which appears to play only a small role in the direct carbon-metal bond may also be stabilized by these neighboring metal-metal bonds. This is suggested in figure 6 by carbon 3. We see that all the metal-metal bonds surrounding it have the same phase, a situation which is uniquely suitable to a stable bonding interaction with the s orbital. This special stabilization, which is particularly appropriate when the wavevector k is zero, may be expected to disappear as the associated bands (see section 9) become half filled. The asymmetry of electron density about the basal plane metal-metal bonds may also be expected to contribute to the stability of the carbon atom both through the enhanced carbon 2s orbital stability and through the three center bonds. Their asymmetry is indicated in the stereogramatic figures 2, 3, and 4 and by the metal bonds near carbon 3 in figure 6. Finally, we note that the unit cell indicated in dotted lines in figure 6 is also the repeat unit cell for the use of nonpaired spin-orbitals for carbon for the three partial phase structures ψ_A,ψ_B, and ψ_C. Note further that the sum of their composites can also correspond to the crystallographic unit cell.

4.4. METALLOID BONDING IN MoP

The bonding scheme described above for carbon in tungsten carbide could be applied to MoP. However, the Pauling metallic radii results suggest (table 2) that a few per cent d character may be involved in the phosphorus bonding. In this section an interpretation of this possibility will be explored through the use of pure C orbitals. We will seek a set of bidirectional orbitals of low d character which are suitable for the trigonal prismatic coordination of phosphorus in MoP.

Assume that we have a pure symmetric C orbital of the form $ap_z + bd_{xz}$ and then rotate it about the x axis by an angle α. Two more orbitals are generated from the first by rotations about the z direction of 120° and 240°. The amount of d character, b^2, is determined by mutual orthonormality and is given in eq (22) derived earlier [38] in a somewhat different form. In order

$$(1-b^2)\cos^2\alpha = 1/3 \qquad (22)$$

to see the effect of changes in the angle α, we refer to figure 8 in which we are looking down the axis (z direction) of a twisted trigonal prism. Assume that the main C orbital lobes of the first orbital point in the direction of atoms 1 and 1′, figure 8. The triangular top of side length $a = \bar{a}$ is in solid lines while the prism base is in dotted lines. The angle in projection between atoms 1 and 1′ is taken to be the angle 2ω as shown and the height of the prism is taken as $\bar{c}/2$.

The results in terms of coordination $\bar{c}/\bar{a}$ ratio and ω is given in figure 9. Notice that when ω is 0° and 60° one has trigonal prismatic coordination and when ω is 30° and 90° the coordination is antiprismatic. The latter case occurs at 54° 44′ and $b^2 = 0$ and corresponds to the octahedral coordination of three pure p orbitals.

The case of most interest here is for $\omega = 60°$. This occurs at $\alpha = 53° 4'$ and has a d character of 7.8% which agrees rather well with the metallic radii results (4-8%) obtained in section 2.1. for phosphorus in MoP. While the correspondence between the observed coordination $\bar{c}/\bar{a}$ of 1.90 and the ratio 1.50 obtained for 8% d character is less than impressive, it is hardly worse than the alternative of using pure p orbitals for the phosphorus. In addition, the use of a small amount of d character in these C orbitals raises the bond hybridization strength to 1.91 compared to 1.73 for pure p orbitals.

Before considering the effect of bond formation in tungsten carbide on its surfaces of constant energy in k-space, we first discuss the transition metal diborides from the same general viewpoints as we have treated the tungsten carbides. While certain similarities are found, it will be seen that differences in the successes of the treatments raise questions as to the correctness of the unpleated AlB_2 structure for some of the diborides.

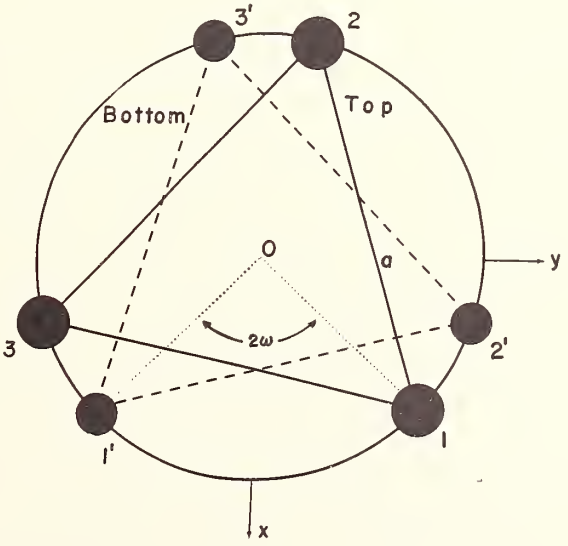

Fig. 8. Looking down the axis of a general twisted trigonal prism we see that the top triangular base of side $a = \bar{a}$ is rotated from the position over the base triangle by the angle 2ω. If the height of the prism is $\bar{c}/2$, then the effective or coordination c/a ratio is $\bar{c}/\bar{a}$.

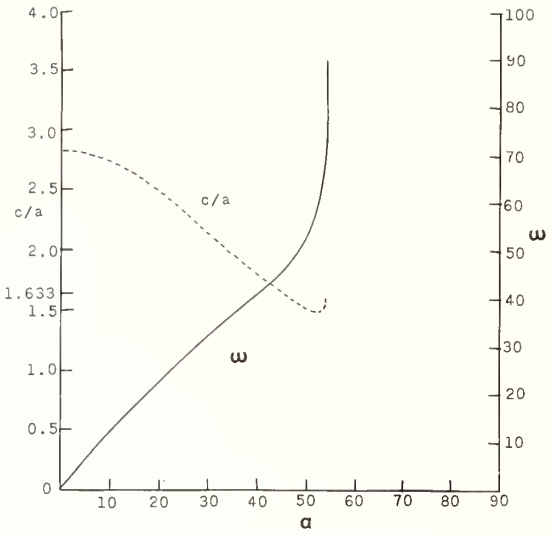

Fig. 9. For a twisted trigonal prismatic coordination using C orbitals the coordination $\bar{c}/\bar{a}$ ratio and the angle ω is given as a function of the rotation α of the C orbital out of the xz plane. When ω = 0 and 60 degrees the coordination is trigonal prismatic while ω = 30 and 90 degrees correspond to antiprismatic and octahedral coordinations respectively.

5. METALLIC RADII TREATMENT OF THE TRANSITION METAL DIBORIDES

The results for the treatment of the nonrare earth transition metal diborides via the metallic radii formalism of Pauling [10] are given in tables 5 and 6 for those diborides listed by Post [3] and Pearson [39] as having the $A\ell B_2$ structure. These selfconsistent calculations were not performed under the "neutral cell" restriction since in many of these compounds the bond polarization of the boron-metal bonds and the transfer of charge for increased bond-forming power are effects which act in the same direction. That is, in some diborides both effects increase the effective negative charge of the boron. Generally it was assumed also that the boron parameter for planar boron layers, that is z(B) = 0.50, is correct and that the lattice parameters taken from the literature [3,15, and 39] were for stoichiometric materials. However, generally speaking, these assumptions are subject to correction as more detailed and critical data is collected. The calculations which are exceptions to these two assumptions in table 5 and 6 are entries 4 and 5 which deal with the effect of changing z(B) in VB_2, and entries 14 and 15 which are nonstoichiometric results for the tantalum diboride compositions, $TaB_{1.97}$ and $TaB_{2.70}$. Also we note here that variations in the boron radius in table 5 are primarily due to charge transfer effects.

When the boron layer is planar and graphite-like (z(B) = 0.50) each boron has three short boron-boron bonds and six boron-metal interactions such that the boron sits in the center of a trigonal prism of metal neighbors. The bond orders for these two different kinds of bonds are given in table 5. It is clear that the strongest bonds are for the B-B interactions and the next strongest are the M-B bonds. The boron valence electrons are, roughly, equally divided between these two kinds of interactions. Each metal atom has twelve boron neighbors in the form of a hexagonal prism and six metal neighbors in the basal plane. Table 5 shows that only in the case of ScB_2 are the M-M bonds stronger than M-B bonds. In addition, there are two weaker metal-metal bonds perpendicular to the basal plane whose bond order is generally three-quarters or less than that shown in table 5 for the M-M bonds. While these two bonds are included in the metal valences shown in table 6, the author doubts that these are significant bonds considering the multiplicity and bond order of the M-B bonds. Generally, speaking for the metal atom, we see that more than two-thirds of the metal's valence electrons are employed in the formation of bonds with the boron atoms and less than a third

Table 5

Metallic Radii and Bond Orders for the Transition Metal Diborides

ENTRY[a]	cpd.	RADIUS		BOND ORDERS		
		Metal	Boron	B-B	B-M	M-M
1.	ScB_2	1.351	0.816	0.43	0.19	0.28
2.	TiB_2	1.250	0.796	0.64	0.24	0.12
3.	VB_2	1.230	0.791	0.73	0.30	0.11
4.	VB_2[b] z = 0.42	1.225	0.800	0.49	0.59 0.16	0.11
5.	VB_2[b,c] z = 0.42	1.227	0.797	0.51	0.54	0.11
6.	CrB_2	1.183	0.778	0.84	0.25	0.17
7.	MnB_2	1.167	0.778	0.77	0.24	0.11
8.	ZrB_2	1.407	0.809	0.45	0.24	0.26
9.	NbB_2	1.336	0.795	0.53	0.29	0.16
10.	MoB_2[d]	0.295	0.799	0.57	0.38	0.17
11.	RuB_2	1.202	0.781	1.11	0.43	0.20
12.	AgB_2	1.318	0.778	0.78	0.34	0.38
13.	HfB_2	1.384	0.805	0.47	0.24	0.24
14.	$TaB_{1.97}$[e]	1.339	0.800	0.53	0.31	0.18
15.	$TaB_{2.70}$[e]	1.339	0.800	0.55	0.30	0.21
16.	OsB_2	1.220	0.782	1.06	0.43	0.20
17.	AuB_2	1.368	0.800	0.43	0.23	0.23

(a) Entries with the same number in tables 5 and 6 correspond to the same calculation.
(b) The position parameter of the boron atom is given by z = 0.42.
(c) The longer boron-metal bonds are not included in the metallic radii calculations.
(d) The high temperature form ($A\ell B_2$ structure) of MoB_2 is stable above 1600 °C and is metal deficient [3].
(e) The self-consistent calculations were carried out for the stoichiometries as indicated.

Table 6

Metallic Radii Summary for the Transition Metal Diborides

ENTRY[a]	cpd.	ELEM.	CHARGE Trans.	CHARGE Eff.	CALC. VALENCE[b]	d-CHARACTER[c]	UNSHARED ELECTRONS
1.	ScB_2	Sc	-1.08	-0.70	4.08(4.14)	0.25(0.20)	0.0
		B	+0.54	+0.35	2.46	--	0.0
2.	TiB_2	Ti	+0.29	+0.43	3.71	0.34(0.27)	0.0
		B	-0.15	-0.22	3.37(3.15)		0.0
3.	VB_2	V	+0.57	+0.67	4.43	0.35(0.35)	0.0
		B	-0.29	-0.33	3.99(3.29)	--	0.0
4.	VB_4 z=09.42[d]	V	0.00	+0.15	5.00	0.35(0.35)	0.0
		B	0.00	-0.08	3.55(3.00)	--	0.0
5.	VB_2 z=0.42[d,e]	V	+0.22	+0.33	4.06	0.35(0.35)	0.71
		B	-0.11	-0.17	3.11	--	0.0
6.	CrB_2	Cr	+1.50	+1.57	4.192	0.39(0.39)	0.30
		B	-0.75	-0.78	4.00(3.75)	--	0.0
7.	MnB_2	Mn	+1.44	+1.46	3.67(3.72)	0.40(0.40)	1.99
		B	-0.72	-0.73	3.73	0.40(0.40)	0.0
8.	ZrB_2	Zr	-0.60	-0.32	4.58	0.34(0.31)	0.0
		B	+0.30	+0.16	2.70	--	0.0
9.	NbB_2	Nb	+0.33	+0.42	4.67	0.40(0.39)	0.0
		B	-0.16	-0.21	3.34(3.16)	--	0.0
10.	MoB_2 H.T. [f]	Mo	+0.08	+0.12	5.92	0.44(0.39)	0.0
		B	-0.04	-0.06	4.00(3.04)	--	0.0
11.	RuB_2	Ru	+1.28	+1.15	6.72	0.53(0.50)	0.0
		B	-0.64	-0.58	5.90(3.64)	--	0.0
12.	AgB_2	Ag	+1.50	+1.51	6.69	0.41(0.35)	2.81
		B	-0.75	-0.75	4.38(3.75)	--	0.0
13.	HfB_2	Hf	-0.38	-0.07	3.49	0.35(0.29)	0.0
		B	+0.19	+0.03	2.81	--	0.0
14.	$TaB_{1.97}$[g]	Ta	+0.09	+0.27	4.91	0.39(0.39)	0.0
		B	-0.06	-0.14	3.40(3.05)	--	0.0
15.	$TaB_{2.70}$[g]	Ta	0.0	+0.19	4.67	0.39(0.39)	0.32
		B	0.0	-0.07	2.98	--	0.02
16.	OsB_2	Os	+1.21	+1.09	6.79	).53(0.49)	0.0
		B	-0.61	-0.55	5.78(3.61)	--	0.0
17.	AuB_2	Au	0.0	+0.10	4.16	0.30(0.36)	6.84
		B	0.0	+0.05	2.64	--	0.36

(a) Entries with the same number in tables 5 and 6 correspond to the same calculation.
(b) Generally the "calculated" valence equals the "estimated" valence, when this is not the case the estimated valence is given in parentheses.
(c) The d-character in parentheses is that given by Pauling or calculated from his table of single bond metallic radii [6,10].
(d) The position parameter of the boron atom is given by z = 0.42.
(e) The longer boron-metal bonds are not included in the metallic radii calculations.
(f) The high temperature form of MoB_2 is stable above 1600 °C, has the AlB_2 structure, and is metal deficient [3].
(g) The self-consistent calculations were carried out for the stoichiometries as indicated.

of the valence electrons is involved in the formation of metal-metal bonds. These results support the observations and interpretations of Post [40,3] who explained the c/a ratios in the transition metal diborides on the basis of a strong B-B bond and a relatively constant metal-boron distance in contrast to a weaker metal-metal bond. As Post has indicated, these conditions permit a qualitative appreciation of what occurs except when the metal atoms are especially large.

Prior to discussing boron charges, magnetic moment, nonstoichiometry, and boron layer pleating, it is noted that, while the rare earth metal diborides might be properly treated here, they will not because the metallic radii results for the lattice parameter data [3,39, and 41] indicate such a high d character increase that an additional complicating effect must be operating. A similar effect was observed by the author [17] in the rare earth compounds having the $CaCu_5$ structure and it was suggested that it was the result of an anisotropic radius of the rare earth atom due to anisotropic f electron shielding [17].

5.1. EFFECTIVE CHARGE AND MAGNETIC MOMENT IN THE DIBORIDES

The metallic radii results for effective charges vary in a systematic way as one progresses across the periodic table. Considering only those calculations for z(B) = 0.50, it is seen by starting with the entries 1, 8, and 13 for ScB_2, ZrB_2, and HfB_2 respectively, that the boron is first positively charged to a maximum extent of +0.54 (ScB_2) and then becomes increasingly negatively charged as one increases atomic number along the row. This appears to be the case for the 3d and 4d series and would apply to the 5d series were it not for AuB_2 where the effective charge is small because charge transfer is not required by boron for the formation of bonds and the electronegativity difference is minimal. The maximum negative charge of the boron for each of these rows is -0.78 (CrB_2), -0.75 (AgB_2) and -0.61 (OsB_2). It is seen that this charge picture generally supports no one theory, neither the transport of three electrons from boron to the metal d band as Juretschke and Steinitz [8] have interpreted their electrical data, nor the loss of 1.7 boron electrons to the metal atom as magnetic data on CrB_2 and MnB_2 as has been discussed by Cadeville [9], nor the gain of an electron by boron to form a graphite-like plane of B^- ions. This later picture is discussed by several authors based both on earlier chemical considerations, (*e.g.*, Nowotny [4] and Muetterties [5]) and on NMR data (Silver, Bray, and Kushida [42,43]). The boron charges generally range from +0.54 for ScB_2 to -0.75 in a few cases where selfconsistency[5] was not achieved.

Experimental checks on the above charges are generally not available from the literature, however, some results for the diborides of titanium and vanadium have been reported by Ramqvist [21] and Fischer [44] respectively. For TiB_2, shifts in the metal K absorption edge, the emission edge, and the metal $2p_{3/2}$ bonding energy (ESCA) were inconclusive except to indicate that the absolute metal charge was smaller than 0.5 [21]. In vanadium L x-ray emission studies of VB_2, the shift to higher energy was interpreted as indicating a charge flow from the metal to boron [44]. Both of these results are in agreement with the present studies. However, clearly, much more work in this area is indicated.

Since magnetic data is becoming available, let us now consider the number of unshared electrons for the 3d elements listed in table 6. For the corresponding diborides, we will confine our interest to those metallic radii results with the z(B) = 0.50, for the moment. The elements Sc, Ti and V (entries 1, 2 and 3) have no unshared electrons available, so a magnetic moment is not expected in their compounds. However, in CrB_2 and MnB_2 the transition metal is associated with 0.30 and 1.99 unshared electrons respectively (entries 6 and 7). Since these electrons are expected to be essentially d electrons and since only 1.63 and 1.47 d orbitals per metal atom are used in CrB_2 and MnB_2 respectively for bond formation, we may expect Hund's rule to be obeyed and find these electrons unpaired as well as unshared.

Magnetic susceptibility data for the 3d diborides summarized by Carter and Swartz [45] supports the above results. From NMR studies, CrB_2 has been reported by Barnes and Creel [46] as antiferromagnetic with a moment estimated by Castaing, Caudron, Toupance, and Costa

[5]The maximum negative charge of -0.75 on boron is program limited by reason of the author's expectation that a metal charge of +1.50 is as large as might be supported by a metal atom in a good conductor. This forces the program to find other ways to seek selfconsistency than by massive charge transfer.

[47] to be below 1 μ_B per metal atom. From a susceptibility curve which cannot readily be fitted with a Curie-Weiss law [47] above the Neel point, paramagnetic susceptibility has been analyzed by Cadeville [9] as corresponding to 1.3 magnetic electrons per metal atom. This is about 1 electron greater both than that estimated in table 6 and that considered to be appropriate to antiferromagnetic CrB_2 [47]. Manganese diboride has been found to be ferromagnetic by both Cadeville [9] and Anderson, Dellby, and Myers [48]. At 0°K the saturation magnetization indicates 0.19 u_β per metal atom while the paramagnetic data gives an effective number of unpaired electrons as 1.55 [9,48] in reasonable agreement with table 6.

The difficulties associated with preparing or obtaining pure CrB_2 and MnB_2 are considerable in the light of recent attempts at NBS [49] and the NMR data reported by Barnes and Creel [46], Anderson, Dellby, and Myers [48], and Carter and Swartz [45]. Apparently the sensitivity for the detection of boride impurities in these materials by the NMR technique is significantly greater than by the usual x-ray powder method. However, if we take exception to the high paramagnetic value of 1.3 magnetic electrons per metal atom in CrB_2 found by Cadeville, because he did not report or correct his measurements for the presence of magnetic second phases, then it is only appropriate to suggest some of the weaknesses in the metallic radii approach. These are indicated in the next two subsections where we consider the effects of nonstoichiometry and the pleating of the boron layer.

5.2. EFFECT OF NONSTOICHIOMETRY

In applying the metallic radii formalism to nonstoichiometric compounds, it is assumed, out of ignorance: 1) that nonstoichiometry is the result of vacancy rather than interstitial formation, 2) that lattice relaxation does not occur at the vacancy site, and 3) that the vacancy locations are purely random. Under these assumptions the effect of nonstoichiometry is fairly predictable. For example, let us consider the $A\ell B_2$ form of MoB_2, a material which must be quenched from high temperature if it is to retain its structure. From entry 10, table 6, we see that selfconsistent results were not obtained since the estimated boron valence is 3.04 while that calculated from the sum of bond orders is 4.00 electrons. Since the molydenum d character is 5% larger than its normal value, it is apparent that the calculated valence of the metal would also be too high if the normal d character, and hence normal single bond radius, were assumed. If it is accepted that the lattice parameters are reasonably correct, then we see that the more reasonable calculated valences would be obtained if metal vacancies (or boron vacancies) were assumed. That this is the case is indicated by the literature [3, p. 342]; however, the lack of sufficient data precludes further calculation.

For tantalum diboride the situation is different in that information on lattice parameters *vs* composition is available [39]. In entries 14 and 15, table 6, we have given the results for $TaB_{1.97}$ and $TaB_{2.70}$ under the condition that d character of tantalum is constant at its normal value of 39%. The nonselfconsistency of the calculated boron valence 3.40 compared to its estimated valence 3.05 can be removed by a d character increase of about 1% and a charge transfer of a couple tenths of an electron. However, for the composition $TaB_{2.70}$ (assuming metal vacancies) it is seen that the normal values of Pauling apply and that the valency of both elements is lowered by the metal vacancies in the ratio $\Delta V_B/\Delta V_{Ta} = 1.75$.

Even though the general strength of tables 5 and 6 is weakened by the lack of accurate compositional and vacancy (density) data, the tables are sufficiently internally consistent to make certain of its members deserving of critical scrutiny. In particular, note the extreme disparities between the calculated and estimated boron valences for RuB_2, 5.90 *vs* 3.64, and OsB_2, 5.78 *vs* 3.61. These differences exist even though reasonable adjustments of metal d character have been made and sizable charge transfer has taken place. It would appear that either the lattice parameters are much too small or that the structure is wrong. Przybylska, Reddoch, and Ritter [41] have called attention to the anomalous positions of the ruthenium and osmium compounds on a lattice parameter chart of the diborides. Earlier Aronsson, Stenberg, and Aselius [50] questioned the interpretation of the osmium and ruthenium boride data and suggested that the composition is more nearly $RuB_{1.1}$ and $OsB_{1.2}$, and that these materials have the tungsten carbide-type structure. If this is correct, then the unusually strong B-B bonds (for the $A\ell B_2$ structure) of table 5, entries 11 and 16, would be eliminated and the calculated boron valence would be restored to a reasonable value of about 3. In addition, the high charge transfer would not occur, the metal d character would be restored to normal, and unpaired electrons might be expected on the metal atoms.

The metallic radii results also suggest that further work on the diborides of silver and gold might be rewarding. These were reported by Obrowski [51] in a simple note without chemical analytical support. While the lattice parameters for the silver compound are in line [41] with other diborides, the calculated results given in table 6, entry 12, suggests the real composition is nonstoichiometric and probably boron deficient compared to AgB_2. The results for AuB_2 are even more suspect both in terms of the "c" lattice parameter [41] and the decreased, not increased, d character of the gold atom, entry 17. The boron unpaired electrons indicated by table 6 for this compound are not expected, in fact.

5.3. THE PLEATING OF THE BORON SHEET

A variable to be considered in addition to stoichiometry is the effect on bonding due to the variation of the boron position parameter, z(B), away from the value 0.5. Such a movement conserves the axial symmetry of the boron, as is required by NMR data [42,45,46], and gives rise to a double (or triple) hexagonal pleated sheet in which the borons are alternately vertically displaced plus and minus from the planar graphite positions. The pleating of boron layers in other compounds is well known and the alternation of pleated and unpleated layers in W_2B_5 and Mo_2B_5 was given a special notation by Kiessling [52] as early as 1947. More recently, it has been found by LaPlaca and Post [53] that the diboride of rhenium has a pleated structure. In addition, a new (perhaps only) modification of ruthenium diboride has been assigned by Roof and Kempter [54] a pleated structure of a different sort.

On the basis of size considerations alone, one might expect that pleating is most likely to occur in the $A\ell B_2$ structure when the transition metal atoms have their smallest radius. This occurs in the 3d series for cobalt and nickel for which diborides have not been reported. The pleating of the boron layer might be tested using the lattice parameters of CrB_2 and MnB_2 and z(B) as a variable in an attempt to remove the nonselfconsistency for boron in these compounds, entries 6 and 7, table 6. However, since these compounds are associated with a poorly determined number of unpaired (or magnetic) transition metal electrons, we elect instead to examine the effect for vanadium diboride for which a magnetic moment is unknown. Accordingly, all outer electrons in VB_2 are bonding electrons since unshared electrons on boron are unlikely for that electron deficient element.

In table 6, entries 3, 4, and 5, three metallic radii calculations are carried out for VB_2 under the condition that the d character of vanadium has its normal value of 35%. In the first case for z(B) = 0.5, entry 3, we see that all of the outer vanadium electrons are used for bonding except for 0.29 electrons which are transferred to boron. This gives an estimated boron valence of 3.29 which is 0.7 electrons short of the calculated valence of 3.99. In order to decrease the difference between the estimated and calculated boron valence, let us develop a pleated boron sheet by moving the boron to a z(B) = 0.42 position. This increases the three boron-boron distances and three of the boron-metal distances, while it decreases the other three boron-metal distances. The effect of these changes on the respective bond orders is indicated in table 5, entry 4. This decreases the nonselfconsistency in the boron valence to 0.55 electrons, however, the decrease seems small and a weak argument for the pleated boron sheet.

In entry 5, table 5 and 6, we give the results for the metallic radii under the assumption that the longer boron-metal interaction is nonbonding. This assumption is justified below (section 8.2) as a combination of the greater distance and the lack of suitable available boron bonding orbitals. In table 6, entry 5, it is seen that overall selfconsistency is obtained. The presence of 0.71 unshared vanadium electrons, however, is not in agreement with experimental data and suggests that z(B) is somewhat greater than 0.42 and that the assumption of the nonbonding longer metal-boron interaction is too strong.

The results constitute the first of four arguments that the boron layer may be expected to be pleated in circumstances of small metal radius and high boron negative charge. Applying this approach to CrB_2 and MnB_2 it is clear that the CrB_2 calculation could be made self-consistent and the boron negative charges could be reduced in magnitude. Experimental evidence for or against this suggestion of a pleated sheet is slight. The single crystal x-ray results of Post and Miksic have been reviewed [3, p. 350] and show that the boron layer in TiB_2 is unpleated. However, in this case the boron effective charge is small, table 6, and the metal atom is large and under compression (compare the calculated d character of 34% to the normal value of 27%). Evidently more experimental work on other diborides is desirable in this area.

Recent new results in combination with previous NMR studies of the 3d and 4d transition metal diborides shows that the electric field gradient at the boron site cannot be correlated with either the c/a ratio or the molecular volume. In this work [45], Carter and Swartz point out that the pleating of the boron layer may be responsible for the lack of correlation, which is especially bad for CrB_2 and MnB_2.

6. VOLUME CHANGES IN VB_2

The variation of the atomic volume change of boron as its positional parameter z(B) decreases from the value 0.5 will now be considered for the representative case of VB_2. The results will constitute the second argument against the transfer of negative charge to a boron layer which remains unpleated. We have seen from the metallic radii results above that there is little evidence for supposing that any transferred electrons to the boron are involved in boron-boron bond formation. If it were the case, the corresponding bond order would be 1.33 and a graphite analogy would be understandable; however, instead, the boron-boron bond order is approximately half that. In view of the absence of such supporting experimental information, it seems reasonable to argue that negative charge transfer to the boron should be associated with a net increase in the atomic volume. In the case of a purely ionic representation, such a volume change with charge is certainly expected, for example, see the large variation of ionic radii with charge suggested by Pauling [10, p. 512ff]. A similar, though smaller, change may be argued on the basis of coulomb repulsion for transferred electrons which are covalently employed.

From simple structural considerations, it is quite clear that the effective boron atomic volume is a minimum when z(B) = 0.50, this is due to the short boron-boron distances. However, it is not at all clear how the volume of the unit cell should be divided up between the constituent vanadium and boron atoms. A hard sphere approach is immediately rejected as it accounts for less than 50% of the unit cell volume. A more reasonable definition of an effective atomic volume is developed below.

For atoms of equal size an approach that was published by the mathematician G. Voronoi [55] in 1908 seems to be most appropriate. Voronoi formed space filling polyhedra about each member of an aggregate of selected points by constructing perpendicular planes at the bisecting position of each interpoint vector. The smallest polyhedron about each member point of the aggregate is known as its Voronoi polyhedron, the complete set of which fill all space. When the aggregate of points correspond to a single type of crystallographically equivalent points, these polyhedra are mathematically termed "stereohedra", although they are better known to the solid-state physicists as Wigner-Seitz cells. In the present case we will have two types of atoms in the unit cell[6] and will describe the resultant polyhedra as Voronoi polyhedra or cells.

The boron Voronoi cells were computed [56] as a function of the boron positional parameter z(B). The boron and vanadium cells are shown in figures 10 and 11, respectively, for the values of z(B) = 0.50 and 0.43. The volume of two boron Voronoi polyhedra plus that of a corresponding vanadium Voronoi polyhedron is equal to the unit cell volume. When fitted together in the ratio of two to one, such cells fill all space. As indicated earlier and illustrated in figure 12, the volume of the boron Voronoi cell is clearly a minimum in VB_2 for z(B) = 0.50. This supports the contention, that with respect to negative charge accumulation, the boron planar configuration at z(B) = 0.50 is unstable.

On the other hand, it might be appropriately argued that the original assumption of equal atomic radii is not a good chemical or physical approximation. This, however, makes no substantial difference as related polyhedra may be also computed under the assumption that the atomic radii are different for vanadium and boron. The resultant polyhedra can no longer be described as Voronoi polyhedra as they are not all-space filling. However, the volume occupied is almost space filling. In the case radii are assumed to be the single bond metallic radii as per Pauling (V, 1.224A; B, 0.80A) these new cells may be taken as newly

---

[6]Perhaps it is appropriate to extend the generality of the term, Wigner-Seitz cell, beyond its original usage, where it was exclusively applied to parallellohedra and stereohedra, to the present case involving two different crystallographic sites, however, the author prefers the term, Voronoi polyhedra, both for its greater generality and its earlier conception.

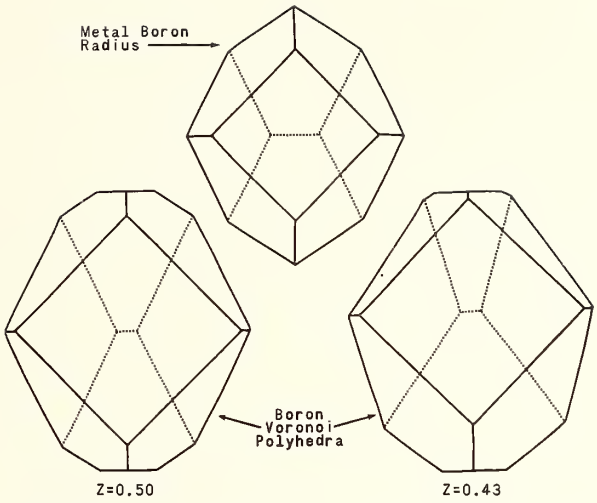

Fig. 10. The boron Voronoi polyhedra are illustrated in the lower two drawings for the boron position parameter z = 0.50 and z = 0.43. The top polyhedron illustrates the smaller volume of the polyhedron obtained by using the same construction method but with atomic sizes corresponding to Pauling's metallic radii.

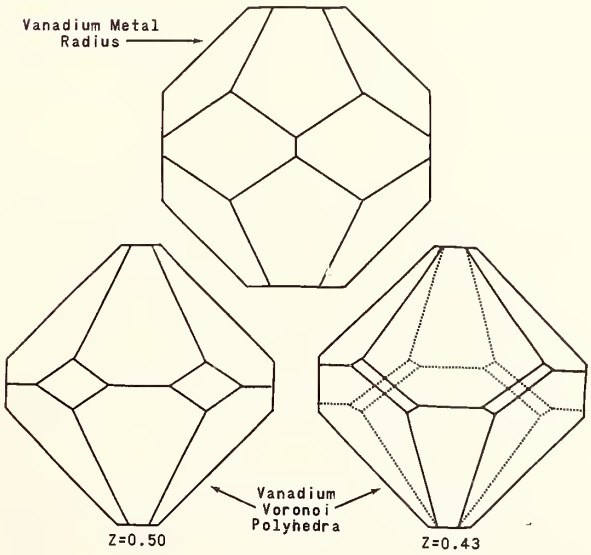

Fig. 11. These vanadium metal polyhedra correspond to those of boron in figure 10. While the metal Voronoi polyhedra plus the corresponding boron polyhedra fill all space the polyhedra associated with different size atoms do not.

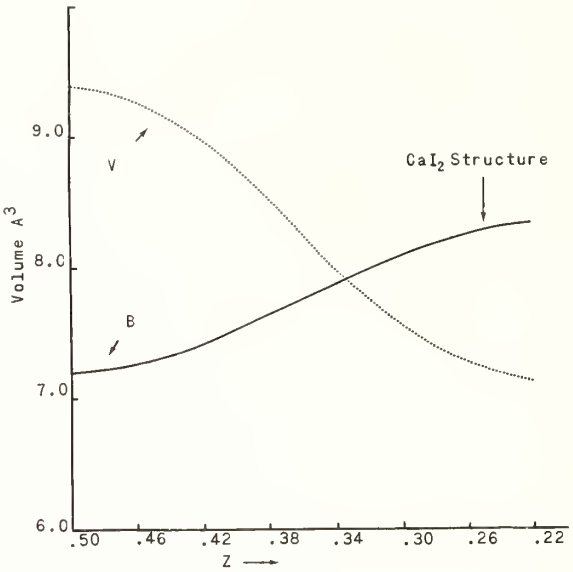

Fig. 12. The volume of boron Voronoi polyhedra in the AlB_2 structure is seen to increase steadily in VB_2 as the boron layer becomes increasingly pleated and approaches the CdI_2 structure type.

defined atomic volumes. Now, the total volume is better than 99.92% occupied by these new cells. The variation of the boron atomic volume for z = 0.50, 0.46, 0.43, and 0.40 is $4.866A^3(7.202)$, $4.894A^3(7.254)$, $4.952A^3(7.360)$, and $5.037A^3(7.520)$ where the numbers in parentheses are the corresponding Voronoi volumes for comparison. Accordingly, we note that the boron is unstable in the graphite position with respect to volume increase resulting from an increased negative charge. This is true in terms of the Voronoi cell volume or in terms of a reasonable definition of atomic volume. In the next section a more forceful argument, based on electrostatic considerations, will also be used to suggest the boron planar configuration is unstable when charged.

7. MADELUNG CONSTANTS FOR THE AlB_2 - CdI_2 STRUCTURE[7]

There is no doubt that, from an electrostatic energy viewpoint, the concentration of charge on a planar boron layer is unstable with respect to a pleated boron layer. This can be argued on the basis of the short boron-boron distance and the known Bozorth form of CdI_2 which is the resultant structure that would evolve from a continuous but extreme pleating of the boron layer. In order to provide rigorous support for this third argument for the pleating of the boron layer when negatively charged, we have calculated the Madelung constant for the $A\ell B_2$ - CdI_2 structure for a variation of the c/a ratio from 0.8 to 1.8 and a variation of the boron position from z(B) = 0.5 to z(B) = 0.0. The method used was the Bertaut series as discussed above (section 3) and the results are given in tables 7 and 8. The Jones and Templeton correction [25] to be subtracted from the Madelung constants of table 7 varies as a function of c/a only, from $\Delta A = 0.000027$ for c/a = 0.8 to $\Delta A = 0.000035$ for c/a = 1.8. The associated Madelung potentials (V_iL/ε) for both the metal and metalloid atoms are given in table 8 for the convenience of the reader and for the future interpretation of ESCA and x-ray data. The series termination correction to be made to the data of this table is uncertain, however, a correction of the form $\Delta V_iL = 2\Delta AZ_i/(\Sigma Z_i^2)$ appears to be consistent with the current information as in table 3.

For the $A\ell B_2$ structure with z(B) = 0.5, there is uncertainty in the correct calculation of $A(R_o)$, of the reduced Madelung constant α, and in the correct manner of calculating α by Templeton's [28,31] empirical relation, eq (11). This is because the anion-anion distance

[7]The $A\ell B_2$ and CdI_2 structure belong to the same space group and differ only in the nonmetal positional parameter (z(B) $\cong$ 0.5, z(I) $\cong$ 0.25) and hence coordination.

Table 7

Madelung Constants for the AlB_2 - CdI_2 Structure, D^3_{3d} - $P\bar{3}m$

z	0.50	0.45	0.40	0.35	0.30	0.25	0.20	0.15	0.10	0.05	0.00
C/A											
0.8	1.57166	1.57962	1.60150	1.63210	1.66490	1.69409	1.71585	1.72902	1.73491	1.73646	1.73657
0.9	1.55707	1.57003	1.60553	1.65493	1.70781	1.75507	1.79073	1.81267	1.82269	1.82537	1.82556
1.0	1.50367	1.52284	1.57507	1.64733	1.72454	1.79392	1.84700	1.88036	1.89597	1.90023	1.90054
1.1	1.41954	1.44600	1.51766	1.61608	1.72099	1.81586	1.88961	1.93706	1.95988	1.96626	1.96674
1.2	1.31049	1.34521	1.43857	1.56570	1.70082	1.82387	1.92117	1.98540	2.01719	2.02634	2.02703
1.3	1.18085	1.22472	1.34167	1.49937	1.66648	1.81977	1.94315	2.02675	2.06943	2.08206	2.08304
1.4	1.03390	1.08774	1.22987	1.41947	1.61971	1.80477	1.95640	2.06187	2.11744	2.13440	2.13573
1.5	0.87215	0.93673	1.10540	1.32781	1.56186	1.77977	1.96148	2.09119	2.16172	2.18392	2.18572
1.6	0.69755	0.77363	0.97001	1.22581	1.49402	1.74554	1.95885	2.11499	2.20258	2.23104	2.23339
1.7	0.51161	0.59993	0.82507	1.11463	1.41711	1.70273	1.94887	2.13346	2.24021	2.27603	2.27906
1.8	0.31552	0.41683	0.67167	0.99518	1.33192	1.65193	1.93192	2.14675	2.27474	2.31909	2.32293

Table 8

Madelung Potentials for the AlB_2 - CdI_2 Structure, D_{3d}^3 - $P\bar{3}m$

C/A	Site	z = 0.50	0.45	0.40	0.35	0.30	0.25	0.20	0.15	0.10	0.05	0.00
0.8	1a	-2.15051	-2.15443	-2.16583	-2.18369	-2.20636	-2.23172	-2.25731	-2.28061	-2.29924	-2.31127	-2.31543
	2d	0.99280	1.00481	1.03718	1.08051	1.12344	1.15646	1.17439	1.17743	1.17059	1.16165	1.15771
0.9	1a	-2.16559	-2.17184	-2.19009	-2.21876	-2.25533	-2.29647	-2.33825	-2.37650	-2.40726	-2.42719	-2.43409
	2d	0.94854	0.96822	1.02097	1.09109	1.16029	1.21368	1.24320	1.24884	1.23813	1.22356	1.21704
1.0	1a	-2.13718	-2.14622	-2.17261	-2.21426	-2.26769	-2.32821	-2.39015	-2.44728	-2.49350	-2.52360	-2.53405
	2d	0.87016	0.89946	0.97754	1.08041	1.18139	1.25962	1.30385	1.31344	1.29843	1.27685	1.26703
1.1	1a	-2.07512	-2.08724	-2.12273	-2.17900	-2.25167	-2.33464	-2.42029	-2.49998	-2.56495	-2.60750	-2.62232
	2d	0.76396	0.80476	0.91259	1.05317	1.19030	1.29708	1.35892	1.37415	1.35481	1.32503	1.31116
1.2	1a	-1.98617	-2.00157	-2.04679	-2.11883	-2.21252	-2.32041	-2.43287	-2.53853	-2.62541	-2.68269	-2.70271
	2d	0.63481	0.68886	0.83035	1.01257	1.18912	1.32733	1.40948	1.43227	1.40898	1.36999	1.35135
1.3	1a	-1.87519	-1.89398	-1.94929	-2.03782	-2.15380	-2.28857	-2.43047	-2.56520	-2.67705	-2.75133	-2.77739
	2d	0.48650	0.55546	0.73405	0.96093	1.17916	1.35097	1.45583	1.48830	1.46181	1.41280	1.38870
1.4	1a	-1.74581	-1.76802	-1.83356	-1.93900	-2.07810	-2.24122	-2.41479	-2.58139	-2.72114	-2.81468	-2.84765
	2d	0.32199	0.40745	0.62617	0.89995	1.16132	1.36831	1.49801	1.54234	1.51374	1.45411	1.42382
1.5	1a	-1.60072	-1.62635	-1.70215	-1.82466	-1.98740	-2.17995	-2.38702	-2.58804	-2.75847	-2.87354	-2.91429
	2d	0.14358	0.24711	0.50865	0.83096	1.13632	1.37959	1.53594	1.59434	1.56497	1.49431	1.45714
1.6	1a	-1.44201	-1.47103	-1.55704	-1.69663	-1.88328	-2.10604	-2.34811	-2.58581	-2.78960	-2.92844	-2.97786
	2d	-0.04692	0.07623	0.38299	0.75499	1.10476	1.38504	1.56959	1.64417	1.61555	1.53364	1.48893
1.7	1a	-1.27129	-1.30366	-1.39978	-1.55639	-1.76705	-2.02055	-2.29882	-2.57522	-2.81491	-2.97975	-3.03874
	2d	-0.24808	-0.10380	0.25037	0.67286	1.06717	1.38490	1.59893	1.69170	1.66550	1.57230	1.51937
1.8	1a	-1.08983	-1.12551	-1.23163	-1.40514	-1.63983	-1.92439	-2.23983	-2.55671	-2.83470	-3.02776	-3.09724
	2d	-0.45879	-0.29184	0.11171	0.58523	1.02401	1.37948	1.62401	1.73680	1.71478	1.61041	1.54862

(B-B) is shorter than the shortest anion-cation distance, usually taken as R_o. If we use a prime to indicate R'_o as referring to the boron-boron distance, then for VB_2 we have $A(R_o) = 1.1939$, $A(R'_o) = 0.8950$, and $\alpha = 1.5918$, and $\alpha' = 1.1934$. Using the empirical calculation of α by eq (11) and ignoring the boron-boron interaction, we have $\alpha = 1.75$ which is in 9% disagreement with $\alpha = 1.592$ above. With the boron-boron interaction and the boron-metal interaction, we have $\alpha'' = 1.52$ which is 4% too small. It is not, of course, surprising that the simple empirical relation of Templeton should fail in such a case.

The expected instability of the aluminum diboride, with respect to the pleating of the boron layer, is clearly demonstrated in table 7 for all values of the Madelung constant calculated from c/a = 0.8 to 1.8. The position at z(B) = 0.50 for all values of c/a is a minimum of electrostatic stability. This instability for the boron is also emphasized by the actual reversal in sign for the boron Madelung potential for c/a ratios greater than 1.6. The increase in the electrostatic stability (Madelung constant) with decreasing c/a ratio is to be expected since all static ionic structures tend to collapse and since a decreasing c/a ratio at constant volume tends to separate the ions of like charges, that is, increases the boron-boron distances and the metal-metal distances in their respective layers.

8. BONDING ORBITALS FOR THE DIBORIDES

8.1. THE TRANSITION ELEMENT

The application of the BOA approach to the problem of finding suitable bonding orbitals for the transition metal when the boron is in the planar graphite sheet (z(B) = 0.50) does not yield wholly satisfying results. This will be briefly indicated in this section for three different conceivable configurations of bidirectional orbitals. The effect of the pleating of the boron sheet on the coordination of the metal atom will also be considered. It will be seen that pleating leads to a more satisfactory bonding scheme.

Two of the principal restrictions of the BOA method [11] are: 1) all neighbors should be simultaneously bonded and, 2) equivalent neighbors should be bonded in an equivalent manner. When applied to atoms of high coordination, these restrictions are usually sufficient to reduce the number of possible combinations of bonding orbitals to a few that can be managed in an elementary discussion. When these restrictions are not maintained, the combinations that should be considered in a "resonating bond" description of a three dimensional structure with high coordination are staggering. Now, when the boron position is at z(B) = 0.5, the metal atom has two boron hexagons directly above and below to give twelve equivalent boron-metal bonds. These bonds are in addition to the six metal-metal bonds in the basal plane. If we just consider the twelve boron-metal bonds, it would appear that six general orbitals as in eq (13) or six C orbitals or G orbitals would be appropriate.

The first approach which might be attempted is to consider six general orbitals ϕ_i obtained by rotating one of them eq (13) by 60° successively five times. This approach, however, quickly leads to impossible conditions among the coefficients. Similar results clearly obtain for either pure C or G orbitals under a six-fold rotation. The second approach which might be considered is two interpenetrating general trigonal prisms formed by C orbitals. For example, if a C orbital in the xz plane is rotated about the x axis out of the vertical plane by about $\alpha = 28°$ it is seen from figure 9 that the corresponding trigonal antiprism ($\omega = 30°$) has a coordination $\bar{c}/\bar{a}$ ratio of about 2.1 in reasonable agreement with the generally observed ratio of 2.0. The second required trigonal prism may be formed by reflecting this one in the yz plane. The six C orbitals are not mutually orthogonal, however. The orbital of their largest overlap is the p_z orbital which is completely used by either of the trigonal prisms. This requires then that one has "resonance" between these two sets of C orbitals and that the metal-boron bond orders are 0.25 or less (as is generally observed in table 5). The presence of "resonance" is not satisfactory since the two tenets of the bidirectional orbital approximation (BOA), as discussed above, are negated along with many of their advantages.

In the third approach we will attempt to employ six general G-type orbitals of the form (eq 23). In this case the approach will be general, although the twelve boron-metal

$$\phi_G = A\ s + B\ p_x + G\ d_{xz} + H\ d_{x^2-y^2} + I\ d_{z^2} \qquad (23)$$

interactions will be considered as composed by two interpenetrating twisted trigonal prisms. For the first trigonal prism the orthogonality conditions eqs (24) and (25), can be obtained from eq (23) and its trigonally related orbitals.

$$\frac{2}{3} = B^2 + G^2 + H^2 \tag{24}$$

$$\frac{1}{3} = A^2 + I^2 \tag{25}$$

By rotating a pure G type orbital (B = 0) of the form $\bar{a}s + \bar{I}d_{z^2}$ about the x axis by an angle α a trigonal antiprismatic coordination is obtained. The corresponding coordination $\bar{c}/\bar{a}$ ratio, bond hybridization strength S, and d character is indicated in figure 13. The introduction of p_x character (B $\neq$ 0) produces a general twisted trigonal prism.

The second of the two interpenetrating prisms is considered to be rotated about the z axis by an angle δ from the first prism and is accordingly composed of an orbital such as ϕ_g, eq (26). Mutual orthonormality for this

$$\phi_g = A\ s + b\cos\delta\ p_x - b\sin\delta\ p_y - 2\cos\delta\sin\delta\ h\ d_{xy}$$
$$+ g\sin\delta\ d_{xz} + g\cos\delta\ d_{yz} + (\cos^2\delta - \sin\delta)h\ d_{x^2-y^2} + i\ d_{z^2} \tag{26}$$

trigonal prism results in orthogonality conditions such as eqs (24) and (25) but in lower case symbols. Orthogonality between the two sets of orbitals gives the conditions of eqs (27), (28), (29), which, from comparison of eqs (28) and (29) is seen to

$$0 = Aa + Ii \tag{27}$$

$$0 = Bb + Gg + Hh\frac{(\cos^2\delta - \sin^2\delta)}{\cos\delta} \tag{28}$$

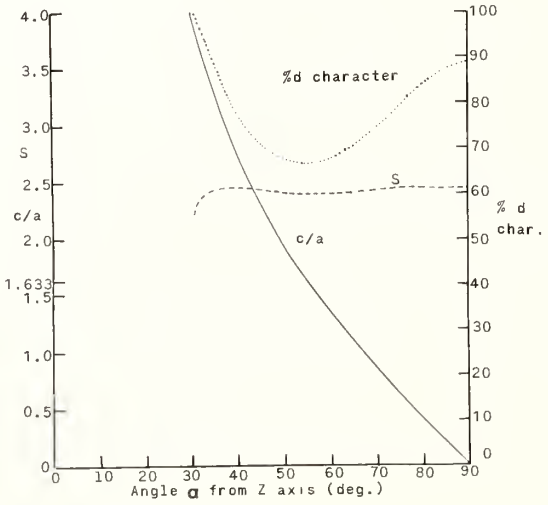

Fig. 13. When G orbitals without p character are used to bond six atoms in a trigonal prismatic coordination one is concerned only with the antiprismatic configuration. This figure illustrates the corresponding variation of the coordination $\bar{c}/\bar{a}$ ratio, the hybridization strength S, and the percent d character as a function of the rotation angle α.

$$0 = Bb \sin\delta + Gg \sin\delta - 2Hh \cos\delta \sin\delta \tag{29}$$

$$\frac{\cos^2\delta - \sin^2\delta}{\cos\delta} = -2 \frac{\cos\delta \sin\delta}{\sin\delta} \tag{30}$$

yield eq (30). This latter equation requires that $\cos\delta = +\frac{1}{2}, -\frac{1}{2}$ and that the corresponding angle δ is 60° and 120°. The trigonal character of these prisms informs us that these results correspond to δ = 180° and 0°, respectively. The former is obtained from the latter by reflection in a mirror plane containing the z and y axes; or equivalently by no restrictions in the signs of the lower case coefficients. In short, we may assume δ = 0° without loss of generality. We also note that the s orbital and the d_{z2} orbital are completely used by the orbitals of the two prisms.

In the case at hand, namely the $A\ell B_2$ structure with z(B) = 0.5, we will want the six G orbitals for the metal to boron bonds to be in some sense equivalent. This requires from eq (25) that $A^2 = I^2 = a^2 = i^2 = 1/6$. Now, if we assume that the signs of the coefficients A and I are positive ($A = I = I/\sqrt{6}$), then we see from the orthogonality condition, eq (27), that the coefficients a and i must be different in sign, *i.e.*, $a = -i = \pm 1/\sqrt{6}$. The net result, then, is that the two trigonal prisms are certainly nonequivalent, independent of the values of the other coefficients, B, G, H, b, g, and h. If, for example, the orbitals of one trigonal prism have high strengths and are thus suitable for bond formation, then the orbitals of the other prism have low strengths and are more suitable for localized electrons[8] than for bonding.

To summarize the above, we have not been able to devise, in the framework of the BOA method, six equivalent bonding orbitals for the coordination of twelve (or eighteen) in the form of two (or three) parallel hexagons of ligands. On the other hand, the BOA approach has been used by the author in the coordination of twelve in a CCP or icosahedral coordination [35,57], of fifteen [58] in one of Kasper's [59] metal coordinations, of sixteen in a Friauf polyhedron [57], of fourteen in WC (this paper), and even of eighteen as in the metallic LaS in the $NaC\ell$ structure. In this latter case, the metal can use six bonding C orbitals to bond the twelve neighboring metal atoms and three pure G orbitals to bond the six neighboring metalloids. In view of the above indicated versatility of the BOA method and its lack of success in the $A\ell B_2$ (z(B) = 0.5) case, the question of the local electron stability of this coordination arises. The feeling that this coordination might be unstable is strengthened by the remainder of this section which offers bonding orbitals for the metal coordination when the boron layer becomes pleated.

As the boron position parameter decreases from the value z(B) = 0.50 the coordination of the borons about the metal atom changes from that of a hexagonal prism to that of two interpenetrating trigonal antiprisms, a long one having a coordination $\bar{c}/\bar{a} = 4(1-\mu)(c/a)_{crystal}$, and a short more important antiprism with a coordination $\bar{c}/\bar{a} = 4\mu(c/a)_{crystal}$ where $\mu = z(B)$. Different methods of using bidirectional orbitals for bonding in these antiprisms is indicated by the data in figure 9 for C orbitals (ω = 30° or 90°) and figure 13 for G orbitals. In addition, we must consider bond formation between the metal atoms in the basal plane. This is possible using G orbitals of high d character (89%) as is also suggested by figure 13 at α = 90°. A combination of such G orbitals and the C orbitals of an antiprism for the short boron distances are readily shown to be orthonormal. We further note that, when z(B) = 0.408, the coordination about the metal atom of the six closest borons and the six metal neighbors is, from a point of view of bond angles, the same as a cubic-close-packed coordination. In this case, six orthogonal C orbitals could be used [35] to bond the twelve nearest neighbors. However, we note that bond orders of the boron-metal bond and the metal-metal bond are different.

We have seen that just as the hexagonal coordination with z(B) = 0.50 is difficult to satisfactorily formulate, any significant pleating of the boron layer leads readily to a variety of reasonable bonding possibilities. In the following section we will find a similar but less extreme situation exists for the boron atom.

---

[8] If equivalence between the prisms is not required, then six bonding G orbitals are obtainable, three corresponding to a twisted trigonal prism of high $\bar{c}/\bar{a}$ and the other prism with a very low $\bar{c}/\bar{a}$.

8.2. BOND FORMATION BY BORON

Valence bond formation in the diborides by the boron atom presents another interesting problem in that boron has nine neighbors but only four bonding orbitals, the 2s and three 2p orbitals. The consideration of this problem is quite germane to understanding the diborides since both the strongest bonds (boron-boron) and next strongest bonds (boron-metal) are involved. We shall attempt to shed some light on this problem by two simple valence bond discussions in which the vertical location of the boron is treated as variable. In the first discussion a traditional valence bond approach is employed, in the second some freedom is added to the general approach by the use of the nonpaired spin-orbitals (NPSO) of Linnett.

The coordination of the six metal atoms about the boron atom in the planar configuration (z(B) = 0.5) is that of a trigonal prism with a coordination $\bar{c}/\bar{a}$ ratio of twice that of the unit cell c/a ratio. If the traditional boron configuration sp^2p_z is used where the single p_z orbital is employed for the boron-metal bonds, then the direction of a boron-metal bond is 49° away from the direction of the p_z orbital. This, of course, gives rise to six rather badly bent boron-metal bonds. Further, it is to be noticed that since only one boron orbital is available to form six bonds, the boron-metal bond order must be 1/6 = 0.167 or less. However, the results of the metallic radii calculations suggest that it is almost always greater than 1/6 and closer to 0.23.

Let us now consider the changes in the traditional hybridization and coordination as we vary the boron parameter away from the planar value of z = 0.5. Independent of electrostatic considerations, there are several effects which give this approach an air of reasonableness. Since the boron-boron bond order (n < 1.0) indicates that π-bonds do not play a role in the interboron bonding, there is no obvious reason for the stabilization of sp^2 hybridization. Thus as z(B) decreases, the strength of the bond hybridization[9] increases slightly from 1.991 for sp^2 hybridization to 2.00 for the best tetrahedral hybridization, sp^3, at z(B) = 0.40. Thus, as far as the boron-boron bonds are concerned, there is little reason for a preference of z(B) = 0.50.

With respect to boron's metal coordination, there are two significant changes; the first is that as z(B) decreases the three metal atoms at the top of the prism become more distant while the base metal atoms become closer. In the exaggerated position at z(B) = 1/3, the boron has a coordination of six in a twisted trigonal prism having a small boron top directly opposed to a larger metal base through the central boron atom. The second significant change which takes place as z(B) decreases from 0.5 is that s character is added to the p_z orbital so that the bond hybridization strength is 2.00 (z(B) = 0.40) toward the metal atoms in the base, but only 1.02 in that part of the boron tetrahedral orbital (sp^3) directed toward the top three metal atoms. This suggests that the effective coordination of boron changes from nine to six with three of the boron metal interactions being decreased in importance, both because of increased distance as well as bond hybridization and direction. These effects were employed in an earlier section (5.4.) in the consideration of VB_2 with z(B) ≠ 0.5.

In the traditional valence bond approach above, the decrease of the boron position parameter improves the bond strength of the $(sp^3)_z$ hybrid, but it increases the misfit between direction of the boron-metal interaxis and direction (z-axis) of $(sp^3)_z$ hybrid. Thus at z(B) = 0.50, this angle is 49° but at z(B) = 0.40 it has increased to 55°. This suggests that Linnett's nonpaired spin-orbitals (NPSO) be used to obtain the boron-metal bond in the form of the pure three p-orbitals which give a good fit at the angle 54° 44'. This is conceivable because the boron-boron bond order is less than 1.0 and nearer to 2/3. If the latter is the case, then at sp^3 hybridization for the boron-boron bonds (z(B) = 0.40 assumed) then 1.5 p orbitals are available for the formation of three boron-metal bonds of half-bond order. This is generally more than required for these compounds. We note that some bending of the boron-metal bond may be expected, both because it is doubtful if z(B) becomes as small as 0.40 and because some s character might be employed for energetic reasons. The use of NPSO for the boron also indicates that the boron-boron bond and the metal-boron bond formation are not only nonorthogonal in the phase structure sense, but are indeed closely coupled. We also note that the use of NPSO's are also quite feasible when z(B) is equal to 0.50 since this gives rise to three boron-metal bonds which are bent only 6° rather than 49°.

---

[9]For a definition bond hybridization strength see Pauling [10, Chapter 4].

In the next main section, we will inquire into the effect that bond formation in the tungsten carbide compounds and diborides has upon the electrical properties of these materials. This will be approached in two ways, through the concept of the Fermi surface and through the use of the orthogonality of some of the phase structures.

9. BOND FORMATION AND THE FERMI SURFACE

The abundance of information inherent in a careful crystal structure analysis is surprisingly rich, especially when used in conjunction with a bond formation scheme. For materials like the transition metal carbides and diborides such information enables one to discuss transport properties at many levels of understanding using rather crude models. The principal consideration, which will be developed here for application to these materials, is the relationship between the chemical bond and the Fermi surface topology. For the purposes of clarity, we consider wave number or k-space as a "good quantum number space" of three dimensions which is rigidly attached to the crystal of interest[10]. The Fermi surface may be taken as the outermost or most energetic of the occupied surfaces of constant energy in k-space. In the 3rd NBS Materials Research Symposium [11], we indicated that the equation for a surface of constant energy in k-space could be written as eq (31). Here m is the electron mass and k is taken as the magnitude of the

$$E_k = \frac{k^2}{2m} - \frac{\bar{\omega}^2_k}{2m} - V_k + \text{neglected terms} \tag{31}$$

unreduced wave vector in k-space in the first term, but as the corresponding triplet index, (k_1, k_2, k_3), in the subscript use. The second term is an average over the contents of the unit cell of the momentum squared of the coordinate and periodic part, $U_k(r)$, of the Bloch wave function ψ_k. of eq (32). The third term, V_k, is a potential

$$\psi_k(r) = e^{ik\cdot r}\, U_k(r) \tag{32}$$

term which behaves similarly to $\bar{\omega}^2_k$ and need not be considered further here.

By focusing our attention on the first two terms of the energy, one a "crystal" momentum term, the second a "molecular" momentum term, we can readily deduce the effects of bond formation in a crystal on the Fermi surface of the crystal. We see immediately that the energy associated with the first term is a minimum (zero) when k = o and large for higher filled or excited states. Just the opposite situation pertains with the second term. In order to see this, it is desirable to indicate the correctness of the appellation, "molecular momentum" term. When k = 0 then the $-\bar{\omega}^2_o/2m$ term corresponds to the energy of a "molecule", which in this case consists of the contents of a single unit cell in its ground state. The associated energy then is large and negative. However, a molecule in its excited state is less negative in energy. This is also true for the general $-\bar{\omega}_k{}^2/2m$ term where an increase in k corresponds to an increasing frequency of nodal planes and a shift of electron density away from areas of greatest potential. However, what we really are interested in is the variation of $\bar{\omega}^2_k$ with respect to k (magnitude) as a function of the direction of the wave vector k.

Qualitatively the variation of $\bar{\omega}^2_k$ with unique directions in a structure can be understood by assuming that we have a crystal composed of diatomic molecules, one per unit cell, with the nuclear axis along the x axis. Now for a k vector along x axis, the magnitude of $\bar{\omega}^2_k$ will decrease strongly with k (magnitude) as an increasing number of nodal planes perpendicular to the internuclear axis begins to decrease the density of the binding electrons. However, the variation of $\bar{\omega}^2_k$ with k in the y or z direction will be much less because the nodal planes are now parallel to the internuclear axis and most will fall between the molecules in areas of low electron density. When this variation is combined with eq (31) it is found that surfaces of constant energy in k space will project, in the unreduced zone scheme, in the directions which are perpendicular to the bond direction. A generalization of this result will be used below to predict the approximate shape of the Fermi surface for compounds having the tungsten carbide and the aluminum diboride structures.

---

[10] The description of k-space as "momentum space" is seriously misleading unless it is further understood as a "crystal momentum" space and not as an electron (p) momentum space.

First, however, let us verify this result with an exact calculation using a square-well potential. Figure 14 shows a square-well potential of period c with four potential step discontinuities per unit cell. The discrete potentials are given by V_i corresponding to hills and valleys of width d_i. The energy of the electron, W, is indicated by the dotted line. Although the solution for the two-step discontinuities per unit cell has been available from the work of Kronig and Penny [60] published in 1931, the general solution to the n-step problem has not been available until recently [61]. Kronig and Penny also indicated in their classic paper [60] that if the assumption is made that the three-dimensional periodic square-well potential of a model crystal may be decomposed into a sum of potentials of single variables, eq (33), the problem of the motion of

$$V(r) = V_x + V_y + V_z \tag{33}$$

the electron is separable and may be solved exactly. Using this approach in figure 15 we show the effect in two dimensions of the combination of a two-step potential for the y direction (left side of fig. 15) and a four-step potential in the x direction (bottom of fig. 15). The depth of the potential is indicated by the amount of cross-hatching. Accordingly, we can imagine a molecule composed of two atom cores, dark squares, separated by a binding region of intermediate potential. The lattice-related molecules are at greater distances and separated by potentials which are more positive. The solutions for these two linear potentials in general are eq (34), taken from the work of Kronig and Penny, and eq (35) (Carter [61]).

Two-step discontinuities

$$\text{Cos } kc = C_1C_2 - \frac{1}{2}\left[\frac{\beta_1}{\beta_2} + \frac{\beta_2}{\beta_1}\right] S_1S_2 \tag{34}$$

Four-step discontinuities

$$\begin{aligned}\text{Cos } kc = {} & C_1C_2C_3C_4 + \frac{1}{2}\left[\frac{\beta_2\beta_4}{\beta_1\beta_3} + \frac{\beta_1\beta_3}{\beta_2\beta_4}\right] S_1S_2S_3S_4 \\ & - \frac{1}{2}\left[\frac{\beta_1}{\beta_2} + \frac{\beta_2}{\beta_1}\right] S_1S_2C_3C_4 - \frac{1}{2}\left[\frac{\beta_1}{\beta_3} + \frac{\beta_3}{\beta_1}\right] S_1C_2S_3C_4 \\ & - \frac{1}{2}\left[\frac{\beta_1}{\beta_4} + \frac{\beta_4}{\beta_1}\right] S_1C_2C_3S_4 - \frac{1}{2}\left[\frac{\beta_2}{\beta_3} + \frac{\beta_3}{\beta_2}\right] C_1S_2S_3C_4 \\ & - \frac{1}{2}\left[\frac{\beta_2}{\beta_4} + \frac{\beta_4}{\beta_2}\right] C_1S_2C_3S_4 - \frac{1}{2}\left[\frac{\beta_3}{\beta_4} + \frac{\beta_4}{\beta_3}\right] C_1C_2S_3S_4\end{aligned} \tag{35}$$

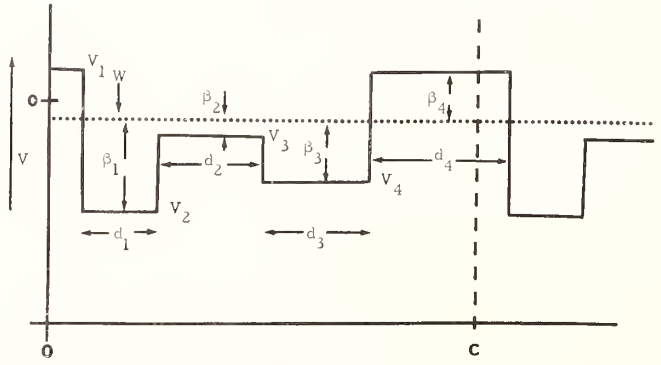

Fig. 14. A general one-dimensional square well potential with four step potential discontinuities per repeat distance is illustrated. The dotted horizontal line indicates the electron energy W in comparison to the constant potentials V_i.

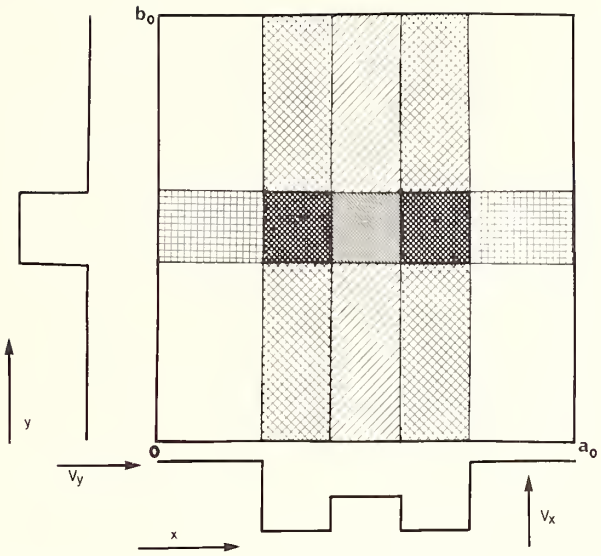

Fig. 15. This figure illustrates the use of two one-dimensional square well potentials to construct a "bimolecular molecule" in a square unit cell. The potentials shown at the left, V_y, and bottom, V_x, add to give a molecule whose internuclear axis is in the x direction.

where c is the unit cell edge, k the wave vector and β_i, C_i, and S_i are defined by eq (36).

$$
\begin{array}{ll}
V_i \leqslant W & V_i > W \\
\beta_i = \sqrt{W - V_i} & \beta_i = \sqrt{V_i - W} \\
C_i = \cos \beta_i d_i & C_i = \cosh \beta_i d_i \\
S_i = \sin \beta_i d_i & S_i = \sinh \beta_i d_i
\end{array}
\tag{36}
$$

The results for the "molecule" of the figure 15 are illustrated in figure 16 for the square unit cell case where $c = a_o = b_o = 6.0$ atomic units, dimensions which roughly correspond to the van der Waals packing of hydrogen molecules. Here it is clearly seen that for a surface of constant energy - constant ordinate in figure 16 - that the Fermi surface projects furthest from the origin in the direction perpendicular to the bond direction. While figure 16 illustrates essentially a core state this condition clearly obtains at large k values also. Since a potential of the separable form eq (33) gives [60] the total energy W_T as the sum, eq (37),

$$W_T = W_x + W_y + W_z \tag{37}$$

it is easy to see that the Fermi surface is roughly ellipsoidal in k when the form of $W_i(k_i)$ is proportional to k_i^2. This ellipsoidal distortion of the Fermi surface due to bond formation is not surprising considering 1) the close relationship between ω_k^2 and the p-momentum distribution for binding, and 2) the ellipsoids of constant p-momentum density found for diatomic molecules by Coulson in 1941 [62]. What is surprising is how well the molecule of "rectangular" atoms of figure 15 appears to mimic the results expected for spherical atoms as used by Coulson [62].

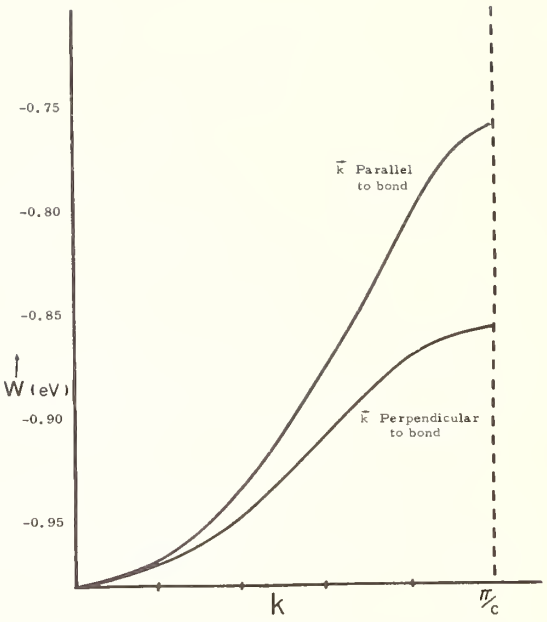

Fig. 16. The solution for the 'diatomic' molecule of figure 15 can be solved exactly if the potentials are additive. The solution for the lowest band is indicated here. It is seen that for constant energy the Fermi surface projects furthest in k-space in those directions which are perpendicular to the internuclear axis.

These elementary conditions can then be summed up in a simple model which can be used for roughly predicting the shape of the Fermi surface given only the crystal structure, or in particular, the relevant bond orders and directions of the stronger interactions or bonds (*i.e.*, n ~ > 0.05). Using the unreduced zone scheme assume a spherical Fermi surface whose volume is determined by the number of electrons outside the filled rare gas cores. Now in the plane perpendicular to each bond imagine a great circle around the sphere which indicates the outward distortion of the sphere due to that bond. If this construction is made for each relevant bond and the amount of distortion is taken as indicated by the bond strength or bond order, then the principal directions of distortion will occur at the intersections of these great circles. Of course the volume of the sphere must be maintained constant during these distortions and the effects of zone boundaries should be considered, especially for insulating materials and the more polar semiconductors or semimetals. The usual reciprocal lattice translations may be employed to obtain the results of the distortions in the reduced zone scheme, see for example [63] or the standard solid state physics references. In the next sections this model will be applied to the materials having the tungsten carbide and aluminum diboride structures.

9.1. THE BOND FORMATION - FERMI SURFACE RELATION IN TUNGSTEN CARBIDE

The Fermi surface is of central importance, of course, in discussions of transport properties of crystalline materials, however, before considering how the Fermi surface is distorted by bond formation let us first discuss those electronic transport properties which may be deduced from our previous description of bond orbitals and their occupancy in the tungsten carbide structure.

The bonding for the tungsten atom has been described in terms of G orbitals linking tungsten atoms together along the c axis and C orbitals which link tungsten atoms together in the basal plane as well as providing the basis for the tungsten-carbon bond. Now the two

principal phase structures which correspond to the use of the G and C-type orbitals are orthogonal and are not mixed by the mirror plane symmetry which must be employed to provide the total wave function with the symmetry of the structure. Accordingly, we then have in real space, in p-momentum space, and in k-space two orthogonal "bands" which we might term for the purposes of this discussion a G-band and a C-band and which (both) would be filled when the corresponding tungsten bidirectional orbitals in the valence state were occupied by one electron. Thus, the G-band is filled to give halfbonds when each tungsten donates one electron to it and the C-band is filled to give halfbonds when each tungsten donates six electrons and carbon three electrons. Such a filling would result in a small band gap semiconductor. However, since the valence of tungsten (table 2) in these compounds is more nearly 6.5 than 7.0, we may expect tungsten carbide to be a low mobility p-type conductor. Since bond order calculations (table 1) suggest that both the W-W (vertical) and W-W (basal) bonds are less than half filled (0.46 and 0.35 respectively) but more than quarter filled both corresponding bands would contribute to the hole-type conductivity. Further, since both bands are intimately involved in bond formation low mobility may be expected.

These results are in agreement with the experimental transport data of L'vov, Nemchenko, and Samsonov [64] for the case of tungsten carbide which differs qualitatively from the other transition carbides (NaCℓ structure) studied[11]. The data are also in agreement with what would be expected from BOA considerations for body centered cubic tungsten metal if the eight near neighbors form halfbonds.

The effect of bond formation in reciprocal k-space for tungsten carbide type compounds is summarized in table 9 which indicates the principal directions of the distortions of the unreduced Fermi surface according to the model of section 9. For example, in the first entry three great circles perpendicular to the metal-metal bonds in the basal plane intersect in the [00$\bar{1}$] and [001] directions to give a strong outward distortion of the Fermi surface. Similarly a medium strength distortion due to the intersection of great circles corresponding to a tungsten-tungsten bond in the basal plane and to a tungsten-carbon bond occurs in the direction [10ℓ], where ℓ is noninteger and is determined such that its angle with the [001] direction is 49°.

Chemical intuition based on training as an organic chemist suggests that carbon should be in a sense "saturated" and have little character at the Fermi surface. However, one might expect that the amount of carbon character should be largest at the Fermi surfaces projections involving the tungsten-carbon bonds. Accordingly, the relative amount of carbon character at the Fermi surface might be expected to increase as one progresses down table 9.

9.2. CONSIDERATION ON THE ELECTRONIC STRUCTURE OF THE DIBORIDES

In the earlier section treating bonding in the transition metal diborides we argued on the basis of four crystal chemical considerations against the charge transfer by the metal of one electron to each boron to form a B^- graphite-like net with a valence configuration of sp^2p_z. It was also indicated that any significant charge transfer should be associated with a pleating of the boron layer. Here we would like to discuss in further detail the electronic structure of the transition metal diborides, both with respect to a proposed semiconducting model [65] and with respect to the distortion of the Fermi surface by bonding effects.

The possibility of a new group of semiconducting compounds based on the $A\ell B_2$ structure has been proposed by George, Goodman, Sterling, and Warren [65]. The stated criteria for semiconductivity included high bond strength (or low thermal motion) and the possibility of an ionic-covalent bond formulation associated with a small charge separation. Experimental support for their contention was their careful preparation and characterization of high mobility-low carrier concentration TiB_2 and ZrB_2. In vapor grown TiB_2 the carrier concentration was sufficiently low ($\sim 8 \times 10^{20}$ electrons/cm^3) that the authors were unable to distinguish between the characterization of the material as a semimetal or a highly impure (nonstoichiometric) semiconductor. However, it was felt that such a low carrier concentration did largely eliminate the description of TiB_2 as a metal. This latter characterization is in contrast to that applied to the electronic specific heat results of Castaing, Caudron,

---

[11] In the discussion of these authors [64] for the carbides it will be seen that the case of tungsten carbide was not considered and should not be included.

Table 9

Projections in Surfaces of Constant Energy[(a)]
Due to Bond Formation in the Tungsten Carbide Structure

DIRECTION	BONDS	STRENGTH
[001]	3 W-W (basal)	Strong
[110]	W-W (basal) W-W (vert.)	Med.
[10ℓ], $\theta_z = 49°$	W-W (basal) W-C	Med.
[10ℓ], $\theta_z = 68°$	2 W-C	
[110]	2 W-C W-W (vert.)	Strong
(11ℓ], $\theta_z = 53°$	2 W-C	Med.

(a) Unreduced Zone Scheme

Toupance and Costa [47] who measured the electronic properties of the diborides of Sc, Ti, V, Cr, and Mn. However, of these, the electronic specific heat of TiB_2 was indeed the lowest suggesting a minimum in the density of states and partial support for the semiconducting model.

The proposed bonding in the model, however, is not consistent with the metallic radii results. In the model of George et al. [65], the boron uses three electrons to form single B-B bonds (n = 1.0) in the graphite network, this number is significantly greater than that indicated by the metallic radii calculations where for the B-B bonds, n = 0.64 (table 5). Further, the titanium metal atom in the model is to contribute one electron to each boron p_z orbital for use as a boron valence electron in the formation of the Ti^{+2}-B^- bond. This results in the use of the four titanium electrons to form twelve bonds with boron of bond order 0.166; this leaves no electrons for the metal-metal bond, as would be required for the proposed semiconductivity. However, the metallic radii results suggest that Ti-B bonds are stronger (n = 0.24) and that the metal-metal bonds are indeed significant (n = 0.12) and sufficient for metallic or at least semimetallic conductivity.

A low density of states model for TiB_2 which is related to the semiconducting model of George et al., but which is in better agreement with the interpretation of the observed bond distances will now be given. Let us assume that for the boron layer a bond order[12] of 2/3 is to be associated with a low density of states corresponding to either a small or zero energy bond gap. In support of this we will recall that for the p_z orbital occupation in graphite, Wallace [66] obtained a zero energy bond gap when the orbitals were 1/3 filled. It would be surprising if a 2/3's filling did not give similar results. Recall also that Pauling noted with interest the frequency of occurrence of fractional bond orders [10]. In addition to the p_z orbital this leaves the boron with one-third of an s orbital and two-thirds of a p_x,p_y orbital available for bond formation with the six equidistant metal neighbors. However, using the valence bond version of the NPSO approach as for carbon in tungsten carbide it seems likely from bond angle considerations that these bonds will predominantly be of p orbital character. This gives a maximum Ti-B bond order of 0.278 (or of 0.333 if the remaining boron s character is available), and this is somewhat larger than is generally

[12]For AlB_2 itself Pauling [10] also obtains a bond order of 2/3.

observed, table 5. If boron uses two electrons for the formation of its three B-B bonds, then the corresponding bond is filled and at a low density of states. The weak metal-metal bonds also appear to correspond to a low density of states since the number of electrons involved is approximately one per metal atom. Accordingly, one would expect the predominant character to be n-type associated with high mobility. The latter property might be expected from the low filling of the metal-metal band and from the high Debye temperature and low thermal motion [3] of the B layer as well as from the restriction of electron scattering to a predominantly two-dimensional process.

Let us now take another viewpoint of the $A\ell B_2$ type structure and consider the distortion of the unreduced Fermi surface due to nearest-neighbor bond formation as a function of the boron position parameter. When the boron layer is unpleated (z = 0.5), the characteristic that over-whelms all others is a very strong distorition of surfaces of constant energy in the [001] direction, not unlike that calculated for graphite by Wallace [66]. This peak is due to the confluence of three great circles of strong distortion due to the boron-boron bonds with three weaker (by 1/6 to 1/3) great circles of distortion due to the basal plane metal-metal bonds. In addition there is a still weaker distortion by another factor of 1/6, around the equator due to the marginal vertical metal-metal bond through the boron layer. The other strong peaks of distortion on the surfaces of constant energy are due to the crossing of the great circles of the boron-metal interactions with those of the metal-metal and boron-boron interactions. For example, in the direction [10ℓ] the metal-boron great circle adds to the metal-metal distortion; here ℓ is determined by the angle θ_z which measures the angle between the projection and the z axis [001]. This angle is readily calculated for this distortion as $\tan\theta_z = \sqrt{3}z(B)(c/a)$. In the [11ℓ] direction with a slightly larger θ_z the metal-boron great circle crosses the boron-boron great circle to give a medium intense distortion. However, as the boron moves away from the planar position this distortion rapidly weakens.

Some distortion peaks will change direction as the boron parameter decreases from z(B) = 0.5. This is shown in figure 17 for c/a = 1. The calculations for this figure are simple ones and require little more than spherical trigonometry. From the figure we see that the strongest peak in the [001] direction rapidly decreases in intensity due to its separation

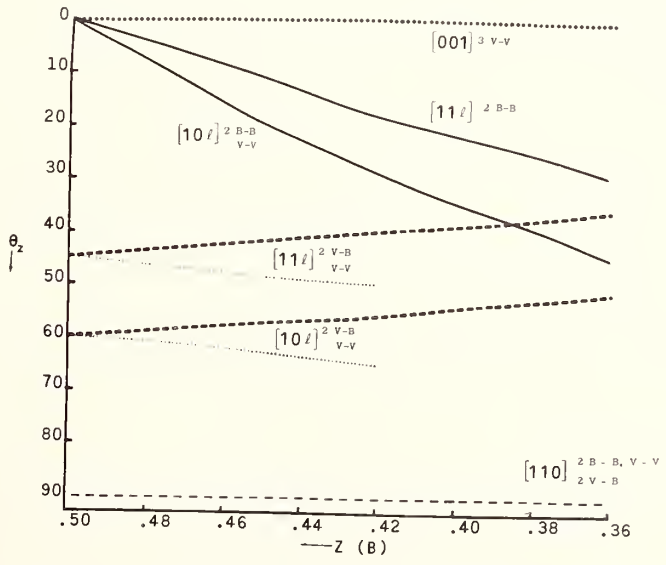

Fig. 17. The distortions of the unreduced Fermi surface for VB_2 are given as a function of the boron positional parameter z(B) neglecting zone boundary crossings. The bonds responsible for the major Fermi surface projections are indicated in the figure along with their general directions.

into other peaks. These number nineteen and include the stationary basal metal-metal distortion, six peaks in the [10ℓ] direction, six in the [11ℓ] direction and six weaker ones in the [10ℓ] position at smaller θ_z values. These latter six are not indicated in figure 16. However, as this peak diffuses the next strongest peak in the [110] direction remains undiminished and unmoved (see fig. 16). Also shown in the figure is the splitting of peaks in the [10ℓ] and [11ℓ] directions with θ_z equal respectively to 60° and 45°. This splitting reflects the splitting of the six boron-metal bonds for each boron into a set of three strong bonds (heavy dashed line) and a set of three weak bonds (weak dotted line). These latter become essentially nonbonding at z(B) = ~ 0.43.

The above material is useful in discussing the effect of the boron z parameter on the density of states N(E). If the length of the normal derivative to a surface S of constant energy in k space is $|\delta E/\delta k_n|$ then the density of states is calculated [67] as indicated by eq (38) where V is the crystal

$$N(E) = (V/8\pi^3) \int |\delta E/\delta k_n|^{-1} d.s \qquad (38)$$

volume. Now since $|\delta E/\delta k_n|^{-1}$ may be approximated as m*/k where m* is the effective mass, we see that the density of states is just the integral of the surface area weighted by m*/k. Looking at figure 17 it may be expected that as z(B) decreases from 0.50 and the number of peaks proliferate the surface area will increase. Accordingly, we may anticipate an increase in the density of states as the boron layer becomes pleated if the effective mass remains relatively stable[13]. An increase in density of states has been observed by Castaing et al. [47] for the diborides on either side of TiB_2. Accordingly, then such information is not inconsistent with the pleating of the boron layers as they become positive (ScB_2) or negative (VB_2) as suggested by the metallic radii results.

10. CONCLUSIONS AND SUMMARY

In general it is seen that the description of transition metal compounds with the tungsten carbide and aluminum diboride structures is possible using a modified valence bond approach with a fair measure of success. Not only are experimental properties understood but the anomalous members and compounds which are erroneously included as members are readily spotted. The fact that a large percentage of the compounds of each group seem to be improperly characterized experimentally is not only indicative of the casualness associated with the lack of chemical analyses and the tendency to eschew adequate determinations of the simpler structures but also of the inordinate difficulties associated with the preparation of pure (single phase) and/or stoichiometric compounds of these refractory structures.

In both of these compound types it was found that the metal-nonmetal bond plays a very important role, nevertheless the effective charges calculated, and partly confirmed by Madelung constant calculations, were not excessive and almost always less than 0.5 (plus or minus). In the tungsten carbide case the combination of bidirectional orbitals and nonpaired spin-orbitals led to the expected high valence of tungsten (6.5) and a less than tetravalent (3.5) carbon atom. However, the presence of three center bonds and a possible high concentration of metal orbitals near the carbon atom may not only compensate for carbon's nontetravalency but may also account for the larger negative effective charge on carbon calculated from chemical shift data (ESCA) than expected from a "neutral" cell metallic radii calculation.

Effective boron charges in the diborides were found to change sign near the compounds of the group V elements and become negative. This has not been previously predicted by any of the more popular models. While the boron bond formation can now be better understood by the use of Linnett's nonpaired spin-orbitals, the transition metal bonding still remains obscure if the original tenets of BOA is strictly followed. On the other hand, the boron-metal bond orders are compatible with a simple form of "resonance" using bidirectional orbitals (nonorthogonal). For emphasis we note here that the boron-boron bond order is not compatible with boron-boron single bond as required by several previous models of the

[13] Changes in the effective mass are difficult to predict from this model without parameterization of the distortion with respect to the bond order, bond length, and electronegativity differences. This information is needed in order to obtain the separation of the Fermi surface from the Bullouin zone faces and hence estimate zone edge effect.

diborides.

For diborides of the smaller transition metals it was indicated that any large negative charging of the boron should result in the pleating of the boron layer. The arguments for this included metallic radii results, anionic volume instability at z(B) = 0.5, electrostatic instability at z(B) = 0.5, and the inability of bidirectional orbitals to form twelve equivalent bonds in a hexagonal prismatic coordination. If compounds of large negative boron charge are found to be unpleated then a proper response to the above arguments must be made. The only clues to where such a response may be found are in the Madelung constant calculations and the fractional boron-boron bond order of 2/3. The special stability of such a bond order for a planar (only) boron configuration might be found in a band calculation. The Madelung constant calculations show that electrostatic energy for z(B) = 0.5 increases rapidly for a c/a decrease. The observed [45] c/a decrease as one moves across the periodic table toward the more negative boron compounds is at least consistent with these considerations.

Finally, we note that Madelung constants and potentials have been calculated for the WC, CdI_2, and $A\ell B_2$ structures as a function of c/a ratios and positional parameters. In addition, Fermi surface distortions due to bond formation in these compounds have been predicted.

11. ACKNOWLEDGMENTS

It is with pleasure that I acknowledge many useful discussions of the transition metal diborides with my wife, Dr. G. C. Carter and that I thank Dr. L. Bennett (both of NBS) for interesting me in this series of compounds. In addition I wish to thank Margaret O'Hara and Walter C. Sadler for their patient and complete assistance in the preparation of the figures and their subsequent photography.

12. REFERENCES

[1] Nowotny, H., in *Electronic Structure and Alloy Chemistry of The Transition Elements*, P. A. Beck, Ed., (Interscience Publishers, New York, 1963), p. 179.
[2] Carter, G. C., Kahan, D. J., Bennett, L. H., Cuthill, J. R., and Dobbyn, R. C., The NBS Alloy Data Center: Permuted Materials Index. (Spec. Pub. 324, 1971).
[3] Post, B., in *Boron, Metallo-Boron Compounds and Boranes*, Roy M. Adams, Ed., p. 301, (Interscience Publishers, New York, 1965).
[4] Nowotny, H., Berg-und Huttenmannische Monatshefte 95, 109 (1950).
[5] Muetterties, E. L., Z. Naturforschg. 12b, 411 (1957).
[6] Pauling, L., Proc. Roy. Soc., 196A, 343 (1949).
[7] Kiessling, R., Acta Chem. Scand., 4, 209 (1950).
[8] Juretschke, H. J., and Steinitz, R., J. Phys. Chem. Solids 4, 118 (1958).
[9] Cadeville, M. C., J. Phys. Chem. Solids 27, 667 (1966).
[10] Pauling, L., *Nature of the Chemical Bond*, 3rd ed. (Cornell University Press, Ithaca, New York, 1960).
[11] Carter, F. L., in Electron Density of States, (NBS Special Publication No. 323, 1971) p. 385.
[12] Hirst, R. M., and Linnett, J. W., J. Chem. Soc. 1035, 3844 (1962).
[13] Empedocles, B. P., and Linnett, J. W., Proc. Roy. Soc. (London) A282, 166 (1964); Trans. Faraday Soc. 62, 2004 (1966).
[14] Carter, F. L., Algol program, Calculation of Chemical Valences using Paulings Metallic Radii. Listing can be obtained from author.
[15] Wyckoff, R. W. G., *Crystal Structures* Volume 1, Second Ed., (Interscience Publishers, 1965).
[16] Hedberg, K., J. Amer. Chem. Soc. 74, 3486 (1952).
[17] Carter, F. L., in *Proceedings of the Ninth Rare Earth Conference* Vol. 2, P. E. Field, Editor (Virginia Polytechnic Institute and State University, Blacksburg, Va., Oct. 1971) p. 617.
[18] Schönberg, N., Acta Chem. Scand., 8, 204, (1954).
[19] Phillips, J. C., Science 169, 1035 (1970).
[20] Siegbahn, K., in ESCA - Atomic Molecular, and Solid State Structure Studied by Means of Electron Spectroscopy, 1st Ed., (North Holland Publishing Co., Amsterdam-London 1967).

[21] Ramqvist, L., Jernkont, Ann. 153, 1 (1969).
[22] Bertaut, F., J. Phys. Radium 13, 499 (1952).
[23] Bertaut, F., Ferroelectric and Dielectric Crystals: Contribution To The Theory of Fields, Potentials and Energies in Periodic Lattices, (U. S. Air Force Report AD-22696, July, 1953), Unpublished.
[24] Templeton, D. H., J. Chem. Phys. 23, 1629 (1955).
[25] Jones, R. E., and Templeton, D. H., J. Chem. Phys. 25, 1062 (1956).
[26] Carter, F. L., Algol program, Madelung Constant Calculations for the WC, VB_2, and NiAs Structures. Listings can be obtained from the author.
[27] Zemann, J., Acta Cryst. 11, 55 (1958).
[28] Templeton, D. H., J. Chem. Phys. 23, 1826 (1955).
[29] Hartman, P., Acta Cryst., 11, 365 (1958).
[30] Hund, F., Z. Phys., 34, 833 (1925).
[31] Johnson, Q. C., and Templeton, D. H., J. Chem. Phys. 34, 2004 (1961).
[32] Leciejewicz, J., Acta Cryst. 14, 200 (1961).
[33] Brumel, M., and de Bergevin, F., C. R. Acad. Sc. Paris 260, 3598 (1965).
[34] Carter, F. L., Vacancy and Charge Ordering in the Th_3P_4 Related Structures, J. of Solid State Chemistry, in press.
[35] Carter, F. L., Proceedings of the Fifth Rare Earth Research Conference, held at Iowa State University, Ames, Iowa (Aug. 30 - Sept. 1, 1965), Book Two, p. 103.
[36] Ganzhorn, K., Z. Naturforschg. 7A, 291 (1952): 8A, 330 (1953).
[37] Pauncz, R., Alternate Molecular Orbital Method, (W. B. Saunders Co., Philadelphia 1967).
[38] Carter, F. L., *Rare Earth Research III*, L. Eyring, Editor (Gordon and Breach, New York, 1965) p. 495.
[39] Pearson, W. B., *A Hand Book of Lattice Spacings and Structures of Metals and Alloys* Vol. 8, G. V. Raynor, Editor (Pergamon Press 1967).
[40] Post, B., Glaser, F. W., and Moskowitz, D., Acta Metallurgica 2, 20 (1954).
[41] Przybylska, M., Reddoch, A. H., and Ritter, G. J., J. Amer. Chem. Soc. 85, 407 (1963).
[42] Silver, A. H., and Bray, P. J., J. Chem. Phys. 32, 288 (1960).
[43] Silver, A. H., and Kushida, T., J. Chem. Phys. 38, 865 (1963).
[44] Fisher, D. W., J. Appl. Phys. 40, 4151 (1969).
[45] Carter, G. C., and Swartz, J. C., J. Phys. Chem. of Solids 32, 2415 (1971).
[46] Barnes, R. G., and Creel, R. B., Phys. Letters 29A, 203 (1969).
[47] Castaing, J., Caudron, R., Toupance, G., and Costa, P., Third International Conference on Solid Compounds of Transition Elements, Oslo, June 1969.
[48] Anderson, L., Dellby, B., and Myers, H. P., Solid State Commun. 4, 77 (1966).
[49] Carter, G. C., personal communication.
[50] Aronsson, B., Stenberg, E., and Aselius, J., Nature 195, 377 (1962).
[51] Obrowski, W., Naturwiss 48, 428 (1961).
[52] Kiessling, R., Acta. Chem. Scand. 1, 893 (1947).
[35] LaPlaca, S., and Post, B., Acta Cryst. 15, 97 (1962).
[54] Roof, R. B., and Kempter, C. P., J. Chem. Phys. 37, 1473 (1962).
[55] Voronoi, G., J. reine and angew, Math. 134, 199 (1908).
[56] Carter, F. L., Algol program, Interatomic Distances for Metallic Valence Program and Voronoi Polyhedra Construction. Listing can be obtained from the author.
[57] Carter, F. L., Proceedings of the Seventh Rare Earth Research Conference, held at Coronado, California (Oct. 28-30, 1968) p. 283.
[58] Carter, F. L., work to be published.
[59] Kasper, J. S., in Theory of Alloy Phases (American Society of Metals, Cleveland, Ohio, 1956), p. 264.
[60] Kronig, R., and Penny, W. G., Proc. Roy. Soc. A130, 499 (1931).
[61] Carter, F. L., work to be published.
[62] Coulson, C. A., Proc. Cambridge Phil. Soc. 37, 55 (1941).
[63] Carter, F. L., *Proc. Eighth Rare Earth Research Conference*, Reno, Nevada, T. A. Henrie and R. E. Lindstrom, Editors, (April 1970) p. 460.
[64] L'Vov, S. N., Nemchenko, V. F., and Samsonov, G. V., Soviet Physics - Doklady 135, 1334 (1960).
[65] George, W. P. R., Goodman, C. H. L., Sterling, H. F., and Warren, R. W., Phys. Stat. Sol. 21, 205 (1967).
[66] Wallace, P. R., Phys. Rev. 71, 622 (1947).
[67] Smith, R. A., Wave Mechanics of Crystalline Solids (John Dickens and Co., Ltd. Northampton, G. B. 1963) p. 307.

DISCUSSION

B. Post: Would this request for single crystal work apply to titanium diboride?

F. L. Carter: I think it would be interesting to do most of the series.

B. Post: Well, this was done about ten years ago in my lab with extremely high, good precision.[1] I forget the R factor, but it's a no-parameter structure and if those borons are not in a plane they are as close to a plane as anything I could imagine. That is, we can detect no contrary evidence whatsoever; they are in just about perfect agreement right down the line. Actually, everything agrees better than it should; that is, within statistical error and even better.

F. L. Carter: Is that assuming that the boron *can* move and checking the space group statistically for the equivalence of reflections?

B. Post: Oh, of course, I mean it was a good structure analysis, a complete structure analysis, and there is no indication at all that the borons are out of plane. This is not vanadium diboride of course, vanadium has a smaller metal atom. I just thought you would be interested.

A. L. Bowman: I did the same calculations for both titanium and zirconium diboride looking for the puckered plane and I agree, no indication at all. As soon as I moved the borons out, all the calculations pushed them back into the plane, but again, I have not done it with vanadium.

F. L. Carter: In the titanium case we have essentially no charge transferred to the boron, so that's a case where one might expect not too much electrostatic instability.

S. LaPlaca: You feel that it is particularly important that you have d-orbital participation in these diborides. What about the stability or instability of AlB_2? How important does this become? You mentioned this in your abstract as the parent compound.

F. L. Carter: I have attempted to understand the diboride structures through the transition metal diborides where d character is generally available. I have not attempted to understand compounds like MgB_2 and AlB_2 for which d character participation is much less likely and which are much harder for me to understand except through overly naive models.

S. LaPlaca: It is certainly one of the series. It's the structure type. I just might mention that rather recently lithium diboride has been found and prepared by Paul Schmidt at Bell Labs and it is isomorphous with this structure. The boron-boron distances in that structure turned out to be exactly what you might expect, it's down around 1.58 for just a single electron pair bond, and I doubt whether you have any d-orbital participation to any extent in lithium diboride.

F. L. Carter: On the basis of our current and rather weak understanding of these compounds it is probably inappropriate to make *a* priori structure stability predictions. While such predictions are entertaining and useful in that they lead to new work, both theoretical and experimental, it should be noted that Mother Nature is able to generate more and better models from which to chose than are generally available to mere mortals.

---

[1] M. G. Miksic, Ph.D. Thesis - Brooklyn Polytechnic , June 1962.

National Bureau of Standards Special Publication 364, Solid State Chemistry, Proceedings of 5th Materials Research Symposium, issued July 1972.

CRYSTAL CHEMISTRY OF REFRACTORY CARBIDES*

Allen L. Bowman

Los Alamos Scientific Laboratory
University of California
Los Alamos, New Mexico 87544

The crystal structures of most of the refractory metal carbides may be described generally on the basis of a close-packed metal sublattice, with the carbon atoms occupying all or part of the octahedral sites. Close-packed carbide structures have been observed with composition MC and packing type c, M_4C_3 and hhcc, M_3C_2 and hcc or hhc, and M_2C and h or c. All of these structures have one octahedral site per metal atom, and thus an apparent possible composition MC. This is reached however, only with the c-type packing, and it has been suggested that only one half of the sites adjacent to an h layer can be filled. This is found to be an upper limit that is not always reached. These carbide structures thus have carbon vacancy concentrations ranging from ~0 up to ~70%, with a possibility of vacancy ordering. Neutron and electron diffraction studies have shown ordering to exist in the M_2C compounds and in carbon-deficient VC.

The order-disorder transformation of the carbon vacancies in Mo_2C has been studied in detail with high-temperature neturon diffraction. The kinetics data are consistent with a nucleation-growth mechanism involving nucleation on grain boundaries and linear growth across the interface. The reaction between Mo_2C and Mo_3C_2, involving the transformation of the close-packed metal lattice (h $\rightleftharpoons$ hcc) has been studied less thoroughly, but the kinetics data also appear to be consistent with a nucleation-growth mechanism.

Key words: Carbide; crystal structure; molybdenum carbide; niobium carbide; reaction mechanism; solid state; tantalum carbide; tungsten carbide; vanadium carbide

1. INTRODUCTION

The refractory metal carbides to be discussed here are those of the third to sixth group of the periodic table. Most of these carbides have melting points above 2000 °C, exceptions being the chromium carbides with melting points of 1500-1800° [1][1], and the lower carbides of the third group metals.

The crystal structures of most of these carbides may be described on the basis of a close-packed metal sublattice, with the carbon atoms occupying the octahedral interstitial sites. The interstitial carbon atom and its nearest metal neighbors may be considered as a coordination polyhedron, and the crystal structure may alternately be described in terms of the stacking of coordination polyhedra. The latter description is particularly useful for those carbides that do not have close-packed metal sublattices.

2. DISCUSSION

The known refractory carbide phases are listed in table 1, with holmium arbitrarily selected to represent the rare-earth metals, and with the non-close-packed structures separated on the sides. The structures of Y_2C_3, Ho_2C_3, and U_2C_3 may be described in terms of stacking of C_2M_8 polyhedra, with C_2 groups of bond-length ~1.3 Å. The Sc_4C_3 differs only in having CM_8 polyhedra, a single carbon atom replacing the C_2 of the M_2C_3 structure.

* Work done under the auspices of the U.S. Atomic Energy Commission.

[1] Figures in brackets indicate the literature references at the end of this paper.

465-504 O - 72 - 37

Table 1

The Refractory Carbides

REFRACTORY CARBIDES

*Sc_2C c	TiC c	*V_2C h	$Cr_{23}C_6$
Sc_4C_3		V_4C_3 hhcc	Cr_7C_3
$ScC_{\sim 1.3}$		*VC c	Cr_3C_2
*Y_2C c	ZrC c	*Nb_2C h	*Mo_2C h
$YC_{\sim 1.2}$, Y_2C_3		Nb_4C_3 hhcc	Mo_3C_2 hcc
YC_2		NbC c	MoC c
*Ho_2C c	HfC c	*Ta_2C h	*W_2C h
Ho_2C_3		Ta_4C_3 hhcc	WC(β) c
HoC_2		TaC c	WC(α)
U_2C_3, UC_2, UC c			

Phases noted by * have well-established ordered vacancy structures. The close-packed structures are indicated by their Jagodzinski-Wyckoff symbol.

The dicarbides, YC_2, HoC_2 and UC_2, are approximately close-packed structures with C_2 groups (bond length ~1.34 Å) occupying the octahedral sites. The crystal structures of the $YC_{\sim 1.2}$ and $ScC_{\sim 1.3}$ phases have not yet been determined. On the other side of the table, the structures of WC (α), Cr_3C_2 and (probably) Cr_7C_3 can be described in terms of stacking of CM_6 trigonal prisms. The structure of $Cr_{23}C_6$ should probably be considered in terms of chromium-metal polyhedra bonded together by carbon atoms.

The carbides in the central portion of table 1 have close-packed structures. The Jagodzinski-Wyckoff symbols for each lattice are also shown (a layer is denoted by h if the two adjacent layers are of the same type, by c if they are of different types). The (110) planes of each of the observed stacking arrangements are shown in figure 1. The hhc sequence, which has been observed in the ternary carbide Ta_2VC_2 [2], is also included. Since each close-packed structure has one octahedral site per metal atom, the maximum carbon composition of each close-packed arrangement would seem to be MC. However, this ideal composition is approached only with the c-type of stacking, while the maximum carbon composition of the h-type carbides is M_2C. It has been suggested [3] that where two sites are located above each other in the (110) plane (which occurs with each h-layer), only one site can be occupied. Following this argument, which is valid for the h-type stacking, and assuming complete occupation of sites adjacent to a c-layer, maximum carbon compositions were defined as M_2C for h, M_3C_2 for hcc and hhc, M_4C_3 for hhcc and MC for c.

The carbon compositions based on 50% vacancies for an h-layer and no vacancies for a c-layer must be considered as upper limits which need not be reached. The composition M_2C appears to be the approximate upper limit for all the h-type phases, while for the c-type phases, TiC, ZrC, HfC, NbC, TaC and UC reach almost 100% occupancy of carbon sites, but $MoC_{0.7}$, $WC_{0.7}$ and $VC_{0.9}$ are always deficient in carbon. The c-type carbides of the group three metals have a maximum composition M_2C at low temperature (<1000°) but form a continuous solid solution field with the dicarbides at higher temperatures. The carbides with mixed stacking sequences are all deficient, with approximate compositions of C/M ~ 0.64.

The close-packed carbides thus tend to have large percentages (up to ~65%) of their carbon sites vacant. Even the c-type carbides with composition MC (except UC) have large ranges of homogeneity based on carbon vacancies. These vacancies could be either ordered or random in the c- and h- type structures. Ordered vacancy structures have been identi-

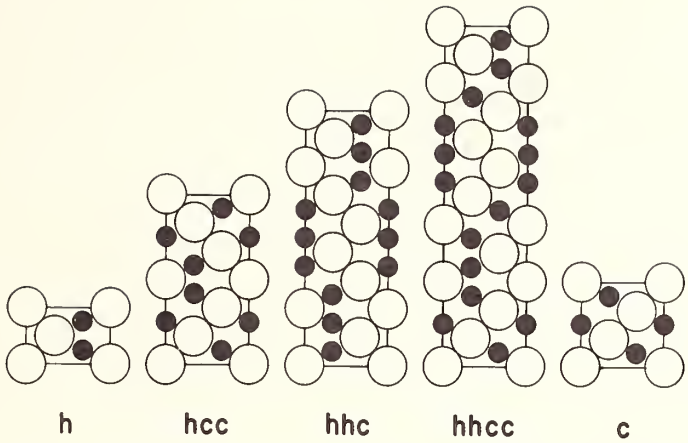

Fig. 1. The known close-packed carbide structures. The (110) plane.

fied in the c-type vanadium carbide phase at V_8C_7 (cubic) [4] and V_6C_5 (trigonal) [5]. Above ~1200° the VC phase has only random vacancies. A complete long-range ordered vacancy structure has not yet been clearly observed in the other monocarbides. Ordered vacancy and identified structures have been observed in all of the M_2C carbides, including the c-type of the third group metals. These structures are listed, and the references cited, in table 2. The structures of the ordered h-type M_2C carbides are shown in figure 2 as projections in the plane perpendicular to the c-axis (V_2C has the same structure as Mo_2C). The c-type structures have the same vacancy arrangement as Ta_2C, with alternate C-planes completely filled and empty. It appears that all of the M_2C carbides transform to the corresponding random vacancy structure at temperatures ranging from ~600° to over 2000°.

The intermediate phases with mixed stacking sequences have two different kinds of carbon sites, those adjacent to an h-layer (H), and those that are not (C). There are thus three possible types of vacancy arrangement, random distribution over all sites, random distribution over H-sites with C-sites filled (partial ordering), and ordered arrangement among specific sites (more probably H-sites), as well as possible intermediate states. The neutron diffraction pattern of Mo_3C_2, obtained at 1750°, appears to agree better with the calculated random vacancy pattern than with the partially ordered vacancy pattern. The completely ordered structure is not possible. The neutron diffraction patterns of Ta_4C_3 also do not appear to be consistent with even partial ordering, although an ordered structure has been proposed from an electron diffraction study [14].

Two solid-state reactions are possible with the close-packed carbides, the transformation between the ordered and disordered vacancy structures, and the reaction with metal or graphite to yield a new phase with a different stacking sequence (the reaction between two carbide phases to yield a third carbide phase is considered equivalent to the second reaction). The molybdenum-carbon system is particularly well suited for the study of both types of reaction, with three possible cases

$$Mo_2C(\alpha) \rightleftarrows Mo_2C(\beta) \quad (1)$$

$$Mo_2C(\beta) + C \rightleftarrows Mo_3C_2 \quad (2)$$

$$Mo_3C_2 + C \rightleftarrows MoC \quad (3)$$

The order-disorder transformation of Mo_2C (eq 1) has been studied with high-temperature neutron diffraction [15]. The volume transformed (ζ) was measured as a function of time by following the change of intensity of the (111) peak of the α-phase when the sample temperature was changed across the equilibrium temperature. The results are shown in figure 3 for Mo_2C in the presence of Mo and C, for an initial temperature 30° from the equilibrium value and a final value 15° to the other side. The data are consistent with a nucleation-growth

Table 2

The Ordered M_2C Phases

V_2C	ζ-Fe_2N	[6]
Nb_2C	α-Nb_2C	[7]
Ta_2C	CdI_2 (C6)	[8]
Mo_2C	ζFe_2N	[9]
W_2C	ε-Fe_2N	[10]
Sc_2C	$CdCl_2$ (C19)	[11]
Y_2C		
Tb_2C		[12]
Ho_2C		[13]

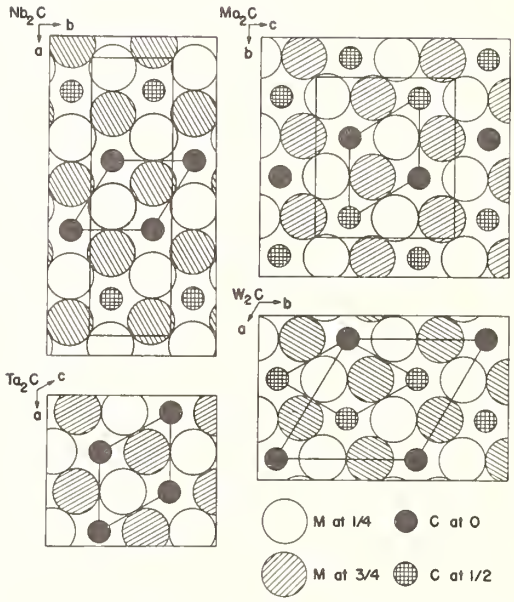

Fig. 2. The ordered M_2C structures. Projection on plane perpendicular to the *c*-axis.

mechanism involving nucleation primarily on grain boundaries and linear growth across the $\alpha \rightleftharpoons \beta$ interface. The data were fitted by the method of least squares to the equation

$$\zeta = 1-\exp\left\{-k_1 t\left[1-\int_0^1 \exp\left(-k_2 t^3[1-3x^2+2x^3]\right)\,dx\right]\right\}. \qquad (4)$$

The rate constants k_1 and k_2 are composites of the nucleation and growth rates and of the grain boundary area available for nucleation.

The reaction between Mo_3C_2 and Mo_2C (eq 2) involving a change in stacking sequence has been studied to a small degree by high-temperature neutron diffraction. The data appear to fit the simpler equation

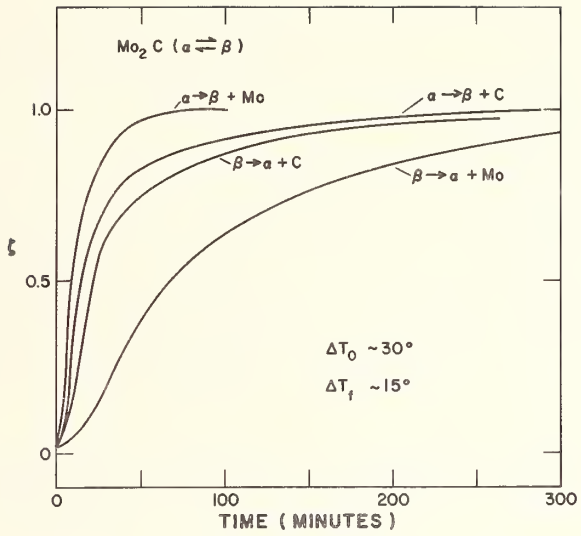

Fig. 3. The rate of the order-disorder transformation of Mo_2C, in the presence of molybdenum and of carbon.

$$\zeta = 1-\exp\ (-kt^n) \qquad (5)$$

with n = 3-4. This is consistent with a nucleation-growth mechanism with decreasing nucleation rate, but further work is required to obtain a quantitative final result. The reaction between Mo_3C_2 and MoC (eq 3) is too fast to study.

2. REFERENCES

[1] Rudy, E., *Compendium of Phase Diagram Data,* AFML-TR-65-2, Part V (1969).
[2] Rudy, E., J. Less-Common Metals 20, 49 (1970).
[3] Parthé, E. and Yvon, K., Acta Cryst. B26, 153 (1970).
[4] deNovion, C. H., Lorenzelli, R., and Costa, P., Compt. Rend. 263, 775 (1966).
[5] Venables, J. D., Kahn, D., and Lye, R. G., Phil. Mag. 18, 177 (1968).
[6] Yvon, K., Rieger, W., and Nowotny, H., Monatsh. Chem. 97, 689 (1966).
[7] Yvon, K., Nowotny, H., and Kieffer, R., Monatsh. Chem. 98, 34 (1967).
[8] Bowman, A. L., Wallace, T. C., Yarnell, J. L., Wenzel, R. G., and Storms, E. K., Acta Cryst. 19, 6 (1965).
[9] Parthé, E. and Sadogopan, V., Acta Cryst. 16, 202 (1963).
[10] Yvon, K., Nowotny, H., and Benesovsky, F., Monatsh. Chem. 99, 726 (1968).
[11] Atoji, M. and Kikuchi, M., J. Chem. Phys. 51, 3863 (1969).
[12] Atoji, M., J. Chem. Phys. 51, 3872 (1969).
[13] Bacchella, G. L., Meriel, P., Pinot, M., and Lallement, R., Bull. Soc. franc. Miner. Crist. 89, 226 (1966).
[14] Martin, J.-L., Rocher, A., Jouffrey, B., and Costa, P., Phil. Mag. 24, 1355 (1971).
[15] Bowman, A. L., Wallace, T. C., and Arnold, G. P., 8th International Congress of Crystallography, Stony Brook, New York, p. 226 (1969).
Bowman, A. L., Arnold, G. P., and Wallace, T. C., 25th Southwest Regional Meeting, A.C.S., Tulsa, Oklahoma, p. 107 (1969).

W. S. Williams: Have you looked at any transport properties through the molybdenum carbide, Mo_2C, order-disorder transition?

A. L. Bowman: Primarily diffusion you're thinking of?

W. S. Williams: I'm thinking of electrical and thermal conductivity primarily.

A. L. Bowman: No, all we have ever worked with has been powder samples and for this it just didn't seem worthwhile to bother. We have done a few diffusion studies, and of course many other people have also done this. This is more of what we are interested in, and in particular what I wanted to find is the change in diffusion as you go through the transition. We don't really know about the other properties, I'm sorry. I'd like to.

H. Nowotny: Your alpha, the ordered alpha Nb_2C is our ζNb_2C?

A. L. Bowman: I believe so. The other one that was found originally that Yvon reported[1] which agrees with electron diffraction data would seem to be an oxide stabilized phase, not part of the system.

H. Nowotny: With respect to stabilization, I want to mention that Dr. Jack in the May meeting of AIME in Atlanta asserts that a nice ordered Mo_2C structure is also stabilized by nitrogen.

A. L. Bowman: Well, if it is, it is stabilized by nitrogen in the 100 ppm range.

H. Nowotny: Well, it may happen.

A. L. Bowman: That's certainly true, but that's about as low as we can get. Certainly all of the M_2C compounds that I described here seem to be stable with just 100 or 200 ppm of nitrogen and oxygen. As soon as you add more of the non-metal impurity, other things can certainly happen. It has been shown by Yvon, of course, with the Nb_2C that this indeed did happen, but we don't know beyond that.

R. Ward: I wonder if it's possible that one could have order within the planes and unless you then have order between the planes also you wouldn't recognize it as an ordered phase. In other words, you may have order between the planes but there would be no relationship between planes, then you wouldn't see the order. It would look like a random phase.

A. L. Bowman: There are all sorts of very grim possibilities along this line. The ordering for the zeta phase that has just been suggested by Martin and Costa and others[2]. What they are now thinking of is the case where four carbon planes are ordered and then the next four are also ordered, but these two blocks of four are random with respect to each other. This is a pretty difficult picture, but it's the best explanation so far for the data that they have.

---

[1] Yvon, K., Nowotny, H., Kieffer, R., Mh. Chem. 98, 34 (1967).

[2] Phil. Mag. 24, 1355 (1971).

National Bureau of Standards Special Publication 364, Solid State Chemistry, Proceedings of 5th Materials Research Symposium, issued July 1972.

A SIMPLE MODEL FOR THE STABILITY OF TRANSITION METAL CARBIDES

Robert G. Lye

Research Institute for Advanced Studies
Martin Marietta Corporation
Baltimore, Maryland 21227

The origins of the unusual and complex combination of physical properties exhibited by the transition metal carbides remain somewhat obscure despite extensive studies of the problem in recent years. Even the qualitative nature of the bonding has not yet been described in a manner that accounts satisfactorily for the diverse and sometimes apparently contradictory experimental observations made on these compounds.

One theme, however, recurring through the years of study, draws attention to the similarity of these compounds to the parent transition metals. This characteristic of the carbides is considered briefly in the present study in an attempt to provide a qualitative explanation for the manner in which the stability of the carbide phases varies with the position of the parent metal in the periodic chart of the elements. A simple model for the d band bonding in the transition metals, discussed by Cyrot-Lackmann, is modified for this purpose. In particular, it is assumed that a major component of the bonding in the carbides arises from crystalline electronic energy bands derived for the d states of the metal atoms. Because of changes in crystal structure, these bands are modified somewhat from the shape of the corresponding bands in the parent metal. Of greater importance for the stability of the carbides, however, is the increase in the width of the band, discussed by Costa and Conte, that results from the presence of the carbon atoms within the interstitial positions in the metal sublattice.

As for the parent metals, the cohesion of the carbides is determined by the number of electrons in the d band. In the carbides, however, it is assumed that some of these electrons are provided by transfer from the 2p states of the carbon atoms. Thus, the stability, as measured by the heat of formation, results from the combined effects of the increase in the width of the d band and in the number of electrons it contains.

Despite the considerable simplifications employed, an analytical formulation of this model yields estimates for the heats of formation of the carbides that agree remarkably well with the experimental data presently available.

Key words: Bonding; carbides; cohesive energy; density of states; electronic structure; heat of formation; $L_{II,III}$ spectra; refractory hardmetals; Ti; TiC; transition metal compounds.

1. INTRODUCTION

Transition metals from Groups IV, V and VI of the Periodic Table combine with boron, carbon or nitrogen to form related series of compounds having remarkable combinations of properties [1-5][1]. In particular, many of these compounds exhibit strong deviations from Dalton's Law of Constant Proportions, resulting in considerable variations in their physical properties. Thus, although $NbC_{0.977}$ has a superconducting transition temperature of 11.1 K

[1] Figures in brackets indicate the literature references at the end of this paper.

and that for an alloy of NbC-NbN is 17.8 K, not far below the highest value yet observed, $NbC_{0.70}$ does not become superconducting above 1.05 K [6,7]. Most of these compounds are hard and brittle at room temperature, reminiscent of covalent solids, yet they exhibit metallic conductivities comparable with those of the parent metals. In addition, they are highly refractory, $TaC_{0.89}$ having the highest melting temperature known, 3985 °C [8]. Some of the carbides become deformable and have remarkably high ratios of strength to density at elevated temperatures [9], which suggests numerous possible technological applications if the undesirable brittleness at low temperatures can be overcome.

Although many of the carbide phases extend over broad compositional ranges, a trend is exhibited, in each transition series, for the region of stability to move toward lower carbon-to-metal atom ratios as the atomic number of the parent metal increases. Brewer and Krikorian [10] and Dempsey [11] have noted that the variation of various physical properties of the carbides approximately parallels that for the metals but is displaced somewhat, as though the carbon atoms contributed additional electrons to the electron energy bands characterizing the transition metals. Similar conclusions have been drawn by Ubbleohde [12], Umanskii [13], Kiessling [14,15] and Robins [16] from a variety of considerations. This point of view was provided some support by the results of an LCAO calculation of the electronic energy band structure TiC by Lye and Logothetis [17], which suggested that the energy bands derived from the 2s and 2p states of the carbon atom were displaced upward in energy relative to the bands arising from the 3d states of the metal atom. The resultant disposition of the energy bands required a transfer of approximately 1.3 electrons from electronic states of 2p symmetry into states of 3d symmetry. Accordingly, the principal component of the interatomic bonding was associated with electronic energy bands similar in most respects to those of the parent transition metal but broadened somewhat by the effect of the carbon atom core potential [18], and occupied more fully by the electron transfer.

This interpretation of the bonding in TiC has been placed in question by the results of APW calculations of the band structure by Ern and Switendick [19] and similar calculations to self-consistency by Conklin and Silversmith [20], who concluded that the carbon 2p bands lie relatively low in energy and accept between 2 and 3 electrons transferred from the titaium electron orbitals.

Ramqvist and coworkers [21-26] in a recent series of papers have reported the results of measurements made by the ESCA technique to determine changes in the binding energy of atomic core electrons upon formation of the carbides. In all of the cubic carbides studied, the binding energy of the carbon 1s state was found to be less in the carbides than in carbon, *i.e.*, the 1s state is raised in energy in the carbides relative to its position in carbon. For TiC, the displacement observed experimentally, 3.3 eV, agrees in direction and approximately in magnitude with the displacements applied to the 2p level (2.77 Ev) and the 2s level (4.15 eV) in the LCAO band structure calculation by Lye and Logothetis [17].

Ramqvist equates this displacement solely to ionic interactions arising from charge transfer between the carbon and metal atoms, and concludes that 0.4 electrons are transferred from 3d states of the Ti atom into carbon electronic states. According to this argument, the electrostatic (Madelung) energies of the cubic carbide lattices are very nearly equal to the heats of formation of these compounds. Ramqvist asserts also that the electrostatic energy of the carbides is approximately one-sixth to one-third of the total binding energy of these compounds. He defines the total binding energy of the carbides, however, as the sum of the cohesive energy of the metal, $-\Delta H_{Me}$, and the heat of formation of the respective carbide, $-\Delta H_{MeC}$, whereas thermodynamic arguments require the inclusion of the cohesive energy of carbon, $-\Delta H_C$ = 710 kJ/mole, in this sum. When Ramqvist's calculations are revised in this manner, his estimated ionic contributions to the cohesive energy vary from 8% to 13% of the total. Qualitative discussions will be given later in this paper to suggest that the effective charge associated with the ions in TiC may be approximately one-half the value indicated by Ramqvist. Thus, the ionic contribution to the bonding would be approximately 4% of the total binding energy or one-quarter of the heat of formation. For either estimate of the ionic charge, however, questions are raised again regarding the origins of the principal components of the bonding.

Additional support for the APW band structure of TiC [19,20] has been offered recently by Holliday [27] and Fischer [28,29] from the results of their measurements of x-ray emission and absorption spectra. Although their interpretations are plausible, they should not be

considered conclusive. Indeed, Fischer [29] correctly emphasized that the x-ray spectra cannot be correlated quantitatively with the electronic density of states curve unless proper account is taken of the influence of the electronic transition probabilities. Accepting this limitation, it may be noted that the titanium $L_{II,III}$ emission and absorption spectra of TiC can be interpreted in the alternative manner illustrated in figure 1. Shown there are the $L_{II,III}$ spectra of Fischer and Baun [29], used by Fischer [28,29] in subsequent discussions also. The emission spectrum is similar to that reported by Holliday [27], but appears to exhibit differences in detail. The significance of these slight differences is unclear. Superimposed on these spectra is a plot of the density-of-states curve derived from the LCAO band structure calculated by Lye and Logothetis [17], adjusted in energy so that the Fermi level lies near the position of the $L_{II,III}$ absorption edge. Some uncertainty resides in this choice [28,30], so the adjustment has been made to optimize the correlation between the x-ray spectra and the density-of-states curve. On this basis, the structure in the x-ray emission spectrum from -4.5 eV to -6 eV may be attributed to charge exchange transitions involving the carbon 2s electrons, the large peak near -1 eV primarily to 3d electrons, and the shoulder near -2.5 eV to titanium 3d and some carbon 2p electrons. Similarly, the small feature near +1.5 eV in both the emission and absorption spectra is correlated with a peak in the density-of-states curve that arises largely from titanium 3d states, although carbon 2p and titanium "4p" states also contribute. The peak in the density of states near 2 3/4 eV arises primarily from $3d_{\varepsilon}$ states, and may cause the abrupt increase in absorption in this region. Although Fischer and Baun [29] do not place great confidence in the details of the absorption spectrum at high energies, their results can be correlated qualitatively with the density-of-states curve in this energy region also. In particular, peaks in the density of states curve near 4.8 eV and 5.6 eV, which result from (4s+"4p") states, respectively, agree rather well with structure in the absorption spectrum. The peak due to "4p" states near 6.6 eV does not correspond to obvious structure in the absorption.

This alternative interpretation of the x-ray spectra differs from that proposed by Fischer [27] primarily in associating the structure near -5 eV with the carbon 2s electrons. Fischer [28], together with Ern and Switendick [19] and Conklin and Silversmith [20], estimate that the carbon 2s band lies somewhat lower in energy, near -9.5 eV. The titanium K emission spectrum obtained by Chirkov et al. [30] appears to support the lower energy of the

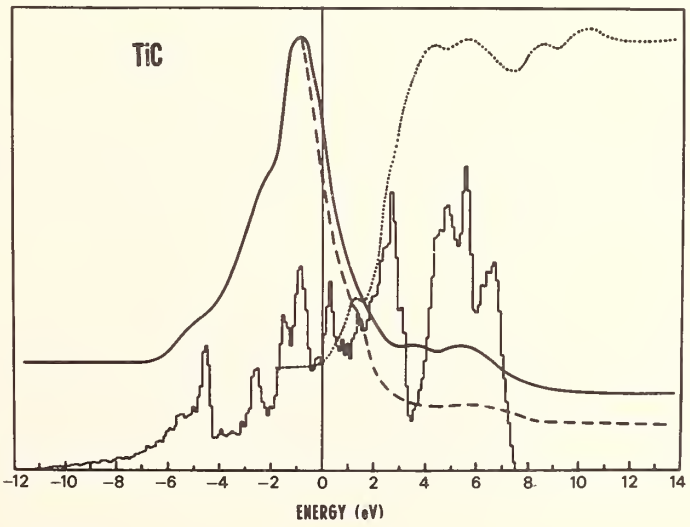

Fig. 1. Structure in the electronic density-of-states histogram for TiC obtained by Lye and Logothetis [17] shows a pronounced correlation with that in the $L_{II,III}$ emission and absorption spectra observed by Fischer and Baun [30] if the Fermi level, at the zero of energy, is placed relative to the x-ray spectra in the manner shown here.

carbon 2s bands employed by Fischer in his analysis; but additional confirmation would be desirable. For either position of this band, however, the carbon 2s electrons would be expected to contribute little to the total binding energy of TiC. To evaluate the principal sources of the bonding with useful accuracy requires knowledge of the relative positions of the carbon 2p and metal d bands with greater precision than appears possible using current techniques of x-ray spectroscopy. The necessary precision may be attainable, however, with other experimental approaches. In particular, the use of modulated piezoreflectance and similar techniques should permit analysis of both the symmetry properties of the energy bands involved and the location of the corresponding optical transitions within the Brillouin zone. Lacking quantitative experimental information on the energy distribution of the carbon 2p states prohibits making a quantitative evaluation of the energy band structures [17,19,20] or of the origins of the bonding. Nevertheless, the qualitative features of the LCAO band structure [17] are in better accord with the broad spectrum of physical characteristics exhibited by the transition metal carbides than is the APW calculation [19,20]. Two aspects of this LCAO band structure may be considered of primary importance: i) electrons are transferred from the carbon 2p states into bands derived from the metal d states, and ii) the introduction of carbon atoms broadens the energy bands of the carbide relative to the metal [18] and thereby increases their contribution to the binding energy. In the next section, these concepts will be employed in an effort to provide a qualitative explanation for i) the manner in which the compositions of the stable carbide phases vary with the position of the metal atom in each transition series, and ii) the manner in which the heats of formation of the carbides vary with the position of the parent metal in each transition series and with carbon content.

2. STABILITY OF THE CARBIDES

An elementary model will be developed in this section to illustrate the concepts mentioned in section 1. For this purpose, it will be supposed that the cohesion of the parent transition metals arises from the superposition of contributions from an s-p band, E_{spo}, and a d band, E_{do}. The s-p band will be assumed to provide a bonding energy of 20 kcal mol^{-1} (83.5 kJ mol^{-1}). The d band will be represented by a uniform distribution in energy of electron states in a band having the same width for each metal within one series. In that case, the d band provides a contribution to the binding energy dependent on α, the fractional occupation of the band [31]:

$$E_d = 4E_{dm}\ \alpha\ (1-\alpha), \tag{1}$$

where E_{dm} is the maximum value assumed by E_d. This parameter will be assigned the values E_{dmo} = 115, 165, or 190 kcal mol^{-1} (480, 690, and 795 kJ mol^{-1}) for the first, second and third transition series metals, respectively, in their pure state. To produce qualitatively the variation of the cohesive energies [3] of these metals, the fractional occupation of the d band is assumed to have the form

$$\alpha_o = N_{do}/10 = (Z-1)/11, \tag{2}$$

where α_o is the fractional occupation and N_{do} is the number of electrons in the d band of the pure metals, and Z represents the number of outer electrons on the metal atom (3 for Sc, Y, La, 4 for Ti, Zr, Hf, etc.). By using this simple form for α_o, with a constant density of states in the d band, only the broad features of the cohesive energy variation will be represented, as shown in figure 2; the detailed fluctuations will be suppressed.

2.1. d BAND WIDTH, w_d

As discussed in section 1, it is assumed that the introduction of carbon to form the carbides causes the electron energy bands to broaden and increases the number of electrons in the d band. The increase in the width, w_d, of the d band will be assumed to be proportional to the atomic ratio, x, of carbon to metal. This increase in width depends on the increase in the magnitude of overlap integrals between orbitals on adjoining metal atoms, and consequently on the change in the effective potential in the overlap region caused by the introduction of the carbon atoms. If it is supposed that the effective potential contributed by the carbon atoms is the same in all carbides, then

$$w_d = w_{do} + xw_c, \tag{3}$$

where w_c is the increase in the width of the d band for a carbon to metal atom ratio of unity. For this simple model [31],

$$E_{dm} = 10w_d/8 \tag{4}$$

Consequently, for the carbides,

$$E_{dm} = 10(w_{do} + xw_c)/8 = E_{dmo} + xE_c = E_{mdo}(1 + xE_c/E_{mdo}) \tag{5}$$

where $E_c = 10w_c/8$ is chosen to have the value 170 kcal mol^{-1} (710 kJ mol^{-1}), in order to be qualitatively consistent with the results of calculations by Costa and Conte [18] and to provide a heat of formation for TiC approximately equal to the value observed experimentally.

For simplicity, it will be assumed that the carbon atoms increase the cohesion provided by the s-p band in a manner silimar to that for the d band. In particular, if the ratio E_c/E_{mdo} approximates the relative strength of the pctential in the overlap region contributed by the carbon, compared with that contributed by the metal atoms, the s-p bonding in the carbides becomes:

$$E_{sp} \cong E_{spo}\ (1 + x\ E_c/E_{mdo}). \tag{6}$$

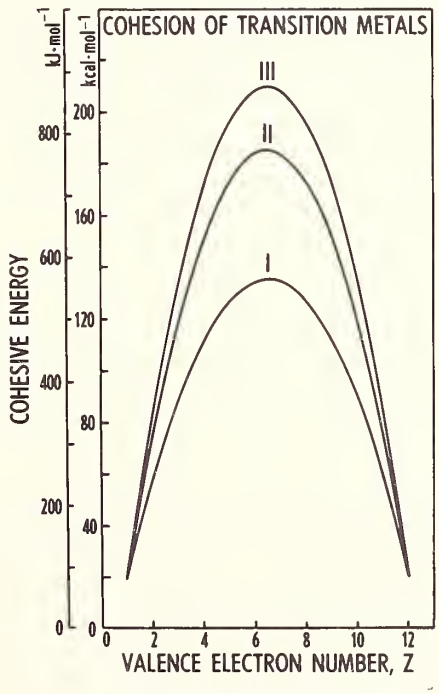

Fig. 2. The cohesive energies of the pure metals from the I, II and III transition series, as represented by the simple model employed here. The detailed fluctuations from the smooth curves observed experimentally [32] are neglected in this model.

2.2. OCCUPATION OF THE d BAND

If it is assumed that all of the n_t electrons donated by each carbon atom are introduced into the d band, then for the carbides,

$$\alpha = N_d/10 = (N_{do} + xn_t)/10. \tag{7}$$

It becomes necessary now to estimate the manner in which n_t varies with the valence electron number, Z, and with the carbon concentration, x. It is expected that n_t will increase with Z, because the d levels of the metal atoms are depressed relative to the 2p level of carbon as Z increases in each series. For simplicity, differences between the energies of the d bands in the three transition series will be neglected for the present purposes even though they may be expected to influence the number of electrons transferred. The variation of n_t with carbon concentration may be understood similarly if the carbon 2p levels are displaced in energy relative to the d bands by an amount that depends on the carbon concentration in the carbide. A qualitative estimate may be made for the elevation of the carbon 2p band in the following manner.

2.3. ELEVATION OF THE CARBON 2p BAND

To be specific, consider a substoichiometric cubic carbide. The metal sublattice is treated as a face-centered cubic packing of spherical metal atoms having radius $r_m = a/2\sqrt{2}$, where a is the lattice parameter. The carbon atoms, of radius $r_c = (\sqrt{2}-1)r_m$, are distributed over the octahedral interstitial sites within the metal sublattice. At the site of a missing carbon atom, the electron charge distribution associated with the surrounding metal atoms provides a negative charge, $-z_o$, within the volume $4/3\ (\pi r_c^3)$ associated with the carbon atoms. This negative charge raises the electron energy levels of a carbon atom inserted into the interstitial site. If the 2p levels then lie above the Fermi level, n_t electrons per carbon atom will be transferred into lower lying states, principally into bands derived from the 3d states of the metal atom. Because of this electron transfer, each carbon atom will lose a negative charge, $-\zeta n_t$, and each metal atom will gain a negative charge, $-x\zeta n_t$. The new electrons received by the metal atoms also will overlap onto the carbon atomic spheres, depositing there an additional negative charge, $-x\beta n_t$.

For a specified carbon concentration, x, the x occupied carbon atomic spheres have a net negative charge

$$z_c = -(z_o - \zeta n_t + x\beta n_t), \tag{8}$$

the (1-x) unoccupied carbon atomic spheres have a net negative charge $-(z_o + x\beta n_t)$, and the metal atomic spheres have a net positive charge

$$z_m = (z_o - x\zeta n_t + x\beta n_t). \tag{9}$$

If these charges are assumed to be uniformly distributed over their respective atomic spheres, they provide average potentials ϕ_{cz} and ϕ_{mz} at the carbon and metal atom sites given by:[2]

$$\phi_{cz} = \frac{6}{5}\frac{z_c e}{r_c}, \tag{10a}$$

$$\phi_{mx} = \frac{6}{5}\frac{z_m e}{r_m}. \tag{10b}$$

The presence of these positive and negative charges in the lattice will provide also Madelung potentials, ϕ_{cM} and ϕ_{mM}. For the present purpose, the Madelung potential will be

[2] The following discussion was suggested in part by J. W. McClure.

calculated by using the positive charge z_m at the metal atom sites and the average negative charge $\bar{z}_c$ at the carbon atom sites, where $\bar{z}_c$ is given by:

$$\bar{z}_c = -x(z_o-\zeta n_t + x\beta n_t)-(1-x)(z_o + x\beta n_t)$$

$$= -(z_o-x\zeta n_t + x\beta n_t) = z_m. \tag{11}$$

Consequently,

$$\phi_{cM} = -\alpha\bar{z}_c e/(a/2) \tag{12a}$$

$$\phi_{mM} = -\alpha z_m e/(a/2), \tag{12b}$$

where α is the Madelung constant for the carbide lattice. The total potentials at the carbon and metal atoms are given by:

$$\phi_c \cong \phi_{cz} + \phi_{cM} = \frac{6}{5}\frac{z_c e}{r_c} - \frac{2\alpha\bar{z}_c e}{a} \tag{13a}$$

$$\phi_m \cong \phi_{mz} + \phi_{mM} = \frac{6}{5}\frac{z_m e}{r_m} - \frac{2\alpha z_m e}{a}. \tag{13b}$$

The difference, ΔV, between the potential energies of an electron on a carbon atom and one on a metal atom determines approximately the upward displacement of the carbon electron energy levels relative to those of the metal atom electrons. This displacement is given by:

$$\Delta V = -e(\phi_c-\phi_m)$$

$$\cong (4.6e^2/a)\ \{z_o-1.78\zeta n_t[1-x(0.44 + 0.56\beta/\zeta)]\}\ \text{ergs}. \tag{14}$$

For TiC,

$$\Delta V \cong 15.3\ \{z_o-1.78\zeta n_t[1-x(0.44-0.56\beta/\zeta]\}\ \text{eV}, \tag{15}$$

and at x = 1, this equation reduces to

$$\Delta V(x = 1) = 15.3\ \{z_o-n_t(\zeta-\beta)\}\ \text{eV}. \tag{16}$$

The effective negative charge on the carbon atoms at the stoichiometric composition is $-q_c$, where,

$$q_c = \{z_o-n_t(\zeta-\beta)\} = \frac{\Delta V(x = 1)}{15.3} \tag{17}$$

Ramqvist [21-26] has determined experimentally that in TiC the carbon 1s levels are displaced upward in energy by approximately 3.3 eV at x = 1. The effective charge on the carbon atoms in TiC is indeed negative, therefore, and has approximately the magnitude 0.215 electron units. It should be noted, however, that this effective charge is the difference between the negative charge, $-z_o$, deposited within the carbon atomic spheres by the metal atoms, and the net negative charge, $-n_t(\zeta-\beta)$, transferred out because of the elevated position of the 2p states relative to the d bands. The magnitude of z_o for TiC could be estimated using the value n_t = 1.33 determined in [17], if $(\zeta-\beta)$ were known. The atomic structure calculations of Herman and Skillman [33] suggest a value of 0.3 for ζ, but β cannot be estimated so directly. Using very coarse approximations for i) the effects of directionality of the d orbitals, and ii) the increased radial extent of the electron wave functions in the crystal relative to the free atom, the charge deposited in the carbon atom sphere is found to be $\beta_s \cong 0.088$ and $\beta_d \cong 0.117$ for each s and d electron respectively. If the average s and d electron densities,

n_s and n_d, at the Fermi level are in the proportions $n_s/n_d \cong 0.17$ [17], then

$$\beta \cong (n_s\beta_s + n_d\beta_d)/(n_s + n_d) \cong 0.11, \tag{18}$$

with a large uncertainty. In that event, z_o has a magnitude near 0.47 electron units.

By assuming that i) β_s and β_d are independent of valence electron number, and ii) the numbers of s and d electrons vary in accord with equation (2), a second estimate is obtained for z_o:

$$z_o = 0.114Z - 0.026 \quad (Z \geq 1). \tag{19}$$

This equation yields $z_o \cong 0.43$ for TiC, in fortuitously good agreement with the previous estimate. Despite the admittedly large uncertainties, both estimates of z_o suggest that the 2p levels are elevated in energy considerably by the overlap charge from the metal atoms. Using equation (19), the amount of this initial displacement, ΔV_o, is found to be

$$\Delta V_o = 15.3z_o = 1.75Z - 0.4 \quad \text{eV}. \tag{20}$$

This large upward displacement permits the carbon 2p electrons to relax into lower lying states. The resulting electron transfer removes charge from the carbon atom spheres, thereby cancelling a portion of the initial upward displacement. The net upward displacement is given approximately by equation (15) using equation (19) for z_o.

2.4. THE NUMBER OF ELECTRONS TRANSFERRED

The simple model discussed above may now be employed to estimate the number of electrons transferred out of the 2p levels of the carbon atoms. For this purpose, as before, the electronic energy bands of the solid are represented by a mean energy and a constant density of states within a prescribed bandwidth. For simplicity, only three bands are considered, the d and s bands of the metal and the p band of carbon. The total number of valence electrons, N, is given by:

$$N = N_s + N_d + N_p, \tag{21}$$

where the N_i's are the numbers of electrons in the respective bands.

If the mean energy of the d band is selected as the zero of energy, and E_F is the Fermi level, equation (21) becomes:

$$N = n_s[E_F - (E_s - w_s/2)] + n_d[E_F + w_d/2] + xn_p[E_F - (E_p + \Delta E_p - w_p/2)], \tag{22}$$

where the n_i's represent the densities of electron states in the respective bands at x = 1, E_s and E_p are the mean energies of the metal s and carbon 2p bands respectively; the w_i's represent the widths of the indexed bands, and ΔE_p, assumed to be equal to ΔV, is the upward displacement of the carbon 2p band discussed in the preceding section. It is implied that the Fermi level intersects each of these three bands.

For the present purposes, only the s and d electrons of the metal atom, a total of Z, and the 2p electrons of the carbon atom are included. Thus, the total number of electrons available for distribution in the three bands is given by

$$N = Z + 2x, \tag{23}$$

for a carbon to metal atom ratio, x. This relation may be used in equation (22) to solve for the position of the Fermi level, E_F:

$$E_F = (Z - 6 - x + xn_p(E_p + \Delta E_p) + n_sE_s)/(n_s + n_d + xn_p), \tag{24}$$

where use has been made of the identities $n_s w_s = 2$, $n_p w_p = 6$ and $n_d w_d = 10$.

The numbers of electrons transferred per carbon atom may then be calculated from the relation:

$$n_t = 2 - N_p/x = 2 - \{n_p[E_F - (E_p + \Delta E_p)] + 3\} \tag{25}$$

The result is:

$$n_t = \frac{n_p[(n_s + n_d)(E_p + 15.3z_o) - (Z - 6 + n_s E_s)] - (n_s + n_d)}{n_p\{(n_s + n_d)(27.4\zeta)[1 - x(0.44 + 0.56\beta/\zeta)] + x\} + (n_s + n_d)} \ . \tag{26}$$

In this form, n_t differs somewhat between the three transition series if, for example, the one-electron energies of the atoms provided by Herman and Skillman [33] are used to define E_s and E_p, but for each series it increases with increasing Z and x in approximately the same manner. In keeping with the approximations made previously, these differences will be neglected in the following discussion and a common form will be used for n_t in the three transition series. The principal conclusions regarding the heats of formation, discussed in the next section, are not affected seriously thereby, but quantitative agreement with experiment cannot be expected.

2.5. THE HEATS OF FORMATION OF THE CARBIDES

The heats of formation of the carbides can be estimated by using expressions (1), (5), (6) and (7) in the relation

$$-\Delta H_f = [E_d(Z,x) + E_{sp}(Z,x)] - [E_d(Z,0) + E_{sp}(Z,0) + x(-\Delta H_c)] \tag{27}$$

where $-\Delta H_c$ is the cohesive energy of carbon, taken to be 170 kcal mol^{-1} (710 kJ mol^{-1}) [32].

If E_s and E_p are assumed to be approximately linear functions of Z, as indicated by Herman and Skillman [33], and the widths of the s, p and d bands are linear functions of x, as in equation (3), expression (26) for n_t assumes the form:

$$n_t = (a_1 + a_2 Z + a_3 x + a_4 xZ)/(b_1 + b_2 x + c_2 x^2) \tag{28}$$

A first approximation to this relation, n_t = constant, when substituted into equation (27), yields results that are reminiscent of the behavior observed experimentally [4], if the value $n_t = 1.332$ estimated for TiC [17] is employed. Discrepancies are observed for a constant value of n_t, however, in that large heats of formation are calculated for the dicarbides of the elements immediately preceding the transition metals, *i.e.*, Z = 1-3. Somewhat similar results are found if n_t is allowed to vary slowly with Z.

An improved approximation is given by the empirical relation:

$$n_t = 1/3(Z - 1)/(1 - x/4) \tag{29}$$

$$\text{and} \quad n_t \leq 2,$$

which vanishes for Z = 1, matches the value 1.332 for $TiC_{1.0}$ [17], and varies with Z and x in approximately the manner required by equation (26). When this expression is used to calculate the heats of formation, equation (27), the results illustrated in figures 3 to 8 are obtained.

As shown in figures 3 to 5, both the regions of stability and the magnitudes of the heats of formation calculated in this simple approximation follow the trends of experimental data in a remarkably consistent manner:

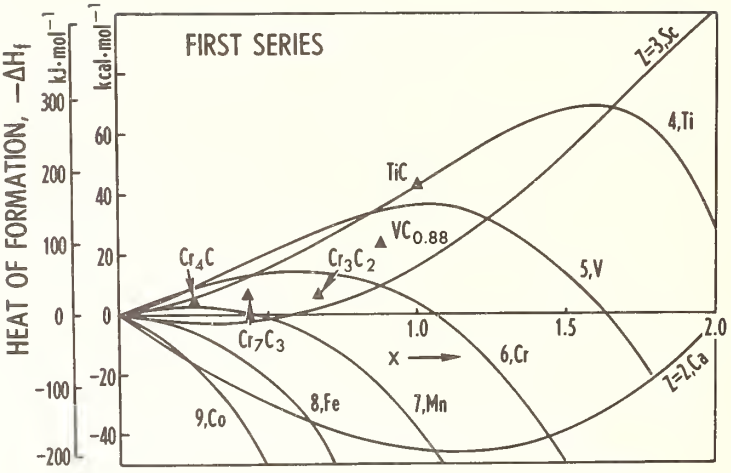

Fig. 3. The heats of formation, $-\Delta H_f$, of the first transition series carbides, as calculated from the model discussed in the text. Experimentally determined heates of formation of some compounds [3] are shown for comparison.

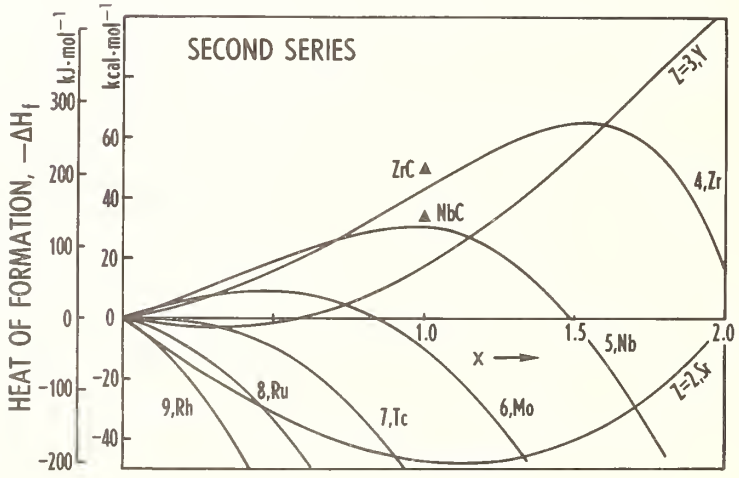

Fig. 4. The heats of formation, $-\Delta H_f$, of the second transition series carbides, as calculated from the model discussed in text. Experimentally determined heats of formation of some compounds [3] are shown for comparison.

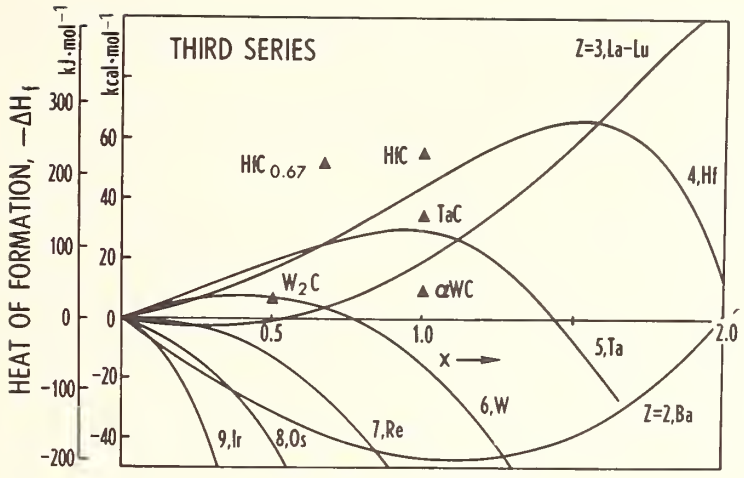

Fig. 5. The heats of formation, $-\Delta H_f$, of the third transition series carbides, as calculated from the model discussed in the text. Experimentally determined heats of formation of some compounds [3] are shown for comparison.

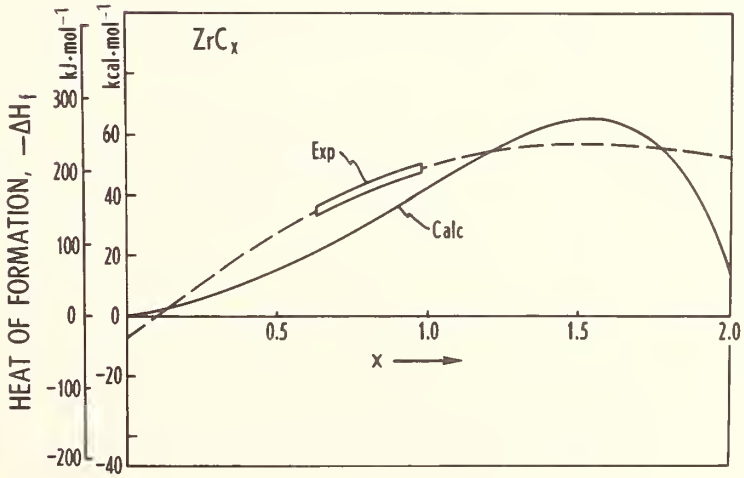

Fig. 6. The variation of the heat of formation, $-\Delta H_f$, of ZrC_x with carbon concentration, x, as calculated from the model discussed in the text, compared with that observed experimentally. The dashed curve represents the analytic expression for $-\Delta H_f(x)$ deduced from experimental data [35].

465-504 O - 72 - 38

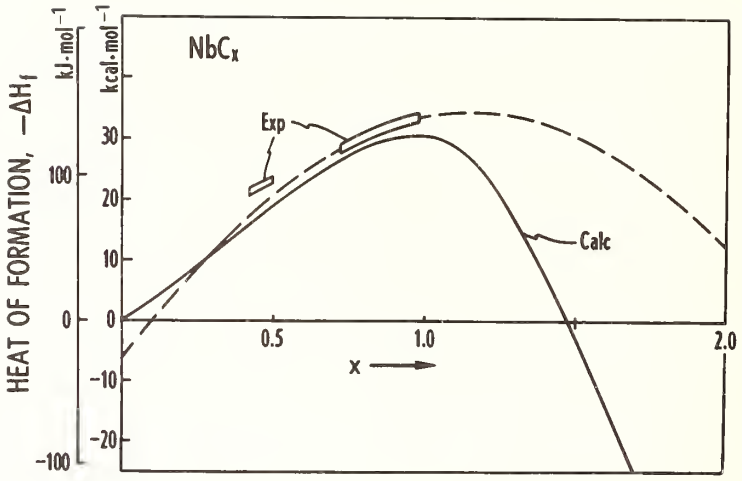

Fig. 7. The variation of the heat of formation, $-\Delta H_f$, of NbC_x with carbon concentration, x, as calculated from the model discussed in the text, compared with that observed experimentally. The experimental value of $-\Delta H_f$ for Nb_2C is shown also. The dashed curve represents the analytic expression for $-\Delta H_f(x)$ deduced from experimental data [36].

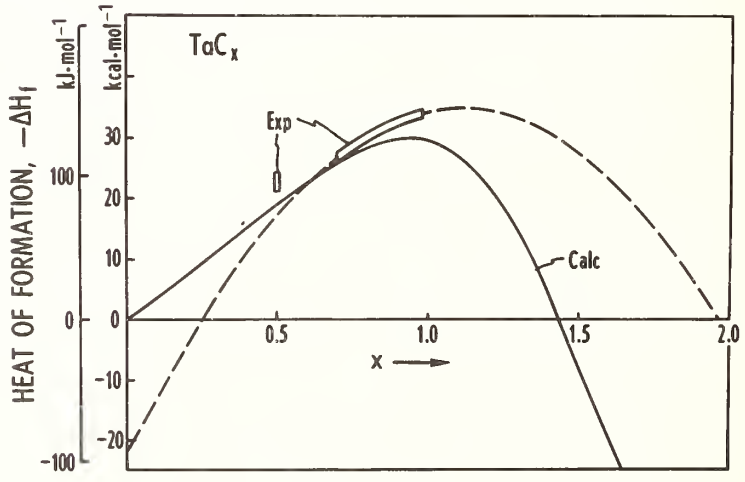

Fig. 8. The variation of the heat of formation, $-\Delta H_f$, of TaC_x with carbon concentration, x, as calculated from the model discussed in the text, compared with that observed experimentally. The experimental value of $-\Delta H_f$ for Ta_2C is shown also. The dashed curve represents the analytic expression for $-\Delta H_f(x)$ deduced from experimental data [37].

i) No stable carbides are indicated for the alkali metals. M_2C_2 carbides having small heats of formation have been reported [34] for these metals[3].

ii) Stable dicarbides are suggested for the alkaline earth elements, as is observed experimentally.

iii) Stable dicarbides having large heats of formation are expected for the elements of Group III, but the ionic radius of scandium, being substantially smaller than those of the Group II metals, would be expected to lead to a reduction in stability when the metal atoms were separated widely by the introduction of a large concentration of carbon atoms. Yttrium and most of the rare earth metals, on the other hand, have relatively large ionic radii and would be expected to accommodate larger concentrations of carbon. Indeed, most of these elements do form higher carbides, including dicarbides. The present model suggests that their heats of formation should increase with increasing carbon content until geometric constraints interfere, but experimental information is not available for confirmation. Uranium also forms higher carbides, despite its small ionic radius, but the heats of formation per mol UC_x do not appear to change much with composition [4]. The fact that $-\Delta H_f$ for UC_2 is slightly *less* than that of $UC_{3/2}$ may perhaps reflect the influence of geometric constraints. Modest heats of formation are expected for the Group III monocarbides.

iv) Large heats of formation are indicated for the Group IV monocarbides. The calculated heats of formation continue to increase beyond x = 1, but, as for the Group III metals, geometric constraints probably prohibit the formation of higher carbides.

v) The Group V carbides exhibit maxima in their heats of formation near x = 1, close to the composition at which the d band is half filled.

vi) Stable carbides are indicated for the Group VI metals only for $x < 1$. Their maximum heats of formation, appreciably less than those of the Group IV and V monocarbides, occur near x = 1/2.

vii) Of the Group VII metals, only Mn is indicated as forming stable carbides, in accord with experimental data, and the region of stability of MnC_x is restricted to $x < 0.5$. The calculated maximum heat of formation, near x = 0.25, is small and therefore of dubious validity, but agrees qualitatively with the small heat of formation of $MnC_{1/3}$, 1.2 kcal mol^{-1} [34].

viii) None of the iron group metals are indicated as forming stable carbides. The heat of formation, $-\Delta H_f$, for the metastable $FeC_{1/3}$ is reported to be -1.9 kcal mol^{-1} (-8 kJ mol^{-1}) [33], compared with the value -10 kcal mol^{-1} (-42 kJ mol^{-1}) estimated here.

ix) No stable carbides are expected on the basis of this calculation for the Co group metals or for the subsequent metals in each transition series, in accord with experimental observations.

x) Detailed experimental information is available for the variation of the heat of formation with carbon concentration for only a few carbides, ZrC_x [35], NbC_x [36], and TaC_x [37]. Analytic expressions for the heats of formation deduced from these studies are given below and are plotted in figures 6-8 for comparison with the results obtained from the present model calculation:

$$ZrC_x \text{ [35]:} \quad -\Delta H_f = -7.4 + 84.1x - 27.2x^2 \text{ kcal mol}^{-1} \tag{30}$$

$$NbC_x \text{ [36]:} \quad -\Delta H_f = -6.60 + 70.95x - 30.75x^2 \text{ kcal mol}^{-1} \tag{31}$$

$$TaC_x \text{ [37]:} \quad -\Delta H_f = -22.81 + 103.78x - 46.88x^2 \text{ kcal mol}^{-1} \tag{32}$$

---

[3] The intercalation compounds of graphite may, perhaps, form another exception at carbon concentrations much larger than those considered here.

Experimentally determined heats of formation for Nb_2C [36] and Ta_2C [37] also are shown in these figures. The calculated curves are seen to agree remarkably well with the experimental data, particularly for the Group V carbides. The good agreement for the latter carbides probably is somewhat fortuitous, however, because no account has been taken here of the energy involved in the structural transformation of the metal lattice in forming these carbides. Pettifor [38] has estimated an energy of approximately 5.65 kcal mol^{-1} for the bcc-fcc crystallographic transformation in Group V and VI metals. On the other hand, the hcp-fcc transformation of Group IV metals appears to involve a substantially smaller energy ($\tilde{=}$ 0.3 kcal mol^{-1}[38]), which has only an insignificant influence on the present comparison.

xi) One experimental point stands in significant disagreement with the calculated curves. According to the experimental data of Zhelankin and Kutsev [39], the heat of formation of $HfC_{0.67}$ is approximately 51.8 kcal mol^{-1} (216 kJ mol^{-1})(fig. 5). If a stability ratio, R_s, is defined by the relation:

$$R_s(x) = -\Delta H_f(x)/(-\Delta H_m - x\Delta H_c), \tag{33}$$

where $-\Delta H_m$ and $-\Delta H_c$ are the cohesive energies of the parent metal and carbon respectively, the results of Zhelankin and Kutsev indicate that this ratio is 15% *greater* for $HfC_{0.67}$ than for $HfC_{0.99}$. The present model suggests, instead, that this stability ratio should decrease as the carbon content of HfC_x is decreased. Allowing for the considerable uncertainties in these calculations, the present results would suggest that the heat of formation of $HfC_{0.67}$ is approximately (40 ± 5) kcal mol^{-1} (167 kJ mol^{-1}), rather than the higher value reported by Zhelankin and Kutsev [39].

3. SUMMARY AND DISCUSSION

A simple model has been proposed to account for the broad trends in the stabilities of the transition metal carbides for different values of the valence electron number, Z, and carbon concentration, x. In this model, it is assumed that the principal components of the bonding in the carbides are similar to those in the parent metals, which are represented as arising from the contributions of an s-p band and a d band. The s-p contribution is assumed to change little throughout the three transition series, whereas that from the d band is assumed to vary with the level of occupation in the parabolic manner suggested by the simple "constant density of states" model of Cyrot-Lackmann [31]. The increase in cohesion in each succeeding transition series is represented as resulting from a corresponding increase in the width of the d band, with the widths assumed to be constant within each series.

It is assumed further that the effects of carbon on the stability of the carbides are two-fold: i) the carbon atoms provide an additional potential that causes a broadening of the electron energy bands proportional to the concentration of the carbon [18], ii) the carbon atoms contribute some of their 2p electrons to the energy bands derived from the electronic states of the metal atom, principally to the metal d band. An elementary calculation is given to indicate the manner in which the number of d electrons, n_t, transferred from the carbon 2p states, varies with Z and x (eq (26)). For simplicity, however, an empirical approximation to this relation is employed in subsequent calculations, the same approximation for each of the three transition series. The expression for n_t used for this purpose is fitted to the value estimated for $TiC_{1.0}$ by Lye and Logothetis [17].

It may be noted that this transfer of electrons from the carbon 2p states into the metal d band is consistent with and, indeed, results from the presence of a small negative charge within the carbon atomic spheres. The LCAO band structure of TiC [17] has been criticized [21-26] on the erroneous basis that it indicates the presence of a positive charge on the carbon atoms. Clearly, the upward displacement of carbon 2s and 2p states employed in the LCAO calculation requires the presence of a small net negative charge, and the upward displacement of these levels is required to permit the transfer of approximately 1.3 electrons from the carbon states to bands derived from electronic states of the metal atom.

No account is taken in this model of the bonding contributed by the carbon 2p band in the carbides, nor of the energy involved in crystallographic transformations of the metal sublattice accompanying the formation of the carbides. Moreover, the contribution to the bonding from the s-p band is dealt with in a rather casual manner for both the metals and

the carbides. A fully consistent model probably should consider the s and p bands of the metal atoms in a manner parallel to that used here for the d bands.

Despite these inadequacies and numerous other simplifications, the stabilities of the carbides as calculated from this model agree remarkably well with experimental observations, particularly with regard to: i) the composition ranges in which the stable carbides occur, ii) the variation of the heats of formation, $-\Delta H_f$, with Z and x, and iii) the magnitudes of the heats of formation for many of the carbides.

It should be noted that the variations of $-\Delta H_f$ calculated here are a direct consequence of the transfer of some 2p electrons from the carbon atoms into bands derived from the d states of the metal atom. It remains to be demonstrated that similar agreement with experimental observations can be provided by a model in which the electron transfer is in the opposite direction. In the meantime, the success of the model discussed here provides justification for accepting at least the principal features of the LCAO band structure for TiC presented by Lye and Logothetis [17], in particular the relative positions of the 2p and 3d bands indicated by that calculation. Additional support for this conclusion is provided by the good correlation between the x-ray spectra of Fischer and Baun [30] and the electron density-of-states curve of Lye and Logothetis [17], as shown in figure 1.

Finally, it would appear entirely feasible to make the model presented here more nearly quantitative: i) by including specific consideration of the metal s and p bands, ii) by using a more realistic representation for the variation of the density of states within the d bands, iii) by allowing for variations in the width of the d band within each transition series, iv) by calculating more precisely the displacement of the carbon 2p levels relative to the d levels and v) by using an estimate for the number of electrons transferred that is specific for each transition series, rather than the empirical approximation employed for all three series in the present calculation. Consideration of these factors may be included in subsequent studies, in which the nitrides and other refractory hardmetals will be examined. Additional attention should be given, however, to developing improved methods for determining the electronic structures and bonding characteristics of the individual members of this interesting and useful class of compounds.

4. ACKNOWLEDGEMENTS

It is a pleasure to acknowledge useful discussions with J. W. McClure and J. D. Venables. Thanks for due to E. Parkison and W. Furth for some of the computer calculations. Grateful appreciation is expressed for financial support provided by NASA Research Division, Code RRS, Materials Research Branch, under Contract NASw-1290.

5. REFERENCES

[1] Kieffer, R. and Benesovsky, F., Hartstoffe, Springer-Verlag, Wien (1963).
[2] Schwarzkopf, P. and Kieffer, R., Refractory Hard Metals, Macmillan, New York (1953).
[3] Storms, E. K., The Refractory Carbides, Academic Press, New York (1967).
[4] Goldschmidt, H. J., Interstitial Alloys, Plenum Press, New York (1967).
[5] Toth, L., Transition Metal Carbides and Nitrides, Academic Press, New York (1971).
[6] Giorgi, A. L., Szklarz, E. G., Storms, E. K., Bowman, A. L., and Matthias, B. T., Phys. Rev. 125, 837 (1962).
[7] Matthias, B. T., Phys. Rev. 92, 874 (1953).
[8] Rudy, E., Ternary Phase Equilibria in Transition Metal-Boron-Carbon-Silicon Systems, Part V. Compendium of Phase Diagram Data, Air Force Materials Laboratory, Wright-Patterson AFB, Ohio (1969).
[9] Hollox, G. E., Mater. Sci. Eng. 3, 121 (1968/69).
[10] Brewer, L. and Krikorian, O., J. Electrochem. Soc. 103, 38 (1956); Univ. Calif. Rad. Lab. Rep. UCRL-3352 (1956).
[11] Dempsey, E., Phil. Mag. 8, 285 (1963).
[12] Ubbleohde, A. R., Trans. Faraday Soc. 28, 284 (1931).
[13] Umanskii, Ya.S., Ann sect. anal. phys.-chim., Inst. chim.gén. (USSR) 16, No. 1, 127 (1943).
[14] Kiessling, R., Acta Chem. Scand. 4, 209 (1950).
[15] Kiessling, R., Met. Rev. 2, 77 (1957).
[16] Robins, D. A., Powder Met. 1/2, 172 (1958).

[17] Lye, R. G. and Logothetis, E. M., Phys. Rev. 147, 622 (1966).
[18] Costa, P. and Conte, R. R. in Nuclear Metallurgy Symposium, Met. Soc. AIME, New York, Vol 10, p. 3 (1964).
[19] Ern, V. and Switendick, A. C., Phys. Rev. 137, A1927 (1965).
[20] Conklin, J. B. and Silversmith, D. J., Int. J. Quantum Chem. Symposium No. 2, 243 (1968).
[21] Ramqvist, L., Jernkont. Annlr. 153, 159 (1969).
[22] Ramqvist, L., Hamrin, K., Johansson, G., Fahlman, A., and Nordling, C., J. Phys. Chem. Solids 30, 1835 (1969).
[23] Ramqvist, L., Ekstig, B., Kallne, E., Noreland, E., and Manne, R., J. Phys. Chem. Solids 30, 1849 (1969).
[24] Ramqvist, L., Hamrin, K., Johansson, G., Gelius, U., and Nordling, C., J. Phys. Chem. Solids. 31, 2669 (1970).
[25] Ramqvist, L., Ekstig, B., Kallne, E., Noreland, E., and Manne, R., J. Phys. Chem. Solids 32, 149 (1971).
[26] Ramqvist, L., J. Appl. Phys. 42, 2113 (1971).
[27] Holliday, J. E., J. Phys. Chem. Solids 32, 1825 (1971).
[28] Fischer, D. W., J. Appl. Phys. 41, 3561 (1970).
[29] Fischer, D. W., J. Appl. Phys. 41, 3922 (1970).
[30] Fischer, D. W. and Baun, W. L., J. Appl. Phys. 39, 4757 (1968).
[31] Cyrot-Lackmann, F., J. Phys. Chem. Solids 29, 1235 (1968).
[32] Gschneider, K. A., in Solid State Physics, ed. F. Seitz and D. Turnbull, Academic Press, New York, Vol. 16, p. 276 ff (1964).
[33] Herman, F. and Skillman, S., Atomic Structure Calculations, Prentice-Hall, Inc., Englewood Cliffs, New Jersey (1963).
[34] Wicks, C. E. and Block, F. E., Thermodynamic Properties of 65 Elements-Their Oxides, Halides, Carbides, and Nitrides, U. S. Bureau of Mines Bulletin 605 (1963).
[35] Baker, F. B., Storms, E. K., and Holley, C. E., J. Chem. and Eng. Data 14, 244 (1969).
[36] Huber, E. J., Head, E. L., Holley, C. E., Storms, E. K., and Krikorian, N. H., J. Phys. Chem. 65, 1846 (1961).
[37] Huber, E. J., Head, E. L., Holley, C. E., and Bowman, A. L., J. Phys. Chem. 67, 793 (1962).
[38] Pettifor, D. G., J. Phys. C 3, 366 (1970).
[39] Zhelankin, V. I. and Kutsev, V. S., Zhur, Fiz. Khim. 38, 562 (1964).

DISCUSSION

B. Post: Were you speaking of x-ray adsorption spectra in the soft x-ray region?

R. G. Lye: The $L_{II,III}$ x-ray emission and adsorption spectra, yes.

B. Post: I had heard that there was some work done by electron spectroscopy on titanium carbides and I wondered whether you were familiar with the results.

R. G. Lye: That's Ramqvist's work[1] that I was talking about. The principal result of that was that it says that the electron energy levels of the carbon are displaced *upward* relative to their position in carbon.

B. Post: Well, it's good to know that the carbides resemble the borides in at least that respect. There are some that think the transfer is to the left and others who think it's to the right. I think it depends on whether you're a physicist or a chemist and I'm serious about that, but it's a long story.

[1] Ramqvist, L., J. Appl. Phys. 42, 2113 (1971) and references listed there.

National Bureau of Standards Special Publication 364, Solid State Chemistry, Proceedings of 5th Materials Research Symposium, issued July 1972.

ORDERING EFFECTS IN NbC AND TaC

J. D. Venables and M. H. Meyerhoff

Research Institute for Advanced Studies
Martin Marietta Corporation
Baltimore, Maryland 21227

Studies of the phase equilibria in the MC transition metal carbides have shown that they retain their nominal NaCl structure over a relatively wide phase field. Although it is well known that this wide latitude in composition is accomplished through the incorporation of carbon vacancies in the carbon sublattice, there is considerable uncertainty regarding the degree of order exhibited in most of the carbides by the remaining carbon atoms. In this investigation, an attempt has been made to resolve this question for NbC and TaC using some of the techniques applied previously in a study of ordering in the vanadium-carbon system.

By means of transmission electron microscopy and electron diffraction, evidence has been obtained for the existence of long range carbon atom ordering in single-crystal niobium carbide that has a carbon-to-metal ratio close to the integral composition Nb_6C_5. The ordering, which gives rise to superlattice and domain structures similar to those observed in V_6C_5, appears, however, only in samples that have been cooled slowly (~8 °C/h) through the order-disorder temperature of 1025 °C. In TaC of similar composition, the ordering, although present, remains very imperfect even after the crystals are subjected to the same thermal treatment.

The results are interpreted in terms of the electronic structure of the transition metal carbides as it is currently understood, and their relevance to the mechanical properties of NbC and TaC are discussed.

Key words: Carbides; electron diffraction; interpretation of ordering effects; niobium carbide; ordering effects; superlattice; tantalum carbide; transition metal compounds; vanadium carbide.

1. INTRODUCTION

In a previous report [1][1], evidence was presented that vanadium carbide having a carbon-to-metal ratio close to the integral composition V_6C_5 exhibits an ordered structure. Material of this composition occurs within the nominally cubic (rocksalt) phase field of the vanadium-carbon phase diagram, but because of the ordering its structure is more appropriately described in terms of a derivative structure in the trigonal space group, $P3_1$, or its enantiomorph, $P3_2$. Thus, the ordered structure is based on two interpentrating fcc lattices, only one of which (the metal lattice) is completely occupied. The other is only 83% filled, but the carbon atoms (and carbon vacancies) are distributed in an ordered manner over the available octahedral lattice sites.

From an analysis of supplementary spots in electron diffraction patterns, and nuclear magnetic resonance spectra of the principal vanadium isotope, V^{51}, it was established that the carbon atoms and carbon vacancies are arranged so that all the vanadium atoms have exactly five nearest neighbor carbon atoms in the perfect ordered structure [1]. The observation that ordering in material of this composition leads to a distribution of atoms

[1] Figures in brackets indicate the literature references at the end of this paper.

that is homogeneous on an atomic scale is consistent with the model for stability of the transition metal carbides discussed in the previous paper by Lye [2]. Considerations based on this model suggest that the most stable composition in the vanadium-carbon system occurs when the carbon-to-metal atom ratio is close to 5/6 and that ordering effect arise in order to maintain this ratio as nearly as possible on an atomic scale.

On the basis of these same considerations, Lye has also suggested that ordering effects similar to those observed for V_6C_5 may also arise in the other Group V transition metal carbides, namely NbC and TaC, with minor modifications imposed by the slight differences in their electronic structure. Accordingly, in this investigation, an attempt has been made to examine the structure of these carbides using some of the techniques applied previously in a study of the ordering in V_6C_5 [1].

2. EXPERIMENTAL

2.1. CRYSTAL GROWTH

Single crystals of niobium carbide and tantalum carbide were grown by the floating zone technique described by Precht and Hollox [3]. Isostatically pressed and sintered rods of an appropriate composition were heated with an r.f. induction unit, and a molten zone about 1 cm in height was passed along the rod at a rate of approximately 1 cm/h. To obtain a composition of the crystalline product close to the integral composition M_6C_5, it was found necessary to add 10% by weight of the appropriate metal to the stoichiometric carbide powders. The actual compositions of the samples used in the experiments were determined by lattice parameter measurements [4] and chemical analysis to be $NbC_{0.84}$ and $TaC_{0.83}$.

2.2. PREPARATION OF ELECTRON MICROSCOPE FOILS

Thin foils suitable for transmission electron microscopy were prepared by jet dimpling 3 mm disks with a 20% sulphuric acid - 80% methonal solution at 4-5 volts, followed by electrolytic polishing in the same solution at the same voltage.

3. RESULTS

3.1. NIOBIUM CARBIDE

3.1.a. EVIDENCE FOR ORDERING IN $NbC_{0.84}$

A typical transmission electron diffraction pattern obtained from an $NbC_{0.84}$ crystal in the "as grown" state is shown in figure 1(a). The pattern exhibits a series of primary diffraction spots which map out the (110) reciprocal lattice of the nominal rocksalt structure of NbC. In addition, a supplementary pattern is observed, which, except for the diffuse nature of the diffraction spots, resembles those derived from V_6C_5 [1]. This evidence suggests that although ordering effects are present in the samples, the long range ordering parameter is less than unity. The imperfect nature of the ordering in the "as grown" crystals can be improved dramatically with a suitable heat treatment, however.

Previous studies on V_6C_5 have indicated that the ordering time constant near the order-disorder temperature of 1250 °C may be as short as 10^{-4} sec [5]. Thus, it is observed that the high temperature disordered state cannot be retained by quenching with readily attainable cooling rates. On the basis of the considerations discussed in Part 3.2 below, however, the ordering time constant in $NbC_{0.84}$ is expected to be at least 5 orders of magnitude greater than in V_6C_5. The degree of order exhibited by a crystal of NbC, therefore, may depend critically upon its prior thermal history. In view of this, sections of the crystal used in the preliminary examination were heated in vacuum to 1130 °C and then cooled linearly to 940 °C in a programmed furnace at a rate of 8 °C/h. Although the cooling rate was selected somewhat aribtrarily, the temperature span was chosen after measurements were made to determine the order-disorder (O-D) transformation temperature.

These measurements were made by heating a sample in the electron microscope hot stage while the degree of order was estimated from visual observations of the superlattice spot intensities in the diffraction pattern. Initial results were limited in accuracy because the diffuse nature of the superlattice spots made it difficult to monitor their intensity

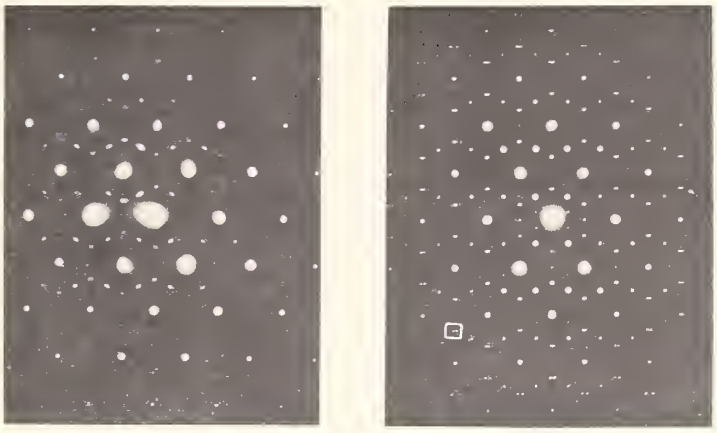

Fig. 1. Transmission electron diffraction patterns obtained from (110) foil of single crystal $NbC_{0.84}$, (a) in "as grown" condition and (b) after slow cool through the order-disorder temperature. The pattern in (b) resembles those derived from V_6C_5 [1] except for extensive spot doubling (circled) and streaking.

on the fluorescent screen. Nonetheless, the results were sufficiently accurate to establish reasonable upper and lower temperature limits for the thermal treatment. Later experiments, in which similar measurements were made on more perfectly ordered material, yielded a value for the O-D temperature of 1025 °C ± 25 °C.

The diffraction patterns derived from the slowly cooled material exhibited a marked increase in the sharpness and intensity of the superlattice spots relative to those derived from as-grown samples, figure 1(b). Moreover, the samples exhibited a domain structure, figure 2, which was not evident before the thermal treatment. This evidence suggests that the long range order parameter was increased to nearly unity by the heat treatment.

3.1.b. CRYSTALLOGRAPHIC STRUCTURE OF Nb_6C_5

The crystallographic structure of vanadium carbide having a carbon-to-metal ratio close to the integral composition V_6C_5 was determined by combining the results of electron diffraction and nuclear magnetic resonance (NMR) studies [1]. The supplementary spots exhibited in the diffraction patterns provided information regarding the symmetry and size of the superlattice unit cell, whereas the NMR of the principal isotope, V^{51}, exhibited spectra that provided information about the disposition of carbon atoms within the unit cell. Similar complementary studies would be desirable to establish the crystallographic structure of niobium carbide, but unfortunately previous investigations [6] have shown that the NMR spectra of Nb^{93} provide insufficient information to determine the disposition of carbon atoms in NbC. Thus, Froidevaux and Rossier [6] have observed that second order quadrupolar line broadening effects in NbC are so great that no satellite line structure is observed in the spectra. They were unaware, however, that slow cooling rates are necessary to promote a high degree of order in NbC and it is possible therefore that studies on well ordered material would provide useful information. For the present, however, a determination of the crystallographic structure of $NbC_{0.84}$ has been based on a comparison of the electron diffraction patterns of $NbC_{0.84}$ and V_6C_5, using as a reference the known structure of V_6C_5.

Selected area diffraction patterns obtained from (100) and (110) foils of $NbC_{0.84}$ are similar in most respects to those obtained from equivalently oriented foils of V_6C_5. However, the NbC patterns exhibit extensive spot doubling and streaking, figure 1(b), which were not so prominent in the VC patterns. Both of these effects are known to result from the presence of planar lattice imperfections that distort the shape of reciprocal lattice points into reciprocal lattice rods (rel-rods). The rel-rods appear as streaks in a dif-

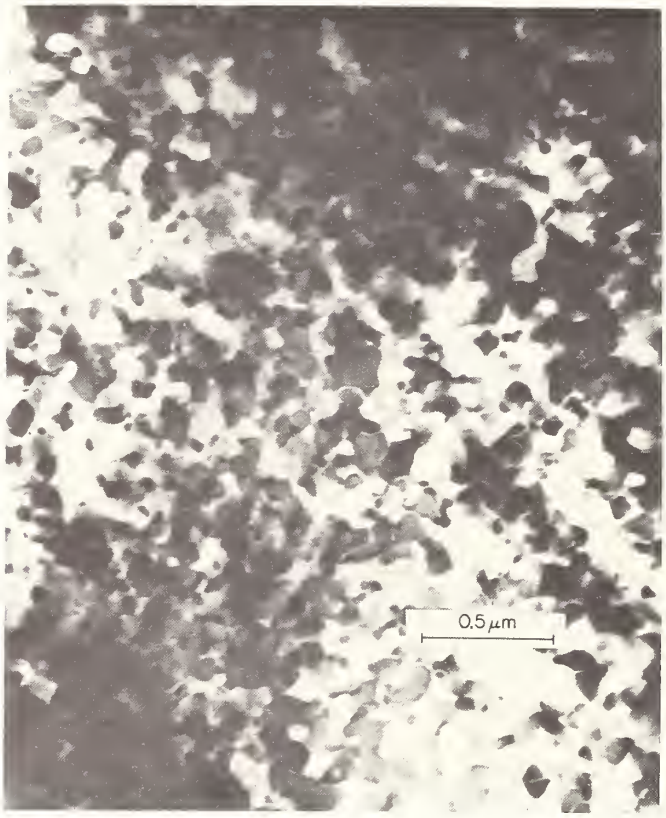

Fig. 2. Bright field transmission electron micrograph of the domain structure which forms in single crystal $NbC_{0.84}$ after heat treatment. No domains can be resolved in the as grown material.

fraction pattern when they are tangent to the reflecting sphere, and (except at the origin) give rise to displaced or extra spots when they intersect the reflecting sphere [7].

In the present case, it has been established that the planar imperfections giving rise to the rel-rods lie parallel to {111} planes. The orientations of the streaks that appear in figure 1(b) can be accounted for on this basis, and the position of all the double spots in the pattern is consistent with this hypothesis also. It is suggested that anti-phase boundaries, similar to those proposed to account for certain contrast effects observed in V_6C_5, [1] may be responsible for the effect.

In the perfect V_6C_5 structure, carbon vacancies are arranged in an ordered manner on alternating carbon layers in two-dimensional hexagonal nets parallel to {111} planes. The nets are sequentially positioned along the third dimension so as to define either a right-handed or left-handed triad screw axis [1]. This sequence is disrupted if one or more of the carbon layers that contain vacancies is displaced by any vector in the {111} plane connecting nearest-neighbor carbon atoms. Such displacements do not change the near-neighbor or next-nearest-neighbor distribution of carbon atoms surrounding metal atoms. For this reason, it is expected that faults of this type (anti-phase boundaries) would be low energy configurations with a high probability for forming in the V_6C_5 structure.

The presence of anti-phase boundaries alone is not a sufficient condition to promote the formation of streaking such as that observed in the patterns. The boundaries must occur in pairs so as to form a thin platelet of anti-phase material embedded in an otherwise perfect matrix. Moreover, the thickness of the platelet, t, determines the length of the streak, ℓ, on the diffraction pattern. Thus, from the relationship $t = k/\ell$ (where k is a geometrical constant), the thickness of the platelets may be computed [7]. In the present

case, the measured streak length implies a platelet thickness of ~10 Å, which is approximately the spacing, 10.32 Å, between four carbon layer planes.

Although there are some indications that similar anti-phase boundaries occur in V_6C_5, [1,8] they do not give rise to such pronounced streaking or spot doubling in the diffraction pattern. This suggests that the spacing between them must be sufficiently great, on average, that the reciprocal lattice points do not become extended in the same manner as in NbC. The reason for this difference is not understood, but it could be related to differences in the driving force for ordering, which, based on the difference in O-D temperatures, is expected to be somewhat smaller in NbC than in VC.

In summary, a comparison of the diffraction patterns obtained from $NbC_{0.84}$ and V_6C_5 suggest that there are only minor differences between the structures of the two materials. Both materials appear to contain anti-phase boundaries parallel to {111} planes, but, in $NbC_{0.84}$, some of them are spaced close to each other and give rise to extensive streaking and spot doubling in the diffraction pattern. Thus, it can be concluded that the structure of niobium carbide having a composition close to that of Nb_6C_5 is isomorphous with that of the V_6C_5 structure.

3.2. TANTALUM CARBIDE

The electron diffraction patterns derived from "as grown" samples of $TaC_{0.83}$ do not exhibit discrete superlattice spots, but evidence for some ordering is suggested by the presence of diffuse bands which appear in addition to the primary spots. The geometry of the bands is consistent with an M_6C_5 type of ordering, but their diffuse nature suggests that the ordering is extremely imperfect. Moreover, the ordering is improved only slightly, figure 3, when the samples are subjected to slow cooling (~8 °C/h) through the temperature range 1150 °C to 775 °C. On the basis of the following arguments, these results suggest that the O-D temperature for $TaC_{0.83}$ is lower than that of $NbC_{0.84}$ and occurs in a temperature range where the carbon atom diffusivity is extremely small.

A measurement of ordering time constants in V_6C_5 [5] has demonstrated that τ varys exponentially with reciprocal temperature

$$\tau = \tau_o \exp(W/kT) \qquad (1)$$

Fig. 3. Transmission electron diffraction pattern obtained from (110) foil of a single crystal $TaC_{0.83}$ sample which had been given a heat treatment similar to that used to develop the ordering in $NbC_{0.84}$. The presence of diffuse bands, rather than discrete superlattice spots, suggests that the ordering is very imperfect.

where W is taken as the activation energy for carbon diffusion. The constant, τ_o, may be evaluated from a knowledge of the Debye temperature since θ_D implies a characteristic atomic vibration frequency, $\nu_D = \theta_D k/h$, which will be fully excited at elevated temperatures. Disordered carbon atoms undergoing these vibrations will have one chance in six tries to jump into an ordered position in a nearest-neighbor site of the carbon sublattice because, on the average, 5/6 of the nearest-neighbor sites are already occupied. Thus, the ordering time at very elevated temperatures is expected to be approximately $\tau_o = 6/\nu_D$. On this basis, if the O-D temperature for $TaC_{0.83}$ were equal to that of Nb_6C_5, it can be shown that the ordering time constants of the two materials should not be appreciably different. For example, using values of θ_D = 761 K [9], W = 3.5 eV [10] for NbC and θ_D = 616 K [9], W = 3.7 eV [11] for TaC, the expected ratio of ordering times τ (NbC)/τ(TaC)=0.2 at 1025 °C. The experimental results imply a much larger difference in the ordering rates, so it must be concluded that the O-D transformation temperature for $TaC_{0.83}$ lies below that for Nb_6C_5.

Although it has not been possible to make quantitative measurements for the ordering effects in $TaC_{0.83}$, it is interesting to note that the present results establish a pattern for the Group V transition metal carbide O-D temperatures. Thus, it appears that the O-D temperature of the Group V metal carbides decrease progressively from the first to the third transition series. This observation has implications for the interpretation of ordering effects in these materials, which will be discussed in the next section.

4. DISCUSSION

The observations presented here, and those which have been discussed previously [1], demonstrate that all the Group V transition metal carbides tend to form an ordered structure of the M_6C_5 type when their carbon-to-metal ratio is close to the value 5/6. In the perfect M_6C_5 structure, the metal atoms occupy their normal fcc lattice sites, but the carbon atoms (and carbon vacancies) are distributed on their fcc sublattice in such a manner that all the metal atoms have only five nearest neighbor carbon atoms. The fact that material of this composition tends to exhibit a distribution of atoms that is homogeneous on an atomic scale is consistent with the electronic structure of the transition metal carbides as developed by Lye [2]. Moreover, it appears that the depression of the O-D transformation temperature in carbides of the higher numbered series Group V transition metals, relative to those of the lower series may be accounted for on the same basis.

In particular, Lye has developed a qualitative description of the bonding in these materials that is based on a semi-empirical LCAO band structure calculations [2]. According to the model, the outer electrons of the six metal atoms surrounding a carbon atom overlap onto the carbon atom site depositing a negative charge there. This raises the potential energy of electrons on the carbon atoms enough to elevate electrons in the upper portion of the bands derived from carbon 2p states above those of vacant states in the d and s bands associated with the metal atoms. To minimize their energy these electrons are redistributed into the lower lying bands, mostly d bands, where they occupy normally vacant states. Thus, the occupancy of these bands is influenced by the carbon concentration even though the bands are initially derived from metal atom d states.

In VC those d states whose orbitals overlap in a *bonding* configuration become completely filled when the carbon-to-metal atom ratio is close to 5/6 [2]. At this composition the anti-bonding states are empty, or nearly so, but an increase in the carbon concentration beyond this ratio would serve to increase their occupancy with electrons contributed by the carbon atoms. Since the electronic interactions between neighboring metal atoms are important in determining the band structure as well as the total cohesive energy of the transition metal carbides, it has been suggested by Lye [12] that the most stable structure would occur when the local concentration of carbon atoms is equal to the integral number five. This condition is not met in VC if the carbon atoms assume a random distribution on their fcc lattice sites even though the carbon-to-vanadium atom ratio is 5/6. In these circumstances the fraction, p, of vanadium sites having n ($n \leqslant 6$) nearest neighbor carbon atoms is given by the binominal distribution function

$$p(n) = C_n^{\,6}(r)^n(1-r)^{6-n} \qquad (2)$$

where r is the fraction of the carbon sites that are occupied, and C_n^6 are the binominal coefficients. Thus, for a random distribution, 33% of the vanadium sites will have six nearest neighbor carbon atoms, whereas only 40% will have five. On the other hand, the condition of homogeneity on an atomic scale is readily satisfied without any modification of the metal lattice, if the carbon atoms assume the ordered arrangement deduced for V_6C_5.

Similar arguments also appear to account qualitatively for the ordered structure V_8C_7 which has been described by de Novion et al. [13]. In this case the fraction of vanadium sites having six, and five, near neighbor carbon atoms would be 45% and 38%, respectively, for a random distribution, but in the ordered structure the corresponding ratios are 25% and 75%. Such an ordered arrangement would be expected to exhibit less stability than V_6C_5 because anti-bonding d states are necessarily occupied, but it should be more stable than the random distribution.

The argument that ordering in VC occurs to avoid the occupation of antibonding d states can be extended to account for the nature of the ordering in NbC and TaC also. For these materials, Lye's calculations indicate that the bonding portion of the d bands become fully occupied at increasingly higher carbon concentrations in progressing from the first to the third series carbides [2]. Consequently, it would be expected that the tendency to form an ordered structure should prevail in these materials also, but that the driving force for ordering would be diminished relative to that in V_6C_5. The observation that the O-D temperatures for V_6C_5, Nb_6C_5 and $TaC_{0.83}$ are 1250 °C, 1025 °C, and <1025 °C, respectively is consistent with this hypothesis because, as a general rule, the O-D temperature of a solid may be taken as a measure of its ordering energy [14].

Finally, it should be noted that Hollox and Venables [15] have demonstrated that the O-D temperature of V_6C_5 corresponds rather closely to its brittle-ductile transition temperature, both effects occurring within the range 1250 °C to 1300 °C. On the basis of this observation, it was suggested that the ordering imposes restraints upon dislocation mobilities in addition to those which arise from the usual Peierls stress. The exact nature of the hardening mechanism has not been determined, but in any event the results, when interpreted in terms of Lye's model for ordering, appear to provide an example of the way in which the electronic energy band structure of solids can influence their mechanical behavior. Moreover, it is reasonable to expect that NbC, and perhaps TaC, will exhibit related effects. However, the characteristics of their electronic structure which impose a sluggish O-D transformation may promote mechanical properties that will depend in a complex manner on prior thermal history.

5. ACKNOWLEDGEMENTS

It is a pleasure to record our indebtedness to R. G. Lye, RIAS, for communicating some of his results on the electronic structure of the carbides prior to publication. Thanks are also due to W. Precht, RIAS, who grew the single crystals, and to R. Huntington, RIAS, who made the lattice parameter measurements. In addition, the authors are grateful for financial support provided by NASA Research Division, Code RRS, Materials Research Branch, under Contract NASw-1290.

6. REFERENCES

[1] Venables, J. D., Kahn, D. and Lye, R. G., Phil. Mag. 18, 177 (1968).
[2] Lye, R. G., this symposium, in paper entitled *A Simple Model for the Stability of Transition Metal Carbides*.
[3] Precht, W. and Hollox, G. E., J. Crystal Growth 3, 4, 818 (1968).
[4] Rudy, E., *Ternary Phase Equilibria in Transition Metal-Boron-Carbon-Silicon Systems*, Part V. *Compendum of Phase Diagram Data* (Clearinghouse, U.S. Dept. of Commerce, Springfield, Va., 1969).
[5] Venables, J. D., *The Ordered Compound V_6C_5 -- Its Structure and Susceptibility to Radiation Damage*, Ph.D. Dissertation, University of Warwick, England (1970).
[6] Froidevaux, D. and Rossier, D., J. Phys. Chem. Solids 28, 1197 (1967).
[7] Hirsch, P. B., Howie, A., Nicholson, R. B., Pashley, D. W., and Whelan, M. J., *Electron Microscopy of Thin Crystals* (London, Butterworths, 1965).
[8] Lewis, M. H., University of Warwick, private communication (1971).
[9] Chang, Y. A., Toth, L. E., and Tyan, Y. S., Metall. Trans. 2, 315 (1971).

[10] Resnick, R., Steinitz, R., and Seigle, L., Trans. Metall. Soc. AIME, 233, 1915 (1965).
[11] Resnick, R. and Seigle, L., Trans. Metall. Soc. AIME, 236, 1732 (1966).
[12] Lye, R. G., private communication.
[13] deNovian, C. H., Lorenzelli, R., and Costa, P., Compt. Rend. 263, 775 (1966).
[14] Muto, T. and Takagi, Y., in "Solid State Physics", ed. F. Seitz and D. Turnbull, Vol. 1 (Academic Press, New York, 1956), p. 212 ff.
[15] Hollox, G. E. and Venables, J. D., Proc. Intl. Conf. on Strength of Metals and Alloys, in Suppl. Trans. Japan. Inst. Metals 9, 295 (1968).

DISCUSSION

J. S. Anderson: It seems this time that you have been able to get ordering in NbC. My colleague, Dr. Fender, and one of his pupils, Alan Henfrey, some two years ago examined the diffuse neutron scattering from materials which had been quenched from 1450° and (I think) 1250°. Henfrey[1] was able to show that in the disordered phase there was still a very strong correlation; there was a strong third neighbor site preference energy. That, I think, is precisely the same spacial relation that you have in the defect structure that you've found.

J. Venables: As we have pointed out in this paper, the degree of order exhibited in NbC is critically dependent on the cooling rate through the order-disorder temperature. The quenched material you describe would undoubtedly exhibit only short range order, but the atomic configuration should be related to that in the long range ordered structure we've described here.

H. Nowotny: The band formation you have shown for tantalum carbide also occurs in vanadium carbide.

J. Venables: Yes, Billingham and Lewis[2] have shown similar patterns for low carbon VC. The order-disorder temperature for this material is considerably lower[3] than that of V_6C_5 and is probably in the range where carbon atom diffusivity is low. Under these circumstances, long range ordering would be more difficult to develop. It appears that this may be the explanation for the presence of banding, rather than sharp diffraction spots, in low carbon VC.

---

[1] Fender, B. E. F. and Henfrey, A. W., to be published; Henfrey, A. W., D. Phil. Thesis, Oxford 1970.

[2] Billingham, J. and Lewis, M. H., Phil. Mag. 24, 231 (1971).

[3] Lewis, M. H., Univ. Warwick, private communication.

National Bureau of Standards Special Publication 364, Solid State Chemistry, Proceedings of 5th Materials Research Symposium, issued July 1972.

THE CdP_2-Ge SYSTEM AND THE GROWTH OF CRYSTALS OF $CdGeP_2$

E. Buehler and J. H. Wernick

Bell Laboratories
Murray Hill, New Jersey 07974

The macroscopic features of the phase relationships in the CdP_2-Ge system have been determined. The tetragonal $CdGeP_2$ phase melts congruently at 790 ± 5 °C. Two eutectics are present: one between CdP_2 and $CdGeP_2$ at ~ 700 °C and 20 mol % Ge, and the other, between $CdGeP_2$ and Ge at ~ 750 °C and 65 mol % Ge. Techniques and results for the growth of crystals from stoichiometric melts, by chemical transport, and from liquid Cd and Sn are presented.

Key words: $CdGeP_2$; CdP_2-Ge system; Ge; phase diagram; single crystals.

1. INTRODUCTION

$CdGeP_2$, a direct band gap (1.72 eV) [1][1] diamond-like ternary semiconductor, is one of a group of isostructural II-IV-V compounds receiving attention in the search for new emitters and detectors of visible and near infrared radiation and new nonlinear optical materials. Shay et al. [1] have reported the electro-reflectance, absorption coefficient, and energy band structure results for $CdGeP_2$ near the direct energy gap on single crystals prepared by chemical transport. These crystals exhibited resistivities of the order of 10^8 ohm-cm at room temperature.

In general, crystals grown by chemical transport are relatively small and growth from melts is desirable for obtaining large single crystals. $CdGeP_2$ had been reported to melt congruently at 800 °C [2] and 779 °C [3] and our early x-ray results and metallographic observations were generally in agreement with this published work. The congruent nature of $CdGeP_2$ is an asset in growth from the melt. On the other hand, it has been known for sometime that glasses of $CdGeP_2$ and CdP_2-rich Ge solutions can be prepared [4,5] suggesting that supercooling and glass formation might be important factors in determining successful growth from the melt. Since $CdGeP_2$ glass has an energy gap of ~ 0.8 eV, it can be detected by use of an infrared microscope [1]. Another important feature of the II-IV-V_2 phosphides relevant for the choice of growth technique is the rather large dissociation pressures exhibited by a number of these materials [6]. Since large single crystals of $CdGeP_2$ are required for a number of electrical and optical studies, the above facts prompted us to investigate some of the macroscopic features of the phase relations in the Cd-Ge-P system and to develop suitable growth techniques .

In this paper we report the results of our study of the CdP_2-Ge join in the Cd-Ge-P[2] system and the successful growth of fairly large single crystals from stoichiometric melts. In addition, we briefly describe our experience in the growth of crystals by chemical transport and from liquid Cd and Sn. Previous workers have grown small crystals from Sn solution [7], from the vapor phase [8] and from the melt [9].

---

[1] Figures in brackets indicate the literature references at the end of this paper.
[2] A complete investigation of the Cd-Ge-P system is in progress and results will be published elsewhere.

2. CdP_2-Ge SYSTEM

Differential thermal analysis was used to determine the liquidus and eutectic temperatures. Thermocouples were calibrated against the melting points of pure metals spanning the temperature range of interest to us. The starting composition for each DTA run was prepared from CdP_2, Ge, and $CdGeP_2$[3] (average weight of charge 0.7 g) and sealed into evacuated quartz ampoules which contained a thermocouple receptacle as shown in figure 1. An additional amount of phosphorous was added for each run so as to yield a phosphorous pressure (as P_4) of approximately 10 atmospheres at 800 °C. In all cases, several SiO_2 granules were added to the charges so as to promote nucleation and thus minimize supercooling. Even so, it was found for cooling rates of 2.9°/min and 3.6°/min, supercooling was observed (as much as 30 °C, for example) for the CdP_2 rich melts. Reproducible DTA data were obtained for a cooling rate of 1.7°/min. Typical DTA curves are shown in figure 2. No evidence of a solid state transformation for $CdGeP_2$ (which occurs for $ZnGeP_2$ at ~ 75 °C below the melting point) was detected, although the occurrence of one close to the melting point is not ruled out. X-ray and metallographic examinations were made after each DTA experiment to properly label the coexistence regions.

The CdP_2-Ge join (fig. 3), determined as described above, shows that the phase relationships are rather simple and the chalcopyrite phase melts congruently. The melting points of CdP_2 and Ge determined in this study are 770 ± 5 °C and 930 ± 5 °C respectively. Berak and Pruchnik [10] reported 782 °C for CdP_2. The generally accepted value for Ge is 936 °C. We were not able to detect the $\beta \rightarrow \alpha$-CdP_2 transition (~ 420 °C) [10]. Our x-ray results show only the presence of β-CdP_2, indicating the sluggishness of this transition [11,12].

We have found that a solution of Br in methanol (1:1000 by volume) is a sensitive etching reagent for metallographic examination of CdP_2-Ge alloys. With this reagent, coring, when present in the primary $CdGeP_2$ phase, can be delineated and is observed for cooling rates in excess of 2°/min for DTA compositions differing from stoichiometric. This is an important observation because it indicates to us that a homogeneity region having the $CdGeP_2$ structure exists at the elevated temperatures. Metallographic and x-ray examination of several $CdGeP_2$ and off-stoichiometric samples homogenized and quenched from 770 °C indicates that the maximum solid solubilities of CdP_2 and Ge in $CdGeP_2$ are less than 2.5 mol %. We have indicated the existence of a homogeneity range at the elevated temperatures based on the metallographic observation of coring and the flatness of the liquidus curve, which from thermodynamic arguments, also suggests the existence of a homogeneity region. It is important to note, however, that we do not yet know the maximum solid solubilities and thus the shapes of the solidus curves and whether or not the stoichiometric composition exhibits the maximum freezing point.

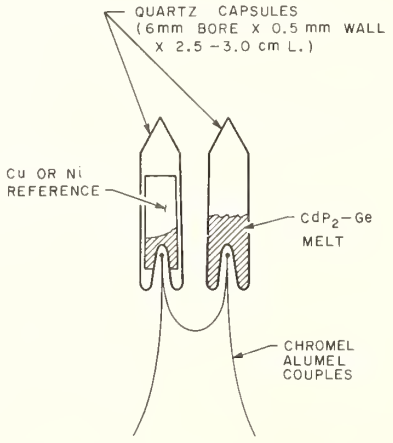

Fig. 1. Ampoules for the DTA experiments showing the reentrant cavities for thermocouples.

[3]Cd, 99.9999%, P, 99.9999%, and Ge, single crystal, 10 ohm-cm p-type.

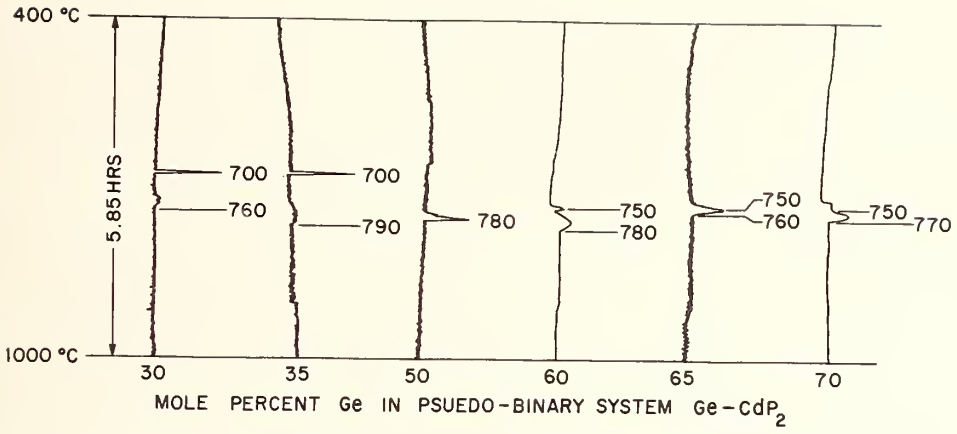

Fig. 2. Examples of DTA curves. The curves for 60 and 70 mol % Ge were obtained with an electrically quieter system.

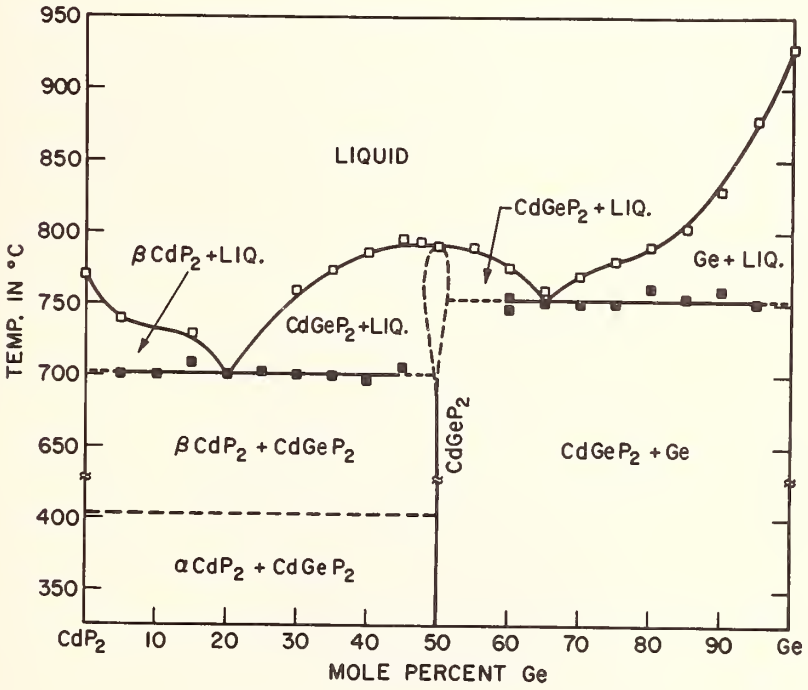

Fig. 3. The CdP_2-Ge system.

Detailed equilibrium partial pressure-temperature-composition information in the context of the whole Cd-Ge-P system is required for a clearer understanding of this phase. The work reported here is a step in this direction.

3. CRYSTAL GROWTH FROM MELTS

Early attempts to grow $CdGeP_2$ crystals from stoichiometric melts contained in quartz crucibles or boats were unsuccessful. The ingots were polycrystalline, contained numerous cracks, and tended to stick to the quartz. Successful single crystal growth has been carried out by directional freezing in pyrolytic graphite and vitreous carbon boats sealed into evacuated quartz ampoules. Charges consisted of stoichiometric amounts of Cd, Ge, and P with or without excess P. When excess P was used, the amount was such so as to yield a P pressure

465-504 O - 72 - 39

(as P_4) of 5-10 atmospheres at 850 °C. In order to avoid explosions, the assembly is usually heated to 500 °C over a period of 24 hours and then to 850 °C at a rate of ~ 100°/day. The melt is then cooled to room temperature by decreasing the furnace temperature at rates which varied from 10-30°/day, depending on the experiment. The furnace gradient established at one end of the assembly is about 4°/cm which we estimate results in a linear growth rate of approximately 2.5 to 7.5 cm/day through the melting point. Ingots prepared in this fashion from stoichiometric melts are not completely single, since no seeding is done. They usually contain from three to ten large crystals. Examples are shown in figure 4. A few cracks are still present and may result from differential thermal contraction or a phase change occurring close to the melting point. Nevertheless, the number of cracks present do not hinder preparing crystals of sufficient size for most electrical and optical experiments presently underway. The room temperature resistivities of crystals prepared in this manner are essentially similar to those prepared by chemical transport (of the order of 10^8 ohm-cm). The presence of $CdGeP_2$ glass could not be detected by Shay by infrared microscopy and thus the tendency for glass formation in this system appears not to be an impediment in growing large crystals from stoichiometric melts. These crystals also yield sharp powder x-ray diffraction peaks. All α_1 and α_2 doublets were well resolved.

4. CRYSTALS VIA CHEMICAL TRANSPORT

The procedure we have used consists of placing the desired quantities of Cd, Ge and P with I_2[4] at the closed end of a quartz tube (15 cm long, 1.5 cm inside diameter, and .15 cm wall thickness), evacuating and sealing. The ampoule containing the charge is placed in a furnace in such a way that on heating over a period of a week, a temperature gradient is maintained whereby the charge-containing end is the coldest. The maximum temperature reached for the colder end was usually 800 °C. At 800 °C, the alloy is molten. The melt is then cooled to ~ 750 °C, where it is solid. The longitudinal temperature gradient is then eliminated because we have found that the largest crystals grow normal to the ingot surface (natural furnace gradient ~ 1-2°/cm) after 10-30 days. Crystals are fewer in number but larger if the starting charge contains enough Ge in excess of the stoichiometric amount such that the solid ingot contains Ge second phase. The optimum amount of excess Ge is ~ 15 mol %.

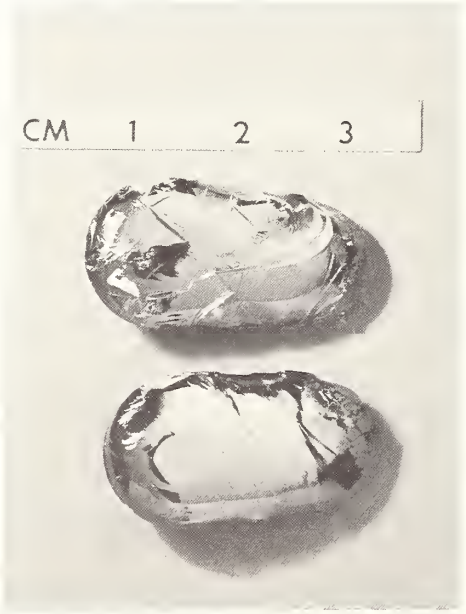

Fig. 4. Examples of two directionally solidified samples of $CdGeP_2$, each containing three or four large crystals.

[4] I_2 is required for the transport of Ge. Six mg of I_2/cc of ampoule volume. For our ampoules, this amounted to ~ 2 wt % of the total weight of charge.

Metallographic examination shows the crystals tend to nucleate and grow at those points on the surface of the ingot which are Ge-rich. Crystals as large as 8 mm^3 have been grown by the above procedure using excess Ge. If the charge is not heated initially to a temperature where it is completely molten but only to the growth temperature, a Cd-Ge liquid phase is always present (Cd-Ge eutectic exists below 400 °C) during the growth period and it is found that only very small crystals are formed under these conditions, similar to that observed for $ZnGeP_2$ [6].

5. GROWTH FROM LIQUID Cd AND Sn

Only a limited amount of effort was expended in this direction. In general, eight mol % of prereacted, polycrystalline $CdGeP_2$ obtained by cooling stoichiometric melts was added to Sn or Cd in pyrolytic graphite boats and sealed into evacuated quartz ampoules. The mixtures were cooled from 750 °C to room temperature at a rate of ~ 2/hr. The crystals were separated from the Sn or Cd by heating the ingots in Hg held at 200 °C, followed by etching in concentrated HNO_3. The crystals obtained by this technique were generally quite small, ~ 2-4 mm^3, and the quality, extremely poor, as indicated by powder x-ray patterns; the high angle lines were not sharp.

6. SUMMARY

The macroscopic features of the phase relationships in the CdP_2-Ge join of the Cd-Ge-P system have been determined as a first step towards understanding the results of crystal growth and physical measurements. The largest crystals of $CdGeP_2$ have been grown from the liquid state and it appears that the tendency towards glass formation in this system is no impediment for the growth of large single crystals from stoichiometric melts.

7. ACKNOWLEDGMENTS

We thank Messrs. J. D. Wiley and J. L. Shay for their efforts in behalf of the crystal growth work and helpful comments on the manuscript.

8. REFERENCES

[1] Shay, J. L., Buehler, E., and Wernick, J. H., to be published in Phys. Rev. Sept. 15, 1971.
[2] Masumoto, K., Iomura, S., and Goto, W., J. Phys. Chem. Solids 27, 1939 (1966).
[3] Mughal, S. A., Rayne, A. J., and Ray, R., J. Materials Science 4, 895 (1969).
[4] Goryunova, N. A., Kuzmenko, G. S., and Osmanov, E. O., Mater. Sci. Eng., 7, 54-56 (1971).
[5] Boltovets, N. S., Borshchevskii, A. S., and Osmanov, E. O., Mater. Sci. Eng., 7, 56-58 (1971).
[6] Buehler, E. and Wernick, J. H., J. Cryst. Growth, 8, 324 (1971).
[7] Spring-Thorpe, A. J. and Pamplin, B. R., J. Cryst. Growth, 3-4, 313 (1968).
[8] Fedorov, A. E., Bychkov, A. G., and Tychina, I. I., UKr. Fix. Zh. 15: 1568-9, Sept. 1970.
[9] Goryunova, N. A., Ryvkin, S. M., Spenikov, G. P., Tychina, I. I., and Fedotov, V. G., Phys. Stat. Sol. 28, 489, (1968).
[10] Berak, J. and Pruchnik, Z., Roczni, Chem. 42, 1403 (1968); we previously reported a value of ~ 725 °C obtained by DTA for a cooling rate of 3.5 deg/min; Mat. Res. Bull. 6, 303 (1971).
[11] von Stackelberg, M. and Paulus, R., Z. Phys. Chem. B28, 427 (1935).
[12] Horn, J., Bull. Acad. Polonaise des Sciences, 17, [2] 69 (1969).

National Bureau of Standards Special Publication 364, Solid State Chemistry, Proceedings of 5th Materials Research Symposium, issued July 1972.

HIGH BORON CONTENT RARE-EARTH BORIDES

K. E. Spear and G. I. Solovyev[1]

Materials Research Laboratory
The Pennsylvania State University
University Park, Pennsylvania 16802

Investigations were performed to determine which rare-earth metals form LnB_{66} phases, and to measure some of the properties of these compounds. Similar rare-earth borides have been recently reported with B:Ln ratios of 50 to 100 for metals Y, Gd, Tb, Ho, and Yb. A single crystal structure analysis published on the yttrium compound shows the structure to be face-centered cubic with an ideal stoichiometry YB_{66}. In the present studies, ten representative metals were used: Y, La, Ce, Pr, Nd, Sm, Gd, Dy, Er, and Yb. Boron-rich compositions were prepared by arc-melting mixtures of the elements. Identification of the phases in each sample was performed with the use of x-ray and metallographic techniques. All of the investigated systems except La, Ce, and Pr formed the LnB_{66} phase, and it is predicted that all rare-earth metals from Nd through Lu will form this phase. Lattice parameters were measured and show a general, but not regular decrease with atomic number. The LnB_{66} phases are extremely hard, with Vickers microhardness values ranging from about 3600 to 4000 kp/mm^2. Melting temperatures for the LnB_{66} phases were essentially the same for all metals, and equal to approximately 2150 °C.

Key words: Borides; lattice constants; LnB_{66} compounds; melting temperatures; microhardness; rare-earth borides.

1. INTRODUCTION

Metal borides are very unique and interesting compounds. Their stoichiometric relationships are extraordinary, with common M:B ratios of 4:1, 2:1, 3:2, 1:1, 3:4, 1:2, 1:4, 1:6, 1:12, and 1:66. The more metal-rich phases are most commonly formed with transition metals, and the boron-rich phases are most commonly formed with lanthanide and actinide metals. Nothing analogous to the higher borides with boron contents of 80 at. % and greater is found in other high temperature materials such as carbides,nitrides, oxides, silicides, etc.; they are unique with the borides.

This paper reports the results of survey studies on the most boron-rich borides of the lanthanide elements, the LnB_{66} phases. Ten representative Ln-B systems were studied. Attempts were made to prepare the LnB_{66} phases, and lattice constants, microhardness, and melting temperatures were measured on these boron-rich compounds. Before reporting and discussing the present results, previous studies on phases of this type will be reviewed.

2. PREVIOUS STUDIES

Seybolt [1][2] discovered a phase in the Y-B system that was very rich in boron, and designated it by the formula YB_{70}. Since that time boron-rich phases have been given formulas of LnB_{50}, LnB_{66}, LnB_{70}, and LnB_{100}. Lundin [2] tentatively assigned a tetragonal

[1]During the time this research was performed, Dr. G. I. Solovyev was a visiting exchange scientist at The Pennsylvania State University. His present address is: Moscow Engineering Physical Institute, Moscow, USSR.

[2]Figures in brackets indicate the literature references at the end of this paper.

cell to a material described as YB_{70}. LaPlaca [3] prepared cubic borides of Tb, Ho, and Yb with approximate composition LnB_{70}, and later reported [4] he could not prepare these phases for the larger rare-earth metals. However, the specific metals are not identified. Smith and Gilles [5] produced similar compounds with Gd and Yb, and gave them formulas LnB_{100}. Eick [6] reported the existence of PuB_{100}.

Richards and Kasper [7] recently performed a single crystal structure analysis of the boron-rich yttrium compound and assigned it a formula of YB_{66} based on this structure analysis. The structure is face-centered cubic with space group Fm3c, and a_o = 23.440 Å with a standard deviation of 0.006 Å. The unit cell contains approximately 1584 boron atoms and 24 yttrium atoms. A single crystal structure analysis by Naslain, Etourneau, and Kasper [8] on ThB_{66} indicates that this phase is isotypic with YB_{66}.

The basic nature of the crystal structure is not difficult to grasp, as has been illustrated by Oliver and Brower [9]. Icosahedra made up of thirteen B_{12} icosahedra are the basic units of the structure. Figure 1 shows how these 156-atom $B_{12}(B_{12})_{12}$ groups are formed. One B_{12} icosahedron is in the center of an icosahedron formed by twelve B_{12} icosahedra. Two orientations of the 156-atom group are shown because the crystal framework as shown in figure 2 is made up of two interpenetrating fcc lattices of $B_{12}(B_{12})_{12}$ units

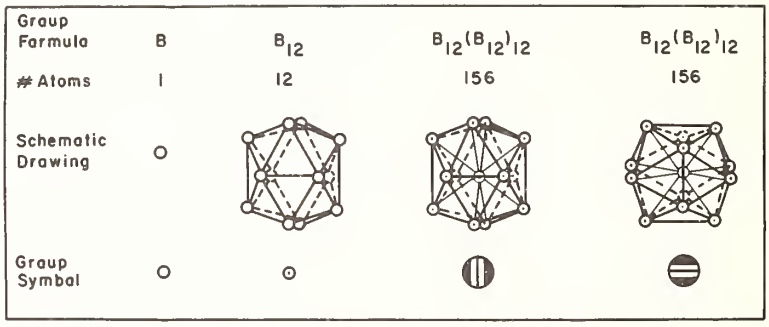

Fig. 1. Schematic illustration showing the formation of B_{12} icosahedra from boron atoms, and of a $B_{12}(B_{12})_{12}$ icosahedra from thirteen B_{12} icosahedra.

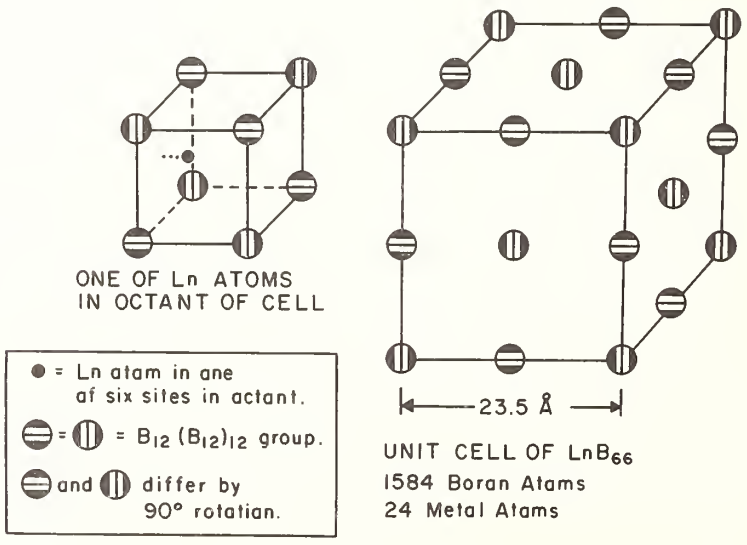

Fig. 2. Schematic drawing of the YB_{66}-type crystal structure. A description of this structure is given in the text.

that differ only by the 90° rotation of these units. Thus, there are eight of these 156-atom groups per unit cell -- or 1248 boron atoms in these icosahedra. The metal atom positions and the locations of the remaining boron atoms in the structure can be most easily pictured by referring to an octant of the cell, also shown in figure 2. Six metal atom sites exist in each octant of the cell, and these are statistically half-filled. The sites are located 1.27 Å (for YB_{66}) inside the cell from the center of each face of an octant; one such site is depicted in the figure. The center of each octant is occupied by either a 36 or a 48 boron atom group. In a random fashion, half of the octants contain 36-atom groups, and half contain the 48-atom groups. The average formula for the structural units present in one octant of the cell may be written as $Ln_3[B_{12}(B_{12})_{12}]_1[B_{36}]_{1/2}[B_{48}]_{1/2}$.

Oliver and Brower [9] have grown single crystals of YB_{66} from the melt by a pedestal growth technique. Their studies have indicated that YB_{66} melts congruently at 2100 °C, and that the YB_{12}-YB_{66} eutectic temperature is 2050 °C, both values have uncertainities of ± 50 °C. Smith and Gilles [5] determined that the melting temperature of YbB_{66} in contact with more metal-rich ytterbium borides must be greater than 2000 °C.

3. EXPERIMENTAL

3.1. SAMPLE PREPARATION AND ANALYSIS

All samples were prepared from elemental boron and the rare-earth metals. The boron from A. D. MacKay, Inc. was -325 mesh powder with a purity of 99.5+%. The major impurities were carbon, 0.20%, and iron, 0.22%. The metals from Research Chemicals had metallic element impurities of 0.05% or less except for the following: *Y*-Ta (1.0%); *Gd*-Y (0.5%); *Dy*-Ta (0.5%). Most detected impurity elements were present in quantities smaller than 0.01%.

The elemental powders were weighed to give a B:Ln atomic ratio of 80 ± 1, mixed, pressed into pellets, and then melted on a water-cooled copper hearth in an argon atmosphere with an arc-furnace utilizing a tungsten electrode. Before melting the samples, zirconium metal was melted to purify the argon atmosphere. The mass of each sample ranged from 5 to 10 grams.

Two of the samples, SmB_{66} and NdB_{66}, were analyzed qualitatively by spectrographic analysis for metallic impurities. The elements Fe and Cu were detected as minor impurities (0.02-1% range), Mn and Cr were detected as trace impurities (< 0.02%), and all other elements including W were not detected. Rare-earth metal impurities were not looked for in these samples. In addition to the boron as a source of Fe impurity, the prepared samples were ground in a hardened steel mortar. The extreme hardness of the samples probably resulted in the pickup of at least part of the Fe and Cr detected. The Cu probably resulted from the arc-melting on a water-cooled hearth.

3.2. HEATING TECHNIQUES

The annealing of samples and melting point determinations were performed in a Centorr Associates Series 15 tungsten mesh resistance furnace under an argon atmosphere. A borided tantalum setter plate suspended into the hot zone by molybdenum wires was covered with a powdered layer of SmB_6 containing a small amount of SmB_{66}. The samples to be heated were placed on this powdered layer. The eutectic temperature of 2055 °C for TaB_2-B mixtures [10], and the boron-like nature of the LnB_{66} compounds make it likely that a similar eutectic would occur between TaB_2 and LnB_{66}. It was for this reason that the powdered layer of SmB_6 was used to separate the LnB_{66} phases and the TaB_2.

Temperatures were measured with a Leeds and Northrup optical pyrometer by sighting through an optical window, through holes in the radiation shields, onto the surface of the sample. In some cases, black-body holes were made in the samples with a spark-cutter. Observed temperatures were corrected with the use of a calibration based on the melting point of platinum. The metal was observed to melt at a pyrometer reading of 1710 °C, 59° below the reported melting temperature of 1769 °C [11]. The melting point of the LnB_{66} compounds was determined by observing the rounding of sharp edges on the samples as the temperature was slowly raised toward this melting point. Some samples completely collapsed at this point.

3.3. CHARACTERIZATION METHODS

3.3.a. X-RAY DIFFRACTION

X-ray diffraction patterns were taken of all samples with a Siemens diffractometer and Ni-filtered CuKα radiation. Scan rates of 2°/min were used for identification of the phases that were present, while rates of 1/2°/min were used in determining lattice constants. The instrument was calibrated with the use of gold and silicon standards. Lattice parameters were calculated by a least-squares technique and a ($\cos^2\theta/\sin\theta$) extrapolation function.

3.3.b. METALLOGRAPHY

Standard metallographic mounting and polishing techniques were used. The extreme hardness of the boride samples made the use of a diamond-paste compound necessary for polishing. The microstructures were examined with the use of a Leitz Panphot photomicrographic apparatus.

3.3.c. MICROHARDNESS

A Leitz Miniload hardness tester was used in measuring the microhardness of samples. The indentations were made with a pyramidal Vickers diamond using a load of 200p (p = pond = 980.665 dynes). A standard supplied with the instrument (MPA 7760.65) was determined to have a microhardness of 594 kp/mm^2, while the value given for a 100p load was 581 $\pm$ 14 kp/mm^2. An average of ten measurements was used to calculate the hardness of each sample.

4. RESULTS

A tabulation of the present results is given in table 1. The phase results of attempts to prepare the LnB_{66} compounds are given for the ten metal-boron systems looked at, and these results are followed by lattice constants, microhardness, and melting temperatures of LnB_{66} for the systems forming this phase.

The three largest rare-earth metals -- La, Ce, and Pr -- did not form LnB_{66} compounds, but gave mixtures of the hexaboride and boron. The seven remaining systems studied all formed the YB_{66}-type phase. Lattice parameters of these phases were calculated using the indexing scheme of Richards and Kasper [7] for YB_{66}. The lines in the diffraction patterns could be readily indexed, and the intensities were approximately the same as given by Richards and Kasper and also by Smith and Gilles [5]. The uncertainties given with the lattice constants in table 1 are computed standard deviations. A general decrease in lattice constant with atomic number is apparent, but this decrease is not regular. A regularly decreasing trend would require that the SmB_{66} and DyB_{66} values be larger.

The microhardness values range between 3610 and 3960 kp/mm^2. No systematic trend with atomic number or cell volume is observed. However, estimated uncertainty limits of $\pm$ 200 kp/mm^2 indicate that not too much emphasis should be placed on differences in these values.

The measured melting temperatures for the LnB_{66} phases were essentially identical for all samples. The same value of 2150 °C was given all samples with a rather large, but realistic uncertainty of $\pm$ 100 °C. The neodymium and samarium values are probably for peritectic melting of LnB_{66}; the other values are believed to correspond to either the congruent or peritectic melting of single phase LnB_{66}, but the mode of melting is unknown. The evidence used to deduce these results is given below.

The LnB_{66} samples were single phase except for the NdB_{66} sample which contained minor amounts of NdB_6, and the YB_{66} and GdB_{66} samples which contained trace amounts of second phase detectable by metallographic, but not by x-ray techniques. In terms of visually observing the melting of a sample, all samples except the neodymium sample would act like single phase materials.

Previous studies of the Sm-B system [12] gave evidence for the peritectic melting of SmB_{66} to give SmB_6 plus a boron-rich melt. The microstructure of the neodymium sample in the present studies indicates that NdB_{66} melts by a similar reaction. The evidence is not conclusive, but a eutectic structure was not observed in the two-phase NdB_6-NdB_{66} mixture.

Table 1

Experimental Results for Measurements on LnB_{66} Compounds[a]

Metal	Phases Present[b]			LnB_{66} Lattice Constant[c] (Å)	Microhardness[d] (kp/mm^2)	Melting Temperature[e] (°C)
	mj	mn	tr			
Y	YB_{66}	-	YB_{12}[g]	23.451 ± 0.002	3860	2150
La	B	LaB_6	-			
Ce	B	CeB_6	-			
Pr	B	PrB_6	-			
Nd	NdB_{66}	NdB_6	-	23.508 ± 0.004	3910	2150
Sm[f]	SmB_{66}	-	-	23.474 ± 0.002	3610	2150
Gd	GdB_{66}	-	GdB_6[g]	23.476 ± 0.005	3660	2150
Dy	DyB_{66}	-	-	23.422 ± 0.005	3840	2150
Er	ErB_{66}	-	-	23.438 ± 0.003	3635	2150
Yb	YbB_{66}	-	-	23.415 ± 0.003	3960	2150

(a) Data were taken on samples quenched from the melt except as noted.

(b) Phases present as determined by x-ray and metallographic techniques: mj = major, mn = minor, tr = trace.

(c) The uncertainties given with the cubic lattice constants are computed standard deviations.

(d) Estimated uncertainty is ± 200 kp/mm^2.

(e) Estimated uncertainty is ± 100 °C.

(f) Lattice constant and microhardness values were measured on an SmB_{66} sample annealed at 2000 °C for 2 hrs. Before annealing, the microhardness was 3710 kp/mm^2.

(g) Identification was by color of the trace phase present.

It appears that the NdB_6 precipitated out first, then NdB_{66}, but elemental boron or a eutectic mixture of NdB_{66} and boron was not detected.

The x-ray and metallographic examination of these samples showed no evidence for LnB_{66} formation by a solid state reaction occurring after solidification of the melt, which leads to the conclusion that these boron-rich compounds do not decompose by a solid state reaction before melting.

5. DISCUSSION

Including the present and previous studies, attempts have been made to form LnB_{66} phases with all the rare-earth elements except Pm (radioactive), Eu, Tm, and Lu. Since only the three largest rare earths -- La, Ce, and Pr -- did not form this phase, it is almost certain that Pm, Eu, Tm, and Lu will form LnB_{66} phases.

Since the starting materials in the present studies were mixed in a molar ratio of B:Ln = 80 ± 1, it might at first seem surprising that all prepared samples were either single phase LnB_{66}, or LnB_{66} plus a more metal-rich phase. One might conclude that the LnB_{66} phases actually have B:Ln ratios closer to 80 or higher, as indicated by Smith and Gilles [5], rather than a ratio of about 66. This explanation could be valid, but another one also seems plausible. From Smith's studies [13] on which rare-earth boride phases vaporize congruently, one concludes that all of the presently studied LnB_{66} phases, with the exception of YbB_{66}, lose boron preferentially upon vaporization. Therefore, one would not be surprised if boron were lost during the arc-melting preparation of the samples so that the final B:Ln ratios were less than 80. Careful preparation and characterization studies are needed on these phases, as they are on essentially all boride phases.

Detailed crystallographic studies of boron-rich chromium samples by Andersson and Lundström [14] showed chromium to dissolve in β-rhombohedral boron to the extent given by the formula $CrB_{\sim 41}$. No unique boron-rich phase such as the YB_{66}-type phase was detected. In latter studies of solution hardening of β-rhombohedral boron by Carlsson and Lundström [15], samples with compositions corresponding to MB_{20} were prepared with metals Sc, Ti, V, Cr, Mn, Fe, Co, Ni, and Cu. No unique boron-rich phases were detected. Perhaps with larger transition metals, YB_{66}-type or similar type phases will form, but thus far, only some of the lanthanide and actinide elements and yttrium have produced these compounds.

The powder diffraction patterns of the LnB_{66} phases studied in the present research indicate that all of these compounds are structurally isotypic with YB_{66}. However, no attempts were made to determine the B:Ln ratios of the samples, nor were samples with a specific metal prepared so that lattice parameters of metal-rich and of boron-rich LnB_{66} could be compared. Such comparisons would indicate the extent of each phase's homogeneity range. Compositions either rich in metal or boron could also be annealed at different temperatures, quenched, and lattice parameters measured. These values would give an indication of the changes in phase boundary composition with temperature.

The hardness values of the LnB_{66} phases are greater than that of pure β-boron, which is given as 3410 kp/mm^2 by Carlsson and Lundström [15], and are about the same as the solution hardened boron values reported by these same authors. The boron was saturated with the metals mentioned in the discussion above, and gave hardness values ranging from 3610 kp/mm^2 for boron containing dissolved V, to 4210 kp/mm^2 for boron containing either dissolved Sc or Mn.

The value of 2150 ± 100 °C given for the melting temperatures of the studied LnB_{66} phases is in agreement with the few reported values. Oliver and Brower [9] give a value of 2100 ± 50 °C for the congruent melting of YB_{66} and 2050 ± 50 °C for the YB_{12}-YB_{66} eutectic temperature. Smith and Gilles [5] report that the melting temperature of YbB_{66} must be higher than 2000 °C. Although the few reported values are in general agreement, more detailed studies of melting temperatures and behavior are needed on these LnB_{66} compounds.

6. ACKNOWLEDGMENTS

The authors want to acknowledge C. W. Gregg for providing the computer program for the least-squares lattice parameter calculations, and E. G. Imperato for his assistance in the experimental portion of these investigations.

7. REFERENCES

[1] Seybolt, A. U., "An Exploration of High Boron Alloys," Trans. Am. Soc. Metals 52, 971-989 (1960).

[2] Lundin, C. E., "Rare Earth Metal Phase Diagrams," in *The Rare Earths*, (F. H. Spedding and A. H. Daane, eds.), Wiley, New York, Chapter 16, 248 (1961).

[3] La Placa, S., private communication quoted on page 330 in Ben Post, "Refractory Binary Borides," in *Boron, Metallo-Boron Compounds and Boranes*, (R. M. Adams, ed.), Interscience Publishers, New York, Chapter 5, 301-371 (1964).

[4] La Placa, S., private communication quoted on page 91 in J. L. Hoard and R. E. Hughes, "Elementary Boron and Compounds of High Boron Content: Structure, Properties, and Polymorphism," in *The Chemistry of Boron and Its Compounds*, (E. L. Muetterties, ed.),

Wiley, New York, Chapter 2, 25-154 (1967).
[5] Smith, P. K. and Gilles, P. W., "Rare Earth Hectoborides," J. Inorg. Nucl. Chem. 26, 1465-1467 (1964).
[6] Eick, H. A., "Plutonium Borides," Inorg. Chem. 4, 1237-1239 (1965).
[7] Richards, S. M. and Kasper, J. S., "The Crystal Structure of YB_{66}," Acta Cryst. B25, 237-251 (1969).
[8] Naslain, R., Etourneau, J., and Kasper, J. S., "Structure Cristalline de la Phase du Systeme Bore-Thorium. Un Nouveau Borure a Structure Type YB_{66}," J. Solid State Chem. 3, 101-111 (1971).
[9] Oliver, D. W. and Brower, G. G., "Growth of Single Crystal YB_{66} from the Melt," Report No. 71-C-162 (June 1971); General Electric Co., Schenectady, New York 12301.
[10] Rudy, E., "Ternary Phase Equilibria in Transition Metal-Boron-Carbon-Silicon Systems, Part V. Compendium of Phase Diagram Data," Tech. Rept. AFML-TR-65,2, Part V, 209 (May 1969).
[11] Hultgren, R., Orr, R. L. and Kelley, K. K., private communication in form of "Supplement to Selected Values of Thermodynamic Properties of Metals and Alloys," University of California, Berkeley, California.
[12] Solovyev, G. I. and Spear, K. E., "Phase Behavior in the Samarium-Boron System", (Submitted for publication J. Am. Ceram. Soc.).
[13] Smith, P. K., "Lanthanide Boride Systems and Properties," Ph.D. Thesis, University of Kansas, May 1, 1964. Also USAEC Report No. COO-1140-103 (May 1964).
[14] Andersson, S. and Lundström, T., "The Solubility of Chromium in β-Rhombohedral Boron as Determined in $CrB_{\sim 41}$ by Single-Crystal Diffractometry," J. Solid State Chem. 2, 603-611 (1970).
[15] Carlsson, J. O. and Lundström, T., "The Solution Hardening of β-Rhombohedral Boron," J. Less-Common Metals 22, 317-320 (1970).

DISCUSSION

B. Post: Did you worry about the fact that all the rare earth B66 ($R.E.B_{66}$) compounds melt within 20 degrees of each other, which is within 20 degrees of the melting point of boron?

K. E. Spear: Yes, we worried some about it. We melted these on a borided tantalum setter plate. That's what we were using to anneal samples and the eutectic temperature between the tantalum diboride and the boron is about 2050°. We were afraid SmB_{66} or any of the metal boron 66 (MB_{66}) phases and tantalum diboride would have a similar low melting eutectic. Therefore, we put a layer of essentially pure samarium hexaboride powder between the tantalum diboride and the specimen to be melted. I think the melting points are correct within ± 100 degrees.

B. Post: What I was wondering about is the possibility that you drove off the metal and had boron left.

K. E. Spear: No, at least ytterbium was the only possible case. The rest of these metal borides should lose boron preferentially according to the work of Smith and Gilles[1].

S. LaPlaca: Just to update your phase diagram[2], the compound samarium boron approximately 2.1 ($SmB_{2.1}$) turns out to be Sm_2B_5. The work in collaboration with Paul Smith at Bell Labs is being published in Acta Cryst. very shortly.

K. E. Spear: Oh, very good, do you know the crystal structure?

S. LaPlaca: Yes, in fact that is how the composition was determined, by doing the crystal structure. It is a derivative of the MB_4 structure where you just separate the layers and put intervening B_2 units in.

[1] P. K. Smith, "Lanthanide Boride Systems and Properties," Ph.D. Thesis, University of Kansas, May 1, 1964. Also USAEC Report No. COO-1140-103, May 1964.

[2] Refers to Sm-B phase diagram shown during oral presentation to illustrate melting behavior of SmB_{66}. This phase diagram appears in the paper: G. I. Solovyev and K. E. Spear, "Phase Behavior in the Samarium-Boron System," J. Am. Ceram. Soc. (submitted for publication).

K. E. Spear: Very good! We had x-ray data and it wasn't like any known boride structure, so I'm glad to hear the structure has been solved.

K. Kahan: Is there any evidence that these MB_{66} phases are intercallation compounds?

K. E. Spear: No, the structure disproves this. The structures are similar to elemental boron in many ways. In fact, the easiest way to answer your question is with two slides that I have. I think I can do this in about one minute. Actually the structure is fairly simple to see when you look at the slides. It is a face-centered cubic structure and is made up chiefly from groups of 156 boron atoms. If you consider these groups as individual units, then you can see fairly easily how the 1608 atoms per unit cell are arranged. The first slide (Fig. 1 in text of paper) just briefly shows how you build up the 156-atom groups. You go from single boron to the icosohedra B_{12} groups. The 156-atom groups have a B_{12} group in the center, and 12 such groups around the outside. This gives you the 156-atom group. I've shown two orientations, of this group, just 90 degrees twisted, because that's the way it is in the structure. If I could have the next slide (Fig. 2 in text of paper); consider this the sodium chloride structure. If you substitute a 156-atom group for each sodium atom and each chlorine atom in NaCl, then you account for 1248 of the boron atoms. Other groups of boron atoms are in the center of each octant of the cell. You have either a 36- or 48-atom group in there. As for the metal atoms, you have an average of 3 metals in each octant. Just one of the six metal sites per octant is shown. The metals are statistically placed with an average of three per octant, or 24 per cell. That finishes filling the cell. This explanation of the structure is a simplified version that I can easily understand.

B. Post: I think it should be emphasized that this structure was done by Kasper and Richards[3] and is really quite a job, it is very good.

[3]Reference 7 in paper under discussion.

National Bureau of Standards Special Publication 364, Solid State Chemistry, Proceedings of 5th Materials Research Symposium, issued July 1972.

PREPARATION AND CHARACTERIZATION OF BORON SUBOXIDE

D. R. Petrak and Robert Ruh

Air Force Materials Laboratory, Wright Patterson Air Force Base, Ohio 45433

B. F. Goosey

Department of Materials Science, University of Cincinnati, Cincinnati, Ohio 45221

Fabrication techniques have been developed to produce specimens of near theoretical density by reaction hot pressing of boron and boric acid in vacuum at temperatures of 1900-2000 °C and pressures of 0.41 kbars. The composition range 80 to 89 atomic % boron was investigated by chemical analysis, lattice parameter studies, pycnometric density determinations, electron probe analysis and infrared analysis. Results support the $B_{12}O_2$ chemical formula and the R3m space group with twelve boron atoms in the 18h positions and two oxygen atoms in the 6c positions. Thus, on the basis of the experimentally determined hexagonal lattice parameters of a = 5.386±0.003 Å and c = 12.326±0.004 Å, the calculated density is 2.602 $g \cdot cm^{-3}$ and this is in good agreement with the experimentally determined value of 2.600 ±0.007 $g \cdot cm^{-3}$. The occupancy of the 3b position by either boron or oxygen (to allow the B_4O or $B_{13}O_2$ stoichiometry) is ruled out since this would require increases in density and/or lattice parameters and none were observed. Also these configurations do not satisfy the Longuet-Higgins and Roberts counting rule. The boron suboxide phase has been studied by electron probe and infrared analyses. The oxygen K emission spectra as well as the infrared reflection spectra are presented. Boron suboxide has been studied by mass spectrometric analysis and found to decompose to rhombohedral boron and B_2O_2.

Key words: Amorphous boron; anhydrous boric acid; boric oxide; boron carbide structure type; boron suboxide; crystal structure; decompose; electron microbeam probe; infrared spectrum; lattice parameters; pycnometer; reaction-hot pressing; rhombohedral boron; x-ray diffraction.

1. INTRODUCTION

Boron suboxide is a material of Air Force interest because of its low theoretical density, high hardness and other characteristics. However, insufficient basic information and property data were known to adequately evaluate the potential of this material. Thus one of our research goals has been to determine structure and property relationships as well as processing techniques so that a meaningful evaluation was possible. A review of the literature on boron suboxide has been accomplished in an earlier study [1][1]. This study was a rather broad one and investigated boron suboxide as well as the 80-100 atomic % B composition range using chemical, metallographic, petrographic, x-ray diffraction, electron probe and elastic properties analysis. Results revealed that with increasing boron content the phases present were: B_2O_3 plus rhombohedral boron suboxide, boron suboxide, boron suboxide plus rhombohedral boron and boron. Hardness was investigated and values somewhat greater than those obtained for boron carbide were found. Elastic properties were determined for boron suboxide and two phase boron-oxygen compositions. Results revealed Young's moduli of up to 4830 kbar for boron suboxide and the value decreasing to 4480 kbar as the composition moved through the two phase region to boron. Poisson's ratio was found to be 0.156 for boron suboxide and to decrease through the two phase region to 0.130 at the boron composition.

[1] Figures in brackets indicate the literature references at the end of this paper.

The current investigation was a more basic and detailed analysis of boron suboxide and study of the structure as well as the thermodynamic and physical properties. Since boron suboxide has the same structure type as boron carbide and other attractive high boron compounds, information gained in this investigation will help to provide a better understanding of this whole family of compounds.

2. FABRICATION TECHNIQUES

2.1. STARTING MATERIALS

The compositions studied were prepared from appropriate mixtures of anhydrous boric acid and amorphous boron powders[2]. Emission spectrographic analyses revealed an impurity level of less than 0.1% for the boric acid and approximately 1% for the boron exclusive of boric oxide. While the impurity level was relatively high, this was the only boron available with the necessary fine (0.5 μm) particle size.

2.2. REACTION HOT PRESSING

The hot pressing of specimens in this study was accomplished in two steps. The first was a prepressing operation which consisted of heating the dry mixed starting powders in a steel die to approximately 450 °C at 0.206 kbar. (Under these conditions the boric acid was molten.) The steel die was lined with Grafoil[3] and tantalum sheet before filling with the powder mixture. The grafoil facilitated easy removal of the specimen from the die while the tantalum sheet assured a smooth specimen surface. The purpose of the prepressing operation was (1) to disperse the anhydrous boric acid throughout the compact and (2) to consolidate the compact and impart green strength.

The second step was a more conventional hot pressing operation. This was accomplished in vacuum using inductively heated graphite dies with barrier layers of boron nitride and tantalum sheet. A schematic diagram of the furnace and die assembly is shown in figure 1. The boron nitride was applied to grooved cylindrical surfaces of the die and plungers using a suspension in toluene. Initial pressings without the tantalum barrier revealed a ring of boron carbide 3 to 5 mm thick on the circumference of the specimen. The use of tantalum prevented the formation of boron carbide in most cases and tantalum was not found to diffuse significantly into the billet. However, as an added precaution, the outer ring of material was always discarded. A billet size of 5 cm in diameter by 1.2 cm in thickness was used so that adequate material was available for many different analyses and tests.

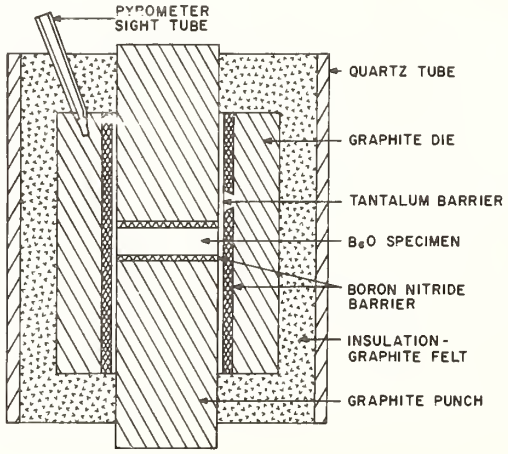

Fig. 1. Schematic diagram of the furnace and die assembly.

[2] U. S. Borax Research, U. S. Borax and Chemical Corporation, Anaheim, California

[3] Union Carbide Corporation, Carbon Products Division, Cleveland, Ohio

Pressings were made at 1900 to 2000 °C for 15 to 30 minutes at 0.41 kbar. Densification was monitored by means of a dial guage mounted on the press ram. Densification due to sintering was not observed until the 1750 to 1800 °C temperature range was attained. Pressure was maintained at 0.069 kbar up to the sintering temperature and then increased to 0.41 kbar. These pressing procedures were found to work equally well for compositions in the 80-100 atomic % boron range and bulk densities of 96-100% of theoretical were obtained.

3. CRYSTAL STRUCTURE

Boron suboxide reflection data were first indexed on an orthorhombic unit cell by Pasternak [2] who also determined the composition to be $B_{6.6}O$ by chemical analysis and the measured density to be 2.64 $g \cdot cm^{-3}$. Based on these data, he assigned a stoichiometric formula of B_7O. Later LaPlaca and Post [3] showed that the powder pattern for the boron suboxide phase could be more satisfactorily indexed on a rhombohedral cell of the boron carbide structure type. The ambiguity in indexing the pattern was the result of a special intensity ratio which existed; namely, $[d_{(001)}/d_{(100)}]^2 = 7$. LaPlaca and Post suggested a $B_{13}O_2$ stoichiometry which agreed well with Pasternak's $B_{6.6}O$ composition but required a calculated density of 2.80 $g \cdot cm^{-3}$. Rizzo et al. [4] found the composition to be B_6O or a $B_{12}O_2$ structural formula, which was later supported by Post [5]. The $B_{12}O_2$ structure (modified from Silver and Bray [6] and shown in figure 2) together with the hexagonal lattice parameters of a = 5.395 and c = 12.342 Å determined by Rizzo et al. gave a calculated density of 2.59 $g.cm^3$. The crystal structure work of both Novak [7] on powder patterns and Corfield [8] on a twinned crystal support the $R\bar{3}m$ space group for boron suboxide. Assuming this rhombohedral symmetry, Hoard and Hughes [9] have noted that the only dimensionally satisfactory structure that satisfies the Longuet-Higgins and Roberts electron counting rule [10] for a filled band configuration is $B_{12}O_2$ where no bond exists between oxygens. This would rule out any stoichiometry range for boron suboxide analagous to the B_4C-$B_{13}C_2$ range in boron carbide.

In this study precision lattice parameters were determined at room temperature on hot-pressed specimens with nominal starting compositions of B_4O, B_5O, B_6O, B_7O and B_8O. Two different methods were used for determining peak positions, namely (1) slow scan diffractometer traces and (2) Debye-Scherrer film techniques using a camera with a radius of 71.62 mm. Agreement between the two methods was very good. However, the film technique yielded the more precise results, and these results are given. Further description of the experimental techniques and the computation of lattice parameters were given in an earlier paper [11]. The hexagonal lattice parameters for all five specimens were within the range of a = 5.386 ± 0.003 and c = 12.326 ± 0.004 Å, thus indicating no significant change. Furthermore, decreasing amounts of B_2O_3 were noted in the B_4O and B_5O specimens by x-ray diffraction, while free boron was found in the B_7O and B_8O specimens. The free boron in the B_7O specimen could not be detected by x-ray diffraction but was observed by metallographic analysis. As shown in table 1, chemical analyses[4] on the nominal B_6O and B_7O specimens gave 79.7 and 80.7 wt. %

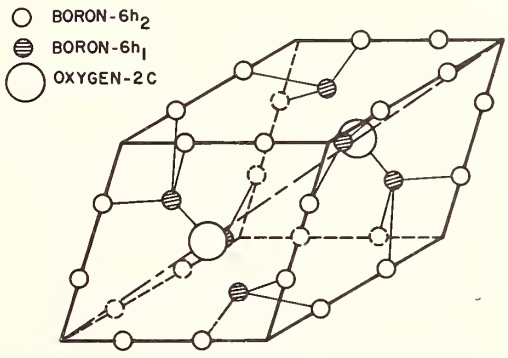

Fig. 2. Proposed rhombohedral unit cell of $B_{12}O_2$ (modified from Silver and Bray [6]).

[4]Ledoux and Company, Teaneck, New Jersey

Table 1
Nominal and Analyzed Compositions and Phases Present in Boron-Oxygen Specimens

Nominal Composition	Analyzed Composition B(wt%)	O(wt%)	Total	Phases Present
B_5O	77.5	22.0	99.5	$B_6O+B_2O_3$
B_6O	79.7	20.7	100.4	B_6O
B_7O	80.7	18.3	99.0	B_6O+B
B_8O	82.5	16.8	99.3	B_6O+B

boron respectively. This would support a B_6O stoichiometry of 80.2 wt. % boron. Oxygen analyses, although not considered as accurate, were performed and gave total boron and oxygen contents of 99.0 to 100.4 percent.

Pycnometric densities were also determined on all but the B_8O specimen. At least 5 grams of each composition were ground to minus 325 mesh in a boron carbide mortar and pestle, then boiled in distilled H_2O to dissolve any B_2O_3 present. After filtering and drying the density was measured using a 25 cm^3 pycnometer with butyl alcohol at 24 °C. All density values were within the range 2.600 ± 0.007 $g \cdot cm^{-3}$. This agrees well with a calculated value of 2.602 $g \cdot cm^{-3}$ obtained by assuming a B_6O stoichiometry and the lattice constants determined in this study. Thus all of the above data support the $B_{12}O_2$ structural formula in agreement with the Longuet-Higgins and Roberts theory. However the data do not preclude the possibility of a small change in stoichiometry.

4. ELECTRON PROBE STUDIES

Polished specimens of the nominal compositions mentioned previously were studied by Baun and Solomon [12] using a Perkin-Elmer (Hitachi) XMA-5 electron microbeam probe. Typical Oxygen K spectra for boron suboxide and B_2O_3 are given in figure 3. It is seen that boron suboxide has two maxima separated by approximately 3 eV[5], while B_2O_3 has a major peak with a much weaker component at the low energy side.

The existence of the two peaks indicates the formation of split molecular orbitals. Although a complete molecular orbital treatment has not been performed for boron suboxide, the two transitions could be explained by the crossover theory. On this basis, transitions from the boron 2p to the oxygen 1s level as well as the oxygen 2p to 1s are allowed. Using published values for these energy levels, the two bonds should be 2.5 to 3 eV apart and this separation was observed.

Baun and Solomon [12], in comparing the spectra from the nominal compositions, have noted changes in the relative intensities of the two peaks. They have explained these changes on the basis of compositional changes due to boron or oxygen occupying the interstitial sites in the rhombohedral structure of figure 2. In light of the present work it appears that the oxygen atoms occupy the 6c sites and that the 3b site is vacant. However the existence of a defect structure cannot be ruled out. The observed changes in relative intensities could also be explained by the presence of B_2O_3 in different amounts.

5. INFRARED REFLECTION SPECTRA

The infrared reflection spectra for the B_6O phase has been determined by Phillipi [13]. The main reflection band at 1060 wave numbers is shown in figure 4. Other weaker reflection bands were observed at 880, 780, 710 and 420 wave numbers. Similar reflection spectra were observed for the nominal compositions of B_4O, B_5O, B_6O and B_7O. However, no large wavelength shifts that could be related to changes in composition were evident. A multioscillator dis-

[5] 1 eV = 1.6021 x 10^{-9}J

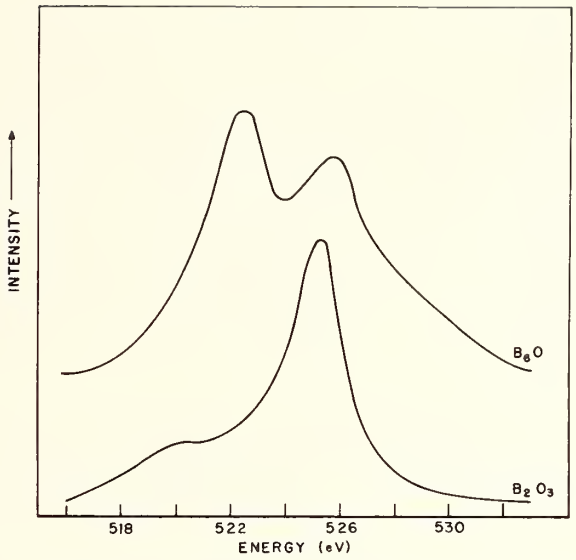

Fig. 3. Oxygen K emission spectra from boron suboxide and B_2O_3 (after Baun and Solomon [12]).

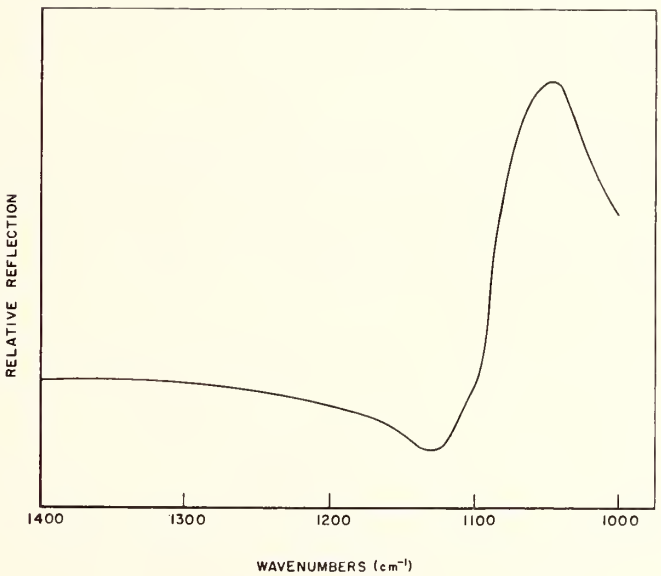

Fig. 4. The major infrared reflection band at 1060 cm^{-1} (after Phillipi [13]).

persion analysis is presently being performed on the spectra to aid in the characterization of these materials.

6. STABILITY AND MASS SPECTROMETRIC STUDIES

The stability of boron suboxide was investigated as a function of temperature in a flowing helium atmosphere. A 97% dense hot pressed pellet was repeatedly heated to temperature, held for two hours, cooled and weighed. Results are presented in figure 5. After the final heating cycle the specimen had an extremely porous appearance and could be crushed easily.

465-504 O - 72 - 40

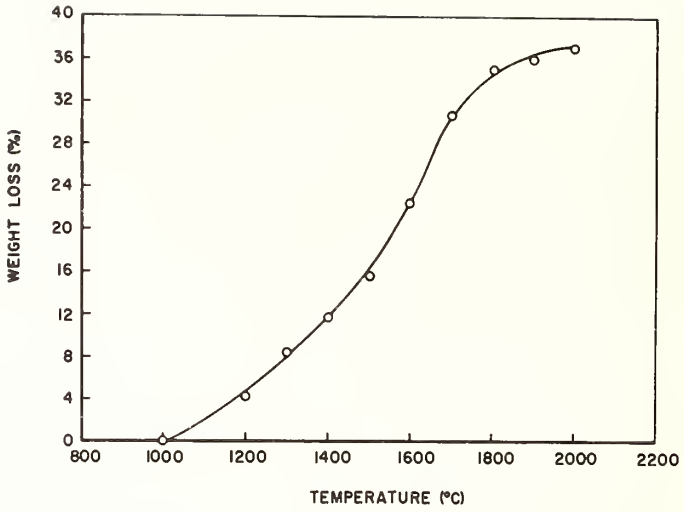

Fig. 5. Weight loss versus temperature for a solid boron suboxide specimen in a helium atmosphere.

X-ray diffraction analysis of the decomposed material revealed rhombohedral boron and a small amount of boron suboxide. This would explain the decrease in rate of weight loss at the higher temperatures, since most of the boron suboxide had already been decomposed. This work is in reasonable agreement with that of Rizzo et al. [4] who determined weight loss in helium for the 1300-1750 °C temperature range.

The vaporization characteristics of boron suboxide were investigated by Carbonara [14] for the authors to determine the vapor species and the thermodynamic quantities involved. An analyzed 79.7% boron composition was contained in a BeO-lined niobium Knudsen cell. A Nuclide HT-90-12 mass spectrometer was used to identify the vaporizing species to temperatures as high as 2000 °C. The predominate vapor components were BO and B_2O_2. Small amounts of B, B_2O, BO_2 and B_2O_3 were also found. This information was used to confirm thermal gravimetric analysis made in an Ainsworth microbalance and the BeO-lined niobium Knudsen cell.

The TGA data were converted to equilibrium total pressure and ΔH_v and ΔS_v were calculated for the reaction:

$$2B_6O(s) \rightleftharpoons B_2O_2(g) + 10B(s)$$

$$\Delta H_v = 90.9 \text{ Kcal/mol}^6$$

$$\Delta S_v = 40.2 \text{ eu}^7$$

X-ray diffraction analysis on the condensed phases after testing gave both boron suboxide and rhombohedral boron. No reaction with BeO was detected.

The above values for ΔH_v and ΔS_v compare well with $\Delta H_v = 94 \pm 8$ Kcal/mol and $\Delta S_v = 41.4$ eu found by Inghram et al. [15] for the vaporization of mixtures of boron and boric oxide. Their work was done in the temperature range 1030 to 1230 °C on molar ratios of boron to boric oxide greater than one. Since Inghram et al. reported no analysis on their condensed phases an attempt was made to reproduce them. A 2:1 molar ratio of boron to boric oxide was mixed and placed in a covered alumina crucible (Inghram et al. used an alumina Knudsen cell). The crucible was then heated to 1230 °C in vacuum for 7 hours. The condensed phases under these conditions were found to be boric oxide and boron suboxide with only a small indication for boron. Since it is doubtful that this experiment had reached equilibrium it is likely that Inghram et al. actually observed the vaporization of boron suboxide and boric oxide. This would explain the similarities in the results of the two mass spectrometric studies.

---

[6] 1 Kcal/mol = 4,184J/mol

[7] 1 eu = 4.184J/mol K

7. SUMMARY

Fabrication techniques have been developed to produce dense specimens of boron suboxide by reaction hot pressing at 1900-2000 °C at pressures of 0.41 kbars in vacuum. The structure of boron suboxide has been investigated in light of chemical analyses, lattice parameter studies, pycnometric density determinations, electron probe analysis and infrared analysis. Results support the $B_{12}O_2$ chemical formula and the R3m space group with twelve B atoms in the 18h positions and two oxygens in the 6c positions. The occupancy of the 3b position by either boron or oxygen (to allow the B_4O or $B_{13}O_2$ stoichiometry) is ruled out by chemical analysis, density and lattice parameter studies, as well as by the Longuet-Higgins and Roberts electron counting rule. However the experimental data does not preclude small changes in stoichiometry. Boron suboxide was found to decompose to $B + B_2O_2$ by mass spectrographic analysis.

8. ACKNOWLEDGMENTS

The writers express sincere appreciation to W. L. Baun, P. W. R. Corfield, T. C. Joyce, C. M. Phillipi and E. J. Rolinski for helpful discussions, to E. G. Charles for assistance in the x-ray diffraction analysis, to V. A. Patel for assistance in the density determinations and to Miss Sally Allen for typing the manuscript.

9. REFERENCES

[1] Ruh, Robert, Petrak, D. R. and Goosey, B. F., *Processing and Fabrication and Some Properties of Boron Suboxide,* Presented at the Seventy-Second Annual Meeting, The American Ceramic Society, Philadelphia, Pennsylvania, May 4, 1970 (Society Symposium 4, Ceramic Armor, No. 7-S4-70)

[2] Pasternak, R. A., Acta Cryst. 12, 612-13 (1959).

[3] LaPlaca, S. and Post, B., Planseeber Pulvermet, Bd 9, 109-12 (1961).

[4] Rizzo, H. F., et al., J. Electrochem. Soc. 109, 1079-82 (1962).

[5] Post, B., *Refractory Binary Borides* in Roy M. Adams, Ed., Boron, Metalloboron Compounds, Interscience Publishers, New York, 301-71 (1964).

[6] Silver, H. A., and Bray, P. J., J. Chem. Phys., 11, 247 (1959).

[7] Novak, R., RCA Laboratories, private communication, Princeton, New Jersey.

[8] Corfield, P. W. R., Chemistry Department, Ohio State University, private communication, Columbus, Ohio.

[9] Hoard, J. L. and Hughes, R. E., *Elementary Boron and Compounds of High Boron Content: Structure, Properties and Polymorphism* in E. L. Muetterties, The Chemistry of Boron and Its Compounds, John Wiley and Sons, Inc. New York, 25-154 (1967).

[10] Longuet-Higgins, H. C. and Roberts, M. deV., Proc. Roy. Soc. (London) 230A, 110-19 (1955).

[11] Domagala, R. F. and Ruh, Robert, ASM Trans Quart. 62, 915-925 (1969).

[12] Baun, W. L. and Solomon, J. S. *Boron Bonding Studies Using the Electron Probe* Presented at the Twenty-Second Pittsburgh Conference on Analytical Chemistry and Applied Spectroscopy, Cleveland, Ohio, Feb. 28-March 5, 1971.

[13] Phillipi, C. M. Analytical Branch, Air Force Materials Laboratory, Wright-Patterson Air Force Base, Ohio, private communication.

[14] Carbonara, R. S., Letter Report on Contract F33615-71-C-1070 *Preliminary Experiments on the High Temperature Behavior of Boron Suboxide,* Sept. 3, 1971, Battelle Columbus Laboratories, Columbus, Ohio.

[15] Inghram, M. G., Porter, R. F. and Chupa, J., J. Chem. Phys. 25, 498-501 (1956).

DISCUSSION

R. S. Kirk: Your slide didn't show what was the temperature stability on your suboxide. How high could it go?

D. R. Petrak: That was the slide that wasn't shown. In a flowing helium atmosphere it begins to decompose at approximately 1000 °C.

National Bureau of Standards Special Publication 364, Solid State Chemistry, Proceedings of 5th Materials Research Symposium, issued July 1972.

TERNARY TRANSITION METAL SILICIDES AND GERMANIDES: ORDERING AND METAL-METAL BONDING IN Ni_2In-RELATED PHASES

Vancliff Johnson and Wolfgang Jeitschko

Central Research Department*
E. I. du Pont de Nemours and Company
Experimental Station
Wilmington, Delaware 19898

Ternary transition metal silicides and germanides with structures related to Ni_2In ("filled" NiAs) are reviewed. For compositions TT'Si and TT'Ge, where T is a transition metal from groups IV, V and VII and T' is from the iron group, the structures adopted are TiNiSi (ordered anti-$PbCl_2$), ordered Fe_2P, TiFeSi or Ni_2In. We describe and illustrate how these as well as the hexagonal Mn_5Si_3 structure are related.

Metal site occupancies in ternary TiNiSi and Fe_2P-type silicides and germanides and pseudobinaries with Ni_2In and Mn_5Si_3 structures are also reviewed. We discuss the importance of the relative size and electronegativity of the transition metal atoms and their d-electron configurations in determining site preferences.

Bonding in these Ni_2In-related phases, $(TT')_{2-x}Si(Ge)$, is discussed. The structures differ principally in the strengths of the respective T-T, T-T', and T'-T' metal-metal interactions. Questions as to how these are determined by electronegativities, size and d-electron configuration, and how they in turn affect phase stability and metal-site occupancies are raised.

Key words: Fe_2P and Mn_5Si_3; metal-metal bonding; metal-site occupancies; Ni_2In; ordered ternary silicides and germanides; silicides and germanides; ternary Ni_2In-related phases; TiNiSi.

1. INTRODUCTION

Ordered versions of the Co_2P (anti-$PbCl_2$), Fe_2P, and closely-related structures frequently occur among ternary silicides and germanides at compositions TT'Si and TT'Ge where T and T' are transition metals. These as well as the Mn_5Si_3 type are all closely related to Ni_2In ("filled" NiAs). True ternary phases, $(TT')_5Si_3$ based on the Mn_5Si_3 structure have not been found; however, in substitutional solid solutions ordering of the transition metal atoms occurs. The factors influencing ordering in all these phases pose interesting questions.

2. EQUIATOMIC TERNARY SILICIDES AND GERMANIDES

Many ternary phases are found at the compositions TT'Si and TT'Ge when T is a large, electropositive transition metal, for example Ti, and T' is from the iron group. With T from groups IV, V, and VII, the structures adopted are TiNiSi (ordered anti-$PbCl_2$), ordered Fe_2P, its distorted version, TiFeSi, or Ni_2In. With T from group VI, the known equiatomic ternary phases possess the $MgZn_2$ structure (T = Mo or W). The occurrence of these phases [1-12][1] is summarized in table 1. The TiNiSi type occurs most frequently with silicides and germanides while the Fe_2P and TiFeSi types occur mainly with rare earths as T component and elements from the aluminum group replacing Si or Ge [13]. The Ni_2In and $MgZn_2$ structures

*Contribution No. 1879

[1] Figures in brackets indicate the literature references at the end of this paper.

Table 1

Occurrence of Ternary Equiatomic Transition Metal Silicides and Germanides TT'Si(Ge).

	SILICIDES					GERMANIDES				
T= \ T'=	Mn	Fe	Co	Ni	Cu	Mn	Fe	Co	Ni	Cu
Ti	○	●	□	□	□		●	○	□	□
Zr		□	□	□	□		□	□	□	□
Hf		□	□	□	□		○	□	□	□
V			□	□				□	□	
Nb	○	□	□	□		○	●	□	□	
Ta	●	□	□	□		●	□	□	□	
Cr										
Mo		x	x	x						
W		x	x	x						
Mn			□	□			△	△	△	
	Tc	Ru	Rh	Pd	Ag	Tc	Ru	Rh	Pd	Ag
Ti		●	□	□						
Zr		○		□			●	□	□	
Nb								□		
Mn			□							

□ TiNiSi (anti-$PbCl_2$) x $MgZn_2$

○ Fe_2P △ Ni_2In

● TiFeSi

occur infrequently at these compositions though the latter occurs in most of the ternary systems in the pseudobinary sections $T(T'_{1-x}Si_x)_2$ with $x \sim 1/3$ [14-16]. The $MgZn_2$ structure is not apparently related to the others and will not be further discussed.

3. STRUCTURAL RELATIONSHIPS

The Ni_2In structure is generally regarded as a "filled-up" version of the NiAs structure. In NiAs the metalloid atoms (As) form a hexagonal close-packed array with octahedral and trigonal by-pyramidal voids. Metal atoms occupy only octahedral voids in NiAs but both in Ni_2In. MnP and TiNiSi are similarly related. The MnP structure derives from NiAs by small atomic displacements (figure 1); likewise the TiNiSi structure may be regarded as a distorted Ni_2In structure [17]. The Fe_2P type structure is not directly derived from Ni_2In. However, as can be seen in figure 1, nearest neighbor environments are very similar to TiNiSi. The TiFeSi structure is very closely related to the ordered Fe_2P type structure [9] and nearest neighbor environments are virtually identical. For the purpose of the present paper it may be regarded as identical to ordered Fe_2P.

In all these structures the basic triangular prismatic coordination of the metalloid atom is retained; the metalloid has six close metal neighbors in NiAs and MnP while three additional metal atoms are in the center of the rectangular prism faces in Ni_2In, TiNiSi and Fe_2P. Nearest neighbor environments for the metal atoms are summarized in table 2. In TiNiSi and ordered Fe_2P (*e.g.* TiCoGe) the large transition metal, T, has five Si or Ge atoms as nearest neighbors which form a quadratic pyramid. The small transition metal, T', has four Si or Ge neighbors in a tetrahedral configuration. The number of nearest metal neighbors is the same for the corresponding T and T' atoms although their relative arrangements differ somewhat (figure 1).

The Mn_5Si_3 structure may also be regarded as related to NiAs [18]. Figure 2 shows in projection the Ni_2In and Mn_5Si_3 structures. The hexagonal close-packed arrangement of metalloid atoms is retained in Mn_5Si_3 but 1/3 of the octahedral positions which are filled in Ni_2In are empty. The remaining octahedral and trigonal prismatic voids of the hexagonal close-packed metalloids are filled. A shift of the T' atoms towards the empty octahedral sites distorts the structure from the ideal Ni_2In arrangement. These voids are filled with C, Ga or Cu in $Mo_{\leq 5}Si_3C_{\leq 1}$ [19], Ti_5Ga_4 [20] and Hf_5Sn_3Cu [21]. Transition metal atoms are in two

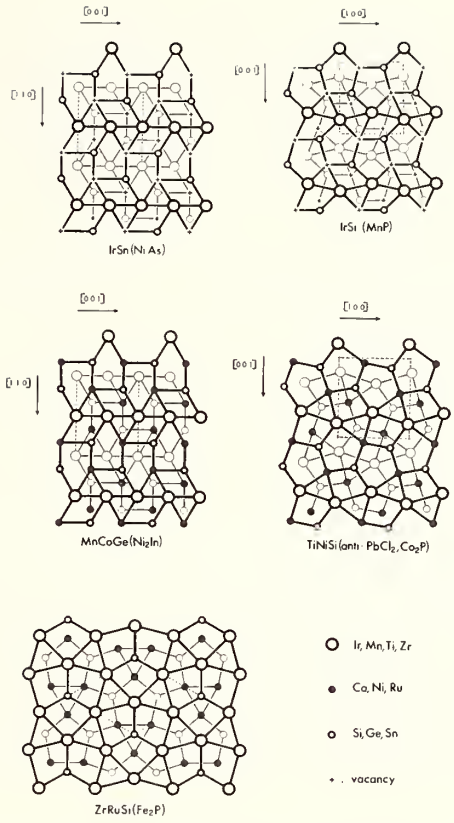

Fig. 1. Projections of the structures of IrSn, IrSi, MnCoGe, TiNiSi, and ZrRuSi. The respective structure types are given in parentheses. Atoms connected by thick lines are separated by half a translation period in the projection direction. Atoms and vacancies are connected to emphasize relationships and differences among the structures [12].

Table 2

Atomic Coordinations of the Transition Metal Atoms in Some Ni_2In-related Phases

Structure	Space Grp	Position	Metalloid Coordination	Total Coordination[a]	Metal Atom
Ni_2In	$P6_3/mmc$	2a	octahedral	6 + 2 + 6	T
		2d	trigonal bi-pyramidal	5 + 0 + 6	T'
TiNiSi	Pnma	4c	pyramidal	5 + 4 + 6	T
		4c	tetrahedral	4 + 2 + 6	T'
Fe_2P	$P\bar{6}2m$	3g	pyramidal	5 + 4 + 6	T
		3f	tetrahedral	4 + 2 + 6	T'
Mn_5Si_3	$P6_3/mcm$	4d	octahedral	6 + 2 + 6	T
		6g	trigonal bi-pyramidal	5 + 6 + 4	T'

[a]The three sequential coordination numbers refer to metalloids, metal atoms of like kind, and unlike metal atoms, respectively.

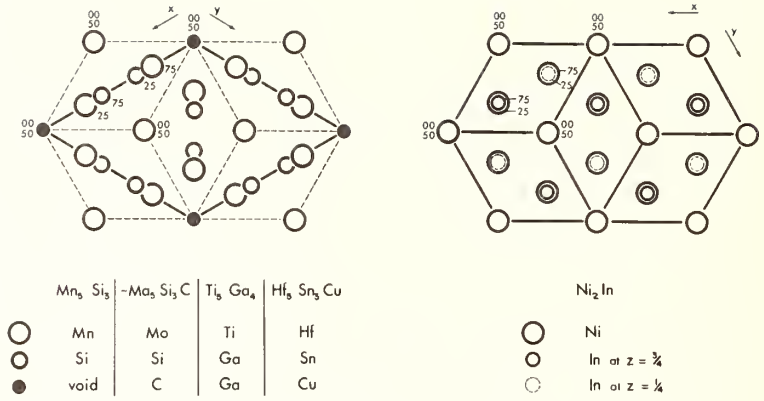

Fig. 2. Relationship between Ni_2In, Mn_5Si_3 and filled Mn_5Si_3 structures.

inequivalent sites (T in 4*d* and T' in 6*g*). The T atom has six metalloid neighbors in a distorted octahedral arrangement. The octahedra share faces along the *c* axis thus giving two close T neighbors (figure 3). Six T' neighbors also forming an octahedron complete the T environment. The T' atom is surrounded by a distorted bypyramid of metalloid atoms, six T' and four T atoms. The T' atoms form octahedra that share faces along c at each corner of the unit cell. The metalloid atoms are coordinated by 4 T and 5 T' atoms in a distorted triangular prismatic arrangement.

4. METAL-SITE OCCUPANCIES

4.1. Ni_2In-TYPE PHASES

This structure is infrequently found for true equiatomic ternary silicides and germanides but is frequently found among binaries and pseudobinaries with large homogeneity ranges not including the T_2X composition. In fact its nonstoichiometry and frequent existence as a high temperature phase are marked characteristics. This is also true of the parent NiAs phases.

For phases with compositions between $Fe_{1.67}Ge$ and $Fe_{1.77}Ge$ it has been shown [22,23,24] that the vacancies occur on the T' (trigonal by-pyramidal, 2*d*) sites. Yasukochi et al. [25] suggest this also for $Mn_{2-x}Sn$, $Fe_{2-x}Sn$, $Co_{2-x}Sn$, and $Ni_{2-x}Sn$ with this structure. Castelliz

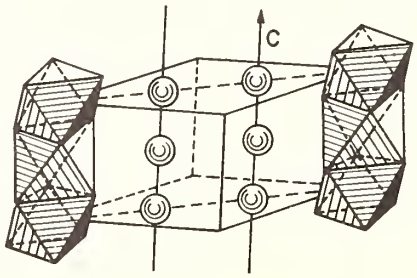

Fig. 3. Mn_5Si_3 structure showing chains of 4*d* metal atoms and chains of octahedra formed by 6*g* metal atoms. Si atoms and octahedral chains at two corners of the unit cell are omitted [38].

[1] was the first to determine the ordering scheme for MnNiGe from x-ray data and this places Mn on the T position. This is plausible since Mn is the larger of the two transition metals and the T position has the higher coordination number. One of the most studied pseudobinary is $(MnFe)_{2-x}Ge$. Suzuoka et al. [26] have reported an ordered ternary phase $Mn_{0.9}Fe_{0.9}Ge$ in which Mn also occupies the T (octahedral, 2*a*) sites. Austin [27] has also shown that Mn perferentially substitutes for Fe in the T positions for the part of the $(Mn,Fe)_{1.67}Ge$ system that has the Ni_2In structure.

4.2. TiNiSi-TYPE PHASES

Ordering of the metal atoms in ternary anti-$PbCl_2$ type structures has been determined by single crystal x-ray studies for TiNiSi [3], ZrFeP [28] and MoCoB [29]. In all cases the larger and more electropositive T atom occupies the site of higher coordination.

It has been pointed out [30] that compounds with the anti-$PbCl_2$ structure can be divided into two main groups, depending on the a/c ratio (setting Pnma) with considerable differences in the number of nearest neighbors. The length of the short b axis has been taken as an additional parameter determining the coordination number [29]. A convenient expression for this is (a + c)/b. The two parameters group the various $PbCl_2$ structures (figure 4). Since the atomic parameters are similar within any one group, the coordination polyhedra differ only slightly within the group, but are entirely different going from one group to another. The ternary anti-$PbCl_2$ phases therefore belong to the Co_2P sub-group whereas the binary silicides and germanides belong to the Co_2Si sub-group.

An interesting question is whether the size factor is the only factor determining the site ordering of the metal atoms in these phases. In all cases where the T atoms were found on the site with the higher coordination number the T atoms also possess a lower number of d electrons and are more electropositive, hence these results do not separate size and electronic effects. Wäppling et al. [31] have emphasized this and have also shown from Mössbauer

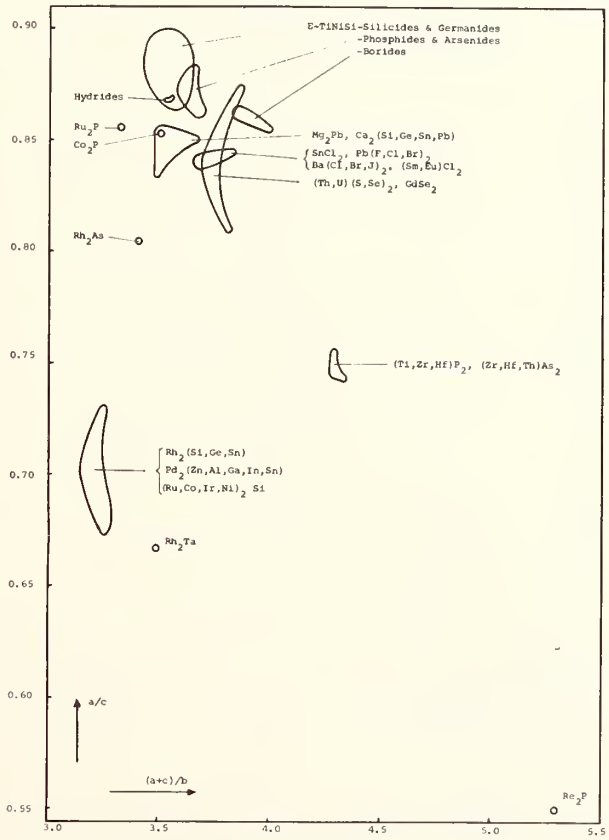

Fig. 4. Grouping of $PbCl_2$ type compounds according to their axial ratios [29].

measurements on $Fe_xCo_{2-x}P$ and $Ru_{2-x}Fe_xP$ with the anti-$PbCl_2$ structure that the larger atoms prefer the T site. In both cases, however, the materials could possess large degrees of disorder depending on composition, suggesting that the size factor is not overwhelming.

We have found that MnRhSi has the anti-$PbCl_2$ structure. Since Rh is larger than Mn (Mn has fewer d electrons) site occupancies for this compound should indicate the relative importance of size and electronic factors. Calculated x-ray intensities for both ordering schemes as well as a disordered arrangement of Mn and Rh are compared in table 3. The data indicate that Mn preferentially occupies the T site, while the larger atom, Rh, prefers the T' site[2]. These results therefore point to d-electron configuration or electronegativity of the participating atoms as most influential in site occupancies.

It has previously been pointed out [32] that in phosphides, silicides, and germanides with TiNiSi and Fe_2P structures the ordering energy is apparently large since their homogenity ranges are extremely restricted to ideal compositions such as ZrFeP, NbMnSi and MnNiSi. For example though atomic sizes are favorable and Ni_2Si and Co_2Si possess the anti-$PbCl_2$ structure (Co_2Si branch), Mn is not soluble in them to a large extent, but the phases MnCoSi and MnNiSi are found with the TiNiSi structure. Furthermore the ternary phases also have restricted phase fields so that mutual substitution of the metal atoms is probably quite small. These results also suggest that factors other than size contribute greatly to the ordering energy.

Table 3

Calculated and observed intensities (powder diffractometer data; CuKα radiation) for MnRhSi. Positional parameters of TiNiSi [3] were used for the calculation.

hkℓ	d_c	I_c [a]			I_o	Fit [b]
		Geometric	Random	Valence		
101	4.681	2	25	71	24	R
002	3.569	4	0	9	7	
011	3.352	27	5	1	2	V,R
200	3.100	27	24	29	19	
102	3.093					
111	2.949	17	41	72	39	R
201	2.843	0	0	3	--	
210	2.401	100	100	100	100	
112	2.398					
202	2.340	19	13	9	11	R,V
211	2.276	84	58	35	43	V,R
103	2.221	53	41	29	14	V
013	2.016	21	28	36	32	V,R
212	1.992	2	7	17	17	V
301	1.985	23	28	33	36	V
113	1.917	4	5	7	13	V
020	1.898	37	42	46	50	V
203	1.888					
302	1.788	4	5	5	6	
004	1.785					

a/ Intensity calculations were done for the ordering schemes: Geometric - Mn in tetrahedral and Rh in pyramidal site; Random - random distribution of Mn and Rh; Valence - Mn on pyramidal and Rh on tetrahedral site.

b/ It can be seen that the data indicate site preferences according to the valence scheme.

[2]It would appear that the space-filling principle is violated; however, the coordinations of these sites probably adjust to give a slightly different structure from that of TiNiSi. A complete structure determination on MnRhSi should therefore be of interest.

4.3. Fe_2P-TYPE PHASES

Kripjakevic et al. [33] were the first to report the ordering (table 4) for the equiatomic phases in the systems (Zr,Hf)-Ni-(Al,Ga). Analogous occupancies were found for CeNiAl [13]. In these structures the Al atom is on the 3*f* site, and the T' atom is found on 2*c* and 1*b* which sites correspond to the metalloid positions in TiNiSi. On the other hand, the site occupancies found for the ternary borides, silicides, germanides and the pseudobinary phosphides listed in table 4 correspond to the ones found for the TiNiSi structure.

At first it may seem surprising that, for example, the Ni atoms in CeNiAl and ZrNiAl do not correspond to the Fe atoms in NbFeB. There are, however, structure-chemical arguments for the support of both ordering schemes [9]: (a) Both Ni and B are the elements with the smallest atomic volume in their respective compounds; they are therefore well-suited for the 2*c* and 1*b* sites which have the lowest coordination number. (b) Although aluminum is chemically related to boron, silicon and germanium, it is known to behave sometimes like a transition metal. For example, it is found in such typically inter-transition-metal structures as the σ-phase structure (σ-Nb_2Al and σ-Ta_2Al). This makes the correspondence of the Al atom in ZrNiAl with the Fe atom in NbFeB at least plausible. (c) In intermetallic phases of the large transition metals of groups three and four with group eight elements, the elements of the eighth group frequently occupy the boron positions in structure types such as CrB, FeB and AlB_2 (for examples see the compilation by Pearson [16]) and thus have a coordination of nine nearest neighbors which is also the case for the Ni atoms in CeNiAl and ZrNiAl. (d) The isotypy of many borides, phosphides, silicides and germanides, on the other hand, supports the atomic order of NbFeB, NbMnSi, and TiCoGe.

In all Fe_2P-type ternary phases the T atom is on the 3*g* site which has the larger coordination number. Thus the principle of good space filling is well preserved.

4.4. $(TT')_5Si_3$

The number of binary and ternary Mn_5Si_3 type and the various "filled" Mn_5Si_3 type phases is close to 200. In this account we limit ourselves to a review of site ordering on the 4*d* and 6*g* metal positions.

Several $(TT')_5Si_3$ systems have been studied. Schachner et al. [35] showed that in the pseudobinary section Ti_5Si_3-Mo_5Si_3 the Mn_5Si_3 structure extends from Ti_5Si_3 up to $Ti_3Mo_2Si_3$ while in Ti_5Si_3-W_5Si_3 the substitution of Ti extends only up to $Ti_{3.75}W_{1.25}Si_3$. In both systems it was shown through x-ray studies that both Mo and W preferentially occupy the 4*d* position. In $(Mn,Re)_5Si_3$, Re occupies the 6*g* position preferentially [36].

Recent Mössbauer effect and magnetic studies of the $(Mn,Fe)_5Si_3$ series have been carried out by Narasimhan et al. [37] and by Johnson et al. [38]. The two studies are not in complete agreement but both show that Fe preferentially enters 4*d* with a small amount of disorder. Compositional dependence of the lattice parameters, c/a ratios and magnetic moments of ferromagnetic compositions are also consistent with this ordering scheme [38].

Table 4

Atomic Order in Fe_2P-Type Structures (Space Group $P\bar{6}2m$-D_{3h}^3)

Phase	Pyramidal 3(g)	Tetrahedral 3(f)	2(c) and 1(b)	Reference
ZrNiAl	Zr	Al	Ni	33
CeNiAl	Ce	Al	Ni	13
NbFeB	Nb	Fe	B	34
NbMnSi	Nb	Mn	Si	6
TiCoGe	Ti	Co	Ge	9
ZrRuSi	Zr	Ru	Si	12
MnFeP	Mn	Fe	P	32
CrFeP	Cr	Fe	P	32

In all these systems, the larger atom occupies the position of higher coordination; again, with the exception of $(Mn,Re)_5Si_3$, the larger atom is both more electropositive and has fewer d electrons so these studies do not distinguish what influences atomic order most. That the $(Mn,Fe)_5Si_3$ system is ordered despite the relatively small size difference between Mn and Fe does point to the importance of electronic factors.

5. BONDING

In all the structures discussed, the basic triangular prismatic coordination of the metalloid is retained as in NiAs. This suggests similar metal-metalloid bonding. Axial ratios of these Ni_2In-related phases indicate that metal-metal interactions are important. We attempt to assess the importance of these for the formation of these phases and in the particular structure type adopted.

For highly positive cations short metal-metal distances introduce core electrostatic repulsions, so these structures are not adopted by ionic compounds. However, in compounds of the transition metals with the less-electronegative metalloids (IIIB, IVB and VB), the effective charges on the metal atoms are small, and metal-metal bonding more than compensates for the electrostatic repulsions due to short metal-metal distances. These ideas have been suggested by Goodenough [39] who discussed the crystal chemistry of binary pnictides and chalcogenides with NiAs-related structures. The influence of metal-metal bonding and its increased importance in the highly covalent metalloid phases are illustrated by the following empirical findings [40]:

(a) NiAs phases do not occur among the more ionic oxides and halides, nor with nontransition metals that are not capable of d-electron metal-metal bonding.

(b) The MnP structure, with an even greater number of short metal-metal distances than the NiAs structure, occurs when the metalloid is of groups IVB and VB but seldom when it is the more electronegative chalcogen.

(c) There is a tendency to form "metal-filled" NiAs-related structures with more and shorter metal-metal distances as the metalloid component becomes less electronegative.

Since bonding between transition metals and silicon or germanium is essentially covalent, metal-metal bonding apparently contributes enough to the binding energy so that "metal-filled", NiAs-related structures are frequently found for phases with these elements. The structures in general differ in the strengths of the respective metal-metal interactions T-T, T-T', and T'-T'[3] [12]. In TiNiSi and ZrRuSi all three interactions are significant whereas in Ni_2In only the T-T and T-T' are present. In these three types the T-T' interaction is strongest whereas in Mn_5Si_3 the T-T and T'-T' interactions are much stronger than the T-T'. The metal-metal interactions are obviously quite sensitive to electronegativities, d-electron configurations, and relative size of the metal and metalloid. The particular structure is therefore stabilized where these factors are such as to give the optimum binding energy. It has also been argued [38] that the extremely close approach of metal atoms in 4*d* of Mn_5Si_3 may account for this site preference by the less electropositive atom.

In TiNiSi and ZrRuSi the T'-T' distances are much shorter than in MnCoGe. There is therefore a larger number of metal-metal bonds in the TiNiSi and ordered Fe_2P types than in Ni_2In. The seeming unimportance of the T'-T' interactions to the stability of the Ni_2In structure may well account for the frequent occurrence of this structure for phases with extended homogeneity ranges arising from variability in the T' concentration. Conversely, phases with the anti-$PbCl_2$ and Fe_2P structures usually exist over more restricted ranges. Also, the Ni_2In structure in preference to the Co_2Si structure is found for iron group phases with the larger metalloids Ge and Sn presumably because, with Ge and Sn in combination with the relative small iron group metals, metal-metal bond strengths are necessarily reduced. This is also consistent with the fact that Ni_2In frequently occurs as a high temperature phase.

---

[3] The relative strengths of the various interactions can be approximated by the Pauling valence method [38], or more qualitatively by comparing interatomic distances to radius sums [12].

For $(Mn,Fe)_5Si_3$, it has been shown [38] that the magnetic moments of the component atoms can be explained in terms of MO theory if valences of III and II are assumed for M_I and M_{II}. These valences are also consistent with Mössbauer results and Pauling valences of the metal atoms with respect to Si. High or low-spin configurations for these atoms are not meaningful concepts since the magnetic moments will depend on the details of the metal-metal interactions (total d-band structure).

6. CONCLUSION

Additional studies of site occupancies and d-electron configurations of the metal atoms in these phases will allow further insight into the factors that determine stabilities and site preferences.

7. REFERENCES

[1] Castelliz, L., Monatsh. Chem. 84, 765 (1953).
[2] Gladysheveskii, E. I., and Kuz'ma, Yu B., Russ. J. Structural Chem. (Eng. Trans.) 1, 57 (1960).
[3] Shoemaker, C. B. and Shoemaker, D. P., Acta Crystallogr. 18, 900 (1965).
[4] Ganglberger, E., Nowotny, H., and Benesovsky, F., Monatsh. Chem. 98 95 (1967).
[5] Nickl, J. J. and Sprenger, H., Naturwissensch. 54, 248 and 515 (1967).
[6] Deyris, B., Roy-Montreuil, J., Fruchart, R., and Michel, A., Bull. Soc. Chim. Fr. 1968, 1303 (1968).
[7] Roy-Montreuil, J., Deyris, B., Fruchart, R., and Michel, A., C. R. Acad. Sci. Paris 262C, 615 (1968).
[8] Jeitschko, W., Jordan, A. G., and Beck, P. A., Trans. Met. Soc. AIME 245, 335 (1969).
[9] Jeitschko, W., Acta Cryst. B26, 815 (1970).
[10] Jeitschko, W., Met. Trans. 1, 2963 (1970).
[11] Deyris, B., Roy-Montreuil, J., Roault, A., Fruchart, R., and Michel, A., C. R. Acad. Sc. Paris 273C, 47 (1971).
[12] Johnson, V. and Jeitschko, W., J. Solid State Chem. 4, 123 (1972).
[13] Dwight, A. E., Mueller, M. H., Conner, R. A., Jr., Downey, J. W., and Knott, H., Trans. Met. Soc. AIME 242, 2075 (1968).
[14] Kuz'ma, Yu B., Gladyshevskii, E. I., and Cherkashin, E. E., Russ. J. Inorg. Chem. (Engl. Trans) 9, 1028 (1964).
[15] Bardos, D. I. and Beck, P. A., Trans. Met. Soc. AIME 236, 64 (1966).
[16] Pearson, W. B., *Handbook of Lattice Spacings and Structures of Metals and Alloys*, Vol 2, Pergamon Press, N. Y. (1967).
[17] Jellinek, F., Österr. Chem. Zeit. 60, 311 (1959).
[18] Nowotny, H., and Parthé, E., Planseeber. 2, 34 (1954).
[19] Parthé, E., Jeitschko, W., and Sadagopan, V., Acta Cryst. 19, 1031 (1965).
[20] Pötzschke, M. and Schubert, K., Z. Metallkde. 53, 474 (1962).
[21] Rieger, W., Nowotny, H., and Benesovsky, F., Monatsh. Chem. 96, 98 (1965).
[22] Kanematsu, K. and Yasukochi, Ko., J. Phys. Soc. Japan 18, [10], 1429 (1963).
[23] Forsythe, J. B. and Brown, P. J., *Proc. Int. Conf. Magnetism, Nottingham, England,* 1964, p. 524.
[24] Adelson, E., and Austin, A. E., J. Phys. Chem. Solids 26, 1795 (1965).
[25] Yasukochi, Ko and Kanematsu, K., J. Phys. Soc. Japan 17, Suppl. B-I, 165 (1962).
[26] Suzuoka, T., Adelson, E., and Austin, A. E., Acta Cryst. A24, 513 (1968).
[27] Austin, A. E., J. Appl. Phys. 40, 1381 (1969).
[28] Rundqvist, S., and Nawapong, P., Acta Chem. Scand. 20, 2250 (1966).
[29] Jeitschko, W., Acta Cryst. B24, 930 (1968).
[30] Rundqvist, S., Arkiv Kemi 20, 67 (1962).
[31] Wäppling, R., Häggström, L., Rundqvist, S., and Karlsson, E., J. Solid State Chem. 3, 276 (1971).
[32] Fruchart, R., Roger, A., and Senateur, J. P., J. Appl. Phys. 40, 1250 (1969).
[33] Kripjakevic, P. I., Markiv, V. Ja., and Melnyk, Ja. V., Dopov. Akad. Nauk, Ukr. RSR A29, 750 (1967).
[34] Kuz'ma, Yu B., Dopov. Akad. Nauk. Ukr. RSR A29, 939 (1967).
[35] Schachner, H., Cerwenka, E., and Nowotny, H., Monatsh. Chem. 85, 245 (1954).
[36] Setz, S., Nowotny, H., and Benesovsky, F., Monatsh. Chem. 99, 2004 (1968).

[37] Narasimhan, K. S. V. L., Reiff, W. M., Steinfink, H., and Collins, R., J. Phys. Chem. Solids 31, 1511 (1970).
[38] Johnson V., Weiher, J. F., Frederick, C. G., and Rogers, D. B., J. Solid State Chem. 4, 311 (1972).
[39] Goodenough, J. B., *Lincoln Technical Report 345*, 1964, p. 11-12.
[40] Kjekshus, A., and Pearson, W. B., Prog. in Solid State Chem. 1, 89 (1964).

DISCUSSION

E. Kostiner: You seem to be treating these compounds as having stoichiometries that are as written. Have you investigated, chemically or physically, deviations of stoichiometry?

V. Johnson: This point has been looked at by several people, in particular for the titanium nickel silicide and the Fe_2P type structures. I have looked at this myself and what was initially quite surprising is that in these two structures the range of homogeneity is quite narrow. This would suggest that there is very little mutual replacement of the two transition metal atoms on the two sites. This is not true for the nickel 2 indium (Ni_2In) structure where the ranges of homogeneity are much, much wider.

III. CHALCOGENIDES

National Bureau of Standards Special Publication 364, Solid State Chemistry, Proceedings of 5th Materials Research Symposium, issued July 1972.

STRUCTURAL TRANSITIONS OF SOME TRANSITION-METAL CHALCOGENIDES

F. Jellinek

Laboratorium voor Anorganische Chemie
Materials Science Center of the University
Groningen, The Netherlands

A survey is given of some recent investigations on transition-metal chalcogenides (sulfides, selenides, tellurides) carried out in the author's laboratory; particular attention is paid to compounds undergoing structural transitions at elevated temperatures. Examples are given of transitions involving a change of the coordination of the metal ($NbSe_2$, TaS_2, $TaSe_2$, $MoTe_2$; Ni_3Se_2), of order-disorder transitions ($AgCrSe_2$ and related compounds; chromium sulfides, $Ni_{3\pm x}Te_2$), and of transitions involving distortions of the structure (CrS; VS, $Nb_{1-x}S$). The occurrence of trigonal-prismatic coordination in several transition-metal chalcogenides is ascribed to d-covalency which stabilizes trigonal-prismatic with respect to octahedral coordination for ions with a d^0, d^1 or spin-paired d^2 configuration. The effect of the metal coordination on the physical properties of the compound is also described. The distributions of occupied and vacant metal sites in transition-metal chalcogenides $M_{1+p}X_2$ are discussed (chromium sulfides, zirconium selenides), as is the concept of "occupation waves" (titanium sulfides). In $Ni_{3\pm x}Te_2$ occupation waves lead to a phase lacking three-dimensional periodicity; the intervention of this phase allows smooth transitions from the disordered high-temperature form to the ordered low-temperature forms (two-step second-order transition).

Key words: Dichalcogenides; intercalation compounds; layer structures; modulated structures; occupation waves; selenides; semiconductor-to-metal transitions; structure transitions; sulfides; tellurides; transition-metal chalcogenides; trigonal-prismatic coordination.

1. INTRODUCTION

The crystal chemistry of the chalcogenides (sulfides, selenides, tellurides) of transition metals differs greatly from that of the oxides of the same elements. There are several reasons for this difference in behaviour. Sulfur, selenium and tellurium are much less electronegative than oxygen. While most transition-metal oxides may be described as containing O^{2-} ions, in several chalcogenides (part of) the non-metal is present as X^- (X = S, Se, Te); often, the X^- ions form pairs $(X_2)^{2-}$ [1][1]. The chalcogenide ions S^{2-}, Se^{2-} and Te^{2-} have much higher polarizabilities than has the oxide ion O^{2-}. Therefore, layer structures and other structures with polar surroundings of the anions are quite common among the chalcogenides, but not for oxides. Actually, all dichalcogenides of transition metals have either layer structures or structures with $(X_2)^{2-}$ anions. Finally, the chalcogenide ions have d-orbitals of accessible energy, which may participate in covalent bonds with the transition metal. Therefore, the chalcogenide ions often have surroundings that are unusual for oxide ions, for instance the trigonal-prismatic coordination of the anions found in chalcogenides of the NiAs type and related structure types [2].

In the present communication we shall discuss some recent investigations carried out in Groningen, particularly those on transition-metal chalcogenides that undergo structural transitions at elevated temperatures. It need not be emphasized that such transitions have great

[1] Figures in brackets indicate the literature references at the end of this paper.

465-504 O - 72 - 41

influence on the high-temperature behaviour of the materials; often, the structure transitions also affect the mechanical, electrical, optical or magnetic properties which are of importance for various applications. The examples we shall discuss comprise changes of the coordination of some ions, distortions of the structures, order-disorder transitions and combinations of these phenomena.

2. DICHALCOGENIDES

As mentioned, many dichalcogenides of transition metals have layer structures [3]. The dichalcogenides of Ti, Zr, Hf have structures of the $Cd(OH)_2$ type with axial ratios c/a near the ideal value of 1.63; the coordination of the metal is octahedral. The same structure type is found for the ditellurides of some group VIII metals, but here the c/a ratio is considerably smaller, probably due the mutual repulsion of the electrons in the dt_{2g} levels of the metals, which levels are more than half filled. These levels are less than half filled in the ditellurides of V, Nb, Ta, Mo (h.t. form) and W which also have layer lattices with the metal in essentially octahedral coordination; however, their structures are distorted due to the presence of (zigzag or more complex) metal-metal chains. In $ReSe_2$ [4], ReS_2, and probably also in the corresponding Tc compounds [5] the metal atoms form clusters which are again linked to chains.

The disulfides and diselenides of Nb, Ta, Mo and W are polymorphic [1,3]. At room temperature these compounds (and also $MoTe_2$) have layer structures with trigonal-prismatic coordination of the transition metal. Molecular-orbital calculations indicate that d-covalency provides a stabilizing factor for trigonal-prismatic with respect to octahedral coordination for ions with a d^0, d^1 or spin-paired d^2 configuration. In trigonal-prismatic coordination the (antibonding) d-level lowest in energy is an a_1 level. This explains that the disulfides and diselenides of Nb and Ta, where the metal has d^1 configuration, are metallic, while the corresponding compounds of Mo and W with d^2 metal ions are diamagnetic semiconductors [2].

At about 850 °C, $MoTe_2$ undergoes a transition leading from trigonal-prismatic to (distorted) octahedral coordination of the cation; this transition is accompanied by a change from semiconducting to metallic properties, as can readily be understood from a band-structure model [6]. In $NbSe_2$ [7], TaS_2 [8,9] and $TaSe_2$ [10] again trigonal-prismatic coordination of the metal is stable at room temperature, octahedral coordination at high temperatures; in the intermediate temperature range modifications are found in which layers with the two types of coordination alternate. The structures of the various forms of $TaSe_2$ are shown in figure 1, their thermal relationships in the following scheme [10]:

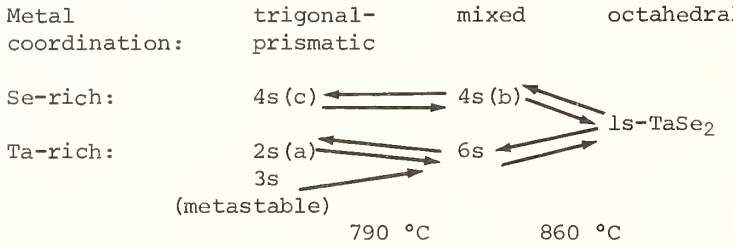

The ls-forms of TaS_2 and $TaSe_2$ with structures of the $Cd(OH)_2$ type can easily be retained at room temperature by quenching. Remarkably enough, these forms are diamagnetic semiconductors at low temperatures [9,11], while the other forms of TaS_2 and $TaSe_2$ are metallic. The diamagnetism of ls-TaS_2 and ls-$TaSe_2$ may be explained by considering the term scheme of a d^1 ion in octahedral coordination [12]; the $^2T_{2g}$ level is split by spin-orbit coupling giving a ground state (Γ_8) with zero magnetic moment, since g = 0. Nevertheless, the spins of the Ta^{4+} ions (S = 1/2) will probably order at low temperatures; indeed, ls-TaS_2 and ls-$TaSe_2$ may be diamagnetic antiferromagnets or even diamagnetic ferromagnets at low temperature! Thus, spin-orbit coupling stabilizes the d^1 configuration in octahedral coordination, while the stabilization of $d^2(+d^0)$ is smaller. Probably, this difference in stabilization causes ls-TaS_2 (and also $BaTaS_3$, $BaTaSe_3$) to be a semiconductor at low temperatures, while isostructural VSe_2 (and $BaVS_3$) where spin-orbit coupling is much weaker, is metallic [11].

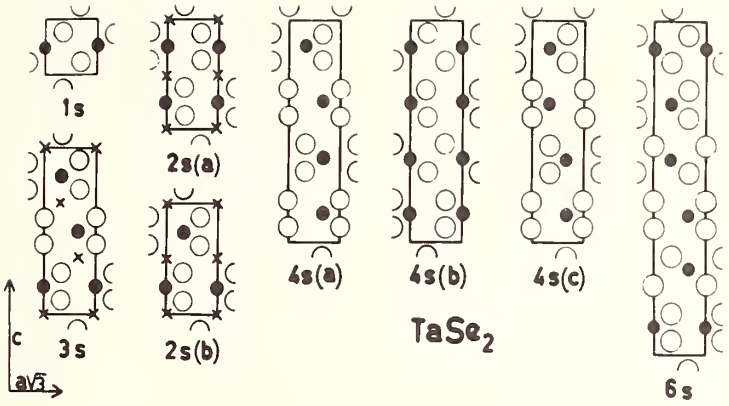

Fig. 1. Sections through the hexagonal (110) planes of the polymorphic forms of $TaSe_2$. Metal atoms are indicated by black circles, chalcogen atoms by open circles.

3. INTERCALATION COMPOUNDS A_pMX_2

The dichalcogenides of Nb and Ta with trigonal-prismatic coordination of the metal exist in several polytypic forms of nearly the same energy, which differ only in the stacking of the XMX slabs (X = S, Se; M = Nb, Ta). It is understandable, therefore, that stacking faults are frequently observed, for instance by the broadening and weakening of diffraction lines with $h-k \neq 3n$ in x-ray powder patterns. The stacking order is greatly improved if additional metal atoms are inserted between the NbX_2 or TaX_2 slabs. This is the case in the phases $M_{1+p}X_2$ ($0 < p < 0.3$ for X = Se [13]) shown in figure 2, and also in ternary phases A_pMbX_2 and A_pTaX_2, where A may be Cu or Ag ($p \simeq 2/3$), a 3d transition metal ($p \leq 1/2$ or $1/3$), an alkali metal ($p \simeq 2/3$) or Eu. The Cu and Ag atoms lie in tetrahedral holes between the NbX_2 or TaX_2 slabs [14], 3d transition metals [15,16] and the light alkali ions in octahedral holes, the heavy alkali ions [17] and Eu^{2+} [18] in trigonal-prismatic holes. The latter surrounding can be understood by regarding the metal ions as d^0 ions [2].

In all these phases A_pMX_2 the Nb or Ta atoms in the MX_2 slabs have an electron configuration between d^1 and d^2 and again a trigonal-prismatic coordination. In corresponding compounds of Mo and W these atoms would have a configuration between d^2 and d^3 and trigonal-prismatic coordination is no longer expected to be stable. Indeed, such intercalation compounds derived from MoX_2 or WX_2 are not known, except for the highly reactive and unstable compounds A_pMoX_2 and A_pWX_2 ($p \simeq 1/2$) where A is an alkali metal [19]. $CoMo_2S_4$ [20] and similar compounds have Mo in essentially octahedral coordination.

Many other compounds A_pMX_2 are known where M is a transition metal in octahedral coordination. We mention only a few examples. In A_pTiS_2 where A is an alkali metal ($p = 0.5 - 0.8$), the coordination of Ti is octahedral; the coordination of the alkali metals Li and Na is also octahedral, but that of K and Cs trigonal-prismatic [21]. In $CuCrX_2$ and $AgCrX_2$ (X = S, Se) the Cu and Ag atoms lie in tetrahedral holes between the CrX_2 slabs [22], though not in the centers of these holes. At room temperature Cu and Ag occupy half of the tetrahedral holes in a polar arrangement, at high temperatures they are distributed over all tetrahedral holes (fig. 3). The transition temperature of this order-disorder transformation lies at 200 °C for $AgCrSe_2$, at about 400 °C for the sulfide compounds [23].

4. PHASES $M_{1+p}X_2$

Several transition-metal chalcogenides $M_{1+p}X_2$ have structures intermediate between the $Cd(OH)_2$ type ($p = 0$) and the NiAs type ($p = 1$) with octahedral coordination of the cations. Completely and partly (fraction p) filled metal layers alternate (fig. 4a). In most phases

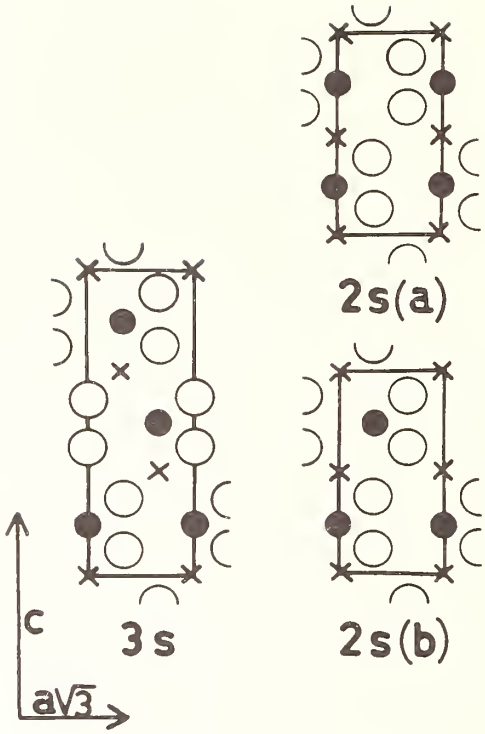

Fig. 2. Sections through the hexagonal (110) planes of the phases $Nb_{1+p}X_2$ and $Ta_{1+p}X_2$ (X=S,Se). Chalcogen atoms are indicated by open circles, fully occupied metal positions by black circles, partly occupied metal positions by crosses.

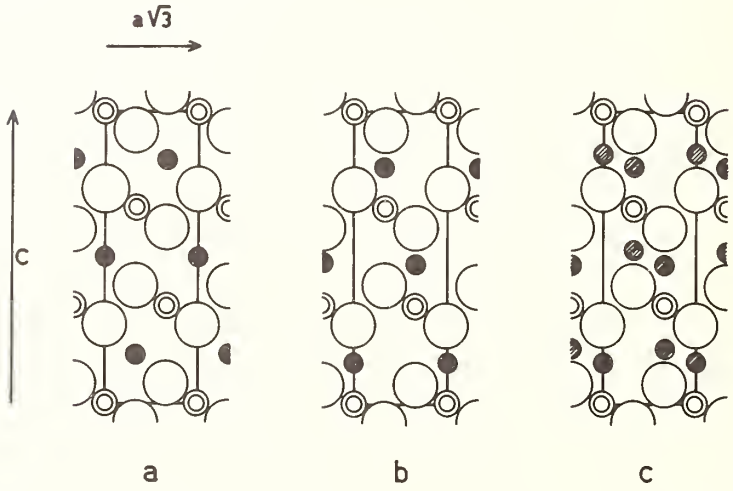

Fig. 3. Sections through the hexagonal (110) planes of (a) $NaCrX_2$, (b) the low-temperature form and (c) the high-temperature form of $CuCrX_2$ and $AgCrX_2$ (X=S,Se). Chalcogen atoms are shown as open circles, Cr as double circles, fully occupied positions of Na, Cu, Ag as black circles, statistically occupied positions as hatched circles.

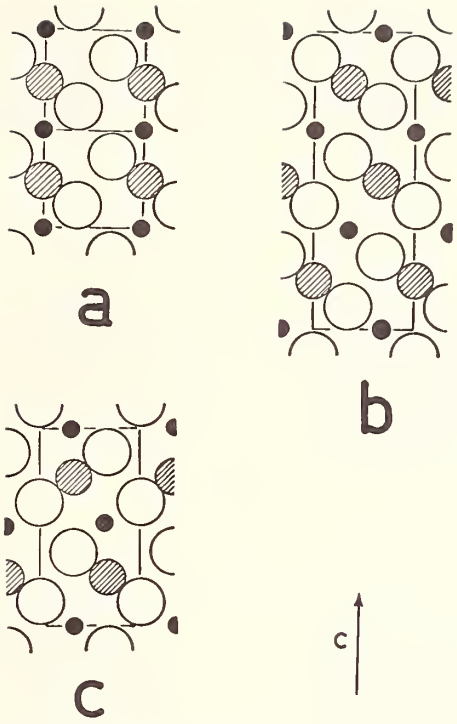

Fig. 4. Sections through the hexagonal (110) planes of phases $M_{1+p}X_2$ with octahedrally coordinated metal atoms M. Chalcogens X are shown as open circles, fully occupied metal positions as hatched circles, partly occupied metal positions as black dots. The chalcogen atoms are in (a) hexagonal close packing; (b) cubic close packing; (c) packing of the type chch.

$M_{1+p}X_2$ the distribution of vacant and occupied metal sites in the partly filled layers is ordered, at least at room temperature. A good example is provided by the chromium sulfides where ordered arrangements of ideal formulas Cr_7S_8 [24], Cr_5S_6, Cr_3S_4, $Cr_{2+x}S_3$, Cr_2S_3 [25] and Cr_5S_8 [26] have been established (fig. 5). However, since the surroundings of occupied and vacant metal sites are almost identical, unusually large proportions of Schottky defects are present [27,28] and the various chromium sulfides are actually somewhat richer in metal than indicated by the ideal formulas given [25]. The three-dimensional order of the vacancies in Cr_7S_8 [24] and Cr_5S_6 [29] disappears at about 320 °C, that in Cr_3S_4 at 880 °C [30], but the vacancies remain confined to alternate metal layers.

Many other transition-metal chalcogenides $M_{1+p}X_2$ have quite analogous structures based on a hexagonal close packing of the anions. In some cases, however, other packings of the anions are found, again with the metal atoms in octahedral holes. The structure of $Zr_{1+p}Se_2$, for instance, is based on a hexagonal close anion packing for small values of p, on a packing of type chch for intermediate values and on a cubic close packing for large values of p [31], as shown in figure 4. Obviously, the radius ratio r_{Zr}/r_{Se} is too large for structures with a hexagonal packing of the anions to be stable, except for small values of p.

Similar arguments hold for the titanium sulfides in the range TiS_2 - TiS. In the phases TiS_2 (hexagonal close sulfur packing), Ti_5S_8 (packing cchh), and Ti_2S_3 (packing ch) completely and partly occupied metal layers alternate, as in the other $M_{1+p}X_2$ phases discussed so far.

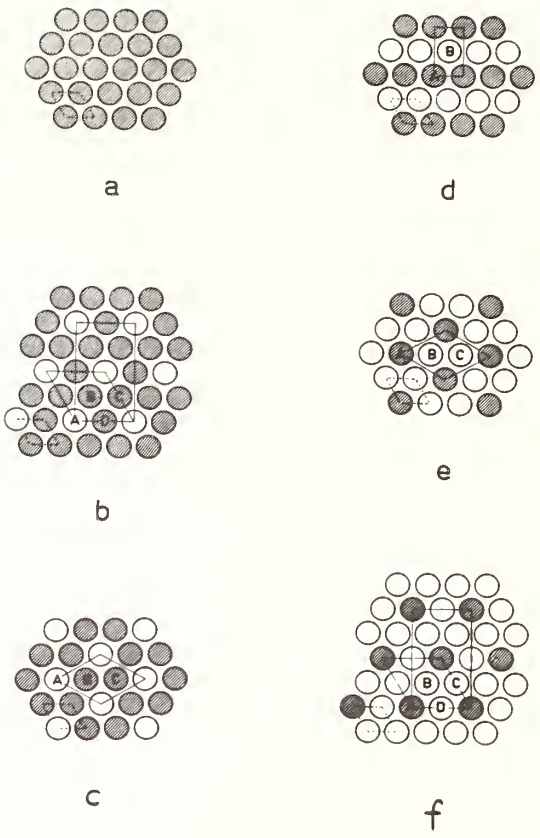

Fig. 5. In the room-temperature forms of the chromium sulfides completely filled metal layers (a) alternate with partly filled layers (b-f), in which the metal atoms (hatched circles) and vacancies (open circles) are ordered. Ordering of type (b) is found in Cr_7S_8, (c) in Cr_5S_6, (d) in Cr_3S_4, (e) in $Cr_{2+x}S_3$ and Cr_2S_3, (f) in Cr_5S_8.

In Ti_3S_4 (packing chchchh), Ti_4S_5 (chchh), and Ti_8S_9 (chh), however, the occupancy of subsequent metal layers is more complicated, as shown by figure 6. The figure suggests that the occupancy may be described by "occupation waves". There are n such waves for 2n + 1 metal layers; n = 0 for TiS (NiAs type), n = 1 for Ti_8S_9, n = 2 for Ti_4S_5, n = 3 for Ti_3S_4, and n $=\infty$ for Ti_2S_3 [32]. The "occupation waves", in this case, are commensurate with the crystallographic lattice.

5. MONOCHALCOGENIDES

TiS is one of the few monochalcogenides which have a NiAs-type structure at room temperature. In several transition metal - chalcogen systems the composition of the NiAs-like phase $M_{1+p}X_2$ does not reach the limit of p = 1, in other systems it reaches it only at high temperatures. In some cases, however, the structures stable at room temperature may be regarded as simple distortions of a NiAs-type structure. The monoclinic distortion of the structure of CrS causes the octahedra about the metal atoms to become elongated: Cr has four sulfur neighbors at distances of 2.43 Å, two more sulfurs at 2.88 Å [25]. Evidently, the deformation of the structure is to be regarded as a Jahn-Teller distortion, due to the free-spin d^4 configuration of Cr^{2+}. This stabilization of the d^4 configuration causes pure CrS to be a semiconductor. At about 600 °C a transition to metallic conduction takes place; this

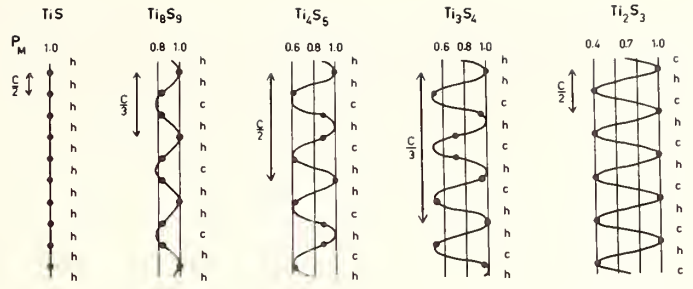

Fig. 6. The fractional occupation P_M of successive metal layers in the phases TiS, Ti_8S_9, Ti_4S_5, Ti_3S_4, and Ti_2S_3; observed values of P_M are indicated by black dots. The stacking of the sulfur layers between the metal layers is also given; c = cubic, h = hexagonal close packed.

transition is not due to a simple structure transformation, but rather to the peritectoidal decomposition of CrS into the high-temperature phase $Cr_{1-x}S$ and chromium metal [24].

Other distortions of the NiAs type may be ascribed to the formation of chains, clusters or three-dimensional networks of metal atoms. Three-dimensional networks of metal atoms are found in the hexagonal superstructure of FeS, stable below 140 °C [33] and in the orthorhombic structure (MnP type) of VS, stable below about 500 °C; the transition from the NiAs to the MnP type is of first order [34]. In the case of the phase $Nb_{1-x}S$ ($0 \leq x \leq 0.08$) a MnP-type form is stable at high temperatures; the distortion from the NiAs type is more pronounced than in VS, resulting in the formation of zigzag Nb-Nb chains (fig. 7a). At 780 °C a transition takes place to a hexagonal low-temperature form of composition $Nb_{11}S_{12}$, the structure of which again is closely related to the NiAs type; nine of the metal atoms per formula unit form triangular clusters, the remaining two being isolated, as shown in figure 7b [35].

6. METAL-RICH NICKEL CHALCOGENIDES

The metal-rich chalcogenides of Ni, Ag, and particularly of Cu undergo many structure transformations of various types. We shall confine our discussion to the transitions of $Ni_{3\pm x}Te_2$ and Ni_3Se_2 which show some remarkable features. Above about 770 °C the phase $Ni_{3\pm x}Te_2$ has a f.c.c. structure; the metal atoms are distributed over a number of positions in the cubic close packed lattice of the chalcogen [36,37]. At lower temperatures structures are found derived from the Cu_2Sb type. In this type the non-metal atoms form a (distorted) cubic close packing; half of the metal sites have tetrahedral, half have octahedral (or rather square-pyramidal) coordination. In $Ni_{3\pm x}Te_2$ the tetrahedrally coordinated metal sites are

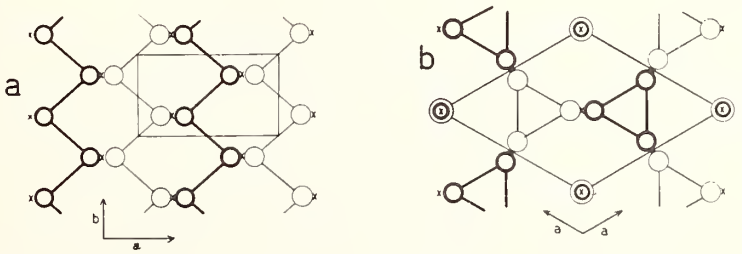

Fig. 7. Projections of (a) the high-temperature form, (b) the low-temperature form of $Nb_{1-x}S$. Metal atoms in alternate layers are indicated by heavy and light contours, respectively; metal positions in an undistorted NiAs-type lattice are indicated by crosses. The sulfur atoms are not shown.

fully occupied, while about half of the square-pyramidal sites are vacant (fig. 8). The occupation of the latter sites is random above about 300 °C (tetragonal structure); ordered arrangements of the atoms in these sites are found below 170 °C (Ni-rich side; monoclinic superstructure) or 130 °C (Te-rich side; tetragonal superstructure), as shown in figure 9 [36,38]. In the intermediate temperature range the structure is orthorhombic, but the (single-crystal and powder) x-ray diffraction patterns of the phase contain additional reflections which cannot be indexed in terms of the orthorhombic cell. The satellite-like extra reflections can be explained by assuming a modulated occupation of the square-pyramidally surrounded metal sites; the period of the occupancy wave is 2.33 times the orthorhombic a-axis [36]. It may be remarked that the room-temperature form of $Cu_{3-x}Te_2$, stable below 140 °C, also has a structure derived from the Cu_2Sb type and modulated in a similar way [39].

The heat effects of the transitions of $Ni_{3\pm x}Te_2$ at about 300° and 150 °C (and of $Cu_{3-x}Te_2$ at 140 °C) are very small and the transformations are close to second order. Analysis in terms of Landau's theory shows that second-order phase transitions from the tetragonal disordered phase directly to the ordered superstructures of $Ni_{3\pm x}Te_2$ are not possible. However, second-order transitions (of type II) are allowed from either of these structures to the orthorhombic structure which lacks three-dimensional periodicity. It appears, therefore, that the intervenient modulated structure makes a smooth path possible from the disordered high-temperature form to the ordered superstructures of $Ni_{3\pm x}Te_2$ [36].

Another interesting transition is shown by Ni_3Se_2. At room temperature this phase has a rhombohedral structure based on a (slightly distorted) body-centered cubic packing of selenium. On heating, a transition to a f.c.c. form of the type described for $Ni_{3\pm x}Te_2$ occurs at 600 °C. When Ni_3Se_2 is cooled again, a transition of the f.c.c. form to a metastable tetragonal form is observed at 560 °C; at about 530 °C this metastable form is converted to the stable rhombohedral form [40]. The structure of the metastable tetragonal form is of the $(Ni,Fe)_{11}Se_8$ type [41]; it is based on a cubic close packing of selenium, just as the high-temperature form of Ni_3Se_2. It is understandable, therefore, that the transition from the high-temperature f.c.c. form to the metastable tetragonal form is kinetically more favorable than a transition to the stable rhombohedral form which has a structure based on a b.c.c. packing of the chalcogen [37].

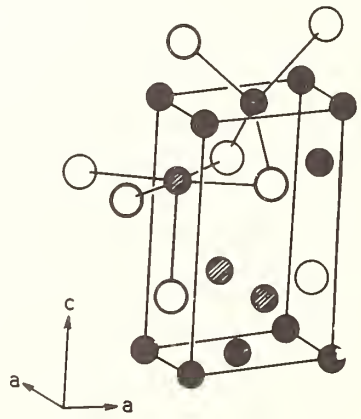

Fig. 8. The structure of tetragonal $Ni_{3\pm x}Te$. Tellurium atoms are shown by open circles, fully occupied metal positions (in tetrahedral coordination) by black circles, partly occupied metal sites (square-pyramidal coordination) by hatched circles.

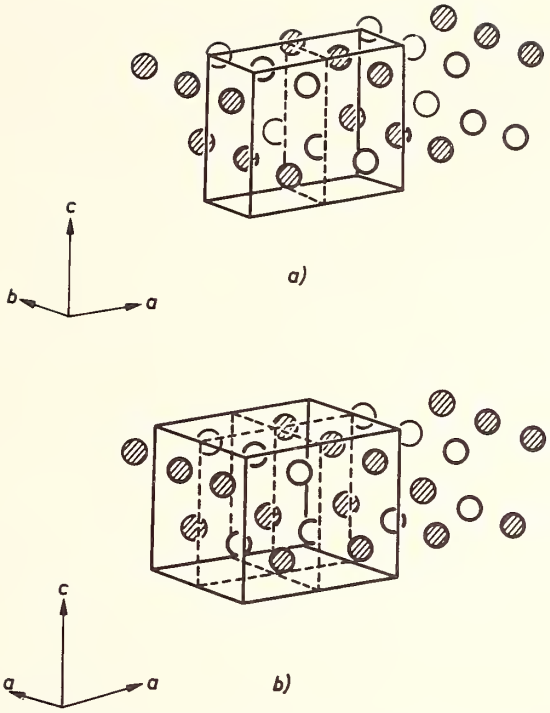

Fig. 9. Low-temperature orderings of metal atoms (hatched circles) and vacancies (open circles) in the square-pyramidal metal sites of $Ni_{3\pm x}Te_2$ in (a) the monoclinic superstructure of Ni-rich samples, (b) the tetragonal superstructure of Te-rich samples. The tellurium and the tetrahedrally coordinated metal atoms are not shown; cf. figure 8.

Several of the investigations discussed were supported by the Netherlands Foundation for Chemical Research (SON) with financial aid from the Netherlands Organization for the Advancement of Pure Research (ZWO).

7. REFERENCES

[1] Jellinek, F., Chapter 19 in: *Inorganic Sulphur Chemistry*, G. Nickless, ed., Elsevier, Amsterdam-London-New York (1968).
[2] Huisman, R., de Jonge, R., Haas, C., and Jellinek, F., J. Solid State Chem., 3, 56 (1971).
[3] Wilson, J. A. and Yoffe, A. D., Adv. In Physics, 18, 193 (1969).
[4] Alcock, N. W. and A. Kjekshus, Acta Chem. Scand., 19, 79 (1965).
[5] Wildervanck, J. C. and Jellinek, F., J. Less-Common Metals, 24, 73 (1971).
[6] Vellinga, M. B., de Jonge, R., and Haas, C., J. Solid State Chem., 2, 299 (1970).
[7] Kadijk, F. and Jellinek, F., J. Less-Common Metals, 23, 437 (1971).
[8] Jellinek, F., J. Less-Common Metals, 4, 9 (1962).
[9] Thompson, A. H., Gamble, F. R., and Revelli, J. F., Solid State Commun., 9, 981 (1971).
[10] Huisman, R. and Jellinek, F., J. Less-Common Metals, 17, 111 (1969).
[11] Geertsma, W., Haas, C., Huisman, R., and Jellinek, F., Solid State Commun., 10, 75 (1972).
[12] Ballhausen, C. J., *Introduction to Ligand Field Theory*, McGraw-Hill, New York (1962).
[13] Huisman, R., Kadijk, F., and Jellinek, F., J. Less-Common Metals, 21, 187 (1970).
[14] van den Berg, J. M. and Kort, C. W. F., J. Less-Common Metals, 13, 363 (1967).
[15] Anzenhofer, K., van den Berg, J. M., Cossee, P., and Helle, J. N., J. Phys. Chem. Solids, 31, 1057 (1970).
[16] van Laar, B., Rietveld, H. M., and IJdo, D. J. W., J. Solid State Chem., 3, 154 (1971).

[17] Omloo, W. P. F. A. M. and Jellinek, F., J. Less-Common Metals, 20, 121 (1970).
[18] Jellinek, F., Mater. Res. Bull., 6, 169 (1971).
[19] Rüdorff, W., Chimia, 19, 489 (1965).
[20] van dan Berg, J. M., Inorg. Chim. Acta, 2, 216 (1968).
[21] Grams, G., Dissertation, Univ. of Tübingen (1961).
[22] Bongers, P. F., van Bruggen, C. F., Koopstra, J., Omloo, W. P. F. A. M., Wiegers, G. A., and Jellinek, F., J. Phys. Chem. Solids, 29, 977 (1968).
[23] Engelsman, F. M. R., van Laar, B., Wiegers, G. A., and Jellinek, F., to be published.
[24] Popma, T. J. A. and van Bruggen, C. F., J. Inorg. Nucl. Chem., 31, 73 (1969).
[25] Jellinek, F., Acta Cryst., 10, 620 (1957).
[26] Sleight, A. W. and Bither, T. A., Inorg. Chem., 8, 566 (1969).
[27] van Laar, B., Phys. Letter, 25A, 27 (1967).
[28] Popma, T. J. A., Haas, C., and van Laar, B., J. Phys. Chem. Solids, 32, 581 (1971).
[29] van Bruggen, C. F. and Jellinek, F., Propr. Thermodyn. Phys. Struct. des Dériv. Semi-Métal., CNRS, Paris, p. 31 (1967).
[30] Erdös, E., Brezina, P., and Scheidegger, R., Werkst. u. Korrosion, 22, 148 (1971).
[31] Salomons, W. and Wiegers, G. A., Rec. Trav. Chim. Pays-Bas, 87, 1339 (1968).
[32] Wiegers, G. A. and Jellinek, F., J. Solid-State Chem., 1, 519 (1970).
[33] Evans, H. T., Jr., Science, 167, 621 (1970).
[34] de Vries, A. B., Dissertation, Univ. of Groningen (1972).
[35] Kadijk, F. and Jellinek, F., J. Less-Common Metals, 19, 421 (1969).
[36] Stevels, A. L. N., Dissertation, Univ. of Groningen (1969); Philips Res. Reports Suppl. 9 (1969).
[37] Stevels, A. L. N. and Jellinek, F., Monatsh. f. Chem., 102, 1679 (1971).
[38] Kok, R. B., Wiegers, G. A., and Jellinek, F., Rec. Trav. Chim. Pays-Bas, 84, 1585 (1965).
[39] Stevels, A. L. N. and Wiegers, G. A., Rec. Trav. Chim. Pays-Bas, 90, 352 (1971).
[40] Stevels, A. L. N., Bouwma, J., Wiegers, G. A., and Jellinek, F., Rec. Trav. Chim. Pays-Bas, 87, 705 (1968).
[41] Røst E. and Haugsten, K., Acta Chem. Scand., 23, 1601 (1969).

DISCUSSION

J. M. Honig: The model presented for explaining the semiconductivity of ls-TaS_2 would imply that the band gap is quite narrow and, therefore, the activation energy quite small; is this correct?

F. Jellinek: The apparent activation energy of semiconducting ls-TaS_2 at room temperature is about 0.02 eV (reference 9), that of $BaTaS_3$ (also with Ta^{4+} in octahedral coordination) about 0.06 eV (R. A. Gardner et al., Inorg. Chem. 8, 2784 (1969)). Although it is not certain whether these observed activation energies are the intrinsic values, they are quite consistent with the model presented.

F. Holtzberg: Can one determine the anisotropy in electrical conductivity in the layer type dichalcogenides?

F. Jellinek: The measurements on the electrical anisotropy are delicate, since the crystals we obtained of the layer-type compounds were quite thin. Preliminary measurements on the metallic forms of $NbSe_2$ and $TaSe_2$ indicate the conductivity perpendicular to the layers to be somewhat smaller (by about one order of magnitude) than that within the layers. However, these experiments may have been affected by several types of errors, again due to the pronounced plate-like habit of the compounds under discussion.

F. Holtzberg: Have optical measurements been performed on layer-type dichalcogenides?

F. Jellinek: Due to the plate-like habit of these compounds transmission spectra through the plates can readily be obtained (cf. reference 3). The energy-band diagrams proposed for these compounds (cf. reference 2) are partly based on such spectra.

A. Wold: In the model presented for ls-TaS_2 the t_{2g} level of the metal in octahedral coordination is split by spin-orbit coupling. However, it is also split if the symmetry of the environment of the metal is lower than cubic. By taking account of the latter splitting we could explain some properties and structural features of marcasite-type compounds.

F. Jellinek: The term scheme presented (cf. reference 11) refers to a d^1 ion in octahedral coordination. Actually, the environment of the metal in ls-TaS_2 has only trigonal symmetry D_{3d} (perhaps even lower at low temperatures). This leads to an additional splitting of some of the energy levels, but the essential features of the scheme are not changed; the ground state still has zero magnetic moment (g = 0).

National Bureau of Standards Special Publication 364, Solid State Chemistry, Proceedings of 5th Materials Research Symposium, issued July 1972.

SOLID SOLUBILITY IN THE FACE CENTERED CUBIC Gd_xSe_{1-x} SYSTEM

F. Holtzberg*, D. C. Cronemeyer, T. R. McGuire* and S. von Molnar*

IBM Thomas J. Watson Research Center
Yorktown Heights, New York 10598

The range of homogeneity has been studied in the face centered cubic Gd_xSe_{1-x} system. The solid solution field is bounded by the composition x = 0.443 for excess Se and extends through the stoichiometric composition to at least 0.512 for excess Gd. The lattice constant decreases linearly with decreasing Gd concentration except at lowest values of x. The materials have been characterized by resistivity, reflectivity and magnetic measurements. The results of the transport and reflectivity measurements are explained on the basis of a simple single rigid band model. Magnetization measurements show that all compositions order antiferromagnetically with the Neél temperature, T_N, varying from ~ 20 to ~ 60 K and θ from -25 to -135 K with increasing Gd or electron concentration.

Key words: Color-concentration dependence; gadolinium monoselenide; Hall effect; homogeneity range; magnetic ordering; reflectivity; resistivity; single crystal growth.

1. INTRODUCTION

The rare earth chalcogenides have been of considerable interest primarily because of the relationship of their magnetic properties to electron concentration. This has been dramatically demonstrated in the semiconducting divalent europium chalcogenides EuS, EuSe and EuTe and particularly in EuO, the only confirmed rare earth monoxide [1-5][1]. Similar effects have been observed in the Th_3P_4 type RE_3Se_4-RE_2Se_3 solid solution systems [6,7]. During a recent attempt to grow crystals in the Gd_3Se_4-Gd_2Se_3 system in the vicinity of the 3:4 composition, the primary crystalization phase was found to have a NaCl type structure with a deep blue metallic color, the remaining phase being a eutectic composition of NaCl and the Th_3P_4 type defect structures. The blue phase had a smaller lattice constant than that expected for GdSe.

There has been evidence for some time in the literature, of compositional variation in the trivalent monochalcogenides. Iandelli [8] noticed a color variation from yellow gold to red violet in the sulfides and selenides, which he attributed to incomplete or non-homogenous reaction. These were polycrystalline materials which were reacted in quartz at temperatures up to 1450 °C. M. Guittard [9] studied the range of homogeneity of all the rare earth monosulfides using lattice constant variations of polycrystalline material to explore the range of solid solubility. She found that the range of homogeneity increased with atomic number. Furthermore, she determined from density measurements that the solid solubility was on the metal-rich side with sulfur vacancies for all the rare earth sulfides except Lu, for which the homogeneity range extended to both sides of the stoichiometric composition. In all cases the lattice constant increased with increasing sulfur concentration.

---

*This research was supported in part by the Advanced Research Projects Agency of the Department of Defense and was monitored by the U. S. Army Missile Command under Contract No. DAAH01-71-C-1319.

[1]Figures in brackets indicate the literature references at the end of this paper.

The rare earth monochalcogenides are gold colored because the electron not used in bond formation is believed to be in a band formed by 5d and 6s wave functions giving rise to the metallic character. The $^8S_{7/2}$ ground state of Gd^{+++} provides an atomic moment of $7\mu_B$ and is, as a pure spin state insensitive to lower order crystalline field splittings. The Gd-Se system was chosen for a study of compositional variation in the monoselenides since the interpretation of magnetization data does not present the complication of having to consider orbital contributions to the magnetic moment.

2. EXPERIMENTAL

2.1. SYNTHESIS AND CRYSTAL GROWTH

Since, among other measurements, we elected to examine transport properties and reflectivity as a function of concentration, it became apparent that it would be useful to obtain single crystals. In order to study the homogeneity range, two large charges on either side of the stoichiometric composition were synthesized using the following procedure: All materials were handled in a He purged dry box. Metallic Gd sponge obtained from the Lunex Corp. having a nominal 99.9 concentration and 99.999 Se from the United Mineral and Chemical Corp. were reacted by the vapor transport of Se to the gadolinium side of an evacuated and sealed dual chamber quartz reaction tube. This reaction was carried out at a maximum temperature of 600 °C because at higher temperatures there was evidence of quartz attack. Transport was considered complete when the characteristic color of Se vapor disappeared. The product of this reaction is quite inhomogeneous. The entire charge was transferred to a large tungsten crucible which was covered and sealed by electron beam welding. The crucible was then heated to 1600 °C in the vacuum heated RF furnace described below. The two samples were powdered and chemical analysis gave the Gd rich composition as $GdSe_{.96}$ and the Se rich composition as $Gd_{.72}Se$. A series of samples developed from mixtures of these two compositions were used for crystal growth. Samples of approximately 6 grams were pressed into pellets which were sealed into 3/8 x 2 in. tungsten crucibles. Crystals were grown in an induction heated RF furnace (fig. 1) using a 10^{-6} torr vacuum to protect the crucible from surface reaction. A split Ta shield surrounding the crucible reduced gradients and the crucible, suspended from a fine Ta wire, was positioned to adjust the temperature profile along its length. Temperature measurement and control were achieved with an NBS calibrated L&N automatic optical pyrometer, surface temperature having been calibrated with a black body measurement obtained with the same geometry. Samples were heated to the melting point and cooled at about a degree per minute to 700 °C at which point the power was turned off.

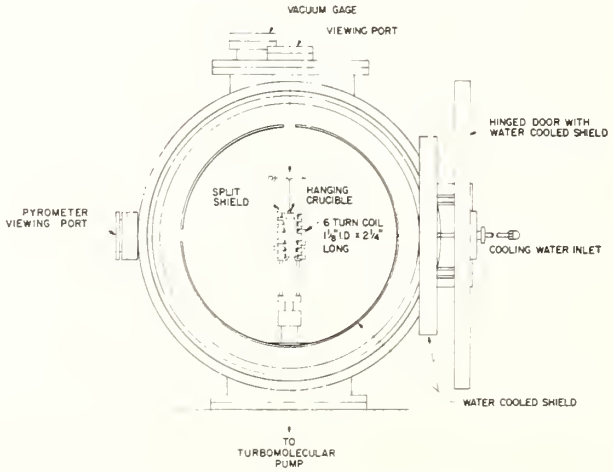

Fig. 1. High temperature vacuum RF furnace.

2.2. X-RAY ANALYSIS

X-ray data were obtained with a Guinier focussing camera using Si as an internal standard. A least squares fit to the data gave a standard deviation of 0.001 Å.

2.3. CHEMICAL ANALYSIS

Relative sample concentrations were obtained using an ARL EMX-SM electron microprobe with Gd metal as a standard. The error in concentration from sample to sample was estimated to be of the order of 0.5%. The composition scale was fixed with wet chemical analysis of three of the microprobe samples. Gd was determined by a EDTA titration and Se by a permanganometric titration. The error in the analysis was estimated to be of the order of 1%.

An AEl MS-7 double focussing solid state mass spectrometer was used for impurity analysis of the Gd metal and several single crystals of the selenide. Y and Ho were found in the 100-200 ppm range and Cu, Si, 0, C and Na at the 100-300 ppm level. Synthesis and crystal growth of the selenide led to small increases in Na and Cu concentrations and considerable reduction in the C and 0 impurity levels. Since the small increase in Na and Cu concentrations (about 50 ppm) was not found to scale with Gd content, the effects of impurities on physical properties were considered to be negligible.

2.4 MAGNETIC MEASUREMENTS

Magnetization data were obtained with a force balance in fields up to 20 Kilogauss in the temperature range 4.2 K to room temperature.

2.5. REFLECTIVITY

A Cary 14 R spectrometer, modified with a reflectivity jig for 10° incidence was used for measuring the shift in reflectance spectra with composition. Instrumental corrections were obtained with an evaporated gold film standard.

2.6 TRANSPORT MEASUREMENTS

A standard 5 probe D.C. technique was used to measure the resistivity as a function of temperature as well as the Hall effect, wherever possible. Measurements were limited to signals greater than 10^{-7} volts.

3. RESULTS

A striking result of the crystal growth experiments is the dramatic variation of sample color as a function of composition. The Gd rich samples were a bright yellow gold color and as the Gd concentration decreased the color changed progressively to bronze, copper, red gold, purple and at the lowest Gd concentration, a deep metallic blue. Since there was a small temperature gradient along the crucible during crystal growth, a concentration gradient developed as the sample crystallized. Each single crystal ingot, therefore, graphically represented the crystallization process of the system. The initial crystallization was found to have the highest Gd concentration or most gold-like color and the final crystallization the lowest Gd concentration or most blue-like color, reflecting the range of solidus concentrations for a particular melt composition. Crystals of uniform color were cleaved from an ingot for analysis and it was found that by carefully matching the color of crystals from different areas it was possible to reproduce all physical measurements within the error of each determination. The gadolinium rich compositions were found to melt at approximately 2350 °C. Melting temperatures decreased smoothly to about 1750 °C for the blue, selenium rich, phase.

Figure 2 is a plot of lattice constant as a function of concentration. The overall decrease of lattice constant with increasing Se concentration is unexpected and contrary to Guittard's [9] results for Lus. It is possible that density determinations will shed some light on the nature of the defect structure and provide an explanation for the lattice contraction. A straight line has been drawn through the stoichiometric composition. It is reasonable, however, to expect differences in slope on either side of this concentration. Al-

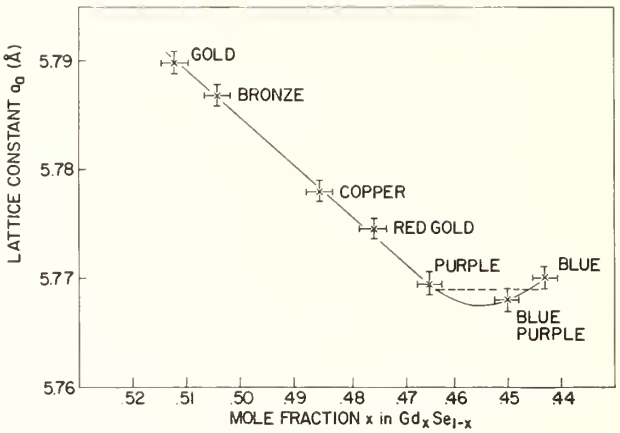

Fig. 2. Lattice constant a_o as a function of composition x in Gd_xSe_{1-x}.

though the data illustrates the general trend shown by the straight line, additional measurements are necessary to show any detailed changes in slope.

In the composition range x = 0.443 to 0.463 the lattice constant goes through a minimum as shown by the solid line. The lattice constant for the blue phase, (x = 0.443), is 5.770 Å, which is identical with the value obtained from the NaCl pattern of the two phase region. This composition therefore, represents the limiting concentration of the Se rich field.

It is also possible to draw a horizontal line (dashed line) which just touches the error bars for the three data points used to define the minimum. Such a line of constant a_o would indicate that this is a two phase region. This would place the solubility limit in the Se rich field at x ~ 0.465. However, neither x-ray nor metallographic analyses showed any evidence of a second phase.

The results of the resistivity measurements can be summarized as follows: i) The bronze and gold colored samples, which have comparably low resistivities, ρ, exhibit a temperature dependence in ρ normal for magnetically ordered metals (lower curves in fig. 3). The resistivity is linear in the paramagnetic region with a knee near T_N and drops precipitously as the temperature decreases towards 0 K. This is readily analyzed with three contributions to resistivity

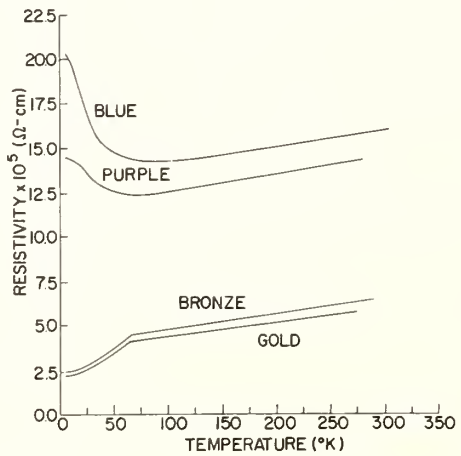

Fig. 3. Resistivity, ρ, as a function of temperature (°K) for four compositions, x, in the Gd_xSe_{1-x} system.

$$\rho = \rho_L + \rho_i + \rho_m, \quad (1)$$

where ρ_L = lattice, ρ_i = impurity and ρ_m = magnetic contributions to the resistivity. For these two samples ρ_m is constant above T_N (only spin disorder scattering) which accounts for the observed curve. ii) The resistivity as a function of temperature for both the blue and purple samples are plotted in the upper part of figure 3. The room temperature resistivity is higher (because the free electron concentration is lower) and the linear decrease in with decreasing temperature reaches a minimum near 75 K, thereafter increasing to a constant value at low temperatures. Again we might analyze the data with equation (1) with the assumption that ρ_m includes a critical scattering term. On the other hand T_N, from magnetic data has not changed appreciably and it is unlikely that the resistivity will remain constant below T_N.

The Hall effect was measured at room temperature for the purple sample ($Gd_{.465}Se_{.535}$) and the carrier concentration derived by assuming a simple band was $n = 1.4 \times 10^{22}$ cm^{-3}. It is possible to check the consistency of this number with other independent measurements as follows: if we assume that each Gd contributes one electron to the conduction band, simple valence arguments lead to the expression

$$N_o\,[3x - 2(1 - x)]\,x2 = N \quad (2)$$

where N_o = carrier concentration for the stoichiometric composition (x = 0.5) where x = composition. Solving for N_o, using the experimental values x = 0.465 and $n = 1.4 \times 10^{22}$ cm^{-3}, one obtains $N_o = 2.2 \times 10^{22}$ cm^{-3}. On the other hand we can also calculate N_o using the lattice parameter for stoichiometric material as $N_o = 4/a_o^3 = 4/(5.78 \times 10^{-8})^3 = 2.1 \times 10^{22}$ cm^{-3}. The agreement is very satisfying and lends evidence to our model of a simple rigid band in which the number of free carriers is determined by the stoichiometry.

It is also tempting to attribute the dramatic changes in color simply to changes in carrier concentration. Figure 4 shows reflectivity data for three representative samples. For the case that the reflectivity minimum, R_{min}, is ~ 5%, the dispersion relation for free carriers yields the following expression:

$$m_s \propto \frac{n\,\lambda^2_{min}}{\varepsilon_\infty - 1} \quad (3)$$

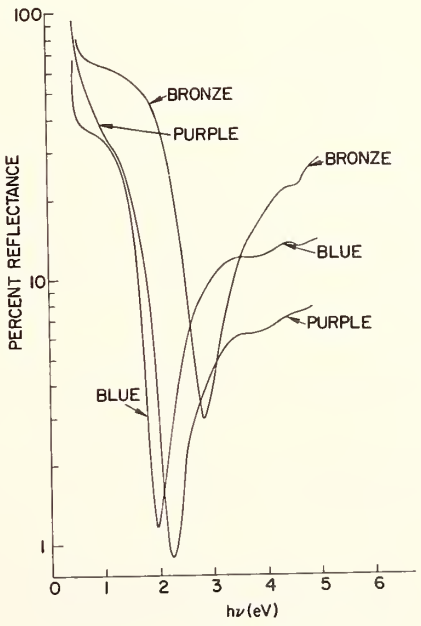

Fig. 4. Percent reflectance R as a function of energy hν.

465-504 O - 72 - 42

where m_s is the effective mass ε_∞ is the high frequency dielectric constant, n is the number of free carriers per unit volume and λ_{min} is the wavelength at which R_{min} occurs. Since $\nu \propto \frac{1}{\lambda}$, (3) can be rewritten as $(h\nu)^2_{min} \propto n$, and, assuming that m_s and ε_∞ do not vary substantially throughout the series, a plot of log n *vs* $h\nu$ should yield a straight line with a slope equal to 2. We have assumed here that the reflectivity is dominated by free carriers and that interband transitions, inc. perturb the spectra only slightly. Figure 5 exhibits the results of such a plot. It is apparent that the curve is consistent with our model with the exception of the lowest point.

All compositions in the solid solution system order antiferromagnetically. A rough measure of Neel temperatures indicates that they vary from ~ 20 K for x = 0.443 to ~ 60 K for x = 0.512. A plot of paramagnetic θ values as a function of composition (fig. 6) is essentially linear with composition except for x = 0.443. Comparing these with the resistivity results we see that the negative exchange interaction increases strongly with electron concentration.

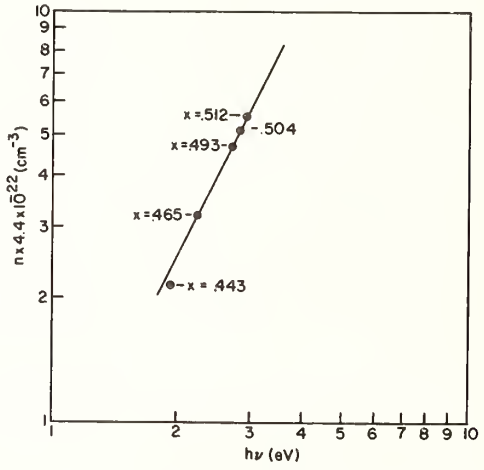

Fig. 5. Carrier concentration, n, derived from experimental composition, x, as a function of $h\nu$ for which the reflectivity is a minimum. The data is plotted on a log-log scale to demonstrate that $n \propto (h\nu)^2$ in the Gd_xSe_{1-x} system.

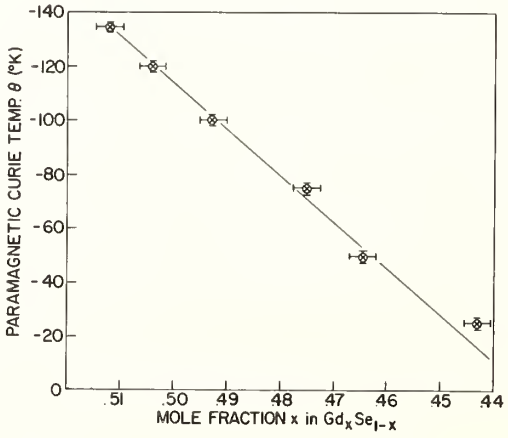

Fig. 6. Paramagnetic Curie temperature, θ, as a function of composition, x, for Gd_xSe_{1-x}.

As we have shown the relationship between observed experimental parameters and composition is surprisingly direct, and in the case of resistivity and reflectivity is well explained by the simplest of all models, a single rigid band. It should of course be noted that in all cases the lowest Gd composition appears to be anomolous, but the explanation probably lies in the breakdown of the free electron approach at lowest Gd concentrations. The possibility of two phases can be ruled out from the lattice constant argument given earlier as well as on the basis of a more detailed examination of the susceptibility data. The limiting concentration of the Gd - Th_3P_4 solid solution system forming the boundary of the two phase region is strongly ferromagnetic with θ positive and equal to 88 K [6]. Measurements on the eutectic phase also gave a positive θ. Any small amount of this ferromagnetic material in the composition x = 0.443 would show a deviation from the linear plot in figure 6 towards a more positive θ, which is contrary to experimental results.

4. ACKNOWLEDGMENT

We wish to thank P. G. Lockwood for sample preparation, R. B. Hamilton for resistivity measurements, H. R. Lilienthal for magnetic measurements, J. D. Kuptsis for microprobe analysis, R. W. Johnson for mass spectrometric analysis and B. O. Olson for chemical analysis.

5. REFERENCES

[1] Holtzberg, F., McGuire, T. R., Methfessel, S. and Suits, J. C., Phys. Rev. Letters, 13, 18 (1964).
[2] Holtzberg, F., McGuire, T. R. and Methfessel, S., J. Appl. Phys., 37, 976 (1966).
[3] Von Molnar, S. and Methfessel, S., J. Appl. Phys., 38, 959 (1967).
[4] Oliver, M. R., Kafalas, J. A., Dimmock, J. O. and Reed, T. B., Phys. Rev. Letters, 24, 1064 (1970).
[5] Final Report, Contract No. DAAH01-70-C-1309, IBM, June 1971, AD-729355.
[6] Holtzberg, F., McGuire, T. R., Methfessel, S. and Suits, J. C., J. Appl. Phys., 35, 1033 (1964).
[7] Loginov, G. M., Sergeeva, V. M. and Bryzhina, Soviet Phys. Solid State, 12, 2942 (1971).
[8] Iandelli, A., *Rare Earth Research* Ed. E. V. Kleeber, MacMillan, 1961, New York, 1, 135.
[9] Guittard, Mlle M., Compt. Rend., 261, 2109 (1965).

DISCUSSION

M. J. Sienko: What is the magnetic moment? Does it correspond to gadolinium 3+?

F. Holtzberg: The C_m values or molar Curie constants are very close to theoretical values for trivalent gadolinium but there is some variation over the concentration range. There have been several discussions with various people at this conference of why this lattice constant decreases and why the sulfide one increases. One explanation could be, in this system, and I don't think this is necessarily correct, that at the high electron concentration you have a d-electron that is localized around gadolinium giving the ion a larger size. As you decrease the electron concentration, the lattice constant would shrink. I favor the picture that we just have vacancies on the rare earth site and that the lattice shrinks around those vacancies.

R. S. Roth: Do you think there is any chance of low temperature annealing giving rise to any ordering in such a system?

F. Holtzberg: We did not anneal below 1600 °C, and I don't have any idea as to whether we would find ordering at lower temperatures; it is something we should study. We did examine some samples from the higher temperature annealing but found no evidence of ordering.

J. Flahaut: I want to first say that the monochalcogenides are very difficult to prepare, and you have made a very good contribution to this program. It seems to me that in your solid solutions through the 1:1 composition don't you observe some discontinuence in the properties, the physical properties, to the 1:1 composition?

F. Holtzberg: That is one of the problems. We don't see it in the magnetization data but I'm not sure that would be the most sensitive way to look for it. The most sensitive way would be, I think, to do all the conductivity around that region and to do more samples at the 1:1. If you noticed, we did not have that composition in time for this slide.

National Bureau of Standards Special Publication 364, Solid State Chemistry, Proceedings of 5th Materials Research Symposium, issued July 1972.

TERNARY CHALCOGENIDES OF LIGHT RARE EARTH ELEMENTS WITH TRANSITION ELEMENTS

G. Collin, H. D. Nguyen, O. Gorochov, M. Guittard,
P. Laruelle and J. Flahaut

Laboratoire de Chimie Minérale - Laboratoire de Physique
Faculte Des Sciences Pharmaceutiques et Biologiques
Universites Paris V et Paris XI - 4
Avenue de l'Observatoire, Paris 6°

Description of three new crystal families. Crystal structures. Magnetic properties. 1) $La_2Fe_2S_5$-type - orthorhombic $A2_1am$. 2) $La_8Fe_3S_{15}$-type - monoclinic Bm. These two structures have similarities. The rare earth atoms are 7-8 coordinated. The Fe atoms have two kinds of environments: 4-coordinated in a distorted tetrahedron of S atoms, 6-coordinated in a distorted octahedron of S atoms. In both cases 2 neighboring Fe atoms are associated by 2 intermediate S atoms. These 4 atoms form a distorted quadrilateral with Fe-S-Fe angles not far from 90°. 3) $CeCrSe_3$-type - orthorhombic Pnam. The rare earth atoms are 9-coordinated, and the Cr atoms are 6-coordinated, inside a nearly regular octahedron of selenium. As in the preceding structures, 2 neighboring Cr atoms form with 2 intermediate Se atoms a nearly regular square.

These compounds are antiferromagnetic at low temperature (Néel temperature for $LaCrSe_3$: 165 K). Weak ferromagnetism appears at lower temperature.

Key words: Crystal structure; magnetic properties; rare earth; ternary chalcogenides; transition metals.

1. INTRODUCTION

We describe here three kinds of new compounds, which contain transition elements - especially Fe and Cr - and light lanthanides - especially La -. There are:

$La_2Fe_2S_5$
$La_8Fe_3S_{15}$
$LaCrSe_3$

and related compounds. The two first are only known with sulfides, the last one exclusively exists with selenium.

First of all, the crystal structures were established, with single crystals, before studying the magnetic and electrical properties. For some of these compounds, the study of the physical properties is still in progress. The formula of the second compound, which was approximately deduced from chemical evidence as being La_2FeS_4, was definitely established from the crystallographic study.

2. COMPOUNDS OF THE $La_2Fe_2S_5$ TYPE

2.1. STRUCTURE OF $La_2Fe_2S_5$.

The tetramolecular orthorhombic cell has the dimensions:

$a = 11.40$ Å $\quad b = 16.55$ Å $\quad c = 4.055$ Å.

The space group is A 2_1am (N° 36), with all atoms in the special positions (with (000; 1/2, 1/2) +):

$$4\ a \quad \bar{x}\ y\ 0 \quad -(x + 1/2),\ \bar{y},\ 0$$

with:

	x	y
4 La I	0.058	0.377
4 LaII	0.443	0.376
4 Fe I	0.231	0.702
4 Fe II	0.211	0.071
4 S I	0.098	0.199
4 S II	0.404	0.199
4 S III	0.241	0.849
4 S IV	0.025	0.000
4 S V	0.299	0.542

The reliability factor is 0.068 for 342 independent reflections. The two La atoms (fig. 1) are surrounded by 8 S atoms; 6 of which are on the corners of a trigonal prism, and the two others in the equatorial plane of the prism, in front of the lateral faces. The Fe I atom is at the center of a distorted octahedron with 3 Fe-S distances of 2.43-2.53 Å, and 3 other ones of 2.75-2.81 Å. The Fe II atom is inside a distorted tetrahedron of S atoms, with Fe-S distances of 2.29, 2.29, 2.43 and 2.49 Å.

Each kind of Fe atom forms a zig zag chain Fe - S - Fe - S --- parallel to the c axis. The chain formed by Fe I is directly bonded to the chain formed by Fe II, and together they constitute a column through the structure, parallel to the c axis. In the column, the interatomic distances are: Fe II - S I: 2.48 Å; S I - Fe I: 2.53 Å; Fe I - S V: 2.76 Å; S V - Fe II: 2.25 Å. The Fe I - Fe II distance is 2.98 Å.

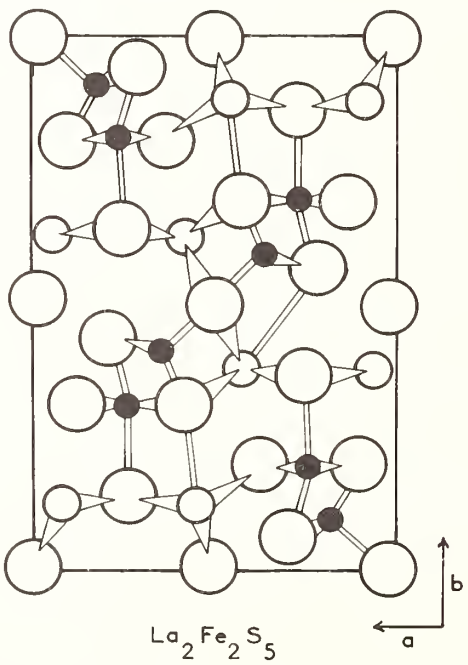

Fig. 1. Projection along the c axis of the orthorhombic structure of $La_2Fe_2S_5$. The iron atoms are black. The sulphur atoms are large circles and the lanthanum atoms are small circles.

Two neighboring columns are bounded by lanthanum atoms. A recent study of this compound showed the presence of vacancies on the Fe II tetrahedral positions, in relation to a partial substitution of Fe^{2+} by Fe^{3+}. At the limit the true composition would be $La_2Fe^{2+}(Fe^{3+}_{2/3}\square_{1/3})S_5$, with a possibility of a small homogeneity range.

2.2. OTHER COMPOUNDS

The two kinds of Fe atoms have quite different coordinations, and the synthesis of other compounds having this crystal type is in agreement with this observation. Really the general formula of these compounds is L_2BCX_5. The B site can only be occupied by usually tetracoordinated atoms, as Zn. The C site is only occupied by usually hexacoordinated atoms: Ti", V", Cr", Mn", Co". These compounds exist with the biggest rare earth atoms: La in each case and Ce in a few cases (for $Ce_2Fe_2S_5$, Ce_2ZnMnS_5 and Ce_2ZnFeS_5).

3. COMPOUNDS OF THE $La_8Fe_3S_{15}$ CRYSTAL TYPE

3.1. STRUCTURE OF $La_8Fe_3S_{15}$.

The tetramolecular monoclinic cell has the dimensions

$a = 16.55$ Å $b = 10.85$ Å $c = 13.98$ Å $\gamma = 102.91°$.

It is related to a pseudo hexagonal subcell, with

$$a_h = 8.10 \text{ Å} \quad c_h = 7.24 \text{ Å}$$

which correspond the only reflections observe on the powder diagrams. This pseudo hexagonal cell is six times smaller than the monoclinic cell.

The atoms are on the positions 2a and 4b of the space group Bm (N° 8). The reliability factor is 0.077 for the 1000 strongest independent reflections.

All the La atoms have coordination 7 - 8, with La-S distances from 2.76 Å to 3.20 Å. The Fe atoms, as in the preceding structure, have two different environments: in each cell 4 Fe atoms have four-fold coordination, inside distorted tetrahedra and the other 8 Fe atoms are 6-coordinated, inside distorted octahedra.

In this structure, from which the asymmetric part of the cell is viewed figure 2, the Fe atoms form clusters with Fe - S - Fe - S arrangements, separated by lanthanum and sulphur atoms and by large cavities.

3.2. OTHER COMPOUNDS

As in the preceding structure, the two kinds of sites of the Fe atoms should be distinguished, and the general formula of this compound should be $L_8BC_2X_{15}$ where the B sites are occupied by usually tetracoordinated atoms, and the c sites by usually hexa-coordinated atoms. At the present time, only four compounds are known with the lightest rare earths: $La_8Fe_3S_{15}$, $La_8Mn_3S_{15}$, $La_8Cr_3S_{15}$ and $Ce_8Fe_3S_{15}$.

4. THE $LCrSe_3$ FAMILY

4.1. STRUCTURE OF $CeCrSe_3$.

The tetramolecular orthorhombic cell has the dimensions:

$$a = 8.08 \text{ Å} \qquad b = 13.74 \text{ Å} \qquad c = 3.952 \text{ Å}.$$

The atoms have the positions 4c of the space group Pnam (N°62):

$$\pm\ x,\ y,\ \tfrac{1}{4} \text{ and } \pm\ (\tfrac{1}{2} + x,\ \tfrac{1}{2} - y,\ \tfrac{1}{4})$$

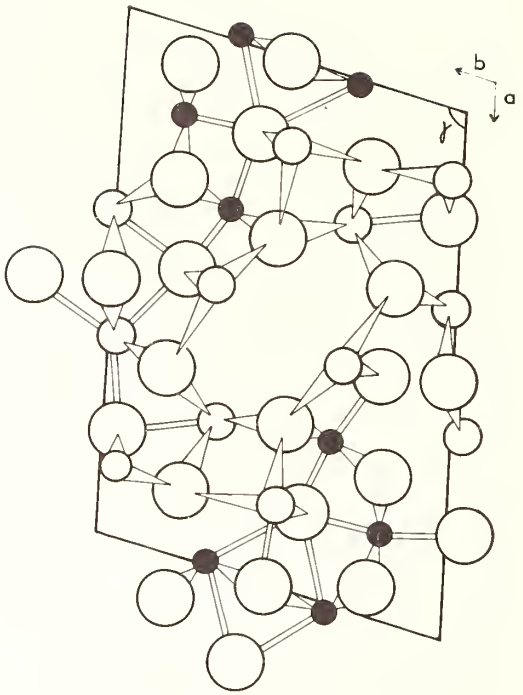

Fig. 2. Projection along the c axis of the structure of $La_8Fe_3S_{15}$. The iron atoms are black. The sulphur atoms are large circles and the lanthanum atoms are small circles.

with

	x	y
Ce	0.0950	0.1711
Cr	0.3427	0.9480
Se I	0.1907	0.7889
Se II	0.3407	0.5040
Se III	0.4832	0.1099

The reliability factor is 0.046 for 487 independent reflections. This structure is identical to that of NH_4CdCl_3, which was previously known for 4 ternary chlorides.

The Ce atoms are nine-coordinated. They are at the center of a triangular prism of selenium atoms, with three other Se atoms in front of the rectangular faces, in the equatorial plane. The Ce-Se distances have an average value of 3.08 Å for the 6 Se atoms at the corners of the prism, and of 3.19 Å for the 3 Se atoms in front of the faces.

The Cr atoms are at the center of a nearly regular Se octahedron with 6 distances Cr-Se between 2.50 and 2.59 Å. There appears in this structure nearly regular square arrangements of 2 Cr atoms and 2 Se atoms: the lengths of the sides are 2.50 and 2.55 Å, and the angles are 88.25° and 91.35° (fig. 3).

4.2. OTHER COMPOUNDS

The high coordination number of the lanthanide sites is the reason why this family is only known with the first elements of the rare earths from La to Nd.

Similar compounds do not exist with other trivalent transition elements, or with sulphur instead of selenium. Large single crystals of the La, Pr and Nd compounds were obtained by a flux method using the iodides of the corresponding rare earth.

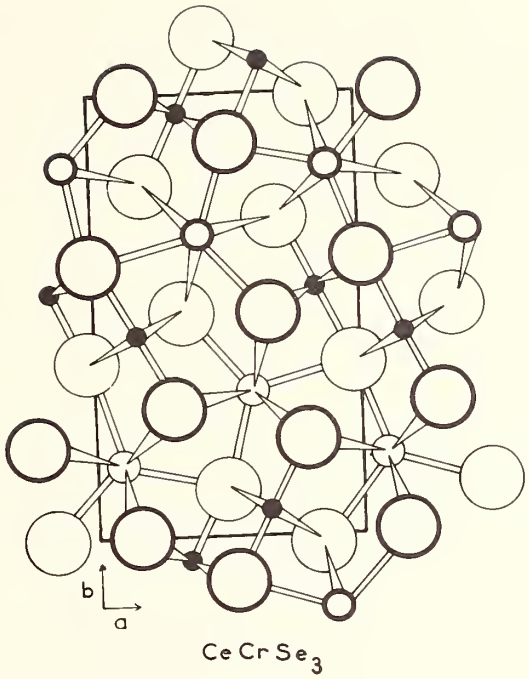

Fig. 3. Projection along the c axis of the structure of $CeCrSe_3$. The chromium atoms are black. The selenium atoms are large circles and the cerium atoms are small circles.

4.3. MAGNETIC PROPERTIES

The magnetic susceptibility of these four compounds was studied between 7 K and 800 K. Powder and large single crystals lead to the same results. All these compounds are antiferromagnetic and we sum the results in table 1. At a temperature slightly lower than the Néel point we observed the appearance of an added weak ferromagnetism. But this phenomenon remains very weak for all low temperatures (down to 7 K). At high temperature these compounds show a paramagnetic law ($X = \frac{C}{T-\Theta}$). The Curie constant related to chromium as calculated for these compounds is about 1.6.

The curves (fig. 4) show that only chromium is oriented below Néel temperature. On the other hand the rare earth follows a paramagnetic law at all temperatures.

We interpreted the magnetic properties in direct relation with the crystal structure.

The three kinds of new compounds which have been described above have two different environments for the transition element: a mixture of 4 and 6 coordination in the $La_2Fe_2S_5$ and $La_3Fe_3S_{15}$ types, and a 6 coordination with a nearly regular octahedron in the $CeCrSe_3$ type. But in both cases two transition element atoms have neighboring positions; so, direct and indirect M - X - M interactions are possible. Known magnetic properties show that magnetic ordering appears at low temperature, and depends only on the transition element.

Table 1

Magnetic Properties of $LCrSe_3$ Compounds

	Preparation	Θ_p (°K)	T_N (°K)	T_f (°K)	C_{exp} (Mol.)	$C_{Ln^{3+}}$	$C_{Cr^{3+}}=C_{Mol}-C_{Ln^{3+}}$
$LaCrSe_3$	A_1	+99	160	110	1.63	0	1.63
	A_2		165	<77			
	A_3		160	<77			
	A_4		160	107			
	B_1		165	<77			
	B_2		165	<77			
	C_1		167	77			
	C_2		165	90			
	C_3		160	-			
$CeCrSe_3$	A_1	+50	171	130	2.30	0.82	1.48
	B_1		175	135			
$PrCrSe_3$	A_1						
	C_1	+10	(170)	(160-165)	3.26	1.64	1.62
$NdCrSe_3$	A_1	-25	(183)	(172)	3.41	1.69	1.72

A : preparation from oxides + H_2Se at 1200° C.
B : preparation from elements in sealed evacuated tubes.
C : crystals.
T_N : Néel temperature.
Θ_P : Curie paramagnetic temperature.
T_f : antiferro $\rightleftharpoons$ ferromagnetic transition.
C_{exp} : experimental Curie constant.
$C_{Ln^{3+}}$: calculated Curie constant for L^{3+}.
$C_{Cr^{3+}}$: Curie constant for Cr^{3+}.

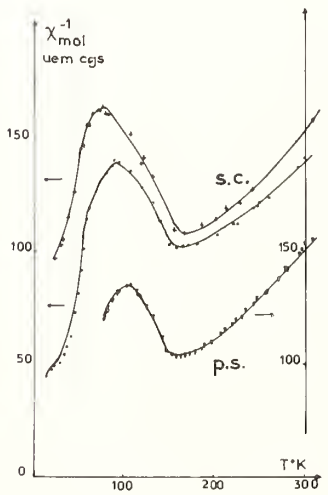

Fig. 4. Variation of the inverse of the magnetic susceptibility, for 3 samples of $LaCrSe_3$: 2 single crystals and one polycrystal sample.

National Bureau of Standards Special Publication 364, Solid State Chemistry, Proceedings of 5th Materials Research Symposium, issued July 1972.

CRYSTAL CHEMISTRY OF METAL-RICH REFRACTORY SULFIDES*

Horng-yih Chen and Hugo F. Franzen

Institute of Atomic Research and Department of Chemistry
Iowa State University
Ames, Iowa 50010

Systematization of the crystal structures of metal-rich chalcogenides was attempted with emphasis on the coordinations of a few key metal atoms. This approach gave a more complete interpretation of many chalcogenide structures, notably those of Ta_2S, Ta_6S and Nb_2Se, than did the conventional descriptions using the packing of the coordinations of the chalcogen atoms. The pursuit of this approach led to the recognition of a polyhedron, which, owing to its repeated presence in many metal-rich compounds, appeared to be of great importance in crystal chemistry. It is a two-centered polyhedron formed by the interpenetration of two C. N. 14 Kasper polyhedra in such a way that the center of one of the Kasper polyhedra is the apex of another. The presence of a very short interatomic distance between the two centers is one of the important features of this polyhedron. With the help of this polyhedron as the building block, the structures of Zr_9S_2, α-V_3S and β-V_3S were satisfactorily described and correlated; the short interatomic distances in the structures could be explained semi-quantitatively; and the structural differences expressed by the different packing schemes of the polyhedra and the different positions the sulfur atoms occupied in the polyhedra. The description using the two-centered polyhedra as the basic units was extended to the structures in phosphide systems and provided new structural evidences to the similarities and distinctions among the Zr_9S_2-, α-V_3S-, β-V_3S-, Fe_3P- and Ti_3P-type structures, and to the correlation that the Fe_3P structure is the high temperature form of the Ti_3P structure. The smooth correlation between the sulfides, Zr_9S_2, α-V_3S and β-V_3S, and the phosphides and related compounds renders further support to the speculation that these sulfides possess the nature of intermetallic compounds.

Key words: Crystal structure; intermetallic; phosphides; refractory; sulfides; transition metal; coordination polyhedra.

1. INTRODUCTION

Earlier studies on refractory metal sulfides by high temperature techniques were focused mainly on the composition range from sesquisulfides to monosulfides. In recent years composition ranges under study were extended to the metal-rich regions, and the results revealed a number of new compounds. Owing to the fact that the compositions of these new compounds are not predictable on the basis of conventional concepts in chemistry, the identification and characterization of these compounds relies very heavily on their structure determinations. Because of the insufficiency in available data the metal-rich sulfide structures have not yet been systematized, and the descriptions and the interpretations of these structures have, so far, been carried out by the extension of the concepts generally accepted for metal-rich borides, silicides and phosphides. The idea was to regard the structures of the sulfides as being built up of trigonal-prismatic coordination polyhedra for sulfur atoms. In general, this approach has yielded satisfactory understanding of the sulfide structures. Difficulties

*Work was performed in the Ames Laboratory of the U. S. Atomic Energy Commission. Contribution No. 3127.

were encountered, however, in the application of this description to the cases of Nb_2Se [1][1], Ta_2S [2] and Ta_6S [3], in which, particularly the former two, the presence of trigonal-prismatic coordination for the chalcogenide atoms was not apparent. Instead, very clear pictures could be obtained when the Ta_2S and Ta_6S structures were described as the packing of icosahedral tantalum coordination polyhedra. Similarly, the interpretation of the crystal structure of Zr_9S_2 can be accomplished with greater ease if the coordination polyhedra of the metal, instead of the sulfur atoms, are used as the basic building units [4]. Clearly, a new approach to the description and systematization of the sulfide structures is desirable. The present study was undertaken with the purpose of systematizing the structures of the refractory transition-metal sulfides with emphasis on the coordinations of the metal atoms.

2. SURVEY ON METAL-RICH SULFIDES

Some sulfides and the structure types to which these sulfides belong are listed in table 1. Also listed in the table are the sulfur coordinations and the coordination of the metal atoms which form the basic units. All the listed compounds are hard and brittle and exhibit metallic luster. They are refractory and do not exhibit appreciable homogeneity ranges. Most of the compounds listed were synthesized easily by high temperature techniques, such as arc-melting, high temperature annealing, etc. $Nb_{14}S_5$, however, formed with great difficulty. More entries to the listing are likely in the near future. Structure-wise, these structure types can be grouped into four classes as indicated in the table.

Table 1

Structural Classification of Refractory Metal-Rich Chalcogenides.

Structure type	Compound	Chalcogen coordination	Metal coordination
Ta_2P	Ti_2S[5], Zr_2S[6], Zr_2Se[6]	capped tri. prism.	cubic
$Nb_{21}S_8$	$Nb_{21}S_8$[7], $Zr_{21}S_8$[6]	capped tri. prism.	cubic
$Nb_{14}S_5$	$Nb_{14}S_5$[8]	capped tri. prism.	cubic
Hf_2S	Hf_2S[9], Hf_2Se[6]	tri. prism.	octahedral
Nb_2Se	Nb_2Se[1]	incomplete tri prism.	cubic
Ta_2S	Ta_2S[2]	incomplete tri. prism.	icosahedral
Ta_6S	Ta_6S[3]	capped tri. prism.	icosahedral
α-V_3S	α-V_3S[10]	square-antiprism.	C.N. 14 Kasper polyhedral
β-V_3S	β-V_3S[10]	square-antiprism.	C.N. 14 Kasper polyhedral
Zr_9S_2	Zr_9S_2[4]	square-antiprism	C.N. Kasper polyhedral

[1] Figures in brackets indicate the literature references at the end of this paper.

3. STRUCTURE OF COMBINED SULFUR AND METAL COORDINATIONS

The first group of structure types to be discussed contains the Ta_2P, $Nb_{21}S_8$ and $Nb_{14}S_5$ structures. These structures have been well recognized for the ubiquitous presence of capped trigonal-prismatic coordinations of sulfur atoms in the diverse structures. Also clearly observable is the presence of fragments of the body-centered cubic structures of the metals. Chains of metal-atom cubes perpendicular to mirror planes are formed in a variety of ways in these structures. The unit of the chains in the Ta_2P structure is formed by two body-centered cubes sharing faces. There are two different kinds of cube-chains in $Nb_{14}S_5$ and $Nb_{21}S_8$ structures. In $Nb_{14}S_5$, there is one type of cube-chain made up of two body-centered cubes interpenetrating in such a way that the body-center of one cube is the corner of another, and another chain is made up of three cubes arranged in a T-shape. In $Nb_{21}S_8$ one chain is made up of four cubes in a cross-shape and another of single cubes. However, because of the complexity of the structures, the description can only be completed with the additional consideration of the trigonal-prismatic coordination polyhedra of the sulfur atoms. Since the trigonal prism has a very high compatibility with cubes and there is a variety of ways to form the cube-chains, a large number of compounds, including many borides, silicides and phosphides [11], have structures formed with the cube-prism combination. This group of structures is characterized by the presence of a short axis equal to the edge of the cubes and parallel to the cube-chains.

The two hafnium compounds form a group. In this group there is a short axis but hafnium does not form cube-chains as has been commented upon by Franzen, Smeggil and Conard [6], based on the Engel-Brewer correlation [12].

4. STRUCTURES BY PACKING OF METAL-CHAINS

The third group of compounds includes Nb_2Se, Ta_2S and Ta_6S. While in Nb_2Se and Ta_2S the chalcogen coordinations are not clearly trigonal-prismatic, the Ta_2S and Ta_6S structures contain one type of Ta-atom which has no sulfur atoms as its nearest neighbor, and the structures can not be satisfactorily described based on the chalcogen coordinations alone. The difficulties encountered can be avoided if the coordinations of the metal atoms are emphasized in the structure description. From the point of view of metal coordinations, the description of the structures of Ta_2S and Ta_6S is quite obvious, namely the packing of Ta atoms arranged in continuously interpenetrating icosahedra with the sulfur atoms filling the voids created in the packing. In Ta_2S, the packing is rectangular and the relatively large voids are filled by clusters of sulfur atoms forming octahedra with a void in the center. In Ta_6S, it is two-dimensional close-packing, and the voids are only large enough to accommodate a single sulfur atom. It has been suggested that the tendency for tantalum to form icosahedral coordination is associated with its low-lying d^5 state.

This approach can also be successfully applied to the Nb_2Se structure. The structure of Nb_2Se is extremely similar to that of Ta_2S if the icosahedral chains of Ta atoms in the latter are replaced with cube-chains of Nb atoms, as shown in figure 1. The basic unit of the cube-chains of Nb atoms is formed by the interpenetration of two body-centered cubes as the one found in the $Nb_{14}S_5$ structure. The voids created in the packing of the cube-chains are again filled with clusters of chalcogen atoms in an octahedral arrangement. The chains are parallel to the short axis and are packed rectangularly as in the case of Ta_2S. Based on the Engel-Brewer correlation, the preference of Nb atoms to form cube-chains instead of icosahedron-chains, is understandable in terms of the low-lying sd^4 state of the Nb atom and the relatively high-lying d^5 state [2].

5. COMPLEX PACKING OF TWO-CENTERED POLYHEDRA

The structure interpretation emphasizing the transition-metal coordinations becomes the most interesting and probably the most significant when applied to the fourth group of the sulfides. There are only three known compounds in this group, namely Zr_9S_2, α-V_3S and β-V_3S. However, the conclusions reached can be extended smoothly to include no less than 30 phosphides and related compounds. A tetragonal symmetry and the absence of a short axis distinguish these structures from those discussed earlier. The structures of these compounds have very similar polyhedra built around metal atoms as basic units, and resemble in many ways the structures of intermetallic compounds, even though they contain sulfur or phosphorus which are conventionally not considered as metallic. The complete listing of the compounds known

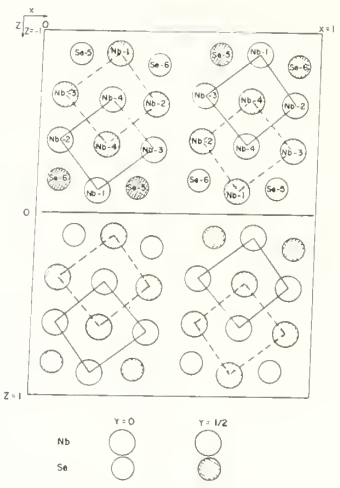

Fig. 1. Two unit cells of Nb_2Se structure projected on (010), emphasizing the units formed by the interpenetration of the body-centered cubes of Nb atoms.

in this group, including phosphides and the related compounds according to Lundström [13], and the five structure types they belong to, are shown in table 2. The structures of Zr_9S_2 and α-V_3S will be discussed in detail and comparison will be made with the other three structure types.

Table 2

Sulfides, Phosphides and Related Compounds with the Two-Centered Polyhedra as Their Structural Unit.

Structure type	Compound
Zr_9S_2	Zr_9S_2
α-V_3S	α-V_3S, Mo_3P, W_3P
β-V_3S	β-V_3S
Fe_3P	Cr_3P, Mn_3P, Fe_3P, Ni_3P, $Fe_3(P_{0.71}B_{0.29})$, Pd_3As, Zr_3Sb, Hf_3Sb, Ti_3Ge, Ta_3Ge (h.t.)
Ti_3P	$(Fe_{0.8}Re_{0.2})_3B$, $Fe_3(P_{0.37}B_{0.63})$, Ti_3P, V_3P, Zr_3P, Nb_3P, Hf_3P, Ta_3P, Zr_3As, Nb_3As, Ti_3Si, Zr_3Si, Nb_3Si, Ta_3Si, Zr_3Ge, Hf_3Ge, Ta_3Ge (l.t.)

5.1. Zr_9S_2

The crystallographic data and atomic parameters for Zr_9S_2 are tabulated in table 3 and 4, respectively, and the coordinations for the six independent atoms are shown in figure 2. The sulfur atoms are coordinated with eight metal atoms in a square-antiprismatic arrangement as in the cases of α-V_3S and β-V_3S. But, for the purpose of this study, the most important coordination is that for Zr(2), around which the two sulfur and 12 zirconium nearest neighbors form a distorted C.N. 14 Kasper polyhedron [14]. This polyhedron differs from the icosahedron around Ta atoms in Ta_2S and Ta_6S in that two sulfur atoms replace two zirconium

Table 3

Crystal Data for Zr_9S_2.

Composition	:	Zr_9S_2
Density	:	d_{obs} = 6.38g/cc (d_{calc} = 6.442g/cc)
Diffraction Symbol	:	I4/mmm Body-centered tetragonal system
Space Group	:	$I4_1/amd$ (No. 141)
Lattice Parameters	:	a = 9.752 Å c = 19.216 Å
Number of Atoms	:	Z = 8

Table 4

Refined Atomic Parameters for Zr_9S_2.

Atom	Wyckoff notation	Point sym.	x	y	z	β(Å^2)
Zr(1)	16(f)	2	0.1788(2)	0	0	0.51(4)
Zr(2)	16(h)	m	0	0.3014(1)	0.3014(1)	0.39(5)
Zr(3)	16(h)	m	0	0.0789(3)	-0.4309(1)	0.53(5)
Zr(4)	16(h)	m	0	-0.0289(3)	0.1422(1)	0.51(5)
Zr(5)	8(e)	mm	0	0.25	0.0106(2)	0.63(7)
S	16(g)	2	0.2723(4)	0.25 + x	7/8	0.37(10)

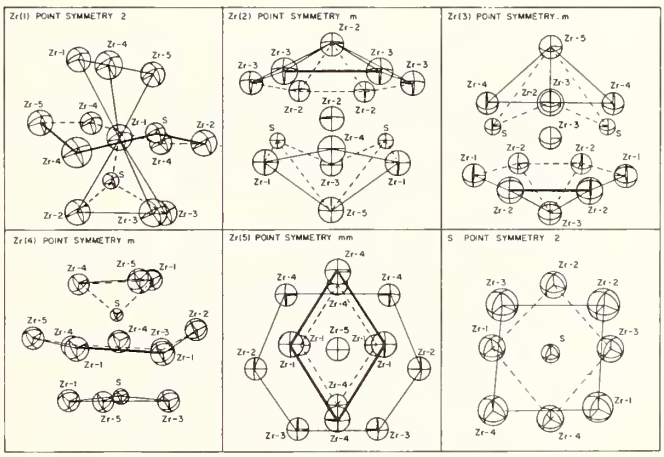

Fig. 2. Coordinations and nearest neighbors of Zr and S atoms in Zr_9S_2.

atoms at 1 and 3 positions in one of the hexagons. As will be concluded later, the polyhedron is a basic unit of the building blocks of the structure, the sulfur atoms in Zr_9S_2 do therefore participate in the formation of the basic unit and are not located in the regions created by the packing of the basic units. The substitution of zirconium atoms by two sulfur atoms in the hexagon results in a distortion of the hexagon from a planar configuration. The other hexagon containing only zirconium atoms lies in a mirror plane, but is not a perfect hexagon either. The distortion of this hexagon is an important feature of the structure and will be discussed later. The central and the apical Zr(2) atoms are related by the mirror plane and have a short interatomic distance of 2.889 Å, about 10% shorter than the sum, 3.20 Å, of the Goldschmidt radii. The prediction, based on a purely geometric argument, proposed by Frank and Kasper [14] will yield a shortening of this interatomic distance by about 15%, which is slightly larger than the 10% observed in Zr_9S_2 case. Since the lower hexagon in figure 2c lies in a mirror plane it can be seen that the coordination polyhedra for the two Zr(2) atoms interpenetrate and form a two centered polyhedron. The axis of this two-centered polyhedron is parallel to the *a*-axis, hence perpendicular to the four-fold, or the *c*-axis, and its length defines the value of *a*. It is proposed here that this polyhedron is the basic building block of Zr_9S_2 structure and the entire structure can be described as the complex packing of such polyhedra. To show how the polyhedra are packed to form the structure a projection picture, emphasizing the arrangement of the Kasper polyhedra, is shown in figure 3. It is projected along the *b*-axis and for clarity only the structure between the two mirror planes, at y = 1/4 and y = 3/4, is shown. There are two zigzag chains in a unit cell propagating along the *a*-axis. The chains are formed by the two-centered polyhedra, around a pair of Zr(2) atoms and with their axes parallel to the *b*-axis, joining together side by side sharing triangular faces. A point to be emphasized is that there is a pair of Zr(2) atoms in the planar hexagon of the polyhedra, which, at the same time, are the two centers of the other polyhedra with their axes parallel to the *a*-axis, in accord with the four-fold screw symmetry. Thus, each pair of Zr(2) atoms has a dual character: as central atoms for one polyhedron and as a part of a hexagonal ring for another. No shortening in interatomic distances will be expected for ring atoms according to Frank and Kasper. Because of the dual character, the Zr(2) - Zr(2) distance of 2.889 Å represents a 10% shortening for the ring atoms and, at the same time, a lengthening for the central-apical atoms by about 33% of the values for a perfect C.N. 14 Kasper polyhedron. Mainly because of the presence of a short Zr(2) - Zr(2) distance in the planar hexagon, the hexagon is distorted. A picture of the structure model constructed by the packing of the two-centered polyhedra is shown in figure 4. It is shown in this picture that the polyhedra join together along their axes by sharing the apical atoms, and that the two chains of polyhedra join together at the closest points by forming tetrahedra of three atoms from one chain and one from another.

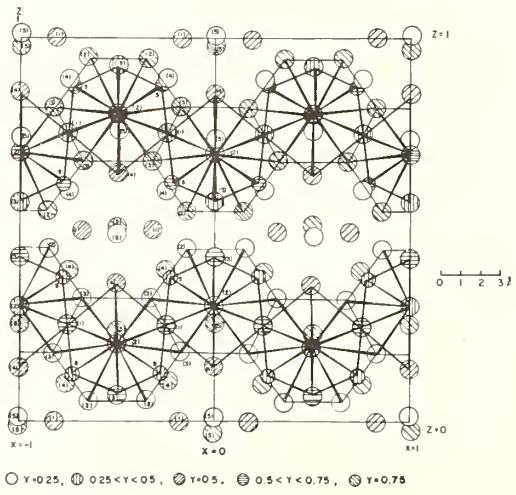

Fig. 3. Crystal structure of Zr_9S_2 with $0.25 \leq y \leq 0.75$ viewed along y-axis.

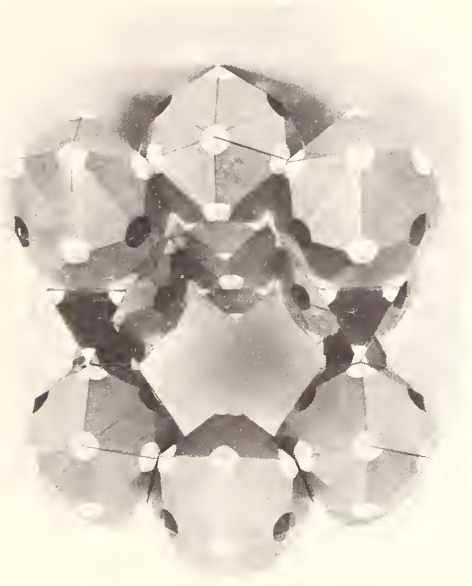

Fig. 4. Crystal structure of Zr_9S_2 constructed with the models of the two-centered polyhedra.

5.2. V_3S

The structures of α-V_3S and β-V_3S were reported by Pedersen and Grønvold [10] and the reported structures are reproduced in figure 5. The presence of short vanadium-vanadium distances was recognized and the structural similarity with β-W structure was discussed. If the structure of α-V_3S is projected along the [110] direction perpendicular to the four-fold axis, the view shown in figure 6 is obtained. Again for clarity only the partial structure, one half unit along the viewing direction, is shown and the presence of the Kasper polyhedral arrangement of atoms, around V(1) atoms and parallel to the [110] direction, is emphasized. From this figure it is readily apparent the structure unit in α-V_3S is very similar to that in Zr_9S_2. The differences between these two structures lies in the packing of the basic units. In α-V_3S, straight chains, formed by the two-centered polyhedra joined together by sharing triangular faces, propagate along the *c*-axis. Along the axes of the polyhedra, the polyhedra join together by sharing, instead of the apical atoms, an edge of the hexagonal pyramid around the apices. In other words, the apical atom of one polyhedron lies in the hexagonal ring of another. This last difference in packing gives rise to the difference in composition between Zr_9S_2 and α-V_3S. There are no important differences between the two basic units, and the V(1) - V(1) distance, 2.50 Å, is shortening from the sum, 2.72 Å, of radii by about 8.2%.

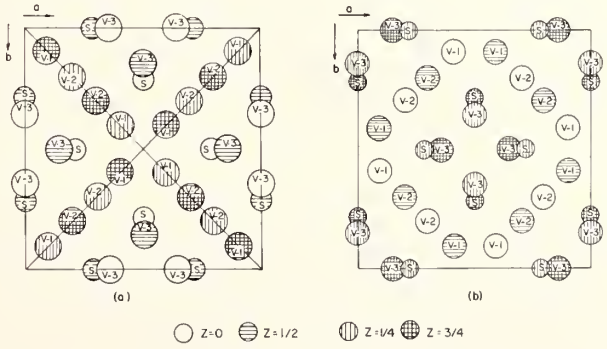

Fig. 5. The structures of (a) α - V_3S and (b) β - V_3S, viewed along the four-fold axes. (Data taken from the paper by Pedersen and Grønvold [10]).

465-504 O - 72 - 43

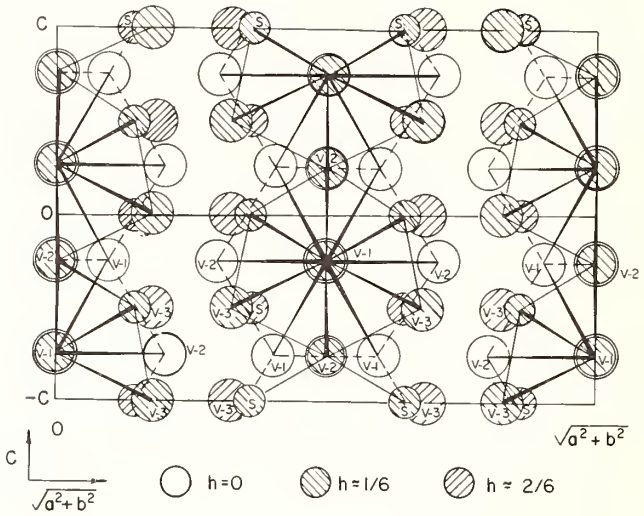

Fig. 6. Crystal structure of α-V_3S projected along the [110] direction, emphasizing the C.N. 14 Kasper polyhedral coordination of Ti(1) atoms.

The structure difference between α-V_3S and its low temperature form, β-V_3S, has been recognized as very small. Crystallographically speaking, it lies in replacement of a mirror plane perpendicular to the [110] direction in α-V_3S with a two-fold symmetry along that direction in β-V_3S. From the viewpoint of the two-centered polyhedral unit, the difference arises from the fact that the two sulfur atoms in the β-V_3S structure units occupy the 1 and 4 positions in the hexagon instead of the 1 and 3 positions as in the cases of α-V_3S and Zr_9S_2, and the upper part of the two-centered polyhedron is related to the lower part by a two-fold axis, instead of a mirror plane. The short V(1) - V(1) distance is 2.44 Å, corresponding to 10% shortening. The polyhedra in β-V_3S are packed in the same way as those in α-V_3S.

It is thus quite clear that the interpretation of the crystal structures of metal-rich sulfides based on the coordinations of the transition-metal atoms is very useful in the discussion of the structures. The presence of some of the atoms, such as Zr(5) in Zr_9S_2, Ta(1) in Ta_6S and Ta(3) in Ta_2S, which have no sulfur atoms as nearest neighbors, can be discussed without relying on any additional model. The presence of short interatomic distances and their values can also be explained semiquantitatively. The successful structural correlation among Zr_9S_2, α-V_3S and β-V_3S regardless of their significant difference in composition is very striking. The correlation will be later extended to phosphides with trigonal-prismatic coordination for phosphorus atoms. Most important of all, this approach sheds some light on the bonding in the crystal. The present interpretation clearly indicates that bonding situations for sulfur atoms in Zr_9S_2, α-V_3S and β-V_3S are different from that in Ta_2S. Since the Kasper polyhedral arrangement of atoms is characteristic of intermetallic compounds, the fact that sulfur atoms can replace the metal atoms in the formation of the Kasper polyhedra indicate the intermetallic characters of these compounds. In other words, sulfur in these compounds behaves as a metal and should probably be regarded as utilizing its outer orbitals to take on metallic character.

6. DISCUSSION

The structural similarity among α-V_3S, β-V_3S, Ti_3P and Fe_3P has been well recognized [13]. The fact, established by Rossteutschen and Schubert [15], that the low temperature form of Ta_3Ge has the Ti_3P structure type and the high temperature form has the Fe_3P structure type, seems to indicate that the α-V_3S to β-V_3S transition is related to the Fe_3P to Ti_3P transition. There is however no correlation among these structures at present. If a partial structure of Ti_3P is projected along the [110] direction the picture such as the one shown in figure 7 will be obtained. The appearance of this picture is so similar to that in

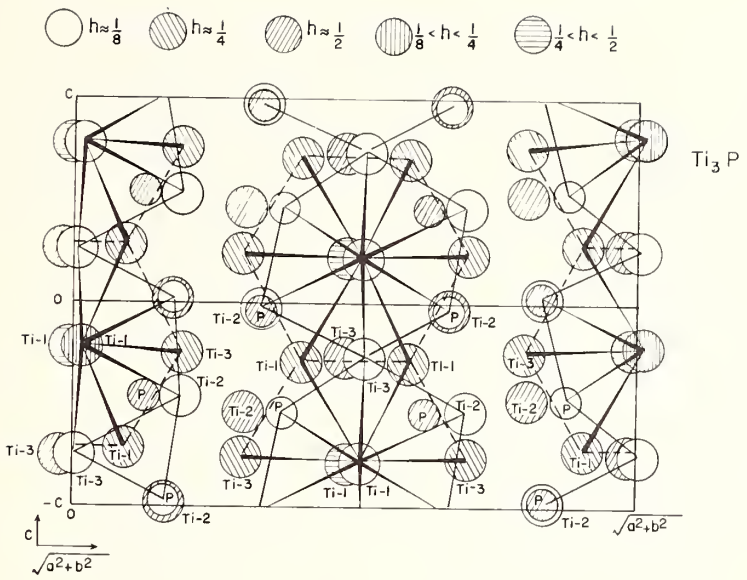

Fig. 7. The structure of Ti_3P projected along the [110] direction, emphasizing the C. N. Kasper polyhedral coordination of Ti(1) atoms.

figure 6 for α-V_3S that only by a close examination can the differences be revealed. It can be readily concluded that a similar two-centered polyhedron should be used as the basic building units of the structure. As it turns out, for the Ti_3P structure the two phosphorous atoms in the distorted hexagon are located at 1 and 4 positions as in the case of β-V_3S, a character of the low temperature form as discussed earlier. Furthermore, the Ti_3P structure has a similar two-centered polyhedral building unit with the two phosphorus atoms at 1 and 3 positions of the distorted hexagon, thus providing the relationship between the phase transitions discussed above. The packing scheme of the polyhedra for Ti_3P and Fe_3P is identical to that for the V_3S structures, and hence they have the same compositions. The Fe(1) - Fe(1) distance, 2.41 Å, in Fe_3P represents a shortening of 5.1% while the Ti(1) distance, 2.712 Å in Ti_3P represents a 6.6% shortening. In the polyhedra for the sulfides the apical vanadium atoms lie on the axes of the polyhedra while the apical atoms of the phosphide polyhedra are off the axes, shifted toward one of the phosphorus atoms resulting in a very long M-P and a shorter M-P distance. Therefore, the phosphorus coordinations in these phosphides are different from the sulfur coordinations in the vanadium sulfides.

It has been suggested earlier that in Zr_9S_2 the presence of sulfur atoms in the hexagon is the major cause for its distortion, and it follows that the distortion will be greater if the metal atoms are larger relative to the sulfur or phosphorus atoms. It will thus be expected that a compound, M_3X, will prefer the Ti_3P structure to the Fe_3P structure if the r_x/r_m is small, where r_x and r_m are the radii of X and M atoms, respectively. In the Ti_3P structure, the X atoms will be located in the 1 and 4 positions in the hexagon of the polyhedra, allowing the distortion forces to come from opposite directions and to cancel one another to a greater extent, while the Fe_3P structure, with the X atoms located off to one side of the hexagon, can tolerate only smaller distortion and will be stable when r_x/r_m is not very much smaller than unity. This conclusion is in agreement with the one arrived at by Lundström [13] that the Fe_3P and Ti_3P structures are characterized by $r_x/r_m > 0.82$ and $r_x/r_m < 0.82$ respectively.

As a summary of this discussion, the structures of the five types, Zr_9S_2, α-V_3S, β-V_3S, Fe_3P and Ti_3P, are compared in table 5 and the models of the five two-centered polyhedra are shown in figure 8.

The extension of the discussion to include the Fe_3P and Ti_3P structures enables one to show the similarities among Zr_9S_2, α-V_3S, β-V_3S and a large group of M_3X compounds involving many heavy Group IV_B and V_B elements. Many of these heavy elements have a highly metallic character. The inclusion of these compounds in the same group with the Zr_9S_2 and V_3S com-

Table 5

Comparison of the Zr_9S_2-, α-V_3S-, β-V_3S-, Fe_3P- and Ti_3P- Structures.

	Zr_9S_2	α-V_3S	β-V_3S	Fe_3P	Ti_3P
Fundamental Data					
Space group	$I4_1/amd$	$I\bar{4}2m$	$P4_2/nbc$	$I4$	$P4_2/n$
Lattice parameters: a	9.752	9.470	9.381	9.107	9.9592
c	19.216	4.589	4.663	4.460	4.9869
Atomic radii ratio (r_x/r_m)[a]	0.65	0.76	0.76	0.87	0.76
Coordinations					
Metal atom	C.N. 14 Kasper polyhedral	C.N. 14 Kasper polyhedral	C.N. 14 Kasper polyhedral	C.N. 14 Kasper polyhedral	C.N. 14 Kasper polyhedral
S or P atom	square-anti-prism	square-anti-prism	square-anti-prism	Tetrakai-decahedral	Tetrakai-decahedral
Two-centered polyhedra					
Point symmetry	mm	m	2	2	2
S or P position	1 and 3	1 and 3	1 and 4	1 and 3	1 and 4
Shortening[a] of central M-M	10%	8.2%	10%	5.1%	6.0%
Apex position	off the axis	on the axis	on the axis	off the axis	off the axis
Linking					
Along the poly. axes	apex-sharing	edge-sharing	edge-sharing	edge-sharing	edge-sharing
Chain shape	zigzag	straight	straight	straight	straight
Chain direction	along a	along c	along c	along c	along c
Link along the chains	face-sharing	face-sharing	face-sharing	face-sharing	face-sharing
Link between the chains	tetrahedron of M atoms	tetrahedron of M atoms	tetrahedron of M atoms	tetrahedron of M atoms	tetrahedron of M atoms

[a] References to sums of Goldschmidt radii.

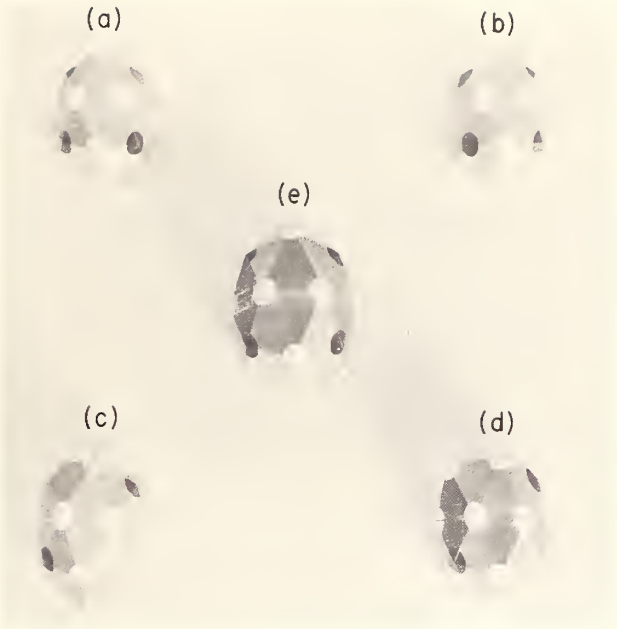

Fig. 8. The models of the two-centered polydra for the crystal structures: (a) α-V_3S, (b) β-V_3S, (c) Fe_3P, (d) Ti_3P and (e) Zr_9S_2.

pounds provides further support for the suggestion that these three sulfides should be regarded as intermetallic compounds.

There are many other compounds between transition metals and Group III_B, IV_B and V_B elements, for which the transition metal atoms have the C.N. 14 Kasper polyhedral coordinations, in particular those with the β-W, W_3Si and Mn_5Si_3 structures. In these structures, there are present even shorter interatomic distances between pairs of transition metal atoms. For example, 2.70 Å between the Zr atoms in Zr_5Al_3 [16] and 2.544 Å between two Ti atoms in Ti_5P_3 [17], corresponding to 15.6 and 12.3% shortening, respectively. All these Kasper polyhedra as in the cases discussed earlier. The major difference is that the axes of the Kasper polyhedra in Zr_5Al_3 and Ti_3P are parallel to the six-fold axes and the pairs of atoms involved do not have the dual characters mentioned earlier. According to Frank and Kasper a shortening of about 15% will be expected, in pretty good agreement with the observed values. While their prediction is useful in the interpretation of crystal structures, it is desirable that some fundamental study on the chemical bonding be carried out to explain the Kasper polyhedral coordination and the presence of very short bonds along the axis of the polyhedron.

7. REFERENCES

[1] Conard, B. R., Norrby, L. J. and Franzen, H. F., Acta Cryst. B25, 1729 (1969).
[2] Franzen, H. F. and Smeggil, J. G., Acta Cryst. B25, 1736 (1969).
[3] Franzen, H. F. and Smeggil, J. G. Acta Cryst. B26, 125 (1970).
[4] Chen, H.-Y. and Franzen, H. F., paper submitted to Acta Cryst.
[5] Owens, J. P., Conard, B. R. and Franzen, H. F., Acta Cryst. 23, 77 (1967).
[6] Franzen, H. F., Smeggil, J. G. and Conard, B. R., Mat. Res. Bull. 2, 1087 (1967).
[7] Conard, B. R. and Franzen, H. F., High Temp. Sci. 3, 49 (1971).
[8] Tuenge, R., Chen H.-Y. and Franzen, H. F. to be published.
[9] Franzen, H. F. and Graham, J., Z. Kristallogr. 123, 133 (1966).
[10] Pedersen, B. and Grønvold, F., Acta Cryst. 12, 1022 (1959).
[11] Aronsson, B., Lundström and Rundqvist, S., *Borides, Silicides and Phosphides*, John-Wiley, New York (1965).
[12] Brewer, L., *Electronic Structure and Alloy Chemistry*, edited by A. Beck, 223-235, Interscience Publishers, New York (1963).
[13] Lundström, T., Arkiv. Kemi, 31, 227 (1969).

[14] Frank, F. C. and Kasper, J., J. Acta Cryst. 11, 184 (1958); 12, 483 (1959).
[15] Rossteutscher, W. and Schubert, K., Z. Metal K. 56, 813 (1965).
[16] Edshammer, L.-E., Acta Chem. Scand. 16, 20 (1962).
[17] Lundström, T. and Snell, P.-O., Acta Chem. Scand., 21, 1343 (1967).
[18] Moore, C. E., National Bureau of Standards Circular 467 (1949).

National Bureau of Standards Special Publication 364, Solid State Chemistry, Proceedings of 5th Materials Research Symposium, issued July 1972.

MIXED CATION DISULFIDES OF TITANIUM, VANADIUM, AND CHROMIUM* +

Lawrence E. Conroy and Kondayoor Raghavan Pisharody

Department of Chemistry
University of Minnesota
Minneapolis, Minnesota 55455

Mixed cation disulfides of the types $Ti_{1-x}V_xS_2$ and $Ti_{1-x}Cr_xS_2$ have been prepared with compositions in the range $0 < x < 1$ in the Ti-V system and $0 < x < 0.4$ in the Ti-Cr system. Polycrystalline materials were prepared by direct reaction of the elements in vacuo at 950°. Single crystals of the Ti-V compounds were prepared by chemical transport reactions, employing iodine as the transport agent. The Ti-Cr disulfides failed to transport by this technique. The chemical properties of the mixed cation materials were found to be very similar to those of TiS_2. X-ray diffraction data indicated a random substitution of V or Cr for Ti in the normal Ti sites in the TiS_2 structure. A regular variation of lattice parameter with the vanadium content was observed in the Ti-V system. The magnetic properties of both the Ti-V and Ti-Cr compounds were characteristic of ferrimagnetic materials, with magnetic susceptibilities in the range of $3 \times 10^{-11} m^3/g$ to $12 \times 10^{-11} m^3/g$ (corrected) at room temperature. All of the mixed cation materials exhibited metallic electrical conductivity in contrast with the degenerate semiconductor behavior of TiS_2, with resistivities of the order of 10^{-5} ohm-m at room temperature. No superconductivity was observed at temperatures above 1.3 K. A band model for the description of the electronic properties of these materials is discussed.

Key words: Disulfides; electrical conductivity; magnetic properties; sulfides; titanium disulfide; titanium-vanadium disulfides; vanadium disulfide.

1. INTRODUCTION

The transition metals form numerous dichalcogenide compounds with the group VI elements. Some sixty-odd have been reported to date. The metals of groups IV, V, VI and VII typically form layered structures, whereas the group VIII dichalcogenides usually crystallize in the pyrite or marcasite structure. In electrical properties the dichalcogenides range from diamagnetic insulators like HfS_2 to true metals such as NbS_2. The entire scope of transition metal dichalcogenides has recently been treated in an elegant and extensive review by Yoffe and Wilson [1][1]. We have been particularly interested in the disulfides of the group IV transition metals because within this isostructural group of compounds is found the full range of electron transport properties. Titanium disulfide is metallic, ZrS_2 is a semi-conductor, and HfS_2 is a large gap insulator [2,3]. All crystallize in a layered structure (C6 in the Strukturbericht classification) consisting of close-packed anion planes in a hexagonal stacking array. The metal atom planes interleave every second pair of sulfur planes to produce a sequence -S-M-S-S-M-S- along the c-axis direction. In the group IV disulfides each metal atom is octahedrally coordinated to six sulfur atoms in the two adjacent layers. Each S-M-S sandwich layer is bonded to adjacent layers by relatively weak Van der Waal's forces with the result that these compounds cleave readily along the layers, *i.e.*, along the *a* plane of the hexagonal lattice. Although superconductivity occurs in the dichalcogenides of group V metals, none has been reported among the group IV compounds.

*Based upon a thesis presented by K. R. Pisharody to the Graduate School of the University of Minnesota in partial fulfillment of the requirements for the Ph. D. degree.

+This work was supported in part by the U. S. Army Research Office - Durham

[1]Figures in brackets indicate the literature references at the end of this paper.

Previous workers have found that substitutional doping of the layered dichalcogenides occurred quite readily in the case of the groups V and VI. Thus $(Nb/Mo)Se_2$ and $(Ta/W)Se_2$ mixed cation compounds have been studied [1,4]. This type of substitution offers intriguing possibilities for the manipulation of the *d* electron population and the examination of the effects of that population on the electrical, magnetic, and optical properties of the system. It is for that purpose that we undertook the preparation and examination of a number of mixed cation disulfides, with special attention to the 3d compounds which have been less studied than the heavier metal systems. This paper reports our studies on the $(Ti/V)S_2$ and $(Ti/Cr)S_2$ systems in which mixed cation disulfides with the type formulas $Ti_{1-x}V_xS_2$ and $Ti_{1-x}Cr_xS_2$ were prepared.

2. EXPERIMENTAL

Starting materials were: titanium metal sponge, 99.9% (United Mineral and Chemical Corp.); vanadium metal powder, 99.9% (Electronic Space Products, Inc.); chromium metal powder, 99.7% (Fisher Scientific Co.); resublimed 99.9% sulfur, and reagent grade 99.9% iodine. Titanium disulfide was prepared by the reaction of stoichiometric quantities of titanium metal sponge and sulfur in sealed, evacuated (10^{-5}torr) Vycor ampules. Each sample was heated slowly to 900° and held at that temperature for one week. The product was a yellow, crystalline powder. The x-ray powder diffraction pattern of this material showed only the reflections for hexagonal TiS_2. To prepare the $Ti_{1-x}V_xS_2$ and $Ti_{1-x}Cr_xS_2$ ($0 < x > 1$) materials, appropriate quantities of vanadium or chromium, sulfur, and TiS_2 were mixed thoroughly by grinding them together in a mortar. Each mixture was pressed into pellets at a pressure of 30,000 lb/in^2. The pellets were heated in sealed, evacuated (10^{-5} torr) ampules at 950° for one week. Each sample was examined for homogeneity by recording its x-ray powder diffraction pattern. Inhomogeneous samples were reheated another week under the same conditions.

The products at this point consisted of polycrystalline masses that exhibited a silvery luster. For the $Ti_{1-x}V_xS_2$ series, a homogeneous phase was produced for each composition over the entire range of x values, but the $Ti_{1-x}Cr_xS_2$ system yielded homogeneous products only in the range $0 < x > 0.4$.

2.1. PREPARATION OF SINGLE CRYSTALS

Samples containing 1 to 2 grams of each composition of the polycrystalline disulfides, described above, were employed in chemical transport [5] reactions to produce single crystals of useful size. Each sample was sealed in an evacuated (10^{-5} torr) Vycor ampule (25 mm diameter x 15 or 20 cm long) along with 5 mg/ml of resublimed iodine. The technique used for loading and evacuating the ampules has been described previously [6]. The transport ampule was heated in a two-zone tube furnace that provided independent temperature control and program for each zone. Initially both zones were heated to 900° and held at that temperature for 12 hours. The growth zone was then allowed to cool at a rate of 10°/hr to 750°. Transport was carried out in the gradient 900° - 750° for 6-7 days.

2.2. CHEMICAL ANALYSIS

Both titanium and vanadium were determined photometrically [7,8]. Samples were dissolved in a H_2SO_4-HNO_3 mixture and the metals were determined in H_2O_2 solution. Because of the interference between these two metals it was necessary to standardize at two wavelengths with pure standard solutions of Ti and V, and to measure the absorbance of each unknown solution at both wavelengths. The concentration of each metal could then be determined from simultaneous equations. Measurements were carried out at 4100 Å and 4500 Å using a Cary 14 spectrophotometer. On known mixtures this method was found to be accurate within 0.5%. Standard solutions were prepared from $K_2Ti(C_2O_4)_3$ and NH_4VO_3.

Chromium was determined spectrophotometrically with diphenyl carbazide [7]. Samples were brought into solution by fusion with a 1:1 mixture of Na_2O_2 and Na_2CO_3.

For sulfur analysis the disulfide sample was fused with a large excess of Na_2O_2-Na_2CO_3 mixture. The cooled cake was dissolved in water, acidified with HCl, and treated with excess $BaCl_2$. Sulfur was weighed as $BaSO_4$. Analytical results are summarized in table 1 of the results section of this paper.

Table 1

Chemical Analysis Data for $(Ti/V)S_2$ and $(Ti/Cr)S_2$ Mixed Cation Disulfides.

Nominal Composition	Composition Found Ti %	V %	Cr %	S %	Formula Found
$Ti_{0.9}V_{0.1}S_2$	35.7	7.2	-	56.9	$Ti_{0.84}V_{0.16}S_2$
$Ti_{0.8}V_{0.2}S_2$	33.8	9.9	-	56.4	$Ti_{0.80}V_{0.20}S_2$
$Ti_{0.5}V_{0.5}S_2$	21.1	22.4	-	56.6	$Ti_{0.5}V_{0.5}S_2$
$Ti_{0.4}V_{0.6}S_2$	17.1	26.7	-	56.1	$Ti_{0.40}V_{0.60}S_2$
$Ti_{0.2}V_{0.8}S_2$	7.0	38.0	-	55.0	$Ti_{0.17}V_{0.87}S_2$
$Ti_{0.1}V_{0.9}S_2$	2.1	43.3	-	54.6	$Ti_{0.05}V_{1.0}S_2$
$Ti_{0.9}Cr_{0.1}S_2$	39.0	-	4.0	56.8	$Ti_{0.92}Cr_{0.09}S_2$
$Ti_{0.8}Cr_{0.2}S_2$	32.9	-	10.5	56.5	$Ti_{0.78}Cr_{0.23}S_2$
$Ti_{0.7}Cr_{0.3}S_2$	29.3	-	14.5	56.1	$Ti_{0.7}Cr_{0.32}S_2$

2.3. OTHER EXPERIMENTAL METHODS

X-ray diffraction data were obtained on powdered samples using a Debye-Scherrer camera and on single crystals by rotation and precession photographs. Nickel-filtered copper radiation was employed. Powder data were refined by a least squares program adapted to Cohen's method [9].

Magnetic susceptibilities were determined by the Faraday method, using an electro-balance. The single-crystal samples weighed approximately 5 mg. Both platinum metal and Hg $[Co(SCN)_4]$ were utilized as calibration standards. The sensitivity of the system was 10^{-6} g and the reproducibility was within 2% on the smallest forces measured. Measurements were carried out over temperatures from 78 K to 300 K. Temperatures were measured with a Cu-constantan thermocouple.

Electrical resistivities were measured on single crystals by the method of Van der Pauw [10]. Electrical contacts to a crystal were made with silver conducting paint at the perimeter of the plate-like crystals. All measurements were made in He atmosphere. Temperatures were measured with a Cu-constantan thermocouple in contact with the center of the crystal.

Hall voltage experiments were carried out by both ac and dc methods. The apparatus has been described previously [11].

3. RESULTS AND DISCUSSION

X-ray powder diffraction data showed that in the preparation of the polycrystalline samples (before transport) a homogeneous phase was formed for each composition in the $Ti_{1-x}V_xS_2$ system. In the $Ti_{1-x}Cr_xS_2$ system, however, homogeneous products were obtained only for compositions having $x \geq 0.4$. Mixtures containing more chromium always yielded mixed phases, even after several weeks of heating at 950°. The chemical transport technique was successful in producing larger crystals $(Ti/V)S_2$ compositions, but all attempts to transport the $(Ti/Cr)S_2$ compositions were unsuccessful in that only TiS_2 was transported. The $(Ti/V)S_2$ crystals deposited as very thin platelets ranging up to approximately 1 cm in diameter and 200 microns in thickness. The color ranged from metallic yellow for the titanium-rich samples to metallic silver for the vanadium-rich compositions. The chemical properties of both the Ti/V and Ti/Cr compounds were very similar to those of TiS_2. All were insoluble in water and organic solvents, and all could be decomposed by concentrated mineral acids, especially oxydizing acids. These compounds were relatively unaffected by aqueous alkali solutions, but fusion with strong oxidants, such as Na_2O_2 or Na_2CO_3-$NaNO_3$ mixtures produced rapid decomposition to sulfates. These substances, like TiS_2, decompose below the melting point when heated in inert atmospheres, and it is this property that makes necessary the chemical transport technique for crystal growth. Heating in air above approximately 450° rapidly converts these compounds to SO_2 and metal oxides. Analytical data on the chemical compositions of the various stoichiometries that were prepared are reported in table 1. Data on the Ti/V composi-

tions are for the crystals prepared by chemical transport, and the Ti/Cr data represent the compositions of the polycrystalline material. Column 1 lists the nominal compositions that were prepared for the starting mixtures of TiS_2, metal, and sulfur.

Both the $(Ti/V)S_2$ and $(Ti/Cr)S_2$ compositions crystallize in the same C6 structure as does TiS_2, having the $P\bar{3}m$ space group (D_{3d} symmetry). Thus both the V and Cr atoms must be in octahedral coordination with sulfur atoms between alternate sulfur layers. The plate-like habit and ready cleavage along the *a* plane are very similar to those properties of the other C6 structure transition metal disulfides [1,12]. Lattice parameters for the crystals are listed in table 2, along with those for nominally pure TiS_2. These data show that the substitution of Ti atoms by V or Cr atoms has negligible effect on the *c* parameter but causes a decrease in the *a* dimension, *i.e.* within the close-packed sulfur planes. A plot of the *a* dimension vs. the vanadium fraction of the metal, shown in figure 1, indicates a Vegard's Law proportionality between the lattice constant and the vanadium content. This contraction is consistent with approximate core radii of 0.60Å and 0.68Å for tetravalent vanadium and titanium, respectively. It is to be noted that, like TiS_2 itself [2], the Ti/V and Ti/Cr disulfides usually crystallize with excess metal in the structure. The C6 structure can accommodate metal atoms in excess of the MS_2 composition both by adding metal atoms within the S-M-S sandwich layers, since half of the octahedral sites and all of the tetrahedral sites are still empty, or by adding them to the nominally empty layers between adjacent sandwiches.

Table 2

Crystallographic Data for $(Ti/V)S_2$ and $(Ti/Cr)S_2$ Mixed Cation Disulfides.

Composition	a (Å)	c (Å)	c/a
TiS_2	3.405 ± 0.005	5.701 ± 0.006	1.67_4
$Ti_{0.84}V_{0.16}S_2$	3.390 ± 0.004	5.707 ± 0.006	1.68_3
$Ti_{0.80}V_{0.20}S_2$	3.382 ± 0.004	5.710 ± 0.006	1.68_8
$Ti_{0.50}V_{0.50}S_2$	3.352 ± 0.002	5.706 ± 0.002	1.70_2
$Ti_{0.4}V_{0.60}S_2$	3.345 ± 0.005	5.710 ± 0.006	1.707
$Ti_{0.17}V_{0.87}S_2$	3.318 ± 0.005	5.710 ± 0.009	1.72_1
$Ti_{0.05}V_{1.0}S_2$	3.296 ± 0.005	5.666 ± 0.01	1.72_1
$Ti_{0.92}Cr_{0.09}S_2$	3.395 ± 0.004	5.701 ± 0.006	1.67_9
$Ti_{0.78}Cr_{0.23}S_2$	3.395 ± 0.002	5.701 ± 0.005	1.67_9
$Ti_{0.70}Cr_{0.32}S_2$	3.381 ± 0.003	5.712 ± 0.006	1.68_9

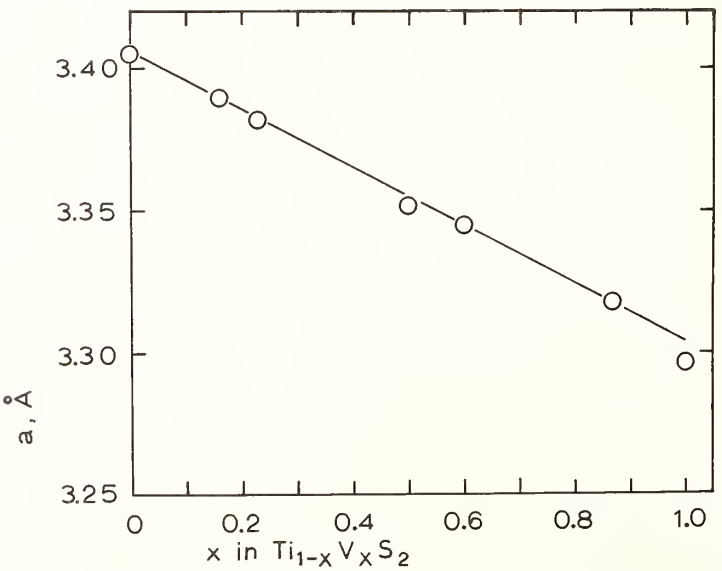

Fig. 1. Lattice parameter, *a*, *vs.* composition, x, for $(Ti/V)S_2$ mixed cation disulfides.

The substitution of Ti atoms by V or Cr atoms must occur on a random basis because our x-ray diffraction data showed no evidence of ordering beyond that of the C6 structure of TiS_2. Similarly the accommodation of excess metal atoms must take place randomly because no structural evidence of the extra metal was found.

Both the $(Ti/V)S_2$ and $(Ti/Cr)S_2$ systems exhibited paramagnetism at temperatures below 300 K. Figures 2 and 3 show the plots of reciprocal susceptibility *vs.* temperature for the $(Ti/V)S_2$ systems, respectively. χ', the susceptibility per gram of $Ti_{1-x}M_xS_2$, has been corrected for diamagnetic contributions using the values (in $m^3/mol \times 10^{11}$) of -6 for Ti^{+4}, -9 for V^{+4}, -10 for Cr^{+4} and -40 for S^{-2} [13,14].[2] The susceptibility data fit a Curie-Weiss law between 120 and 300 K. Least-squares fits of the linear portions of these plots yield the magnetic constants that are listed in table 3. The low-temperature deviations from Curie-Weiss dependence are characteristic of ferrimagnetic structures. An examination of the magnetic moments tabulated in table 3, column 5, reveals no direct relationship to the vanadium or chromium content. Thus the magnetic evidence points to the existence of interactions between two or more magnetic sublattices in antiferromagnetic array. We have no evidence thus far concerning the distribution of the two types of metal ions in the crystals. Our powder

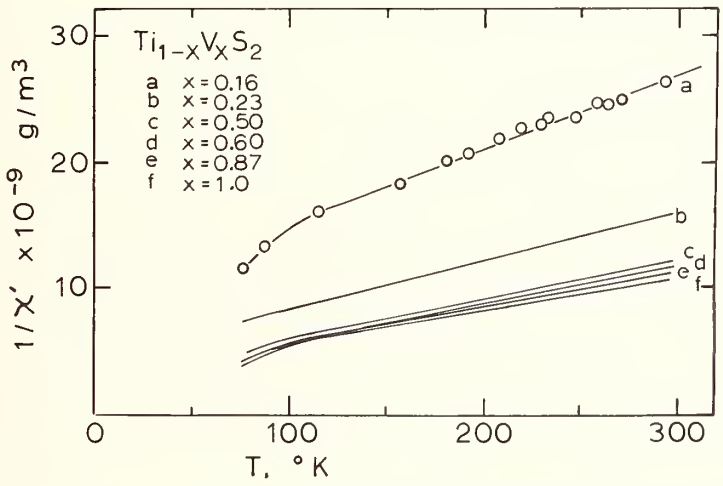

Fig. 2. Reciprocal magnetic susceptibility of $(Ti/V)S_2$ as a function of temperature.

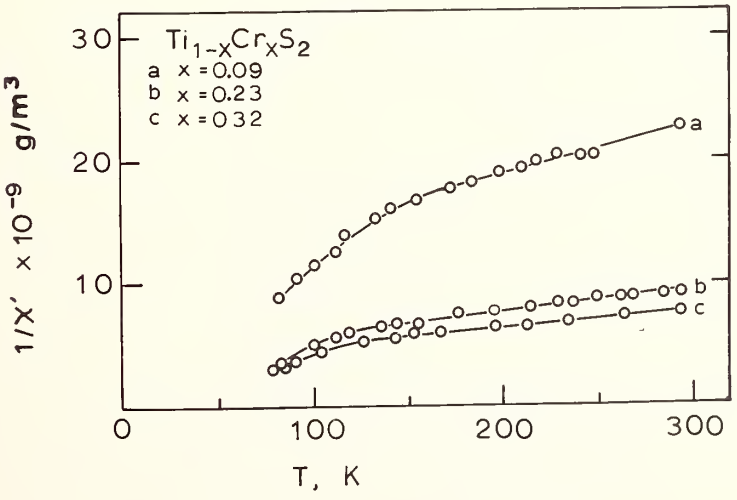

Fig. 3. Reciprocal magnetic susceptibility of $(Ti/Cr)S_2$ as a function of temperature.

Table 3

Magnetic Constants for $(Ti/V)S_2$ and $(Ti/Cr)S_2$ Mixed Cation Disulfides.

1 Composition M,x in $Ti_{1-x}M_xS$	2 Weiss Constant θ (K)	3 Curie Constant C	4 Magnetic Moment per Metal Atom at 300 K μ (BM)	5 Magnetic Moment per V or Cr Atom at 300 K μ (BM)
0	---	---		
V 0.16	-161 ± 19	0.16	0.897	5.6
V 0.23	-120 ± 20	0.24	1.14	5.0
V 0.50	- 97 ± 10	0.30	1.31	2.6
V 0.60	- 92 ± 16	0.30	1.35	2.2
V 0.87	-105 ± 19	0.33	1.41	1.8
V 1.0	- 94 ± 15	0.29	1.55	1.6
Cr 0.09	-257 ± 20	0.21	1.33	1.3
Cr 0.23	-214 ± 20	0.42	1.99	8.7
Cr 0.32	-250 ± 30	0.71	2.40	7.5

x-ray diffraction data could not distinguish any such sublattices occupied by atoms as closely similar as Ti, V, and Cr.

Electrical resistivity data were obtained on single crystals of the $(Ti/V)S_2$ compositions. No crystals sufficiently large for electrical measurements were obtained in the transport of the $(Ti/Cr)S_2$ system. Resistivities were measured in the *a* plane for all compositions of $(Ti/V)S_2$. No reliable data could be obtained for resistivity parallel to the *c* axis because of the extremely thin flake-like habit of the crystals. The *a* plane resistivity *vs.* temperature data for the titanium-vanadium disulfides are shown in figure 4, along with similar data for pure TiS_2. The room temperature resistivity of 2.35×10^{-5} ohm-m obtained for TiS_2 in this work is in fair agreement with that obtained in earlier work in this laboratory 1.35×10^{-5} ohm-m and reported by Conroy and Park [6], and with the results of McTaggart and Wadsley [3], 7.7×10^{-5} ohm-m. The dependence of the electrical resistivity upon the composition is indicated by the plot in figure 5.

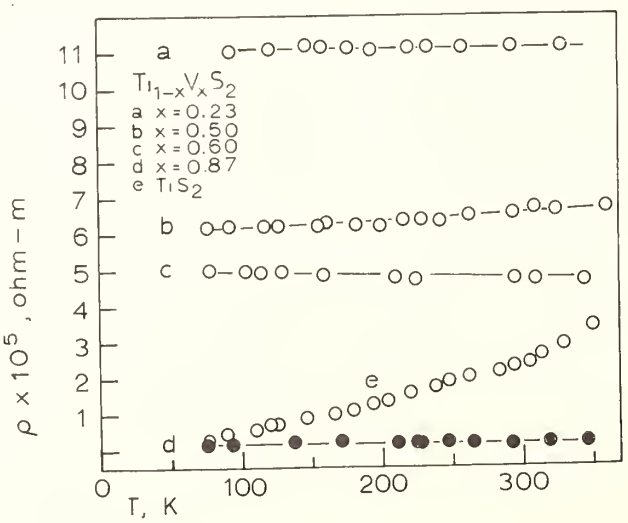

Fig. 4. Electrical resistivity of $(Ti/V)S_2$ as a function of temperature.

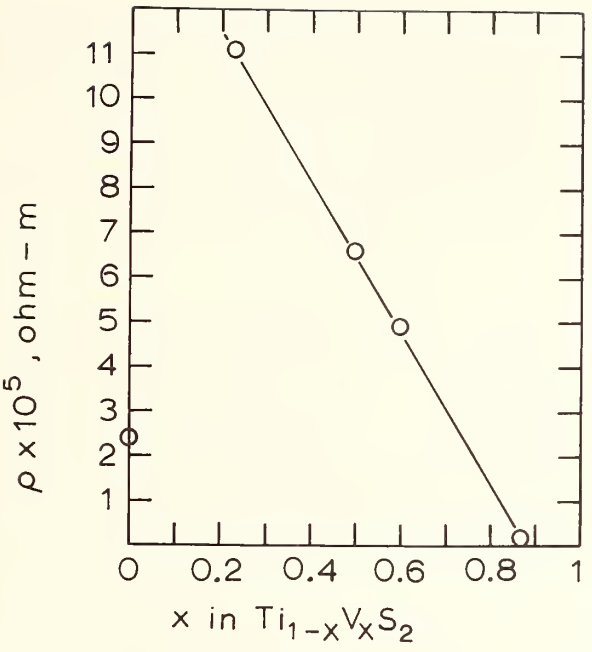

Fig. 5. Electrical resistivity of $(Ti/V)S_2$ as a function of composition.

A comparison of the resistivity *vs.* temperature data for the $(Ti/V)S_2$ system (fig. 4) with that for TiS_2 shows that the substitution of vanadium for titanium in this lattice has changed the electrical characteristics from that of a degenerate semiconductor in TiS_2 to metallic conductivity. Some preliminary Hall coefficient measurements on this system indicate that each vanadium atom contributes a fractional additional electron to the system. No superconductivity could be detected in any of these $(Ti/V)S_2$ or $(Ti/Cr)S_2$ materials down to 1.3 K.

The effect of the substitution of vanadium or chromium atoms for titanium atoms in the TiS_2 structure is to confer properties of a paramagnetic (or ferrimagnetic) metal on the system. An energy level model to describe such a nonmetal-metal transition in compounds having the C6 structure has been proposed by Vellinga, de Jonge, and Haas [15]. Their schematic energy level diagram is reproduced in figure 6. For trigonally distorted octahedral coordi-

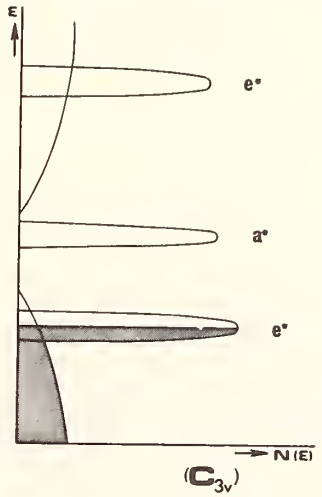

Fig. 6. Schematic one-electron energy level diagram for C6 disulfides with trigonally distorted octahedral (C_{3v}) coordination.

nation, with the metal atom shifted along the trigonal axis (symmetry C_{3v}), the ligand field splitting produces two degenerate e* antibonding levels and a nondegenerate a* (d_{z^2}) level, with one of the e* levels (d_{x2-y2} and d_{xy}) being lowest. Employing this model, Vellinga, de Jonge, and Haas have successfully explained the metallic behavior of β-$MoTe_2$. Although TiS_2 and our substituted disulfides have the same C6 structure as β-$MoTe_2$, it has not yet been established in any of these compounds that the octahedral coordination around the metal is trigonally distorted as it is in β-$MoTe_2$. However it is reasonable to expect such distortions since it is found in TaS_2, also a C6 structure. The smaller first row transition metal atoms Ti, V, and Cr, would be more easily displaced in the relatively large octahedral voids in the sulfide lattice than would a Ta atom.

Application of the Vellinga-deJonge-Haas model to TiS_2 would predict that the energy bands that arise from the overlap of the antibonding orbitals would all be empty, so that TiS_2 would be an insulator or semiconductor. The substitution of the d^1 ions of the V^{+4} or d^2 ions of Cr^{+4} would contribute electrons to the low-lying e* band and bring about metallic conduction. Because of the smaller radial extent of the d orbitals in Ti as compared with Ta, one would expect the interaction with adjacent atoms to be less, so that the conduction bands would be narrower in TiS_2 than in TaS_2. The greater binding of the d band electrons to the ion cores may be responsible for the observed paramagnetic susceptibility in these substituted disulfides.

4. ACKNOWLEDGMENT

This research was supported in part by the U. S. Army Research Office - Durham.

5. REFERENCES

[1] Wilson, J. A. and Yoffe, A. D., Advan. Phys., 18, 193 (1969).
[2] Conroy, L. E. and Park, K. C., Inorg. Chem., 7, 459 (1968).
[3] McTaggart, F. and Wadsley, A. D., Aust. J. Chem., 11, 471 (1958).
[4] Brixner, L. H. and Teufer, G., Inorg. Chem., 2, 992 (1963).
[5] Schäfer, H., *Chemical Transport Reactions*, Academic Press, New York, 1964.
[6] Conroy, L. E., Inorg. Syntheses, 12, 158 (1970).
[7] Sandell, E. B., *Colormetric Determination of Traces of Metals*, 2nd ed., Interscience Publishers, New York, 1960, p.572.
[8] Weissler, A., Ind. Eng. Chem., 17, 775 (1945).
[9] Cohen, M., Rev. Sci. Instrum., 6 68 (1935) 7, 155 (1936).
[10] Van der Pauw, L., Phillips. Res. Repts., 13, 1 (1958).
[11] Vergamini, P., M. S. Thesis, University of Minnesota, Minneapolis, Minnesota (1969).
[12] Jellinek, F., Ark. Kemi., 20, 447 (1963).
[13] Angus, W., Proc. Roy. Soc., Ser. A., 136, 573 (1932).
[14] Klemm, W., Z. Anorg. Allg. Chem., 246, 347 (1941).
[15] Vellinga, M. B., de Jonge, R., and Haas, C., J. Solid State Chem., 2, 299 (1970).

---

[2] To convert to cgs units, divide by $4\pi \times 10^{-6}$.

DISCUSSION

F. Holtzberg: Did you analyze your compounds for sulfur as well as for metals?

L. E. Conroy: Yes, all components were determined. Samples were oxidized by fusion with a large excess of Na_2O_2-Na_2CO_3 mixture. The cooled cake was dissolved in water, acidified, and the sulfur was precipitated as $BaSO_4$. Attempts to determine sulfur as SO_2 were unsuccessful, apparently because the presence of V_2O_5 or TiO_2 catalyzes the conversion to SO_3.

National Bureau of Standards Special Publication 364, Solid State Chemistry, Proceedings of 5th Materials Research Symposium, issued July 1972.

CRYSTAL GROWTH AND PROPERTIES OF SOME I-III-VI_2 COMPOUNDS

H. M. Kasper

Bell Telephone Laboratories, Incorporated
Murray Hill, New Jersey 07974

The I-III-VI_2 compounds are ternary analogues to the II-VI semiconductors and are interesting both as possible nonlinear optical materials and as semiconductors. They usually crystallize in the chalcopyrite structure which belongs to the uniaxial acentric crystal class $\bar{4}2m$. In order to study their optical and semiconductor properties, single crystals of $AgGaS_2$, $CuGaS_2$ and $CuInS_2$ have been grown by slowly cooling melts of stoichiometric composition, and the conditions of growth by directional freezing are reported. $AgGaS_2$ crystallizes as yellow and green crystals. The yellow crystals seem to be gallium rich. $CuGaS_2$ does not melt congruently. Stoichiometric melts first crystallize a composition near $Cu_{0.88}Ga_{1.04}S_2$ as light orange crystals. Later darker, nearly stoichiometric crystals are obtained. $CuInS_2$ crystallizes between 1050 °C and 1000 °C with all crystals transparent to beyond 10 μ. There is a strong absorption in $CuGaS_2$ near 1.8 μ, which extends toward the visible and causes the darker color. The bandgaps are 2.72 eV for $AgGaS_2$, 2.53 eV for $CuGaS_2$ and 1.55 eV for $CuInS_2$ at 2 K. Both the light and dark crystals of $CuGaS_2$ as well as $CuInS_2$ and $AgCuS_2$ show sharp line luminescence. The linear and nonlinear optical properties of $AgGaS_2$, $Cu_{0.88}Ga_{1.04}S_2$ and $CuInS_2$ have been investigated. Unfortunately in both $Cu_{0.88}Ga_{1.04}S_2$ and $CuInS_2$ the birefringence is not large enough to permit three frequency phase matching, but $AgGaS_2$ can be phase matched in the infrared for both parametric oscillation and second harmonic generation. With both $CuGaS_2$ and $CuInS_2$ a pronounced structure has been observed in electroreflectance near the bandgap and at higher energies. From this structure is concluded that the crystal field splitting of the d bands is about 0.7 eV and that the d bands lie about 2 eV below the valence band edge in both compounds. Stimulated emission has been observed in $AgGaS_2$, $CuGaS_2$ and $CuInS_2$. $AgGaS_2$ is usually of high resistivity, whereas $CuGaS_2$ is p-type and $CuInS_2$ can be made both p- and n-type.

Key words: $AgGaS_2$; chalcogenides; chalcopyrite; I-III-VI_2 compounds; crystal growth; $CuInS_2$; $CuGaS_2$; d-bands; direct bandgap semiconductors; nonlinear optical materials; semiconductor materials.

1. INTRODUCTION

Luminescent materials, especially zinc sulfide and cadmium sulfide, have been of considerable interest for a long time both scientifically and technically. More recently, encouraged by the success of many useful semiconductor devices, investigators have begun to study in detail electroluminescent devices, in which minority carriers are injected at a junction so that light is produced by recombination with majority carriers. These studies have generally focused on two classes of materials, II-VI compounds [1][1] and III-V compounds [2]. Both the II-VI's and the III-V's are deficient in some respect insofar as being ideal electroluminescent materials [3]. In the III-V compounds visible light emission is relatively inefficient, while the II-VI sulfides and selenides have so far only been obtained with useful n-type conductivity, so that no efficient electroluminescence has been achieved. ZnTe is only p-type and CdTe has the bandgap in the infrared. Thus, we were led to consider alternative electroluminescent materials.

[1]Figures in brackets indicate the literature references at the end of this paper.

In contrast to our extensive knowledge of the physical properties of the II-VI compounds, there is presently very little known about ternary compounds related to the II-VI's. The most obvious related class is the I-III-VI_2 compounds, where the bivalent cation is substituted half by a monovalent and half by a trivalent cation, *e.g.*, in ZnS Zn is substituted half by the element to its left in the periodic table (Cu) and half by the element to its right (Ga). A number of materials in this class were first prepared by Hahn and coworkers [4], who determined that all ABC_2-compounds (A = Cu, Ag; B = Al, Ga, In; C = S, Se, Te) had the chalcopyrite ($CuFeS_2$ type) crystal structure. This structure can be derived from the zincblende lattice by an ordered substitution at the cation sites. The superstructure formed leads to a doubling of the c-axis in the chalcopyrite with respect to the cubic zincblende lattice [5] (figure 1).

Previous investigations of these materials [6] have mostly concerned the thermoelectric properties of the ABC_2 members with lower bandgaps. It has been shown that small crystals of many ABC_2 can be obtained by hydrothermal methods [7]. Robertson obtained crystals of $AgGaS_2$ by a Bridgman technique [8], and Lerner those of $CuGaSe_2$ and $AgInSe_2$ by zone refining methods [9]. We have found that $CuGaS_2$ and $CuInS_2$ can be transported with iodine vapor [10], but we were unsuccessful in transporting $AgGaS_2$. However, sulfides generally incorporate insignificant amounts of iodine which can change transport and optical properties quite drastically. There have also been some studies on the compound formation of pseudobinaries of I-III-VI_2 compositions with either II-VI compounds as by Hahn [4] and Parthe [11] or with the III_2VI_3 compounds as in the investigation of the system $CuGaS_2$-Ga_2S_3 by Belova and coworkers [12].

We will report here on the preparation and properties of crystals of $AgGaS_2$, $CuGaS_2$ and $CuInS_2$, which we have studied more extensively than other members of the I-III-VI_2 family and which have the most interesting electroluminescent and nonlinear optical properties of those members so far examined.

2. EXPERIMENTAL

In each case crystals were obtained by slowly cooling melts of stoichiometric composition. Starting materials were 99.999% pure copper, 99.999% pure silver, 99.9999% pure gallium, and 99.9999% pure sulphur obtained from United Minerals Corporation. The melts were prepared similar to Belova and coworkers [12] by heating stoichiometric amounts in silica boats contained in evacuated and sealed silica ampoules. Slowly cooling the melt was used to initiate directional freezing and crystals up to several mm in size were obtained of all three materials.

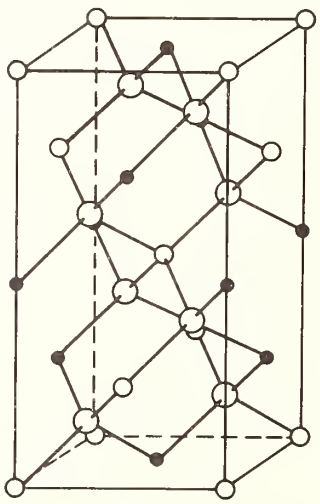

Fig. 1. Model of $CuGaS_2$ crystallizing in the chalcopyrite lattice.

3. RESULTS AND DISCUSSION

(a) *Silver gallium sulfide, $AgGaS_2$ - Preparation:* The melting point has been reported to be at 980 °C [12] or 1040 °C [8], although our quenching experiments indicate that crystallization occurs closer to 950 °C. The melts were cooled from 1020 °C at a rate of about 1 °C/hour. In many cases the silica boats were cracked because of the thermal contraction of the crystals on cooling. Generally when the starting composition was exactly $AgGaS_2$ the ingot consisted of a light yellow part, which had crystallized first, blending into a green part, which crystallized last. Luminescence investigations showed, that exciton emission was sharper for the green material [13]. Growth experiments where the initial stoichiometry was $Ag_{0.97}Ga_{1.01}S_2$ resulted in completely yellow material. On the other hand when oxygen got into the ampoule, when crystals were formed they were green. Thus, it is apparent that the color of the crystals depends strongly on the defect concentration and that $AgGaS_2$ does not melt completely congruently. It is likely that the solid in equilibrium with a stoichiometric melt has Ga/Ag >1. This may be part of the reason for the observed difference of melting point (980 °C) and the reported crystallization temperature (950 °C).

Properties: The lattice constants (a = 5.75 and c = 10.305) of the yellow and green material did not show any difference within the accuracy of our measurement and agreed well with previous measurements [4]. The absorption spectrum for a yellow crystal is shown in figure 2. The absolute reliability of the absorption coefficient as shown in figures 2, 4, and 7 is discussed by Boyd et al. [14]. $AgGaS_2$ is transparent in the infrared to about 13 μ, where multiple phonon absorption starts. There was some residual absorption in the visible in all the samples measured, and it is not clear at this time how it can be eliminated. The bandgap deduced from reflectivity measurements by Tell et al. [13] is 2.727 eV at 2 K. It is shifted at 77 K to a slightly higher energy (2.732 eV) in contrast to the decrease of the bandgap with increasing temperature normally observed for II-VI compounds. This may be caused by the anisotropic thermal expansion. Unfortunately no measurements of thermal expansion of $AgGaS_2$ are reported in the literature. The indices of refraction at 1 μ are n_o = 2.4582 and n_e = 2.4053 with a birefringence of 0.0529 [14]. This birefringence in connection with the acentricity of the chalcopyrite structure and a large coefficient of second harmonic generation allows phase matched second harmonic generation with the wavelength of the fundamental between 1.8 μ and 11 μ. Chemla et al. [15] and Boyd et al. [14] have observed the phase matched second harmonic with a CO_2-laser output at 10.6 μ as a pump. Measurement of the nonlinear optical coefficient shows that it is about three times that of $LiNbO_3$ [14]. However, the residual absorption of unidentified origin below the bandgap and problems with crystal quality have first to be worked out before $AgGaS_2$ can serve as a useful nonlinear optical material. The class $\bar{4}2m$ of $AgGaS_2$ is nonenantiamorphous and the allowed optical activity is normally unobservable. Hobden [15] detected optical rotation in $AgGaS_2$ at 4974Å where $n_o = n_e$ and it should also be detectable in $CuGaS_2$ where $n_o = n_e$ at 6400Å [14].

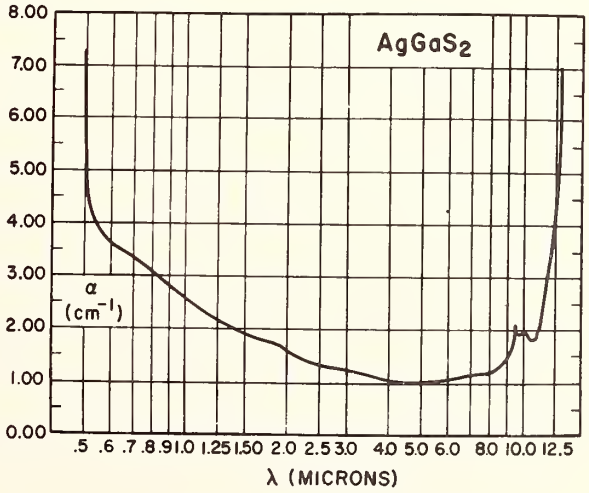

Fig. 2. Absorption coefficient of $AgGaS_2$.

465-504 O - 72 - 44

Investigation of the electrical transport properties of $AgGaS_2$ have shown no useful conductivity [13]. All crystals, both yellow and green, are semi-insulating but of very low ($\sim 10^{-7}$ Ω cm) conductivity and it was not possible to determine the nature of the few carriers. Various doping and annealing experiments did not change the situation. The low conductivity is disappointing from a semiconductor point of view, but of course connotes an absence of free carrier absorption in the infrared which is desirable for optical applications.

(b) *Copper gallium sulfide, $CuGaS_2$ - Preparation:* The preparation and crystallization of $CuGaS_2$ is more complicated than that of silver gallium sulfide. Belova et al. [12] studied the pseudobinary $CuGaS_2$-Ga_2S_3 system with samples quenched from 1100 °C and measured the dependence of the lattice constants on composition. In figure 3, which is adapted from their publication, two homogeneity regions for $Cu_{1-x}Ga_{1+x/3}S_2$ with $0 < x < 0.13$ and $0.65 < x < 0.9$ can be recognized. In the region $0 < x < 0.13$ the diffraction pattern corresponds to the chalcopyrite structure and for $0.65 < x < .9$ to an ordered alloy $CuGa_5S_8$. Cooling stoichimetric melts of $CuGaS_2$ we found that the results depend strongly on three parameters: (1) the maximum temperature to which the melt had been raised, (2) the soaking time at this temperature, and (3) the cooling rate. Generally, it was found that at the beginning of the crystallization lighter orange crystals formed, while later darker crystals with some black material crystallized. This indicates that at first gallium richer phases grew and after some depletion of the melt at lower temperatures more copper rich crystals appeared. When the melt was raised to temperatures above 1160 °C, invariably the first material crystallizing was yellow and obviously lay in the region $0.65 < -x < 0.9$. Below 1160 °C all crystals were always orange and darker. This shows that the jump in the solidus curve of the phase diagram between $Cu_{0.34}Ga_{1.22}S_2$ and $Cu_{.88}Ga_{1.04}S_2$ occurs near 1160 °C. The reported melting point of $CuGaS_2$ is, however, 1280 °C according to Apple and Fischer [17] and >1200 °C according to Belova et al. [12]. We think that the difference is not a supercooling effect but due to the presence of other valence states such as Cu^{++} and Ga^{++} in the melt, which may make the treatment of these systems as pseudobinaries inappropriate. We obtained crystals with reasonable reproducibility, when we soaked the stoichiometric melt at 1150 °C for a day and then slowly cooled at a rate of about 1-1/2 °C/hour. The crystals were several mm in diameter with concoidal cleavage. The first crystals were deep orange or deep red; the later ones darker.

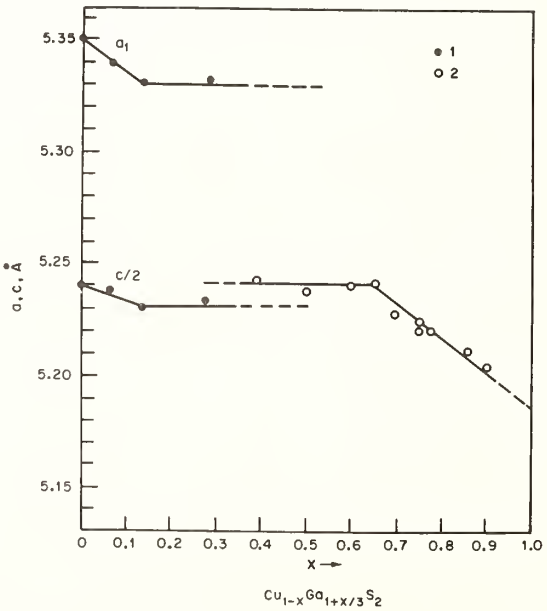

Fig. 3. Lattice constants and their dependence on composition for the system $Cu_{1-x}Ga_{1+x/3}S_2$ (adapted from Belova, Koshkin and Palatnik [12]).

Properties: Spectrographic analysis showed that the crystals contained about 5 ppm Si and Mg, 3 ppm Al and Fe, and 2 ppm Ca. Twenty-nine other elements were checked but not found. The lattice constants for the orange crystals were a = 5.328Å and c = 10.462Å, while the dark crystals had a = 5.351Å and c = 10.484Å. This suggests (using the data of figure 3) compositions of $Cu_{0.88}Ga_{1.04}S_2$ or x = 0.12 for the orange crystals and nearly stoichiometric $CuGaS_2$ for the dark crystals. The absorption spectrum in figure 4 shows transmission in the infrared to 13 μ. Reflectivity measurements give 2.53 eV for the bandgap of $CuGaS_2$ at 2 K. In addition, there is an absorption in the red crystals in the infrared (figure 5) and a much stronger broad absorption in the dark crystals at about 1.8 μ. We suspect that defects connected with Cu^{2+} are responsible for the absorption in the dark crystals. The indices of refraction at 1 μ are n_o = 2.5406 and n_e = 2.5349 with a birefringence of only $n_e - n_o = -.0053$ [14]. The small birefringence does not allow phase matched second harmonic generation at any wavelength in $CuGaS_2$. The electroreflectance spectrum of $CuGaS_2$ shows pronounced structure at about 2.4 eV and between 3.5 and 5 eV (figure 6). The electroreflectance spectra of the II-IV-V_2 compounds with chalcopyrite structure like $CdSnP_2$ have been very satisfactorily explained by Shay [18] and coworkers with the quasicubic model, which assumes that the band structure is insensitive if two atoms like In are replaced with an atom to the right and to the left of In in the periodic table (*i.e.*, Cd and Sn substituting for 2 In). This model also assumes that the only important change in the band structure going from the zincblende to the chalcopyrite lattice is due to the relative size of the tetragonal distortion. While this model works beautifully for the II-IV-V_2 compounds, it breaks down for the change ZnS → $CuGaS_2$ [19]. This breakdown can be seen from the fact that there is a big difference in the size of the bandgap in ZnS (3.8 eV) and $CuGaS_2$ (2.40 eV). The model probably is inappropriate because of the d-electrons present in copper. We can assign the structure of the electroreflectance spectrum [20] near 4.5 eV to a transition near the Γ-point from a d_ε electron band mostly on the copper to the s-type conduction band and similarly the structure near 3.8 eV to a transition d_γ to the conduction band (figure 4). This corresponds to a crystal field splitting for the d-electrons near the copper of 0.7 eV, which is very close to the value found for tetrahedral Cu^{2+} in many oxides [21]. The location of the d-bands in $CuGaS_2$ with respect to the conduction band edge coincides with the position of the upper valence band edge in ZnS, which is made up mostly from p-orbitals. Since there is strong orbital overlap between d and p-electron distribution, we conclude that the breakdown of the pseudocubic model is due to this interaction. The position of the d-bands ~ 1.5 eV below the valence band edge is consistent with the observation that the chemically most stable valence of tetrahedral copper in sulfides is monovalent, in contrast to oxidic tetrahedral copper compounds, where an inversion of these bands would be expected, but instead mostly bivalent copper is observed.

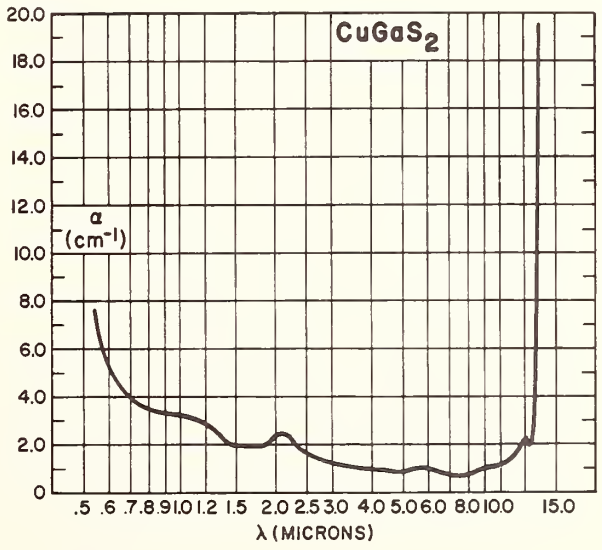

Fig. 4. Absorption coefficient of orange $Cu_{1-x}Ga_{1+x/3}S_2$.

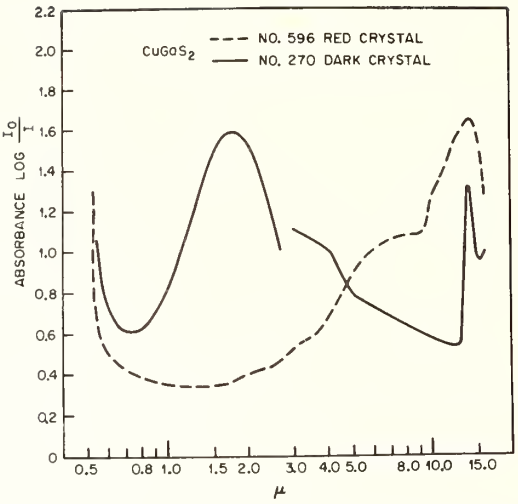

Fig. 5. Absorbance log I_o/I of red and dark $Cu_{1-x}Ga_{1+x/3}S_2$.

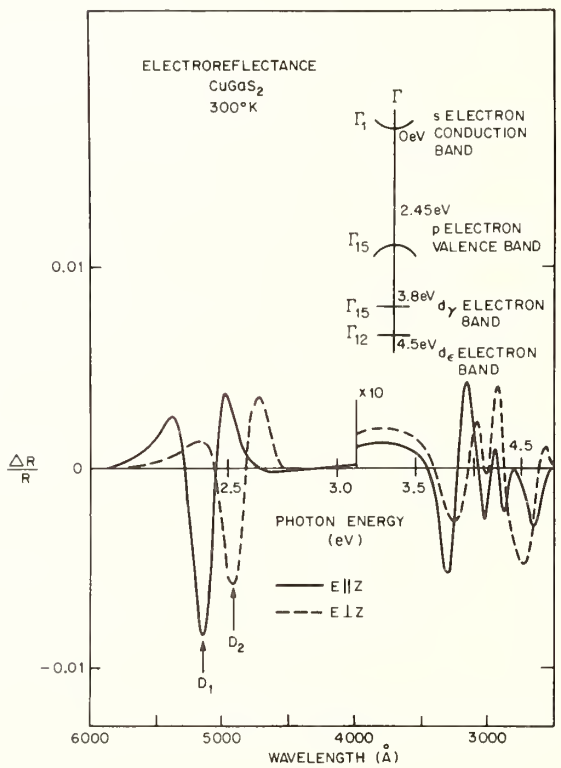

Fig. 6. Electroreflectance spectrum and simplified energy band diagram neglecting the ordering of the cations and tetragonal distortion of the chalcopyrite lattice and using the band designations of the zincblende structure (adapted from Tell, Shay and Kasper [20]).

The investigation of the transport properties showed that as-grown crystals are mostly semi-insulating [20]. However, in contrast to all II-VI sulfides, which are semi-insulating or n-type, $CuGaS_2$ can be made p-type with a resistivity of $\rho \sim 0.4\ \Omega$ cm and a Hall mobility $\mu_h \sim 20\ cm^2$/volt sec by doping and annealing procedures [20]. Tell et al. found that as in the II-VI compounds the conductivity depends strongly on the anion vapor pressure.

(c) *Copper indium sulfide, $CuInS_2$ - Preparation:* We cooled the melts from 1100 °C at a rate of about 1 °C/hour and presume that the crystallization temperature lies somewhere between 1050 and 1000 °C. $CuInS_2$ is opaque to visible light; however, it is transparent in the infrared and crystals were selected by use of a microscope equipped with an infrared image converter. Although we observed differences in transparency in various crystals in the infrared image converter, we did not note stoichiometry variations as spectacular as in $CuGaS_2$.

Properties: The lattice constants were determined to a = 5.524 and c = 11.13Å in agreement with previous work [4]. The absorption spectrum of $CuInS_2$ is shown in figure 7, and we see that it is transparent in the infrared to 15 μ. The bandgap is 1.55 eV as determined from reflectivity at 2 K [20], and is considerably higher than a previously reported value of 1.2 eV [22]. The absorption coefficient shows some absorption, probably due to impurities, near the band edge. The indices of refraction at 1 μ are $n_o = 2.7225$ and $n_e = 2.7067$ with birefringence $n_e - n_o = -0.0158$, which is insufficient to allow the phase matched generation of second harmonic laser light [14].

The electroreflectance spectrum of $CuInS_2$ [20] is similar to that of $CuGaS_2$ with a general shift of all structure to the infrared corresponding to the smaller bandgap. The d_ε band is about 4 eV and the d_γ band about 3.3 eV below the conduction band edge and the transitions due to the valence band edge are seen at about 1.55 eV. Again we have the disagreement with the quasicubic model in the infrared shift of the bandgap compared with $Zn_{0.5}Cd_{0.5}S$ (3 eV). The splitting of the d-bands is ~ 0.7 eV as in $CuGaS_2$. The energy difference of the d-bands and the valence band edge is here about 0.5 eV larger than in $CuGaS_2$ and the perturbation of the valence band through d-electrons should be slightly less. As grown $CuInS_2$ is usually low conductive p-type. Annealing and/or doping leads to highly conductive p-type [20] material with a resistivity $\rho = 7\ \Omega$ cm and a mobility of 12 cm^2/V sec. After better crystals were available it was found that $CuInS_2$ can also be made n-type with a resistance $\rho \sim 1\ \Omega$ cm and a Hall mobility $\mu \sim 200\ cm^2$/volt sec. Recently rectifying junctions have been obtained in $CuInS_2$ [23].

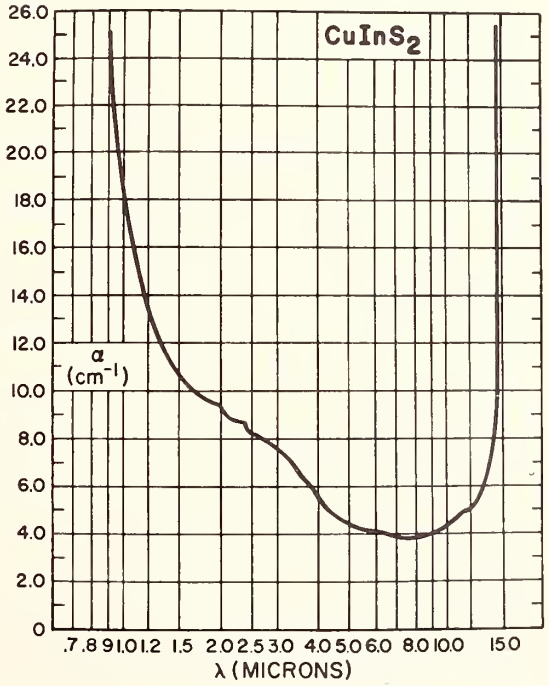

Fig. 7. Absorption coefficient of $CuInS_2$.

4. VISIBLE STIMULATED EMISSION AND POSSIBLE APPLICATIONS

We have already mentioned that $AgGaS_2$ has very desirable nonlinear optical properties. However, the properties of $CuGaS_2$ and $CuInS_2$ are even more interesting. It is important that $CuGaS_2$ and $CuInS_2$ are direct bandgap semiconductors with the top of the valence band and the bottom of the conduction band at the Γ-point of the Brillouin zone. This implies a strong interaction of valence and conduction band electrons with photons of bandgap energy, and it is a precondition for efficient semiconductor luminescence. Experimentally, Shay et al. [24] have recently demonstrated the emittive qualities of $AgGaS_2$, $CuGaS_2$ and $CuInS_2$. At ~ 2 K, electrons were pumped with a pulsed nitrogen laser (3371Å) from the valence band to the conduction band. It was possible to observe stimulated emission in a small solid angle normal to the incident beam in $AgGaS_2$ at 4620Å, $CuGaS_2$ at 5000Å and in $CuInS_2$ at 9175Å.

For the design of light emitting devices p-n junctions are required in addition to the luminescent properties. $CuInS_2$, which can be made of both p- and n-type conductivity and which has a bandgap slightly larger than GaAs, shows all the requirements of a homojunction laser material. Fisher [3] distinguishes quasi-homojunctions as defined as a p-n junction between two materials, one being n-type, the other p-type, which form a complete series of solid solutions from hetrojunctions made of unrelated materials. Up to now all quasi-homojunctions of the II-VI compounds had to be based on ZnTe, which was the only material with native p-type properties and which had to be combined with the n-type sulfides and selenides. The p-type conductivity and the luminescent properties of $CuGaS_2$ make, in our opinion, this sulfide a much stronger contender for quasi-homojunctions with II-VI sulfides than ZnTe.

5. CONCLUSIONS

We have reported on the preparation and the properties of crystals of the I-III-VI_2 compounds $AgGaS_2$, $CuGaS_2$, and $CuInS_2$. We find that growth from the melt is probably the best way to obtain crystals of I-III-VI_2 compounds, which are able to meet the purity and perfection standards required for semiconductor and nonlinear optical applications, in contrast to the preparation of quality II-VI compounds from the vapor phase [25]. $AgGaS_2$ has been shown to have good potential for nonlinear optical applications. The most remarkable property of the copper compounds is their p-type conductivity. $CuInS_2$ is the first tetrahedral sulfide which has shown good conductivity of both types. The outstanding luminescent properties of the tetrahedral chalcogenides, and specifically sulfides, leads to the expectation that the p-type conductivity will enable the design of useful visible light and laser sources.

6. ACKNOWLEDGMENT

I would like to thank R. A. Laudise and A. G. Chynoweth for their initiation of and their continued interest in this work. The encouragement and uninterrupted cooperation of G. D. Boyd, J. H. McFee, G. E. Peterson, J. L. Shay, and B. Tell have been extremely helpful and they have contributed greatly to the author's knowledge about the physics of these materials. I would like to thank R. L. Barns for obtaining lattice constants, J. L. Shay and B. Tell for their enthusiastic investigation of modulation and luminescence spectra and of electrical properties, G. D. Boyd for his untiring effort to uncover better nonlinear optical materials and Miss B. E. Prescott for the transmission spectra.

7. REFERENCES

[1] See for example *"Physics and Chemistry of II-VI Compounds"*, edited by M. Aven and J. S. Prener, John Wiley and Sons, New York (1967).
[2] See for example O. Madelung, Physics of III-V Compounds, John Wiley and Sons, New York (1964).
[3] Fischer, A. G., Journal of the Electrochem. Soc. 118, (6), 139C (1971).
[4] Hahn, H., Frank, G., Klinger, W., Meyer, A., and Störger, S., Z. Anorg. allg. Chem. 271, 153 (1953).
[5] Gross, R., Gross, N., Neues Jahrb. f. Min. Bull. 48, 113-135 (1923).
[6] Zhuse, V. P., Sergeeva, V. M. and Shtrum, E. L., Zhurnal technischeskoi Fiziki 28, 2093 (1958); translation: Soviet Physics, Tech. Phys. 3, 1925 (1958).
[7] Cambi, L., Elli, M., Chimica e Industria 48, 944 (1966).
[8] Cound, V. M., Davies, P. H., Hulme, K. F., and Robertson, D., J. Physics C 3, L83 (1970).

[9] Lerner, L. S., J. Phys. Chem. Solids 27, 1 (1966).
[10] For the vapor transport method compare H. Schafer, Chemical Transport reactions, Academic Press, New York (1964).
[11] Parthe, E., Yvon, K., and Deitch, R. H., Acta Cryst. B25, 1164 (1969).
[12] Belova, C. K., Koshkin, V. M., and Palatnik, L. S., Izvestia Akad Nauk SSSR, Neogranicheskia Materialy 3, 617 (1967).
[13] Tell, B., Kasper, H. M., Phys. Rev. B, 4, 4455 (1971).
[14] Boyd, G. D., Kasper, H. M., and McFee J. H., IEEE Journal of Quantum Electronics, QE7, 563 (1971).
[15] Chemla, D. S., Kupecek, P. J., Robertson, D. S. and Smith, R. C., Optics Comm. 3, 29 (1971).
[16] Hobden, M. V., Acta Cryst. A24, 676 (1968).
[17] Apple, E. F., J. Electrochem. Soc. 105, 251 (1958); Fischer, A. G., J. Electrochem. Soc. 106, 839 (1959).
[18] See for example, Shay, J. L., Buehler, E., and Wernick, J. H. , Phys. Rev. B3, 2004 (1971).
[19] Shay, J. L., Tell, B., Kasper, H. M., and Schiavone, L. M., to be published (Phys. Rev. B).
[20] Tell, B., Shay, J. L., and Kasper, H. M., Phys. Rev., B4, 2463 (1971).
[21] Ballhausen, C. J., Introduction to Ligand Field Theory, McGraw Hill, New York (1962).
[22] Austin, G., Goodman, C. H. L., and Pengelly, A. E., J. of the Electrochem. Soc. 103, 609 (1956).
[23] Tell, B., and Kasper, H. M., unpublished.
[24] Shay, J. L., Tell, B., Kasper, H. M., Appl. Phys. Lett. 19, 366 (1971).
[25] Henry, C. H., Faulkner, R. A., and Nassau, K., Phys. Rev. 183, 798 (1969).

National Bureau of Standards Special Publication 364, Solid State Chemistry, Proceedings of 5th Materials Research Symposium, issued July 1972.

CRYSTAL CHEMISTRY AND MAGNETIC PROPERTIES OF PHASES IN THE Ba-Fe-S(Se) SYSTEMS*

H. Steinfink, H. Hong and I. Grey[1]

Materials Science Laboratories
Department of Chemical Engineering
The University of Texas at Austin
Austin, Texas 78712

The crystal structures of a number of new phases synthesized in the Ba-Fe-S and Se systems were investigated by x-ray diffraction techniques. Ba_2FeS_3 is orthorhombic, Pnma, a = 12.087(5) A, b = 4.246(2) A, c = 12.359(5) A, ρ_{meas} = 4.0 g/cc, ρ_{calc} = 4.47 g/cc, Z = 4, m.p. > 1300 °C. The compound is isostructural with Ba_2ZnS_3 and the structure consists of FeS_4 tetrahedra sharing corners to form an infinite linear chain. Ba_2FeSe_3 is isostructural with the sulfide and its parameters are a = 12.350(7) A, b = 4.439(2) A, c = 12.921(5) A. $BaFe_2S_3$ is orthorhombic, Cmcm, a = 8.7835(9) A, b = 11.219(1) A, c = 5.2860(5) A, ρ_{meas} = 4.0 g/cc, ρ_{calc} = 4.40 g/cc, Z = 4, m.p. = 765 ± 10 °C. Three dimensional x-ray diffraction data was used to refine the structure which consists of two FeS_4 tetrahedra sharing edges and this binuclear unit in turn shares edges with others to form an infinite chain. The structure of $BaFe_2Se_3$ is essentially the same as that of the sulfide but they are not isostructural. The selenide is orthorhombic, Pnma, a = 11.878(3) A, b = 5.447(2) A, c = 9.160(2) A, ρ_{calc} = 5.44 g/cc, Z = 4; decomposes above 750 °C. $Ba_6Fe_8S_{15}$ is tetragonal, I4/m, a = 11.408(2) A, c = 10.256(2) A, ρ_{meas} = 4.30 g/cc, ρ_{calc} = 4.36 g/cc, Z = 2, m.p. 880 ± 10 °C. The structure was determined from three dimensional x-ray diffraction data and consists of a tetranuclear unit formed by 4 FeS_4 tetrahedra sharing corners and these units then share edges to form an infinite column. $Ba_3Fe_3Se_7$ is hexagonal, $P6_3mc$, a = 10.843(3) A, c = 7.384(2) A, ρ_{calc} = 5.00 g/cc, Z = 2. The structure was determined using three dimensional single crystal x-ray diffraction data and consists of isolated trinuclear units formed by edge sharing of three FeS_4 tetrahedra. The Fe-Fe distances between chains are 6 A, and vary from 2.6 A to 4.2 A within the chains. The Fe-S distances are 2.3 - 2.4 A, the S-Fe-S angles are tetrahedral and the Ba-S distances are essentially equal to the sum of the ionic radii. The corresponding distances in the selenides reflect the larger size of the anion.

The magnetic characteristics of Ba_2FeS_3, $Ba_7Fe_6S_{14}$ and $Ba_6Fe_8S_{15}$ were investigated; all three compounds are antiferromagnets. The values of the exchange forces, J/k, correlate with the observed Fe-Fe distances.

Key words: Crystal structures of Ba_2FeS_3, Ba_2FeSe_3, $BaFe_2S_3$, $BaFe_2Se_3$, $Ba_7Fe_6S_{14}$, $Ba_6Fe_8S_{15}$, $Ba_3Fe_3Se_7$; magnetic characteristics of Ba_2FeS_3, $Ba_7Fe_6S_{14}$ and $Ba_6Fe_8S_{15}$.

1. INTRODUCTION

A series of new compounds has been synthesized in the barium-first row transition metal-sulfur and selenium systems which is based on a common structural scheme consisting of tetrahedra linked by corner and edge sharing into linear chains or columns.

The crystal structure of $Ba_7Fe_6S_{14}$ [1][2] and the structures and magnetic behavior of Ba_2MnS_3 and Ba_2MnSe_3 [2] have been reported and a preliminary account of the structures of the other phases has been given [3].

---

* Research sponsored by the Robert A. Welch Foundation, Houston, Texas

[1] Present address: CSIRO, Division of Mineral Chemistry, Port Melbourne, Victoria, Australia.

[2] Figures in brackets indicate the literature references at the end of this paper.

2. EXPERIMENTAL SECTION

BaS, BaSe, Fe, S and Se constitute the starting materials for the ternary compound preparations. Commercial, yellow BaS, containing free S, was heated at 500 °C for 4-5 hours under a current of H_2. BaSe was prepared by the reduction of $BaSeO_3$ under a current of H_2 at 500 °C for 4-5 hours. The Fe, S and Se powders were nominally 99.9% pure and no impurities were detected on examination of their x-ray powder patterns. Different ratios of BaS, BaSe, Fe, S or Se were mixed in a graphite tube and sealed under vacuum of 10^{-3} to 10^{-4} mm in vycor tubing and preheated at temperatures of 300 °C for sulfides and 350 °C for selenides for 4-5 hours. The temperature was then raised and kept in the range of 750 °C to 1050 °C for two days. At the end of the reaction the sample was slowly cooled to room temperature by cutting off the power to the furnace or was quenched by dropping it into ice water.

Melting points of the compounds were obtained by selecting single crystals and placing them on a thermocouple junction to which an A.C. voltage was applied. Melting temperatures were obtained by observing the crystals microscopically. An x-ray powder diffraction diagram was obtained after the material had solidified to check whether melting had occurred congruently.

Densities of the compounds were obtained by the liquid displacement method using benzene and the values have ± 10% precision.

3. STRUCTURES OF Ba_2FeS_3 AND Ba_2FeSe_3

The initial mixtures of 2BaS:Fe:S and 2BaSe:Fe:Se were heated at 850-870° for 2 days. The x-ray powder patterns of the two products were quite similar indicating that they were probably isostructural. Weissenberg and precession diagrams of a single crystal selected from the selenide showed that the space group is either Pnma or $Pn2_1a$, with lattice parameters a = 12.350(7) A, b = 4.439(2) A, c = 12.921(5) A. The powder pattern of Ba_2FeS_3 was also indexed on the basis of an orthorhombic cell with lattice constants a = 12.087(5) A, b = 4.246 (3) A and c = 12.359(7) A. With an assumed stoichiometry based on the initial composition and a knowledge of the lattice constants and space group it was found that the compounds could be isostructural with Ba_2ZnS_3 [4]. A calculation of the powder intensities for Ba_2FeS_3 and single crystal intensities for Ba_2FeSe_3 using the atomic coordinates of Ba_2ZnS_3 gave good qualitative agreement and confirmed that the structures were identical. The measured density of Ba_2FeS_3 is 4.02 g/cc, calculated ρ = 4.47 g/cc, Z = 4 formula weights per unit cell; m.p. > 1300 °C.

The projection of the structure of Ba_2FeS_3 on (010) is shown in figure 1. A linear infinite tetrahedral iron chain, formed by corner sharing, exists parallel to the b axis and the Fe-Fe distance between shared tetrahedra is 4.246(3) A, the b axis dimension of the unit cell. In Ba_2FeSe_3 this distance is 4.439(2) A. Bond distances were calculated on the basis of the Ba_2ZnS_3 parameters and the Fe-S distance where S is shared between two Fe ions is 2.45 A, considerably longer than the other Fe-S distances of 2.30 A and 2.38 A. One Ba^{+2} is surrounded by six S ions at the corners of a trigonal prism and an additional S ion is approximately centered above one rectangular face. Seven S ions surround the other Ba^{+2}, four at the corners of a square plane and three at the corners of a triangle whose plane contains the barium ion and is perpendicular to the plane of the square. Ba_2FeS_3 is isostructural with Ba_2ZnS_3, K_2CuCl_3, $(NH_4)_2CuBr_3$, Cs_2AgCl_3, Cs_2AgI_3 and CuPbBiS$_3$ [5].

4. CRYSTAL STRUCTURE OF $BaFe_2S_3$

A mixture of BaS:2Fe:2S was prepared and heated at 790 °C for two days and then slowly cooled to room temperature. Weissenberg and precession pictures indicated space groups C2cm, $Cmc2_1$ and Cmcm. The lattice constants were a = 8.7835(9) A, b = 11.219(1) A, and c = 2860(5) A. The measured density is 4.00 g/cc, ρ_{calc} = 4.40 g/cc, Z = 4; m.p. = 765 ± 10 °C. An examination of lattice constants and space groups for compounds with stiochiometry AB_2C_3 [5] showed that $CsCu_2Cl_3$ might be isostructural with the unknown phase. Single crystal intensities were collected using the stationary crystal-stationary counter method with balanced filters for molybdenum radiation and 336 independent reflections were measured. The data were reduced to F(hkℓ) in the usual manner.

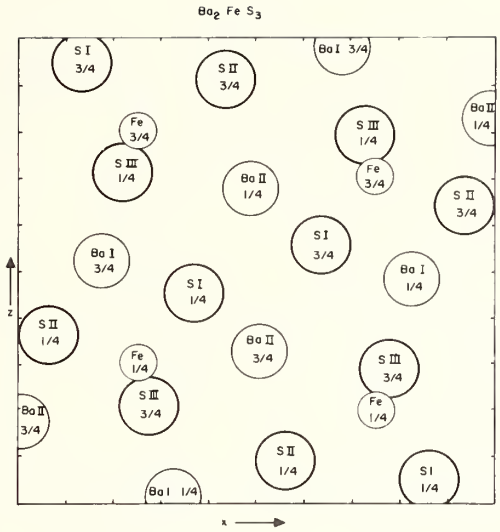

Fig. 1. The projection of Ba_2FeS_3 on (010). The numbers inside the circles denote fractional heights along the b axis.

The atomic parameters for $CsCu_2Cl_3$ [6], space group Cmcm, were used as starting parameters for a least squares refinement of the structure and after 3 cycles with anisotropic temperature factors R was 0.064 and wR was 0.067; ($R = \Sigma||F_o| - |F_c||/\Sigma|F_o|$, $wR = [\Sigma w(F_o - F_c)^2/\Sigma wF_o^2]^{1/2}$). The final parameters are shown in table 1, and bond distances and angles are shown in table 2.

4.1. DISCUSSION OF THE STRUCTURE

Two FeS_4 tetrahedra share an edge with the line formed by the two Fe ions parallel to the a axis of the unit cell, figure 2. This unit of two tetrahedra, in turn, shares edges with another unit above it and parallel to the c axis and forms an infinite chain along [001], shown stereoscopically in figure 3. The Ba^{+2} is coordinated to 8 sulfur ions, six are located at the corners of a trigonal prism at 3.29 A and 3.45 A and two are approximately above the rectangular faces at 3.35 A. Two additional sulfur atoms are located near the third rectangular face of the prism but at 3.92 A and can't be considered as part of the coordination sphere.

Table 1

Atomic Parameters and Their Standard Deviations in Parentheses ($\times 10^4$) for $BaFa_2S_3$*

Atom	x	y	z	B_{11}	B_{22}	B_{33}	B_{12}	B_{13}	B_{23}
Ba	1/2	1859(3)	1/4	66(3)	41(2)	94(9)	0	0	0
Fe	3464(4)	1/2	0	26(4)	14(3)	33(11)	0	0	0
S(I)	1/2	6147(9)	1/4	35(12)	10(7)	70(34)	0	0	0
S(II)	2074(9)	3768(7)	1/4	52(9)	41(7)	50(23)	0	0	0

*The temperature factor is $[\exp-(B_{11}h^2 + B_{22}k^2 + B_{33}\ell^2 + 2B_{12}hk + 2B_{13}h\ell + 2B_{23}k\ell)]$.

Table 2

Bond Distances and Angles in $BaFe_2S_3$[a]

Distances (A)

2[b] Fe-S_1	2.28(1)	4Ba-S_2	3.29(1)
2Fe-S_2	2.27(1)	2Ba-S_2	3.35(1)
Fe-Fe	2.643(5)	2Ba-S_2	3.92(1)
Fe-Fe	2.699(5)	2S_2-S_1	3.69(1)
Ba-Fe	3.998(5)	S_1-S_1	3.69(1)
2Ba-S_1	3.46(1)	2S_2-S_1	3.70(1)
		S_2-S_2	3.82(1)

Angles (°)

S_2-Fe-S_1	108.1(4)
S_2-Fe-S_1	107.6(4)
S_1-Fe-S_2	108.1(4)
S_2-Fe-S_2	114.9(4)
S_2-Fe-S_1	108.9(4)
S_1-Fe-S_2	108.9(4)

[a] Standard deviations are shown in parentheses.

[b] The number in front of a bond length indicates how frequently this length occurs.

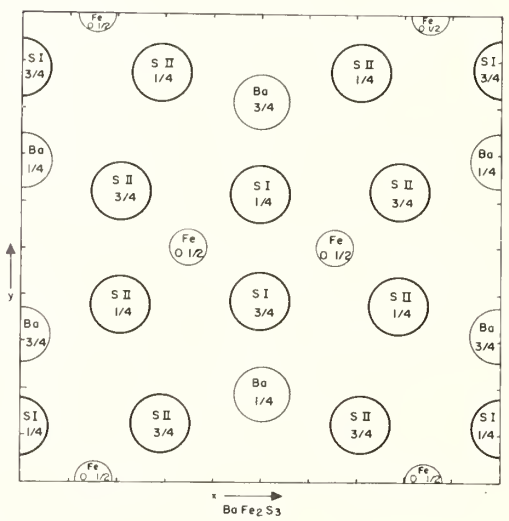

Fig. 2. The projection of the structure of $BaFe_2S_3$ on (001).

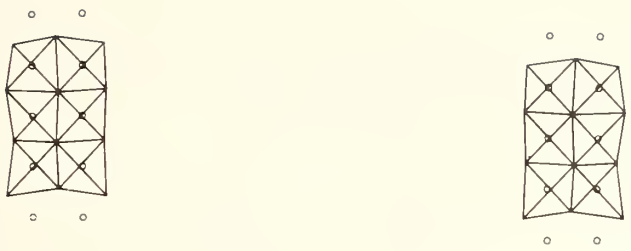

Fig. 3. Stereoscopic drawing of the double tetrahedral chain in $BaFe_2S_3$. The horizontal direction is [100] and the vertical [001].

5. CRYSTAL STRUCTURE OF $BaFe_2Se_3$

A mixture of BaSe:2Fe:Se was heated at 790 °C for 2 days followed by slow cooling. The x-ray powder pattern of the material showed great similarity to $BaFe_2S_3$ and initially these two compounds appeared to be isostructural. Weissenberg and precession pictures showed that the possible space groups were Pnma or $Pn2_1a$; the lattice constants were a = 11.878(3) A, b = 5.447(2) A, c = 9.160(2) A; ρ_{calc} = 5.44 g/cc, Z = 4; decomposes above 750 °C. The different space group showed that this compound was not isostructural with $BaFe_2S_3$ and a search of lattice constants and space groups for compounds with a stoichiometry AB_2C_3 [5] indicated that constants for $CsAg_2I_3$ were similar to those of the unknown phase. A single crystal structure determination was undertaken on the assumption that the compound was $BaFe_2Se_3$ and was isostructural with $CsAg_2I_3$.

Single crystal x-ray intensities were collected in the range $3° \leq 2\theta \leq 50°$ using unfiltered AgK radiation and a scintillation counter. The integrated intensities of 1160 reflections were obtained and reduced to $F(hk\ell)$. The atomic parameters for $CsAg_2I_3$ were used as starting parameters for a least squares refinement. After four cycles of refinements using anisotropic temperature factors, R was 0.0725 for 983 reflections greater than σ and R = 0.0891 for all 1160 reflections. The final parameters are shown in table 3; bond distances and angles are shown in table 4.

5.1. DISCUSSION OF THE STRUCTURE

The structure shown in projection on (101) in figure 4 is basically identical with that of $BaFe_2S_3$ but sufficient distortions exist to change the symmetry operations relating the atoms and the coordination of the Ba^{+2} is thereby affected. The Ba^{+2} is surrounded by 6 Se^{-2} at the corners of a trigonal prism with Ba-Se distances of 3.368 A, 3.455 A, and 3.534 A. Two additional Se^{-2} are above the centers of two rectangular faces of the prism at distances

Table 3

Atomic Parameters and Their Standard Deviations in Parentheses ($x10^4$) for $BaFe_2Se_3$*

Atom	x	y	z	B_{11}	B_{22}	B_{33}	B_{12}	B_{13}	B_{23}
Ba	1847(1)	1/4	5185(1)	49(1)	89(3)	69(0)	0	15(1)	0
Fe	4947(1)	3(3)	3515(1)	28(1)	76(4)	31(1)	-2(1)	-0(1)	0(2)
SeI	3590(1)	1/4	2272(2)	40(1)	71(4)	45(2)	0	-21(1)	0
SeII	6259(1)	1/4	4915(1)	28(1)	66(4)	34(1)	0	0(1)	0
SeIII	3976(1)	1/4	8125(2)	47(1)	92(5)	53(2)	0	28(1)	0

*The temperature factor is $[\exp-B_{11}h^2 + B_{22}k^2 + B_{33}\ell^2 + 2B_{12}hk + 2B_{13}h\ell + 2B_{23}k\ell)]$.

Table 4

Bond Distances and Angles in $BaFe_2Se_3$[a]

Distances (A)

$Fe-Se_1$	2.396(2)	$Ba-Se_3$	3.455(1)
$Fe-Se_3$	2.399(2)	$Ba-Se_3$	3.455(1)
$Fe-Se_2$	2.434(2)	$Ba-Se_1$	3.377(2)
$Fe-Se_2$	2.444(2)	$Ba-Se_3$	3.694(2)
Fe-Fe	2.721(3)	$Ba-Se_3$	3.745(2)
Fe-Fe	2.726(3)	Se_1-Se_3	3.988(2)
Ba-Fe	3.963(2)	Se_1-Se_2	3.418(2)
$Ba-Se_1$	3.368(1)	Se_1-Se_2	3.753(2)
$Ba-Se_1$	3.368(1)	Se_3-Se_2	3.999(2)
$Ba-Se_2$	3.534(1)	Se_3-Se_2	3.906(2)
$Ba-Se_2$	3.534(1)	Se_2-Se_2	3.826(2)

Angles (°)

$Se_1-Fe-Se_3$	112.55(8)
$Se_1-Fe-Se_2$	111.32(6)
$Se_1-Fe-Se_2$	101.67(7)
$Se_3-Fe-Se_2$	107.83(7)
$Se_3-Fe-Se_2$	111.35(6)
$Se_2-Fe-Se_2$	112.13(6)

[a]Standard deviations in the last decimal place in parentheses

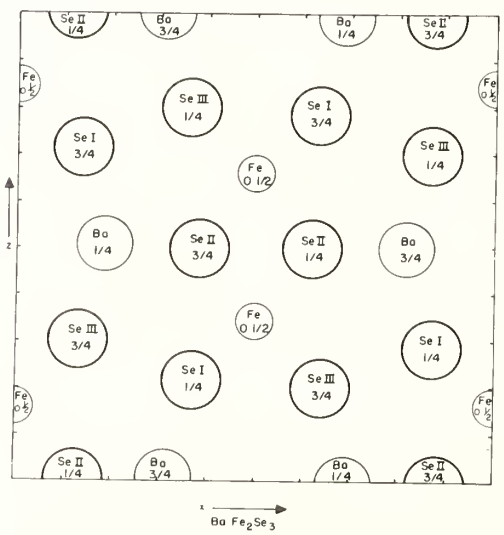

Fig. 4. The projection of the crystal structure of $BaFe_2Se_3$ on (010).

of 3.377 A and 3.694 A from Ba^{+2}. The corresponding Ba-S distances in $BaFe_2S_3$ are equal. A ninth Se^{-2} is near the third rectangular face at a distance of 3.745 A while the tenth selenium atom is at a distance of 4.47 A. If the Ba^{+2} coordination is taken as 8 in $BaFe_2S_3$ then it can be considered as 9 in $BaFe_2Se_3$. In the former compound the coordination polyhedron is also more symmetric.

6. CRYSTAL STRUCTURE OF $Ba_7Fe_6S_{14}$

This structure has been published [1] and is included here for the sake of completeness. The basic structural unit is a trinuclear iron cluster, $Fe_3S_6S_{2/2}$, which consists of three FeS_4 tetrahedra, where the central tetrahedron shares its two opposing edges with two other tetrahedra. The trinuclear groups link together by corner sharing of the tetrahedra to produce infinite zigzag chains in the general direction of the "b" axis. The chains are held together by the packing of the barium ions.

Within a Fe_3S_7 group, the Fe-Fe distances are unequal, with Fe_1 distances to the two terminal iron atoms 2.747(7) and 2.829(7) A. The bridging angles of Fe-S-Fe are in the range 72-75° and the sequence Fe_2-Fe_1-Fe_3 is almost linear (177.1(2)°). These distances and angles are closely similar to those observed in $KFeS_3$ [7], containing infinite chains of edge-sharing tetrahedra . Each of the FeS_4 tetrahedra is considerably distorted as reflected in the large variation in the tetrahedral angles and in the Fe-S bond lengths. The distance between adjacent iron atoms of two corner-shared trinuclear groups is 3.670(7) A which is considerably greater than the distances between irons within a cluster. It is, however, shorter than the Fe-Fe separation in Ba_2FeS_3. Further details of the structure are presented in reference 1.

7. CRYSTAL STRUCTURE OF $Ba_6Fe_8S_{15}$

The crystal, which eventually was shown to have this stoichiometry, was found in the product obtained from a quench of a starting mixture having the composition BaS:2Fe:2S which had been held at 800 °C for two days. It was evident from the x-ray powder pattern that the product was polyphasic. Weissenberg and precession photographs showed that the possible space groups were $I\bar{4}$, I4, and I4/m. The lattice constant were a = 11.408(2) A, c = 10.256(2) A; Z = 2, ρ_{cal} = 4.36 g/cc, ρ_{meas} = 4.30 g/cc; the compound melts congruently at 880 ± 10 °C, (the number of formula weights and calculated density are based on the subsequently determined stoichiometry).

Three dimensional data were collected with MoK radiation. A total of 1033 reflections was measured, of which 956 were considered to be above background.

The structure was determined by the use of the direct method for phase determinations. Wilson statistics indicated a centric distribution and I4/m was selected as the proper space group. The sequence of computer programs FAME-MAGIC-LINK-SYMPL [8] was used to generate about 300 phases from five symbol assigned reflections. A three dimensional E(hkℓ) map showed peaks which could be interpreted as due to two Ba and one Fe atoms. A three dimensional electron density map calculated with signs obtained with these positions revealed additional peaks which were due to S and it became evident that the compound had the formula $Ba_6Fe_8S_{15}$. The final parameters shown in table 5 were obtained by a least squares refinement. The final R = 0.0800, wR = 0.0678 for 1034 reflections and R = 0.0714, wR = 0.0673 for 928 reflections greater than σ.

7.1. DISCUSSION OF THE STRUCTURE

The [001] projection of the structure is shown in figure 5. Four FeS_4 tetrahedra share corners and their arrangement can be described with reference to an octahedron. Two opposing faces of the upper half of an octahedron, (111) and $(\bar{1}\bar{1}1)$, form the bases for two tetrahedra and they share a corner which is the apex of the octahedron; two opposing faces of the lower half of the octahedron, $(1\bar{1}\bar{1})$ and $(\bar{1}1\bar{1})$, form the bases of the other two tetrahedra and they share a corner which is the lower apex of the octahedron. The sets of two tetrahedra share corners which are the 4 points 100, 010, $\bar{1}00$, and $0\bar{1}0$ of the octahedron. This unit of 4 FeS_4 tetrahedra is propagated by mirror planes perpendicular to [001] into an infinite column parallel to the c axis as illustrated in figure 6. The Fe-Fe distances between edge sharing tetrahedra are 2.81 A and are 3.34 A, 3.54 A and 3.78 A for Fe-Fe distances when tetrahedra

Table 5

Final Atomic Parameters and Their Standard Deviations in Parentheses ($\times 10^4$) for $Ba_6Fe_8S_{15}$[a]

Atom	x	y	z	B_{11}	B_{22}	B_{33}	B_{12}	B_{13}	B_{23}
Ba_1	0	0	3044(2)	14(1)	14(1)	25(2)	0	0	0
Ba_2	2484(1)	1304(1)	0	15(1)	15(1)	38(1)	0(1)	0	0
Fe	1537(2)	4384(2)	1365(2)	13(1)	14(1)	25(2)	0(1)	-1(1)	1(1)
S_1	790(3)	2700(3)	2266(4)	17(2)	14(2)	31(3)	3(2)	6(2)	4(2)
S_2	3035(5)	3951(4)	0	17(3)	15(3)	25(5)	0	0	0
S_3	0	1/2	0	12(5)	13(5)	28(7)	4(4)	0	0
S_4	0	0	0	16(8)	16(8)	16(9)	0	0	0

[a]The temperature factor is $\exp[-(B_{11}h^2 + B_{22}k^2 + B_{33}\ell^2 + 2B_{12}hk + 2B_{13}h\ell + 2B_{23}k\ell)]$.

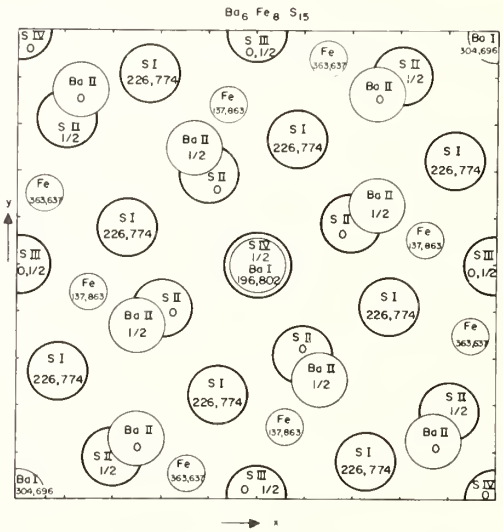

Fig. 5. The projection of the structure of $Ba_6Fe_8S_{15}$ on (001).

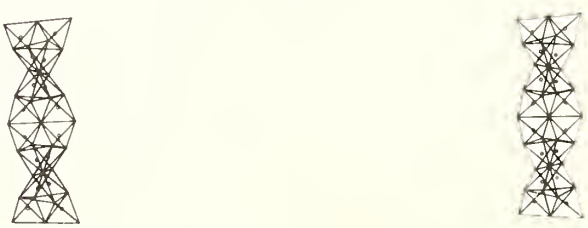

Fig. 6. Stereoscopic view of the infinite column of tetrahedra in $Ba_6Fe_8S_{15}$. The vertical direction is [001] of the unit cell.

share corners. The Fe-Fe distance between atoms in adjacent chains is 6.10 A. The Ba ions are in ninefold coordination. Eight S ions form a square antiprism around Ba_1 and the 9th atom, S_4, is in the center of one square face, along the c axis. The S_4 atom is not part of a FeS_4 tetrehedron. The polyhedron around Ba_2 consists of a capped trigonal prism. The Ba-S distances are essentially equal to the sum of the ionic radii. The bond distances and angles are listed in table 6.

The formula of this compound can be written as $Ba_3Fe_2(III)Fe_1(II)S_7$ and since the Fe ions are crystallographically indistinguishable we can consider the average oxidation number as 2.25. There is a possibility that electrical conduction can occur via a hopping mechanism and that this material should display conductivity in one dimension similar to the recently reported mixed valence square planar complexes, [9].

8. CRYSTAL STRUCTURE OF $Ba_3Fe_3Se_7$

In addition to Ba_2FeSe_3 an unknown phase was occasionally observed in the reacted material obtained from an initial mixture of 2BaSe:Fe:Se. The unknown phase, which was later found to be $Ba_3Fe_3Se_7$, consisted of black hexagonally shaped crystals.

Weissenberg and precession photographs indicated the possible space groups $P\bar{6}2c$, $P6_3mc$, and $P6_3/mmc$. The lattice parameters are a = 10.843(3) A, c = 7.384(2) A; Z = 2, ρ_{cal} = 5.00 g/cc. Peak height intensities from a single crystal were obtained with balanced filters and MoKα radiation. A total of 455 independent reflections was measured of which 397 were considered observed.

Table 6

Bond Distances and Angles in $Ba_6Fe_8S_{15}$[a]

Distances, Å

$Fe-S_2$	2.27(1)	Ba_1-S_2	3.23(1)
$Fe-S_1$	2.29(1)	Ba_1-S_2	3.23(1)
$Fe-S_1$	2.30(1)	Ba_1-S_1	3.31(1)
$Fe-S_3$	2.36(1)	Ba_1-S_1	3.31(1)
Ba_2-S_2	3.09(1)	Ba_1-S_1	3.31(1)
Ba_2-S_3	3.23(1)	Ba_1-S_1	3.31(1)
Ba_2-S_4	3.20(1)	S_2-S_1	3.74(1)
Ba_2-S_1	3.34(1)	S_1-S_3	3.95(1)
Ba_2-S_1	3.34(1)	S_2-S_3	3.67(1)
Ba_2-S_1	3.36(1)	S_1-S_3	3.61(1)
Ba_2-S_1	3.36(1)	S_2-S_1	3.61(1)
Ba_2-S_1	3.61(1)	S_1-S_1	3.95(1)
Ba_2-S_1	3.61(1)	Fe-Fe	2.811(7)
Ba_1-S_4	3.119	Fe-Fe	3.539(7)
Ba_1-S_2	3.23(1)	Fe-Fe	3.783(7)
Ba_1-S_2	3.23(1)	Fe-Fe	3.342(7)
		Fe-Fe	6.102(7)

Angles (°)

S_2-Fe-S_1	110.3(3)
S_1-Fe-S_3	115.8(3)
S_1-Fe-S_1	118.8(3)
S_2-Fe-S_3	104.9(3)
S_1-Fe-S_3	102.1(3)
S_2-Fe-S_1	104.2(3)
$Fe-S_1-Fe$	100.8(3)
$Fe-S_3-Fe$	106.8(1)
$Fe-S_1-Fe$	108.8(3)

[a]Standard deviations in the last decimal place in parentheses.

465-504 O - 72 - 45

The structure was solved from an interpretation of the three dimensional Patterson function even though the formula was unknown. The interactions observed in the various Harker sections indicated that the probable space group was $P6_3mc$. The positions of one Ba and one Se were located from the Patterson map and phases were calculated. A three dimensional electron density map based on these phases revealed positions for one Fe and two additional Se atoms. It was evident now that the compound was $Ba_3Fe_3Se_7$. The atomic coordinates were refined by least squares and after three cycles of refinements with antisotropic temperature factors and using 381 reflections greater than σ, R was 0.0704, wR = 0.071; for all 455 reflections R = 0.0887, wR = 0.0725. The final atomic parameters are shown in table 7.

8.1. DISCUSSION OF THE STRUCTURE

The structure of $Ba_3Fe_3Se_7$ consists of isolated trinuclear units formed by three $FeSe_4$ tetrahedra sharing edges, figure 7. The Fe-Fe distances within the unit are 2.85 A and are 5.91 A between iron ions of different units. Ba is in eightfold coordination consisting of a distorted trigonal prism which is capped on two rectangular faces. The (001) projection of the structure is shown in figure 8. The Fe and Ba ions lie in planes at z = 0.486 and z = 0 respectively and they are separated by selenium lying in planes at z = 0.311 and 0.590. The bond distances and angles of interest are shown in table 8. The formula can be expressed as $Ba_3Fe_2(III)Fe(II)Se_7$ and the crystallographically equivalent Fe can be considered to have the average oxidation number 2.66.

Table 7

Final Atomic Parameters and Their Standard Deviations in Parentheses ($x10^4$) for $Ba_3Fe_3Se_7$[a]

Atom	x	y	z	B_{11}	B_{22}	B_{33}	B_{12}	B_{13}	B_{23}
Ba	1911(2)	3822(2)	0	21(2)	21(2)	69(4)	-6(2)	0	0
Fe	2458(6)	4916(6)	486(1)	38(7)	38(7)	5(1)	36(5)	0	0
Se_1	4573(5)	9146(5)	3110(7)	35(5)	35(5)	50(7)	25(4)	0	0
Se_2	1252(4)	2504(4)	5895(7)	23(5)	23(5)	73(8)	13(4)	0	0
Se_3	1/3	2/3	738(1)	17(7)	17(7)	30(1)	0	0	0

[a] The temperature factor is $\exp[-(B_{11}h^2 + B_{22}k^2 + B_{33}\ell^2 + 2B_{12}hk + 2B_{13}h\ell + 2B_{23}k\ell)]$.

Fig. 7. Stereoscopic view of 3 $FeSe_4$ tetrahedra forming the trinuclear unit in $Ba_3Fe_3Se_7$.

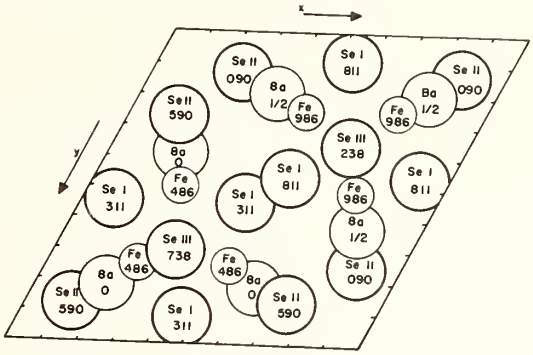

Fig. 8. Projection of the structure of $Ba_3Fe_3Se_7$ on (00.1).

Table 8

Bond Distances and Angles in $Ba_3Fe_3Se_7$[a]

Distances, Å

Fe-Se_1	2.44(1)	Ba-Se_3	3.30(1)
Fe-Se_2	2.39(1)	Ba-Se_2	3.27(1)
Fe-Se_3	2.48(1)	Ba-Se_2	3.26(1)
Fe-Se_1	2.44(1)	Ba-Se_2	3.26(1)
Fe-Fe	2.85(1)	Se_1-Se_3	3.92(1)
Ba-Fe	3.84(1)	Se_1-Se_2	3.98(1)
Fe-Fe	5.91(1)	Se_2-Se_3	4.06(1)
Ba-Se_1	3.75(1)	Se_1-Se_1	4.03(1)
Ba-Se_1	3.75(1)	Se_1-Se_3	3.92(1)
Ba-Se_1	3.41(1)	Se_1-Se_2	3.98(1)
Ba-Se_1	3.41(1)		

Angles, (°)

Se_1-Fe-Se_3	105.5(5)
Se_1-Fe-Se_2	110.8(5)
Se_2-Fe-Se_3	112.8(5)
Se_1-Fe-Se_1	111.2(5)
Se_1-Fe-Se_3	105.5(5)
Se_1-Fe-Se_2	110.8(5)

[a]Standard deviations in the last decimal place in parentheses.

9. MAGNETIC PROPERTIES OF Ba_2FeS_3, $Ba_7Fe_6S_{14}$ AND $Ba_6Fe_8S_{15}$

A Faraday type magnetic balance was used to measure the magnetic susceptibilities of the $Ba_xFe_yS_z$(Se) compounds. Each datum point is an average measurement on two samples and the differences are all within 8%. The results are shown in the form of the usual $1/\chi_A$ *vs.* temperature (°K) plots; χ_A is expressed in electromagnetic units in the cgs system. The linear portions of the curves (Curie-Weiss behavior) were extrapolated to obtain a value for the Weiss constant θ.

The curve of $1/\chi_A$ *vs* T for Ba_2FeS_3, figure 9, exhibits a minimum at 110 K and is typical for an antiferromagnet. A theoretical equation has been proposed for the susceptibility of a one-dimensional array of Ising spins for S = 1/2, and S = 3/2. A reduced spin model

$$\chi = \frac{Ng^2\beta^2 S(S+1)}{3kT} e^{J'/kT}$$

[illegible] applied with good results for S = 2 and S = 5/2. Therefore, log $[(3k/N\beta^2)\chi T]$ was [illegible] against 1/T in figure 9 for Ba_2FeS_3 (S = 2) and the data fit the straight line relationship rather well. The intercept, $g^2S(S+1)$, yields a magnetic moment of 5.29 BM which is reasonable for a tetrahedral iron (II) ion in a weak ligand field having S = 2. The g factor [illegible] in Ba_2FeS_3 shows that the orbital moments are quenched. Table 9 summarizes the magnetic parameters for the three compounds. The value of μ_{eff} for Ba_2FeS_3 obtained from the Curie-Weiss plot is too high for Fe^{+2} and is actually the value for Fe^{+3}. A value closer to [illegible] would be obtained from the reduced spin plot. A much larger number of experimental

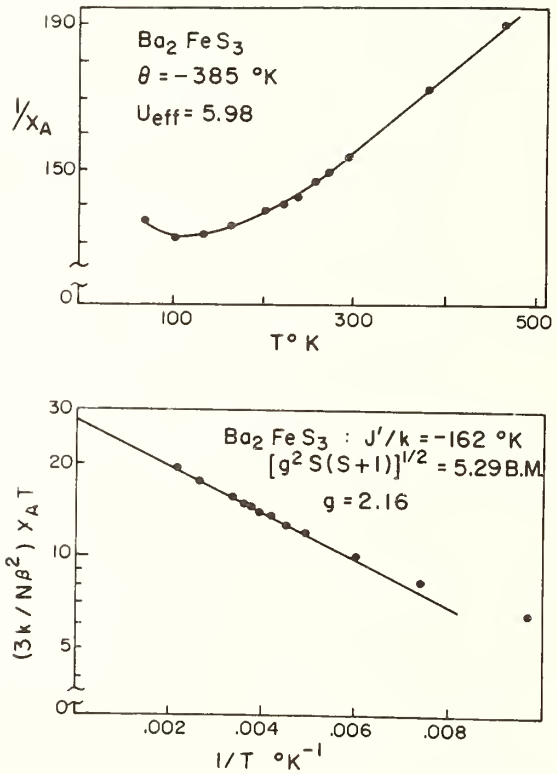

Fig. 9. Magnetic susceptibility as a function of temperature for Ba_2FeS_3.

Table 9

Magnetic Parameters[a]

Compound	Curie-Weiss Plot T K	θ K	μ_{eff} B.M.	Reduced Spin Plot J'/k K	$[g^2S(S+1)]^{1/2}$	Metal-Metal[b] Distances Å
Ba_2FeS_3	110	-385	5.98(2.44)	-162	5.29(2.16)	4.246
$Ba_3Fe_2S_{14}$	200	-152	5.30(2.02)	-228	5.70(2.18)	2.747-3.670
$Ba_3Fe_2S_{15}$	250	-937	5.57(2.15)	-304	4.39(1.70)	2.810-3.780
$BaFe_2S_3$	600	-395	4.00(1.64)	-480	4.70(1.92)	2.643

[a] g values are given in parentheses

[b] nearest transition metal distances

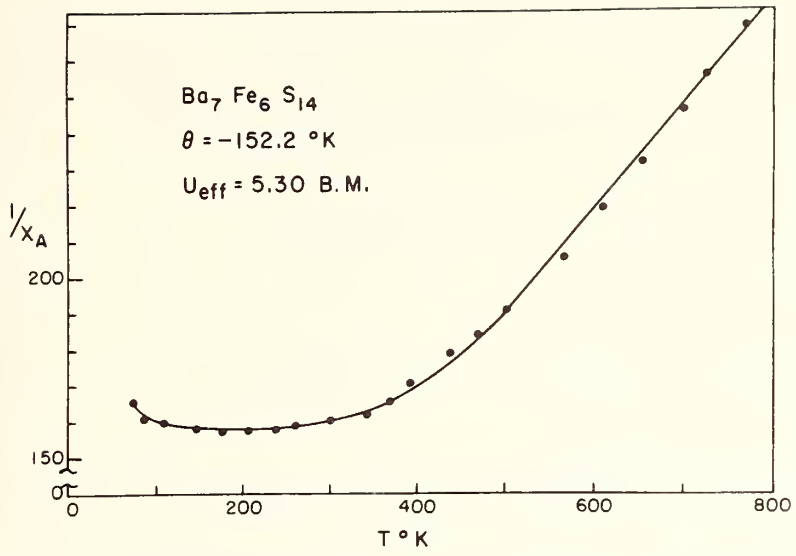

Fig. 10. Magnetic susceptibility as a function of temperature for $Ba_7Fe_6S_{14}$.

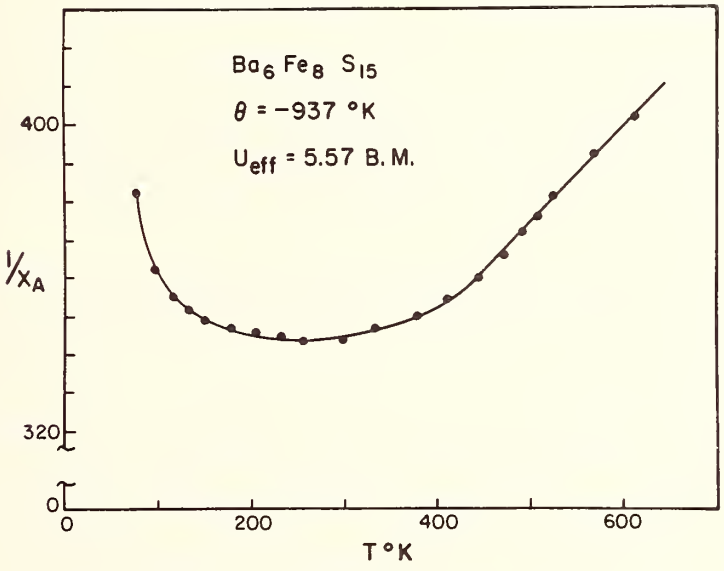

Fig. 11. Magnetic susceptibility as a function of temperature for $Ba_6Fe_8S_{15}$.

points follow a linear relationship when this interpretation is used and the intercept is thus much better defined than the slope obtained from the Curie-Weiss plot. The curves of atomic reciprocal susceptibility $1/\chi_A$ *vs.* temperature observed for $Ba_7Fe_6S_{14}$ and $Ba_6Fe_8S_{15}$, figures 10 and 11, show that these materials are also antiferromagnets. The Néel temperatures are 200 K and 250 K, respectively.

If the trinuclear unit in $Ba_7Fe_6S_{14}$ is treated as a single unit, then the zig-zag iron chain can be considered as a linear chain in which each unit shares corners as observed in Ba_2FeS_3. Therefore the reduced spin model was tried and log $[(3k/N\beta^2)\chi T]$ was plotted against $1/T$, figure 12. The intercept, $g^2S(S+1)$, yields a magnetic moment of 5.70 BM which is reasonable for an iron ion having average S = 2.17. This suggests that the reduced spin model may be applicable and that the effective spins of the clusters can be considered as forming a one dimensional antiferromagnet.

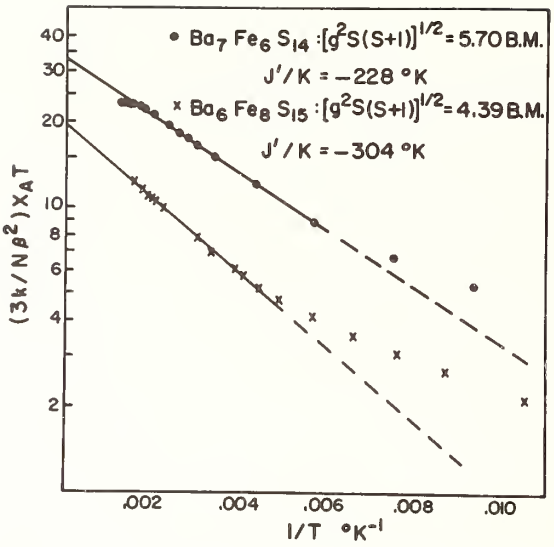

Fig. 12. Plot of magnetic susceptibility as a function of temperature using the reduced spin model.

The reduced spin model was also tried for $Ba_6Fe_8S_{15}$ and the plot is shown in figure 12. The intercept gives a magnetic moment of 4.39 BM which is unreasonable for iron ions with an average S = 2.125. This suggests that the antiferromagnetism of $Ba_6Fe_8S_{15}$ can not be expressed as a simple linear interaction. This is not too surprising since the linear structure is columnar rather than a chain. The very high Curie-Weiss constant, θ = -937 K, implies a strong interaction among iron atoms.

The slope of the straight line portion permits the calculation of the effective exchange energy J'/k and these values are listed in table 9. It is evident that the exchange energy correlates very well with the Fe-Fe distances found in these structures.

10. REFERENCES

[1] Grey, I. E., Hong, H. and Steinfink, H., Inorg. Chem. 10, 340 (1971).
[2] Grey, I. E. and Steinfink, H., Inorg. Chem. 10, 691 (1971).
[3] Hong, H. and Steinfink, H., Abstracts, American Crystallographic Association, Winter Meeting 1971.
[4] Schnering, H. G. and Hoppe, R., Z. Anorg. Allg. Chem., 312, 99 (1961).
[5] Wyckoff, R. W. G., *Crystal Structures*, 2, Interscience Publishers, J. Wiley & Sons, New York (1964).
[6] Brink, C., Binnendijk, N. F. and van de Linde, J., Acta Cryst. 7, 176 (1954).
[7] Boon, J. W. and MacGillavry, C. H., Recl. Trav. Chim, Pays-Bas, 61, 910 (1942).
[8] Dewar, R. B. K., *Proceedings of the 1969 International Summer School on Crystallographic Computing*, Ed. F. R. Ahmed, Munksgaard, Copenhagen, 1970.
[9] Minot, M. J. and Perlstein, J. H., Phys. Rev. Lett. 26, 371 (1971).

DISCUSSION

R. S. Roth: Did you try to determine whether the compounds you have described can be considered part of a homologues series?

H. Steinfink: There doesn't seem to be a general expression that would cover the various stoichiometries described in this presentation.

National Bureau of Standards Special Publication 364, Solid State Chemistry, Proceedings of 5th Materials Research Symposium, issued July 1972.

STUDY OF SULFOSPINELS

R. E. Tressler and V. S. Stubican

Department of Material Sciences
The Pennsylvania State University
University Park, Pennsylvania 16802

Several new compounds with the formula AB_2S_4 were synthesized. Pressure-induced polymorphism of the sulfospinels was investigated. Sulfospinels which produced new high-pressure phases were $NiRh_2S_4$, $FeYb_2S_4$, In_2S_3, $CrIn_2S_4$, $NiIn_2S_4$, $CoIn_2S_4$ and $MnIn_2S_4$. The only sulfospinels which transformed to the NiAs derivatives were those in which A and B atoms had unfilled d-orbitals. P-T phase relations were investigated for a series of sulfochromites.

Thin films of several ACr_2S_4 (A = Mn, Fe, Co, Cu and Zn) sulfospinels were prepared by a flash evaporization technique on the (111) and (100) planes of NaCℓ and on the (100) plane of MgO.

Key words: Flash evaporation; high pressure phases; sulfospinels; thin films.

1. INTRODUCTION

The existence of well defined sulfospinels has been known for some time [1][1]. Structures of complex sulphides with composition $M^{II}M_2^{III}S_4$ have been reported by several authors. Hahn et al. [2], Lotering [3], Bouchard et al. [4], Blasse and Schipper [5], Flahaut et al. [6,7,8], Pinch et al. [9], Romers et al. [10], Omloo and Jellinek [11], Patrie et al. [12], Donahue [13], Lugscheider et al. [14], Steigmann [15], Bouchard and Wold [16], Bouchard [17], Plovnik [18] have studied the preparation and the structure of the $M^{II}M_2^{III}S_4$ compound. The purpose of this paper is to summarize our recent results on (i) the synthesis of some previously unreported $M^{II}M_2^{III}S_4$ compounds (ii) the polymorphism of sulfospinels at high pressures and (iii) the preparation of thin films of some sulfospinels.

2. EXPERIMENTAL PROCEDURE

2.1. SYNTHESIS OF $M^{II}M_2^{III}S_4$ COMPOUNDS

Usually the two metals and sulfur were mechanically mixed, pelletized, sealed under vacuum in fused silica tubes, heated slowly from 200 °C to 800 °C, held for several days, ground, pelletized, heated at 700 to 800 °C for several days, and then recycled until the sample was single phase. Exceptions were the use of rare-earth and scandium sulfides, cupric sulfide and cadmium sulfide. When two sulfides were mixed to form a ternary compound, heat treatment was begun at high temperatures.

2.2. HIGH PRESSURE EXPERIMENTS

The high pressure experiments were performed with externally heated uniaxial devices, using pistons of cemented carbides and hardened steel. The high pressure apparatus is described fully elsewhere [19]. The samples were pelletized into platinum rings, sandwiched between two platinum sheets to assure a closed system, and placed between two pistons on

[1] Figures in brackets indicate the literature references at the end of this paper.

which high pressure was applied. After 1 to 14 days the specimens were quenched to room temperature by a cold air blast, and the pressure was released. With some specimens, the same treatment was repeated several times to assure equilibrium. Temperatures and pressures were automatically controlled to ± 5 °C and ± 5% respectively

2.3. PREPARATION OF THIN FILMS

The technique of flash evaporation [20] was used to prepare thin films of sulfospinels which contained elements with different vapor pressures. The spinels $MnCr_2S_4$, $FeCr_2S_4$, $CoCr_2S_4$, $NiCr_2S_4$ and $ZnCr_2S_4$ were prepared as previously described. The evaporation was accomplished using a Hitachi vacuum evaporator fitted with a copper block substrate heater against which the substrate was held by stainless steel clips. The substrates were Harshaw NaCℓ crystals cut, and polished on the (111) plane and NaCℓ crystals cleaved on the (100) plane. General Electric MgO crystals cleaved on the (100) plane were also used. A thin wafer of the spinel was evaporated from the W-strip. The substrate to strip distance was held constant at 1 1/8". Spinel film could be obtained by preheating the substrate to 170 - 180 °C, evaporating for 2 to 6 seconds, and annealing in place at 210 - 220 °C for 24 hrs. The vacuum before evaporation was consistently 0.9 - 1.0 x 1.0^{-4} Torr as measured by an ionization gauge, calibrated against a Stokes McLoad gauge. By weight gain measurements and knowing the spinel densities, the film thicknesses were calculated to be between 500 Å and 1500 Å, the 1500 Å film being opaque.

The thin films were floated off the substrate in water or alcohol onto a copper grid and were examined in transmission on a Hitachi electron microscope.

3. RESULTS AND DISCUSSION

3.1. SYNTHESIS OF COMPOUNDS

Table 1 includes the conditions of preparation and the proposed structures of the AB_2S_4 compounds which were previously unreported.

Table 1

Syntheses of Previously Unreported Compounds

Compound	Preparation	X-ray Diffraction Results
$NiAl_2S_4$	300 °C 1 day, 800 °C 4 days	Isostructural with $FeAl_2S_4$
$ZnSc_2S_4$	800 °C 1 day, 1200 °C 1 day (2 cycles), 950 °C 1 week	Spinel, a_o = 10,478 ± 0.001 Å
$NiYb_2S_4$*	400 °C 1 week, 800 °C 1 week 1200 °C 1 day, 950 °C 1 week	Isostructural with α- CaY_2S_4
$NiRh_2S_4$	400 °C 1 week, 800 °C 1 week	Spinel, a_o = 9.701 ± 0.001 Å
$FeRh_2S_4$†	600 °C 6 days, 800 °C 4 days 900 °C 6 days, 600 °C 11 days	Unidentified

* $CuYb_2S_4$, $CdYb_2S_4$, $ZnYb_2S_4$, $ZnLu_2S_4$, $CdLu_2S_4$, and $CoLu_2S_4$ were prepared under the same conditions as $NiYb_2S_4$ and appear to be isostructural with this compound.

† $CrRh_2S_4$, $MnRh_2S_4$, $ZnRh_2S_4$ and $CdRh_2S_4$ were prepared under the same conditions as $FeRh_2S_4$ and appear to be isostructural with this compound.

From the results in table 1 and from literature sources [2-18] the octahedral radius of the A^{II} ion can be plotted versus the radius of the B^{III} ion for $A^{II}B^{III}_2S_4$ compounds. Sulfides are more covalent than oxides because of the lesser electronegativity of sulfur [21]. The use of ionic radii for characterization of a "structural field" has a limited value in this case. Because of many variables involved (coordination change, degree of covalency, etc.) no single type of radii is completely satisfactory. However, strictly for the matter of relative comparison, figure 1 was prepared. Some regularities in this figure are obvious. For large B^{III} ions there is some overlap of the spinel and α-CaY_2S_4 structure type. Pressure or temperature polymorphism of the compounds near the boundary is a possibility which was not investigated. For large B^{III} and A^{II} ions, the Th_3P_4-type structure is predominant. With small B^{III} ions the $FeAl_2S_4$ type structure, where both A^{II} and B^{III} ions are in fourfold coordination, overlaps with spinels. The compounds with the spinel type structure surround a central area of compounds with the defect Ni-As structure which has predominately covalent bonding. With the small B^{III} and large A^{II} ion hexagonal $PbCr_2S_4$ type structure appears [11]. However, the shortcomings of the presentation of the structural relationships as given in figure 1 become evident if one considers the polymorphism of some AB_2S_4 compounds at high pressure or temperature. $NiIn_2S_4$ and other In-spinel containing transition elements, all form a high pressure phase which is not isostructural with NiAs or CaY_2S_4. $ZnAl_2S_4$ possesses a normal spinel type of structure at room temperature. The high temperature polymorph has a layered structure with an orthorhombic cell [15].

3.2. HIGH PRESSURE RESULTS

The appearance of the NiAs structure field and the known spinel-NiAs polymorphism promoted the investigation of the effect of pressure on other sulfospinels [22]. The results are listed in table 2. It is evident from table 2 that only spinels which transformed to the NiAs derivatives are those in which A^{II} and B^{III} ions have unfilled d-orbitals, *i.e.*, a d-d interaction is necessary to stabilize the face-shared octahedral arrangement in the NiAs structure.

In_2S_3 transformed to a high pressure form which could not be indexed as an NiAs structure. The other In-spinels produced a similar high-pressure phase. The d-spacings for high pressure In_2S_3 and $NiRh_2S_4$ are given in table 3.

The chromite series of sulfospinels was selected for quantitative investigation of the pressure-temperature relations between the spinel and NiAs structures. The experimental P-T curves for several spinels are given in figures 2A and 2B. The P-T curve for $FeCr_2S_4$ was in excellent agreement with the data of Albers and Rooymans [22]. For the P-T conditions near

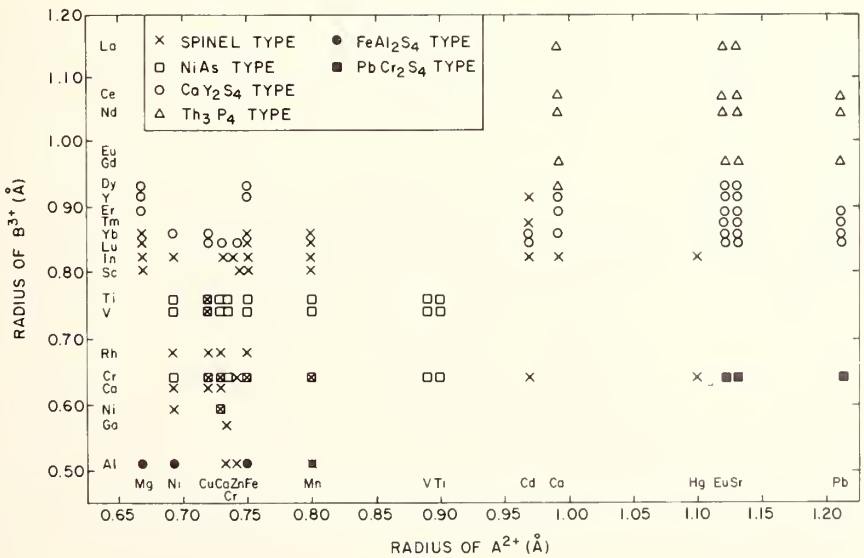

Fig. 1. Structure of AB_2S_4 compounds.

Table 2

High Pressure Results

Compound	Treatment P (kbars)	Treatment T (°C)	Treatment t (days)	Phases	Lattice Parameters (Å)
$CoNi_2S_4$	50	500	2	Disordered NiAs	a = 3.42±0.01, c = 5.33±0.01
CuV_2S_4	60	415	3	Ordered NiAs	a = 5.82±0.01, b = 3.30±0.01 c = 11.44±0.01, β = 91.90°
$CuTi_2S_4$	58	510	4	Disordered NiAs	a = 3.44±0.02, c = 5.65±0.05
$MnCr_2S_4$	60	520	7	Ordered NiAs	a = 5.98±0.01, b = 3.45±0.01 c = 11.74±0.05, β = 91.2°±0.10°
$FeCr_2S_4$*	55	520	7	Ordered NiAs	a = 5.94±0.01, b = 3.44±0.01 c = 11.47±0.01, β = 90.85°±0.05°
$CoCr_2S_4$	40	520	7	Ordered NiAs	a = 5.91±0.01, b = 3.41±0.01 c = 11.10±0.05, β = 91.7°±0.1°
$CuCr_2S_4$**	80	600	4	Spinel	No transformation
$ZnCr_2S_4$	80	600	4	Spinel	No transformation
$NiCr_2S_4$	50	500	4	Ordered NiAs (same as starting material)	a = 5.90±0.01, b = 3.42±0.01 c = 11.04±0.05, β = 91.5°±0.05°
In_2S_4†	45	500	3	High-pressure phase, not NiAs	Unidentif. d spacings (table 3)
$FeYb_2S_4$	60	485	3	High-pressure phase, not NiAs	Similar to In_2S_3, unidentif.
$NiRh_2S_4$	45	497	3	High-pressure phase, not NiAs	Unidentif., apparently complex distortion of spinel

* Albers and Rooymans [22] reported hexagonal NiAs cell parameters, a = 3.4 Å, c = 5.7 Å

† $NiIn_2S_4$, $CoIn_2S_4$, $CrIn_2S_4$, and $MnIn_2S_4$ all form high-pressure phases isostructural with high pressure In_2S_4.

** Bouchard [17] reported the transformation of $CuCr_2S_4$ to the NiAs type structure.

Table 3

X-ray Diffraction Powder Patterns of High Pressure Phases

In_2S_4		$NiRh_2S_4$	
d spacings (Å)	(I/Io)obs	d spacings	(I/Io)obs
4.58	30	3.07	20
4.40	60	3.00	100
3.47	50	2.14	15
3.29	70	2.11	40
3.10	80	1.99	10
2.68	80	1.89	25
1.89	100	1.76	10
		1.73	60

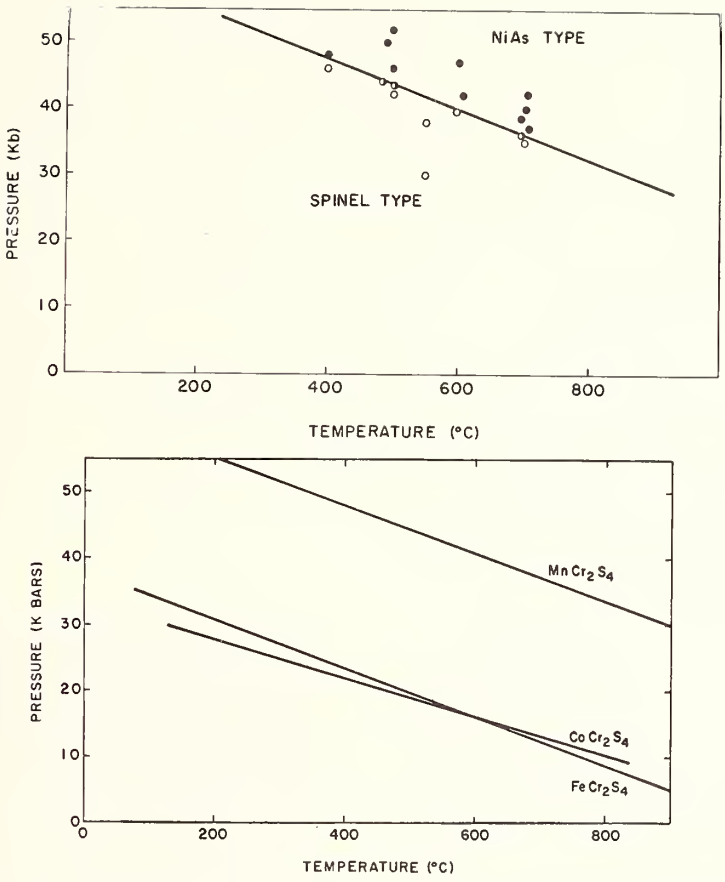

Fig. 2. Univariant P-T curve for the transition spinel type $\overleftrightarrow{}$ NiAs-type structure, (A) in $MnCr_2S_4$ (B) in $CoCr_2S_4$, $FeCr_2S_4$ and $MnCr_2S_4$.

the transition, the hexagonal NiAs structure was observed for $FeCr_2S_4$ and $MnCr_2S_4$, after they were held for short times. At longer times and more extreme pressures, the monoclinic NiAs phase appeared as shown in figure 3. However, for all conditions of treatment in the NiAs field, $CoCr_2S_4$ transformed directly to the ordered monoclinic NiAs phase.[2] In figure 4, x-ray densities for the spinel-type and NiAs-type phases are compared. The difference in the densities of the low- and high-pressure polymorphs increases from 6.6% for $FeCr_2O_4$ to 9.1% for $CoCr_2S_4$.

Considering the equilibrium transition pressure at 600 °C versus the various parameters for the A^{II} ion, such as ionic radius, number of d-electrons, and octahedral site preference energy, there are no definite trends. The equilibrium transition pressure decreases with increasing octahedral site preference, however, $CuCr_2S_4$ does not fit this trend. It is evident from these results that the magnitude of the transition pressure depends on the crystal chemical parameters in a complex way.

3.3. PREPARATION OF THIN FILMS

The selected area diffraction patterns showed all compositions deposited onto the (111) plane of NaCℓ gave polycrystalline spinel patterns with some preferential orientation on the substrate. The excellent agreement of lattice parameters determined by electron diffraction on thin films and by x-ray diffraction on polycrystalline samples showed that the films were not far from AB_2S_4 stoichiometry [23].

[2] In a concurrent investigation, Bouchard [17] obtained also monoclinic high-pressure polymorphs of Mn-, Fe-, and $CoCr_2S_4$ well above the equilibrium transformation conditions.

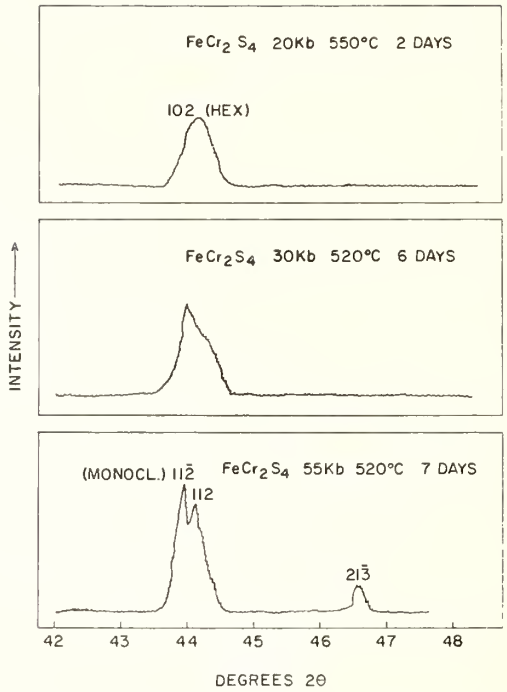

Fig. 3. X-ray diffractometer tracings showing the transition from disordered (hexagonal) to ordered (monoclinic) NiAs-type structure in $FeCr_2S_4$.

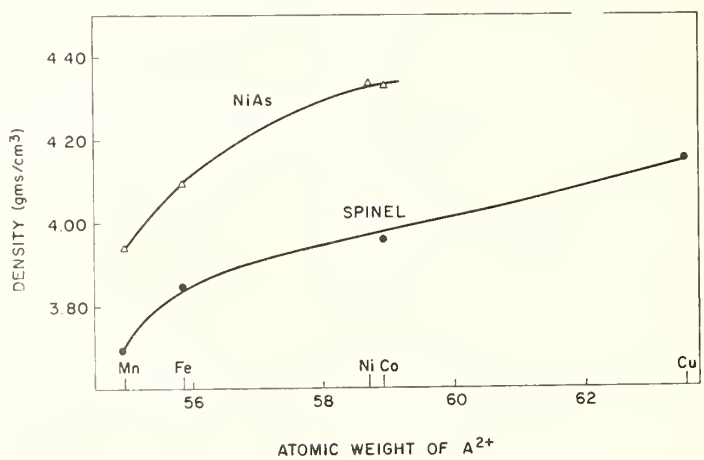

Fig. 4. X-ray densities of spinel-type and NiAs-type structures as a function of the atomic weight of the A^{II} ions.

Deposition of $FeCr_2S_4$ on the (100) plane of NaCℓ at 215 °C and subsequent annealing in vacuum at 200 °C for 24 hrs. resulted in electron diffraction patterns represented by figure 5(A) and figure 5(B). Figure 5(A) appears to be a textured polycrystalline pattern or a single crystal pattern superimposed on a random polycrystalline pattern. Figure 5(B), taken from a different area of the same film as in figure 5(A), appears to be a single crystal pattern with double diffraction and twin diffraction with a weak diffraction pattern of textured polycrystalline material. From figure 5(A), the preferred orientation can be determined from the bright diffraction spots which are indexed in figure 5(C).

Some spinel crystals grow epitaxially with the {001} type planes parallel to the (100) plane of the NaCℓ substrate. The set of four diffraction points around the (400) point in figure 5(B) is typical of the pattern observed for twinning and double diffraction in face-centered cubic metals with (111) twin planes. The spinel situation is analogous with (111) twinning except the (200) reflection is extinct in spinel causing the satellite reflections around the primary (400) reflection.

Higher temperature deposition on the (100) plane resulted in flaking of the film possibly due to the vaporizing of contaminants or to the difference in thermal expansion between the substrate and film.

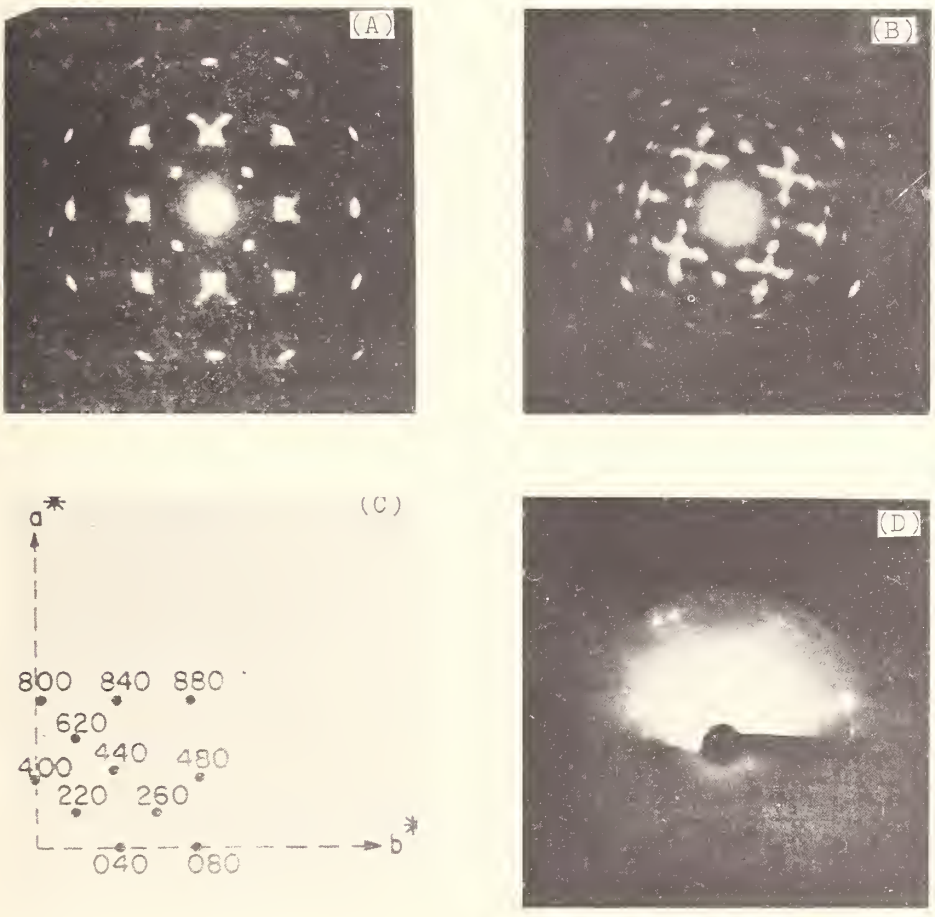

Fig. 5. (A) and (B), electron diffraction patterns of a thin film of $FeCr_2S_4$ spinel deposited on the (100) plane of NaCℓ; (C) indexing of the strong diffraction spots in (A); (D) reflection electron diffraction pattern of a $FeCr_2S_4$ spinel thin film deposited on the (100) of MgO.

Because of the poor insulating properties of NaCℓ, it was of technological interest to deposit films on a good insulating substrate. Single crystals of MgO were the logical choice because the rocksalt structure was known to induce epitaxial growth. $FeCr_2S_4$ was deposited on the (100) plane of the MgO substrate. Because the film could not be floated from the MgO without destroying the film, it was necessary to use a reflection electron diffraction technique where the plane of the film and substrate is nearly parallel to the incident beam. Figure 5(D) is the resulting diffraction pattern. By matching the two strong rings with the (400) and (440) rings in the spinel pattern and comparing radius ratios $R_1/R_2 = d_1/d_2$ the K value for the diffraction pattern could be calculated. The remaining spots on the diffraction pattern could all be indexed as spinel reflections. Thus the $FeCr_2S_4$ does crystallize on the (100) plane of MgO as spinel, but no texturing effect could be observed because of the diffraction technique used.

Recently, single crystal films of several chromium sulfospinels were grown by the chemical vapor transport method [24].

4. ACKNOWLEDGMENT

R. E. Tressler was supported in this work by the National Science Foundation and the National Aeronautics and Space Administration.

5. REFERENCES

[1] Passerini, L. and Baccaredda, Atti Accad. Lincei 14, 33 (1931).
[2] Hahn, H., Z. Anorg. Allgem. Chem. 264, 184 (1951); Hahn, H., Frank, G., Klinger, W., Storger, A. D., and Storger, G., Z. Anorg. Allgem. Chem. 279, 241 (1955).
[3] Lotering, F. K. and VanSteen, G. H., Solid State Commun. 7, 1827 (1969).
[4] Bouchard, R. J., Russo, P. A., and Wold, A., Inorg. Chem. 4, 685 (1965).
[5] Blasse, G. and Schipper, D. J., J. Inorg. Nucl. Chem. 26 1467 (1964).
[6] Flahaut, J., Domange, L., and Patrie, M., Bull. Soc. Chim. France 105 (1961).
[7] Flahaut, J., Domange, L., and Patrie, M., ibid, pg. 1887 (1961).
[8] Flahaut, J., ibid. pg. 1282 (1962).
[9] Pinch, H. L., Woods, M. J., and Lopatin, E., Mat. Res. Bull. 5, 425 (1970).
[10] Romers, C., Blaisse, B. A., and Ijdo, D. J. W., Acta Cryst. 23, 634 (1967).
[11] Omloo, W. P. and Jellinek, F., Receuil 87, 545 (1968).
[12] Patrie, M., Guittard, M., and Pardo, M. P., Bull. Soc. Chim. France 11, 3832 (1969).
[13] Donahue, P. C., J. Sol. State Chem. 2, 6 (1970).
[14] Lungscheider, W., Pink, H., Weber, K., and Zinn, W., Z. Angew. Phys. 30 36 (1970).
[15] Steigmann, G. A., Acta Cryst. 23, 142 (1967).
[16] Bouchard, R. J. and Wold, A., J. Phys. Chem. Solids 27, 591 (1966).
[17] Bouchard, R. J., Mater. Res. Bull. 2, 459 (1967).
[18] Plovnik, R. H., Ph.D. Thesis, Brown University, 1969.
[19] Dachille, F. and Roy, Rustom, pg. 163 in *Modern Very High Pressure Techniques*, ed. by Wentorf, R. H., Jr., Butterworth & Co. (Publishers) Ltd. London, 1962.
[20] Harris, L. and Siegel, B. M., J. Appl. Phys. 19, 739 (1948).
[21] Wells, Structural Inorganic Chemistry 3rd ed; pp. 31 725 and 427, Oxford University Press, London, 1962.
[22] Albers, W. and Rooymans, C. J. M., *High-Pressure Polymorphism of Spinel Compounds*, Solid State Commun. 3, 417 (1965).
[23] Tressler, R. E. and Stubican, V. S., Mater. Res. Bull. 2, 1119 (1967).
[24] Pinch, H. L. and Ekstrom, L., RCA Review December, 1970 pg. 692.

National Bureau of Standards Special Publication 364, Solid State Chemistry, Proceedings of 5th Materials Research Symposium, issued July 1972.

PHASE CHANGES IN Cu_2S AS A FUNCTION OF TEMPERATURE

William R. Cook, Jr.

Gould Inc., Gould Laboratories
Cleveland, Ohio 44108

and

Case Western Reserve University
Cleveland, Ohio 44106

The high-copper phase boundary of Cu_2S deviates from stoichiometry above 300 °C, first becoming copper deficient, then above ~ 1075 °C becoming copper rich. The maximum copper content occurs at the monotectic temperature of 1104 °C. The strong effect of oxygen on the hexagonal-cubic transition in Cu_2S was confirmed; the transition was also found to be sensitive to the type of pretreatment of the material. The high temperature tetragonal "$Cu_{1.96}S$" phase is stable between $Cu_{1.95}S$ and Cu_2S, at temperatures of ~ 90° to ~ 140 °C. The transition to the tetragonal phase is extremely sluggish. The true composition of djurleite has been shown to be approximately $Cu_{1.93}S$.

The phases near the chalcocite-digenite region of the diagram may be grouped into those with hexagonal close packing of sulfur atoms and those with cubic close packing of sulfurs. This is important in understanding rates of transformation among the various phases that occur in this area of the diagram.

Key words: Chalcocite; Cu_2S; digenite; djurleite; nonstoichiometry; phase relations.

1. PREVIOUS WORK

Fairly thorough explorations of the Cu-S phase diagram between Cu_2S and $Cu_{1.7}S$ have been made by a number of previous workers [1-8][1]. The resulting diagram may be seen in figure 1 taken largely from Roseboom [7] and Rau [8]. The principal phases are chalcocite (Cu_2S), orthorhombic (or monoclinic [9]) below 103.5° and hexagonal above it; djurleite (~ $Cu_{1.96}S$)[2], and digenite ($Cu_{2-x}S$), cubic with a wide range of solid solution at high temperatures, pseudocubic rhombohedral below 78° with a narrow range of solid solution. Additional phases which have been reported but which have not been confirmed as stable phases in the diagram are a tetragonal "$Cu_{1.96}S$," obtained between ~ 100° and ~ 150° [10-12], hexagonal $Cu_{1.91}S$, obtained by only one group [13], a hexagonal [14] polymorph of digenite [15], and a new "stable" ordering of digenite, known as anilite [16,17].

Several studies have examined the changing stoichiometry of chalcocite. Posnjak et al. [1] and Jensen [3] found the maximum melting point to be at a composition slightly deficient in copper. Rau [8] found approximately a linear relation for the maximum copper composition of chalcocite between $Cu_{1.9988}S$ at 516° and $Cu_{1.9939}S$ at 1048°. Wagner and Wagner [18] obtained a limiting composition of $Cu_{1.9996 \pm .0002}S$ at 400°. Wehefritz [19] obtained a formula of ~ $Cu_{1.998}S$ at 443° (cubic phase) but found no detectable deviation from stoichiometry in the hexagonal phase (*i.e.* copper content > $Cu_{1.9998}S$).

---

[1] Figures in brackets indicate the literature references at the end of this paper.

[2] All chemical formulas will be given as the number of atoms of copper per atom of sulfur. All temperatures are °C.

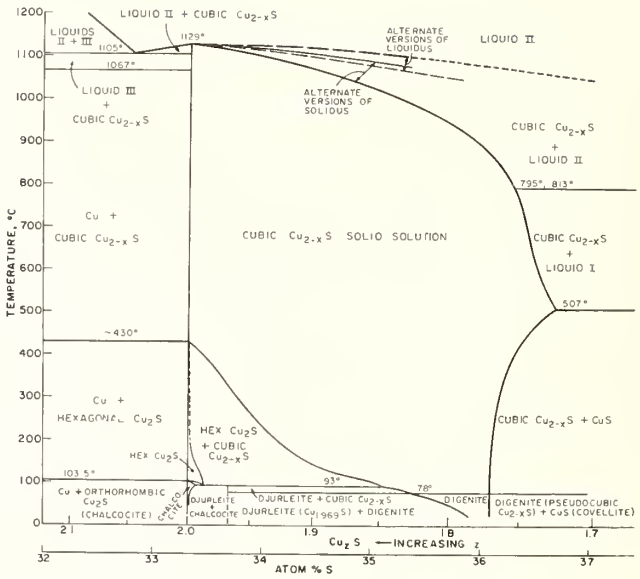

Fig. 1. Cu-S phase diagram in the vicinity of chalcocite and digenite [3, 6-8].

Much of the previous work, particularly near room temperature, was done in air on the assumption that little if any reaction with air occurs. Buerger [2] pointed out that this assumption was not valid, but his work was later criticized [5] because much of it had been done in air. Studies on chalcocite crystals chemically converted from CdS [14] re-emphasized that it was necessary to completely exclude air at all temperatures if the objective was to determine the two component diagram. The only one to have done so is Jensen [3], and our results are in agreement with his.

2. MATERIALS AND EXPERIMENTAL TECHNIQUES

Raw materials were 99.999% Cu in either rod or 1 mm wire form and 99.999% S, both from American Smelting and Refining Co. The major impurity in the sulfur is organic material. The copper was etched in 1:2 or 1:3 HNO_3 to remove the oxide and superficial impurities, washed with distilled water, and kept in vacuum until use. Copper filings were not used because of the increased amount of oxygen impurity that would be present due to the large surface area. The sulfur was kept in vacuum briefly before use also in order to remove as much adsorbed oxygen and H_2O as possible. Only chunk sulfur was used so that none would be lost. Compositions were recalculated after weighing and applying the buoyancy correction to give the exact composition of the mix. From the time they were made, all compositions were kept sealed in vacuum except when being ground of x-rayed.

For the usual mixes, which ranged between 1 and 2-1/2 grams, compositional uncertainty was 0.05 to 0.1% in the Cu:S ratio, $Cu_{1.9599 \pm .0019}S$, for example. For the "whisker" compositions, which were weighed on a semi-microbalance, the estimated precision of the final compositions was ~ 2 to 4 ppm, equivalent to a formula of $Cu_{2.001151 \pm .000005}S$, for example. At this inaccuracy level, impurities can constitute an error up to ten times the weighing error. However, it is here assumed that due to the similar nominal level of impurities in the two raw materials, no substantial increase in error existed. If this is incorrect, it could shift the abscissa laterally in figure 3 by a small amount.

This work used mainly three techniques: observation of changes at high temperature (Cu "whisker" growth of Cu_2S samples), differential thermal analysis (DTA), and low temperature equilibrium at several temperatures, particularly 120° ± 1°, 73° ± 0.4°, and room temperature (24° ± 2°). Powder x-ray diffraction patterns were taken on most of the samples using film or a diffractometer.

Fig. 2. $Cu_{2.00115}S$ composition showing the effect of heating to 608° for 1.3 hours. The upper picture (with cm scale) shows sample after equilibration at 100° (no whiskers). The lower picture shows the presence of numerous fine copper whiskers, particularly along the bottom edge of the sample.

After reaction (generally at 600° for 16 hours to several days, followed by slow cooling over several more days to allow re-equilibration), most samples were ground, divided into several parts, and resealed in fused silica. One part was used for the DTA (Dupont 900 unit with 1600° furnace); other parts were held at 120°, 73°, and room temperature. Where an appreciable vapor pressure was expected, the vapor space was reduced to a minimum by inserting a hollow slug before sealing. The DTA equipment was calibrated against the melting point of tin (231.89°) [20], cadmium (320.9°) [20], zinc (419.505°) [21], silver (960.8°) [20], and gold (1064.5°) [22], both at the beginning and near the end of the work. The temperature correction was never more than 3°. Temperatures normally reproduced to better than 1°.

The determination of the copper-rich Cu_2S phase boundary rests on an observation by Shiozawa [23]. If a Cu_2S sample has been saturated with copper at a low temperature and is heated somewhat hotter, very fine copper whiskers will grow out of the surface of the Cu_2S, indicating it is now supersaturated and is in the two-phase Cu-Cu_2S region of the diagram. When the sample is cooled the whiskers redissolve in the Cu_2S. Since very small amounts of free copper can be detected visually, this is therefore a very sensitive means of plotting this phase boundary. An example showing the same sample with and without the copper whiskers is seen in figure 2.

The large samples to be used for the copper-saturated Cu_2S phase boundary were not ground after reaction, but were used as is. It is believed that the slow cooling permitted equilibration as low as 150°. The reaction progressed by copper migrating through the already-formed copper sulfide to the surface, where it reacted with sulfur vapor. This resulted in a hollow core at the completion of the reaction of almost the size of the original copper rod. Any free copper remaining after the reaction was completed remained as a solid lump in the hollow core.

465-504 O - 72 - 46

A thermocouple (calibrated against a NBS standardized reference thermocouple) was fastened to the outside of the container with the bead aligned with the middle of the Cu_2S piece, and the assembly was put in a temperature-stabilized furnace for a length of time necessary to establish equilibrium. For low temperatures, > 16 hours was used, while near 1000° times of 15 minutes to 1/2 hour were sufficient. The length of the samples meant that at high temperatures a small temperature gradient (< 5°) existed within the sample. The magnitude of the gradient was estimated with the thermocouple, and corrected for.

After heating, the sample was very quickly removed from the furnace and examined for the presence of copper whiskers. Most of the time, samples not showing copper whiskers were heated in order to see if whiskers appeared, but occasionally the reverse procedure was used: samples in which whiskers had been formed were heated at a different temperature to see if the whiskers disappeared. As far as could be determined, both methods gave the same results.

Two observations should be made on problems encountered, in case others should wish to repeat the experiments. Whiskers that formed quickly at low temperatures tended to redissolve quickly, but if they remained for 16 hours, extensive treatment (usually at very high temperature) was necessary in order to get rid of them. Thus for the tests involving disappearance of copper whiskers, the whiskers had to be "fresh". Also at high temperatures, the presence of a very small sulfur (or copper sulfide) vapor pressure resulted in whiskers converting to Cu_2S on the surface after a few hours, after which it was virtually impossible to get rid of them and the sample would have to be abandoned (since one is depending on visual appearance of whiskers). This caused premature abandonment of one of the compositions used in this study, that at about $Cu_{2.00115}S$.

3. EXPERIMENTAL RESULTS AND DISCUSSION

The results of the present work and the previous literature are summarized in figures 3 - 5. The values of Rau [8], Roseboom [7], Ruhl and Sauer [24] and Wehefritz [19] have been accepted for the copper-deficient phase boundary of digenite ($Cu_{2-x}S$) between 130° and 1000°.

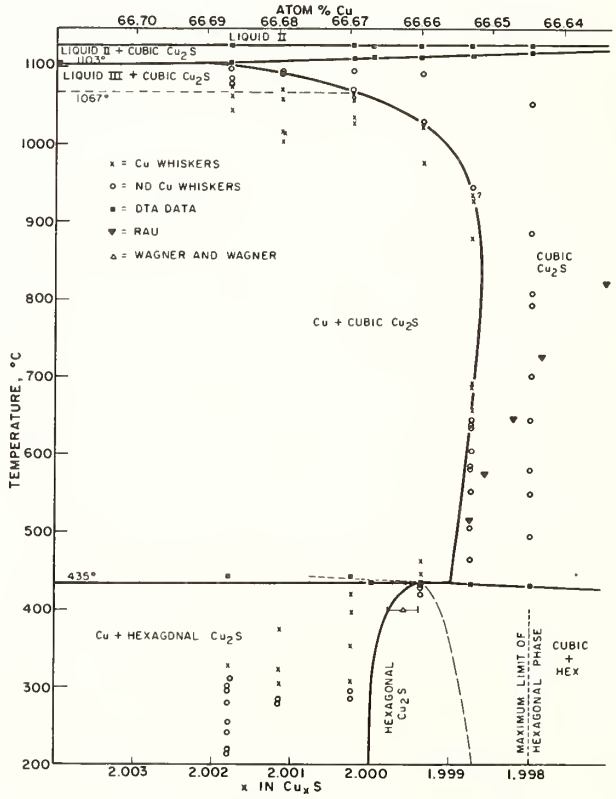

Fig. 3. The phase boundary between Cu_2S and Cu_2S + Cu.

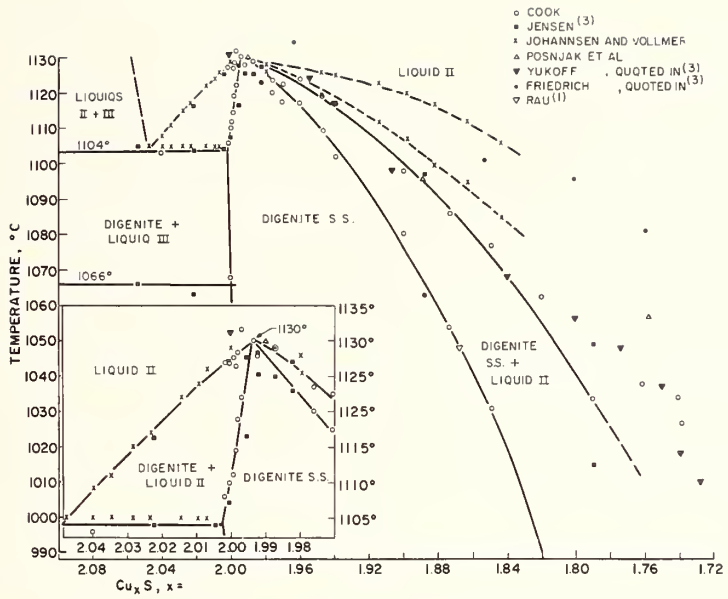

Fig. 4. Melting relations from $Cu_{2.1}S$ to $Cu_{1.72}S$. The previous literature is summarized along with results from the present study.

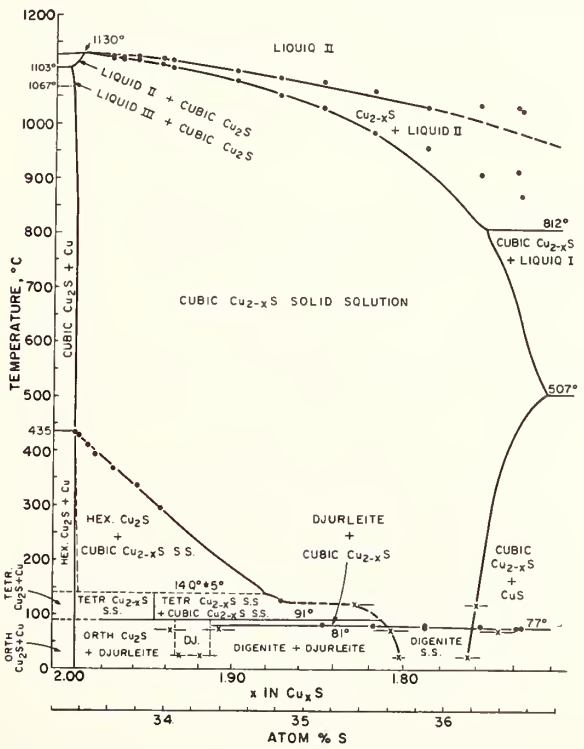

Fig. 5. Phase diagram from $Cu_{2.00}S$ to $Cu_{1.72}S$.

3.1. *Copper Solubility in Cu_2S and High Temperature Phase Relations*

The observation of Cu whiskers due to supersaturation with copper was used to determine the (Cu + Cu_2S) - Cu_2S phase boundary between 165° and 1070 °C, as shown in figure 3. At low temperatures, copper whiskers were most numerous at the hottest spot, which follows from the shape of the phase boundary (fig. 3). The copper whiskers varied in length up to half an inch or more. Long whiskers were usually bent or coiled. Widths of whiskers ranged from barely detectable under the microscope (< 10 microns) to several tenths of a millimeter. One whisker was found to be polycrystalline by x-ray diffraction. In at least some cases, the whiskers grew into the inner void as well as on the outside, but this did not appear to interfere with the observations. When the samples were broken open at the end of the experimentation, a very minor amount of whiskers was found in those samples with more than two copper atoms per sulfur, but no trace was found of the original copper core, indicating that at some stage all of the copper was in solid solution in the Cu_2S.

The initial deviation from stoichiometry is in the direction of copper deficiency as expected. However, as may be seen in figure 3 the boundary unexpectedly curves back towards copper at high temperature. This is in the opposite direction to what has been reported previously [8].

At low temperatures, all three samples with excess copper ($x > 2.0$) formed Cu whiskers on heating above ~ 305 °C. Since all were equilibrated with Cu near 150°, all showed whiskers at the same temperature, the excess copper at 150° remaining in the core as a solid piece. It must be only above 300° that the phase boundary deviates significantly from the stoichiometric composition. One sample was heated for long times near 305°, 320°, 400°, 415°, 435°, and 445° and the amount of free copper was qualitatively observed. At 304.5° no copper was detected. At 306° one exceedingly small whisker was found. At 320.5°, both the number and length of the copper whiskers had increased considerably, but the amount was still small. At 415° a further increase in amount of copper was observed. At 435° and at 445° the number of whiskers had probably not increased, but the thickness and length were both quite large. The longest whiskers were probably at least half an inch in length, and strongly coiled. These qualitative observations are the basis for the shape of the phase boundary below 435° as drawn in figure 3. It is assumed that copper-saturated compositions below 300° are stoichiometric, but the limits of uncertainty are $Cu_{2.0001}S$ and $Cu_{1.9999}S$ from compositions of samples adjacent to the phase boundary and observation of changes in amount of copper whiskers with temperature above 305°.

High temperature results were supplemented by data from the DTA curves, which showed the existence of solidus and liquidus curves on *both* sides of the maximum melting temperature of the Cu_2S phase as indicated in figures 3 and 5. The maximum melting point is in the composition range $Cu_{1.994}S$ to $Cu_{1.986}S$, probably at the high copper end of this range, and the maximum temperature of melting is 1130 ± 2°, in excellent agreement with 1130 ± 1° at $Cu_{1.990} \pm .004S$ and 1129° at $Cu_{1.989}S$ reported previously [1,3]. It is probable that the occurrence of the maximum melting point slightly on the sulfur-rich side of Cu_2S led previous workers to suspect that the copper-rich phase boundary of the Cu_2S phase was shifted in the same direction at high temperatures [8,3], which is incorrect or oversimplified as seen above.

One notices in figure 3 that the "solid solution" of copper in Cu_2S at 1103° is appreciable. The data points from the "whisker" data just below 1095° indicating no formation of copper whiskers have been disregarded. The lack of apparent rise of the Cu-Cu_2S phase boundary is due to the circumstance that the specimens needed to be equilibrated at least 20° above the phase boundary for the whiskers to appear. The fact that the sample with composition $Cu_{2.001797}S$ was not supersaturated with copper at 1097° (the highest temperature to which it was heated) is shown by the absence of any core of unreacted copper when the piece was broken open.

The monotectic was measured at 1103 ± 2° for a composition with appreciable excess Cu (fig. 4) compared with 1105° determined previously [6,3]. Jensen [3] chose 1105° although his data contained both 1104° and 1105° as possible data points. The value of 1104° ± 1° is used for figure 1.

3.2. *The Hexagonal-Cubic Phase Transition Near 435°*

There has been a good deal of difficulty in determining the transition temperature in the past due to its sluggish nature, with temperatures between 350° and 470° reported; in this study it was *not* a problem, largely because of the rigorous efforts to exclude oxygen from the samples. The strong effect of oxygen on the phase transition was pointed out by Roseboom [7]. The minimum temperature hysteresis for the transition was 7°, considerably under most other studies, but still of significant size. Wehefritz [19] explained this large hysteresis as due to the extremely small heat of transition, estimated by him as 110 ± 40 cal/mole. This can be expected to be not far in magnitude from enthalpies due to structural defects and therefore arising from other than thermodynamic equilibrium.

An additional effect on the hysteresis was found arising from the past thermal history of the sample. All samples in which the composition contained more copper than the stable limit near 435° showed increased hysteresis with temperature cycling, even when oxygen was excluded, the increase in hysteresis amounting to a factor of three after several cycles. The effect was temporary, since re-equilibrating the sample at high temperature sharpened the DTA peaks and eliminated the excess hysteresis. The transition temperature was unchanged between samples equilibrated at 1105° (near maximum Cu content) and at 835° (near minimum Cu content). Thus the increased temperature hysteresis is caused by slow kinetics, probably caused by lattice defects connected with the Cu precipitation, rather than a shift of transition temperature with copper content.

There appears also to be a continued rise of the hexagonal-cubic phase transition as a metastable extension of the phase boundary into the two phase region (dotted in on figure 3) but the increase in temperature is small and is barely significant.

The shape of the DTA curves for the hexagonal-cubic transition in compositions near Cu_2S can also suggest a location for the minimum copper content of the hexagonal phase since a single phase sample will transform more sharply than a sample which is a mixture of the limiting hexagonal composition plus a cubic phase. From the curve shapes the limiting low copper content of the hexagonal phase is no lower than $Cu_{1.998}S$, and may be as high as $Cu_{1.9994}S$. This uncertainty is indicated on figure 3 by dashed lines. Roseboom [7] by a different method judged that the solid solution limit of hexagonal chalcocite at 180° was at higher copper content than $Cu_{1.998}S$, which is in agreement.

3.3. *Low Temperature Phase Relations*

A brief summary is given of other findings, since they affect the structural interpretation of the results.

No evidence was found for solid solution in "orthorhombic" chalcocite at 73° or 76° by the method of disappearing phases. No evidence near 100° (where solid solution was reported to be maximum [7]) could be obtained, since samples transformed to the tetragonal phase. By the same method the composition of djurleite was found to be $Cu_{1.93 \pm .015}S$. Results were not precise enough to be certain of the existence of solid solution. It is probable that previous studies used material that was slightly contaminated with oxygen, and thus contained less Cu in the lattice than was believed to be the case. Djurleite decomposes at 91 ± 1°, in reasonable agreement with the previously determined [7] 93°.

The transformation to tetragonal "$Cu_{1.96}S$" is very sluggish, and may again become more so in the presence of oxygen contamination. All compositions between $Cu_{2.00}S$ and $Cu_{1.95}S$ transformed completely to the tetragonal phase in a matter of months between the temperatures of 94° and 120°, and partially transferred at 137°. The phase transforms back by at least 146°. Lesser times were frequently insufficient for complete conversion.

$Cu_{1.91}S$ [13], the hexagonal polymorph of digenite [14,15], and anilite [16,17] were not obtained as stable phases in this study, and are not believed to exist in the equilibrium Cu-S phase diagram. The details of the attempts to obtain anilite will be reported elsewhere.

4. COMPARISON OF THE STRUCTURE OF THE COPPER SULFIDES

X-ray diffraction on small CdS crystals which had been chemically converted to chalcocite, djurleite, or "hexagonal digenite" demonstrate a great similarity in the structure [14], which can be explained by assuming that the sulfur atoms remain fixed while the copper atoms, which are known to be unusually mobile in Cu_2S [4, 25], rearrange themselves in accordance with the proportion of copper atoms to sulfur. Chalcocite, both hexagonal [26] and "orthorhombic" [9,26] forms, has its sulfurs essentially in hexagonal close packing. Psuedo-hexagonal [27] djurleite and the hexagonal polymorph of digenite are both obtainable from chalcocite as *single* crystals [14], indicating the same sulfur arrangement. Eliseev's [13] $Cu_{1.91}S$ phase can also be fitted to this sulfur arrangement (fig. 6).

The cubic close packed sulfur arrangement typified by sphalerite and hawleyite (cubic CdS) is found in digenite [28] (or anilite [16,17]) and tetragonal "$Cu_{1.96}S$" [10]. This is the obvious explanation for the very sluggish transition between "$Cu_{1.96}S$" and djurleite or chalcocite, and the somewhat sluggish transition between hexagonal chalcocite and digenite at 435°. On the other hand, while the cubic high temperature form of digenite can be at least partially quenched, the phase transformation to the low temperature ordered phase is sufficiently fast that the DTA peak occurs with no hysteresis. The hexagonal form for chalcocite is widely reported as unquenchable; the hexagonal-orthorhombic transition, though almost certainly first order and showing 10 to 15° hysteresis, occurs rapidly.

All of the above results are completely consistent with the picture of the two basic sulfur arrangements with the interstices filled by highly mobile copper atoms. Transitions between phases with the same sulfur arrangements are rapid while transitions between phases with different sulfur arrangements are sluggish. This same approach to phase relation among the copper sulfides has been clearly expressed in a recent paper by Cavallotti and Salvago [15]. It is obvious that the copper atoms, being highly mobile and able to take a wide variety of orderings, are very poorly bonded to the sulfur atoms. In fact a statistical distribution of copper atoms along channels has been proposed [26] for the structure of hexagonal chalcocite.

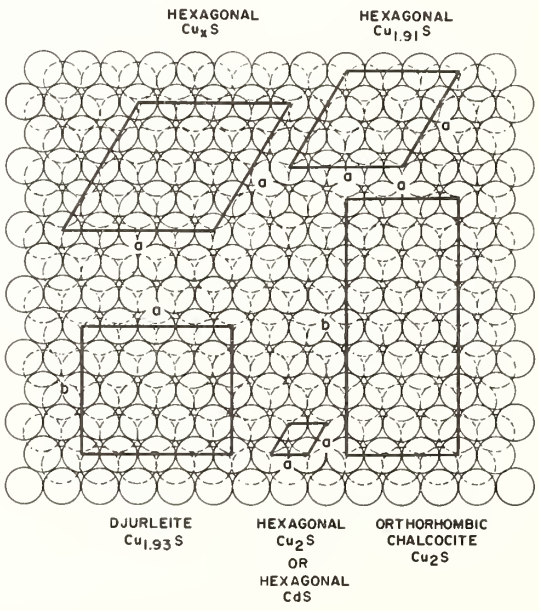

Fig. 6. Idealized unit cells in the plane perpendicular to *c* for copper sulfides, showing orientation and size of unit cells with respect to hexagonal close packed sulfur layers.

An additional problem is the reason for the wide solid solution in the structures with a cubic close packed sulfur arrangement and very limited solid solution in those with hexagonal close packed sulfurs. Cavallotti and Salvago [15] offered the following structural explanation. In the cubic type the coppers tend to be in the tetrahedral antifluorite position, whereas in the hexagonal close packed structures the coppers tend to be in the sulfur layer and are thus more tightly bonded to three sulfurs than when they are bonded to four in the cubic arrangements. This favors the cubic sulfur arrangement when the ratio of copper to sulfur deviates from 2:1.

5. ACKNOWLEDGMENTS

This work was performed while a Ph.D. candidate at Case Western Reserve University, and was supported in part by Aerospace Research Laboratories, Air Force Systems Command, United States Air Force, Contract F33615-68-C-1732. I am indebted to P. O. Banks and J. Hower of the Geology Department, Case Western Reserve University and L. R. Shiozawa and J. M. Jost of Gould Inc. for many stimulating discussions.

6. REFERENCES

[1] Posnjak, E., Allen, E. T., and Merwin, H. E., Econ. Geol. 10, 491-534 (1915).
[2] Buerger, N. W., Econ. Geol. 36, 19-44 (1941).
[3] Jensen, E., Avhandl. Norske Videnskaps-Akad. Oslo I. Mat.-Naturw. Klasse 1947, No. 6, 1-14.
[4] Hirahara, E., J. Phys. Soc. Japan 2, 211-13 (1947), ibid. 6, 422-27 (1951).
[5] Djurle, S., Acta Chem. Scand. 12, 1415-26 (1958).
[6] Johannsen F. and Vollmer, H., Erzbergbau u. Metallhuttenw. 13, 313-22 (1960).
[7] Roseboom, E. H., Jr., Econ. Geol. 61, 641-72 (1966).
[8] Rau, H., J. Phys. Chem. Solids 28, 903-16 (1967).
[9] Evans, H. T., Jr., Nature Phys. Sci. 232, 69-70 (1971).
[10] Janosi, A., Acta. Cryst. 17, 311-12 (1964).
[11] Skinner, B. J., Boyd, F. R., and England, J. L., Am. Geophys. Union Trans. 45, 121-22 (1964).
[12] Kullerud, G., *Handbook of Physical Constants*, Geol. Soc. Am. Mem. 97, 323-44 (1966).
[13] Eliseev, E. N., Rudenko, L. E., Sinev, L. A., Koshurnikov, B. K., and Solovov, N. I., Mineralog. Sb. L'Vovsk. Gos. Univ. 18, 385-400 (1964).
[14] Cook, W. R., Jr., Shiozawa, L., and Augustine, F., J. Appl. Phys. 41, 3058-63 (1970).
[15] Cavallotti, P. and Salvago, G., Electro-chim. Metal. 4, 181-210 (1969).
[16] Morimoto, N., Koto, K., and Shimazaki, Y., Am. Mineral 54, 1256-68 (1969).
[17] Morimoto, N. and Koto, K., Am. Mineral. 55, 106-17 (1970).
[18] Wagner, J. B. and Wagner, C., J. Chem. Phys. 26, 1602-6 (1957).
[19] Wehefritz, V., Z. Phys. Chem. (Frankfurt) 26, 339-59 (1960).
[20] Weast, R. C., Ed., *Handbook of Chemistry and Physics*, 45th Ed., Chemical Rubber Co., Cleveland, Ohio (1964).
[21] Simson, H. F., NBS J. Res. 65A [3] 139-45 (1961).
[22] Moser, H., Otto, J., and Thomas, W., Z. Physik 175, 327-36 (1963).
[23] Shiozawa, L. R., personal communication, Aug. 1968.
[24] Rühl W. and Saur, E., Ber. Oberhess. Ges. Natur-u. Heilk. Giessen, Naturw. Abt. 28, 35-47 (1957).
[25] Pavlyuchenko, M. M. and Pokrovskii, I. I., Vestsi Akad. Navuk Belarus, SSR, Ser. Khim. Navuk 1967 (3), 35-41.
[26] Buerger, M. J. and Wuensch, B. J. Science 141, 276-77 (1963); Wuensch, B. J. and Buerger, M. J., Mineral Soc. Am. Special Paper 1, p. 164-70 (1963).
[27] Takeda, H., Donnay, J. D. H., Roseboom, E. H., and Appleman, D. E., Zeit. Krist. 125, 404-13 (1967).
[28] Morimoto N. and Kullerud, G., Am. Mineral. 48, 110-23 (1963).

DISCUSSION

H. T. Evans: In connection with your testimony that most natural chalcocite specimens actually are djurleite, I may say that from my own experience I can confirm this observation. However, I do not agree that the djurleites are psendomorphous after original low chalcocite. The specimen labelling is not important because djurleite closely resembles low chalcocite in physical properties, and djurleite was not known to be a distinct species before 1958. I have found that each has distinct and characteristic crystal habit, and from this evidence it appears that both have been formed as primary phases in the veins at temperatures below 100 °C. The djurleite crystals are flat, roughly hexagonal tablets, fresh in appearance, with blue-black submetallic luster. Low chalcocite crystals are more prismatic with dome terminations, highly striated, and have a dark, reddish brown-black patina resulting from surface oxidation. X-ray diagrams show that low chalcocite crystals are often intergrown with djurleite. Allowing for low temperatures of formation that are quite feasible in vein deposits, these observations are consistent with the equilibrium system you have shown.

W. R. Cook: In all cases but one, the crystals examined were old (mined over 43 years ago), and were almost entirely djurleite. One larger crystal that had been attached to copper sulfide matrix was still partly chalcocite, and one crystal which was unattached had gone all the way to digenite. However, all but one of these crystals (including the digenite) had shapes explicitly or implicitly hexagonal. Some were flat hexagonal plates, some were hexagonal prisms. The crystal retaining a little chalcocite was prismatic.

Basically, I have trouble visuallizing djurleite being as hexagonal in appearance as chalcocite, which *is* hexagonal above 103 °C. Therefore, I believe that all of these crystals were hexagonal to start with, and were chalcocite. The one crystal that was different was the Bristol Conn. specimen, which had the shape shown for it in Dana. The long axis of the crystal was the djurleite *a* axis. This crystal obviously grew below the stability range of the hexagonal form, and therefore could have been either low chalcocite or djurleite. My preference is for djurleite, because the composition is "different" and so is the crystal shape, but it is purely intuitive, and may be entirely incorrect.

National Bureau of Standards Special Publication 364, Solid State Chemistry, Proceedings of 5th Materials Research Symposium, issued July 1972.

PREPARATION AND PROPERTIES OF THE SYSTEMS $CuFeS_{2-x}$ AND $Cu_{1-x}Fe_{1+x}S_{2-y}$

R. L. Adams, P. Russo, R. J. Arnott, and A. Wold

Division of Engineering
Brown University
Providence, Rhode Island 02912

Stoichiometric samples of $CuFeS_2$ were prepared by direct combination of the elements in sealed evacuated silica tubes. The products were characterized by x-ray diffraction, density determination, magnetic susceptibility and Mössbauer spectroscopy. Homogeneous single phase products gave a density of 4.18 ± 1 g/cc and cell parameters of a_o = 5.292 ± (5) Å and c_o = 10.407 ± (5) Å. In addition, all of the iron was found to be trivalent and located on tetrahedral sites. The plot of inverse susceptibility versus temperature was nearly temperature independent from 77 K to 300 K, and the magnetic susceptibility measurements gave a χ_M = 9.8×10^{-4} emu/mole. Single crystals of $CuFeS_2$ were grown from the melt by means of a modified Bridgman technique.

Samples having the composition $CuFeS_{2-x}$ were also prepared by the direct combination of the elements. X-ray diffraction studies indicated that existence of a single phase, tetragonal γ - form, when x was varied from 0.17 to 0.24. The compound $CuFeS_{1.8}$ had cell dimensions of a_o = 10.598 ± (5) Å and c_o = 5.380 ± (5) Å. Contrary to previous reports, this phase was found to be stable from room temperature to 800 °C. In addition, this phase was stable at room temperature for a period of time in excess of 250 days. It was concluded from density measurements that the structure is best represented as a close packing of sulfur with excess metal ions occupying additional lattice sites.

Compounds having the composition $Cu_{1-x}Fe_{1+x}S_{1.80}$ ($0.25 > x > 0.08$) were prepared and found to be cubic with an average cell size of a_o = 5.32 Å. However, attempts to prepare single phase products with a composition of $Cu_{1+x}Fe_{1-x}S_{2-y}$ were unsuccessful.

Key words: Chalcopyrite; $CuFeS_2$, $CuFeS_{2-x}$, $Cu_{1-x}Fe_{1+x}S_{2-y}$; Cu-Fe-S system; $CuFeS_2$ crystal growth.

1. INTRODUCTION

Chalcopyrite ($CuFeS_2$) has been examined by many investigators [1,2,3,4][1] and found to have an ordered zinc blende structure (a_o = 5.28 Å, c_o = 10.41 Å) with the c-axis doubled. Hiller and Probsthain [5] reported that on removal of sulfur from chalcopyrite, a stable cubic β phase ($CuFeS_{2-x}$) was formed; Nambu [6] and Kano indicated that the stability range of the β phase was with x varying from 0.144 to 0.260. This phase was reported [5] to be body centered with a_o = 10.60 Å. In addition, they indicated the existence of a high temperature γ - form of $CuFeS_{2-x}$ which was tetragonal with a_o = 10.58 Å and c_o = 5.37 Å. This phase was reported to be stable at elevated temperature and converts slowly to the β - phase at room temperature. When heated to 230 °C the β - phase transforms to the γ - phase. Hiller and Probsthain concluded from density determinations that neither of these phases contains sulfur vacancies, but that excess metal ions occupy additional lattice sites.

[1] Figures in brackets indicate the literature references at the end of this paper.

Neutron diffraction studies showed $CuFeS_2$ to be antiferromagnetic at room temperature [7,10]. Teranishi [7] reported a Néel temperature of 550 °C with a moment at liquid nitrogen temperature of $\chi_M = 8 \times 10^{-4}$ emu/mole; the susceptibility was temperature independent below the Néel temperature. These measurements were carried out on natural single crystals of chalcopyrite which had the composition $CuFe_{1.08}S_{2.01}$. Efforts by Teranishi to synthesize single crystals of $CuFeS_2$ were unsuccessful. There appear conflicting reports in the literature [8,9,10] concerning the oxidation states of the copper and iron in chalcopyrite. A recent Mössbauer study [10] indicates the probable valence of +3 iron located on the tetrahedral sites. However, +2 iron is undoubtedly present in the non-stoichiometric phase.

There are numerous other reports on the preparation and properties of chalcopyrite and related phases. However, these studies have been carried out on either naturally occurring minerals or poorly characterized polycrystalline samples. There have been no successful reports of the growth of stoichiometric $CuFeS_2$ single crystals. There appears to be sufficient confusion in the literature concerning the preparation and characterization of phases related to chalcopyrite to warrant further investigation.

2. EXPERIMENTAL

2.1. PREPARATION OF SAMPLES

Samples were prepared by the direct combination of the elements. Freshly reduced copper (Gallard-Schleisenger, 99.999%), iron (Gallard-Schleisenger, 99.999%), and sulfur (Gallard-Schleisenger, 99.9999%) were combined and sealed in evacuated silica tubes. Initially, the samples were heated from room temperature to 800 °C at a rate of 25 °C/hour, were maintained at that temperature for 2 days, and were allowed to cool to room temperature over a period of 18 hours. This cooling was essential to allow time for the complete reaction of the sulfur. The sintered samples were then removed and ground in an agate mortar and pestle under a dry nitrogen atmosphere. The materials were again sealed in evacuated silica tubes and heated at 800 °C for 4 days and slow cooled. This procedure was repeated for two additional cycles in order to ensure sample homogeneity. It was found that extreme caution was necessary in order to prevent oxidation of the sample by exposure to air. However, once the reaction was completed, there was a dramatic increase in sample stability.

2.2. PHASE BOUNDARY STUDIES

The problem of phase analysis was studied by both Thermal Gravimetric Analysis (TGA) and x-ray diffraction. For TGA studies, samples were heated in a dynamic vacuum, and the weight loss was measured as a function of temperature. $CuFeS_2$ was heated for a period of time, was allowed to lose a certain amount of sulfur and then was slow cooled; the product was weighed and x-rayed in order that the phase(s) present in that particular composition could be identified. Small samples (5 mg) were chosen as the optimum size because the final product had a uniform color and appeared homogeneous under microscopic examination. In addition, compounds of a specific composition near the phase boundaries, defined by the TGA studies, were synthesized and examined by x-ray diffraction. The use of these two methods resulted in sharply defined phase boundaries.

2.3. CHARACTERIZATION OF SAMPLES

Cell parameters of products were obtained with a Norelco diffractometer using monochromatic radiation (AMR-202 focusing monochrometer) and a high intensity copper tube. The diffractometer was calibrated relative to a silicon standard.

Densities were determined by a hydrostatic technique using a modified Sartorious model 2604 analytical balance. The density medium, chosen for its ability to wet the samples, was 1,1,2,2 tetrachloroethane. This simple method gives precision and accuracy of 0.5%, but care must be taken to outgas the samples throroughly before weighing them.

The bulk magnetic susceptibility of the samples was measured with a Faraday balance from 77 K to 300 K. The susceptibility was also measured as a function of field (Honda-Owens method [12] up to 10.3 kilogauss in order that the presence of any ferromagnetic impurities could be ascertained.

2.4. CRYSTAL GROWTH

Crystals of $CuFeS_2$ have been grown by a modified Bridgman technique. The samples were lowered from 925 °C to 825 °C over a period of 10 days at a rate of 1/2 inch per day. The thermal characteristics of the furnace were such that an extremely slow rate of cooling (2-3° / inch) occurred during the initial growth period, and then the rate of cooling was continuously increased as the crystal was lowered through the temperature gradient. When the temperature of the crystal reached 825 °C, the furnace was programmed to room temperature at a rate of 100 °C/day. The resulting crystal was usually found to be sulfur deficient. The density of the crystal was measured, and the amount of sulfur to be added was calculated to give a stoichiometric composition ($CuFeS_2$). The crystal and sulfur were then annealed in an evacuated silica tube at 700 °C for a period of 5 days and again were slow cooled. The crystal was x-rayed by both Laue (using molybdenum radiation) and diffractometer methods before and after annealing. Densities were also used to verify the final composition after annealing.

3. RESULTS AND DISCUSSION

3.1. $CuFeS_{2-x}$

The results of the phase studies for the system $CuFeS_{2-x}$ are summarized in table 1. Tetragonal α - $CuFeS_2$ was found to lose sulfur at 390 °C under a dynamic vacuum. This is considerably lower than the value of 550 °C reported in a previous study [5]. Some of the α - $CuFeS_2$ samples prepared contained magnetic impurities that could be detected by means of density and magnetic measurements, although they appeared to be homogeneous by x-ray diffraction. For such samples, the measured density was higher than the calculated value of 4.18 ± (1) g/cc. In addition, the Honda-Owens plot showed the presence of ferromagnetic impurities. This is evident, in figure 1, by the field dependence of the susceptibility. The presence of the apparent ferromagnetic impurity is undoubtedly a result of the lack of homogeneity of the sample. When such samples were annealed, with sufficient sulfur to decrease the density to 4.18 ± (1) g/cc, the magnetic susceptibility showed no field dependency. This can be seen in figure 1. Magnetic susceptibility can, therefore, be used to determine sample homogeneity, beyond the sensitivity of x-ray analysis, when a deviation in stoichiometry results in a separation of a magnetic phase.

Table 1

$CuFeS_{2-x}$

Value of x	a_o (Å)	c_o (Å)	Theoretical++ Density (g/cc)	Experimental Density (g/cc)	Structure	c/a
x = 0	5.292±(5)	10.407±(5)	4.18±(1) 4($CuFeS_2$)	4.18±(1)	α- tetragonal	1.97
x = 0 to x = .16	MIXED PHASE				α+γ tetragonal**	
x = .17 to x = .24	10.598±(5)*	5.380±(5)*	4.32±(1)* 8($Cu_{1.11}Fe_{1.11}S_{2.00}$)	4.30±(1)	γ- tetragonal	0.51

* Values given represent composition for x = 0.2.

** It is possible that the β-phase (cubic) is also present as pointed out by Dr. L. J. Cabri (personal communication).

++ All theoretical densities based on a close-packing of sulfur with excess metal ions occupying additional lattice sites.

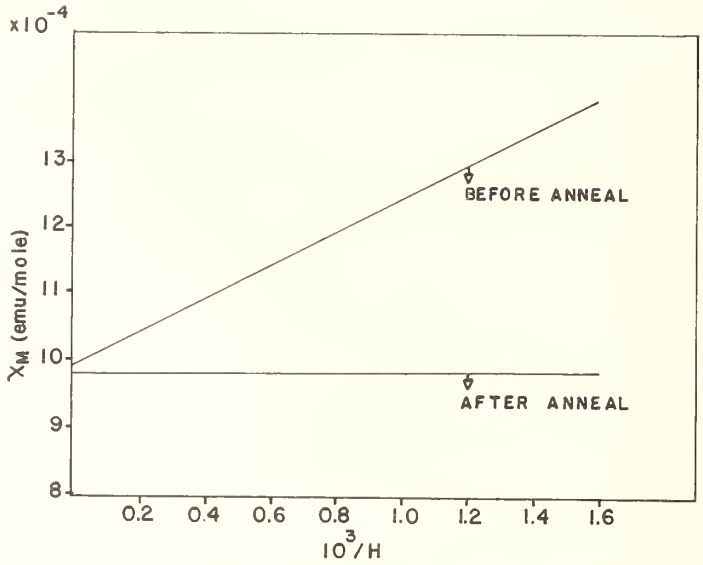

Fig. 1. Magnetic susceptibility of $CuFeS_2$.

Magnetic susceptibility measurements of stoichiometric $CuFeS_2$ gave a value of χ_M = 9.8 x 10^{-4} emu/mole as compared to the reported value of natural crystals of χ_M = 8 x 10^{-4} emu/mole [7]. The plot of inverse susceptibility versus temperature, shown in figure 2, was nearly temperature independent from 77 K to 300 K. Mossbauer examinations of polycrystalline samples of $CuFeS_2$ [11] indicated that all the iron was present as +3 and located on tetrahedral lattice sites.

Attempts were made to reproduce the cubic β-phase reported by Hiller and Probsthain [5] by direct combination of the elements. In all cases, the final products were found to have the tetragonal γ-form. This phase was found to be present in all samples whether quenched from elevated temperatures or slow cooled and annealed below 230 °C. The γ-$CuFeS_{2-x}$ phase has a range from x = 0.17 to x = 0.24. For the composition $CuFeS_{1.8}$, the cell parameters are a_o = 10.598 ± (5) Å and c_o = 5.380 ± (5) Å which is in agreement with a previous report [5]. However, whereas Hiller and Probsthain [5] reported this phase to be unstable at low temperatures, this study indicated the γ-phase to be stable when quenched from any temperature

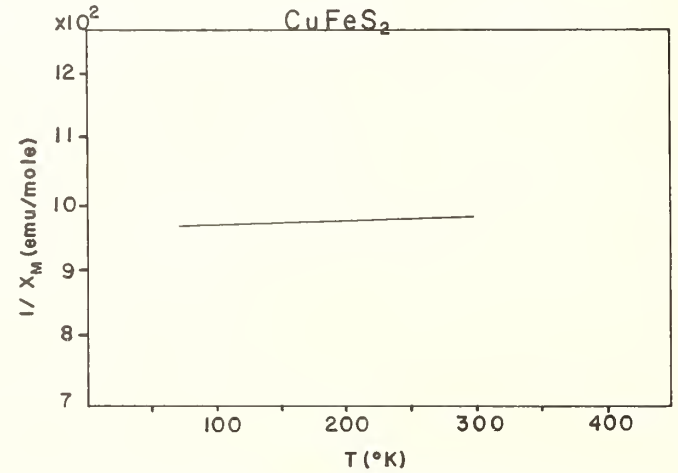

Fig. 2. Inverse magnetic susceptibility of $CuFeS_2$ as a function of temperature.

between room temperature and 800 °C; also, the γ-phase was stable at room temperature for an extended period of time (250 days). In addition, the product does not transform to the cubic β-phase. The β-phase can be prepared by heating $CuFeS_2$ in a stream of hydrogen at 450 °C, but the pure phase cannot be obtained by the direct combination of the elements. For compounds having the composition $CuFeS_{2-x}$, density measurements indicate the structure to be based on a close-packing of sulfur with extra cations occupying additional lattice sites. This was demonstrated for the composition $CuFeS_{1.8}$ by comparing its measured density (4.30 ± (1) g/cc) with the theoretical density for the close-packed case (4.32 ± (1) g/cc) and the value for the sulfur deficient model (3.89 ± (1) g/cc). Therefore, the formula for $CuFeS_{1.8}$ can be represented as $Cu_{1.1}Fe_{1.1}S_2$ indicating the existence of additional metal occupancy.

3.2. $Cu_{1-x}Fe_{1+x}S_{2-y}$

Attempts to produce polycrystalline samples of $Cu_{1-x}Fe_{1+x}S_2$ and $Cu_{1+x}Fe_{1-x}S_2$ were unsuccessful. In each case, α -$CuFeS_2$ and other unidentified phases appeared in the diffraction pattern. However, a single phase could be obtained for compounds having the general formula $Cu_{1-x}Fe_{1+x}S_{2-y}$ (for $0.25 > x > 0.08$ and y chosen as 0.2). The stability range of this phase with respect to sulfur content is still to be determined. The compounds in the above compositional range have a cubic structure with a_o varying from 5.31 Å to 5.33 Å. This phase contains no superlattice lines requiring a doubling of the cell edge as is observed in the cubic β case. The change in structure as the copper to iron ratio is varied from x = 0 to x = 0.25 is shown in table 2. The tetragonal γ - phase exists only when the value of the copper to iron ratio approaches unity. Efforts to prepare $Cu_{1+x}Fe_{1-x}S_{1.8}$ were unsuccessful, and the phases identified by x-ray diffractions were: $CuFeS_2$ or $CuFeS_{2-x}$ in addition to a bornite solid solution (Cu_5FeS_4).

3.3. $CuFeS_2$ SINGLE CRYSTALS

The growth of well characterized single crystals of $CuFeS_2$ and associated phases is desirable for the elucidation of both the structural and magnetic properties of the materials. Earlier work has shown this to be a formidable problem [7]. Crystals grown from the melt, as discussed earlier, weighed as much as 500 mg. and were 1 cm. in diameter and approximately 1 cm. in length. Density measurements were used to ascertain deviations from stoichiometry. The crystals were reannealed with sufficient sulfur to produce the desired stoichiometry. In all cases, Laue patterns were taken, and the growth of single crystals was verified. However, the Laue diffraction spots were always diffuse indicating either strain or microtwinning. This has also been observed for many natural chalcopyrite crystals.

Table 2

$Cu_{1-x}Fe_{1+x}S_{1.8}$

Value of x	a_o (Å)	c_o (Å)	Theoretical++ Density (g/cc)	Experimental Density (g/cc)	Structure	c/a
x = o to x = .01	10.598±(5)	5.380±(5)	4.32±(1) 8.($Cu_{1.11}Fe_{1.11}S_{2.00}$)	4.30±(1)	γ- tetragonal	0.51
x = .02 to x = .07	MIXED PHASE				γ- tetragonal cubic	
x = .08 to x = .25	5.328±(5)		4.28±(1)* 2($Cu_{.89}Fe_{1.33}S_{2.00}$)	4.28±(1)*	cubic	1.00

* Values given represent composition for x = 0.2.

++ All theoretical densities based on a close-packing of sulfur with excess metal ions occupying additional lattice sites.

4. ACKNOWLEDGMENT

This work has been supported by the Kennecott Copper Corporation and by the United States Army Research Office, Durham, North Carolina.

The technical support of the Marc Vassiliadis and Roland Beaulieu, in the growth of chalcopyrite single crystals, is greatly appreciated.

5. REFERENCES

[1] Burdick, C. L. and Ellis, J. H., Proc. Natl. Acad. Sci. U. S. 3, 644 (1917), J. Am. Chem. Soc. 39, 2518 (1917).
[2] Pauling, L. and Brockway, L. O., Z. Krist. 82, 188 (1932).
[3] Donney, G., Corliss, L. M., Donnay, J. D. H., Elliot, N., and Hastings, J. M., Phys. Rev. 112, 1917 (1958).
[4] Buerger, N. W. and Buerger, M. J., Amer. Min. 19, 289 (1934).
[5] Hiller, J. E. and Probsthain, K., Z. Krist. 108, 108 (1956).
[6] Nambu, M. and Kano, S., Ganeski Kobutsu Kosho Gakkaishi, 60 (5), 127-145 (1968).
[7] Teranishi, T., J. Phys. Soc. Jap. 16, (10) 1881 (1961).
[8] Raj, D. and Puri, S. P., Il. Nuovo Cimento LXB (2), (1969).
[9] Aramu, F. and Bressani, T., Il. Nuovo Cimento LIB (2), (1967).
[10] Frank, E., Il. Nuovo Cimento 58B (2), 407 (1968).
[11] Chen, J., personal communication.
[12] Bates, L. F., Modern Magnetism (Cambridge University Press, New York, 1961).

DISCUSSION

L. J. Cabri: I found this paper most interesting since we have been studying these phases, both as minerals and as synthetic compounds for the past five years and have recently submitted new mineralogical, Mössbauer, magnetic, and crystallographic data on talnakhite (β-phase), chalcopyrite and mooihoekite (γ-phase) for publication and are presenting some of this work at the 17th Annual Conference on Magnetism and Magnetic Materials in November. As a consequence, I have a few comments and questions I would like to put to the authors.

Firstly, we have prepared homogeneous γ-phase and found it to be stable at room temperature for a period of over 3 years. But we have observed that it transforms to two high-temperature *non-quenchable* phases at 165° and 236 °C. This has been confirmed by high-temperature x-ray powder diffraction. These results appear to disagree with the authors' statement that γ-phase is stable from room temperature to 800 °C. Can the authors comment on this?

R. L. Adams: I did not mean to imply that there were no other phases when the γ-phase is heated to 800 °C. What was meant was that on quenching from any temperature from room temperature to 800 °C, only lines of the γ-phase appeared on the powder diffraction patterns. Also, the study presented here did not employ high temperature x-ray equipment.

L. J. Cabri: Secondly, in a recent paper (Cabri and Harris, 1971, New Compositional Data for Talnakhite, $Cu_{18}(Fe,Ni)_{16}S_{32}$. Econ. Geol. 66, p. 673) it was shown that the β-phase can be synthesized from the elements provided that a specific proportion of Cu:Fe is employed. Have the authors determined the composition of the phase they formed by heating $CuFeS_2$ in hydrogen?

R. L. Adams: No. The composition has not been determined because this phase was not prepared as a pure single phase material. The preparation was made to obtain some idea as to the diffraction pattern found for this phase. More important, however, was that the phase was not studied because the area of interest in this work is only with pure single phase materials and not mixed phases.

L. J. Cabri: And lastly, we also synthesized a phase which can be indexed on a primitive cubic cell a≃5.32 Å for the composition $Cu_{0.98}Fe_{1.27}S_{2.00}$. However this phase transforms on heating between room temperature and ~200 °C to give a powder pattern which is similar to that of f.c.c. high-temperature chalcopyrite. This phase is *non-quenchable* and can only be observed with a high-temperature x-ray camera.

R. L. Adams: Again, high temperature x-rays were not used in the study. Therefore, the phases observed at these elevated temperatures were not observed and not studied. The emphasis in this work deals with materials that are stable at room conditions only.

I believe these comments cover the areas discussed.

National Bureau of Standards Special Publication 364, Solid State Chemistry, Proceedings of 5th Materials Research Symposium, issued July 1972.

LASER RAMAN SPECTRA OF POLYCRYSTALLINE ZnS AND $Zn_xCd_{1-x}S$ SOLID SOLUTIONS†

Jacob Shamir and Simon Larach*

Department of Inorganic and Analytical Chemistry
Hebrew University
Jerusalem, Israel

Raman spectra of polycrystalline ZnS and of CdS have been recorded. The instrument consisted manily of a He-Ne laser, Spectra-Physics, model 125 and a 1400 Spex double monochromator [1]. The lines observed were in good agreement with those observed before in a single crystal [2]. Some of these lines are not as sharp and intense as in a single crystal; however the LO frequency of ZnS at 351 cm^{-1} is a very sharp and intense line.

In addition we studied the spectra of $Zn_xCd_{1-x}S$ solid solutions. These materials have been prepared by firing mixtures of pure ZnS and CdS, in the proper compositions, at 1100 °C, in an atmosphere of purified Argon. It has been observed that the LO frequency of CdS at 306 cm^{-1} shifts toward higher frequencies as the concentration of zinc increases. This behavior indicates a type I change as discussed by Pershan and Lacina [3], namely a linear shift of the frequency as the concentration varies from zero to one in the $Zn_xCd_{1-x}S$. These results resemble the ones obtained in a Vegard plot of lattice constants as determined by x-rays.

Key words: Laser Raman spectra; polycrystalline; ZnS; $Zn_xCd_{1-x}S$.

REFERENCES

[1] Claassen, H.H., Selig, H. and Shamir, J., Appl. Spectr. 23, 8 (1969).
[2] Nilsen, W.G. in *Light Scattering Spectra of Solids*, G. B. Wright (editor), Springer-Verlag 1969, p. 129.
[3] Pershan, P.S. and Lacina, W.B., Appl. Spectr. 23, 439 (1969); Phys. Rev. B1, 1765 (1970).

†As this is a post-deadline paper only a brief abstract is presented here.

*Permanent address: RCA Laboratories, Princeton, New Jersey.

465-504 O - 72 - 47

National Bureau of Standards Special Publication 364, Solid State Chemistry, Proceedings of 5th Materials Research Symposium, issued July 1972.

NOVEL METHOD FOR THE SYNTHESIS OF RARE EARTH CHALCOGENIDES†

C. Paparoditis and R. Suryanarayanan

Centre National de la Recherche Scientifique
Laboratoire de Physique des Solides
Bellevue, France

A description is given of an all-metal vacuum system for the synthesis of rare earth tellurides and selenides by the coevaporation of the elements. The evaporation chamber is provided with three crucibles so that ternary compounds can also be prepared. Forty or more deposits can be obtained in a single operation. A wide range of compositions can thus be obtained if desired. The substrates, amorphous or crystalline, can be heated up to 600 °C. The following compounds have been obtained as polycrystalline, highly textured or single crystal films: EuTe, EuSe, YbTe, YbSe, $YbSe_{1+\delta}$, SmTe, SmSe, $SmSe_{1+\delta}$ (Th_3P_4 structure), $Eu_{1-x}Pb_xTe$, $Eu_{1-x}Gd_xSe$, $Eu_{1-x}Yb_xTe$ [1]. Evidence of high quality is given by x-ray, electron microscopy, electron diffraction and electron microprobe analysis. Optical absorption spectra up to 6 eV, reflection spectra up to 10 eV, magnetic circular dichroism spectra in the visible have been obtained. Transition assignments have been proposed for the first time in the case of Yb and Sm monochalcogenides [1,2].

Results of optical and magneto optical investigations have been presented for the ferromagnetic EuS obtained by coevaporation and for EuO obtained by reactive evaporation. Finally, electrical and other transport properties of stoichiometric EuO have also been presented [3].

Key words: Coevaporation of elements; rare earth chalcogenides; synthesis.

REFERENCES

[1] Paparoditis, C., et al., ICCG-3, Marseille, July 1971, to be published in J. Crystal Growth 1972.
[2] Suryanarayanan, R., et al., Conference on Rare Earths and Actinides, Durham, July 1971.
[3] Paparoditis, C., et al., Sol. State Comm. 9, 1871 (1971).

† As this is a post-deadline paper only a brief abstract is presented here.

IV. OPEN DISCUSSION

SUBJECT: NONSTOICHIOMETRY

ORDERING AND CLUSTERING OF DEFECTS
EQUILIBRIUM vs NON-EQUILIBRIUM

National Bureau of Standards Special Publication 364, Solid State Chemistry, Proceedings of 5th Materials Research Symposium, issued July 1972.

THE TITANIUM AND TITANIUM-CHROMIUM OXIDE SYSTEMS AND SWINGING SHEAR PLANES

L. A. Bursill
School of Chemistry
University of Western Australia
Nedlands, Australia 6009

L. Bursill: Earlier this week Mike O'Keeffe and also Professor Anderson talked about some of our interpretations of electron microscopy and diffraction results on the titanium and titanium-chromium oxygen systems. I would like to show and discuss our evidence for what we call *swinging shear planes*. The first slide (fig. 1) shows a single (100) layer of reduced rutile idealized so that the anions (white balls) are close-packed. The pattern of filled octahedral cation sites (black balls) is identical for each layer and these are stacked to give an approximately hexagonal close-packed anion lattice. You will see what appear to be *out-of-phase* boundaries running from top to bottom (X-X). At the top is n = 8 of M_nO_{2n-1} with (121) *CS* planes[1]. The (121) structures n = 4-9 occupy the composition range $1.75 \leqslant x \leqslant 1.89$. At the bottom of figure 1 is n = 13 of M_nO_{2n-1} with (132) *CS* planes. These occupy the composition range $1.93 \leqslant x \leqslant 1.98$. The difference between (121) and(132) will be seen by looking at the sequence of steps along the trace of the *CS* planes. Two types of step occur in the (132) structures, labelled *C* and *A* at the right of figure 1. *C* is a *CS* step and it consists of an anti-phase boundary (*APB*) step *A* plus an *extra* metal (which of the cations 1 or 2 is interstitial?). *C* and *A* alternate along the *CS* plane for (132) but for (121) all the steps are *C*-type (top of fig. 1). On stacking the layers in three-dimensions *C* and *A* steps become strings of corundum (*e.g.*, Cr_2O_3) and α-PbO_2 type structure respectively. These strings are parallel to $[1\bar{1}1]$ rutile.

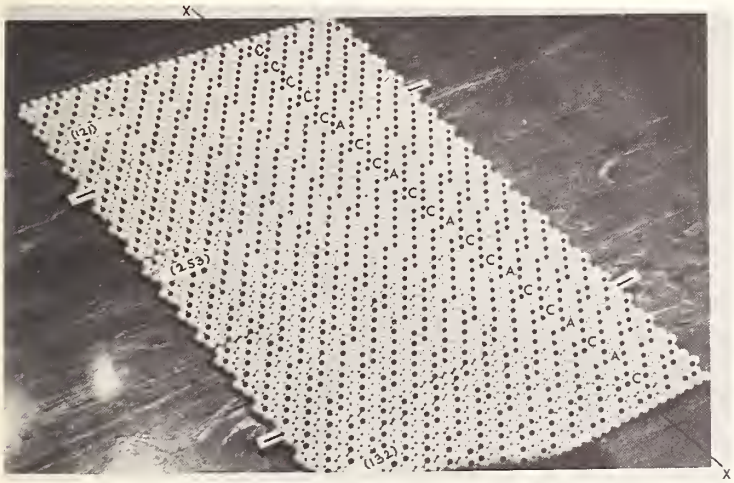

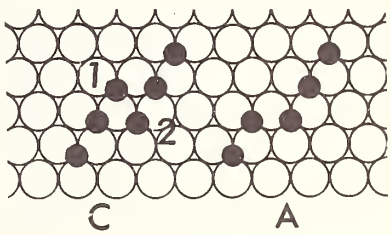

Fig. 1.

[1] The crystallographic shear (*CS*) plane indices (hkℓ) define the plane of infinite extent of basic structure while the shear vector [uvw] is the ideal displacement of the basic structure across this plane.

Our problem was to decide which structures occurred in the intermediate composition range $1.89 \leqslant x \leqslant 1.93$ and we built models like this. We also had some diffraction patterns which showed rows of spots along (253) suggesting ordered intermediate *CS* structures. A n=21 (253) structure is shown in the center of figure 1. The sequence along the *CS* plane is ...*C C A C C A*... and we note that (253) = (121) + (132).

R. S. Roth: I would like to give people a chance to interrupt if they want to, so I am going to have these microphones on and if anyone wants to ask you a question, they can.

L. Bursill: Okay. Well I'll go on. The next slide (fig. 2) shows an electron diffraction pattern which is evidence for (253) *CS* planes. It is a carefully oriented $[1\bar{1}1]_{rutile}$ zone. Look at the origin O. There is a row of superlattice spots running out to (253). The angle between (132) and(121) is 11.5 degrees and the superlattice rows clearly do not go to either of these. Three members of this family with n=23, 24 and 25 were found.

In a parallel study of the Ti-Cr-O system Don Philp in our laboratory found 12 members of this family with n=28 to about 40 ($1.93 \leqslant x \leqslant 1.95$). No (132) structures occurred. At about x=1.93 the *CS* plane began to swing. The next slide (fig. 3) shows a very sharp diffraction pattern, but the superlattice rows run from the origin- we shifted the origin here- to (374). Figure 4a and b shows rows which, as accurately as can be measured, are along (495) and (5, 11,6). Now you see what is happening. The superlattice pattern rotates from (132) for TiO_x, or (253) for $(Ti,Cr)O_x$, around towards (121). Figure 5 shows (7,15,8). A striking feature of the patterns is the sharpness of the spots and this suggests that even the very high index *CS* planes are very well ordered. Instead of a disordered mixture of (121) and(132) structures or large grains of *e.g.*, n=9 (121) and n=16 (132) we have many intermediate *CS* structures. Figure 6a shows a very high index *CS* plane, very close to (121), giving rise to what has been called spacing and orientation *anomalies*. Finally, (fig. 6b) we find the *CS* plane has, we think!, swung to (121). This occurs for n=9 for TiO_x but for n=8 for $(Ti,Cr)O_x$.

An important question is "just how well ordered are these structures? Is it an artifact we see in the diffraction patterns, and as we see no two-phase mixtures on the patterns, are we really seeing a continuous series of ordered structures with no two-phase regions in between?" Yes?

F. Carter: How many unit cells does it take to show up good sharp spots like this in electron diffraction?

L. Bursill: Well, we have very large areas, half to one micron, so we are not worried.

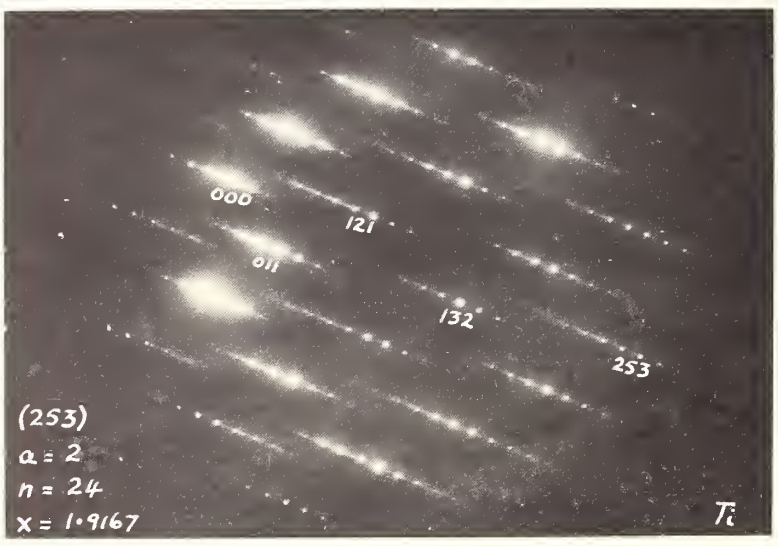

Fig. 2.

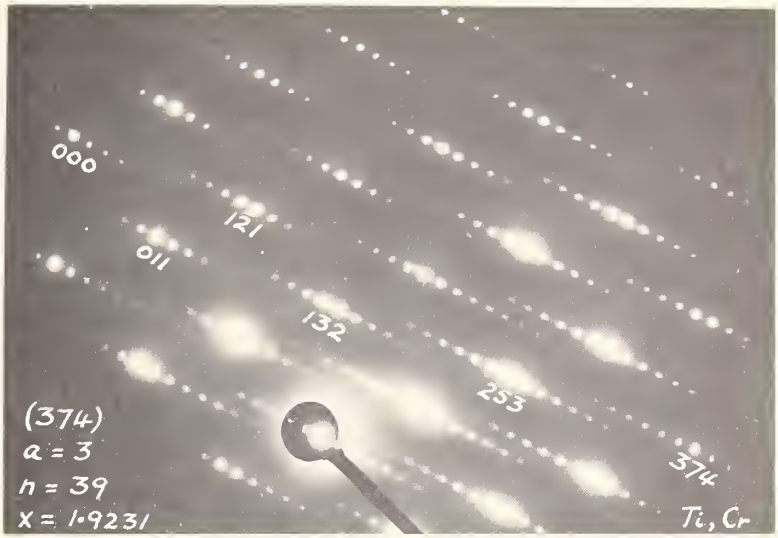

Fig. 3.

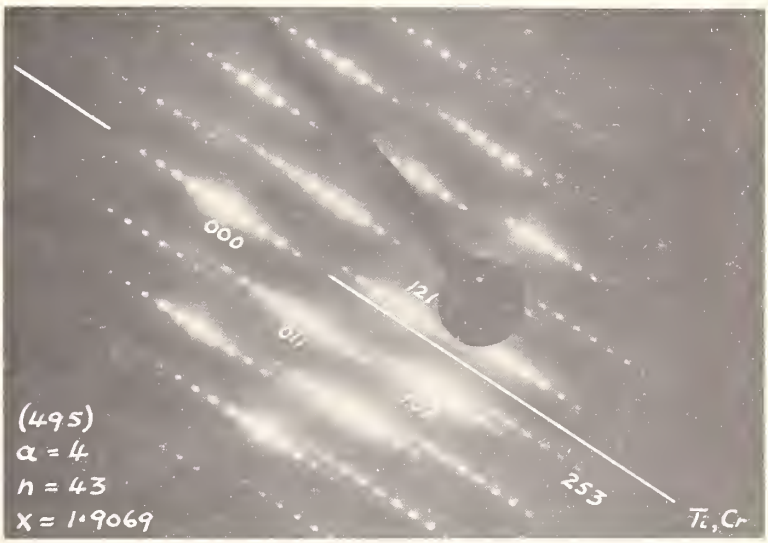

Fig. 4a.

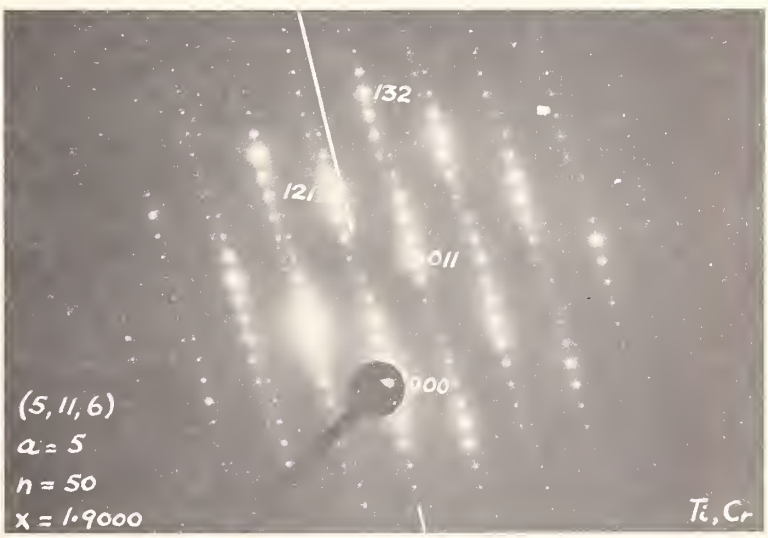

Fig. 4b.

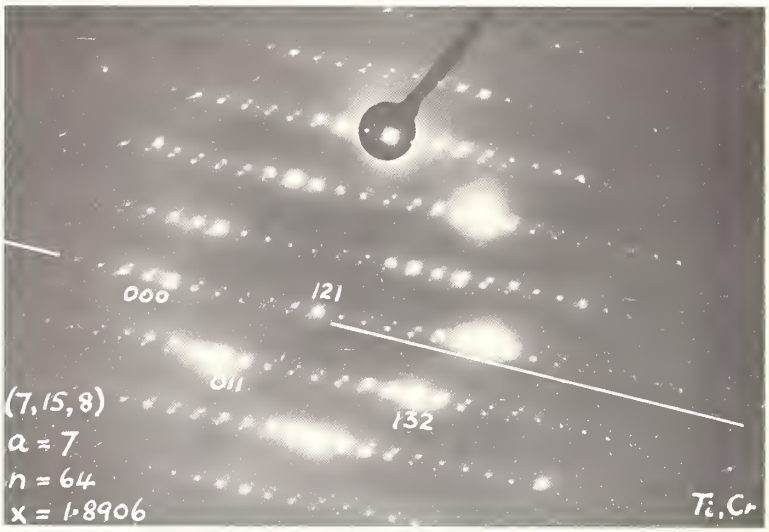

Fig. 5.

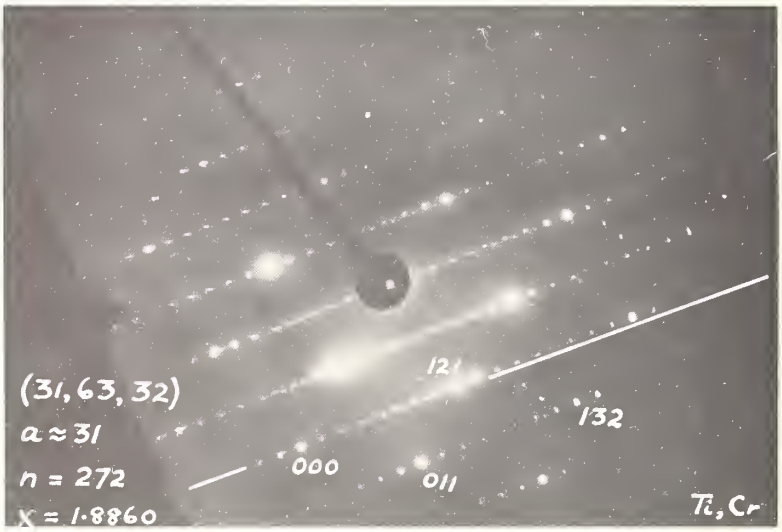

Fig. 6a.

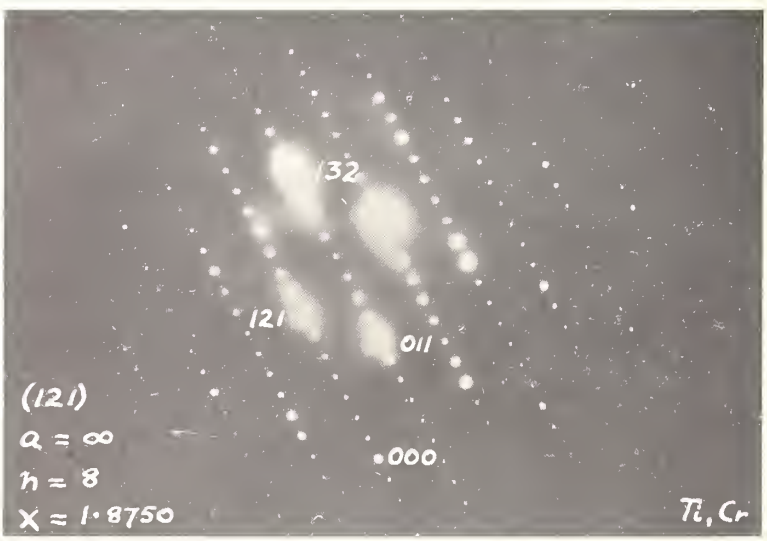

Fig. 6b.

F. Carter: What is the minimum number?

L. Bursill: I don't know, how sharp do you want the spots? Ten to 100 would give sharp spots, we have many more than this.

I have now examined a number of compositions in both systems by lattice imaging in the hope of clarifying the extent of order. Figure 7a shows a lattice image of a crystal indicating (5,11,6) *CS* on the diffraction pattern (fig. 7b). As you see both the spacing and orientation of the fringes are constant and across what appears to be a twin boundary *T* we find the *equivalent CS* plane (11,5,$\bar{6}$). So this crystal of (Ti,Cr)O_x appears to be a very well ordered stable phase. Even more interesting than this is that Don Philp has now oriented at least 77 flakes into the [$1\bar{1}1$] zone, which is the one you must obtain, and at least 50 of these are different, measurably different.

R. S. Roth: What was the method of preparation of these specimens that can produce such a well ordered phase? At what temperature were they heated?

L. Bursill: Pellets were melted in an argon arc, sealed in air in platinum tubes and annealed at 1300° C for three days. (The powdered pellets were black (reduced) after melting but brown (oxidized) on annealing.) No great attempt was made to reach equilibrium.

As I said, of 77 patterns 50 were measurably different. As well as different *CS* plane indices a number of different *n* values occur for each family, although not in the same flake. All the intermediate *CS* planes may be written (hkℓ)=*p*.(121)+*q*.(132) and are therefore ordered intergrowths in this sense (see fig. 14).

The next slide (fig. 8) shows an image of a crystal which, on the diffraction pattern, seemed to have *CS* plane intermediate between (495) and (5,11,6). We wondered whether these would order also. It seems from this that you get wobbly fringes, and it is tempting to

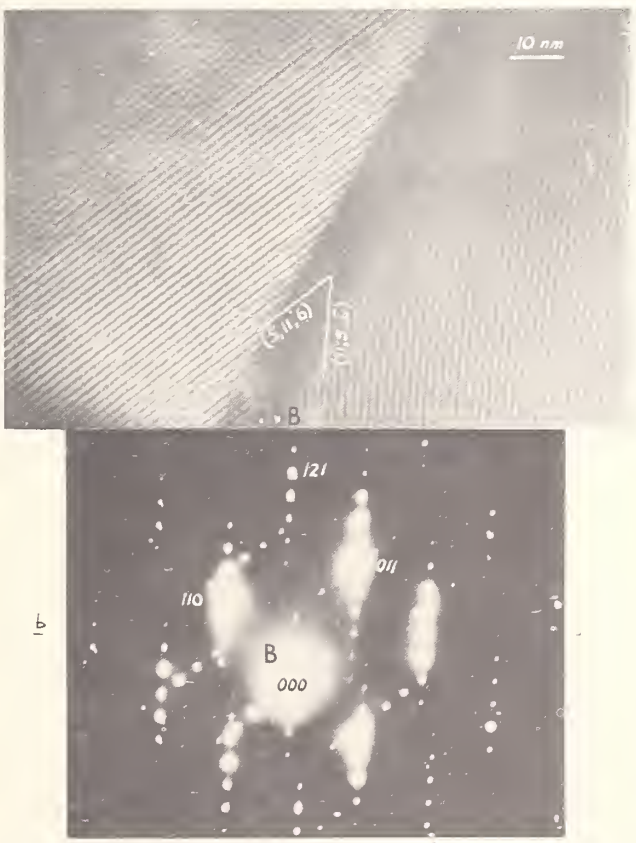

Fig. 7.

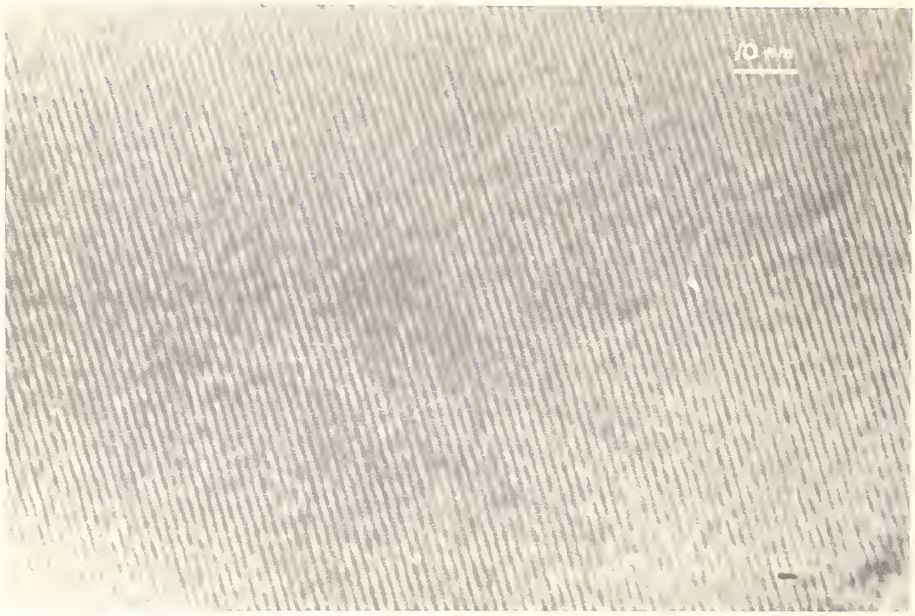

Fig. 8a.

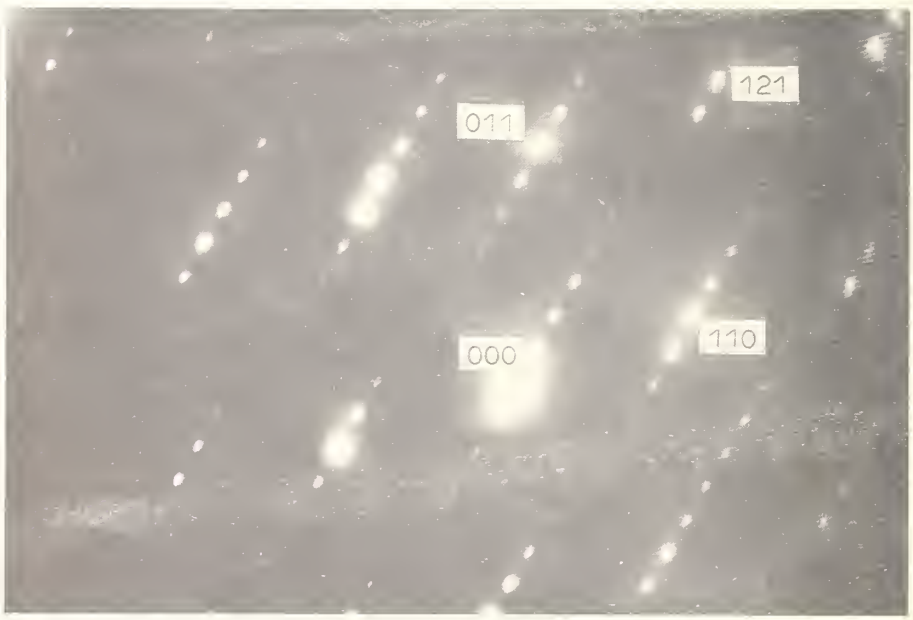

Fig. 8b.

think that we have partly resolved the *A* steps and that the sequence ...*C C C C A C C C C C A*... is not perfectly ordered. It is very difficult to interpret. The fringe spacing is 15 Angstrom. We need to obtain cross grating images to check this. In the region around the origin of the diffraction pattern (fig. 8b) the row of reflections B-B is very weak. To resolve the *APB* or *CS* steps we need to use the strong rutile reflections. This means resolution better than about 3 Angstrom. We are attempting this.

In the next slide we return to the binary system TiO_x and these patterns (fig. 9) are from a specimen quenched from 1450 C. You see that we have a whole range of streaks, spots and arcing of spots. We still have the same basic effect but with a whole range of intermediate *CS* planes in the same small area. On annealing in vacuum at 1000 C TiO_x specimens can be made which have quite sharp diffraction spots, but not as sharp as for chromia doped

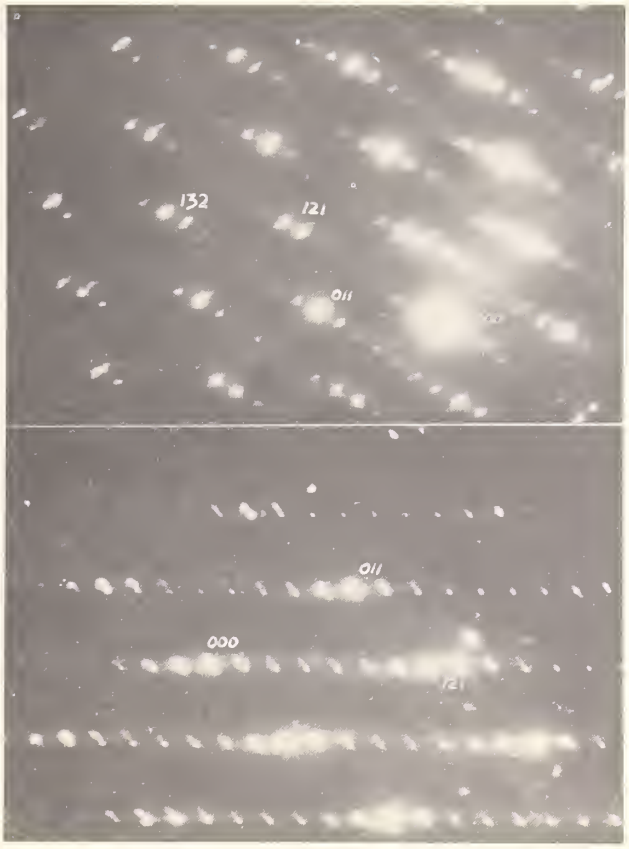

Fig. 9.

rutile. Figure 10a is a lattice image of reduced rutile where the *CS* plane lies between (132) and (253), *i.e.*, approximately (385) (see fig. 10b). If you sight along the fringes you can resolve them into, to a first approximation, units parallel to (132) and (253), which differ by 4°. The diffraction pattern (fig. 10b) is much better than figure 9 but not as sharp as the Ti-Cr-O ones. The *CS* and *APB* steps are not ordered as well. Figure 11 shows very wobbly fringes in TiO_x. We cannot interpret this in detail at this stage, but this to me gives an impression of what a nonstoichiometric phase in the strict sense would look like. You have a variable *CS* plane. The steps are not ordered and if[2] this is the high temperature situation you can imagine a dynamical situation with steps moving to and fro. An oversimplified conclusion is that the results on TiO_x provide a nice model for true non-stoichiometry while those on $(Ti,Cr)O_x$ provide a model system for a continuous series of ordered phases.

The next slide shows a model where by a series of ...

L. Eyring: Before you get too far from those wavy fringes have you taken diffraction patterns on those particular areas?

L. Bursill: Yes.

L. Eyring: What are they? Are they the ones that we saw just before?

L. Bursill: No, not as bad as figure 9 and sharper than figure 10b. They look sharp until you compare them with the chromia ones. This is a big problem, even if the *CS* planes are wobbly you may still get a *sharp* diffraction pattern. It just depends how wobbly they are.

[2] Reduced rutile will oxidize on cooling if any oxygen is present thereby introducing disorder and there is also evidence that the *CS* plane, at a given composition, swings towards (121) at higher temperatures.

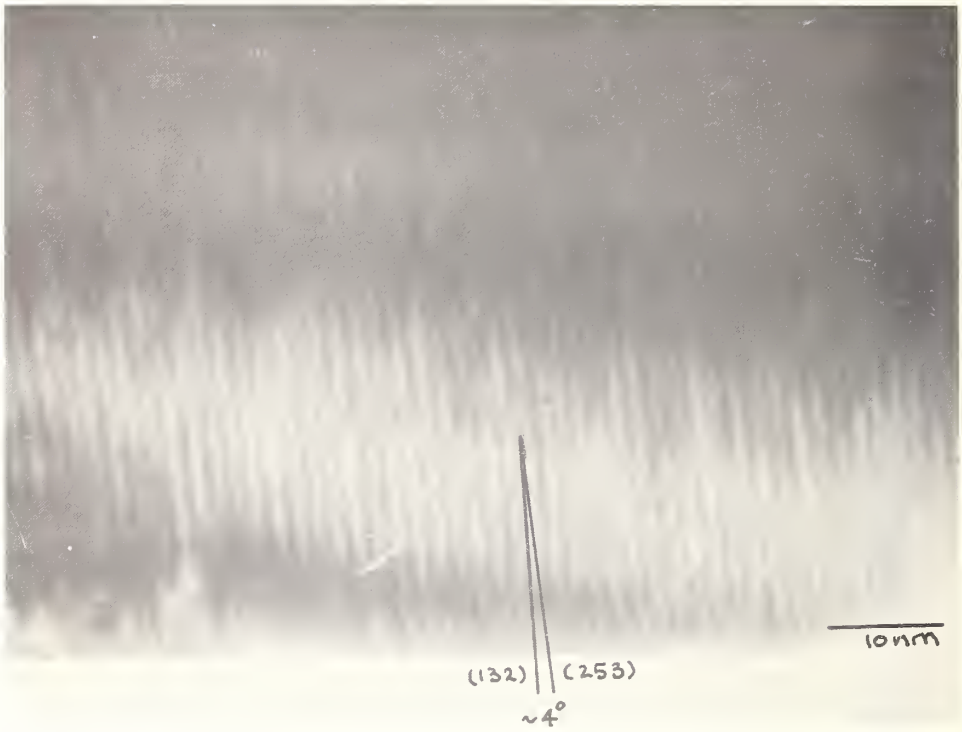

Fig. 10a.

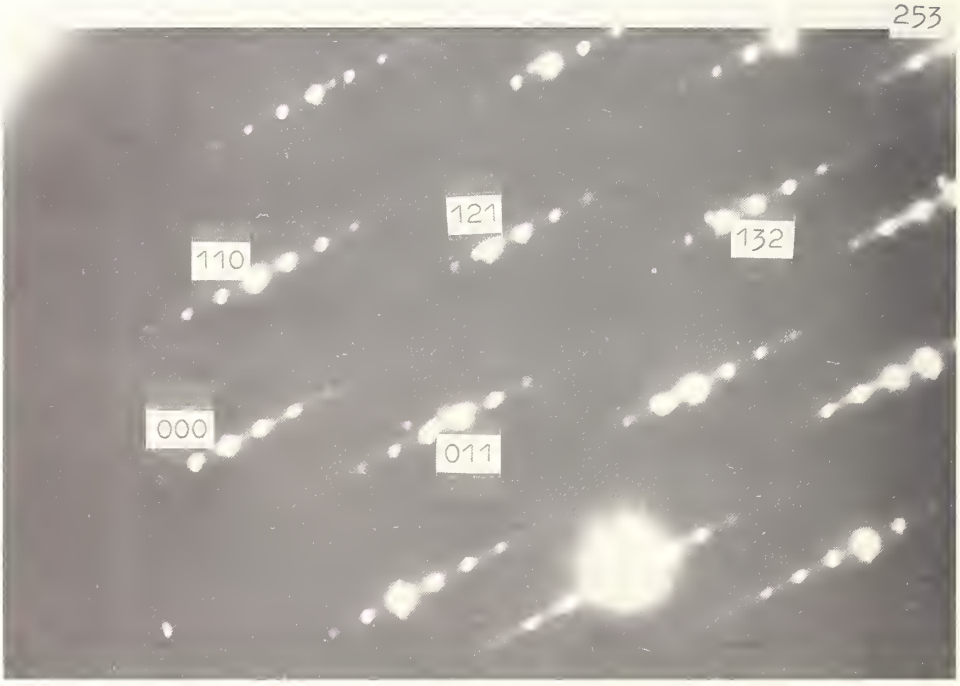

Fig. 10b.

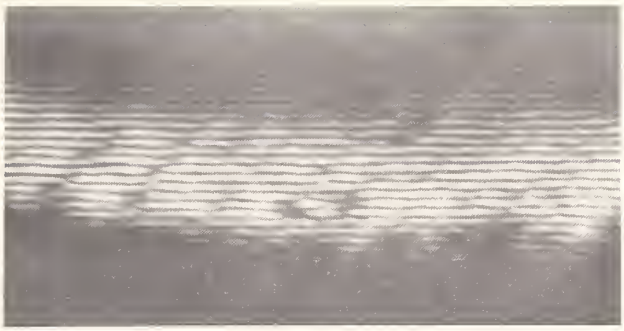

Fig. 11.

J. Allpress: Some of those wobbles may be due to dynamical effects, because I noticed some bend contours crossing.

L. Bursill: In figure 10a yes. I wouldn't interpret it. It is impressionistic. (Note added in proof: The bend contour runs parallel to the fringes and the crystal thickness varies slowly in this area so the diffraction conditions are constant along the fringes. The wobbles must be due to *CS* plane fluctuations but what the wobbles are in terms of structure must await higher resolution.)

Figure 12 shows a schematic model mechanism for swinging the *CS* planes from (132) towards (121). Cations (small balls) are added on the surface at *APB* steps (top left fig. 12) and these are fed along the *CS* plane by the hopping mechanism described by Mike O'Keeffe on Monday[3]. At each hop a cation jumps from a *CS* step onto an adjacent *APB* step. The latter becomes a *CS* step and the former an *APB* step closer to the surface. Thus the *CS* plane may swing continuously through all the intermediate high index planes by controlling the sequence of *C* and *A* type steps. Remarkably few hops are required for a perfectly ordered structure to occur at each stage. It appears that in reduced rutile the sequences disorder at high temperature but can be made to order at approximately 1000 C but for Ti-Cr-O the intermediate sequences are very well ordered at 1300 C. The process is continued in figure 13; after about (5,11,6) it is difficult to see the complete repeating sequence. We need a bigger model. The number of steps becomes smaller and it is easier to make a continuous series of ordered structures.

The next slide (fig. 14) shows how a n=25 (253) structure may be resolved, at right, into a unit cell of n=9 (121) plus a unit cell of n=16 (132); or alternatively, at left, into two unit cells of n=9 (121) plus a unit cell of *APB* structure n=7 (011). Many other possibilities exist for coherent intergrowth of different *CS* planes and n values. Not only do the *CS* plane indices follow as sums but the structures may also be regarded as ordered intergrowths. We may extend this a little further and note that the corundum-like strips along $[1\bar{1}1]$ at the *CS* steps contain the correct number of sites to accomodate all the Cr in the *CS* structures which therefore may also be regarded as ordered intergrowths of Cr_2O_3 plus TiO_2.

The next slide (fig. 15) shows a more general situation, *i.e.*, two reciprocal lattice nets, the finer derived from a super-cell corresponding to the coarser net. The dots indicate reflections you might see using x-ray diffraction, *i.e.*, doublets or triplets about strong sub-cell positions. Now I ask you the question *what happens to your powder pattern as the fine net is rotated relative to the sub-cell?* If a reflection is exactly on a sub-cell position the line will not shift but reflections on either side will, and with increasing distance from the sub-cell position. This is just the kind of diffraction pattern which is taken to represent a solid solution! No two phase regions will be seen even though we have a different perfectly ordered crystal at each stage. We believe that this sort of swinging or this sort of behavior in the reciprocal lattice will be a quite general crystallographic phenomenon; it could occur for ordered intergrowth of any two unit cells which have a common face. It will be found in many cases. So we look for similar effects in other systems.

[3] See: L. Bursill, B. Hyde and M. O'Keeffe this volume.


(132)
1
6
(253)
2
7
3
8
4
9
(374)
5
10

Fig. 12.


11
16
(495)
12
17
(5,11,6)
13
18
14
19
(6,13,7)
(121)
15
20

Fig. 13.

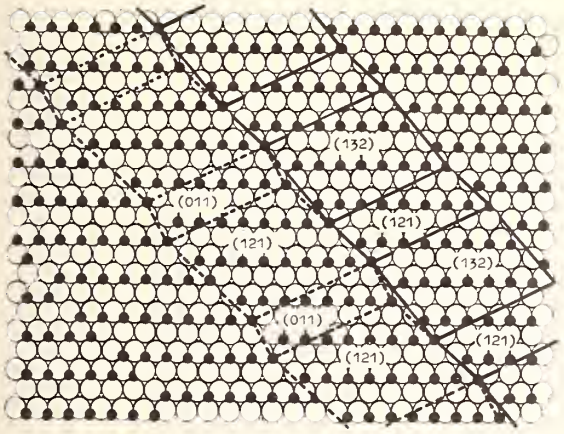

Fig. 14.

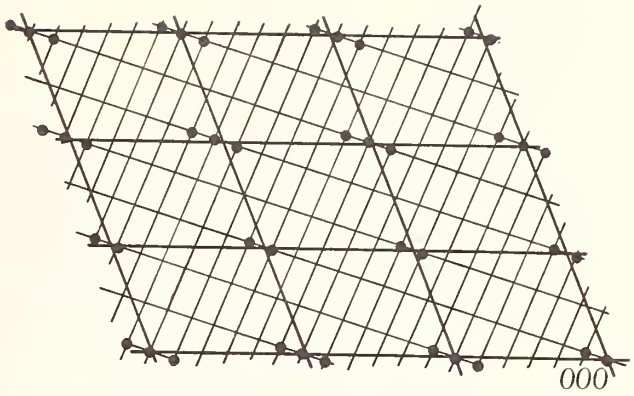

Fig. 15.

The next slide (fig. 16) shows a *CS* plane in the ReO_3-type structure. It changes from (120) at the top through (130), (140), (150) to (010) at the bottom. Only (120) and (130) *CS* structures were known. So we searched to find high index *CS* planes *i.e., swinging shear-planes* in R_eO_3-type systems.(unaware of John Allpress' work- this conference)[4]. Figure 17 shows some diffraction patterns we obtained from niobia doped WO_3. On the top (fig. 17a), we have the (140) structure with n about 60 in M_nO_{3n-3}, *i.e.*, $MO_{2.95}$.

R. S. Roth: Can you give me a one or two sentence definition of *swinging shear planes?*

L. Bursill: A composition change occurs by a cooperative change in *CS* plane orientation, at close to constant shear plane spacing.

On the bottom, figure 17b, we have a mixture of highly ordered (140) and (150) structures.

B. Cox: Do these shear planes only rotate in one plane or are they moving in three dimensions. In other words, do they all remain parallel to one direction?

L. Bursill: All the *ordered* structures we observe are parallel to $[1\bar{1}1]_{rutile}$ or $[001]_{ReO_3}$.

B. Cox: Then can you be sure that you don't get steps in the other direction?

L. Bursill: Yes. We are very careful in orienting these patterns. (Note added in proof: we refer only to ordered structures, there may be a low density of faults.)

Figure 18 shows a lattice image of a crystal of $(Nb,W)O_{2.93}$ (c.f. fig. 10 in John Allpress' paper). The *CS* plane spacing is very regular but they change orientation, in this system (c.f. chromia doped rutile), over a very small volume - in a few 1000 Angstrom. Note the stepped fringes at *X*, a long row of steps aligned along *Y-Y*, cooperative inflections in the *CS* planes at *P*, and a (140) *CS* plane ending at *Q*. In the large area of well ordered *CS* planes from the center to the right of this picture their orientation changes from (140) to (150) and back again, a range of 2.7 degrees. To the left the *CS* plane is (010) which is the one you have in *e.g.*, V_2O_5. Here all the *A* type steps have been eliminated. In the region *Y-Y* steps are regularly organized over quite large distances. These are very high index *CS* planes or, if you prefer, regularly stepped (010) *CS* planes.

Recently Grey and Reid[5] reported some shear structure compounds $(Cr,Fe)_2Ti_{n-2}O_{2n-1}$ derived from the α-PbO_2 type structure. The next slide (fig. 19) shows a model of α-PbO_2 structure. If the rows of balls A and B are moved to the left and right as indicated, and a zig-

[4] See J. Allpress, this volume.

[5] I. E. Grey and A. F. Reid (1971) J. Solid State Chem. (to be published).

465-504 O - 72 - 48

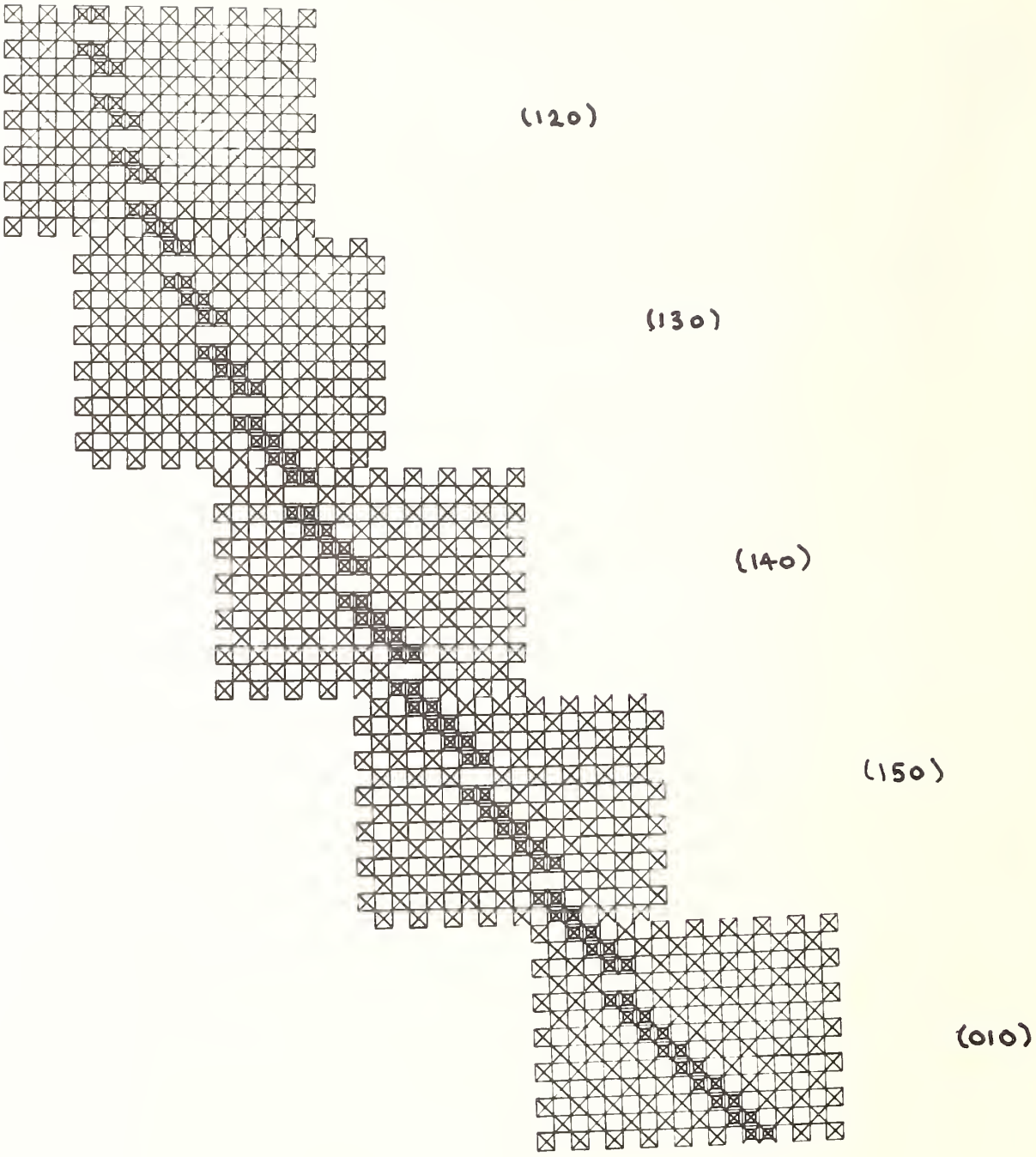

Fig. 16.

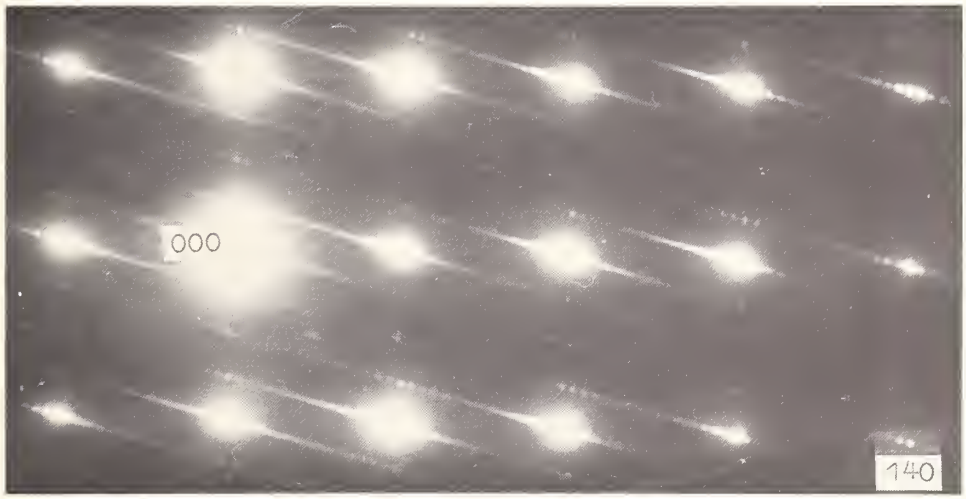

Fig. 17a.

Fig. 17b.

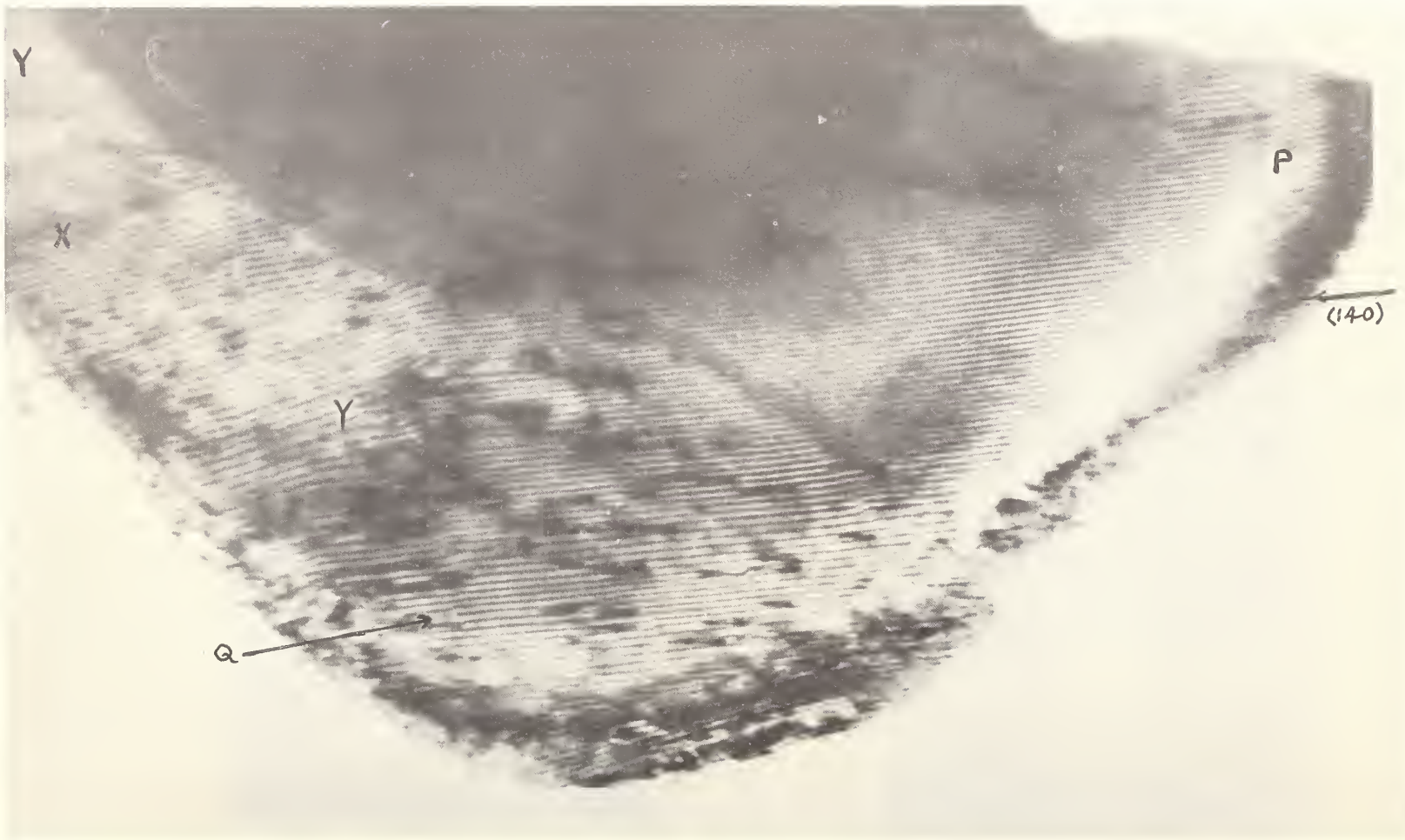

Fig. 18.

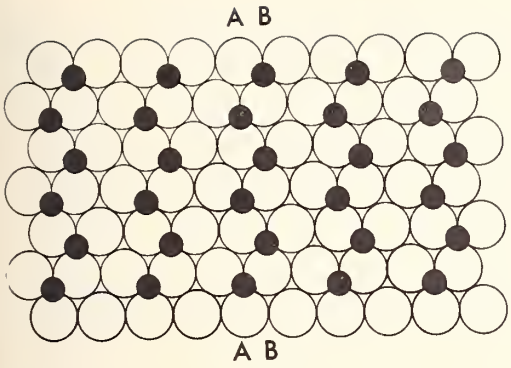

Fig. 19a.

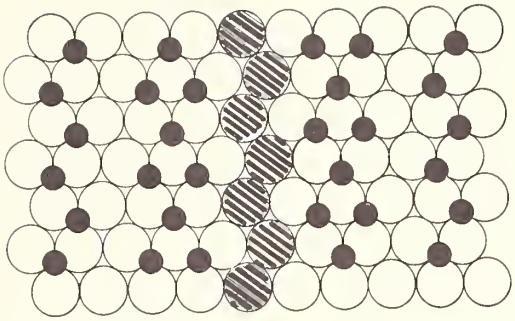

Fig. 19b.

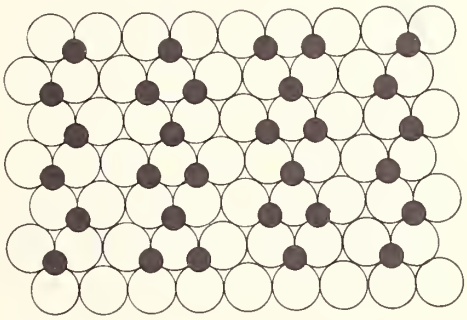

Fig. 19c.

zag plane of oxygens is removed and the gap closed we obtain a double strip of V_3O_5. This is a *CS* plane in the α-PbO_2 structure. In figure 20 a slab of M_4O_7 (121) structure (the original Sten Andersson structure) is shown (top) joined coherently to a slab of M_4O_7 (derived from α-PbO_2) at the bottom. The *CS* plane is $(110)_{\alpha\text{-}PbO_2}$. We may take p unit cells of (121) rutile and q unit cells of $(110)_{\alpha\text{-}PbO_2}$ and add these together to give intermediate *CS* structures. As q increases the basic structure changes from rutile to α-PbO_2. This type of intermediate *CS* structure may possibly explain some of the misorientation anomalies observed by John Allpress in $(Cr,Fe)Ti_{n-2}O_{2n-1}$ for compositions around n=4.

Just before I finish I would like to stress that we predict this special type of reciprocal lattice behavior will be very common in other systems, particularly the so-called isomorphous replacement series in mineralogy.

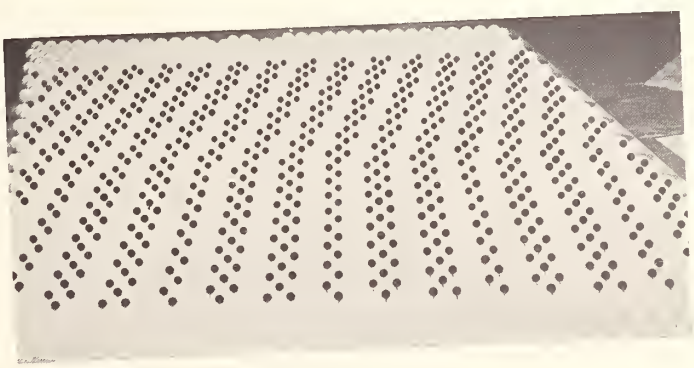

Fig. 20.

R. S. Roth: One other thing. I assume with all these beautiful pictures and diagrams that they have been or will be published in the very near future. Can you give us a reference of some sort on what you are going to do with them?

L. Bursill: The diffraction patterns for Ti-O and Ti-Cr-O were published a few months ago in Philosophical Magazine[6]. More of these and the lattice images are being written up. Some of these and a discussion of structural principles and reaction mechanisms will appear in Progress in Solid State Chemistry Vol. 7. A paper on reduced WO_3 and related psuedo-binaries is to be published in J. of Solid State Chemistry.

R. S. Roth: Is there anybody in the audience that would like to explain the effects that we have seen in these slides today on the basis of solid solution? No? I didn't think there would be.

J. Allpress: I am not going to do that, but we did find Bob, that if you doped WO_3 with niobium, you can put a couple of mol.% in before you start seeing shear planes[7], and I think that the same is true for chromium in rutile. Is that so Les?

L. Bursill: We have observed that also with chromia doped rutile samples.

J. Allpress: I'd like to know what the reason for that is.

R. S. Roth: I think that what you have to say is that there is some other type of defect which occurs at very, very low concentrations and I think that many people have believed for a long time that there *are* other ways to make a solid solution. Maybe one of these might actually exist, who knows?

L. Bursill: What? A point defect? A cluster?

R. S. Roth: One question I would like to ask is what do the x-ray diffraction powder patterns of a series of compositions across one of these swinging shear plane areas look like? Do they look anything like the powder patterns that I showed on that niobium-zirconia phase; that is, substructure not moving much and superstructure moving continuously?

L. Bursill: Well, this is exactly how.....Sten Andersson has published these for Ti-Cr-O and reduced rutile.

R. S. Roth: But you can't see that two-phase region.

L. Bursill: No, above $TiO_{1.90}$ you cannot see two-phase regions.

S. Andersson: If we take the $Ti_2Cr_2O_7$ compound, as an example, the low angle superstructure lines move more than the parent lines, but we never saw any sort of two phase region.

L. Bursill: I could add that Don Philp has taken Guinier diffraction patterns and has computed the unit cells for a list of intermediate structures and calculated line positions. These come out as groups of very closely spaced lines which show up on the diffraction patterns as a slightly unsharp line.

S. Andersson: Of course, we do agree that if you had a tremendous resolution we would see two phase regions wouldn't we?

L. Bursill: Well, not so, because the samples always show a range, you never get a sample with just two phases.

S. Andersson: No, but you would see doublets here and there wouldn't you?

L. Bursill: Yes, if you have the resolution.

---

[6] L. A. Bursill, B. G. Hyde and D. K. Philp, Phil. Mag. 23, 1501 (1971).

[7] R. S. Roth and J. L. Waring, J. Res. NBS 70A, 281 (1966).

[8] J. G. Allpress, J. Solid State Chem. 4 (1971).

R. S. Roth: If the specimen was completely equilibrated with a given composition and the true composition and the theoretical composition derived from the observed shear planes matched each other, which nobody has really proved, then you should *have* to see either one or two phases if you have the proper resolution. But that's practically theoretical.

S. Andersson: It depends on the degree of swinging, doesn't it?

L. Bursill: Yes. You would get a slightly unsharp line. I wouldn't say it was a broad line, at first glance it is sharp, but it is really the superposition of many.

R. S. Roth: Have you examined a specimen of a given composition with respect to how the shear planes changed with temperature and time of annealing? I would say they should change, until you reach some certain equilibrium condition, maybe.

L. Bursill: Well this is a big problem. What is the high temperature structure in the reduced rutile system? Is it wobbly or is it ordered?

R. S. Roth: I was referring particularly to the titanium-chromium oxide system.

L. Bursill: That *can* be done by annealing because it doesn't oxidize.

R. S. Roth: But at various temperatures will it change?

L. Bursill: We have worked mainly at one temperature so far. If you melt a pellet and then anneal at 1000°C for three days you do not anneal out the structure of the melt which is a reduced rutile. That's a mess (c.f. fig. 9). At 1000°C you do not seem to have the mobility to get an ordered structure and you have to go up in temperature. A further point here is that to change the *CS* plane in reduced rutile (fig. 12) no long range diffusion of cations is required (all the cations are the same colour, say red), Ti^{3+} and Ti^{4+} may interchange by electron switching. For Ti^{4+}-Cr^{3+} you require long-range diffusion of Cr^{3+} (blue balls must diffuse along the *CS* plane) and this requires a more complex series of jumps and presumably a higher activation energy.

R. S. Roth: What I am predicting is that for the temperature-time annealing sequence you quoted, you have, and you see with electron diffraction, two or three or four different orientiations of shear planes in the crystal because you have not yet approached equilibrium far enough. As you go to higher temperatures and longer periods of time you should gradually anneal everything out until any given specimen will show always one set of shear planes. This would be your equilibrium condition. Now, if you could demonstrate that after you have done that, if you come down to lower temperatures it changes again then I will take back everything I have said.

B. Hyde: That's a theological statement and not a scientific one.

R. S. Roth: Yes, but it can be checked.

L. Bursill: It should be checked.

R. S. Roth: All right. I think it's about time to give somebody else a chance up here.

National Bureau of Standards Special Publication 364, Solid State Chemistry, Proceedings of 5th Materials Research Symposium, issued July 1972.

A DEFECT CLUSTER IN MAGNESIUM FLUOROGERMANATE

E. Kostiner
Department of Chemistry
Cornell University
Ithaca, New York 14850

E. Kostiner: I would like to turn away from electron diffraction and describe a defect cluster which we investigated using single crystal x-ray diffraction. First, let me give proper credit; my co-workers are Bob Von Dreele (who is now at Arizona State University) and Paul Bless and Bob Hughes at Cornell.

The genesis of this problem was an investigation of phosphor host lattices, in particular, the fluorescence of Mn^{+4} in the so-called magnesium germanate and magnesium fluorogermanate structures. To completely determine the correct identity of these materials, it was necessary to grow crystals and do complete structural analyses. It turns out that the material that has been considered[1] to be magnesium germanate with a stoichiometry Mg_4GeO_6 is in reality $Mg_{28}Ge_{10}O_{48}$[2]. It is a rather intriguing structure which can best be described as a mixture of cubic and hexagonal packing of oxygen atoms with a packing sequence $(ABACBC)_n$. Structurally, it can be described as a layer structure made up of olivine blocks and magnesium oxide blocks. The space group is P_{bam} with a = 14.512(2), b = 10.219(2), and c = 5.944(1) Å.

Figure 1 illustrates the structure. What we have, starting from the bottom, is an alternation of magnesium oxide layers with olivine layers in the sequency MgO, olivine, MgO, olivine, MgO with the packing direction along the a-axis. The olivine layer has the composition Mg_2GeO_4; the magnesium oxide layer, however, has two magnesium ions replaced by a germanium ion and a vacancy in an ordered arrangement to produce the stoichiometry Mg_6GeO_8, rather than Mg_8O_8. The stacking sequence and the orientation of the layers is not the same as in the norbergite-type minerals which are made up of olivine and brucite [$Mg(OH)_2$] layers. The full three-dimensional crystal structure analysis was refined completely to an R = 0.044.

My interest in this problem is the effect of structure on the fluorescence properties of Mn^{+4}. (We are now investigating these properties, and the manganese evidently substitutes for an octahedrally coordinated germanium.) It was found empirically by the phosphor people that by adding magnesium fluoride to the ceramic preparation there was an increase in the luminescence efficiency and there was discussion as to whether the fluoride actually went into the lattice. It turns out that fluoride is incorporated into the lattice. The composition of the fluorogermanate single crystals is $Mg_{28}Ge_{7.5}O_{38}F_{10}$. In other words, about 9 w/o fluorine substitutes into the structure and charge compensation is accomplished by a deficiency in germanium. There is nothing unusual about fluoride-substitution in oxide materials; it is known to occur in perovskites, spinels, garnets, etc.

We grew single crystals of the fluorogermanate and made a detailed crystallographic investigation[3] of the defect site (one of the germanium sites). The germanate and the fluorogermanate are isostructural (crystallographic parameters for the fluorogermanate are a = 14.343(1), b = 10.196(1), and c = 5.9075(4) Å). We had an ample amount of single crystal data so that a number of possible models for the defect site could be investigated. For example, perhaps there is not a germanium vacancy but a magnesium ion substitute at the germanium site.

[1] Robbins, C. R. and Levin, E. M., Amer. J. Sci., 257, 63 (1959).
[2] Von Dreele, R. B., Bless, P. W., Kostiner, E. and Hughes, R. E., J. Solid State Chem., 2, 612 (1970).
[3] Bless, P. W., Von Dreele, R. B., Kostiner, E. and Hughes, R. E., J. Solid State Chem. 4, 262 (1972).

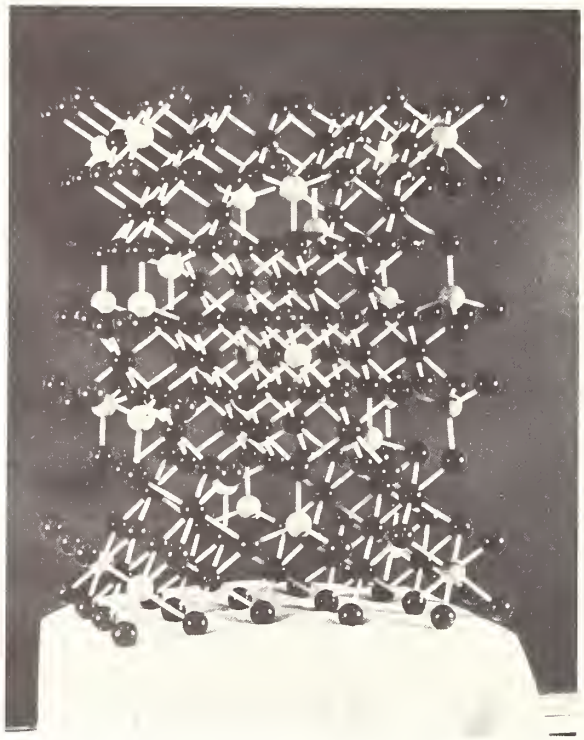

Fig. 1.

(Germanium occupies both tetrahedral and octahedral sites; magnesium could substitute at either site.) The possibility of magnesium surrounded by fluorine, germanium surrounded by oxygen, germanium surrounded by fluorine was also investigated. The final arguments[3], which I will not go into here, are based on occupancy factors, thermal parameters at the various sites, and a statistical analysis of the resultant *R* factors.

We found that the basic difference between the two structures, as first deduced from the Patterson maps, is that the Ge(III) site (tetrahedrally coordinated) is 38% occupied. This site is illustrated in figure 2. Three of the anions (actually two, since anion VI lies on a mirror plane) have highly anisotropic thermal parameters, while anion IV is nearly isotropic. These thermal ellipsoids point toward the germanium sites. From our previous arguments we felt that the fluorine was localized at these sites. Since one can approximate a thermal ellipsoid of vibration by two fractionally weighted atoms placed along its major axis, we placed two half-weighted fluorines at either side of the center of this axis for each of the highly anisotropic anion sites. Refinement converged to an $R = 0.046$ with one half-fluorine exactly at the position of the oxygen in the germanate structure and the other displaced about 0.2 Å farther away from the Ge(III) site. It is very tempting to say that when the germanium site is occupied fluorines occupy these sites and when the germanium site is vacant the anion (possibly oxygen) moves away from the vacancy.

Complex as the basic germanate structure may seem, it is really very simple if one considers the building blocks of olivine and magnesium oxide. In the fluorogermanate, the defect cluster is a partially occupied germanium site with the charge compensating anions localized about it. If one has a germanium deficiency one must have some sort of compensation and in this case it is the substitution of fluorine for oxygen.

We have some other very preliminary information. We have done some electron diffraction, but rather crude compared to what we have seen here during the past few days. This diffraction work indicates that we may have some sort of lamilar structure. In fact, if we take very long exposure x-ray photographs, the glide that relates the two Ge(III) atoms in the fluorogermanate is violated. Therefore, there may be some ordering of defects within the structure as it stands. We are at present investigating this possibility of a lamilar structure. Thank you.

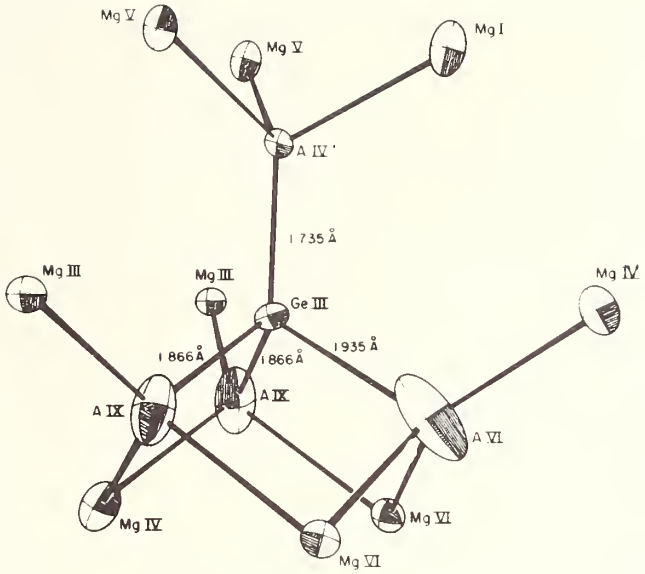

Fig. 2.

R. S. Roth: I would like to take the Chairman's right by asking the first question. I think there are lots of ways that people could think of disagreeing with you if they wanted to. There are obviously other interpretations. Now, one of the first things that comes to mind is ... I remember the paper that was in the Journal of Solid State Chemistry ...

E. Kostiner: That was the germanate structure.

R. S. Roth: The crystals themselves were grown by a flux technique and there was the question of did they or did they not have manganese fluoride or something like that?

E. Kostiner: They were grown with the activator ion (Mn^{+4}) added, that's correct. But no fluoride was present in the preparation of the germanate.

R. S. Roth: And yet there was no account taken of the manganese in the structure analysis and the question is, how much is in there? How does it affect the x-ray results?

E. Kostiner: That's a very good question. The manganese concentration (by analysis) is 0.72%, which corresponds to 0.3 atom of manganese per unit cell. It is very small and it does not affect the structural details at all. One can make the material and grow crystals of it without the activator ion. It is very handy to use the activator because you just use a UV lamp to find the crystals. We did spectroscopic analyses for platinum contamination from the crucible (0.67%), lead contamination from the flux (<0.1%), and they are at a very low level such that there is a very small fraction of an atom per unit cell. Yes, I did worry about the possibility of this intentional contaminant causing this layer structure to form. Are you satisfied?

R. S. Roth: I wouldn't say I was satisfied, but right at the moment I don't have any more questions.

Is there anybody else who would like to take a crack at this? From the crystallographer's point of view?

E. Kostiner: I think the structure should stand as it is. It is a good structure. There are no anomalies in the data.

R. S. Roth: How about the defect data?

E. Kostiner: This is certainly an interesting example of what one might call a defect cluster.

R. S. Roth: I once ran into a similar thing in a germanium partial occupancy problem that I simply couldn't solve and this, of course, was because I insisted that it was going to have to come out stoichiometric. This was the germanium: 9 niobia which is isostructural with vanadium or phosphorus: 9 niobia ($P_2O_5 \cdot 9Nb_2O_5$)[4]. Whether it's nine or not, the germania compound hasn't been proven, but it is some sort of a defect problem which nobody has ever solved.

B. M. Gatehouse: I don't think you commented on the anisotropic thermal ellipsoids in the compound without fluoride.

E. Kostiner: We went fully anisotropic in the germanate structure. The thermal parameters for all of the atoms are essentially isotropic.

R. S. Roth: Any more comments? Questions? I think that we should give Dr. Bevan the next chance.

---

[4]Roth, R. S., Wadsley, A. D. and Andersson, S., Acta Crystallographica 18, 647 (1965).

National Bureau of Standards Special Publication 364, Solid State Chemistry, Proceedings of 5th Materials Research Symposium, issued July 1972.

THE ORTHORHOMBIC PHASES IN THE SYSTEM YTTRIUM-OXYGEN-FLUORINE

D. J. M. Bevan

Flinders Univ. of S. Australia
Bedford Park, South Australia 5042

D. J. M. Bevan: On this same theme of a continuous sequence of ordered phases or an apparently continuous sequence of ordered phases in a nonstoichiometric region, following on what Bob Roth said the other day and what we have just heard about the chromium doped rutile systems, I thought it might be of some interest to tell you something of the work that Dr. Alan Mann and I have been doing on the yttrium oxide-fluoride system. I'll try and be as brief as I can. The first slide (fig. 1) defines the region of interest. The X stands for oxygen plus fluorine and you can see that somewhere between about 2.12, or something like that, and 2.22 there is this orthorhombic phase. At the lower end it co-exists with stoichiometric rhombohedral YOF; at the high end with stoichiometric YF_3.

The second slide (fig. 2) shows a plot of the orthorhombic parameters of the subcell. This is very closely related to the fluorite structure. The slightly distorted fluorite-type subcell parameters are about five and a half angstroms or thereabouts. You might think you have the nice simple sort of situation of 5 or 10 years ago, continuous variation of lattice parameter with composition.

Phase data for samples investigated by powder and single crystal diffraction.

Composition	Phase Analysis	fluorite-type sub-cell parameters (±0.001Å) a_F	b_F	c_F
$YX_{2.13(6)}$	orthorhombic phase	5.425	5.508	5.527
$YX_{2.11(5)}$	YOF + orthorhombic phase	5.420	5.512	5.527
$YX_{2.14(8)}$	orthorhombic phase	5.419	5.519	5.529
$YX_{2.14(9)}$	orthorhombic phase	5.419	5.516	5.527
$YX_{2.16(5)}$	orthorhombic phase	5.416	5.520	5.528
$YX_{2.17(1)}$	orthorhombic phase	5.413	5.52(8)	5.52(8)
$YX_{2.18(3)}$	orthorhombic phase	5.410	5.53(3)	5.53(3)
$YX_{2.18(7)}$	orthorhombic phase	5.407	5.53(3)	5.53(3)
$YX_{2.22(0)}$	YF_3 + orthorhombic phase	5.402	5.541	5.535
$YX_{2.22(5)}$	YF_3 + orthorhombic phase	5.400	5.544	5.534
$YX_{2.25(9)}$	YF_3 + orthorhombic phase	5.399	5.546	5.535

Fig. 1.

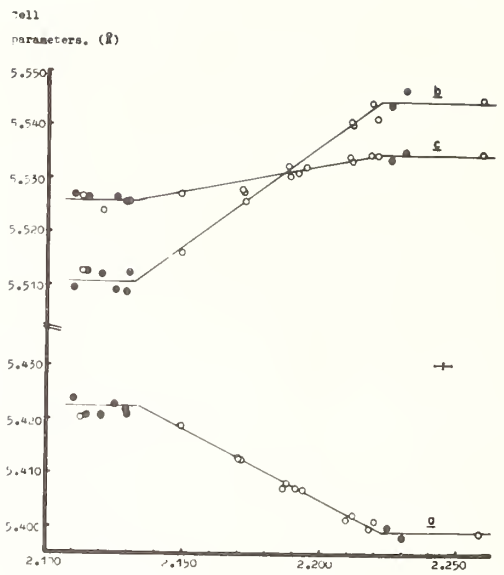

Fig. 2. Composition → o = analyzed composition
● = estimated composition (2P)

The next slide (fig. 3) shows the sort of situation that Bob Roth described the other day. These are three Guinier powder patterns of different compositions. You can see the (111) fluorite-type line, the (200) fluorite group, and the set of superstructure reflections. This one, this ($1k_32$) one moving left and the other one, over here, ($0k_22$) moving right. So this rather gives the lie to the idea of continuous solid solution. The next slide.....

R. S. Roth: Judge, can I interupt before you move that slide. Why does the (111) orthorhombic line appear to be split into three lines?

D. J. M. Bevan: Oh, there's an internal standard in there. That's thoria.

R. S. Roth: Thank you, that means the (111) orthorhomibc line is only split into two lines, not three. (There is probably some YOF in this pattern, too.) Comment?

D. J. M. Bevan: Yes, on the lowest of the three pictures. There is, of course, no splitting of the orthorhombic (111) reflection.

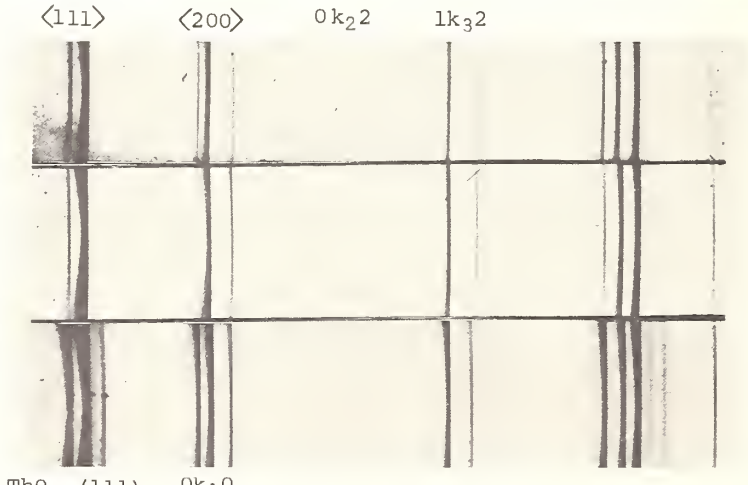

Fig. 3.

Next slide (fig. 4). This is a Weissenberg picture of a single crystal which turned out, very fortunately for us, to be a comparatively simple superstructure; a one-dimensional superstructure which shows seven spaces between the main fluorite type reflections. We have gone some way towards getting the single crystal structure of this. Sten Andersson has seen the results. I think the next slide will show you the sort of structure which this substance has (fig. 5). This is one quarter of the unit cell, which consists of seven fluorite-type subcells stacked one on top of the other in the *b* direction. Down at the bottom the distortions are relatively small. As you move up you start to get rather larger distortions and the additional anion. The ideal formula for this substance is $Y_7O_6F_9$, it's an M_7O_{15} structure. The additional anions go in here, these A9 anions on the y = 1/4 mirror plane. I'm not going to say anything more about the structure except this: in its simplest terms you can think of a layer, a two-dimensional layer of interstitial anions, going in at the y = 1/4 position. Sten Andersson has a very nice geometric model for this (in terms of his geometry) where the coordination in this region becomes square anti-prismatic. He might like to comment on that later on.

Fig. 4.

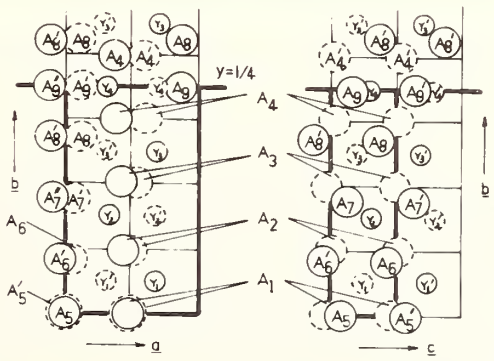

Projection onto (001) Projection onto (100)

○ = Y atom projected from near z=1/4 onto (001)
or Y atom projected from near x=1/4 onto (100)

◌ = Y atom projected from near z=3/4 onto (001)
or Y atom projected from near x=3/4 onto (100)

◯ = anion projected from near z=0 onto (001)
or anion projected from near x=0 onto (100)

◌ = anion projected from near z=1/2 onto (001)
or anion projected from near x=1/2 onto (100)

Fig. 5.

Let me just move on very quickly to the next slide (fig. 6) which again shows the coordination polyhedra. Two of the cations in the asymmetric unit are now 9-coordinated. There are the additional anions coming in here (A9). On the next slide (fig. 7) is one attempt that we have made to arrive at the structural relationships. This is the coordination polyhedron in the YF_3 phase itself. You can see that there is quite a close similarity, geometrically, to the 9-coordinated metals in the region of the interstitial layer. A crude description might be given in terms of an intergrowth of the YF_3 type structure; a two-dimentional intergrowth with regions of a fluorite-type sturcture. However, I don't want to press that analogy too far. A great deal more needs to be done on the detailed structure before we can say too much about that. We also have discovered the phase $Y_6O_5F_8$, and we believe that there is indeed an homologous series of simple ordered phases, which one can write as $Y_nO_{n-1}F_{n+2}$. That's enough for that slide, thank you.

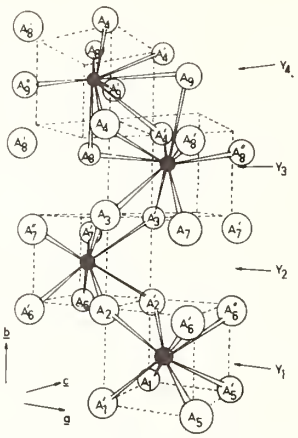

Fig. 6. Metal coordination polyhedra in $(Y_7O_6F_9)_4$ (Primes refer to symmetry related atoms in adjacent asymmetric units.)

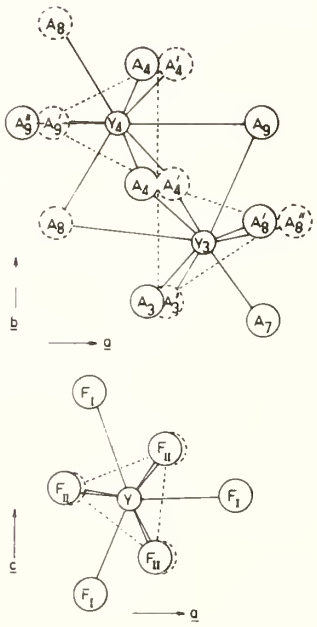

Ⓨ = yttrium atom at close to z=1/4.
Ⓐ = anion at close to z=0.
(A) = anion at close to z=1/2.

Ⓨ = yttrium atom at y=3/4.
$Ⓕ_{II}$ = fluorine atom at close to y=0 (and 1/2)
$Ⓕ_{I}$ = fluorine atom at y = 3/4.

Fig. 7. Coordination of metals Y_3, Y_4 in $(Y_7O_6F_9)_4$.

Let us come back for a moment to the powder patterns. Both of the simple homologs n = 7 and n = 6, have been found as single crystals and indexed completely, and this indexing related back to the powder patterns. The superstructure reflections which are of interest are the ones which move the most and are of the form $0k_{2}2$ and $1k_{3}2$. Then there is another reflection which is one of the fluorite 200 family, which we can write $0k_{1}0$ where, in the case of the fluorite subcell, of course, this is 2. In these simple homologs the values of these indices are related to the number of fluorite subcells in the stack. The index $0k_{1}0$ is simply (0,*n*,0) where *n* is the number of fluorite units in the stack. This one is (0,*n*-1,2) and this one is (0,*n*+1,2). Let's now move on to the next slide (fig. 8). This just lists the homologs of the series. The 7 and the 6 homologs have been found. Let me be quite honest and say that we haven't found the 5 homolog in the pure state, although we have certainly found super-superlattices, as we call them, which are quite clearly *based* on the 5 homolog. The compositions of the members *n* = 8 and *n* = 4, do not fall within the region of what one might call "nonstoichiometry."

The next slide please (fig. 9). This is another Weissenberg pattern of one of the intermediate phases. As you can see this one is based on the member *n* = 5. The very strong reflections are the fluorite subcell spots. You can see that there are 5 spaces in between these, giving the *n* = 5 homolog superlattice. You then have the *super*-superlattice on top of this, where you have the satellite spots occurring. I think, just speaking from memory, that we have here a *b* axis of something like 250 angstroms.

Basic unit orthorhombic phases.

Unit	Composition	Formula	Unit Cell Parameters		
			a	*b*	*c*
8F	$YX_{2.125}$	$(Y_8O_7F_{10})_4 = Y_8X_{17}$	not stable as a discrete entity		
7F	$YX_{2.143}$	$(Y_7O_6F_9)_4 = Y_7X_{15}$	5.420A°	38.58A°* (=7x5.512A°)	5.527A°*
6F	$YX_{2.167}$	$(Y_6O_5F_8)_4 = Y_6X_{13}$	5.416A°	33.12A° (=6x5.520A°)	5.520A°
5F	$YX_{2.200}$	$(Y_5O_4F_7)_4 = Y_5X_{11}$	5.406A°	27.69A° (=5x5.538A°)	5.532A°
4F	$YX_{2.250}$	$(Y_4O_3F_6)_4 = Y_4X_9$	not stable as a discrete entity		

*Originally reported as *c* = 38.58A°, *b* = 5.526A° (D. J. M. Bevan, R. S. Cameron, A. W. Mann, G. Brauer, and V. Roether, Inorg. Nucl. Lett. 4 [4], 241-7 (1968)). This designation has been interchanged in accordance with the structural findings.

Fig. 8

Fig. 9.

465-504 O - 72 - 49

Now, how to sort this out? What we have been able to do, and I think this is probably shown in the next slide (fig. 10), no, I'm sorry this just shows the indexing of the superlattice lines for the simple members of the homolog. At any rate there is the $(n-1)k$ index and the $(n+1)k$ index showing up. Next one, please (fig. 11).

Now, this is the way in which we have approached this analysis. I'm not going to go through this in detail, but what one can do is to get experimental ratios of sine square thetas from the Guinier patterns and these values of sine square thetas can be obtained fairly precisely from Guinier patterns. We use strictly monochromatic $CuK\alpha_1$ radiation and the precision in these measured sine square thetas is quite high. R_1 & R_2 are the ratios of the sine square theta for the $0,k_1,0$ reflection, which is one of the 200 fluorite subcell group, and the sine square thetas for $0k_2 2$ and $1k_3 2$ reflections respectively. These are experimental ratios. Now you can match these to the ratios of the squares of integers. In this way you can see what sort of values for n are within the limit of error, where n now is the number of fluorite subcells in the stack. You never find more than about 2 or possibly 3 which are reasonable at all. Then you combine this sort of information with the measurements that you get from those single-crystal Weissenberg patterns showing super-superlattice reflections.

$\sin^2\theta$ and $\{hk\ell\}$ values for $\{0k_10\}$, $\{0k_22\}$, and $\{1k_32\}$ reflections.

Basic Unit	$\{0k_10\}$ (Fluorite-type)		$\{0k_22\}$ (Superstructure)		$\{1k_32\}$ (Superstructure)	
	$\sin^2\theta$	$\{hk\ell\}$	$\sin^2\theta$	$\{hk\ell\}$	$\sin^2\theta$	$\{hk\ell\}$
7F	0.07811	{0(14)0}	0.09199	{0 6 2}	0.12359	{1 8 2}
6F	0.07786	{0(12)0}	0.09125	{0 5 2}	0.12430	{1 7 2}
5F	0.07750*	{0(10)0}	0.08995*	{0 4 2}	0.12568*	{1 6 2}

*By interpolation of $\sin^2\theta$ values from patterns at nearby compositions.

Fig. 10

In the orthorhombic system $\sin^2\theta_{\{hk\ell\}} = h^2A + k^2B + \ell^2C$

$$\text{where } A = \frac{\lambda^2}{4a^2},\ B = \frac{\lambda^2}{4b^2},\ C = \frac{\lambda^2}{4c^2}$$

Thus for the $\{0k_10\}$ reflection: $\sin^2\theta_{\{0k_10\}} = k_1{}^2B$

for the $\{0k_22\}$ reflection: $\sin^2\theta_{\{0k_22\}} = k_2{}^2B + 4C$

and for the $\{1k_32\}$ reflection: $\sin^2\theta_{\{1k_32\}} = 1A + k_3{}^2B + 4C$

In these expression the values of A and C are determined quite precisely from the a and c parameters of the fluorite-type subcells (see figure 1) since, for any given intermediate phase, these are unaffected by an uncertainty in the number of sub-cells comprising the one-dimensional (b-axis) superstructure.

It then follows that two ratios, R_1 and R_2, can be defined such that

$$R_1 = \frac{k_1{}^2}{k_2{}^2} = \frac{\sin^2\theta_{\{0k_10\}}}{\sin^2\theta_{\{0k_20\}} - 4C}$$

and

$$R_2 = \frac{k_1{}^2}{k_3{}^2} = \frac{\sin^2\theta_{\{0k_10\}}}{\sin^2\theta_{\{1k_32\}} - A - 4C}$$

Fig. 11.

These are not terribly accurate, not good to better than about ± 4% on the *b* parameter from those single crystals. I think the next slide shows the results of this (fig. 12). Here are the experimental ratios as determined from the powder data and the values of the *b* parameter as determined from the single crystal data, and then going back again to the powder data, one comes up with more precise values of *b*. You see now the biggest we got is 315 angstroms for a 57 times fluorite stack. This just indicates the number of fluorite subcells in the one-dimensional stack.

Overall the picture has been rationalized in terms of an ordered intergrowth of the basic homologs, and the next slide (fig. 13) shows the possibilities. There is, for example, a 23 stack, 2 lots of eight and one of seven, although the 8 homolog, of course, doesn't occur on its own. It's outside of the homogeneity region, although it can still be invoked in the ordered intergrowth explanation. The only other thing I need to add by way of justification for this is that if this generalization for the indexing is correct, (this is an assumption, but works out quite well) then one might expect to have the same sort of approach apply in the case of the ordered intergrowth. So, if you take k_1 for example, it is obvious that if you have 23 fluorites, then the k index is going to be 46 because it's a fluorite-type reflection. However, for the two super-lattice reflections of the 23 stack, the k_2 index for a pure 8 phase would be 7, then twice 7 equals 14, and the k_2 index for the 7 phase is 6, so the k_2 index for this superlattice phase is 14 + 6 = 20. The k_3 of this would be twice 9 or 18 plus 8, 9 + 9 + 8 = 26. On the basis of this sort of rationalization, we claim (whether we are justified in claiming this or not, I don't really know, but it certainly works,) we can make a distinction between the two possibilities for the 47 stack and the 57 stack, as shown, because only in the case of this first one do the indices fit. According to this pattern and the ratios that you get from these indices, only then do these agree with the measured ratios of the sine square thetas from the powder data.

Unit cells for Intermediate Phases.

Derived Unit Cell *n*	Powder Pattern Ratios		Unit Cell *b*	
	Experimental	Derived Cell	Experimental	Derived Cell
23F	R_1 = 5.25±0.06	5.29	128 ± 5Å	126.7Å
	R_2 = 3.11±0.03	3.13		
7F	R_1 = 5.46±0.06	5.44	38.5 ± 2Å	38.6Å
	R_2 = 3.04±0.03	3.06		
19F	R_1 = 5.66±0.06	5.64	105 ± 5Å	104.9Å
	R_2 = 2.98±0.03	2.98		
45F	R_1 = 5.58±0.06	5.61	248 ± 10Å	248.2Å
	R_2 = 3.00±0.03	3.00		
6F	R_1 = 5.72±0.06	5.76	33 ± 1Å	33.1Å
	R_2 = 2.94±0.03	2.94		
17F	R_1 = 5.90±0.06	5.90	91 ± 4Å	94.0Å
	R_2 = 2.90±0.03	2.89		
47F	R_1 = 6.08±0.06	6.12	252 ± 10Å	260.0Å
	R_2 = 2.82±0.03	2.82		
57F	R_1 = 6.16±0.06	6.14	317 ± 12Å	315.4Å
	R_2 = 2.80±0.03	2.81		
28F *	R_1 = 6.42±0.06	6.48	155 ± 6Å	155.2Å
	R_2 = 2.73±0.03	2.71		
28F *	R_1 = 6.45±0.06	6.48	157 ±6Å	155.2Å
	R_2 = 2.71±0.03	2.71		
41F	R_1 = 6.54±0.06	6.51	222 ± 9Å	227.4Å
	R_2 = 2.69±0.03	2.69		

* However, for the two samples with the same (28F) unit cell, a unit with half the indicated *b* axis (*i.e.* 14F) must also be considered, but for the structural interpretation of this intermediate phase, the ambiguity is, at this stage, trivial.

Fig. 12.

Ordered intergrowth models.

Unit	Ordered Interspersion	Calculated Composition	k indices from theoretical ratios k_1	k_2	k_3
23F	2 x (8F) + 1 x (7F)	$YX_{2.130}$	46	20	26
7F	1 x (7F)	$YX_{2.143}$	14	6	8
19F	1 x (7F) + 2 x (6F)	$YX_{2.153}$	38	16	22
45F	3 x (7F) + 4 x (6F)	$YX_{2.155}$	90	38	52
6F	1 x (6F)	$YX_{2.167}$	12	5	7
17F	2 x (6F) + 1 x (5F)	$YX_{2.176}$	34	14	20
47F	2 x (6F) + 7 x (5F)	$YX_{2.191}$	94	38	56
	7 x (6F) + 1 x (5F)	$(YX_{2.170})$			
57F	2 x (6F) + 9 x (5F)	$YX_{2.193}$	114	46	68
	7 x (6F) + 3 x (5F)	$(YX_{2.175})$			
28F	4 x (5F) + 2 x (4F)	$YX_{2.214}$	56	22	34
28F	4 x (5F) + 2 x (4F)	$YX_{2.214}$	56	22	34
41F	5 x (5F) + 4 x (4F)	$YX_{2.220}$	82	32	50

Fig. 13.

So that's the story! This is I think another example of a continuous series of ordered phases in a range which in the early days, when Zachariasen[1] first studied this system, was thought to be a classical non-stoichiometric phase. It is related to the fluorite system. Crystallographic shear planes are not involved here and we have a different sort of principle. Paul Caro thinks that he can explain this in terms of his $(LnO)_n$ cation. I think that we need to do some more work on that to see if it fits. Sten Andersson has a very nice description of the square anti-prism coordination polyhedron in the center whereby the extra anions are introduced. Altogether we'll need to sort all these things out before we can give a final definitive statement on this. This preliminary work will be published in the J. Solid State Chemistry as soon as possible. Thank you Mr. Chairman.

R. S. Roth: I have several questions. The first one is the same question that I've asked everybody else, how did you make the specimens?

D. J. M. Bevan: Solid state reactions, no doubt with the aid of a little bit of vapor phase transport, in sealed platinum capsules at about 1150° for a week, slow cooled; mixtures of yttrium oxide and yttrium trifluoride.

R. S. Roth: How near were you to the melting points, to the solidus temperatures?

D. J. M. Bevan: Yttrium fluoride, I think, melts somewhere around about 1350°. We have some of the specimens which have obviously been close to melting. The crystal growth that takes place at high temperatures is very, very considerable indeed.

R. S. Roth: My second question is, how near was the experimental composition to the theoretical one derived from the crystal taken from that batch, and how close do you think the real composition is to that?

[1] W. H. Zachariasen, Acta Cryst. 4, 231 (1951).

D. J. M. Bevan: The real compositions were determined by chemical analysis. They didn't always agree with the as-prepared compositions because the specimens tend to hydrolyze, and indeed one makes use of this in the analytical procedure. In using this hydrolysis technique, steam plus oxygen over the specimens at about 1000°, the HF comes off and you have quite a nice method for analyzing the fluorine. You are left behind with pure Y_2O_3 which you can weigh, so the analysis is for example 2.155 ± 3 or so in the third figure.

R. S. Roth: Now the question becomes, how close does the chemically analyzed composition fit the x-ray theoretical composition?

D. J. M. Bevan: In the case of the seven homolog, that single crystal came from a mixture in which some YOF was present. The analyzed composition was 2.116 if I remember correctly. The theoretical composition of the 7 phase was 2.143. The chemical analysis of the 6 phase, which is about 2.186 if I remember rightly, agrees with the theoretical to about within experimental error.

R. S. Roth: I've been hogging the questions here. Does anybody else wish to contribute?

Do you think that a stacking sequence of 47 or 57 in a unit cell dimension of 315 angstroms has any real meaning?

D. J. M. Bevan: I've only been talking about the facts as observed.

R. S. Roth: Oh, I quite agree with the facts as observed, that wasn't the question.

J. S. Anderson: I think that is a very interesting question, Bob. I really find it hard to believe that a crystal can remember what it did 700 angstroms ago even if it has a faint recollection of what it did 350 angstroms ago. I have a feeling that when one comes to look at these stacking sequences, made up as they are of a number of sub-units, we are almost bound to find that there is some variation from specimen to specimen, and some disorder. It seems to me that these questions about the thermal preparation, are particularly cogent in cases like this. It is very hard to believe that some disordering does not take place at high temperatures. It may be that they are stable right up to the melting points, but I strongly suspect that there will be some randomization of stacking, that it will be very hard to prepare an absolutely uniform crystal.

R. S. Roth: Well, one point on this is that . . . I might be hogging the answers too, but my feelings on this subject is that you can introduce *more* order into the system by high temperatures. This is not a crystallographic shear type system at all that we are referring to. In this system I feel that you get a better stacking sequence, more order to that sequence with more time and temperature as more energy is applied to the system.

D. J. M. Bevan: Well, with respect, Bob, because it is not a CS system then your comment is irrelevant because in fact if you heat these things up at about 400° or 500°, you lose your super-structure; they disorder. These are low temperature phases.

R. S. Roth: How do you know? What experiment has led you to this hypothesis?

D. J. M. Bevan: We have seen the disordering process occur in electron diffraction, even under normal operating conditions.

J. S. Anderson: You see, this is kinetics versus thermodynamics. One must distinguish between the real equilibrium state - the absolute minimum of the free energy surface at any temperature - and the practicability of getting to that state. As prepared, there may be fluctuations of order and composition within a crystal, leading to variations in local order. Its properties correspond to some point on a metastable free energy surface. To get to the absolute equilibrium state, kinetic processes must intervene: diffusion, or next neighbor place exchange or at least a jump across a potential barrier to a site of different coordination. To achieve a new order in both CS phases and stacking structures, these steps have to be highly cooperative. This is perhaps why such ordering processes sometimes seem to show peculiar kinetics: they can set in rather abruptly at high enough temperatures, as if the activation energy was far greater than that of any individual unit step. For example, in our electron microscopy of the niobium oxides we have found that H-Nb_2O_5 reduces rapidly

below 1000° to give a product with domains of the $Nb_{25}O_{62}$ structure in unchanged domains of H-Nb_2O_5 structure, and can be annealed indefinitely at 1000° without change. The preparation process already involves cooperative atom movements that shift all the CS planes (using that term loosely) in the transformed structure. At 1300°, quite rapidly, the CS planes re-shuffle themselves to transform the domain structure into the large-cell regular intergrowth structures. That would seem in line with Bob's argument, but I believe it is a kinetic effect. As we go up the temperature scale - and each structure has its own effective temperature scale - a second kinetic effect comes in. The atoms are not immobile vibrators: they have a finite mean lifetime on any site, and this is strongly temperature dependent. If the mean life time is short, a significant proportion of sites of any one type is always 'wrongly' occupied. On the ultramicrostructural level, perfect order cannot prevail throughout the crystal at high enough temperatures. Two questions then arise. How much disorder must there be before we recognise it? How much disorder must there be before the crystal loses track of the correlations upon which its superstructural organization depends? Returning to the thermodynamics, there is now no doubt that the coulombic part of the lattice energy of ionic crystals confers significant disadvantage to random structures as compared with ordered structures - any kind of order. In CS and stacking structure, the difference in energy between a perfectly regular and an irregular, but locally ordered, stacking sequence is likely to be much smaller. The energetic gain, the driving force, behind attainment of true order is small, so that the crystal can hang up on a metastable free energy surface. *However, as long as the planar structural units retain their integrity*, there is very little entropy to be gained by randomising their spacing. Hence, under these conditions, equilibrium is dominated and the superstructure order can persist - once reached - up to the highest temperatures. However, if the mean life time factor erodes the perfection of the planar structural units, the situation changes. Instead of involving a small number of entities in a 1-dimensional disorder problem, the configurational entropy arises from a much larger number of local clusters, or even every site in the crystal. The entropy gain from disorder can then take control. In principle, these seem to be the considerations behind the range of behavior that is found.

P. E. Caro: I would like to point out that the strict chemical order I am suggesting for those phases in terms of a succession of definite planar chemical entities does not necessarily imply a crystallographic order. This then will be "ordering" but not with the crystallographic meaning: we may have several polymorphs with the same composition (*i.e.* a chemical order). The fact is well known for silicate structures. The chemical order then came first, and the crystallographic one only second, and more, it may not be necessary after all.

D. J. M. Bevan: Well, I agree entirely with what Stuart Anderson said, too, because there is no doubt these things are not perfectly ordered and when we can get around, if ever we can get around to looking at them under the electron microscope then we are going to see stacking faults. That is, if they don't disorder in the process, which I suspect they may do. I don't think there is any doubt about that, but Bruce Hyde, it was Fujiyawa or someone, wasn't it, who has done a theoretical analysis of these stacking faults? But you still get the repeat unit.

B. G. Hyde: Why bother to speculate? Wait and see!

D. J. M. Bevan: All right, we'll wait and see.

F. Jellinek: I don't think these very large unit cells are really as frightening as they look at first sight. You have two mechanisms of some kind of ordering. You have both the metal positions which you studied and also the arrangement of oxygen and fluorine which you have not studied and could not with this method of course. It may well be similar to what we have found to be the case in some other compounds. One of the orderings may have, say a repetition distance of 4 subcells; the other one a repetition distance of, say, three and a half subcells and you add up to a unit cell repitition distance commensurable with both of them, that means in this example 28 subcells (7x4=8x3 1/2). So if you have two mechanisms, as you do have, you are bound to have large unit cells if the two mechanisms are not exactly commensurate. This may well be the explanation of these phenomena you observe.

R. S. Roth: Any other comments: Let me get back to my argument then. You said that if you have a system that does not have shear planes, then the argument I was making about high temperature annealing is invalid. I disagree with that. It could be that in your yttrium oxide fluorides all the super structures disappear at ~400°, you hadn't made that point earlier. However, we can mention other systems that do not contain shear planes, for instance, consider the paper that Stephenson gave at the Arizona meeting on the tantalum tungsten oxides[2]. Now, there are no shear planes in that low temperature form of tantalum oxide, yet it is a high temperature annealed system where increased temperature causes *better* order. The same is true of almost any high temperature oxide that I have ever worked with that has such things, and there are certainly many such. Do you call the Aurivillius type phases shear planes, or the Ruddelson-Popper type phases shear planes? These phases, stacking sequence type things, all have similar phenomena, hundreds and hundreds of angstrom unit cells and increased high temperatures contribute to ordering; contribute to a much sharper super-structure pattern. Now, that isn't quite the same thing, is it? But this is the experimental observation. Comment on that?

D. J. M. Bevan: I don't quite understand what you are saying. You are saying that if I heat to higher temperatures, then I will get better ordered phases on cooling.

R. S. Roth: I didn't really mean your system, although I wouldn't be surprised, yes.

D. J. M. Bevan: Well, obviously you have to heat to high enough temperatures in order to react the specimens. They will, in fact, react at about 850° and you get perfectly well-ordered phases. It might be worth pointing out in this context that this is not the only system we are looking at. We are looking at the other rare earth oxide fluorides as well. When you move up to the lighter rare earths, neodymium oxide fluoride, the specimens have been heated up to about 1600° or thereabouts, and very good single crystals obtained and there is only a partial ordering of these. The fluorite subcell distorts in a monoclinic fashion, but none of the super-superlattice phases have been observed, even after six months annealing at 350 °C. As you go down the series the super-superlattice phases begin to come in at temperatures where you can expect to have a reasonably mobile system. I believe as far as the neodymium system is concerned that we just cannot achieve this sort of order if it is stable at temperatures where--well, what I am trying to say is that the way you would get the ordering is at temperatures so *low* that you have lost mobility for ordering to take place. You are beaten by a kinetic problem.

R. S. Roth: Well, maybe the difference is between a mixed cation oxide and a mixed oxyfluoride with only one cation, but yet I think of Sten Anderson's work on the tatalum oxyfluoride which was the same structure type as the one I originally referred to.

D. J. M. Bevan: But there again, the mobil species is the tantalum is it not?

R. S. Roth: I wouldn't know.

Shall we give Dr. Eyring a chance now?

---

[2]R. S. Roth and N. C. Stephenson, in *The Chemistry of Extended Defects in Non-Metalic Solids*, p 167, North Holland Publ. Co., Amsterdam

National Bureau of Standards Special Publication 364, Solid State Chemistry, Proceedings of 5th Materials Research Symposium, issued July 1972.

PHASE REACTIONS NOT EXHIBITED ON THE USUAL PHASE DIAGRAM

LeRoy Eyring

Department of Chemistry
Arizona State University
Tempe, Arizona 85281

L. Eyring: I thought it would be worthwhile to call attention to some results obtained by sensitive yet antediluvian methods of observing phase reactions in solids not usually represented. I refer to oxygen pressure, temperature, composition studies on rare earth oxides utilizing thermogravimetric techniques. For example, let us look at the phase diagram of the praseodymium oxide-oxygen system shown in the first figure[1]. This is an interesting phase diagram, a fraud to say the least, ostensibly describing all the relationships between oxygen and praseodymium atoms in the temperature-composition limits shown. People have, whenever this slide has been shown in my presence, rarely asked about the funny spots veering off to the right of the $PrO_{1.714}$ composition at higher temperatures. Well, therein lies a tale.

The fact is that above about 750° at higher pressures this most thermally stable of the intermediate phases (iota) does not form as a single phase in reduction (see curve 650 in fig. 2). This is true even with annealing for as long as a month--there is simply no measurable drift toward $PrO_{1.714}$ under these conditions. On the other hand, if the pressure over a sample at say 850° and high pressure(stranded at higher composition) is reduced to 10 Torr the composition goes immediately to ~ $PrO_{1.714}$ and the sample does not reoxidize upon returning to the original pressure[2]. All this in spite of the fact that reaction rates for phase reactions are very fast under these conditions.

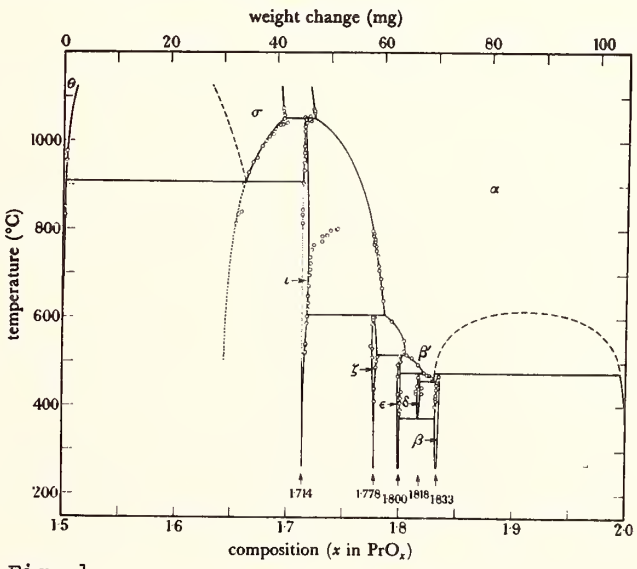

Fig. 1.

[1] B. G. Hyde, D. J. M. Bevan and L. Eyring, Phil. Trans. Roy. Soc., London Ser. A, No. 1106, 259, pp 583-614 (1966).

[2] R. P. Turcotte, M. S. Jenkins and L. Eyring, unpublished results.

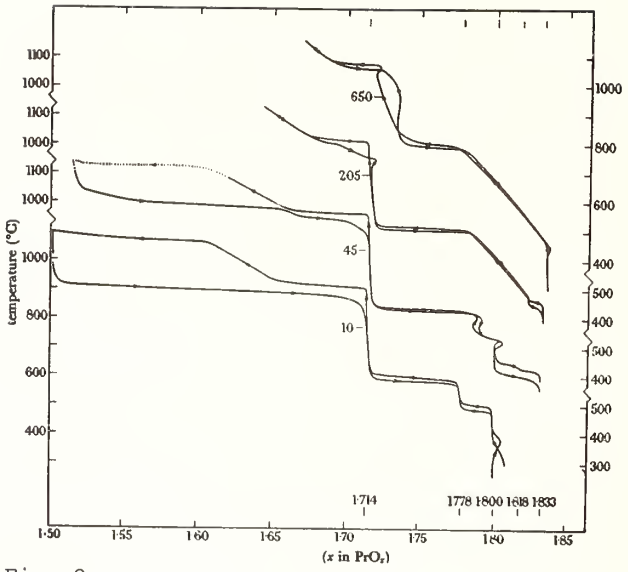

Fig. 2.

In the region of the delta, epsilon and zeta phases a phenomenon quite analogous to that just described in the hyperiota region occurs (see fig. 2 curve 45). At low pressures almost classical isobars are seen yet such curves show marked hypercomposition at higher pressures. This behavior is inadequately explained and is presently undergoing further study[2].

The alpha phase is formed at higher pressures and temperatures as shown in the diagram by an apparent disordering of the intermediate phases belonging to the homologous series. At suitable pressures one can cross the alpha region by changing the temperature and when one does so, the isobars are reversible and reproducible even with very careful measurements. Curiously there is an indication, outside the limits of error, that the nature of the alpha phase depends upon its origin. It depends upon what the ordered phases were which formed it in disordering[3]. In addition, whereas the high temperature Guinier photographs of the fluorite alpha phase show no superstructure when one is well within the stability region--at the boundaries there is indication of blackening of the film in the regions where a superstructure appears when the transition to the ordered phase is reached. There is also broadening of the main reflections which are split in the ordered phase being formed[2].

Another common feature of the tensimetric or gravimetric studies in the rare earth oxide system is the occurrence of hysteresis and pseudophase behavior in the two-phase regions. The next slide (fig. 3) shows this as revealed by an isobaric cycle in the TbO_x system between the delta and iota region. (Similar behavior may be seen in the two-phase regions of figure 2.) Notice that a sample at 380 Torr at a composition $TbO_{1.818}$ (the delta phase) being heated slowly does not reduce appreciably before a quite sharp decomposition temperature ($\sim$525°) is reached. At this point it reduces smoothly and rapidly but not discontinuously to the iota phase. If the temperature is then reversed a temperature is reached at which rapid oxidation occurs but this is below the temperature at which reduction occurred in heating hence a hysteresis loop is formed. Furthermore, before delta phase is reached the loop suddenly deviates into a bivariant curve which approaches the delta phase more slowly[4] (see dashed curve in fig. 3). This bivariant region is called a pseudophase (δ'). Although in this case the rate of heating in traversing the loop has some effect on its size the occurrence of the pseudophase is unchanged. The path taken point-by-point with long annealing

---

[3] M. S. Jenkins, R. P. Turcotte and L. Eyring in *The Chemistry of Extended Defects in Non-Metallic Solids*, (Eyring and O'Keeffe, eds.) North-Holland Publishing Co., Amsterdam, 1970, p. 36.

[4] B. G. Hyde and L. Eyring in *Rare Earth Research III*, (L. Eyring, ed.) Gordon and Breach, New York, p. 623 (1965).

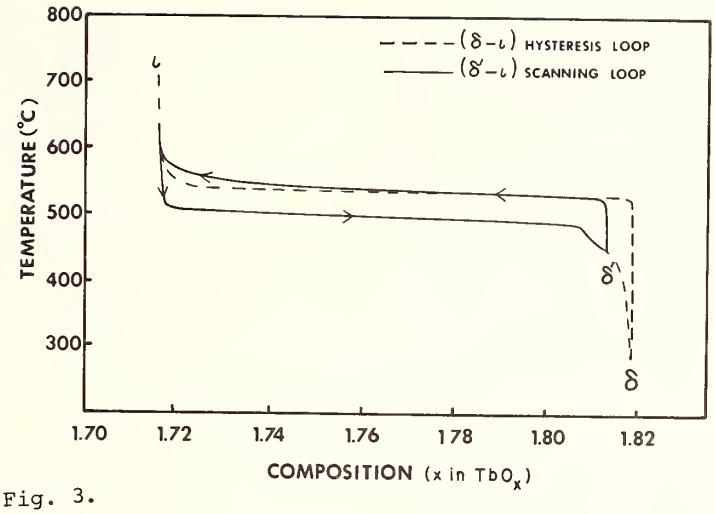

Fig. 3.

times has been observed to shrink the hysteresis loop[5] but not the δ´ pseudophase. The loop is also much smaller if one studies single crystals of ~10^6 times the volume of the powder but the δ´ feature remains essentially unchanged[6].

High temperature diffraction diagrams taken over many weeks as the sample is cooled in the δ´ region show a distinct and different pattern from δ which is formed at the lower temperatures. In this case δ´ is never seen in reduction--always in oxidation[7].

Scanning hysteresis loops are being studied at present[6]. One of the interesting features is that if one is in the cooling (oxidation) branch of the loop but reverses the temperature anywhere in the δ´ region the sample behaves as a line phase with no loss of oxygen until a decomposition temperature is reached (see fig. 3, the hysteresis envelope is indicated by a dashed line). If cooling is initiated before decomposition of δ´ occurs the cooling curve is reversible.

The point of these remarks is that the tensimetric and gravimetric observations reveal exceedingly complex behavior not yet explicable but surely associated with coherent intergrowth of neighboring phases of the homologous series resulting in hysteresis and pseudophase formation. This will be an important system to study utilizing the powerful techniques of electron microscopy and electron diffraction for structure elucidation discussed earlier by several authors. Such studies are underway. So far it is clear that one can follow the reduction of a crystal of PrO_2 in the microscope vacuum as a result of electron heating. It appears that the complex reduction path may be interpretable when more experience is gained.

[5] J. Kordis and L. Eyring, J. Phys. Chem. 72, 2044 (1968).
[6] Arthur Lowe and L. Eyring, unpublished results.
[7] L. Eyring, unpublished results.

PARTICIPANTS

Mr. Robert Adams
Brown University
Division of Engineering
Providence, Rhode Island 02912

Dr. John G. Allpress
CSIRO, Div. of Tribophysics
University of Melbourne
Parkville, Victoria, 3052, AUSTRALIA

Dr. J. S. Anderson
University of Oxford
ENGLAND

Dr. S. Andersson
Lund Inst. of Technology
Lund, SWEDEN

Dr. Ronald J. Arnott
Brown University
Providence, Rhode Island 02912

Dr. C. E. Bamberger
Oak Ridge National Lab.
Reactor Chemistry Division
P. O. Box X
Oak Ridge, Tennessee 37830

Dr. E. Banks
Polytechnic Institute of Brooklyn
Department of Chemistry
333 Jay Street
Brooklyn, New York 11201

Dr. Y. Baskin
Ferro Corp. Technical Center
7500 E. Pleasant Valley Road
Independence, Ohio 44131

Dr. Lewis J. Beaudin
Norton Research Corp.
8001 Daily Street
Niagara Falls, Ontario, CANADA

Dr. Lawrence H. Bennett
National Bureau of Standards
Institute for Materials Research
Washington, D.C. 20234

Dr. D. J. M. Bevan
Flinders Univ. of S. Australia
Bedford Park, SOUTH AUSTRALIA 5042

Dr. William Bindloss
DuPont Central Research Department
DuPont Experimental Station
Wilmington, Delaware 19898

Dr. Tom A. Bither
E. I. duPont de Nemours & Co.
Central Research Dept., Experimental Sta.
Wilmington, Delaware 19898

Dr. C. R. Boston
Oak Ridge National Lab.
P.O. Box X
Oak Ridge, Tennessee 37830

Dr. Robert J. Bouchard
E. I. duPont de Nemours & Co.
Central Research Dept., Experimental Sta.
Wilmington, Delaware 19898

Mr. W. S. Brower, Jr.
National Bureau of Standards
Room B214, Matls. Bldg.
Washington, D.C. 20234

Dr. Frank J. Bruni
Oak Ridge National Laboratory
P. O. Box X
Oak Ridge, Tennessee 37830

Dr. Jorulf Brynestad
Oak Ridge National Laboratory
P. O. Box X
Oak Ridge, Tennessee 37830

Dr. Ernest Buehler
Bell Telephone Laboratories, Inc.
600 Mountain Avenue
Murray Hill, New Jersey 07974

Dr. L. A. Bursill
School of Chemistry
Univ. of Western Australia
Nedlands, AUSTRALIA 6009

Mr. A. D. Butherns
Bell Telephone Labs.
Murray Hill, New Jersey 07974

Dr. H. Radford Byerly, Jr.
National Bureau of Standards
Institute for Materials Research
Washington, D.C. 20234

Dr. L. J. Cabri
Dept. Energy, Mines & Resources
555 Booth Street
Ottawa, CANADA K1A 0G1

Dr. J. J. Cacciotti
Philip Morris Inc.
Richmond, Virginia 23201

Dr. David F. Cahen
Northwestern University
Chemistry Department
Evanston, Illinois 60201

Prof. C. Calvo
McMaster University
Chemistry Department
Hamilton, Ontario, CANADA

Dr. R. J. Campbell
ITT Lamp Division
330 Lynnway
Lynn, Massachusetts 01901

Dr. George A. Candela
National Bureau of Standards
Room A259, Materials Bldg.
Washington, D.C. 20234

Dr. Paul E. Caro
Lab. Terres Rares - CNRS
1 P. A. Briand
92 Bellevue, FRANCE

Dr. Forrest Carter
Naval Research Laboratory
CMRA, Code 6062
Washington, D.C. 20390

Dr. Gesina C. Carter
National Bureau of Standards
Room B150, Materials Bldg.
Washington, D.C. 20234

Dr. William S. Castor, Jr.
American Cyanamid Company
1937 West Main Street
Stamford, Connecticut 06904

Dr. E. David Cater
University of Iowa
Dept. of Chemistry
Iowa City, Iowa 52240

Dr. Bert Chamberland
University of Connecticut
Department of Chemistry
Storrs, Connecticut 06268

Dr. Horng-yih Chen
Iowa State University
Ames, Iowa 50010

Dr. T. Chen
Xerox Palo Alto Research Center
3180 Porter Drive
Palo Alto, California 94304

Dr. P. Cichy
The Carborundum Company
P. O. Box 423
Niagara Falls, New York 14302

Dr. LeRoy R. Clavenna
Esso Research & Engineering Co.
P. O. Box 45
Linden, New Jersey 07036

Dr. Lawrence E. Conroy
University of Minnesota
Department of Chemistry
Minneapolis, Minnesota 55455

Dr. William R. Cook, Jr.
Gould, Inc.
540 E. 105th Street
Cleveland, Ohio 44108

Dr. Jean-Pierre Coutures
Laboratoire des Ultra Refractaires, CNRS
B.P. N°5, 66 - Odelio, FRANCE

Dr. B. Cox
Atomic Energy of Canada, Ltd.
Chalk River Nuclear Labs.
Chalk River, Ontario, CANADA

Dr. Thomas D. Coyle
National Bureau of Standards
Room A329, Materials Bldg.
Washington, D.C. 20234

Dr. William J. Croft
Materials Sciences Division
Army Matls. and Mech. Res. Center
Arsenal Street
Watertown, Massachusetts 02172

Dr. Lynton W. R. Dicks
Shell Development Company
P. O. Box 24225
Oakland, California 94623

Prof. R. J. Diefendorf
Rensselaer Polytechnic Institute
Materials Division
Troy, New York 12181

Dr. Louis P. Domingues
Trans-Tech. Inc.
P. O. Box 457
Gaithersburg, Maryland 20760

Dr. P. C. Donohue
E. I. duPont de Nemours & Co.
Central Research Dept.
Wilmington, Delaware 19898

Dr. Sunil K. Dutta
Army Matls. and Mech. Res. Cen.
Watertown, Massachusetts 01901

Dr. A. E. Dwight
Northern Illinois University
DeKalb, Illinois 60115

Dr. Howard T. Evans, Jr.
U. S. Geological Survey
Washington, D.C. 20242

Dr. LeRoy Eyring
Arizona State University
Department of Chemistry
Tempe, Arizona 85281

Dr. Winston Farrar
National Bureau of Standards
Institute for Materials Research
Washington, D. C. 20234

Dr. Homer Fay
Union Carbide Research Institute
Tarrytown Technical Center
Tarrytown, New York 10591

Dr. Douglas R. Fitchmen
Ford Motor Company
20,000 Rotunda Drive
Dearborn, Michigan 48121

Prof. J. Flahaut
Universite de Paris
Faculte de Pharmacie
4, Ave. de l'Observatoire
Paris, FRANCE (VI^{e})

Dr. A. D. Franklin
National Bureau of Standards
Room A355, Materials Bldg.
Washington, D.C. 20234

Dr. Hugo F. Franzen
Iowa State University
Chemistry Department
Ames, Iowa 50010

Dr. H. P. R. Frederikse
National Bureau of Standards
Room A259, Materials Bldg.
Washington, D.C. 20234

Dr. Lois J. Frolen
National Bureau of Standards
Institute for Materials Research
Washington, D.C. 20234

Dr. Shun Chong Fung
Esso Research & Engineering Co.
P. O. Box 45
Linden, New Jersey 07036

Dr. G. Gafner
South African CSIR
NPRL Box 395
Pretoria, SOUTH AFRICA

Dr. J. Galy
Centre National de la
Recherche Scientifique
Bordeaux, FRANCE

Dr. Richard A. Gardner
IBM Corporation
East Fishkill Facility
Hopewell Junction, New York 12533

Dr. Bryan M. Gatehouse
Monash University
Chemistry Department
Wellington Road
Clayton, Victoria, AUSTRALIA

Mr. James O. Gibson
McDonnell Douglas Astronautics Co.
2955 George Washington Way
Richland, Washington 99352

Prof. Paul W. Gilles
Department of Chemistry
University of Kansas
Lawrence, Kansas 66044

Dr. F. P. Glasser
University of Aberdeen
Chemistry Department
Old Aberdeen AB9 ZVE
SCOTLAND

Dr. Denis R. Gonseth
Wolfram & Molybdene S.A.
CH-1260 Nyon
SWITZERLAND 022/61.31.01

Dr. John B. Goodenough
M.I.T., Lincoln Laboratory
P. O. Box 73
Lexington, Massachusetts 02173

Dr. Dane C. Grenoble
Esso Research & Engineering Co.
P. O. Box 45
Linden, New Jersey 07036

Dr. Reginald Gruehn
University of Giessen
Institute of Inorganic Chemistry
63 Giessen, WEST GERMANY

Dr. E. Gugel
Forschunginstitut der Cremer-Gruppe
D-8633
Rodental, GERMANY

Dr. G. Haacke
American Cyanamid Company
1937 W. Main Street
Stamford, Connecticut 06904

Dr. P. Hagenmuller
Univ. of Bordeaux
351 Cours de la Liberation
33 Talence, FRANCE

Dr. Sydney R. Hall
E.M.R., Mineral Science Division
555 Booth Street
Ottawa, Ontario, CANADA

Mr. C. A. Harding
National Bureau of Standards
Room B214, Materials Bldg.
Washington, D.C. 20234

Dr. Richard W. Hess
DuPont Company
Pigments Department
Wilmington, Delaware 19898

Dr. David G. Hilson, II
Sel-Rex Corporation
Electronic Materials Division
1302 E. St. Gertrude Place
Santa Ana, California 92705

Dr. Karl E. Hoekstra
Corning Glass Works
Corning, New York 14830

Dr. John D. Hoffman
National Bureau of Standards
Institute for Materials Research
Washington, D.C. 20234

Dr. F. Holtzberg
I.B.M. Corporation
Thomas J. Watson Research Center
Yorktown Heights, New York 10598

Dr. J. M. Honig
Purdue University
Department of Chemistry
West Lafayette, Indiana 47907

Dr. Emery J. Hornyak
Owens-Illinois, Inc.
P. O. Box 1035
Toledo, Ohio 43651

Dr. Emanuel Horowitz
National Bureau of Standards
Institute for Materials Research
Washington, D.C. 20234

Dr. William S. Horton
Inorganic Materials Division
National Bureau of Standards
Washington, D.C. 20234

Dr. William R. Hosler
National Bureau of Standards
Room A259, Materials Bldg.
Washington, D.C. 20234

Dr. Earl Hoyt
Stanford Linear Accelerator Center
Box 4349
Stanford, California 94305

Dr. R. A. Huggins
Center for Materials Research
Stanford University
Stanford, California 94305

Dr. R. E. Hughes
Cornell University
627 Clark Hall
Ithaca, New York 14850

Dr. James J. Hurst
Brookhaven National Laboratory
Upton, New York 11973

Dr. B. G. Hyde
Univ. of Western Australia
School of Chemistry
Nedlands, WESTERN AUSTRALIA 6009

Dr. Donald L. Janes
3-M Center, Building 201-2E
St. Paul, Minnesota 55101

Dr. W. Jeitschko
E. I. duPont de Nemours & Co.
Central Research Laboratory
Wilmington, Delaware 19898

Dr. F. Jellinek
University of Groningen
Laboratory of Inorganic Chemistry
Bloemsingel 10
Groningen, NETHERLANDS

Mr. Garrett K. Johnson
Union Carbide Research Inst.
P. O. Box 278
Tarrytown, New York 10591

Mr. Ronald B. Johnson
National Bureau of Standards
Institute for Materials Research
Washington, D.C. 20234

Dr. V. Johnson
E. I. duPont de Nemours & Co.
Central Research Department
Wilmington, Delaware 19898

Capt. Thomas E. Joyce
Air Force Materials Laboratory
AFML/LPT
Wright Patterson AFB, Ohio 45433

Mr. Z. T. Jugovic
Universal Atlas Cement Division
U. S. Steel Corporation
Buffington Station
Gary, Indiana 46401

Dr. J. A. Kafalas
M.I.T., Lincoln Laboratory
P. O. Box 73
Lexington, Massachusetts 02173

Dr. A. H. Kahn
National Bureau of Standards
Room A259, Materials Bldg.
Washington, D.C. 20234

Dr. Roy I. Kaplan
Goodyear Atomic Corp.
P. O. Box 628
Piketon, Ohio 45661

Dr. Ronald Karam
Xerox Corporation
Xerox Square (W-103)
Rochester, New York 14644

Dr. H. M. Kasper
Bell Telephone Lab., Inc.
Murray Hill, New Jersey 07974

Dr. Paul P. Keat
Norton Company
New Bond Street
Worcester, Massachusetts 01606

Dr. Richard Keezer
Xerox Corporation
800 Phillips Road
Webster, New York

Dr. Y. S. Kim
Bell Telephone Lab., Inc.
555 Union Blvd.
Allentown, Pennsylvania 18103

Dr. Robert S. Kirk
Allied Chemical Corporation
P. O. Box 1021R
Morristown, New Jersey 07960

Dr. O. J. Kleppa
James Franck Institute
University of Chicago
5640 South Ellis Avenue
Chicago, Illinois 60637

Prof. E. Kostiner
Cornell University
Baker Laboratory of Chemistry
Ithaca, New York 14850

Mr. John Krc, Jr.
Parke, Davis & Company
Joseph Campau at the River
Detroit, Michigan 48232

Dipl.Phys. W. H. Kuhlmann-Schaefer
Preussag AG, Erdol und Erdgas
3 Hannover, Postfach 4829
WEST GERMANY 3000

Dr. Richard G. LaBar
The Carborundum Company
Box 367
Niagara Falls, New York

Dr. Irwin M. Lachman
Corning Glass Works
Corning, New York 14830

Dr. D. Laguitton
Universite Laval
Departement de Mines et Metallurgie
Quebec, CANADA

Dr. A. Lamprecht
Institute of Petrologie
Frankfurt/Senckenberganl. 28
Frankfurt, GERMANY

Dr. Sam LaPlaca
Brookhaven National Lab.
Department of Chemistry
Upton, Long Island, New York 11973

Dr. John J. Larkin
AFCRL (LQP)
L. G. Hanscom Field
Bedford, Massachusetts 01730

Dr. John I. Lauritzen, Jr.
National Bureau of Standards
Institute for Materials Research
Washington, D.C. 20234

Mr. E. M. Levin
National Bureau of Standards
Room B214, Materials Bldg.
Washington, D.C. 20234

Dr. George G. Libowitz
Ledgemont Laboratory
Kennecott Copper Corp.
128 Spring Street
Lexington, Massachusetts 02173

Dr. Jacob W. Lin
Honeywell Corporation
500 Washington Avenue, South
Hopkins, Minnesota 55343

Dr. D. J. Lloyd
Service de Chimie Minerale
Universite de Bordeaux
33-Talence, FRANCE

Dr. John M. Longo
Esso Research & Engineering Co.
P. O. Box 45
Linden, New Jersey 07036

Prof. J. Lucas
Universite de Rennes
Lab. de Chimie Minerale D
Avenue du General Leclerc
35 Rennes, FRANCE

Dr. Robert G. Lye
R.I.A.S.
1450 South Rolling Road
Baltimore, Maryland 21227

Prof. G. J. McCarthy
Pennsylvania State University
Materials Research Lab.
University Park, Pennsylvania 16802

Dr. James W. McCauley
Ceramics Division
Army Materials & Mechanics Res. Cen.
Watertown, Massachusetts 02172

Mr. C. L. McDaniel
National Bureau of Standards
Room B214, Materials Bldg.
Washington, D.C. 20234

Dr. William J. McDonough
U. S. Naval Research Lab.
Code 6136
Washington, D.C. 20390

Dr. Thomas D. McGee
Iowa State University
Ceramic Engineering Dept.
Ames, Iowa 50010

Dr. Howard L. McKinzie
Brown University
Division of Engineering
Providence, Rhode Island 02912

Dr. James R. McNesby
National Bureau of Standards
Institute for Materials Research
Washington, D.C. 20234

Dr. D. B. McWhan
Bell Telephone Labs., Inc.
600 Mountain Avenue
Murray Hill, New Jersey 07974

Dr. J. B. MacChesney
Bell Telephone Labs.
Murray Hill, New Jersey 07974

Dr. George D. MacKenzie
TRW Philadelphia Laboratories
401 North Broad Street
Philadelphia, Pennsylvania 19108

Dr. Arnulf J. Maeland
W.P.I.
Worcester, Massachusetts 01609

Dr. Massimo Marezio
Bell Telephone Labs., Inc.
600 Mountain Avenue
Murray Hill, New Jersey 07974

Dr. William J. Marshall
E. I. duPont de Nemours & Co.
Newport, Delaware 19804

Mr. Robert F. Martin
National Bureau of Standards
Institute for Materials Research
Washington, D.C. 20234

Dr. Richard W. Meyer
Owens-Illinois, Inc.
1700 N. Westwood
Toledo, Ohio 43607

Dr. Ralph O. Moyer, Jr.
Trinity College
Clement Chemistry Lab.
Hartford, Connecticut 06106

Dr. G. M. Muchow
Owens-Illinois, Inc.
P. O. Box 1035
Toledo, Ohio 43601

Dr. Ronald A. Munson
U. S. Bureau of Mines
College Park, Maryland 20740

Dr. M. K. Murthy
Ontario Research Foundation
Sheridan Park
Ontario, CANADA

Dr. Clifford E. Myers
State Univ. of New York at Binghamton
Vestal Parkway East
Binghamton, New York 13901

Dr. Kurt Nassau
Bell Laboratories
600 Mountain Avenue
Murray Hill, New Jersey 07974

Dr. T. Negas
National Bureau of Standards
Room B214, Materials Bldg.
Washington, D.C. 20234

Dr. Gordon L. Nichols
Keystone Carbon Co.
State Street
St. Marys, Pennsylvania 15857

Dr. Arthur S. Nowick
Columbia University
School of Mines
New York, New York 10027

Dr. H. Nowotny
University of Vienna
Vienna, AUSTRIA

Dr. John J. O'Connor
AFCRL (LQP)
L. G. Hanscom Field
Bedford, Massachusetts 07130

Dr. Roger W. Ohnsorg
The Carborundum Company
P. O. Box 367
Niagara Falls, New York 14302

Dr. M. O'Keeffe
Arizona State University
Chemistry Department
Tempe, Arizona 85281

Dr. Jean Pannetier
Universite de Rennes
Lab. de Chimie Minerale D
35-Rennes, FRANCE

Dr. C. Paparoditis
Laboratoire de Physique des Solides
CNRS
92-Bellevue, FRANCE

Mr. H. S. Parker
National Bureau of Standards
Room B214, Materials Bldg.
Washington, D.C. 20234

Dr. Jerome H. Perlstein
Johns Hopkins University
Department of Chemistry
Baltimore, Maryland 21218

Dr. Daniel R. Petrak
Air Force Materials Laboratory
AFMS/LLM
Wright Patterson AFB, Ohio 45433

Dr. James W. Pierce
M.I.T., Lincoln Laboratories
244 Wood Street
Lexington, Massachusetts 02173

Dr. Roos H. Plovnick
Cornell University
Materials Science Center
Ithaca, New York 14850

Dr. Ralph H. Plumlee
Sandia Laboratories
Box 5800
Albuquerque, New Mexico 87115

Dr. Ben Post
Polytechnic Inst. of Brooklyn
Department of Physics
Brooklyn, New York 11201

Dr. Stephen F. Prest
Quebec Iron and Titanium Corp.
P. O. Box 40
Sorel, Quebec, CANADA

Mr. Abbaraju Raju
Zenith Radio Corp.
1851 Arthur Avenue
Elk Grove Village, Illinois 60007

Dr. J. P. Remeika
Bell Telephone Laboratories
600 Mountain Avenue
Murray Hill, New Jersey 07974

Dr. R. R. Rettew
W. R. Grace & Co.
Washington Research Center
Clarksville, Maryland 21029

Dr. Morton Robinson
Hughes Research Laboratories
3011 Malibu Canyon Road
Malibu, California 90265

Dr. Donald B. Rogers
E. I. duPont de Nemours & Co.
Central Research Department
Wilmington, Delaware 19898

Dr. R. D. Rosenstein
Crystallography Department
University of Pittsburgh
Pittsburgh, Pennsylvania 15213

Mr. Gaylon S. Ross
National Bureau of Standards
Institute for Materials Research
Washington, D.C. 20234

Dr. R. S. Roth
National Bureau of Standards
Room B214, Materials Bldg.
Washington, D.C. 20234

Dr. W. L. Roth
General Electric Company
Corporate Research & Development
Schenectady, New York 12301

Dr. Robert J. Rubin
National Bureau of Standards
Washington, D.C. 20234

Dr. P. H. Schmidt
Bell Telephone Laboratories
600 Mountain Avenue
Murray Hill, New Jersey 0797

Mr. S. J. Schneider
National Bureau of Standards
Room B214, Materials Bldg.
Washington, D.C. 20234

Dr. S. Scholes
James A. Jobling & Co., Ltd.
Advance Res. & Technology Unit
Brancepeth Castle, Durham, ENGLAND

Dr. H. Schäfer
University of Munster
Munster, GERMANY

Dr. Jacob Shamir
Dept. of Inorganic and Analytical Chemistry
Hebrew University
Jeursalem, Israel

Dr. Joseph R. Shannon
E. I. duPont de Nemours & Co.
335 Experimental Station
Wilmington, Delaware 19898

Dr. M. J. Sienko
Cornell University
Baker Laboratory
Ithaca, New York 14850

Dr. Arthur W. Sleight
E. I. duPont de Nemours & Co.
Central Research Department
Wilmington, Delaware 19898

Dr. John Smeggil
G. E. Research & Development Center
P. O. Box 8
Schenectady, New York 12301

Dr. Doug Smith
Owens-Illinois, Inc.
1700 N. Westwood
Toledo, Ohio 43606

Dr. Charles A. Sorrell
Dept. of Ceramic Engineering
University of Missouri
Rolla, Missouri 65401

Dr. K. E. Spear
Pennsylvania State University
Materials Research Lab.
University Park, Pennsylvania 16802

Dr. B. F. Spielvogel
Army Research Office-Durham
Box CM, Duke Station
Durham, North Carolina 27706

Dr. Donald A. Stanley
Department of Interior
Bureau of Mines
P. O. Box L
University, Alabama 35486

Dr. B. C. H. Steele
Metallurgy Department
Imperial College
London SW7, ENGLAND

Dr. Hugo Steinfink
Chemical Engineering Department
University of Texas
Austin, Texas 78712

Dr. N. C. Stephenson
University of New South Wales
AUSTRALIA

Dr. Kurt H. Stern
Naval Research Lab.
Washington, D.C. 20390

Dr. G. Bryan Street
IBM Research Laboratory
Bldg. 028, Monterey Road
San Jose, California 95114

Dr. V. S. Stubican
Dept. of Matls. Science
Pennsylvania State Univ.
University Park, Pennsylvania 16802

Dr. George D. Sturgeon
University of Nebraska
Department of Chemistry
Lincoln, Nebraska 68508

Mr. Robert M. Sullivan
Hercules Inc., Drakenfeld Colors
P. O. Box 519
Washington, Pennsylvania 15301

Dr. Lydon J. Swartzendruber
National Bureau of Standards
Room B150, Materials Bldg.
Washington, D.C. 20234

Dr. Gunter Teufer
E. I. duPont de Nemours & Co.
Pigments Department
Wilmington, Delaware 19898

Dr. Robb Thomson
National Bureau of Standards
Washington, D.C. 20234

Dr. Richard E. Tischer
Corning Glass Works
Sullivan Park
Corning, New York 14830

Dr. John L. Torgesen
National Bureau of Standards
Institute for Materials Research
Washington, D.C. 20234

Dr. Louis Toth
Chemical Engineering & Materials Science
University of Minnesota
Minneapolis, Minnesota 55455

Dr. R. P. Turcotte
Battelle Memorial Institute
Pacific Northwest Laboratories
P. O. Box 999 (308 Trailer)
Richland, Washington 99352

Mr. George A. Uriano
National Bureau of Standards
Institute for Materials Research
Washington, D.C. 20234

Dr. W. Van Gool
State Univ. of Utrecht
A.C.L., Croesestraat 77A
Utrecht, NETHERLANDS

Dr. John Venables
R.I.A.S.
1450 South Rolling Road
Baltimore, Maryland 21227

Dr. Robert B. Von Dreele
Arizona State University
Department of Chemistry
Tempe, Arizona 85281

Dr. John B. Wachtman, Jr.
Inorganic Materials Division
National Bureau of Standards
Washington, D.C. 20234

Mr. Fritz Wald
Tyco Laboratories, Inc.
16 Hickory Drive
Waltham, Massachusetts 02154

Dr. Roland Ward
University of Connecticut
Storrs, Connecticut

Mr. J. L. Waring
National Bureau of Standards
Room B214, Materials Bldg.
Washington, D.C. 20234

Dr. D. Watanabe
Tohoku University
JAPAN

Dr. Edward A. Weaver
Owens-Illinois, Inc.
1700 N. Westwood Avenue
Toledo, Ohio 43607

Dr. Cletus Welch
PPG Industries, Inc.
P. O. Box 31
Barberton, Ohio 44203

Dr. Paul F. Weller
SUNY College at Fredonia
Department of Chemistry
Fredonia, New York 14063

Dr. William B. White
Pennsylvania State University
Materials Research Laboratory
University Park, Pennsylvania 16802

Dr. M. Stanley Whittingham
Center for Materials Research
Stanford University
Stanford, California 94305

Dr. J. P. Williams
Corning Glass Works
Research & Development
Corning, New York 14830

Dr. Morgan L. Williams
National Bureau of Standards
Room B150, Materials Bldg.
Washington, D.C. 20234

Dr. Wendell S. Williams
University of Illinois
Dept. of Ceramic Engineering
Urbana, Illinois 61801

Dr. David E. Witter
Crystal Product Dept.
Union Carbide Corp.
8888 Balboa Avenue
San Diego, California 92123

Dr. E. Woermann
Institute fur Kristallographie
RWTH Aachen
D-51, Templergraben 55
Aachen, GERMANY

Dr. Aaron Wold
Brown University
Division of Engineering
Providence, Rhode Island 02912

Dr. Takashi Yamaguchi
Pennsylvania State University
313 Mineral Industries Bldg.
University Park, Pennsylvania 16802

Dr. Daniel F. W. Ydo
University of Leyden
Gorleans Laboratory
Leiden, NETHERLANDS

Dr. H. Thomas Yolken
National Bureau of Standards
Institute for Materials Research
Washington, D.C. 20234

Dr. Howard Young
Department of Geological and
Geophysical Sciences
Princeton University
Princeton, New Jersey 08540

Dr. John E. Young, Jr.
Gulf Research and Development
P. O. Drawer 2038
Pittsburgh, Pennsylvania 15230

Dr. Susan Zador
Department of Metallurgy
University of Toronto
Toronto 5, Ontario, CANADA

Dr. Saul Zolotov
Chemistry Department
Baker Laboratory
Cornell University
Ithaca, New York 14850

FORM NBS-114A (1-71)

U.S. DEPT. OF COMM. BIBLIOGRAPHIC DATA SHEET	1. PUBLICATION OR REPORT NO. NBS-SP-364	2. Gov't Accession No.	3. Recipient's Accession No.

4. TITLE AND SUBTITLE
SOLID STATE CHEMISTRY

5. Publication Date
July 1972

6. Performing Organization Code

7. AUTHOR(S)
R. S. Roth and S. J. Schneider, Co-editors

8. Performing Organization

9. PERFORMING ORGANIZATION NAME AND ADDRESS

NATIONAL BUREAU OF STANDARDS
DEPARTMENT OF COMMERCE
WASHINGTON, D.C. 20234

10. Project/Task/Work Unit No.

11. Contract/Grant No.

12. Sponsoring Organization Name and Address

Same as No. 9.

13. Type of Report & Period Covered
Final

14. Sponsoring Agency Code

15. SUPPLEMENTARY NOTES

16. ABSTRACT (A 200-word or less factual summary of most significant information. If document includes a significant bibliography or literature survey, mention it here.)

This book presents the Proceedings of the 5th Materials Research Symposium on "Solid State Chemistry" held at the National Bureau of Standards, Gaithersburg, Maryland on October 18-21, 1971. The symposium was sponsored by the Institute for Materials Research, NBS. The purpose of the conference was to explore the realm of new inorganic crystalline materials emphasizing crystal chemical and structural aspects, providing a forum for discussion of new research problems and techniques. A total of 56 invited and contributed papers were presented. In addition, the symposium included three unscheduled talks and an open discussion period consisting of four impromptu lectures on very current subjects dealing with nonstoichiometry. The Proceedings are divided into four main groupings, I Oxides, II Borides, Carbides, Silicides, and Related Materials, III Chalcogenides, and IV Open Discussion on Nonstoichiometry. An edited version is given of the floor discussion following each paper.

17. KEY WORDS (Alphabetical order, separated by semicolons) Chalcogenides; crystallographic shear; electron optical lattice images; lone pair geometry; nonstoichiometry; oxides; refractory hard metals; Solid State Chemistry

18. AVAILABILITY STATEMENT

[X] UNLIMITED.

[ ] FOR OFFICIAL DISTRIBUTION. DO NOT RELEASE TO NTIS.

19. SECURITY CLASS (THIS REPORT)
UNCLASSIFIED

21. NO. OF PAGES
799

20. SECURITY CLASS (THIS PAGE)
UNCLASSIFIED

22. Price
$7.50

USCOMM-DC 66244-P71

U. S. GOVERNMENT PRINTING OFFICE : 1972 O - 465-504